

L · U · N · A · R

s o u r c e b o o k

a user's guide to the moon



*edited by Grant H. Heiken, David T. Vaniman,
and Bevan M. French*

foreword by Harrison H. Schmitt

The *Lunar Sourcebook*, a concisely presented collection of data gathered during the American and Soviet missions, is an accessible and complete one-volume reference encyclopedia of current scientific and technical information about the Moon. This book provides a thorough introduction to lunar studies and a summary of current information about the nature of the lunar environment. It explores the formation and evolution of the Moon's surface, the chemical and mineralogical nature of lunar rocks and soils, and the current state of scientific knowledge about the nature, origin, and history of the Moon.

The book is written and edited by scientists active in every field of lunar research, all of whom are veterans of the Apollo program. The contributors are from universities, national laboratories, industry, and NASA.

Lunar Sourcebook

LUNAR SOURCEBOOK

A User's Guide to the Moon

GRANT H. HEIKEN

Los Alamos National Laboratory

DAVID T. VANIMAN

Los Alamos National Laboratory

BEVAN M. FRENCH

National Aeronautics and Space Administration



CAMBRIDGE
UNIVERSITY PRESS



LUNAR AND PLANETARY INSTITUTE

Houston, Texas

*Published by the Press Syndicate of the University of
Cambridge The Pitt Building, Trumpington Street, Cambridge,
CB2 1 RP 40 West 20th Street, New York, NY 10011, USA
10 Stamford Road, Oakleigh, Melbourne 3166, Australia*

© Cambridge University Press 1991

First published 1991

Printed in the United States of America

Library of Congress Cataloging-in-Publication Data applied for.

ISBN 0-521-33444-6 Hardcover

*To those who have been there —
And to those who will return.*

CONTENTS

Contributors	xi
Foreword	xiii
Editor's Preface and Acknowledgments	xv
Units and Abbreviations	xvii
Lunar Databases and Archives	xix
Chapter 1: INTRODUCTION	1
1.1. USING THE MOON: AVAILABLE DATA	1
1.2. THE CONTENTS OF THIS BOOK	2
Chapter 2: EXPLORATION, SAMPLES, AND RECENT CONCEPTS OF THE MOON	5
2.1. LUNAR EXPLORATION	5
2.2. LUNAR SAMPLES	6
2.2.1. The Apollo Collection	6
2.2.2. Lunar Sample Identification	8
2.3. NEW VIEWS OF THE MOON FROM EXPLORATION	10
2.4. NEW CONCEPTS OF THE MOON FOLLOWING EXPLORATION	13
2.4.1. Origin of the Moon	13
2.4.2. Diversity of Lunar Rock Types	13
2.4.3. Differentiation of the Moon and Origin of the Lunar Crust	15
2.4.4. The Present View of Lunar Magmatic Evolution	19
APPENDIX: APOLLO SAMPLE TYPES AND LUNAR SAMPLE CURATION	21
A2.1. Apollo Sample Types	21
A2.2. Lunar Sample Curation	23
A2.3. Curation History	25
Chapter 3: THE LUNAR ENVIRONMENT	27
3.1. EARTH AND MOON COMPARED	27
3.2. THE ASTRONAUT EXPERIENCE	27
3.3. TERRAIN	30
3.3.1. Mare Surfaces	31
3.3.2. Large-scale Ejecta Ridges	31
3.3.3. Lunar Highlands	32
3.3.4. Highlands-Mare Boundaries (Basin Margins)	32
3.3.5. Other Parts of the Moon	34
3.4. DUST	34
3.5. TEMPERATURES ON THE LUNAR SURFACE	34
3.6. LUNAR HEAT FLOW	36
3.6.1. Heat Flow at the Apollo 15 Landing Site	37
3.6.2. Heat Flow at the Apollo 17 Landing Site	37
3.6.3. Conclusions	38
3.7. SEISMIC ACTIVITY	38
3.8. POLAR ENVIRONMENT	39
3.9. ATMOSPHERE	40
3.9.1. Contamination	41
3.9.2. The Real Lunar Atmosphere	42
3.9.3. The Past and Future of the Lunar Atmosphere	43

3.10. METEOROID BOMBARDMENT	45
3.10.1. Meteoroid Velocities and Impact Rates	46
3.10.2. Meteoroid Distributions in Lunar Orbit and on the Lunar Surface	46
3.10.3. Meteoroid Hazards	46
3.11. IONIZING RADIATION	47
3.11.1. Solar Wind	48
3.11.2. Solar-Flare-Associated Particles	49
3.11.3. Galactic Cosmic Rays	52
3.11.4. Modes of Interactions with the Moon	53
3.11.5. Implications of the Lunar Radiation Environment	55
APPENDIX	57
A3.1. Motion of the Earth-Moon System	57
A3.2. Brightness of the Lunar Surface	59
A3.3. Locating Points on the Moon	60
Chapter 4: LUNAR SURFACE PROCESSES	61
4.1. IMPACT PROCESSES	62
4.1.1. The Morphology of Impact Structures	62
4.1.2. The Cratering Process	65
4.1.3. Crater Frequency and Bombardment History	79
4.1.4. Geological Processes	85
4.2. BASALTIC VOLCANISM	94
4.2.1. Volcanic Landforms	95
4.2.2. Filling of the Maria	102
4.2.3. Volume Estimates of Basaltic Mare Fill	105
4.3. TECTONIC ACTIVITY	107
4.3.1. External Forces	108
4.3.2. Internal Forces	111
4.4. LUNAR STRATIGRAPHY	111
Chapter 5: LUNAR MINERALS	121
5.1. SILICATE MINERALS	123
5.1.1. Pyroxene	123
5.1.2. Plagioclase Feldspar	126
5.1.3. Olivine	130
5.1.4. Silica Minerals: Quartz, Cristobalite, and Tridymite	132
5.1.5. Other Silicate Minerals	133
5.1.6. Comparative Silicate Mineralogy: Earth-Moon	135
5.2. OXIDE MINERALS	137
5.2.1. Ilmenite	140
5.2.2. Spinels	143
5.2.3. Armalcolite	147
5.2.4. Other Oxides	149
5.3. SULFIDE MINERALS	150
5.3.1. Troilite	150
5.3.2. Other Sulfides	151
5.4. NATIVE FE	151
5.4.1. Meteoritic Contamination	151
5.4.2. Native Fe in Lunar Rocks	152
5.4.3. Native Fe in Lunar Soil	154
5.5. PHOSPHATE MINERALS	154
APPENDIX: COMPOSITIONS OF LUNAR MINERALS	155

Chapter 6: LUNAR ROCKS	183
6.1. MARE BASALTIC LAVAS AND VOLCANIC GLASSES	186
6.1.1. Chemical Composition, Classification, and Properties of Mare Basalts	186
6.1.2. Mineralogy of Mare Basalts	193
6.1.3. Textures of Mare Basalts	195
6.1.4. Crystallization Experiments on Mare Basalts	198
6.1.5. Cooling Rates of Mare Basalts	201
6.1.6. Vesicles and Nature of the Gas Phase	201
6.1.7. Lunar Pyroclastic Deposits	202
6.1.8. Experimental Petrology and Phase Relations	205
6.1.9. Ages of Mare Basalts	208
6.2. EXTENDED MAPPING OF MARE LAVAS AND PYROCLASTIC DEPOSITS BY REMOTE SPECTRAL OBSERVATIONS	209
6.2.1. Techniques	209
6.2.2. Regional Distribution of Mare Basalts and Pyroclastic Glasses	210
6.3. HIGHLAND PRISTINE ROCKS: IGNEOUS ROCKS AND MONOMICT BRECCIAS	212
6.3.1. Classification of Pristine Igneous Highland Rocks	214
6.3.2. KREEP Rocks	216
6.3.3. Ferroan Anorthosites	220
6.3.4. Mg-rich Rocks	225
6.3.5. Other Pristine Highland Rock Types	228
6.4. HIGHLAND POLYMICHT BRECCIAS	232
6.4.1. Nomenclature and Classification	233
6.4.2. Fragmental Breccias	235
6.4.3. Glassy Melt Breccias and Impact Glasses	246
6.4.4. Crystalline Melt Breccias or Impact-Melt Breccias	249
6.4.5. Clast-poor Impact Melts	252
6.4.6. Granulitic Breccias and Granulites	254
6.4.7. Dimict Breccias	256
6.4.8. Regolith Breccias	257
6.5. SPECTRAL PROPERTIES OF HIGHLAND ROCKS	257
APPENDIX: CHEMICAL DATA FOR LUNAR ROCKS	261
Chapter 7: THE LUNAR REGOLITH	285
7.1. LUNAR SOIL	287
7.1.1. General Description	287
7.1.2. Petrography	288
7.1.3. Agglutinates	296
7.1.4. Other Unusual Soil Components	302
7.1.5. Grain Shapes and Surfaces	304
7.1.6. Grain-size Characteristics	304
7.1.7. Chemical Composition of Lunar Soils	306
7.2. SPECTRAL PROPERTIES OF THE LUNAR REGOLITH	307
7.3. REGOLITH EVOLUTION AND MATURITY	307
7.3.1. Maturation by Meteoroid Bombardment	310
7.3.2. Maturation by Ionizing Radiation	315
7.3.3. Maturity Indices and Their Use	317
7.3.4. Regolith Processes and Maturity	321
7.4. VARIATION OF SOILS WITH DEPTH: THE LUNAR CORE SAMPLES	321
7.4.1. General Characteristics of Lunar Regolith Core Samples	321
7.4.2. Variations with Depth in Regolith Core Samples	325
7.4.3. Regolith Stratigraphy	337

7.5. MODELS FOR REGOLITH FORMATION	342
7.5.1. Regolith Dynamics	342
7.5.2. Grain-size Distributions	343
7.5.3. Differential Comminution	344
7.5.4. Comparison of Soil Chemistry with Bedrock Chemistry	345
7.5.5. Variation of Soil Chemistry Within Sites	345
7.5.6. Variation of Soil Chemistry Between Sites	351
7.6. REGOLITH BRECCIAS	352
7.7. THE RECORD OF SOLAR HISTORY PRESERVED IN THE LUNAR REGOLITH	354
7.7.1. A Summary of Historical Results	354
7.7.2. Solar-Wind History	355
7.7.3. Solar-Flare History	356
7.7.4. Galactic-Cosmic-Ray History	356
Chapter 8: CHEMISTRY	357
8.1. WHERE TO FIND A PARTICULAR ELEMENT DISCUSSED	359
8.1.1. Organization of the Data	359
8.1.2. Types of Lunar Materials Considered	359
8.1.3. Cautions on Data Use	361
8.2. OVERVIEW OF PLANETARY SEPARATION PROCESSES	361
8.3. MAJOR ELEMENTS	363
8.3.1. Concentrations of Major Elements in the Moon	363
8.3.2. Minerals and Rocks Formed by Major Elements	363
8.3.3. Abundances and Correlations Among Major Elements	366
8.3.4. Ores of Major Elements	371
8.4. INCOMPATIBLE TRACE ELEMENTS	372
8.4.1. Abundances of Incompatible Trace Elements in Lunar Crustal Materials	372
8.4.2. Incompatible Trace Elements in Lunar Highland Materials: KREEP	380
8.4.3. Incompatible Trace Elements in the Lunar Maria	386
8.5. MISCELLANEOUS MINOR ELEMENTS	390
8.5.1. Data Sources	390
8.5.2. Phosphorus, Potassium, and Barium	390
8.5.3. Scandium, Vanadium, Chromium, and Manganese	391
8.5.4. Sulfur, Cobalt, and Nickel	398
8.5.5. Gallium and Strontium	398
8.5.6. Possible Lunar Ores of the Miscellaneous Minor Elements	398
8.6. SIDEROPHILE ELEMENTS	399
8.6.1. Analytical Difficulties	400
8.6.2. Iridium: The "Type" Siderophile Element	404
8.6.3. Other Siderophile Elements	405
8.6.4. Siderophile-Element Fractionations Related to Grain Size in Lunar Soils	413
8.6.5. Possible Lunar Ores of Siderophile Elements	414
8.7. VAPOR-MOBILIZED ELEMENTS	414
8.7.1. Concentration Levels	414
8.7.2. Meteoroid Additions to the Regolith	419
8.7.3. Vapor-Mobilized Elements as Incompatible Trace Elements: Indigenous Concentrations in Lunar Materials	422
8.7.4. Vapor-Phase Transport of Vapor-Mobilized Elements	424
8.7.5. Pyroclastic Volcanic Emissions as an Indigenous Source of Vapor-Mobilized Elements	427
8.7.6. Surface Mobility of Vapor-Mobilized Elements	430
8.7.7. Sulfur	432

8.7.8. Halogens	434
8.7.9. Possible Lunar Ores of Vapor-Mobilized Elements	435
8.8. SOLAR-WIND-IMPLANTED ELEMENTS	436
8.8.1. The Solar Wind	436
8.8.2. Noble Gases (He, Ne, Ar, Kr, and Xe)	437
8.8.3. Biogenic Elements (H, C, and N)	443
8.8.4. Solar-Wind-Implanted Elements as Lunar Resources	448
APPENDIX: STATISTICAL SUMMARIES OF LUNAR CHEMISTRY	449

Chapter 9: PHYSICAL PROPERTIES OF THE LUNAR SURFACE **475**

9.1. GEOTECHNICAL PROPERTIES	475
9.1.1. Particle Size Distribution	477
9.1.2. Particle Shapes	478
9.1.3. Specific Gravity	481
9.1.4. Bulk Density and Porosity	483
9.1.5. Relative Density	494
9.1.6. Compressibility	500
9.1.7. Shear Strength	506
9.1.8. Permeability and Diffusivity	517
9.1.9. Bearing Capacity	517
9.1.10. Slope Stability	521
9.1.11. Trafficability	522
9.2. ELECTRICAL AND ELECTROMAGNETIC PROPERTIES	530
9.2.1. Electrical Conductivity	531
9.2.2. Photoconductivity	532
9.2.3. Electrostatic Charging and Dust Migration	532
9.2.4. Dielectric Permittivity	536
9.2.5. Electromagnetic Sounding	552
9.3. REFLECTION AND EMISSION OF RADIATION FROM THE MOON	558
9.3.1. Optical Astronomy	558
9.3.2. Radar Astronomy	562
9.3.3. Thermal Infrared Astronomy	566
APPENDIX: SUPPLEMENTARY DATA ON LUNAR PHYSICAL PROPERTIES	567

Chapter 10: GLOBAL AND REGIONAL DATA ABOUT THE MOON **595**

10.1. GLOBAL AND REGIONAL IMAGERY AND DATA SOURCES	595
10.1.1. Earth-based Telescopic Data	596
10.1.2. Lunar Orbiter Photographic Images	597
10.1.3. Apollo Orbital Photography	597
10.1.4. Coverage and Resolution of Lunar Photography	599
10.2. SURFACE MINERALOGIC AND GEOCHEMICAL DATA	599
10.2.1. Spectral Reflectance Measurements and Multispectral Imagery (Earth-based)	599
10.2.2. Apollo Gamma-ray Spectrometer	602
10.2.3. Apollo X-ray Fluorescence Spectrometer	603
10.3. GEOPHYSICAL DATA	603
10.3.1. Lunar Gravity Field	603
10.3.2. Lunar Surface Magnetic Field	605
10.3.3. Radar Data for the Lunar Nearside	605
10.4. REGIONAL DISTRIBUTION OF LUNAR ROCK TYPES	607
10.4.1. Mare Basalt Lavas	607
10.4.2. Petrologic Map of the Moon from Apollo Gamma-ray Data	608

10.4.3. Mineralogy of Highland Rock Types Inferred from Near-Infrared Reflectance Spectra	608
10.5. STRATIGRAPHY AND RELATIVE AGES	609
10.6. GEOLOGY OF THE APOLLO AND LUNA LANDING SITES	609
10.6.1. Apollo 11	609
10.6.2. Apollo 12	610
10.6.3. Apollo 14	610
10.6.4. Apollo 15	610
10.6.5. Apollo 16	631
10.6.6. Apollo 17	631
10.6.7. The Luna Landing Sites	631
Chapter 11: AFTERWORD	633
11.1. RETURN TO THE MOON	633
11.2. CURRENT UNDERSTANDING OF THE MOON: A BASE FOR PLANNING	633
11.2.1. The Post-Apollo Moon	633
11.2.2. Environmental Impacts	635
11.3. GOALS FOR FUTURE LUNAR EXPLORATION	636
11.3.1. Science	636
11.3.2. Transportation	636
11.3.3. Resources	636
11.3.4. Benefits to Future Astronauts: <i>Terra Firma Nova</i>	637
11.4. UNANSWERED QUESTIONS ABOUT THE MOON	637
11.4.1. The Lunar Environment	638
11.4.2. Lunar Surface Processes and Evolution	638
11.4.3. Lunar Minerals, Rocks, and Soils	638
11.4.4. Lunar Chemistry	639
11.4.5. Lunar Physical Properties	639
11.4.6. Global Lunar Data and Future Mapping	639
11.5. THE NEXT STEPS	639
11.6. A PERMANENT PRESENCE	640
APPENDIX A11.1: STUDIES IN LUNAR UTILIZATION	644
APPENDIX A11.2: LUNAR RESOURCES	647
A11.2.1. Aluminum	647
A11.2.2. Helium-3	647
A11.2.3. Hydrogen	647
A11.2.4. Iron	648
A11.2.5. Oxygen	648
A11.2.6. Regolith	649
APPENDIX A11.3: SUMMARY OF UNANSWERED QUESTIONS ABOUT THE MOON	650
References	655
Sample Index	717
Subject Index	721

CONTRIBUTORS

Editors

Grant H. Heiken, Los Alamos National Laboratory
David T. Vaniman, Los Alamos National Laboratory
Bevan M. French, National Aeronautics and Space Administration

Contributors

Abhijit Basu, Indiana University
Alan Binder, Lockheed Engineering and Science Company
George Blanford, University of Houston, Clear Lake
W. David Carrier III, Lunar Geotechnical Institute
John Delano, State University of New York, Albany
John Dietrich, NASA Johnson Space Center
Bevan M. French, National Aeronautics and Space Administration
Richard Grieve, Geological Survey of Canada
Larry Haskin, Washington University
Grant Heiken, Los Alamos National Laboratory
Gary Lofgren, NASA Johnson Space Center
Friedrich Hörz, NASA Johnson Space Center
David S. McKay, NASA Johnson Space Center
Wendell Mendell, NASA Johnson Space Center
Gary Olhoeft, U.S. Geological Survey
James J. Papike, South Dakota School of Mines and Technology and University of New Mexico
Carlé Pieters, Brown University
Robert Reedy, Los Alamos National Laboratory
Graham Ryder, Lunar and Planetary Institute
Steven Simon, University of Chicago
Paul Spudis, U.S. Geological Survey
G. Jeffrey Taylor, University of New Mexico and University of Hawaii
Lawrence A. Taylor, University of Tennessee
David Vaniman, Los Alamos National Laboratory
Paul Warren, University of California, Los Angeles

Lunar and Planetary Institute Publications Services Staff

Editorial:

Renee Dotson
Stephanie Tindell
Sarah Enticknap
Joan Shack
Karen Hrametz

Lunar and Planetary Institute Publications Services Staff *(continued)*

Graphic Design:

Stephen L Hokanson
Donna Jalufka
Pam Thompson
Shirley Brune
Ronna Hurd
Christy Owens

Typesetting

Linda Tanner
Deborah Barron
Shantha Elluru
Pam Thompson
Carl Grossman
Cindy Schwartz
Janet Martin

Lunar and Planetary Institute Computer Services

Kin Leung
Jackie Lyon

Lunar and Planetary Institute Center for Information and Research Services

Cathy Fischer
Mary Ann Hager
Debra Rueb
Stephen Tellier
Fran Waranius

Other Editing Assistance

Mary-Hill French

Chapter Reviewers

Mark Cintala, NASA Johnson Space Center; Mike Gibson, CarboteK; Stephen Haggerty, University of Massachusetts; Steve Howe, Los Alamos National Laboratory; John Kerridge, University of California, Los Angeles; Randy Korotev, Washington University; James K. Mitchell, University of California, Berkeley; William Phinney, NASA Johnson Space Center; Ron Scott, California Institute of Technology; John Shervais, University of South Carolina; Jeffrey L Warner, Chevron Oil Field Research Company; Herb Zook, NASA Johnson Space Center; and contributors who reviewed chapters other than their own.

FOREWORD

Humankind sought and attained greatness with the first field explorations of the Moon between 1966 and 1976. Apollo spacecraft and the various automated probes launched by the U.S. and the U.S.S.R., which successfully collected samples and information from the Moon during this period, pushed the species along its first clear steps of evolution into the solar system and eventually into the galaxy. A sense of reality began to surround a lesson taught to the Pueblo Indians by their ancestors: “We walk on the Earth, but we live in the sky.”

Early explorers of the sky took their eyes and minds into space and became the eyes and minds of billions of other explorers on the starship Earth. They also began the long process of transplanting civilization into space. This fundamental change in the course of history has occurred as humans have also gained new insight into themselves and their first planetary home. With the conclusion of the Apollo 17 mission and the Apollo program in December 1972, humankind had reached the “end of the beginning” of its movement into the universe.

Human evolution into the universe began with the 1968 Christmas Eve mission of Apollo 8. The presence of Frank Borman, Jim Lovell, and Bill Anders in orbit around the Moon, and the words and pictures they shared with us, gave human beings a new awareness not only of the Moon but of the Earth’s own place as a lonesome, lovely, and potentially fragile life-bearing planet in the black void of space. Hundreds of millions of human beings throughout the world simultaneously thought new thoughts about a familiar object in the night sky—the Moon. The men of Apollo 8 were there, and the Moon would never be the same for anyone.

Now we should realize that the Earth will also never be the same. Through new communication, information, and space technologies, solutions can be found to the age-old problems of the human condition on Earth—ignorance, poverty, hunger, and disease. Opportunities have been created to realize the more modem dream of living permanently in space. Such solutions and opportunities exist, however, only *if* we are wise enough to reach out and grasp them.

President George Bush’s statement on the occasion of the 20th anniversary of Apollo 11’s landing on the Moon provides a vision of human beings as a perpetual spacefaring species. The President’s words implied a commitment to protect the Earth, settle the solar system, and move toward the stars.

The Moon’s proximity to the Earth, lack of atmosphere, gravity (only one-sixth that of the Earth), planetary position as the smallest of the terrestrial planets, and potential resources almost certainly assure a role for lunar activities in support of human exploration and utilization of space.

Proximity, one-sixth gravity, and potential resources essential to sustaining human life require that the Moon be considered as both a stepping stone toward Mars and the outer planets and a low-cost supply depot for exploration and settlement. Its planetary characteristics and lack of atmosphere justify the continued use of the Moon as a natural laboratory for comparative planetology and for solar and stellar astronomy.

In the context of these possibilities, as well as in even more general terms, *Lunar Sourcebook* provides an extremely important and heretofore unavailable first reference for those who may consider a return to the Moon for whatever purpose. The information compiled within and the guide to other data provided distills and, in one sense, immortalizes the dedication, imagination, and extraordinary hard work of hundreds of managers, scientists, engineers, and their supporters. Now others can begin to move forward to plan, in President Bush’s words, a “. . . return to the Moon, this time to stay . . .”

One can only vaguely imagine the ultimate legacy of the data from Apollo, the automated probes, and Earth-based observation through which *Lunar Sourcebook* guides its reader. The more easily conceived possibilities include permanent and self-sustaining settlements on the Moon,

serving solar and stellar observatories and far-ranging lunar surface expeditions; lunar engineering and training sites supporting the development of Mars exploration and settlement; huge solar collector arrays on the Moon producing the energy needed to support lunar activities as well as for potential export to Earth and to stations in space; underground mines in stratified mineral deposits within the mare that provide raw materials to space equipment manufacturing facilities on the Moon or in lunar orbit; and great farms that produce the food required by increasing numbers of men and women living in space, on the Moon, and on Mars.

Perhaps most critically, one can imagine large mobile processing plants, periodically stepping their way across the lunar maria, mining, extracting, and processing solar-wind gases from the regolith, to provide the life-sustaining consumables (H_2 , O_2 , H_2O , CO_2 , NO_x , and 4He) required by a spacefaring species. From solar-wind materials implanted in the lunar regolith, we may also extract the environmentally benign fusion fuel 3He , which can be used on Earth to sustain civilization as well as protect the biosphere.

On behalf of those privileged few who helped gather the samples, collect field information, and deploy the experiments that provided the data upon which much of this book draws, I wish to thank the editors and their contributor team for stepping once more into the breach. They have added great new value to the lunar exploration community's efforts. Unless what has been learned as a consequence of our activities becomes accessible, we, like the tree falling in the forest, have made no sound for those not present to hear. *Lunar Sourcebook* not only brings many individual sounds together into the beginnings of a symphony, but it serves waiting and appreciative new generations of composers and audiences.

*Harrison H. Schmitt, Apollo 17 astronaut
Albuquerque, New Mexico
September 20, 1990*

EDITORS' PREFACE AND ACKNOWLEDGMENTS

Lunar Sourcebook is intended for the post-Apollo generation of scientists, engineers, teachers, and students. It has two purposes. First, it summarizes what we know about the Moon as a result of U.S. and U.S.S.R. lunar missions and the continuing analysis of lunar samples and data here on Earth. Second, it provides a convenient, accessible sourcebook for planning the future study of the Moon and the eventual use of the Moon by spacefaring humans.

This book began in 1984, and we were at the active manuscript-editing stage on July 20, 1989, when President George Bush marked the 20th anniversary of the Apollo 11 landing by initiating what is now called the Space Exploration Initiative (or sometimes the Moon-Mars initiative), a program for the return of humans to the Moon, followed by human exploration of the planet Mars. We hope that *Lunar Sourcebook* will be a timely response to the renewed scientific and exploration interest in our nearest planetary neighbor, the only other world so far explored in person by human beings. We also hope that the book will help in our return to the Moon, and in the intelligent use of the Moon when we establish a permanent presence there.

The task of putting everything we know about the whole Moon into a single book is far more difficult now than it was before the Apollo program. Before Apollo, only a few people were needed to summarize the available information about the Moon, and they could (and did) produce books from their own knowledge. The Apollo and Luna programs, with their intensive close-up studies and the return of samples to Earth, have produced an explosion in lunar knowledge. The available scientific information about the Moon is now scattered throughout many books and thousands of articles in journals from a wide range of scientific disciplines: astronomy, geosciences, nuclear chemistry, space physics, materials science, life sciences, and engineering, to name just a few.

In this post-Apollo age, assembling *Lunar Sourcebook* would have been impossible without help from many different people. We owe the most to our scientist-authors for sifting the immense amount of knowledge in each field, organizing it, and then patiently enduring multiple syntheses, continuing editorial changes, extensive rewriting, and doubts that their work would ever see daylight on a printed page.

The editorial and production staff at the Lunar and Planetary Institute (LPI) in Houston, Texas, worked hard and patiently—literally for years—to turn an overwhelming amount of manuscript pages and disorganized art work into an attractive and readable text. Renee Dotson, as technical editor at the LPI, suffered (with remarkable equanimity) through enough versions of this book to fill her bookshelves. The excellent illustration work by Donna Jalufka, Pam Thompson, Shirley Brune, and others at the LPI, with special notice of the herculean effort and dedication of Steve Hokanson, resulted in a set of polished figures that were often compiled from crude sketches and all too often forced through time-consuming revisions. We also thank our editors at Cambridge University Press in New York, Peter-John Leone and Nancy Seltzer, for their faith in the whole project and their patience with an unexpectedly long process.

The support of NASA, through contract NASW-4066 to the Lunar and Planetary Institute, was critical to this work, and we are particularly grateful for the patience and steady encouragement of Dr. William L. Quaide, Chief Scientist for the Solar System Exploration Division.

At Los Alamos, the continued moral support by Wayne Morris, Wes Myers, and P. W. Keaton made it possible for us to carry through the editing process over many years; Marcia Jones and Barbara Hahn contributed to the word processing when we could not keep up. We also owe a great deal to our families, who gave up countless weekends and evenings for the book. Finally, we especially thank Mary-Hill French for intense and meticulous proofreading, with an uncanny knack for finding errors that had eluded us.

Grant H. Heiken and David T. Vaniman
Earth and
Environmental Sciences Division Los Alamos
National Laboratory
Los Alamos, New Mexico 87545

Bevan M. French
Solar System Exploration Division
National Aeronautics and Space Administration Headquarters
Washington, DC 20546

UNITS AND ABBREVIATIONS*

Unit	Abbreviation	Unit	Abbreviation
absolute permeability	K	Kelvin	K
activation energy	E	kilobar	kbar
angstrom	Å	kilocalorie	kcal
antenna gain	G	kiloelectron volt	keV
ampere	A	kilogram	kg
astronomical unit (1.496×10^8 km)	A.U.	kilohertz	kHz
atomic mass unit	amu	kilometer	km
billion years	b.y.	kilopascal	kPa
bulk density	ρ	kilowatts electric	kWe
centimeter	cm	kurtosis (statistical)	K_G
coefficient of lateral stress	K_o	loss tangent	$\tan \delta$
cohesion	c	magnetic field strength	A/m, γ
Cole-Cole frequency distribution		mean (statistical)	\bar{x} , Mz
parameter	α	median (statistical)	Md
compression index	C_c	megaelectron volt	MeV
conductance (1/ohm)	mho	meter	m
conductivity	σ	metric ton (tonne)	t
cone penetration resistance	q	microgram	μ g
degree Celsius	$^{\circ}$ C	micrometer	μ m
degree of polarization	P	milligal	mgal
density of water	ρ_w	milligram	mg
depth into regolith (cm)	z	millimeter	mm
equivalent surface area ratio	ESAR	million years	m.y.
electron volt	eV	millisecond	msec
factor of safety	F.S.	milliwatt	mW
ferromagnetic resonance intensity	Is	minutes	min
flow rate	Q	mole	mol
Fresnel reflection coefficient	ρ	mole percent	mol.%
friction angle	ϕ (degrees)	nanogram	ng
galactic cosmic ray	GCR	nanometer	nm
gamma (10^{-5} oersted)	γ	normal stress	σ
geometrical albedo	p	newton	N
gigaelectron volt	GeV	nucleon	u
gram	g	parts per billion by weight	ng/g
gross pull per wheel (N)	H	parts per million by weight	μ g/g
Hertz	Hz	parts per thousand	‰
horizontal stress	σ_h	Pascal	Pa
hour	hr	phase angle (optical)	g
initial relative density	D_{Ri}	phase integral (optical)	q
integrated mass depth	d_m	phi scale (grain size)	ϕ
joule	J	poise	p

* Note multiple uses of the symbols G, k, p, W, α , and σ . Units and abbreviations that are explicitly defined where they are used in the text are not listed here.

UNITS AND ABBREVIATIONS *(continued)*

Unit	Abbreviation	Unit	Abbreviation
porosity (in situ)	n	specific gravity	G
P-wave velocity	α	specific surface area	SSA
radar cross-section	σ	static allowable bearing capacity	q_{all}
received echo power (radar)	P_r	static ultimate bearing capacity	q_{ult}
recompression index	C_r	steradian	sr
relative density	D_R	subradar point	i
relative dielectric permittivity	k	torricelli	torr
seismic attenuation	Q	wavelength	γ
second	sec	wheel load (N)	W
shear strength	τ	vertical stress	σ_v
skewness (statistical)	SK, α_3	void ratio	e
soil compaction resistance per wheel (N)	R_c	volume percent	vol.%
solar cosmic ray	SCR	watt	W
sorting (statistical)	σ	weight percent	wt.%
		year	yr

LUNAR DATABASES AND ARCHIVES

Manned and unmanned missions to the Moon were responsible for an enormous volume of diverse data, ranging from measurements of the tenuous lunar magnetic field to sample analyses. Most of these data and reports are available to researchers, at the cost of transferring the information or images.

Lunar and Planetary Institute (LPI). The best place to begin your search for lunar data is the Lunar and Planetary Institute, 3303 NASA Road 1, Houston, Texas 77058-4399. The LPI was established by NASA as the Lunar Science Institute in 1969 and is managed by the Universities Space Research Association. The Center for Information and Research Services (CIRS) contains lunar and planetary photographs, maps, reports, and lunar sample information. CIRS also maintains a lunar and planetary bibliography and a literature collection to support the bibliography. The LPI Geophysical Data Facility has a selection of Moon datasets.

National Space Science Data Center (NSSDC). Documents, imagery, and geophysical data are available from the NSSDC. For U.S. investigators, the address is National Space Science Data Center, Code 601.4, NASA Goddard Space Flight Center, Greenbelt, Maryland 20771. For researchers outside of the United States, the address is World Data Center A, Rockets and Satellites, Code 601, NASA Goddard Space Flight Center, Greenbelt, Maryland 20771 USA. The database includes images, reports, and geophysical data from the Ranger, Surveyor, Lunar Orbiter,

Apollo, Luna, and Zond Programs. A comprehensive catalog was published by W. S. Cameron, E. J. Mantel, and E. R. Miller (1977) *Catalog of Lunar Mission Data*, NSSDC/WDC-A-RS Document #77-02, 204 pp.

National Technical Information Service (NTIS). For out-of-print reports, facsimile paper copies or microfiche can be ordered from NTIS, 5825 Port Royal Road, Springfield, Virginia 22152.

NASA Johnson Space Center History Office. Over 30,000 documents from the Apollo program have been saved as an archive for the purpose of historical studies by the History Office, NASA Johnson Space Center, Code BY4, 2101 NASA Road 1, Houston, Texas 77058-3696. The materials are arranged and described according to accepted archival practice and in a computer index. This office has also published excellent histories of the Apollo program [C. G. Brooks, J. Grimwood, and L. Swenson Jr. (1979) *Chariots for Apollo: A History of Manned Lunar Spacecraft* NASA SP-4205, 553 pp.; W. D. Compton (1989) *Where No Man Has Gone Before: A History of Apollo Lunar Exploration Missions*, NASA SP-4214, 415 pp.]

NASA Johnson Space Center Lunar Sample Curatorial Facility. To obtain lunar samples, a researcher must submit a request to the Lunar Sample Curator, Code SN2, NASA Johnson Space Center, Houston, Texas 77058-3696. This request will be reviewed by NASA's Lunar and Planetary Sample Team. Sample histories are also available from the Curator (see Appendix to Chapter 2).

Regional Planetary Image Facilities. The system of Regional Planetary Image Facilities (RPIF) represents a coordinated effort to provide easy access to planetary data products by scientists, students, educators, and the general public. Although each facility has different specific strengths, the close cooperation among RPIF members permits accessing materials without unnecessary trips to more distant centers. The RPIFs are not designed to provide hard-copy products for permanent retention, but are established to provide assistance in both locating the necessary data products and in accessing them through the NSSDC. RPIF facilities are located:

Arizona State University
Department of Geology
Tempe, Arizona 85287

Brown University
Box 1846
Department of Geological Sciences
Providence, Rhode Island 02912

Cornell University
Center for Radiophysics and
Space Research
Ithaca, New York 14853

Jet Propulsion Laboratory
Mail Stop 202-101
4800 Oak Grove Drive
Pasadena, California 91109

Lunar and Planetary Institute
Center for Information and
Research Services
3303 NASA Road 1
Houston, Texas 77058-4399

National Air and Space Museum
Center for Earth and Planetary
Studies
Room 3101
Washington, DC 20560

U.S. Geological Survey
Branch of Astrogeologic Studies
2255 N. Gemini Drive
Flagstaff, Arizona 86001

University of Arizona
Lunar and Planetary Laboratory
Tucson, Arizona 85721

University of Hawaii
Planetary Geosciences Division
Hawaii Institute of Geophysics
2525 Correa Road
Honolulu, Hawaii 96822

Washington University
Department of Earth and
Planetary Sciences
One Brookings Drive
St. Louis, Missouri 63130-4899

Istituto Astrofisica Spaziale
Reperto di Planetologia
Viale Dell Universita, 11
00185 Roma ITALY

University of London Observatory
33/35 Daws Lane
Observatory Annexe
London, NW7 4SD
UNITED KINGDOM

Phototheque Planetaire
Université Paris-Sud
Laboratoire de Geologie
Dynamique Interne
Orsay Cedex FRANCE

Abt. Planetare Erkundung
DLR - Institut fur Optoelektronik
8031 Oberpfaffenhofen
GERMANY

*** Note added in proof: These addresses were current at the time of publication (1991). For an updated list of RPIFs, go to <http://www.lpi.usra.edu/library/RPIF/index.shtml>.**

INTRODUCTION

1.1. USING THE MOON: AVAILABLE DATA

This book was written to provide a single, complete, and annotated description of our present knowledge of the Moon. It is intended for a wide range of readers, including scientists who are studying the Moon and trying to understand its place in the solar system, designers now planning missions to return to the Moon, and engineers and astronauts who may participate in the future exploration of the Moon. We dedicate this book to all of them, because their wide range of thoughts and activities will be essential to the intelligent future use of the Moon.

During the last 20 years, the Moon has developed a dual role in human thought. As the Apollo explorations have shown, the Moon is a scientifically important planet. It preserves a unique history of planetary formation and early development, and also serves as a probe that has recorded the space environment and cosmic radiation for billions of years. Because of its closeness to Earth, the Moon is also an obvious target for long-term human exploration beyond Earth. Knowledge of the Moon's characteristics, especially its potential usefulness and resources, has become critical for planning the human future in space.

Many conceptual designs for lunar bases have already been prepared by Americans as well as by European and Japanese engineers. The National Aeronautics and Space Administration (NASA) now receives a steady flow of requests from engineers, student groups, and others involved in such planning.

These groups want detailed information about the Moon, and their requests have not been easy to answer. Most handbooks containing data about the Moon were written in the 1960s for the Apollo missions and are therefore out of date; they are also out of print. Much of their information was intended for spacecraft design and is not useful for planning long-term surface activities or a permanent outpost on the Moon.

To address these problems, the authors of this book have attempted to combine their aggregate experience in different areas of lunar research in order to summarize, in one place, the currently available data about the Moon and its environment.

The great accumulation of post-Apollo lunar science information, although rich in details, is an inconvenient database. This information is scattered through dozens of technical journals, making the search difficult. Many data are found only in government publications, contractor reports, and abstract volumes that are now virtually unobtainable. In addition, complete information on specific matters is not easily collected. For example, a particular lunar parameter, such as soil density or radiation exposure, may have been measured by several scientific groups over several years. Published values of that parameter may be valid only for a specific set of conditions or for specific sample materials, and these limitations are not obvious in a casual literature search. The most current or best

available measurement may have been published in a journal that is not readily accessible. It is not uncommon for errors to be found years after the original data appear, but the corrections are difficult to discover, even if they were formally published.

The data are separated into individual chapters by topic, and the goal has been to make each chapter independent, so that a minimum of cross-referencing is required to extract the data. Within each chapter the data are presented in their scientific context, and the limitations are described so that the reader can make the best use of the data. Extensive references have been included for access to the original scientific and technical literature. Finally, much remains to be discovered about the Moon, and the authors have tried to identify areas where data are lacking, rather than to leave such subjects unmentioned.

1.2. THE CONTENTS OF THIS BOOK

The substantive parts of this sourcebook begin in Chapter 2 with a summary of lunar exploration, a description of the sample collections that have resulted from this exploration, and a brief summary of the new ideas on lunar origin and evolution that have resulted from exploration and sampling.

Chapter 3 focuses on the lunar environment as a set of boundary conditions for the designer. Values for physical parameters of the lunar surface are presented. The critical data on radiation and temperature are also covered. This information is adequate for planning a wide variety of surface operations.

Chapter 4 discusses the large-scale geologic processes that have shaped the surface of the Moon. Foremost are the impact craters that cover the face of the Moon. Every piece of lunar real estate has been affected by cratering, whether it is part of a crater or has been blanketed by impact ejecta. Another major mechanism of terrain formation is volcanic eruption. Lava flows tend to occur in the gigantic impact basins excavated much earlier in the history of the Moon. In many of the maria there are ridges and domes of apparent tectonic origin, formed by compressive stresses associated with cooling and settling of the vast volcanic plains.

Careful study of lunar minerals, rocks, and soils is a primary tool for deciphering the history and structure of the Moon, and Chapters 5 through 7 summarize the great body of data that has been collected on lunar materials. Lunar minerals are discussed in Chapter 5. Chapter 6 begins with the description of lunar igneous rocks that crystallized from magmas (a process also common on Earth) and then covers the many rocks created by impacts, such as impact breccias and impact melt rocks.

Sedimentary rocks and water-bearing minerals are absent on the Moon because of the total absence of water. On the other hand, the fragmentary debris (regolith) blanketing the Moon is an impact-formed "physical weathering" product unknown on the Earth, having its own set of physical and chemical properties. These are described in Chapter 7.

Chapter 8 first relates the well-studied chemistry of the Apollo samples to the important primordial processes of planetary accretion and the subsequent differentiation of the lunar crust to produce the lunar highlands. In a concise format, this chapter then illustrates where each chemical element of interest can be found on the Moon, as well as the range of its abundance. The rarity of volatile elements in lunar materials exacerbates the problem of supporting life and industry there. However, the Apollo missions sampled only a small part of the lunar surface and it is possible that isolated concentrations of volatile elements or ores do occur somewhere on the Moon. Insights gained from our partial knowledge of lunar geochemistry can direct the exploration needed to find important resources.

Although most studies of the Moon have been carried out for purely scientific objectives, ongoing lunar operations will require engineering data. Such data will be necessary for planning lunar bases. Chapter 9 reviews the physical quantities that characterize the lunar surface environment. The geotechnical information comes from the work of the few civil engineers who participated in lunar exploration. These data come both from measurements made on the lunar surface and from measurements made on returned samples. The collection of engineering measurements was overshadowed by exciting scientific discoveries, but the engineering studies now assume new importance. The thermal, optical, and electromagnetic parameters come from astronomical and remote-sensing investigations coupled with a few lunar surface experiments and many laboratory studies of returned samples. The values derived from very-large-scale remote measurements do not always agree with data taken on specific samples because the techniques differ and the lunar environment cannot be reproduced exactly in the laboratory. Therefore, the experimental conditions and constraints are described in the text to aid the reader in interpreting the data properly for any given application.

Exploration produces maps; development requires them. Chapter 10 summarizes the lunar maps derived from quantitative spectral imaging, astronomical measurements, and orbital remote sensing. Even the casual reader will note the startling lack of completeness in the information. Mars is more completely photomapped than the Moon, and the

global cartographic control for Mars is better than that for the Moon. Very important geochemical remote-sensing data are limited to narrow strips in the equatorial regions of the Moon, along the ground tracks of the brief Apollo missions. Some of the data are presented as geologic maps that interpret photographic or remotely-sensed data. While these maps are often easier for the nonspecialist to understand, they sometimes embody data interpretations that are still controversial in the scientific community. The geologic cross-sections shown in Chapter 10 are most speculative. Planners must keep an open mind and utilize this information carefully.

Chapter 11 looks to the future. Many gaps in this book's data can be filled with relatively modest unmanned spacecraft placed in lunar orbit. Plans for

such missions are discussed, and the significance of new findings is placed in the context of future manned explorations as well as advancement of our understanding of the planets, Earth included.

The authors intend this publication to be a succinct but quantitative summary of what is known about the Moon. In most chapters the quantitative aspect has been emphasized, because numerical data are needed to bridge the gap between speculation and planning. The information has been organized to be accessible and has been discussed in enough detail to make it useful even when incomplete. Inevitably, condensation of much knowledge and opinion into one volume has its price. We trust the compromises have been the right ones and that the users of the book are not frustrated by omissions.

EXPLORATION, SAMPLES, AND RECENT CONCEPTS OF THE MOON

David Vaniman, John Dietrich, G. Jeffrey Taylor, and Grant Heiken

2.1. LUNAR EXPLORATION

Beyond Earth, the Moon is the only body in space that has been systematically sampled. Meteorites have provided chance samples of solar system debris from the asteroids, and may even include fragments of Mars, but the Moon is the only other planet from which samples have been chipped, scooped, raked, spaded, and collected in cores. These samples were collected by the six U.S. Apollo and three U.S.S.R. Luna missions from known locations on the lunar surface. Analyses of rocks and soils from these sites have allowed their use as “ground-truth” points for remotely-sensed physical and geochemical maps of the Moon.

Although exploration of the Moon is incomplete, the effort expended has been extensive (Table 2.1, Fig. 2.1). The first imaging missions (Luna, Zond, and Ranger) were flown from 1959 through 1965. At the same time, systematic Earth-based mapping of the Moon by telescope began (*Kuiper*, 1960) and led to the determination of a lunar stratigraphy (*Wilhelms and McCauley*, 1971). Luna 10 provided the first orbital gamma-ray chemical data in 1966. Lunar Orbiter missions returned high-resolution images of the lunar surface in preparation for the U.S. manned missions. Unmanned soft landings and surface operations (Surveyor and Luna) continued between 1964 and 1976, with the first data on soil physics and chemistry radioed back from the lunar surface in 1966 and the first Soviet robot-collected samples returned by Luna 16 in 1970. The greatest achievements in lunar sampling were the six Apollo manned landings between 1969 and 1972.

Each Apollo landing increased in exploration complexity and returned ever greater amounts of lunar samples. The last three Apollo landings included Lunar Roving Vehicles (LRVs) that expanded the sample collections across traverse distances of about 30 km. From the standpoint of sample mass returned, the 381.7 kg from six Apollo landings far outweigh the 0.3 kg returned by the three Luna robots. This comparison should not be viewed as a denigration of the Luna contribution; Luna 16, 20, and 24 provided important new sample types from areas on the lunar surface that were not visited by Apollo. The number and diversity of the Apollo samples is particularly valuable, however, when consideration is given to the careful human observations that went into their selection and to the extensive range of analyses and measurements possible with larger samples. At our present stage of technological development, robots are still second-rate geologists.

Current interpretations of the global distribution of lunar rock types (Chapter 10) use the gamma-ray and X-ray fluorescence data collected by the orbiting Apollo command modules and spectral data obtained from telescopes on Earth, but the deciphering of these data depends on the “ground truth” now offered by the large suite of samples collected by Apollo astronauts (Chapters 5 through 7). The Apollo astronauts also deployed surface experiments and made personal observations that provided most of the environmental and physical data we now have for the Moon (Chapters 3 and 9).

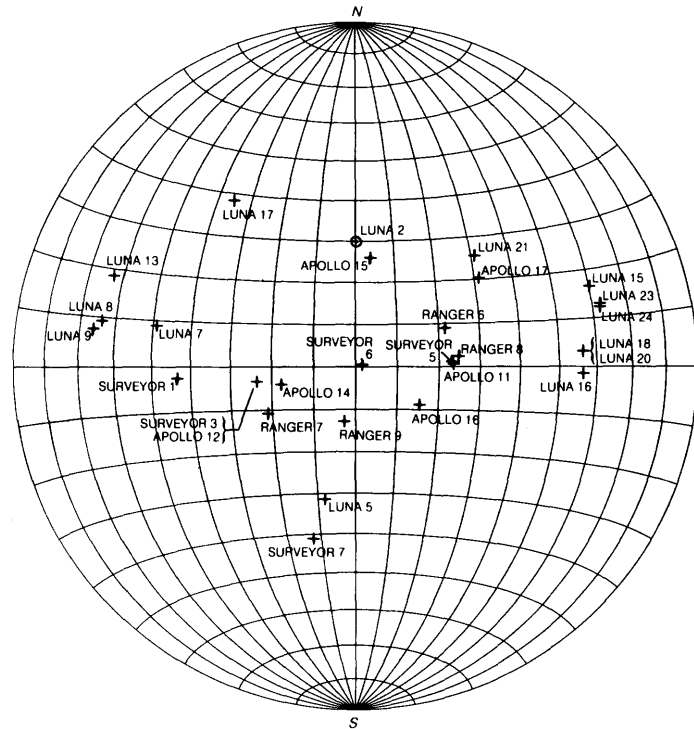


Fig. 2.1. Landing spots of lunar exploration missions, including the impact spots of crashed missions (see Table 2.1). The impact spot of Ranger 4, the only craft to have landed on the farside of the Moon, is shown in Fig. 2.3b. This figure is an equal-area projection drawn to the same scale as the global lunar figures in Chapter 10; it can be copied as a transparency on most copying machines and used as an overlay for the color plates in Chapter 10.

As a direct result of sample studies, we now know that the Moon is not a primitive body that has remained unchanged since the origin of the solar system. We know instead that the Moon had a violent early half-billion years of impact and melting, followed by at least a billion years of volcanic activity. Our knowledge is not comprehensive; the lunar samples are too few and represent only a tiny fraction of the lunar surface. Nevertheless, the study of lunar samples has led to sound hypotheses that address many age-old questions about the Moon. This study goes on still, for the lunar samples continue to reward closer inspection and newer analytical approaches with fresh insight.

2.2. LUNAR SAMPLES

There are three sources of lunar samples for study on Earth. First and most significant are the Apollo samples, 381.7 kg of rock and soil (Table 2.2) collected at six sites from the central part of the Moon's nearside (facing the Earth). The second source is from three Luna robot landers that collected soil and small rock fragments by drilling 35, 27, and 160 cm into the surface. The Luna missions returned a total of 321 g of lunar material to the U.S.S.R. These first two sources provide samples that can be keyed to known locations on the Moon (Fig. 2.1). The third

source consists of lunar meteorites collected on the Antarctic ice cap by both U.S. and Japanese expeditions. Since the first such meteorite was collected in 1979, 10 have been recovered (see Table 2.3), and it is almost certain that more will be found in the future. Chemical studies of these meteorites have provided convincing evidence for a lunar origin; slight differences suggest that they come from other locations than the nine sites sampled by the Apollo and Luna missions. It is thought that the meteorites were blasted off the Moon and sent to Earth by large crater-forming impacts that took place thousands or possibly millions of years ago. Landing on the icecap, the meteorites were preserved to the present.

Data from all three sources are used in this book, but the bulk and complexity of the Apollo sample source requires a more detailed description. A discussion of the Apollo sample types, a description of lunar sample curation, and the history of curation can be found in the Appendix to this chapter. Aspects of the Apollo sample collection and sample identification that are most important for effective use of this book are described below.

2.2.1. The Apollo Collection

Each of the six successful Apollo landings returned a larger number of samples and a greater mass of lunar materials than the previous mission. Table 2.2

TABLE 2.1. History of lunar exploration.

Mission	Launch Date	Accomplishment	Data*
Luna 1	01/02/59	first lunar flyby	
Luna 2	09/12/59	first lunar impact	
Luna 3	10/04/59	first photos of lunar farside	P
Ranger 3	01/26/62	missed the Moon by 36,793 km	
Luna 4	04/02/63	missed the Moon by 8,500 km	
Ranger 4	04/23/62	crashed on the lunar farside	
Ranger 5	10/18/62	missed the Moon by 724 km	
Ranger 6	01/30/64	impact lander; television failed	
Ranger 7	07/28/64	impact lander	P
Ranger 8	02/17/65	impact lander	P
Ranger 9	03/21/65	impact lander	P
Luna 5	05/09/65	crashed on the Moon	
Luna 6	06/08/65	missed the Moon by 161,000 km	
Zond 3	07/18/65	photographed lunar farside	P
Luna 7	10/04/65	crashed on the Moon	
Luna 8	12/03/65	crashed on the Moon	
Luna 9	01/31/66	first lunar soft landing	P
Luna 10	03/31/66	first lunar satellite	SE,CO
Surveyor 1	05/30/66	first soft-landed robot laboratory	P,SM
Lunar Orbiter 1	08/10/66	lunar satellite	P,R,SE,M
Luna 11	08/24/66	lunar satellite	P
Luna 12	10/22/66	lunar satellite	P,M,SE
Lunar Orbiter 2	11/06/66	lunar satellite	P,R,SE,M
Luna 13	12/21/66	soft landing on the Moon	P,C
Lunar Orbiter 3	02/05/67	lunar satellite	P,R,SE,M
Surveyor 3	04/17/67	soft-landed robot laboratory	P,SM
Lunar Orbiter 4	05/04/67	lunar satellite	P,R,SE,M
Explorer 35	07/19/67	lunar satellite	
Lunar Orbiter 5	08/01/67	lunar satellite	P,R,SE,M
Surveyor 5	09/08/67	soft-landed robot laboratory	P,SM,C
Surveyor 6	11/07/67	soft-landed robot laboratory	P,SM,C
Surveyor 7	01/07/68	soft-landed robot laboratory	P,SM,C
Luna 14	04/07/68	lunar satellite	
Zond 5	09/14/68	first lunar flyby and Earth return	
Zond 6	11/10/68	lunar flyby and Earth return	P
Apollo 8 (G) [†]	12/21/68	first humans to orbit the Moon	P
Apollo 10 (G) [†]	05/18/69	first docking maneuvers in lunar orbit	P
Luna 15	07/13/69	crashed on the Moon	
Apollo 11 (H) [†]	07/16/69	first humans on the Moon (07/20/69)	P,S,SM,G, M,SW,D
Zond 7	08/08/69	lunar flyby and Earth return	P
Luna 16	09/12/70	first robot sample return (100 g)	S
Luna 17	11/10/70	first robot rover (322 days, 10.5 km)	P,C,SM,R
Apollo 12 (H) [†]	11/14/69	second human landing on the Moon	P,S,SM,G,M,SW,D,A
Apollo 13 (H) [†]	04/11/70	aborted human landing	P
Zond 8	10/20/70	lunar flyby and Earth return	P
Apollo 14 (H) [†]	01/31/71	third human landing on the Moon	P,S,SM,G,SW,D,A
Apollo 15 (J) [†]	07/26/71	fourth human landing on the Moon	P,S,C,SM, R,G,CO,SE,SW,D,A
Luna 18	09/02/71	crashed on the Moon	
Luna 19	09/28/71	lunar satellite	P,SE
Luna 20	02/14/72	second robot sample return (30 g)	P,S
Apollo 16 (J) [†]	04/16/72	fifth human landing on the Moon	P,S,C,SM, R,G,CO,SE,A
Apollo 17 (J) [†]	12/07/72	sixth human landing on the Moon	P,S,SM,R, G,SE,M
Luna 21	01/08/73	robot lunar rover (139 days, 37 km)	P,C,SM,R
Luna 22	05/29/74	lunar satellite	P
Luna 23	10/28/74	failed robot sampler	
Luna 24	08/09/76	third robot sample return (170 g)	S

TABLE 2.1. (continued).

Apollo Lunar Missions	Crew
8	F. Borman, J. Lovell Jr., W. Anders
10	T. Stafford, J. Young, E. Cernan
11	N. Armstrong, E. Aldrin Jr., M. Collins
12	C. Conrad Jr., R Gordon Jr., A. Bean
13	J. Lovell Jr., J. Swigert Jr., F. Haise
14	A. Shepard Jr., S. Roosa, E. Mitchell
15	D. Scott, J. Irwin, A. Worden
16	J. Young, T. Mattingly II, C. Duke Jr.
17	E. Cernan, R. Evans, H. Schmitt

* Data types are abbreviated as follows: A = atmosphere and ion studies; C = surface chemistry; CO = chemical mapping from orbit; D = dust analysis; G = surface-based geophysics; M = meteoroid studies; P = photography; R = radiation environment studies; S = samples returned to Earth; SE = selenodesy measurements; SM = soil mechanics studies; SW = solar wind studies. More detailed descriptions of individual experiments are given in Chapters 3, 9, and 10.

†The Apollo manned missions fall into three major categories with the following letter designations: G (lunar orbit without lunar landing); H (lunar landing with limited mobility); and J (lunar landing with Lunar Roving Vehicle). The H missions (30 metric tons) were three times as heavy as the Apollo 8 and Apollo 10 G missions (10 metric tons); the J missions (50-60 metric tons) were twice as heavy as the H missions.

Detailed information on U.S. missions can be found in *Mantell and Miller (1977)*; comparable information on U.S.S.R. missions is in *Johnson (1979)*.

summarizes sample data for each Apollo mission and for the total program. The number of samples and total weight entries at the top of each column document the total size of the collection.

The status of the Apollo samples as of 1989 is reported in Table 2.2. By 1989, almost two decades after the first samples were obtained, the Apollo collection was probably the most intensively studied suite of rocks on Earth. The original 2196 samples had been split into more than 78,000 subsamples, but 87% of the sample mass remained "pristine." These samples, protected from chemical alteration inside nitrogen-filled cabinets, are available for future study. A sample is considered pristine if it has been stored continuously in dry nitrogen since its preliminary examination at the Lunar Receiving Laboratory (LRL). Many of the pristine samples have been studied and sampled extensively in the nitrogen-filled cabinets of the Lunar Sample Laboratories at NASA Johnson Space Center (JSC). The lower proportion of pristine samples (71-84%) in the collections returned by Apollo 11 through 14 is due, in part, to the quantity of samples allocated for tests related to biological quarantine early in the Apollo program.

The Apollo astronauts collected a variety of rock and fine-grained regolith samples at each site. Detailed descriptions of the various sampling techniques and resulting sample types are given in the Appendix to this chapter. Table 2.2 also summarizes the relative abundances of igneous rocks, rocks produced by impact processes, fine-grained regolith

collected from the surface, and cores at the six Apollo sites. The relative abundances of mare rocks (basalt, dolerite) are also reported.

Cores provide the only samples suitable for detailed studies of variations in regolith properties with depth. Apollo cores were collected with 31.8-to 72-cm-long drive tubes (for a detailed description of Apollo sampling tools, see *Allton, 1989*). At some locations the astronauts collected cores with a single drive tube; at other locations they sampled deeper layers by connecting two drive tubes. At Apollo sites 15 through 17 a battery-powered drill was used that could drive up to eight connected 40-cm-long core tube sections. The bottom of Table 2.2 lists the types of cores collected at each Apollo site.

2.2.2. Lunar Sample Identification

A system of sample identification had to be developed before records of samples could be maintained. The basic format of identification numbers for the Apollo samples was adopted before the first samples were returned, but refinements of the system appeared from time to time through the program.

Following each Apollo mission, the Lunar Sample Preliminary Examination Team (LSPET) assigned a unique five-digit generic sample number to each of the following types of returned samples: (1) each coherent fragment larger than 1 cm in diameter; (2) each sieved fraction of a single fine-grained soil sample; (3) each unsieved portion of a single fine-

TABLE 2.2. Apollo sample summary.

	Apollo 11	Apollo 12	Apollo 14	Apollo 15	Apollo 16	Apollo 17	Apollo Total
<i>Original Collection</i>							
Number of samples	58	69	227	370	731	741	2196
Total weight (kg)	21.6	34.3	42.3	77.3	95.7	110.5	381.7
<i>Sample Status as of 1989 (% of total weight)</i>							
<i>In Curator's Custody</i>							
Pristine samples at JSC *	63.5	70.3	65.8	69.7	78.6	75.8	72.9
Pristine samples at BAFB †	6.9	13.7	16.0	15.7	12.5	14.8	14.0
Returned samples at JSC	16.8	7.8	10.5	7.4	4.4	4.4	6.9
<i>Allocated Samples</i>							
For analysis	3.7	2.3	2.1	1.9	1.8	1.3	1.9
For educational display	1.3	2.7	3.0	4.1	1.2	2.5	2.5
Consumed	7.8	3.2	2.7	1.3	1.5	1.2	1.8
<i>Lithology (% of total weight)</i>							
Rocks (>10 mm)	44.9	80.6	67.3	74.7	72.3	65.9	69.5
Anorthosite				(0.4)	(10.5)	(0.5)	(2.8)
Basalt	(19.9)	(52.2)	(9.1)	(37.9)		(29.1)	(22.9)
Dolerite (coarse basalt)		(26.3)					(2.4)
Other igneous rocks	(2.1)	(0.2)				(4.0)	(1.3)
Breccia	(22.9)	(1.9)	(58.2)	(34.1)	(36.8)	(32.3)	(33.4)
Impact melt				(2.3)	(25.0)		(6.7)
Fines (<10 mm)	54.6	16.8	30.6	17.0	19.3	26.7	24.0
Unsieved	(54.6)	(16.8)	(0.8)	(5.1)	(8.5)	(11.3)	(11.1)
<1 mm			(27.3)	(10.7)	(9.2)	(13.9)	(11.5)
1-2 mm			(1.0)	(0.4)	(0.7)	(0.6)	(0.5)
2-4 mm			(0.8)	(0.4)	(0.5)	(0.5)	(0.4)
4-10 mm			(0.8)	(0.4)	(0.5)	(0.4)	(0.4)
Cores	0.4	1.2	0.9	6.0	7.4	6.6	5.2
Other		1.4	1.0	2.4	1.2	0.9	1.2
<i>Cores Collected</i>							
2-cm Drive Tube							
Single	2	2	2				6
Double		1	1				2
4-cm Drive Tube							
Single				1	1	2	4
Double				2	4	3	9
2-cm Drill Core							
Number				1	1	1	3
Maximum depth (cm)				237	221	292	

* JSC = Johnson Space Center, Houston, Texas.

BAFB = Brooks Air Force Base, San Antonio, Texas.

Numbers in parentheses represent subtotal percentages within a group.

TABLE 2.3. Lunar meteorites.

Discovery	Location/Number	Weight (g)
<i>Anorthositic Breccias</i>		
1982	Allan Hills 81005	31.4
1984	Yamato 791 197	52.4
1985	Yamato 82192	36.7
1986	Yamato 82193	27.0
1987	Yamato 86032	648.4
1987	Yamato 793274	8.7
1989	MacAlpine Hills 88104	61.2
1989	MacAlpine Hills 88105	662.5
<i>Basaltic Compositions</i>		
198	Elephant Moraine 87521 (breccia)	30.7
199	Asuka 31 (unbrecciated cumulate)	- 500

grained soil sample; (4) each section of a drive tube or drill stem containing a lunar soil core; (5) each special sample.

The numbering system became more organized as succeeding missions explored larger areas and returned more samples. A description of the system used for each mission may be found in the Sample Information Catalogs issued by the Lunar Sample Curator (JSC, Houston, Texas). A brief summary is given in the adjacent sidebar.

2.3. NEW VIEWS OF THE MOON FROM EXPLORATION

Until lunar samples were returned by the Apollo missions, our understanding of the Moon, especially of its composition and history, was severely limited. Since meteorites had been the only extraterrestrial materials available for laboratory analysis, there had

been speculation that the Moon might be like some meteorites: an ancient body condensed from the solar nebula (Urey, 1965, 1966) and unaffected by the terrestrial processes of segregation into crust, mantle, and core. The Apollo samples proved that the Moon was not a primitive body, unchanged since its origin. The samples provided ample evidence for over a billion years of planetary evolution, catastrophic meteorite bombardment, and intense igneous activity that have altered the Moon since its origin about 4.6 b.y. ago. The major problem in understanding the Moon's early history then became the need to see through this early history of chemical segregation, bombardment, and volcanism to the Moon's primordial origins.

The most visible evidence of lunar chemical segregation is the existence of two very different terrains on the Moon: the highlands and the maria.

LUNAR SAMPLE NUMBERING

A two-part number identifies each sample in the Apollo collection. The first part is a five-digit "generic" number; the second part is a one- to four-digit "specific" number. The specific number is placed to the right of the generic and separated from it by a comma (e.g., 15362,28).

The first one or two digits of the five-digit generic number always identify the Apollo mission, as follows:

10 — Apollo 11	14 — Apollo 14	6 — Apollo 16
12 — Apollo 12	15 — Apollo 15	7 — Apollo 17

The Luna samples have similarly been given five-digit numbers, of which the first two correspond to the mission:

16—Luna 16	20—Luna 20	24—Luna 24
------------	------------	------------

Lunar meteorite names and numbers are listed in Table 2.3.

For samples collected during Apollo missions 11 through 14, the LSPET assigned the last three digits of the generic numbers without regard to sample type or location within the landing site. For samples collected during Apollo missions 16 and 17, the second digit of the generic number generally identifies the location where the sample was collected. For samples collected during Apollo missions 15 through 17, the fifth digit of the generic number generally identifies the sample as unsieved fines, a sieved fraction of fines, or a rock as follows:

---- y0	Unsieved <10-mm fines	---- y4	4-10-mm sieved fraction
---- y1	<1-mm sieved fraction	---- y5	a >10-mm rock from the same sample bag
---- y2	1-2-mm sieved fraction	---- y6 to	---- y9 for additional rocks from the same sample bag
---- y3	2-4-mm sieved fraction		

When more than five rocks were in a bag, the LSPET assigned numbers 5 through 9 in successive decades ($y + 1$, $y + 2$, $y + 3$, etc.) until each rock received a unique generic number. Gaps are common in lists of sample numbers for these later missions because a sample bag rarely contained exactly five rocks and a sample of fines large enough to provide four sieved fractions plus an unsieved reserve.

The specific part of the sample number, located to the right of the comma, provides a unique identification for each subdivision of a sample. Usually, the LSPET assigned specific number "0" to the whole sample. Each subsample (chip, aliquant, thin section, etc.) retains the generic number of its source and receives the next higher unused specific number for that sample.

This sample numbering scheme can be confusing to those who are not involved in lunar sample studies. Lunar researchers are often guilty of reciting lunar sample numbers as if they were the names of old friends, expecting their listeners to draw a physical or chemical image of the "famous" sample mentioned. However, the Apollo sample numbering scheme also serves a very useful purpose in helping to track down data. In this book the Apollo generic sample numbers are used extensively, not to confuse but to provide easier access to more information about the sample being discussed. The indexes of this book and of many other references list generic sample numbers; a search based on generic sample number is a powerful method for obtaining a broad range of data on a particular lunar sample.

Physically, the highlands are rough and intensely cratered while the maria are relatively smooth. Although these bright (highlands) and dark (mare) areas of the Moon have been obvious since prehistoric times when they were given mythical anthropomorphic shapes, it required actual sampling of these two terrains to provide the fundamental clues about lunar origin and evolution.

From low orbit the Apollo astronauts were impressed by the sharp contrasts between juxtaposed mare and highland regions (Fig. 2.2). At an orbital altitude of only 60 km, the passage over highland mountain ranges rising abruptly 3 km above the flat maria was spectacular.

Studies of the Apollo and Luna samples have provided direct evidence of the major differences between these terrains. Chemically, the lunar highlands are enriched in Ca and Al while the maria are richer in Fe and Ti. In rock type, the highlands consist mostly of old impact-shocked plutonic (deep-seated) rocks while the maria consist of basaltic lavas. Mineralogically, the highlands are dominantly feldspar while the maria have more abundant pyroxene.

The first probe to orbit behind the Moon, Luna 3, showed a surprising absence of mare terrain on the lunar farside. Although mare basalts cover about 16% of the lunar nearside, less than 1% of the farside



Fig. 2.2. A view from orbit of the sharp terrain differences between mare and highland regions on the Moon. This is an oblique view of the rim of Mare Crisium. Mount Fuji, 3776 m high, has been drawn in for scale.

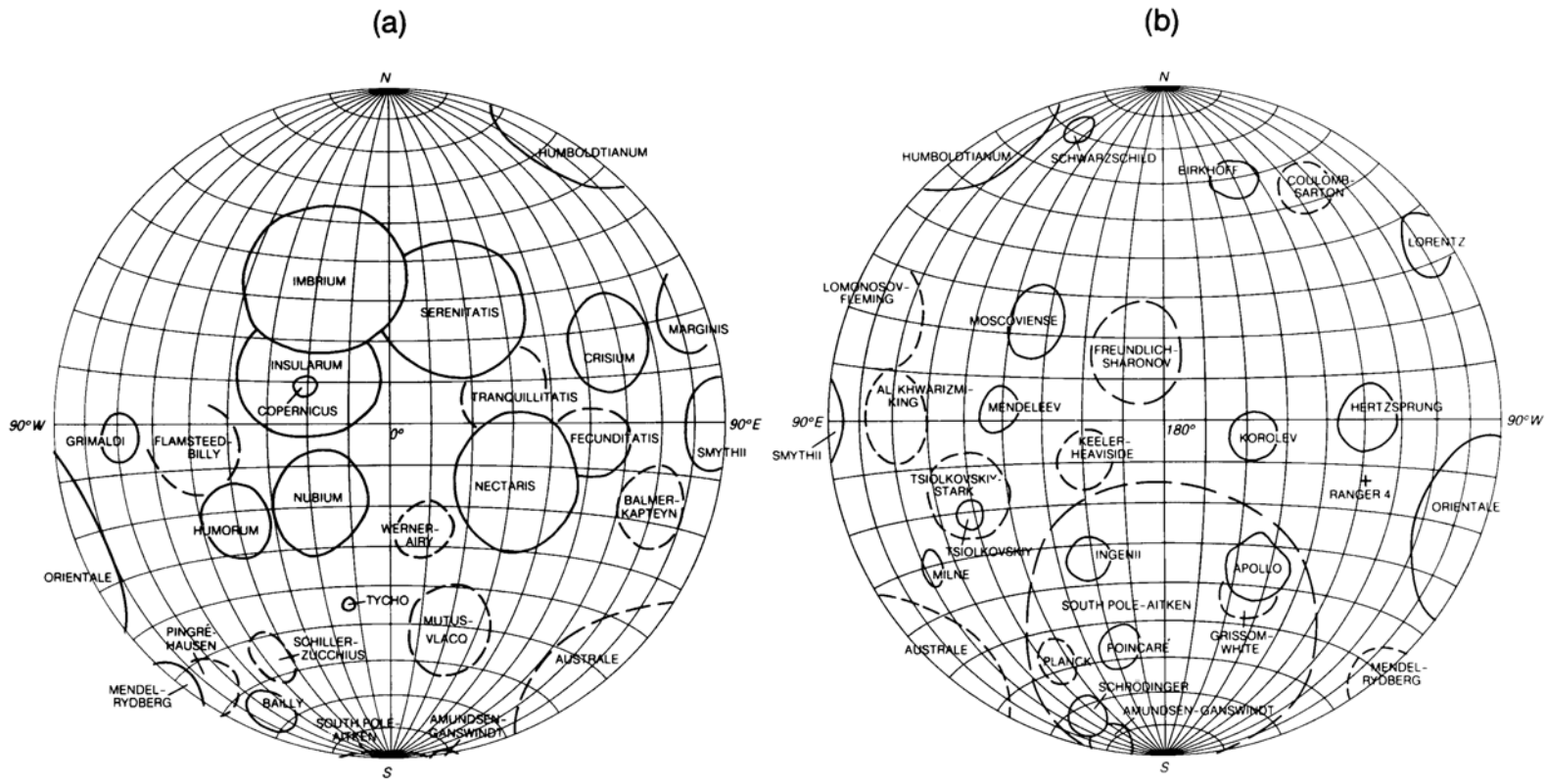


Fig. 2.3. Major impact basins on the (a) nearside and (b) farside of the Moon. These are equal-area projections drawn to the same scale as the global lunar figures in Chapter 10; they can be reproduced as transparencies on most copying machines and used as overlays for the color plates in Chapter 10.

has mare basalt cover. The cause of this imbalance in the distribution of lunar maria is still unknown; suggestions range from a thickened farside crust, through which basalt could not rise, to the absence of deep mantle melting beneath the farside. A gap in our lunar sample collection is the absence of any samples—mare or highland—obviously from the lunar farside. (Some lunar meteorites may be from the farside.)

The deposits from mare basalt eruptions have done much to soften some of the relief on the nearside of the Moon. However, the topography of all parts of the Moon remains dominated by major impact basins. Figure 2.3 shows the sizes, locations, and names of many of the most prominent lunar impact basins. These basins are useful geographic reference features for discussing locations on the Moon, and the names listed in Fig. 2.3 are used throughout this book (see Chapter 4 for detailed discussion of basin-forming impacts).

2.4. NEW CONCEPTS OF THE MOON FOLLOWING EXPLORATION

Although this book is focused on the data from the Moon instead of interpretations, it would be incomplete without a discussion of recent models of lunar origin and evolution based on these data.

2.4.1. Origin of the Moon

The origin of the Moon, like the origin of the Earth, has been cause for speculation since prehistoric times. Modern speculation began when George Darwin (1879) hypothesized that the Moon formed from the Earth by fission of a single larger body. Two other modern hypotheses that are considered “classical” are formation along with the Earth as a sister planet (*Schmidt*, 1959) and gravitational capture of a body formed elsewhere in the solar system (*Gerstenkorn*, 1955).

Many people anticipated that the Apollo program would be more than sufficient to provide the final answer on the origin of the Moon. This probably would have been the case if the Moon were a primitive undifferentiated, homogeneous body (*Urey*, 1966). The differentiation of the Moon into concentric zones of differing chemical composition and its active geologic past, however, have obscured its origins. We have sufficient data on celestial mechanics (gravitational effects) to know that the dynamical constraints (shape, gravity, moment of inertia) alone are not sufficient to pin down the Moon’s origin; the data available for lunar geophysical analyses and particularly for lunar geochemistry are too few to be conclusive. However, as often happens in science, the post-Apollo work, especially on lunar samples, has

combined the earlier, simpler hypotheses and added a new twist. It has been proposed (*Hartmann and Davis*, 1975; *Cameron and Ward*, 1976) that a large object, possibly Mars-size, impacted Earth to expel large amounts of material (fission hypothesis), condense much of that vaporized material in orbit (sister planet hypothesis), and incorporate much of the exotic collider (capture hypothesis). This new combined hypothesis goes a long way toward reconciling the strong points and solving the dilemmas in dynamics, chemistry, and geophysics that are coupled with adherence to any of the individual classical hypotheses. *Hartmann et al.* (1986) summarize the development of these hypotheses in their book, *Origin of the Moon*. Figure 2.4, from a computer model by *Kipp and Melosh* (1986), illustrates this new view of the first 12.5 minutes of the impact process that may have led to the origin of the Moon.

To truly understand the origin of the Moon, more data are needed. From future geophysical surveys, we need to learn more about the Moon’s heat flow, its mantle thickness and seismic velocity structure, and whether it has a metallic core. From future geochemical studies, we need to determine the lunar inventory of heat-producing radioactive elements, the abundances of refractory and volatile elements, and the abundances of siderophile elements (those that tend to be miscible with iron). The magnesium-to-iron ratio must also be known for comparison with the Earth. These seem at first glance to be simple measurements, but they are measurements that can now only be obtained from a few of the varied parts of the differentiated Moon. The reassembly of these parts can be done with confidence only after the history of lunar differentiation is known, by the determination of volumes and ages of rock types at the surface, and by the use of geophysics and geochemistry to infer their sources at depth. Future lunar global data from orbit and from the lunar surface will be required to create and test a convincing theory of the Moon’s origin.

2.4.2. Diversity of Lunar Rock Types

One of the fundamental discoveries of the Apollo program was that the Moon is made up of a variety of igneous rock types that differ widely in both their chemistry and mineral composition. The first-order differences are between the dark basalts of the maria and the lighter-colored feldspar-rich rocks of the highlands, as described in section 2.3. There is also a great diversity among the highland rocks themselves. Three major types have been identified:

Ferroan anorthosites, which are rich in Ca and Al and composed largely of the mineral *plagioclase feldspar* ($\text{CaAl}_2\text{Si}_2\text{O}_8\text{-NaAlSi}_3\text{O}_8$), are one of the most

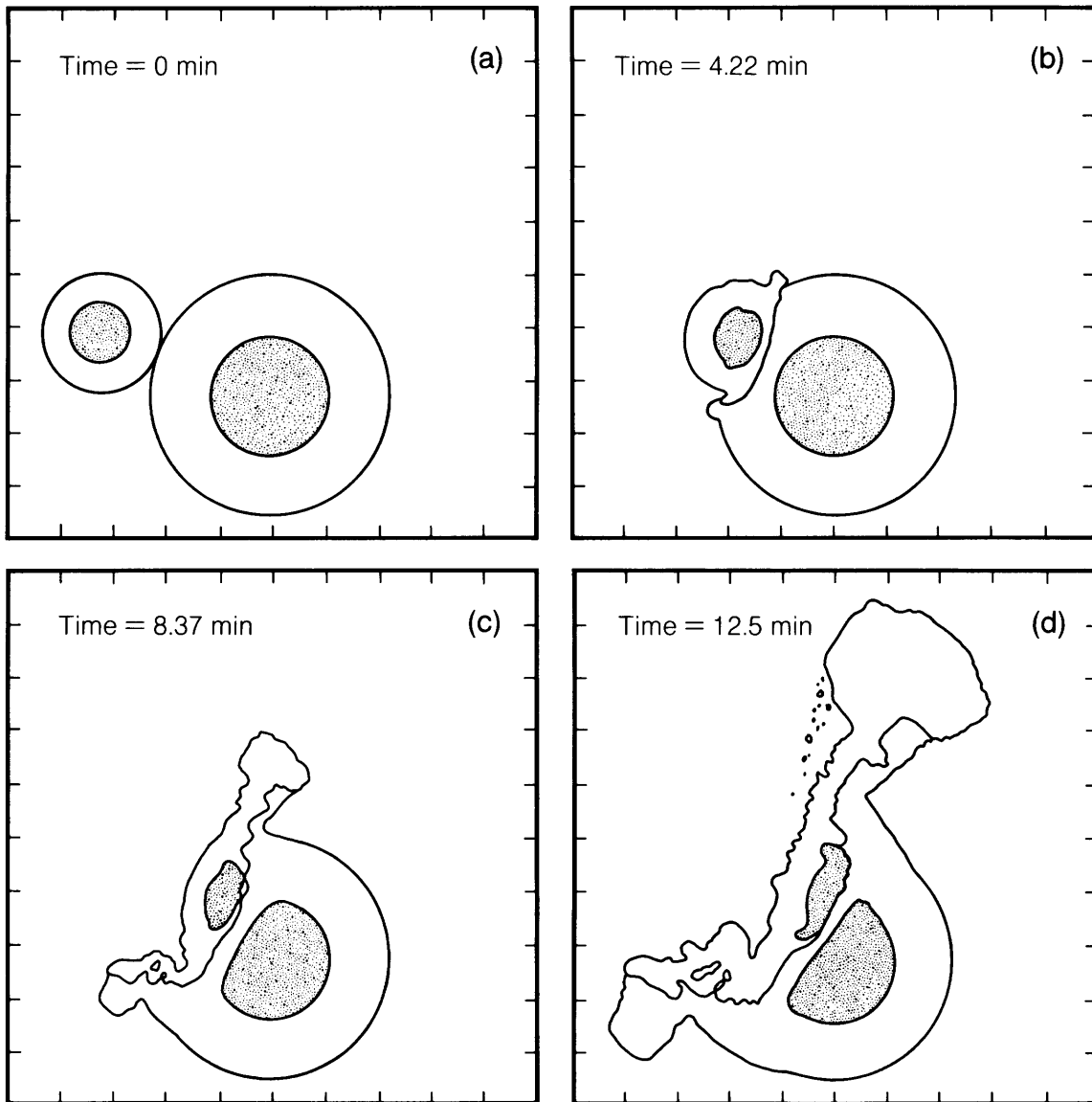


Fig. 2.4. A computer simulation showing 12.5 minutes in the duration of a hypothetical collision between a Mars-sized planet and the proto-Earth. The dotted circles at the center of each planet represent their metallic cores, which are surrounded by silicate mantles. In this illustrated hypothesis the “jetted” silicate material being ejected in the last frame will provide a large part of the Moon, while the metallic parts of both bodies will coalesce in the Earth; the result would be a Moon with little or no metallic core, which fits our present knowledge of our natural satellite (after *Kipp and Melosh, 1986*).

ancient of highland rock types. Ferroan anorthosites are relatively common among samples from the Apollo 16 landing site and among the anorthositic lunar meteorites (Table 2.3).

Magnesium-rich (Mg-rich) rocks are clearly distinct from the ferroan anorthosites. They may contain

nearly as much plagioclase as the ferroan anorthosites, but they also contain Mg-rich grains of minerals such as olivine $[(\text{Mg,Fe})_2\text{SiO}_4]$ and pyroxene $[(\text{Ca,Mg,Fe})\text{SiO}_3]$. Different rock names within this group—such as *norite* (plagioclase plus low-Ca pyroxene), *troctolite* (plagioclase plus olivine), and

dunite (abundant olivine)—reflect differences in the proportions of plagioclase, olivine, and pyroxene that make up these rocks.

KREEP rocks are crystalline highland rocks that contain a chemical component enriched in such elements as potassium (K), the lanthanides or “rare-earth elements” (REE), and phosphorus (P). The KREEP component is also generally accompanied by relatively high concentrations of the radioactive elements U and Th. The appearance of KREEP in lunar rocks indicates extensive chemical separation within the Moon, and the enrichment of the heat-producing elements U and Th makes KREEP-bearing rocks important in understanding the Moon’s thermal history.

Detailed descriptions of these three categories of highland igneous rocks are given in section 6.3, but the descriptions given above are sufficient for this chapter. The chemical and mineralogical diversity among highland and maria igneous rocks has been a major problem in understanding the origin and early history of the Moon. Extensive analytical studies, laboratory experiments, and theoretical modeling have attempted, ever since the first samples were returned to Earth, to explain how the different rocks formed, how they are related to each

other, and how one type may have been derived from (or may have given rise to) others. This active debate continues at the present time.

2.4.3. Differentiation of the Moon and Origin of the Lunar Crust

The major differences between the lunar maria and highlands indicate large-scale chemical segregation (differentiation) of the original materials that accreted to form the Moon. There is general agreement on this point, but the details of differentiation are still mysterious. Early recognition of the fact that the highlands are composed mostly of Ca-rich plagioclase ($\text{CaAl}_2\text{Si}_2\text{O}_8$), a relatively light mineral, led to the suggestion that this mineral represents crystal flotation at the top of a very deep (400 km?) “magma ocean” (Wood *et al.*, 1970). This startling concept—a planet drowned in a molten silicate sea with temperatures greater than 1400°C —has survived in several modifications since its introduction. The evolution of this concept from 1969 to 1985 is illustrated in Fig. 2.5; the discussion that follows is a summary of the major data that have led to these variations in the magma-ocean hypothesis.

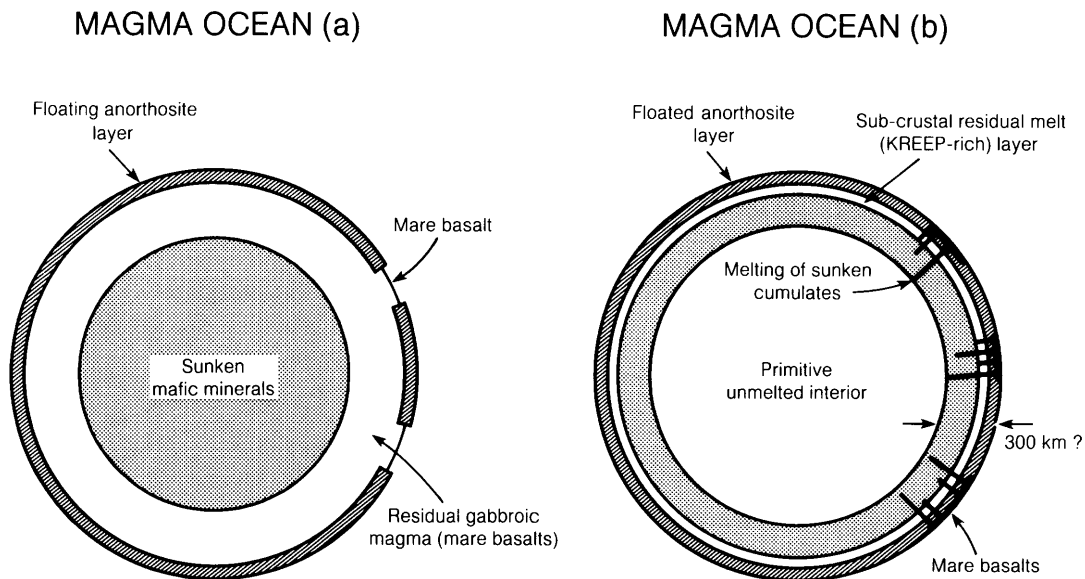


Fig. 2.5. Evolution of the “magma ocean” concept. **(a)** An early model (after Wood *et al.*, 1970) that supposed the entire Moon was initially molten and the mare basalts seen from Earth were parts of the chilled magma ocean exposed through holes in the crust. **(b)** A synthesis of several studies done between 1970-1974 that limited the magma ocean to the outer ~300 km and allowed the mare basalts to form later by remelting (black lines ascending through the sunken cumulates; LAPST, 1985).

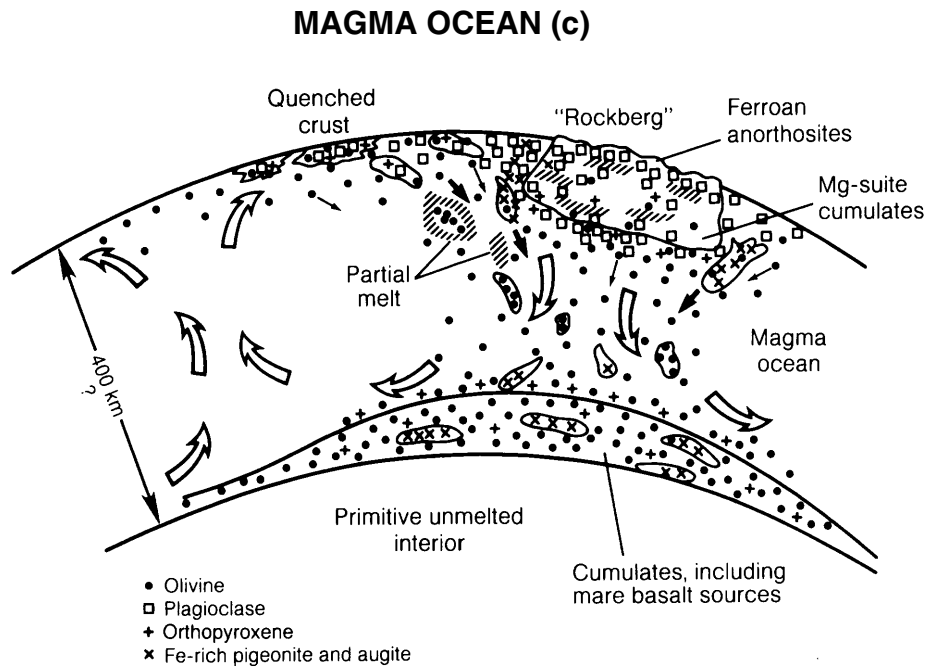


Fig. 2.5. (continued) (c) This figure incorporates details required to account for the differences between ferroan anorthosites and the Mg-suite rocks by forming “rockbergs” on the magma ocean above down-flowing regions within the magma ocean (Longhi and Ashwal, 1985). See Chapter 5 for descriptions of the minerals shown.

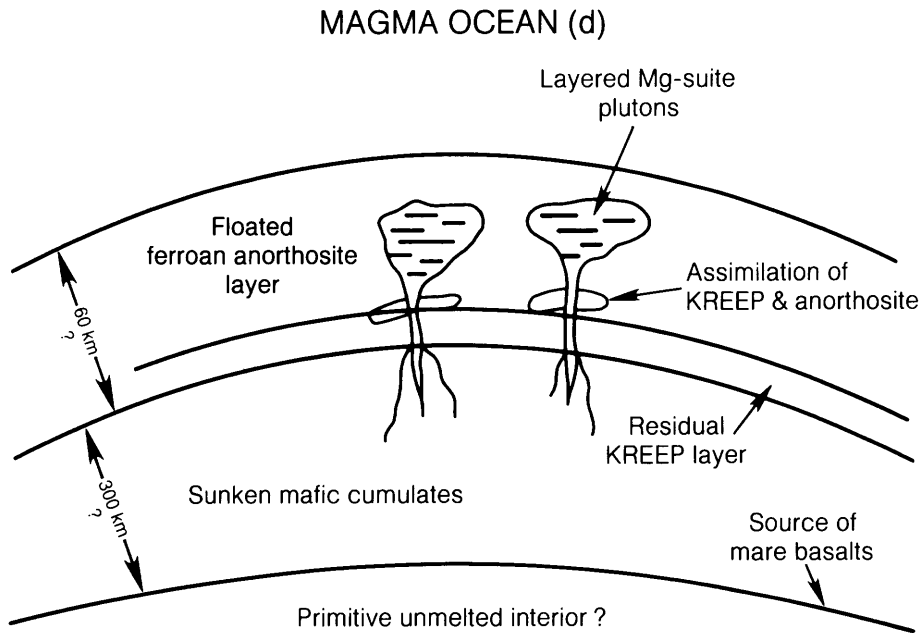


Fig. 2.5. (continued) (d) A more recent model that allows for the ferroan anorthosites to form by flotation on the magma ocean but accommodates a younger age for the Mg-suite rocks by formation through partial melting in the interior with assimilation of older KREEP and anorthosite compositions (synthesis of several studies by LAPST, 1985).

The basic argument for a “magma ocean” has been the need for a mechanism to float a plagioclase-rich crust, while denser minerals such as olivine and pyroxene sank. The idea soon developed that these sinking dense minerals accumulated into deep layers that subsequently became the source areas for at least some mare basalts. The main data constraints on the magma-ocean hypothesis follow; for details, see Warren (1985).

A global, plagioclase-rich crust. Although we lack global coverage, available data from Apollo samples, remote measurements from lunar orbit, and gravity data indicate that the lunar highlands’ surface material averages about 75% plagioclase. Seismic data and the composition of ejecta from large impact basins indicate that this enrichment in plagioclase extends to depth as well. This high abundance of one mineral indicates that some global process concentrated it; flotation in a huge magma system is most likely.

Uniformity of incompatible trace-element ratios. “Incompatible” trace elements are those not required to make the common minerals that crystallize in igneous rocks. Instead, these elements end up concentrated in the last liquid dregs of the magma ocean. This may be the ultimate origin of KREEP (see the section below on formation of the

anorthositic crust). Lunar rocks rich in incompatible trace elements may have quite variable total abundances of these elements, but the ratios of these elements to each other are remarkably constant. This suggests that the enrichments in trace elements derive from a single global source, such as a residuum from a magma ocean.

Possibly extensive melting. Assuming the existence of a magma ocean, estimates of its depth vary from about 100 km to virtually the center of the Moon, a depth of 1738 km. As summarized by Warren (1985), calculations on the depth of melting are based mostly on mass-balance arguments about the abundances of plagioclase and incompatible elements in the crust, estimates of the stresses causing thrust faults in the crust, and estimates of the depths of mare basalt source regions that formed as a consequence of magma ocean crystallization. On balance, the evidence favors a possible magma shell deeper than about 250 km but probably no more than 1000 km deep.

The nature of the hypothetical magma ocean is also uncertain. It is not known whether it would have been a melt of whole-Moon composition or a partial melt. The tendency of partial melts to separate from their source regions and for a solid-melt system to convect suggests that total melting is unlikely,

SERIAL MAGMATISM (e)

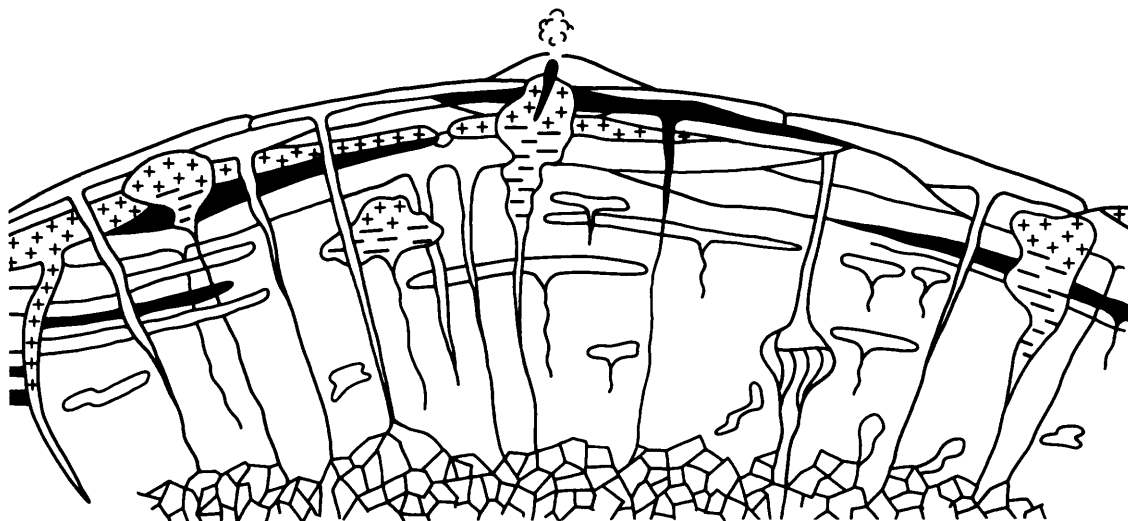


Fig. 2.5. (continued) (e) A model by Walker (1983) that allows for production of the entire range of lunar crustal rock types without any magma ocean. This model generates the Eu anomalies in Fig. 2.6, which led to the magma ocean concept, by an open-system series of melting events with fractionation and admixture of residual liquids. This panel shows the complex series of aluminous basalt flows, sills (black horizontal layers), and intrusions allowed by the model. The evolving and sometimes conflicting hypotheses illustrated in these five panels are evidence of the vital debate that continues over the data from a handful of lunar samples.

although this assumes that the Moon was originally solid. It is possible that the magma ocean was derived from partial melting of the lunar interior and was continuously fed by a "magmifer" (a term analogous to "aquifer" and used to describe the quasisolid mantle, beneath a magma ocean, with extractable partial melt; see Shirley, 1983). Some models for the Moon's origin, such as fission from Earth, however, depict the Moon beginning as a molten body, so a totally molten magma ocean cannot be ruled out.

Complementary europium anomalies. The average highlands crust has a positive europium (Eu) anomaly relative to other REE, indicating an Eu enrichment in plagioclase (Fig. 2.6). This chemical signature is an important and fundamental part of the lunar database, worth considering in some detail. Europium is in the middle of the lanthanide elements (atomic numbers 57 to 71) in the periodic table; these lanthanides (or REE) play an important role in understanding rock and mineral origins (see Chapters 5, 6, and 8). The Eu anomaly considered here is seen when the REE abundances in a sample are ratioed to a fixed standard, commonly their abundance in very primitive meteorites (chondrites) that have not undergone any form of planetary segregation, although a model REE composition for the bulk Moon has also been used (Fig. 2.6). In contrast to the average highlands crust, mare basalts have negative Eu anomalies that were apparently inherited from their deep source regions in the lunar mantle. Plagioclase must therefore have been separated from the magmas from which these mare basalt source regions formed, implying that the source regions now contain the dense olivines and pyroxenes that sank (or at least did not float) as plagioclase floated in the magma ocean.

Geochemical distinctiveness of ferroan anorthosites. As shown in section 6.3, some of the most ancient of lunar samples are ferroan anorthosites. Warren (1986) finds evidence that an already solid crust of ferroan anorthosites was there to be assimilated by somewhat younger Mg-rich highland magmas that rose through the crust. In this view, the ferroan anorthosites formed earlier and from a different magma than the bulk of the highlands crust. Ferroan anorthosites have large positive Eu anomalies, consistent with an origin coupled to plagioclase flotation. This is also consistent with the magma ocean hypothesis.

Antiquity of highland igneous rocks. Age data clearly indicate that the Moon underwent extensive chemical fractionation prior to 4.4 b.y. ago. Ferroan anorthosites and many (but not all) Mg-suite rocks have crystallization ages and model ages older than 4.4 b.y., and model ages for other highland igneous

rocks and mare basalts indicate that their source regions had formed by 4.4 b.y. ago. A magma ocean would be a very efficient mechanism for concentrating these igneous source regions so early in lunar history.

Serial magmatism: Alternatives to the magma ocean. Some investigators have suggested that there never was a magma ocean, favoring instead

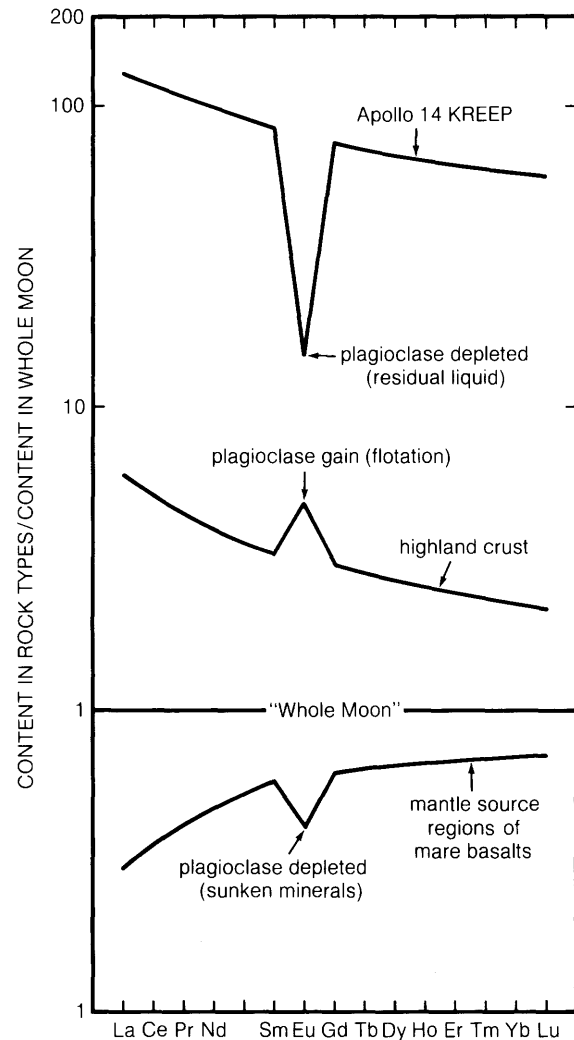


Fig. 2.6. Rare-earth element (REE) concentrations and Eu anomalies in the plagioclase-rich lunar crust, in the source regions for lunar mare basalts, and in KREEP basalts from the Apollo 14 site. The Eu anomalies are due to excursions from smooth trends in the ratio of lanthanide element abundances of a rock compared to a model whole-Moon composition. The Eu anomalies are caused by accumulation or removal of Eu-enriched plagioclase (after S. R. Taylor, 1982).

the formation of anorthosites and other feldspathic cumulates in numerous magmas that intruded the primeval crust. This idea has been dubbed “serial magmatism.” *Longhi and Ashwal* (1985) have developed the most elaborate model for the formation of ferroan anorthosites by this mechanism. They depict anorthosites rising as solid but plastic masses from layers deep in the lunar crust. This would account for the enrichment of plagioclase in the crust, but it requires that the crust be extremely hot (partially molten) for 50 to 100 m.y.

Serial magmatism is now almost universally evoked to explain the formation of Mg-suite magmas. Opinion is split about whether ferroan anorthosites came from a magma ocean or were produced by serial magmatism, although most investigators favor the magma ocean idea. A test to distinguish between the magma ocean and serial magmatism hypotheses for the formation of ferroan anorthosites is to determine accurately the abundance of plagioclase in the crust. Serial magmatism implies that the average crustal composition is roughly noritic or basaltic, containing 15-20 wt.% Al_2O_3 , corresponding to a plagioclase abundance of less than 55%. The magma ocean hypothesis requires a crust richer in plagioclase. This test awaits the completion of the Lunar Observer mission, which will produce global geochemical, mineralogical, and geophysical data (Chapter 11).

2.4.4. The Present View of Lunar Magmatic Evolution

Our sampling of the Moon is limited. We lack global photogeologic, geochemical, and geophysical coverage, and many details of lunar history are controversial. Nevertheless, a broad outline of lunar igneous evolution can be constructed; for details and numerous references, see *Warren* (1985).

Formation of the anorthositic crust. As the Moon formed, its outer portions consisted of a layer of molten silicate magma in which plagioclase floated and accumulated into the first stable lunar crust. At the same time, the heavier olivine, pyroxene, and eventually ilmenite ($FeTiO_3$) sank to form the source areas for mare basalts. As the ocean crystallized, it evolved to produce a residual liquid rich in trace elements; this residuum is the first of the KREEP constituents formed on the Moon and has been dubbed “urKREEP” by *Warren and Wasson* (1979a). Meteoritic bombardment continuously reduced mountains of anorthosite to rubble, leaving only remnants for geologists to study 4.5 b.y. later.

Formation of Mg-rich rocks. Although some authors have developed complicated, quantitative models to explain how both anorthosites and the

Mg-suite rocks could come from a magma ocean (e.g., *Longhi and Boudreau*, 1979), it seems almost certain that most Mg-suite magmas are the products of melting events that postdate the magma-ocean epoch. Nevertheless, some of them might have formed even before the magma ocean had totally solidified. Chemical data and petrologic modeling indicate that Mg-suite magmas assimilated urKREEP and ferroan anorthosites. Different amounts of assimilation produced the diversity seen within the Mg-suite. The sources of the magmas are not known; they could represent partial melts of previously undifferentiated lunar material at depth in the Moon or they may be partial melts of Mg-rich mineral cumulates deep in the magma ocean. They might even be products of melting at the interface between the primitive interior and the bottom of the magma ocean. The melting could have been started by convective overturn of the magma ocean cumulate pile, which would originally have had the less dense Mg-rich rocks on the bottom and progressively denser Fe-rich rocks above.

Formation of KREEP basalts and the subsequent fate of urKREEP. The residual material remaining after 99% of the magma ocean had crystallized would have been rich in FeO and trace elements and enriched somewhat in silica. This material oozed its way into the lower crust, altering the original rock compositions. Some might have undergone liquid immiscibility, producing granitic and FeO-rich complementary melts. Low-K Fra Mauro (LKFM) basalt, which exists as impact melt sheets associated with large basins (Chapter 6), could contain a component that is the product of this process. Partial melting of lower crustal rock contaminated with urKREEP probably gave rise to KREEP basalts. The zone of KREEP-rich material in the lower crust seems to have acted as a source of trace elements for rising magmas to assimilate. Both Mg-suite and mare basalt magmas seem to have been affected by it. At this point in the Moon’s history, it may have appeared as shown in Fig. 2.7a. This conjectural reconstruction of the Moon at about 3.9 b.y. ago dramatically shows that up until that time the process of cratering predominated over igneous processes in determining lunar geomorphology.

Formation of mare basalts. The chemical diversity of mare basalts demonstrates that their genesis is very complicated. Their Eu anomalies indicate that they formed by partial melting of cumulates that developed from the magma ocean after plagioclase had crystallized (Fig. 2.6). Experiments at elevated temperatures and pressures on melts thought to represent primary magmas indicate that they formed at depths ranging from 100 to

(a)



Fig. 2.7. Historical evolution of the nearside (Earth-facing) face of the Moon; modified from *Wilhelms and Davis (1971)*. **(a)** Features as they probably appeared immediately following most of the major basin-forming impact events, but just prior to the formation of the Imbrium basin about 3.8-3.9 b.y. ago (see Fig. 2.3a and section 4.4). Figure is by Don Davis.

(b)



Fig. 2.7. (continued) **(b)** Features as they appeared immediately after the most extensive mare lava floods (about 3 b.y. ago). Figure is by Don Davis.



Fig. 2.7. (continued) (c) The present appearance of the Moon. Figure is by Don Davis.

500 km from source rocks rich in olivine and orthopyroxene (pyroxene without Ca), sometimes accompanied by clinopyroxene (pyroxene with Ca). The abundances of the source rock minerals and the percentage of partial melting varied. Most of the magmas so produced began to crystallize and therefore fractionated (lost crystals) before reaching the surface. Also, most mare basaltic magmas assimilated small amounts of KREEP or (in a few cases such as the “very-high-K” basalts; see section 6.1) granite prior to eruption.

Mare volcanism is known to have been active by about 3.9 b.y. ago, while the Moon was still being heavily bombarded; Fig. 2.7a shows small amounts of lava—some impact melts, some mare basalts—in the bottoms of large impact craters. However, at about 3.9 b.y. ago the rate and scale of cratering decreased. There followed a period of perhaps 1 b.y. in which many of the larger craters on the lunar nearside were inundated by mare basalts (Fig. 2.7b). From ~3 b.y. ago to the present it appears that igneous activity on the Moon was very sparse, and the terrain-forming processes were controlled by sporadic meteorite impacts that have led to the Moon we see today (Fig. 2.7c). Chapter 4 provides greater detail on these surface processes.

APPENDIX: APOLLO SAMPLE TYPES AND LUNAR SAMPLE CURATION

A2.1. Apollo Sample Types

The Apollo astronauts collected several types of samples that can be distinguished on the basis of collection techniques and/or types of equipment used. As a result, the type and amount of data about the lunar surface environment and the type of information contained within the sample can differ from sample to sample. Descriptions of the major types of samples in the Apollo collection follow. The type of sample can generally be determined from the lunar sample catalog or other documents available at the Planetary Materials Laboratory (PML; NASA Johnson Space Center, Houston, TX 77058 USA).

Contingency sample. At the first four Apollo landing sites, the first astronaut to step onto the lunar surface sampled the loose, fine-grained regolith and rocks by scooping at several places with the contingency sampler; this was a combined scoop and bag on the end of a rod that allowed it to be quickly swept through the uppermost few centimeters of the lunar surface. He then removed the bag from the sampler and stored it in a pocket of his suit. This ensured the return of some lunar material

from the site if surface exploration had to be aborted on short notice. The crews of Apollo 16 and Apollo 17 did not collect a contingency sample.

Rocks were present but generally small (<6.5 cm) in the contingency sample. The rocks and fines of the sample represent a small area of the lunar surface near the lunar module (LM). Although the astronauts tried to scoop up a variety of rocks, they spent little time deciding where to collect the contingency sample. The fine-grained component is a mixture of material from several points within the area sampled.

Bulk sample. The bulk sample was collected only at the Apollo 11 site. It consists of 38.3 kg of regolith scooped from several points near the LM and combined as a single sample. Astronaut Armstrong scooped small rocks and fine-grained regolith from the surface at 22 or 23 locations a few meters northwest and west of the LM. He returned to the LM nine times to pour the contents of the scoop into one of the two Apollo Lunar Sample Return Containers (ALSRC) that remained on the Modularized Equipment Storage Assembly (MESA) of the LM. Some of the activity was within the field of the TV camera; some was outside the range of any imagery.

Documented sample. The astronauts documented the settings of many rock and fine-grained regolith samples with down-sun and cross-sun photographs of the undisturbed area before collecting the sample and a down-sun photograph of the area after the sample was removed. When the gnomon (a vertical scale on a small tripod) was within the area photographed, its image and shadow could be used to determine precisely the vertical vector and the down-sun direction. The gnomon also served as a scale, a color chart, and a reflectivity reference for the sample and surface features near the sample.

The “before” photographs documented the relationship of a sample and its surroundings before astronaut activity disturbed the surface. The “after” photograph showed the effects of collection activity on the surface characteristics and supported the identification of the collected sample. The Lunar Sample Preliminary Examination Team (LSPET) successfully determined depth of burial and lunar surface orientation for many documented rock samples by comparing the rock shape and shadow patterns recorded in the “before” photographs with the shape and shadows observed under artificial illumination in the laboratory. These rock orientations were needed to evaluate directions of micrometeoroid impacts and radiation effects on the surface samples.

The procedure for fully documenting a lunar sample required participation by both astronauts and

consumed several minutes of the limited time available for exploring the lunar surface. Note that the Apollo 11 samples discussed as “documented” samples in the catalog are “selected” samples according to the definitions presented here. At the Apollo 11 site, the astronauts did not have adequate time to provide photographic documentation or voice descriptions of the lunar surface setting.

Selected sample. Astronaut teams collected many samples of rock and fine-grained regolith without the full set of photographs required to document the sample in its lunar setting. They placed each “selected” sample in a numbered bag and generally discussed the sample and its lunar setting while collecting and bagging the sample.

Without the documentation photographs, members of the LSPET could not determine the lunar surface orientation or depth of burial for the sample. Also, the reflectivity of the sample before handling and packaging could not be measured without these photographs.

On the positive side, the astronauts could work independently while collecting the selected samples, and many selected samples could be collected within the time required to fully document one sample. Collection of lunar material in the “selected sample” mode provided a larger number and a wider variety of lunar samples than would have been possible if all samples had been fully documented.

Rake sample. The Apollo 11 bulk sample of fine-grained regolith included a few marble-sized and larger rocks of varied lithology. The rocks were large enough to support extensive tests and yet small enough to permit the return of a significant population if the finer fraction could be left on the Moon.

A new lunar tool, the lunar sampling rake, was therefore developed for the later Apollo missions to support collection of the rocks distributed through the upper few centimeters of the fine-grained regolith. When the astronaut pulled it through the regolith, the rake retained rocks larger than a centimeter across but the finer material remained on the surface. Commonly, the astronaut added one or more scoops of the fine-grained regolith to a rake sample before closing the sample bag. The crews of Apollo 15 and later missions collected rake samples.

Rake samples include rocks that represent the population distributed across a few square meters of the lunar surface. Fines in the rake sample bag are a mixture of samples of fine-grained regolith collected from one or more spots in the raked area plus fines attached to the rocks when they were collected.

Cores. Cores are only 5.2% by mass of the total collection, but they are extremely valuable. They are the only source of reliable information about the

near-surface texture and stratigraphy of the lunar regolith. At some localities the astronauts dug shallow trenches, photographed the layering observed, and scooped samples from the bottom and walls of the trench. However, a returned core is the only type of Apollo sample that permits the detailed study of variations in the physical and chemical properties of the lunar regolith with depth. The samples provide information on the Moon's cratering history, a record of solar activity and cosmic-ray flux, and structure of the lunar regolith.

The Apollo astronauts collected 21 cores from the 6 landing sites by pushing or hammering drive tubes into the regolith. They used a battery-powered drill to sample deeper layers of the regolith at one point in each of the last three Apollo sites.

Drive tubes used during the first three missions were 2 cm in diameter. Each tube could hold a core 31.6 cm long, but the lengths of six cores collected with single drive tubes during these missions ranged from 10.5 to 19.3 cm. Lengths of the two cores collected with double drive tubes (units made of two drive tubes threaded together) were 37.7 and 41.1 cm.

Improved drive tubes used during the last three missions were 4 cm in diameter and capable of holding a core 34.3 cm long. Of the 22 core segments collected with the large-diameter drive tubes, 14 had been dissected as of spring 1988. These included six cores (lengths ranging from 46.7 to 66.3 cm) collected with double drive tubes and two cores (31.4 and 29.3 cm) collected with single drive tubes.

The Apollo 15 and 16 astronauts used six drill-stem segments each to sample the upper 237 and 221 cm, respectively, of the regolith. The Apollo 17 crew, using eight drill-stem segments, sampled to a depth of 292 cm. Cores collected with the battery-powered drill are about 2 cm in diameter.

A2.2. Lunar Sample Curation

Three major objectives of lunar sample curation are to (1) protect the samples physically, (2) preserve chemical integrity, and (3) maintain accurate records. These objectives could be met by counting the samples accurately, surrounding them with an inert atmosphere, and sealing them in a secure vault. But the main value of the collection lies in the use of lunar materials to determine the nature of the Moon and to test new hypotheses about its origin and history.

Therefore, curation of the Apollo collection (and of U.S.S.R. Luna samples in U.S. possession) also requires the allocation of samples to support current

scientific studies while meeting the major objectives that are designed to conserve this resource for future studies. This balance is accomplished through a combination of special facilities, controlled access to sample processing and storage areas, and strictly enforced procedures. Similar protective curation is maintained for the lunar meteorites from Antarctica, but these have already been long exposed on the Earth's surface, and they are therefore maintained in a separate facility with less stringent environmental controls. The lunar meteorites are curated by the Johnson Space Center (JSC) and the Smithsonian Institution. The Meteorite Working Group at JSC handles all sample requests.

Physical security. One major objective of Apollo and Luna sample curation is to protect samples in the collection from unauthorized removal or loss due to natural hazards such as hurricanes and tornados. Two vaults in the Lunar Sample Building (Johnson Space Center Building 31-A), which was completed in 1979, provide good physical protection for stored samples. The vaults meet the Bank Protection Act requirements for class 9R bank vaults and they are designed to withstand tornadic winds even though the rest of the building may be demolished. Flooding should not endanger lunar samples stored in the vaults because the elevation of the vault floor is above the highest tide predicted for a maximum hurricane at the Johnson Space Center.

In 1976, before the Lunar Sample Building was constructed, the Curator moved about 14% of the Apollo collection to a remote storage facility at Brooks Air Force Base (BAFB) in San Antonio, Texas, as a precautionary measure in case of damage or loss of the main collection at Houston. These samples are still retained there in remote storage. To ensure selection of a representative subset of the samples, all the larger rocks and many smaller rocks were sawed to provide major subsamples for storage at the remote facility.

Samples for allocation to approved investigators are prepared in the Planetary Materials Laboratory (PML) adjacent to the storage vaults on the second floor of the Lunar Sample Building. The vaults, laboratories, and adjacent corridors are a NASA Limited Area. NASA regulations restrict access to such areas; operational procedures further restrict access to the vaults and the corridor outside the vault during working hours. At other times, unauthorized entry or movement within the Limited Area will activate alarms that alert Johnson Space Center security.

Two individuals witness each movement of samples within the PML. They transfer samples from the vault to the laboratory processing cabinets only when the samples are required for study or for

allocation. Excepting three samples on display near the visitor area, samples are returned to the vault promptly when processing or study is completed. When a hurricane warning is issued, all samples in the laboratory are moved to the vault.

Protection from contamination. Contamination control is a major concern of lunar curation. The abundant oxygen and water vapor in the Earth's atmosphere could react with samples from the dry, near-vacuum environment of the lunar surface; contaminants introduced as the samples are stored or processed could bias the results of critical analyses (for example, Pb solder or Rb in wallboard). The small size of typical samples allocated for analysis accentuates the effects of contamination.

Pristine lunar samples are stored, studied, and prepared for allocation inside cabinets filled with flowing, high-purity nitrogen gas that carries less than 5.7 ppm H₂O, 20 ppm O₂, and 2 ppm Ar. This relatively inert atmosphere protects the samples from reactions with oxygen and water vapor and from contamination by other components of the Earth's atmosphere. For storage or transfer outside a processing cabinet, a lunar sample is sealed in three teflon bags or in a rigid container plus two bags. All are filled with nitrogen. Since the packaging is permeable to gases over a long period, the packaged samples are stored in nitrogen. In the pristine sample vault, the samples are stored in glove cabinets supplied with flowing nitrogen. At the BAFB remote facility, the samples are sealed in a nitrogen-filled, thick-walled stainless steel cabinet. Periodically, personnel from Johnson Space Center visit the remote facility, analyze the gas in the cabinet to check the integrity of the system, and flush the old gas from the cabinet with fresh nitrogen.

Overall cleanliness of the lunar sample vaults and laboratories is important because dust could enter the processing or storage cabinets when they must be opened for cleaning or glove replacement. Both facility construction and operating procedures prevent such contamination. Careful selection of building materials used inside the processing and storage areas reduces the number of particles contributed by the structure, and the use of materials with the lowest levels of critical elements (e.g., Pb, Au, Hg, and the rare-earth elements) reduces the impact of contamination if it should occur.

Operating procedures are designed to reduce the numbers and types of particles introduced into the laboratory. Access to the laboratories is controlled. Workers and visitors preparing to enter must remove all gold jewelry and put on nylon coveralls, caps or snoods, gloves, and booties to reduce contamination from material on their shoes and the lint and dust carried by their clothes. An air shower between the

change room and the laboratory-vault area replaces air from the change room with filtered air before the individual enters the cleaner area.

A high-efficiency filtration system removes dust and other particles from the conditioned air fed to the vaults and laboratories of the Lunar Sample Building. Air in these work areas meets or exceeds Class 1000 Clean Room specifications. Positive air pressure blocks the entry of unfiltered air and directs air movement from all rooms within the laboratory-vault complex toward the exterior. Pressure is highest in the Pristine Sample Vault and lowest, but still positive, in the change room at the entrance.

The floor plan and operational procedures restrict access to the vaults; most of the traffic is downstream (in the air flow) from areas where packaged samples must be handled briefly outside the protective nitrogen atmosphere of the cabinets.

As a lunar sample is subdivided by prying, chipping, or sawing, any contact with other materials can result in contamination. The effects of this potential contamination are minimized by (1) restricting the materials allowed to contact the sample and (2) selecting materials that are relatively abundant in the lunar samples, where possible. Only aluminum, teflon, and stainless steel are allowed to touch the lunar samples during processing in the JSC Lunar Sample Laboratory.

Actually, a rock is its own best container. Therefore, for extremely critical analyses, a sample larger than the mass required for a proposed test will be allocated. The investigator can remove an exterior layer, using techniques and tools that will not affect the results of the test and thereby have an absolutely pristine sample for the analysis.

Operational procedures reduce the probability of cross contamination between Apollo sites or between samples from the same site. Samples from only one Apollo site can be transferred into a nitrogen cabinet. Before a sample from a different site can be moved in, all samples, equipment, and supplies must be removed and the cabinet cleaned according to established procedures. Different samples from the same Apollo site can be transferred into a processing cabinet, but only splits from one sample can be open at the same time.

Lunar sample records. The Lunar Sample Curator maintains extensive records, both paper and electronic, for each lunar sample. These include photographs that document the surface features of rocks as they were before any laboratory operations other than a thorough dusting, the initial description prepared by one or more members of the LSPET, and the original copies of laboratory records that document all processing of the sample in facilities operated by the Lunar Sample Curator.

Sample location, mass, and some of the other information in the datapack are included in the Lunar Sample Data Base (LSDB) that is currently maintained on the Solar System Exploration Division computer at JSC. This database provides ready access to an accurate inventory of the Apollo collection and of Luna samples that have been received from the U.S.S.R. Planetary Materials Laboratory personnel update this interactive database each time a sample is moved. Updates to the interactive file are checked daily using a backup file that is accessible only to the system operator. The electronic lunar sample inventory permits a real-time check on the status of any split of a lunar sample in the collection. The ease of access to the basic inventory data has led to the development of several auxiliary files with expanded descriptions and operational details.

A2.3. Curation History

The opportunity to study lunar samples excited the global scientific community. NASA carefully reviewed the proposed studies and evaluated the qualifications of the individuals and their laboratories. Many organizations expended great effort to demonstrate the capability to obtain reproducible results with small samples. More than two years prior to the first lunar landing, 110 scientists in the United States, England, Germany, Canada, Japan, Finland, and Switzerland had been selected as principal investigators by the NASA Office of Space Science and Applications.

To support this massive program of study and analysis, NASA and representatives of the scientific community developed plans for the curation and study of lunar samples during several years prior to the first lunar landing. Isolation of persons (astronauts and others exposed to lunar samples) and materials that had either direct or indirect contact with the lunar surface became a central element in the plans because existing scientific evidence could not demonstrate conclusively that the Moon was lifeless. Precautions against potentially pathogenic life forms therefore had to be taken.

Sterilization of lunar samples would destroy their value for many scientific experiments (for example, determination of the presence of gases in lunar samples). Therefore, the astronauts, samples, and other equipment were placed in a quarantine facility while the lunar examples were being examined for potential biological activity. The Lunar Receiving Laboratory (LRL) was designed to satisfy the interrelated requirements of contamination control, quarantine, and time-dependent experimentation.

Construction of the LRL at the NASA Manned Spacecraft Center (MSC; now JSC) in Houston, Texas, was completed prior to the first lunar landing.

Facilities for biological tests associated with the quarantine and other time-dependent scientific tests were provided within the sample isolation area. A comprehensive scientific examination of the lunar samples was conducted during the quarantine period within sterile gloveboxes to provide the world with initial descriptions of the samples, to curate those samples, and to provide an advisory committee with information needed to allocate the samples to investigators.

The Apollo astronauts packed some samples from each mission in aluminum boxes designed to seal and maintain the vacuum of the lunar surface environment during the trip to Earth and the LRL. For various reasons, some boxes did not maintain that low pressure. After the first mission, the crews also packed other samples in a variety of closed but unsealed bags. Samples in the leaking boxes and unsealed bags experienced limited exposure to the atmosphere of the LM and command module (CM) as the containers underwent two or more decompression/compression cycles during the several days between their removal from the lunar surface and splashdown in the Pacific Ocean. Within a few hours of landing, the sample boxes and other sample containers were sealed in plastic bags on the recovery ship prior to the flight to Houston.

The original plan for sample quarantine and examination at the LRL was to examine the samples and perform the initial processing tasks in a vacuum environment (10^{-6} torr). A large vacuum chamber with ports for observation and photography and glove ports for sample manipulation had been installed in the LRL. After a few samples from the Apollo 11 selected sample box had been processed, a leak developed rapidly in one of the gloves. Unprotected samples were shifted quickly to another section of the cabinet before the section with the leaking glove was isolated for repair. The entire vacuum system had to be sterilized with dry heat in order to replace the glove without violating the biological containment.

Following that accident, the unopened Apollo 11 bulk sample box was transferred from the vacuum lock to a nitrogen cabinet in the Biological Preparation Laboratory. Rocks and fines in the bulk sample were examined, described, photographed, and chipped in nitrogen cabinets. The two cores and the contingency sample were also processed in those cabinets. Most of the core samples and material from the bulk and contingency samples remained in the nitrogen cabinets until the end of the Apollo 11 sample quarantine.

The Apollo 12 documented sample box leaked during the return to Houston. When tested at the LRL, the internal pressure was a significant fraction of atmospheric pressure and the ratios of nitrogen, oxygen, and argon approximated those in Earth's atmosphere. Internal pressure of the selected sample box was 40 to 60 μm when probed; that box was opened in the vacuum system. The LSPET processed rocks and fines from the documented sample box, the contingency sample, the tote-bag samples (four large rocks returned in an unsealed bag), and cores in nitrogen-filled cabinets.

No samples were returned from the Apollo 13 mission. Because of an accident during the trip to the Moon, the crew was not able to land on the lunar surface.

The LRL biological barriers remained intact during the preliminary examination of samples returned by the Apollo 14 crew. All samples were examined and processed in nitrogen-filled glove cabinets. Because of the importance of biological protection in handling the Apollo 11, 12, and 14 samples, nitrogen pressure in the glove cabinets was held slightly below atmospheric pressure to maintain the biological barrier. When a leak occurred, nitrogen that had contacted lunar materials would not escape. Instead, the terrestrial atmosphere would enter the cabinet. To protect the lunar samples from contamination, they were removed from sealed containers only while being studied or subdivided.

By 1971, detailed scientific studies of the Apollo 11, 12, and 14 samples had clearly established that lunar rocks and soils contained no life forms (living or fossil), no toxic materials, and no water. As a result, the biological protection requirements were dropped and no quarantine was imposed for the lunar samples returned by Apollo 15

and later missions. The cabinets of the lunar sample processing lines were therefore operated with a positive nitrogen pressure throughout the preliminary examination period to protect the lunar samples from terrestrial contamination should a leak occur.

Lunar Receiving Laboratory facilities were used for the preliminary examination, initial processing, and time-critical physical and chemical tests of lunar samples from all the Apollo missions. The growing collection of lunar samples was also stored in the LRL until 1971. Part of the operation moved to JSC's Building 31 when a new vault for storing lunar samples and a laboratory for processing lunar samples returned by investigators became operational. All laboratories for processing lunar samples were concentrated on the second floor of Building 31 in 1973. Lunar samples were stored in vaults distributed around JSC (in Buildings 1, 16, 31, and 45) until late 1979.

The Curator moved representative samples totaling about 14% of the collection to a remote storage facility at BAFB in February 1976. After evaluating several proposed sites for the active collection, NASA decided to keep the collection in Houston. At this time the Lunar Sample Building (Building 31-A) was constructed at JSC.

The Curator consolidated lunar samples stored at JSC in the vaults of Building 31-A during August and September 1979. Pristine sample processing began in the second-floor laboratories of the new building after the samples were moved. All lunar sample activity at JSC was consolidated in 1982 when the returned sample processing laboratories moved from Building 31 to the first floor of the Lunar Sample Building.

THE LUNAR ENVIRONMENT

David Vaniman, Robert Reedy, Grant Heiken, Gary Olhoeft, and Wendell Mendell

3.1. EARTH AND MOON COMPARED

The differences between the Earth and Moon appear clearly in comparisons of their physical characteristics (Table 3.1). The Moon is indeed an alien environment. While these differences may appear to be of only academic interest, as a measure of the Moon's "abnormality," it is important to keep in mind that some of the differences also provide unique opportunities for using the lunar environment and its resources in future space exploration.

Despite these differences, there are strong bonds between the Earth and Moon. Tidal resonance between Earth and Moon locks the Moon's rotation with one face (the "nearside") always toward Earth, the other (the "farside") always hidden from Earth. The lunar farside is therefore totally shielded from the Earth's electromagnetic noise and is—electromagnetically at least—probably the quietest location in our part of the solar system. The Moon has also been moving away from Earth over time, because the dissipation of tidal energy by bottom friction in the Earth's seas (especially in shallow seas) has gradually slowed the Earth's rotation (e.g., *Lambeck*, 1975). To keep the angular momentum of the Earth-Moon system constant, the Moon has been moving slowly outward at a rate of a few centimeters per year.

The relationships between the Earth and Moon in origin, composition, and orbital dynamics are as important for the basing of people and equipment on the Moon as they are for scientific understanding. However, in considering routine terrestrial processes transplanted to the Moon, it is primarily the many differences in Table 3.1 that stand out.

On the Moon the most obvious environmental factors that concern people are extreme temperature

fluctuations, low gravity, and the virtual absence of any atmosphere. Other environmental factors are not so evident. Of these the most important is ionizing radiation, and much of this chapter is devoted to the details of solar and cosmic radiation that constantly bombard the Moon. Of lesser importance, but necessary to evaluate, are the hazards from micrometeoroid bombardment, the nuisance of electrostatically charged lunar dust, and alien lighting conditions without familiar visual clues. To introduce these problems, it is appropriate to begin with a human viewpoint—the Apollo astronauts' impressions of environmental factors that govern the sensations of working on the Moon.

3.2. THE ASTRONAUT EXPERIENCE

Working within a self-contained spacesuit is a requirement for both survival and personal mobility on the Moon. Spacesuits overcome the extreme lunar temperatures and the lack of air, and they are adequately mobile (although awkward) in the low gravity. Current technology in spacesuit design provides for survival but is far from the optimum in comfort. Spacesuits used on the Apollo missions were bulky; maneuvering in the awkward suits was compensated for by low lunar gravity, so that mobility on the Moon was not much different from mobility on Earth without a suit. The Apollo 11 astronauts remarked that "the lunar gravity field . . . has differing effects on Earth-learned skills. Although the gravitational pull on the Moon is known to be one-sixth of the gravitational pull on the Earth, objects seem to weigh approximately one-tenth of their Earth weight. [Objects are] easy to

TABLE 3.1. Physical comparison of the Moon and Earth.

Property	Moon	Earth
Mass	7.353×10^{22} kg	5.976×10^{24} kg
Radius (spherical)	1738 km	6371 km
Surface area	37.9×10^6 km ²	510.1×10^6 km ² (land = 149.8×10^6 km ²)
Flattening*	0.0005	0.0034
Mean density	3.34 g/cm ³	5.517 g/cm ³
Gravity at equator	1.62 m/sec ²	9.81 m/sec ²
Escape velocity at equator	2.38 km/sec	11.2 km/sec
Sidereal rotation time	27.322 days	23.9345 hr
Inclination of equator/orbit	6°41'	23°28'
Mean surface temperature	107°C day; -153°C night	22°C
Temperature extremes	-233°C(?) to 123°C (Table 3.3)	-89°C to 58°C
Atmosphere	$\sim 10^4$ molecules/cm ³ day 2×10^5 molecules/cm ³ night	2.5×10^{19} molecules/cm ³ (STP)
Moment of inertia (1/MR ²)	0.395	0.3315
Heat flow (average)	~ 29 mW/m ²	63 mW/m ²
Seismic energy	2×10^{10} (or 10^{14} ?) J/yr†	10^{17} - 10^{18} J/yr
Magnetic field	0 (small paleofield)	24-56 A/m

* (Equatorial-ideal)/ideal radii.

† These estimates account for moonquakes only and do not account for seismicity from meteoroid impacts; see discussion of seismic energy in section 3.7.

handle in the reduced lunar atmosphere and gravitational field. Once moving, objects continue moving, although their movements appear to be significantly slower in the lunar environment" (*Aldrin et al.*, 1969).

The Apollo 12 astronauts (*Bean et al.*, 1970) explained that the characteristic "loping" gait seen in all the films of astronauts on the lunar surface was the most natural way to move; heel-to-toe "Earth" walking was more difficult and energy-consuming in the reduced lunar gravity. *Scott* (1973) equated walking on the Moon with the sensation of walking on a trampoline. Although low weight compels this peculiar gait, the mass of an astronaut's body and personal gear remain unchanged. For this reason it takes considerable exertion to start or stop. "I . . . get under way by thrusting my body forward, as though I were stepping into a wind. To stop, I dig in my heels and lean backward" (*Scott*, 1973).

Energy consumption by the astronauts working on the lunar surface was high (about 1 MJ/hr) but not excessive (*Bean et al.*, 1970). During the Apollo missions no astronauts were placed in the situation

of having to negotiate steep slopes; climbing abilities on crater walls or steep hills are still untested. However, the Apollo 12 astronauts reported that recovery from falls was relatively simple in low gravity, despite the awkward suits. "When a fall begins, you first lose your balance rather quickly, particularly if you try to back up, because the ground is uneven and there is a possibility of stepping in holes or on rocks. [Their spacesuits also had an aft displacement of center-of-gravity.] The fall progresses so slowly, though, that there is plenty of time to almost turn around or to catch your footing before you actually fall to the surface. Because a fall begins so slowly on the Moon, it is usually possible to spin around, bend the knees, and recover. Several times, in trying to bend over to get something, we would start to fall over, but the fall progressed so slowly we could start moving our feet and keep moving until they came back under us again" (*Bean et al.*, 1970).

The senses of taste, smell, and hearing are dominated by the artificial environment of the spacesuit and have nothing to do with the Moon.

Touch is secondary, transmitted through the skin of the suit, but is an important factor in an astronaut's ability to move and manipulate. The most critical of the senses is sight, for the lunar environment's most direct impact on a spacesuited astronaut is visual.

Difficulties in visibility were evident in orbit before the astronauts even arrived on the lunar surface. Visibility was poor in areas viewed at low phase angle (i.e., with the sun more or less behind the observer; Fig. 3.1), but topographic details could still be seen. Visibility in subsolar areas is essentially that of zero phase angle. In this condition there is a complete lack of shadows, but albedo differences are clearly visible. Navigation from orbit, using landmarks under these conditions, is very difficult.

From orbit, after a few minutes of adaptation, features on the dark side of the Moon could be viewed clearly in earthshine. Landmark tracking is difficult but not impossible (NASA, 1969).

Once on the surface, other visibility problems were noticed. Apollo 11 astronauts Armstrong and Aldrin first commented on this problem: "Distances on the lunar surface are deceiving. A large boulder field located north of the LM [lunar module] did not appear to be too far away when viewed from the LM cockpit. However, on the surface we did not come

close to this field, although we traversed about 100 ft toward it. The flag, the television camera, and the experiments, although deployed a reasonable distance away from the LM and deployed according to plan, appeared to be immediately outside the window when viewed from the LM cockpit. Because distance judgement is related to the accuracy of size estimation, it is evident that these skills may require refinement in the lunar environment" (Aldrin et al., 1969).

Right after touchdown, the Apollo 12 astronauts observed that "we were positive of where we were, but it was difficult to pinpoint our exact location because of the limited field of view out the LM windows, because of the general tendency to underestimate distances . . . and because of the difficulty of seeing even large craters beyond a distance of about 100 ft. None of the shadows that were visible in flight, the ones in the bottoms of craters, were visible after touchdown . . . it was difficult to find the craters." They also found that "lunar surface visibility was not too unlike Earth visibility, with the exception that the sun was extremely bright . . . shadows were visible only when viewing cross-sun. It was difficult to view down-sun exactly along the zero-phase direction, but this

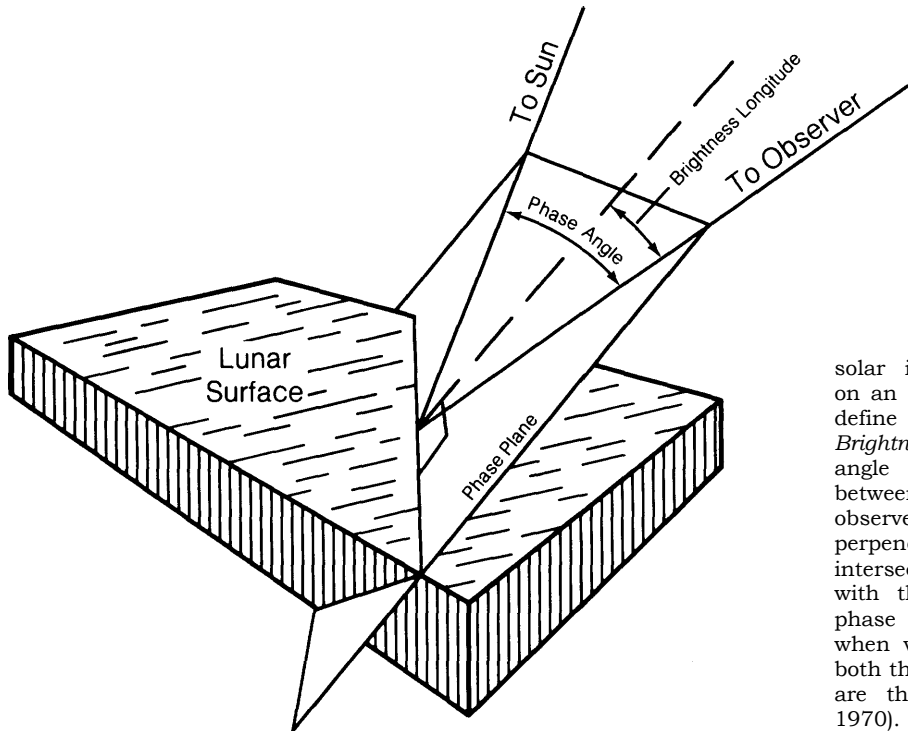


Fig. 3.1. Illustration of *phase angle*, which is the angle between an observer's line of sight and the line of solar illumination impinging on an object. These two lines define the *phase plane*. *Brightness longitude* is the angle in the phase plane between the light path to the observer and a line perpendicular to the intersection of the ground with the phase plane. Zero phase angle is the condition when vectors to a spot from both the sun and the observer are the same (from Mutch, 1970).

deficiency did not hinder normal lunar surface operations because the eyes could be scanned back and forth across these bright zones for visual assimilation. Objects in shadows could be seen with only a slight amount of dark adaptation" (*Bean et al., 1970*).

"Walking in the up-sun direction posed no problem, although the light was very bright with the sun shining directly into the visor. While walking in the down-sun direction, most objects were visible, but the contrast was washed out. Varying shapes, sizes, and glints were more easily identified in the cross-sun directions" (*Aldrin et al., 1969*). The Apollo 12 astronauts added the observation that colors were deceptive and changeable, depending largely on sun angle, with the same surface changing from gray to dark or tannish brown during their short 32-hour stay on the Moon (*Bean et al., 1970*).

In summary, the combination of low gravity, awkward suit mobility, and harsh sunlight without atmospheric filtering leads to significant disorientation in the unfamiliar lunar terrain. Spacesuit improvements and longer periods for acclimatization may improve this situation for future astronauts. A

completely different set of visual conditions will be experienced by astronauts who will someday operate on the nighttime lunar surface with illumination by earthshine. The Apollo legacy is only a brief taste of the lunar experience and much remains unknown.

3.3. TERRAIN

"One salient impression we have of our journey was the variety of lunar terranes and geologic structures. We suspect that there is a general lack of appreciation for the complexity of lunar processes and probably of lunar geologic history. We believe that lunar studies will prove fascinating and rewarding for many years and through many programs" (the Apollo 16 astronauts; *Young et al., 1972*).

The Moon's terrain has been controlled by two factors, high-velocity impacts and volcanism. The mare basins are rimmed with high mountains formed during impact of planetesimals; many of these same basins were smoothed when filled or partly filled with basaltic lavas. Deep channels (rilles) cut the mare surfaces, and faults and wrinkle ridges buckle those same surfaces. All of the Moon's

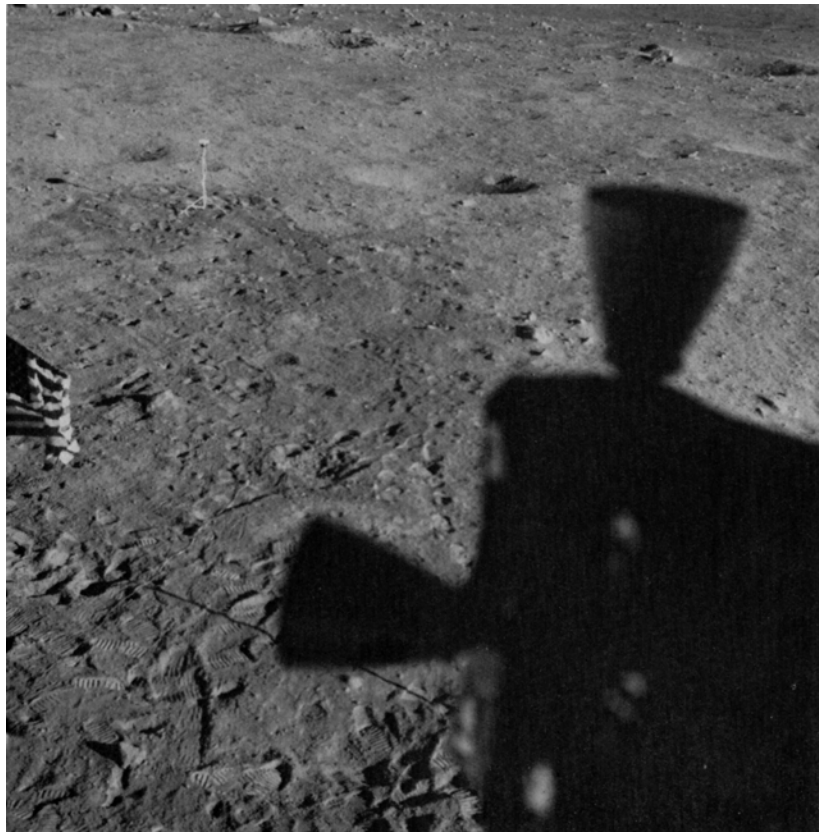


Fig. 3.2. View of the Apollo 11 landing site from a window in the lunar module (NASA Photo AS 11-37-5468). Note the abundance of well-preserved footprints.

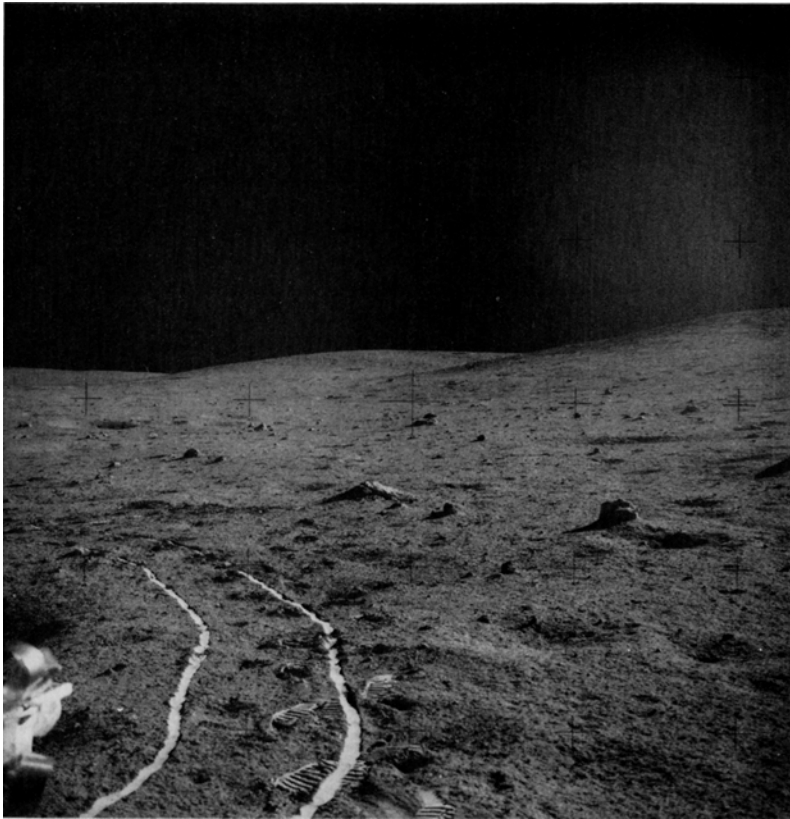


Fig. 3.3. View of a ridge at the Apollo 14 landing site (NASA Photo AS14-64-9058). Slope angles are gentle, but small meter-scale craters are abundant. Sunlight is reflected from the compressed soil in the wheel tracks of the equipment cart (the “modularized equipment transporter”). Note the difficulty of judging distance without familiar visual clues.

surface is cratered, with craters ranging from subdued shallow depressions to sharp-rimmed features littered with large boulders. (For a detailed treatment of crater shapes, sizes, and ages, see Chapter 4.) Nearly all the lunar surface is covered with several meters to tens of meters of loose regolith.

The Apollo astronauts visited a variety of sites on the lunar surface. The examples of terrain described here have been walked upon, driven over, sampled, and tested.

3.3.1. Mare Surfaces

Apollo 11. The Apollo 11 landing site is located on the flat surface of Mare Tranquillitatis. It is, however, far from smooth, being covered with craters ranging in diameter from 0.3 to 20 m (not including the occasional large crater; *Aldrin et al.*, 1969). A fresh, 180-m-diameter, 30-m-deep crater, located 400 m east of the site, is surrounded by a 250-m-wide apron of blocky ejecta with blocks as large as 5 m long. Most of the craters have subdued rims covered with fine-grained regolith (Fig. 3.2). Although there were fresh craters in the area, the

astronauts commented that no crater rims were truly sharp. Block fields correspond with crater rays visible on orbital photographs.

Apollo 12. The cratered surface at the Apollo 12 site, on Oceanus Procellarum, was similar to that of Apollo 11. Craters range from very subdued, rimless depressions to sharp, well-defined features. The sharper craters contain concentrations of angular blocks. The small, fresh craters have rubbly rims (*Shoemaker et al.*, 1970). Most of the larger craters near the landing module, ranging from 50 m to 250 m in diameter, have subdued rims; traversing the rim and interior of Surveyor Crater (200 m in diameter, 28 m deep) was easy for the astronauts. Two peculiar mounds were described, each being 1.3 m high and 1.6 m wide, perched on a 6.5-m-diameter base (*Bean et al.*, 1970).

3.3.2. Large-scale Ejecta Ridges

Apollo 14. The Apollo 14 landing site is located on the Fra Mauro Formation, which is characterized by elongate ridges 1 to 4 km wide and a few to tens of meters high. These are large impact-ejecta ridges that radiate away from the Imbrium Basin. Craters

with diameters of 400 m to 1000 m are two to three times more abundant here than in the mare regions. The ridges consist mostly of highland debris, but they contain a variety of mare basalt fragments. One of the ejecta ridges is penetrated by 340-m-diameter Cone Crater, located 1100 m east of the lunar module; its crater rim is littered with blocks 1 to 16 m in diameter with spaces between blocks of several meters. The “smooth” terrain of the site is more or less level over distances of one to several kilometers (Fig. 3.3) but is saturated with craters several tens of meters to hundreds of meters in diameter and meters to tens of meters deep. The walls of older, larger craters have slopes of 10° to 15°.

3.3.3. Lunar Highlands

Apollo 16. The central nearside lunar highlands consist of plains between hilly and “furrowed” mountainous areas (Muehlberger *et al.*, 1972). Adjacent to the heavily cratered plains at the Apollo 16 site are the Descartes highlands; projecting into the area traversed by the astronauts is 540-m-high Stone Mountain. The slopes of Stone Mountain are

subtly terraced and have a maximum angle of 18°. Smoky Mountain, located north of the landing site, has a plateau-like top but is steep-sided, with slopes up to 40°.

Both plains and hilly terrain are heavily cratered. Two of the largest and youngest craters studied are 0.5 and 1.0 km in diameter and 100 m and 200 m deep, respectively. Most crater walls are not steeper than 40° to 45°; the walls are covered with loose, thin regolith, boulders, and some outcrops (Mitchell *et al.*, 1972b). South Ray Crater, the freshest large crater in the area, has a high block concentration near the crater rim; the astronauts noted that it would have been impossible to drive to the rim because of the blocks (Young *et al.*, 1972). Stone Mountain was also littered with large blocks; here the astronauts had to park their lunar rover in a small crater to keep it from rolling down the slope (Fig. 3.4).

3.3.4. Highlands-Mare Boundaries (Basin Margins)

Apollo 15. This landing site at the eastern margin of the Imbrium Basin was chosen for its

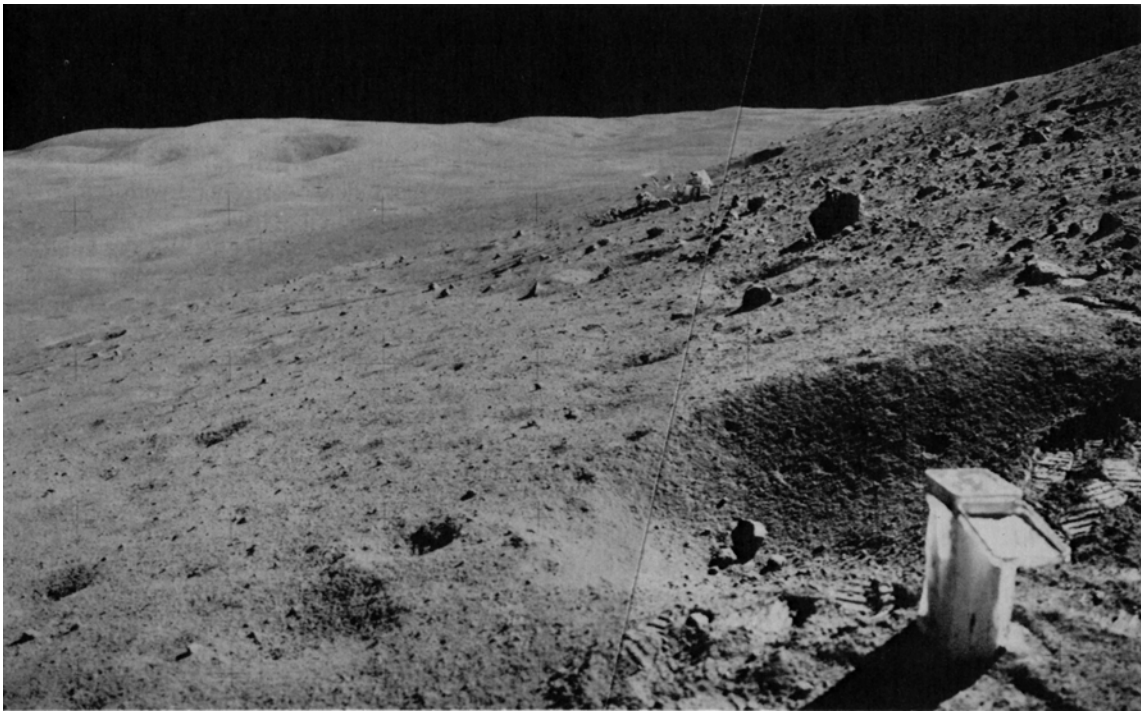


Fig. 3.4. The lunar roving vehicle (LRV), parked below a boulder field on Stone Mountain at the Apollo 16 site (NASA Photos AS16-107-17472 and -17473). The LRV was parked in a small crater to keep it from rolling downhill. Many of the larger boulders are about the size of the tires on the LRV (80-cm diameter). A sample collection container is in the foreground.

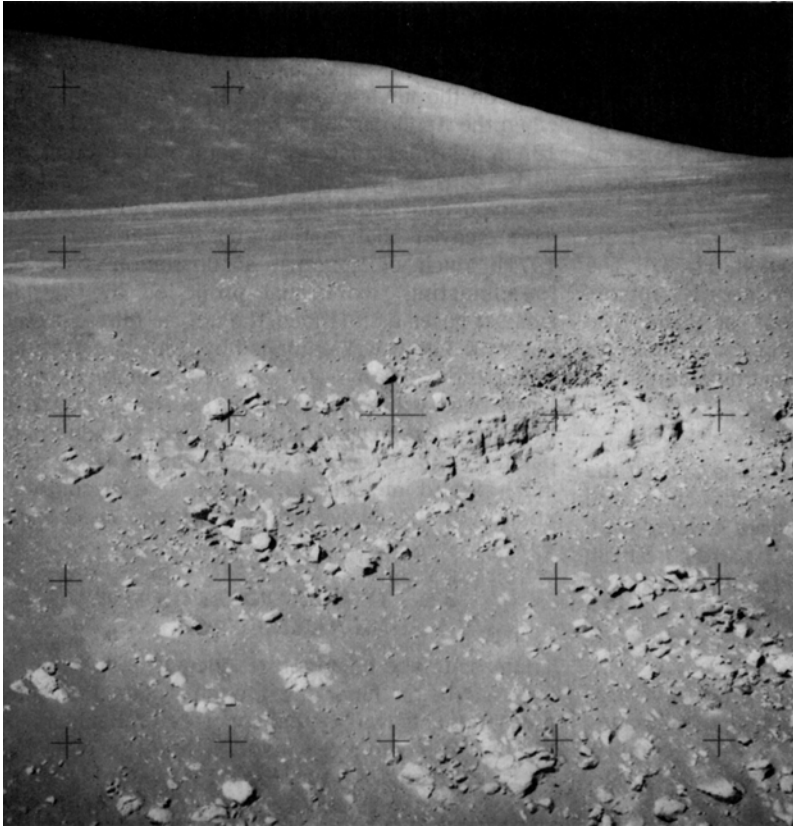


Fig. 3.5. Telephoto view of out-crops of mare lava flows in Hadley Rille at the Apollo 15 landing site (NASA Photo AS15-89-12116). Both massive and thin-bedded lava flows can be seen. The massive flows have well-developed columnar jointing; some of the thin-bedded layers are less than 1 m thick. For scale, the largest boulders in the rille wall are 8 to 10 m in diameter.

geologic and physiographic diversity. The landing was on an embayment of mare lavas that projects into high mountains.

The Apennine Mountains are a chain of rectangular fault blocks that rise 2 to 5 km above the mare surface, rivaling in height many of the mountains of the Earth (Swann *et al.*, 1972). Slopes on these massifs range from $>30^\circ$ on Mount Hadley to 26° on the western flank of Hadley Delta. The steep massifs grade toward the east into low hummocky hills and to the west into a line of hills across a band of mare lava. Numerous “passes” separate these fault blocks and some have been flooded by mare lavas.

The major physiographic feature of this site that would present an obstacle to travel is Hadley Rille. It is 1500 m wide, 400 m deep, and 100 km long. The mare surface slopes gently toward the rille and the regolith is thinner; this is one of the few locations where astronauts came close to sampling bedrock from below the regolith. The rille walls have slope angles of 25° to 30° . There are discontinuous outcrops 35 m to 60 m below the rille rim to the top of talus deposits that partly fill it (Fig. 3.5).

Apollo 17. The last Apollo mission to the Moon visited an area that is physiographically similar to

that visited by the Apollo 15 crew: a basin margin where large, steep-sided massifs are bounded by narrow valleys flooded with mare basalt flows. Taurus-Littrow Valley is flanked by 2000- and 2300-m-high massifs with average slopes of 25° (Schmitt and Cernan, 1973). Many of the craters are buried by regolith emplaced during mass wasting; large (>10 m) boulders have rolled down the slopes of the massifs, leaving visible trails up to 2 km long (Mitchell *et al.*, 1973a). Adjacent to the massifs are low, rounded hills referred to as the “sculptured hills,” which are believed to be a separate physiographic province within the highland terrains (Muehlberger *et al.*, 1973). The upper slopes of these hills are 20° to 27° . Below a visible slope change and change in albedo, slopes range from 15° to 20° .

The Apollo 17 area is covered with craters representing a full spectrum of sizes and ages (maturities) (see Chapter 4 for crater descriptions). The valley floor is nearly flat, sloping 1° toward the east. It is, of course, broken by craters, especially by several crater clusters that may be groups of secondary craters (craters formed by lunar fragments ejected from a primary crater, rather than by meteoritic or cometary impacts). It is also partly

covered by a thin avalanche deposit from the South Massif; this deposit consists of fine-grained debris that obscures older craters. The eastern end of the valley is cut by a fault scarp up to 80 m high. This scarp is generally broken into a pair of subdued steps (Muehlberger *et al.*, 1973). Further north, the scarp changes to an irregular wrinkle ridge and is dome-shaped in cross-section.

The contrast between prelanding terrain and the terrain at mission's end is shown in Fig. 3.6. The vehicle tracks and footprints will probably remain visible for hundreds of thousands of years. The equipment left behind will remain for millions of years under the slow battering of micrometeoroids.

3.3.5. Other Parts of the Moon

Parts of the Moon visited by humans and by the unmanned landers, including Surveyor, Luna, and Lunokhod, all have cratered surfaces covered with loose regolith. The most common hazards are fresh craters with steep walls and boulder-strewn rims. In general, the surface can be traversed easily, although diligence will be required to avoid random blocks, fresh craters, and rilles.

We can only infer the nature of the terrain in large craters like Copernicus from Lunar Orbiter images. Traverses may be possible through the complex blocky hills of the central uplift and across crater walls, but little detail will be available until lunar exploration is resumed.

3.4. DUST

"After lunar liftoff... a great quantity of dust floated free within the cabin. This dust made breathing without the helmet difficult, and enough particles were present in the cabin atmosphere to affect our vision. The use of a whisk broom prior to ingress would probably not be satisfactory in solving the dust problem, because the dust tends to rub deeper into the garment rather than to brush off" (Bean *et al.*, 1970).

The lunar regolith has grain-size characteristics similar to a silty sand, with mean grain sizes mostly between 45 to 100 μm (Chapter 7). Many of the grains are sharp and glassy; analogies have been made to fine-grained slag or terrestrial volcanic ash. This fine material has very low electrical conductivity and dielectric losses, permitting accumulation of electrostatic charge under ultraviolet (UV) irradiation. The sharp gradient in UV flux across the solar terminator (the boundary between day and night) may generate clouds of electrostatically-supported dust and set them into motion as the terminator moves across the Moon (section 9.2.1 discusses this process in more detail).

Dust accumulation and adhesion to equipment was demonstrated by the examination and recovery of parts from the Surveyor 3 robot lander, which had been on the lunar surface for two and a half years when the Apollo 12 lunar module (LM) landed about 183 m away. Discoloration of painted and aluminum parts, caused by solar irradiation, was found as expected. Dust accumulation and adhesion, however, were heavier than anticipated (Carroll and Blair, 1971). Much of the dust accumulation indicated "sandblasting" from dust propelled by the LM exhaust gases as it landed; the optical mirror on the Surveyor 3 craft was damaged by dust accumulation and pitting. Clearly, any exposed equipment at a lunar base will have to be protected or removed from landing areas. Soil was found to adhere to painted surfaces with a strength of about 10^4 dynes/cm², and to metallic surfaces with a strength of about 2 to 3×10^3 dynes/cm² (Scott and Zuckerman, 1971).

3.5. TEMPERATURES ON THE LUNAR SURFACE

Lunar surface temperatures increase about 280 K from just before lunar dawn to lunar noon. Heat flow measurements within the upper several meters of the lunar regolith were made at the Apollo 15 and 17 sites (Langseth *et al.*, 1973), where surface temperatures were also monitored by thermocouples in cables placed several centimeters above the lunar surface. At the Apollo 15 site (26°N, 3.6°E), the maximum temperature was 374 K (101°C) with a minimum of 92 K (-181°C). Temperatures at the Apollo 17 site (20°N, 30.6°E) were about 10° higher (Langseth and Keihm, 1977). These observed temperatures are quite close to those determined by Earth-based instruments (maximum = 390 K, minimum = 104 K; Glasstone, 1965).

The temperature at lunar noon varies throughout the year because of varying distance from the sun. The noon temperature increases about 6 K from aphelion to perihelion (Langseth *et al.*, 1973).

Langseth and Keihm (1977) describe a large difference in mean temperature (i.e., the temperature averaged over a complete day-night cycle) just below the lunar surface. At the Apollo 15 site, the mean temperature at a depth of 35 cm is 45 K higher than that of the surface; at the Apollo 17 site, the difference is 40 K. This increase in the mean temperature is related mostly to the temperature dependence of thermal conductivity of the topmost 1 to 2 cm of lunar soil.

Estimated average surface temperatures and temperature extremes for different areas of the Moon were made by the Lunar Colony Study Group (see Dalton and Hoffman, 1972) and are presented in

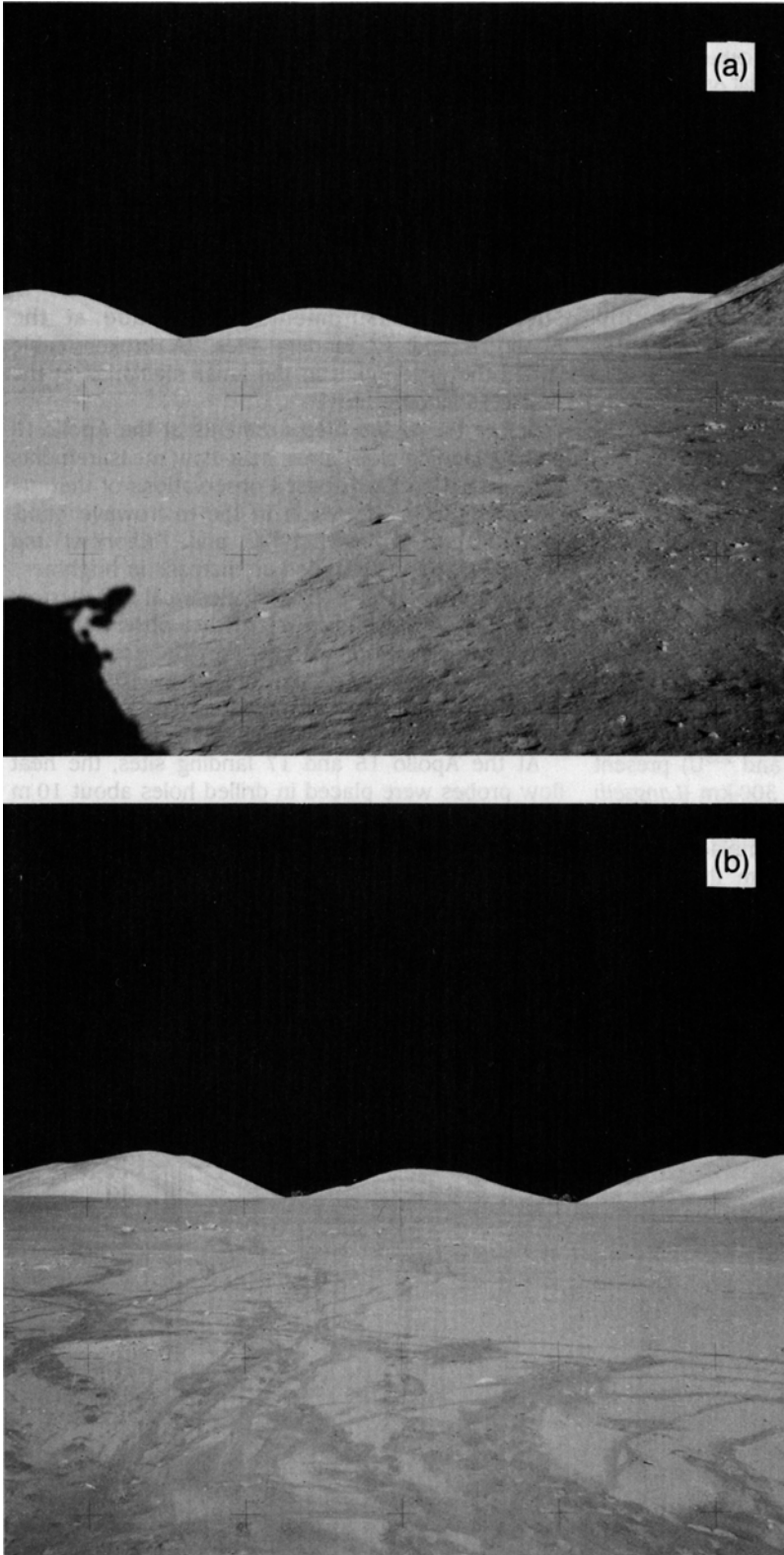


Fig. 3.6. The Apollo 17 landing site **(a)** before (NASA Photo AS17-147-22470) and **(b)** after (NASA Photo AS17-145-22200) the astronaut movements near the lunar module. Note the distribution of tracks and footprints that will remain visible for hundreds of thousands of years. The mountain on the left is 11 km away and 1 km high.

TABLE 3.2. Estimated lunar surface temperatures.

	Shaded Polar Craters	Other Polar Areas	Front Equatorial	Back Equatorial	Limb Equatorial	Typical Mid-Latitudes
Average temp.	40 K(?)	220 K	254 K	256 K*	255 K	220 < T < 255 K
Monthly range	none	±10 K†	±140 K	±140 K	±140 K	±110 K

* The farside of the Moon is closer to the sun at noon than the nearside is, so it gets ≈1% more solar energy.

† Average temperature has a yearly variation that makes it very cold ($T < 200$ K) for several weeks.

Table 3.2, along with the estimated very cold temperatures likely to prevail in permanently shadowed polar craters (*J. D. Burke, 1985*). The Lunar Colony Study Group also studied possible temperature variations within craters of lower latitudes and found that the crater floors may be a few degrees warmer than the walls and outer slopes. This has since been verified by thermal infrared mapping (see section 9.2).

3.6. LUNAR HEAT FLOW

The Moon is a small planetary body, and there is good reason to believe that it has lost most of its initial heat during its 4.6-b.y. history. Most of the present heat flux is probably generated by radioisotopes (mainly ^{40}K , ^{232}Th , ^{235}U , and ^{238}U) present in the interior to a depth of about 300 km (*Langseth and Keihm, 1977*). During the Apollo 15, 16, and 17 missions, heat-flow probes were emplaced in the holes left after extracting cores from the regolith.

Successful measurements were made at the Apollo 15 and 17 landing sites. (A broken cable ended the experiment in the lunar highlands at the Apollo 16 landing site.)

Before the *in situ* measurements at the Apollo 15 and 17 landing sites, lunar heat-flow measurements were based on Earth-based observations of thermal emissions from the Moon in the microwave band. *Krotikov and Troitsky (1964)* and *Tikhonova and Troitsky (1969)* determined an increase in brightness temperature of $0.6^\circ/\text{cm}$. Using electrical and thermal properties deduced from microwave observations in the 1-mm to 3-cm range, they interpreted this gradient in terms of a heat flow of $3 \times 10^{-6} \text{ W/cm}^2$ to $4 \times 10^{-6} \text{ W/cm}^2$. This estimated heat flow is very close to that actually measured on the Moon.

At the Apollo 15 and 17 landing sites, the heat flow probes were placed in drilled holes about 10 m apart (*Fig. 3.7*). Dual probes enabled two independent measurements of heat flow and measurement of the lateral variation of heat flow within the regolith. Each

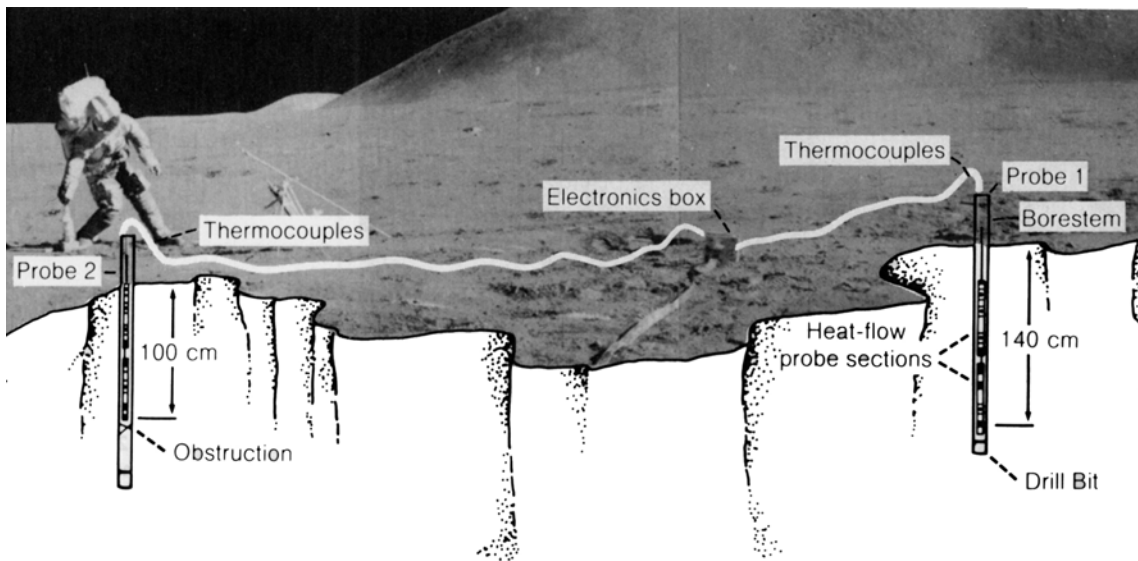


Fig. 3.7. Diagram showing emplacement of lunar heat-flow probes at the Apollo 15 landing site (from *Langseth et al., 1972*).

probe had two nearly identical 50-cm-long sections; each section had two differential thermometers (accuracy ± 0.001 K) that measured temperature differences between points separated by about 47 cm and 28 cm (gradient bridge and ring bridge spacings, respectively; see Fig. 3.8). Measurements of absolute temperature could be made at four points on each probe (Langseth *et al.*, 1972). Additional temperature measurements were made by four thermocouple units in the cables that connected the probes to the central station. Conductivity measurements were made by means of heaters surrounding each of eight gradient-bridge sensors. A heater was energized at 0.002 W and the temperature rise of the underlying gradient sensor recorded as a function of time for a period of 36 hr. The temperature rise and rate of temperature rise was interpreted in terms of the conductivity of the surrounding lunar regolith.

3.6.1. Heat Flow at the Apollo 15 Landing Site

The Apollo 15 heat flow measurements were made in regolith developed on the mare surface 1.8 km east of Hadley Rille and about 4 km north of the base of the Apennine Massif (Hadley Delta). The regolith was sampled to a depth of 237 cm at this location and consists of 42 textural units of mostly fine-grained lunar soil (Heiken *et al.*, 1973). The first probe was inserted to a depth of 1.4 m and the second probe to a depth of 1.0 m; the original planned depth of 3 m could not be reached because of difficult drilling conditions (Langseth *et al.*, 1972).

The subsurface measurements indicated that conductivity must increase substantially with depth, and values of 1.5×10^{-4} W/cm K are found at a depth of 1 m; this increase correlates well with increasing bulk soil density with depth (Chapter 9).

At Hadley Rille, both the rille and the Apennine Front should affect the heat flow, but in opposite ways; both effects are about 5% and thus appear to be self-canceling. The best value for heat flow at this site is an uncorrected value of 3.1×10^{-6} W/cm², with an uncertainty of $\pm 20\%$.

3.6.2. Heat Flow at the Apollo 17 Landing Site

The heat flow experiment at Apollo 17 was located about 200 m west of the landing site and 9 m north of the ASLEP (Apollo Lunar Scientific Experiments Package) on the floor of the Taurus-Littrow Valley. The valley floor consists of irregular, heavily cratered regolith developed on lava flows that partly fill an embayment between 2-km-high massifs; the valley is about 8 km wide at this point. A 400-m-diameter crater is located within 500 m of the heat flow probes. The regolith, sampled to a depth of 292 cm, consists of interbedded fine- to coarse-grained lunar

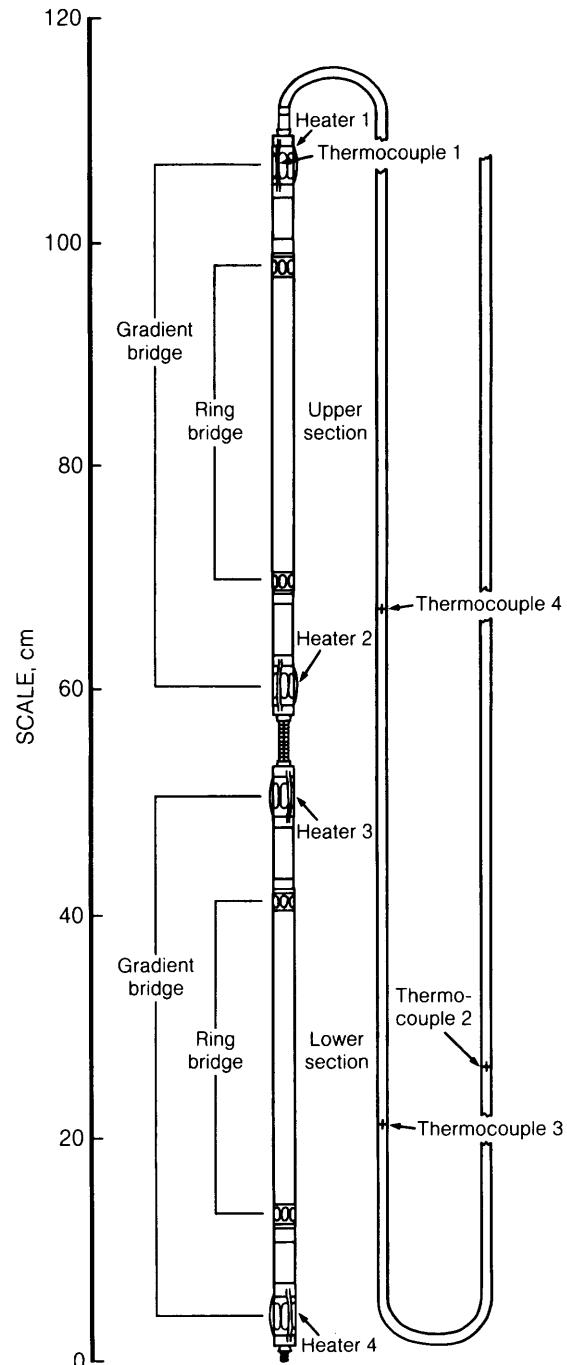


Fig. 3.8. Diagram of a lunar heat-flow probe (after Langseth *et al.*, 1972). Differential thermometers measured temperature differences between gradient bridge and ring bridge spacings in each section. Surface temperature measurements were made by thermocouples in the connecting cable. Activation of the heaters allowed measurement of conductivity.

soil layers. The heat-flow probes were about 11 m apart and emplaced to depths of 2.36 m (probe 1) and 2.3 m (probe 2).

Thermal conductivity measured by the Apollo 17 heat-flow probes ranged from 1.72 to 2.95×10^{-4} W/cm K $\pm 20\%$ (Langseth et al., 1973). This range is related to the bulk density of the regolith. At this site heat flow appeared to be uniform over the probe lengths, with an overall value of 2.8×10^{-6} W/cm² (probe 1) and 2.5×10^{-6} W/cm² (probe 2). The large massifs flanking the Taurus-Littrow Valley have a significant effect on the heat flow. It is estimated that a correction of -15% to -20% should be applied; the resulting best heat flow value is 2.2×10^{-6} W/cm² $\pm 20\%$.

3.6.3. Conclusions

The upper 1 to 2 cm of lunar regolith must have extremely low thermal conductivities (1.5×10^{-5} W/cm²), with conductivity increasing 5 to 7 times at a depth of 2 cm. At the Apollo sites, mean temperatures 35 cm below the lunar surface are 40 to 45 K above those at the surface. This is primarily related to the temperature dependence of thermal conductivity in the topmost 1 to 2 cm of lunar regolith

(Langseth and Keihm, 1977). Thermometers buried 80 cm below the lunar surface show no perceptible variation in temperature related to the lunar day/night temperature cycle. Below these depths, thermal gradients should reflect heat flow from the lunar crust. Figure 3.9 shows the relationship between near-surface day/night temperature fluctuations superimposed on the steady heat-flow profiles in the regolith. It is noteworthy that an insulating blanket of only about 30 cm of regolith is sufficient to dampen out the ~ 280 K lunar surface temperature fluctuation to ± 3 K variation. This indicates that a lunar habitation buried beneath a thick regolith radiation shield will not be subjected to monthly temperature extremes, but rather will have to find an efficient method for dissipating its waste heat.

The heat flow measured at two points on the lunar surface and estimated from microwave emission is 2 to 4×10^{-6} W/cm², about half that of the average heat flow for the Earth (6.3×10^{-6} W/cm²).

3.7. SEISMIC ACTIVITY

As a result of the Apollo Passive Seismic experiments, the release of seismic energy from the Moon is commonly assumed to be small, only $\sim 2 \times 10^{10}$

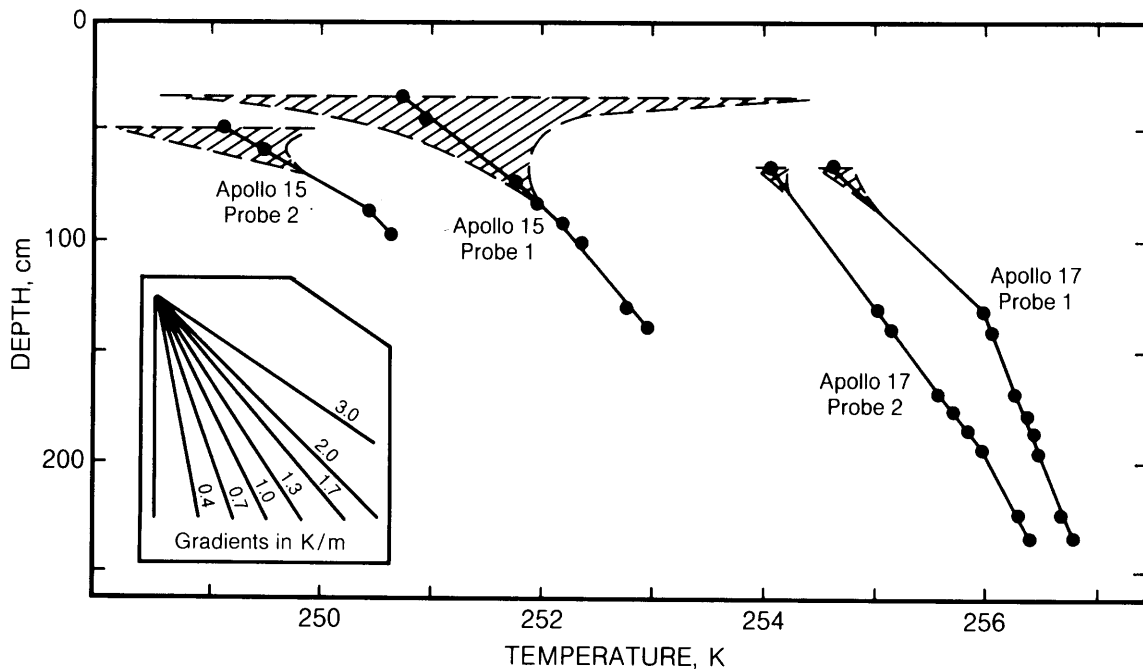


Fig. 3.9. Temperature fluctuations in the lunar regolith as a function of depth (after Langseth and Keihm, 1977). Note that the small temperature scale at the bottom of the diagram does not permit plotting of the extreme temperature fluctuations at depths less than ~ 30 cm; this region is left blank. Hatched areas show day-night temperature fluctuations below ~ 30 to 70 cm. Below ~ 50 cm there is essentially no temperature fluctuation due to the lunar day-night temperature cycles, and the steady temperature gradients recorded are due to internal lunar heat flow.

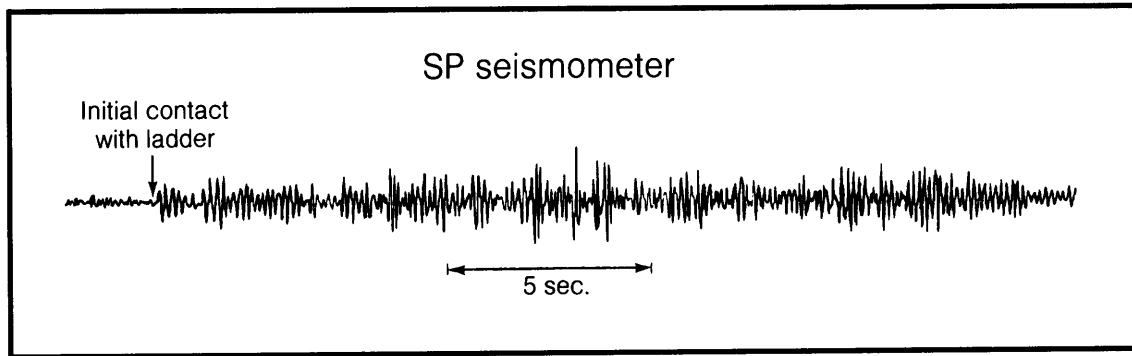


Fig. 3.10. The short-term (SP) seismometer could detect all of the Apollo 11 astronaut movements on the lunar surface. This figure shows the signal recorded by the SP seismometer, ~17 m away, as Neil Armstrong climbed the ladder of the lunar module (after *Latham et al.*, 1970c).

J/yr compared to Earth's 10^{17} to 10^{18} J/yr (e.g., *Goins et al.*, 1980). This is the lower value listed in Table 3.1. Note, however, that larger but rarer moonquakes may not have occurred during the eight years of lunar seismic monitoring, and the actual average lunar seismic energy could be as high as 10^{14} J/yr (*Nakamura*, 1980); this is the queried higher value in Table 3.1. In either case, the Moon's low seismic activity, coupled with extremely low elastic wave propagation losses (e.g., low attenuation, sometimes referred to as "high Q"), means the Moon is an extremely quiet place, even though seismic events and the resulting elastic "sounds" carry for long distances through the rock and soil with great clarity. (Note that there is no sound transmission through the air as the atmosphere is too thin.) The Apollo 11 passive seismic instrument clearly recorded Astronaut Armstrong climbing the ladder into the LM (Fig. 3.10). This sensitivity to seismic energy because of low attenuation gave rise to the phrase "the Moon rings like a bell," as seen in the characteristically long seismic signatures of moonquakes and of meteoroid impacts on the Moon (Fig. 3.11).

Over the eight years of Apollo passive seismic recording, the largest recorded moonquakes have Earth-equivalent magnitudes of about 4. The sources of seismicity on the Moon include the monthly *deep-focus moonquakes* caused by Earth-Moon tidal stresses (sometimes appearing as moonquake swarms), a few stronger (but rarer) *shallow moonquakes* (also known as high-frequency teleseisms or "HFT") that may be due to tectonic processes, and *meteorite impacts* (*Hood et al.*, 1985; *Dorman et al.*, 1978; *Goins et al.*, 1978; *Latham et al.*, 1978; *Nakamura*, 1978). *Nakamura et al.* (1982) also distinguish some small *thermal moonquakes* that may be due to thermal degradation of young lunar

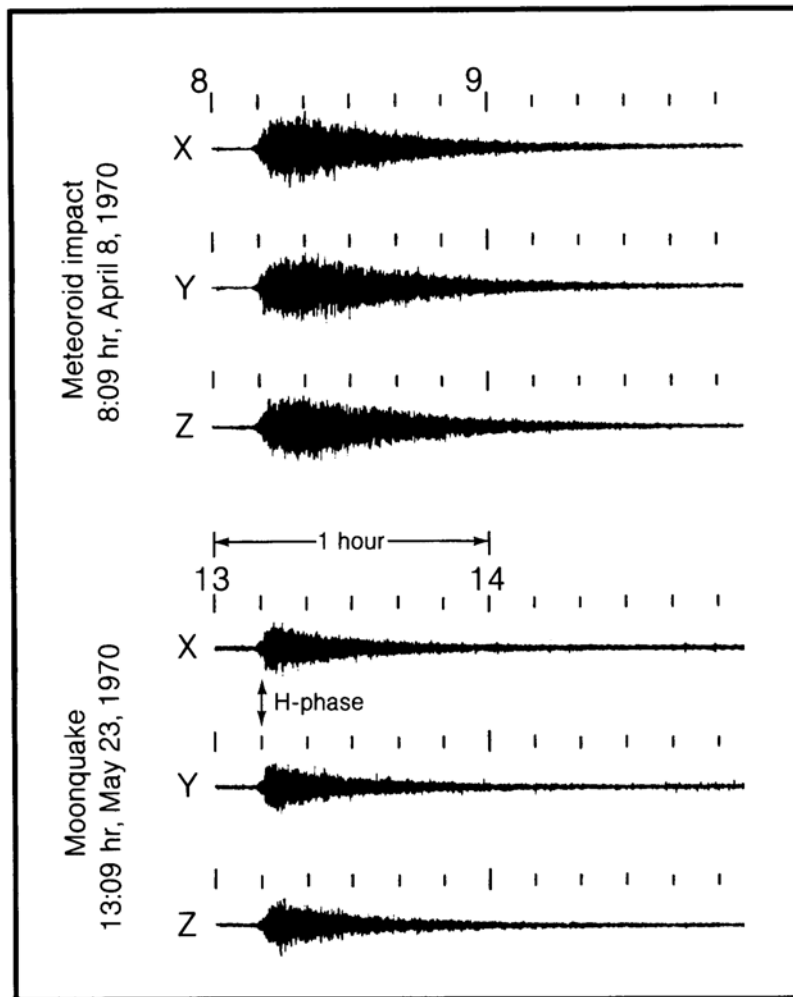
surface features (e.g., thermal cracking of fresh boulders around young craters). Although there were only about four or five shallow moonquakes per year during the period of lunar seismic monitoring, they account for most of the seismic energy released in the Moon (*Nakamura*, 1980). Table 3.3 lists the events recorded during the nearly eight years of seismic station operation during the Apollo program.

Seismic events due to meteoroid impact vary widely in energy. Meteoroid impacts of all energies tend to be most common when meteoroid showers peak (*Dorman et al.*, 1978), particularly among the largest meteoroid impacts that tend to occur in the months of April through July. The largest recorded impacts, in July 1972 and May 1975, represented meteoroids of about 5 t. In all, seven meteoroid impacts of 1 t or more were observed within five years during lunar seismic monitoring (*Latham et al.*, 1978; *Dorman et al.*, 1978). Major impacts are very rare (Chapter 4), but the effects can be widespread; for example, a major landslide visited at the Apollo 17 site in the northern hemisphere was probably caused by impact of debris from the crater Tycho (~100 m.y. old), which is some 2000 km away in the southern hemisphere (*Arvidson et al.*, 1976). Landslides or slumping of crater walls may be triggered seismically as well as by impact. Even though such events are rare it may be prudent to locate permanent lunar establishments away from potentially unstable slopes (section 9.1).

3.8. POLAR ENVIRONMENT

The Apollo missions and most of the Lunar Orbiter missions concentrated on the equatorial regions of the Moon, leaving the poles little better known than in the pre-Apollo era. Image resolution by Lunar Orbiter 4 was only ~100 m at the poles; also, many

Fig. 3.11. Natural seismic activity on the Moon. Top: probable meteoroid impact of April 8, 1970; bottom: moonquake of May 23, 1970, with probable focal depth of 800 km. Such deep moonquakes have monthly cycles and are apparently due to tidal forces. One difference between the moonquake and the meteoroid impact is the presence of a distinct "H-phase," recorded as a primarily horizontal (X,Y) motion, suggesting a shear-wave mechanism (after *Latham et al.*, 1972). The Z motion is vertical.



features in the polar areas were obscured by shadows. Much of the speculation about environmental conditions at the poles has been summarized by *J. D. Burke* (1985).

The very small inclination of the Moon's equator to the ecliptic ($1^{\circ}32'$; see Fig. A3.2) leads to the most interesting of these speculations, that there may be ice preserved in permanently shadowed craters or valleys where surface and subsurface temperatures may be relatively constant and as low as 40 K. Debate over the presence or absence of lunar polar ice has developed over several years; summaries of the problems involved (reradiated sunlight, solar wind sputtering, and whether ice can be protected by regolith blankets) are given by *Arnold* (1987) and by *Svitek and Murray* (1988). Similarly, there may be elevated "mountains of perpetual light" at the poles, which could serve as sites for continuous solar

power collection. However, the combination of rough terrain plus the slight but not insignificant inclination of the Moon's spin axis makes such features unlikely. If nothing else, our ignorance of the lunar poles should spur future exploration.

3.9. ATMOSPHERE

The lunar atmosphere is extremely tenuous. The undisturbed gas concentration is only about 2×10^5 molecules/cm³ during the lunar night, falling to perhaps 10^4 molecules/cm³ during the lunar day (*Hodges et al.*, 1975). This is about 14 orders of magnitude less than Earth's atmosphere, a difference so extreme that the Moon is often said to have no atmosphere at all—a misstatement that arises from the terrestrial perspective. Much of our present understanding of the lunar atmosphere is based on

TABLE 3.3. Summary of the Apollo passive seismic experiment data (after *Latham et al., 1978*).

<i>Period of Observation</i>		
1 station (July-Aug., Nov. 1969 - Feb. 1971)		1.27 yr
2 stations (Feb. 1971 - July 1971)		0.48 yr
3 stations (July 1971 - Apr. 1972)		0.73 yr
4 stations (Apr. 1972 - Sept. 1977)		5.44 yr
Total		7.92 yr
<i>Number of Seismic Events Detected</i>		
	Total*	Major Events†
Artificial impacts	9	5
Meteoroid impacts	1700‡	95
Shallow moonquakes (HFT)	32‡	7
Deep moonquakes		
confirmed	973‡	9
unconfirmed	1800‡	2
Unclassified events	7300‡	0
Total	11,800‡	118

* The total does not include signals detected only by the short-period seismometers of each station, or the large number of signals detected by the Apollo 16 station only.

† "Major events" are those signals with amplitude >10 mm at two or more stations.

‡ These numbers represent estimated data as compiled by *Latham et al. (1978)*. Final numbers of 1743 meteoroid impacts, 28 shallow moonquakes, 3145 deep moonquakes, and 7633 unclassified events are given by *Nakamura et al. (1982)*.

theory, not because the instruments deployed during the Apollo missions were inadequate (they were in fact extremely accurate and sensitive) but rather because the gases released during the missions flooded the data. This problem is easy to visualize when it is considered that the total ambient lunar atmosphere is only about 10^4 kg, and each Apollo landing released as much gas while on the Moon (*Vondrak, 1974*). The six Apollo landings delivered six times as much gas to the lunar surface as there is in the ambient atmosphere.

3.9.1. Contamination

The results of the Cold Cathode Gage experiments in Apollo missions 12, 14, and 15 clearly show the ease with which the ephemeral lunar atmosphere is contaminated (*Johnson et al., 1970, 1972*). These gages were extremely sensitive, and were easily driven off-scale by the waste gas clouds emitted from the astronauts whenever they approached within a few meters of the experiment. Contamination remained evident long after the astronauts left.

Figure 3.12 shows the fluctuation of gas concentration at the Apollo 14 landing site for 10 lunar days (about three-quarters of a year) following the landing. Discontinuities in the curves shown are due to periods when the instrument was turned off for fear of high-voltage arcing, and days 6 through 8 are not shown because they would clutter the diagram between days 5 and 9. At the first lunar day

after the astronauts left (day 2), there was a sharp rise in gas concentration as the area around the landing site was heated up. This suggests that a large amount (perhaps 10%) of the lunar module exhaust gas (a mixture of about 20% H₂O with a wide variety of C-H-O-N species; *Freeman et al., 1972*) was adsorbed onto the lunar surface during the first lunar night after the astronauts departed, to be released rapidly as the sun rose again. These adsorbed gases were probably widely scattered, because the adsorptive capacity of lunar soil is low (10^{-4} to 10^{-5} g gas/g soil) and lunar rocks are 10 to 100 times less adsorptive than soil (*Vondrak, 1974*). Release profiles for the subsequent lunar days probably reflect losses from both the lunar module and the contaminated equipment and regolith. These later losses appear to be very long-lived, with a time constant of about three or four months.

A miniature mass spectrometer, the Lunar Atmospheric Composition Experiment (LACE), was placed in the Taurus-Littrow Valley during the last Apollo landing (Apollo 17). This instrument was able to show that helium, neon, and argon are native to the lunar atmosphere. Hydrogen is also native, but the hydrogen data were swamped by contamination (*Hoffman et al., 1973*). Contamination makes interpretation of the data difficult, but much effort has been put into this interpretation and we now have a reasonably good understanding of what the lunar atmosphere contains.

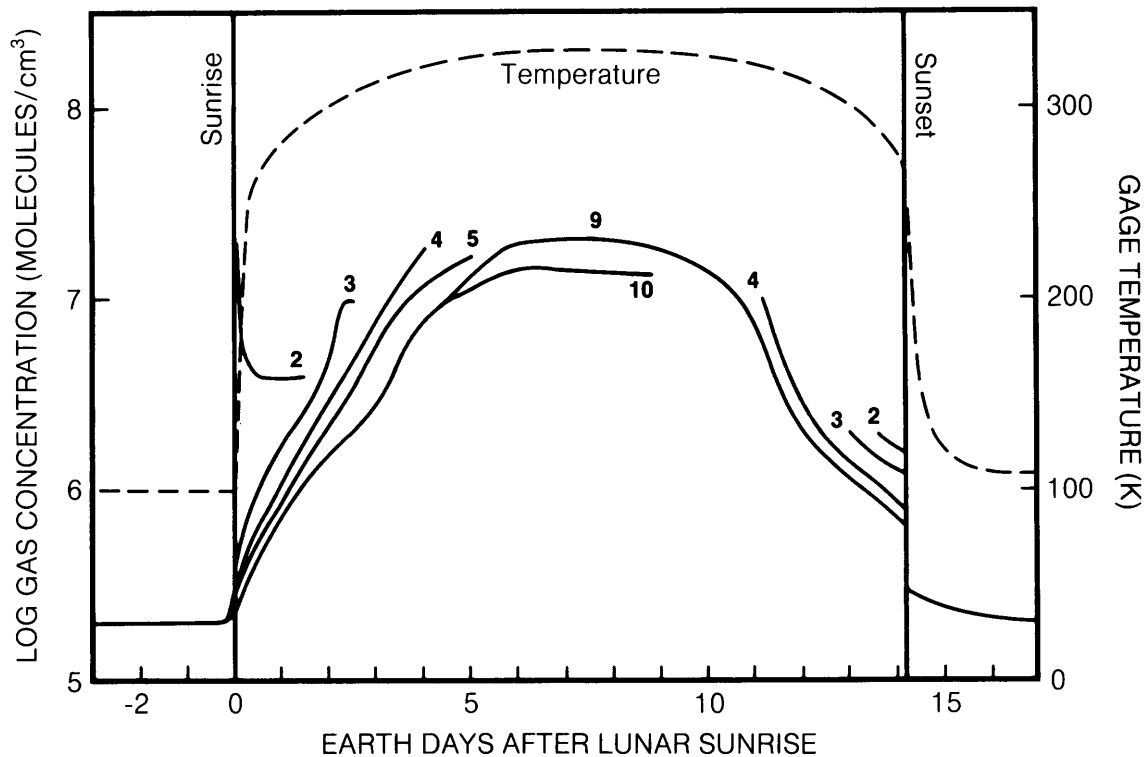


Fig. 3.12. Variation in total gas concentration (molecules/cm³) in the near-surface atmosphere at the Apollo 14 landing site, over nine lunar days (curves numbered 2 to 10) following the Apollo 14 landing (counting day 1 as the day of the landing, when no data were obtained). Surges in gas concentration during the lunar daytime are not a feature of the undisturbed lunar environment (see Fig. 3.13); these daytime gas surges are due to the solar heating of soil and equipment at the landing site with resulting contaminant gas release. To avoid crowding, days 6 to 8 are not shown; these curves fall between those for days 5 and 9. Data were not collected through a full day cycle until day 9, for fear of high voltage arcing at midday temperatures. The monthly temperature cycle is also plotted (after *Johnson et al.*, 1972).

3.9.2. The Real Lunar Atmosphere

The major constituents of the ambient lunar atmosphere are neon, hydrogen, helium, and argon. Neon and hydrogen are derived from the solar wind. Helium is mostly derived from the solar wind, but ~10% may be radiogenic and lunar in origin (*Hodges*, 1975). Argon is mostly ⁴⁰Ar that is derived from the radioactive decay of lunar ⁴⁰K (only about 10% of the argon is ³⁶Ar of solar wind origin). Table 3.4 lists the most probable abundances of these and a few other species in the undisturbed lunar atmosphere.

The numbers listed in Table 3.4 are subject to several causes of both variability and unreliability. First, the contamination problem is particularly severe for the daytime gas determinations. Second, the variability in abundance of the impinging solar wind will affect the solar-wind species. Gases escape thermally (H₂, He) or they are ionized and lost (Ne, Ar) within about four months (10⁷ sec; *Johnson et al.*,

1972; *Hodges et al.*, 1974); these processes allow recycling of the lunar solar-wind atmosphere within weeks to months. Third, the lunar day-night temperature differential becomes smaller at higher latitudes, resulting in smaller differences between daytime and nighttime atmospheres as the poles are approached. The fluctuations correlative with latitude are summarized for the four most abundant atmosphere species (²⁰Ne, He, H₂, and ⁴⁰Ar) in Fig. 3.13. The Apollo 17 LACE data for He and ⁴⁰Ar used for this figure are particularly well constrained; the data for ²⁰Ne and H₂ are less precise.

Both Table 3.4 and Fig. 3.13 show a major distinction in the behavior of argon compared to the lighter simple gases. Argon abundances in the atmosphere drop rather than rise during the lunar night, and do so rather gradually. This is because argon is a condensable gas at lunar nighttime temperatures, whereas neon, helium, and hydrogen are not. The complex C-H-O-N gases are also

condensable and follow argon in behavior. Note that the noncondensable gases (Ne, He, H₂) increase in concentration by night, and decrease by day; this is because the noncondensable gas concentrations vary as an inverse power of surface temperature ($T^{-5/2}$; Hodges *et al.*, 1974), resulting in their concentration on the night side. As found in the Cold Cathode Gage experiments of Apollo 12, 14, and 15, the lunar module contaminant gases are almost completely condensable (Fig. 3.12).

3.9.3. The Past and Future of the Lunar Atmosphere

On Earth, Precambrian rocks (especially those rocks older than about 1200 m.y.) provide evidence of major changes in the chemical composition of earlier terrestrial atmospheres. In contrast, there is little in the lunar geologic record to provide detailed evidence for any variation in the Moon's past atmosphere. There has been some speculation,

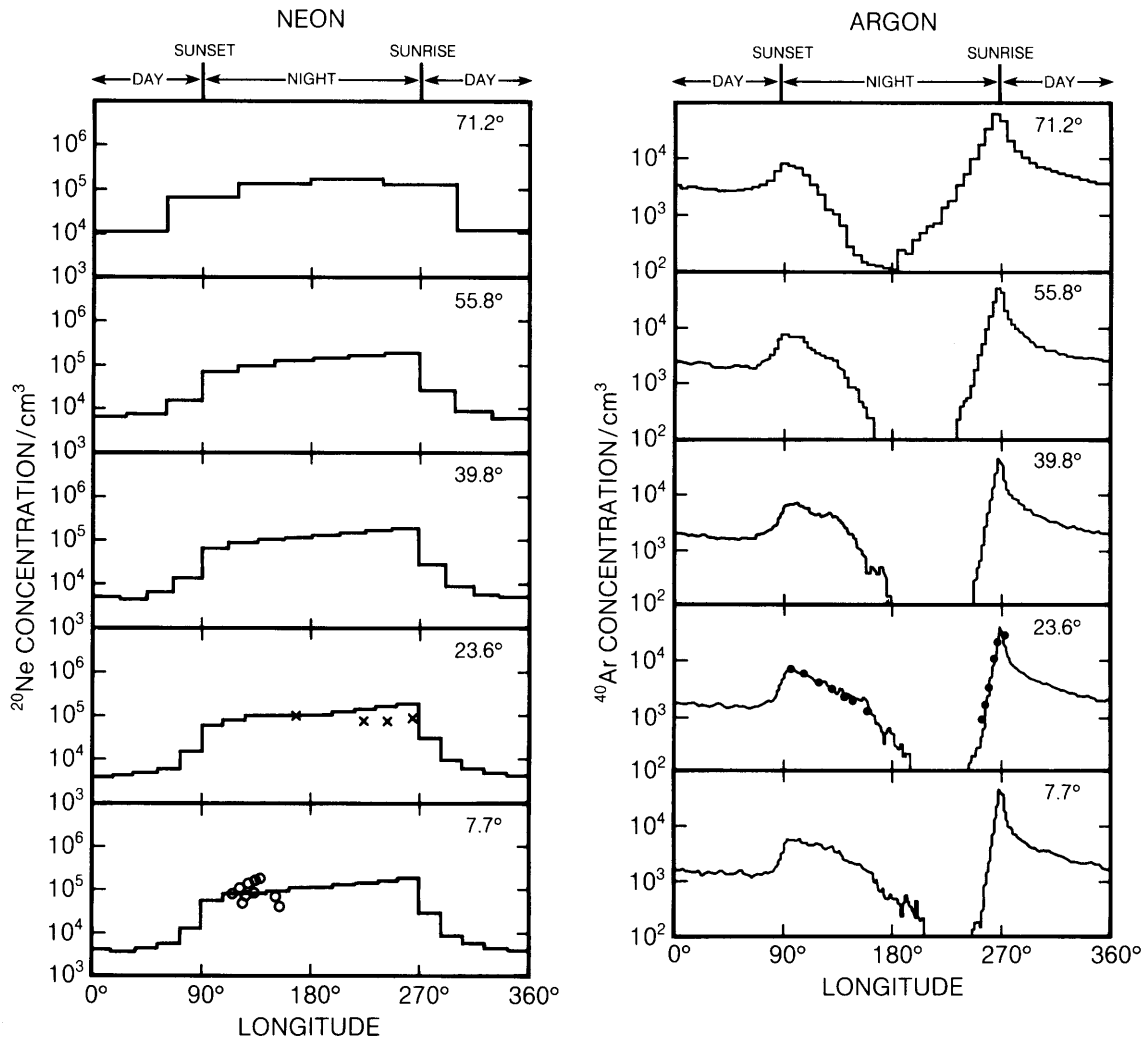


Fig. 3.13. Calculated variations in abundances of the four principal lunar atmospheric gases over day/night cycles at five latitudes (circumferential bands at 7.7°, 23.6°, 39.8°, 55.8°, and 71.2° away from the equator). The day/night cycle is depicted with sunrise at 270° long., the subsolar point at 0° (or 360°), and sunset at 90°. The calculated ²⁰Ne gas concentrations at 7.7° and 23.6° lat. are compared with actual data from Apollo 16 and Apollo 17, respectively; the calculated ⁴⁰Ar concentration at 23.6° is compared with the Apollo 17 data. Line thicknesses for He and H₂ allow for ±5°C uncertainty in the nighttime temperature (after Hodges *et al.*, 1974).

however, that the lunar atmosphere may have been about 5×10^7 times as massive as it presently is at some time in the past 10^8 years. This speculation is based mostly on an apparent lack of some micrometeoroid effects in buried soils, leading to a model that calls for a thicker atmosphere to screen out impactors in the 10^{-7} to 10^{-11} g range (Chernyak, 1978; Hughes, 1978).

Much more certain are the possible effects of large-scale human operations on the lunar surface. Irreversible pollution of the lunar atmosphere is a real possibility. Each Apollo mission left behind a mass of gases equivalent to the ambient lunar atmosphere; many of these gases have large molecular weights and are condensable. Some of the

Apollo gases may prove to be particularly pernicious, and permanent pollution may already have occurred.

Vondrak (1974) points out that most gases are presently removed from the lunar atmosphere through ionization from interaction with the solar wind and the interplanetary electric field. Thermal escape (heating to escape velocity) is a much less significant process. However, if the lunar atmosphere were >100 times as massive as it presently is, the roles of these two processes would be reversed. At a total mass of about 10^7 to 10^8 kg these loss mechanisms would reach steady or declining rates and the Moon would obtain a long-lived atmosphere (Fig. 3.14). The Apollo missions did not cause such a drastic change, and even a small lunar base would

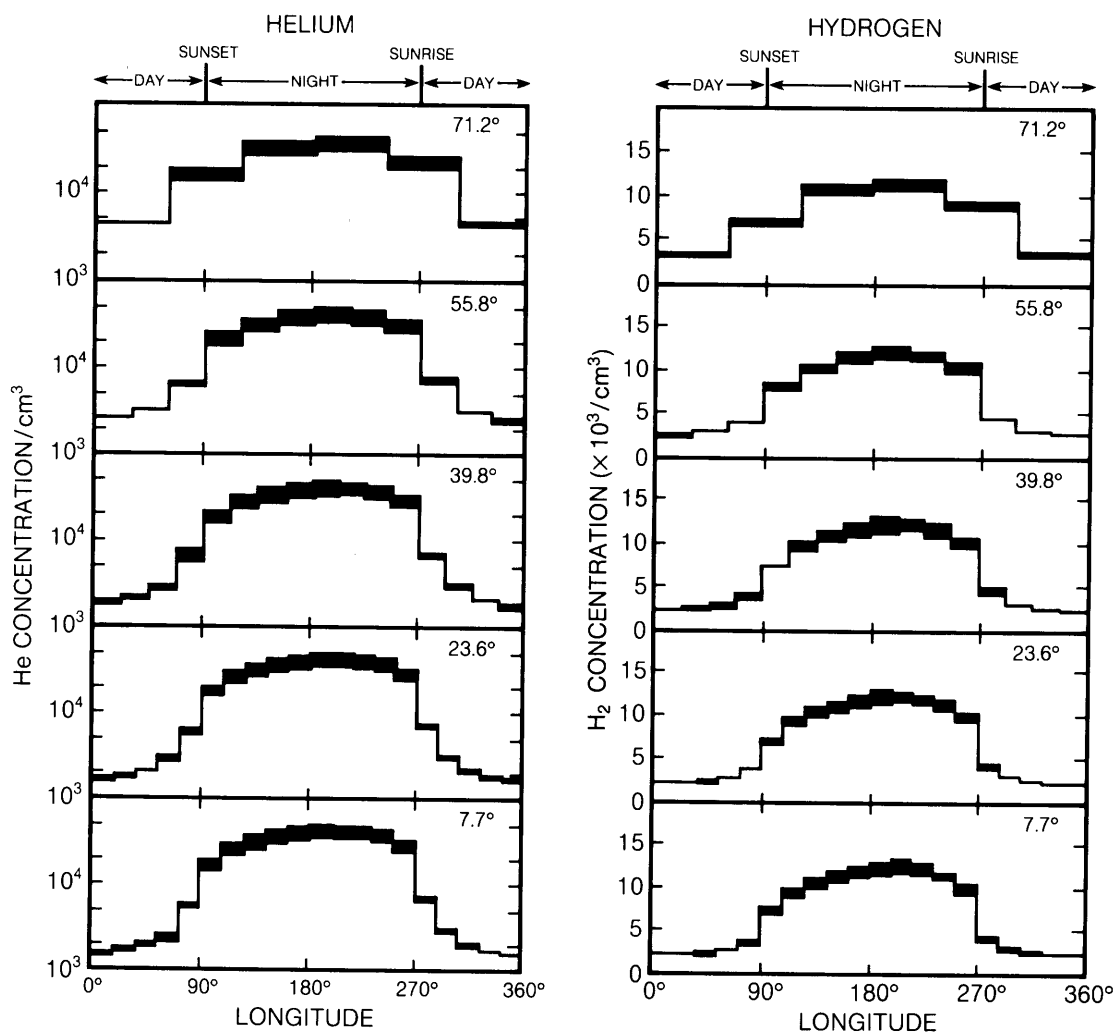


Fig. 3.13. (continued)

TABLE 3.4. Gas abundances and some scale heights in the lunar atmosphere.

	Abundances (molecules/cm ³)		Scale Heights*	
	Daytime	Nighttime	Daytime	Nighttime
²⁰ Ne	~4 × 10 ³ to 10 ⁴	10 ⁵	100 km	25 km
He	~8 × 10 ² -4.7 × 10 ³	4 to 7 × 10 ⁴	511 km	128 km
H ₂	~2.5-9.9 × 10 ³	10 ⁴ to 1.5 × 10 ⁵	1022 km	256 km
⁴⁰ Ar	~2 × 10 ³	to <10 ²	55 km	
CH ₄	~1.2 × 10 ³			
CO ₂	~10 ³			
NH ₃	~4 × 10 ²			
OH+H ₂ O	~0.5			

*"Scale height" refers to the altitude at which the amount of an atmospheric constituent drops to 1/e (0.368) of its surface abundance in an isothermal atmosphere.

Based on calculations reported in Hodges et al. (1974), Hodges (1973), Hoffman and Hodges (1975), Mukherjee (1975), and Johnson et al. (1972).

fall short of such a consequence; however, extensive lunar operations may be capable of releasing sufficient waste gases to create such an atmosphere. Vondrak (1974) suggests that any process producing more than 100 kg/sec of gas will produce a long-lived lunar atmosphere. He concludes his analysis with a summary of Kraft Ehrlicke's suggestion that buried 1 kt nuclear detonations might be used to create caverns of about 40 m diameter on the Moon, each cavern yielding about 10⁷ kg of oxygen. The problems of polluting the present lunar atmosphere would certainly be swamped by such a massive planetary manipulation. Any possible benefits of such

a project would have to be carefully weighed against the loss of a very unique high-vacuum environment, a loss that would produce a major degradation in many lunar-based science and engineering activities.

3.10. METEOROID BOMBARDMENT

The term "meteoroid" is used for a naturally occurring solid body, traveling through space, that is too small to be called an asteroid or a comet. Meteoroids with diameters less than about 1 mm (and hence with masses less than about 10⁻² g) are commonly classified as micrometeoroids. The suffix

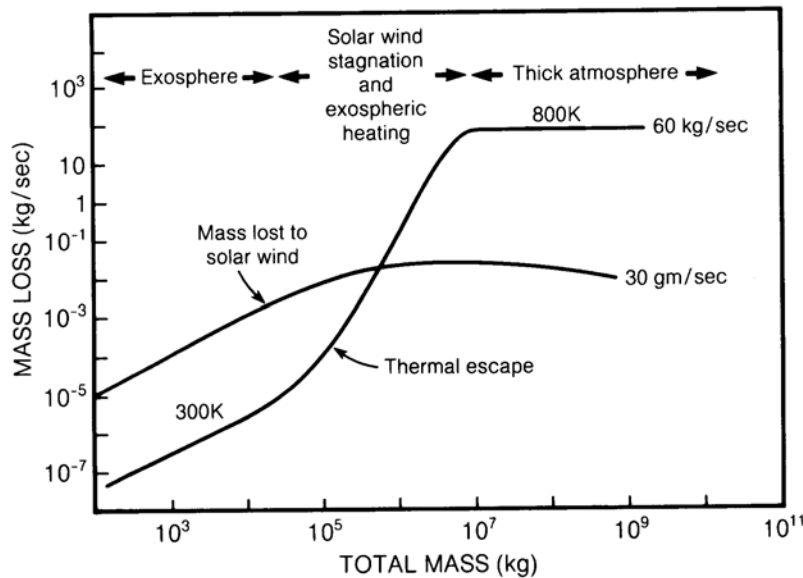


Fig. 3.14. Variations between thermal and electrostatic gas loss mechanisms as a function of lunar atmosphere mass (hypothetical; after Vondrak, 1974). A pure oxygen atmosphere (mass 16 amu) is assumed for this model; thermal escape gas losses from the thick atmosphere are probably overestimated because the model atmosphere is assumed to be isothermal. Relative gas temperatures for thermal escape at ~2 × 10³ kg and at ~10⁸ kg are shown.

“ite” (e.g., meteorite) is used for meteoroids that have fallen through an atmosphere and been recovered. However, the terms “meteorite” and “meteoroid” are often used generically as in, for example, the “meteorite complex.”

From the size and frequency distributions of meteoroids discussed in Chapter 4, it can be estimated that micrometeoroids of about milligram mass should be expected to strike lunar features as large as facilities and equipment almost yearly; impacts by smaller objects will be more frequent, and by larger objects more rare. Although much is known about the size-frequency distributions of meteoroids, the consequences of these objects for prolonged space missions are still poorly understood.

3.10.1. Meteoroid Velocities and Impact Rates

Direct measurements of meteoroid impact were obtained in the vicinity of the Moon by Lunar Orbiters 1 through 5 (Table 2.1). These orbiters were ringed by sets of pressurized semicylinders made of 0.025 mm metal with pressure-sensitive switches to record perforation by meteoroids. Data from the five orbiters, corrected for geometry and exposure orientation, suggest 0.16 perforations per m^2 per day (Gurtler and Grew, 1968). This is about half the perforation rate in comparable experiments flown on Explorer spacecraft in near-Earth orbit. Erickson (1969) suggests that this difference is related to an increase in meteoroid flux caused by the Earth’s gravitational attraction. In addition, the increase in velocity resulting from the Earth’s pull causes the near-Earth impacts to be more penetrating.

Meteoroid velocities have been measured near Earth by photographic and radar tracking. If corrected to constant meteoroid mass, the velocities of meteoroids at the Moon can be calculated to range from 13 to 18 km/sec (Zook, 1975). The meteoroid flux at the lunar surface shows a significant enhancement from small meteoroids ($<1 \mu m$) traveling toward the Moon from the sun and a somewhat lesser enhancement of large particles ($>1 \mu m$) arriving from the direction in which the Earth is traveling (Fechtig et al., 1974; Zook and Berg 1975; Oberst and Nakamura, 1986). Whichever side of the Moon is facing into the direction of the Earth’s motion in its orbit around the sun will be more exposed to the larger and more hazardous meteoroids (Gurtler and Grew, 1968).

3.10.2. Meteoroid Distributions in Lunar Orbit and on the Lunar Surface

The size distributions and frequencies of micrometeoroids are discussed in section 4.1.3 and shown in Fig. 4.14. The distribution shown in Fig. 4.14 is fairly

well defined as far as the spacecraft-collected data are concerned. Although there has been some suggestion that the meteoroid flux may be much higher on the lunar surface than it is in lunar orbit, such a variation has not been established (Fechtig et al., 1974). There are also indications that the present meteoroid flux, as measured by spacecraft, may be more than an order of magnitude higher than the time-averaged prehistoric flux calculated from impact microcraters on lunar samples (Hartung and Storzer, 1974; Cour-Palais, 1974; Grün et al., 1985). More data are needed to constrain the current and past meteoroid fluxes on the Moon.

3.10.3. Meteoroid Hazards

Meteoroids of about 10^{-6} g can produce craters of 500 μm diameter in metal. In most materials, depth of the crater will be comparable to or less than the diameter; however, fracturing effects in brittle materials may extend the damage to greater depth. Figure 3.15 shows the number of perforations per day that may be expected for a given thickness of Be-Cu metal as used in the spacecraft meteoroid detectors (Gurtler and Grew, 1968). Two to three millimeters of a tough composite material is relatively effective shielding against damage by micrometeoroids in the milligram mass range.

Although rarer, the impacts of larger meteoroids are a more significant hazard. For meteoroid masses of about 1 g, craters of centimeter scale and somewhat lesser depth are formed; the damage

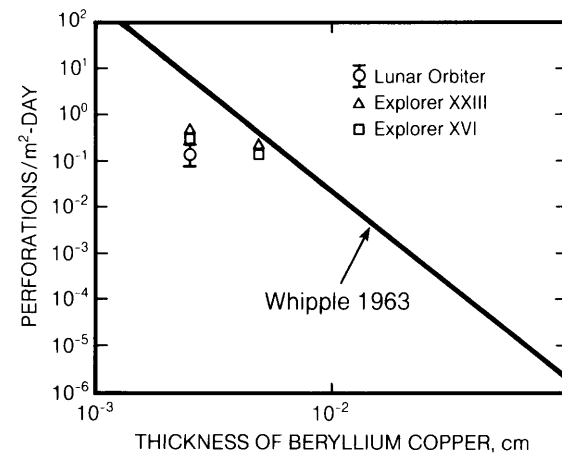


Fig. 3.15. Hazards of perforation by meteoroids in lunar orbit as a function of metal thickness (after Gurtler and Grew, 1968). Explorer and Lunar Orbiter data are compared with Whipple’s (1963) predicted curve, modified to compare with the beryllium copper used on the spacecraft instruments.

inflicted may be more than cosmetic. The probability of such a meteoroid striking an astronaut on the lunar surface is very small—about one chance in 10^6 to 10^8 for one year of cumulative time exposed on the surface. The most significant hazard, therefore, is to large and critical structures—habitats, base support facilities, processing plants, or research instruments—that are expected to last on the lunar surface for many years.

The actual risk to an object exposed on the Moon is difficult to estimate. Risk is commonly expressed as some compound measure of both probability and consequences (Lowrance, 1976). The current probabilities of impact by meteoroids of particular sizes are now fairly well known, but the consequences of damage will depend very much on the nature and function of each component for which risk must be assessed. For a large but inert structure, the consequences may be very small; for a small but vital life-support package, the consequences may be great. Meteoroid hazards at a lunar base therefore cannot be fully constrained until a detailed base layout is considered.

3.11. IONIZING RADIATION

The space around the Moon contains many types of ionizing radiation: large fluxes of low-energy solar-wind particles, smaller fluxes of high-energy galactic cosmic rays, and rare but occasionally intense particle fluxes emitted by solar flares. The radiation fluxes and energies typically span at least eight orders of magnitude. Radiation energy is traditionally expressed in units of electron volts (eV) or multiples of eV (such as keV, MeV, or GeV) with $1 \text{ eV} = 1.6022 \times 10^{-12} \text{ erg}$. The lunar radiation environment also changes with time, usually reflecting the level of solar activity, such as the modulation of galactic cosmic rays and the irregular emission of energetic particles from the sun.

Three major types of radiation at the Moon are discussed here: the solar wind, solar-flare-associated particles (also called solar energetic particles or solar cosmic rays), and galactic cosmic rays. The radiation consists mainly of protons and electrons with some heavier nuclei. These particles interact with the Moon in different ways, depending on their energy and composition, resulting in penetration depths that vary from micrometers to meters. The results of interactions with exposed lunar rocks and soils also vary considerably; the effects include solar-wind implantation, heavy-nuclei tracks, spallation reactions, and the generation of secondary neutrons and gamma rays. A summary of the three radiation types in terms of their energies, fluxes, compositions, and lunar interaction depths is given in Table 3.5. The

numbers in this table are averages or more probable ranges, and most of the values can vary widely with time and/or energy.

Not discussed below are other types of gamma, electron, antimatter, and other charged-particle radiation that have been observed in space around the Earth-Moon system. These particles are present in such low fluxes or low energies that their interactions with the Moon are very difficult to detect, and some have not been well characterized. The gamma rays that come from galactic sources or that are emitted from the sun in large solar flares have low fluxes. There also are several varieties of low-energy particles (usually $<0.1 \text{ MeV}$ for electrons and $<1 \text{ MeV}$ for protons) that have been seen near the Earth-Moon system or that have been inferred from studies of lunar samples. Some particles near the Moon have origins other than the sun or the “galaxy.” These include electrons emitted by Jupiter’s magnetosphere or nuclei like ^{40}Ar that have diffused from the lunar surface and then been ionized and carried along with plasmas near the Moon. During the rare times that the Moon is in the Earth’s magnetotail, even some terrestrial particles can reach the lunar surface.

The majority of the observations about radiation presented here were collected by instruments on spacecraft beyond the Earth’s magnetosphere; these observations are representative of what hits the Moon. The Earth’s strong magnetic field and thick atmosphere make it hard to use Earth-based methods to study these radiations, even though observations on Earth led to their discovery. For example, the galactic cosmic radiation was identified by ionization chambers carried aloft with Victor Hess on balloons in 1911-1912, and Forbush’s ionization chambers detected high-energy (GeV) particles from the sun in the 1940s (Pomerantz and Duggal, 1974).

The Earth’s magnetic field scatters particles back into space, except near the magnetic poles where even low-energy solar particles reach the Earth’s atmosphere. The ionization at the top of the Earth’s atmosphere by large fluxes of particles absorbs cosmic radio noise (“polar cap absorption” or PCA). Since 1952, riometers have been used routinely to measure polar cap absorptions caused by solar particles (see, e.g., Pomerantz and Duggal, 1974). The Earth’s atmosphere is thick enough (1000 g/cm^2) that very few cosmic-ray particles penetrate to the surface. Among those that reach the surface are the weakly-interacting muons and a few neutrons. Ionization chambers and neutron detectors on the Earth’s surface have monitored galactic and solar cosmic radiations since 1936, with energy discrimination being provided by the strength of the geomagnetic field at various locations. While used

TABLE 3.5. Summary of the three major types of radiation in the lunar environment.

Type	Solar Wind	Solar Cosmic Rays	Galactic Cosmic Rays
Nuclei energies	~0.3-3 keV/u*	~1 to >100 MeV/u	~0.1 to >10 GeV/u
Electron energies	~1-100 eV	<0.1 to 1 MeV	~0.1 to >10 GeV/u
Fluxes (protons/cm ² sec)	~3 × 10 ⁸	~0-10 ⁶ †	2-4
<i>Particle ratios</i> ‡			
electron/proton	~1	~1	~0.02
proton/alpha	~22	~60	~7
L (3 ≤ Z ≤ 5)/alpha	n.d.	<0.0001	~0.015
M (6 ≤ Z ≤ 9)/alpha	~0.03	~0.03	~0.06
LH (10 ≤ Z ≤ 14)/alpha	~0.005	~0.009	~0.014
MH (15 ≤ Z ≤ 19)/alpha	~0.0005	~0.0006	~0.002
VH (20 ≤ Z ≤ 29)/alpha	~0.0012	~0.0014	~0.004
VVH (30 ≤ Z)/alpha	n.d.	n.d.	~3 × 10 ⁻⁶
<i>Lunar Penetration Depths</i>			
protons and alphas	<micrometers	centimeters	meters
heavier nuclei	<micrometers	millimeters	centimeters

* eV/u = electron volts per nucleon.

† Short-term SCR fluxes above 10 MeV; maximum is for the peak of the August 4, 1972 event. Flux above 10 MeV as averaged over ~1 m.y. is ~100 protons/cm²sec.

‡ Ratios often vary considerably with time for the solar wind and SCR particles and with energy for SCR and GCR. The symbols L (light), M (medium), H (heavy), VH (very heavy), etc., are historical terms for nuclei charge (Z) groups greater than 2 in the cosmic rays.

n.d. = not determined (usually because the ratio is too low to measure). Composition data from *Feldman et al.* (1977) and *Bame et al.* (1983) for the solar wind, *McGuire et al.* (1986) for the SCR, and *Simpson* (1983) for the GCR.

mainly to study the galactic cosmic rays, about once a year these surface detectors observe signals called "ground level enhancement" (GLE) due to solar particles. Such effects as PCA and GLE are not present on the Moon with its very weak magnetic fields and tenuous atmosphere, but are mentioned here because of the considerable information that they have given us about cosmic-ray particles.

3.11.1. Solar Wind

Besides the radiant energy continuously emitted from the sun, there is also a steady plasma emission. This plasma consists of an equal number of ions and electrons with an embedded magnetic field that expands from the solar corona (*Hundhausen, 1972*). The solar wind streams outward from the sun through the solar system creating interplanetary magnetic field lines that have spiral shapes because of the sun's rotation. The solar wind is electrically neutral, and the composition of the nuclei in it is approximately that of the sun. At a distance of 1 A.U. from the sun, the mean energy of the, solar-wind ions is ~1 keV/u (keV/atomic-mass-unit or, for nuclei, keV/nucleon), and all particles move at nearly the same velocity. The solar-wind velocity typically

ranges from 300 to 700 km/sec, and its particle concentrations normally range from 1 to 20 per cm³ (*Feldman et al., 1977*). The solar-wind proton flux generally ranges from 1 × 10⁸ to 8 × 10⁸ protons/cm² sec.

The composition of the solar wind is not well known, especially for heavier nuclei. The short-term alpha-particle-to-proton ratio has been observed to range from ~0 to 0.25, although the longer-term average over periods of months is in a smaller range, 0.037-0.055 (*Hundhausen, 1972; Bame et al., 1983*). Both direct satellite measurements and analyses of artificial materials exposed at the lunar surface (*Walker, 1975*) have helped to characterize abundances of heavier nuclei in the solar wind. The abundance ratios given in Table 3.5 are from *Feldman et al.* (1977) and *Bame et al.* (1983). As noted in section 3.9 and in Chapter 8, the solar wind is the main source for several volatile elements in the lunar atmosphere and on the lunar surface, such as H, He, C, and N, that are otherwise rare on the Moon. The solar wind also serves as a minor cause of long-term erosion of lunar samples by producing sputtering reactions on exposed surfaces (the main agent of lunar erosion is the cratering produced by micrometeoroid impacts).

3.11.2. Solar-Flare-Associated Particles

The sun also produces intermittent high fluxes of energetic charged particles that are associated with some major solar flares. These solar-flare-associated particles are also called solar energetic particles or solar cosmic rays (SCR). As only the higher-energy particles are emphasized here and some other writers use the expression “energetic particles” for lower-energy species, the term solar cosmic rays or SCR will be used below.

Solar-cosmic-ray particles can be accelerated either in the sun’s corona or in interplanetary space. These particles reach the Earth-Moon system in less than a day. After a big solar flare, electrons with energies of ~0.5-1 MeV arrive at 1 A.U., usually traveling along interplanetary field lines, within tens of minutes to tens of hours. Solar protons with energies of 20-80 MeV usually arrive within a few to ~10 hours (*Van Hollebeke et al.*, 1975). Some high-energy SCR particles can arrive in as little as 20 minutes from flares on the sun’s western hemisphere that are well connected to the Earth (see, e.g., *Rust*, 1982). For many flares, mainly low-energy (~10-100 keV) electrons reach the Earth (*Simnett*, 1974). Very large flares also can accelerate electrons and energetic nuclei to relativistic velocities (i.e., traveling close to the speed of light).

The locations of most flares producing these high-energy particles that reach the Earth are in the sun’s western hemisphere (*Pomerantz and Duggal*, 1974), although in some cases the flare is not visible from the Earth, making prediction of the solar particle event more difficult. The nature of solar flares and how they accelerate particles to high energies are not very well known, although recent observations are giving us a better picture of high-energy processes in solar flares (see, e.g., *Rust*, 1982; *Chupp*, 1988). In several cases, particles are accelerated to high energies in interplanetary space by multiple reflections between two converging shock fronts (*Pomerantz and Duggal*, 1974). We shall not discuss solar flares further or the origin or propagation of these solar high-energy particles but will concentrate on SCR properties as observed near the Earth, at 1 A.U. from the sun.

Because relativistic electrons ($E > 0.5$ MeV, the rest mass of an electron) and nuclei with energies above a few MeV/u are emitted only in large fluxes by major flares at the sun (*Pomerantz and Duggal*, 1974), they are present at the Moon only a small fraction of the time. Very few SCR particles are present during periods of minimum solar activity; most are emitted during the time near solar maximum. Figure 3.16 shows the occurrence of major fluxes of SCR particles for three 11-year solar cycles along with a smoothed curve for the sunspot

number (the sum of the number of individual sunspots, plus 10 times the number of sunspot groups). Sunspot curves have been used as one indicator of solar activity (see *Pomerantz and Duggal*, 1974). Solar-cosmic-ray particles are seldom emitted during the period of the 11-year solar cycle when solar activity is near a minimum but can be present near the Moon at any time when the sun is fairly active, usually when the sunspot number is above ~50. However, the sunspot number is only a qualitative indicator of SCR fluxes (*Goswami et al.*, 1988).

The temporal distribution of solar protons during a month when the sun was very active is shown in Fig. 3.17. This period is more active than most but shows some typical features for the fluxes of solar protons at 1 A.U. Detectable fluxes of high-energy protons are only present for a few days after a solar flare. The flux of low-energy solar protons persists for longer periods of time. The flux of SCR particles rises fairly rapidly right after a flare and then decays at rates that vary with their energy, with higher-energy particles decaying faster. The periods of maximum SCR fluxes are typically a few hours. During a solar particle event, the directions and amounts of anisotropy of the SCR particles can vary (*Pomerantz and Duggal*, 1974). The largest anisotropy usually occurs in the early phases of an event, with the maximum flux generally about 50° west of the sun-Earth line, the direction of the solar wind magnetic field at 1 A.U. The lower-energy particles near the end of a SCR event tend to arrive more isotropically.

The particle compositions in typical SCR events are given in Table 3.5. Most nuclei are protons or alpha particles. Electrons usually arrive ahead of these nuclei because they travel faster at these energies (*Simnett*, 1974). There are some heavier nuclei, of which the more easily ionized elements are enriched relative to those with high ionization potentials (*McGuire et al.*, 1986). The ratios of various elements in the SCR can vary within an SCR event and from event to event (*McGuire et al.*, 1986). Elemental ratios can also vary with energy (*McGuire et al.*, 1986; *Reedy et al.*, 1983). Very unusual elemental ratios (e.g., high $^3\text{He}/^4\text{He}$) have been observed in some small events, but these events account for a very small fraction of the total fluence at the Moon over long periods of time.

As indicated in Fig. 3.17 and shown in Fig. 3.18, the SCR particle energy spectrum drops rapidly with increasing energy, most particles having energies below ~30 MeV. The spectral shape varies during an SCR event and, as shown in Fig. 3.18, can be very different from event to event. Most SCR events have soft spectra with few high-energy particles. However,

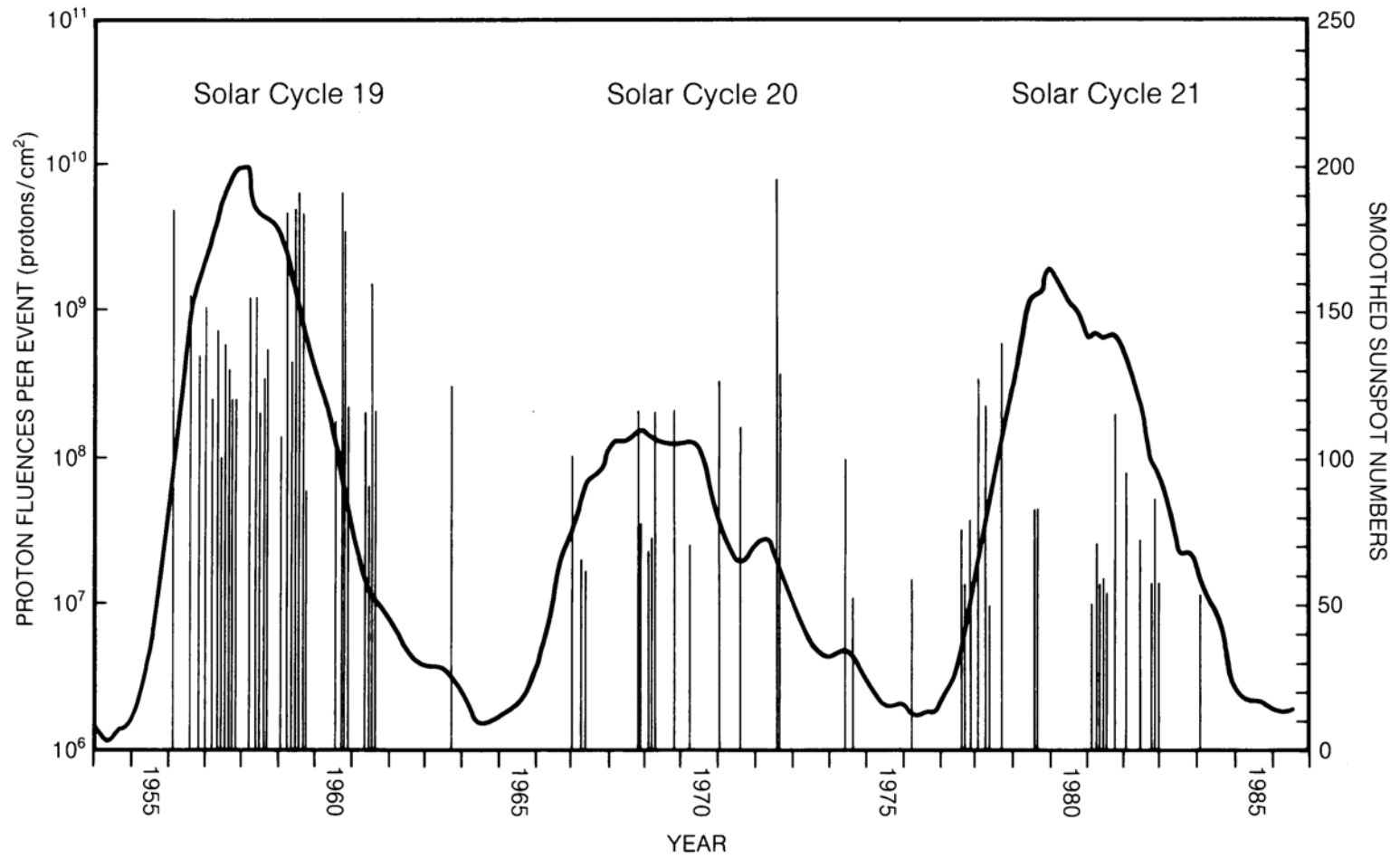


Fig. 3.16. Vertical lines mark individual event-integrated fluxes of solar protons above 30 MeV (Reedy, 1977; Goswami et al., 1988). The curve shows the smoothed sunspot number, an indicator of the level of solar activity, over three 11-year solar cycles.

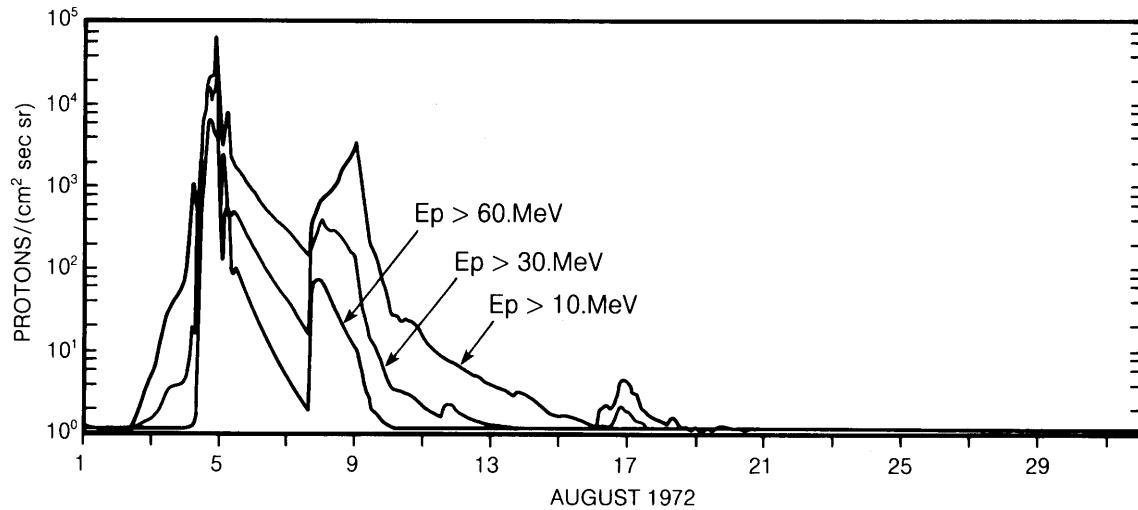


Fig. 3.17. Time distributions of the fluxes of solar protons (protons per cm²-sec-steradian) integrated above energies of 10, 30, and 60 MeV during August 1972, a month when the sun was very active (Kohl et al., 1973). Note the sharp (few hours) rise and the long (days) decay in the proton fluxes during each event.

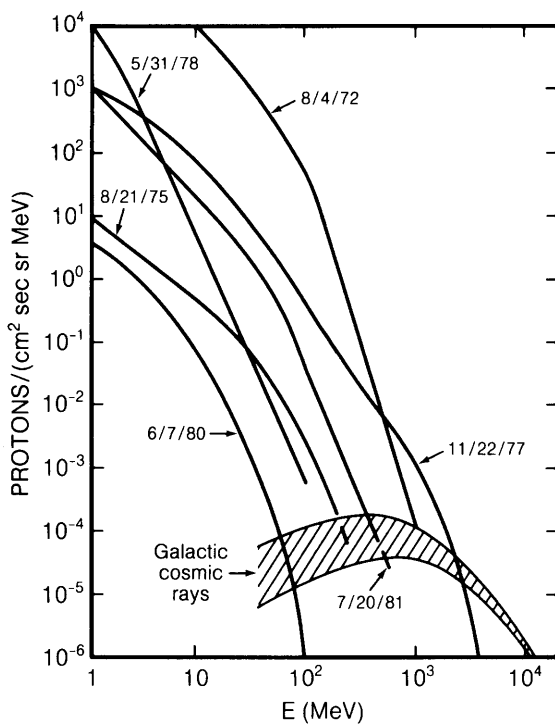


Fig. 3.18. Solar-cosmic-ray (SCR) proton fluxes vs. energy. The highest proton fluxes observed at a given energy during each event are shown as a function of energy for six representative medium to large solar-particle events. Also shown are the usual ranges of GCR proton fluxes over a

typical 11-year solar cycle (see also Fig. 3.19). For the August 4, 1972 event, the time-of-maximum fluxes below 100 MeV are based on the integral fluxes in Fig. 3.17 and the fluxes above 100 MeV are from Simnett (1976). The maximum fluxes shown for the five other events are from McGuire and von Rosenvinge (1984), except that the fluxes above 400 MeV for the November 22, 1977 event are from Debrunner et al. (1984). Note the large differences in proton fluxes and spectral shapes among different events.

a few events can have large fluxes of high-energy particles that extend to GeV or higher energies (see, e.g., Pomerantz and Duggal, 1974). It is these rare events, with high fluxes of very energetic particles, that are of the most serious concern for men and material exposed in space or on the lunar surface. The intensity of high-energy particles in these rare, intense SCR events is such that neutron monitors or ionization chambers on the surface of the Earth record very large increases (up to 90 times normal levels during the February 23, 1956 event) for several hours during the peak of the event (Pomerantz and Duggal, 1974). On the Moon, an astronaut caught outside his shielded habitat during such an event could easily receive a debilitating or lethal radiation dose in a few days; at peak fluxes the dose may cause nausea and vomiting within an hour (Rust, 1982). Prediction of SCR events and ready access (on ~30 minutes notice) to a buried shelter will be requirements for safe long-term astronaut exposure on the lunar surface.

Our ability to accurately estimate the probabilities of very large SCR particle fluxes is limited by the fact that observation of such particles has only been done qualitatively since 1942 and by direct measurements using detectors on satellites since the 1960s (*Pomerantz and Duggal, 1974; Reedy, 1977; Goswami et al., 1988*). Rough intensity estimates of the solar protons emitted during solar cycle 19 (1954-1964) were made by *Reedy (1977)* using indirect measures of the relative intensities of solar-proton events and using the solar-proton-produced radioactivities in lunar rocks. Some of the indirect estimates of solar-proton intensities during this period were low by factors of 3 to 5, and this solar cycle appears to have had a much larger flux of solar protons and many more events with very high fluxes than the two more recent solar cycles (*Goswami et al., 1988*). During the last two decades there has only been one very large solar-particle event, in August 1972. It should also be noted that solar-particle events occurred in 1942 (two events), 1946, and 1949 that, based on terrestrial GLE data, were larger than any seen from 1957 to 1988 (*Pomerantz and Duggal, 1974*).

Thus our ability to predict the probabilities of large solar-particle events is limited by the fact that such events are rare and have seldom been measured (cf. *Goswami et al., 1988; King, 1974*). The data for the last few solar cycles suggest that large particle events with integral proton fluences above 10^{10} protons/cm² are fairly rare. Estimates for the probabilities of solar-particle events with proton fluences above 10^{10} protons/cm² vary widely (*King 1974; Lingenfelter and Hudson, 1980; Goswami et al., 1988*). The activities of long-lived radionuclides made in lunar rocks by SCR particles have been used to determine the average fluxes of solar protons over time periods of 10^4 to 10^7 years (*Reedy, 1980*). These average solar-proton fluxes and the absence of detectable solar-proton-produced ¹⁴C in tree rings over the last 7000 years has led *Lingenfelter and Hudson (1980)* to conclude that extremely large solar proton fluxes are rare and that the probability curve as a function of integral event fluence takes a sharp drop for fluences above $\sim 10^{10}$ protons/cm².

However, several of the intense events observed since 1953, such as the February 23, 1956 event with a very hard spectrum and the August 4, 1972 event, would have been hazardous to humans exposed in space (*Rust, 1982; Letaw et al., 1987*). The existing data indicate that there could be several hazardous solar-particle events per solar cycle, and that there is only a period of a few years around solar minimum when such events are unlikely. Habitats shielded under 2 m (about 400 g/cm²) of densely packed regolith are a minimum requirement for a lunar base; for full protection from the rare gigantic

flare events, shielding of about 3.5 m thickness will be necessary (*Silberberg et al., 1985*).

3.11.3. Galactic Cosmic Rays

The main matter in the solar system that originates far from the solar system is that in the galactic cosmic rays (GCR). The GCR particles with energies below $\sim 10^{15}$ eV come from our galaxy, and their flux at the Earth is very isotropic (*Simpson, 1983*). Energies of GCR particles extend up to $\sim 10^{20}$ eV, although such ultrahigh energies are very rare. The actual sources of GCR particles and the reasons for their great energies are not well known (*Simpson, 1983*). The GCR nuclei typically take $\sim 10^7$ years to reach us and, during that time, have passed through ~ 5 g/cm² of interstellar matter. Spallation reactions during their interstellar passages result in a significant abundance of the rare elements lithium, beryllium, and boron and enhancements in other minor elements, such as those just below iron (see composition in Table 3.5). The amount of antimatter in the GCR is low, with the measured ratio of antiprotons to protons in the range of 10^{-3} to 10^{-4} (*Simpson, 1983*).

The main source of variations in the fluxes and energies of GCR particles at the Moon is solar activity. Magnetic fields carried by the solar wind as it expands from the sun cause the GCR particles to lose energy as they penetrate into the solar system. During a typical 11-year solar cycle, the flux of GCR particles with energies above 1 GeV/u varies by a factor of 2, with the highest GCR fluxes during periods of minimum solar activity. As shown in Fig. 3.19, the modulation of the GCR energy spectrum is greatest at low energies, and GCR particles with energies above ~ 10 GeV/u are barely affected by the magnetic fields in the solar wind.

The actual amount of modulation of GCR particles varies from solar cycle to solar cycle, and the curves in Fig. 3.19 are based on measured GCR fluxes during the last two solar cycles (*Reedy, 1987*). Deviations from this range of GCR fluxes are expected only during very rare periods of unusually low or high solar activity (*Reedy et al., 1983*). The largest possible flux of GCR particles at the Moon would be for a long period of very low solar activity, at which time the GCR particle flux would approach that of the local interstellar medium. Estimates for the interstellar GCR particle flux vary, and the interstellar GCR flux curves in Fig. 3.19 span the range of estimates (*Reedy, 1987*). Galactic-cosmic-ray particle fluxes as a function of energy at the lunar surface probably will never exceed the local interstellar space curve. The last time that the GCR particle flux was much above the typical range was probably during the

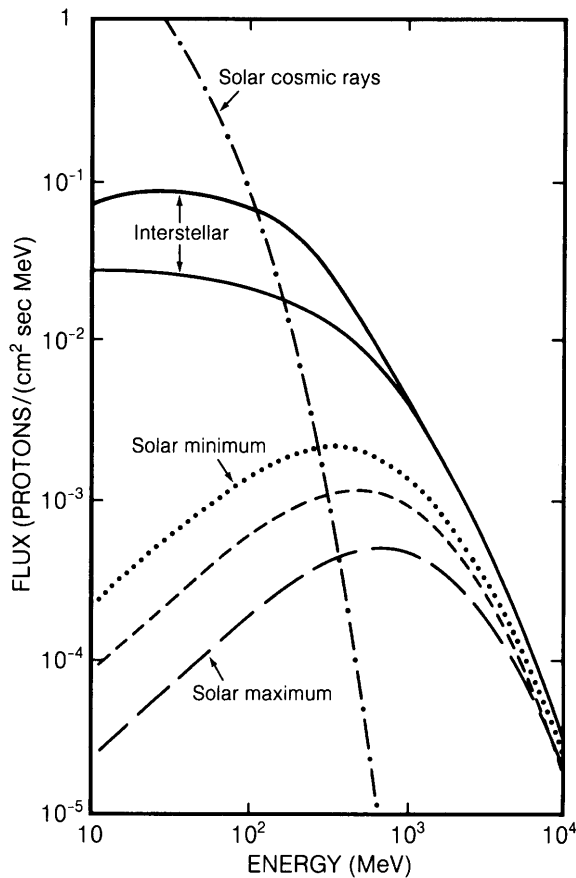


Fig. 3.19. Galactic-cosmic-ray proton fluxes vs. energy (from *Reedy, 1987*). The curves for minimum and maximum of solar activity are the same as those in Fig. 3.18 but are integrated over 4π solid angle. The dashed curve between “solar min.” and “solar max.” is the GCR flux near the Moon averaged over an 11-year solar cycle. The two solid curves at the top represent the range of estimates for GCR particle fluxes in interstellar space, which would be the GCR flux near the Moon if there were no solar activity. The dot-dashed curve shows for comparison the long-term (thousands to millions of years) averaged fluxes of solar protons.

Maunder Minimum, which was a period of very low solar activity lasting from the years 1645 to 1715 (*Reedy et al., 1983*).

3.11.4. Modes of Interactions with the Moon

All energetic particles interact with matter by a few well-known processes. Most energetic particles and all neutrons can induce nuclear reactions with the nuclei in the lunar surface. These nuclear reactions range with the energy of the incident

particle from neutron capture and elastic scattering to high-energy spallation. The products of these nuclear reactions range from the initial target nucleus to nuclei far from the target and also can include a wide range of secondary particles, such as neutrons, pions, gamma rays, and various nuclear fragments.

The energy of the incident particle determines what nuclear reactions are possible and the probabilities for these reactions. Nuclear reactions, especially elastic-scattering reactions, are the only way that energetic neutrons can interact (although particles can escape from the Moon and thus stop interacting with it). Typical energetic (MeV) particles will induce nuclear reactions with an interaction mean free path of ~ 100 g/cm². Thus even the highest-energy GCR particle will have interacted before passing through ~ 1000 g/cm² of matter, which is the thickness of the Earth’s atmosphere or of ~ 5 m of lunar regolith.

The nuclear reaction induced by a high-energy particle ($E > \sim 10$ MeV) usually initiates a cascade of particles. Typically, a number of secondary particles, and possibly even the incident particle with degraded energy, are emitted by the initial nuclear reaction. Most low-energy secondary charged particles are stopped by ionization-energy losses before reacting, but the secondary neutrons and higher-energy charged particles can induce additional nuclear reactions (*Armstrong and Alsmiller, 1971; Reedy and Arnold, 1972*). The secondary particles, especially neutrons, made in the cascades started by GCR particles, are an important part of the lunar radiation environment.

One way that charged particles interact with matter is to ionize atoms and molecules, thereby losing energy. Most low-energy (below ~ 30 MeV/u) charged particles are slowed down so fast (within < 1 g/cm²) that they usually are stopped before they can induce a nuclear reaction. The heavy nuclei in the GCR, especially those with higher charges, also are rapidly stopped by ionization energy losses. It is because of their short ranges (the distances over which they are stopped) that the penetration depths of heavy nuclei, as shown in Table 3.5, are much less than those of protons and alpha particles. The nuclei that are stopped are then implanted in that material, and most SCR and all solar-wind nuclei end up as implanted species in the upper layers of the Moon. Most GCR protons induce reactions, as the range of a 400 MeV proton is about equal to its interaction mean free path (~ 100 g/cm²), and most GCR protons have energies much higher than 400 MeV and very long ranges in the Moon.

The energetic particles in the lunar environment also induce a variety of radiation damage effects. The

radiation damage induced by nuclei with $Z > 20$, near the end of their range, is so high that it can be seen by transmission electron microscopy in certain minerals. Simple chemicals can preferentially dissolve the damaged areas in these minerals (Walker, 1975; Reedy *et al.*, 1983); the etched holes are called *tracks*. Tracks from the iron group (VH) nuclei typically have lengths of 10-20 μm . Electrons can occasionally become trapped in metastable energy states and are very slowly released. The light emitted when these trapped electrons are released during heating is called *thermoluminescence* (Walker, 1975), and the amount of light released can sometimes be used to estimate how long a sample was exposed to radiation.

Energetic particles can displace the nuclei in the target material. If the displaced atom is on the surface, it can be removed from that material, a process called *sputtering*. On the lunar surface, erosion of exposed surfaces is mainly by micrometeoroid impacts and not by sputtering (Walker, 1975). If the dose of energetic particles to which a material is exposed is high enough, the structure of the material can be changed. The very outer layers (about 0.05 μm thick) of some lunar grains are amorphous because of their bombardment by the intense flux of solar-wind nuclei (Walker, 1975).

While similar processes occur on the Earth, two major differences between the Earth and the Moon affect the nature of these interactions. The Earth has a very strong magnetic field that deflects almost all SCR particles and most GCR particles. The only places on Earth where the magnetic fields are not important are above the geomagnetic poles. Magnetic fields on the Moon are generally so weak that even the very low-energy ions in the solar wind can hit the lunar surface. The other major difference is the Earth's atmosphere, which has a thickness of about 1000 g/cm^2 . The atmosphere is thick enough that the dose of particles at the surface is much lower than that at the top of the atmosphere. The cascade of particles in the atmosphere is partially affected by its low density, as pions can travel far enough before interacting that they decay into muons, while on the lunar surface with its density of $\sim 2 \text{ g}/\text{cm}^3$ the pions usually react with nuclei, producing secondary neutrons, before decaying (Lingenfelter *et al.*, 1961, 1972). Therefore the number of secondary neutrons in the lunar surface is higher than that in the atmosphere above the Earth's magnetic poles by a factor of $\sim 50\%$, and the flux of muons on the Moon is much less than that for the Earth.

Solar wind. Solar wind particles have such low energies ($\sim 1 \text{ keV}/\text{u}$) that they only interact with the lunar surface by rapidly stopping (in much less than

a micrometer) in the uppermost layer. This interaction also can produce sputtering and, if the dose of solar wind particles is intense enough, can change crystalline regions on the surfaces of grains into amorphous layers (Walker, 1975). As noted by Walker (1975), the amount of solar wind atoms hitting the Moon over 4 b.y. is about equal to the number of lunar atoms in the top 10 m of the lunar regolith. However, many solar wind atoms are not retained and eventually escape into space (see section 3.9.2). The solar wind is the major source of certain elements that are very rare on the Moon, such as H, C, N, and the noble-gas elements (see section 8.8).

Solar cosmic rays. Most particles in the solar cosmic rays are stopped by ionization energy losses in the top few centimeters of the lunar surface. The heavy nuclei in the SCR are rapidly stopped in the outer millimeter of the Moon and can produce high densities of radiation damage there (Walker, 1975; Reedy *et al.*, 1983). Solar proton fluxes, especially those at lower energies, drop rapidly with depth in the Moon because of the slowing down of these fairly low energy particles (Reedy and Arnold, 1972). The few reactions induced by SCR particles are mainly in the top centimeter of the lunar surface, and few secondary particles are emitted in these reactions. Over many years, the average flux of secondaries from SCR particles is much less than those from GCR particles (Armstrong and Alsmiller, 1971), although the flux of secondaries in the top $\sim 100 \text{ g}/\text{cm}^2$ of the Moon could be relatively high during the peak of an intense, hard SCR event. The relatively small cascade of particles induced by SCR particles does not penetrate deeply.

Galactic cosmic rays. The heavy nuclei in the galactic cosmic rays are usually stopped by ionization energy losses within $\sim 10 \text{ cm}$ of the lunar surface. Most of the radiation damage induced by these heavy GCR nuclei occurs within the top few centimeters. This radiation damage is so intense that it can be seen as high densities of tracks in lunar samples (Walker, 1975; Reedy *et al.*, 1983) and can cause problems in sensitive electronic components (Adams and Shapiro, 1985). Shielding of a few g/cm^2 is usually adequate to remove most of these highly-ionizing heavy GCR nuclei.

The lighter nuclei in the GCR, mainly protons and alpha particles, are very penetrating and induce a cascade of particles that extends meters into the lunar surface. The number of secondary particles in this GCR cascade is much greater than the number of incident primaries. For example, the flux of GCR primary particles hitting the lunar surface is about two particles/ $\text{cm}^2 \text{ sec}$, while the number of secondary neutrons made in the lunar surface is about 13

neutrons/cm² sec (Reedy *et al.*, 1983). Additional secondary particles, such as pions, are also present in this cascade (Armstrong and Alsmiller, 1971), although the dominant particle in the cascade is the neutron (mainly because neutrons are not slowed by ionization energy losses). For energies below ~100 MeV, most particles in the Moon are neutrons (Armstrong and Alsmiller, 1971; Reedy and Arnold, 1972). These neutrons are typically produced with energies of a few MeV and travel through the Moon until they interact (most effectively with elements lighter than oxygen) or escape into space (Lingenfelter *et al.*, 1961, 1972). As elements lighter than oxygen are very rare in the Moon, neutrons lose energy slowly and many collisions are required to

degrade the energy of a neutron to near thermal (below ~0.1 eV) energies (Lingenfelter *et al.*, 1961, 1972).

Galactic-cosmic-ray particle fluxes, both the incident primaries and the secondaries, are shown in Fig. 3.20 as a function of depth in the Moon for several energy groups. Armstrong and Alsmiller (1971) give a plot of the fluxes of neutrons for eight energy groups. The particles with energies above 1 GeV/u are mainly the primary nuclei and some high-energy secondaries (Reedy and Arnold, 1972). The particles below ~100 MeV/u are mainly secondary neutrons, and the particles between 100 MeV/u and 1 GeV/u are a mixture of primaries and secondaries, although secondaries usually dominate, especially at greater depths in the Moon. The curves in Fig. 3.20 are based on the model of Reedy and Arnold (1972) for energies above 0.5 MeV and the neutron-transport calculations of Lingenfelter *et al.* (1972) for thermal neutrons. The fluxes of high-energy particles decrease almost immediately below the lunar surface because these particles are removed from the primary GCR by attenuation. The lower-energy secondaries have flux-vs.-depth profiles that reflect both their buildup and subsequent attenuation. The deep peak for the thermal neutrons is largely due to the fact that many neutrons near the surface escape from the Moon before they can be slowed to thermal energies.

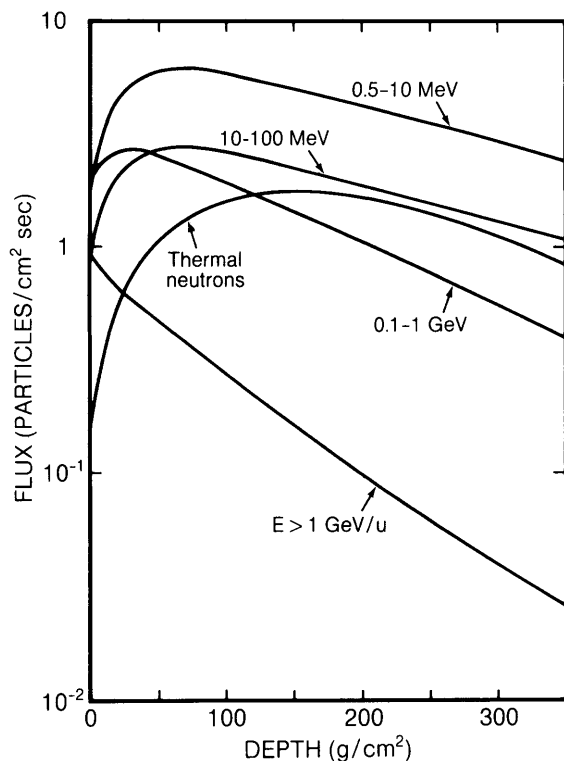


Fig. 3.20. Fluxes of galactic-cosmic-ray particles, both incident primaries and secondaries, as a function of depth in the Moon (a depth of 350 g/cm² is about 2 m of lunar regolith). Profiles were calculated with the lunar-GCR-particle model of Reedy and Arnold (1972), except for the thermal neutron profile (from Lingenfelter *et al.*, 1972). High-energy (>1 GeV/u) particles are removed rapidly with increasing depth while lower-energy particles first increase but eventually decrease with depth. For doses vs. depth in the Moon, see Silberberg *et al.* (1985) or Letaw *et al.* (1987).

3.11.5. Implications of the Lunar Radiation Environment

Scientific studies. The products of the interactions of the solar wind, the solar cosmic rays, and the galactic cosmic rays with the Moon have been used for a large variety of scientific studies (Reedy *et al.*, 1983; Walker, 1975). The solar wind and cosmic ray records of lunar materials have been investigated in detail. These studies, which determine how these radiations interacted with lunar samples, have provided records of the histories of both the radiation and the lunar samples themselves. The results of some of these investigations will only be briefly discussed here (see Reedy *et al.*, 1983, Walker, 1975, and references therein for additional details).

As mentioned above, lunar samples have provided a good record of solar wind and SCR particles in the past. It is largely based on the lunar record for SCR particles over the past ~10⁷ years that we can make many of the statements in section 3.11.2 about the SCR particle fluxes expected at the lunar surface. The amounts of the products from solar wind, SCR, or GCR interactions can be used to determine the length of time that a lunar sample was within

micrometers, centimeters, or meters, respectively, of the lunar surface. Such “exposure ages” cover a wide range, from material freshly ejected from craters to pieces of the regolith that have been near the surface for ~1 b.y.

These exposure ages have been used to help date a number of lunar features, such as craters. Profiles of cosmic-ray-produced nuclides have been used to determine the rate that the regolith has been disturbed by impacts (see *Reedy et al.*, 1983). The top few centimeters of the regolith have been mixed on timescales of a few millions of years. The deepest parts of the ~2-m-long cores brought back from the Moon usually have been disturbed on much longer timescales. Most rocks have been on the lunar surface for much less than 1 b.y., and usually have been knocked around on timescales of ~10 m.y. Very old rocks are extremely rare because rocks on the lunar surface eventually are destroyed or deeply buried by impact processes.

Another use of the lunar radiation environment has been the study of gamma rays and neutrons emitted as the result of the interaction of GCR particles in the lunar surface. Some of these gamma rays and neutrons subsequently escape into space. Many of the gamma rays have energies that uniquely depend on the nuclide from which they were produced (*Reedy*, 1978). By measuring the gamma rays above the lunar surface, the elemental composition of the top layers of that surface can be determined. This was the basis of the Apollo orbiting gamma-ray spectrometer, which provided useful chemical maps of Th, Ti, Fe, Mg, and K (see section 10.2.2). The neutrons leaking from the lunar surface are also sensitive to the surface chemical composition, especially its hydrogen content (*Lingenfelter et al.*, 1961); detection of neutrons could be used as an exploration tool for near-surface hydrogen or water (especially at the lunar poles; see section 3.8).

Radiation effects in the Moon. Each of the three radiation types in the lunar environment produces its own set of effects. The solar wind can produce sputtering and amorphous material in the very outermost layers (<1 μm) of the particles on the lunar surface and many of these ions become implanted. Lunar grains with these near-surface solar-wind effects usually become buried deeper by impact debris.

The solar cosmic rays typically interact with the top millimeter to top few centimeters of the lunar surface, mainly by ionization energy loss. The heavy SCR nuclei can induce locally high doses near the end of their ranges. Solar-cosmic-ray events occur irregularly, mainly at times when the sun is relatively active, and the dose rates from SCR particles range

from nothing to very high levels for several hours during rare, very intense events (*Rust*, 1982; *Letaw et al.*, 1987). These rare, very intense SCR events are potentially the greatest radiation hazard on the Moon; it is difficult to predict their occurrence and severity.

The GCR particles are the most penetrating of the radiation types but also are very predictable. The heavy nuclei in the GCR typically penetrate only a few centimeters, but the cascade of secondary particles, especially neutrons, made by the GCR protons and alpha particles penetrates meters into the Moon. Fairly high radiation doses result from these GCR particles (*Silberberg et al.*, 1985). The incident fluxes of GCR particles vary by about a factor of 2 over a typical 11-year solar cycle and are expected to be most intense during solar minima. During rare (every ~200 years), long periods of low solar activity (like the Maunder Minimum), the fluxes of GCR particles could be up by a factor of ~3 when compared with a typical solar minimum.

Summary. The radiation that hits the Moon is very diverse. It includes huge fluxes of ~1 keV/u solar-wind ions, a few high-energy (>1 GeV) GCR particles, and high-energy SCR particles intermittently emitted from the sun. The radiations at the lunar surface are very different from those on the Earth because the Moon lacks both a strong magnetic field and a thick atmosphere.

At the lunar surface, this radiation produces distinct, permanent, and depth-dependent effects. These effects, studied in lunar samples, have been used for a number of valuable scientific studies that include dating the ages of lunar features, determining the rate of “gardening” of the lunar regolith by meteoroids, and establishing a historical record for the past behavior of the sun.

The energies and fluxes of the particles hitting the Moon span many orders of magnitude (Table 3.5). Furthermore, their compositions differ and can vary with time and energy. Their lunar penetration depths vary from less than a micrometer to several meters. The solar-wind ions are implanted in the very surfaces of grains on the lunar surface, and these solar particles are the main source of certain volatile elements in the lunar regolith. The heavy nuclei in the galactic cosmic rays and the many secondary particles, especially neutrons, that the GCR generate in the lunar soil require the use of shielding to protect humans and sensitive electronic equipment on the Moon. Energetic particles from the sun are generally a minor concern on the Moon, but a few very large solar particle events, produced by flares, can occur each decade. These events would be very serious radiation hazards for humans and equipment exposed on the lunar surface.

APPENDIX

A3.1. Motion of the Earth-Moon System

Viewed from above the north pole of the Earth, the Moon travels counterclockwise in a slightly elliptical path around the Earth. At closest approach (perigee) the Moon is 356,410 km from the Earth and at farthest distance (apogee) it is 406,697 km away. From the Earth the apparent diameter of the lunar

disk varies systematically with these changes in distance (Glasstone, 1965; Mutch, 1970).

The average period of revolution of the Moon about the Earth, using the stars as fixed reference points, is 27.322 days or a *sidereal month* (Fig. A3.1). Because of the gravitational effects of the sun on the Moon, the period of revolution varies from one revolution to the next; variation from the mean value can be several hours. The *synodic month* is the time

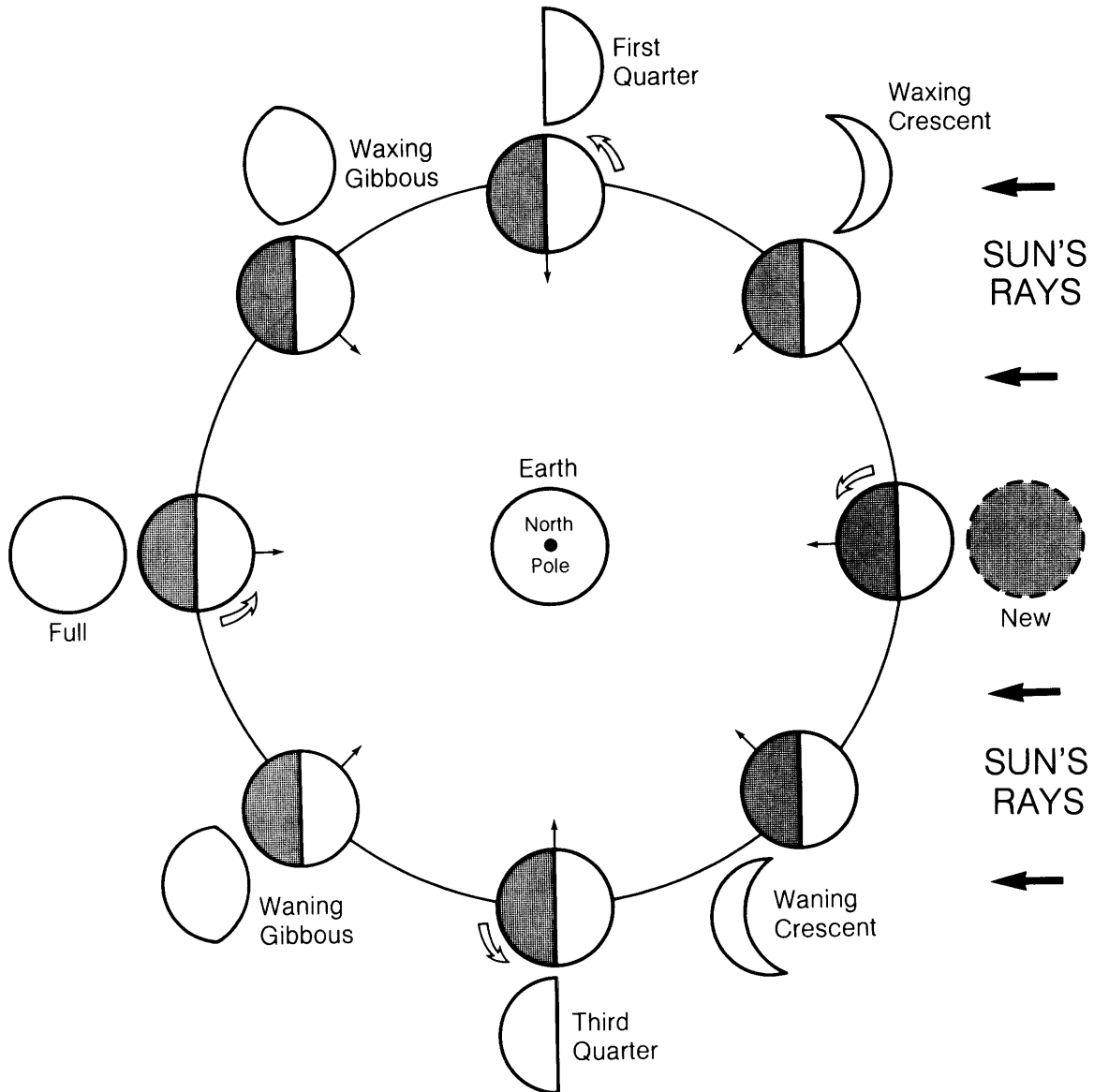


Fig. A3.1. Revolution of the Moon around the Earth, showing the combination of its orbital motions with its gravitationally "locked" rotation that causes it to present only one face to the Earth (from Mutch, 1970).

between two successive alignments of the Moon with the sun, observed from the Earth; this is also the time between successive new Moons and is called the *lunar month* (Fig. A3.1). The observed average lunar month is 29.531 days; variation from this value can be up to 13 hours.

The geometry of the Moon's rotation about its axis and orbit around the Earth is shown in Fig. A3.2. The periods of rotation and revolution are virtually identical, with a fixed lunar *nearside* that faces the Earth and a *farside* that faces away (Fig. A3.1). The relative motions and orientations of the Earth and

Moon (Figs. A3.3 and A3.4), however, do allow the Earthbound observer to see slightly more than half of the lunar surface because of *librations* in both longitude and latitude.

Longitudinal libration, caused by the slight non-circularity of the Moon's orbit, is an apparent rocking back-and-forth motion of the Moon in an east-west direction (Fig. A3.3). Because of this libration, it is possible to see an additional 7.7° along both eastern and western limbs of the lunar disc (Glasstone, 1965). *Latitudinal libration* is caused by the inclination of 6.7° of the Moon's axis of rotation to a line

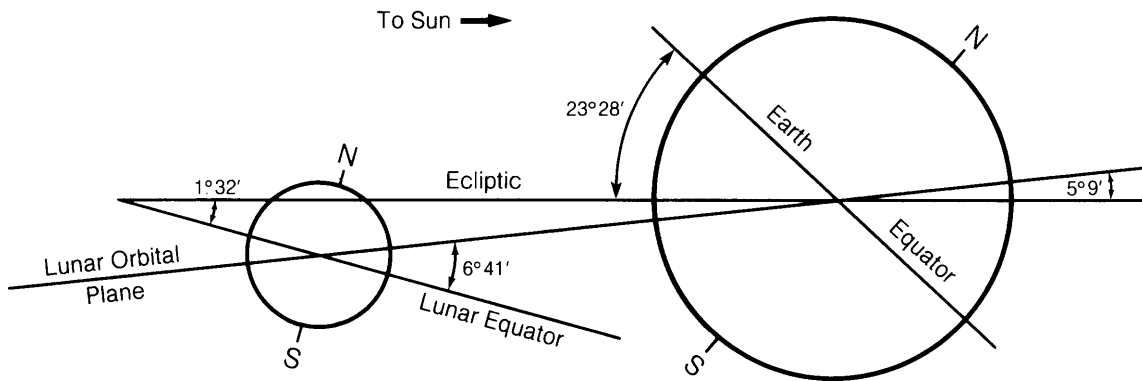


Fig. A3.2. Geometric relationship between the planes of revolution and rotation in the Earth-Moon system. Note that angular relationships have been exaggerated (from Mutch, 1970).

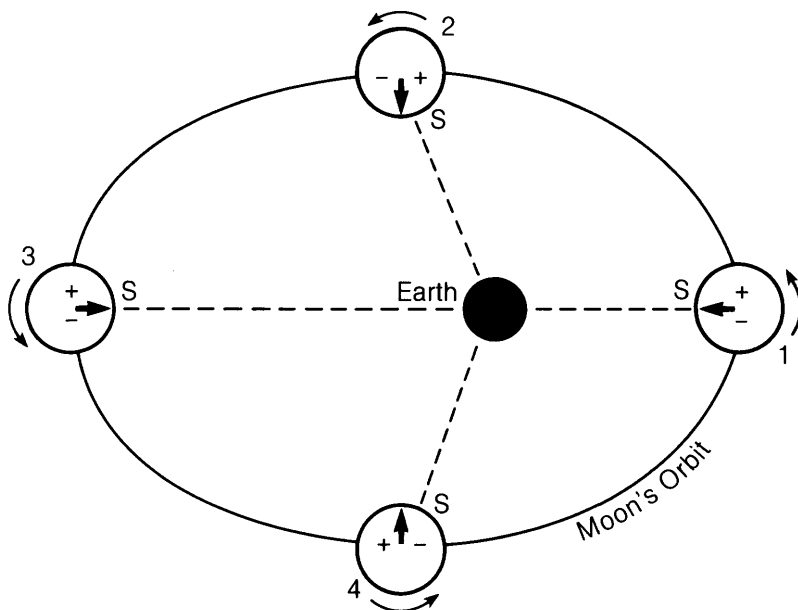


Fig. A3.3. Illustration of longitudinal libration. Because of the elliptical orbit of the Moon, positions 2 and 4 present slightly displaced subterrestrial viewpoints(s); this libration is positive (to the right of the arrow that marks the lunar prime meridian) at point 2 and negative (to the left of the lunar prime meridian) at point 4. The net result is that we see slightly more of the Moon's near-equatorial surface than we otherwise would from Earth (from Mutch, 1970).

perpendicular to the lunar orbital plane (Fig. A3.4). Because of this, it is possible to see an additional 6.7° at the north and south poles, over two-week intervals.

The *diurnal libration* is a parallax effect caused by rotation of the Earth. The position of an observer on the Earth's equator will move laterally about 13,000 km during a 12-hr period. This gives a libration of 1° at the western edge of the Moon upon rising and 1° at the eastern edge when it sets.

Because of these combined librations, we can see about 60% of the lunar surface from the Earth.

A3.2. Brightness of the Lunar Surface

Brightness of any spot on the Moon is dependent upon *phase angle*, *brightness longitude*, and *albedo* of the rocks or regolith. *Phase angle* is the angle measured between incident solar radiation and the

emergent ray as seen by the observer (see Fig. 3.1). *Brightness longitude* is "the angle measured in the plane between the emergent ray and a line perpendicular to the intersection of the ground with the phase plane" (Mutch, 1970).

Albedo is the fraction of visible electromagnetic radiation reflected by the surface of a material. Overall, in visible light, the Moon is a dark object with albedos ranging from about 7% to 24%. The light-colored rocks of the lunar highlands have variable but generally high albedos (mostly about 11% to 18%) whereas the basaltic lavas of the lunar maria have low albedos (about 7% to 10%). Earth-based albedo measurements are made during full Moon.

Brightness varies systematically with changing phase angle, so that total lunar brightness is lower than the fraction of the lunar surface illuminated

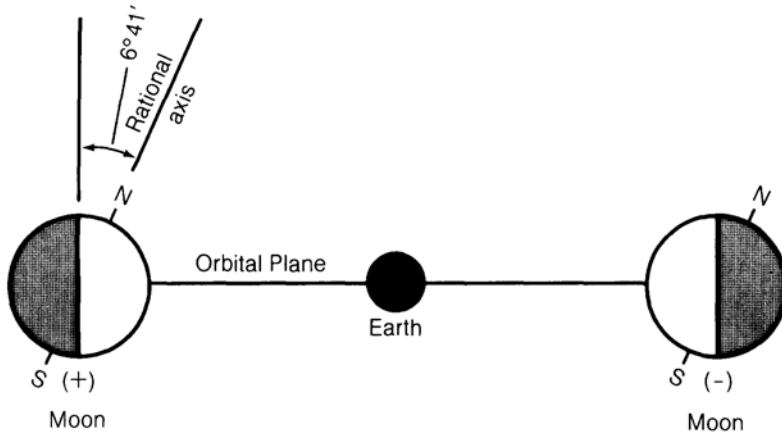
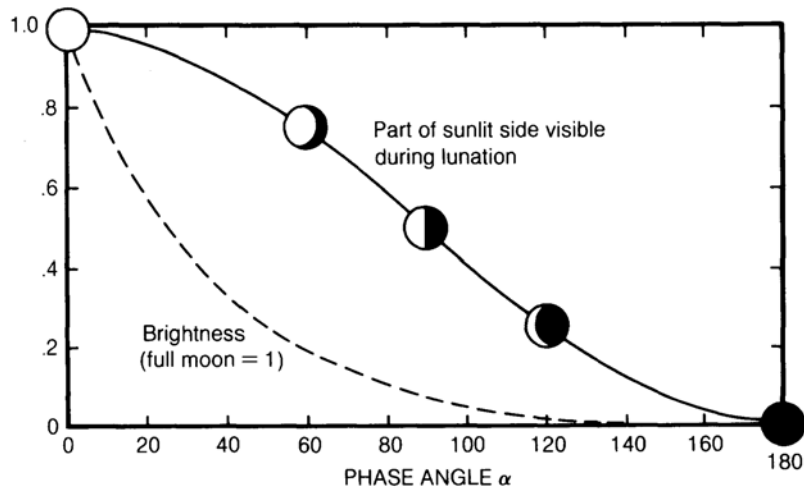


Fig. A3.4. Illustration of latitudinal libration (from Mutch, 1970). Views of the north polar region result from positive latitudinal libration; views of the south polar region result from negative latitudinal libration. The net result is that we see more of the Moon's polar regions than we otherwise would from Earth.

Fig. A3.5. Variation of total lunar brightness detected at Earth (scale of 0 to 1.0, dashed curve) compared with the fraction of the lunar surface visible from Earth (also on a scale of 0 to 1.0, solid curve with lunar images). Brightness decreases more rapidly than the fraction of surface illuminated as the Moon wanes, and increases more slowly as the Moon waxes (after Mutch, 1970).



(Fig. A3.5). For a review of photometric studies of the lunar surface and lunar materials, see *Wilson* (1971).

A3.3. Locating Points on The Moon

Selenodesy, or mapping of the Moon, began with Aristotle (384-322 B.C.) and has continued to today, building on the work of such famous astronomers as Galileo (1610), Langrenus (1645), Cassini (1680), Schroter (1791), and many others. Beginning in 1959, the U.S. Air Force Aeronautical Chart and Information Center (ACIC) began an international cooperative project to map the Moon's nearside at a scale of 1:1,000,000; 44 individual maps were prepared and completed in 1967. All of this work was based upon Earth-based telescopic photographs.

As a result of the Lunar Orbiter flights of 1966-1967, most of the Moon was photographed. However, because of photographic distortions, few of these images have been used for cartography other than general mapping of surface features. Mapping cameras (panoramic and metric) carried on the last three Apollo missions were used to produce topographic maps of a near-equatorial band around the Moon below the command module flight paths. For a complete review of lunar mapping, see the Lunar Cartographic Dossier by *Schirmerman* (1973).

Lunar maps have followed Earth convention since 1961, with north at the top and the prime meridian referenced to Crater Moring A on the Moon's nearside. Before 1974, maps expressed lunar longitude in terms of 0° -180° east (+) and 0° -180° west (-) of the prime meridian; this convention is used in this book. After 1974, a lunar longitude system of 360°, proceeding counterclockwise (increasing to the east) from the prime meridian, was adopted by international agreement for future cartography.

The names of lunar features varied from map to map until 1907 when a committee of the International Association of Academies was appointed to bring some uniformity to the problem; a collated list was published in 1913. Eventually the International Astronomical Union took on the responsibility of naming lunar features and keeping track of nomenclature. The following resolution was made:

“For designating the lunar surface features, it is recommended to follow the previous rules, revised and improved as follows: (i) Craters and rings or walled plains are designated by the name of an astronomer or prominent scientist deceased, written in the Latin alphabet, and spelled according to the recommendation by the country of origin of the scientist named. (ii) Mountain-like chains

are designated in Latin by denominations allied with our terrestrial geography. Names are associated with the substantive Mons according to the Latin declension rules and spelling. (Three exceptions, Montes d'Alembert, Montes Harbinger, and Montes Leibnitz are preserved, due to former long use).

(iii) Large dark areas are designated in Latin denominations calling up psychic states of mind. These names are associated, according to the Latin declension rules and spellings, to one of the appropriate substantives Oceanus, Mare, Lacus, Palus, or Sinus. (The exceptions Mare Humboldtianum and Mare Smythii are preserved, due to former long use).

(iv) Isolated peaks are designated according to the same rules as for the craters, as well as promontories, the latter being preceded by the Latin substantive Promontorium. (v) Rifts and valleys take the name of the nearest designated crater, preceded by the Latin substantives Rima and Vallis (The exception Vallis Schroter is preserved). (vi) Undenominated features can be designated by their coordinates. They can equally be designated according to the former classical system, by taking the name of the nearest crater, followed by a block letter of the Latin alphabet for craters, depressions and valleys, by a minor letter of the Greek alphabet for hills, elevations and peaks, and by a Roman number followed by the letter r for the clefts.”

At an IAU Assembly in 1973, the surface of the Moon was divided into 144 named regions at a scale of 1:1,000,000, by means of parallels of latitude and meridian arcs. It was also resolved to drop Greek letter designations for lunar elevations and crater names by use of a Roman capital letter. Ridges will be called *dorsa* and crater chains designated *catena*. Future name assignments will also contain the names of distinguished and deceased contributors to human culture and knowledge; political, military, and religious figures were excluded. Maps with all lunar names are too large for this sourcebook.

The reader is referred to The Rectified Lunar Atlas (*Whitaker et al.*, 1964; *Wilhelms*, 1987) for more details.

LUNAR SURFACE PROCESSES

Friedrich Hörz, Richard Grieve, Grant Heiken, Paul Spudis, and Alan Binder

The Moon's surface is not affected by atmosphere, water, or life, the three major agents for altering terrestrial surfaces. In addition, the lunar surface has not been shaped by recent geological activity, because the lunar crust and mantle have been relatively cold and rigid throughout most of geological time. Convective internal mass transport, which dominates the dynamic Earth, is therefore largely absent on the Moon, and so are the geological effects of such internal motions—volcanism, uplift, faulting, and subduction—that both create and destroy surfaces on Earth. The great contrast between the ancient, stable Moon and the active, dynamic Earth is most clearly shown by the ages of their surfaces. Nearly 80% of the entire solid surface of Earth is <200 m.y. old. In contrast, >99% of the lunar surface formed more than 3 b.y. ago and >70% of the lunar surface is more than ~4 b.y. old.

Despite the fact that lunar surface processes are less varied and dynamic than those of the Earth, complex alterations of the lunar surface do occur; the most important source of such alterations, at least during the last 3 b.y., is external to the Moon. The Moon's stable but heavily cratered surface provides evidence that planets are continuously bombarded by external objects ranging from small dust specks to giant bodies tens of kilometers in diameter.

The Moon and all other planets are not isolated, closed systems. They are an integral part of a dynamic solar system that continues to evolve under largely gravitational forces. Orbits of predominantly small bodies are continually rearranged by close

encounters with each other and with larger planets throughout the lifetime of the solar system. These orbital alterations are generally minor, but they ensure that, over geological periods, collisions with other bodies will occur.

When such a collision happens, two outcomes are possible. If "target" and "projectile" are of comparable size, collisional fragmentation and annihilation occurs, producing a large number of much smaller fragments. If the target object is very large compared to the projectile, it behaves as an "infinite halfspace," and the result is an impact crater in the target body. For collisions in the asteroid belt, many of the resulting collisional fragments or crater ejecta escape the gravitational field of the impacted object; many of these fragments are then further perturbed into Earth-crossing orbits to form the majority of the projectiles that impact the Earth and Moon.

The Moon's population of impact craters represents a faithful record of these collisional processes over most of the lifetime of the solar system. By comparison, only the barest outlines of the cratering history of Earth can be reconstructed, even for just the last 200 m.y., and only a few structures older than 500 m.y. have been identified.

Typical impact velocities of asteroidal objects on the Moon at present are between 15 and 25 km/sec; they were apparently somewhat lower prior to 4 b.y. ago. Such high velocities, combined with a high frequency of impact events (especially before 3.8 b.y. ago), have expended a cumulative kinetic energy on the lunar surface that exceeds the lunar internal energy released by volcanism and seismicity. As a

result, meteorite impact has been, and continues to be, the dominant lunar surface process, although volcanic and tectonic processes were also important in the Moon's distant past.

In this chapter, lunar surface processes are grouped by decreasing importance into impact-related phenomena (section 4.1), volcanic processes (section 4.2), and tectonic activity (section 4.3). A summary of lunar geologic history and associated stratigraphy is presented in section 4.4.

4.1. IMPACT PROCESSES

The projectiles that now enter the Earth/Moon system are derived from the asteroid belt and from comets. The most massive objects are entire asteroids or comets, which are generally a few kilometers in diameter, but rarely a few tens of kilometers across. Most projectiles, however, are smaller fragments from asteroidal collisions that vary widely in size; small specimens reach the Earth's surface as meteorites a few grams to a few metric tons in weight. The exceedingly fine-grained "micrometeoroids" (fragments <1 mm in diameter, with masses $\lesssim 10^{-2}$ g; see section 3.10) may be either the most fine-grained collisional debris from asteroids or small particles released from comets (e.g., *Gehrels, 1979; Shoemaker, 1983*).

Projectile masses impacting the lunar surface have ranged over 35 orders of magnitude, from microscopic dust particles weighing 10^{-15} g to huge asteroids of 10^{20} g; associated kinetic energies vary from a small fraction of an erg to $\sim 10^{32}$ ergs per individual impact. By comparison, the total internal energy released by the Earth, which drives such visible processes as volcanism and tectonism, is estimated at 10^{26} to 10^{27} ergs per year (*Lammlein et al., 1974*). The "geologic" manifestations of impacts on the Moon range from microscopic craters <0.1 μm in diameter on tiny grains of lunar soil to impact basins hundreds of kilometers across on the lunar surface. Lunar global surface evolution has thus been dominated by a small number of discrete but rare, large-body, basin-forming impacts as well as by the more continuous pounding from numerous smaller and less energetic projectiles. The latter group produces smaller craters, together with some unique cumulative surface effects.

Characterization of many lunar surface processes therefore requires an understanding of the consequences of single hypervelocity (>3 km/sec) impacts of vastly different scales. Section 4.1.1 provides a phenomenologic and geometric description of fresh impact craters. This is followed by a summary of our current understanding of impact physics and its major geologic consequences (section 4.1.2). When combined with isotopically-determined ages of

returned lunar samples, the statistical number of lunar craters per unit area provides important constraints on both the relative and absolute ages of various surface units and on the nature of the projectile flux through geologic time (section 4.1.3). Such calculations permit an assessment of cumulative cratering effects by modeling the stochastic nature of repetitive impacts (section 4.1.4).

The importance of impacts on the Moon extends far beyond the simple formation of crater-shaped landforms. The largest impact structures, which are the multiring basins that constitute major topographic and structural features of the Moon, have also served as sites for later volcanic and tectonic activity. Furthermore, the lunar surface materials and deeper crustal rocks that are excavated from impact craters are also processed by impacts in ways that greatly affect their petrographic appearance (Chapter 6), surface debris (Chapter 7), chemical composition (Chapter 8), and physical properties (Chapter 9).

4.1.1. The Morphology of Impact Structures

Terminology. The fundamental shape of an impact feature is that of a bowl-shaped depression (a crater) surrounded by a raised rim. Impact crater shapes vary with crater diameter (measured from rim to rim). With increasing diameter, they become proportionately shallower and develop more complex rims and floors, including the appearance of central peaks and rings. Such morphologic changes are found in craters on all the terrestrial planets and moons (*Pike, 1980*). Some basic terms for the range of features associated with fresh, uneroded impact craters are illustrated by the examples in Fig. 4.1, and schematic views of various crater features are shown in Fig. 4.2.

The basic morphologic subdivisions of impact structures are (1) *simple craters*, (2) *complex craters*, and (3) *basins*. *Simple craters* are generally bowl-shaped with rounded or, in some cases, small, flat floors (*Smith and Sanchez, 1973*). They have smooth rims that lack terraces. With increasing diameter, simple craters develop scalloped walls as large masses of rock and regolith are slumped onto a generally hummocky crater floor (Figs. 4.1 c,d).

With larger diameters, simple craters evolve into *complex craters*, which are characterized by terraced and crenulated rims, or by zones of broad-scale (inward) slumping, and by an uplifted central peak or peaks protruding from a relatively broad, flat floor.

On the Moon, the transition from simple to complex craters takes place in the 15–20 km diameter range (*Pike, 1977*). *Central peaks* are rarely observed in craters <10 km, but most fresh craters >35 km and <100 km have central peaks (*Wood and*

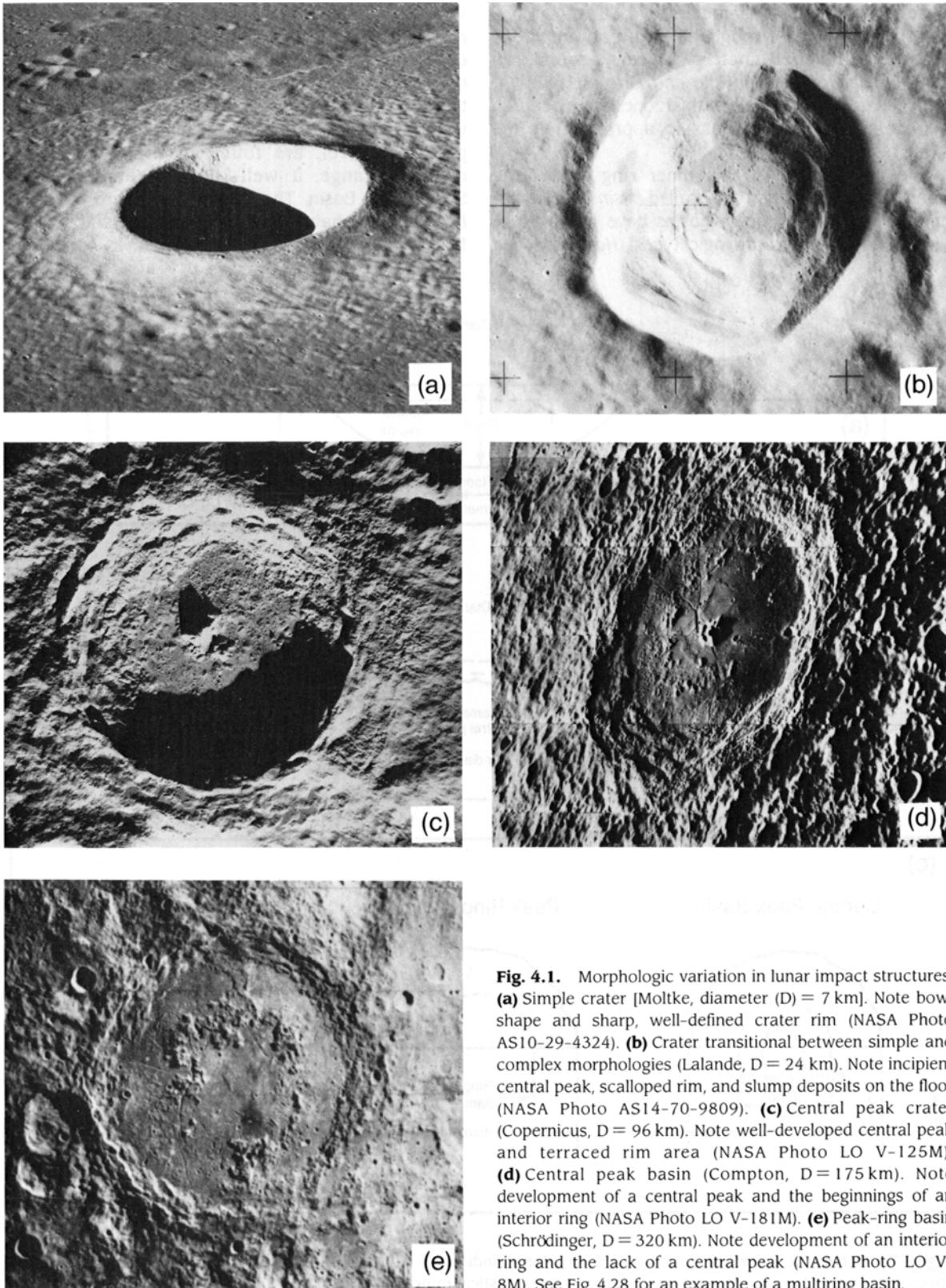


Fig. 4.1. Morphologic variation in lunar impact structures. **(a)** Simple crater [Moltke, diameter (D) = 7 km]. Note bowl shape and sharp, well-defined crater rim (NASA Photo AS10-29-4324). **(b)** Crater transitional between simple and complex morphologies (Lalande, D = 24 km). Note incipient central peak, scalloped rim, and slump deposits on the floor (NASA Photo AS14-70-9809). **(c)** Central peak crater (Copernicus, D = 96 km). Note well-developed central peak and terraced rim area (NASA Photo LO V-125M). **(d)** Central peak basin (Compton, D = 175 km). Note development of a central peak and the beginnings of an interior ring (NASA Photo LO V-181M). **(e)** Peak-ring basin (Schrödinger, D = 320 km). Note development of an interior ring and the lack of a central peak (NASA Photo LO V-8M). See Fig. 4.28 for an example of a multiring basin.

Andersson, 1978). At diameters of >80 km, a concentric zone of floor roughening with an amplitude of several hundred meters appears around the central peak or peaks (Hale and Grieve, 1982). At larger diameters (>100 km) this zone is replaced by a fragmentary ring of peaks in approximately the same region (Figs. 4.1 d,e).

The appearance of this inner ring marks the transition from craters to so-called *basins* (Hartmann and Kuiper, 1962). Impact basins have been subdivided into three morphologic types (Hartmann and

Wood, 1971). *Central peak basins*, such as Compton, are relatively small basins with a fragmentary ring of peaks surrounding a central peak (Fig. 4.1d). They occur in the 140–175 km diameter range and are transitional to peak-ring basins. *Peak-ring basins*, which have a well-developed ring but lack a central peak (Fig. 4.1 e), are found in the 175–450 km diameter range; a well-known example is the Schrödinger Basin. The largest basins are *multiring basins*, which have as many as six concentric rings. Multiring basins are generally more than 400 km in

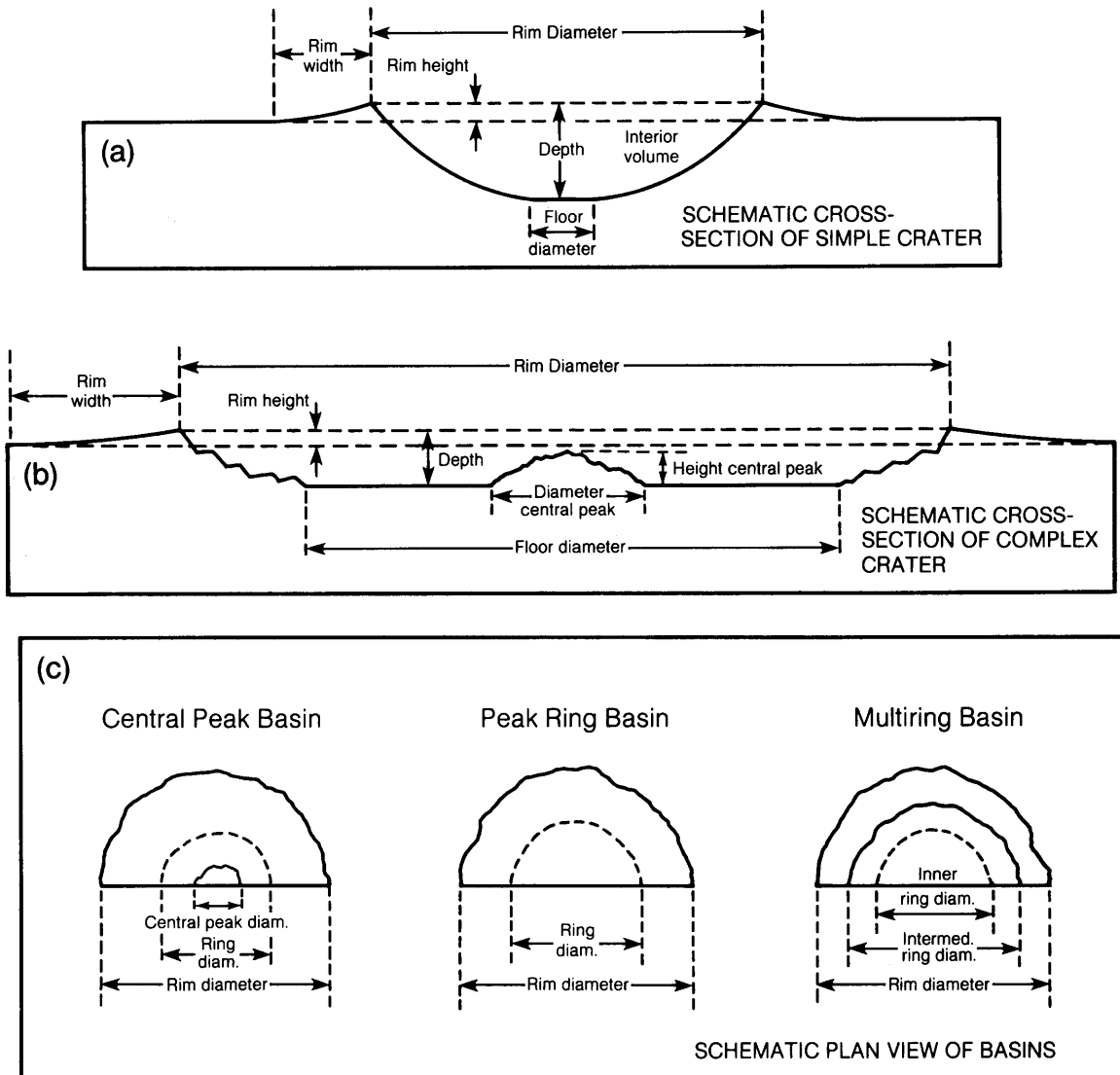


Fig. 4.2. Schematic views of lunar impact structures, indicating principal morphologic elements. (a) Simple crater, (b) complex central peak crater, (c) various basins. For statistical (morphometric) data on these elements, see Table 4.1.

diameter; the best example is the Orientale Basin, which has been only partly flooded by lavas (Fig. 4.28). The definition of diameters for the various basin shapes can vary among workers, depending on the exact criteria and datasets examined.

The most comprehensive classification of lunar crater shapes is that of *Wood and Andersson* (1978). Their catalog, which is based on observations from Lunar Orbiter IV photographs, is a compilation of morphologic and morphometric data for 11,462 craters. In the catalog, crater shape classification is more detailed than that outlined above, and 18 different crater types are recognized. Some, however, represent rare variants. There also is some argument as to whether all observable crater forms represent distinct morphologic types, whether some forms are transitional stages between accepted end members (*Ravine and Grieve*, 1986), or whether some forms are the result of the effects of varying target properties on crater shape (*Cintala et al.*, 1977).

The catalog of *Wood and Andersson* (1978) also includes criteria for the classification of progressively eroded and degraded impact structures. Estimates of "degradation" (extent of erosion) are based on such features as rim continuity, rim sharpness, and infilling of the crater cavity by mass wasting. *Class 1* craters are the freshest and least eroded; *class 5* craters are the most degraded and are only marginally recognizable as impact features. Obviously, the signature of a 1-km-diameter crater is obliterated faster than that of a 100-km-diameter crater. Degradational state and the associated classification become important, therefore, when one evaluates the relative formation ages of specific craters or crater populations (*Soderblom*, 1970; *Wilhelms*, 1985; see also section 4.4).

Morphometry. Morphometric studies are concerned with the measurement of landform shape and dimensions. For fresh lunar craters, they describe the fundamental diameter-dependent variations in crater shape as outlined above, such as the statistical variation of crater depth with rim diameter. Morphometric measurements are based on Lunar Orbiter and higher-resolution Apollo imagery, or on derivative map products such as Lunar Topographic Orthophotomaps.

Detailed measurements of lunar imagery have made it possible to represent the different geometrical characteristics of lunar impact craters by equations of the form

$$y = aD^b$$

where y is a given crater characteristic (e.g., depth, rim height), D is the diameter of the crater (measured from rim to rim), and a and b are constants.

Specific equations for a large number of crater characteristics are summarized in Table 4.1, which also shows variations in such features as the volume of central peaks.

4.1.2. The Cratering Process

Upon impact, the projectile's kinetic energy is transformed into *shock waves* that travel forward from the interface into the target and rearward into the projectile (Fig. 4.3). In the target, particle motion induced by the shock wave accelerates the impacted materials radially downward and outward. At the same time, the projectile is decelerated by shock waves that propagate rearward, opposing the direction of flight. Specific energies of the highly compressed target and projectile materials are increased; upon adiabatic decompression after passage of the shock wave, this increase appears as waste heat. At cosmic impact velocities (15–20 km/sec) and associated pressures (up to several hundred GPa), substantial volumes of the target and virtually all of the projectile may be melted, vaporized, or even ionized. Subsequent unloading from these high-pressure states is initiated by the release waves or *rarefaction waves* that form as the shock wave reaches free surfaces, such as the rear of the projectile or the ground surface at some distance from the impact point. Rarefaction waves modify the initial shock particle motions and ultimately set up a flow field that initiates and eventually completes the actual crater excavation (e.g., *Maxwell*, 1977; *Orphal*, 1977; *Croft*, 1980).

Cratering mechanics. The processes that form small simple craters are well understood from experiments (*Gault et al.*, 1968; *Stöffler et al.*, 1975), calculations (*Maxwell*, 1977; *Orphal et al.*, 1980), and observations at terrestrial and lunar impact structures (*Roddy et al.*, 1977; *Dence et al.*, 1977; *Grieve et al.*, 1981; *Basilevski et al.*, 1983; *Stöffler et al.*, 1985). During early penetration of the projectile, a roughly hemispherical cavity with a radius not much larger than that of the projectile is formed, and most of the impactor's energy and momentum are rapidly transferred to the target (*Holsapple and Schmidt*, 1986). A roughly hemispherical shock front propagates outward from this cavity into the target. Total energy transfer, combined with the radial engulfment of increasing volumes of material and the resultant associated decrease in specific energy, will determine the attenuation rate of the shock wave and the fractional target volumes shocked to specific peak pressures (e.g., *Ahrens and O'Keefe*, 1977).

Interaction of the shock wave with the target's free surface begins very early and essentially at the impact point; a rarefaction wave results. Because the

TABLE 4.1. Morphometric relations for fresh lunar impact craters (see Fig. 4.2).

Crater Characteristic	D, km*	N	Exponent (b)	Coefficient (a)	Source
<i>Simple Craterforms</i>					
Depth	<15	171	1.010	0.196	Pike (1974b)
Rim height	<15	124	1.014	0.036	Pike (1977)
Rim width	<15	117	1.011	0.257	Pike (1977)
Floor diameter	<20	38	1.765	0.031	Pike (1977)
Interior volume	<13	47	3.00	0.040	Croft (1978)
<i>Complex Craterforms</i>					
Depth	12-275	33	0.301	1.044	Pike (1974b)
Rim height	15-375	38	0.399	0.236	Pike (1977)
Rim width	15-375	46	0.836	0.467	Pike (1977)
Floor diameter	20-125	53	1.249	0.187	Pike (1977)
Diameter (central peak)	17-175	175	1.05	0.016	Hale and Head (1979)
Basal area central peak	17-136	19	2.19	0.09	Hale and Grieve (1982)
Height central peak	17-51	15	1.969	0.589×10^{-3}	Hale and Grieve (1982)
Central peak volume	17-51	15	5.078	0.987×10^{-7}	Hale and Grieve (1982)
Central peak volume	80-136	4	3.599	0.397×10^{-5}	Hale and Grieve (1982)
Interior volume	19-150	21	2.31	0.238	Croft (1978)
<i>Basins</i>					
Diameter ring in central peak and peak ring basins	140-435	12	1.125	0.245	Head (1977)
Diameter inner ring in multiring basins	420-1160	13	0.943	0.708	Pike and Spudis (1987)
Diameter intermediate ring in multiring basins	420-1160	13	0.970	0.845	Pike and Spudis (1987)

* This column indicates the range of rim-to-rim crater diameter values (D) used to establish relations for other crater characteristics; N is the number of craters used. Relations are of the form $y = aD^b$, where y is the crater characteristic (e.g., crater depth, rim height, etc.), D is the rim-to-rim crater diameter, and a and b are constants. Linear crater dimensions (depth, height, diameter, etc.) are in km. Volumes (central peaks, crater interiors, etc.) are in km³.

shock-induced particle motions are small when compared with shock-wave and rarefaction-wave velocities, the shocked material near the impact point has not moved substantially by the time the rarefaction waves arrive. The initial shock-produced particle motions are therefore modified because the rarefaction wave fronts generated at the target surface are not parallel with the direction of shock acceleration (other than along the centrosymmetric axis).

Through the interactions of the shock waves and rarefaction waves, the initial radial accelerations in the target are changed to motions with distinct upward components, especially for near-surface strata. A subsurface flow field (Fig. 4.3) is thus established and controls both excavation and ejection processes. In detail, the exact geometry and other aspects of this flow field are poorly understood for impacts. However, qualitatively analogous flow fields occur during explosive cratering events, as described and analyzed for nuclear explosion craters by Maxwell (1977) and for laboratory explosion and impact experiments by Oberbeck (1977).

Components of the target volume that travel along upward and outward flowlines at sufficient velocity to be excavated and thrown above the initial target surface will form crater *ejecta* and will define the *excavation cavity* of the crater. Materials beyond this excavation cavity are also set in motion, but their flow directions and velocities do not result in ejection. These materials are displaced, either by downward compression in the central part of the crater or by structural uplift in the rim area outside the excavation cavity (Fig. 4.3).

At the instant that the shock-induced particle flow ceases, the total excavated and (temporarily) displaced target materials define the so-called *transient cavity*. The latter is substantially deeper than the excavation cavity, but their diameters are similar. This is an important concept: *A crater's maximum depth of excavation is shallower than the maximum depth of the transient cavity.* As the name implies, the latter is a temporary phenomenon. The compressed materials immediately unload, leading to predominantly upward motion in the crater's center. Some of the materials temporarily displaced

as structural rim uplifts are gravitationally unstable and slide downward and inward, thus modifying the transient cavity by collapse. Once all motion ends, the result is a geometrically simple, bowl-shaped cavity that resembles neither the “excavation” nor the “transient” cavity precisely.

Reconstructions of well-studied terrestrial simple craters suggest that the transient cavity has a depth-to-diameter ratio of $\sim 1/3$ (Dence *et al.*, 1977). There is, however, no direct information on the equivalent dimensions of lunar simple craters. The maximum depth of excavation at terrestrial simple craters has been estimated as $\sim 0.14 D$ by Grieve *et al.* (1981) and

as $\sim 0.1 D$ based on a first-order analytical model of Maxwell (1977; see also Croft, 1980), where D is the diameter of the transient cavity.

The transient crater may be an ideal that never truly exists as a physical reality. Computer models, using continuum mechanical code calculations, indicate that maximum cavity depth is reached prior to maximum radial growth (Orphal *et al.*, 1980). As a consequence, incipient rebound of the crater floor may occur before ejection and radial growth are finished. In any case, the brecciated and fractured walls of the transient cavity and the elevated rim area are highly unstable and collapse inward,

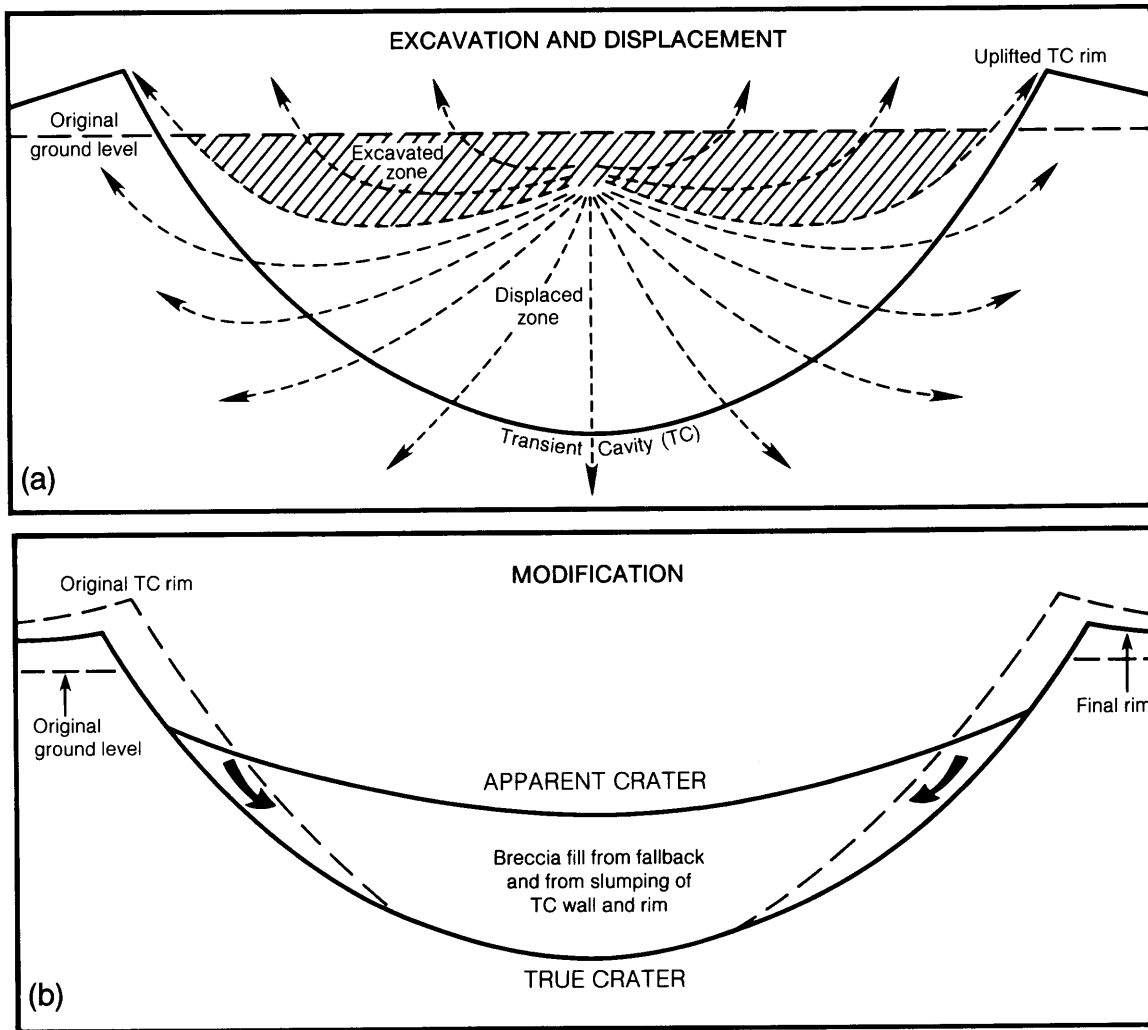


Fig. 4.3. Model of the formation of a simple crater. **(a)** Formation of the transient cavity by a combination of excavation and displacement induced by the cratering flow field, which in turn is established by the shock and rarefaction waves. **(b)** Inward collapse of the transient cavity walls and rim to form an interior breccia lens and the final apparent crater [see text (section 4.1.2) for further details].

enlarging the diameter slightly and partially filling the crater with a lens of brecciated material that is commonly observed in terrestrial simple craters (Grieve and Garvin, 1984; Fig. 4.3). Thus the final form of a simple crater is a bowl-shaped depression underlain by a breccia lens (Fig. 4.3). The visible crater form is known as the *apparent crater*, while the form that includes the continuation of the wall under the breccia lens is known as the *true crater* (Grieve, 1981; Fig. 4.3).

There is less consensus on the details of cratering mechanics during formation of complex craters and basins (Schultz and Merrill, 1981). Considerable observational evidence from complex terrestrial craters (Dence et al., 1977) supports the hypothesis that the rim terraces and central structures are indicative of extensive structural movement. Terraces are clearly composed of material that has collapsed inward from the rim area. Central peaks are uplifted from beneath the transient crater floor (Grieve et al., 1981).

The majority of cratering models for complex craters focus on uplift and collapse hypotheses in which the transient cavity is modified under conditions of low material strength (Melosh, 1977, 1982). The driving forces for modification have been considered to be gravity and elastic rebound (Ulrich et al., 1977; Grieve and Robertson, 1979). Small central uplifts are obscured in lunar craters with smaller diameters than those that display rim terraces (Wood and Andersson, 1978; Pike, 1980), supporting the hypothesis that rebound of the crater floor produces central peaks by inward and upward material flow, which in turn may facilitate rim collapse and terrace formation.

In lunar ring basins the major structural ring is usually interpreted as a collapse feature and taken to be the actual crater "rim" (Figs. 4.2c, 4.28a). However, the formation of additional rings interior and exterior to this main ring, or rim, is not well understood. As the diameter of a complex crater increases, the size of the central peak also increases up to ~80 km diameter (Hale and Head, 1979), where the height appears to stabilize at an equilibrium elevation. At this diameter, concentric floor roughening is obscured in the approximate position at which an interior ring appears in larger-diameter structures (Hale and Grieve, 1982). Observations at terrestrial structures indicate increasing degrees of structural uplift with increasing diameter. Floor roughening, and ultimately an interior ring, may represent the excess volume of uplifted material that could not be accommodated in a central peak.

These observations have led to models of ring formation in which an initial central peak is uplifted beyond its equilibrium height and collapses to form

a peak and ring (Fig. 4.4d). To form additional interior rings, it has been suggested that the central uplifted area may oscillate up and down to produce a series of rings (Murray, 1980). This is a variant of the "tsunami" hypothesis (Baldwin, 1974), in which the rings are likened to frozen ripples formed after throwing a stone into water. Other hypotheses have been offered for basin rings, for example, the "nested crater" hypothesis (Hodges and Wilhelms, 1978). The origin of rings outside the main rim is obscure but some attempts have been made to explain them as a structural discontinuity associated with impact-induced rupturing and fracturing (Croft, 1981). It is clear that our understanding of basin-sized events, which involve energies in the range of 10^{32} ergs (O'Keefe and Ahrens, 1975) or the equivalent of billions of megatons of TNT, is incomplete. Many of the unanswered questions must await detailed on-site geologic investigations of basin rings on the Moon.

At present, the uplift and collapse hypotheses, in which the uplifted material behaves hydrodynamically during modification, appear most promising. These hypotheses are based on the assumption that much of the target material behaves as if it has little or no strength for some time following initial cavity formation, similar to the behavior of experimental craters in water and mud (Gault and Greeley, 1978; Gault and Sonett, 1982). The model of basin formation shown in Fig. 4.4 considers that at least initially the transient cavity is similar to that of simple craters. It is rapidly modified, however, by extensive uplift, while minor near-surface excavation may be continuing. Thus the reconstructed cavity would appear like a sombrero with the volume corresponding to the high crown limited to the central region (Croft, 1981). Whether this model corresponds to reality is speculation. It does, however, have points in common with some observational data at smaller terrestrial structures and with cratering experiments in low-strength materials.

The initial cavity shape of a ring basin is related to excavation depth. This concept is especially important in trying to establish the source of lunar samples, all of which have been collected as loose fragments on the surface. Such studies are especially important in two areas: attempting to estimate depths from which deep-seated fragments have been excavated by impact basins (Spudis, 1984), and attempting to construct a lunar stratigraphy (Wilhelms, 1985) from the isolated fragments sampled by astronauts and robot missions.

A lack of consensus still exists on these matters, partly because of some confusion about terminology and partly from disagreement over the details of cratering mechanics for large basin-forming events.

In particular, there has been disagreement over which ring in a multiring structure, if any, corresponds to the rim of the original excavated cavity. These difficulties can be illustrated by considering the range of estimates in the literature for the maximum diameter and depth of excavation for the Orientale Basin (Table 4.2; see also Fig. 4.28).

In summary, the processes occurring during formation of relatively small, simple, bowl-shaped craters appear to be well understood from terrestrial and lunar field observations, laboratory experiments, and theory (see the summary by *Holsapple and Schmidt*, 1986). The phenomena associated with complex craters, especially with basin-forming impacts, are poorly understood, despite considerable efforts to "scale" observations from controlled laboratory experiments to large natural structures.

The problems in such scaling efforts arise less from dimensional aspects than from uncertainties about material properties and behavior, for example, (1) the finite (tensile) failure strengths of severely shocked rocks (*Curran et al.*, 1977), (2) possible

differences in energy partitioning between laboratory experimental velocities and impacts at cosmic speeds (*Ahrens and O'Keefe*, 1977), and (3) estimating the proper balance between work done against the intrinsic dynamic strength of rocks *vis-à-vis* work done against the prevailing gravity field. After all, a crater can form only if rock is broken and lofted out of the growing cavity. At small cratering scales the strength parameter dominates, but the growth of large structures is controlled primarily by gravity.

Such theoretical scaling calculations are critical to understanding the cratering process. They are important in attempts to reconstruct the characteristics (size, velocity, density) of the populations of projectiles responsible for an observed crater population. Ideally, one would like to relate some measured crater properties (e.g., diameter) to the total kinetic energy of the projectile and thus determine the mass, momentum, and velocity of the projectile that formed it. Such reconstruction is difficult at present and is still highly model-dependent. Indeed, as illustrated by the Orientale

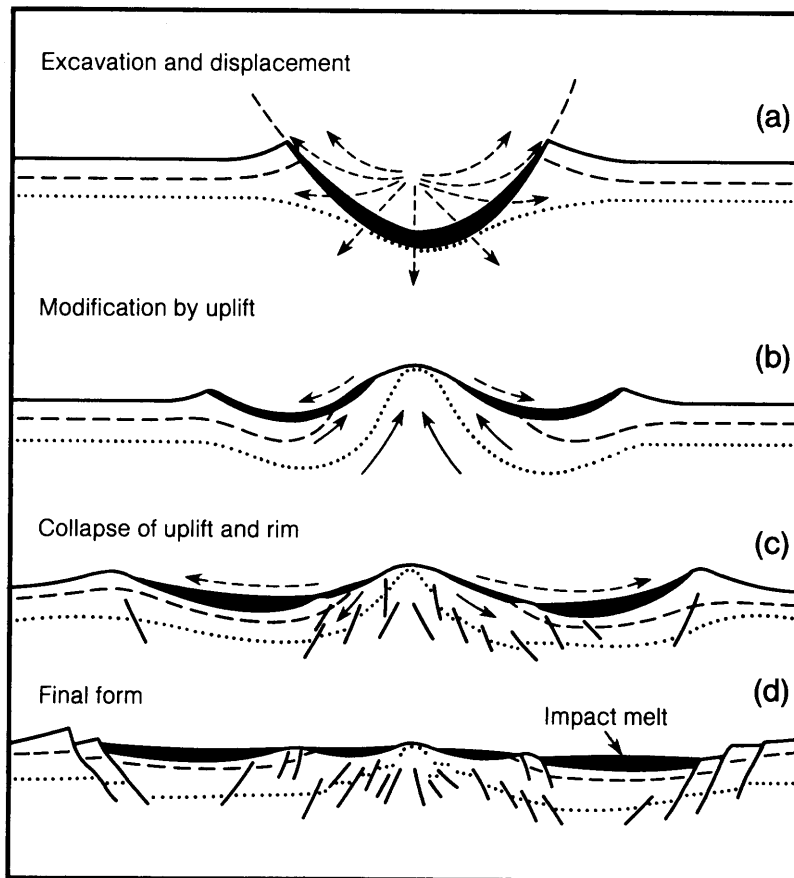


Fig. 4.4. Possible model for the formation of an impact basin with a central peak and interior ring. **(a)** Excavation and displacement to form a transient cavity initially similar to that of a simple crater. **(b)** Modification of the transient cavity by uplift of the cavity floor above the original ground surface, accompanied by minor near-surface excavation. **(c)** Collapse of the overheightened central peak uplift. **(d)** Formation of outer final rim by downfaulting to form terraces and the appearance of an interior ring, which contains the excess of the originally uplifted material that could not be accommodated in the central peak. See text for further details and alternate models (after *Grieve et al.*, 1981).

TABLE 4.2. Estimates of maximum excavation diameter and depth for the Orientale Basin (Fig. 4.28a).

Excavation Diameter, km	Morphologic Feature Used to Estimate Diameter of Excavation	Excavation Depth, km	Source
—	—	130	<i>Dence (1973)</i> , as cited by <i>Head et al. (1975)</i>
600	Outer Rook Mts.	85	<i>Moore et al. (1974)</i>
620	Outer Rook Mts.	6–20	<i>Head et al. (1975)</i>
850	Cordillera Mts.	85	<i>Hodges and Wilhelms (1978)</i>
850	Cordillera Mts.	—	<i>Murray (1980)</i>
500–600	Inner-Outer Rook	50	<i>Spudis et al. (1984)</i>
480	Inner Rook Mts.	50	Terrestrial analogy, calculated from <i>Grieve et al. (1981)</i>

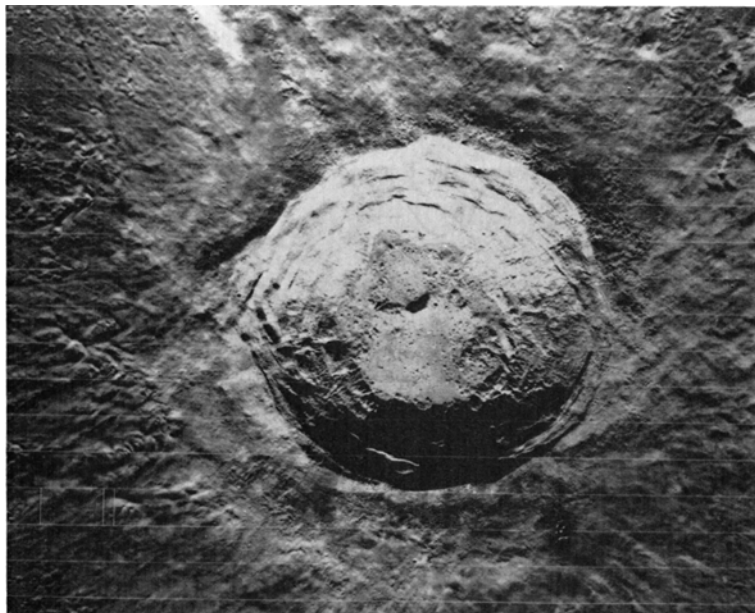
Basin (Table 4.2), there is not even consensus on what feature marks the rim of the original excavation cavity.

The nature of ejecta. Ejection of debris from an impact crater is a remarkably ordered process. With increasing radial distance from a crater, the material ejected from the crater (*ejecta*) forms successively continuous deposits, discontinuous deposits, and rays (Fig. 4.5). Materials ejected early in the cratering process originate close to the target surface and close to the point of impact. Pressure gradients are highest in this zone, and the ejecta are therefore dominated by small fragments traveling at high speeds. They also take off at relatively high ejection angles. As the excavation process continues, mate-

rials of larger average size, slower velocity, and lower ejection angle emanate from the growing cavity. While individual ejecta fragments follow their own ballistic trajectories, they cumulatively form a relatively thin, coherent “curtain” of material, as illustrated in Fig. 4.6 (*Shoemaker, 1962; Oberbeck, 1975*). There is distinct order in such an ejecta curtain; the near-surface target strata produce a relatively fine-grained high-velocity component, with steep take-off angles, higher in the curtain. More deepseated target strata occur predominantly as coarser fragments and boulders at the curtain’s base.

Both theory and models of cratering predict that ejecta deposited near the crater rim should be coarser grained than ejecta far from the rim. This

Fig. 4.5. The well-preserved central peak crater Aristarchus (D = 40 km). The crater is surrounded by a hummocky, continuous ejecta deposit. At greater radial distance, the deposits become discontinuous, as evidenced by chains and clusters of secondary craters. Near the limit of the lobate continuous deposits, the secondary craters are partially filled and draped by mixed primary ejecta and by local materials that moved outward by ground-hugging flow. Also note the well-developed wall terraces and other evidence for slumping in the crater interior (NASA Photo LO V-198M).



prediction has been confirmed by observations on the maximum size of ejecta blocks (Moore, 1972; Table 4.3) and by the decreasing number of discernible blocks in lunar photographs with increasing distance from the crater (Cintala et al., 1982).

This relation between the original position of an ejecta fragment within the target and the resulting ejection velocity, ejection angle, and particle size produces a high degree of order during ejecta deposition. Deep-seated, coarse materials barely make it over the crater rim and compose essentially the coarse rim deposits, while materials of decreasing target depth are deposited at increasingly larger radial distances. This situation produces an inverted stratigraphy in the ejecta deposits, relative to the stratigraphy in the original target. Any radial traverse from the periphery of an ejecta blanket toward the crater rim will encounter materials from progressively deeper target strata.

This concept, which has been demonstrated at terrestrial impact structures (e.g., Hörz et al., 1983) is paramount for any geologic exploration of the lunar surface (Shoemaker, 1972; Gault et al., 1968; and many others). For example, it is possible to use the morphometric information summarized in Table 4.1 to determine that the near-rim deposits of a specific crater originated at or close to the bottom of the excavation cavity and thus at some absolute depth. A series of craters, with increasingly larger diameters, may thus be used to probe deeper and deeper formations in a given geologic terrane, thus enabling reconstruction of first-order stratigraphic and structural relationships at depth principally from simple surface observations. Such considerations indeed greatly affect our current perception of the lithologic make-up of the lunar crust based on rocks and remote-sensing information gathered from the surface (Spudis et al., 1984; Wilhelms, 1985).

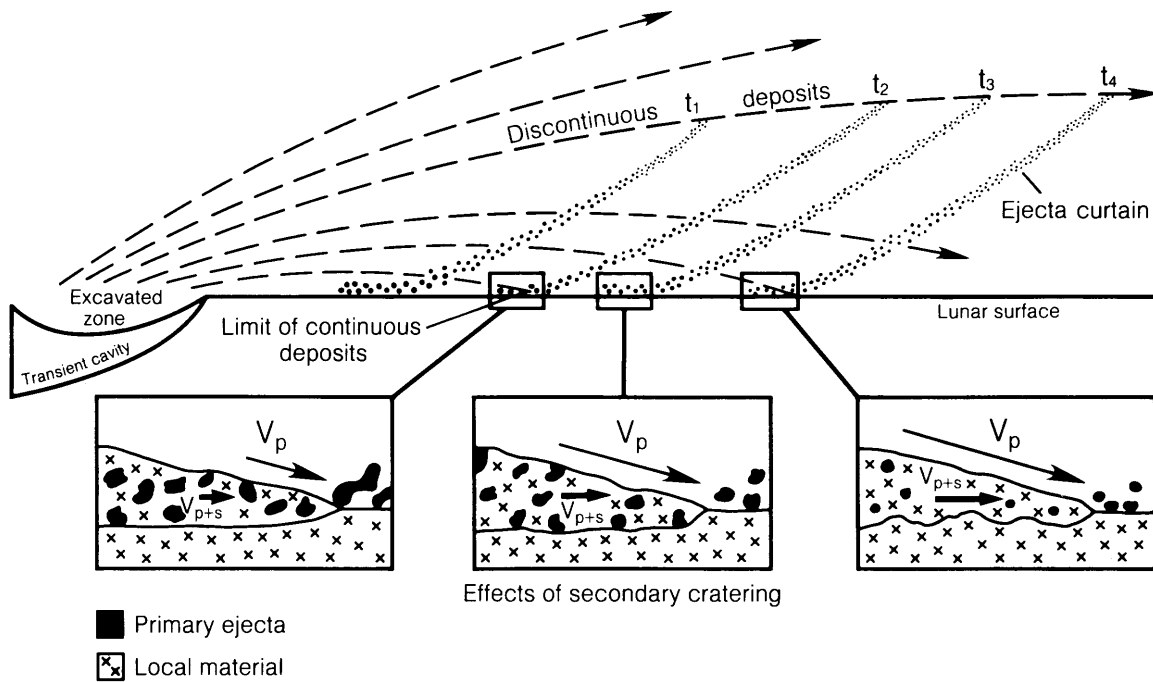


Fig. 4.6. Ejection processes and interaction of ejecta with the lunar surface. Ejecta leave the crater cavity along discrete, relatively shallow ballistic trajectories. At any given time (t) these trajectories define an outrunning ejecta curtain. Coarse-grained, low-velocity ejecta travel along low-angle trajectories and are concentrated at the base of the curtain. They impact close to the crater and excavate modest amounts of local substrate material (see insert; V_p = impact velocity of ejecta; V_{p+s} = radial flow velocity of the resultant debris surge combining “primary” and “secondary” ejecta). Finer-grained fragments reside higher in the ejecta curtain, having been ejected at increasingly higher V_p and steeper angles. As the curtain sweeps radially across the surrounding target, higher-velocity ejecta impact the surface causing local materials to be incorporated in the debris surge, resulting in increasingly higher flow velocities of the debris surge (after Oberbeck, 1975).

TABLE 4.3. Dimensional relations of crater ejecta.

Crater Characteristic	D, km*	N	Exponent (b)	Coefficient (a)	Source
Radial distance of continuous ejecta	1.3-436	84	1.006	1.169	Moore et al. (1974)
Radial distance of continuous ejecta	0.56-1300	8	0.976	1.064	Oberbeck et al. (1974)
Distance rays can be traced from rim	3.2-132	50	1.25	4.41	Moore et al. (1974)
Maximum diameter of ejecta blocks	0.1-98	60	0.66	2.99×10^{-2} 9.97×10^{-3}	Moore (1972)
Thickness of ejecta at the rim*	1.2-970	5	0.74	0.014	McGetchin et al. (1973)

* This column indicates the range of rim-to-rim crater diameter values (D) used to establish relations for other crater characteristics. N is the number of craters used. Relations are of the form $y = aD^b$, where y is the crater characteristic (e.g., crater depth), D is the rim-to-rim crater diameter, and a and b are constants. Linear dimensions (crater diameter, distances, etc.) are in km.

†Includes terrestrial crater and nuclear explosion crater data.

The ejecta deposits surrounding impact sites are generally highly centrosymmetric, regardless of the angle at which the projectile struck the surface. This condition reflects the fact that, for most impact angles, the shock and rarefaction waves are propagated with near-spherical symmetry. Experiments summarized by Gault (1973) indicate that, at cosmic velocities, projectile trajectories inclined at $<15^\circ$ to the local horizontal are required to produce elongated, noncentrosymmetric crater cavities and associated, noncentrosymmetric ejecta blankets. Therefore, for most craters, the ejecta distribution is generally centrosymmetric, and three "facies" can be recognized with increasing radial distance (see, e.g., Moore et al., 1974 and Fig. 4.6).

1. The *continuous ejecta*, deposited closest to the crater, completely drape all preexisting ground around the impact site. The extent of such continuous ejecta blankets increases linearly with crater diameter (Moore et al., 1974). The outer periphery of the continuous ejecta is lobate and grades into the zone of discontinuous ejecta.

2. *Discontinuous ejecta* deposits are characterized by patchy and localized deposition of ejecta material. These deposits frequently contain shallow and elongate *secondary craters* that tend to occur in clusters.

3. *Ejecta rays*, which are an extreme form of discontinuous ejecta deposits, occur beyond the zone of discontinuous ejecta as relatively thin, long streaks oriented radially to the crater. For large lunar craters, such as Copernicus and Tycho, these streaks may extend over a substantial fraction of the lunar

globe, while ejecta rays emanating from large ring basins may extend over the entire surface of the Moon.

The ejecta thickness at the crater rim and the variation of that thickness with crater diameter in different craters has been estimated from both lunar and terrestrial data (Table 4.3). One relationship derived from both lunar and experimental craters, including nuclear explosion events, is

$$t = 1.7 \times 10^{-3} r^3 D^{2.74}$$

where t is ejecta thickness at increasing range from the crater center, r is radial range from the crater center, and D is crater diameter (all units in kilometers; McGetchin et al., 1973). Unfortunately, predictions from this relationship for the most important ejecta deposits on the Moon, those from the large multiring basins, can be 'ambiguous. The crater diameter in the relationship is the diameter of the excavated cavity, estimates of which, as noted previously, can vary widely, as in the case of Orientale (Table 4.2). Pike (1974a) has also called into question the validity of the relationship defining ejecta thickness at the crater rim because it is based in part on nuclear explosion craters, which may not be exactly analogous to impact craters.

Secondary craters. Based on laboratory impact experiments related to ejecta dynamics, Oberbeck (1975) was able to expand on the early calculations by Shoemaker (1962) to estimate the fraction of crater ejecta that travels at sufficient velocities to produce secondary craters upon landing. This fraction increases with increasing crater diameter. In

fact, the cumulative volume of material excavated by these secondary impacts can exceed the primary crater volume, because low-velocity impactors (such as ejecta) excavate more efficiently than high-velocity meteoroid projectiles, which partition large fractions of their energy into waste heat.

This model for secondary crater formation leads to the conclusion that large-scale ejecta blankets are mixtures of material from the primary crater and additional material from relatively local sources that served as target(s) for the secondary craters. As illustrated in Fig. 4.6, this local fraction *increases* with radial range, because primary ejecta velocity increases systematically with distance. Many large-scale, mappable lunar ejecta deposits, especially those associated with basins, may be entirely dominated by locally excavated materials (e.g., Morrison and Oberbeck, 1975; Hörz *et al.*, 1983; Pieters *et al.*, 1986). For this reason Oberbeck (1975) suggested using the term “continuous deposits” rather than “ejecta.”

Shock metamorphism. During a typical lunar impact the shock pressures in the target rocks readily exceed millions of bars. Such pressures are generally expressed in GPa (1 GPa = 10 kbar or 150,000 psi). During impact events, large volumes of

the target are subjected to pressures of tens to hundreds of GPa. Such high pressures are not known from internally-driven processes, especially within planetary crusts (see Fig. 4.7). In addition, temperatures and strain rates in impact events can be orders of magnitude higher than those produced by internal processes. Rocks traversed by shock waves respond irreversibly to these unusual conditions by producing unique deformation features and phase changes known collectively as *shock metamorphism* (French and Short, 1968).

An example of calculated shock pressures for representative impact conditions on the Moon is illustrated in Fig. 4.8 (Ahrens and O’Keefe, 1977). This figure illustrates how the peak pressure generated at the target/projectile interface attenuates (along the vertical axis of symmetry). Such calculations form the basis for estimating the fractional crater volumes that are subjected to specific shock stresses and the associated thermodynamic states of the compressed target and projectile materials.

At high shock pressures, a significant amount of shock energy is deposited in the target rocks, raising their temperatures far above the melting or vaporization points. Model calculations indicate that extensive melting and vaporization occur in a typical

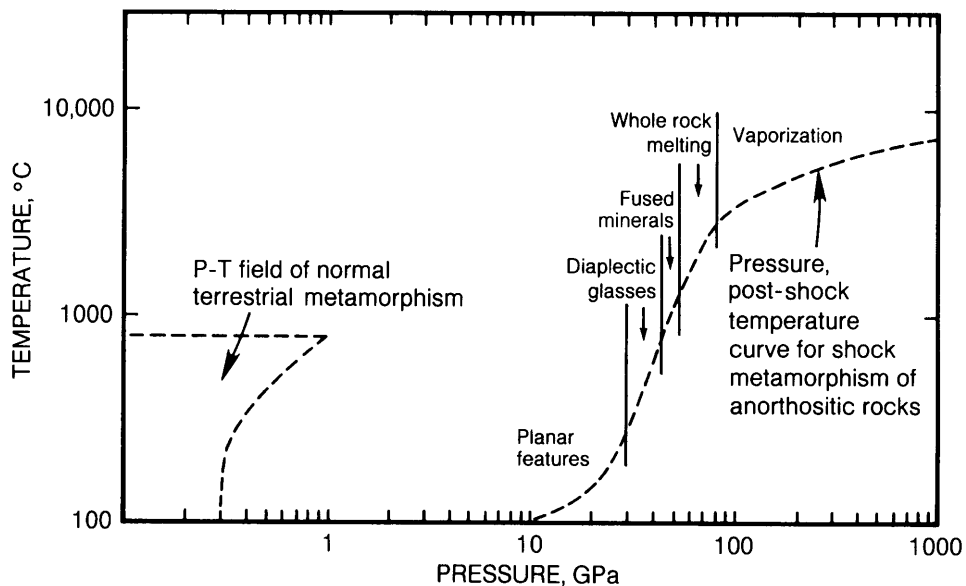


Fig. 4.7. Comparison of pressures and temperatures typical for internally driven metamorphism of crustal rocks on Earth with those characteristic of shock-induced metamorphism. The range of shock pressures for specific shock deformation effects and phase transitions apply to the feldspar-rich rock, anorthosite. Shock metamorphism also differs from internally driven metamorphism by orders of magnitude in timescales and strain-rates. Relatively modest stresses and temperatures may be generated and sustained in the Earth’s crust for millions of years; in contrast, shock metamorphism operates on timescales of minutes, seconds, or less, depending on crater size (after Stöffler, 1971).

pressure (along the vertical axis) in a gabbroic anorthosite (igneous rock type) target impacted by gabbroic anorthosite projectiles at 5, 15, and 45 km/sec impact velocity. The radial distance (R) is normalized to the diameter of the projectile (R_0). Note that (1) absolute peak pressure is strongly related to impact velocity; (2) the decaying shock is divided into (a) a near-field attenuation, characterized by relatively slight pressure decay impact. Vapor masses on the order of a few projectile masses and melt masses about 100 times the projectile mass can be generated (O'Keefe and Ahrens, 1975; Orphal *et al.*, 1980).

The degree of shock metamorphism produced by a given shock pressure depends heavily on a material's behavior at ultrahigh pressures and temperatures, i.e., on its so-called *equation of state*, which relates such parameters as compressibility, specific energy, entropy, specific volume, and phase changes at such conditions (e.g., Kinslow, 1970; Marsh, 1980). The transition from elastic to plastic behavior of dynamically loaded rocks and minerals occurs at relatively high stresses, typically on the order of 5–12 GPa. At pressures between 40 and 100 GPa thermal effects begin to dominate, and melting begins. Pressures exceeding 150 GPa will cause vaporization; ionization will occur at a few hundred GPa.

At shock stresses <10 GPa, crystals of most minerals, especially silicates, respond by brittle failure, producing fractures, shattering, microbrecciation, mosaic textures, and occasionally twinning (e.g., in ilmenite; Sclar and Bauer, 1973; Fig. 4.9a). These microdeformations are not readily distinguished from those generated by other means, for example, tectonic deformation (Stöffler, 1972, 1974; Bauer, 1979). However, the development of unusual striated

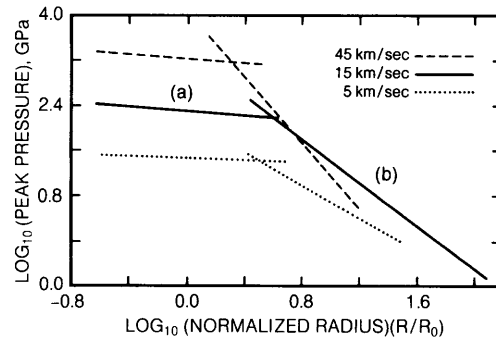
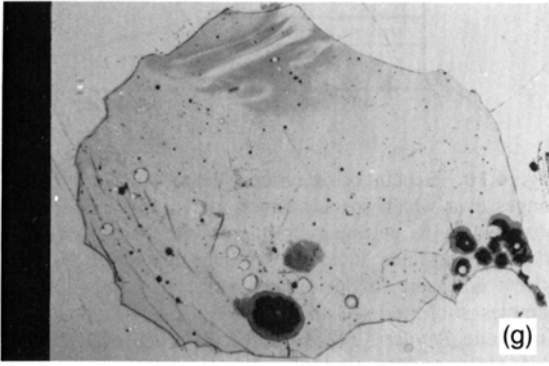
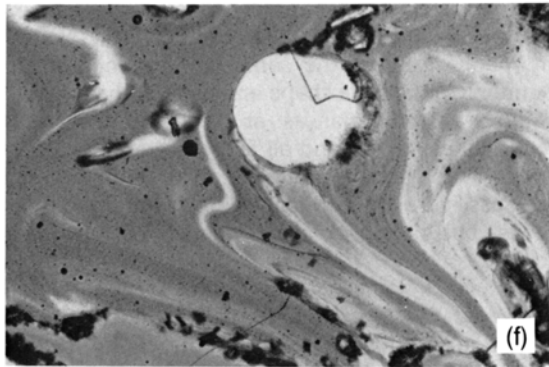
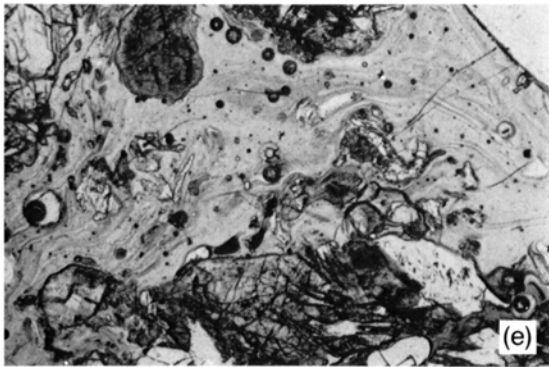
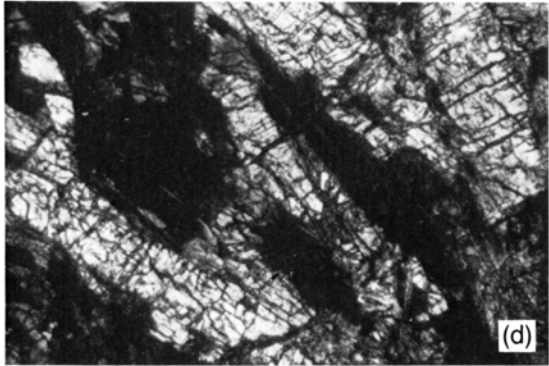
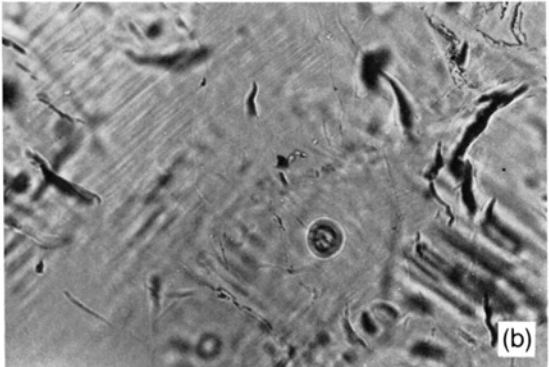
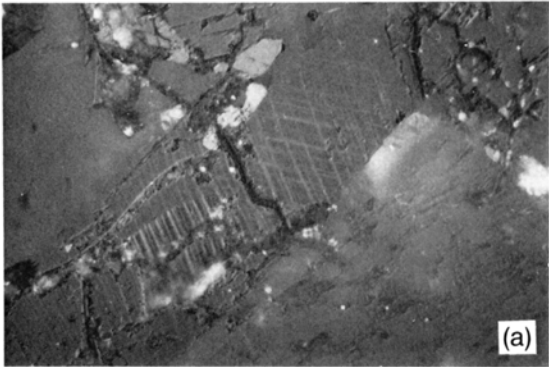


Fig. 4.8. The attenuation of the peak shock with distance, and (b) a far-field regime of relatively rapid pressure decay; (3) the near-field attenuation rate is relatively insensitive to impact velocity, but the far-field rate increases with increasing impact velocity. As a consequence, energetically equivalent impacts caused by projectiles of different sizes and velocities will not necessarily produce identical effects in the target (after Ahrens and O'Keefe, 1977).

Fig. 4.9. Typical shock-metamorphic effects in lunar rocks and minerals, arranged in order of increasing shock pressure from (a) through (h). (For systematics of the lunar rock numbering system see section 2.2.) FOV is field of view (horizontal dimension). (a) Shock-induced twinning of ilmenite indicates modest shock-stress (<10 GPa). Lunar rock 10085,319; reflected light; FOV = 0.22 mm. (b) "Planar elements" (shock lamellae), shown here in a lunar feldspar, are among the most diagnostic shock features formed at pressures of 10–30 GPa. Lunar rock 79155; transmitted light; FOV = 0.22 mm. (c) "Diaplectic feldspar glass" (white areas); plane polarized light (see (d)). (d) Identical field of view as (c) under crossed polarizers; the isotropic feldspar areas are black, revealing their amorphous, glassy state. Note that the original outlines of feldspar grains are perfectly preserved, which implies that no melting took place during formation of these unusual glasses. Such glasses are known only from shocked rocks and form at pressures of 30–45 GPa. The glassy feldspar is surrounded by highly fragmented, but still crystalline, pyroxene; such intense fracturing (mosaicism) is typical of shocked pyroxene, but it is not a unique shock indicator. Lunar rock 15684; FOV = 2.2 mm. (e) Incipient shock-melting in lunar rock 15684. The schlieren-rich, flow-banded nature of these glasses indicates that they are chemically heterogeneous; they are in fact composed of different proportions of feldspar and pyroxene melts. The contacts with mineral grains in the host rock are thermally eroded (i.e., rounded) and in various stages of disaggregation, and abundant broken-off fragments (clasts) occur in the melt. Such mixed melts are typical of shock-stresses of 45–60 GPa. Plane-polarized light; FOV = 2.2 mm. (f) Heterogeneous "whole rock" impact melt produced by conversion of the entire target rock to a melt at high shock pressures (>80 GPa). Flow lines (schlieren) of different colors generally differ only modestly in chemical composition. Many schlieren are the result of incomplete clast digestion by the probably superheated melt. Lunar sample 65315,82; FOV = 2.2 mm. (g) Relatively homogeneous glassy "whole rock" impact melt; note, however, that some faint schlieren are still present, at least locally. This is one of the optically most homogeneous lunar impact melts and as such is somewhat atypical [(f) is more typical of impact-produced melts and glasses.] Lunar sample 60095,34; plane-polarized light; FOV = 1.8 mm. (h) Completely crystallized impact melt. Depending on the cooling history of an impact melt, different types of crystallization products and textures may be produced, resulting in a wide variety of rock textures. Many textures may be similar to those that develop during the cooling of normal igneous melts, such as this "ophitic-subophitic" example, a textural term derived from the study of conventional basaltic lavas. Lunar rock 68415; plane-polarized light; FOV = 2.2 mm.



conical fractures (*shatter cones*) in rocks shocked at about 5–10 GPa is apparently a unique shock wave effect.

Solid-state deformations that are diagnostic of shock are generally produced at shock levels >10 GPa. Pressures in this region exceed the transition between low-pressure elastic failure and the high-pressure *Hugoniot Elastic Limit*. Two prominent and easily observed deformation phenomena develop only under such shock conditions: the so-called *shock lamellae* (also called *planar elements* and *planar features*) and the isotropic mineral *diaplectic glasses* (also called “*thetomorphic*” glasses). Shock lamellae are microscopic sets of parallel deformation planes a few micrometers in width that occur along specific crystallographic planes (Fig. 4.9b) (see Hörz, 1968; Roberts, 1968). These features develop prominently in quartz and feldspar, but they are also known from pyroxenes and olivines (Chapter 5). At pressures between 20 and 30 GPa, one commonly observes multiple sets of shock lamellae of differing crystallographic orientations in individual mineral grains. The crystallographic orientation of shock lamellae in quartz is related to peak shock pressure, and the observed fabric of shock lamellae may be used to estimate the pressure history of naturally-shocked samples (e.g., Robertson and Grieve, 1977).

Diaplectic glasses are produced at higher shock pressures by *in situ* conversion of the crystal into an amorphous glass of the same composition, which commonly retains the shape and habit of the original grain. Diaplectic glasses are only known from tectosilicates (quartz and all feldspars), and they are formed over a pressure range of about 28 to 45 GPa. The glasses are optically isotropic and amorphous to X-rays, but they lack any evidence of flow and melting.

Both shock lamellae and diaplectic glasses are considered the most unique and diagnostic solid-state deformation features produced by shock waves. There is an extensive literature describing their detailed mechanisms of formation and especially the structural states of diaplectic glasses, which possess, for example, higher densities and refractive indexes than glasses produced from quenched silicate melts (see, e.g., French and Short, 1968; Stöffler, 1972, 1974; Hörz and Quaide, 1973; Arndt et al., 1982; Ostertag 1983; Stöffler, 1985).

Above 50–70 GPa, postshock temperatures are high enough to melt most minerals and rocks (Figs. 4.9e–h and 4.10). Feldspars may display signs of incipient melting at pressures as low as 45 GPa (Stöffler, 1972; Schaal and Hörz, 1977). Such mineral-specific melting is also a diagnostic indicator of shock processes; monomineralic melts are essen-

tially unknown in more conventional melt processes that are governed by equilibrium thermodynamic processes. Incipient melting during shock generally favors the phases with highest compressibility, unlike phase-equilibrium melting. For instance, the juxtaposition of genuine feldspar melts with intact mafic minerals, which have lower intrinsic melting temperatures, is commonly observed in shocked rocks. Furthermore, shock melting commences at grain boundaries, especially in porous materials, where reverberations of the shock wave may deposit extra waste heat. As a result, highly localized melts (*mixed mineral melts*) are produced that are clearly mixtures of the two neighboring phases. As illustrated in Fig. 4.11, shock-induced melting phenomena occur over a wide pressure range, and the amount of melt produced is related to peak pressure. At pressures at or above 70–80 GPa, depending somewhat on the nature of the major constituent minerals, the entire rock will be melted to form a glass.

There are substantial differences between the effects of shock on coherent crystalline materials (rock), or on porous, granulated materials (e.g., lunar soil) of the same composition (Kieffer, 1971, 1975; Ahrens and Cole, 1974). Shock-recovery experiments indicate that, in porous targets, intragranular solid-state deformation effects are less obvious and

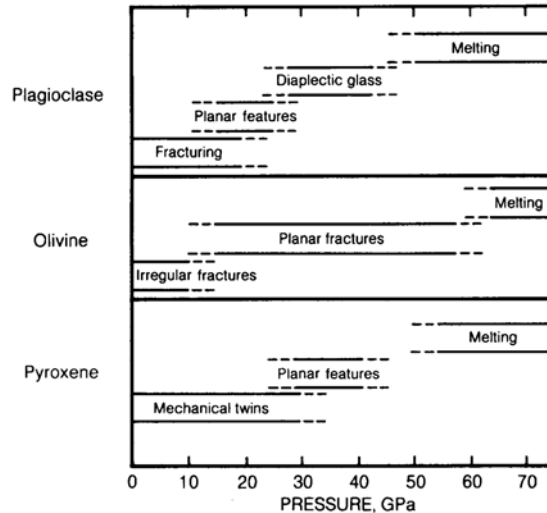


Fig. 4.10. Schematic diagram illustrating the pressure ranges over which specific shock-metamorphic effects, as observed in the petrographic microscope, appear in major rock-forming lunar minerals. Pressure calibration of these effects is based on the optical analysis of single crystal samples subjected to laboratory shock waves of known amplitude (Stöffler, 1972, 1974; Schaal et al., 1979; Reimold and Stöffler, 1978; Bauer, 1979; Ostertag, 1983).

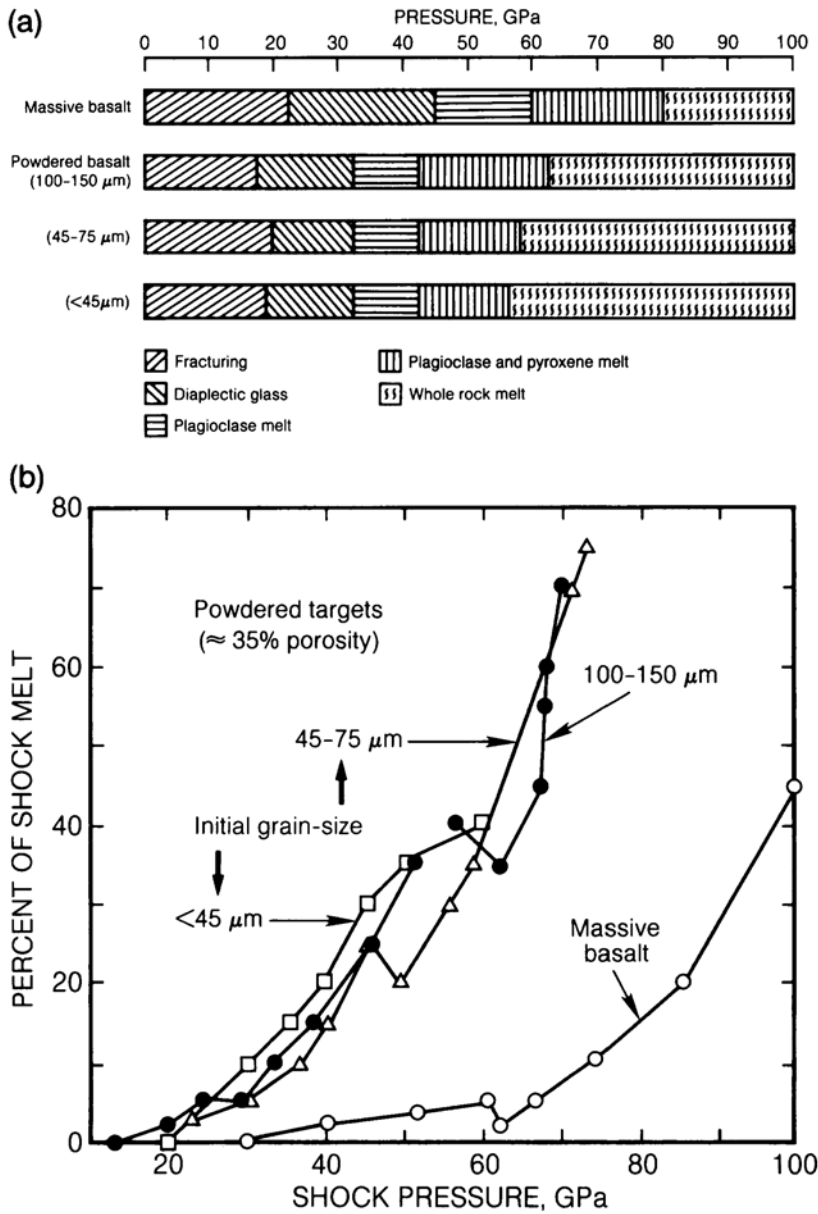


Fig. 4.11. Schematic diagram of experimental shock pressure ranges over which particular shock effects appeared in a typical, nonporous lunar basalt and in powders of various grain-sizes (regolith analogs) prepared from the same sample. **(a)** Summary of petrographic observations. Note that qualitatively similar effects occur in both the dense and powdered samples, but the threshold pressures for development of equivalent features are lower in the powdered materials. **(b)** Detailed comparison of the melting behavior of dense, nonporous basalt and its powdered, porous equivalent. Note that powdered samples melt with substantially greater ease than nonporous targets (after *Schaal et al., 1979*).

intergranular effects dominate (*Gibbons et al., 1975; Schaal et al., 1979*). In addition, the onset of melting occurs at lower shock pressures in porous or granulated materials. Intergranular melts develop in powdered lunar basalt at shock pressures as low as 20 GPa, and whole-rock melts are formed at 55 GPa (*Fig. 4.11*). This more pronounced shock melting in lunar regolith and similar materials, compared to more coherent equivalents, is due to increased reverberation(s) of the shock wave at the free

surfaces of component grains, where the density contrast between “solids” and “voids” is maximized. This condition leads to highly localized stress concentrations and to a highly heterogeneous deposition of energy, including the local production of high residual temperatures at relatively modest average shock stress.

The overall response of individual rocks to shock waves is controlled largely by the response of their major component minerals. While differences are

observed between diverse rock types, all rocks become completely molten at or above 100 GPa. Impacts at cosmic velocities will produce such pressures within a large volume of target, so that a significant part of the target will therefore be melted no matter what its detailed lithology and mineral composition.

Impact melts. The above considerations have important implications for naturally-occurring *impact melts*, a term that designates completely molten target material produced by the intense shock waves of meteoroid impact. This section emphasizes lunar impact melts, which constitute a prominent rock type in the Apollo sample suite. Material identified as impact melt composes some 30–50% of all hand-specimen-sized rocks returned from highland landing sites and some 50% of all soil materials, including mare collections (Ryder, 1981). How can such impact melts, which range in texture from completely noncrystalline glasses to completely crystalline rocks, be distinguished from internally-derived volcanic melts and their crystallization products?

The *melt zone* of a crater is the region within which shock pressures are high enough (~80 GPa or higher) to produce complete melting of the target rock. Even if this zone is composed of dramatically different lithologies, all will melt, and the melt will become part of the material that flows during the crater's excavation stage. Detailed studies of terrestrial impact melt sheets (e.g., Masaytis et al., 1975; Dence et al., 1977; Phinney and Simonds, 1977; Grieve, 1981; and many others) show that the divers melts tend to be homogenized, and that the resulting glasses or crystalline rocks, depending on cooling rate, represent remarkably homogenized mixtures of the original target lithologies.

Chemical composition is therefore one criterion applied to distinguish impact melts from conventional igneous rocks. The criterion is simple: Impact melts are simple mixtures of preexisting target rocks. In many cases, the mixed compositions of impact melts have unique characteristics that cannot be produced by conventional internal melting processes, which involve the partial melting of a compositionally restricted source rock.

A second criterion for recognizing impact melts is the special nature of rock and mineral inclusions and the effects they produce on the surrounding melt. During crater excavation, the impact melt bodies move along the crater floor and walls. In the process they pick up numerous inclusions (*clasts*) of the target rocks ranging in size from large blocks to small mineral grains. Impact glasses, which obviously cooled and quenched rapidly, always contain large amounts of these clasts, which may

extend down to submicroscopic sizes (e.g., *Stahle*, 1972). These clasts frequently show distinct shock effects. Partial digestion of these clasts by the melt typically results in texturally heterogeneous glasses with variegated streaks (*schlieren*), consisting of glasses of different compositions.

Progressively more crystallized impact melts, reflecting slower cooling rates, display an increased tendency to digest this clastic material. In completely crystallized impact melts, clastic material may no longer be observed on the scales of thin section and even hand specimens (millimeter to centimeter), yet larger clasts are always observed in the field (*Phinney and Simonds*, 1977). However, the digestion of these relatively cold clasts by the superheated impact melt produces local disturbances of the average thermal environment within the cooling impact melt sheet, giving rise to textural heterogeneities on unusually small scales (<1 cm) relative to those observed in rocks produced by igneous processes. In addition, all clasts found in impact melts are samples of the primary target rocks and can be used to determine the exact nature of those rocks and to model the melting process. As described by *Stahle* (1972) and *Phinney and Simonds* (1977), the observed clast population does not necessarily reflect the exact mixture of lithologies originally present in the melt zone. The surviving clasts are biased toward "cold" (unshocked) and refractory starting materials.

A third criterion for distinguishing between conventional igneous rocks and impact melts is the identification of projectile remnants in the impact melts, as pioneered by *Anders* and coworkers (e.g., *Anders et al.*, 1973). In the impact process, the entire projectile suffers shock stresses sufficient to melt, if not to vaporize and ionize, virtually all of the projectile. Part of this melted and vaporized projectile will be disseminated throughout the melt zone.

Chemical analyses have been the most effective means of detecting such projectile remnants in impact melts. In particular, siderophile elements such as Ni, Co, Ir, Au, Pt, and others have been especially diagnostic. They are highly enriched in meteorites relative to the indigenous target rock (lunar or terrestrial) concentrations, so that small amounts of a projectile can be readily detected in an impact melt. Furthermore, specific elemental ratios differ as well between and among diverse classes of meteorites, allowing the projectile type to be identified from its chemical signature in the impact melt.

For these reasons, siderophile elements have been used extensively as clues in identifying melts of impact origin on the Moon (see section 6.3) and on the Earth. The siderophile content in lunar and

terrestrial melt rocks can be used to demonstrate an impact origin by detecting an enrichment of meteoritic siderophiles over indigenous values. Furthermore, from the elemental ratios, it is possible in many cases to determine what type of projectile may have struck (e.g., *Palme*, 1980). Clearly, these methods require a detailed knowledge of the siderophile element content in the initial target rocks, and it has not been successfully applied to all lunar impact melts because there is uncertainty about the initial siderophile concentrations in the lunar rocks (e.g., *Anders*, 1978; *Wänke et al.*, 1978; *Ringwood*, 1978).

On Earth, this geochemical approach was applied by *Alvarez et al.* (1980) to interpret their discovery of a siderophile-rich layer at the Cretaceous-Tertiary boundary (65 m.y. ago) as the result of a giant impact that seemingly triggered a major mass extinction in the "recent" geologic record of Earth.

Studies of terrestrial impact melt sheets, some several hundred meters thick (e.g., Manicouagan Crater, Canada; *Floran et al.*, 1978), indicate that compositional and textural arguments can be combined to distinguish successfully between impact melts and internally-derived igneous rocks. For a few lunar samples, however, these arguments can become interpretative and are not settled (e.g., *Anders*, 1978; *Ryder et al.*, 1980).

By studying diverse lunar impact melts in detail, a variety of major questions related to the evolution and composition of the lunar crust were successfully resolved, as detailed in section 6.4. Many others still remain open. For example: What are the original pristine igneous rocks composing the initial lunar crust that gave rise to the observed, "mixed" impact melts? What was the stratigraphic and selenographic distribution of these pristine rocks? Do grossly similar impact melt compositions, as revealed by cluster analysis, imply a common parent crater for a number of melt specimens, or do they result from a number of separate impacts into grossly similar targets? Many of these questions can only be answered by further field work to provide the necessary structural and stratigraphic control.

Unfortunately for resolving these problems, most information on terrestrial impact melts derives from melt sheets inside the crater cavity, where they typically pool in the bottoms of simple craters or form an annulus between the central uplift and topographic rim of large complex craters (see Fig. 4.12). Few terrestrial impact melts have been recovered as ejecta outside the crater rim; the well-preserved and relatively young Ries Crater of Germany is one example where this has been done (*Pohl et al.*, 1977). No terrestrial analog for the melt pools mapped in the rim vicinity of lunar craters (e.g., *Hawke and Head*, 1977) is known on Earth. Are the

impact melt ejecta identical both inside and outside the crater rim? The make-up of the unmelted ejecta no doubt differs vastly between those regions.

Furthermore, the concept of close compositional homogeneity of impact melts is demonstrably violated by terrestrial tektite melts (*tektites* are small bodies of heterogeneous silicate glass generally believed to have formed in terrestrial impact craters). While the exact origin of tektites is poorly known (*Engelhardt et al.*, 1987), they undoubtedly formed during the early cratering stages as high-velocity ejecta. But major chemical differences exist between the tektites or the tektite-like impact melts found around and undoubtedly related to several terrestrial craters [the Ries Crater (moldavites; *Engelhardt et al.*, 1987), Lonar Crater (lonarites; *Murali et al.*, 1987) and Zhamanshin impact structure (irghizites; *Florensky*, 1975)] and the much larger volumes of impact melt found inside the craters.

4.1.3. Crater Frequency and Bombardment History

The statistical study of lunar crater populations provides several kinds of critical data. The distribution of crater diameters reflects the mass distribution of incoming projectiles, and the number of craters in a given area tells us how many objects struck. This information gives fundamental insights into the collisional dynamics of the solar system, because it defines both the mass frequency and time-integrated flux of impacting objects. Crater statistics are also indispensable to understanding lunar surface evolution because of one simple fact: Older surfaces accumulate more impact craters than young ones. The number of craters observed in any region therefore defines important chronological information because it can tell us the relative ages and times of emplacement of different geological formations. If we can then determine the absolute emplacement ages of these formations (e.g., by age-dating of samples), then we can calculate absolute crater production rates and absolute projectile fluxes. Such measurements have indeed been accomplished for the Moon as one of the greatest successes of the Apollo program, and from them we have learned a great deal about collisional processes in the inner solar system and about lunar geologic evolution during the past 4 b.y.

Crater frequencies. The relative frequencies of lunar crater diameters are illustrated in Fig. 4.13. In these plots, ΣN , which is defined as the number of craters equal to or larger than a given diameter D in a unit area, is plotted against d , which is measured in meters. The three panels cover three different diameter intervals: 10^{-5} mm to 1 mm (a), 1 cm to 1 km (b), and 100 m to 1000 km (c).

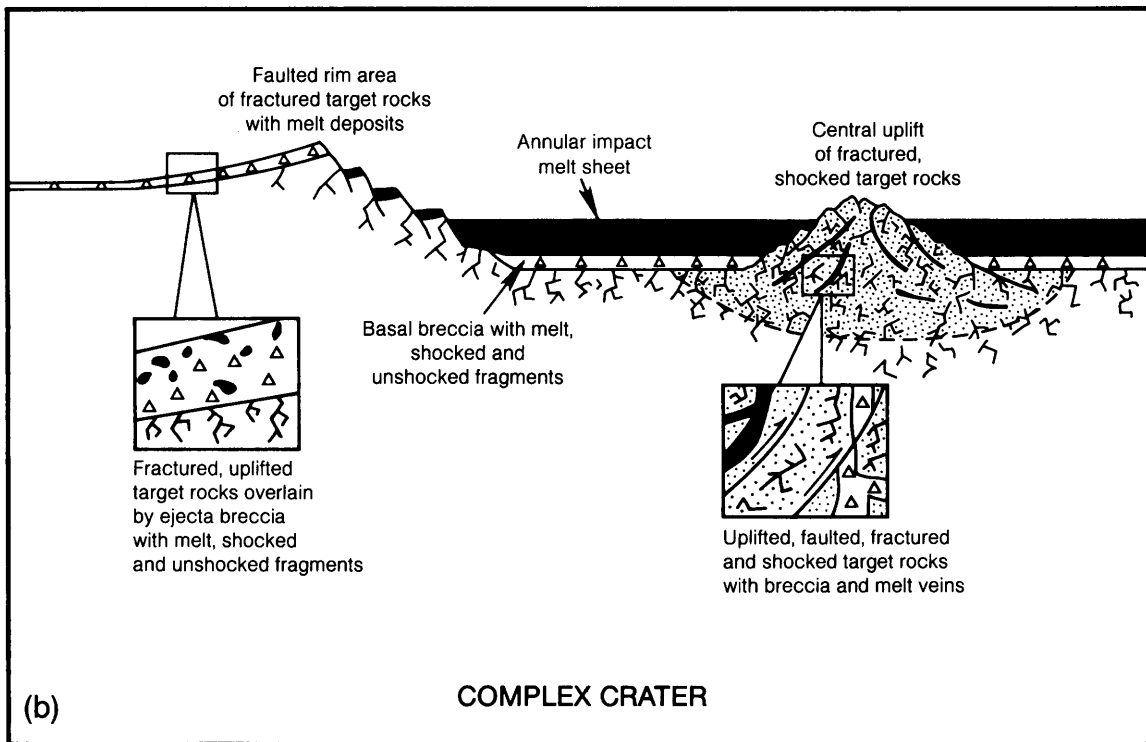
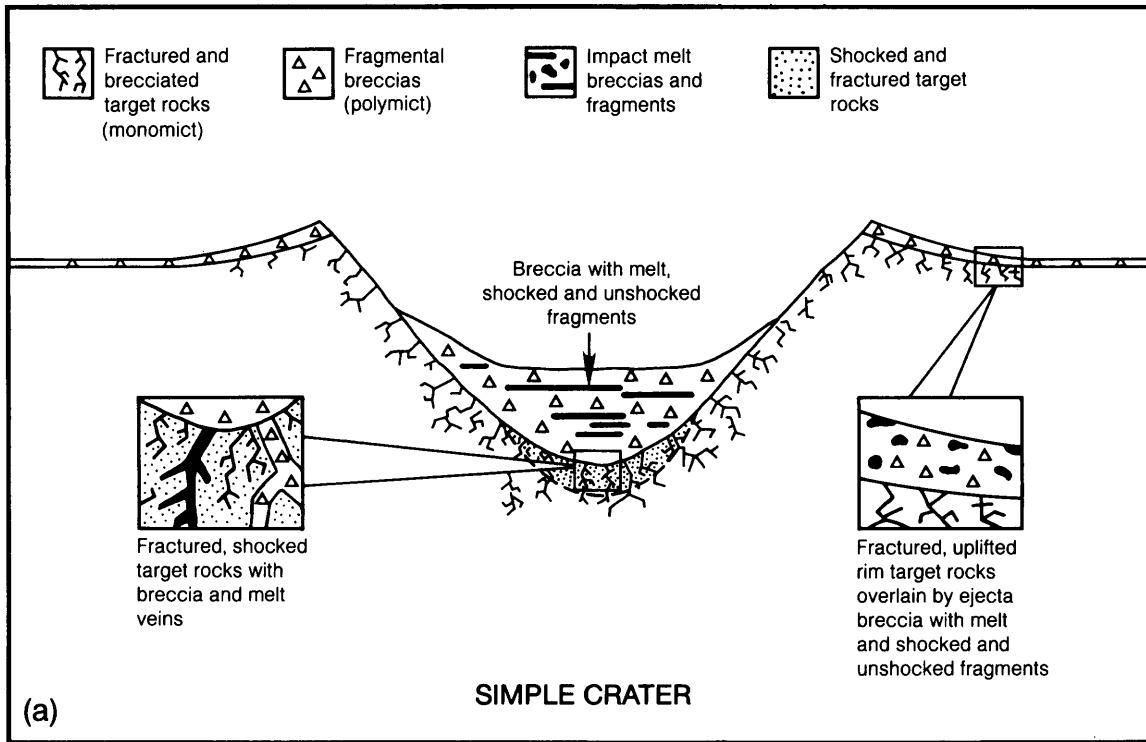


Fig. 4.12. Schematic cross-sections of simple and complex impact craters indicating the spatial distribution of impact-produced rock types; for emphasis and clarity, cross-sections are not to exact scale. **(a)** Simple craters are characterized by an interior, fragmental *breccia lens* containing both unshocked and shocked materials, including impact melt. This breccia lens overlies the highly fractured and shocked crater floor. The floor may have been slightly displaced as a result of the impact, but it still preserves the original structural and stratigraphic relations of the target. Veins of impact melt or fine-grained breccias may be injected into this crater floor along impact-induced fractures. The uplifted rim is composed of (1) highly fractured target rocks that have been slightly displaced and (2) ejecta from the crater. The ejecta are fragmental, but the deposits preserve an inverted stratigraphy, and increasing amounts of shocked and melted materials occur toward the top. **(b)** The interior of a complex crater is characterized by a fragment-containing, massive, impact-melt sheet that surrounds the central peak as an annulus. Breccias, which contain fragments derived from a number of sites within the crater (*polymict breccias*), occur at the base of the melt-sheet and overlie highly fractured, moderately shocked, bedrock. Fracturing and deformation of this bedrock may continue to depths (d) approaching substantial fractions of the crater diameter (D) (i.e., $d = 0.1$ to $0.2 D$). The central uplift exposes originally deep-seated, highly disturbed shocked rocks, cut by breccias whose fragments tend to be of a single rock type (*monomict breccias*). The rim area is structurally displaced, terraced, and pervasively fractured. The underlying bedrock of the terrace is covered by ballistic ejecta; most of the latter are highly polymict and moderately shocked. Bodies of ejected melt tend to pool in surface depressions on top of the breccias. Impact melts, together with both polymict and monomict breccias, may also be injected into fractures in the crater basement, as well as into the central uplift. Some of these veins may even have been generated in place during rapid subsurface movements of large blocks. Such rapid movements can produce intense fracturing along the block margins and can generate sufficient frictional heating to produce local melting.

These three different diameter ranges are studied by different observational techniques; they also reflect real differences between major geologic units and processes. Microcraters (panel a) largely control the evolution of particulates in the lunar soil, the erosion of surface rocks, and the exposure history of individual soil components to the space environment. Intermediate-size craters (panel b) are largely responsible for the comminution of near-surface bedrock and the build-up of the lunar regolith (see Chapter 7). Finally, the “large” lunar craters and multiring basins (panel c) have profoundly affected lunar crustal evolution, have dominated global morphology and stratigraphy, and were particularly important during early lunar history.

The <1-mm data (panel a) are based on optical and electron microscope observations of returned lunar rock surfaces; smooth glassy surfaces make particularly good microcrater detectors, as illustrated by the glass-coated surface of rock 64455 (Fig. 4.13d). At this size range, measured crater diameters may be used to calculate projectile masses with a fair degree of confidence because high-fidelity impact simulations and calibrations can be performed on the same scale in the laboratory (e.g., Gault, 1973; Vedder and Mandeville, 1974). Because the surface-exposure ages of many of these cratered rocks are also known, thus giving the integrated time that the rock has been at the surface (e.g., Arvidson et al., 1975a), the flux of micrometeoroids may be calculated as well.

Within experimental error, this calculated lunar micrometeoroid flux is consistent with totally independent measurements by contemporary space-

craft, as recently summarized by Grün et al. (1985). Figure 4.14 represents current best estimates for the flux of small particles; the data reflect spacecraft measurements, augmented at the large mass end ($>10^{-3}$ g) by a variety of astronomical observations (see Grün et al., 1985). This particle population has apparently interacted with the lunar surface for aeons. It also defines the major collisional hazard to humans and machines, a major concern for large-scale and long-term lunar surface operations (see section 3.10).

Panels b and c in Fig. 4.13 represent crater studies made using photogeologic methods. The craters shown in panel b are largely confined to young basaltic mare surfaces, those in panel c to ancient highland terrains; crater counts for structures >200 km in diameter refer to the entire Moon. The data in panel b are characterized by substantial uncertainties, with a possible gap at the smallest crater sizes. These deficiencies result partly from the fact that the imaging systems employed in lunar orbit have limited spatial resolution, and thus fail to detect smaller craters. However, the effect is largely due to natural causes. The lunar surface is not a simple and easily interpreted projectile detector for craters <100 m in diameter because it is not possible to distinguish with confidence between small primary impact craters and the numerous craters formed by secondary impacts from larger craters.

An additional problem with craters <100 m in diameter is that the lunar surface does not permanently record all the small primary impact craters that form on it. In most regions of the Moon, so many 100-m craters have formed over geologic time

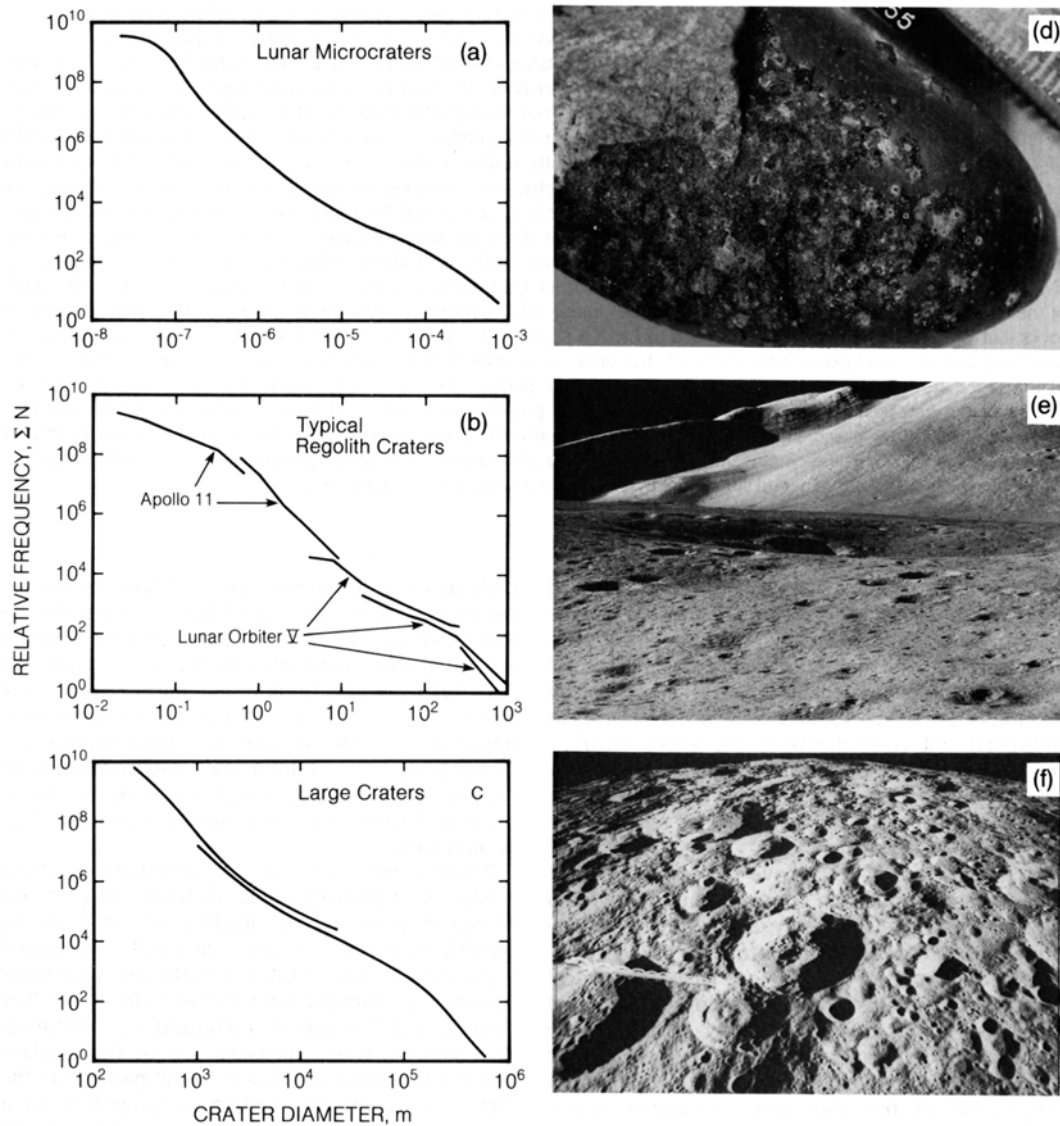


Fig. 4.13. The cumulative size-frequency distributions of lunar impact craters ranging from submicrometer-size features to structures 1000 km across. Horizontal axes show crater diameters (in meters). Vertical axes show cumulative number of craters equal to or larger than a given diameter per unit area, or ΣN . **(a)** Lunar microcraters, **(b)** typical regolith craters, and **(c)** large impact structures (see text for details). Also shown are representative lunar scenes that illustrate the dominant geological effects of these crater-size regimes: **(d)** lunar rock 64455, a sample draped with impact-produced glass, in which small craters have been produced; this sample illustrates the erosive capabilities of the micrometeorite environment (NASA Photo S-73-22656); **(e)** typical lunar surface scene from Apollo 15 showing numerous craters in the 1–10-m diameter range; such craters are responsible for much of the regolith gardening and evolution (NASA Photo AS15-87-1148); **(f)** heavily-cratered lunar highlands displaying large numbers of craters >10 km in diameter (NASA Photo AS16-M-0594). A large body of information (collected by various groups) is synthesized in this figure. For summaries see (for **(a)**) Morrison and Clanton (1979); Hartung et al. (1978); (for **(b)**) Shoemaker (1970); Soderblom (1970); Neukum (1977); and (for **(c)**) Neukum et al. (1975); Wilhelms (1985); BVSP (1981).

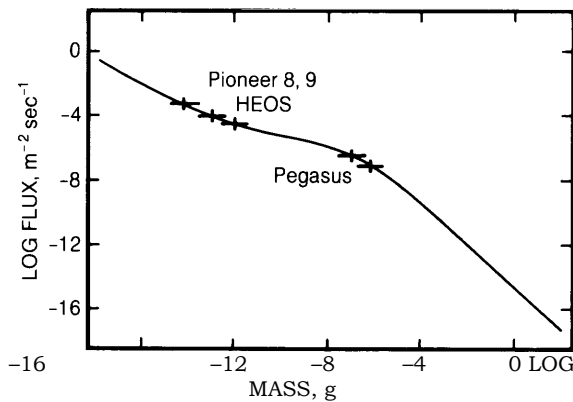


Fig. 4.14. The flux of micrometeoroids ($\sim 10^{-17}$ to 10^2 g in mass) at 1 A.U., as estimated from lunar rock analyses, direct *in situ* measurements by various spacecraft (Pioneer, HEOS, and Pegasus), and divers Earth-based observations (after McDonnell, 1977; Grün *et al.*, 1985).

that a “steady state” has been reached where each freshly created crater destroys a preexisting one. The lunar surface has thus been “saturated” with small craters (Gault, 1970) and only the “survivors” can be observed, which may be a small fraction of all the craters formed. On the Moon, the younger mare basalt surfaces, 2–3 b.y. old, yield excellent statistics for craters approximately 0.5–10 km in diameter (Neukum *et al.*, 1975). Unfortunately, most mare surfaces are too young to have recorded large numbers of craters >10 km diameter.

These problems of saturation and differential obliteration also affect the interpretation of the “large” structures shown in panel c. In the geologically older lunar highlands, so many craters >10 km in diameter have formed that the crater populations may be saturated at this level, causing relatively “small” craters (<10 km in diameter) to be underrepresented. Additional complexities stem from the different views of individual workers as to what constitutes the actual crater diameter, especially in large multiring basins, and on individual and somewhat subjective identifications of highly degraded craters. In addition, secondary craters from large basins may be as large as a few tens of kilometers across (Wilhelms *et al.*, 1978) and may therefore affect the crater frequencies shown in panel C at the small size end.

Crater densities and projectile flux. Since the lunar surface records impact history in a cumulative, time-integrated fashion, measurement of the absolute spatial crater density (N/km^2 , where N is the cumulative number of craters with diameters greater than a specified size) constitutes a measure of relative exposure age. Absolute and relative crater

densities have therefore become valuable tools for lunar stratigraphy, a discipline that attempts to establish the chronologic sequence(s) of geologic events (section 4.4).

Relative age-dating of different craters can also be obtained from quantitative measurements of their degradational states. Impact is the most active erosional process on the Moon, and the relative degradation of different craters, measured in various ways, is therefore a measure of the cumulative exposure time to the meteorite flux (e.g., Soderblom, 1970; Soderblom and Lebofsky, 1972; Boyce, 1976; BVSP, 1981).

The return of actual basalt samples from several different lunar maria made it possible to use radioactive age-dating methods to determine the crystallization ages of specific basalt flows and therefore their time of eruption and solidification. Measured basalt eruption ages range from 3.1 to 3.9 b.y. (Wasserburg and Papanastassiou, 1971; see also section 6.1). The absolute crater densities for craters >4 km in diameter obtained from these dated flows are illustrated in Fig. 4.15. Other lunar data in Fig. 4.15 are model-dependent to some degree, but are still valuable in understanding crater production rates through geologic time.

Most rocks returned from the older lunar highlands have narrowly restricted ages between 3.8 and 4.0 b.y. and are for the most part only slightly older than the oldest basaltic mare surfaces. Highland regions, however, typically display 10 to 50 times as many large impact craters (>15 km) than do the volcanic flows of the maria. The conclusion is therefore inescapable that there was a markedly higher crater-production rate between 3.8 and 4.0 b.y. ago than over the last 3.8 b.y. Some workers interpret this difference as the tail end of the original planetary accretionary process and use the data to calculate half-lives for the depletion of the initial inventory of impacting planetesimals (e.g., Hartmann, 1975; Neukum and Wise, 1976; Wetherill, 1981; Baldwin, 1981). Others propose that a cataclysmic increase of infalling projectiles occurred at approximately 3.8–4.0 b.y. ago (Tera *et al.*, 1974).

Samples of lunar impact melts collected from nonvolcanic surfaces are clearly the materials needed to obtain formation ages of individual craters (e.g., Grieve, 1982). For this reason, the relatively narrow age distribution of these samples, from about 3.8–4.0 b.y., is surprising. The simplest interpretations of this observation entail a high projectile flux between 3.8 and 4.0 b.y. ago, yet significant differences exist in the details of different mechanisms. Much current debate focuses on whether impact melts from large basin-forming events are present in the sample collection and, if so, how many (e.g.,

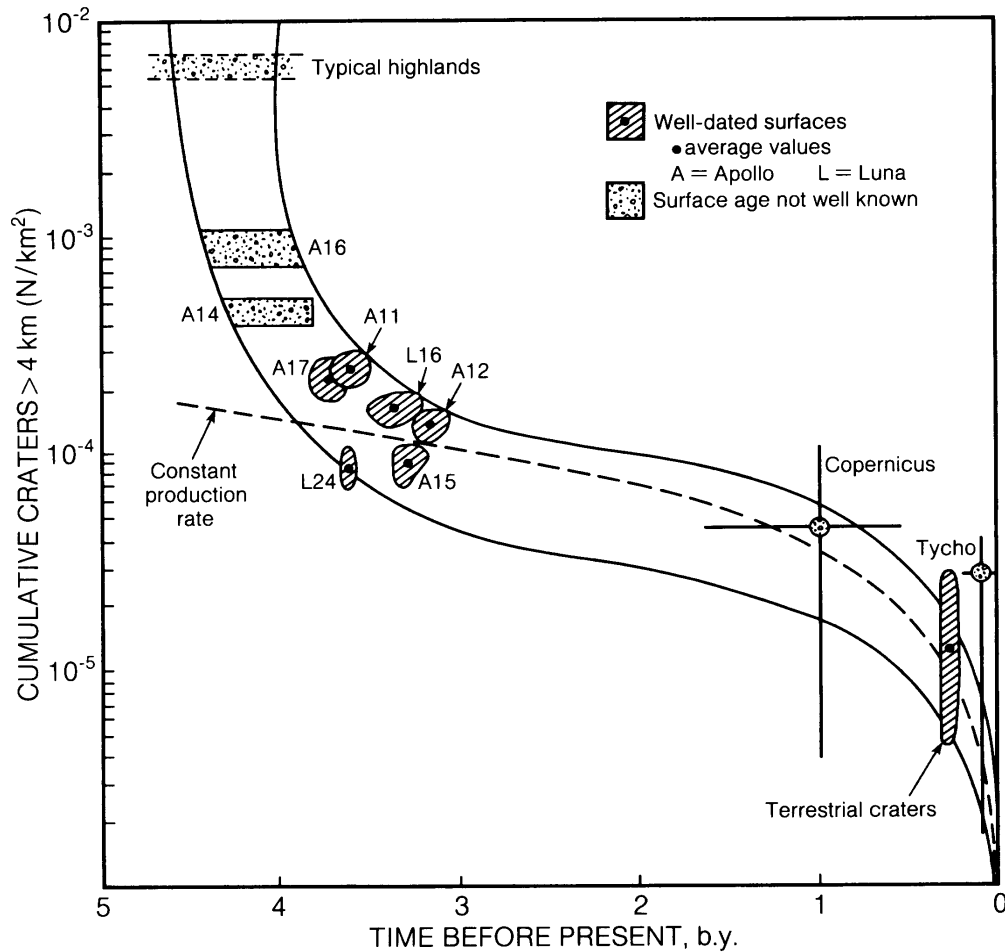


Fig. 4.15. Lunar crater production rates through geologic time, as reconstructed from the measurement of crater densities on the lunar surface and from absolute age dating of returned lunar rocks. As indicated in the text, firm correlations may be reconstructed only for (1) the well-characterized basalt surfaces (3.8–3.2 b.y. old) and (2) the contemporary meteorite flux, based on current astronomical observations ($t = 0$). The terrestrial cratering rate applies to only the last 200 m.y., and the ages for lunar craters Tycho and Copernicus are inferred from indirect evidence. Cratering activity was clearly very high prior to 3.8 b.y., as indicated by the lunar highland rocks, but details of this bombardment history cannot yet be reconstructed. The absolute production rates refer only to craters >4 km in diameter (and are expressed as number formed per km^2). Note that the inferred crater production rate differs markedly from the curve representing a constant crater production rate around 4 b.y. ago (based on BVSP, 1981).

James, 1981; Wilhelms, 1985). If the sample collection were dominated by impact melts from a few basins, the ages measured would represent chiefly the times of basin formation, regardless of other crater-forming events. In the Apollo sample collections, the oldest basin represented would likely be Nectaris (from Apollo 16), variously interpreted to have formed at 3.8 b.y. (James, 1981; Spudis, 1984) to ~3.9 b.y. ago (e.g., Wetherill, 1981). A large number

of basins are younger than Nectaris (Wilhelms, 1984), including Serenitatis and Imbrium, impact melts of which are possibly present in the Apollo 17 and Apollo 15/14 sample collections, respectively.

All interpretations involving the presence of numerous samples of basin-related impact melts in the collection and the associated formation ages of 3.8–4.0 b.y. require that several gigantic, basin-forming impactors collided with the Moon up to

approximately 3.8 b.y. ago. Other workers, however, point out that a very large fraction of all smaller, non-basin-forming impacts occurred after formation of the Nectaris Basin and they attribute most melt samples and their formation ages to these subsequent non-basin-forming impacts. In summary, the true production rate for large lunar highland craters is not well known, and the flux implied by Fig. 4.15 for periods older than 3.8 b.y. remains speculative. While we are confident that intense bombardment occurred in early lunar history, absolute cratering rates remain uncertain.

The age of <1 b.y. estimated for the relatively young craters Copernicus and Tycho (Fig. 4.15) is based on circumstantial evidence and is uncertain. This young age is, however, in accord with independent estimates of the terrestrial cratering record for the past 200 m.y. (Grieve, 1982) and with present-day astronomical observations of solar system objects that cross the Earth/Moon space to become potential projectiles (Shoemaker, 1983).

The question of the apparent exponential increase in projectile fluxes in early lunar history is intimately related to the equally fundamental question of how many large impact craters and multiring basins were formed at all on the Moon (e.g., Baldwin, 1974, 1981; Strom, 1977; Neukum, 1977; Hartmann, 1980; Wetherill, 1981; and many others). Does the observable crater population faithfully reflect all the large craters that formed (Strom, 1977; Neukum, 1977), or does it merely reflect the survivors? The fact that many craters are partly to nearly obliterated is taken by some workers to suggest that large numbers of "early" craters were indeed destroyed (Hartmann, 1980) and that current crater populations reflect the surface saturation conditions described by Gault (1970).

The nature of the returned highland samples has been used in attempts to resolve this problem. Ryder (1981) has estimated that the Apollo collection contains 30% (by volume) of impact melt. If this figure is indeed representative of all highlands, then the existence of multiple cratering is strongly indicated, because single (terrestrial) impacts never seem to produce more than 10% impact melt in their ejecta (Grieve *et al.*, 1977). In addition, Lange and Ahrens (1979) have emphasized that the observed age distribution of lunar highland impact melts is incompatible with models involving simple exponential decays of the impactor populations that are required to produce the observed crater population. Most workers therefore agree that the highlands have been saturated for craters <4 km in diameter and that the current crater populations merely represent the survivors, rather than all impact structures formed.

4.1.4. Geological Processes

As indicated in section 4.1.2, meteorite impact is a major transport process, because it redistributes materials both laterally and vertically, either by sedimentation from ballistic trajectories or by upward subsurface motion. Impact is also a major erosional process. Depending on the size of the event, impacts can pulverize surface boulders, shatter subsurface bedrock, or even dislodge crustal sections tens of kilometers deep. Impact is also the most important metamorphic process on the Moon, causing characteristic shock deformation, heating, melting, vaporization, and even ionization of pre-existing minerals and rocks. Impact processes alter the textures of rocks and generate new ones, such as glasses, impact melts, and fragmental rocks (*breccias*) containing either a single rock type (*monomict*) or multiple rock types (*polymict*). A detailed classification of impact-generated rock types and their nomenclature is presented in Table 6.11 in Chapter 6 (see also Stöffler *et al.*, 1980).

The ejection of material from impact structures, and the subsurface effects beneath them, combine to produce a lunar crust and surface composed of lithologically diverse impact deposits. Some ejecta deposits from individual young impact basins are distinctive enough to be mapped as discrete geological formations and stratigraphic units; they have distinct surface characteristics and well-defined structural/temporal relations to neighboring units (e.g., Wilhelms and McCauley, 1971; see geological map, Plate 10.10). Despite their apparent uniformity, these lunar ejecta units must be highly complex. Even within the relatively small ejecta deposits surrounding terrestrial craters, there is exceptional textural and structural complexity, diversity of grain size, and variability in rock types (Hörz *et al.*, 1983). The complexity and internal variability of large-scale lunar ejecta deposits must be larger still, partly because many individual components have been repeatedly processed by impact cratering. For example, it is typical for lunar impact breccia samples to contain fragments of impact melts and older breccias from a number of craters. Textural, mineralogical, chemical, and chronological evidence for these "breccia within breccia" relationships is common (e.g., Quick *et al.*, 1981 a,b).

Multiple cratering on the lunar surface is a random process in space and, to some extent, in time. Therefore, a variety of statistical (probabilistic) models have been used to explore the effects of continuous meteorite bombardment, and especially of multiple impacts on the lunar surface. Figure 4.16 illustrates some first-order results by plotting the relative times necessary to cover specified fractions

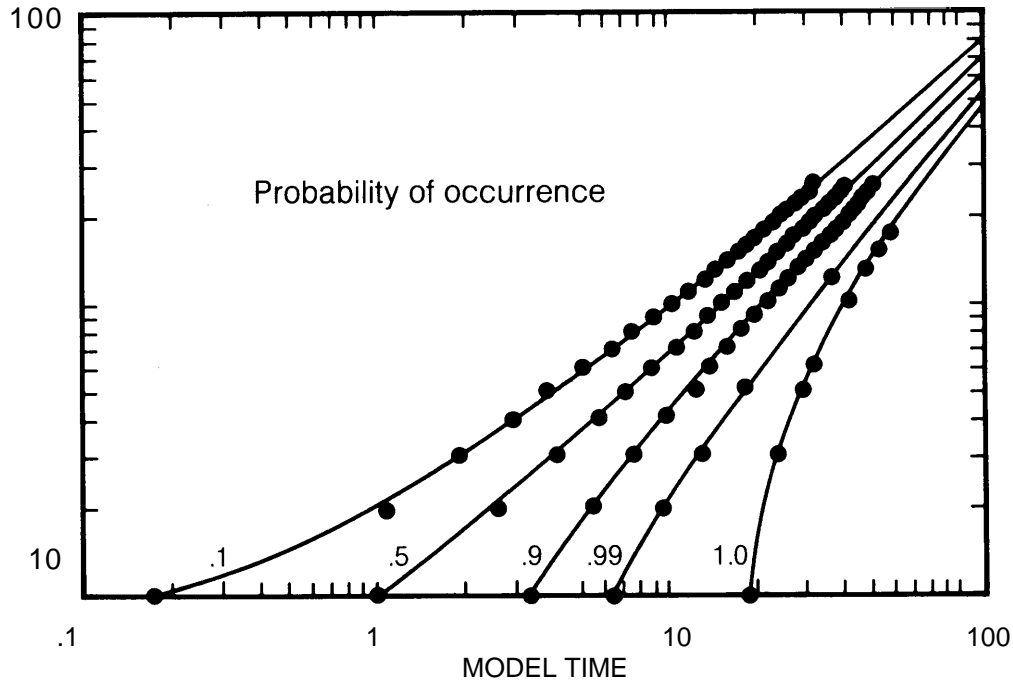


Fig. 4.16. Statistical results, using a probabilistic Monte Carlo technique, which illustrate how often a given area of the lunar surface may be impacted. The analysis uses an arbitrary model time that is linearly related to the number of impacts generated by computer. The smallest surface element considered is equivalent to the surface area of the smallest impact crater employed in the calculation. Unit time is defined as the interval that is long enough to provide a probability of 0.5 for impact to occur in any surface element; a period of time about 7 times longer is needed to increase this probability to 0.99 (i.e., 99% of the surface is cratered). At the end of this time 90% (probability 0.9) of the surface has been impacted twice, 50% has been impacted at least five times, and 10% has suffered approximately eight impacts. By the time the last surface element is cratered for the first time (with probability 1.0), >90% of the entire surface has already suffered more than 10 impacts.

of the lunar surface with craters. In this model, craters were represented by simple circles simulating measured crater-diameter size frequencies; they were allowed to form at random surface coordinates and times. "Unit" time is defined as the period necessary for any given point to be impacted at least once with a probability of 0.5; this time corresponds, by definition, to the time necessary to crater 50% of any given model surface. Note that it takes approximately 20 times longer to crater every surface point at least once (probability 1.0) (Fig. 4.16). While this is being accomplished, many surface points will simply suffer repeated impacts; 90% of the given surface will have received about 10 impacts and 10% will have been cratered 20 times. This example demonstrates that any fractional element within a large surface area may have experienced a substantially different impact history when compared with the "average" of the entire exposed surface.

Lunar rock erosion. Small impacts by particles less than one micrometer to several centimeters in diameter will erode lunar rocks by two principal mechanisms. Very small impacts have an "abrasive" effect, akin to energetic sandblasting, and each impact removes a relatively small amount of rock. In contrast, more energetic events, involving larger projectiles up to centimeters in size, will completely shatter an entire rock by "collisional fragmentation" (Gault and Wedekind, 1969; Matsui et al., 1982). Examples of these erosive processes are illustrated in Fig. 4.17. These processes are clearly gradational and partial disruption of surface boulders has been commonly observed.

"Abrasive" impacts may be thought of as impacts into infinite half-space targets, with a large mass ratio of target rock/projectile. With larger projectiles, and smaller rock/projectile ratios, the target rock acts as a finite-sized object and shatters if the

impact energy exceeds a definite value. The erosion rate by abrasion has been calculated to be on the order of 1 mm/ 10^6 years for typical kilogram-sized lunar rocks (Ashworth, 1977). Larger, more massive rocks have higher erosion rates, because increasingly larger impacts begin to contribute to the abrasive process. Absolute abrasion rates, therefore, increase with increasing mass of the target rock.

The survival times of lunar surface rocks for collisional fragmentation by large impacts are much shorter than for abrasion (Fig. 4.18). The experiments of Gault and Wedekind (1969), Gault (1973), Fujiwara *et al.* (1977), Matsui *et al.* (1982), and others have shown that collisional fragmentation destroys rocks faster and more effectively than abrasion.

These calculated abrasion rates and collisional lifetimes for lunar rocks compare favorably with the observed size population of lunar rocks (Hörz, 1977; Langevin and Arnold, 1977). A typical surface rock of 1 kg mass can be expected to survive on the Moon for approximately 10 m.y. Observed rocks, including many Apollo samples, have therefore resided on the lunar surface for periods comparable to the time it took the Colorado River to carve out the Grand Canyon (about 15 m.y.). Terrestrial erosion processes are orders of magnitude more efficient at wearing down exposed rock surfaces.

The “gardening” of the regolith. Small meteorite impacts, involving submillimeter-sized projectiles, dominate the small-scale evolution of the lunar surface. Such repetitive and frequent impacts agitate the lunar surface by shattering, burying, exhuming, tumbling, and transporting individual grains in a random fashion. These processes gradually develop a fine-grained powdery layer on the lunar surface above the actual bedrock. This layer, called the *regolith*, is then continuously “gardened” and churned (Morris, 1978a). The actual “gardening” process has been investigated through detailed lunar soil studies described in Chapter 7.

A number of models have been developed to describe the rate and depth of this gardening process (Shoemaker, 1970; Gault *et al.*, 1974; Langevin and Arnold, 1977). Two typical results are illustrated in Fig. 4.19. Owing to the steep mass-frequency distribution of the micrometeoroid population (i.e., smaller projectiles are much more abundant than larger ones), the rate of gardening or “turn-over” decreases rapidly with depth. In 10^6 years, the regolith is gardened (overturned) once to a depth of almost 1 cm at the 50% probability level, but during the same period the uppermost millimeter is turned over a few tens of times and the outermost 0.1 mm a few hundred times (Fig. 4.19a).

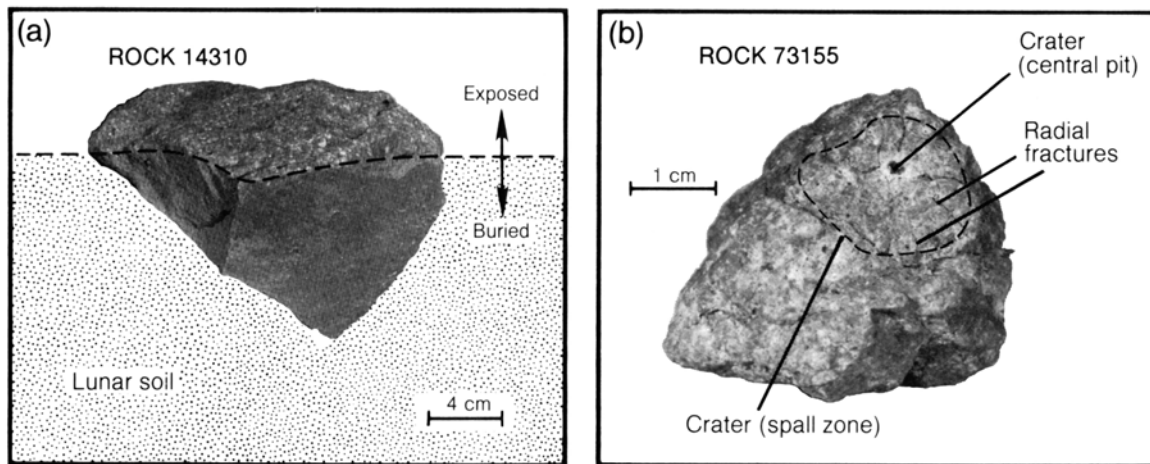
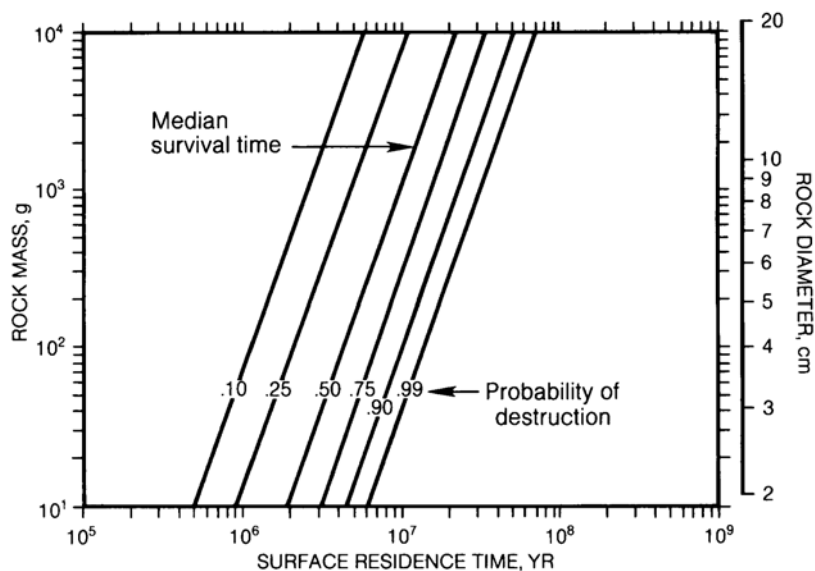


Fig. 4.17. Erosional processes recorded by lunar surface rocks. **(a)** Abrasion by multiple, small-scale impacts, akin to energetic sandblasting. The upper rock surfaces, rounded and smooth, were exposed to space and thus to micrometeoroid impacts; they contrast strongly with the lower, angular, fresh fracture surfaces that were buried in the soil. Such rocks with simple exposure histories are rare in the Apollo collection; most lunar rocks have tumbled on the surface a number of times. As a result, they display microcraters and other signs of space erosion on all surfaces (NASA Photo S-71-21830). **(b)** A rare example of a more energetic impact that almost broke up an exposed lunar rock. The large impact crater is characterized by (1) a central, glass-lined depression (central pit, commonly termed “pit-crater”), around which occur (2) a prominent “spall zone,” characterized by mass loss and removal of surface material by tensile failure, and (3) prominent, penetrative fractures that emanate radially from the impact. A slightly more energetic event would have largely destroyed the entire rock (NASA Photo S-73-17057).

Fig. 4.18. Possible surface residence times of lunar rocks before they are destroyed by collisional breakup caused by energetic impacts. This model combines probabilistic modeling with experimentally determined threshold energies that are necessary to destroy a given rock mass (after Hörz *et al.*, 1975).



In developing the regolith, a major role is played by the rare larger impacts (Fig. 4.19b). Such impacts can create a layered regolith column, despite the tendency of more numerous smaller impacts to homogenize the upper part of the regolith. The model illustrated in Fig. 4.19b emphasizes the role of larger craters and illustrates how a typical layered regolith column may be produced. Random impacts are allowed to remove materials from a surface point initially at “0” elevation by excavation and negative elevation change or to deposit materials onto the same point by ballistic sedimentation (positive elevation change). Over time, constructive and destructive impact events are continually competing; in this hypothetical regolith, a particularly destructive event occurred at 240 m.y., destroying all previous sedimentary history.

Because of these infrequent but large-scale events that destroy the preexisting record, stratigraphic gaps (*unconformities*) must therefore be common in lunar regolith profiles. Profiles in core samples collected only meters apart may reveal very different depositional histories, and unique interpretations of the profiles in core samples, some a few meters deep, is possible only in rare cases (see Chapter 7). Despite these diversities in depositional histories and surface exposures between individual grains or individual soil samples, there are not necessarily any great differences in the mineralogy, rock types, or chemical composition. Most regoliths are largely derived from underlying local bedrock, and they show a relatively limited compositional variety at any given Apollo site (Papike *et al.*, 1982).

Large-scale regolith evolution. The projectiles responsible for pulverizing rock and for macroscopic regolith evolution are largely in the 10- to 1000-cm diameter range. The effects of such impacts can be modeled by Monte Carlo statistical simulations, such as those of *Quaide and Oberbeck* (1975; Fig. 4.20). Figure 4.20a shows how the median regolith thickness evolves as a function of absolute number of impact events. Crater populations on the younger mare surfaces do not exceed $N = 10^8/\text{km}^2$ (diameter, $D > 1$ m) and regolith thicknesses are typically only a few meters. Regolith thicknesses >10 m, however, may occur in the highlands. Figure 4.20b addresses the macroscopic evolution of regoliths at the Apollo 11 and 12 sites, for which both the crater populations and the regolith thicknesses are well understood.

These figures also compare the effects of time-constant vs. exponentially decaying meteorite fluxes for the Apollo 11 and 12 sites. The important point is that, for either type of flux, the overall growth rates of the regolith decrease with time. This is caused by the gradual development of the regolith itself, which acts to shield the bedrock. As time goes on, and the regolith thickens, increasing numbers of “small” craters develop entirely in the regolith layer and fail to penetrate bedrock. It takes increasingly larger craters, which are relatively rare, to deepen the regolith by penetrating the entire layer and excavating new bedrock. Therefore, today’s regolith growth rates are significantly lower than those in early lunar history, when the regoliths were thinner and the overall impact flux was higher.

Because all Apollo rock samples are loose pieces in the regolith, there is substantial interest in estimating the source depths from which individual bedrock fragments have been derived. Figure 4.20c illustrates the progressive change of mean source depths in an evolving mare regolith, while Fig. 4.20d portrays fractional regolith volumes derived from specific depths. Such models can place constraints on the nature and stratigraphy of the local bedrock beneath the regolith, using the data obtained by analyzing the surface soils.

The many crater cavities that penetrate the regolith combine to produce a highly irregular surface at the bedrock/regolith interface, although

much of the relief is subsequently filled and smoothed by mass wasting and ejecta deposition (Soderblom, 1970; Shoemaker, 1970; Boyce, 1976). As a result of these processes, regolith thickness can be highly variable locally. Figure 4.21 illustrates the distribution of regolith depths calculated from Monte Carlo methods and compares them with depths inferred from photogeologic measurements for specific lunar surface areas. In these measurements regolith depths are determined from the presence of distinct "benches" within small craters. These benches form because of the contrast in physical strength between the relatively competent bedrock and the overlying unconsolidated, fragmental rego-

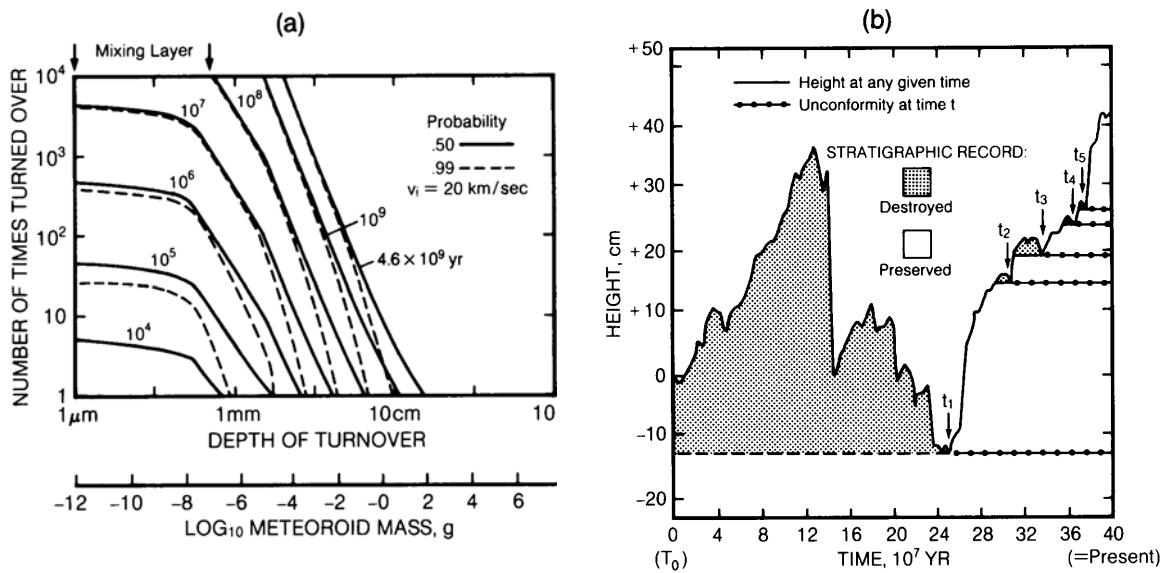


Fig. 4.19. Gardening of the near-surface regolith. **(a)** This figure combines probabilistic calculations with laboratory cratering experiments in fine-grained unconsolidated targets. These data are used to convert projectile kinetic energy into realistic estimates of crater volumes, diameters, and depths. The figure shows the number of times a given area of lunar surface is affected by cratering and the excavation and overturning depths involved for a specific time interval (indicated by a number adjacent to the curves), for both 0.50 and 0.99 levels of probability. This complex figure is best read along a vertical line corresponding to a fixed depth below the surface. Intersections of this line with the curves indicate varying time durations, and the number of overturns during that period can be read from the vertical axis. It is clear that near-surface zones (a few millimeters or less) of the regolith are highly active (e.g., 10–100 turnovers in a million years). However, the turnover rate decreases very rapidly with depth; zones deeper than 10 cm have little probability of being turned over during the entire lifetime of the Moon at present cratering rates (after Gault *et al.*, 1974). **(b)** Results of probabilistic calculations that model successive deposition or erosion of fine-grained regolith material at an arbitrary point on the lunar surface. This model incorporates both crater excavation (negative relief changes) and the addition of crater ejecta (positive relief changes). The time axis gives absolute time duration (i.e., it begins at the left side of the graph, at T₀). The vertical axis indicates the elevation change of the regolith surface relative to a starting point of 0 elevation at T₀. The graph thus depicts the historical evolution of a regolith profile. In this model, substantial buildup of the regolith occurred early, but a large impact at 12–16 × 10⁷ yr destroyed almost the entire deposit. Additional buildup and modest destruction then continued, but at 24 × 10⁷ yr, all previous regolith history (to a depth of 12 cm) was destroyed by an even larger impact. Continuous buildup dominates after that and is only slightly affected by minor mass removal. Considering the absolute scales involved, it appears obvious that highly diverse and complex regolith histories will be encountered over small distances, i.e., on the scale of Apollo landing sites and between the locations of cores collected on a single mission (after Langevin and Arnold, 1977).

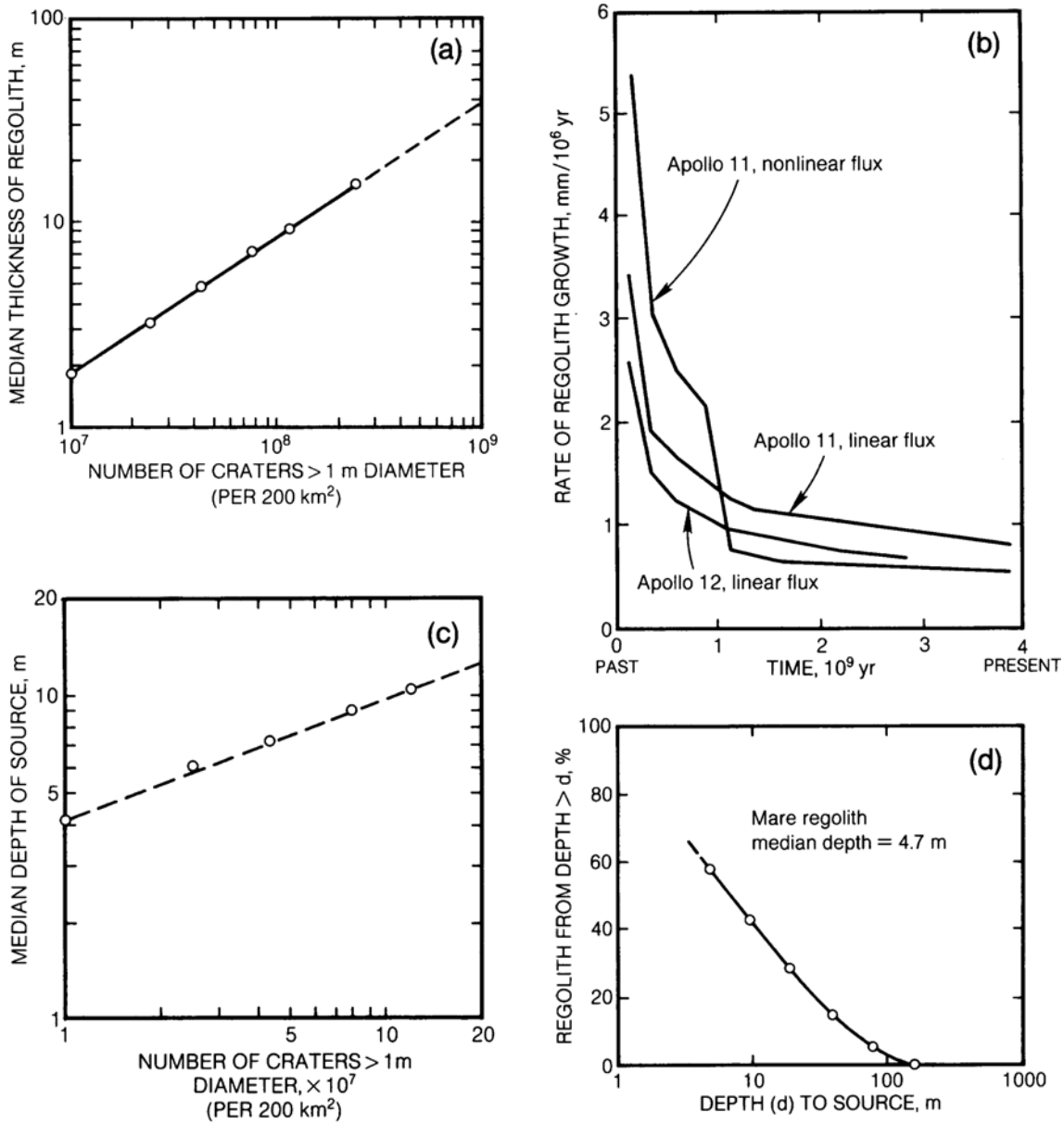


Fig. 4.20. Some aspects of large-scale lunar regolith evolution, using models that combine probabilistic calculations, impact experiments, and photogeologic analyses of lunar mare surfaces. **(a)** How the median regolith thickness increases as a function of absolute number of craters on the surface. The regolith thickness is not linearly proportional to the number of craters because, as time goes on, increasingly larger (and less frequent) craters are needed to penetrate the regolith and to produce fresh bedrock ejecta. **(b)** The rate of regolith growth at the Apollo 11 and 12 landing sites, allowing for differences in crater density and assuming linear and nonlinear impact flux models. The regolith originally developed at >3–5 mm/m.y., but typical contemporary regolith growth rates have dropped to <1 mm/m.y. **(c)** Calculated median source depth for fragments located in an evolving regolith. Note that median source depths for most mare regoliths are a few meters; such regoliths are dominated by the comminution of local bedrock. **(d)** Cumulative mass fractions derived from sources deeper than a few meters for a regolith typical of Apollo 12, having a median depth of 4.7 m. Virtually no fragments are derived from >100-m depth (all figures after *Quaide and Oberbeck, 1975*).

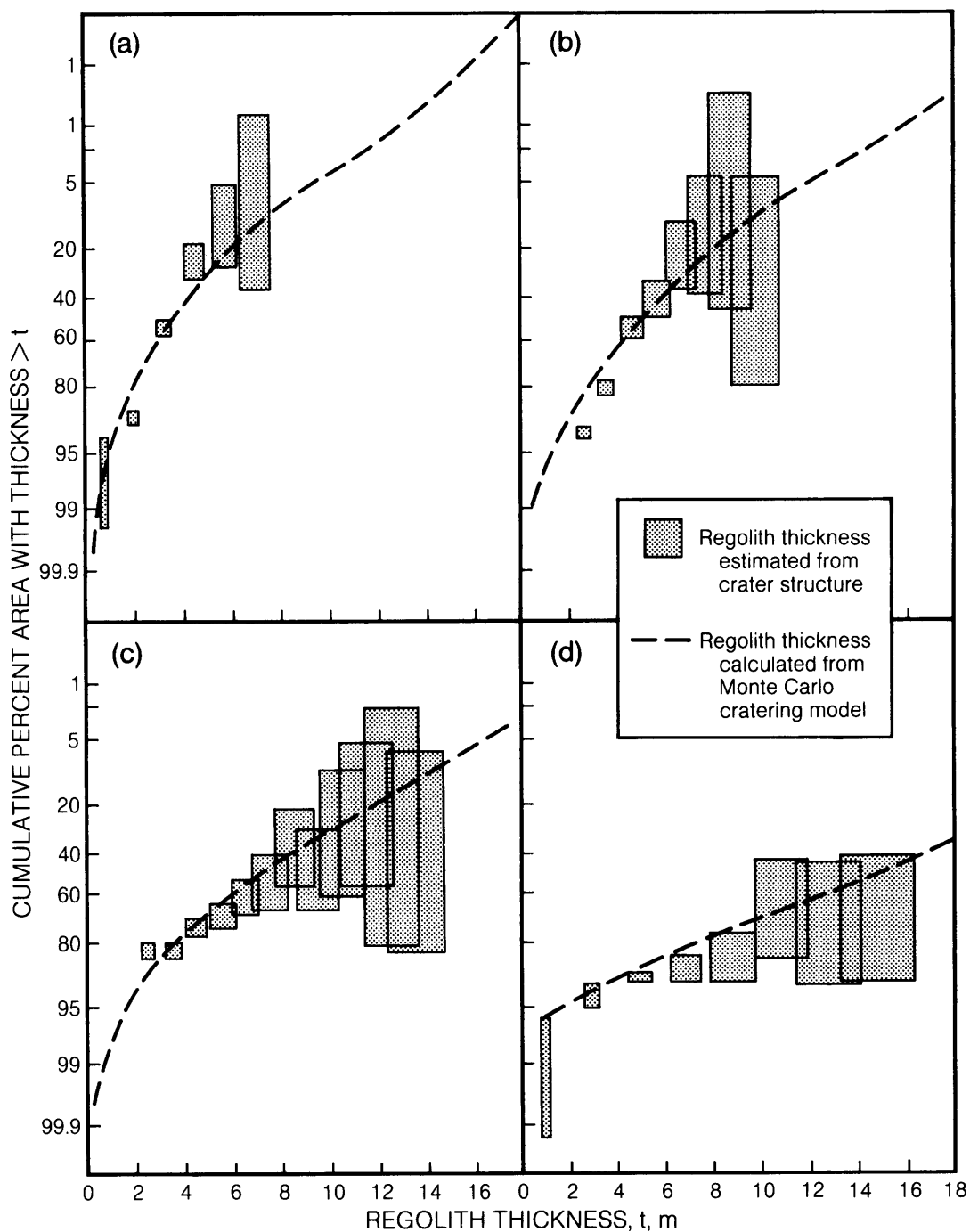


Fig. 4.21. Thickness variations of the lunar regolith obtained by photogeologic studies of four representative lunar surface areas, compared with thickness distributions obtained from Monte Carlo calculations. [(a) Apollo 12; (b) Apollo 11; (c) densely cratered mare; (d) Apollo 16 (after Oberbeck and Quaide, 1968).] The close agreement between calculated and observed results provides strong support for the general models of regolith formation by random meteorite impacts.

lith (Oberbeck and Quaide, 1968). The close agreement between observed and calculated regolith depths supports the Monte Carlo calculations of Quaide and Oberbeck (1975).

Large-scale bombardment of the highlands. The epoch of intense bombardment that occurred in early lunar history is not readily modeled. Many essential parameters have little or no experimental or observational constraints, and major assumptions must be made. The most crucial uncertainties involve estimates of the absolute numbers of large impact craters produced (as discussed in section 4.1.3). There are also serious uncertainties about the shapes and sizes of the transient crater cavities and the volumes of material excavated from them. As a result, current models are highly divergent.

Short and Foreman (1972) were the first to suggest that the aggregate volume of ejecta from all major lunar craters, evenly spread over the entire Moon, must be at least 2.5 km deep. Similar results were obtained by Monte Carlo modeling by Hörz *et al.* (1977) and Aggarwal and Oberbeck (1979), and by analytical approaches (Hartmann, 1980). Calculations by Cashore and Woronow (1985) produced estimates of much deeper ejecta stacks, possibly tens of kilometers in thickness. Regardless of these differences, there is little doubt that cumulative ejecta thicknesses on the lunar highlands must be measured in kilometers. Hörz *et al.* (1977) and Hartmann (1980) calculate thicknesses approaching 10 km using model bombardment histories about 10 times more intense than that indicated by the present crater populations.

These calculations refer to ballistic ejecta only. They do not consider the substantial subsurface mass movements typical of large-scale impacts. In these events, the lunar crust must be disturbed to great depths, as illustrated in Fig. 4.22. In a terrestrial analog, Pohl *et al.* (1977) have shown that the bedrock beneath a young, 26-km-diameter crater (Ries Crater, Germany) is seismically disturbed to depths of 4.5 km, although its excavation cavity is estimated to be only 1.5 km deep. By analogy, the lunar crust may well be fractured and brecciated to depths approaching 10 km, judging from the sizes of preserved craters, and significant fracturing, cataclasis, and brecciation may be present at average depths approaching 20 km. Still greater depths of disturbance may have been developed over large areas of the Moon if substantial numbers of large, multiring basins once covered the entire Moon, but have since been obliterated.

Because of these uncertainties, the average depth to which the lunar crust is mechanically disturbed is not known. Conservative estimates conclude that

ejecta blankets are at least 2–3 km thick (mega-regolith) and that structural disturbance (fracturing, brecciation, etc.) is over 10 km deep in the highland areas. These are average values; data for specific regions may be substantially different. As illustrated in Fig. 4.22, these estimates appear consistent with seismic profiling and measured sound-velocities (V_p).

Available data are not sufficient to test these estimates. Seismic measurements can, in principle, distinguish between solid and fragmented rock, but many fragmented and displaced masses may have been recompacted and densified by subsequent impacts. The occasional occurrence of recrystallized lunar rocks (*granulites*) in the Apollo samples (see section 6.4.6) may imply that recrystallization at elevated temperatures has occurred at depth within the Moon. Even highly-fragmented ejecta from large craters may recrystallize if heated sufficiently. These compaction and recrystallization effects can blur the ideally sharp contact between impact-transported melt or breccia and underlying fractured bedrock. Actual seismic measurements do not reveal a pronounced discontinuity in the lunar highlands akin to the sharp regolith/bedrock interfaces detected on the younger mare basalt surfaces (see Chapter 7). The limited seismic profiling of the lunar crust reveals a gradual velocity increase with depth, which may be consistent with the presence of disturbed rock masses as deep as a few tens of kilometers (Fig. 4.22).

Lateral mass transport. Most current models for impact craters spread the ejecta centrosymmetrically around the crater, typically within <2.5 crater diameters from the center. These models are based on photogeologic studies of the “continuous” deposits around lunar craters (Moore *et al.*, 1974; see Fig. 4.5). Unfortunately, the ejection velocities for the more distant “discontinuous” ejecta are not sufficiently known to be meaningfully incorporated into these models. This omission is a significant flaw in these models, for the discontinuous deposits clearly consist of high-speed ejecta, and the amount of such material ultimately determines the transport efficiency of the impact event at large distances from the crater (Pieters, 1986). Distant ejecta is also geologically significant, because it may distribute “exotic” components across the Moon (or even farther away; see discussion of “lunar meteorites” in Chapter 2). At the global scale, our views on the homogeneity or heterogeneity of the present lunar crust also depend on the efficiency of lateral mass transport. Considerable quantities of ejecta from large multiring basins may be distributed globally, and these continuous deposits can cover and conceal substantial surface areas (Moore *et al.*, 1974; Davis and Spudis, 1985). All remote-sensing informa-

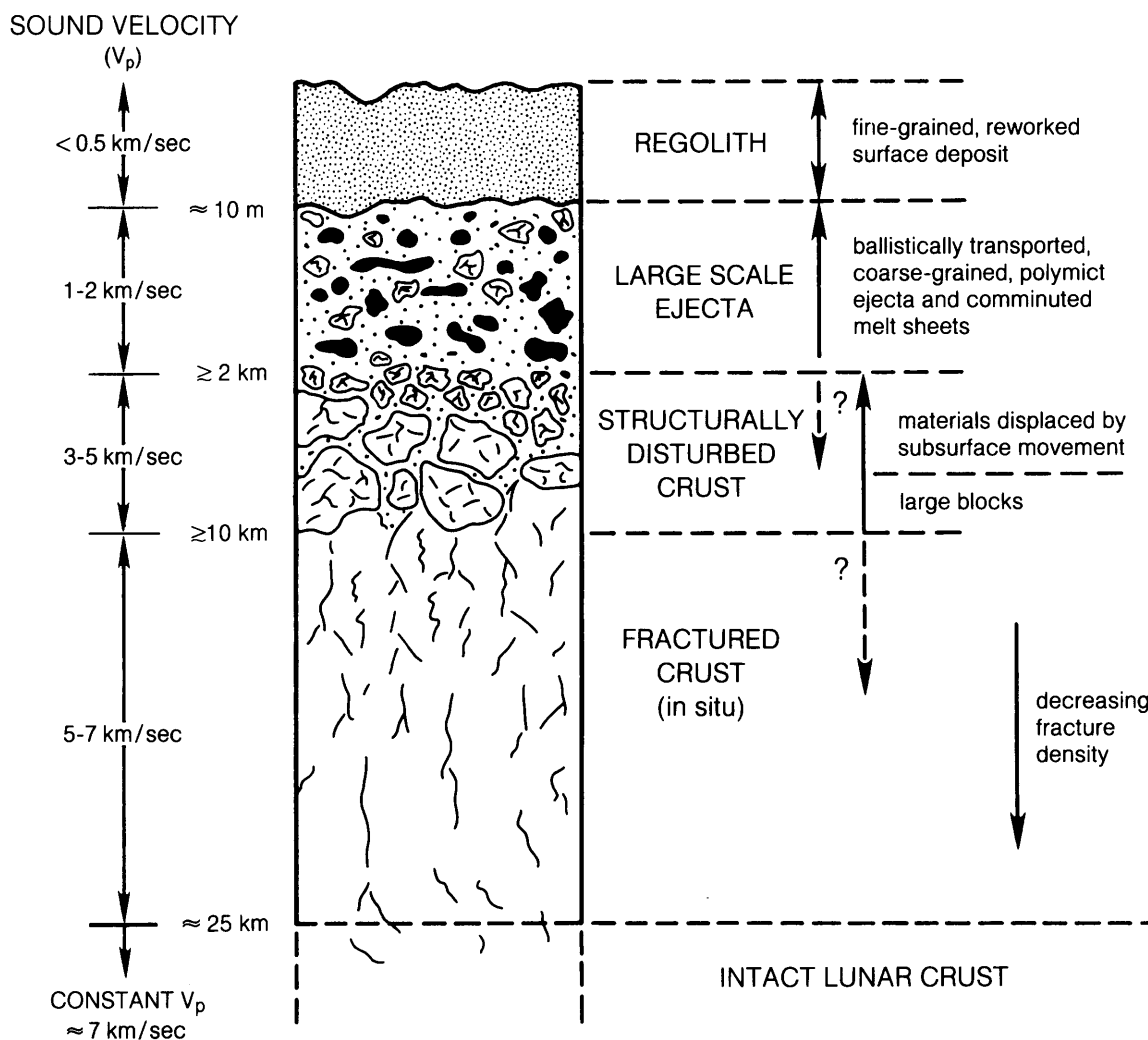


Fig. 4.22. Highly schematic cross-section illustrating the idealized effects of large-scale cratering on the structure of the upper lunar crust; see discussion of megaregolith in the text. A structurally disturbed lunar crust is also inferred from seismic measurements, e.g., from sound velocity (V_p) (Toksöz *et al.*, 1973). The depth scale in the figure is highly uncertain, because the total number of large craters and basins remains unknown. Highly variable depth effects must exist in different regions, depending on the degree to which an area has been affected by basin-sized impacts.

tion (optical imagery, infrared spectra, chemical data) is obtained from the surface layer and can therefore refer only to the last swath of ejecta deposited over any given province.

Arvidson *et al.* (1976) calculated the mass fraction of regolith material at any specific sampling site that is derived from specific craters at given radial ranges (Fig. 4.23). The results suggest that regolith is largely locally derived, with only about 1% of the ejecta derived from distances >10 km from the sampling

site. The models of Quaide and Oberbeck (1975) yield similar results. Petrologic-geochemical studies (e.g., Rhodes, 1977) also indicate that the bulk of the regolith at any site is derived from fairly local sources. In general, substantial (>10%) amounts of "exotic" materials from distant terrains are not observed in most lunar soils (Hörz, 1978). Nevertheless, because of the potential importance of such components, considerable effort has been spent in petrographic and geochemical searches for exotic

components from distant and lithologically different terrains (e.g., *Basu and Bhattacharya, 1986*; see Chapter 7).

At regional and global scales, the lunar surface is both chemically and lithologically heterogeneous, a conclusion supported by the diversity of the Apollo sample suite, by compositional remote sensing from lunar orbit, and by Earth-based telescopic methods (see Chapter 10). Major outstanding questions are whether and to what degree this observed surface heterogeneity reflects the existence and preservation of an initially heterogeneous lunar crust beneath the surface. In other words, we do not know whether the observed lunar surface patterns are only a superficial reflection of the last large-scale ejecta deposits, or whether they are in fact related to properties of the deeper lunar crust (*Warren and Taylor, 1981*; *Davis and Spudis, 1985*).

Basin-related ejecta deposits are clearly massive enough to conceal substantial fractions of the underlying original lunar surface. A better understanding of ejection processes from large craters and multiring basins is necessary to determine whether the current surface distribution of the diverse lunar rock types reflects their initial distribution, or if the observed provinces are the simple result of large-area ejecta deposition. In evaluating this mechanism, it is important to remember that the crater ejecta are confined to within <2.5 diameters of the parent crater, even around multiring basins. The currently recognized basins cover only a small portion of the Moon; if those are all the basins ever formed, it

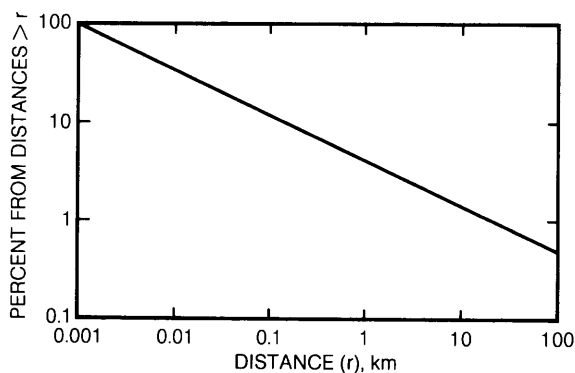


Fig. 4.23. Graph showing analytical model results for the cumulative mass fraction of the regolith at a given location that has been brought to the site as ballistic ejecta from varying distances. Virtually all ($>95\%$) of the regolith material is locally derived (from <5 km); only $<1\%$ apparently comes from sources >10 km distant (after *Aavidson et al., 1975b*).

seems likely that only a modest redistribution of crustal rocks has occurred; if so, then the observed differences arise from the heterogeneous nature of the lunar crust.

Although many unanswered questions remain, it is possible to identify the next steps that must be taken to solve them. Concerted laboratory efforts are needed to understand impact and ejection processes in more detail, with emphasis on the high-speed ejecta components. Better observational constraints are also needed for the lunar surface itself. Improved remote geochemical sensing at high spatial resolution would provide precise and high-resolution compositional gradients across highland/mare boundaries or across the contacts between chemically contrasting lava flows. Exact measurements of the compositional gradients across such chemically contrasting contacts would greatly help to establish the time-averaged fraction of surface components that derives from known distances and the extent of transport of "exotic" materials into local regions.

4.2. BASALTIC VOLCANISM

The presence of volcanic activity and lavas on the surface of a planet reflects the planet's thermal state and its evolution. Unless the planet somehow generates high enough internal temperatures to melt rocks, volcanic activity may never begin or, having begun, may not last long. On the Earth, melts form in the mantle, the deep layer that underlies the Earth's outer crust; the necessary heat is provided by the decay of natural radioactive elements. A complex method for melting rocks in the Earth's mantle is by the movement of large crustal plates that drag down (*subduct*) crustal rocks to lower depths where they can melt. Subduction does not occur on the Moon, where all lunar volcanism apparently resulted by melting of mantle rocks mixed with little or no recycled crust.

Although we have well-documented samples from only two terrestrial planets, the Earth and the Moon, there is indirect evidence that the lavas produced by partial melting of the mantles of all the terrestrial planets are chemically similar (*BVSP, 1981*). This situation reflects the fact that the mantle compositions are also similar, because all of the terrestrial planets were probably assembled from similar materials when the solar system formed.

When mantle materials are heated, melts are generated from those minerals that melt most easily at mantle pressures. These are *partial melts*, and they do not have the same composition as the original mantle material from which they form. The most common partial melts produced are called *basalts*. They are characterized by relatively low SiO_2

contents (45–55%) and by relatively high MgO and FeO contents. None of them resemble the higher-SiO₂ lavas produced on Earth by the deep reprocessing of crustal rocks.

Because such melting has apparently occurred on all the terrestrial planets—and is still occurring on Earth—many scientists are now studying complex mantle processes such as partial melting, the pooling of melt (*magma*) into deep *magma chambers*, and the ascent of magma to the surface.

For the necessary melting and basaltic volcanism to occur on the Moon, temperatures of >1100°C at depths of 150–200 km are required. The mere existence of basaltic lavas at the lunar surface therefore provides important data about past temperatures within the Moon.

The duration of lunar volcanic activity is related to the thermal state of the mantle and thus to the thermal evolution of the Moon. Current data indicate that major lunar volcanic activity ceased at approximately 3 b.y. ago, implying that mantle temperatures had then dropped below those necessary to sustain partial melting.

Studies of lunar basalts are important for determining the composition of the Moon's mantle. Because they are “partial” melts, the lunar basalts are chemically complementary to the residual unmelted mantle materials left behind. Using the thermodynamic principles involved in equilibrium partial melting, the complementary residue may be characterized and the original bulk composition of the Moon's mantle may then be calculated.

All of the smooth, dark regions visible on the Moon's nearside consist of lavas that partly or completely fill the multiring basins (Figs. 4.24 and 4.25). Basaltic lavas cover an area of 7×10^6 km², 17% of the Moon's surface (Head, 1976). Nearly all of the basalts occur on the nearside.

Most of the facts concerning lunar basaltic volcanism are derived from the analysis of returned samples (section 6.1) and from the characterization of volcanic landforms (section 4.2.1). The sequence and duration of volcanic activity, as exemplified by successive filling of multiring impact basins, is described in section 4.2.2, and estimates of the total volume of basaltic lavas generated are summarized in section 4.2.3. The possibility that there was early volcanic activity on the Moon is discussed in section 4.4.

Not all products of basaltic volcanism are necessarily lava flows. “Fire fountaining,” driven by gases exsolving from the magma, occurs during basaltic lava eruptions, dispersing the melt as fine droplets. These droplets form *pyroclasts* or *volcanic ash* that may be strewn over large areas. Pyroclastic materials are recognized in the lunar sample collection and

can also be identified by remote-sensing techniques, especially by infrared reflectance spectra that reveal their glass-rich nature (Adams *et al.*, 1974; Hawke *et al.*, 1979). Pyroclastic deposits on the Moon are widely dispersed and are readily worked into the regolith by impact gardening; identification of these deposits in surface photographs is possible only at a few well-preserved locations.

4.2.1. Volcanic Landforms

Mare lava flows. The dark-colored flat mare plains were formed by large-volume eruptions of low-viscosity basaltic lavas (BSVP, 1981; see section 6.1). Samples of lava and volcanic ash returned to Earth confirmed the commonly held hypothesis of a volcanic origin for the mare plains (Baldwin, 1948, 1963). Several other hypotheses for the flat basin fills had been put forth, including pyroclastic flows (Mackin, 1964) and deep dust, mass-wasted from the highlands (Gold, 1966). Much earlier, Galileo had likened these smooth surfaces to water, i.e., “oceans,” thus the Latin term “mare.” In current usage, *mare basin* designates a circular, multiring impact structure and *maria* the dark-colored lavas within such basins.

Although lunar lava flows were identified through pre-Apollo telescopic observations and on Lunar Orbiter imagery, the best descriptions of these landforms are based upon maps and panoramic photography generated during the extended Apollo J missions (Apollo 15–17; Schaber, 1973a). Figure 4.26 shows in detail several lava flows of Mare Imbrium, but qualitatively similar observations also apply to other mare basins. In the Imbrium Basin, lavas were erupted from the southwest basin edge (18° to 23°N, 28° to 32°W; Fig. 4.26). From this center, three successive sets of flows extend into the basin for 1200 km, 600 km, and 400 km, respectively, over slopes of about 1:1000 (Fig. 4.26b). Lobate flow scarps bounding these flows have heights ranging from 10 m to 63 m and average ~35 m (Gifford and El Baz, 1978). These combined flows cover an area of $\sim 2 \times 10^5$ km² (an area equal to that of Nebraska or Senegal), with an estimated basalt volume of 4×10^4 km³. The presence of leveed flow channels and localized lava ponds (dammed by wrinkle ridges; see below) on these lava flows provide strong support for the concept of extraordinarily large flow distances over essentially flat terrain.

Such thin flows, 20–40 m thick, would be expected to chill and solidify quickly; the apparently long flow distances are therefore surprising. This apparent inconsistency was in part solved by direct viscosity measurements of molten lunar basalt (Weill *et al.*, 1971). The viscosities are unusually low, only a few tens of poise at 1200°C. Furthermore, similar

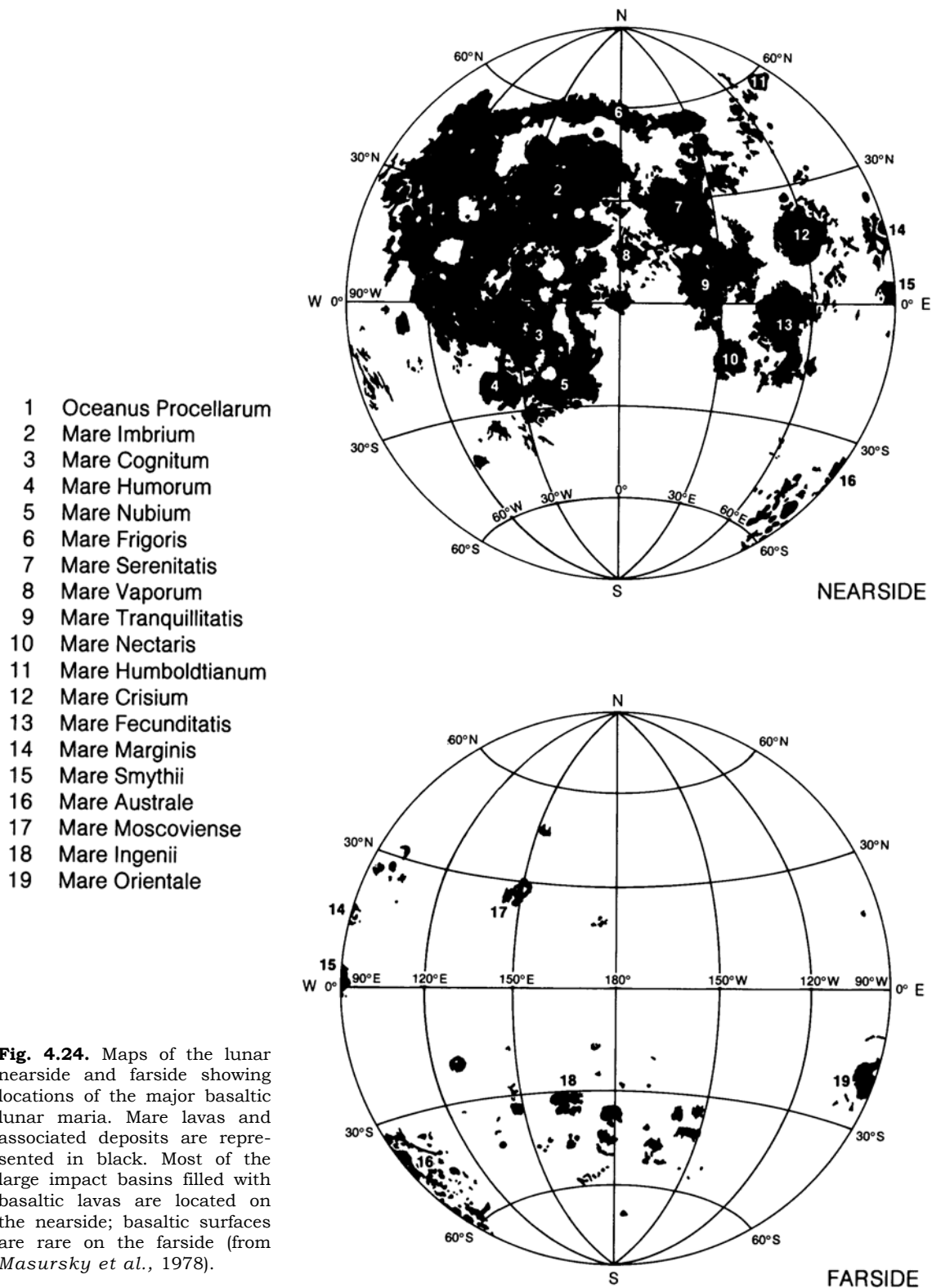


Fig. 4.24. Maps of the lunar nearside and farside showing locations of the major basaltic lunar maria. Mare lavas and associated deposits are represented in black. Most of the large impact basins filled with basaltic lavas are located on the nearside; basaltic surfaces are rare on the farside (from Masursky *et al.*, 1978).

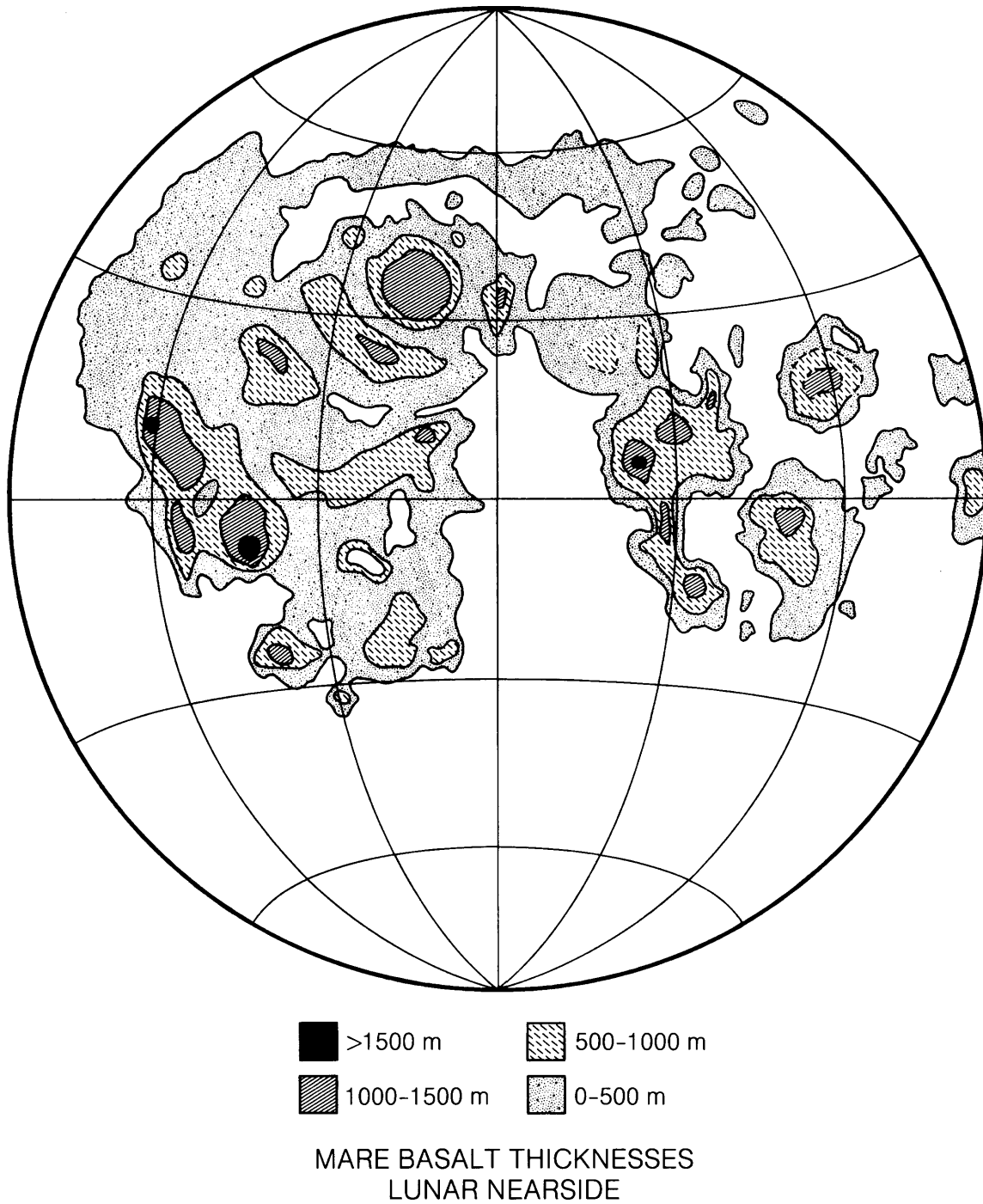


Fig. 4.25. Estimated thickness of mare basalts in the nearside maria based on the “flooded crater” method of DeHon (1974, 1979) and DeHon and Waskom (1976). Isopach interval is 500 m. Note the substantial basalt depths in the basin centers, where no flooded craters are seen because they have been totally inundated by basalt flows. Most flooded craters occur in the relatively shallow shelf areas.

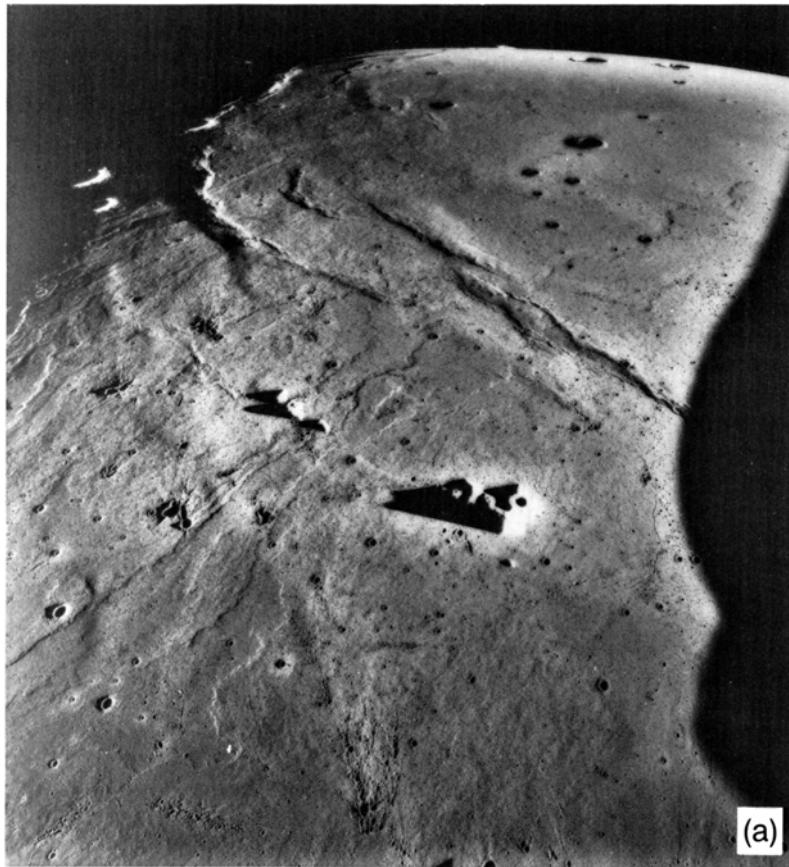
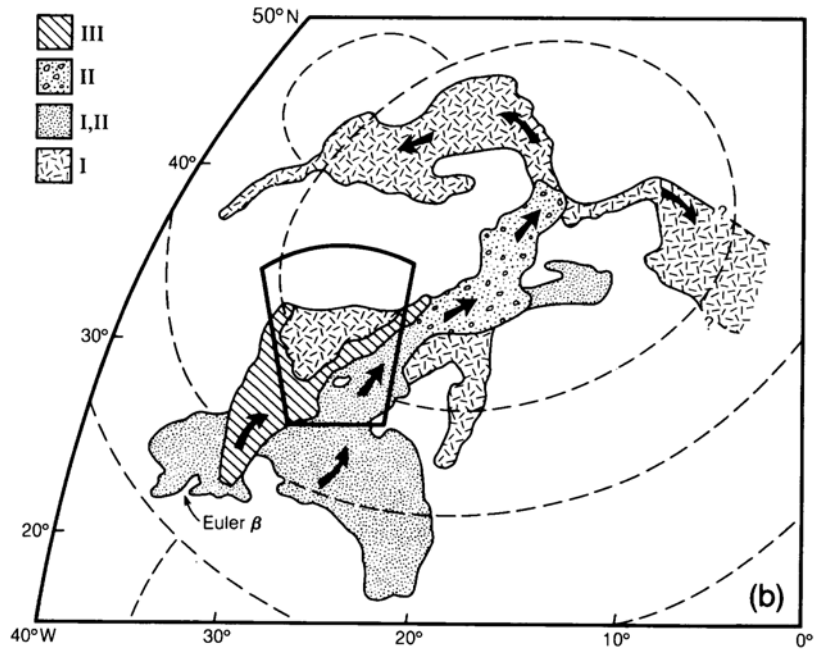


Fig. 4.26. Sequence of eruption of large-scale lava flows in Mare Imbrium, a 1200-km-diameter impact basin. **(a)** Oblique, northwest-facing photograph of Mare Imbrium, illustrating lobate flows-carps, leaved channels (running southwest to northeast), and con-centric wrinkle ridges. Mount La Hire (center-right), about 30 km long at the base, is surrounded and partially submerged by lavas. Lavas are channeled between La Hire and part of a massif to the northwest (NASA Photo ASI5-1556). **(b)** Location and extent of the major basalt flows of Mare Imbrium according to Schaber (1973a). Crater counts reveal three major episodes (I, II, III) of basalt extrusion, spanning approximately 0.5 b.y. The sources for these flows are believed to be fissure vents located in the southwest rim of Mare Imbrium. Arrows indicate direction of flow; dashed lines are basin ring structures. "I, II" are areas where lava flows from episodes I and II overlap and cannot be individually mapped. The heavy outline shows the area of **(a)**.



eruption processes on Earth have formed the flood basalts of the Columbia River Plateau, Washington State, and have been reconstructed through studies by *Shaw and Swanson* (1970). At high eruption temperatures (~1250°C), low viscosities (<30 p), and high eruption rates, the Columbia River basalts are believed to have erupted 10^{-1} to 10^{-2} km³/day of lava for each kilometer of active fissure. For comparison, the youngest of the Imbrium lava flows was erupted from a 20-km-long fissure located at the intersection of major basin rings. By analogy with the Columbia River basalt flows, 0.1 to 2.0 km³ of lava per 24-hour period could have erupted from this Imbrium fissure, assuring the high eruption rates required for lava to flow to great distances.

The thin lava flows studied in the Imbrium Basin are not unique. By applying petrologic models to basalt samples from the Apollo 11, 12, and 15 sites, *Brett* (1975a) determined that those samples had come from lava flows less than 10 m thick. In the walls of Hadley Rille, at the Apollo 15 site, there are at least three different basalt flow layers observed within 60 m below the mare surface. Supporting evidence for flows about 20 m thick came from many additional photogeologic and petrogenetic studies (*Howard et al.*, 1973; *Gifford and El Baz*, 1978; *Spudis and Ryder*, 1985).

Many lunar lava flows lack distinct scarps, an observation that could reflect several possible causes— even lower viscosities, higher eruption rates, pooling of flows in shallow depressions, or subsequent destruction by impact cratering. In areas of continuing eruption, younger thin lava flows could also have covered and subdued older flow fronts (see maps in Chapter 10).

The primary landforms resulting from lunar basaltic volcanism are vast, smooth plains, indicating low lava viscosities and high eruption rates. Photogeologic, spectral, and other methods have been used to distinguish numerous individual flows, to recognize discrete eruptive periods, and to establish relative ages (e.g., *Schaber*, 1973a,b; *Boyce*, 1976). First, younger flows clearly overlap, spill over, or inundate older flows. Some different flows may have subtly different albedos and photometric properties, indicating different chemical compositions (*Pieters*, 1978). Flows from different eruptive periods invariably display different crater densities, indicating a substantial hiatus between eruption cycles (*Boyce*, 1976).

Crater-density or crater-erosion ages for diverse basaltic mare surfaces indicate that production of basin-filling volcanic lavas lasted about 500 m.y. in most major basins. [Detailed infrared reflectance observations (*Pieters*, 1978), combined with cratering ages (*Boyce*, 1976; BSVP, 1981) for a large number

of flows, are presented in detail in Chapter 10.] These synoptic observations indicate a great diversity in basalt compositions as well as in extrusion ages.

Remote-sensing studies indicate that we have not sampled all the compositional varieties of lunar lavas; neither have we sampled the oldest or youngest flows on the Moon.

Prominent basalt eruptions over the entire Moon lasted a minimum of 800 m.y., i.e., from 3.9 to 3.1 b.y. ago, as determined by radiometric age dates on lunar samples (*Head*, 1976a; also see section 6.1). On the basis of observed low crater densities on some formations, minor eruptions could have continued until as recently as 2 b.y. ago (*Schultz and Spudis*, 1983). The onset of basaltic activity is also not clearly defined. The oldest mare basalt sample, extracted from a highland breccia, apparently crystallized at 4.2 b.y. ago (*Taylor et al.*, 1983). However, corresponding surface units are not visible.

Indications of early basaltic activity are also supported by some photogeologic studies. *Schultz and Spudis* (1979) describe impact craters with low-albedo ejecta blankets (“dark halo craters”) from a number of highland sites peripheral to large mare basins; they explain them as the results of impacts into basaltic deposits that are buried under a thin veneer of highland ejecta. It is also possible that very early basalt flows, buried by younger ones, exist inside the mare basins; clearly only the youngest (last?) flows composing the actual surface can be studied by remote sensing and photogeology. Although neither the onset nor the termination of lunar basaltic volcanism can be accurately defined at present, any activity after 3 b.y. ago is certainly of minor volumetric importance.

Vast expanses of basaltic lava flows dominate the mare basins, but other volcanic landforms, such as ash rings and lava domes, are present. Most are small in scale and of limited lateral extent. Many may be considered accessories to the major flows, and these illuminate the details of processes during flow emplacement. Others indicate different eruptive styles, including explosive volcanic activity. All are, however, a natural consequence of basaltic volcanism.

Sinuuous rilles. Meandering channels, called *sinuuous rilles*, commonly begin at crater or crater-like landforms and end by fading downslope into the smooth mare surface or into a chain of elongate pits (*Greeley*, 1971; Figs. 4.27a,b). Sinuuous rilles range in size from a few tens of meters to 3 km in width and from a few kilometers to 300 km in length (*Schubert et al.*, 1970). The channels are U- or V-shaped, but the original cross-sections have been modified by fallen debris from channel walls or ejecta from nearby craters. Their mean depth is ~100 m.

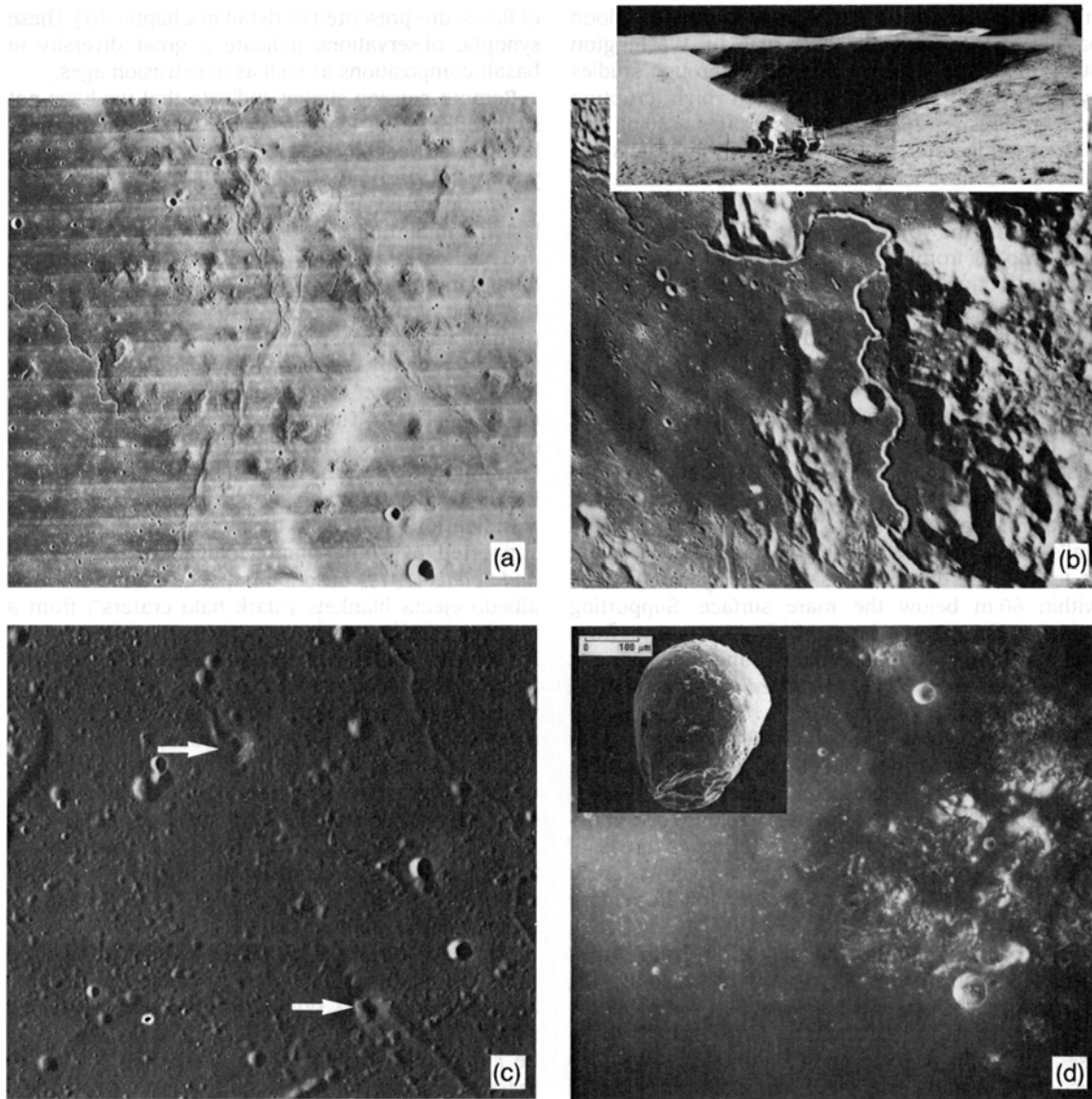


Fig. 4.27. Small volcanic landforms associated with basaltic volcanism. **(a)** Marius Hills, a plateau believed to be of volcanic origin, located in Oceanus Procellarum. This image shows dome-like landforms, sinuous rilles, elongate depressions, crater chains that may be partly collapsed lava tubes, and wrinkle ridges. The width of this image is ~165 km (NASA Photo LO IV-157 H-2). **(b)** Oblique orbital view of Hadley Rille, approximately 120 km long. The rille originates in a deep, wedge-shaped cleft (bottom right of picture) and disappears under the mare surface along the highland massif/mare contact (upper left) (NASA Photo AS15-M-0855). The surface photograph of Hadley Rille (inset) was taken during the Apollo 15 mission. The rille is 1500 m wide and 300 m deep and exposes several basalt flows, cumulatively at least 60 m thick (Greeley and Spudis, 1986) (NASA Photos AS15-84-11450 and 11453). **(c)** A chain of cone-like landforms (arrows), with craters and short rilles, located in Mare Serenitatis. The chain is approximately 25 km long (NASA Photo AS17-P-2317). **(d)** Dark pyroclastic mantle deposits, which cover part of the southeastern Serenitatis Basin and its rim (Taurus Mountains) near the Apollo 17 landing site. These deposits form an irregular band around the basin perimeter and over part of the adjacent highlands. The Apollo 17 landing site is located in the valley, center-right (NASA Photo AS15-M-1115). Inset: Scanning electron photograph of a partly crystalline glass droplet typical of the dark mantle deposit sampled by the Apollo 17 astronauts at Shorty Crater. The irregular coatings consist of flattened glass droplets and vapor condensates. These droplets are believed to have formed in lava fountains.

Although present everywhere on the Moon where there are mare deposits, most rilles are located along basin margins. The highest concentrations of sinuous rilles are in the Marius Hills (14°N, 50°W) and on the Aristarchus Plateau (27°N, 50°W). *Guest and Murray* (1976) mapped their distribution on the lunar nearside and farside.

Before Apollo, the three most popular hypotheses for the origin of sinuous rilles, which had already been detected by telescopic observations, were (1) collapsed lava tubes or open lava channels (*Baldwin*, 1963), (2) erosion of mare lavas by pyroclastic flows (*Cameron*, 1964), and (3) erosion by water (*Firsoff* 1961). The Apollo 15 site was deliberately chosen on the edge of Hadley Rille to study processes of rille formation. No pyroclastic materials were found, much less hydrated minerals or water (*LSPET*, 1972; *Howard et al.*, 1972). The relationship between sinuous rilles and basaltic lava flows was confirmed, but their detailed formation remains poorly understood.

Analogies with terrestrial lava channels and totally enclosed lava conduits, termed *lava tubes*, seem obvious. Molten lava commonly advances in open channels, and the build-up of levees by lateral spattering and overflow frequently accompanies these molten lava rivers. Build-up of substantial levees, together with crusting over of the lava surface may, in extreme cases, lead to lava tubes through which lava continues to flow. Widening and deepening of these channels by melting of the underlying rock by very hot lavas is also observed on Earth (*Hulme*, 1973; *Peterson and Swanson*, 1974). Such processes must have combined to form sinuous rilles on the Moon (*Oberbeck et al.*, 1971). However, there is a problem in scale. The terrestrial rilles are modest in size; the lunar ones are typically a factor of 30–50 larger than the terrestrial features in width, depth, and length. Roofs free-spanning >100 m across lava tubes can exist in the lower gravity of the Moon (*Oberbeck et al.*, 1969), but the unusually large sizes of lunar sinuous rilles seem to require a combination of reduced gravity, high melt temperature, low viscosity, and high extrusion rates.

Mare domes. Domes are broad, convex, circular to oval landforms of modest positive relief on the lunar maria (*Smith*, 1973; *Head and Gifford*, 1980). This term may have been an unfortunate choice because “volcanic dome,” when used on Earth, usually implies eruptions of highly viscous, silica-rich lavas (*MacDonald*, 1972) and, indeed, some observers argued initially for such silicic volcanism on the Moon. At this writing, no observations have been made of silicic lavas on the Moon.

Eighty low domes (slopes of 2° to 3°) have been mapped on the Moon’s nearside (*Guest and Murray*,

1976). Basal diameters range from 2.5 km to 24 km, and the domes may be 100 m to 250 m high. Most of the domes are located in the Marius Hills, where there are many other unusual volcanic features (Fig. 4.27a). Some domes have summit craters or fissures, and some grade laterally into the lavas of the surrounding mare surface. Domes with steep sides (7° to 20°) are also present in the Marius Hills. We know little about the formation mechanism(s) of domes, but they could have been formed by eruption of more viscous basaltic lavas, by intrusion as shallow subsurface laccoliths, or by mantling of large blocks of older rock by subsequent lavas. Interpretation of their origins must wait for future sampling and mapping.

Lava terraces. Small terraces within some craters and along mare-highland boundaries have been interpreted as “shorelines” left after withdrawal of erupted lava, either by drainage back into vents or by flow into a lower basin (*Holcomb*, 1971; *Young*, 1976; *Spudis and Ryder*, 1986).

Cinder cones. On Earth, cinder cones and spatter ramparts are the most common subaerial volcanic landforms developed around vents. They are developed by the explosive ejection of blobs or sprays of molten rock, which are then deposited as lava bombs and cinders around a vent. Less viscous sprays of smaller melt droplets can form fine ash that is interbedded with such coarser-grained deposits. Cones and spatter ramparts are commonly associated with basaltic lava flows, but they make up only a small part of the total volume erupted from a vent.

On the Moon, conelike landforms have been described on the maria in association with rilles. They are generally of very low albedo. Most cones are less than 100 m high, with diameters of approximately 2–3 km at the base (*Guest and Murray*, 1976; *Head and Wilson*, 1979). Some have summit craters less than 1 km in diameter (Fig. 4.27c). Lines of cones associated with rilles are interpreted as fissure vents.

Dark-haloed craters and pyroclastic deposits. Extrapolation to the Moon of the conditions that generate terrestrial cinder cones predicts that such features should be relatively modest, broad, pancake-shaped volcanic landforms, primarily because of the low gravity that allows wider areal dispersion of the spatter and bombs (*McGetchin and Head*, 1973). It has not been established that such features do exist on the Moon, but this origin has been proposed to explain the numerous *dark-haloed craters* on the lunar surface.

Dark-haloed craters are located along the margins of mare basins and along rilles or lineaments. Most are shallow depressions with rim deposits 2 km to 10 km in diameter. Like cinder cones, they generally

have albedos that are distinctly lower than the surrounding basalt surfaces.

A dark-haloed crater, named "Shorty," was sampled at the Apollo 17 site (Fig. 4.27d). It turned out to be nonvolcanic, but is apparently an impact crater that penetrated a deposit of loose glassy and partly crystalline droplets of orange to black color, producing low-albedo ejecta. This material, initially called the "orange soil," turned out to be pyroclastic deposits of volcanic origin (*Heiken et al.*, 1974; *Butler*, 1978; *Delano*, 1986) that clearly predate the formation of Shorty Crater. Whether other "dark-haloed" craters on mare surfaces are also impact craters that penetrate pyroclastic deposits or whether they are genuine volcanic features is currently undetermined (*Schultz and Spudis*, 1979; *Head and Wilson*, 1979).

Dark-haloed craters of unambiguous impact origin are also found in some highland areas adjacent to maria (*Schultz and Spudis*, 1979). It has been suggested that their ejecta consist largely of basaltic materials, excavated from below a thin veneer of material that has been ballistically transported or mass-wasted from the adjacent highlands. These underlying basalt flows may in fact be among the oldest ones on the Moon, indicating the existence of basaltic volcanism before 3.9 b.y. ago.

In summary, a variety of "dark-haloed" craters are recognized on the Moon; they may or may not be of volcanic origin. Dark-haloed craters located along rilles or in straight lines, similar to those located in the basaltic fill of Alphonsus Crater (*Head and Wilson*, 1979) or those spatially associated with the source area of the youngest Imbrium lavas (*Schaber*, 1973a,b), are excellent candidates for volcanic landforms.

The low-albedo volcanic materials around dark-haloed craters, even if exhumed by impact processes, are nevertheless of extreme interest, because they may have been originally associated with explosive, volatile-rich volcanic activity. Some dark albedo materials, e.g., the Apollo 17 "orange soil," are clearly pyroclastic deposits. Studies of this material from Shorty Crater revealed that the orange (glassy) and black (partly or completely crystalline) droplets formed during lava fountaining of low-viscosity, Fe-Ti-rich basaltic magmas (e.g., *Heiken et al.*, 1974). The surfaces of individual droplets have unusual concentrations of condensed volatiles, including Zn and S (*Butler*, 1978). Compositions of the droplets themselves are similar to compositions predicted in unmodified partial melts from the mantle (*Delano*, 1986). However, they could also represent magma that had been contaminated during its ascent by assimilation of wall rocks, so that the "basalt" rock compositions observed would therefore not represent the original mantle melts.

The observations of Apollo 17 orange glasses have helped to confirm the volcanic origin of green glass spherules returned from the Apollo 15 site. In addition, systematic searches for pyroclastic components in regoliths sampled by other missions have revealed the presence of still different pyroclastic glasses (e.g., *Delano*, 1986). Although these glasses are of trivial volume, they are important samples in understanding lunar volcanism, for they demonstrate that lava fountaining took place on the Moon. A similar pyroclastic origin may explain the dark mantle deposits of significant areal extent that occur along the inner rim of Mare Serenitatis (*Adams et al.*, 1974; *Hawke et al.*, 1979).

4.2.2. Filling of the Maria

Basaltic volcanism and large-scale impact basins are spatially related on the Moon. Basin formation, followed immediately by collapse of the transient basin cavity, leads to large-scale fracturing of the crust and thus provides both the structural framework and the conduits along which basaltic magmas generated at depth may ascend to the surface. Most such conduits seem to be located just within the edges of the mare basins, where large-scale slump zones should be prominent (*Schaber*, 1973a,b; *Head*, 1976a).

Deep melting can be produced by several mechanisms associated with the formation of large impact basins. The lower thermal conductivity of thick basin-filling ejecta blankets, which is related to their high porosity, can produce significant upwarping of mantle isotherms, thus promoting localized melting below a basin (*Arkani-Hamed et al.*, 1973). Other factors include the actual physical uplift of mantle materials during basin formation, the decrease in hydrostatic pressure caused by the sudden removal of overburden, and the resulting decrease in melting temperature with decreasing confining pressure (*Brett*, 1976). In addition, massive, unfractured sheets of fresh impact melt produced during basin formation, possibly a few kilometers deep, may act as an impermeable plug that forces the ascending lavas from the center of the basin to its edges.

Significant time may elapse between the formation of a large *mare basin* by impact and its subsequent filling with basaltic lava flows to form the dark lunar *maria*. Current information fixes the formation of the Imbrium Basin at about 3.9 b.y. ago, but the lavas that fill it (sampled by the Apollo 15 mission) are about 3.3 b.y. old.

Many details of how basins are formed and filled with lavas are not well understood, but there is little question that basin formation has provided the

structural framework for widespread basalt eruptions. With few exceptions, the lava flows that form the dark lunar maria are confined to basin interiors, but on occasion the lavas seem to have spilled over the basin rims to flood adjacent terrains.

It is important to note that not all large impact basins have triggered subsequent volcanic activity. Most basins on the nearside are flooded by basalts, but only a few on the farside are flooded. This difference may be caused by the existence of a thicker farside crust, a condition that is also suggested by gravity observations and other geophysical considerations (*Bills and Ferrari, 1976; Solomon et al., 1982*). The processes leading to filling of the basins with lavas also appear to be generally related to the chronology of basin formation. Many old, highly-degraded basins are devoid of volcanic activity and lava fillings; most major, well-preserved basins, i.e., the geologically younger ones, seem to be filled by lavas (*Head, 1976a*). There are exceptions to these trends, however, and there is still no general consensus nor any accepted model to relate volcanic activity directly to the time of basin formation or to the thickness of the lunar crust. Clearly, most volcanic activity has occurred over a limited area of the Moon and is confined, with minor exceptions, to the lunar nearside (*Head, 1976a; BVSP, 1981*).

The sequences of basaltic eruptions, and their implications for basalt origin and for the long-term evolution of the basins themselves, are illustrated best by the youngest basins: *Oriente* (*Head, 1974a; Moore et al., 1974*), *Imbrium* (*Schaber, 1973*), and *Serenitatis* (*Head, 1979; Solomon and Head, 1980; Solomon et al., 1982*). *Mare Orientale*, the youngest large lunar basin, is only partly filled with basaltic lavas. Its interior seems dominated by a relatively flat-lying sheet of nonbasaltic(?) impact melt, which shows modest local topographic relief. The subsequently erupted basaltic lavas have spilled over part of this melt sheet and occupy only the basin interior. *Oriente* may thus represent the earliest phases of basin-filling by lavas. Eruptions began within the innermost ring (the "Inner Rook"; see Fig. 4.28a) and along the ring's concentric fault systems. Well-preserved fissure vents and domes are also visible in association with the next outward ring, the *Rook Mountains*, which form the major inner ring of *Oriente*. Eruption vents are located along ring faults (Figs. 4.28b,c).

Mare Imbrium, although older than *Oriente*, is the youngest major basin located entirely on the lunar nearside; its ejecta deposits cover a substantial fraction of the entire nearside. Total lava fill in the *Imbrium* Basin is more substantial than in *Oriente* (*Head, 1982*). Unlike *Mare Orientale*, no sheet of apparent impact melt is visible. Significantly, most of

the annulus between the major interior ring and the major topographic rim (the *Apennine Mountains*) is also covered by lava flows, except for the *Palus Putredinus* region in *Imbrium's* southeast corner. As described by *Schaber (1973a,b)*, lavas were erupted predominantly from the basin periphery, in this case close to the major topographic rim (Fig. 4.26). Did earlier eruptions occur in more interior locations, as in *Oriente*? We do not know. It is clear, however, that there are three distinct eruptive episodes in *Mare Imbrium*, based on crater-density ages; the volcanic activity represented by these (last) three eruptive episodes spans 0.5 b.y. (3.7 to 3.2 b.y. ago).

The *Serenitatis* Basin is somewhat older than *Imbrium*. Its interior rings are completely flooded, and basaltic lavas occupy the entire basin inside the major topographic rim. As in the case of *Imbrium*, three major episodes of lava flows are observed (Fig. 4.29). The history of the *Serenitatis* Basin has been extensively modeled by *Solomon and Head (1980)*. They propose an early, dilatational stage of the entire lunar crust during basin formation and basaltic activity, followed by a compressional stage as the crust cooled and contracted (*Golombek, 1979; Binder, 1986*). The oldest lavas, Stage I, erupted in the southern basin rim of *Serenitatis*. Some of them spilled over into the adjacent *Mare Tranquillitatis*, where they were collected by the *Apollo 11* mission and dated at 3.65 to 3.85 b.y. ago.

During this period, the center of the *Serenitatis* Basin sank under the load of the Stage I lavas. The subsequent Stage II lavas therefore erupted into a newly created shallow depression. They form an approximately concentric annulus within the Stage I lavas; overlap relationships and crater densities leave little doubt that these lavas were erupted later. The last eruptive episode, Stage III, produced the youngest basalts; these occupy the basin center because downwarping had continued. Some Stage III lavas, however, also spilled into embayments around the adjacent *Imbrium* Basin, illustrating that topographic slopes and gradients were small.

The major conclusion of this model (*Solomon and Head, 1980*) is that basin floors downwarp under successive basalt fillings and it is therefore possible that total basalt-fill thickness, predominantly from early eruptions, may exceed a few kilometers. This process also accounts for the existence of compressional ridges (Fig. 4.29c; see also *Muehlberger, 1974*). The continued downwarping causes centrosymmetric foreshortening, and thus compression, forming concentric bands of compressional ridges.

Most petrologic models of lunar basaltic magmas suggest that they originated by partial melting at depths of 200–400 km (*Kesson, 1975; BVSP, 1981; Delano, 1986; Binder, 1986*; also see section 6.1.8).

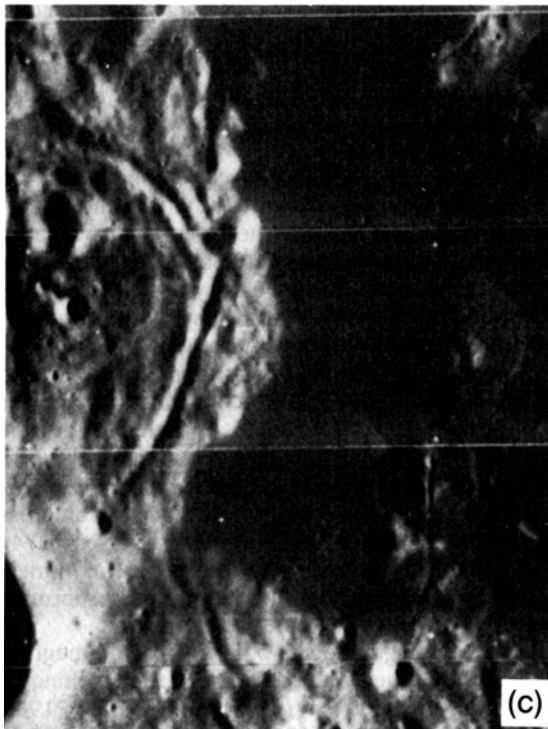
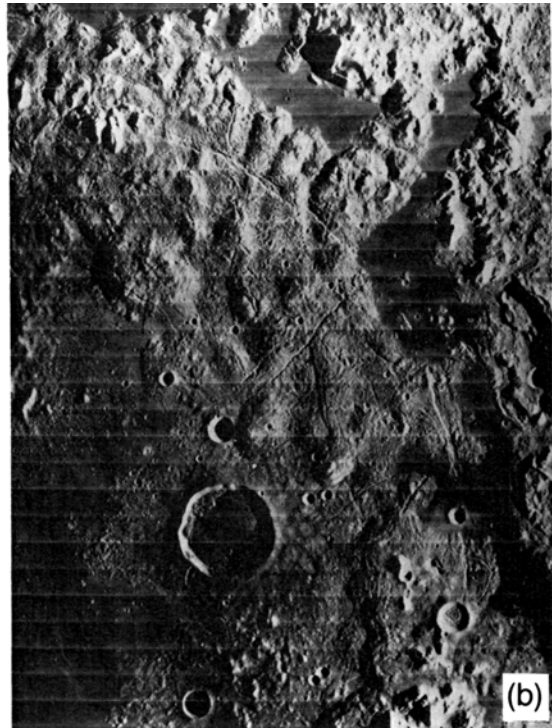


Fig. 4.28. Basaltic volcanism in Mare Orientale (at 20°S, 95°W), showing details of lunar basaltic volcanism that may be applicable to other, more extensively flooded, multiring basins. **(a)** Overview of Orientale, illustrating the well-preserved major rings: Innermost ring (4), 320-km diameter; Inner Rook (3), 480-km diameter; Outer Rook (2), 620-km diameter; and Cordillera (1), 930-km diameter. Note that dark basalts cover part of the basin interior as well as some depressions between the major rings. Occurrence of basalts in such different locations and as isolated patches in a number of depressions appears to require a large number of individual vents within the basin and between the rings (NASA Photo LO IV-187M). **(b)** Detailed view of the northeastern quadrant of Mare Orientale. Dark basaltic lavas have been erupted into the concentric depression formed between the Inner and Outer Rook Mountains, suggesting the existence of a number of conduits associated with basin-generated faults and slump zones. None of these basalts appear to have spilled into the basin interior; the interior fill must therefore have come from more centrally located vent areas. (NASA Photo LO IV-187 H₂). **(c)** Photographic enlargement of the lower right corner of **(b)**, illustrating examples of possible fissure vents (north-south trend) and associated volcanoes. The latter form low, broad shields (some 6 to 8 km in diameter at the base) around the vents. **(d)** Mare filling within the south-central Orientale Basin. Dark, smooth plains are interpreted to be basaltic lavas; the presence of sinuous rilles and of circular subsidence features suggests the presence of surface liquids and flow (NASA Photo LO IV-195 H₁).

These magmas had lower densities than the surrounding rocks, and therefore tended to rise as large bodies of melt. At shallower depths in brittle crust, the magma most likely followed fractures and faults induced by basin-forming impacts or by local extension of the crust caused by basin subsidence (Fig. 4.29c). The location of volcanic conduits is thus strongly affected by impact-basin structures in the crust (Solomon and Head, 1980).

Photogeologic studies reveal that fissures are the sources for some of the lunar lavas. In their models of lunar volcanic eruptions, Head and Wilson (1979) determined that such fissure vents need be no wider than 10 m to allow the high eruption rates required for long lava flows. They also determined that the speed of rising magmas must have been >0.5–1.0 m/sec to maintain lava fountains, even if no explosive lava fountaining activity occurred.

Vesicles (bubbles) occur within lunar lavas and pyroclasts indicating that a volatile phase (or phases) was present when the rocks were molten. The vanishingly small water content of lunar lavas indicates that—unlike terrestrial lavas—water was not a significant gas component. Sato (1978) presents evidence suggesting that CO was the main gas phase. Lunar pyroclastic activity, driven by CO, appears possible. Head and Wilson (1979) determined that only 250–750 ppm of CO is required to disrupt magmas at depths of 15 to 40 m, producing explosive activity by the growth of large bubbles that burst and throw spatter clots. Based upon analysis of orange-glass pyroclasts from the Apollo 17 site, Heiken and McKay (1978) favor semicontinuous lava fountaining as the main type of lunar explosive volcanism.

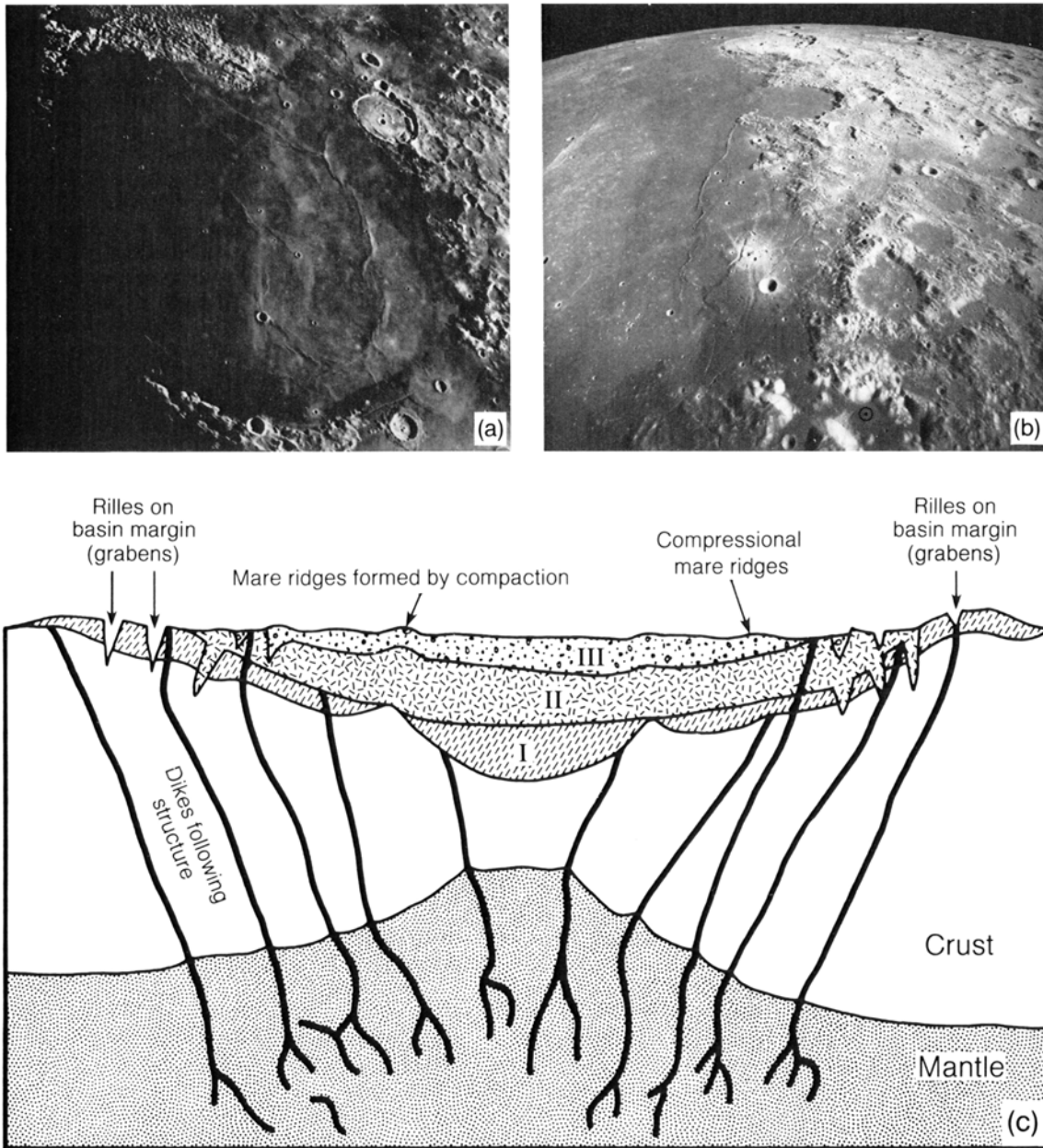
4.2.3. Volume Estimates of Basaltic Mare Fill

The total volume of the Moon's volcanic deposits is an important quantity in defining the extent of melting that took place within the lunar mantle

(Kesson, 1975; Delano, 1986). How much of the lunar mantle was melted to produce the basaltic lavas? This question addresses two important points: (1) What was the degree of partial melting, i.e., the fraction of melt produced per unit volume of mantle material? (2) How much of the entire lunar mantle was involved? A given volume of basalt at the surface can obviously be produced by large degrees of partial melting of a small mantle volume or by a small degree of partial melting of a large part of the mantle. The total volume of erupted basalt—an independently-determined quantity—can be used to constrain geophysical/geochemical models involving various bulk compositions and thermal histories of the lunar mantle.

The area occupied by basaltic deposits is readily measured—about 17% of the Moon's surface, or about 6.4×10^6 km². No direct measurements of the thickness of basaltic mare deposits have been made, however. Active seismic profiling during the Apollo missions did not yield good estimates of basalt depths, even at local scales, at the Apollo landing sites (Kovach and Watkins, 1973). Electromagnetic sounding of the maria from orbit (Peeples et al., 1978) yielded discontinuities (interpreted as the base of the basalt fill) at about 1.6–2 km for Mare Serenitatis, 1.4 km at the center of the Serenitatis Basin, and about 0.8–1.0 km in the peripheral shelf areas of Mare Serenitatis. These data apply to single-line profiles across the basins, and they cannot be readily extended to other areas to calculate total basalt volumes.

Indirect estimates of total lava volume are obtained from studies of impact craters flooded by mare basalts, a technique pioneered by DeHon (1974). By using the ideal crater shapes described in section 4.1.2 (Table 4.1), in particular the height of the fresh crater rim, one can estimate how thick the basalt stack filling the crater must be. The crater diameter and the height of the present rim crest



above the basalt surface can be measured from photographs. Subtraction of the present height from the estimated initial rim height (above the initial lunar surface) yields the cumulative thickness of basaltic fill. This approach was applied to all observable flooded craters, generally only 20–40 craters per mare-filled basin; from these data isopach maps of the thickness of basalt filling were constructed (DeHon and Waskom, 1976; DeHon,

1979). These maps indicate basalt thicknesses of 0.5–1 km in the shelf areas, increasing to a few kilometers in the basin interiors (Fig. 4.25). The total volume of lunar basalt erupted is thus estimated at $\sim 6.5 \times 10^6 \text{ km}^3$, i.e., <1% of the lunar mantle volume.

These estimates by DeHon use the ideal shape of fresh lunar craters; Hörz (1978), on the other hand, suggested that lower rim heights are more commensurate with the average degradational state of

Fig. 4.29. Basaltic volcanism within the Serenitatis Basin. **(a)** Earth-based, telescopic view of Mare Serenitatis. The morphologic rim encloses substantially more dark basaltic fill than is the case for the Orientale Basin. The outermost zone of basalts is the oldest (based on crater density counts) and also has a very low albedo. This outer zone also contains extensive graben systems that formed in response to tensional forces (see section 4.3). The inner basin is flooded by younger basalts. The basalt surfaces display many compressional ridges, produced either by compressional tectonics or by surface buckling over subsurface basalt intrusions. **(b)** Portions of eastern Mare Serenitatis, illustrating the mare/highland contact relationships. Dark basaltic lavas have flowed out of the basin into older craters, such as Le Monnier (near the top of the photograph; 70-km-diameter crater). Dark mantle deposits, which underlie the lowest-albedo areas, are interpreted as volcanic ash. The Apollo 17 landing site (marked by the circled dot) is located slightly outside the major basin rim; this mission returned a variety of highland rocks, mare basalts, and pyroclastic rocks (NASA Photo AS17-M-0939). **(c)** Idealized cross-section of the lunar crust and mantle under Mare Serenitatis, illustrating some general ideas about the volcanic eruption history and the location of magma conduits as inferred from photogeology and from thermal modeling of the lunar crust. The prolonged eruption of basaltic lavas into the Serenitatis impact basin resulted in the downwarping of the basin floor and the gradual filling of this depression by successively younger basalt flows. This filling took place principally during three major episodes, labeled I through III from earliest to last (see also section 4.3). Peripheral downdropped grabens formed early during a period of extension, and compressional or “wrinkle” ridges were produced during a later stage of compression as the crust cooled and shrank. The locations and shapes of the basaltic conduits are highly idealized, as is the assumed upwarping of the lunar mantle.

impact craters. This correction would decrease the basalt thicknesses estimated by DeHon and coworkers by a factor of ~ 2 . A more serious shortcoming, however, affects the technique itself: the implicit assumption that all the now-flooded craters were originally formed on pristine basin floors before any lava had been erupted. The above volume estimates are therefore minimum values.

Larger estimates of erupted lava volume result if one instead assumes a specific geometry for the original impact basin cavities, modeled after the Orientale Basin, which is the youngest and least-filled basin (Head, 1977). Assuming similar cavity geometries for all the other basins, and measuring the present degree of flooding (elevation of the lava-filled mare surface relative to rim height), total erupted lava volumes of $6\text{--}7 \times 10^6 \text{ km}^3$ are obtained. A maximum volume of $3\text{--}4 \times 10^7 \text{ km}^3$ is obtained by assuming that all basins were filled to the brim, which is obviously not the case.

Other constraints on basalt thickness are derived from “mascons,” the positive gravity anomalies observed over many (but not all) of the basalt-filled mare basins (see Chapter 10). When the excess mass required to produce the observed gravity anomaly is assumed to be entirely basalt fill, minimum estimates for basalt thickness of 1–2 km are obtained (Phillips *et al.*, 1972; Phillips and Lambeck, 1980; Solomon and Head, 1980). These are minimum estimates, however. It is not known whether there is additional basaltic fill below the equilibrium gravitational surface used in the modeling. Evidence for the presence of such deeper basalt fill is seen in the fact that most large, unfilled craters have negative gravity (Bouguer) anomalies (Phillips and Dvorak, 1981), even the highly degraded Grimaldi Basin.

Solomon and Head (1980), in addressing the problem of lunar melting, have combined most geophysical, photogeological, and petrographic evidence with rheological and thermal modeling of the lunar crust. Their most recent models allow about $6 \times 10^6 \text{ km}^3$ of basalt to be produced within the Moon.

In summary, the total volume of basaltic magma generated within the Moon is not precisely known, but current estimates yield values of between 10^6 and 10^7 km^3 . Even the maximum estimates are $<1\%$ of the volume of the lunar mantle. It is therefore safe to infer that high degrees of partial melting, involving large regions of the entire mantle, did not take place within the Moon. Uncertain as these estimates are, they are nevertheless adequate to provide useful constraints in reconstructing the composition of the lunar mantle and its thermal history (see BVSP, 1981).

4.3. TECTONIC ACTIVITY

Tectonic activity refers to the deformation of the rocks of a planet by external or internally-produced forces. These forces can produce a wide range of observable deformation features—faults, folds, mountain ranges, and zones of volcanism—at or near the planet’s surface. These features, in turn, provide information about the interior of a planet, its structure, its mechanical properties, its thermal state, and its past history.

The volume of a planet over which such forces are applied (*stress fields*) can vary from local to global, and the stresses themselves can be either compressive or tensional. Depending on the magnitude of the stress, the rate of application, and the nature of the material under stress, deformation can occur by

either gradual (“plastic”) deformation or by abrupt failure (*rupture*). Interpretation of the resulting features is complicated by several circumstances, including the superposition of local stress fields onto global ones and the alternation between tensional and compressional stresses in a given area as time passes.

Most information about lunar tectonic activity has been obtained from surface images, from surface seismometers emplaced at Apollo landing sites, and from modeling the thermal state of the lunar crust and mantle. These data indicate that, in comparison to the geologically active Earth, internal tectonic activity on the Moon is a minor process. The energy released by lunar earthquakes (“moonquakes”) may be $<10^{-12}$ as much as the seismic energy released by the Earth. Furthermore, the crust of the Moon appears to be thick, rigid, immobile, and cool in comparison to the crust of the Earth, which is characterized, even today, by large-scale motions and by a high degree of partial melting. This comparison is reinforced by the fact that the returned lunar samples show virtually no textures typical of slow, low-strain-rate (“plastic”) deformation, features that are abundantly displayed in a wide range of terrestrial rocks.

Under these conditions, much lunar tectonic activity is driven by forces external to the Moon—tidal stresses and large meteorite impacts. Internally-generated tectonic activity results from the changing thermal state of the Moon, and its effects include global expansion and contraction, as well as the production of volcanic lavas.

4.3.1. External Forces

Impact. As discussed in section 4.1, impact events create a large number of tectonic features associated with complex craters and large impact basins. These features include wall terraces, multi-ring mountain scarps, and radial fracture (*fault*) systems (Fig. 4.12). It is likely that additional movement occurred along these impact-produced faults for some time after the impact event itself, especially in the case of multiring basins.

The large cavity created by the basin-forming impact, the extensive subsurface shattering of crustal rocks, and the resulting lateral and vertical movements clearly represent a substantial disturbance of the pre-impact global stress field. After the impact, the lunar crust will tend to adjust to any residual stresses, probably by subsequent movements along the impact-produced faults. Such faults may be kept active for long periods of time, or may be reactivated by seismic energy from subsequent impacts in the vicinity (Titley, 1966; Schultz and Gault, 1975a,b). The

seismic energy emanating from a hypervelocity impact is generally 10^{-3} to 10^{-4} that of the initial projectile kinetic energy (Latham *et al.*, 1970a,b), and should be adequate to produce significant new movement on older, preexisting faults.

Another form of tectonic activity is associated with large-scale impact basins that are subsequently filled with basalts. The additional loads of basalt can produce significant stress within and adjacent to the filled basins. Near the basin edge, the radial and tangential stress components are tensile and mildly compressional, respectively (Melosh, 1978; Maxwell, 1978; Solomon and Head, 1979; Comer *et al.*, 1979). These combined stresses can produce concentric down-dropped valleys (grabens) at the edges of the maria, a situation illustrated by Mare Humorum (Fig. 4.30). The basalt loading also produces down-warping of the basin center, generating compressional stresses and leading to foreshortening of the surface and the formation of wrinkle ridges (Fig. 4.31; Muehlberger, 1974; Lucchitta, 1976; Solomon and Head, 1979).

Post-impact gradual isostatic adjustments of large-scale crater and basin cavities may also have occurred in response to the lunar gravity field. However, the high viscosity of the solid lunar crust has prevented such isostatic adjustment from occurring rapidly, at least throughout the period represented by the preserved cratering record. Many large craters that are not filled with lavas still retain their original negative gravity anomalies (Phillips *et al.*, 1972; Phillips and Lambeck, 1980; Phillips and Dvorak, 1981). Furthermore, the Apennine Mountains, which were formed with the Imbrium Basin 3.9 b.y. ago, are even now not in isostatic equilibrium (Ferrari *et al.*, 1978). These conclusions are complicated by evidence of definite post-impact deformation in other craters. Portions of some large crater floors seem to have been uplifted and cut by grabens. (Hall *et al.*, 1982) have interpreted these features as evidence for tectonic activity associated with isostatic readjustment within craters.

Tidal forces. The body tides on the Moon, which are generated by the gravitational field of the Earth, together with the tidally locked or synchronous rotation of the Moon, cause the Moon to deform from a sphere into a triaxial ellipsoid (Jeffreys, 1962). The amount of deformation varies with the third power of the Earth-Moon distance. At the present Earth-Moon distance of about 60 Earth radii, the theoretical difference between the maximum and minimum radii of the Moon is about 65 m. Since the lunar orbit is elliptical, the monthly variations in the Earth-Moon distance cause this value to vary by about 40%. As a result, tidal stresses of a few bars build up and decay in the lunar crust every month.

These stresses are far too weak to produce independent tectonic activity in the lunar crust. However, the tidal stresses of ~ 0.2 bar at depths of 700 to 1100 km in the Moon seem adequate to generate or trigger the weak, cyclic, deep moonquakes (Lammlein, 1977), for such activity is strongly correlated with the Moon's position in its orbit around the Earth (see section 3.7 for a discussion of seismic stability).

Most theories of the origin of the Moon require that the Earth-Moon distance was only a few Earth radii early in lunar history (MacDonald, 1964; Binder, 1978; Thompson and Stevenson, 1983) and conclude that this distance has increased with time. If this is correct, or if the Moon underwent any reorientation events (Melosh, 1975), then at Earth-Moon distances

of $< 8 R_E$, tidal and synchronous rotational stresses of up to 100 kbar could develop within the early lunar lithosphere. The stresses required to produce major tectonic deformation on the Moon are on the order of 1 kbar at the surface and 10 kbar at the base of the crust. Therefore, these early tidally-induced stresses must have caused intense deformation, with probable faulting throughout the entire crust. Unfortunately, the period during which this intense faulting must have occurred was also the time when the Moon underwent its most intense cratering (section 4.1), a process that would have obliterated the surface effects of such deformation.

Despite the obliterating effects of the intense bombardment, evidence of early, global tectonic deformation may still be preserved. A number of



Fig. 4.30. A system of concentric, down-dropped valleys (*grabens*) at the southeastern edge of Mare Humorum. The width of the graben system is approximately 55 km, and individual grabens are a few hundred kilometers long. Note that the grabens are filled with basaltic lavas, indicating that they were relatively early extensional features. The grabens extend, virtually unobstructed, from the mare into the adjacent highlands, and they also cut across the rim of a large, preexisting flooded crater. These observations indicate that the grabens reflect a substantial, possibly deep-seated, basin-wide stress field. Two younger and much smaller impact craters (center) were clearly formed after the graben. The fact that graben-forming movements had completely ceased by this time is indicated by the sharp, undeformed crater rims. Such observations, combined with crater frequency counts, limit the period of extensional tectonics and graben formation to early lunar history, coincident with the early generation of large volumes of basaltic lava (NASA Photo LO IV-132H₁).

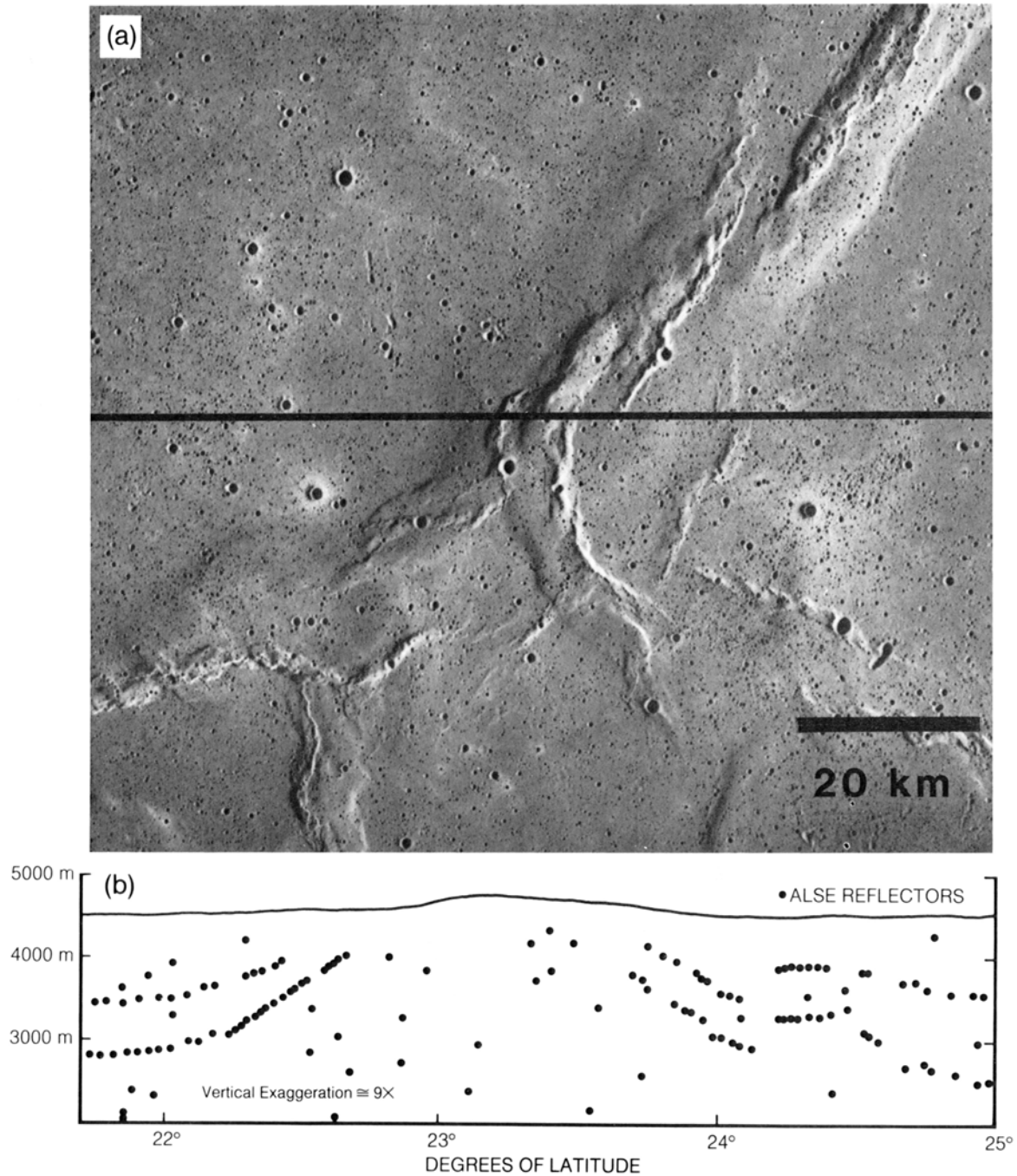


Fig. 4.31. Lunar compressional ridges. **(a)** Orbital photograph of a major wrinkle ridge system in southeastern Mare Serenitatis. The *en echelon* offsets of ridges and crests indicate compressive stress. The arcuate shape of the ridges (concentric to the basin) indicates substantial centrosymmetric foreshortening, perhaps 0.5% to 0.8% (Muehlberger, 1974; Maxwell, 1978) (NASA Photo AS17-M-0451). **(b)** Penetrating radar reflection profile obtained by the Apollo Lunar Sounding Experiment (ALSE) across the ridge depicted in **(a)**; horizontal line in **(a)** represents the ground track of the Apollo 17 spacecraft, along which these measurements were taken. Note substantial upwarping, possibly folding and faulting, of the basaltic subsurface layers down to depths of approximately 2 km below the surface (from Maxwell, 1978).

investigators (*Habakov, 1949; Strom, 1964; Allen, 1975; Fagin et al., 1978; Hale, 1980*) have suggested that a systematic, global pattern of lineaments (grabens, horsts, linear scarps, linear crater wall segments, etc.) exists; this pattern has been called the "lunar grid" system. Because the overall mapping of the Moon is still incomplete, other scientists maintain that only local lineaments occur, unrelated to any global stress system.

4.3.2. Internal Forces

Thermal stress. Models of lunar thermal history indicate that thermal expansion during the first billion years of the Moon's existence would have produced tensional stresses in the lunar crust and that contraction during the subsequent 3.5 b.y. until now have produced compression (*Solomon and Chaiken, 1976; Binder and Lange, 1980*). The exact magnitude of these tensional and compressional stresses is still a matter of debate. Some models indicate that stresses during the early phase of expansion were about 1 kbar, or two orders of magnitude smaller than the stresses produced by tidal effects and synchronous rotation during the same period. Clearly, very early lunar tectonic activity was totally dominated by tidal stresses; internally-generated stresses were insignificant.

There is, however, clear photogeological evidence of tensional stresses in the Moon between 3.9 and 3.6 b.y. ago. A period of normal faulting, mainly characterized by the production of downdropped grabens, began at the time when the oldest mare lavas were deposited (*Lucchitta and Watkins, 1978*). Many of these grabens are found in maria such as Humorum (Fig. 4.30) that display positive gravity anomalies (mascons). Although these grabens are most likely related to stresses caused by filling of the maria with thick layers of basaltic lava, they could not have formed unless mildly tensile global stresses were also present (*Melosh, 1978; Solomon and Head, 1979; Comer et al., 1979*). Similar grabens and normal faults are also observed in areas unrelated to maria and mascons, and these features could reflect global tensional stresses; the Sirsalis, Hyginus, Triesnecker, and Ariadeus Rilles are good examples (Fig. 4.32).

Subsequent to this episode of tensional stresses before 3.6 b.y. ago, the Moon's global stresses became compressional, and internally driven tectonism ceased for the last 2.5 to 3 b.y. These compressional stresses built up so slowly that a few billion years may have been required to accumulate sufficient stress (>1 kbar) to cause small-scale compressional features (*thrust faults*). Photogeologic observations reveal small scarps and thrust faults, generally less than 10 km long. Based on cratering

ages, these faults appear to be less than ~700 m.y. old (*Binder and Gunga, 1985*). Examples of such young thrust faults are illustrated in Fig. 4.33. It is estimated that there are some 2000 such features in the lunar highlands. A few of these scarps extend into the adjacent maria, where they appear as ridges. Other mare ridges could also be thrust faults (*Muehlberger, 1974*).

These compressional tectonic features are interpreted by *Binder and Gunga (1985)* to indicate that, since about 2 b.y. ago, the Moon had cooled and contracted sufficiently to have produced global compressive stresses and associated thrust faulting. In their view, the Moon is not tectonically dead, and it has not been firmly established that there is no seismic hazard to future exploration and habitation (see section 3.7). Long-term seismic observations, combined with other geophysical exploration, are required for a better understanding of the Moon's present thermal state, its detailed crustal structure, and its current deformation.

Volcanic intrusions. While most mare ridges are believed to have been caused by thermally-generated compressive stresses, some ridges may have been produced by intrusion of magma just below the surface (*Strom, 1964*). One model for the development of craters with fractured floors calls for intrusion of magma beneath the crater floors, resulting in uplift (*Schultz, 1976b*). Humboldt Crater may be one example of such uplift and associated fracturing (Fig. 4.34).

4.4. LUNAR STRATIGRAPHY

Stratigraphy is a branch of geology that deals with the recognition of different rock units, the establishment of geometric relations between them, and the use of these relations to determine the origin and history of the rocks involved. The goal of lunar stratigraphic studies is to apply the principles of terrestrial stratigraphy to the Moon in order to decipher its geologic history. Over 25 years ago *Shoemaker and Hackman (1962)* applied a fundamental principle of terrestrial stratigraphy to the Moon, the *Law of Superposition*, which states simply that older rocks are overlain, cut, or intruded by younger rocks. This is an obvious condition, but it is a powerful method for unraveling sequences of geological events on both the Earth and the Moon.

Although the Law of Superposition allows relative ages to be established, absolute age information is necessary to place lunar or terrestrial geologic history into an absolute time frame or to determine how long a specific epoch or event lasted. In terrestrial studies, such absolute ages have been provided by radioactive-decay measurements

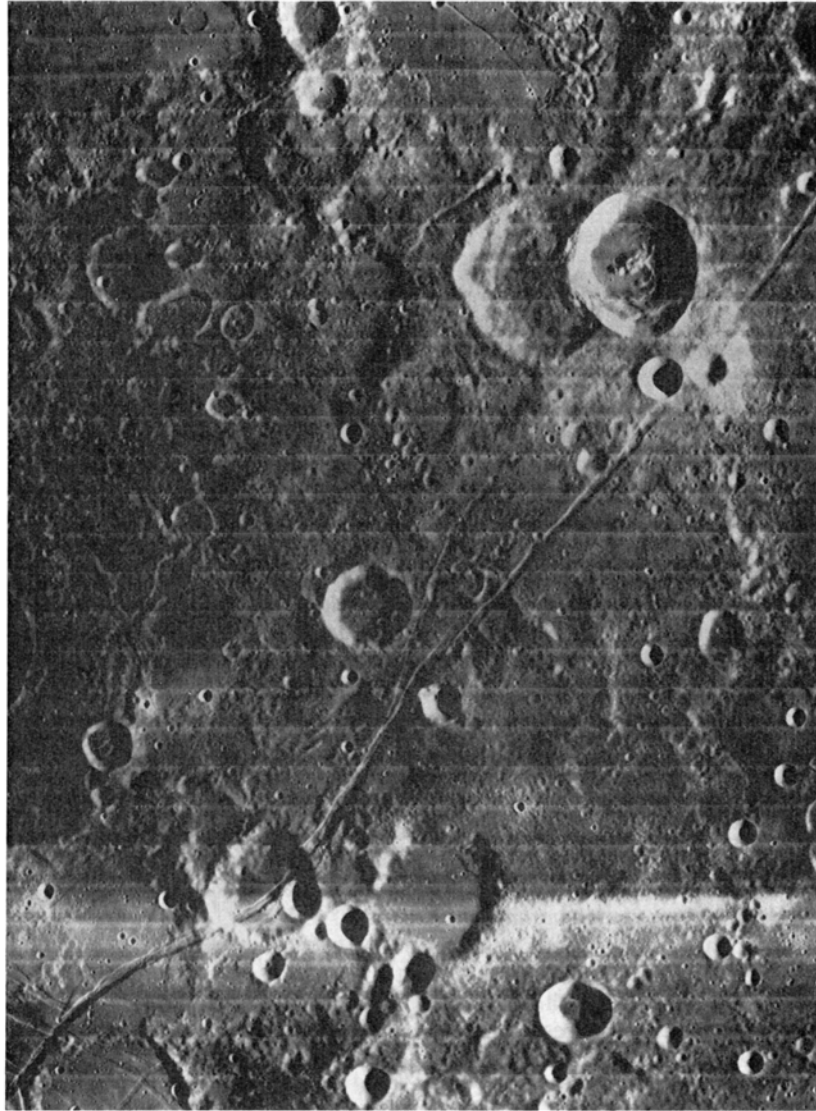


Fig. 4.32. Sirsalis Rille, running from upper right to lower left, a possible example of early extension unrelated to loading of the mare basins by basaltic lavas to produce mascons (NASA Photo LO IV-161 H₂). The northeast-trending rille, located on the outer fringes of the Orientale Basin ejecta blanket, is 300 km long.

applied to well-characterized terrestrial rocks. However, dating of even ideal rocks is complicated and time-consuming, and terrestrial stratigraphers have only a relatively small number of absolute chronological tie-points for the Earth's record. These data provide calibration points for the overall geological record of the Earth. More detailed age measurements can then be made by indirect means that allow interpolation between the absolute chronological reference points. On Earth, such interpolations are based on the fossil record or on the record of polarity-reversals of the Earth's magnetic field.

On the Moon, which lacks both fossils and a significant magnetic field, the impact crater populations and the areal density of craters can be used to determine ages. Using absolute ages for lunar surfaces, determined by age measurements of returned lunar samples, the crater population can then be used to determine the ages of other surfaces. These measurements have only begun, and few lunar surfaces have been precisely dated. Furthermore, for a number of reasons, many lunar rocks may not be dated accurately even when modern isotope-geochronology techniques are used (see sections 6.3 and 6.4).

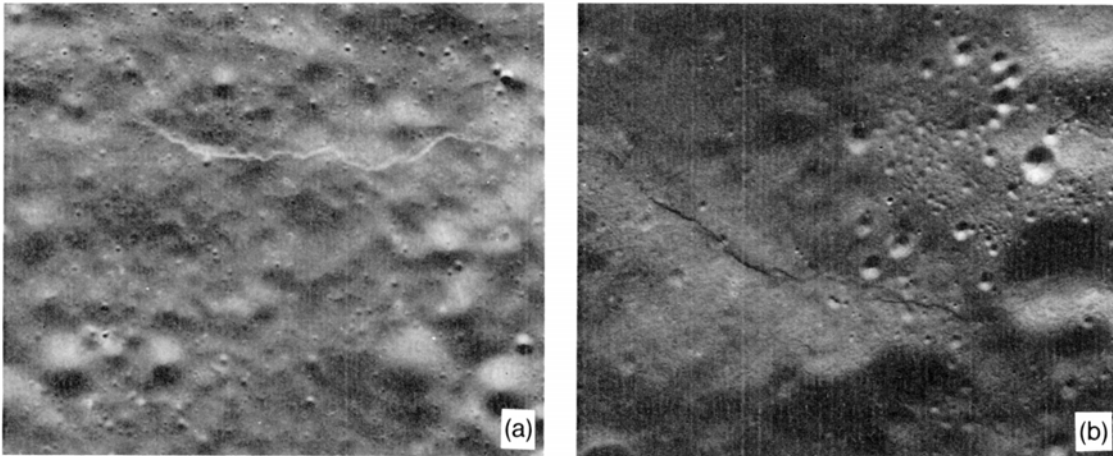


Fig. 4.33. Small scarps produced by compressive thrust faults in the lunar highlands. Such features are interpreted by *Binder and Gunga* (1985) to have formed recently by compression produced as a result of cooling and shrinking of the lunar interior. **(a)** Mandel'shtam Scarp (upper right), approximately 13 km long and located at 7°N/161°E near Mandel'shtam Crater (NASA Photo AS16-P-4150). **(b)** Morozov Scarp, approximately 15 km long, is located at 7°N/130°E, inside Morozov Crater (NASA Photo AS16-P-4970).

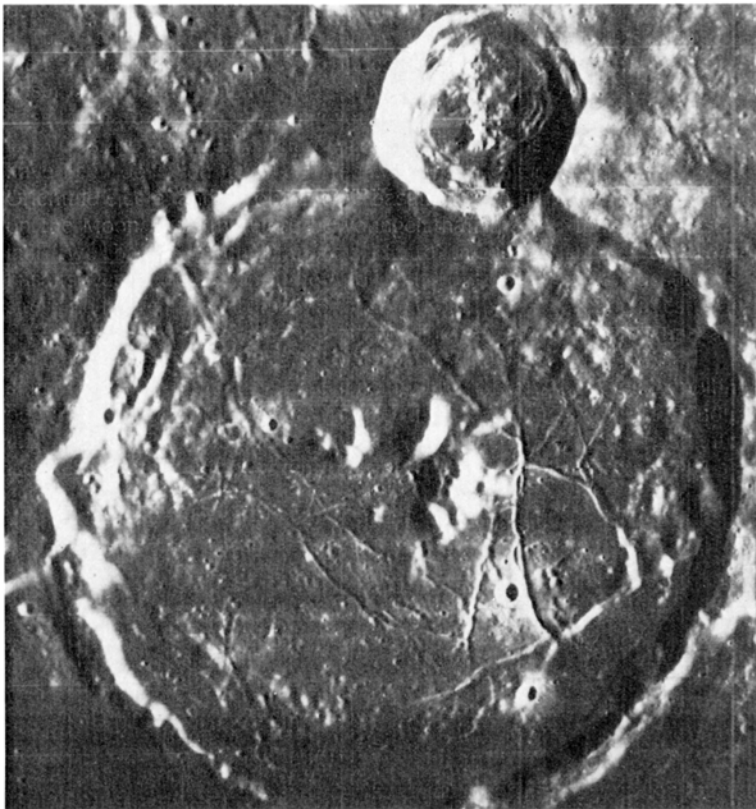


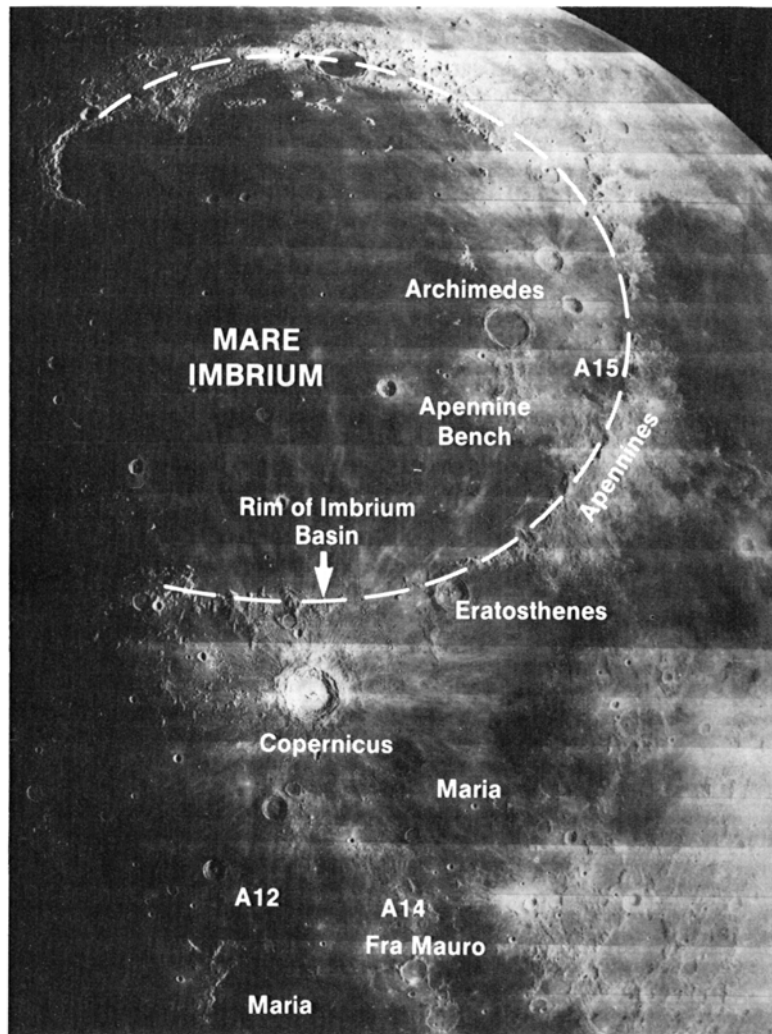
Fig. 4.34. Floor-fractured Gasendi Crater (110 km in diameter). Note the relatively flat crater floor apparently represents a filling of volcanic lava or impact melt. After solidification, this filling of the crater fractured irregularly, either because of contraction, subsidence of the crater floor, or intrusion beneath the crater floor (NASA Photo LO IV-143 H₂).

The techniques of lunar geologic mapping and stratigraphy are well illustrated by the region around Copernicus Crater, studied by *Shoemaker and Hackman* (1962) (Fig. 4.35). Copernicus is the youngest major impact crater in this region, as indicated by the fact that its rays and secondary craters overlie all the other geological units. The nearby Eratosthenes Crater (Fig. 4.35) has been overlain by the rays from Copernicus, so it must have been there when Copernicus formed. Eratosthenes has also been excavated in dark, smooth mare material. From these observations, the relative ages of three events can be established; from young to old, they are (1) Copernicus impact, (2) Eratosthenes impact, and (3) the eruption of mare lavas.

These observations can be carried further back in time. In their turn, the dark maria lavas embay, fill, or overlie other units: (1) Archimedes Crater, (2) a light-colored unit (the Apennine Bench Formation), and (3) the rugged highlands area and mountains associated with the rim of the Imbrium Basin (Fig. 4.35). Moreover, the plains formed by the light Apennine Bench Formation also embay the Imbrium Basin rim. Therefore the entire sequence recognized in this area, from young to old, is as follows: (1) Copernicus, (2) Eratosthenes, (3) the maria, (4) Archimedes, (5) the Apennine Bench plains, and (6) the Imbrium Basin.

Similar observations have been successfully employed to make geologic-stratigraphic maps of

Fig. 4.35. Region of the Moon around the crater Copernicus (97-km diameter, left-center of photograph), where the lunar stratigraphic system was first defined (*Shoemaker and Hackman, 1962*). The formation sequence of features in this region is as follows (from youngest to oldest): Copernicus, Eratosthenes, dark maria filling, Archimedes, Apennine Bench light plains deposits, Imbrium Basin massifs, and surrounding highlands features. These relative age relations define the equivalent time-stratigraphic systems: Copernican, Eratosthenian, Procellarian (epoch of mare lavas), Imbrian, and pre-Imbrian (see Table 4.4 for the current system nomenclature). North at top; portion of NASA Photo LO IV-126M. A12, A14, and A15 mark the Apollo 12, 14, and 15 landing sites, respectively.



the entire Moon (Wilhelms, 1970, 1972, 1984, 1985, 1987). This stratigraphic information has been supplemented by relative ages based on crater densities (see section 4.1.3) and by other age estimates based on the degradation of original crater shapes with time, caused by subsequent continuous bombardment. (See Fig. 4.36 for details on the relationship between a crater's size, its relative age, and the degree of degradation of its original features.)

The original lunar stratigraphic system established by Shoemaker and Hackman (1962) is shown in Table 4.4. Prior to the Apollo landings, the age durations of the various subdivisions of this system were unknown. Most of them were believed to be ancient; indeed, the ages of the maria were estimated to be 4.5 to 3.5 b.y. old (Shoemaker et al., 1962; Hartmann, 1966). The measurement of abso-

lute ages of returned mare basalt samples allowed us to establish absolute dates for these photogeologically recognized systems.

The Moon has been mapped geologically at a variety of scales. A program to systematically map the lunar nearside at 1:1,000,000 scale was begun in 1962 and completed in 1972 (see Wilhelms, 1970). In addition, all the prime and potential Apollo landing sites were mapped at scales ranging from 1:1000 to 1:100,000, including several sites of strong geologic interest that were never visited by Apollo missions. After the Apollo flights, a global synoptic mapping program was undertaken at 1:5,000,000 scale. The resulting maps cover the lunar equatorial region in four sheets (Wilhelms and McCauley, 1971; Wilhelms and El Baz, 1977; Stuart-Alexander, 1978; Scott et al., 1977); the lunar poles are covered in two more sheets (Lucchitta, 1978; Wilhelms et al., 1979).

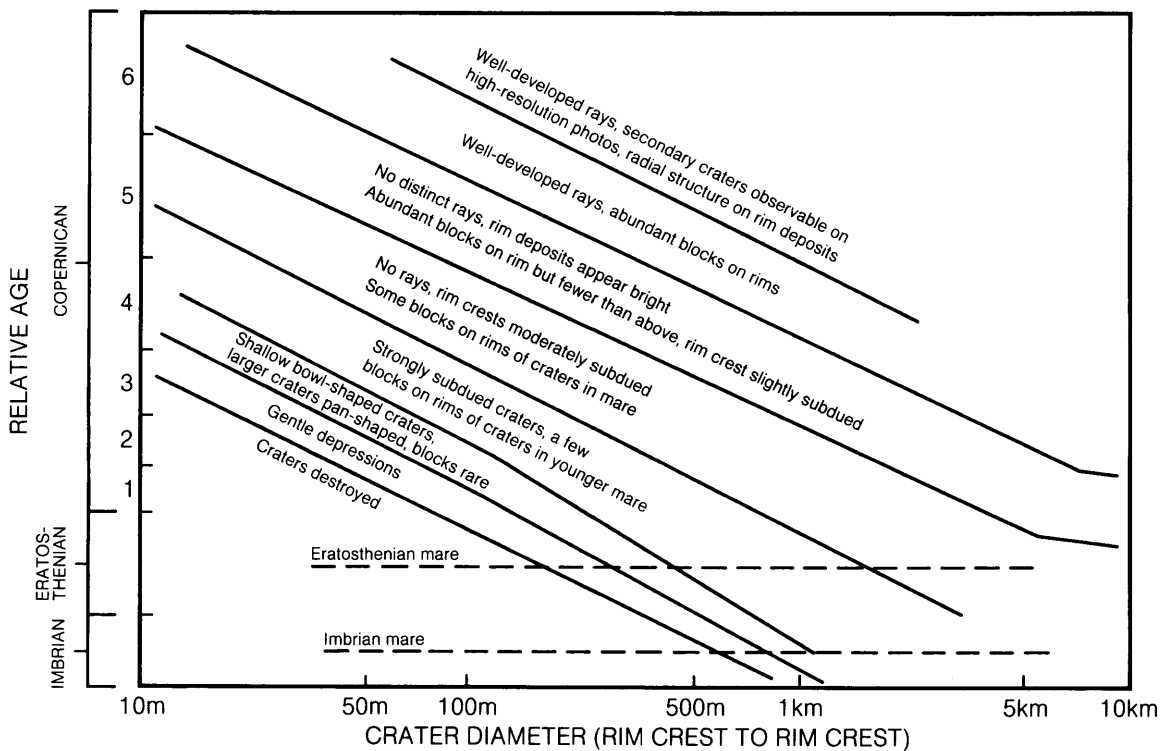


Fig. 4.36. Criteria used to characterize the relative degradational state of lunar impact craters >10 m in diameter. Post-crater degradation (loss of rays, lowering of rims, infilling) is produced by the continuing post-impact bombardment of the crater by smaller meteoroids. For a given original diameter, more degraded craters are older than less degraded ones, and the relative degree of degradation can be used as shown in the figure to establish the relative sequence of crater formation ages. For example, on the older Imbrian mare surface, all craters <500 m across have been completely destroyed, while on the younger Eratosthenian mare surface, craters as small as 200 m are still preserved. Even smaller craters (>50 m across) are preserved on the youngest Copernican mare surface. (Based on Trask, 1977 and after Wilhelms, 1985; see also Soderblom, 1970; Boyce, 1976; Schultz et al., 1976; Basilevski, 1976.)

TABLE 4.4. Lunar stratigraphic systems—original and current (youngest to oldest).

System	Typical Units	Approximate Age (b.y.)
Original (<i>Shoemaker and Hackman, 1962; Shoemaker et al., 1962</i>)		
Copernican	Rayed craters	—
Eratosthenian	Nonrayed craters	—
Procellarian	Maria	4.5
Imbrian	Ringed basins	—
Pre-Imbrian	Terrae	4.6
Current (<i>Wilhelms, 1985</i>)		
Copernican	Fresh, rayed craters; minor maria	1.2-present
Eratosthenian	Slightly degraded craters, significant maria	3.2-1.2
Imbrian	Imbrium and Orientale basins; Cayley plains; degraded craters; most maria	3.85-3.2
Nectarian	Nectaris + 12 other basins; many degraded craters; some light plains	3.92-3.85
Pre-Nectarian	Basins and craters; volcanic and intrusive igneous rocks; megaregolith and crust	Before 3.92

These global maps are our current best summary of the geology of the Moon; a condensed version prepared from them is shown in Plate 10.10 (see also *Wilhelms, 1986*).

The lunar stratigraphy represented in these maps is subdivided into four major periods that are described from youngest to oldest in the following discussion. This arrangement, from young to old, is not normally practiced in stratigraphic descriptions on Earth. However, it is commonly used for the Moon because it aids the attempt to trace well-understood and comparatively recent processes into the distant and much more uncertain past.

Copernican Period (the present to ~1 b.y. ago). Copernicus Crater (96 km diameter) is one of the most recent large lunar craters. Its conspicuous rays cover much of the lunar nearside, and these rays can be used to determine unambiguously which surface units are older or younger than Copernicus itself. Very few large lunar craters (>50 km diameter) are younger than Copernicus; possible examples include Tycho and Kepler. Copernicus is currently believed to be approximately 900 m.y. old (*BVSP, 1981*), and the Copernican Period probably encompasses the last 1 b.y. of lunar history.

Virtually no internally-derived surface units (e.g., lava flows) younger than Copernicus have been identified. The Copernican Period is dominated by continuous and relatively modest impact cratering, which has produced small craters and created much

of the powdery lunar surface layer (regolith). Some minor tectonic activity, indicated by young thrust faults, has apparently also occurred (see section 4.3).

Eratosthenian Period (~1.0~3.2 b.y.). Eratosthenes Crater is similar to Copernicus in size. Although still well preserved, Eratosthenes is demonstrably older than Copernicus because its ray system has been essentially destroyed and its ejecta deposits underlie Copernican rays. Eratosthenes represents a class of abundant, moderately degraded craters >20 km in diameter, all of which are apparently older than Copernicus. Some of these craters and their surrounding ejecta deposits have been flooded by the youngest mare basalts. Although Eratosthenes itself has not been affected by basalt flows, the basalts in which Eratosthenes was formed are, on the basis of crater density measurements, estimated to be older than the youngest mare basalt units.

These observations indicate that the beginning of the Eratosthenian Period and the formation of the Eratosthenian class of craters was coincident with the ending of the great eruptions that more or less filled the mare basins with basaltic lavas. Most, but not all, of the Eratosthenian craters are flooded by the youngest mare basalts, and the end of major volcanic activity is more or less coincident with many Eratosthenian craters. The Eratosthenian Period therefore includes the last stages of major lunar basaltic volcanism, as well as some modest

subsequent basin subsidence and associated graben and ridge formation. Most of the surface debris (*regolith*) covering the lunar maria was also formed during this period. Eratosthenian basalts were collected at the Apollo 12 site, and their measured age dates suggest that initiation of this period can be placed at approximately 3.2 b.y. ago.

Imbrian Period (3.2–3.8 b.y.). The formation of the Imbrium Basin by a huge impact was a major event on the lunar nearside. Ejecta from this basin dominate a substantial fraction of the lunar globe and caused virtually complete reconstruction of the lunar surface in a large annulus around the basin. Imbrium ejecta represent the most important stratigraphic marker unit on the lunar nearside. Crater densities on these deposits indicate that substantial large-scale cratering activity continued for some time after formation of the Imbrium Basin. This activity includes the formation of at least one more basin (Orientale). Although some samples of Imbrium ejecta may have been returned by the Apollo 14, 15, and 16 missions, positive identification is currently not possible because of the intensity and complexity of cratering events at that time. The formation age of the Imbrium Basin is not known precisely, but is estimated to be between 3.8 and 3.9 b.y. ago.

It has become convenient to divide the Imbrian period into two parts, characterized by different kinds of geological activity. The “Early Imbrian” Epoch, which is bracketed by the Imbrium and Orientale basin-forming impacts, was a period of substantial cratering activity. Apollo 14 and 16 landed on heavily-cratered “Early Imbrian” surfaces (*Head, 1974b; Hawke and Head, 1977*). Many impact melts characterizing this period are 3.8 to 3.9 b.y. old, but the exact time boundaries (i.e., the ages of the Imbrium and Orientale Basins) have not been determined.

The “Late Imbrian” Epoch is characterized by less intense cratering and also includes most of the observable lunar volcanism, i.e., virtually all the basaltic mare fill, except for the younger Eratosthenian flows. No surfaces of mare basalt within basins have been observed to be covered with Imbrium or Orientale ejecta, and all observable basaltic basin fill on the Moon must therefore be younger than these last two basin-forming impacts. “Late Imbrian” basalts were returned from the Apollo 11, 15, and 17 sites and range in age from 3.75 to 3.2 b.y. old.

Nectarian Period (3.8–~3.9 b.y.). The Nectaris Basin is typical of several large mare basins that are substantially degraded. Some basins are clearly better preserved and therefore younger than Nectaris (e.g., Serenitatis), while some are older (e.g., Smythii). Isolated patches of apparent Nectaris ejecta are

clearly preserved in the Janssen Formation, and parts of the Nectaris rings occur in such places as the Altai Mountains.

By definition, the Nectarian Period encompasses lunar history between the Nectaris and Imbrium Basin impacts. Formation of the Nectaris Basin is estimated to have occurred between 3.8 b.y. ago (*Wetherill, 1981*) and ~3.9 b.y. ago (*fames, 1981; Spudis, 1984*). These estimates are based on a number of Apollo 16 samples thought to be Nectaris ejecta. The Nectarian Period was therefore relatively short, approximately 200 m.y., compared to the other stratigraphic periods.

During the Nectarian Period, about a dozen lunar basins formed, and numerous other large-scale impacts occurred, indicating an epoch of heavy bombardment that is not reflected in later lunar history. *Wilhelms (1976, 1984)* estimates formation of a minimum of 1700 craters ≥ 20 km in diameter on the whole Moon. Heavy reworking of the lunar crust certainly took place at this time, including substantial vertical and lateral mixing. Early basaltic volcanism may also have occurred during the Nectarian Period (*Schultz and Spudis, 1979; Taylor et al., 1983; Wilhelms, 1984, 1985*).

Samples possibly representing Nectarian age deposits were returned from the Apollo 17 site (located at the rim of Mare Serenitatis), probably from the Apollo 16 site (Nectaris ejecta itself?), and possibly even from Apollo 15 (Serenitatis ejecta?).

Pre-Nectarian Period (~3.9–~4.6 b.y.). As implied by the name, this period encompasses all geologic history prior to the Nectaris impact. Features from this period are still clearly observable, but their complexity and the violence of events during this period has made it impossible at present to do the detailed morphological and chronological classification that would allow systematic geological subdivision and mapping.

This period is clearly characterized by heavy cratering and by the formation of many large impact basins. *Wilhelms (1984)* identifies 30 basins older than Nectaris, some of which are much larger (albeit largely eroded) than the younger, more recognizable major basins and rings. As discussed in section 4.1, one of the unresolved lunar questions is exactly how many of these large, ancient impact structures are preserved and how many have been destroyed. Until this question is settled, little improvement can be made in estimates of the number of large craters and basins that actually formed during pre-Nectarian time.

Global melting, chemical differentiation, crystallization, flotation, and solidification of a feldspar-rich lunar crust must have occurred very early in lunar history (>4.4 b.y. ago; section 2.4.3), but no direct

TABLE 4.5. Relative ages of known and possible (parentheses) ringed impact basins on the Moon, proceeding from youngest (class 1) to oldest (class 15) on the basis of photogeologic observations related to degradational state and crater density (from *Wilhelms, 1984*).

Basin*	Center		Diameters (km) [†]		Age [†]
	Lat	Long	Main rim	Other ring(s)	
Orientele	20 S	95 W	930	620-480-320	1-I
Schrödinger	75 S	134 E	320	150	2-I
Imbrium	33 N	18 W	1200	670	3-I
Sikorsky- Rittenhouse	69 S	111 E	310	—	4-N
Bailly	67 S	68 W	300	150	
Hertzprung	2 N	129 W	570	410-265	
Serenitatis	27 N	19 E	740	420	
Crisium	18 N	59E	1060	635-500-380	
Humorum	24 S	40 W	820?	440-325	
Humboldtianum	61 N	84 E	600	275	
Mendeleev	6 N	141 E	330	140	5-N
Mendel-Rydberg	50 S	94 W	630?	460-200	6-N
Korolev	5 S	157 W	440	220	
Moscoviense	26 N	147 E	445	210	
Nectaris	16 S	34 E	860	600-450-350	
Apollo	36 S	151 W	505	250	7-pN
Grimaldi	5 S	68 W	430	230	
Freundlich- Sharonov	19 N	175 E	600	?	8-pN
Birkhoff	59 N	147 W	330	150	9-pN
Planck	58 S	136 E	325	175	
Schiller-Zucchius	56 S	45 W	325	165	
(Amundsen- Ganswindt)	81 S	120 E	355		
Lorentz	34 N	97 W	360	185	10-pN
Smythii	2 S	87 E	840	(600)-360	11-pN
Couloumb-Sarton	52 N	123 W	530?	400-180	
Keeler-Heaviside	10 S	162 E	780?	540	
Poincaré	58 S	162 E	340	175	12-pN
Ingenii	34 S	163 E	560?	325	
Lomonosov-Fleming	19 N	105 E	620		13-pN
Nubium	21 S	15 W	690		
Fecunditatis	4 S	52 E	690		
Mutus-Vlacq	52 S	21 E	700		
Tranquillitatis	7 N	40 E	775?		
Australe	52 S	95 E	880	(550)	

TABLE 4.5. (continued).

Basin*	Center		Diameters (km) [†]		Age [‡]
	Lat	Long	Main rim	Other ring(s)	
(Al Khwarizmi-King)	1 N	112 E	590		14-pN
(Pingré-Hausen)	56 S	82 W	300?		
(Werner-Airy)	24 S	12 E	500?		
(Balmer-Kapteyn)	16 S	69 E	550?		
(Flamsteed-Billy)	8 S	45 W	570?		
(Marginis)	20 N	84 E	580		
(Insularum)	9 N	18 W	600?		
(Grissom-White)	40 S	155 W	600?		
(Tsiolkovskiy-Stark)	15 S	128 E	700?		
South Pole-Aitken	56 S	180	2500		15-pN
(Procellarum)	26 N	15 W	3200	2400-1700	

* Basin names from two superposed, unrelated craters (*Wilhelms and El-Baz*, 1977) or from contained mare.

† Main rim refers to topographic basin rim.

‡ “Age” ranked from youngest (top) to oldest (bottom). I = Imbrian; N = Nectarian; pN = pre-Nectarian. Fifteen age groups are given; Basins cannot be accurately ranked within a group. Those basins in a group are ranked in order of increasing size.

morphological evidence is available for these processes. Evidence for the Moon’s earliest history and processes must be extracted from the returned rocks by petrogenetic and cosmochemical reasoning that encompasses the accretion and origin of the Moon itself.

Despite the violence and intensity of early lunar history, it is clear that relatively little geological activity has taken place on the Moon during the last 3 b.y. It is also clear that the absolute chronology of the early basin-forming events is not well understood, despite the great importance of these events in the lunar stratigraphic record. Fortunately, photogeologic analysis can successfully establish the relative sequence of most basin-forming events and Table 4.5 lists the relative ages of 42 Nectarian and pre-Nectarian ringed impact basins based on remote mapping.

Some of these basins have probably provided materials that are now among the Apollo returned samples. Ejecta from Orientale, Imbrium, Serenitatis, and Nectaris basins are most likely present in the Apollo sample collection, but it has not yet been possible to unambiguously associate a given sample with a specific basin. Neither is it clear at present how the observed cratering record and the range of measured crystallization ages of impact melts from the lunar highlands relate to each other (see section 6.4).

Despite the small number of places visited by the Apollo and Luna sample-return missions (Fig. 2.1), it is clear that numerous returned soil and breccia samples are related to the younger Copernican Period and Eratosthenian Period and reflect their dominant processes. The Apollo 12 mission provided samples of the young Eratosthenian basalts, and the older Late Imbrian basalts were obtained from several mare landing sites. Other samples have provided evidence for basaltic volcanism as long ago as 4.2 b.y. (*Taylor et al.*, 1983), and these results constitute the strongest argument for very early lunar volcanic activity. The record of intense cratering and basin formation for periods older than 3.8 b.y. is poorly understood, but it must be present in many highland samples obtained from the Apollo 14, 15, 16, and 17 landing sites.

There is general consensus that the lunar geological history as summarized in Fig. 4.37 is well established for the last 3.8 b.y. This historical reconstruction is a remarkable feat considering how few locations were actually sampled. In a sense, the Moon itself collaborated in this work, because it has experienced only a limited variety of geological processes for most of its existence and because it has preserved its records well. The heavily cratered, more active Moon that existed before >3.8 b.y. ago is more difficult to understand. Impact cratering clearly dominated these early surface processes, but

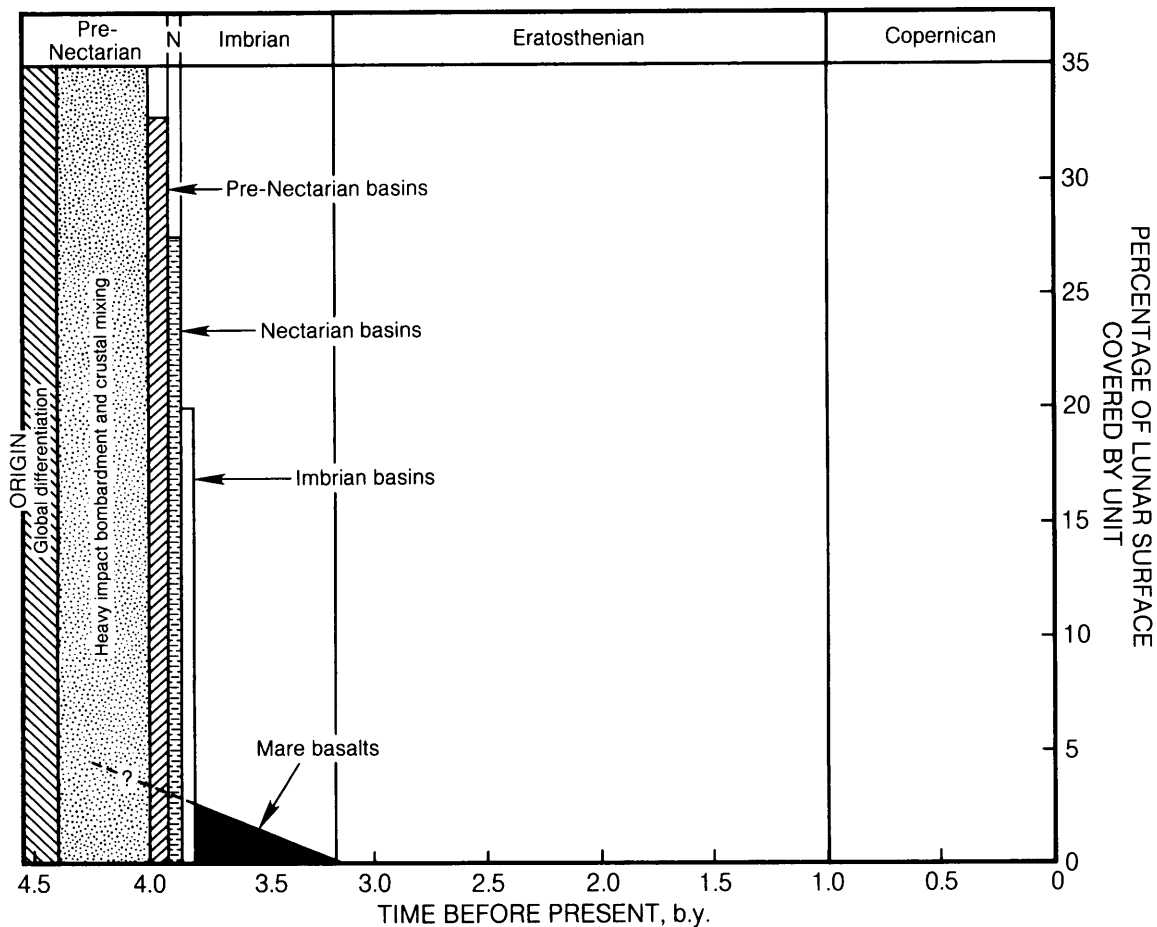


Fig. 4.37. Ages of lunar geological units, plotted against the percentage of the lunar surface covered by each unit or group of units (from *Wilhelms, 1984*). “Basin materials” include basin interior deposits and continuous basin ejecta to a distance of one basin radius beyond the basin margin. Eratosthenian and Copernican Crater deposits cover barely enough area to appear on this diagram. Ages are approximate and may overlap. The extrapolation of eruption rates for mare basalt lava units into the older period of intense cratering is uncertain and highly model dependent; there may have been a steady decline in heavy cratering throughout the early history of the Moon, and it may have continued into the Late Imbrian Period, while the rate of lava eruptions was also declining. Volcanism is shown as having ended at the beginning of the Eratosthenian Period; there may be Eratosthenian- and Copernican-age lavas, but any such deposits are too small to be visible on this diagram.

the details of the bombardment history and the absolute ages of even the youngest multiring basins are still not well known. Upon return to the Moon, this early bombardment history must be attacked with vigor. Extensive field exploration and sampling of materials from known structural/stratigraphic settings will constitute a crucial part of this effort. For example, collection and dating of the Orientale impact melt to determine the formation time of the Orientale Basin itself will provide an important insight into the end of large basin formation, for all other large basins are older. Other impact melts

recording the formation of most “young” multiring basins (e.g., Imbrium) may be collected and dated as well to yield additional insight into the early cratering history of the Moon. Impact melts from Tycho, Copernicus, and Eratosthenes would greatly illuminate the crater production rate over the past 3 b.y. Improved understanding of the lunar crater production rate would be useful not only for lunar stratigraphy; the data would also help us understand the intense collisional environment that must have affected all the planets in the early inner solar system, including Earth.

LUNAR MINERALS

James Papike, Lawrence Taylor, and Steven Simon

The lunar rocks described in the next chapter are unique to the Moon. Their special characteristics—especially the complete lack of water, the common presence of metallic iron, and the ratios of certain trace chemical elements—make it easy to distinguish them from terrestrial rocks. However, the minerals that make up lunar rocks are (with a few notable exceptions) minerals that are also found on Earth.

Both lunar and terrestrial rocks are made up of minerals. A *mineral* is defined as a solid chemical compound that (1) occurs naturally; (2) has a definite chemical composition that varies either not at all or within a specific range; (3) has a definite ordered arrangement of atoms; and (4) can be mechanically separated from the other minerals in the rock. *Glasses* are solids that may have compositions similar to minerals, but they lack the ordered internal arrangement of atoms.

Minerals have provided the keys to understanding lunar rocks because their compositions and atomic structures reflect the physical and chemical conditions under which the rocks formed. Analyses of lunar minerals, combined with the results of laboratory experiments and studies of terrestrial rocks, have enabled scientists to determine key parameters—temperature, pressure, cooling rate, and the partial pressures of such gases as oxygen, sulfur, and carbon monoxide—that existed during formation of the lunar rocks.

The fact that minerals are mechanically separable from the rest of the rock is also a critical characteristic in considering the economic extraction of

resources from lunar materials. For terrestrial resources, mechanical separation without further processing is rarely adequate to concentrate a potential resource to high value (placer gold deposits are a well-known exception). However, such separation is an essential initial step in concentrating many economic materials and, as described later (Chapter 11), mechanical separation could be important in obtaining lunar resources as well.

A mineral may have a specific, virtually unvarying composition (e.g., quartz, SiO_2), or the composition may vary in a regular manner between two or more *endmember* components. Most lunar and terrestrial minerals are of the latter type. An example is *olivine*, a mineral whose composition varies between the compounds Mg_2SiO_4 and Fe_2SiO_4 . The intermediate members, produced by the variable substitution of Mg and Fe, are called *solid solutions* and can be represented by the formula $(\text{Mg,Fe})_2\text{SiO}_4$, a notation indicating that the elements inside the parentheses may substitute for each other. The *crystal structure* of a mineral reflects the regular and ordered arrangement of atoms within it. Within this structure, positively charged *cations* (generally metals such as Si, Al, Mg, Ti, and Fe) are linked into complicated geometric networks with negatively charged *anions* (chiefly O). Within the crystal structure, each cation is shared (*coordinated*) with several anions. Coordination with four anions produces an arrangement of anions surrounding a cation in *tetrahedral* or *fourfold coordination*, while coordination with six anions is called *octahedral* or *sixfold coordination*. These tetrahedral and octahedral units combine to form

larger structures—chains, sheets, or three-dimensional networks—to build up the mineral. Within these networks, certain ions normally occupy specific sites that are given special designations such as M1 and M2 (for metals) and O1 and O2 (for oxygen atoms). The appendix to this chapter lists compositions of important lunar minerals as oxide weight percents and also, in most cases, as cation proportions. Table A5.1 explains the rock descriptions used to indicate which rock types the mineral analyses are from.

The crystal structures of minerals, and the relations between different ions in the structure, provide important clues not only about the nature of the mineral, but also about its origin. The structures can be established using X-ray diffraction methods, and X-ray crystallography was an important and well-established discipline long before the return of lunar samples.

In defining the structure of a mineral, the key element is the *unit cell*. This is a stackable volume of atoms that defines the structure; the crystal is then built up by the infinite stacking of the unit cell in all directions. The unit cell is a three-dimensional prism normally several Angstrom units (Å) on a side (1 Å = 10^{-10} m). Unit cells are defined by specifying the lengths of their *crystallographic axes* (e.g., *a*, *b*, *c*) and the angles between them (α , β , γ). Careful measurement of unit cells is especially important, because unit cell parameters can be indicators of the composition, conditions of formation, and cooling histories of the minerals involved, and therefore of the rocks that contain them.

Lunar rocks are made up of minerals and glasses. Some lunar rocks, called *breccias*, also contain fragments of older rocks. Silicate minerals, composed dominantly of silicon and oxygen, are the most abundant constituents, making up over 90% by volume of most lunar rocks. The most common silicate minerals are *pyroxene*, $(\text{Ca,Fe,Mg})_2\text{Si}_2\text{O}_6$; *plagioclase feldspar*, $(\text{Ca,Na})(\text{Al,Si})_4\text{O}_8$; and *olivine*, $(\text{Mg,Fe})_2\text{SiO}_4$. *Potassium feldspar* (KAlSi_3O_8) and the silica (SiO_2) minerals (e.g., *quartz*), although abundant on Earth, are notably rare on the Moon. Minerals containing oxidized iron (Fe^{3+} rather than Fe^{2+}) are absent on the Moon. The most striking aspect of lunar mineralogy, however, is the total lack of minerals that contain water, such as clays, micas, and amphiboles.

Oxide minerals, composed chiefly of metals and oxygen, are next in abundance after silicate minerals. They are particularly concentrated in the mare basalts, and they may make up as much as 20% by volume of these rocks. The most abundant oxide mineral is *ilmenite*, $(\text{Fe,Mg})\text{TiO}_3$, a black, opaque mineral that reflects the high TiO_2 contents of many

mare basalts. The second most abundant oxide mineral, *spinel*, has a widely varying composition and actually consists of a complex series of solid solutions. Members of this series include: *chromite*, FeCr_2O_4 ; *ulvöspinel*, Fe_2TiO_4 ; *hercynite*, FeAl_2O_4 ; and *spinel (sensu stricto)*, MgAl_2O_4 . Another oxide phase, which is only abundant in titanium-rich lunar basalts, is *armalcolite*, $(\text{Fe,Mg})\text{Ti}_2\text{O}_5$. As with the silicate minerals, no oxide minerals containing water (e.g., limonite) are native to the Moon. There was some debate about the origin of rare FeOOH found in some samples, but it is now generally believed that this material formed after contamination by terrestrial water (section 5.2.4).

Two additional minerals are noteworthy because, although they occur only in small amounts, they reflect the highly-reducing, low-oxygen environment under which the lunar rocks formed. *Native iron (Fe)* is ubiquitous in lunar rocks; this metal commonly contains small amounts of Ni and Co as well. *Troilite*, relatively pure FeS , is a common minor component; it holds most of the sulfur in lunar rocks. The sulfur that is not held in troilite can be mobilized during impact events, producing further sulfurization of native Fe (see below, section 5.3.1).

Rare lunar minerals include *apatite* [$\text{Ca}_5(\text{PO}_4)_3(\text{OH,F,Cl})$], which contains only F or Cl and no OH on the Moon, and the associated mineral *whitlockite* [$\text{Ca}_3(\text{PO}_4)_2$]. Rare sulfides, phosphides, and carbides occur in a variety of lunar rocks. Among these are a few that are largely of meteoritic origin and are very rare indeed: *schreibersite* [$(\text{Fe,Ni})_3\text{P}$], *cohenite* [$(\text{Fe,Ni})_3\text{C}$], and *ninningerite* [$(\text{Mg,Fe,Mn})\text{S}$]. In detail, lunar mineralogy becomes quite complex when rare minerals are considered. An excellent summary of known and suspect lunar minerals, compiled soon after the Apollo era, can be found in *Fronde* (1975).

Not all lunar minerals are described in detail in this chapter. It will be seen that the chapter devotes almost as much text to the description of some minor minerals as to the abundant ones. Although this may seem odd from a pragmatic viewpoint, many minor minerals provide unique and important scientific information that the more abundant ones do not. Furthermore, from the point of view of possible resource utilization, abundance is only one factor to be considered. Composition and ease of separation are also important, and even rare minerals can be valuable economic resources. At one extreme of potential economic use, the abundance of plagioclase is so great in some lunar highland rocks and soils that no concentration would be necessary for some proposed uses (e.g., glass manufacture). At the other extreme, native Fe metal is rare but might still be valuable because concen-

TABLE 5.1. Modal proportions (vol.%) of minerals and glasses in soils from the Apollo (A) and Luna (L) sampling sites (90–20 μm fraction, not including fused-soil and rock fragments).

	A-	A-	A-14	A-(H)	A-(M)	A-16	A-(H)	A-(M)	L-16	L-20	L-24
Plagioclase	21.4	23.2	31.8	34.1	12.9	69.1	39.3	34.1	14.2	52.1	20.9
Pyroxene	44.9	38.2	31.9	38.0	61.1	8.5	27.7	30.1	57.3	27.0	51.6
Olivine	2.1	5.4	6.7	5.9	5.3	3.9	11.6	0.2	10.0	6.6	17.5
Silica	0.7	1.1	0.7	0.9	-	0.0	0.1	-	0.0	0.5	1.7
Ilmenite	6.5	2.7	1.3	0.4	0.8	0.4	3.7	12.8	1.8	0.0	1.0
Mare Glass	16.0	15.1	2.6	15.9	6.7	0.9	9.0	17.2	5.5	0.9	3.4
Highland Glass	8.3	14.2	25.0	4.8	10.9	17.1	8.5	4.7	11.2	12.8	3.8
Others	-	-	-	-	2.3	-	-	0.7	-	-	-
Total	99.9	99.9	100.0	100.0	100.0	99.9	99.9	99.8	100.0	99.9	99.9

Data from Papike *et al.* (1982), Simon *et al.* (1982), Laul *et al.* (1978a), and Papike and Simon (unpublished). (H) Denotes highland. (M) Denotes mare.

tration and collection may be possible. Finally, it is important to emphasize that, although our catalog of lunar mineral types is large, there are almost certainly some minerals on the Moon that are not represented in our currently small and geographically limited sample collection. At the time this book was being prepared, another new mineral was discovered in the Apollo lunar sample collection (*yoshiokaite*; see Vaniman and Bish, 1990). More surprises are to be expected as we explore the geochemically distinct and unsampled parts of the Moon (Chapter 10).

5.1. SILICATE MINERALS

The silicate minerals, especially pyroxene, plagioclase feldspar, and olivine, are the most abundant minerals in rocks of the lunar crust and mantle. These silicate minerals, along with other minerals and glasses, make up the various mare basaltic lavas and the more complex suite of highland rocks (melt rocks, breccias, and plutonic rocks) discussed in Chapter 6. Meteoroid impacts over time have broken up and pulverized the lunar bedrock to produce a blanket of powdery *regolith* (a term for fragmental and unconsolidated rock debris) several meters thick, which forms the interface between the Moon and its space environment (see Chapter 7). The regolith therefore provides a useful sample of lunar minerals from a wide range of rocks, and Table 5.1 shows the average volume percentages of minerals in regolith collected at the Apollo and Luna sites (see section 2.1 for locations). The data are for the 90–20 μm size fraction, normalized so that the rock fragments are subtracted from the total. The resulting soil *modes* (composition by volume percent)

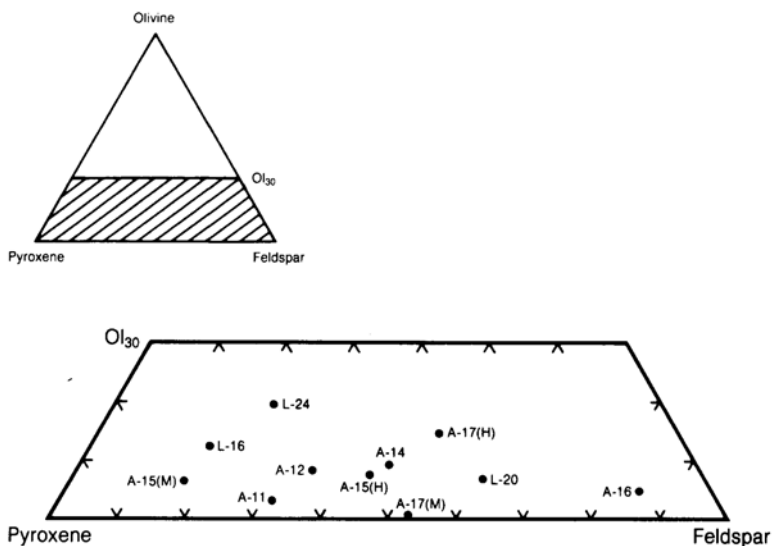
show the predominance of silicate minerals, especially pyroxene (8.5 to 61.1 vol.%), plagioclase feldspar (12.9 to 69.1 vol.%), and olivine (0.2 to 17.5 vol.%).

Figure 5.1 shows the modal proportions of the same three silicate phases. Several features are apparent. First, olivine is usually subordinate to pyroxene and plagioclase, and its maximum abundance occurs in the Luna 24 regolith. Second, there is a wide range of pyroxene/plagioclase ratios; the Apollo 15 mare soils are richest in pyroxene, and the Apollo 16 soils are richest in plagioclase. Because of these variations, any processing scheme designed to extract specific elements from minerals in the regolith will have to consider the variations in mineral abundances across the Moon.

5.1.1. Pyroxene

Pyroxenes are the most chemically complex of the major silicate phases in lunar rocks. They are also informative recorders of the conditions of formation and the evolutionary history of these rocks. Pyroxenes are compositionally variable solid solutions, and they contain most of the major chemical elements present in the host rocks. Figure 5.2 shows the pyroxene crystal structure, which basically consists of chains built up from linked silicon-oxygen tetrahedra, combined with metal-oxygen octahedra. Oxygen atoms define the corners of all of the polyhedral sites shown, and the cations (Si and other metals) are located inside the polyhedra. The structure is composed of *octahedral layers* containing infinite chains of edge-sharing bands of six-cornered (octahedral) polyhedra (called the M1 sites); the chains run parallel to the crystallographic *c*-axis. These chains are cross-linked by distorted six-cornered octahedra or larger eight-cornered

Fig. 5.1. Triangular plot showing modal (vol.%) proportions of pyroxene, olivine, and plagioclase feldspar in the 90-20 μm fractions of typical lunar soils. Soil compositions lie in the trapezoidal area bounded by pyroxene-feldspar-olivine (30%). Sampling sites are indicated, e.g., A-12 is Apollo 12 and L-20 is Luna 20. (H) indicates highland soil while (M) indicates mare soil.



PYROXENE

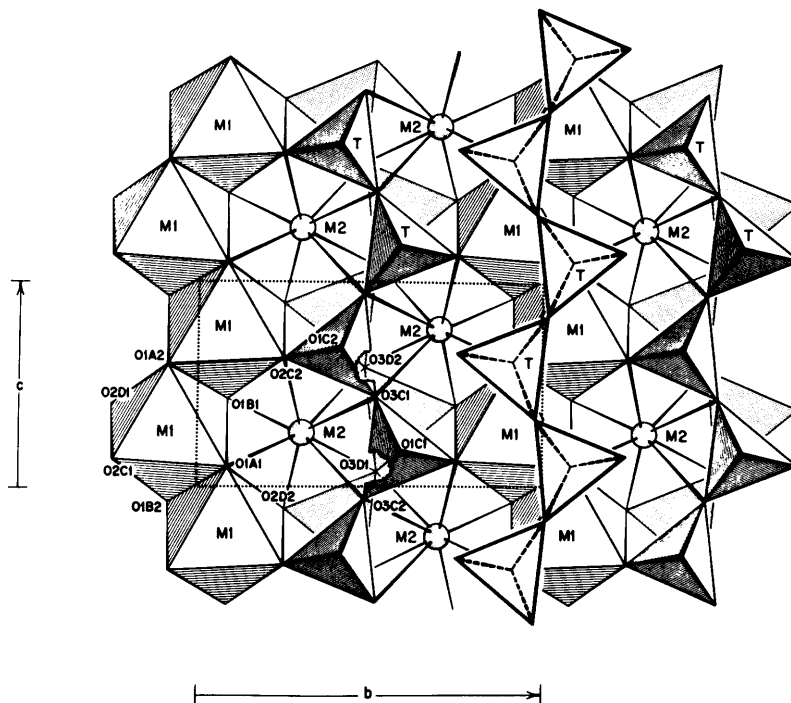


Fig. 5.2. Crystal structure of pyroxene, composed of polyhedra defined by oxygen atoms (O positions). These polyhedra vary in size, from the smaller T (tetrahedral sites) to larger M1 (octahedral sites) and M2 (distorted six to eight coordinated sites). Symbols O1A2, O1B1, etc. represent symmetrically distinct oxygen positions; *b* and *c* show the orientation and dimension of the *unit cell* (dotted outline) along the *b* and *c* axes of the crystal.

polyhedra (collectively called the M2 sites). These M1-M2 layers are in turn separated from each other by layers composed of infinite chains of silicon-oxygen tetrahedra that also run parallel to the crystallographic c-axis.

In such a structure, the M1 and M2 sites provide a variety of volumes; as a result, pyroxenes can accommodate a wide variety of cations, and these cations reflect much of the chemistry and crystallization history of the rocks in which they occur. Ca, Na, Mn, Mg, and Fe^{2+} are accommodated in the large distorted six- to eight-cornered M2 site; Mn, Fe^{2+} , Mg, Cr^{3+} , Cr^{2+} , Ti^{4+} , Ti^{3+} , and Al occur in the six-cornered M1 site; and Al and Si occupy the small four-cornered tetrahedral site. Potassium is too large to be accommodated in any of the pyroxene crystallographic sites.

Pyroxene chemical analyses are listed in Table A5.2 for mare basalts, in Table A5.3 for highland clast-poor melt rocks and crystalline melt breccias (section 6.4) as well as KREEP rocks (section 6.3.2), and in Table A5.4 for coarse-crystalline highland igneous rocks (anorthosites and Mg-rich rocks; sections 6.3.3 and 6.3.4). These tables

show that Fe^{3+} (which would be listed as Fe_2O_3) does not occur in lunar pyroxenes and that sodium is in low abundance.

Figures 5.3, 5.4, and 5.5 illustrate the range of lunar pyroxene compositions, in terms of the end-member components MgSiO_3 (*enstatite*), CaSiO_3 (*wollastonite*), and FeSiO_3 (*ferrosilite*). The diagram shown is a quadrilateral that represents the lower half of the complete triangular plot. This convention is used because compositions more calcium-rich than Ca:Mg = 1:1 or Ca:Fe = 1:1 do not crystallize with the pyroxene structure. The solid dots indicate specific analyses from Tables A5.2, A5.3, and A5.4, while the short dashed lines define the total range of known compositions for those lunar rock types. The long dashed lines in Fig. 5.5, which connect pairs of high-Ca and low-Ca pyroxenes, are called *tie-lines*. These tie-lines connect pairs of pyroxenes that formed in slowly-cooled lunar rocks, in which the component minerals were close to thermal and chemical equilibrium. Much of the chemical variability of pyroxenes is illustrated on pyroxene quadrilateral plots discussed above. More detailed discussion of the correlation between pyroxene

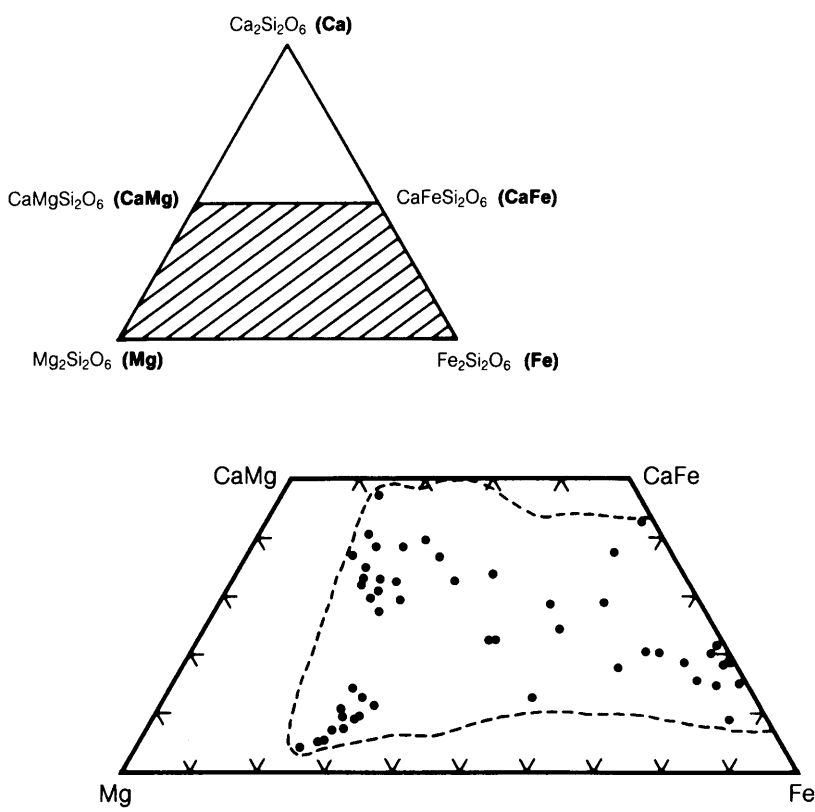


Fig. 5.3. Compositions of pyroxenes from mare basalts, shown in the “pyroxene quadrilateral” part of the triangle $\text{Ca}_2\text{Si}_2\text{O}_6$ (Ca) — $\text{Mg}_2\text{Si}_2\text{O}_6$ (Mg) — $\text{Fe}_2\text{Si}_2\text{O}_6$ (Fe). Inset diagram shows the pyroxene mineral compositions corresponding to the corners of the “quadrilateral” (shaded area) that includes all possible pyroxene Ca:Mg:Fe compositions. Dots represent analyses in Table A5.2. Dashed line encloses the total range of mare basalt pyroxene

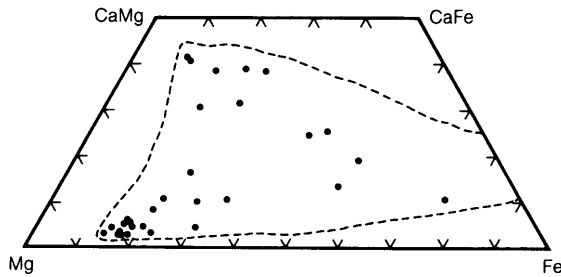


Fig. 5.4. Compositions of pyroxenes from highland breccias, clast-poor melt rocks, and KREEP rocks, shown in the “pyroxene quadrilateral.” Dots represent analyses in Table A5.3. Dashed line encloses the total range of pyroxene compositions reported in the literature for these highland rock types.

compositions, rock types, and cooling rates can be found in *Papike et al.* (1976) and *BVSP* (1981) for mare basalts, and in *Vaniman and Papike* (1980) for lunar highland melt rocks.

Although the major elements that define the quadrilateral plot (Ca, Mg, and Fe) show the important variations discussed above, the other, less abundant elements also show important trends. These other elements include Al, Ti, Cr, and Na. Sodium usually occurs in low concentrations in lunar pyroxenes because of its generally low abundance in lunar rocks. However, the contents of Al, Ti, and Cr in lunar pyroxenes can be significant (see Tables A5.2, A5.3, and A5.4). The very low abundance (partial pressure) of oxygen gas during the crystallization of lunar rocks has resulted in reduced valence states for some Ti atoms (Ti^{3+} rather than Ti^{4+}) and Cr atoms (Cr^{2+} rather than Cr^{3+}). These

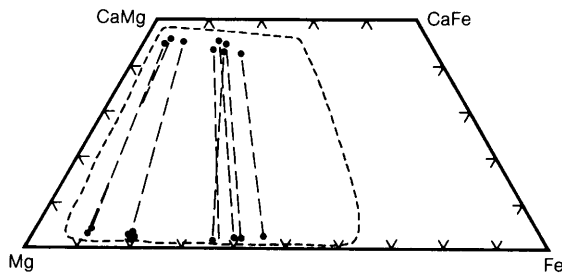


Fig. 5.5. Compositions of pyroxenes from highland coarse-crystalline igneous rocks (ferroan anorthosites and Mg-rich rocks), shown in the “pyroxene quadrilateral.” Dots represent analyses in Table A5.4. Dashed line encloses the total range of pyroxene compositions reported in the literature for these highland rock types. Straight dashed lines connect compositions of high-Ca and low-Ca pyroxenes that coexist in the same rock.

lower valence states are very rare in Ti and Cr of terrestrial pyroxenes. For example, *Sung et al.* (1974) suggest that as much as 30–40% of the Ti in Apollo 17 mare basalts occurs in the trivalent state and that most of this reduced Ti is in pyroxenes.

Lunar pyroxenes also show substantial *subsolidus* reactions (i.e., recrystallization and other changes that take place below melting temperatures). Considerable work has been done to interpret the resulting features. It was discovered soon after the return of the Apollo 11 samples that submicroscopic, subsolidus separation (*exsolution*) of two distinct pyroxenes [*augite* (high-Ca clinopyroxene) and *pigeonite* (low-Ca clinopyroxene)] had taken place within originally uniform pyroxene crystals (e.g., *Ross et al.*, 1970). This process produced distinctive microscopic and submicroscopic *exsolution lamellae*, i.e., thin layers of pigeonite in augite, or vice versa. *Papike et al.* (1971) attempted to relate these exsolution features to the relative cooling histories of mare basalts. They pointed out that certain parameters of the pyroxene crystal unit cell (the length b and the angle β) could be used to estimate the compositions of the intergrown augite and pigeonite. They also suggested that Δ/β (β pigeonite— β augite) could be used to indicate the degree of subsolidus exsolution and thus the relative annealing temperatures of the exsolved pyroxenes. *Takeda et al.* (1975) summarized similar exsolution data for pyroxene grains from Apollo 12 and 15 basalts. They compared the relative cooling rates (determined from exsolution studies) with absolute cooling rates determined from experimental studies. *Ross et al.* (1973) experimentally determined the 1-atmosphere augite-pigeonite stability relations for pyroxene grains from mare basalt 12021. *Grove* (1982) used exsolution lamellae in lunar clinopyroxenes as cooling rate indicators, and his results were calibrated experimentally. These studies all indicate that the cooling and subsolidus equilibration of igneous and metamorphic pyroxenes is a slow process; estimated cooling rates range from 1.5° to 0.2°C/hr for lava flows 6 m thick (e.g., model cooling rates for Apollo 15 mare lavas; *Takeda et al.*, 1975).

Shock lamellae can be produced in pyroxenes by the shock waves due to meteoroid impact. However, these features are relatively rare, and they are much less well characterized than the analogous shock lamellae in plagioclase (*Schall and Hörz*, 1977).

5.1.2. Plagioclase Feldspar

The silicate mineral *feldspar* has a framework structure of three-dimensionally linked SiO_4 and AlO_4 tetrahedra (Fig. 5.6). The ratio Si:Al varies between 3:1 and 1:1. Ordering (i.e., nonrandom

placement) of Si and Al in specific tetrahedral sites can lead to complexities such as discontinuities in the crystal structure. Within this three-dimensional framework of tetrahedra containing Si and Al, much larger volumes with 8 to 12 corners occur that accommodate large cations (Ca, Na, K, Fe, Mg, Ba).

Aside from rare potassium- and barium-enriched feldspars (discussed below in section 5.1.5), most lunar feldspars belong to the plagioclase series,

which consists of solid crystalline solutions between albite ($\text{NaAlSi}_3\text{O}_8$) and anorthite ($\text{CaAl}_2\text{Si}_2\text{O}_8$). Because of the alkali-depleted nature of the Moon (Chapter 8), lunar plagioclases are also depleted in Na (the albite component) relative to terrestrial plagioclases. Tables A5.5, A5.6, and A5.7 list lunar plagioclase compositions for mare basalts, for clast-poor melt rocks and crystalline melt breccias (section 6.4), as well as KREEP rocks (section 6.3.2),

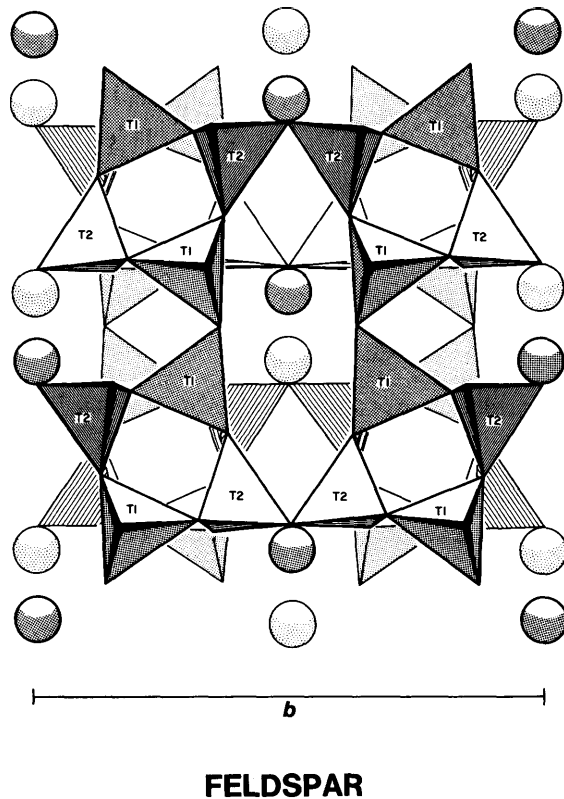


Fig. 5.6. Crystal structure of feldspar, which is composed of tetrahedra (T 1, T2) with oxygen atoms at the apices, combined with larger polyhedra. This structure forms several varieties of feldspar, depending on the chemical composition of the larger cations (shown as spheres). Spheres represent Ca atoms in anorthite, Na in albite, K in potassium feldspar, and Ba in celsian. The ratio of Al:Si within the tetrahedral sites varies from 1:1 when the large cations (spheres) have divalent charge (e.g., Ca) to 1:3 when the large spheres are monovalent (e.g., Na). T1 and T2 are two symmetrically distinct tetrahedral sites in high-temperature feldspar, in which the placement of Si and Al within the tetrahedral sites is random (*disordered*); *b* is the unit cell dimension along the *b* axis of the crystal.

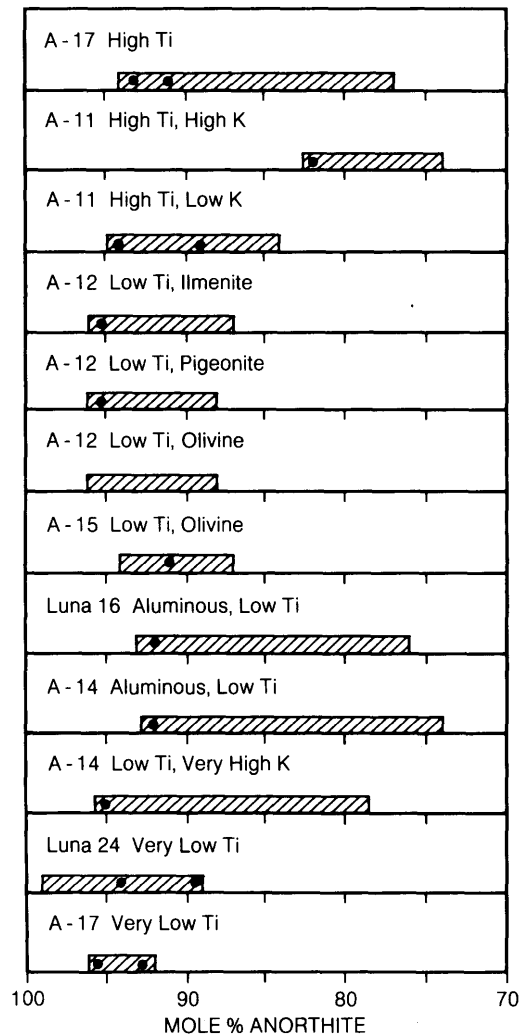


Fig. 5.7. Range of compositional variation in plagioclase feldspars from lunar mare basalts, shown as mol.% anorthite ($\text{CaAl}_2\text{Si}_2\text{O}_8$) in the albite ($\text{NaAlSi}_3\text{O}_8$)-anorthite ($\text{CaAl}_2\text{Si}_2\text{O}_8$) solid solution. Dots represent analyses in Table A5.5. Patterned areas represent the ranges for all mare basalt plagioclases reported in the literature. Mare rock types are described in Table A5.1 and in section 6.1.

and for coarse-crystalline highland igneous rocks (anorthosites and Mg-rich rocks; sections 6.3.3 and 6.3.4). The maximum chemical variation involves solid solution between albite and anorthite, a variability that can also be described as the coupled substitution between NaSi and CaAl, in which the CaAl component represents anorthite. Figure 5.7 illustrates the compositional range of this substitution in plagioclase feldspars from mare basalts. The Ca abundance in the plagioclase (mole% anorthite) correlates positively with the Ca/Na ratio in the host basalts (e.g., *Papike et al.*, 1976; *BVSP*, 1981).

Plagioclases from highland impact melts, from breccias, and from KREEP rocks such as "IKFM" (Fig. 5.8) have more Na-rich compositions (i.e., less anorthite) along with their enrichment in the geochemically similar elements potassium (K), rare earth elements (REE), and phosphorus (P), the association of minor elements referred to as KREEP (see sections 2.4 and 6.3.2). Plagioclases from coarse-crystalline igneous rocks have more restricted compositions (Fig. 5.9); however, there is a positive correlation between the alkali content of the host rock and the plagioclase (note the Na-rich plagioclase from a particular rock type, alkali anorthosite, which is itself also Na-rich).

An interesting aspect of mare basalt plagioclases concerns the problem of where the observed Fe and Mg fit into the crystal structure. *Smith* (1974), in

reviewing this problem, pointed out that (1) the Fe content in mare basalt plagioclase is higher than that in plagioclase from lunar highland rocks and (2) the Fe content is positively correlated with albite (NaSi) content. *Weill et al.* (1971) noted peculiarities in lunar plagioclase cation ratios, and suggested that they might result from substitution of the theoretical "Schwantke molecule," $\text{Ca}_{0.5}\square_{0.5}\text{AlSi}_3\text{O}_8$ where \square = a vacant site normally occupied by a large cation (Na or Ca). *Wenk and Wilde* (1973) reviewed all available chemical data to accurately define the chemical components in lunar plagioclase. They concluded that (1) the deficiency of Al+Si in the tetrahedral sites (up to 0.06 atoms per eight-oxygen formula unit) is largely compensated by Fe and Mg substitution in the same tetrahedral sites; (2) the Ca/Na ratio in the octahedral large-cation sites increases correspondingly to maintain charge balance; and (3) the vacancy-coupled substitution of Ca+ \square (the "Schwantke molecule") for 2Na probably also occurs but is much less significant. *Wenk and Wilde* (1973) also made the interesting observation that the apparent number of vacancies increases with increasing Fe+Mg content. They suggested that the progressive substitution of the larger Fe and Mg ions for the smaller Si in the tetrahedral sites decreases the volume of interstitial space available for the large Ca and Na atoms. *Longhi et al.* (1976) identified the same Fe and Mg components by using a slightly

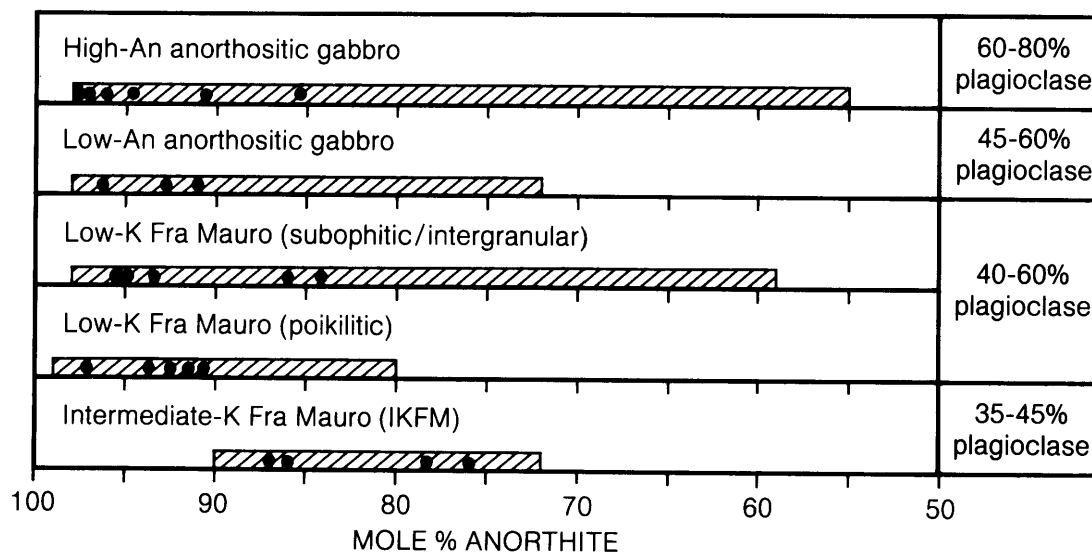


Fig. 5.8. Range of compositional variation in plagioclase feldspars from lunar highland breccias, clast-poor melt rocks, and KREEP rocks, shown as mol.% anorthite ($\text{CaAl}_2\text{Si}_2\text{O}_8$) in the albite ($\text{NaAlSi}_3\text{O}_8$)-anorthite ($\text{CaAl}_2\text{Si}_2\text{O}_8$) solid solution. Dots represent analyses in Table A5.6. Patterned areas represent the ranges for plagioclases reported in the literature for these highland rock types. The rock types listed use the nomenclature of *Vaniman and Papike* (1980); those at the top generally have more plagioclase than those at the bottom.

different approach. *Schurmann and Hafner* (1972) and *Hafner et al.* (1973), using Mössbauer and electron spin resonance techniques, showed that most of the iron in lunar plagioclase is present as Fe^{2+} . These studies all indicate that divalent Mg and Fe are important components in the tetrahedral structural sites in lunar plagioclase.

Plagioclase, like pyroxene, may undergo subsolidus reactions. *Smith and Steele* (1974) suggested that the grains of pyroxene and silica minerals observed as inclusions inside the plagioclase crystals of slowly-cooled highland plutonic rocks (e.g., anorthosites) may have formed by solid-state exsolution of the necessary elements (Ca, Fe, Mg, Si, etc.) from the original plagioclase grain. The original plagioclase, when first crystallized, would have had high contents of Fe and Mg in its tetrahedral sites, perhaps comparable to the Fe and Mg contents of plagioclases in mare basalts. *Smith and Steele* (1974) proposed that, with falling temperature, the plagioclase component $\text{CaSi}_3(\text{Mg}, \text{Fe}^{2+})\text{O}_8$ broke down into pyroxene, $\text{Ca}(\text{Mg}, \text{Fe}^{2+})\text{Si}_2\text{O}_6$, and a silica mineral (SiO_2). However, this interesting suggestion was not supported by the subsequent results of *Dixon and Papike* (1975), who found that the volume of SiO_2 inclusions in plagioclases from anorthosites is much too low relative to the pyroxene inclusions for the two minerals to have formed by such a reaction. These authors preferred the explanation that the pyroxene inclusions and the plagioclase precipitated together from the original melt and later reacted during thermal annealing according to the exchange reaction: $\text{Ca}(\text{pyroxene}) + \text{Fe}(\text{plagioclase}) = \text{Fe}(\text{pyroxene}) + \text{Ca}(\text{plagioclase})$. As a result, the plagioclase became more Ca-rich and the pyroxene more Fe-rich with time.

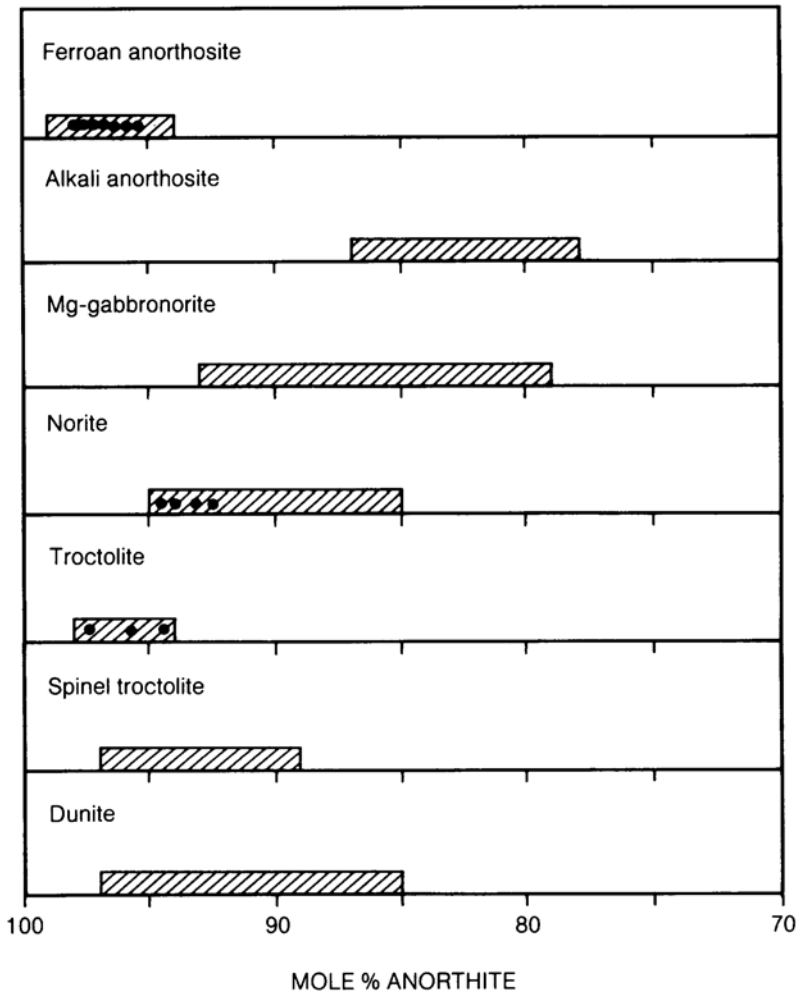


Fig. 5.9. Range of compositional variation in plagioclase feldspars from highland coarse-crystalline igneous rocks (ferroan anorthosites, alkali anorthosites, and five types of Mg-rich rocks), shown as mol.% anorthite ($\text{CaAl}_2\text{Si}_2\text{O}_8$) in the albite ($\text{NaAlSi}_3\text{O}_8$)-anorthite ($\text{CaAl}_2\text{Si}_2\text{O}_8$) solid solution. Dots represent analyses in Table A5.7. Patterned areas represent the ranges for plagioclases from all such rocks reported in the literature. See section 6.3 for description of rock types.

5.1.3. Olivine

The crystal structure of olivine, $(\text{Mg,Fe})_2\text{SiO}_4$, consists of serrated chains formed of edge-sharing octahedra. These chains run parallel to the crystallographic c -axis (Fig. 5.10). The octahedral chains are cross-linked by isolated SiO_4 tetrahedra. The major cations in the octahedral sites, Fe^{2+} and Mg , are distributed with a high degree of disorder (randomness) over both the M1 and M2 octahedral sites. However, the small amounts of Ca that may occur in olivine occupy only the M2 site (see *Papike and Cameron, 1976*, for a review).

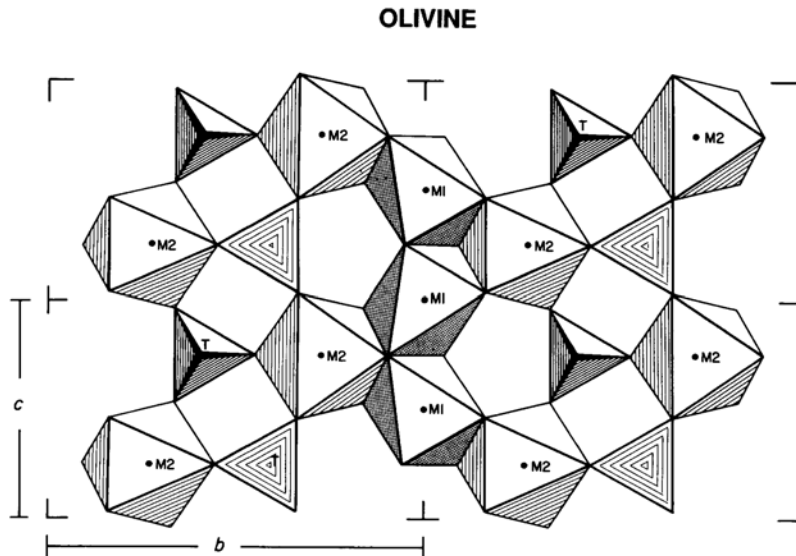
Representative olivine analyses are listed in Tables A5.8 for mare basalts, A5.9 for highland clast-poor melt rocks and crystalline melt breccias (section 6.4), and A5.10 for coarse-crystalline high-land igneous rocks (anorthosites and Mg-rich rocks; sections 6.3.3 and 6.3.4). The major compositional variation within olivines is caused by exchange of Fe for Mg; this exchange, and the resulting variations in composition, are represented by the ratio $\text{Fe}/(\text{Fe} + \text{Mg})$. The Fe end member, Fe_2SiO_4 , is *fayalite*, and the Mg end member, Mg_2SiO_4 , is *forsterite*. Figures 5.11, 5.12, and 5.13 illustrate the variations between forsterite and fayalite within olivines from mare rocks, highland impact melts or breccias, and highland coarse-crystalline igneous rocks.

The most magnesian mare basalt olivine grains contain only 20% fayalite (Fa), represented by the notation Fa_{20} (i.e., 80 mol.% forsterite and 20% fayalite in the solid solution series forsterite—fayalite, Mg_2SiO_4 — Fe_2SiO_4). Most mare basalt olivines have compositions in the range Fa_{20} — Fa_{70} (Fig. 5.11).

Very few olivines in mare basalts have compositions in the range Fa_{70} — Fa_{100} ; however, a number of mare basalts do contain very Fe-rich olivine (Fa_{90} — Fa_{100}). These olivines are part of an equilibrium three-phase assemblage (Ca,Fe pyroxene — Fe olivine — silica) that crystallized stably from the late-stage iron-enriched portions of mare basalt melts. Some mare basalts, which cooled quickly during the late stages of crystallization, contain instead either an Fe-rich pyroxene that crystallized metastably relative to the normal three-phase assemblage or a related silicate mineral, pyroxferroite (see section 5.1.5). The formation of extremely Fe-rich pyroxene violates a so-called “forbidden region” at the Fe-apex of the “pyroxene quadrilateral” (the Fe corner of Figs. 5.3–5.5; see *Lindsley and Munoz, 1969*, for details).

Other significant elements in lunar olivines are Ca, Mn, Cr, and Al. Calcium varies directly with the Fe content, and it may be an indicator of the cooling rate (*Smith, 1974*). The experimental data of *Donaldson et al. (1975)* support this contention. Olivines in mare basalts are significantly enriched in Cr relative to olivines in terrestrial basalts. Cr_2O_3 values, which are commonly below detection limits (~0.1 wt.%) in terrestrial olivines (*Smith, 1974*), range up to 0.6 wt.% in lunar olivines. Much or all of this Cr may be in the reduced Cr^{2+} valence state, and *Haggerty et al. (1970)* identified significant Cr^{2+} in lunar olivine using optical absorption techniques. Cr^{2+} is more readily accommodated into the olivine structure than is Cr^{3+} , which is the normal valence state for Cr in terrestrial olivines. The presence of Cr^{2+} is another result of the low oxygen partial pressures that

Fig. 5.10. Crystal structure of olivine, which is composed of tetrahedra (T) and octahedra (M1, M2) defined by oxygen atoms. Small cations (almost entirely Si^{4+}) are located within the tetrahedra; larger cations (mostly Fe^{2+} and Mg^{2+}) are located within the two symmetrically distinct octahedral sites (M1 and M2). The bars b and c indicate the orientation and dimension of the unit cell along the b and c axes of the crystal.



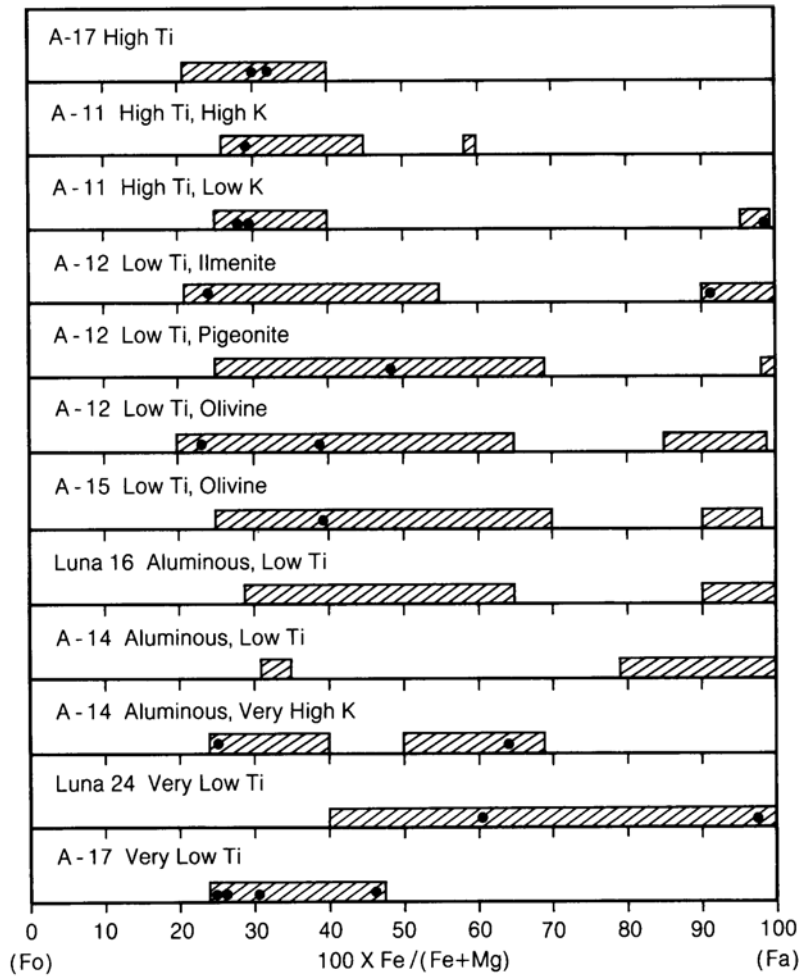


Fig. 5.11. Variation of the atomic ratio Fe/(Fe + Mg) in olivines from lunar mare basalts. Compositions lie between the end members forsterite (Fo), Mg₂SiO₄, at 0, and fayalite (Fa), Fe²⁺₂SiO₄, at 100. Dots represent analyses in Table A5.8. Patterned areas represent the entire compositional range for mare basalt olivines reported in the literature.

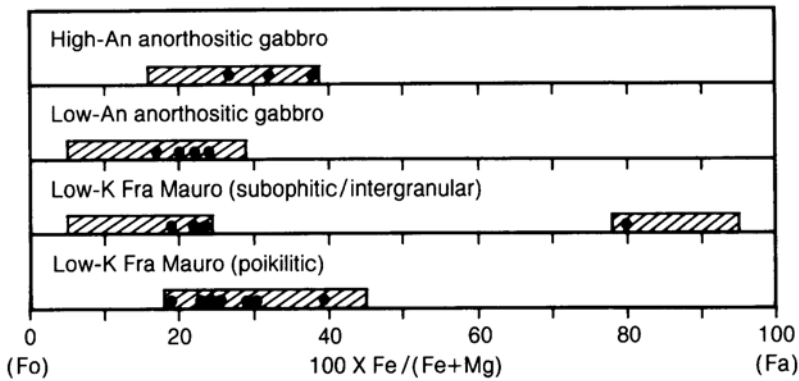
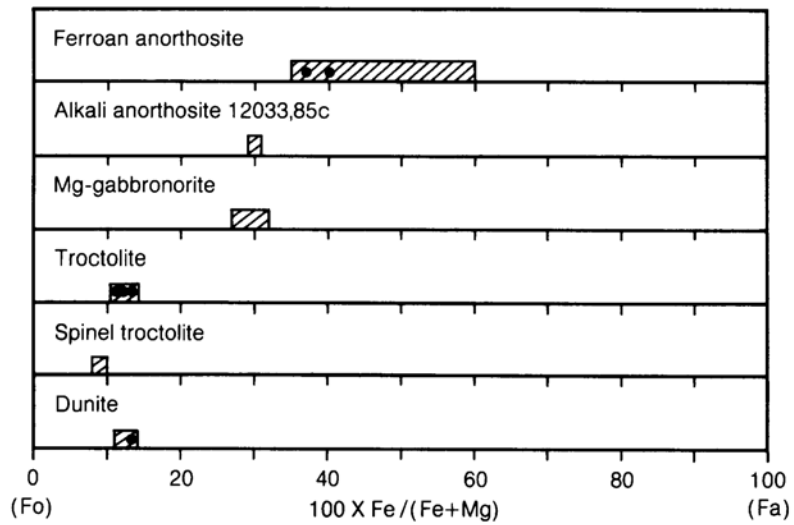


Fig. 5.12. Variation of the atomic ratio Fe/(Fe + Mg) in olivines from lunar highland clast-poor melt rocks. Compositions lie between the end members forsterite (Fo), Mg₂SiO₄, and fayalite (Fa), Fe²⁺₂SiO₄. Dots represent analyses in Table A5.9. Patterned areas represent the entire compositional range for highland melt rock olivines reported in the literature.

Fig. 5.13. Variation of the atomic ratio $Fe/(Fe + Mg)$ in olivines from lunar highland coarse-crystalline igneous rocks (anorthosites and Mg-rich rocks). Compositions lie between forsterite (Fo), Mg_2SiO_4 , and fayalite (Fa), $Fe^{2+}_2SiO_4$. Dots represent analyses in Table A5.10. Patterned areas represent the entire compositional range for lunar plutonic rock olivines



existed during mare basalt crystallization. Similarly, Cr^{2+} is much more abundant in lunar pyroxenes than in terrestrial pyroxenes (BVSP, 1981).

5.1.4. Silica Minerals: Quartz, Cristobalite, and Tridymite

Silica minerals include several structurally different minerals, all of which have the simple formula SiO_2 . These minerals are generally rare on the Moon. This rarity is one of the major mineralogical differences between the Moon and the Earth, where silica minerals are abundant in such common rocks as granite, sandstone, and chert. The relative absence of silica minerals on the Moon is a result of several factors. For one thing, the Moon has apparently not evolved chemically beyond the formation of a low-silica, high-alumina anorthositic crust (see section 2.4), so that high-silica granitic rocks are rare. For another, the Moon lacks hydrous and hydrothermal systems like those that can crystallize silica on Earth.

Despite their rarity on the Moon, the silica minerals are nevertheless important in classifying and unraveling the origin of some lunar rocks (section 6.3). Furthermore, lunar crustal rocks that contain silica minerals may be more abundant than their meager representation among the returned Apollo and Luna samples suggests. The silica minerals tend to concentrate along with chemical elements that are also rare on the Moon, such as the KREEP elements (sections 6.3.2 and 6.3.5). For these reasons, the lunar silica minerals deserve greater consideration than their rarity would otherwise warrant.

The silica minerals found on the Moon are *cristobalite*, *quartz*, and *tridymite*. In spite of the intense impact cratering of the Moon, it is interesting that the high-pressure polymorphs of SiO_2 , *coesite* and *stishovite*, which are known from young terrestrial impact craters, have not been found on the Moon. Explanations for their absence include the rarity of silica grains in the original target rocks and probable volatilization of silica during impact events in the high vacuum at the lunar surface.

The crystal structures of the silica minerals are distinctly different, but they all consist of frameworks of SiO_4 tetrahedra in which each tetrahedral corner is shared with another tetrahedron. A comparison of silica mineral structures, along with structure diagrams, can be found in *Papike and Cameron (1976)*. All of the silica mineral structures contain little or no room for cations larger than Si^{4+} , hence the relatively pure SiO_2 composition of these minerals. The structures become more open in going from quartz to cristobalite to tridymite, and the general abundance of impurities increases accordingly.

Quartz occurs in a few granite-like (*felsite*) clasts (e.g., sample 12013, section 6.3.5) as needle-shaped crystals that probably represent structural transformation (*inversion*) of original tridymite (*Quick et al., 1981a*). Some tridymite is preserved in these felsite clasts. The other rock type in which quartz is abundant is the rare fragments of coarse-grained lunar granites. The largest lunar granite clast yet found, from Apollo 14 breccia 14321, weighs 1.8 g and contains 40 vol.% quartz (*Warren et al., 1983*). A smaller granite clast from sample 14303 was

estimated to have 23 vol.% quartz (Warren *et al.*, 1983). Based on their isotopic work on the large clast, Shih *et al.* (1985) suggested that the sample crystallized in a deep-seated plutonic environment about 4.1 b.y. ago, and it therefore did not form during the earlier crystallization of the magma ocean about 4.5 to 4.3 b.y. ago (section 2.4). Consistent with the general absence of hydrous minerals on the Moon, the lunar granites do not contain mica or amphibole, as would granites on Earth.

The most common silica mineral in mare basalt lavas is not quartz but cristobalite, which can constitute up to 5 vol.% of some basalts. This situation contrasts with the general absence of all silica minerals in terrestrial basalts. Lunar cristobalite commonly has twinning and curved fractures, indicating that it has inverted from a high-temperature crystal structure to a low-temperature one during cooling of the lavas (Dence *et al.*, 1970; Champness *et al.*, 1971). Other mare basalts contain crystals of the silica mineral tridymite that have incompletely inverted to cristobalite, producing rocks that contain both tridymite and cristobalite. In a study of Apollo 12 basalts, Sippel (1971) found that the coarser-grained samples contained tridymite and cristobalite, while the finer-grained basalts contained cristobalite and quartz. Unfortunately, these mineral pairs are stable over fairly large temperature ranges and can also form metastably, outside of their equilibrium stability fields, so they are not useful for inferring the temperatures of lava crystallization.

Cristobalite tends to occur as irregular grains wedged between other crystals, while tridymite forms lathlike crystals. Klein *et al.* (1971) observed tridymite laths enclosed by pyroxene and plagioclase and suggested that tridymite was an early crystallizing phase.

Table A5.11 lists some representative analyses of cristobalite (analyses 13-15) and tridymite (analysis 16). Although the lunar silica minerals are nearly pure SiO₂, they contain such typical contaminants as Al₂O₃, TiO₂, CaO, FeO, and Na₂O.

In contrast to lunar basalts, terrestrial basalts typically lack any evidence for crystallization of silica minerals from the melt. In those cases where silica minerals are observed in terrestrial basalts, they generally occur as rounded or embayed crystals of quartz that have been partly absorbed by the surrounding basaltic magma. These textures are ambiguous, and it is difficult to decide whether this quartz formed directly from the basaltic magma or whether it represents accidental inclusions picked up from other rocks through which the magma flowed. This is not the case in lunar mare basalts, where silica minerals have clearly crystallized from the magma.

5.1.5. Other Silicate Minerals

Several other silicate minerals occur only rarely in lunar rocks. Some of these (e.g., *tranquillityite* and *pyroxferroite*) are unique to the Moon. Others, like *zircon* and *potassium feldspar* (*K feldspar*), are rare on the Moon but common on Earth. These minerals occur in lunar basalts in small patches of high-silica residual melt formed during the last stages of crystallization of the mare lavas, and they are often accompanied by a silica mineral such as cristobalite. The same minerals also occur in unusual high-silica ("KREEPy") highland rocks, which may have formed from a similar residual melt produced during large-scale crystallization of ancient highland igneous rocks (see sections 2.4.3 and 2.4.4).

Despite the rarity of these minerals on the Moon, they are important because (1) they act as recorders of the last stages of basalt crystallization and (2) they are commonly enriched in rare earth elements (REE) and in radioactive elements, some of which are useful in dating the samples.

As the basalt bedrock is gradually pulverized by meteoroid impacts, these rare silicate minerals are released into the lunar soil. These minerals are fine-grained to begin with and, in the case of K-feldspar and cristobalite, are easily broken. As a result, the rare silicate minerals tend to become concentrated in the finer soil fractions. In mare terranes, the finest soil fractions have different compositions from the bulk soils; they are enriched in REE, in radioactive elements, and in Al, K, and Na contained in feldspars. This variation of regolith composition with grain size is discussed in more detail in section 7.5.3.

Tranquillityite. *Tranquillityite* [Fe₈(Y+Zr)₂Ti₃Si₃O₂₄] is named for the Apollo 11 landing site in Mare Tranquillitatis. This mineral was first described in Apollo 11 samples as "new mineral A" (Ramdohr and El Goresy, 1970). Chemical analyses of tranquillityite, together with the structural formula, X-ray data, and density (4.7 g/cm³) were first published by Lovering *et al.* (1971). Some of their analyses of tranquillityite from Apollo 11 and Apollo 12 basalts are listed in Table A5.11b.

Tranquillityite characteristically occurs in lunar mare basalts, where it forms small (<100-μm) lath-shaped crystals associated with other rare minerals such as pyroxferroite and apatite in small pockets where the last minerals to crystallize are clustered. Tranquillityite is semiopaque; it has a nonpleochroic (constant in all crystal directions) deep red color in transmitted light (due to its high TiO₂ content) and a gray to dark gray color in reflected light. Lovering *et al.* (1971) determined crystallographic dimensions for what appeared to be well-crystallized tranquillityite. However, further X-ray diffraction studies

showed that some tranquillityites tend to be *metamict*, a state in which the original crystallographic order is partly or completely destroyed by radiation produced by decay of the relatively large amounts of U (~40–1000 µg/g) that they contain (Gatehouse *et al.*, 1977; Lovering and Wark, 1971). Gatehouse *et al.* (1977) were able to anneal this damage and recrystallize lunar tranquillityite grains by heating them to 800°C. Those heated in air formed a face-centered cubic crystal structure similar to fluorite (CaF₂), with an edge dimension of 4.85 Å. Grains reconstituted in vacuum formed with a slight rhombohedral distortion from cubic symmetry (edge dimension = 4.743 Å). Heating above 900°C caused the tranquillityite structure to break down (Gatehouse *et al.*, 1977). This result is consistent with the observation that tranquillityite is not found in metamorphosed (highly heated) basalt clasts (Lovering and Wark, 1975), in which it appears to have broken down, in part, to zircon.

Zircon. Zircon, ideally ZrSiO₄, is important not only because it tends to concentrate REE, but also because it is useful for age-dating the rocks in which it formed. Zircon is a refractory mineral that resists remelting and often incorporates Hf, Th, and U into its crystal structure, making it well-suited for U-Pb dating (e.g., Compston *et al.*, 1984). Zircons also have a high retentivity for *fission tracks*, microscopic linear zones of damage produced by the recoil of U atoms that decay in the crystal by spontaneous fission. Zircon is especially suitable for age determinations based on the density of such tracks within the crystal (Braddy *et al.*, 1975).

The main source of lunar zircons appears to be the rare, high-silica granitic rocks (Lovering and Wark, 1975). For example, rock 12013, a KREEPy granitic rock, contains 2200 µg/g Zr (LSPET, 1970), which corresponds to approximately 0.1% zircon (Drake *et al.*, 1970). In this sample, zircons range from 4 to 80 µm in size. Taylor *et al.* (1980) found 0.6 vol.% zircon in a fragment of a similar rock type (quartz monzodiorite) from melt breccia 15405, and Keil *et al.* (1971) reported zircon in a “12013-like lithic fragment.” Gay *et al.* (1972) found zircon in an anorthosite clast in breccia 14321. Representative analyses of these zircons are listed in Table A5.11a. Optical and physical properties of lunar zircons are described in Braddy *et al.* (1975).

Because of the rarity of lunar granitic rocks and the durability of zircons, most zircons are found as isolated grains in soils and breccias. Zircons can also be found in metamorphosed basalt clasts, where they possibly form by the breakdown of original tranquillityite (Lovering and Wark, 1975). For their fission track study, Braddy *et al.* (1975) separated zircons from the “sawdust” left after breccia 14321

was cut for other studies. From 20 g of this sawdust they recovered 93 zircons, 70 of which were >100 µm in diameter. The zircons varied in U content from 15 to 400 µg/g, with a median content of 50 µg/g. Braddy *et al.* (1975), using methods of thermal annealing followed by etching, showed that zircons are excellent recorders of fission tracks.

Although they are rare, small, and difficult to work with, zircons are very important in dating lunar samples, especially very old (>4 b.y.) highland rocks. Uranium-lead dating of lunar zircons, using ion microprobe analysis techniques (Compston *et al.*, 1984), has shown that zircons can survive the intense shock and heating of meteorite bombardment without serious disruption of their U-Pb systematics; they can therefore preserve the original rock ages. Compston *et al.* (1984) analyzed four zircons from a *clast* (a fragment of an older rock) within breccia 73217 and successfully determined a formation age for the clast of about 4356 m.y., a measurement that would otherwise not have been obtained.

Pyroxferroite. Although *pyroxferroite* had been synthesized in the laboratory (Lindsley, 1967), the mineral was not observed in natural rocks until the return of the Apollo 11 samples. Pyroxferroite is an iron-rich *pyroxenoid* (a mineral structurally similar to pyroxene), whose formula is approximately Ca_{1/7}Fe_{6/7}SiO₃, with limited substitution of Mg for Fe. Some representative analyses are listed in Table A5.11a. Burnham (1971) determined that the pyroxferroite structure is based on a repeating pattern of seven SiO₄ tetrahedra; this structure is the same as that of a rare terrestrial mineral, *pyroxmangite*. Chao *et al.* (1970) published some of the first X-ray, physical, and chemical data for pyroxferroite.

Pyroxferroite is found in mare basalts and Fe-rich basalts (*ferrobasalts* such as those at the Luna 24 site). As these rocks cooled, the compositions of the crystallizing pyroxenes changed, moving toward the CaFe-Fe side of the pyroxene quadrilateral (Fig. 5.3), and approaching the pyroxferroite composition. However, experimental studies by Lindsley and Burnham (1970) showed that pyroxferroite is only stable at approximately 10 kbar pressure, which on the Moon corresponds to a depth in the crust of several hundred kilometers (Chao *et al.*, 1970). Although the lunar mare basalt magmas may have been derived from such depths, it is highly unlikely that they crystallized under such high pressures. Therefore it is probable that pyroxferroite crystallized *metastably* (out of equilibrium) during rapid near-surface cooling of the basalts. To test this hypothesis, Lindsley *et al.* (1972) heated pyroxferroite crystals and found that those kept at 900°C for three days decomposed, forming the stable mineral assemblage

Ca-rich pyroxene + fayalite (Fe_2SiO_4) + tridymite (SiO_2). This result indicates that the lunar basalts cooled to below 900°C within three days after crystallization of pyroxferroite. If they had remained above this temperature for a longer time, the pyroxferroite would have broken down to the three stable minerals.

Potassium feldspar. Another late-stage mineral found in lunar basalts is potassium feldspar, KAlSi_3O_8 . Because the other basalt minerals (e.g., pyroxene, olivine, and plagioclase feldspar) accept very little of the relatively large K^+ ion into their structures, it becomes concentrated in the residual melt that remains after most minerals have crystallized. Early investigators were therefore not surprised to find minor amounts of late-formed potassium feldspar in Apollo 11 basalts (e.g., *Agrell et al.*, 1970; *Keil et al.*, 1970). *Albee and Chodos* (1970) observed a “K-rich phase” that approached potassium feldspar in composition but was nonstoichiometric.

In high-silica highland rocks, which have granitic or so-called “KREEPy” compositions, potassium feldspar is commonly neither minor nor fine-grained. In sample 12013, a KREEPy breccia that itself contains two different breccias (gray and black), there are abundant patches of fine-grained granitic material (*felsite*) that contain 50% potassium feldspar, 40% silica minerals, 5% Fe-rich augite, and 5% other phases (*Quick et al.*, 1981a). Neither the black nor the gray breccias in 12013 contain any mare basalt components; apparently 12013 was formed from a very unusual, SiO_2 -rich, KREEPy, evolved terrane, probably somewhere in the highlands. Because 12013 appears to be an impact-produced breccia, it is not clear whether the variety of rock types it contains came from a single differentiated intrusion or from a number of unrelated sources (*Quick et al.*, 1981a; see also section 6.3.5).

In addition to the occurrences of K-feldspar in highland samples (KREEPy and granitic rocks), and as a nonstoichiometric phase in some mare basalts, the mineral is also found in an unusual K-rich mare basalt type (very high-K basalt), which has been discovered as clasts in two Apollo 14 breccias (*Shervais et al.*, 1983, 1984b, 1985). These clasts have $\text{K}_2\text{O} > 0.5$ wt.% and contain several percent potassium feldspar. *Shervais et al.* (1985) conclude that these basalts have most likely been produced by the partial assimilation of lunar granite crust by a normal low-Ti mare basalt magma on its way to the surface.

Some analyses of lunar potassium feldspars are listed in Table A5.11a. It is obvious that the feldspars can have a significant BaO content (also expressed as *celsian feldspar*). *Quick et al.* (1981a) reported that, in the potassium feldspar in the felsites of sample 12013, the celsian (Cn) content increases with the

K:Na ratio in the potassium feldspar, and the composition ranges from 0.9 mol.% Cn at K:Na = 1:1 to 2.9% Cn at K:Na = 3:1.

5.1.6. Comparative Silicate Mineralogy: Earth-Moon

Pyroxenes. A complete discussion of pyroxene minerals from basaltic meteorites, terrestrial basalts, and lunar basalts is given in *BVSP* (1981); the interested reader is referred to that book for more detailed figures and tables. One of the first-order differences between terrestrial and lunar pyroxenes is the abundance of Fe^{3+} in the former and its absence in the latter; this difference reflects the more reducing conditions (lower oxygen partial pressure) in gases on the Moon than on Earth. Some compositional differences between lunar and terrestrial pyroxenes are shown in the “pyroxene quadrilateral” plots of Fig. 5.14.

Lunar pyroxenes, including those from both mare basalts and highland rocks, have great chemical variability. They also differ in several respects from terrestrial pyroxenes. Pyroxenes from terrestrial ocean floor basalts, which are the most abundant basalts on Earth, are more magnesian than those from lunar mare basalts, and the lunar mare basalt pyroxenes are thus displaced compositionally toward the Fe^{2+} -rich side of the pyroxene quadrilateral relative to terrestrial ones. The Mg-rich nature of terrestrial oceanic pyroxenes reflects the high Mg content of the ocean-floor basalt magmas themselves, and this difference implies that the source region in the Earth’s mantle is significantly enriched in Mg relative to the source regions for lunar mare basalts.

Other important compositional differences between terrestrial oceanic pyroxenes and mare pyroxenes are seen in elements other than Mg, Fe, and Ca. These include Na, Cr, Fe^{3+} , Al, and Ti. In terrestrial oceanic basalt pyroxenes, the two most important ionic substitutions involving these elements are $\text{Fe}^{3+}(\text{octahedral}) + \text{Al}(\text{tetrahedral})$ and $\text{Ti}^{4+}(\text{octahedral}) + 2\text{Al}(\text{tetrahedral})$ (*Papike and Bence*, 1978). These two substitutions are of roughly equal importance in terrestrial oceanic basalt pyroxenes. However, the low oxygen partial pressures in gases on the Moon preclude the possibility of Fe^{3+} occurring in any mare basalt pyroxenes, and this substitution therefore cannot occur. As a result, lunar pyroxene crystal chemistry and pyroxene-melt interactions are significantly different from those on Earth. In lunar pyroxenes, the most important ionic substitutions involving the same elements are $\text{Ti}^{4+}(\text{octahedral}) + 2\text{Al}(\text{tetrahedral})$, $\text{Cr}^{3+}(\text{octahedral}) + \text{Al}(\text{tetrahedral})$, and $\text{Al}(\text{octahedral}) + \text{Al}(\text{tetrahedral})$.

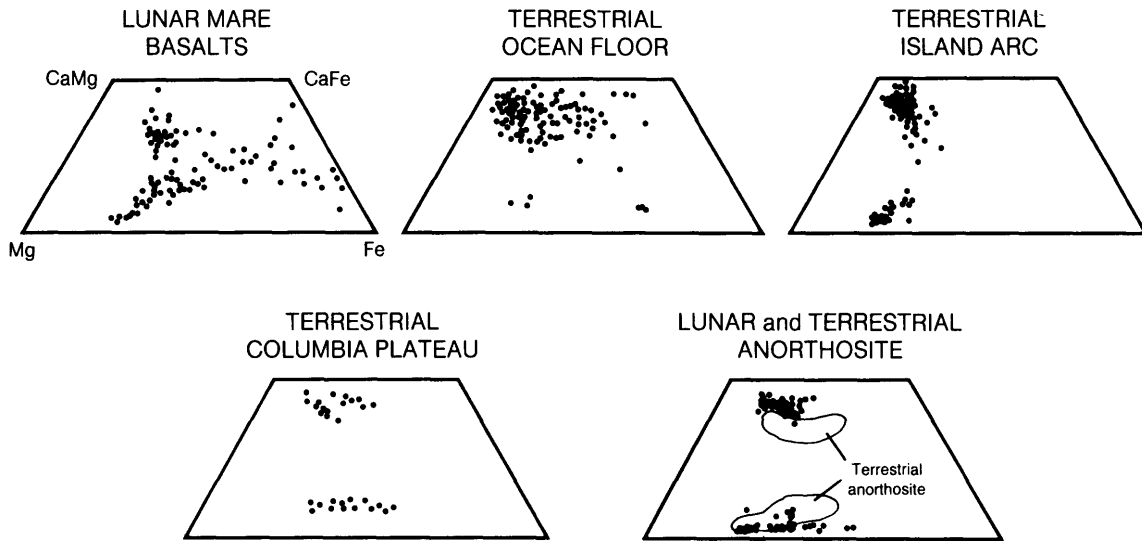


Fig. 5.14. Chemical comparisons between selected suites of lunar and terrestrial pyroxenes, shown on the “pyroxene quadrilateral” part of the compositional triangle CaSiO₃ (Ca) — MgSiO₃ (Mg) — FeSiO₃ (Fe); see Fig. 5.3. Many pyroxenes from lunar mare basalts are more Fe-rich than those from terrestrial lavas. Low-Ca and high-Ca pyroxenes from one group of deep-seated lunar plutonic rocks (*anorthosites*) tend to be more separated in composition than pyroxenes in comparable terrestrial rocks (data from Ashwal, 1990). The greater separation between lunar anorthosite pyroxenes may be a result of lower final crystallization temperatures. In the anorthosite diagram, dots (•) indicate lunar pyroxene compositions; fields of pyroxene analyses from terrestrial anorthosites are shown only in outline.

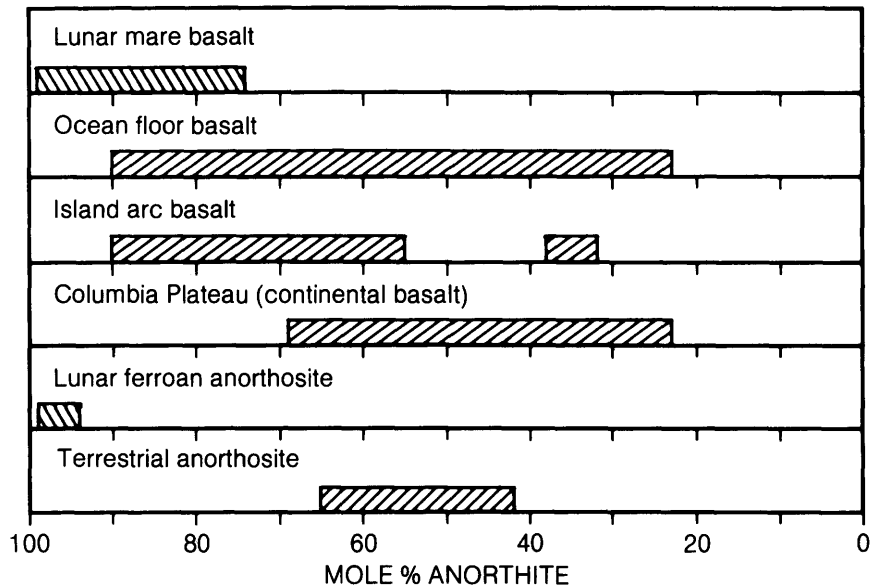


Fig. 5.15. Chemical comparisons between plagioclase feldspar from selected suites of lunar and terrestrial rocks, shown in terms of mol.% anorthite (CaAl₂Si₂O₈) in the feldspar. Feldspars from lunar mare basalts are generally more Ca-rich than those from comparable terrestrial volcanic rocks. Feldspars from lunar coarse-crystalline igneous rocks (e.g., ferroan anorthosites; see section 6.3) are far more Ca-rich than those from terrestrial anorthosites.

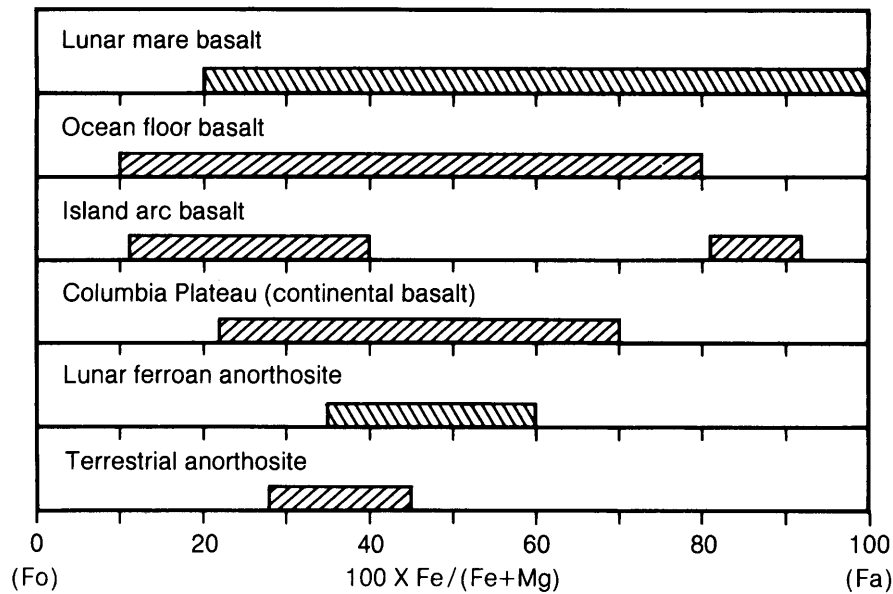


Fig. 5.16. Chemical comparisons between olivines from selected suites of lunar and terrestrial rocks, shown in terms of the atomic ratio $\text{Fe}/(\text{Fe} + \text{Mg})$ in the olivine. Although there is a high degree of overlap between the terrestrial and lunar populations, the most Fe-rich olivines occur in lunar mare basalts, while terrestrial basalts tend to contain the most Mg-rich ones.

Feldspars. The most significant differences between terrestrial and lunar feldspars (Fig. 5.15) are the striking enrichment of sodium in terrestrial plagioclase feldspars relative to lunar ones and the extreme scarcity of potassium feldspar on the Moon. These conditions reflect the overall depletion of the Moon in alkali elements (e.g., Na, K) relative to the Earth.

Olivines. Comparative lunar and terrestrial olivine compositions are illustrated in Fig. 5.16. Two main differences between terrestrial and lunar olivines are apparent. First, although significant Mg:Fe variation is present in both olivine groups, lunar mare olivines include more iron-rich compositions. Second, the most magnesian terrestrial olivines are more magnesian than the most Mg-rich lunar olivines. As with the lunar pyroxenes, this difference almost certainly reflects the more magnesian composition of the Earth's mantle relative to that of the Moon.

5.2. OXIDE MINERALS

The silicates, such as pyroxene, olivine, and feldspar, are the most abundant minerals in lunar rocks. With minor chemical differences, the common lunar silicate minerals are essentially the same as found on Earth. However, the nonsilicate minerals—especially the oxides—are far more distinctive in

lunar rocks. These oxide minerals are likely ores for resource extraction at a lunar base, and they are particularly abundant in some mare basalts (Table 5.2).

As mentioned earlier, several oxide minerals are important constituents of lunar rocks: *ilmenite* (FeTiO_3), *spinel* (with extensive chemical variations: $[(\text{Fe}, \text{Mg})(\text{Cr}, \text{Al}, \text{Fe}, \text{Ti})_2\text{O}_4]$), and *armalcolite* $[(\text{Fe}, \text{Mg})\text{Ti}_2\text{O}_5]$. The less abundant lunar oxide minerals include *rutile* (TiO_2), *baddeleyite* (ZrO_2), and *zirconolite* $[(\text{Ca}, \text{Fe})(\text{Zr}, \text{REE})(\text{Ti}, \text{Nb})_2\text{O}_7]$.

The major differences between the oxide minerals in lunar and terrestrial rocks arise from fundamental differences between both the surfaces and the interiors of these two planets. On the Moon, meteoroid impact and shock-metamorphic processes play a major role in altering rocks. These effects are not the same for all minerals. Shock damage and the formation of shock glasses out of minerals (e.g., *maskelynite* from plagioclase feldspar) are observed chiefly in lunar silicate minerals. Oxide minerals also record shock damage (Fig. 4.9a), but another effect of impact on oxide (and sulfide) minerals is to produce small amounts of chemical reduction where these minerals occur as soil particles.

The Moon has no significant atmosphere (see section 3.9). As a result, the Moon has no insulating blanket to (1) retain solar energy and (2) shield it

from cosmic and galactic rays, solar wind, and meteorite infall. Consequently, the surface of the Moon absorbs tremendous solar and cosmic radiation fluxes and undergoes extreme changes in temperature (section 3.5). Meteoroids of all sizes, from kilometers down to submicrometers in size, have for aeons bombarded the lunar surface at very high speeds (about 40,000–250,000 km/hr; Chapter 4). These meteoroid impacts are the only effective weathering and erosion process on the Moon. In addition, the complete lack of any water on the Moon results in the absence of chemical weathering that is so dominant on Earth. As a result, any unmelted and unvaporized meteoroid components, especially the native Fe metal phases, are preserved in the lunar soil. In addition, a steady flux of protons (hydrogen nuclei) and atoms (e.g., helium and carbon) from the solar wind are continually implanted in the uppermost surface of the lunar regolith. These atomic particles, which then become involved as reducing agents during the meteoroid and micrometeoroid impacts that produce shock metamorphism or complete melting, account for one of the distinctive aspects of lunar soil, namely the presence of slaggy, composite particles (*agglutinates*) that contain myriad minute Fe⁰ grains (i.e., native Fe metal).

In addition to the different surface environments of the Earth and Moon, the original conditions of formation of lunar rocks, most notably the volcanic ones, are different from those on Earth in three main aspects: (1) higher temperatures of formation; (2) lower oxygen partial pressures during formation; and (3) complete absence of water. These factors combine to produce oxide minerals on the Moon that are very different from those found on Earth. The temperatures at which igneous rocks melt and crystallize are much higher on the Moon than on Earth because of the absence of water, a chemical species that has a major effect in lowering the melting temperatures (*fluxing*) of these melts. This temperature differential is not large, generally about 100°–150°C for melting temperatures of about 1200°C, and this difference alone would not produce any major changes between terrestrial and lunar magmas.

In contrast, the differences in oxygen partial pressure between the Earth and Moon (Fig. 5.17) lead to pronounced differences in mineralogy (Sato *et al.*, 1973; Sato, 1978; Haggerty, 1978b). As in the case of the silicate minerals, the low oxygen partial pressure prevents any completely oxidized iron (Fe³⁺) from forming in the oxide minerals as well. Indeed, oxygen partial pressures on the Moon are so low that native iron (Fe⁰) is stable with FeO (the mineral *wüstite*—Wu in Fig. 5.17). As a result, metallic iron (Fe⁰) is

ubiquitous in lunar samples of all kinds. Other elements in lunar minerals are also present in unusually low oxidation states (e.g., Ti³⁺, Co²⁺, Cr²⁺, P³⁻) in comparison to terrestrial minerals.

The oxide minerals, although less abundant than silicates in lunar rocks, are of great significance because they retain signatures of critical conditions of formation (e.g., limited availability of oxygen) from the rocks in which they occur. Whereas most of the silicate minerals differ little from those on Earth, the opaque oxide phases reflect the reducing, anhydrous conditions that prevailed during their formation. By combining analyses of lunar oxide minerals with the results of laboratory experiments on their synthetic equivalents, the temperature and oxygen pressure conditions during formation of lunar rocks can be estimated (Fig. 5.17; see Sato *et al.*, 1973; Usselman and Lofgren, 1976).

Because their oxygen is more weakly bonded than in silicate minerals, oxide minerals are obvious and important potential feedstocks for any future production of lunar oxygen and metals. On Earth, similar oxide minerals commonly occur in economically recoverable quantities called *ore deposits*. However, most of these deposits, and the minerals in them, have formed from *hydrothermal* waters (100°–300°C or hotter). The Moon has little if any water, and the presence of similar hydrothermal ore deposits on the Moon is not probable. However, there are other means of concentrating oxide minerals into exploitable ores. *Crystal settling* of dense minerals (e.g., chromite, ilmenite, and minerals containing the platinum-group elements) is possible within silicate magmas, if the magma remains liquid for a long enough time. On Earth, such accumulations are normally found in *layered intrusions*. These bodies form from large masses of magma that have been emplaced into crustal rocks without reaching the Earth's surface. Under such conditions, cooling is slower, and physical separation processes—which may include convection as well as settling—have time to act. Well-known examples of ore deposits resulting from these processes occur in the Stillwater Anorthosite Complex (Montana) and the Bushveld Igneous Complex (South Africa). Can similar deposits form in the very different environment of the Moon?

The accumulation of dense oxide minerals as they crystallize from a magma depends on their *settling velocity* in the less dense silicate melt. The higher the settling velocity, the further the minerals can fall before the melt solidifies, and the more chance they have to accumulate. The settling velocity in the melt can be approximated by *Stokes' Law*, which relates settling velocity (*v*) to other parameters. For spheres, Stokes' Law is

$$v = (2/9)gr^2[(\rho_s - \rho)/\eta]$$

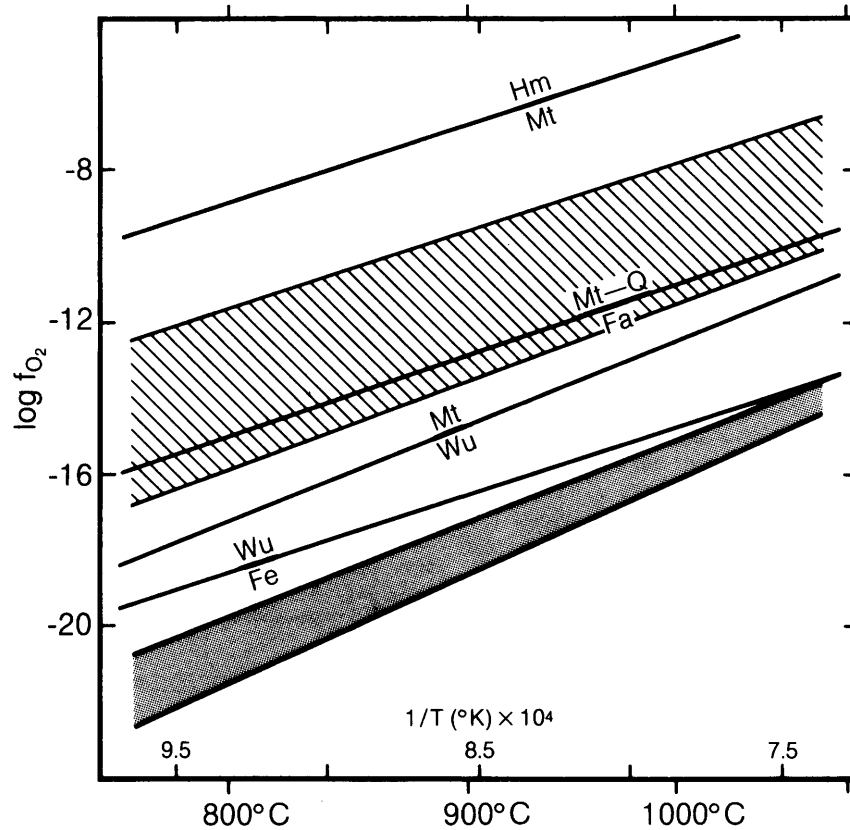


Fig. 5.17. Stability regions for various Fe-bearing minerals, shown as a function of *oxygen fugacity* (f_{O_2}) and temperature (T). Oxygen fugacity is the actual thermodynamic chemical potential of oxygen in a gas mixture, which, because of nonideal gas behavior, is not adequately represented by partial pressure. Minerals shown are metallic iron (Fe), wüstite (Wu)($Fe_{1-x}O$), magnetite (Mt)(Fe_3O_4), the Fe-olivine fayalite (Fa)(Fe_2SiO_4), quartz (Q)(SiO_2), and hematite (Hm)(Fe_2O_3). Mineral assemblages become more oxidized in going from the bottom to the top of the diagram. The f_{O_2} - T region for terrestrial volcanic activity, estimated from the minerals in terrestrial rocks, is shown as a zone marked by diagonal lines and includes the relatively oxidized fayalite/(quartz + magnetite) boundary. The equivalent region for lunar basalts (gray zone) is located entirely below the iron/wüstite boundary. Note that the minerals containing Fe^{3+} (Mt and Hm) are not stable in the lunar region, and that Fe metal is stable in lunar rocks.

where g is the acceleration of gravity, r is the radius of the sphere, ρ_s and ρ_l are the densities of solid and melt respectively, and η is the viscosity of the melt. The most important factors to be considered in comparing lunar and terrestrial environments are the acceleration due to gravity (g), which directly affects v , and the viscosity (η) of the silicate melt, which affects v inversely. The acceleration due to gravity on the Moon's surface is about 160 cm/sec^2 , compared to 980 cm/sec^2 on Earth. This factor will produce a sixfold lesser settling velocity in lunar magmas if all other factors are equal. However, this effect is countered by the fact that the viscosity of an average lunar basaltic melt is 10 to 100 times

less than that of a terrestrial basaltic magma. This viscosity difference results from two circumstances: (1) viscosity decreases with temperature and, as noted above, the average crystallization temperatures of lunar basalts are $100^\circ\text{--}150^\circ\text{C}$ higher than terrestrial basalts; and (2) typical lunar basalts are considerably higher in FeO and lower in Al_2O_3 than their terrestrial counterparts, making them less viscous at any given temperature. These effects combine to greatly lower the viscosities of lunar magmas. The reduction in viscosity (1/10 to 1/100 \times Earth magmas) overwhelms the effect of lower lunar gravity ($1/6 \times$ Earth), and crystals will have greater settling velocities on the Moon. It is therefore

possible that layered ore deposits similar to or even larger than those on Earth may occur on the Moon (see Taylor and Lu, 1990).

The following discussions of individual oxide minerals have drawn upon ideas and data from many references that provide detailed information about the subject, especially BVSP (1981), Frondel (1975), Levinson and Taylor (1971), LAPST (1985), Papike and Vaniman (1978), Papike et al. (1976), Smith (1974), Smith and Steele (1976), and S. R. Taylor (1975, 1982).

5.2.1. Ilmenite

Ilmenite, with the ideal formula FeTiO₃, is the most abundant oxide mineral in lunar rocks. The amount of ilmenite in these rocks is a function of the bulk composition of the magma from which the ilmenite crystallized (Rutherford et al., 1980; Norman and Ryder, 1980; Campbell et al., 1978); the higher the TiO₂ content of the original magma, the higher the ilmenite content of the rock. Ilmenite forms as much as 15-20% by volume of many Apollo 11 and 17 mare basalts (McKay and Williams, 1979). However, the volume percentages of ilmenite in mare basalts vary widely across the Moon as indicated by the range of TiO₂ contents in samples from different lunar missions (Table 5.2 and Fig. 5.18).

The ilmenite crystal structure is hexagonal (Fig. 5.19) and consists of alternating layers of Ti- and Fe-containing octahedra. Most lunar ilmenite

TABLE 5.2. Summary of modal data (vol.%) for mare basalts (after BVSP, 1981, p. 255).

	Oxide		Pyroxen Feldspa	
	Minerals	e	r	Olivine
A-17 high Ti	24.4	47.7	23.4	4.6
A-11 high K	20.6	57.5	21.7	0.1
A-17 low K	15.1	51.6	33.3	-
A-11 low K	14.6	50.9	32.2	2.3
A-12 ilmenite	9.3	61.1	25.9	3.6
A-12 pigeonite	9.1	68.4	21.1	1.4
A-12 olivine	7.1	53.5	19.2	20.2
L-16 aluminous	7.1	51.5	41.2	0.1
A-15 olivine	5.5	63.3	24.1	7.0
A-15 pigeonite	3.7	62.5	33.8	-
A-14 aluminous	3.2	53.8	43.0	-
L-24 ferrobasalt	1.8	48.6	39.1	10.4
L-24	1.4	60.2	34.2	4.2
ferrobasalt	1.0	61.7	31.9	5.4
A-17 VLT				

Modal data normalized to 100% for the four phases considered, in Apollo (A) and Luna (L) samples. Ordered from top to bottom in terms of decreasing modal content of opaque oxide minerals.

contains some Mg substituting for Fe (Table A5.11), which arises from the solid solution that exists between ilmenite (FeTiO₃) and MgTiO₃, the mineral *geikielite*. Other elements are present only in minor to trace amounts (i.e., <1%); these include Cr, Mn, Al, and V. In addition, ZrO₂ contents of up to 0.6% have

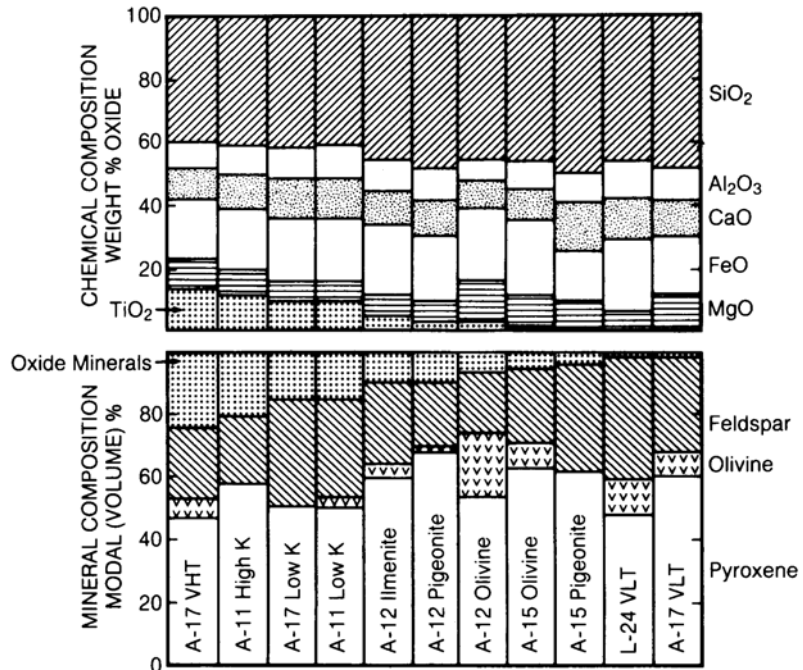


Fig. 5.18. Variations in major-element chemistry and modal (vol.%) mineral content in a range of lunar mare basalts. Analyses are arranged from left to right in order of decreasing TiO₂ (or oxide mineral) content (adapted from BVSP, 1981).

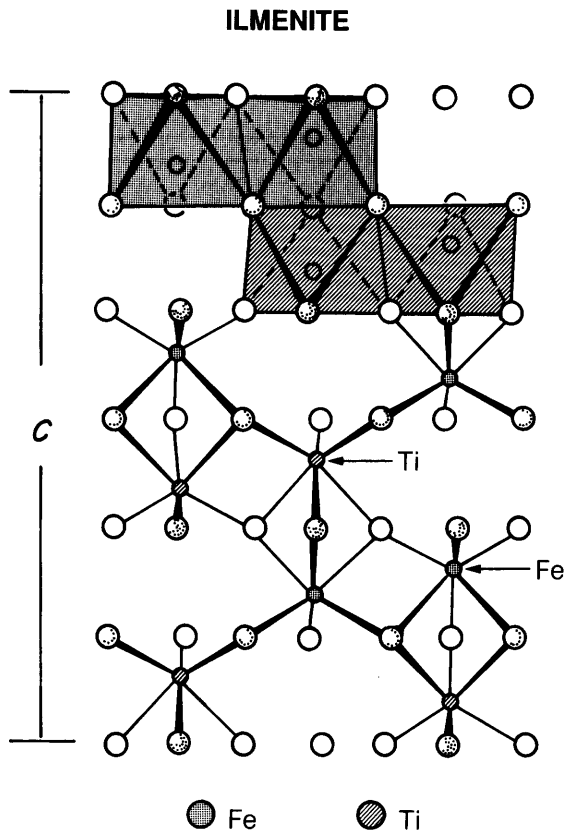


Fig. 5.19. Crystal structure of ilmenite, composed of octahedra defined by oxygen atoms, which contain Fe^{2+} , Ti^{4+} , and other cations. The unit-cell dimension along the c -axis is shown as c (after Papike *et al.*, 1976). The patterns used to distinguish Fe from Ti sites apply to both octahedra (upper part of structure) and cations (lower part of structure).

been reported from ilmenites in Apollo 14 and 15 basalts (El Goresy *et al.*, 1971a,b; Taylor *et al.*, 1973b). In fact, the partitioning of ZrO_2 between ilmenite and coexisting ulvöspinel (Fe_2TiO_4) has been experimentally determined (Taylor and McCallister, 1972) and has been used as both a geothermometer (to deduce temperatures during crystallization) and as a cooling-rate indicator (Taylor *et al.*, 1975, 1978; Uhlmann *et al.*, 1979). Although terrestrial ilmenite almost always contains some Fe^{3+} , lunar ilmenite contains none, a result of the more reducing magmatic conditions within the Moon. Table A5.12 lists representative ilmenite compositions from a wide range of lunar rock types.

The compositions of lunar ilmenites plot along the FeTiO_3 - MgTiO_3 join; variation from FeTiO_3 is often expressed in weight percentage of MgO (Fig. 5.20).

The appreciable MgO contents of many lunar ilmenites (>3% MgO) are similar to terrestrial ilmenites that formed at high pressure in rocks called *kimberlites* (kimberlites come from deep in the Earth's mantle and are the igneous rocks that often contain diamonds). It was originally thought that the high Mg content in some lunar ilmenites was produced, as in terrestrial kimberlites, by high pressures of formation. In general, the ilmenites with the highest Mg contents tend to come from relatively high-Mg rocks; ilmenite composition correlates with the bulk composition of the rock and therefore reflects magmatic chemistry rather than pressure. In detail, the distribution of Mg between ilmenite and coexisting silicate minerals in a magma is related to the timing of ilmenite crystallization relative to the crystallization of the other minerals. This *crystallization sequence* is itself a function of cooling rate and other factors, most notably the oxygen partial pressure (Usselman *et al.*, 1975). However, it is doubtful that the Mg contents in ilmenite all represent equilibrium conditions, because ilmenite compositions can vary significantly, even within distances of a few millimeters, within a single rock (Fig. 5.21).

Ilmenite commonly occurs in mare basalts as bladed crystals up to a few millimeters long. It typically forms near the middle of the crystallization sequence, where it is closely associated with pyroxene. It also forms later in the sequence and at lower temperatures, where it is associated with native Fe and troilite. In Apollo 17 rocks, ilmenite is frequently associated with armalcolite (see section 5.2.3) and occurs as mantles on armalcolite crystals (e.g., El Goresy *et al.*, 1974; Haggerty, 1973a; Williams and Taylor, 1974). In these instances, ilmenite has possibly formed by the reaction of earlier armalcolite with the melt during crystallization.

The stability curve of pure ilmenite as a function of temperature and oxygen pressure is significantly different from that of ulvöspinel (Taylor *et al.*, 1973b), the spinel phase with which it is commonly associated (Fig. 5.22), implying that the two minerals did not crystallize together. The data suggest that, in these mineral assemblages, ilmenite has formed by solid-state reduction (oxygen loss) of this high-Ti spinel at temperatures below their melting points (*subsolidus reduction*, see section 5.2.2). Rare grains of ilmenite also contain evidence for subsolidus reduction of ilmenite to rutile (TiO_2) + native Fe; other grains show reduction to chromite (FeCr_2O_4) + rutile + native Fe.

Ilmenite as a source of oxygen. The production of oxygen on the Moon from lunar materials is a major goal for a lunar base (National Commission on Space, 1986). McKay and Williams (1979), Williams

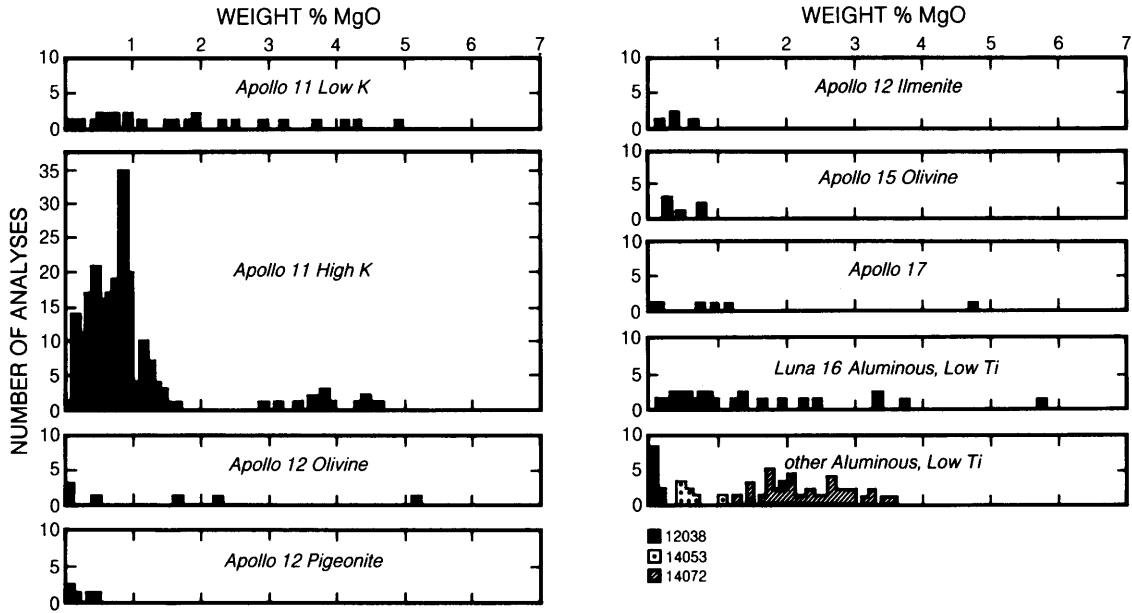
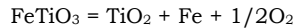


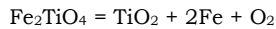
Fig. 5.20. MgO contents (wt.%) of ilmenites in mare basalt samples from various lunar sites (adapted from Papike et al., 1976). The terms “low K,” “high K,” “olivine,” “pigeonite,” “ilmenite,” and “aluminous, low-Ti” are modifiers used to describe various basalt chemical types (for example, olivine basalts are relatively Mg-rich, pigeonite basalts are relatively Si-rich, and ilmenite basalts are relatively Ti-rich within the general group of low-Ti mare basalts from Apollo 12; see section 6.1 and Table A5.1 for more information on mare basalt types).

and Erstfeld (1979), Williams et al. (1979), and Rao et al. (1979) first suggested that ilmenite might usefully be reduced to rutile + Fe with the release of oxygen. The lowest curve below 1150°C in Fig. 5.22 represents the conditions for the reaction of interest



This reaction could ideally produce 10.5 wt.% O₂ from a given mass of ilmenite. The reaction could be carried out by using hydrogen to reduce the ilmenite. The hydrogen might be obtained from the indigenous solar-wind protons (hydrogen nuclei) that are implanted in the lunar soil and in the ilmenite grains within it (Blanford, 1982; Kiko et al., 1979). Preliminary studies have shown the feasibility of this type of oxygen production (Williams, 1985; Gibson and Knudsen, 1985).

Another possible source of oxygen is the spinel phase, ulvöspinel (Fe₂TiO₄), according to the reaction



This reaction would ideally produce 14.3 wt.% O₂ from a given mass of ulvöspinel. Ulvöspinel is a very abundant mineral (several weight percent) in many mare basalts, particularly those from the Apollo 12, 15, and 17 sites. However, the composition of ulvöspinel is quite variable (see section 5.2.2 below), and this variability could introduce complications into its use for oxygen production.

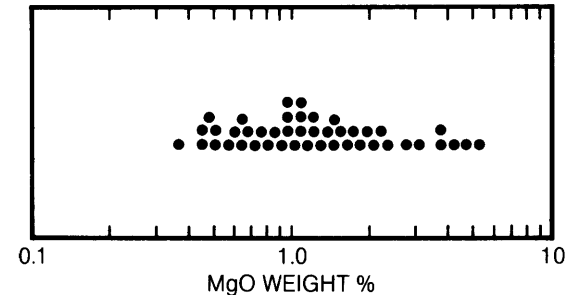


Fig. 5.21. Variations in the MgO (wt.%) content of ilmenites from one sample of lunar mare basalt (sample 12018; see also Fig. 5.26). Each dot represents one analysis. The ilmenite MgO content varies over a wide range, between 0.3% and 6% (adapted from El Goresy et al., 1971b).

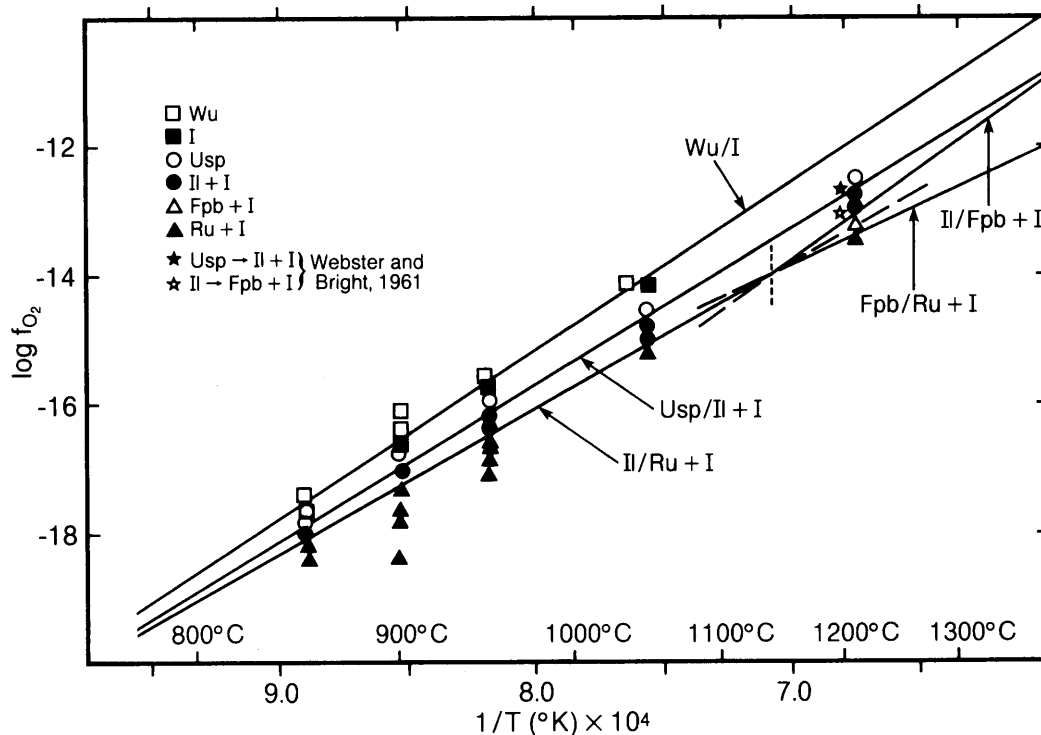


Fig. 5.22. Stability relations of several Fe- and Ti-bearing minerals, shown as a function of oxygen fugacity (f_{O_2}) and temperature (T). The diagram shows possible reactions in the Fe-Ti-O system (adapted from Taylor *et al.*, 1972). Abbreviations: Wu = wüstite; I = iron; Usp = ulvöspinel; Il = ilmenite; Fpb = ferropseudobrookite; Ru = rutile. In labeling the curves, the oxidized side of the reaction (upper side of the curve) is listed before the reduced part (lower side of the curve), e.g., Wu/I ($Fe_{1-x}O/Fe$). The labels for each curve thus show (oxidized side of the reaction)/(reduced side of the reaction). In going from reduced conditions (bottom) to oxidizing ones (top), at temperatures below 1150°C, the sequence of reactions is rutile + iron + oxygen = ilmenite; ilmenite + iron + oxygen = ulvöspinel; and iron + oxygen = wüstite. At higher temperatures, the mineral ferropseudobrookite appears in the sequence.

5.2.2. Spinel

Spinel is the name for a group of minerals, all with cubic crystal symmetry, that have extensive solid solution within the group. Spinel is the second most abundant opaque mineral on the Moon, second only to ilmenite, and they can make up as much as 10% of the volume of certain basalts, most notably those from the Apollo 12 and 15 sites. The general structural formula for these minerals is $^{IV}A^{VI}B_2O_4$, where IV and VI refer to four-cornered (tetrahedral) and six-cornered (octahedral) polyhedra of oxygen atoms.

The basic spinel structure is a cubic array of oxygen atoms. Within the array, the tetrahedral A-sites (black dots in Fig. 5.23) are occupied by one-third of the cations, and the octahedral B-sites

(vertical-line shading) are occupied by the remaining two-thirds of the cations. In a *normal spinel* structure the divalent cation, such as Fe^{2+} , occupies only the tetrahedral sites, and the two different sites each contain only one type of cation (e.g., $FeCr_2O_4$). If the divalent cation occurs in one-half of the B-sites, the mineral is referred to as an *inverse spinel* [e.g., $Fe(Fe,Ti)_2O_4$]. In lunar spinels, the divalent cations (usually Fe^{2+} or Mg^{2+}) occupy either the A- or both A- and B-sites (i.e., there are both normal and inverse lunar spinels), and higher-charge cations (such as Cr^{3+} , Al^{3+} , Ti^{4+}) are restricted to the B-sites.

The relations of the various members of the spinel group can be displayed in a diagram known as the *Johnston compositional prism* (Fig. 5.24). The end members represented include *chromite*, $FeCr_2O_4$; *ulvöspinel*, $FeFeTiO_4$ (commonly written as Fe_2TiO_4 ,

SPINEL

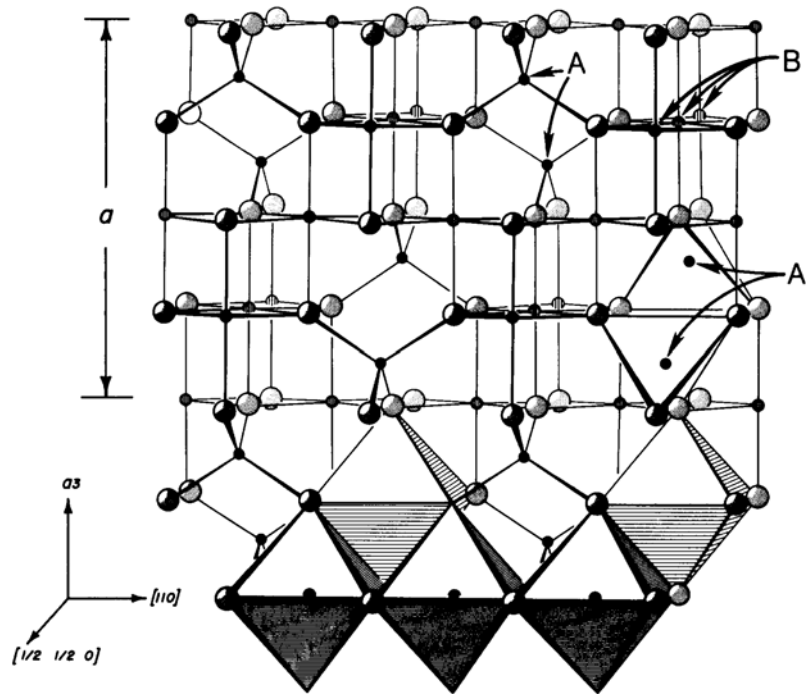
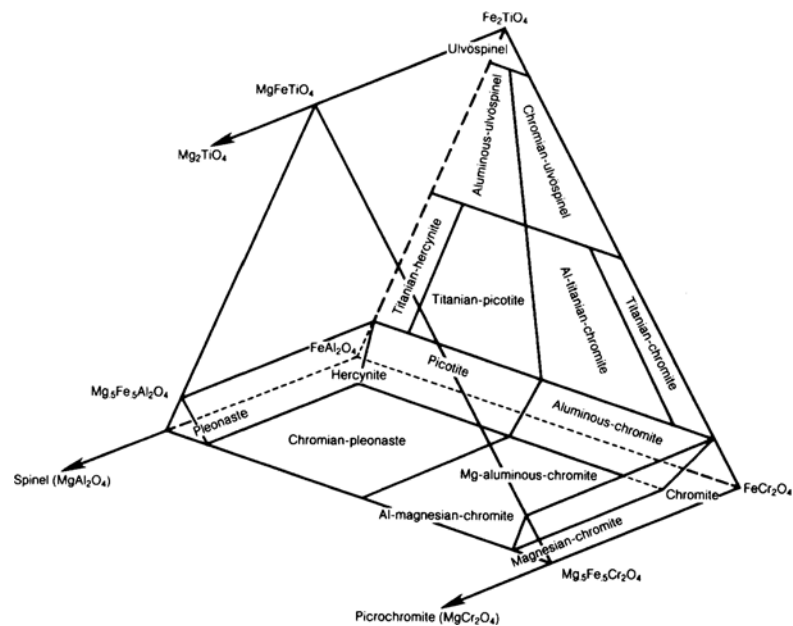


Fig. 5.23. Crystal structure of spinel, composed of a cubic-close-packed array of oxygen atoms. This structure provides two interstitial sites, ^{IV}A (a tetrahedral site coordinated with four oxygens) and ^{VI}B (an octahedral site coordinated with six oxygens). Both A and B can accommodate a wide variety of cations. In this diagram, the A-sites are indicated by small black dots, and the B-sites by somewhat larger shaded spheres. The largest shaded spheres are oxygen atoms. The edge of the cubic unit cell is shown as *a*. The three axes at the lower left indicate reference crystallographic directions for orienting the figure (modified from Papike et al., 1976).

Fig. 5.24. Compositional diagram (modified Johnston prism) showing names used for different chemical varieties of spinels (adapted from Haggerty, 1972a). Fe-rich end-member compositions used in this diagram are *chromite* (FeCr_2O_4), *ulvöspinel* (Fe_2TiO_4 or FeFeTiO_4), and *hercynite* (FeAl_2O_4). The prism is filled in with mineral names only in that half where Fe/Mg proportions are >1 ; the more Mg-rich spinels are relatively rare, but compositions closer to *spinel* (*sensu stricto*; MgAl_2O_4) than to hercynite occur in some highland rocks (Table A5.13, columns 56 and 57).



but this is an inverse spinel with Fe²⁺ in both A- and B-sites); *hercynite*, FeAl₂O₄; and *spinel (sensu stricto)*, MgAl₂O₄. Intermediate compositions among these end members are designated by using appropriate modifiers (e.g., *chromian ulvöspinel* or *titanian chromite*). Some common solid solution compositions also have distinct names, such as *pleonaste* for compositions between MgAl₂O₄ and FeAl₂O₄. Figure 5.25 is a set of modified Johnston compositional prisms that show the compositional ranges in lunar spinels.

As shown in Fig. 5.25, most lunar spinels have compositions generally represented within the three-component system: FeCr₂O₄ — FeFeTiO₄ — FeAl₂O₄, and their compositions can be represented on a flat triangular plot. The addition of Mg as another major component provides a third dimension to this system; the compositions are then represented as points within a limited Johnston compositional prism in which the Mg-rich half (Mg > Fe) is deleted because most lunar spinels are Fe-rich (e.g., *Agrell et al., 1970; Busche et al., 1972; Dalton et al., 1974;*

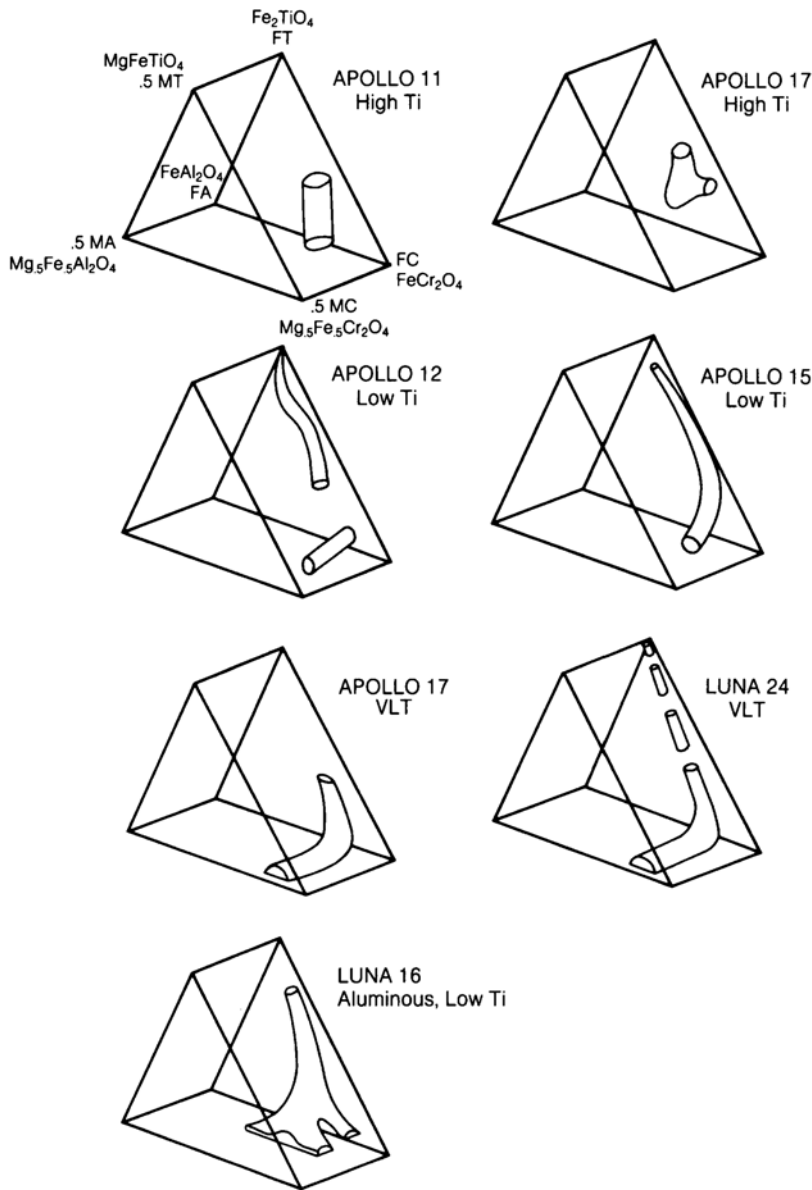


Fig. 5.25. Diagrams showing ranges of chemical variation of lunar spinels in mare basalt samples from individual Apollo and Luna landing sites. Each diagram is a modified Johnston prism, showing only that half for Fe/Mg > 1 (see Fig. 5.24); the mare basalt spinels consist mostly of early-formed chromite varieties and late-crystallizing ulvöspinel. Note the wide variation in spinel compositions between sites and often within a single site (modified from *Haggerty, 1978a*).

El Goresy et al., 1971b, 1976; *Haggerty*, 1971a, 1972b,c, 1973b, 1978a; *Nehru et al.*, 1974, 1976; *Taylor et al.*, 1971). As is apparent from Figs. 5.24 and 5.25, most lunar spinel compositions fall between chromite and ulvöspinel. The principal cation substitutions in these lunar spinels can be represented by $\text{Fe}^{2+} + \text{Ti}^{4+} = 2(\text{Cr,Al})^{3+}$. Other cations commonly present include V, Mn, and Zr. Representative compositions are given in Table A5.13.

Spinel is ubiquitous in lunar mare basalts, where they occur in various textures and associations. These spinels are invariably zoned chemically. Such zoning occurs particularly in Apollo 12 and 15 rocks, in which chromite is usually the first mineral to crystallize from the melt. As the chromite crystals continue to grow, their TiO_2 and FeO contents increase, and their Al_2O_3 , MgO , and Cr_2O_3 contents decrease, with the overall composition moving toward that of ulvöspinel (Fig. 5.25; Table A5.13). In most of the basalts that contain both titanian chromites and chromian ulvöspinel, the latter phase occurs as overgrowths and rims surrounding the

chromite crystals. (Some individual ulvöspinel grains also occur as intermediate to late-stage crystallization products.)

When observed using a reflected-light microscope, the ulvöspinel in these composite crystals appears as tan to brown rims about the bluish chromite. The contact between the two is commonly sharp, indicating a discontinuity in the compositional trend from core to rim (Fig. 5.25). This break probably records a cessation in growth, followed later by renewed crystallization in which the earlier chromite grains acted as nuclei for continued growth of ulvöspinel (*Cameron*, 1971). Some rocks (e.g., 12018; Fig. 5.26) contain spinel grains with diffuse contacts that are also reflected in gradational changes in the composition of the solid solution. These textures could result from continuous crystallization of the spinel or from later reequilibration by solid-state diffusion within the crystal (*Taylor et al.*, 1971).

Although most abundant in mare basalts, spinels also occur in highland rocks such as anorthosites, anorthositic gabbros, troctolites, and impact mix-

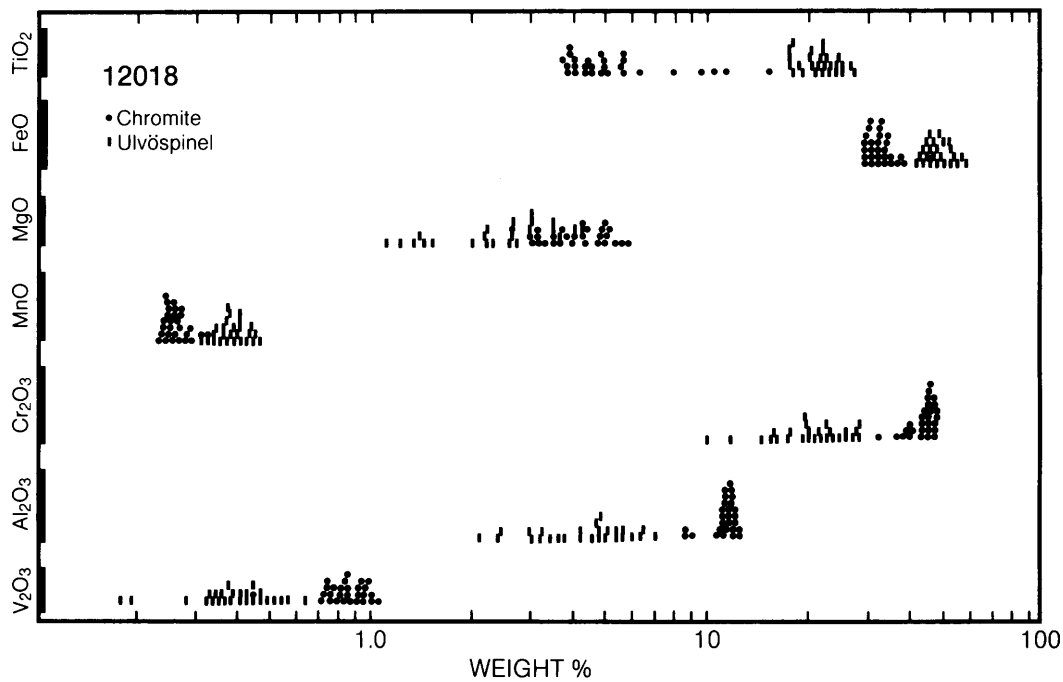


Fig. 5.26. Distribution of chemical compositions (oxide wt.%) of chromites and ulvöspinel in Apollo 12 low-Ti mare basalt 12018 (see also Fig. 5.21) (adapted from *El Goresy et al.*, 1971b). The diagram shows individual analyses for chromite (dots) and ulvöspinel (small bars) in wt.% abundance of several oxide constituents (V_2O_3 , Al_2O_3 , etc.). In major oxide content, chromites (high Cr_2O_3) are readily distinguished from ulvöspinel (high TiO_2 and FeO). Chromites also have relatively high contents of the minor oxides Al_2O_3 , MgO , and V_2O_3 , but are lower in MnO . Note that the ulvöspinel compositions are less tightly clustered than the chromites (i.e., the ulvöspinel are more chemically zoned).

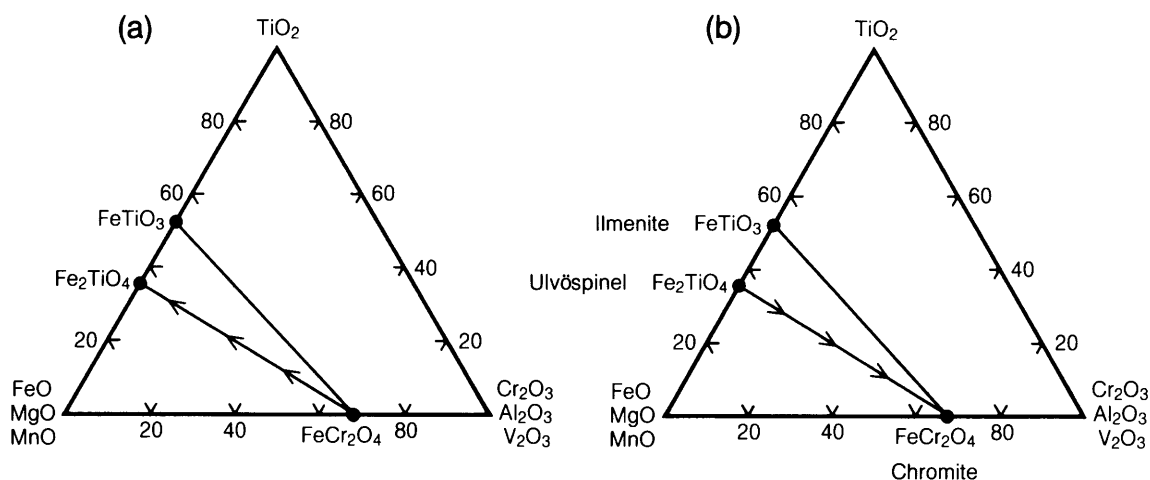


Fig. 5.27. Stability relations between ulvöspinel (Fe_2TiO_4) and chromite (FeCr_2O_4) during (a) crystallization and (b) reduction during cooling of the solid rock (the example here is an Apollo 14 impact melt). During crystallization, spinels change in composition from chromite toward ulvöspinel. As the spinels are reduced when the rock cools, the ulvöspinel breaks down to form ilmenite (FeTiO_3) and Fe metal, while that portion that retains the spinel structure reverts to a more chromite-rich composition (adapted from *El Goresy et al.*, 1972).

tures of these rock types (e.g., *Haselton and Nash*, 1975; see sections 6.3 and 6.4). The spinels in anorthositic (plagioclase-rich) highland rocks tend to be chromite with lesser amounts of MgO, Al_2O_3 , and TiO_2 (Table A5.13). However, certain highland rocks, notably the olivine-feldspar types (*troctolites*), contain pleonaste spinel. The composition of this spinel is slightly more Fe- and Cr-rich than an ideal composition precisely between the end members MgAl_2O_4 and FeAl_2O_4 (Fig. 5.25). This spinel is not opaque; under the microscope, it stands out because of its pink color, high index of refraction, and isotropic character in cross-polarized light.

Subsolidus reduction. Crystals that originally form from a melt may continue to change while the rock is solid but still hot. Such *subsolidus reactions* can occur at temperatures significantly below the melting point. In terrestrial rocks, the oxygen pressure is relatively high during such changes, and terrestrial subsolidus reactions generally involve oxidation. However, in lunar rocks and soils, evidence for *subsolidus reduction* is extremely common. Lunar ulvöspinel grains are often reduced to ilmenite + native Fe; more rarely, ilmenite is reduced to rutile + native Fe or to chromite + rutile + native Fe (*El Goresy et al.*, 1971a, 1972; *Haggerty*, 1971b, 1972a,d, 1977; *McCallister and Taylor*, 1973; *Taylor et al.*, 1971). The causes of this late-stage reduction of ulvöspinel are speculative, but the effects have been quite pervasive (*Brett*, 1975; *Haggerty*, 1978b; *Sato*, 1978). In a few rocks (e.g., 14053, 14072), the Ti-

rich ulvöspinel is reduced to a mixture of Ti-poor spinel + titanian chromite + ilmenite + native Fe (*El Goresy et al.*, 1972; *Haggerty*, 1972a).

Compositional changes of the spinel during later subsolidus reduction are the opposite of those observed during primary crystallization (*El Goresy et al.*, 1972; *Haggerty*, 1972c; *Taylor et al.*, 1971). During normal crystallization of spinel from a melt, the spinel typically begins as chromite and changes its composition toward ulvöspinel as growth continues (Fig. 5.27a). The net effect of later subsolidus reduction on the ulvöspinel is to form ilmenite + native Fe; the residual components enrich the remaining spinel so that its composition moves back toward chromite (Fig. 5.27b). The secondary generation of native Fe during these subsolidus reactions is of some importance. It provides evidence for the reducing nature of the reaction. It also increases the Fe metal content of the rock involved. Spinel grains in the lunar soil also readily undergo reduction when shock metamorphosed by impacting micrometeoroids. This reduction is possibly caused by the presence in the soil of implanted solar-wind particles, notably the elements hydrogen and carbon, which create a reducing environment when heated to high temperatures during impact.

5.2.3. Armalcolite

Armalcolite is named after the Apollo 11 astronauts (ARMstrong, ALdrin, and COLLins). It was first recognized as a new mineral in samples from the

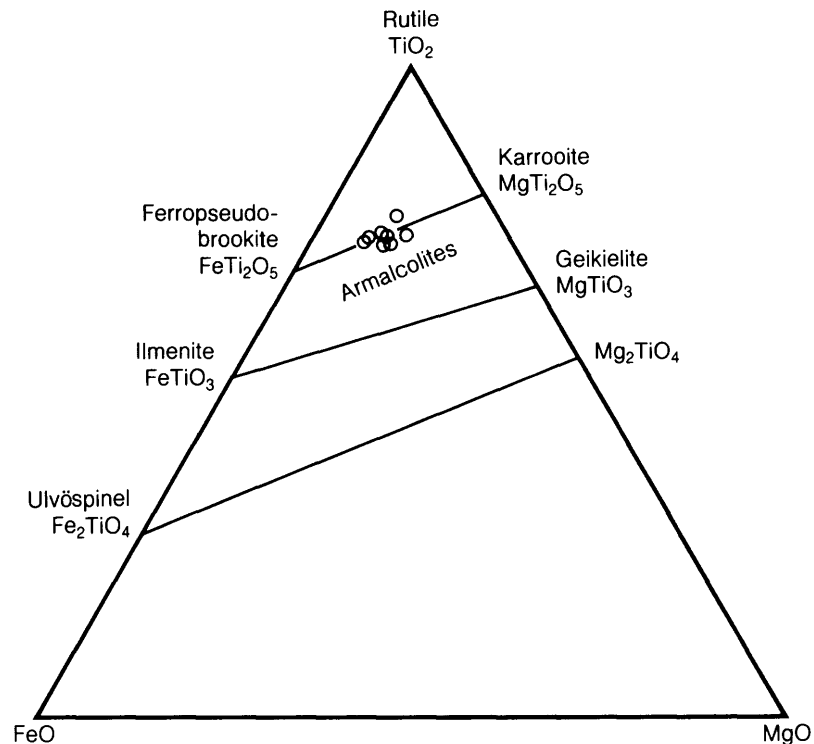


Fig. 5.28. Triangular compositional plot of the system FeO — MgO — TiO₂ (in wt.%), showing armalcolite compositions, which plot along the join FeTi₂O₅ — MgTi₂O₅ (adapted from Anderson *et al.*, 1970).

Apollo 11 site, where it is a minor constituent in Ti-rich basalts (Anderson *et al.*, 1970). Its composition is strictly defined as (FeO₅MgO₅)Ti₂O₅, but the name is also used in a broader sense to describe *solid solutions* whose compositions vary between FeTi₂O₅ and MgTi₂O₅ (Fig. 5.28).

Armalcolite has a crystal structure like that of the mineral *ferropseudobrookite* (FeTi₂O₅; Fig. 5.29). Titanium is restricted to the M2 site, and Mg, Al, and Fe occupy the M1 site. Detailed chemical analyses of armalcolite, with careful consideration of the ionic charge balance required within the crystal structure, have shown that appreciable Ti is present as Ti³⁺ rather than Ti⁴⁺ (Fig. 5.30; Wechsler *et al.*, 1976). Kesson and Lindsley (1975) examined the effects of Ti³⁺, Al³⁺, and Cr³⁺ on the stability of armalcolite, and later work showed that the Ti³⁺ content can be used to deduce the *fugacity* (effective partial pressure in terms of thermodynamic chemical potential) of oxygen during crystallization (Stanin and Taylor, 1979, 1980). The presence of reduced Ti (Ti³⁺) as well as Ti⁴⁺ in lunar armalcolites, due to the strongly reducing lunar environment, serves to distinguish between the lunar mineral from the armalcolites subsequently identified on Earth (Cameron and Cameron, 1973), in which all Ti occurs as Ti⁴⁺.

The occurrence of armalcolite is restricted to rocks with high TiO₂ content that have also cooled rapidly. This rapid cooling (*quenching*) is essential to prevent early-formed armalcolite from reacting with the remaining liquid to form magnesian ilmenite. There are three distinct compositional types of armalcolite in lunar samples (Haggerty, 1973a; Fig. 5.31). The first and most abundant type is *Fe-Mg armalcolite* ("A" in Fig. 5.31), and it is represented by intermediate compositions in the solid solution series FeTi₂O₅-MgTi₂O₅ (Table A5.14). This variety is the typical armalcolite observed in the high-Ti Apollo 11 and 17 basalts, although it is also found in basalt samples from all missions. Two varieties of this type have been characterized by their appearance in reflected-light microscopy as gray- vs. tan-colored; Haggerty (1973b) referred to these as ortho- and para-armalcolite respectively. They have overlapping compositions (Papike *et al.*, 1974; Williams and Taylor, 1974) and appear to be present in a range of different textures. The most common type is the gray variety, which occurs with rims of high-Mg ilmenite, especially in Apollo 17 samples. There were suggestions that these two varieties had different crystal structures, but the crystal structures have since been shown to be identical (Smyth, 1974).

ARMALCOLITE

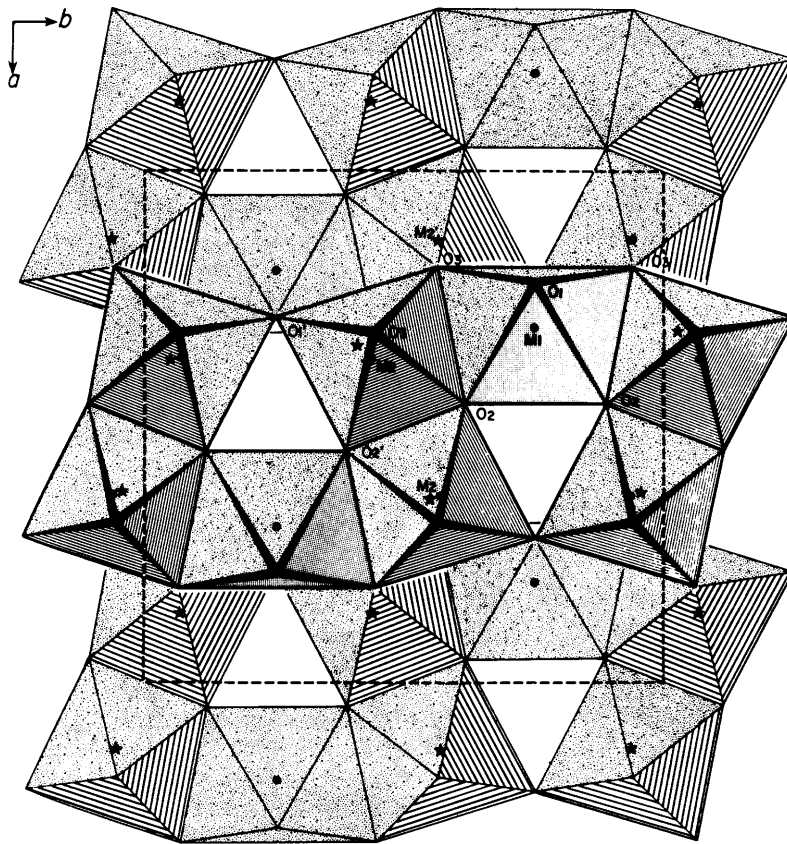


Fig. 5.29. Crystal structure of armalcolite, composed of octahedra defined by oxygen atoms. The octahedra are strongly deformed, and the oxygens do not approach close packing. Cations occur within the octahedra at M-sites. Dots indicate M1 sites, which contain Fe and Mg; stars represent M2 sites, which contain Ti. Directions of *a* and *b* crystallographic axes are shown at upper left, and dashed lines indicate the unit cell (adapted from the pseudobrookite structure of Wechsler *et al.*, 1976).

The second compositional type of armalcolite is characterized by high contents of ZrO_2 (3.8-6.2 wt.%), Cr_2O_3 (4.3-11.5 wt.%), and CaO (3.0-3.5 wt.%). This has been called *Cr-Zr-Ca-armalcolite* ("C-Z-A" in Fig. 5.31). The third type is intermediate in composition between the first type, Fe-Mg armalcolite, and the second type, Cr-Zr-Ca armalcolite. It has been called *Zr-armalcolite* ("Z-A" in Fig. 5.31) and has distinctive amounts of ZrO_2 (2.0-4.4 wt.%), Y_2O_3 (0.15-0.53 wt.%), and Nb_2O_5 (0.26-0.65 wt.%). Detailed descriptions and analyses of these various types of armalcolite are given in Table A5.14 and by Haggerty (1973a).

5.2.4. Other Oxides

The only other oxide minerals of significant abundance in lunar rocks and soils are *rutile* (TiO_2) and *baddeleyite* (ZrO_2); representative compositions

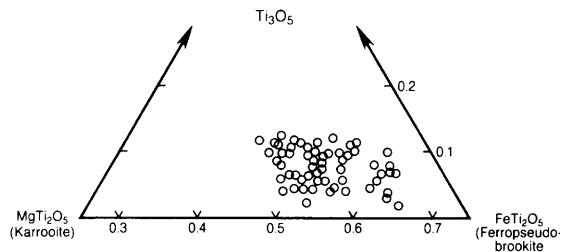


Fig. 5.30. Compositions of armalcolites (in mol.%) from lunar mare basalts, plotted on a triangular composition diagram in the system $MgTi_2O_5 - FeTi_2O_5 - Ti^{3+}_2Ti^{4+}O_5$. Compositions are calculated from electron microprobe chemical analyses. Note that the compositions are all displaced from the $MgTi_2O_5 - FeTi_2O_5$ join, indicating that significant amounts of Ti are present in the reduced form of Ti^{3+} (adapted from Wechsler *et al.*, 1976).

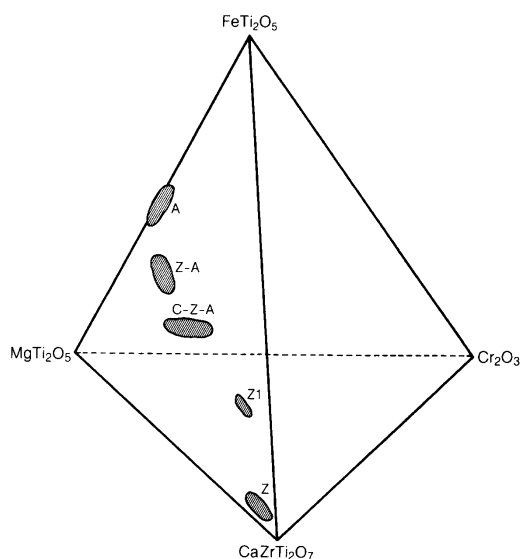


Fig. 5.31. Compositional tetrahedron (in wt.%) showing compositions of different varieties of lunar armalcolites (adapted from *Haggerty, 1973*). Normal armalcolites (A) lie along the line between MgTi_2O_5 and FeTi_2O_5 . Zr-armalcolites (Z-A) and Cr-Zr-Ca armalcolites (C-Z-A) are displaced toward the high-Cr and high-Zr apices. "Phase Z1" is a possible new mineral from the Apollo 15 site, and (Z) indicates the mineral *zirconolite*.

of these phases are given in Table A5.15. Rutile is generally associated with ilmenite, and it occurs most commonly as a reaction product from the reduction of ilmenite and/or armalcolite. Primary rutile occurs as discrete euhedral grains, also typically associated with ilmenite. Rutile in this association often contains Nb, Cr, Ta, and lanthanide elements (*Marvin, 1971; Hlava et al., 1972; El Goresy and Ramdohr, 1975; Table A5.15*). Baddeleyite is common in certain Apollo 14 clast-poor impact melt rocks (e.g., 14310, 14073; section 6.4) where it is associated with schreibersite $[(\text{Fe},\text{Ni},\text{Co})_3\text{P}]$; *El Goresy et al., 1971a*). Although these two minerals were originally thought to be indigenous to the Moon, it is now thought probable that the high Zr and P contents of these baddeleyite- and schreibersite-bearing rocks arise from meteoritic contamination that was incorporated into the original melts, which were produced by large meteoroid impact events.

Although rare on the Moon and not truly an oxide, the compound FeOOH has been found and often described as "rust" in lunar rocks from every mission, particularly those from Apollo 16 (*El Goresy et al.,*

1973a,b; *Taylor et al., 1973a*). It has been conclusively shown that this phase, the mineral *akaganeite* ($\beta\text{-FeOOH}$), is the product of contamination of the lunar rocks by terrestrial water vapor, which caused the oxyhydration of indigenous *lawrencite*, FeCl_2 , to form this water-bearing phase (*Taylor et al., 1973a*). Therefore, to date, no evidence for indigenous water has been found in any lunar minerals.

5.3. SULFIDE MINERALS

Sulfur is a relatively volatile element (section 8.7.7) that plays a dual role on the Moon: in the gases that drove lunar pyroclastic eruptions (section 4.2.1), and in the gases released during impact heating. For a planet with a surface otherwise poor in volatile elements, the Moon has a fair amount of sulfur. Lunar mare basalts, for instance, have about twice as much sulfur as do typical terrestrial basalts. On the Moon, this sulfur is present in sulfide (S) minerals; the low oxygen partial pressures in the lunar environment apparently do not permit the formation of sulfate (SO_4) minerals.

5.3.1. Troilite

Troilite (FeS) is the most common sulfide mineral in lunar rocks. Although it almost always forms less than 1% by volume of any lunar rock, troilite is ubiquitous. It is commonly associated with native Fe, ilmenite, and spinel. The chemical composition of troilite is essentially that of FeS with less than 1 wt.% of all other components (Table A5.16).

Based on study of a small number of early Apollo samples, *Skinner (1970)* proposed that lunar troilite was always associated with native Fe in textures that result from crystallization at the 988°C eutectic point where both FeS and Fe form simultaneously. The formation of an immiscible sulfide melt late in the crystallization of a silicate magma preceded this eutectic crystallization. Some lunar troilite has undoubtedly formed in this way. However, other troilite occurrences are void of native Fe and require precipitation directly from the S-saturated silicate melt.

The most common occurrence of troilite is as an accessory phase in mare basalts, where it is usually a late-stage crystallization product. Such primary troilite forms when the original bulk composition of the melt, in particular the sulfur content, is appropriate. Secondary troilite forms later, in the solid rocks, in cases where the partial pressure of sulfur increases rapidly and sulfurizes native Fe during the high-temperature shock metamorphism produced by meteoroid impacts. Some Apollo 16 rocks, notably 66095, contain troilite that most likely formed as a direct result of this remobilization of sulfur during meteoroid impact.

5.3.2. Other Sulfides

Other sulfide minerals positively identified in lunar rocks include *chalcopyrite* (CuFeS_2), *cubanite* (CuFe_2S_3), *pentlandite* $[(\text{Fe},\text{Ni})_9\text{S}_8]$, *mackinawite* (Fe_{1+x}S), and *sphalerite* $[(\text{Zn},\text{Fe})\text{S}]$. All these minerals are so rare as to be only geologic curiosities, and they have only minor applications in determining the origins of the rocks that contain them.

The Cu-bearing phases have only been found as small grains ($<10\text{-}15\ \mu\text{m}$) in some Apollo 12 basalts (Taylor and Williams, 1973) and in small cavities (vugs) in two Apollo 17 breccias, where chalcopyrite is associated with pentlandite (Carter et al., 1975). Pentlandite has also been reported from an Apollo 14 breccia (Ramdohr, 1972). Mackinawite was identified as small ($<5\ \mu\text{m}$) grains in certain Apollo 12 basalts (El Goresy et al., 1971b; Taylor et al., 1971). Sphalerite (with 28 mol.% FeS in solution with ZnS) was observed in some Apollo 16 breccias, notably 66095 (Table A5.16; El Goresy et al., 1973; Taylor et al., 1973a), where it was probably formed as a result of the mobilization of Zn and S during impact-produced shock metamorphism. It is only present as small grains ($<20\ \mu\text{m}$) and in minor quantities ($<0.01\ \text{vol.}\%$).

5.4. NATIVE FE

Native iron metal, Fe^0 , is only rarely found in terrestrial rocks. However, in lunar rocks it is a ubiquitous minor phase, largely because of the low oxygen partial pressures during original crystallization of lunar magmas (Fig. 5.17) and during subsequent meteoroid impacts.

Native Fe occurs in lunar rocks as three different minerals with different crystal structures. These minerals occur in various proportions and form intricate textures, either from exsolution during cooling or from later subsolidus reequilibration. These three minerals also have different chemical compositions, involving varying amounts of solid solution between Fe and Ni. *Kamacite* (alpha-type iron) has a body-centered cubic crystal structure and contains 0-6 wt.% Ni. *Taenite* (gamma-type iron) has a face-centered cubic crystal structure and contains 6-50% Ni. *Tetrataenite* has a tetragonal crystal structure and is essentially FeNi , with $50\pm 2\%$ Ni.

In lunar samples, kamacite is the most abundant metal phase and taenite the second most abundant. Tetrataenite is only rarely observed, and that which occurs is most likely due to meteoritic contamination. These minerals are apparently formed by four different processes: (1) normal igneous crystallization; (2) subsolidus reduction of oxides (see section 5.2.2), or of troilite and olivine (this process has occurred in rocks 14053 and 14072); (3) reduction of

the FeO component in impact-produced silicate melts in the soil; and (4) meteoroid contamination. Effects of the first and second processes are readily apparent and were easily recognized in the first returned samples. The meteoroid metal component is to be expected because of the large flux of impacting bodies onto the lunar surface. However, the discovery that abundant native Fe could be produced in the soils during impact melting was unexpected. At first, the observation of significant Fe metal in the lunar soils presented a quandary: Was the metal produced by a surface process or was it simply meteoroid contamination? The resolution of this question, and the recognition that Fe metal in the lunar soil comes from several sources, are discussed in more detail in section 5.4.3.

5.4.1. Meteoritic Contamination

It is important to determine how much of the FeNi metal found in the lunar soil is actually extralunar in origin, having been brought in as a component of the meteoroids that have bombarded the Moon over geologic time. Unfortunately, making this distinction is a major problem, and the results to date are controversial. An early method of distinguishing between lunar and meteoroid metal was based on Ni and Co contents. Figure 5.32 shows a plot of Co vs. Ni contents for native Fe metal. The "meteoritic field" is a region originally designated as unique to metal from meteoroids (Goldstein and Yakowitz, 1971). However, these boundaries were established with earlier data, obtained by others, on the whole-rock compositions of iron meteorites, and these data were incorrectly presented as indicative of meteoroid metal as a whole (for further discussion, see Misra and Taylor, 1975a,b). Most meteorites are stony, not iron, and the metal they contain can vary widely from the bulk composition of iron meteorites.

As a result of newer data, it is now clear that these earlier boundaries are no longer valid for distinguishing between lunar and meteoroid metal and that there is extensive overlap between the two. If the composition of metal lies within the "meteoritic" field in Fig. 5.32, this does not imply that it is of meteoroid origin; it may have an indigenous lunar origin. Nor does a composition of Fe metal outside this area mean that it is lunar in origin. The Ni and Co contents of native Fe metal can vary considerably, from 0% to over 50% Ni and from 0% to 8% Co. For example, Fig. 5.33 shows the range of compositional variation (Misra and Taylor, 1975a) in several Apollo 16 highland samples. Of all lunar samples, it is reasonable to suppose that the older highland rocks contain the greatest amount of introduced meteoroid metal; however, determination

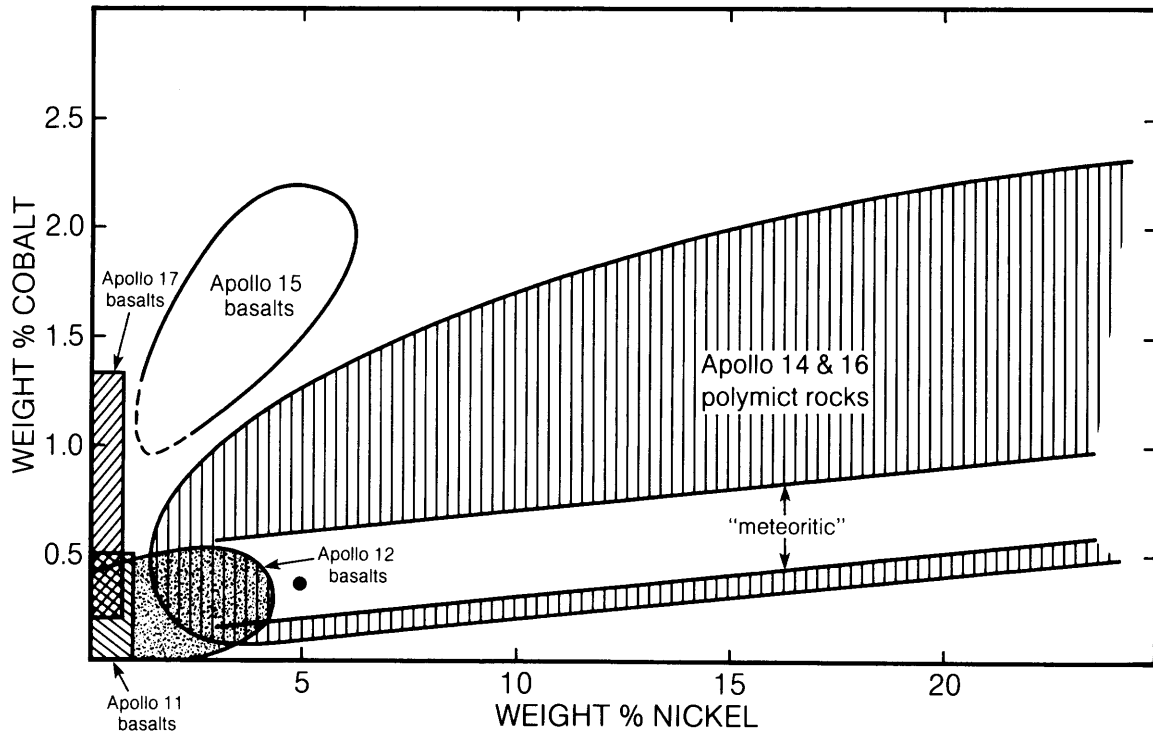


Fig. 5.32. Plot of Co and Ni contents (in wt.%) of the Fe metal phase occurring in mare basalts (*pristine rocks*) and breccias (*polymict rocks*) from different Apollo landing sites. The region for metal from the Apollo 14 and 16 polymict rocks is from *Ryder et al.* (1980). The solid circle at about 5% Ni represents the average composition of chondritic meteorites. The region labeled "meteoritic" was established by early work on iron meteorites (*Goldstein and Yakowitz, 1971*) and is used here only for reference. Later work has shown that the compositions of meteoritic metal can extend far beyond this region (see text for discussion).

of the exact amount is not possible by using the "meteoritic" range of Fig. 5.32. For example, it would appear that many of these rocks do not contain any lunar metal, if the criteria of *Goldstein and Yakowitz* (1971) are used. Based upon other chemical criteria, this is not likely.

The best means of determining the meteoroid contribution to the metal contents of lunar soils and breccias is through use of the rarer *siderophile* (i.e., readily soluble in molten iron) elements, other than Ni (*Ganapathy et al., 1970; Pearce and Chou, 1976; Reed and Taylor, 1974; Wlotzka et al., 1973*). These elements, which tend to concentrate in Fe-metal minerals, especially during melting processes, include Au, Pt, Ir, Os, Mo, and Ge. Because lunar rocks contain relatively small amounts of these elements compared to meteoroid FeNi metal, estimates can be made about the quantity of meteoroid material in a soil or breccia (see sections 6.4 and 8.6). It has been determined, for example, that the average Apollo 16 soil contains

about 2% input from chondritic meteoroids. In addition, the siderophile content of a sample, particularly the amount of iridium (Ir), has been successfully used as a criterion for distinguishing between *pristine* and meteorite-contaminated lunar rocks (sections 6.3 and 6.4).

5.4.2. Native Fe in Lunar Rocks

One of the surprising findings from the first-returned lunar samples, Apollo 11 mare basalts, was the presence of native Fe metal grains in every sample (e.g., *Reid et al., 1970*). These metal grains were produced by the crystallization of normal igneous melts under reducing conditions. Subsequently, native Fe metal was identified in all returned lunar rocks. The amount of metal varies between samples as well as between sites, but is always less than 1% by volume. Representative analyses of metals are listed in Table A5.17. In the mare basalts, native Fe makes up only a small portion of the opaque (i.e., "black" in transmitted-light microscopy)

mineral content, which is mostly formed of the oxide minerals ilmenite and spinel. However, in some highland rocks such as the Apollo 16 breccias, native Fe is virtually the only opaque mineral present (Misra and Taylor, 1975a,b). Some cubic Fe crystals have grown in the open spaces of breccias, apparently from Fe-rich vapor (Clanton *et al.*, 1973).

Although there are substantial variations in the compositions of native Fe among the samples from a single landing site, some differences between sites can still be recognized (Fig. 5.32). Native Fe from Apollo 11 basalts is usually low in Ni (<1%) and Co (<0.5%); metals from the Apollo 17 samples are similar but may have higher Co content. Metals from Apollo 12 and 15 basalts have compositions with 0-

30% Ni and 0-6% Co. The high-Ni and high-Co content metals in these basalts are rare, however, and the majority of lunar metal compositions fall within the areas shown in Fig. 5.32. Such correlations should be treated with caution, however, because major differences in metal composition can exist even within a single sample. Native Fe enclosed within early-formed olivine crystals can contain 30% Ni, whereas that in the later-crystallized parts of the rock can be virtually pure Fe (i.e., <0.2% Ni). The metal in breccias from the Apollo 14 and 16 sites is difficult to distinguish from meteoroid metal and has wide-ranging compositions similar to those reported for meteorites (i.e., 0% to more than 50% Ni; 0-8% Co).

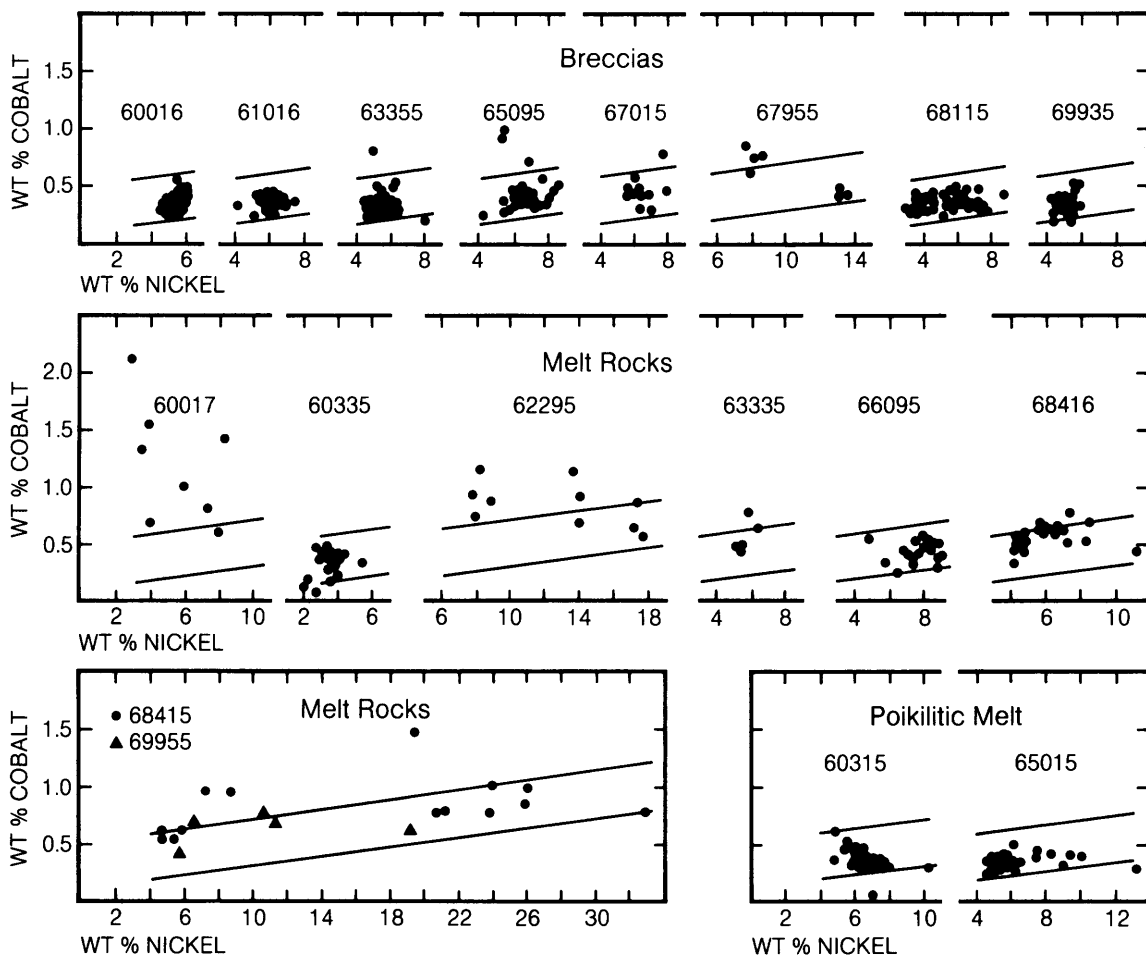


Fig. 5.33. Plots of Ni vs. Co contents (wt.%) of Fe metal grains in Apollo 16 rocks (adapted from Misra and Taylor, 1975a). The samples include fragmental rocks (*breccias*), relatively fine-grained crystallized clast-poor impact *melt rocks*, and coarsely crystalline (*poikilitic*) clast-poor impact melt rocks. The parallel diagonal lines outline the “meteoritic” region of Goldstein and Yakowitz (1971) and are used here only for reference (see text for discussion).

5.4.3. Native Fe in Lunar Soil

The lunar soil consists of comminuted rocks and minerals. Therefore, any mineral occurring in the rocks can become part of the soil (Taylor, 1988). In particular, the native Fe metal grains now observed in the soil can have formed originally by normal crystallization of a silicate melt or by later subsolidus reduction of other minerals (e.g., oxides in the cooling magma). In addition, a large amount of metal can be contributed by impacting meteoroids. As a result of these diverse sources, the compositions of lunar Fe metal vary from essentially pure Fe to virtually any composition in the range reported for meteoritic metal. The compositions of metal grains larger than a few micrometers (i.e., those large enough for *electron microprobe* analysis), when taken as a whole for a given soil, tend to center around a bulk composition of Ni = 5-6% and Co = 0.3-0.5%; these values are the same as the average compositions of metal in chondrite meteorites (Fig. 5.32).

However, magnetic studies of the lunar soil indicate that a significant amount of Fe metal is present as much smaller particles, well below 0.1 μm in size. Tsay *et al.* (1971) noticed that the ferromagnetic resonance (FMR) signal for *single-domain* Fe (i.e., from grains 40 to 330 \AA in size) in the lunar soil was an order of magnitude greater than that from associated rock samples (see review article by Taylor and Cirlin, 1986). These studies indicated that there is considerably more Fe metal in the lunar soils than in the rocks from which they were derived, that much of it is very fine-grained (<300 \AA), and that it is not meteoroid metal. Since the soils are composed of disaggregated rock material, what is inherently different between the lunar rocks and soils? That is, where did this additional Fe metal come from? It must be produced by a process involved in the formation of the lunar soil itself.

There are two principal processes at work in forming lunar soils: (1) simple *disaggregation*, or the breaking of rocks and their minerals into smaller particles; and (2) *agglutination*, the welding together of rock and mineral fragments by the glass produced by melting due to small meteoroid impacts (the glass-welded particles are called *agglutinates*; see section 7.1.3). These two processes compete to decrease and increase, respectively, the grain size of soil particles (Morris, 1977, 1980).

The agglutinates contain much of the fine-grained, single-domain Fe metal particles in the soil. The majority of the metal grains in the agglutinates are from 100-200 \AA in size, well within the single-domain size range of 40-330 \AA for metallic Fe. The composition of most of these minute Fe particles is >99% Fe with only trace amounts of Ni and Co

(Mehta and Goldstein, 1979). By contrast, metal grains that are larger than a few micrometers across have higher Ni, Co, and P contents; these may be finely disseminated particles of meteoroid metal. Further details are contained in numerous studies characterizing the nature of the native Fe in lunar soils from various missions (e.g., Axon and Goldstein, 1973; Goldstein and Axon, 1973; Goldstein and Blau, 1973; Hewins and Goldstein, 1974, 1975; Ivanov *et al.*, 1973; Mehta *et al.*, 1979; Misra and Taylor, 1975a,b).

What is the origin of this abundant single-domain metallic iron? As originally discussed by Tsay *et al.* (1971), and reiterated later by others (e.g., Housley *et al.*, 1973), the soil particles at the surface before the impact are exposed to the solar wind, and they are effectively saturated with solar-wind-implanted protons (hydrogen nuclei) and carbon atoms in the outer 0.1 μm of their surface. When the soil is melted by a small micrometeoroid impact, these elements produce an extremely reducing environment, which causes reduction of the Fe^{2+} in the agglutinate melt to Fe^0 . This Fe metal then precipitates as myriad tiny Fe^0 spheres disseminated throughout the quenched melt, i.e., in the agglutinate glass. This *autoreduction* process is responsible for producing the additional Fe^0 that occurs in agglutinate particles. Unfortunately, although this additional Fe metal is abundant in the soil, it is extremely fine-grained and may be too fine for easy concentration and beneficiation to produce iron metal as a resource. Possibly, heat treatment to produce Fe metal grain coarsening could make agglutinates into a more desirable feedstock for resource applications.

5.5. PHOSPHATE MINERALS

Lunar rocks and soils generally contain about 0.5 wt.% P_2O_5 , most of which is contained in the phosphate minerals *whitlockite* [ideally $\text{Ca}_3(\text{PO}_4)_2$] and *apatite* [ideally $\text{Ca}_5(\text{PO}_4)_3(\text{OH},\text{F},\text{Cl})$]; Friel and Goldstein, 1977], which occur in very minor amounts in most lunar rocks. Whitlockite and apatite generally form crystals with hexagonal cross-sections. Apatite crystals with two well-shaped pyramidal ends (*doubly-terminated*), thought to be vapor-deposited, have been found in gas-formed cavities within lunar rocks.

As is the case for most minor lunar minerals, the phosphates occur as late-stage crystallization products in mare basalts. However, they are more abundant, and crystallize earlier, in certain KREEPY (K, rare earth element, and P-rich) highland samples. Phosphates are also commonly found in association with metal particles (Friel and Goldstein, 1977); in such occurrences they have probably formed by the oxidation of phosphorus out of the metal (Friel and Goldstein, 1976, 1977).

Of the two major lunar phosphates, whitlockite is more abundant and has higher rare earth element (REE; La to Lu) contents. As Table A5.18 shows, lunar whitlockite can also contain significant amounts of FeO, MgO, Na₂O, and Y₂O₃, as well as the REEs (especially the light REEs, La₂O₃, Ce₂O₃, Nd₂O₃). It is also U-enriched; crystals from the Apollo 12 basalts contain ~100 ppm U (*Lovering and Wark*, 1971). These compositions contrast sharply with terrestrial and meteoritic whitlockites, which contain only trace amounts of rare earth elements (*Albee and Chodos*, 1970). Table A5.18 also shows that lunar whitlockites have a fairly wide range of Fe:Mg ratios. On the other hand, the REE contents do not vary so widely, especially in whitlockites from KREEP-rich basalts (e.g., *Simon and Papike*, 1985). These data suggest the existence of a fairly uniform KREEP component across the Moon (*Warren and Wasson*, 1979; *Warren*, 1985).

As shown by the formula given above, apatite contains one OH, F, or Cl position per formula unit, and in terrestrial apatites the OH content may be quite high relative to F and Cl. However, the general lack of water in lunar samples causes lunar apatites to have low OH contents, and analyses indicate that they are Cl- and F-rich. Some nearly pure fluorapatites have been found on the Moon (e.g., *Fuchs*, 1970), containing over 3 wt.% F out of a possible maximum of 3.8%. This F-rich end member (also found in human teeth) is the harder and more durable of apatite variants. The analyses in Table A5.18 also show that some "chlorofluorapatites" have also been found. Chlorine-rich apatites are typically characteristic of high-temperature rocks (*Albee and Chodos*, 1970) and meteorites (*Fuchs*, 1969; *Dodd*, 1981).

There are other major- and trace-element differences between lunar and terrestrial apatites. Lunar apatites have higher Si, Y, and REE contents. The ionic exchanges involved in producing these compositions are largely Si⁴⁺ for P⁵⁺, balanced by REE³⁺ and Y³⁺ for Ca²⁺ (*Fuchs*, 1970).

Both whitlockite and apatite are important REE carriers in lunar rocks, and they are enriched in REE relative to their terrestrial counterparts. The lunar whitlockites have higher REE contents than lunar apatites (e.g., La, Ce, Nd; Table A5.18). At least some of this difference between apatite and whitlockite can be attributed to different crystal/liquid *distribution coefficients* (K_d : the ratio between the amount of

an element in a mineral crystallizing from a melt and the amount of the same element in the melt itself). Experimental work by *Dickinson and Hess* (1983) shows K_d s of about 9.5 for the distribution of light REE (Ce-Sm) in the system whitlockite/melt, compared to K_d s of about 2.5-5 for apatite/melt. The apatite distribution coefficients can approach and even exceed those of whitlockite in Si-rich liquids (*Watson and Green*, 1981; *Dickinson and Hess*, 1983), but Si-rich liquids are rare on the Moon.

APPENDIX

Compositions of Lunar Minerals

Numerous analyses have been made of lunar minerals. Almost all of the analyses made have been done by electron microprobe, a technique of microanalysis that allows accurate determinations of mineral compositions from samples as small as 5-10 μ m. Elements with atomic number equal to or greater than F are routinely determined by this technique; oxygen abundances are assumed based on the relative abundances of the heavier elements. All the data in this appendix were collected by electron microprobe.

These appendix tables provide for each mineral analysis (1) the measured element abundance in weight percent, recalculated as an oxide if it is known to occur with oxygen in the mineral structure, and (2) the cation molecular proportions of the analysis (where the mineral consists of an oxygen framework, these cation abundances are calculated in terms of a given number of oxygens). For most of the silicate minerals, the ratios of certain major cations are also listed; these ratios determine the positions of plotted points in several of the diagrams in section 5.1.

References are provided for each analysis, to provide more detailed information should the reader need it. An indication of the rock type (or soil) from which the analysis was obtained is also listed, based on the categories of rock types described in Chapter 6. These rock types are listed in Table A5.1. For the mare basalts, ranges of host rock chemistry are given in parentheses (Table A5.1) where chemical composition is an important part of the mare rock classification. For highland rocks, features of mineral, glass, and fragmental makeup are listed, for these are more important in rock classification.

TABLE A5.1. Listing of rock types and corresponding abbreviations for Chapter 5 mineral chemistry tables.

Rock Type	Table Symbol
<i>Mare Basalts (see section 6.1 for more detail)</i>	
High-Ti (>9% TiO ₂)	
Apollo 11	
high-K (>0.3% K ₂ O)	A-11 HK
low-K (<0.11% K ₂ O)	A-11 LK
Apollo 17	A-17
Low-Ti (1.5-9% TiO ₂)	
Apollo 12	
pigeonite (<10% MgO, <5% TiO ₂)	A-12 pig
olivine (>10% MgO, <5% TiO ₂)	A-12 ol
ilmenite (<10% MgO, >5% TiO ₂)	A-12 ilm
Apollo 15	
pigeonite (<10% MgO, <5% TiO ₂)	A-15 pig
olivine (>10% MgO, <5% TiO ₂)	A-15 ol
Aluminous, Low-Ti (>10% Al ₂ O ₃ , 2-5% TiO ₂)	
Luna 16	L-16 Al
Apollo 14	A-14 Al
Very-High-K (>0.6% K ₂ O)	VHK
Very Low-Ti (<1.5% TiO ₂)	
Apollo 17	A-17 VLT
Luna 24	L-24 VLT
<i>Highland Igneous and Monomict Rocks (section 6.3)</i>	
KREEP rocks (high K, rare earths, and P)	KREEP
Ferroan Anorthosites (Low-Na plagioclase, low-Mg pyroxene)	Fan
Mg-rich Rocks (variable plagioclase, high-Mg pyroxene)	Mg rock
Alkali Anorthosites (relatively high-Na plagioclase)	Alk an
Granite (or felsite) (K-feldspar, silica minerals)	Granite
<i>Highland Polymict Rocks (see section 6.4)</i>	
Fragmental Breccias (mainly fragments)	Frag br
Glassy Melt Breccias (glass with some fragments)	Glassy br
Crystalline Melt Breccias (crystallized melt with some fragments)	Cryst br
Clast-poor Impact Melt Rocks (crystallized melt with rare fragments)	Melt rock
Granulitic Breccias (recrystallized)	Gran br
Dimict Breccias (two rock types joined)	Dimict
Regolith Breccias (compressed soil)	Reg br
<i>Soil (single crystals in soil, from unknown rock types)</i>	
	Soil

TABLE A5.2. Pyroxene analyses from mare basalts.

	High-Ti Basalts															
	Apollo 17						Apollo 11 High-K						Apollo 11 Low-K			
	1.	2.	3.	4.	5.	6.	7.	8.	9.	10.	11.	12.	13.	14.	15.	16.
<i>Chemical Composition (Weight Percent)</i>																
SiO ₂	44.50	48.50	52.10	50.40	49.20	53.80	50.60	44.10	49.90	45.20	49.80	46.10	46.60	47.00	49.32	47.09
Al ₂ O ₃	7.70	2.73	1.64	2.50	3.93	0.96	3.40	1.43	2.56	0.88	2.79	1.09	5.25	1.85	3.17	0.86
TiO ₂	6.00	2.20	1.33	1.78	3.37	0.78	2.76	1.06	2.47	0.72	2.39	0.79	3.74	1.41	2.49	0.72
Cr ₂ O ₃	0.98	0.52	0.50	0.71	1.00	0.31	0.0	0.06	0.58	0.06	0.61	0.09	0.60	0.29	0.45	0.06
FeO	8.10	19.10	16.70	13.10	9.55	18.40	12.00	45.80	11.10	43.90	11.80	42.80	9.60	28.00	10.95	41.07
MnO	0.28	0.50	0.30	0.29	0.0	0.0	0.0	0.59	0.18	0.59	0.25	0.58	0.25	0.53	0.08	0.67
MgO	12.00	10.70	20.40	15.40	16.10	22.80	16.60	1.72	15.90	1.40	16.40	2.24	14.40	7.20	14.80	2.29
CaO	20.70	16.00	6.80	15.80	17.40	3.68	15.20	3.52	16.50	6.12	15.50	6.57	18.80	12.60	17.95	8.04
Na ₂ O	0.19	0.17	0.0	0.09	0.0	0.0	0.10	0.03	0.0	0.0	0.12	0.0	0.0	0.0	0.0	0.0
Total	100.45	100.42	99.77	100.07	100.55	100.73	100.66	98.31	99.19	98.87	99.66	100.26	99.24	98.88	99.21	100.80
<i>Cation Formula Based on 6 Oxygens (Ideal Pyroxene = 4 Cations per 6 Oxygens)</i>																
Si	1.668	1.873	1.934	1.891	1.820	1.967	1.868	1.923	1.877	1.952	1.866	1.947	1.762	1.908	1.861	1.965
^{IV} Al	0.332	0.124	0.066	0.109	0.171	0.033	0.132	0.074	0.114	0.045	0.123	0.053	0.234	0.089	0.139	0.035
Total tet*	2.000	1.997	2.000	2.000	1.991	2.000	2.000	1.997	1.991	1.997	1.989	2.000	1.996	1.997	2.000	2.000
Ti	0.169	0.064	0.037	0.050	0.094	0.021	0.077	0.035	0.070	0.023	0.067	0.025	0.106	0.043	0.071	0.023
^{VI} Al	0.008	0.0	0.006	0.002	0.0	0.008	0.016	0.0	0.0	0.0	0.0	0.001	0.0	0.0	0.002	0.007
Cr	0.029	0.016	0.015	0.021	0.029	0.009	0.0	0.002	0.017	0.002	0.018	0.003	0.018	0.009	0.013	0.002
Fe	0.254	0.617	0.519	0.411	0.295	0.562	0.371	1.671	0.349	1.585	0.370	1.512	0.304	0.950	0.345	1.433
Mn	0.009	0.016	0.009	0.009	0.0	0.0	0.0	0.022	0.006	0.022	0.008	0.021	0.008	0.018	0.003	0.024
Mg	0.670	0.616	1.129	0.861	0.887	1.242	0.913	0.112	0.891	0.090	0.916	0.141	0.812	0.436	0.832	0.142
Ca	0.831	0.662	0.271	0.635	0.690	0.144	0.601	0.165	0.665	0.283	0.622	0.297	0.762	0.548	0.726	0.359
Na	0.014	0.013	0.0	0.007	0.0	0.0	0.007	0.003	0.0	0.0	0.009	0.0	0.0	0.0	0.0	0.0
Total Cations	3.984	4.001	3.986	3.996	3.986	3.986	3.985	4.007	3.989	4.002	3.999	4.000	4.006	4.001	3.992	3.990
<i>Cation Ratios: Ca : Mg : Fe and Fe/(Fe+Mg)</i>																
Ca	47.4	34.9	14.1	33.3	36.8	7.4	31.9	8.4	34.9	14.5	32.6	15.2	40.6	28.3	38.1	18.6
Mg	38.2	32.5	58.9	45.1	47.4	63.7	48.4	5.7	46.8	4.6	48.0	7.2	43.2	22.5	43.7	7.4
Fe	14.5	32.6	27.0	21.6	15.8	28.9	19.7	85.8	18.3	80.9	19.4	77.5	16.2	49.1	18.2	74.1
Fe/(Fe+Mg)	0.27	0.50	0.31	0.32	0.25	0.31	0.29	0.94	0.28	0.95	0.29	0.91	0.27	0.69	0.29	0.91

TABLE A5.2. (continued).

	Low-Ti Basalts																	
	Apollo 12 Ilmenite		Apollo 12 Pigeonite						Apollo 12 Olivine				Apollo 15 Pigeonite					
	17.	18.	19.	20.	21.	22.	23.	24.	25.	26.	27.	28.	29.	30.	31.	32.	33.	34.
	<i>Chemical Composition (Weight Percent)</i>																	
SiO ₂	49.00	47.32	50.30	45.00	53.51	45.23	51.50	46.80	52.10	49.40	45.60	51.77	54.01	41.43	52.40	43.20	51.50	48.20
Al ₂ O ₃	3.46	1.41	3.06	2.15	0.66	0.54	2.05	0.83	1.21	0.90	1.27	1.51	0.63	10.10	1.89	9.66	2.77	1.43
TiO ₂	2.13	1.14	0.89	1.41	0.35	0.73	0.68	0.89	0.63	1.29	0.99	1.08	0.19	2.96	0.36	3.99	0.63	1.11
Cr ₂ O ₃	0.97	0.18	1.38	0.09	0.74	0.05	0.93	0.09	0.52	0.13	0.0	0.37	0.77	0.02	1.04	0.66	1.06	0.45
FeO	13.31	30.28	17.10	43.10	16.69	46.54	16.90	37.80	19.20	25.70	41.90	16.34	15.76	27.68	16.90	20.10	14.50	30.20
MnO	0.24	0.43	0.36	0.51	0.29	0.56	0.37	0.56	0.38	0.44	0.52	0.32	0.28	0.39	0.0	0.0	0.0	0.0
MgO	15.64	2.64	21.60	0.41	24.26	0.34	21.90	3.80	21.40	11.10	0.29	15.34	26.26	3.90	23.90	8.58	14.20	7.41
CaO	14.44	16.24	4.54	7.69	2.61	6.43	5.10	8.90	4.59	10.50	9.16	13.99	2.02	10.98	2.62	13.80	14.70	10.80
Na ₂ O	0.05	0.01	0.0	0.0	0.0	0.03	0.0	0.0	0.0	0.0	0.0	0.01	0.00	0.09	0.03	0.05	0.03	0.03
Total	99.24	99.65	99.23	100.36	99.11	100.45	99.43	99.67	100.03	99.46	99.73	100.73	99.92	97.55	99.14	100.04	99.39	99.63
	<i>Cation Formula Based on 6 Oxygens (Ideal Pyroxene = 4 Cations per 6 Oxygens)</i>																	
Si	1.853	1.943	1.879	1.910	1.973	1.947	1.916	1.953	1.940	1.948	1.945	1.941	1.96	1.70	1.935	1.676	1.941	1.941
^{iv} Al	0.147	0.057	0.121	0.090	0.027	0.027	0.084	0.041	0.053	0.042	0.055	0.059	0.03	0.30	0.065	0.324	0.059	0.059
Total tet*	2.000	2.000	2.000	2.000	2.000	1.974	2.000	1.994	1.993	1.990	2.000	2.000	1.99	2.00	2.000	2.000	2.000	2.000
Ti	0.061	0.035	0.025	0.045	0.010	0.024	0.019	0.028	0.018	0.038	0.032	0.030	0.00	0.09	0.010	0.116	0.018	0.034
^{vi} Al	0.008	0.012	0.013	0.018	0.001	0.0	0.006	0.0	0.0	0.009	0.007	0.007	0.00	0.19	0.017	0.117	0.064	0.008
Cr	0.029	0.006	0.041	0.003	0.022	0.002	0.027	0.003	0.015	0.004	0.0	0.011	0.02	0.00	0.030	0.020	0.032	0.014
Fe	0.421	1.040	0.534	1.530	0.515	1.675	0.526	1.319	0.598	0.848	1.495	0.512	0.48	0.95	0.522	0.652	0.457	1.017
Mn	0.008	0.015	0.011	0.018	0.009	0.020	0.012	0.020	0.012	0.015	0.019	0.010	0.01	0.01	0.0	0.0	0.0	0.0
Mg	0.882	0.162	1.202	0.026	1.333	0.022	1.214	0.236	1.188	0.652	0.018	0.857	1.42	0.24	1.315	0.496	0.798	0.445
Ca	0.585	0.715	0.182	0.350	0.103	0.297	0.203	0.398	0.183	0.444	0.419	0.562	0.08	0.48	0.104	0.574	0.594	0.466
Na	0.004	0.001	0.0	0.0	0.0	0.003	0.0	0.0	0.0	0.0	0.0	0.001	0.00	0.01	0.002	0.004	0.002	0.002
Total Cations	3.998	3.986	4.008	3.990	3.993	4.017	4.007	3.998	4.007	3.991	3.992	3.990	4.000	3.970	4.000	3.979	3.965	3.986
	<i>Cation Ratios: Ca : Mg : Fe and Fe/(Fe+Mg)</i>																	
Ca	31.0	37.3	9.5	18.4	5.3	14.9	10.5	20.4	9.3	22.8	21.7	29.1	4.0	28.7	5.3	33.3	32.1	24.2
Mg	46.7	8.4	62.7	1.4	68.3	1.1	62.5	12.1	60.3	33.6	1.0	44.4	71.7	14.4	67.8	28.8	43.2	23.1
Fe	22.3	54.3	27.8	80.3	26.4	84.0	27.1	67.5	30.4	43.6	77.4	26.5	24.2	56.9	26.9	37.9	24.7	52.8
Fe/(Fe+Mg)	0.32	0.87	0.31	0.98	0.28	0.99	0.30	0.85	0.33	0.57	0.99	0.37	0.25	0.80	0.28	0.57	0.36	0.70

TABLE A5.2. (continued).

	Low-Ti Basalts				Aluminous, Low-Ti Basalts						Very Low-Ti Basalts					
	Apollo 15 Olivine				Luna 16		Apollo 14		VHK		Luna 24		Apollo 17			
	35.	36.	37.	38.	39.	40.	41.	42.	43.	44.	45.	46.	47.	48.	49.	50.
<i>Chemical Composition (Weight Percent)</i>																
SiO ₂	51.80	49.90	51.40	47.00	49.24	46.28	51.30	45.32	51.21	51.90	49.13	44.95	50.45	48.28	53.09	45.76
Al ₂ O ₃	2.88	1.66	2.15	1.16	3.03	0.98	1.73	1.68	1.97	1.64	3.76	0.88	5.13	2.91	1.45	1.04
TiO ₂	0.90	1.21	0.83	0.92	2.48	1.16	0.84	1.62	0.83	1.45	0.89	0.76	0.39	1.26	0.20	1.19
Cr ₂ O ₃	0.86	0.22	0.75	0.0	0.59	0.10	0.73	0.02	0.72	0.42	0.89	0.00	1.53	0.17	0.73	0.06
FeO	14.50	25.80	13.60	36.60	13.27	38.67	18.60	30.32	19.07	15.17	16.95	43.35	17.42	31.81	17.45	42.54
MnO	0.0	0.0	0.0	0.0	0.28	0.55	0.0	0.30	0.47	0.37	0.28	0.54	0.30	0.43	0.27	0.58
MgO	16.30	11.40	16.80	5.59	13.22	3.13	21.20	0.57	20.21	11.67	11.68	0.12	19.86	11.01	23.60	0.82
CaO	12.80	10.60	14.40	7.81	18.01	8.75	4.37	18.24	5.37	18.16	16.87	7.88	6.10	5.93	3.63	8.58
Na ₂ O	0.0	0.0	0.0	0.0	0.09	0.01	0.02	0.07	-	-	0.00	0.00	0.00	0.00	0.00	0.00
Total	100.04	100.79	99.93	99.08	100.21	99.63	98.79	98.14	99.85	100.78	100.45	98.48	101.18	101.80	100.42	100.57
<i>Cation Formula Based on 6 Oxygens (Ideal Pyroxene = 4 Cations per 6 Oxygens)</i>																
Si	1.928	1.935	1.921	1.948	1.86	1.94	1.928	1.913	1.915	1.956	1.875	1.955	1.853	1.887	1.945	1.938
^{iv} Al	0.072	0.065	0.079	0.052	0.14	0.05	0.072	0.084	0.086	0.044	0.125	0.045	0.147	0.113	0.055	0.052
Total tet*	2.000	2.000	2.000	2.000	2.000	1.99	2.000	1.997	2.000	2.000	2.000	2.000	2.000	2.000	2.000	1.990
Ti	0.025	0.035	0.023	0.029	0.07	0.04	0.024	0.051	0.023	0.041	0.026	0.025	0.011	0.037	0.006	0.038
^{vi} Al	0.054	0.011	0.015	0.005	0.0	0.0	0.005	0.0	0.001	0.029	0.044	0.000	0.075	0.021	0.007	0.000
Cr	0.025	0.007	0.022	0.0	0.02	0.003	0.022	0.001	0.021	0.013	0.027	0.000	0.044	0.005	0.021	0.002
Fe	0.451	0.837	0.425	1.269	0.42	1.36	0.585	1.070	0.596	0.478	0.541	1.577	0.535	1.040	0.535	1.506
Mn	0.0	0.0	0.0	0.0	0.009	0.002	0.0	0.011	0.014	0.012	0.009	0.020	0.009	0.014	0.008	0.021
Mg	0.904	0.659	0.936	0.345	0.74	0.20	1.187	0.036	1.126	0.656	0.664	0.008	1.087	0.641	1.288	0.052
Ca	0.510	0.440	0.577	0.347	0.73	0.40	0.176	0.825	0.215	0.733	0.690	0.367	0.240	0.248	0.142	0.389
Na	0.0	0.0	0.0	0.0	0.006	0.001	0.001	0.006	-	-	0.000	0.000	0.000	0.000	0.000	0.000
Total Cations	3.969	3.989	3.998	3.995	3.995	3.996	4.000	3.997	3.996	3.962	4.001	3.997	4.001	4.006	4.007	3.998
<i>Cation Ratios: Ca : Mg : Fe and Fe/(Fe+Mg)</i>																
Ca	27.4	22.8	29.8	17.7	38.6	20.4	9.0	42.7	11.3	39.3	36.2	18.6	12.8	12.8	7.2	20.0
Mg	48.5	34.0	48.3	17.6	39.2	10.2	61.0	1.9	57.5	35.1	34.9	0.4	58.1	33.0	65.6	2.7
Fe	24.2	43.2	21.9	64.7	22.2	69.4	30.0	55.4	31.2	25.6	28.9	81.0	29.1	54.2	27.2	77.4
Fe/(Fe+Mg)	0.33	0.56	0.31	0.79	0.36	0.87	0.33	0.97	0.35	0.42	0.45	0.99	0.33	0.62	0.29	0.97

Total tet = sum of Si and Al in tetrahedral sites; in ideal pyroxenes, this number = 2. Some Al (listed as ^{vi}Al) may also occur in octahedral sites. Analyses #1 and 2 are from sample 74275 (Hodges and Kushiro, 1974); #3 and 4 are from sample 70017 (Hodges and Kushiro, 1974); #5 and 6 are from sample 70035 (Papike et al., 1974); #7 is from sample 10022 (Smith et al., 1970); #8 is from sample 10022 (Kushiro and Nakamura, 1970); #9 and 10 are from sample 10017 (Kushiro and Nakamura, 1970); #11 and 12 are from sample 10024 (Kushiro and Nakamura, 1970); #13 and 14 are from sample 10045 (Brown et al., 1970); #15 is from sample 10058 (Agrell et al., 1970b); #16 is from sample 10058 (Hollister and Hargraves, 1970); #17 and 18 are from sample 12063 (Hollister et al., 1971); #19 and 20 are from sample 12052 (Bence et al., 1970); #21 and 22 are from sample 12065 (Hollister et al., 1971); #23 is from sample 12021 (Dence et al., 1971); #24 is from sample 12021 (Boyd and Smith, 1971); #25 to 27 are from sample 12020 (Kushiro et al., 1971); #28 is from sample 12040 (Newton et al., 1971); #29 and 30 are from sample 15597 (Weigand and Hollister, 1973); #31 and 32 are from sample 15499 (Bence and Papike, 1972); #33 and 34 are from sample 15058 (Bence and Papike, 1972); #35 and 36 are from sample 15016 (Bence and Papike, 1972); #37 and 38 are from sample 15555 (Bence and Papike, 1972); #39 and 40 are from sample Luna 16 B-1 (Albee et al., 1972); #41 is from sample 14053 (Bence and Papike, 1972); #42 is from sample 14053 (Gancarz et al., 1971); #43 is from sample 14305 (Shervais et al., 1985b); #44 is from sample 14168 (Shervais et al., 1985b); #45 and 46 are from sample 24174 (Laul et al., 1978b); #47 and 48 are from sample 70009 (Vaniman and Papike, 1977c); #49 and 50 are from sample 70008 (Vaniman and Papike, 1977c).

TABLE A5.3. Pyroxene analyses from clast-poor melt rocks, crystalline melt breccias, and KREEP rocks.

	Melt Rocks					Cryst Melt Breccias					Melt Rocks						
	1.	2.	3.	4.	5.	6.	7.	8.	9.	10.	11.	12.	13.	14.	15.	16.	17.
<i>Chemical Composition (Weight Percent)</i>																	
SiO ₂	54.3	52.8	49.8	53.2	52.0	53.1	49.4	53.6	51.8	53.4	51.1	54.6	53.5	45.2	53.2	49.3	54.8
Al ₂ O ₃	4.1	1.6	0.9	1.1	2.1	4.5	1.6	1.8	2.4	1.7	2.8	2.0	0.81	1.3	3.7	2.6	0.89
TiO ₂	0.32	0.50	1.1	0.23	0.69	0.36	1.3	1.1	1.6	1.2	1.7	0.34	0.40	1.5	0.74	2.5	0.36
Cr ₂ O ₃	0.76	0.68	0.01	0.63	0.89	0.61	0.26	0.87	0.87	0.54	0.81	0.53	0.38	0.08	0.67	0.37	0.54
FeO	9.8	14.9	26.4	13.2	11.3	10.4	25.3	10.9	6.4	13.1	13.1	11.2	18.0	41.2	11.4	15.9	11.9
MnO	0.09	0.21	0.38	0.19	0.18	0.16	0.36	0.21	0.15	0.20	0.26	0.28	0.30	0.45	0.23	0.28	0.19
MgO	30.3	21.7	9.9	27.3	18.1	28.3	11.3	29.1	17.3	26.2	24.1	30.0	22.3	4.4	28.2	11.6	28.8
CaO	2.1	8.2	11.6	2.2	14.7	2.5	11.7	2.8	20.4	4.2	5.2	1.6	5.0	4.6	2.6	17.5	2.6
Na ₂ O	0.00	0.00	0.00	0.00	0.10	0.00	0.00	0.00	0.10	0.00	0.00	0.00	0.10	0.10	0.00	0.10	0.00
Total	101.77	100.59	100.09	98.05	100.06	99.93	101.22	100.38	101.02	100.54	99.07	100.55	100.79	98.83	100.74	100.15	100.08
<i>Cation Formula Based on 6 Oxygens (Ideal Pyroxene = 4 Cations per 6 Oxygens)</i>																	
Si	1.882	1.932	1.958	1.952	1.924	1.883	1.916	1.905	1.888	1.919	1.879	1.927	1.962	1.911	1.881	1.872	1.955
^{iv} Al	0.118	0.068	0.042	0.047	0.076	0.117	0.074	0.075	0.103	0.072	0.120	0.073	0.035	0.065	0.119	0.116	0.037
Total tet*	2.000	2.000	2.000	1.999	2.000	2.000	1.990	1.980	1.991	1.991	1.999	2.000	1.997	1.976	2.000	1.988	1.992
Ti	0.008	0.014	0.033	0.006	0.019	0.009	0.037	0.030	0.044	0.033	0.047	0.011	0.014	0.060	0.025	0.089	0.009
^{vi} Al	0.050	0.003	0.000	0.000	0.015	0.070	0.000	0.000	0.000	0.000	0.000	0.010	0.000	0.000	0.035	0.000	0.000
Cr	0.020	0.020	0.000	0.018	0.026	0.017	0.008	0.024	0.024	0.015	0.023	0.015	0.011	0.003	0.019	0.011	0.015
Fe	0.284	0.456	0.869	0.403	0.351	0.309	0.819	0.324	0.194	0.394	0.402	0.330	0.552	1.456	0.337	0.505	0.355
Mn	0.002	0.006	0.013	0.006	0.006	0.005	0.012	0.006	0.005	0.006	0.008	0.008	0.009	0.016	0.007	0.009	0.005
Mg	1.567	1.186	0.582	1.491	0.998	1.498	0.655	1.541	0.945	1.405	1.317	1.578	1.219	0.277	1.486	0.657	1.533
Ca	0.078	0.323	0.491	0.084	0.582	0.095	0.487	0.107	0.797	0.160	0.205	0.060	0.196	0.208	0.099	0.712	0.098
Na	0.000	0.000	0.000	0.000	0.008	0.000	0.000	0.000	0.006	0.000	0.000	0.000	0.007	0.005	0.000	0.007	0.000
Total Cations	4.009	4.008	3.988	4.007	4.005	4.003	4.008	4.012	4.006	4.004	4.001	4.012	4.005	4.001	4.008	3.978	4.007
<i>Cation Ratios: Ca : Mg : Fe and Fe/(Fe+Mg)</i>																	
Ca	4.0	16.4	25.1	4.3	30.1	5.0	24.7	5.4	41.1	8.2	10.6	3.1	10.0	10.7	5.1	38.0	4.9
Mg	81.1	60.2	29.8	75.1	51.5	78.6	33.2	77.9	48.6	71.5	68.2	80.1	62.0	14.3	77.3	35.0	77.0
Fe	14.9	23.4	45.1	20.6	18.4	16.4	42.1	16.7	10.3	20.3	21.2	16.8	28.0	75.0	17.5	27.0	18.1
Fe/(Fe+Mg)	0.15	0.28	0.60	0.21	0.26	0.17	0.56	0.17	0.17	0.22	0.23	0.17	0.31	0.84	0.18	0.43	0.19

TABLE A5.3. (continued).

	Cryst Melt Breccias						KREEP						
	18.	19.	20.	21.	22.	23.	24.	25.	26.	27.	28.	29.	30.
<i>Chemical Composition (Weight Percent)</i>													
SiO ₂	54.1	50.3	53.9	50.4	55.1	50.7	53.4	51.8	49.5	53.5	51.5	49.2	48.3
Al ₂ O ₃	2.9	3.6	2.4	2.7	1.8	4.9	3.0	1.9	1.1	1.6	1.5	2.6	1.4
TiO ₂	0.79	3.0	0.56	2.2	0.54	1.8	0.6	0.85	0.82	0.51	0.97	2.0	0.91
Cr ₂ O ₃	0.83	0.72	0.64	0.48	0.60	0.17	0.92	0.85	0.27	0.79	0.92	1.00	0.37
FeO	9.0	6.6	10.5	10.5	10.9	14.7	11.7	19.0	30.8	14.1	20.4	13.4	32.3
MnO	0.15	0.21	0.13	0.14	0.16	0.20	0.09	0.25	0.49	0.20	0.34	0.24	0.52
MgO	30.9	16.6	29.5	15.3	30.2	14.4	28.9	23.0	11.0	26.9	19.6	13.0	8.8
CaO	1.5	19.5	1.5	18.2	1.7	14.4	1.40	2.2	6.2	1.7	5.1	17.9	8.9
Na ₂ O	0.00	0.2	0.00	0.10	0.00	0.20	0.00	0.00	0.00	0.00	0.00	0.00	0.00
Total	100.17	100.73	99.13	100.02	101.00	101.47	100.01	99.85	100.18	99.30	100.33	99.34	101.50
<i>Cation Formula Based on 6 Oxygens (Ideal Pyroxene = 4 Cations per 6 Oxygens)</i>													
Si	1.901	1.842	1.923	1.881	1.932	1.871	1.901	1.920	1.958	1.941	1.930	1.878	1.920
^{iv} Al	0.099	0.156	0.077	0.118	0.068	0.129	0.099	0.081	0.042	0.059	0.066	0.116	0.066
Total tet*	2.000	1.998	2.000	1.999	2.000	2.000	2.000	2.001	2.000	2.000	1.996	1.994	1.986
Ti	0.021	0.082	0.015	0.062	0.014	0.050	0.016	0.024	0.025	0.014	0.028	0.058	0.027
^{vi} Al	0.019	0.000	0.025	0.000	0.007	0.084	0.026	0.000	0.009	0.009	0.000	0.000	0.000
Cr	0.023	0.021	0.018	0.014	0.017	0.005	0.026	0.025	0.008	0.023	0.027	0.030	0.011
Fe	0.265	0.202	0.314	0.327	0.321	0.454	0.348	0.588	1.019	0.429	0.639	0.427	1.072
Mn	0.004	0.006	0.004	0.004	0.004	0.007	0.003	0.008	0.016	0.006	0.011	0.008	0.017
Mg	1.616	0.906	1.567	0.854	1.580	0.794	1.533	1.269	0.649	1.454	1.092	0.740	0.523
Ca	0.058	0.766	0.057	0.729	0.065	0.568	0.054	0.088	0.263	0.065	0.204	0.732	0.380
Na	0.000	0.013	0.000	0.005	0.000	0.016	0.000	0.000	0.000	0.000	0.000	0.000	0.000
Total Cations	4.006	3.994	4.000	3.994	4.008	3.978	4.006	4.003	3.989	4.000	3.997	3.989	4.016
<i>Cation Ratios: Ca : Mg : Fe and Fe/(Fe+Mg)</i>													
Ca	3.0	40.7	2.9	38.1	3.3	31.2	2.8	4.5	13.5	3.3	10.5	38.4	19.1
Mg	83.1	48.2	80.7	44.6	80.2	43.6	79.1	65.0	33.3	74.4	56.1	38.8	26.2
Fe	13.9	11.1	16.4	17.3	16.5	25.2	18.1	30.5	53.2	22.3	33.4	22.8	54.7
Fe/(Fe+Mg)	0.14	0.18	0.17	0.28	0.17	0.36	0.19	0.32	0.61	0.23	0.37	0.37	0.67

* "Total tet" = sum of Si and Al in tetrahedral sites; in ideal pyroxenes, this number = 2. Some Al (listed as ^{vi}Al) may also occur in octahedral sites.

Analyses #1 to 3 are from sample 67559; #4 and 5 are from sample 68416; #6 and 7 are from sample 63549; #8 and 9 are from sample 60335; #10 and 11 are from sample 66095; #12 to 14 are from sample 14276; #15 and 16 are from sample 14310; #17 is from sample 64455; #18 and 19 are from sample 60315; #20 and 21 are from sample 62235; #22 and 23 are from sample 77135; #24 to 26 are from sample 15386; #27 to 30 are from sample 15434 (all analyses by *Vaniman and Papike*, 1980).

TABLE A5.4. Pyroxene analyses from ferroan anorthosites and Mg-rich rocks.

	Ferroan Anorthosites										Mg-rich Rocks								
	1.	2.	3.	4.	5.	6.	7.	8.	9.	10.	11.	12.	13.	14.	15.	16.	17.	18.	19.
<i>Chemical Composition (Weight Percent)</i>																			
SiO ₂	52.88	53.42	52.71	53.00	53.00	52.40	51.80	51.80	53.60	51.38	54.39	54.18	53.31	55.3	53.91	55.9	53.48	56.05	54.13
Al ₂ O ₃	0.51	0.68	0.28	0.75	0.51	0.87	0.35	0.73	0.45	1.32	1.02	1.02	1.10	1.30	0.99	1.5	1.00	0.96	1.22
TiO ₂	0.26	0.36	0.17	0.45	0.24	0.48	0.20	0.42	0.18	0.42	0.26	0.29	0.66	0.20	0.27	0.4	0.53	0.28	0.11
Cr ₂ O ₃	0.20	0.19	0.11	0.21	0.09	0.24	0.08	0.11	0.19	0.25	0.65	0.67	0.64	0.51	0.67	0.6	0.72	0.26	1.11
FeO	25.22	9.70	24.18	9.01	22.60	8.90	27.70	12.40	22.40	10.40	12.80	12.89	4.80	12.35	12.57	7.4	2.87	6.94	2.71
MnO	0.52	0.24	0.54	0.23	0.62	0.29	0.66	0.39	0.53	0.23	0.20	0.23	0.15	0.25	0.22	0.1	0.06	0.15	0.11
MgO	20.26	13.83	20.36	14.47	21.90	14.90	18.60	13.20	22.40	14.60	29.35	29.50	16.77	28.7	29.25	32.7	18.11	32.29	18.40
CaO	1.02	22.14	1.33	22.33	0.80	21.50	1.30	20.80	0.87	21.50	1.47	1.19	22.29	1.56	1.46	1.5	23.44	2.24	22.50
Na ₂ O	-	0.03	-	0.01	0.00	0.00	0.00	0.00	0.00	0.00	-	-	-	-	-	-	0.02	0.01	0.05
Total	100.87	100.59	99.68	100.46	99.76	99.58	100.69	99.85	100.62	100.10	100.14	99.97	99.72	100.17	99.34	100.1	100.23	99.18	100.34
<i>Cation Formula Based on 6 Oxygens (Ideal Pyroxene = 4 Cations per 6 Oxygens)</i>																			
Si	1.98	1.98	1.99	1.97	1.984	1.962	1.974	1.963	1.985	1.930	1.944	1.940	1.958	1.967	1.942	1.945	1.946	1.967	1.959
^{iv} Al	0.02	0.02	0.01	0.03	0.016	0.038	0.016	0.033	0.015	0.058	0.044	0.044	0.042	0.033	0.042	0.055	0.043	0.033	0.041
Total tet*	2.00	2.00	2.00	2.00	2.000	2.000	1.990	1.996	2.000	1.988	1.988	1.984	2.000	2.000	1.984	2.000	1.989	2.000	2.000
Ti	0.01	0.01	0.01	0.01	0.007	0.014	0.006	0.012	0.005	0.012	0.008	0.008	0.018	0.005	0.008	0.010	0.014	0.007	0.003
^{vi} Al	0.00	0.01	0.00	0.00	0.006	0.000	0.000	0.000	0.005	0.000	0.000	0.000	0.006	0.021	0.000	0.006	0.000	0.007	0.011
Cr	0.01	0.01	0.00	0.01	0.003	0.007	0.002	0.003	0.006	0.007	0.018	0.020	0.018	0.015	0.020	0.017	0.021	0.007	0.032
Fe	0.79	0.30	0.76	0.28	0.707	0.279	0.883	0.393	0.694	0.327	0.382	0.386	0.148	0.366	0.378	0.215	0.087	0.203	0.082
Mn	0.02	0.01	0.02	0.01	0.020	0.009	0.021	0.013	0.017	0.007	0.006	0.008	0.004	0.008	0.006	0.002	0.002	0.004	0.003
Mg	1.13	0.77	1.15	0.80	1.222	0.831	1.056	0.746	1.236	0.817	1.562	1.574	0.918	1.520	1.570	1.697	0.981	1.687	0.991
Ca	0.04	0.88	0.05	0.89	0.032	0.862	0.053	0.845	0.035	0.865	0.056	0.046	0.878	0.060	0.056	0.056	0.914	0.084	0.872
Na	-	-	-	-	0.000	0.000	0.000	0.000	0.000	0.000	-	-	-	-	-	-	0.002	0.001	0.003
Total Cations	4.00	3.99	3.990	4.00	3.997	4.002	4.011	4.008	3.998	4.023	4.020	4.026	3.990	3.995	4.022	4.003	4.010	4.000	3.997
<i>Cation Ratios: Ca : Mg : Fe and Fe/(Fe+Mg)</i>																			
Ca	2.0	45.1	2.5	45.2	1.6	43.7	2.7	42.6	1.8	43.1	2.82	2.28	45.16	3	2.81	2.8	46.1	4.2	44.8
Mg	57.7	39.5	58.7	40.6	62.3	42.1	53.0	37.6	62.9	40.7	78.08	78.47	47.25	78	78.31	86.2	49.5	85.5	50.9
Fe	40.3	15.4	38.8	14.2	36.1	14.1	44.3	19.8	35.3	16.3	19.11	19.25	7.59	19	18.88	10.9	4.4	1.03	4.2
Fe/(Fe+Mg)	0.41	0.28	0.40	0.26	0.37	0.25	0.46	0.35	0.36	0.29	0.20	0.20	0.14	0.19	0.19	0.11	0.08	0.11	0.08

* "Total tet" = sum of Si and Al in tetrahedral sites; in ideal pyroxenes, this number = 2. Some Al (listed as ^{iv}Al) may also occur in octahedral sites.

Analyses #1 to 4 are from sample 15415 (Hargraves and Hollister, 1972); #5 and 6 are from sample 60015 (Dixon and Papike, 1975); #7 and 8 are from sample 60025 (Dixon and Papike, 1975); #9 and 10 are from sample 61016 (Dixon and Papike, 1975); #11 to 13 are from sample 78235 (McCallum and Mathez, 1975); #14 is from sample 78235 (Sclar and Bauer, 1975); #15 is from sample 78238 (McCallum and Mathez, 1975); #16 is from sample 76535 (Smyth, 1975); #17 is from sample 76535 (Dymek et al., 1975a); #18 and 19 are from sample 72415 (Dymek et al., 1975a).

TABLE A5.5. Plagioclase analyses from mare basalts.

	High-Ti Basalts				Low-Ti Basalts			Aluminous, Low-Ti			Very Low-Ti Basalts					
	Apollo 17		Apollo 11 High-K		Apollo Low-K		A-12 Ilmenite	A-12 Pigeonite	A-15 Olivine	L-16 Al	A-14 Al	VHK	Luna 24		A-17 VLT	
	1.	2.	3.	4.	5.	6.	7.	8.	9.	10.	11.	12.	13.	14.	15.	16.
<i>Chemical Composition (Weight Percent)</i>																
SiO ₂	46.9	48.6	49.80	48.30	45.72	46.30	48.10	44.50	46.70	45.18	45.10	44.09	45.54	45.52	45.03	47.01
Al ₂ O ₃	34.5	31.7	30.50	32.40	34.53	34.00	32.00	35.20	31.80	33.87	33.90	35.18	34.31	33.96	34.93	32.67
FeO	0.28	0.63	0.81	0.51	0.30	0.99	1.17	0.81	2.62	0.54	0.29	0.25	0.92	1.32	0.90	1.34
MgO	0.26	0.22	0.25	0.22	0.07	0.30	0.08	0.08	1.16	0.16	0.0	-	0.06	0.00	0.26	0.15
CaO	17.4	17.0	15.80	16.60	18.64	17.10	17.50	19.20	17.30	18.80	18.80	19.54	18.89	17.20	19.42	18.48
Na ₂ O	1.34	1.55	1.95	1.84	0.70	1.05	0.40	0.58	0.88	0.86	0.88	0.55	0.65	1.02	0.46	0.71
K ₂ O	0.05	0.02	0.25	0.19	0.01	0.09	0.20	0.02	0.06	0.06	0.03	0.03	0.00	0.15	0.03	0.12
Total	100.73	99.72	99.36	100.06	99.97	99.83	99.45	100.39	100.52	99.47	99.00	99.64	100.37	99.17	101.03	100.48
<i>Cation Formula Based on 8 Oxygens (Ideal Plagioclase = 5 Cations per 8 Oxygens)</i>																
Si	2.141	2.237	2.295	2.216	2.108	2.136	2.222	2.056	2.160	2.100	2.105	2.048	2.100	2.121	2.067	2.165
^{iv} Al	1.853	1.721	1.657	1.753	1.877	1.849	1.743	1.917	1.734	1.850	1.865	1.927	1.865	1.866	1.891	1.774
Total tet*	3.994	3.958	3.952	3.969	3.985	3.985	3.965	3.973	3.894	3.950	3.970	3.975	3.965	3.987	3.958	3.939
Fe	0.011	0.024	0.031	0.020	0.012	0.038	0.045	0.031	0.101	0.020	0.011	0.009	0.036	0.052	0.034	0.052
Mg	0.018	0.015	0.017	0.015	0.005	0.021	0.006	0.006	0.080	0.010	0.000	-	0.004	0.000	0.018	0.010
Ca	0.850	0.836	0.780	0.816	0.921	0.845	0.866	0.950	0.857	0.930	0.940	0.972	0.933	0.859	0.955	0.912
Na	0.119	0.138	0.174	0.164	0.063	0.094	0.036	0.052	0.079	0.080	0.080	0.049	0.058	0.092	0.041	0.063
K	0.003	0.001	0.015	0.011	0.001	0.005	0.012	0.001	0.004	0.004	0.002	0.001	0.000	0.009	0.002	0.007
Total Cations	4.995	4.972	4.969	4.995	4.987	4.988	4.930	5.013	5.015	4.994	5.003	5.006	4.996	4.999	5.008	4.983
<i>Cation Ratio Fe/(Fe+Mg), and Molecular Proportion of Orthoclase (Or), Albite (Ab), and Anorthite (An)</i>																
Fe/(Fe+Mg)	0.38	0.62	0.65	0.57	0.71	0.65	0.89	0.85	0.56	0.67	1.00	1.00	0.90	1.00	0.65	0.84
Or	0.3	0.1	1.5	1.1	0.1	0.5	1.3	0.1	0.4	0.4	0.2	0.1	0.0	9.6	0.2	0.7
Ab	12.2	14.1	18.0	16.6	6.4	10.0	3.9	5.2	8.4	7.9	7.8	4.8	5.8	0.9	4.1	6.4
An	87.5	85.7	80.5	82.3	93.5	89.5	94.8	94.7	91.2	91.7	92.0	95.1	94.2	89.5	95.7	92.9

* "Total tet" = sum of Si and Al, both of which must be in the 4 tetrahedral sites per 8 oxygens.

Analyses #1 and 2 are from sample 75083 (Papike et al., 1974); #3 is from sample 10022 (Kushiro and Nakamura, 1970); #4 is from sample 10024 (Crawford, 1973); #5 is from sample 10045 (Agrell et al., 1970b); #6 is from sample 10050 (Appelmann et al., 1971); #7 is from sample 12063 (Crawford, 1973); #8 is from sample 12021 (Crawford, 1973); #9 is from sample 15016 (S. R. Taylor et al., 1973a); #10 is from sample Luna 16 B-1 (Albee et al., 1972); #11 is from sample 14053 (Kushiro et al., 1972); #12 is from sample 14305 (Shervais et al., 1985b); #13 and 14 are from sample 24174 (Laul et al., 1978b); #15 and 16 are from sample 70008 (Vaniman and Papike, 1977c).

TABLE A5.6. Plagioclase analyses from highland clast-poor melt rocks, crystalline melt breccias, and KREEP rocks.

	Melt Rocks					Cryst Melt Breccias					Melt Rocks					Cryst Melt Breccias					KREEP				
	1.	2.	3.	4.	5.	6.	7.	8.	9.	10.	11.	12.	13.	14.	15.	16.	17.	18.	19.	20.	21.	22.	23.	24.	25.
<i>Chemical Composition (Weight Percent)</i>																									
SiO ₂	44.5	47.6	43.9	45.4	43.5	44.4	44.6	45.8	43.8	45.5	44.7	47.4	43.8	46.4	45.4	45.9	44.9	45.8	45.5	44.2	45.8	47.3	49.5	47.1	51.3
Al ₂ O ₃	36.4	33.3	36.7	35.7	36.1	35.7	35.9	34.3	36.1	35.4	34.7	33.4	36.1	34.0	36.3	32.7	34.5	34.3	35.4	35.9	35.3	34.0	30.8	32.5	30.8
FeO	0.10	0.52	0.15	0.46	0.07	0.11	0.12	0.18	0.15	0.30	0.21	0.39	0.15	0.06	0.06	0.26	0.27	0.22	0.27	0.18	0.26	0.19	0.38	0.16	0.48
MgO	0.00	0.00	0.05	0.07	0.00	0.07	0.01	0.07	0.00	0.15	0.12	0.14	0.19	0.29	0.36	0.37	0.00	0.00	0.11	0.00	0.00	0.19	0.10	0.17	0.08
CaO	20.0	17.3	20.2	18.1	19.4	18.8	19.3	17.9	19.7	18.7	19.5	17.2	19.2	17.1	18.5	19.0	19.0	18.7	18.6	19.7	18.7	17.1	15.9	17.1	14.7
Na ₂ O	0.26	1.6	0.27	0.97	0.29	0.56	0.40	0.92	0.39	0.71	0.49	1.6	0.51	1.4	0.69	0.78	0.66	0.88	0.91	0.28	0.98	1.4	2.2	1.5	2.4
K ₂ O	0.01	0.10	0.01	0.09	0.00	0.01	0.03	0.06	0.01	0.12	0.05	0.29	0.05	0.21	0.02	0.09	0.06	0.25	0.07	0.07	0.09	0.08	0.34	0.11	0.33
Total	101.27	100.42	101.28	100.79	99.36	99.65	100.36	99.23	100.15	100.88	99.77	100.42	100.00	99.46	101.33	99.10	99.39	100.15	100.86	100.33	101.13	100.26	99.22	98.64	100.09
<i>Cation Formula Based on 8 Oxygens (Ideal Plagioclase = 5 Cations per 8 Oxygens)</i>																									
Si	2.031	2.181	2.009	2.078	2.022	2.053	2.051	2.123	2.024	2.082	2.073	2.173	2.026	2.143	2.062	2.142	2.087	2.112	2.082	2.039	2.090	2.163	2.285	2.191	2.334
^{IV} Al	1.962	1.796	1.980	1.926	1.981	1.949	1.948	1.874	1.968	1.909	1.897	1.804	1.968	1.851	1.946	1.796	1.891	1.864	1.909	1.952	1.896	1.834	1.676	1.783	1.650
Total tet*	3.993	3.977	3.989	4.004	4.003	4.002	3.999	3.997	3.992	3.991	3.970	3.977	3.994	3.994	4.008	3.938	3.978	3.976	3.991	3.991	3.986	3.997	3.961	3.974	3.984
Fe	0.004	0.020	0.006	0.018	0.003	0.004	0.005	0.007	0.006	0.012	0.008	0.015	0.006	0.002	0.002	0.010	0.011	0.009	0.010	0.007	0.010	0.007	0.015	0.006	0.018
Mg	0.000	0.000	0.003	0.005	0.000	0.005	0.001	0.005	0.000	0.010	0.008	0.010	0.013	0.020	0.024	0.026	0.000	0.000	0.008	0.000	0.000	0.013	0.007	0.012	0.006
Ca	0.977	0.850	0.991	0.888	0.970	0.934	0.953	0.888	0.976	0.916	0.969	0.845	0.952	0.846	0.899	0.949	0.946	0.924	0.912	0.971	0.914	0.840	0.787	0.855	0.719
Na	0.023	0.139	0.024	0.086	0.026	0.050	0.036	0.084	0.035	0.063	0.142	0.046	0.125	0.060	0.071	0.060	0.079	0.081	0.025	0.086	0.121	0.196	0.133	0.210	0.003
K	0.001	0.006	0.001	0.005	0.000	0.001	0.002	0.003	0.000	0.007	0.003	0.017	0.003	0.012	0.001	0.005	0.003	0.014	0.004	0.004	0.005	0.005	0.020	0.007	0.019
Total Cations	4.998	4.992	5.014	5.006	5.002	4.996	4.996	4.984	5.009	4.999	5.002	5.006	5.014	4.999	4.994	4.999	4.998	5.002	5.006	4.998	5.001	4.983	4.986	4.987	4.956
<i>Cation Ratio Fe/(Fe+Mg), and Molecular Proportion of Orthoclase (Or), Albite (Ab), and Anorthite (An)</i>																									
Fe/(Fe+Mg)	1.00	1.00	0.66	0.79	1.00	0.44	0.83	0.58	1.00	0.55	0.50	0.61	0.21	0.10	0.09	0.28	1.00	1.00	0.56	1.00	1.00	0.35	0.68	0.34	0.76
Or	0.10	0.60	0.10	0.50	0.00	0.10	0.10	0.30	0.00	0.70	0.30	1.70	0.30	1.30	0.10	0.50	0.30	1.40	0.40	0.40	0.50	0.50	2.00	0.70	2.00
Ab	2.30	14.00	2.40	8.80	2.60	5.10	3.60	8.50	3.50	6.40	4.30	14.20	4.60	12.70	6.30	6.90	5.90	7.80	8.10	2.50	8.60	12.50	19.60	13.30	22.10
An	97.60	85.40	97.60	90.70	97.40	94.80	96.20	91.20	96.50	92.90	95.40	84.10	95.10	86.00	93.60	92.60	93.80	90.80	91.50	97.10	90.90	87.00	78.40	86.00	75.90

Total tet = sum of Si and Al, both of which must be in the 4 tetrahedral sites per 8 oxygens.

Analyses #1 and 2 are from sample 67559; #3 and 4 are from sample 68415; #5 and 6 are from sample 63549; #7 and 8 are from sample 60335; #9 and 10 are from sample 66095; #11 and 12 are from sample 14276; #13 and 14 are from sample 14310; #15 is from sample 64455; #16 is from sample 62295; #17 and 18 are from sample 62235; #19 is from sample 65015; #20 and 21 are from sample 77135; #22 and 23 are from sample 15386; #24 and 25 are from sample 15434 (all analyses from *Vaniman and Papike, 1980*).

TABLE A5.7. Plagioclase analyses from ferroan anorthosites and Mg-rich rocks.

	Ferroan Anorthosites								Mg-rich Rocks						
									Norite				Troctolite		
	1.	2.	3.	4.	5.	6.	7.	8.	9.	10.	11.	12.	13.	14.	15.
<i>Chemical Composition (Weight Percent)</i>															
SiO ₂	44.19	43.92	44.6	44.6	43.4	43.9	43.2	42.8	44.72	45.25	46.48	45.27	43.40	44.1	44.21
Al ₂ O ₃	35.77	36.24	35.2	36.0	35.2	35.7	36.6	35.6	35.15	34.85	32.75	35.18	35.41	35.3	35.89
FeO	0.16	0.09	0.20	0.18	0.19	0.16	0.08	0.10	0.10	0.15	1.21	0.10	0.18	0.04	0.10
MgO	0.00	-	0.06	0.07	0.04	0.04	0.00	0.00	0.08	0.10	1.51	0.08	0.11	-	0.07
CaO	19.66	19.49	20.0	19.5	19.5	19.2	19.6	18.9	19.24	18.73	17.77	18.79	19.22	18.7	19.60
Na ₂ O	0.22	0.26	0.35	0.38	0.42	0.45	0.25	0.33	0.57	0.59	0.71	0.66	0.58	0.43	0.29
K ₂ O	-	-	0.01	0.03	0.00	0.01	0.00	0.00	0.09	0.10	0.09	0.14	0.08	0.07	0.05
Total	100.00	100.00	100.4	100.8	98.8	99.5	99.7	97.7	99.95	99.77	100.52	100.22	98.98	98.64	100.21
<i>Cation Formula Based on 8 Oxygens (Ideal Plagioclase = 5 Cations per 8 Oxygens)</i>															
Si	2.04	2.03	2.057	2.046	2.034	2.040	2.002	2.024	2.068	2.093	2.137	2.083	2.033	2.063	2.04
^{iv} Al	1.95	1.97	1.915	1.947	1.947	1.956	1.999	1.984	1.917	1.900	1.775	1.908	1.952	1.943	1.950
Total tet*	3.99	4.00	3.972	3.993	3.981	3.996	4.001	4.008	3.985	3.993	3.912	3.991	3.985	4.006	3.991
Fe	0.01	0.00	0.008	0.007	0.007	0.006	0.003	0.004	0.004	0.006	0.047	0.004	0.007	0.002	0.004
Mg	0.00	-	0.004	0.005	0.003	0.003	0.000	0.000	0.005	0.005	0.104	0.005	0.008	-	0.005
Ca	0.97	0.97	0.987	0.959	0.981	0.955	0.973	0.957	0.953	0.928	0.876	0.927	0.964	0.937	0.970
Na	0.02	0.02	0.031	0.034	0.038	0.041	0.023	0.030	0.051	0.053	0.063	0.059	0.052	0.038	0.026
K	-	-	0.001	0.002	0.000	0.000	0.000	0.000	0.005	0.006	0.005	0.008	0.004	0.004	0.003
Total Cations	4.99	4.99	5.003	5.000	5.010	5.001	5.000	4.999	5.003	4.991	5.007	4.994	5.020	4.987	4.999
<i>Cation Ratio Fe/(Fe+Mg), and Molecular Proportion of Orthoclase (Or), Albite (Ab), and Anorthite (An)</i>															
Fe/(Fe+Mg)	1.00	1.00	0.67	0.58	0.70	0.67	1.00	1.00	0.44	0.54	0.31	0.44	0.47	1.00	0.44
Or	-	-	0.05	0.2	0.0	0.0	0.0	0.00	0.5	0.6	0.6	0.9	0.4	0.4	0.3
Ab	2.0	2.0	3.0	3.4	3.7	4.1	2.3	3.0	5.1	5.4	6.7	5.9	5.1	3.9	2.6
An	98.0	98.0	96.9	96.4	96.3	95.9	97.7	97.0	94.4	94.0	92.7	93.2	94.5	95.7	97.1

* "Total tet" = sum of Si and Al, both of which must be in the 4 tetrahedral sites per 8 oxygens.

Analyses #1 and 2 are from sample 15415 (Hargraves and Hollister, 1972); #3 and 4 are from sample 60015 (Dixon and Papike, 1975); #5 is from sample 60025 (Dixon and Papike, 1975); #6 is from sample 61016 (Dixon and Papike, 1975); #7 and 8 are from sample 65315 (Dixon and Papike, 1975); #9 to 11 are from sample 78235 (McCallum and Mathez, 1975); #12 is from sample 78238 (McCallum and Mathez, 1975); #13 is from sample 12033,66 (Marvin and Walker, 1985); #14 is from sample 76255 (J. L. Warner et al., 1976a,b); #15 is from sample 76535 (Dymek et al., 1975a).

TABLE A5.8. Olivine analyses from mare basalts.

	High-Ti Basalts						Low-Ti Basalts						Very Low-Ti Basalts							
	Apollo 17		A-11		A-11		A-12		A-12		A-12		A-15		VHK		Luna 24		Apollo 17	
	1.	2.	3.	4.	5.	6.	7.	8.	9.	10.	11.	12.	13.	14.	15.	16.	17.	18.	19.	20.
<i>Chemical Composition (Weight Percent)</i>																				
SiO ₂	37.60	37.53	37.50	37.50	38.60	29.20	38.08	30.60	34.10	37.80	35.40	29.70	37.46	33.50	33.37	29.93	37.24	34.99	37.98	37.71
Al ₂ O ₃	0.02	0.01	0.04	0.05	0.00	0.30	0.02	0.00	0.32	0.00	0.00	0.06	-	-	0.20	0.29	0.17	0.20	0.18	0.21
FeO	28.44	27.44	26.20	25.50	25.40	68.70	22.15	65.30	39.60	21.10	33.80	64.80	24.71	49.79	48.61	67.15	28.25	39.35	23.06	23.43
MgO	34.66	35.93	35.80	36.50	34.90	0.50	38.86	3.54	23.70	39.20	30.10	3.80	37.39	15.75	17.88	0.97	35.23	26.42	37.94	38.30
MnO	0.31	0.28	0.22	0.30	0.36	1.10	0.24	0.00	0.52	0.24	0.36	0.66	0.36	0.71	0.45	0.74	0.28	0.42	0.29	0.26
Cr ₂ O ₃	0.19	0.13	0.21	0.21	0.28	0.02	0.35	0.00	0.24	0.44	0.11	0.04	-	-	0.12	0.10	0.39	0.15	0.55	0.67
CaO	0.33	0.29	0.28	0.33	0.31	0.26	0.27	0.65	0.59	0.30	0.36	0.40	0.23	0.32	0.48	1.03	0.28	0.29	0.41	0.39
Na ₂ O	0.01	0.00	0.00	0.00	0.00	0.00	0.01	0.00	0.00	0.00	0.00	0.00	-	-	-	0.00	-	-	-	-
Total	101.56	101.61	100.25	100.39	99.85	100.08	99.98	100.09	99.07	99.08	100.13	99.46	100.15	100.07	101.11	100.21	101.84	101.82	100.41	100.97
<i>Cation Formula Based on 4 Oxygens (Ideal Olivine = 3 Cations per 4 Oxygens)</i>																				
Si	0.993	0.986	0.993	0.989	1.020	0.987	0.992	1.005	0.984	0.990	0.978	0.987	0.986	1.006	0.985	0.996	0.981	0.975	0.989	0.980
Al	0.001	0.000	0.001	0.002	0.000	0.012	0.001	0.000	0.011	0.000	0.000	0.002	-	-	0.007	0.011	0.005	0.006	0.006	0.006
Fe	0.628	0.603	0.580	0.562	0.561	1.942	0.483	1.794	0.956	0.462	0.781	1.800	0.544	1.251	1.200	1.870	0.622	0.917	0.502	0.509
Mg	1.364	1.407	1.413	1.435	1.374	0.025	1.509	0.173	1.020	1.530	1.240	0.188	1.468	0.705	0.786	0.048	1.382	1.097	1.473	1.483
Mn	0.007	0.006	0.005	0.007	0.008	0.031	0.005	0.000	0.013	0.005	0.008	0.019	0.007	0.018	0.011	0.021	0.006	0.010	0.006	0.006
Cr	0.004	0.003	0.004	0.004	0.006	0.001	0.007	0.000	0.005	0.009	0.002	0.001	-	-	0.003	0.002	0.008	0.003	0.011	0.014
Ca	0.009	0.008	0.008	0.009	0.009	0.009	0.008	0.023	0.018	0.008	0.011	0.014	0.006	0.009	0.015	0.037	0.008	0.009	0.012	0.011
Na	0.001	0.000	0.000	0.000	0.000	0.000	0.001	0.000	0.000	0.000	0.000	0.000	-	-	-	0.000	-	-	-	-
Total Cations	3.007	3.013	3.004	3.008	2.978	3.007	3.006	2.995	3.007	3.004	3.020	3.011	3.011	2.989	3.007	2.985	3.012	3.017	2.999	3.009
<i>Cation Ratio Fe/(Fe+Mg)</i>																				
Fe/(Fe+Mg)	0.32	0.30	0.29	0.28	0.29	0.99	0.24	0.91	0.48	0.23	0.39	0.91	0.27	0.64	0.60	0.97	0.31	0.46	0.25	0.26

Analysis #1 is from sample 70215 (Dymek *et al.*, 1975); #2 is from sample 71055 (Dymek *et al.*, 1975); #3 is from sample 10022 (Kushiro and Nakamura, 1970); #4 is from sample 10020 (Haggerty *et al.*, 1970); #5 is from sample 10045 (Brown *et al.*, 1970); #6 is from sample 10044 (Smith *et al.*, 1970); #7 is from sample 12022 (Weill *et al.*, 1971); #8 is from sample 12063 (El Goresy *et al.*, 1971b); #9 is from sample 12052 (Bence *et al.*, 1970); #10 is from sample 12009 (Butler, 1972); #11 is from sample 12035 (Butler, 1972); #12 is from sample 15555 (Roedder and Weiblen, 1972). #13 and 14 are from sample 14305 (Shervais *et al.*, 1985b); #15 and 16 are from sample 24174 (Laul *et al.*, 1978b); #17 and 18 are from sample 70008 (Vaniman and Papike, 1977c); #19 is from sample 70007 (Vaniman and Papike, 1977c); #20 is from sample 70008 (Vaniman and Papike, 1977c).

TABLE A5.9. Olivine analyses from highland clast-poor melt rocks and crystalline melt breccias.

	Melt Rocks				Cryst Melt Breccias				Melt Rocks				Cryst Melt Breccias							
	1.	2.	3.	4.	5.	6.	7.	8.	9.	10.	11.	12.	13.	14.	15.	16.	17.	18.	19.	20.
<i>Chemical Composition (Weight Percent)</i>																				
SiO ₂	36.5	38.2	37.4	36.1	39.3	38.9	38.8	38.0	31.9	39.0	39.1	38.2	38.4	37.8	38.8	38.4	38.8	35.8	39.5	37.7
Al ₂ O ₃	0.11	0.06	0.02	0.22	0.06	0.10	0.11	0.13	0.44	0.16	0.10	0.11	0.17	0.14	0.15	0.17	0.14	0.54	0.26	0.08
FeO	34.1	25.4	28.8	33.3	15.8	18.0	20.2	22.2	58.3	17.4	20.1	21.4	22.0	26.6	21.4	22.8	22.2	33.7	18.5	26.2
MgO	30.5	37.6	34.5	30.4	44.6	42.0	41.2	39.2	8.4	43.0	41.4	40.0	39.7	35.5	40.6	39.3	38.3	29.5	43.1	36.3
MnO	0.28	0.33	0.28	0.36	0.18	0.21	0.27	0.20	0.55	0.14	0.19	0.22	0.27	0.42	0.21	0.25	0.15	0.31	0.14	0.25
Cr ₂ O ₃	0.09	0.10	0.07	0.12	0.21	0.22	0.20	0.12	0.02	0.09	0.08	0.03	0.10	0.06	0.21	0.20	0.07	0.07	0.20	0.04
CaO	0.40	0.16	0.16	0.26	0.12	0.13	0.17	0.22	0.30	0.15	0.16	0.11	0.15	0.19	0.23	0.19	0.26	0.24	0.39	0.23
Total	101.98	101.85	101.23	100.76	100.27	99.56	100.95	100.07	99.91	99.94	101.13	100.07	100.79	100.71	101.60	101.31	99.92	100.16	102.09	100.80
<i>Cation Formula Based on 4 Oxygens (Ideal Olivine = 3 Cations per 4 Oxygens)</i>																				
Si	0.986	0.989	0.991	0.986	0.989	0.995	0.990	0.987	1.004	0.992	0.994	0.989	0.989	0.996	0.988	0.988	1.006	0.983	0.987	0.992
Al	0.004	0.002	0.001	0.007	0.002	0.003	0.003	0.004	0.016	0.005	0.003	0.003	0.005	0.004	0.004	0.005	0.004	0.017	0.008	0.003
Fe	0.771	0.550	0.638	0.759	0.332	0.385	0.430	0.482	1.535	0.369	0.427	0.463	0.472	0.586	0.456	0.490	0.481	0.774	0.387	0.576
Mg	1.229	1.451	1.363	1.234	1.673	1.604	1.566	1.519	0.394	1.630	1.569	1.543	1.522	1.395	1.540	1.506	1.480	1.207	1.607	1.421
Mn	0.006	0.007	0.006	0.008	0.004	0.004	0.006	0.004	0.015	0.003	0.004	0.004	0.006	0.009	0.004	0.005	0.003	0.007	0.003	0.005
Cr	0.002	0.002	0.001	0.002	0.004	0.004	0.004	0.002	0.000	0.002	0.002	0.001	0.002	0.001	0.004	0.004	0.001	0.002	0.004	0.001
Ca	0.012	0.004	0.005	0.008	0.003	0.004	0.005	0.006	0.010	0.004	0.004	0.003	0.004	0.005	0.006	0.005	0.007	0.007	0.010	0.006
Total Cations	3.010	3.005	3.005	3.004	3.007	2.999	3.004	3.004	2.974	3.005	3.003	3.006	3.000	2.996	3.002	3.003	2.982	2.997	3.006	3.004
<i>Cation Ratio Fe/(Fe+Mg)</i>																				
Fe/(Fe+Mg)	0.38	0.27	0.32	0.38	0.17	0.20	0.22	0.24	0.80	0.19	0.22	0.23	0.24	0.30	0.23	0.25	0.24	0.39	0.19	0.29

Analysis #1 is from sample 67559; #2 and 3 are from sample 68415; #4 is from sample 68416; #5 to 7 are from sample 60335; #8 is from sample 66095; #9 is from sample 14310; #10 and 11 are from sample 64455; #12 is from sample 62295; #13 and 14 are from sample 60315; #15 and 16 are from sample 62235; #17 and 18 are from sample 65015; #19 and 20 are from sample 77135 (all analyses from *Vaniman and Papike, 1980*).

TABLE A5.10. Olivine analyses from ferroan anorthosites and Mg-rich rocks.

	Ferroan Anorthosites		Mg-rich Rocks					
			Troctolite			Dunite		
	1.	2.	3.	4.	5.	6.	7.	8.
<i>Chemical Composition (Weight Percent)</i>								
SiO ₂	37.1	35.59	40.3	39.9	40.85	40.24	40.13	39.84
Al ₂ O ₃	0.08	0.0	0.0	-	0.0	<0.01	0.05	0.00
FeO	31.8	34.58	12.3	12.0	11.0	12.29	13.00	13.13
MgO	30.9	30.11	47.96	47.1	48.45	47.65	48.14	48.30
MnO	-	0.42	0.16	0.1	0.11	0.13	0.15	0.17
Cr ₂ O ₃	-	0.05	0.02	<0.02	0.04	0.04	0.05	0.05
CaO	0.06	0.03	0.03	<0.02	0.09	0.13	0.13	0.08
Na ₂ O	-	-	-	-	0.05	-	0.06	0.02
Total	99.94	100.78	100.77	99.10	100.59	100.48	101.71	101.59
<i>Cation Formula Based on 4 Oxygens (Ideal Olivine = 3 Cations per 4 Oxygens)</i>								
Si	1.009	0.979	0.991	0.994	1.000	0.993	0.980	0.978
Al	0.003	-	-	-	-	-	0.001	-
Fe	0.723	0.795	0.253	0.250	0.225	0.254	0.265	0.269
Mg	1.253	1.235	1.760	1.750	1.768	1.753	1.752	1.768
Mn	-	0.010	0.003	0.001	0.002	0.003	0.003	0.003
Cr	-	0.001	0.000	0.000	0.001	0.001	0.001	0.001
Ca	0.002	0.001	0.001	0.000	0.002	0.003	0.003	0.002
Na	-	-	-	-	0.002	-	0.003	0.001
Total Cations	2.990	3.014	3.008	2.995	3.000	3.007	3.008	3.022
<i>Cation Ratio Fe/(Fe+Mg)</i>								
Fe/(Fe+Mg)	0.37	0.39	0.13	0.12	0.11	0.13	0.13	0.13

Analysis #1 is from sample 67635,2 (Borchardt et al., 1985); #2 is from sample 62237 (Dymek et al., 1975a); #3 is from sample 76535 (Dymek et al., 1975a); #4 is from sample 76535 (Gooley et al., 1974); #5 is from sample 12033 (Marvin and Walker, 1985); #6 is from sample 72415 (Dymek et al., 1975a); #7 and 8 are from sample 72415 (Richter et al., 1976).

TABLE A5.11a. Analyses of miscellaneous lunar silicate minerals.

	Zircon					Pyroxferroite			K-Feldspar				Silica Polymorphs				
	Soil		Reg br		Granite		A-11		A-12	Granite		Soil	A-12	A-14	A-11		A-11
	1.	2.	3.	4.	5.	6.	7.	8.	9.	10.	11.	12.	13.	14.	15.	16.	
<i>Chemical Composition (Weight Percent)</i>																	
SiO ₂	32.2	35.5	32.11	32.41	32.41	46.92	45.86	45.23	60.93	61.0	57.2	63.49	98.0	98.0	97.6	96.9	
Al ₂ O ₃	0.09	1.3	-	0.2	-	0.76	0.36	0.54	22.52	20.5	20.1	19.44	1.56	0.92	1.1	1.03	
TiO ₂	-	0.2	-	0.19	-	0.74	0.37	0.73	-	-	-	-	0.48	0.27	0.2	-	
Cr ₂ O ₃	-	-	-	0.03	-	0.12	0.08	0.05	-	-	-	-	-	-	-	-	
FeO	0.32	0.8	-	0.02	0.35	42.48	44.33	46.54	0.13	-	0.35	0.03	0.18	0.05	0.3	0.35	
MnO	-	-	-	-	-	0.65	0.76	0.56	-	-	-	-	-	-	-	-	
MgO	0.18	0.1	-	0.19	-	2.41	0.90	0.34	0.0	-	-	-	-	-	-	-	
CaO	-	-	-	0.26	-	6.69	6.56	6.43	3.87	2.07	0.55	0.35	0.34	0.16	0.3	0.52	
Na ₂ O	0.09	-	-	-	-	-	-	0.03	3.46	1.24	0.81	0.74	0.19	0.15	0.0	0.05	
K ₂ O	-	-	-	-	-	-	-	-	7.99	10.9	11.1	14.76	-	-	0.0	0.25	
ZrO ₂	64.7	61.5	67.23	66.93	63.48	-	-	-	-	-	-	-	-	-	-	-	
HfO ₂	-	0.6	0.88	-	3.01	-	-	-	-	-	-	-	-	-	-	-	
BaO	-	-	-	-	-	-	-	-	1.19	2.73	9.3	0.44	-	-	-	-	
Total	97.58	100.0	100.22	100.23	99.25	100.77	99.22	100.45	100.09	98.44	99.41	99.24	100.75	99.55	99.5	99.10	
<i>Cation Compositions Based on Relevant Number of Oxygens</i>																	
Si	1.004	1.054	0.986	0.987	1.01	1.965	1.978	1.95	2.788	2.88	2.819	2.954	0.979	0.988	0.986	0.985	
Al	0.003	0.045	-	0.007	-	0.038	0.018	0.03	1.215	1.14	1.168	1.064	0.018	0.011	0.013	0.012	
Ti	-	0.004	-	0.009	-	0.023	0.012	0.02	-	-	-	-	0.004	0.002	0.002	-	
Cr	-	-	-	0.001	-	0.004	0.003	0.00	-	-	-	-	-	-	-	-	
Fe	0.008	0.020	-	0.001	0.009	1.488	1.599	1.68	0.005	-	0.014	0.000	0.002	0.000	0.003	0.003	
Mn	-	-	-	-	-	0.023	0.028	0.02	-	-	-	-	-	-	-	-	
Mg	0.008	0.004	-	0.004	-	0.150	0.058	0.02	-	-	-	-	-	-	-	-	
Ca	-	-	-	0.008	-	0.300	0.303	0.30	0.190	0.105	0.029	0.016	0.004	0.002	0.003	0.006	
Na	0.005	-	-	-	-	-	-	0.00	0.307	0.113	0.077	0.065	0.004	0.003	-	0.001	
K	-	-	-	-	-	-	-	-	0.466	0.656	0.698	0.875	-	-	-	0.003	
Zr	0.984	0.890	1.007	0.994	0.962	-	-	-	-	-	-	-	-	-	-	-	
Hf	-	0.005	0.008	-	0.027	-	-	-	-	-	-	-	-	-	-	-	
Ba	-	-	-	-	-	-	-	-	0.021	0.050	0.180	0.006	-	-	-	-	
Total	2.012	2.022	2.001	2.011	2.008	3.991	3.999	4.02	4.992	4.944	4.985	4.980	1.011	1.006	1.007	1.010	
No. of Oxygens	4	4	4	4	4	6	6	6	8	8	8	8	2	2	2	2	

Analysis #1 is from sample 12070 (Keil et al., 1971); #2 is from sample 12034 (Anderson and Smith, 1971); #3 is from sample 12032 (Brown et al., 1971); #4 is from sample 14321 (Gay et al., 1972); #5 is from sample 12013 (Lunatic Asylum, 1970); #6 is from sample 10058 (Agrell et al., 1970b); #7 is from sample 10058 (Brown et al., 1972); #8 is from sample 12065 (Hollister et al., 1971); #9 is from sample 12013 (Drake et al., 1970); #10 is from sample 10085 (Albee and Chodos, 1970); #11 is from sample 12039 (Keil et al., 1971); #12 is from sample 14305 (Shervais et al., 1985); #13 is from sample 10017 (Brown et al., 1970); #14 is from sample 10058 (Brown et al., 1970); #15 is from sample 10020 (Dence et al., 1970); #16. is from sample 10045 (Keil et al., 1970).

TABLE A5.11b. Tranquillityite analyses from mare basalts.

	A-11					A-12	A-12
	LK					ol	plg
	1.	2.	3.	4.	5.	6.	7.
<i>Chemical Composition (Weight Percent)</i>							
SiO ₂	13.66	13.77	13.98	13.75	13.65	13.00	14.7
Al ₂ O ₃	0.87	0.90	0.83	0.85	0.92	0.70	1.71
TiO ₂	19.75	20.66	20.01	20.28	19.80	17.50	19.7
Cr ₂ O ₃	0.06	0.19	0.13	0.15	-	-	-
FeO	43.00	42.37	42.90	42.34	42.50	41.78	42.3
MnO	0.36	0.30	0.34	0.30	0.50	0.25	0.22
CaO	1.04	1.11	1.17	1.20	1.20	1.00	1.53
Zr ₂ O ₃	16.96	16.79	16.35	16.87	16.90	17.80	17.3
HfO ₂	0.05	0.06	0.04	0.05	0.49	0.60	-
Y ₂ O ₃	2.51	2.73	2.61	2.58	3.50	4.71	1.34
Total	98.26	98.88	98.36	98.37	99.46	97.34	98.80
<i>Cation Formula Based on 24 Oxygens</i>							
Si	2.859	2.849	2.906	2.860	2.836	2.805	3.009
Al	0.141	0.151	0.094	0.140	0.164	0.178	0.000
Subtotal	3.000	3.000	3.000	3.000	3.000	2.983	3.009
Ti	2.916	2.900	2.870	2.907	2.939	2.839	2.587
Al	0.074	0.069	0.109	0.068	0.061	0.000	0.413
Cr	0.010	0.031	0.021	0.025	0.000	0.000	0.000
Subtotal	3.000	3.000	3.000	3.000	3.000	2.839	3.000
Fe	7.527	7.332	7.458	7.365	7.385	7.538	7.241
Ti	0.193	0.315	0.258	0.265	0.155	0.000	0.446
Mn	0.064	0.053	0.060	0.053	0.088	0.046	0.038
Ca	0.233	0.246	0.261	0.267	0.267	0.231	0.336
Subtotal	8.017	7.946	8.037	7.950	7.895	7.815	8.061
Zr	1.731	1.694	1.657	1.711	1.712	1.873	1.727
Hf	0.003	0.004	0.002	0.003	0.029	0.037	0.000
Y	0.279	0.300	0.288	0.285	0.387	0.540	0.146
Subtotal	2.013	1.998	1.947	1.999	2.128	2.450	1.873
Total cations	16.030	15.944	15.984	15.949	16.023	16.087	15.943

Analyses #1 to 5 are from sample 10047; #6 is from sample 12018; #7 is from sample 12039 (all analyses from *Lovering et al.*, 1971).

TABLE A5.12. Ilmenite analyses from lunar rocks and soils.

	A-11 Soil	A-11 HK				A-11 LK	A-12 ol	A-11 ol	A-12 pig	A-12 ilm	A-12 pig	A-12 ilm
	1.	2.	3.*	4.*	5.	6.	7.	8.	9.	10.	11.	12.
<i>Chemical Composition (Weight Percent)</i>												
TiO ₂	56.30	54.2	52.22	54.53	52.1	53.0	53.8	53.0	52.25	52.34	52.91	53.9
Al ₂ O ₃	1.64	0.17	<0.03	<0.03	—	—	0.02	0.03	0.04	0.28	1.13	0.42
Cr ₂ O ₃	0.34	0.72	0.53	0.53	2.12	0.52	0.51	0.75	0.18	0.24	0.19	0.39
V ₂ O ₃	—	—	—	—	—	—	0.07	0.04	—	—	—	0.04
FeO	32.39	41.7	44.38	44.84	44.4	45.1	40.5	44.1	46.74	45.16	46.30	45.4
MgO	9.63	3.12	1.39	1.14	1.35	0.75	5.14	2.28	0.47	0.39	0.01	0.10
MnO	0.34	0.35	0.15	0.15	0.45	0.45	0.42	0.41	0.30	0.34	0.31	0.36
CaO	0.44	0.03	0.21	0.21	0.01	0.10	—	—	—	—	—	—
ZrO ₂	—	—	—	—	—	—	—	—	—	—	—	—
SiO ₂	—	0.04	0.09	0.09	0.12	0.23	—	—	—	—	—	—
Total	101.08	100.33	98.97	101.49	100.55	100.15	100.46	100.61	99.98	98.75	100.85	100.61
<i>Cation Formula Based on 3 Oxygens (Ideal Ilmenite = 2 Cations per 3 Oxygens)</i>												
Ti	0.976	0.997	0.989	1.014	0.974	0.996	0.983	0.985	0.991	1.000	0.988	1.007
Al	0.045	0.002	0.000	0.000	—	—	0.001	0.001	0.001	0.008	0.033	0.012
Cr	0.006	0.014	0.010	0.010	0.042	0.010	0.010	0.015	0.004	0.005	0.004	0.008
V	—	—	—	—	—	—	0.001	0.001	—	—	—	0.001
Fe	0.624	0.853	0.935	0.918	0.923	0.942	0.822	0.912	0.986	0.959	0.962	0.943
Mg	0.331	0.114	0.052	0.042	0.050	0.028	0.186	0.084	0.018	0.015	0.000	0.004
Mn	0.001	0.007	0.003	0.003	0.009	0.009	0.009	0.009	0.006	0.007	0.007	0.008
Ca	0.011	0.001	0.006	0.006	0.000	0.003	—	—	—	—	—	—
Zr	—	—	—	—	—	—	—	—	—	—	—	—
Si	—	0.001	0.002	0.002	0.003	0.006	—	—	—	—	—	—
Total	1.994	1.989	1.997	1.995	2.001	1.994	2.012	2.007	2.006	1.994	1.994	1.983

TABLE A5.12. (continued).

	A-12 ol	Mg Rock (anorth.)	Glassy br	Melt rock	A-14 Al	A-15 ol	A-17 Basalt	Luna 16 Soil		Luna 20 Soil	
	13.	14.	15.	16.	17.	18.	19.	20.	21.	22.	23.
<i>Chemical Composition (Weight Percent)</i>											
TiO ₂	52.7	51.7	59.35	52.66	53.24	50.70	53.1	52.00	50.79	53.7	53.1
Al ₂ O ₃	0.12	0.19	0.60	0.10	0.09	0.09	0.15	0.17	0.28	—	—
Cr ₂ O ₃	0.23	0.58	0.85	0.38	0.35	0.23	0.39	0.58	0.27	0.39	0.16
V ₂ O ₃	0.06	—	—	—	—	—	—	—	—	—	—
FeO	46.7	37.7	34.30	44.62	45.30	46.84	45.7	44.70	48.14	37.1	45.7
MgO	0.09	8.2	3.85	0.83	0.72	0.27	0.72	0.86	0.15	8.0	0.15
MnO	0.37	0.20	—	0.32	0.47	0.52	0.44	0.50	0.45	0.36	0.40
CaO	—	0.31	—	0.12	—	0.16	—	0.11	0.34	0.58	0.04
ZrO ₂	—	—	—	—	0.05	—	0.04	—	—	—	—
SiO ₂	—	0.30	—	0.39	0.16	0.50	—	0.23	0.45	0.18	—
Total	100.27	99.18	98.95	99.42	100.38	99.31	100.54	99.15	100.87	100.31	99.55
<i>Cation Formula Based on 3 Oxygens (Ideal Ilmenite = 2 Cations per 3 Oxygens)</i>											
Ti	0.998	0.943	1.062	0.994	0.998	0.970	0.996	0.987	0.960	0.966	1.008
Al	0.004	0.005	0.017	0.003	0.003	0.003	0.004	0.005	0.008	—	—
Cr	0.005	0.011	0.016	0.008	0.007	0.005	0.008	0.012	0.005	0.007	0.003
V	0.000	—	—	—	—	—	—	—	—	—	—
Fe	0.983	0.765	0.682	0.936	0.944	0.997	0.953	0.943	1.012	0.742	0.964
Mg	0.004	0.297	0.136	0.031	0.027	0.010	0.027	0.032	0.006	0.285	0.006
Mn	0.008	0.004	—	0.007	0.010	0.011	0.009	0.011	0.010	0.007	0.009
Ca	—	0.008	—	0.003	—	0.004	—	0.003	0.009	0.015	0.001
Zr	—	—	—	—	0.001	—	0.000	—	—	—	—
Si	—	0.007	—	0.010	0.004	0.013	—	0.006	0.011	0.004	—
Total	2.002	2.040	1.913	1.992	1.994	2.013	1.997	1.999	2.021	2.026	1.991

*Columns 3 and 4 are averages of multiple analyses.

Analysis #1 is from sample 10085 (Agrell *et al.*, 1970b); #2 is from sample 10072 (Kushiro and Nakamura, 1970); #3 and 4 are from sample 10057 (Lovering and Ware, 1970); #5 is from sample 10017 (Brown *et al.*, 1970); #6 is from sample 10058 (Brown *et al.*, 1970); #7 and 8 are from sample 12018 (El Goresy *et al.*, 1971b); #9 is from sample 12065 (Cameron, 1971); #10 is from sample 12022 (Cameron, 1971); #11 is from sample 12065 (Cameron, 1971); #12 is from sample 12063 (El Goresy *et al.*, 1971b); #13 is from sample 12002 (El Goresy *et al.*, 1971b); #14 is from sample 14258 (Powell and Weiblen, 1972); #15 is from sample 14257 (Klein and Drake, 1972); #16 is from sample 14310 (Gancarz *et al.*, 1971); #17 is from sample 14053 (Haggerty, 1972a); #18 is from sample 15555 (Haggerty, 1972a); #19 is from sample 75035 (Meyer and Doctor, 1974); #20 and 21 are from Luna 16 soil (Haggerty, 1972c); #22 and 23 are from Luna 20 soil (Brett *et al.*, 1973).

TABLE A5.13. Spinel analyses from lunar rocks and soils.

	A-11 LK			A-12 ol		A-12 pig		A-12 ilm		A-12 ol			A-12 ilm		A-12 ol		A-12 pig		
	1.	2.	3.	4.	5.	6.	7.	8.	9.	10.	11.	12.	13.	14.	15.	16.	17.	18.	19.
<i>Chemical Composition (Weight Percent)</i>																			
TiO ₂	20.9	21.2	32.8	3.8	4.7	6.27	7.90	9.33	10.8	20.6	22.0	23.7	25.3	24.70	24.8	28.6	29.1	32.0	33.3
Al ₂ O ₃	8.61	4.20	1.56	12.2	12.5	11.0	12.17	10.99	11.0	8.00	4.24	4.03	3.03	5.89	5.18	3.3	2.35	2.3	2.1
Cr ₂ O ₃	23.5	21.9	0.16	49.1	48.8	43.8	41.61	40.07	34.9	24.1	21.7	17.6	16.6	15.59	15.1	11.9	8.71	2.8	1.2
V ₂ O ₃	0.4	—	—	—	—	0.74	—	—	0.92	0.4	0.54	0.42	0.38	—	0.75	—	0.19	0.3	—
FeO	42.1	46.4	65.7	26.8	26.3	33.3	35.98	34.46	37.8	44.4	49.3	51.7	52.8	49.55	51.6	54.1	57.4	63.3	62.8
MgO	4.23	4.74	—	7.8	7.6	3.92	1.26	4.43	3.94	2.6	2.19	0.81	2.01	2.78	2.63	2.7	0.59	0.1	0.1
MnO	0.25	0.50	0.24	—	0.4	0.27	—	0.38	0.20	0.3	0.38	0.53	0.41	0.37	0.39	0.4	1.31	0.3	0.4
CaO	<0.03	0.15	0.10	—	—	—	0.15	0.13	—	—	—	—	—	0.34	—	—	—	—	—
SiO ₂	—	0.46	0.13	—	—	—	0.36	0.18	—	—	—	—	—	0.18	—	—	—	—	—
ZrO ₂	<0.10	—	—	—	—	—	—	—	—	—	—	—	—	—	—	—	—	—	—
Total	99.99	99.55	100.69	99.70	100.30	99.30	99.43	99.97	99.56	100.40	100.35	98.79	100.53	99.40	100.45	101.0	99.65	101.1	99.9
<i>Cation Formula Based on 4 Oxygens (Ideal Spinel = 3 Cations per 4 Oxygens)</i>																			
Ti	0.541	0.566	0.915	0.096	0.117	0.163	0.205	0.240	0.281	0.537	0.592	0.654	0.685	0.659	0.662	0.764	0.807	0.880	0.924
Al	0.349	0.176	0.068	0.481	0.488	0.449	0.493	0.442	0.446	0.327	0.178	0.174	0.129	0.246	0.217	0.138	0.102	0.100	0.091
Cr	0.638	0.615	0.005	1.299	1.279	1.198	1.138	1.081	0.953	0.660	0.612	0.510	0.473	0.438	0.424	0.334	0.254	0.080	0.035
V	0.011	—	—	—	—	0.021	—	—	0.025	0.012	0.013	0.012	0.011	—	0.021	—	0.006	0.009	—
Fe	1.213	1.378	2.039	0.750	0.729	0.962	1.060	0.984	1.093	1.287	1.478	1.587	1.589	1.471	1.536	1.608	1.770	1.938	1.938
Mg	0.217	0.251	—	0.389	0.375	0.203	0.065	0.225	0.203	0.132	0.117	0.044	0.108	0.147	0.139	0.143	0.032	0.007	0.011
Mn	0.007	0.015	0.008	—	0.011	0.007	—	0.011	0.006	0.008	0.012	0.017	0.013	0.011	0.012	0.012	0.041	0.010	0.013
Ca	0.000	0.006	0.004	—	—	—	0.005	0.005	—	—	—	—	—	0.013	—	—	—	—	—
Si	—	0.016	0.005	—	—	—	0.012	0.006	—	—	—	—	—	0.006	—	—	—	—	—
Zr	0.000	—	—	—	—	—	—	—	—	—	—	—	—	—	—	—	—	—	—
Total	2.976	3.023	3.044	3.015	2.999	3.003	2.978	2.994	3.007	2.963	3.002	2.998	3.008	2.991	3.011	2.999	3.012	3.024	3.012

TABLE A5.13. (continued).

	A-12 pig						A-14 Al						Melt Rocks			A-15 pig		A-15 ol	
	20.	21.	22.* core	23.* core	24.* rim	25.* rim	26.* rim	27.	28.	29.	30.	31.	32.	33.	34.	35.	36.	37.	38.
<i>Chemical Composition (Weight Percent)</i>																			
TiO ₂	33.6	33.8	4.5	4.8	27.0	29.9	33.3	4.95	3.31	2.79	18.57	22.60	23.0	30.23	32.4	32.3	1.71	2.46	4.10
Al ₂ O ₃	2.3	1.6	12.6	12.5	3.6	2.5	2.1	16.11	20.1	21.74	6.00	4.52	4.38	2.21	2.10	1.33	10.64	10.84	11.76
Cr ₂ O ₃	0.8	0.2	49.2	48.6	14.8	7.1	1.2	39.56	39.1	38.17	26.06	18.99	17.3	4.52	0.97	0.32	54.87	53.30	46.28
V ₂ O ₃	0.3	0.2	—	—	—	—	—	0.70	0.63	0.56	—	—	0.45	—	0.01	0.04	1.33	—	—
FeO	63.1	62.9	27.3	28.0	51.6	59.6	62.8	33.29	31.7	29.24	47.59	48.33	52.0	60.53	62.5	63.5	24.38	26.38	35.21
MgO	0.1	0.0	6.7	6.2	1.8	0.3	0.2	4.02	4.62	5.98	0.70	3.22	1.55	0.87	0.66	0.26	7.23	6.15	2.35
MnO	0.3	0.3	0.4	0.4	0.4	0.4	0.4	0.25	0.24	0.18	0.51	0.74	0.71	0.40	0.44	0.47	0.27	0.41	0.44
CaO	—	—	—	—	—	—	—	—	—	—	0.04	0.13	—	0.07	—	—	0.05	—	0.03
SiO ₂	—	—	—	—	—	—	—	—	—	—	0.31	0.29	—	0.30	—	—	0.19	—	0.19
ZrO ₂	—	—	—	—	—	—	—	0.00	0.04	0.00	—	—	0.04	—	0.19	0.08	—	—	—
Total	100.5	99.0	100.7	100.5	99.2	99.8	100.0	98.88	99.74	98.66	99.78	98.82	99.43	99.13	99.27	98.30	100.67	99.54	100.36
<i>Cation Formula Based on 4 Oxygens (Ideal Spinel = 3 Cations per 4 Oxygens)</i>																			
Ti	0.926	0.951	0.112	0.120	0.734	0.829	0.924	0.127	0.082	0.069	0.502	0.612	0.631	0.845	0.908	0.923	0.043	0.063	0.107
Al	0.100	0.069	0.493	0.491	0.153	0.109	0.091	0.646	0.781	0.840	0.254	0.192	0.188	0.097	0.092	0.059	0.418	0.434	0.480
Cr	0.024	0.005	1.291	1.281	0.423	0.207	0.035	1.063	1.020	0.989	0.740	0.541	0.498	0.133	0.029	0.010	1.447	1.433	1.266
V	0.009	0.007	—	—	—	—	—	0.019	0.017	0.015	—	—	0.013	—	0.000	0.001	0.036	—	—
Fe	1.936	1.968	0.758	0.781	1.559	1.838	1.938	0.947	0.875	0.801	1.429	1.456	1.585	1.881	1.948	2.017	0.680	0.750	1.019
Mg	0.007	0.000	0.331	0.308	0.097	0.017	0.011	0.204	0.227	0.292	0.037	0.173	0.084	0.048	0.037	0.015	0.360	0.312	0.121
Mn	0.009	0.009	0.011	0.011	0.012	0.012	0.013	0.008	0.007	0.005	0.016	0.023	0.022	0.013	0.013	0.015	0.008	0.012	0.013
Ca	—	—	—	—	—	—	—	—	—	—	0.002	0.005	—	0.003	—	—	0.002	—	0.001
Si	—	—	—	—	—	—	—	—	—	—	0.011	0.010	—	0.011	—	—	0.006	—	0.007
Zr	—	—	—	—	—	—	—	0.000	0.001	0.000	—	—	0.001	—	0.003	0.001	—	—	—
Total	3.011	3.009	2.996	2.992	2.978	3.012	3.012	3.014	3.010	3.011	2.991	3.012	3.022	3.031	3.030	3.041	3.000	3.004	3.014

TABLE A5.13. (continued).

	A-15 ol				L-16 Soil				L-16 Al				L-20 Soil						
	39.	40.	41.	42.	43.	44.	45.	46.	47.	48.	49.	50.	51.	52.	53.	54.	55.	56.	57.
<i>Chemical Composition (Weight Percent)</i>																			
TiO ₂	6.10	10.01	13.85	18.12	21.10	26.40	28.14	31.56	0.83	6.14	6.93	24.14	30.16	5.25	3.99	15.22	0.54	1.10	0.16
Al ₂ O ₃	11.35	9.66	8.04	6.23	5.03	3.81	2.82	1.95	17.36	9.55	23.33	4.06	1.90	9.37	11.88	6.67	45.50	54.43	64.70
Cr ₂ O ₃	42.79	37.69	30.54	25.57	19.85	13.36	9.16	4.84	49.00	43.07	30.76	18.08	6.68	49.18	45.91	36.32	18.47	10.06	2.29
V ₂ O ₃	—	—	—	—	—	—	—	—	—	—	—	0.53	0.18	—	—	—	—	—	—
FeO	34.35	40.29	42.71	46.12	50.11	53.61	56.19	61.42	25.33	37.81	30.11	50.07	60.04	29.55	28.43	35.70	24.18	15.93	10.70
MgO	3.35	2.01	3.23	2.72	2.20	2.15	1.58	0.40	7.05	1.01	7.90	1.72	0.17	5.02	8.43	4.89	10.76	17.31	21.59
MnO	0.46	0.41	0.33	0.49	0.44	0.43	0.45	0.44	0.53	0.55	0.38	0.47	0.31	0.49	0.44	0.35	0.20	0.13	0.04
CaO	0.20	0.03	0.33	0.17	0.29	0.04	0.23	0.02	0.20	0.35	0.01	0.19	0.05	0.19	0.13	0.07	0.16	0.02	0.07
SiO ₂	0.41	0.19	0.48	0.36	0.31	0.28	0.45	0.33	0.41	0.57	0.13	0.15	0.15	0.29	0.13	0.17	0.43	0.10	0.18
ZrO ₂	—	—	—	—	—	—	—	—	—	—	—	—	—	—	—	—	—	—	—
Total	0.99.01	100.29	99.51	99.78	99.33	100.08	99.02	100.96	100.71	99.05	99.55	99.41	99.64	99.34	99.34	99.39	100.24	99.08	99.73
<i>Cation Formula Based on 4 Oxygens (Ideal Spinel = 3 Cations per 4 Oxygens)</i>																			
Ti	0.159	0.263	0.367	0.484	0.574	0.714	0.776	0.866	0.020	0.165	0.116	0.655	0.840	0.116	0.104	0.379	0.012	0.022	0.003
Al	0.465	0.398	0.334	0.261	0.214	0.161	0.122	0.084	0.664	0.401	0.875	0.173	0.083	0.358	0.422	0.279	1.526	1.719	1.919
Cr	1.175	1.043	0.852	0.719	0.567	0.380	0.266	0.140	1.257	1.213	0.774	0.516	0.196	1.382	1.258	0.989	0.415	0.213	0.046
V	—	—	—	—	—	—	—	—	—	—	—	0.015	0.005	—	—	—	—	—	—
Fe	0.998	1.179	1.260	1.371	1.515	1.611	1.724	1.873	0.688	1.126	0.801	1.510	1.861	0.897	0.824	1.058	0.575	0.357	0.225
Mg	0.174	0.105	0.170	0.144	0.119	0.115	0.086	0.022	0.341	0.054	0.375	0.092	0.009	0.217	0.384	0.258	0.456	0.691	0.810
Mn	0.014	0.012	0.010	0.015	0.013	0.013	0.014	0.014	0.015	0.017	0.010	0.014	0.010	0.015	0.013	0.011	0.005	0.003	0.001
Ca	0.007	0.001	0.012	0.006	0.011	0.002	0.009	0.001	0.007	0.013	0.000	0.007	0.002	0.007	0.007	0.003	0.005	0.001	0.002
Si	0.014	0.007	0.017	0.013	0.011	0.010	0.017	0.012	0.013	0.020	0.004	0.005	0.006	0.011	0.005	0.006	0.012	0.003	0.005
Zr	—	—	—	—	—	—	—	—	—	—	—	—	—	—	—	—	—	—	—
Total	3.007	3.008	3.022	3.013	3.024	3.006	3.014	3.012	3.005	3.009	2.955	2.987	3.012	3.003	3.017	2.983	3.006	3.009	3.011

*Analyses 22 to 26 show the core-to-rim zonation in one spinel crystal.

Analysis #1 is from sample 10020 (Haggerty et al., 1970); #2 and 3 are from sample 10058 (Brown et al., 1970); #4 is from sample 12009 (Brett et al., 1971); #5 is from sample 12052 (Champness et al., 1971); #6 is from sample 12063 (El Goresy et al., 1971b); #7 is from sample 12021 and #8 is from sample 12022 (Weill et al., 1971); #9 is from sample 12063 (El Goresy et al., 1971b); #10 is from sample 12022 (Cameron, 1971); #11 is from sample 12018, #12 is from sample 12002 (El Goresy et al., 1971b); #13 is from sample 12018 (El Goresy et al., 1971b); #14 is from sample 12022 (Weill et al., 1971); #15 is from sample 12063 (El Goresy et al., 1971b); #16 is from sample 12035 (Reid, 1971); #17 is from sample 12002 (El Goresy et al., 1971b); #18 is from sample 12065 (Cameron, 1971); #19 is from sample 12052 (Champness et al., 1971); #20 and 21 are from sample 12065 (Cameron, 1971); #22 to 26 are from sample 12052 (Gibb et al., 1970); #27 is from sample 14053 (El Goresy et al., 1971a); #28 is from sample 14072 (El Goresy et al., 1972); #29 is from sample 14053 (El Goresy et al., 1971a); #30 and 31 are from sample 14053 (Haggerty, 1972a); #32 is from sample 14053 (El Goresy et al., 1972); #33 is from sample 14310 (Haggerty, 1972a); #34 is from sample 14310 (El Goresy et al., 1972); #35 is from sample 14073 (El Goresy et al., 1972); #36 is from sample 15597 (Weigand, 1972); #37 is from sample 15085 (Brown et al., 1972); #38 to 46 are from sample 15555 (Haggerty, 1972b); #47 to 49 are from Luna 16 soil (Haggerty, 1972c); #50 and 51 are from Luna 16 soil (Albee et al., 1972); #52 to 57 are from Luna 20 soil (Haggerty, 1973b).

TABLE A5.14. Armalcolite analyses from lunar rocks and soils.

Armalcolite Type 1: Fe-Mg Armalcolite															
A-11 HK		Frag br	Reg br	A-11 Soil	Reg br	A-14 Soil	A-17 Soil		A-17 Basalt						
1.	2.	3.	4.	5.	6.	7.	8.	9.	10.	11.	12.	13.	14. core*	15. rim*	
<i>Chemical Composition (Weight Percent)</i>															
TiO ₂	70.9	73.4	75.6	72.0	71.9	75.15	69.41	73.4	73.2	73.23	72.93	71.61	73.91	74.3	72.5
FeO	16.9	15.3	11.9	14.7	11.32	14.30	21.23	16.0	15.7	15.35	16.39	16.30	14.44	13.5	17.6
MgO	8.6	7.70	8.12	8.7	11.06	6.95	3.59	6.63	6.77	6.20	5.77	6.63	7.75	7.95	5.32
CaO	—	0.01	—	0.32	—	0.16	0.31	0.28	—	—	—	0.44	0.03	—	—
MnO	0.02	0.08	—	0.07	0.01	0.09	0.10	0.11	0.10	0.08	0.08	0.09	0.17	0.00	0.02
Al ₂ O ₃	1.8	1.62	1.87	1.48	0.97	1.80	2.60	1.96	2.00	1.87	1.87	1.77	1.99	1.93	1.91
Cr ₂ O ₃	1.3	2.15	1.81	1.94	1.26	1.88	2.05	1.65	1.78	1.83	1.62	1.69	2.01	2.17	1.43
V ₂ O ₃	—	<0.5	—	0.07	—	—	—	—	0.71	—	—	—	0.27	0.05	—
SiO ₂	—	—	—	—	—	0.40	0.21	—	—	—	—	0.30	0.08	—	—
Nb ₂ O ₅	—	—	—	—	—	—	0.17	—	—	—	—	—	—	—	—
Y ₂ O ₃	—	—	—	—	—	0.05	0.05	—	—	—	—	—	—	—	—
ZrO ₂	—	—	—	—	—	0.05	0.38	—	—	—	—	—	—	—	—
Total	99.52	100.26	99.30	99.28	96.52	100.83	100.10	100.03	100.26	98.56	98.66	99.10	100.43	99.85	98.78
<i>Cation Formula Based on 5 Oxygens (Ideal Armalcolite = 3 Cations per 5 Oxygens)</i>															
Ti	1.897	1.968	2.012	1.917	1.938	1.926	1.919	1.979	1.967	1.954	1.927	1.952	1.970	1.984	1.993
Fe	0.506	0.456	0.352	0.438	0.342	0.408	0.653	0.480	0.469	0.448	0.482	0.494	0.427	0.397	0.538
Mg	0.459	0.409	0.428	0.462	0.595	0.353	0.197	0.354	0.361	0.323	0.302	0.357	0.409	0.421	0.290
Ca	—	0.000	—	0.012	—	0.006	0.012	0.011	—	—	—	0.016	0.000	—	—
Mn	0.001	0.002	—	0.002	0.000	0.003	0.003	0.003	0.003	0.002	0.002	0.002	0.004	0.000	0.001
Al	0.076	0.068	0.077	0.062	0.041	0.072	0.113	0.083	0.084	0.050	0.045	0.048	0.082	0.081	0.082
Cr	0.037	0.061	0.051	0.055	0.036	0.051	0.060	0.047	0.050	0.050	0.045	0.048	0.056	0.061	0.041
V	—	—	—	0.002	—	—	—	—	0.020	—	—	0.007	0.001	—	—
Si	—	—	—	—	—	0.014	0.008	—	—	—	—	0.010	0.002	—	—
Nb	—	—	—	—	—	—	0.003	—	—	—	—	—	—	—	—
Y	—	—	—	—	—	0.001	0.001	—	—	—	—	—	—	—	—
Zr	—	—	—	—	—	0.083	0.007	—	—	—	—	—	—	—	—
Total	2.976	2.964	2.920	2.950	2.952	2.917	2.976	2.957	2.954	2.827	2.803	2.934	2.951	2.944	2.945

TABLE A5.14. (continued).

	Type 2: Cr-Zr-Ca Armalcolite					Type 3: Zr Armalcolite			
	Cryst br	A-15 Soil	Cryst br	A-15 Soil	L-20 Soil	A-15 Soil	A-15 Soil	A-15 Soil	A-15 Soil
	16.	17.	18.	19.	20.	21.	22.	23.	24.
<i>Chemical Composition (Weight Percent)</i>									
TiO ₂	66.52	68.58	71.2	68.8	65.42	67.94	68.16	71.84	71.72
FeO	9.33	9.78	9.1	13.4	10.66	17.61	17.33	14.08	13.44
MgO	2.31	2.38	1.9	1.7	1.98	7.09	6.78	8.80	9.41
CaO	3.40	3.72	3.1	3.1	3.40	0.35	0.35	0.33	0.35
MnO	0.13	0.21	—	0.2	0.10	0.08	0.02	0.08	0.08
Al ₂ O ₃	1.49	2.12	1.7	0.9	1.48	0.97	0.97	0.94	0.98
Cr ₂ O ₃	10.31	9.67	8.8	4.3	7.67	1.46	1.49	1.49	1.45
V ₂ O ₃	—	—	—	—	—	—	—	—	—
SiO ₂	0.23	0.47	0.6	0.2	0.27	0.18	0.23	0.23	0.19
Nb ₂ O ₅	0.37	<0.05	—	—	—	0.65	0.58	0.20	0.44
Y ₂ O ₃	<0.05	<0.05	—	—	—	0.53	0.53	0.01	0.01
ZrO ₂	6.01	4.4	4.4	6.1	6.55	3.76	3.92	2.76	2.39
REE	—	—	—	1.3	—	—	—	—	—
Total	100.10	101.33	100.8	100.0	97.53	100.62	100.36	100.76	100.46
<i>Cation Formula Based on 5 Oxygens (Ideal Armalcolite = 3 Cations per 5 Oxygens)</i>									
Ti	1.834	1.849	1.915	1.921	1.855	1.871	1.880	1.927	1.923
Fe	0.286	0.293	0.272	0.416	0.336	0.539	0.531	0.420	0.401
Mg	0.126	0.127	0.101	0.094	0.111	0.387	0.371	0.468	0.500
Ca	0.134	0.143	0.119	0.123	0.137	0.014	0.014	0.013	0.013
Mn	0.004	0.006	—	0.006	0.003	0.002	0.001	0.002	0.002
Al	0.064	0.090	0.072	0.039	0.066	0.042	0.042	0.040	0.041
Cr	0.299	0.274	0.249	0.126	0.229	0.042	0.043	0.042	0.041
V	—	—	—	—	—	—	—	—	—
Si	0.009	0.017	0.021	0.007	0.010	0.007	0.008	0.008	0.007
Nb	0.008	—	—	—	—	0.011	0.010	0.003	0.007
Y	—	—	—	—	—	0.010	0.010	0.000	0.000
Zr	0.108	0.077	0.077	0.110	0.120	0.067	0.070	0.048	0.042
REE	—	—	—	0.017	—	—	—	—	—
Total	2.872	2.876	2.826	2.859	2.867	2.992	2.980	2.971	2.977

*Analyses 14 to 15 show the core-to-rim variation in one spinel crystal.

Analysis #1 is from sample 10022 (Anderson *et al.*, 1970); #2 is from sample 10071 (Anderson *et al.*, 1970); #3 is from sample 10059, #4 is from sample 10068 (Anderson *et al.*, 1970); #5 is from sample 10084 (Anderson *et al.*, 1970); #6 is from sample 10021 (Haggerty, 1973a); #7 is from sample 14191 (Haggerty, 1973a); #8 is from sample 74241 (Taylor *et al.*, 1973c); #9 is from sample 75081 (Taylor *et al.*, 1973c); #10 and 11 are from sample 74242 (Williams and Taylor, 1974); #12 is from sample 70017, #13 is from sample 70215 (El Goresy *et al.*, 1974); #14 and 15 are from sample 70035 (Papike *et al.*, 1974); #16 is from sample 66156, #17 is from sample 15102 (Haggerty, 1973a); #18 is from sample 60335 (Levy *et al.*, 1972); #19 is from sample 15102 (Peckett *et al.*, 1972); #20 is from sample 22001 (Reid *et al.*, 1973); #21 to 24 are from sample 15102 (Haggerty, 1973a).

TABLE A5.15. Analyses of other oxides from lunar rocks and soils.

	Rutile					Baddeleyite				
	A-11	A-12	Frag	Cryst	L-20	A-12	A-12	Melt	L-20	
	LK	Soil	br	br	Soil	ilm	pig	Rock	Soil	
1.	2.*	3.	4.	5.	6.	7.	8.	9.	10.	
<i>Chemical Composition (Weight Percent)</i>										
SiO ₂	—	—	0.93	—	0.13	0.39	0.12	<0.01	—	0.18
TiO ₂	96.62	87.9	87.29	98.0	97.23	1.97	3.13	2.4	—	1.82
Al ₂ O ₃	1.91	—	0.13	—	0.02	—	—	<0.01	—	0.54
Cr ₂ O ₃	0.30	3.2	0.56	0.3	0.48	—	—	—	—	0.13
V ₂ O ₃	—	0.4	—	—	—	—	—	—	—	0.06
FeO	0.22	—	7.45	0.1	2.34	3.25	0.96	7.4	—	0.45
MnO	0.03	—	0.14	—	0.01	<0.02	<0.02	—	—	0.17
MgO	0.05	—	3.20	<0.1	0.04	<0.02	0.18	—	0.06	0.14
CaO	0.37	—	0.28	<0.1	0.10	—	—	<0.1	—	0.16
Nb ₂ O ₅	—	6.4	0.55	1.6	—	—	—	—	—	0.49
ZrO ₂	—	—	0.07	0.1	—	91.9	93.2	90.3	98.23	94.7
HfO ₂	—	—	—	—	—	3.23	1.60	—	1.70	1.65
REE	—	1.2	—	—	—	—	—	—	—	—
Total	99.50	99.1	100.60	100.1	100.35	100.74	99.19	100.1	99.99	100.49
<i>Cation Formula Based on 2 Oxygens</i> (Ideal Rutile or Baddeleyite = 1 Cation per 2 Oxygens)										
Si	—	—	0.013	—	0.002	0.008	0.002	—	—	0.004
Ti	0.971	0.915	0.898	0.984	0.980	0.030	0.048	0.037	—	0.028
Al	0.030	—	0.002	—	0.000	—	—	—	—	0.013
Cr	0.003	0.035	0.006	0.003	0.005	—	—	—	—	0.002
V	—	0.004	—	—	—	—	—	—	—	0.001
Fe	0.002	—	0.085	0.001	0.026	0.056	0.016	0.126	—	0.008
Mn	0.000	—	0.002	—	0.000	—	—	—	—	0.003
Mg	0.001	—	0.065	—	0.001	—	0.005	—	0.002	0.004
Ca	0.005	—	0.004	—	0.001	—	—	—	—	0.003
Nb	—	0.040	0.003	0.010	—	—	—	—	—	0.004
Zr	—	—	0.000	0.001	—	0.915	0.929	0.900	0.989	0.933
Hf	—	—	—	—	—	0.019	0.099	—	0.010	0.010
REE	—	0.006	—	—	—	—	—	—	—	—
Total	1.012	1.000	1.078	0.999	1.015	1.028	1.099	1.063	1.001	1.013

*Also 0.2% Ta₂O₅.

Analysis #1 is from sample 10058 (Agrell *et al.*, 1970b); #2 is from sample 12070 (Marvin, 1971); #3 is from sample 14321 (Haggerty, 1973a); #4 is from sample 15445 (Anderson, 1973); #5 is from sample 22003 (Haggerty, 1973b); #6 and 7 are from sample 12036 (Keil *et al.*, 1971); #8 is from sample 12038 (Simpson and Bowie, 1971); #9 is from sample 14310 (El Goresy *et al.*, 1971a); #10 is from sample 22002 (Brett *et al.*, 1973).

TABLE A5.16. Analyses of sulfide minerals from lunar rocks and soils.

	Troilite		Chalcopyrite		Cubanite	Bornite	Sphalerite		
	A-12 ilm	A-12 ol	A-12 pig		6.	A-16 Soil	Cryst br		
	1.	2.*	3.	4.		5.	7.	8.	9.
<i>Chemical Composition (Weight Percent)</i>									
Ti	0.15	0.05	0.24	0.27	—	—	—	—	—
Cr	0.02	0.02	—	—	—	—	—	—	—
Fe	63.2	63.1	63.4	63.58	30.0	40.4	12.7	14.8	17.6
Cu	—	—	—	—	33.6	22.8	60.7	—	—
Mg	—	—	—	0.04	—	—	—	—	—
Zn	—	—	—	—	—	—	—	51.0	48.2
Ni	0.03	0.03	0.10	0.02	—	—	0.07	—	—
Co	0.08	0.06	0.12	0.11	0.85	0.87	0.2	—	—
S	36.4	36.0	36.4	35.66	35.2	35.7	26.2	33.0	33.7
P	—	—	—	—	—	—	0.1	—	—
Total	99.88	99.26	100.26	99.68	99.65	99.77	99.97	98.8	99.5
<i>Atomic Formulae:</i>									
<i>Ideal troilite = FeS, chalcopyrite = CuFeS₂, cubanite = CuFe₂S₃, bornite = Cu₅FeS₄, sphalerite = (Zn,Fe)S</i>									
Ti	0.003	0.001	0.004	0.005	—	—	—	—	—
Cr	0.000	0.000	—	—	—	—	—	—	—
Fe	0.996	1.002	0.996	1.007	0.986	1.964	1.133	0.256	0.300
Cu	—	—	—	—	0.971	0.974	4.758	—	—
Mg	—	—	—	0.001	—	—	—	—	—
Zn	—	—	—	—	—	—	—	0.752	0.701
Ni	0.000	0.000	0.001	0.000	—	—	0.006	—	—
Co	0.001	0.001	0.002	0.002	0.026	0.040	0.017	—	—
S	0.999	0.996	0.996	0.984	2.016	3.022	4.071	0.992	0.999
P	—	—	—	—	—	—	0.016	—	—
Total	1.999	2.000	1.999	1.999	3.999	6.000	10.001	2.000	2.000

Analysis #1 and 2 are from sample 12063 (Taylor et al., 1971); #3 is from sample 12004 (Taylor et al., 1971); #4 is from sample 12021 (Weill et al., 1971); #5 and 6 are from sample 12021 (Taylor and Williams, 1973); #7 is from sample 68841 (Carter and Padovani, 1973); #8 is from sample 66095 (El Goresy et al., 1973); #9 is from sample 66095 (Taylor et al., 1973a).

TABLE A5.17. Analyses of native Fe metal from lunar rocks and soils.

	A-11 LK		A-11 Soil		A-12 pig	A-12 ilm	A-12 ol	Melt Rock	A-15 Soil		Fan	Glassy br	Cryst br	Melt Rock	Cryst br	Melt Rock	
	1.	2.	3.	4.	5.	6.	7.	8.	9.	10.	11.	12.	13.	14.	15.	16.	17.
Fe	98.95	99.2	85.82	97.54	95.7	67.4	91.71	88.4	82.74	37.8	91.33	92.66	94.69	90.45	93.31	94.94	78.41
Ni	—	0.1	13.4	0.61	1.72	26.7	7.45	4.7	5.0	60.0	6.52	4.74	4.45	0.91	5.46	4.16	20.23
Co	0.80	0.7	0.48	1.24	2.59	2.37	—	6.9	11.8	1.3	0.41	0.43	0.30	7.86	0.54	0.39	0.78
P	—	—	—	—	—	—	—	0.02	0.02	0.02	0.31	1.44	0.29	0.01	0.19	0.10	0.14
Si	0.12	—	0.14	0.16	—	—	—	—	—	—	—	—	—	—	—	—	—
Cr	0.09	—	0.04	0.05	—	0.03	—	—	0.46	—	—	—	—	—	—	—	—
Mn	—	—	0.07	0.07	—	—	—	—	—	—	—	—	—	—	—	—	—
S	—	—	—	—	—	—	—	—	—	—	0.06	0.02	0.02	0.05	0.01	0.02	0.03
Σ	100.0	100.0	99.86	99.67	100.01	96.47	99.16	100.0	100.0	100.0	98.63	99.29	99.75	99.28	99.51	99.59	99.59

Analysis #1 is from sample 10058 (*Brown et al.*, 1970); #2 is from sample 10084 (*Agrell et al.*, 1970b); #3 is from sample 10085 (*Brown et al.*, 1970); #4 is from sample 12021 (*Weill et al.*, 1971); #5 is from sample 12051 (*Keil et al.*, 1971); #6 is from sample 12004 (*Taylor et al.*, 1971); #7 is from sample 14276 (*Gancarz et al.*, 1971); #8 is from sample 15261, #9 is from sample 15071, #10 is from sample 15261 (*Axon and Goldstein*, 1973); #11 is from sample 61016 (*Misra and Taylor*, 1975a); #12 is from sample 69935 (*Misra and Taylor*, 1975a); #13 is from sample 68115 (*Misra and Taylor*, 1975a); #14 is from sample 62295 (*Misra and Taylor*, 1975a); #15 is from sample 66095 (*Misra and Taylor*, 1975a); #16 is from sample 60335 (*Misra and Taylor*, 1975a); #17 is from sample 68415 (*Misra and Taylor*, 1975a).

TABLE A5.18. Analyses of lunar phosphates.

	Whitlockite					Apatite			
	Soil	Soil	Cryst br	Melt Rock	Cryst br	Soil	Cryst br	Melt Rock	Cryst br
	1.	2	3.	4.	5.	6.	7.	8.	9.
<i>Chemical Composition (Weight Percent)</i>									
CaO	40.4	40.9	39.31	42.50	42.70	52.0	52.14	56.79	54.36
P ₂ O ₅	43.9	44.1	42.14	45.62	46.65	40.6	39.40	39.70	39.11
FeO	0.90	0.90	1.03	3.68	0.90	0.83	0.35	1.47	0.92
MgO	3.29	3.38	2.91	2.50	2.99	0.39	0.11	-	0.35
Na ₂ O	1.11	0.60	0.14	0.75	-	0.01	0.10	-	-
K ₂ O	0.01	0.04	0.02	-	-	0.02	-	-	-
SiO ₂	0.76	0.31	0.41	-	-	0.75	1.38	-	0.72
TiO ₂	0.07	0.11	-	-	-	0.09	-	-	-
Al ₂ O ₃	0.50	0.10	-	-	-	0.07	0.04	-	-
Y ₂ O ₃	2.76	2.98	3.66	1.68	-	0.10	0.81	-	1.47
La ₂ O ₃	0.91	0.92	1.46	0.69	0.91	0.08	0.28	-	-
Ce ₂ O ₃	2.26	2.45	3.78	1.62	2.69	0.10	0.66	-	-
Nd ₂ O ₃	1.90	2.16	2.30	1.04	1.60	0.12	-	-	-
Cl	0.01	0.01	0.04	-	-	1.40	1.38	0.84	1.80
F	0.10	0.07	0.14	-	-	2.75	2.59	1.10	1.12
Total	98.88	99.03	97.34	100.08	98.44	99.31	99.24	99.90	99.85
<i>Cation Formula Based on 8 Oxygens (Whitlockite) or 12.5 Oxygens (Apatite)</i>									
Ca	2.31	2.35	2.33	2.385	2.400	4.80	4.86	5.325	5.110
P	1.98	2.00	1.98	2.023	2.071	2.97	2.90	2.941	2.904
Fe	0.04	0.04	0.048	0.161	0.039	0.06	0.026	0.108	0.065
Mg	0.26	0.27	0.240	0.195	0.234	0.05	0.014	-	0.046
Na	0.12	0.06	0.015	0.019	-	-	0.017	-	-
K	-	-	0.002	-	-	-	-	-	-
Si	0.04	0.02	0.022	-	-	0.06	0.120	-	0.063
Ti	-	-	-	-	-	0.01	-	-	-
Al	0.03	0.01	-	-	-	0.01	0.004	-	-
Y	0.04	0.05	0.108	0.045	-	-	0.038	-	0.069
La	0.02	0.02	0.030	0.013	0.017	-	0.009	-	-
Ce	0.04	0.05	0.077	0.031	0.051	-	0.021	-	-
Nd	0.04	0.04	0.045	0.019	0.029	-	-	-	-
Total Cations	4.92	4.91	4.897	4.891	4.841	7.96	8.009	8.374	8.257
<i>Anion Contents Including Cl and F (Analyzed) and O (Assumed)</i>									
Cl	-	-	0.004	-	-	0.20	0.204	0.125	0.267
F	0.02	0.01	0.025	-	-	0.75	0.711	0.304	0.311
O	8	8	8	8	8	12.5	12.50	12.5	12.5

*Represents oxide sum of 99.78 less O = F1, Cl(1.52).

Analyses #1 and 2 are from sample 10085-LR-1 (Albee and Chodos, 1970); #3 is from sample 12013 (Lunatic Asylum, 1970); #4 is from sample 14310 (Friel and Goldstein, 1977); #5 is from sample 14321 (Friel and Goldstein, 1977); #6 is from sample 10085-LR-1 (Albee and Chodos, 1970); #7 is from sample 12013 (Lunatic Asylum, 1970); #8 is from sample 14310 (Friel and Goldstein, 1977); #9 is from sample 14321 (Friel and Goldstein, 1977).

LUNAR ROCKS

*G. Jeffrey Taylor, Paul Warren, Graham Ryder, John Delano, Carlé Pieters,
and Gary Lofgren*

INTRODUCTION: A GUIDE TO LUNAR ROCKS

Lunar Rocks

The Moon, like the Earth, is made of rocks. To learn about the Moon and its history, one has to learn something about lunar rocks—what they are made of, how they are studied and classified, and how our experiences in interpreting rocks on the Earth have been applied to rocks on the Moon.

The lunar samples have provided our only direct information about the Moon's minerals, chemical composition, and age. Lunar rocks have also provided information about the Moon's origin, the evolution of its crust, and the timing of critical events such as volcanism and meteorite bombardment.

The Moon is not a uniform, homogeneous planet. It consists of different rocks, formed in different ways at different times. Some of the Moon's rocks are familiar. The *basalt* lava flows that cover the dark maria formed in the same way as many of the lava flows on Earth—by melting deep in the planet, followed by ascent of molten rock to the surface and eruption through fractures and vents. Other lunar rocks are less familiar; the numerous lunar *breccias* are made up of fragments of older rocks that have been shattered, crushed, and melted by meteoroid impacts, either during an ancient episode of intense meteoroid bombardment that ended about 3.8 b.y. ago or by the rarer impacts of more recent times.

Within any group of rocks (e.g., basaltic lavas), the rocks are not identical. There are differences in mineral composition, in mineral shapes and sizes, and in each rock's chemical composition. These

differences have been studied in detail because they are the clues to a rock's origin, history, and relations to other rocks. The immense database for lunar rocks, collected from the Apollo and Luna missions and from lunar meteorites, has made it possible to raise our understanding of some aspects of the origin, evolution, and history of the Moon to a level unmatched for any other planet—maybe even the Earth.

The information obtained from lunar samples can also be applied to larger areas of the Moon, including regions never visited by astronauts or robot sample return vehicles. Natural X-ray and γ -ray signals mapped from orbit by the Apollo command modules provide chemical data from areas on the Moon that were never sampled (Chapter 10). In addition, Earth-based telescopes have been used—and are still being used—to measure the spectral characteristics of the light reflected from the Moon's surface. By making similar spectral measurements in the laboratory on well-studied lunar samples, it is possible to better interpret the spectral data obtained for other lunar regions. The lunar samples provide the “ground truth” for extending our remote mapping to little-known areas of the Moon.

Unfortunately, the many differences among lunar rocks also promote complex classifications, each with many subdivisions that have been developed (sometimes too enthusiastically) by lunar scientists. In some cases, terrestrial rock names have been successfully applied to their lunar equivalents. In others, new terms have had to be coined. These subdivisions, and their technical definitions, are

important, but can be baffling to the nongeologist and even daunting to Earth-oriented geologists. This introduction provides a brief background for the detailed material in subsequent sections.

Classification of Lunar Rocks

The rocks of the Moon fall into four distinct groups: (1) *basaltic volcanic* rocks, including *lava flows* and *pyroclastic* (volcanic ash) rocks; (2) *pristine* rocks from the lunar highlands (i.e., those highland rocks, shattered by impact or not, that have original lunar compositions uncontaminated by impact mixing); (3) complex *polymict breccias*, formed by impacts that shatter, mix, and recompact the lunar surface, and *impact melts* formed by melting of older lunar rocks during meteoroid impacts; and (4) the *lunar soil*, which is the fragmental (<1 cm) unconsolidated debris within the *lunar regolith* that covers the lunar surface. Because of the unique character of the lunar regolith and its importance on the Moon, it is discussed separately in Chapter 7. This chapter discusses only solid, consolidated rocks from the Moon.

All of these rocks were originally *igneous*, that is, they formed by cooling of molten material (*magma*) to form rocks made up of interlocking minerals and sometimes glass. Most of these rocks consist of a few minerals: pyroxenes, olivine, plagioclase feldspar, ilmenite, and silica minerals (tridymite or cristobalite). For detailed information on lunar minerals, see Chapter 5.

Melting and subsequent cooling of the Moon occurred at different places and different times. Early melting occurred soon after the Moon formed and produced the light-colored, Al-rich rocks now exposed in the lunar highlands. Later episodes of internal melting and volcanic eruptions produced the dark-colored lava flows that cover the mare basins.

Some of the samples returned from the Moon are *pristine*, that is, they have not been significantly changed by the effects of meteoroid impacts. However, most lunar rocks have been altered by meteoroid impacts; they have been shattered, crushed, melted, and mixed. Such rocks (breccias and impact melts) are formed by energetic recycling of older rocks and might not correspond to any single igneous rock within the lunar crust. Some of the “recycled” impact-melt rocks can be hard to distinguish from pristine rocks; these distinctions are often controversial among lunar scientists who study them.

Mare basaltic lavas and related volcanic rocks (see sections 6.1 and 6.2). The mare basaltic lavas formed by processes that are both familiar and long-studied on the Earth. In some ways they are the simplest and best understood of lunar rocks. They

were formed by melting of the solid interior of the Moon, probably at depths of 100-400 km, followed by the buoyant rise of molten rock to the lunar surface and its eruption.

Two types of volcanic rocks have been erupted at the lunar surface:

1. *Lava flows*: Lunar lava flows apparently erupted from fissures in the lunar surface. Because lunar basalts contain more Fe and less Si and Al than terrestrial basalts, the lavas were quite fluid and formed thin, widespread flows. The lavas cooled at different rates, dependent on the thickness of individual flows, to produce a variety of mineral textures. Many lava flows accumulated in thick stacks that partly filled many of the mare basins.

2. *Pyroclastic deposits (volcanic ash)*: Gases contained within rising magmas can be explosively released when the magmas reach the surface of a planet. As lavas pour from a fissure vent, gases may be released to drive a fountain of molten droplets. On the Moon, these *lava fountains* associated with eruptions of basalt formed small glassy beads. Deposits of these beads are widely dispersed around lunar volcanic vents because of low gravity and eruption into a vacuum. Such *pyroclastic deposits* are similar to the volcanic ash deposited around lava fountains on Earth. Two striking examples of lunar pyroclastic rocks are the *orange soils* (although they really are not soils, but rather volcanic deposits) from the Apollo 17 landing site and the *green glass* from the Apollo 15 landing site. Orbital photographs of the lunar surface reveal *dark-mantle deposits*, which may also be of pyroclastic origin, surrounding apparent volcanic vents (section 4.2.1).

Pristine highland rocks (see section 6.3). Among the wide variety of rock types collected from the lunar highlands are at least a few that probably represent material from the original lunar crust that formed between 4.6 and 4.3 b.y. ago. The chemical compositions of these rocks indicate that, during this interval, extensive melting occurred in the outermost part of the Moon. According to several models, the Moon was covered by a “*magma ocean*”: a layer of molten silicate perhaps hundreds of kilometers deep (section 2.4).

The question of a lunar magma ocean is fundamental to lunar history. If such an ocean cooled and crystallized, the physical separation of crystals (the floating of lower-density plagioclase feldspar) produced the original lunar crust.

After crustal formation, the long history of intense meteoroid bombardment has masked most of the actual unaltered (*pristine*) lunar crust. Samples of nonbasaltic (e.g., highland) *pristine* rocks are rare. The few such samples that are believed to be *pristine* have been subjected to extensive study because of

the clues they provide to understanding the origin and early history of the Moon. This work has been enlivened by the difficulty in distinguishing between genuine pristine highland rocks and similar rocks produced in large meteoroid impacts.

Classification for pristine highland rocks is roughly parallel to that for similar terrestrial rocks. Pristine highland rocks are divided into several groups:

1. *Ferroan anorthosite*: These rocks are light-colored, rich in Ca and Al, and are composed mostly of plagioclase feldspar. Minor minerals include pyroxene and olivine, which are richer in Fe than those of most Mg-rich crustal rocks (see below); hence the adjective “ferroan” is applied to these anorthosites. These anorthosites may be the pro-ducts of flotation of plagioclase in a magma ocean.

2. *Mg-rich rocks*: This second group of rocks is more varied, including some plagioclase-rich rocks, but many rocks with more pyroxene and olivine and correspondingly smaller amounts of plagioclase. Within the Mg-rich group are several rock types distinguished by their major minerals: *Gabbros* and *norites* are composed of pyroxene and plagioclase, *troctolites* contain mostly olivine and plagioclase, and *dunites* are nearly pure olivine rocks. If a magma ocean did indeed form on the Moon, the Mg-rich rocks probably formed after it had largely solidified.

3. *KREEP rocks*: In contrast to most other lunar rocks, the KREEP rocks are highly enriched in potassium (K), rare earth elements (REE), and phosphorus (P). The few known pristine KREEP rocks are basaltic lavas. They are apparently older than most of the basaltic lavas that fill mare basins. KREEP rocks appear to be most abundant around the Imbrium Basin. Because of its unique chemical character, KREEP is recognized in many breccia samples (see below); only a small amount is needed to produce a distinctive chemical signature.

Breccias (see sections 6.3 and 6.4). Nothing better demonstrates the intensity of meteoroid bombardment of the lunar surface throughout its history than the fact that most rock samples returned by the Apollo missions are *breccias* (consolidated fragmental rocks), which were formed during meteoroid impacts. Breccias are complex rocks composed of discrete rock, mineral, or glass fragments (*clasts*) set in a *matrix* (the fine-grained material between the larger rock and crystal fragments; matrix can be made up of similar fragments that are just smaller, or it may be made of a completely different rock type). The individual clasts may represent a wide range of components of different composition and age, including lunar bedrock, pieces of older breccias, and clots of impact-melted rock (textures of the melt rocks can range from glassy to completely crystalline).

Such complex rocks have bred complex classification schemes, but two fundamental types can be distinguished: *monomict breccias* and *polymict breccias*.

Monomict breccias contain only a single rock type, which has been broken into myriad deformed and crushed clasts. Monomict breccias are, in fact, simply highly crushed samples of a single lunar bedrock type. They have not been mixed with other rock types and may preserve some clasts with their original textural character. For that reason, they have been included with the pristine highland rocks in section 6.3.

Polymict breccias, discussed in section 6.4, are the most common of lunar breccias. As the name implies, they contain a variety of different materials, derived from several types of bedrock, earlier generations of breccias, and impact melts. Their classification is correspondingly complicated, but several general types can be distinguished on the basis of the nature of the fragments and especially the matrix. The breccia types described in section 6.4 are:

1. *Fragmental breccias*: These rocks are composed of fragments of rocks, often including earlier-formed breccias, in most cases just barely stuck together. The matrix consists of finer-grained fragments of the same material.

2. *Glassy melt breccias*: These breccias consist of a similar variety of fragments (clasts), enclosed in a matrix of impact-melt glass. The glassy matrix has not crystallized, implying rapid cooling of the rocks. As the number of fragments decreases, glassy melt breccias grade into fragment-poor *impact glasses*, although no dividing line has been established between the two rock types.

3. *Crystalline melt breccias*: These rocks are similar to the glassy melt breccias, but the melt matrix cooled more slowly. As a result, the originally molten matrix has solidified to form a crystalline igneous rock that often resembles a lava. The ratio of clasts to matrix varies widely.

4. *Clast-poor impact melts*: Crystalline melt breccias sometimes have so few clasts that they may have textures similar to a lava, and can be referred to as clast-poor impact melts. In many cases it is difficult to distinguish between these melt breccias and pristine lunar igneous rocks. A lot of research and discussion between lunar geologists has been directed, not always successfully, to making distinctions between clast-poor impact melts and lavas. Relatively high concentrations of rare elements thought to be introduced by meteoroid contamination (e.g., Ir, Au, Os; see section 8.6) are often used as a criterion of impact-melt origin.

5. *Granulitic (metamorphic) breccias*: Granulitic breccias were formed during the alteration and recrystallization of other breccias that have been subjected to high temperatures (~1000°C) since they were formed. Under these conditions the original textures have been obliterated during recrystallization and replaced by an even-grained *granulitic* texture. A completely recrystallized rock that retains none of its original texture is a *granulite*.

6. *Dimict (two-component) breccias*: Two-component breccias may have been produced in the shattered rocks injected by and mixed with impact melt below an impact crater. Similar rocks have formed this way on Earth, where the impact-melt component is called *pseudotachylite*.

7. *Regolith breccias*: Breccias that preserve distinctive regolith features, such as small glass spheres and vesicular regolith glasses (*agglutinates*), are classified as regolith breccias. These breccias are simply regolith that has just barely been turned into a rock.

These lunar rock classifications are discussed below in approximately the order of their definition above.

6.1. MARE BASALTIC LAVAS AND VOLCANIC GLASSES

Volcanism is a fundamental planetary process. Even though lava flows and pyroclastic deposits form less than 1% of the lunar crust, they provide information about the Moon's internal constitution and its thermal history. Mare basalt lavas were produced inside the Moon by *partial melting* of the lunar mantle. If this melting process involved chemical equilibrium between the melted and unmelted portions, then the lavas will preserve clues to the chemical and mineral compositions of the regions that underwent partial melting. They will also contain information about the pressures (and therefore the depths) at which melting occurred. Furthermore, the ages of lunar volcanic rocks tell when they were erupted; by age-dating different lavas, it is possible to determine how the rate and depth of melting changed with time, revealing details of the Moon's thermal history.

Lunar volcanic rocks and their landforms may also contain important potential resources. The volcanic plains that form the maria are rich in Fe, and many are rich in Ti, most of which is in the mineral ilmenite (FeTiO₃). This mineral can provide TiO₂, Fe, and O by chemical reduction, the TiO₂ useful as a refractory, the Fe for materials fabrication, and the O for life support and rocket propellants. In addition, because the older lunar rocks are pervasively shattered by meteoroid bombardment, virtually the only areas of near-surface intact bedrock on the

Moon are in the younger lunar maria, which might be an important consideration for building large structures. Lava tubes, which are the hollow underground channels where lava once flowed, might even be used as shelters from solar and galactic radiation (Hörz, 1985a).

6.1.1. Chemical Composition, Classification, and Properties of Mare Basalts

Like terrestrial basalts, lunar basalts are low in silica (<54% SiO₂). Most other lunar rocks, however, are also low in silica. This contrasts with Earth, where the crust contains abundant high-silica granitic rocks. The range of compositions among lunar basalts is great, and allows for recognition of a wide variety of lunar mare basalt types. Representative chemical compositions for mare basalts are listed in Tables A6.1 (major elements) and A6.2 (trace elements).

One of the most fundamental features of the Moon is its division into two chemically distinct terrains: the mare basalts and the more abundant highland regions. Mare basalts contain greater concentrations of FeO and TiO₂ and have higher CaO/Al₂O₃ ratios than do rocks from the highland areas, a situation that reflects the lower proportion of Al-rich plagioclase feldspar in the basalts. Fragments of older mare basalts, which have been found in rocks from the highlands, demonstrate that mare-type volcanism actually began before the final flooding of the visible maria (e.g., *Ryder and Taylor, 1976; Taylor et al., 1983; Schultz and Spudis, 1983*).

One of the most striking chemical characteristics of mare basalts is their large variation in TiO₂ contents. This variation has allowed recognition of three major groups of different mare basalts: *high-Ti* (>9 wt.% TiO₂), *low-Ti* (1.5-9 wt.% TiO₂), and *very-low-Ti* (<1.5 wt.% TiO₂). Although these groups have been defined from analysis of returned samples, remotely-sensed spectral data that cover unsampled areas of the Moon suggest that there is in fact a continuous gradation from very-low- to high-Ti mare basalts (*Pieters, 1978*).

Other chemical parameters can be used to subdivide these three groups, as shown in Fig. 6.1, which is a three-axis plot of TiO₂, Al₂O₃, and K₂O. Some low-Ti basalts are richer in Al₂O₃ than others; these have been designated *aluminous low-Ti* mare basalts. Apollo 11 high-Ti mare basalts have been subdivided into high-K (>0.3 wt.% K₂O) and low-K (<0.1 wt.% K₂O). A group of aluminous mare basalts from the Apollo 14 site are, for the Moon, exceptionally rich in K₂O, averaging 0.9 wt.%; these have been designated *very-high-K*, or *VHK*, mare basalts (*Shervais et al., 1985b*). Detailed reviews of mare

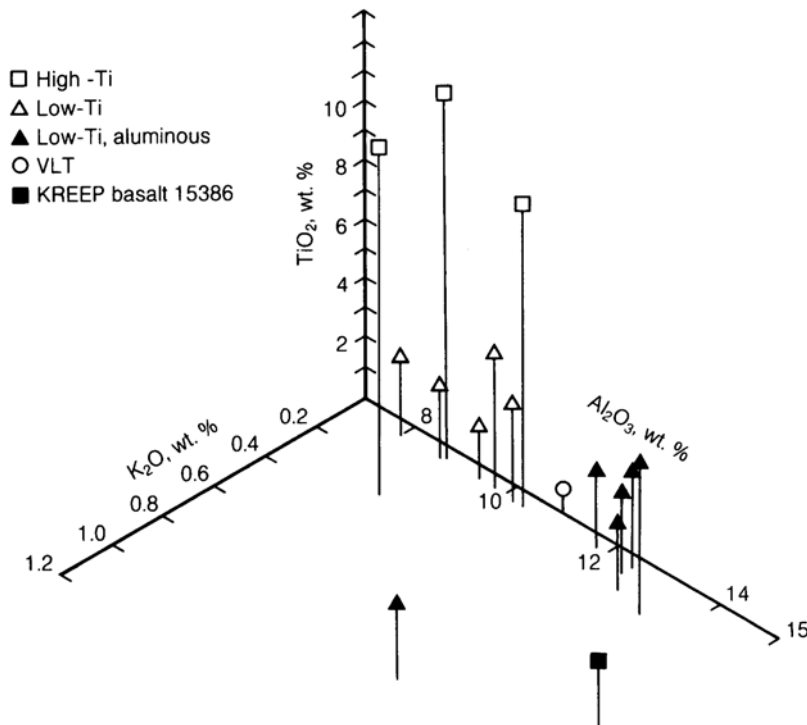


Fig. 6.1. K_2O - TiO_2 - Al_2O_3 plot for chemical compositions of representative lunar mare basalt types. The plot shows the separation of lunar basalts into chemically distinct groups, especially on the basis of TiO_2 content. Data are from Table A6.1.

basalt chemical compositions are given by *Papike et al.* (1976), *Papike and Vaniman* (1978), and *BVSP* (1981).

High-Ti mare basalts. Basalts collected from the Apollo 11 and 17 sites are mainly high-Ti mare basalts. Rare high-Ti mare basalt fragments are also found in the regolith at the Apollo 16 highland site; they were probably thrown to that site by impacts on distant mare basalt surfaces, perhaps on Mare Nectaris (*Delano*, 1975). The Apollo 11 high-Ti basalts have been subdivided into two main groups, low-K and high-K (Fig. 6.1). The Apollo 17 high-Ti basalts include one group that is much like Apollo 11 low-K basalts, as well as another very-high-Ti group, which is more abundant, that contains even more TiO_2 and more of the opaque mineral ilmenite (Table 6.1).

Even within these groups, the compositions of high-Ti basalts vary significantly from sample to sample. Explanations for these differences are complicated by the fact that virtually all mare basalt samples were collected as loose blocks in the regolith, and no identifiable lava flows were sampled directly on the lunar surface (although sampling at the Apollo 15 site came within a few meters of lava bedrock). Nevertheless, studies of terrestrial lava flows suggest that the observed variations from sample to sample reflect variation both within and between individual lava flows.

These variations are thought to result from the crystallization and separation of early-forming minerals. Analyses of numerous samples of high-Ti basalts show that TiO_2 decreases and Al_2O_3 increases as MgO decreases (Figs. 6.2a,b). This variation is consistent with the crystallization of Fe-Ti oxide minerals, such as ilmenite and armalcolite (both Ti-rich), and of olivine (Mg-rich), followed by their separation (e.g., by sinking) from the remaining liquid magma. This early crystallization could have taken place as the erupted lavas cooled while flowing across the lunar surface or sitting in lava ponds. The early-crystallizing minerals contain little or no Al_2O_3 , and this component therefore becomes enriched in the remaining liquid as crystallization proceeds. Removal of roughly equal amounts of ilmenite and olivine drives the chemical trends (referred to as *fractionation trends*) toward lower TiO_2 and MgO contents (Fig. 6.2a). By contrast, the Apollo 11 high-K basalts have little chemical variation, but they still lie along similar fractionation trends.

The contents of trace chemical elements (*trace elements*) in high-Ti mare basalts are listed in Table A6.2. The relative abundances of rare earth elements (*REE*; Fig. 6.3) are of particular interest. Because these elements are chemically similar and dilute enough in the magma to have relatively "ideal" and well-determined behavior, their contents give

TABLE 6.1. Modal mineral abundances (vol.%, normalized to 100%) of the major minerals in lunar mare basalts (from BVSP, 1981).

	Rock Type	Opaques*	Pyroxene	Olivine	Plagioclase
Apollo 17	very-high-Ti	24.4	47.7	4.6	23.4
Apollo 11	high-K	20.6	57.5	0.1	21.7
Apollo 17	low-K	15.1	51.6	—	33.3
Apollo 11	low-K	14.6	50.9	2.3	32.2
Apollo 12	ilmenite	9.3	61.1	3.6	25.9
Apollo 12	pigeonite	9.1	68.4	1.4	21.1
Apollo 12	olivine	7.1	53.5	20.2	19.2
Luna 16		7.1	51.5	0.1	41.2
Apollo 15	olivine	5.5	63.3	7.0	24.1
Apollo 15	pigeonite	3.7	62.5	—	33.8
Apollo 14	aluminous (14053)	3.2	53.8	—	43.0
Luna 24	very-low-Ti	1.8	48.6	10.4	39.1
Apollo 17	very-low-Ti	1.0	61.7	5.4	31.9

* Opaques are minerals that do not transmit light in thin section (e.g., armalcolite, ilmenite, spinel, troilite).

clues to the processes of melting, crystallization, and crystal separation from a melt. In the high-Ti basalts, the REE have pronounced bow-shaped patterns (Fig. 6.3). The relative REE abundances (when normalized to abundances in chondritic meteorites, a common standard; see section 8.4) increase from La to Sm, then decrease from Gd to Lu. The high-K basalts contain greater abundances of REE because these elements tend to concentrate along with K, Rb, and some other elements.

All of the high-Ti mare basalts have low Eu contents (negative *Eu anomalies*) relative to the other REE (see section 2.4.4). The explanation for negative Eu anomalies is that Eu behaves differently from the other REE because a significant amount of it occurs as the divalent ion Eu^{2+} , as well as the trivalent ion Eu^{3+} , in contrast to the other REE, which are only trivalent. This difference causes Eu to concentrate in Ca feldspar, $\text{CaAl}_2\text{Si}_2\text{O}_8$, by substitution for Ca^{2+} . Negative Eu anomalies appear to be a fundamental characteristic of the basalt source regions in the lunar mantle. This condition suggests that there was a Moonwide earlier stage of feldspar removal from the chemical system that produced the source regions, and that the separated feldspar took much of the Eu with it. One possibility, widely accepted, is that plagioclase crystallization and flotation occurred during a magma ocean episode early in the Moon's history, when the outer Moon may have contained a layer of melt tens or hundreds of kilometers thick (section 2.4.3). However, other explanations for the Eu anomaly, involving less extreme conditions, have been proposed (e.g., Walker, 1983).

Low-Ti mare basalts. A wide variety of low-Ti mare basalts were collected at the Apollo 12, Apollo 15, and Luna 16 landing sites on various maria, as well as at the Apollo 14 landing site. The Apollo 12 and 15 varieties each consist of two main basalt types, *olivine basalts* and *pigeonite* (low-Ca pyroxene) *basalts*. In general, the olivine basalts have more MgO and less CaO, Al_2O_3 , and TiO_2 than do the pigeonite basalts at the same site.

Like the high-Ti mare basalts, none of these low-Ti basalts crystallize plagioclase feldspar early as they cool. Both types show clear evidence for the early separation of olivine or pigeonite, but not of ilmenite. The resulting trends of chemical composition show increasing TiO_2 and Al_2O_3 with decreasing MgO (Figs. 6.2c,d). In addition to these basalts, some of the low-Ti basalts collected at the Apollo 12 site are noticeably richer in ilmenite than the others; these have been designated *ilmenite basalts*. The REE abundances in low-Ti basalts (Fig. 6.4) are, in general, lower than in the high-Ti basalts, although both groups have the same bow-shaped pattern and both have negative Eu anomalies. Concentrations of other *incompatible elements* (i.e., those elements that tend to stay in the liquid rather than in the early crystallizing minerals) such as Sr and U are also lower in the low-Ti basalts than in the high-Ti basalts (Table A6.2).

Aluminous low-Ti mare basalts. Some groups of low-Ti basalts contain more Al_2O_3 than do those from the Apollo 12 and 15 sites (Fig. 6.1); these have been called *aluminous*. Three major categories of aluminous mare basalts can be distinguished on the basis of their location and chemistry: those from the

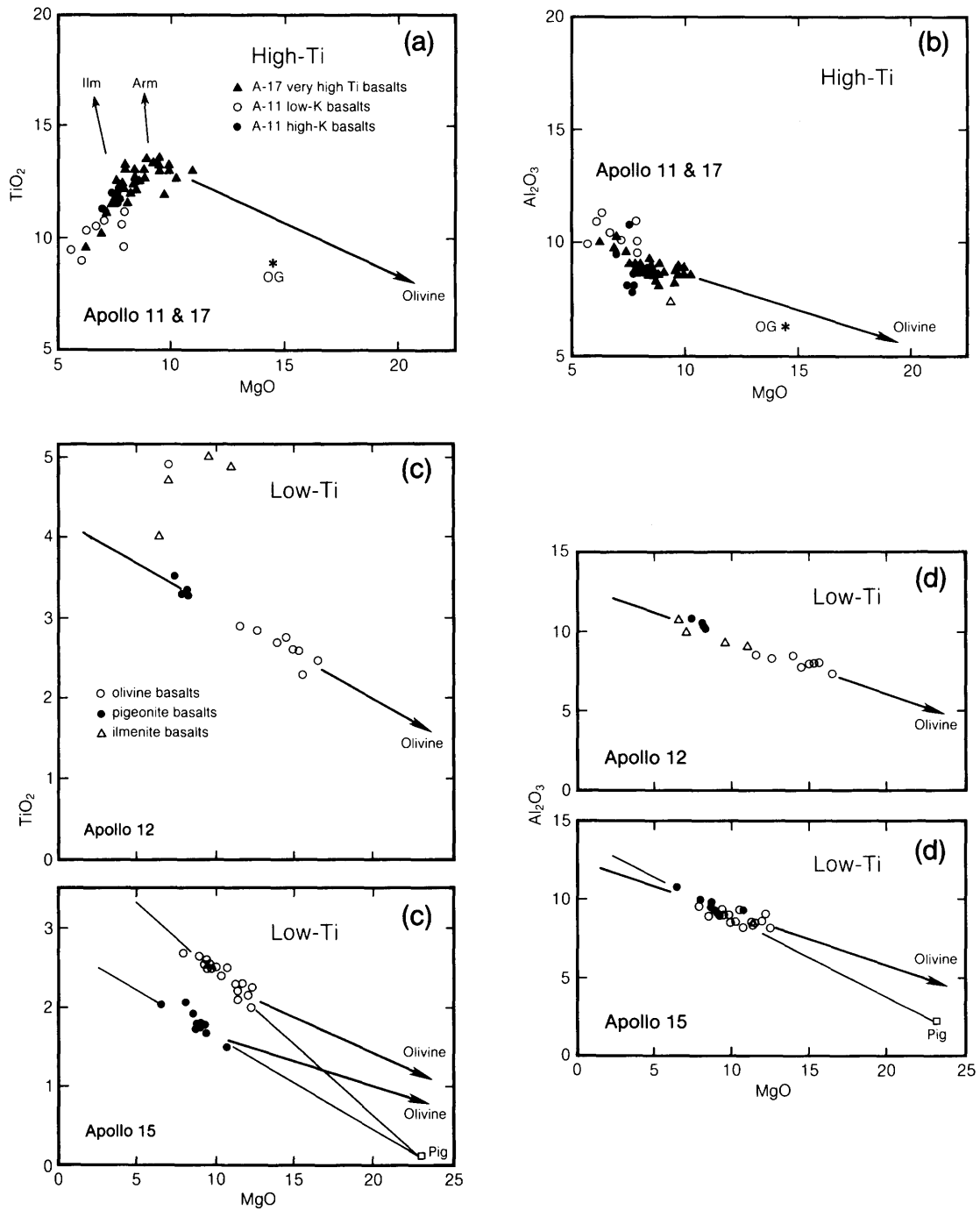
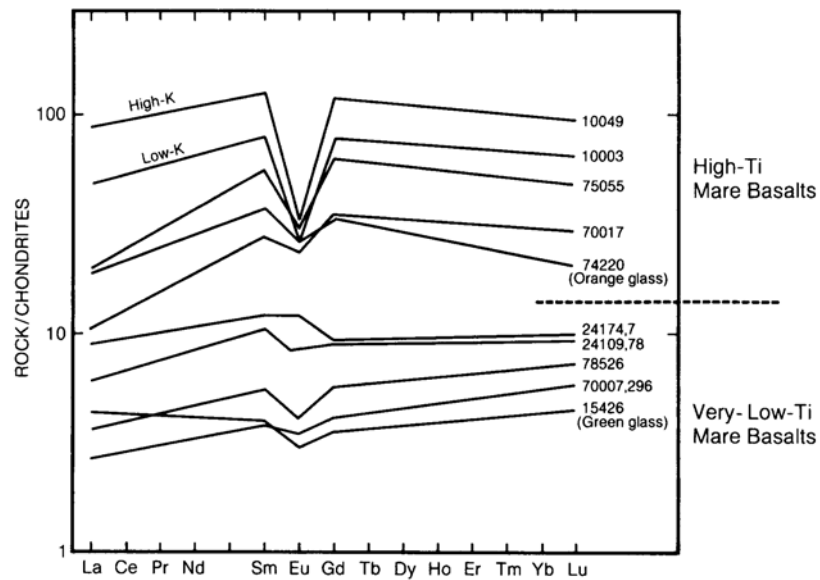


Fig. 6.2. Chemical variation diagrams showing MgO-TiO₂ and MgO-Al₂O₃ relations for high-Ti (a,b) and low-Ti (c,d) lunar mare basalts (Papike et al., 1976). Actual basalt compositions are represented by circles, dots, and triangles. "OG" in panels (a) and (b) shows the composition of Apollo 17 orange glass. Arrows point toward the compositions of specific minerals that crystallize from the basaltic magmas (Ilm = ilmenite, Arm = armalcolite, Pig = the low-Ca pyroxene *pigeonite*). If these minerals or combinations of them are removed, the composition of the remaining liquid will be driven in an opposite direction, producing the trend of plotted points.

Fig. 6.3. Plot of rare earth element (REE) contents in high-Ti and very-low-Ti (VLT) mare basalts (data from Table A6.2 and from *BVSP*, 1981). REE contents are normalized to the contents in chondritic meteorites. The high-Ti basalts have higher REE concentrations in a convex-upward ("bow-shaped") pattern interrupted by a large to small negative Eu anomaly. The VLT basalts have a flatter pattern in which small negative Eu anomalies may or may not be present.



Luna 16 site, some from the Apollo 14 site (mostly from one breccia sample, 14321), and others from the Apollo 14 site that are enriched in K_2O . The Luna 16 mare basalts contain the most TiO_2 of any of the aluminous low-Ti basalts, averaging about 5 wt.%. They also have distinctive REE patterns (Fig. 6.5) that are characterized by much greater abundances of the light REE (La through Sm) than the heavier REE. The Luna 16 basalts do, however, display the same typical bow-shaped pattern, with a negative Eu anomaly, that is characteristic of other mare basalts.

A rich variety of aluminous mare basalts was collected from the Apollo 14 site. Several fragments of aluminous basalt, contained in a single breccia sample (14321), actually represent a suite of related rocks from several distinct lava flows. They have relatively uniform major-element compositions (Table A6.1), but this uniformity is coupled with an eightfold variation in the abundances of REE and other incompatible elements (Table A6.2; Fig. 6.5). None of these basalts has the typical bow-shaped REE pattern that characterizes the mare basalts described above, although all have negative Eu anomalies. The highest REE group, designated Group 1 by *Dickinson et al.* (1985), has a REE pattern lower than but similar to that of the unusual *KREEP basalts* (Fig. 6.5), a highland rock type that is rich in incompatible elements (see section 6.3.2). Some Apollo 14 mare basalts have higher REE contents than do the Group 1 rocks, but they have much flatter REE patterns (*Shervais et al.*, 1985a). The lowest REE group (Group 5) in breccia 14321 has an

REE pattern characterized by a continuous rise from La to Lu; a negative Eu anomaly is still present. Groups 2, 3, and 4 have REE distributions that fall between the extremes of Groups 1 and 5.

A few mare basalt fragments in other Apollo 14 highland breccias, samples 14304 and 14305, contain exceptionally high quantities of K_2O (0.6-1.4%) for mare basalts (*Shervais et al.*, 1985b) and are designated *very-high-K*, or *VHK*, mare basalts. These basalts are high in K_2O for basalt samples from the Moon; they are also high in comparison to terrestrial ocean-floor basalts, with ~0.1-0.3% K_2O , but much lower than many types of terrestrial continental basalts that commonly have K_2O contents of ~2% and may have more than 4% K_2O (this difference between Earth and Moon reflects the depletion of the entire Moon in K relative to Earth). The VHK basalts have major-element compositions much like the Apollo 14 aluminous mare basalts, except for the enrichment in K_2O . Their REE contents, however, are not significantly greater than those of Apollo 14 aluminous basalts, and the REE enrichment that might normally accompany the K_2O enrichment is not observed. Consequently, the VHK magmas could not have been derived from basalts like those in sample 14321 by any simple process involving mixing of Group 5 basalts with *KREEP*. Their unusual characteristics may have been produced by more complex processes involving assimilation of lunar high-silica ("granitic") materials (see section 6.3.5 for descriptions of granitic materials, and *Shervais et al.*, 1985b or *Shih et al.*, 1986, for assimilation models).

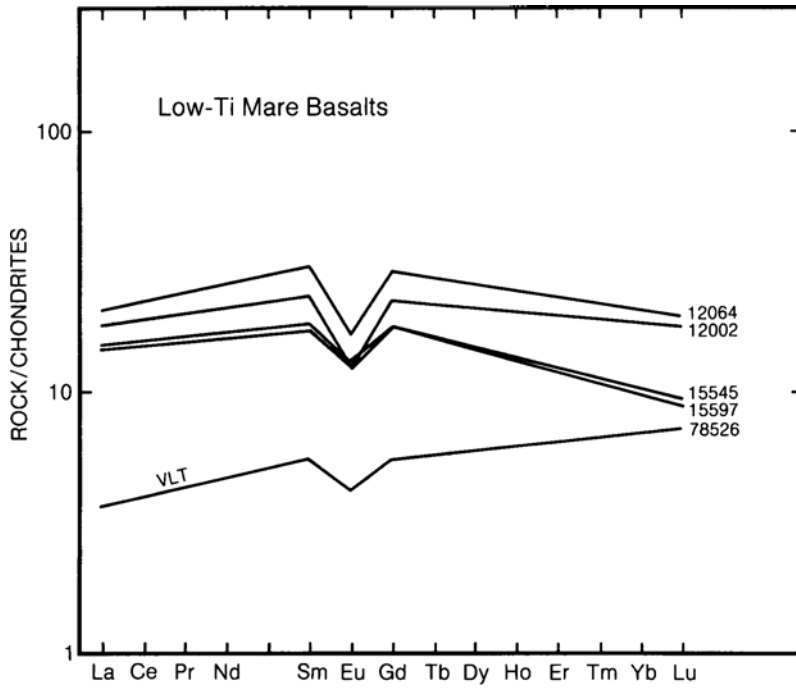


Fig. 6.4. Plot of REE contents in low-Ti mare basalts. These basalts have convex-upward (“bow-shaped”) patterns with small negative Eu anomalies. One very-low-Ti mare basalt (VLT) is shown for comparison (data from Table A6.2).

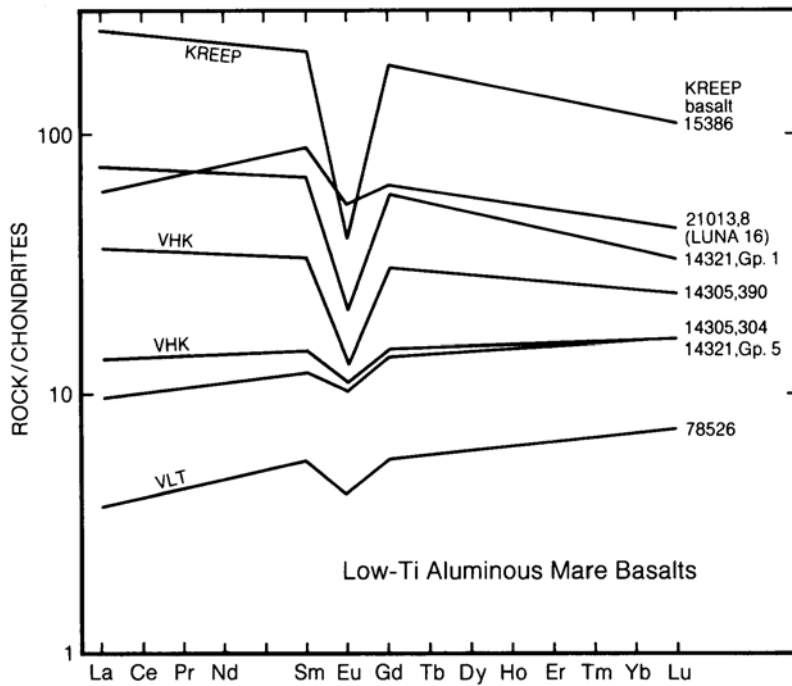


Fig. 6.5. Plot of REE contents in low-Ti, aluminous mare basalts. The REE patterns vary from slightly depleted in the light REE (left side of diagram) to slightly enriched. Curves labeled “VHK” indicate very-high-K basalts that occur as fragments within sample 14305. Data for very-low-Ti (VLT) and KREEP basalts are shown for comparison (data from Table A6.2 and from *Shervais et al., 1985b*).

Very-low-Ti (VLT) mare basalts. VLT mare basalt's were first discovered as tiny fragments in the Apollo 17 drill core (Vaniman and Papike, 1977c). The basalt particles collected by Luna 24 from Mare Crisium were also VLT mare basalt's. Besides containing lower amounts of TiO_2 (<1.5%) than other mare basalt's, VLT basalt's are distinctive in having low abundances of REE and other incompatible elements; they also have REE patterns that are not bow-shaped. Instead, the REE contents (Fig. 6.3) rise continuously from La to Lu, although Luna 24 VLT basalt's have rather flat patterns among the heavy REE (Gd to Lu). All but one fragment of the Luna 24 basalt's have small negative Eu anomalies. A similar basaltic composition, the Apollo 15 green-glass pyroclastic deposits (section 6.1.7), has comparable chemical characteristics.

Comparison with other planetary basalt's. The chemistry of lunar mare basalt's differs in many ways from that of terrestrial basalt's. In general, Ti and Cr concentrations and Fe/Mg ratios are considerably higher in lunar basalt's, and Al, Na, and K concentrations are lower.

Lunar mare basalt's are also depleted in volatile elements (K, Na, Rb, Pb, C, H, etc.) compared to terrestrial basalt's. This condition is illustrated by the low K/U ratios of lunar basalt's (Fig. 6.6). The K/U ratio is especially useful for recognizing volatilization events; K and U behave similarly during melting and crystallization of silicate magmas, but K is volatile (vaporizes at low temperatures) and U is refractory

(vaporizes at high temperatures). Therefore, the K/U ratio will not be much altered by normal melting and crystallization, but it will be sensitive to any high-temperature volatilization events.

Except for some rare meteorites (*eucrites* or *basaltic achondrites*), lunar mare basalt's (and lunar highland rocks as well) have lower K/U ratios than all other planetary samples, including the unusual basaltic SNC meteorites, which may have come from Mars (e.g., McSween, 1985). One might argue that the low K/U ratios in lunar basalt's reflect an enrichment in U instead of a depletion in K. However, there is ample additional evidence for the general depletion of volatile elements in the Moon—the totally water-free nature of lunar basalt's, as well as the extremely low abundances of other volatile elements such as Bi, Cd, and Ti (Wolf *et al.*, 1979). Curiously, S, though usually volatile in its terrestrial behavior, occurs in greater abundance in lunar mare basalt's than in terrestrial basalt's.

Lunar basalt's are also depleted in *siderophile* elements, elements that tend to concentrate in metallic iron (Ni, Co, Au, Ir, etc.). This depletion has been discussed and debated in much detail, because it has great bearing on how the Moon formed and on whether or not the Moon has a metallic core (e.g., Newsom, 1986). An example of this depletion is the relationship between Mo (a siderophile element) and Nd (a rare earth element; Fig. 6.7). Both elements are refractory, so differences in their abundances are not caused by volatilization of one of them. Furthermore,

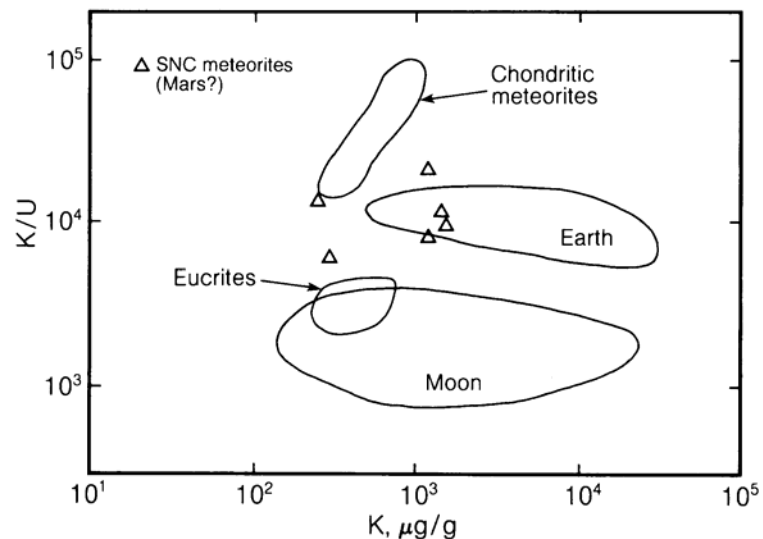


Fig. 6.6. Plot of potassium/uranium (K/U) vs. K for various analyzed solar system materials (after Taylor, 1982). The uniformly low K/U ratios of lunar samples demonstrate the Moon's general depletion of volatile elements and sets it clearly aside from most other solar system objects.

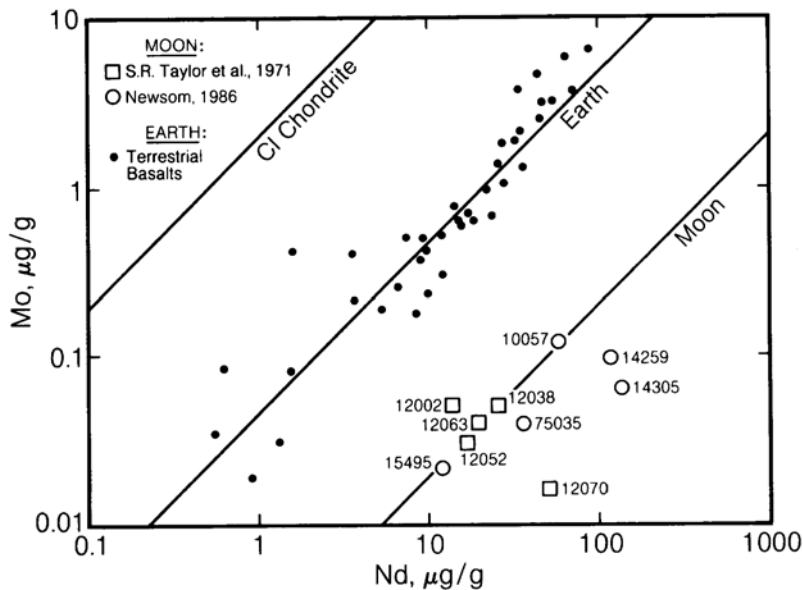


Fig. 6.7. Plot of Mo (a siderophile element) vs. Nd (a lithophile element) in terrestrial basalts (filled circles) and lunar basalts (open symbols with sample numbers). The data show that lunar basalts (and hence the lunar mantle, from which they were derived) are depleted in siderophile elements compared to terrestrial basalts and Earth's mantle (Newsom, 1986).

in systems where no metallic iron is present, Mo behaves geochemically very much like Nd, so the observed depletion cannot be due to any process that occurs in a melt that is free of metallic iron. Consequently, the depletion of Mo (Fig. 6.7) has been interpreted (Newsom, 1986) as an indication that all lunar basalts (and the lunar mantle that melted to form them) contain uniformly lower siderophile element abundances than do terrestrial basalts and the mantle of the Earth. Extensive analyses of lunar rocks have shown that the greater the tendency of an element to concentrate in metallic iron, the more depleted it is in lunar rocks (Newsom, 1986).

Oxygen partial pressures (fugacities) during crystallization. Even a cursory look at lunar basalts shows that they formed under substantially more reducing conditions (lower oxygen partial pressures) than did terrestrial basalts. Lunar basalts invariably contain metallic iron, which occurs naturally on Earth under only the most extraordinary circumstances. However, there is no real contradiction between the widespread presence of metallic iron and the generally low abundances of the siderophile elements (such as Ni) that should associate with metallic iron. Most of the metallic iron in lunar basalts has been formed from the reduction of FeO during the crystallization of the basalts (see section 5.4.2), long after the siderophiles were removed from the mantle materials that melted to produce the basalts. Further evidence of reduction is the fact that there is virtually no Fe₂O₃ in lunar lavas.

Intrinsic oxygen *fugacities* (effective partial pressures in terms of thermodynamic chemical potential) of mare basalts (Figs. 6.8 and 5.17) are about a million times lower than those in terrestrial basalts at any given temperature. The reduced character of lunar lavas causes some elements, such as Eu and Cr, to have lower valence states and thus to have different chemical behavior on the Moon than they do in terrestrial rocks.

Viscosity. The low viscosity of lunar lavas is suggested by the way they spread out in thin, extensive flows on the lunar surface. This low viscosity has been confirmed by measurements of the viscosity of a synthetic liquid with the composition of Apollo 11 high-Ti basalt (Murase and McBirney, 1970). The measured viscosity ranges from 4.5 p at 1495°C to 10p at 1395°C when measured in air. Measurements in an Ar atmosphere yielded similar results. These viscosities are approximately that of heavy motor oil at room temperature. Terrestrial lavas are typically 10 times more viscous (Fig. 6.9). Section 5.2 discusses some of the implications of this viscosity difference for potentially effective concentration of heavy crystals by settling in lunar mare magmas.

6.1.2. Mineralogy of Mare Basalts

The minerals that make up a basaltic rock and their relative amounts are largely dependent on the chemical composition of the lava from which the

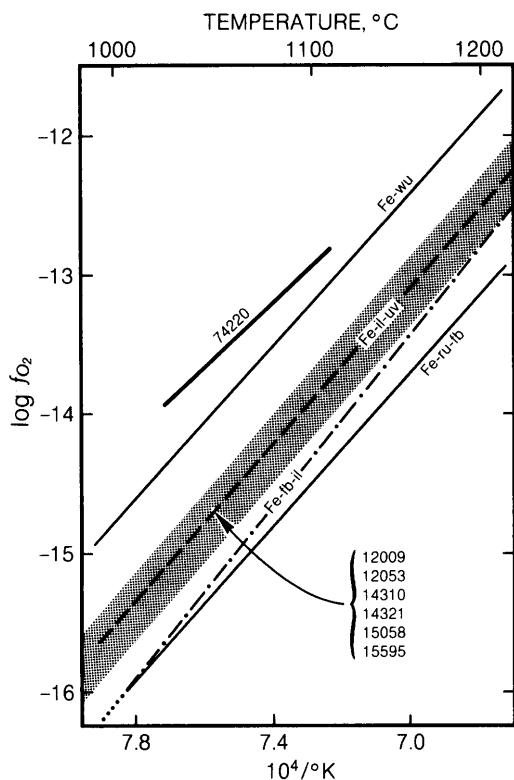


Fig. 6.8. Plot of fO_2 (oxygen fugacity; a measure of effective oxygen chemical potential roughly related to oxygen availability) vs. temperature in equilibrium with lunar mineral assemblages and lunar igneous rocks (sample numbers). Note that sample 74220 is the Apollo 17 orange glass (Table A6.1). Measured oxygen fugacities in lunar igneous rocks fall in the shaded area. Labeled lines are mineral equilibrium “buffer” curves for the Fe-FeO-TiO₂ system: Fe = iron metal; il = ilmenite; uv = ulvöspinel; wu = wüstite; fb = ferropseudobrookite; ru = rutile. Adapted from Taylor (1982). In contrast, terrestrial basalts would plot just above this diagram (see Fig. 5.17).

rock crystallized. Lavas that contain substantial amounts of TiO₂, for example, will crystallize more ilmenite and other Fe-Ti oxide minerals than will lavas that are low in TiO₂.

The mineralogy of a basaltic rock is also affected by how fast the lava cooled. In cases of extremely rapid cooling, as experienced by the particles ejected in lava fountains, no minerals form at all; the resulting rock is all quenched glass. At the other extreme, very slow cooling will allow separation of crystallizing minerals from lava, allowing the remaining liquids to develop a significant range of chemical compositions.

Lunar mare basalts are composed chiefly of four major minerals: pyroxene, plagioclase, olivine, and metal oxides (ilmenite, armalcolite, and spinel). Mare basalts also contain minor amounts of minerals that form near the end of crystallization. These late-stage minerals include silica minerals (cristobalite or tridymite), potassium feldspar, zircon and other Zr-bearing silicates, phosphate minerals (apatite and whitlockite), metallic iron, and iron sulfide (troilite). These minerals are described in detail in Chapter 5. Varying amounts of late-stage glass may also be preserved in mare basalts.

Abundances of the four major mineral types in mare basalts have been normalized to 100% in Table 6.1; the amounts of other minerals rarely exceed 5%. The abundance of metal-oxide minerals varies directly with TiO₂ content, because high TiO₂

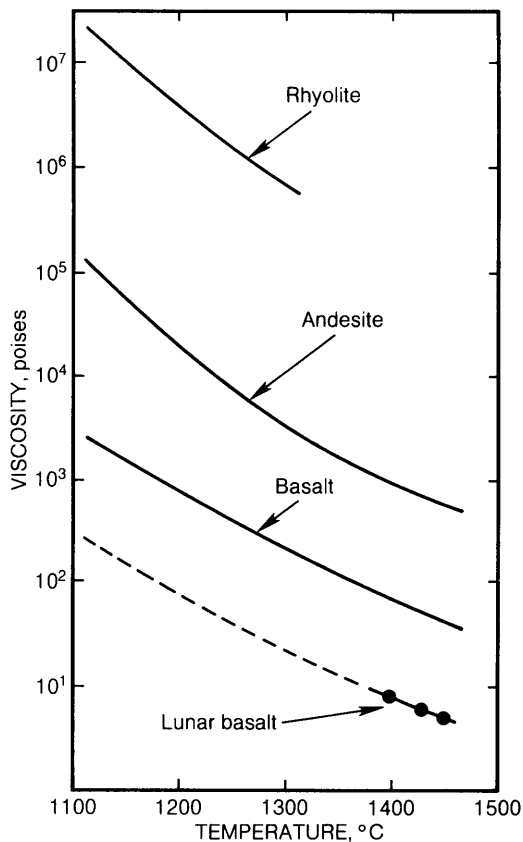


Fig. 6.9. Plot of measured viscosity as a function of temperature for lunar high-Ti mare magma, compared to terrestrial magmas (from Murase and McBirney, 1970). Lunar basaltic magmas are only about one-tenth as viscous as terrestrial basaltic magmas.

contents result in the formation of Ti-rich oxide minerals such as ilmenite (see also Fig. 5.18). Apollo 17 very-high-Ti basalts have the most oxide minerals (largely ilmenite), followed by other high-Ti basalts, low-Ti basalts, and very-low-Ti basalts. Because Al occurs chiefly in plagioclase feldspar, the aluminous mare basalts (14053 and Luna 16 in Table 6.1) have the highest plagioclase-to-pyroxene ratios. A more detailed comparison between major-element composition and mineral abundances is given by *BVSP* (1981, p. 254).

The chemical compositions of the individual minerals reflect both the bulk composition and the cooling rate of the lava in which they formed. These relations are shown most dramatically by the pyroxenes. Individual pyroxene crystals in mare basalts are *compositionally zoned* (i.e., the composition, especially the amounts of Fe, Mg, and Ca, varies significantly) from their centers to their edges, and there are also substantial variations from one pyroxene crystal to another (Fig. 5.3). The chemical variations are not confined to the major elements (Fe, Mg, Ca) alone, but also involve minor elements such as Ti, Al, and Cr. Detailed discussions of pyroxene composition and how it is affected by lava composition, cooling rate, oxidation-reduction conditions, and temperature are given by *Bence and Papike* (1973), *Papike et al.* (1976), and *BVSP* (1981). Extensive chemical zonation is also found in other minerals. In fact, most mineral grains in mare basalts are not entirely uniform in composition, except very small ones and the silica minerals (e.g., cristobalite).

Mineral compositions can also be affected by the sequence in which different minerals crystallize from the cooling lava. This sequence is not the same in all lavas. It depends on the bulk chemical composition of the lava, on the cooling rate, and on the extent to which the first-formed minerals are removed (*fractionated*) from the lava.

6.1.3. Textures of Mare Basalts

The *texture* of a rock is defined by the sizes and shapes of the minerals that compose it and by the mutual geometric relationships between them. Texture is important because it contributes to a rock's physical properties, such as strength. In volcanic rocks, the observed textures reflect the crystallization history, including the cooling rate, and they also provide clues to the amount of crystallization that took place before the lava was erupted.

The texture of a volcanic rock is determined chiefly by the composition, initial temperature, and cooling rate of the lava from which it crystallized. Geologists have given names to many different textures that occur in terrestrial basalts. Applying

these names to lunar mare basalts is complicated by the fact that plagioclase feldspar, which plays an important role in naming a texture, is more abundant in terrestrial basalts than in lunar ones. Nevertheless, geologists have managed to find appropriate textural terms for virtually all lunar basalts. Some of the most important textures are described below and shown in Figs. 6.10 to 6.13. A guide to textural terms appears as Table 1.3.3.1 in *BVSP* (1981).

High-Ti mare basalts. Most Apollo 11 high-K basalts have *intersertal* textures, in which pyroxene and ilmenite crystals form an open fretwork around plagioclase and glass. Other high-K basalts have *ophitic* textures, characterized by pyroxene crystals enclosed by plagioclase. *Grove and Beatty* (1980) prefer to call these two textures "*anti-intersertal*" and "*anti-ophitic*" to distinguish them from the normal intersertal and ophitic textures in terrestrial rocks, where plagioclase forms the fretwork or is enclosed within pyroxene. Some high-K basalts are *vitrophyric*; these contain a glassy matrix (*groundmass*) in which relatively large crystals are embedded. Examples of some textures appear in Fig. 6.10; for details, see *Beatty and Albee* (1978), *Beatty et al.* (1979), *Grove and Beatty* (1980), *Papike et al.* (1974), *Longhi et al.* (1974), and *Warner et al.* (1978b).

Low-K, high-Ti mare basalts have *ophitic* to *subophitic* textures (Fig. 6.10). This variability in texture results primarily from the variability in pyroxene size. Where pyroxene partially encloses the plagioclase, the texture is called *subophitic*; where pyroxene is coarser and fully encloses individual plagioclase crystals, it is called *ophitic*.

The sizes and shapes of individual crystals are also important in defining the textures of mare basalts, and certain crystal sizes and shapes tend to be associated with certain textures. Pyroxene crystals tend to be *euhedral* (i.e., regularly shaped and well faceted) in the more slowly cooled rocks, which commonly have coarsely granular or *ophitic* textures. Large, early-formed crystals (*phenocrysts*) of olivine occur only in the finer-grained *intergranular* basalts, in which the smaller crystals form a network resembling *intersertal* textures but lacking glass. In the coarser ophitic basalts, olivine crystals are smaller (or lacking) and are often mantled by later-crystallizing pyroxene.

Ilmenite in mare basalts forms elongate, bladed grains in the finer-grained subophitic rocks, grading to more equant, *anhedral* grains (lacking crystal faces) in the coarse ophitic samples. Many high-Ti basalts collected at the Apollo 17 site have *porphyritic* or *microporphyritic* textures, in which large crystals of olivine and armalcolite occur in finer-grained matrices. The olivine crystals are often *mantled* (rimmed by another crystal in crystallogra-

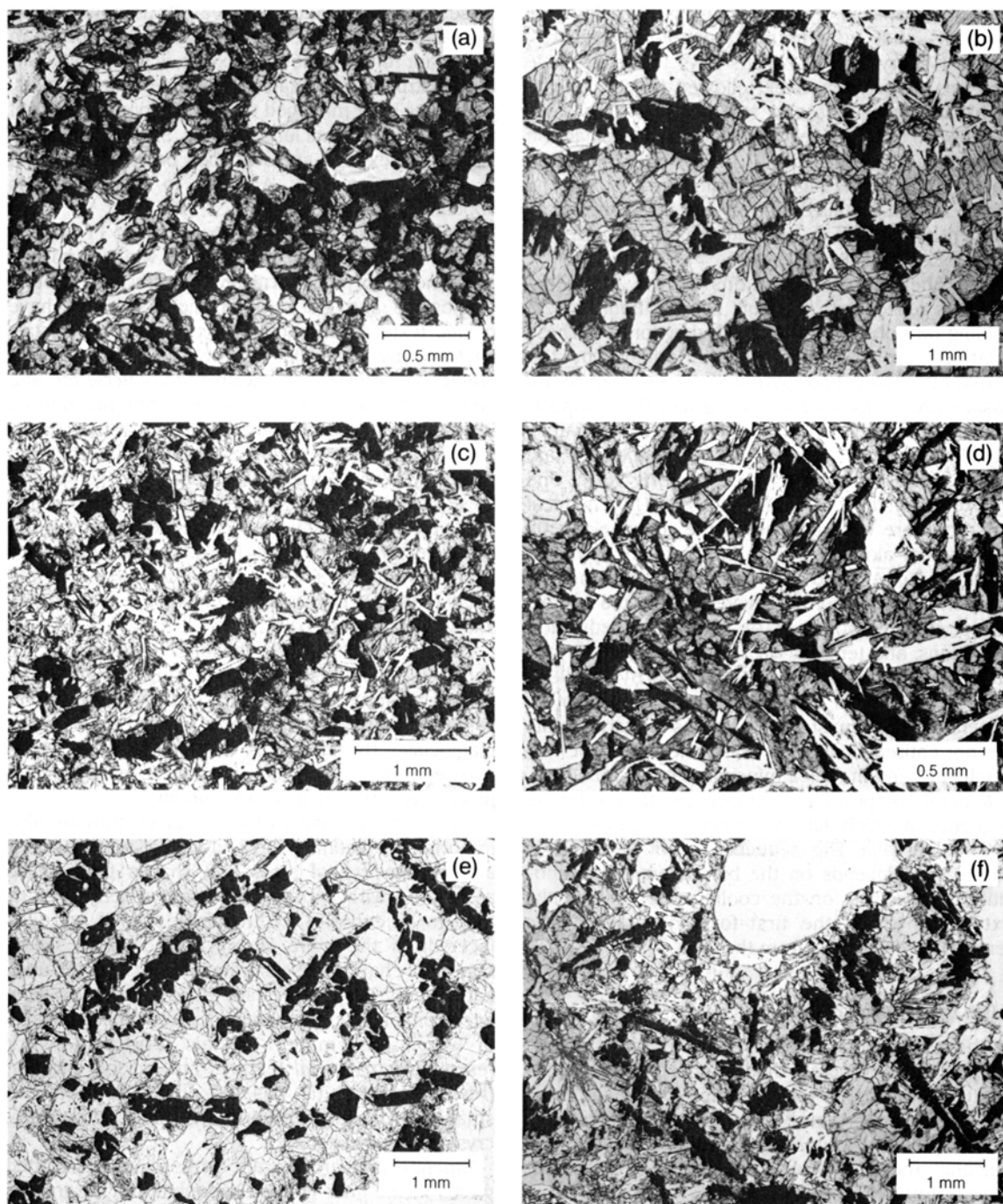


Fig. 6.10. Photomicrographs of high-Ti mare basalts showing the wide range of textures developed during crystallization. The major minerals are pyroxene and olivine (light gray), plagioclase (white), ilmenite (black). **(a)** Sample 10017,20, displaying an anti-ophitic texture; **(b)** sample 10044,55, displaying a subophitic texture; **(c)** sample 10003,40, displaying an intergranular texture; **(d)** sample 10062,44, displaying an ophitic to intergranular texture; **(e)** sample 70035,19, displaying a subophitic texture; **(f)** sample 71035,28, displaying a microporphyritic texture with a coarsely radiate matrix.

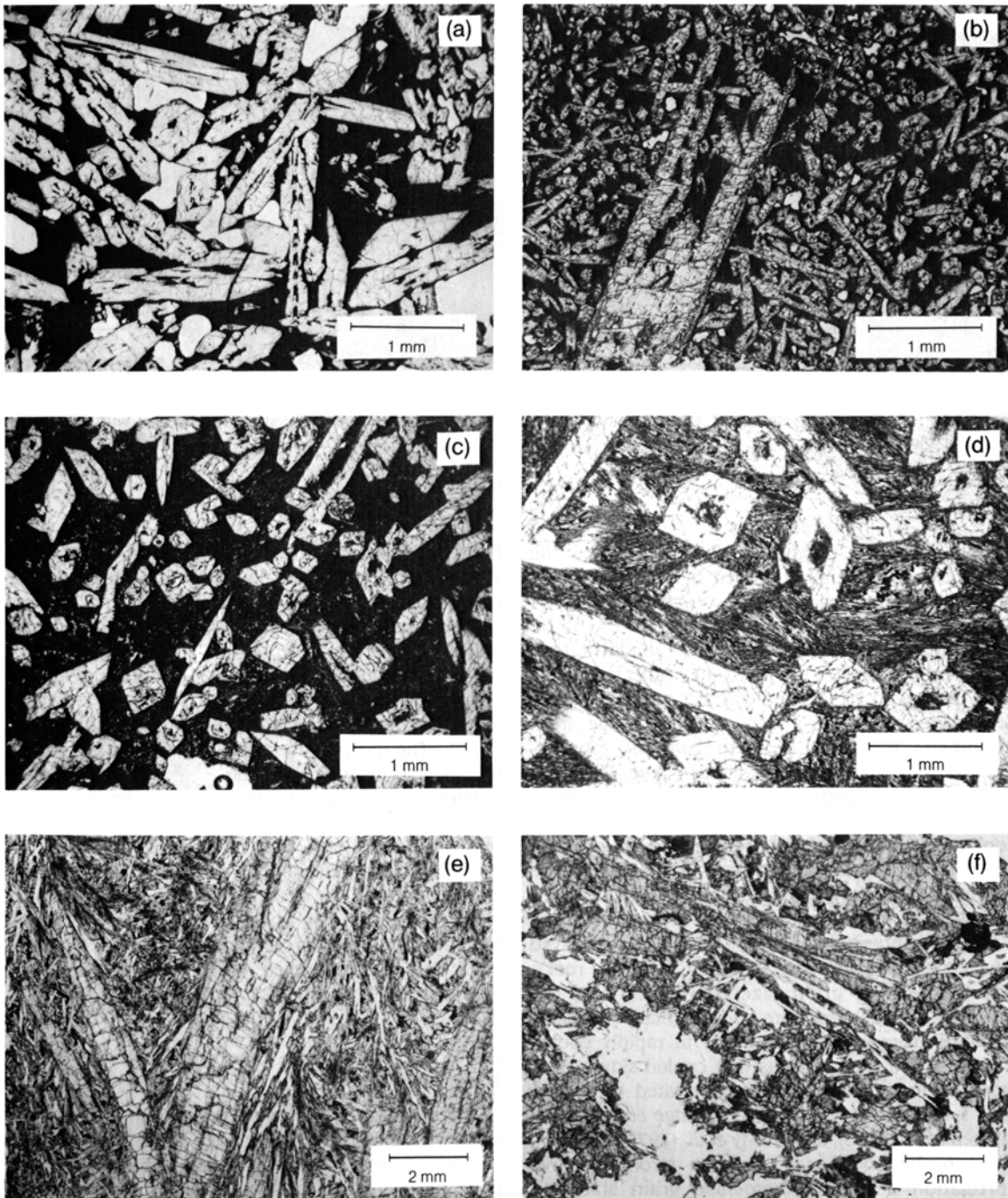


Fig. 6.11. Photomicrographs of low-Ti pigeonite basalts showing a range of textures from completely crystalline (*gabbroic*) to largely glassy (*vitrophyric*). **(a)** Sample 15486,22, porphyritic with an aphanitic groundmass; **(b)** sample 15597,17, microporphyritic with occasional large phenocrysts in an aphanitic matrix; **(c)** sample 15595,37, microporphyritic texture with a fine radiate matrix; **(d)** sample 15596,16, porphyritic with medium radiate matrix; **(e)** sample 15476,32, porphyritic with coarse radiate to intergranular matrix; **(f)** sample 15058,126, subophitic texture; **(g)** sample 15076,12, subophitic texture; **(h)** sample 15085,19, subophitic texture with distinctly coarse plagioclase.

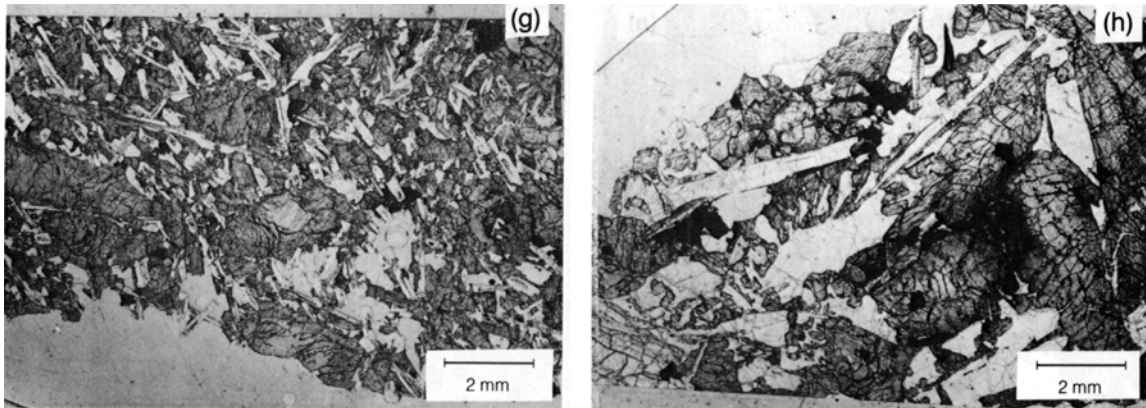


Fig. 6.11. (continued) **(g)** Sample 15076,12, subophitic texture; **(h)** sample 15085,19, subophitic texture with distinctly coarse plagioclase.

phically matched orientation) by augite, and the armalcolite is generally mantled by ilmenite. A few Apollo 17 samples have very coarse-grained subophitic textures.

Low-Ti mare basalts. Low-Ti basalts that contain pigeonite (low-Ca pyroxene), especially those from the Apollo 15 site, show an extraordinary range of textures. In these rocks, textures range from vitrophyric (mostly glassy) to *gabbroic* (coarse-grained and completely crystalline; see Fig. 6.11). Olivine becomes increasingly rare in these rocks as the grain size increases, indicating that with slow cooling olivine reacts with the liquid to produce pyroxene. The finer-grained rocks in this series are *porphyritic*, containing large, early-formed crystals (*phenocrysts*) in a finer, later-formed *groundmass*. Most of the phenocrysts are pigeonite, but embayed olivine phenocrysts occur in the most glassy rocks. With increasing grain size, the texture of the groundmass changes from *radiate* (bladed crystals radiating from common centers) in rapidly cooled rocks to subophitic in lavas that cooled slowly. This variation in groundmass texture, related to cooling rate, is discussed in detail in *Baldrige et al.* (1979), *Lofgren et al.* (1975), and *Dowty et al.* (1973, 1974a).

Olivine-bearing basalts have a strong positive correlation between plagioclase grain size and normative olivine content (*Walker et al.*, 1976). (The *normative* olivine content is calculated from the chemical analysis; the *modal* olivine content is measured from the sample with a microscope.) This relation suggests that the different samples formed by crystal settling inside a single, relatively thick flow. Observed textures range from vitrophyric to gab-

broic; representative textures are shown in Fig. 6.12. Textures of ilmenite basalts range from fine-grained and porphyritic to coarse-grained (Fig. 6.12); this range of textures is also consistent with derivation within a single lava flow.

Most aluminous low-Ti mare basalts have subophitic to ophitic textures, though a few are vitrophyric (*Shervais et al.*, 1985a,b; *Dickinson et al.*, 1985). The porphyritic varieties have plagioclase phenocrysts, as well as olivine.

Very-low-Ti mare basalts. All the known samples of very-low-Ti mare basalts are small fragments found in soils, and determination of textures is therefore more difficult than would be the case for larger samples. The observed textures are generally subophitic to microporphyritic (Fig. 6.13), but fragments with both vitrophyric and ophitic textures have also been observed. For details, see *Vaniman and Papike* (1977c) and *G. J. Taylor et al.* (1978).

6.1.4. Crystallization Experiments on Mare Basalts

A great deal of effort has been spent in trying to understand how the textures of mare basalts developed and what the textures can tell us about how the lavas formed. In addition to studies of the rocks themselves, dynamic crystallization experiments have been performed on small samples with the compositions of lunar basalts. These samples are first completely melted and then cooled from their *liquidus* (completely molten) temperatures at various rates. These experiments have shown that the development of textures in basaltic rocks is con-

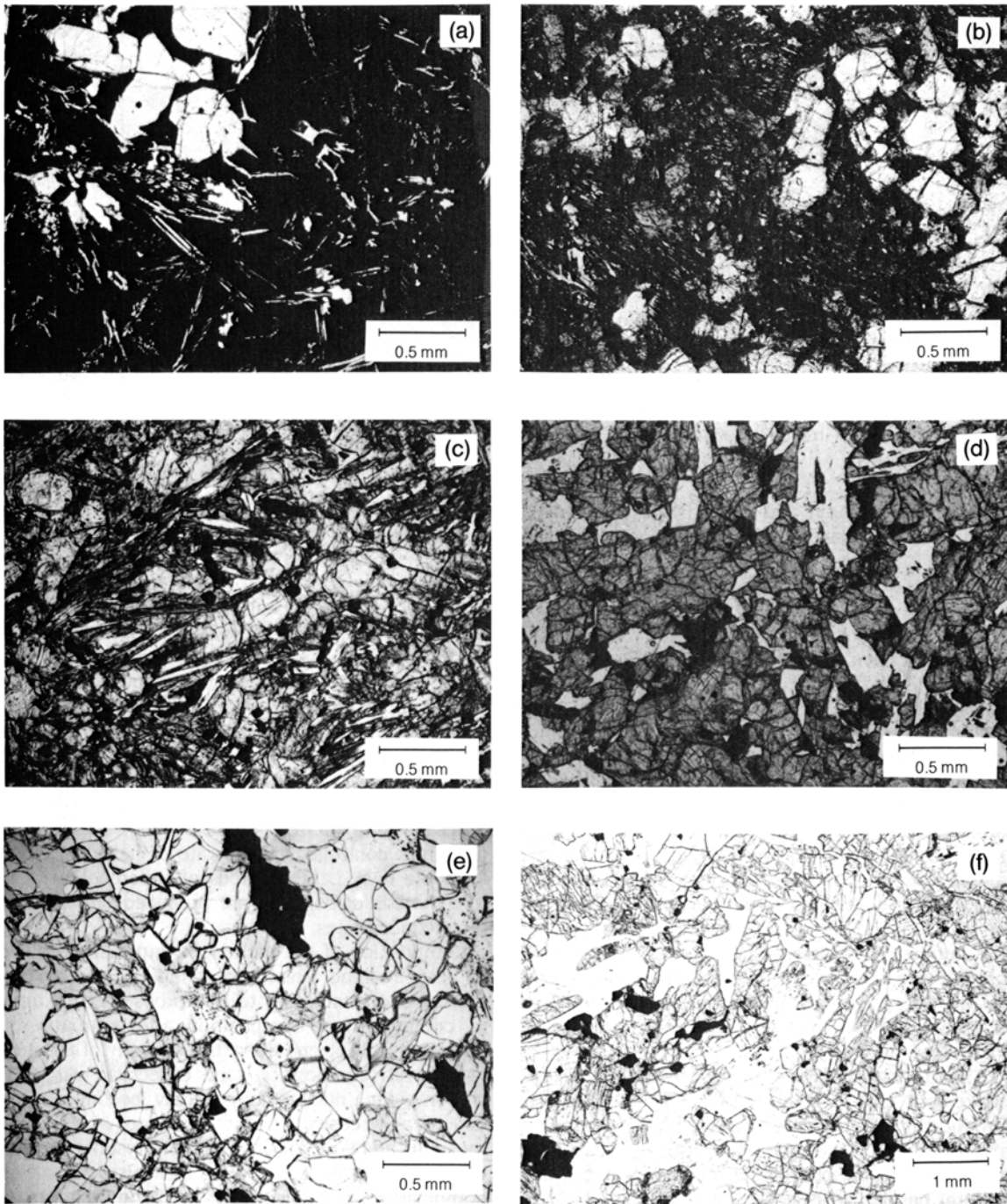


Fig. 6.12. Photomicrographs of low-Ti olivine (**a,c,f**) and ilmenite (**b,d,e**) basalts. (**a**) Sample 12009,11, porphyritic texture with coarse equant and fine dendritic phenocrysts and an aphanitic matrix; (**b**) sample 12022,110, microporphyritic with fine radiate matrix; (**c**) sample 12004,55, subophitic texture; (**d**) sample 12056,7, subophitic texture; (**e**) sample 12005,12, cumulate texture; (**f**) sample 12035,24, ophitic, gabbroic texture.

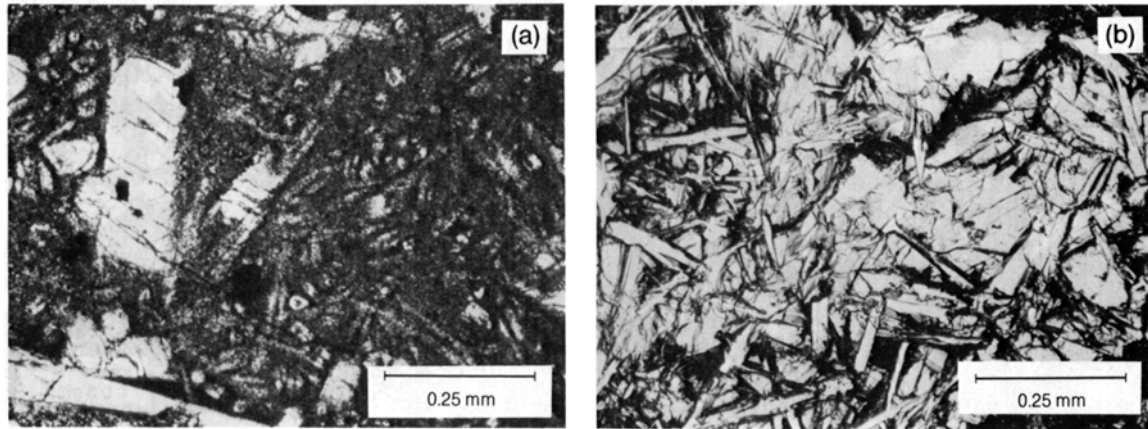


Fig. 6.13. Photomicrographs of very-low-Ti mare basalts. **(a)** Sample 70007,325L1, displaying a microporphyritic texture; **(b)** subophitic texture in sample 70009,295L1.

trolled by nucleation and growth rates of crystals, cooling rates of lavas, compositions of the liquids, and the amount of fluid flow within the lavas (Lofgren, 1980, 1983).

Dynamic crystallization experiments have also shown that the nature of the melt when cooling begins can have a dramatic effect on the resulting textures (Donaldson *et al.*, 1975; Bianco and Taylor, 1977; Lofgren, 1977, 1983; Lofgren *et al.*, 1978). A key factor is the existence of nuclei in the melt, on which crystals can then form and grow. Such nuclei may be either tiny crystalline fragments or specks of debris completely unlike the crystals that form around them. In general, if crystal nucleation occurs more easily for any reason (e.g., because nuclei are already present as a result of incomplete melting), the resulting product will be more completely crystallized. The final grain size will depend more on the number of nuclei per unit volume than on the growth rate of individual crystals. The effect of melt history (e.g., number of nuclei, cooling rate) on texture is most dramatic at cooling rates less than 10°C/hr.

The uncertain effects of nucleation on texture make it difficult to relate the large array of textures produced in experiments to the textures observed in natural rocks. To make direct comparisons, one must have some idea of the number of nuclei in a natural basaltic melt at the onset of cooling. There is virtually no observational information on this matter and none at all for lunar rocks. However, as we accumulate more information about the precooling nucleation condition of the melt, we will ultimately be able to interpret not only the crystallization history of a basalt lava but also the history of the magma prior to eruption.

The cooling rate is determined by the initial temperature, the thickness of the lava flow, and the rate of heat loss from it. This rate controls the time available for nucleation to occur and provides the driving force for crystal growth once nuclei are present. The influence of cooling rate on texture is greatest when the melt is free of nuclei at the start of cooling. In the absence of nuclei, nucleation in the cooling melt can be delayed to create a high degree of *supercooling* (cooling below the normal freezing point), and the shapes and compositions of the resulting crystals are more profoundly affected (Lofgren, 1980). Once nuclei are present, growth proceeds immediately upon cooling; the rate of growth is controlled by the rate of heat extraction from the lava. Large degrees of supercooling (tens to hundreds of degrees) are produced only at very rapid cooling rates.

Composition of the melt is an important variable to keep in mind when comparing textures among basalts and attempting to relate observed textures to cooling rates. Composition affects texture in several ways. For one thing, the viscosity of the melt varies with composition (and especially with SiO₂ content), and nucleation generally becomes more difficult as viscosity increases, as it does in high-SiO₂ rocks. In addition, the intervals of crystallization of different minerals in a cooling melt also depend on composition and affect the resulting textures in complex ways. For example, if a melt of a certain composition is characterized by a significant temperature interval in which the liquidus phase (the first mineral that forms as the lava cools) crystallizes alone before a second mineral appears, the crystals of the first mineral tend to grow larger, producing a greater tendency for a porphyritic texture during

cooling (Lofgren, 1974). However, this porphyritic texture will form only if the density of nuclei in the melt is low (i.e., the crystallization is restricted to a few spots). Porphyritic textures do not form during the cooling of basalts that are saturated (or nearly so) with two or more minerals at the liquidus (Walker *et al.*, 1978; Lofgren, 1980). In these cases, both minerals crystallize together. Porphyritic textures in such lavas, when observed, indicate that the large crystals are inherited from earlier crystallization at depth.

The effects of magmatic flow in bodies of molten lava usually appear as textures containing large or small aligned crystals (*trachytic* or *pilotaxitic* textures). Flow can also suspend larger crystals that might otherwise settle to the bottom of the melt body. This effect is restricted to relatively thin flows. Crystal settling only becomes a factor in the development of textures in mare basalt flows thicker than about 10 m. By mixing different portions of the melt together, flow can also promote *heterogeneous nucleation*, in which crystal growth does not begin spontaneously but starts around a foreign object.

For details of dynamic crystallization experiments and their interpretation, see the following papers: high-Ti basalts: Usselman *et al.* (1975), Usselman and Lofgren (1976), Grove and Beaty (1980); low-Ti pigeonite basalts: Lofgren *et al.* (1974), Grove and Bence (1977), Grove and Raudsepp (1978), Lofgren *et al.* (1975), Walker *et al.* (1977); low-Ti olivine basalts: Donaldson *et al.* (1975), Walker *et al.* (1976), Bianco and Taylor (1977); very-low-Ti basalts: Grove (1978), Grove and Bence (1979).

6.1.5. Cooling Rates of Mare Basalts

The rates at which mare basalt lavas have cooled after eruption have been estimated by two methods. One method is by the dynamic crystallization experiments discussed above (section 6.1.4), in which artificial samples with compositions like mare basalts are melted and then cooled from their melting temperatures at known rates; the resulting textures are compared with those observed in lunar basalts. These comparisons involve qualitative matching of textures as well as quantitative assessments based on such parameters as crystal size. The other method is theoretical, in which mineral compositions and kinetic parameters such as diffusion coefficients are combined to calculate the rate at which a basalt cooled (e.g., Onorato *et al.*, 1978). These two methods are complementary, and they give the same results to well within an order of magnitude.

These studies indicate that most mare basalts cooled at rates ranging from about 0.1°C to 30°C/hr. This range can be produced by cooling in lava

flows only a few meters thick. Brett (1975a), using petrographic and geologic data, estimated that most mare basalts formed in flows thinner than 8 m, and his conclusions are consistent with photogeologic observations of lunar lava flows. For example, the flows in the walls of Hadley Rille at the Apollo 15 landing site (Howard *et al.*, 1972) average less than 10 m thick (Schaber *et al.*, 1976), although some individual flows appear to be 10-20 m thick. The heights of flow fronts photographed in Mare Imbrium are generally less than 15 m, although they range from 1 to 96 m (Gifford and El-Baz, 1981). Thicker flows, or ponding of flows in depressions to form lava lakes, will result in much slower cooling rates and may produce basalt textures very different from any yet observed.

6.1.6. Vesicles and Nature of the Gas Phase

Many mare basalts contain numerous frozen gas bubbles, now empty, called *vesicles* (Fig. 6.14), which almost certainly formed when gases dissolved in the melt came out of solution in response to decreasing pressures associated with eruption. Rapid cooling of the lavas has preserved these bubbles. However, none of the gas remains, and its original nature is still a matter for speculation.

On Earth, vesicles are formed by outgassing of H₂O and CO₂, the dominant volcanic gases of terrestrial lavas. However, because there is no water in lunar rocks, CO₂ was likely to be more important than H₂O. Because of the chemically reducing conditions

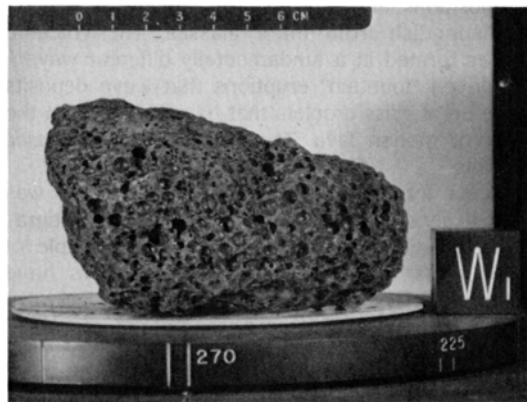


Fig. 6.14. Specimen of low-Ti, vesicular mare basalt 15016 collected from the Apollo 15 site at Hadley Rille. The specimen is about 10 cm long; the cube marked "W₁" is 2 cm on each edge. The numerous large cavities (*vesicles*) are frozen gas bubbles, now empty. In similar terrestrial rocks, the main gas phase in such bubbles would be H₂O, but on the Moon it was probably CO₂.

in lunar rocks, a significant amount of CO was probably present along with CO₂. Other gases may also have been present. For example, sulfur contents are high in lunar pyroclastic deposits (see section 6.1.7 below), suggesting that sulfur species may be another component of lunar volcanic gases.

These speculations are supported by analyses of mare basalts, which contain from 3 to 80 µg/g carbon (Gibson, 1977, and Table A8.6). When the basalts are analyzed by acid hydrolysis, both CO and CO₂ are released; the CO/CO₂ ratio ranges from 1/2 to 1/4. These gases appear to have been produced during the crystallization of the lavas, possibly by the reaction of carbon or carbides in the magma with FeO, to produce metallic iron (which is observed in mare basalts) and CO and CO₂. Sulfur contents are much higher in lunar basalts (up to 0.3 wt.%) than in terrestrial basalts (less than 0.15 wt.%), but the nature of the sulfur-bearing gases present during crystallization is still speculative (see sections 8.5, 8.7, and 8.8 for a more quantitative discussion of carbon and sulfur).

6.1.7. Lunar Pyroclastic Deposits

Glass droplets and fragments are a common component in the lunar soil; they have a broad range in both composition and texture. Lunar glasses have been produced by two very different processes, meteoroid impacts (impact melting) and volcanic eruptions. Glasses formed by impact melting are discussed in section 6.4.3; such glasses can generally be recognized by their heterogeneous textures and compositions, although they are sometimes difficult to distinguish from mare glasses. The volcanic glasses formed in a fundamentally different way, in gas-driven "fountain" eruptions that leave deposits made up of glass droplets that have chilled from the spray of molten lava. These are called *pyroclastic* deposits.

Except for Apollo 17 orange glass, which was most likely collected in place, no field or stratigraphic evidence exists to show that any sample of lunar glass is volcanic, but investigators have developed other criteria for distinguishing between these two types of glasses. These criteria, discussed in detail by Delano (1986), are the following:

1. *Absence or presence of schlieren and exotic inclusions:* Volcanic liquids are unlikely to become contaminated with large quantities of chemically and mineralogically exotic material. The result is a fairly uniform glass. In contrast, glasses of impact origin are commonly heterogeneous; they contain streaks of fine-grained debris, called *schlieren*, together with inclusions with compositions different from that of the glass.

2. *Homogeneity of composition:* Individual pieces of volcanic glass, which are samples of hot, magmatic reservoirs, should be chemically uniform, at least for the nonvolatile elements. Impact glasses have cooled rapidly, and have not remained as liquids long enough for diffusion to homogenize them. Consequently, individual pieces of impact glass tend to be chemically heterogeneous.

3. *Clustering of chemical compositions:* Volcanic glasses are quenched samples of a magma reservoir that was probably chemically uniform over substantial distances. As a result, the droplets produced by the eruption of lava from this reservoir will tend to be chemically uniform as well. Tight compositional clustering is therefore a frequently observed aspect among the volcanic glasses. In magma bodies and lava flows, crystal/liquid fractionation can also produce tight chemical trends within the resulting suite of volcanic glasses. In contrast, impact glasses are produced by the instantaneous fusion of multi-component, chemically heterogeneous targets; as a result, their compositions tend to define chemically diffuse clusters.

4. *Volatile element enrichments:* The best-known examples of lunar volcanic glasses, the Apollo 15 green glass and Apollo 17 orange glass, are highly enriched in volatile elements compared to most lunar samples (Butler and Meyer, 1976). This characteristic was apparently related to the presence of a transient gas phase that accompanied the eruption and not to implantation from the solar wind while these glasses resided on the lunar surface (see section 8.8 for details on the solar-wind component of lunar rocks).

5. *Ferromagnetic resonance intensity:* As described in sections 5.4.3 and 7.3.1, the ferromagnetic intensity is a measurement of the amount of small particles of single-domain iron in a glass sample. These particles are a common component of impact glasses and they apparently form by the reduction of small amounts of divalent iron (Fe²⁺) during impact melting. Clearly volcanic glasses, particularly the Apollo 15 green glass and Apollo 17 orange glass, have been found to possess lower ferromagnetic resonance intensities and thus less single-domain iron than impact glasses (Stone et al., 1982).

6. *High Mg/Al ratios:* Areas of pyroclastic deposits on the Moon whose chemistry has been measured from orbital instruments (see section 6.2) are known to have higher Mg/Al ratios than do mare regoliths (e.g., Schonfeld and Bielefeld, 1978). Samples of volcanic glasses have high Mg/Al ratios between 1.7 and 3.3; impact glasses have ratios similar to sampled regoliths, i.e., <1.5.

Chemical compositions and varieties of volcanic glasses. Twenty-five distinct varieties of

volcanic glasses have been identified from the Apollo landing sites (Delano, 1986). Their major-element compositions are given in Table A6.3. In some cases, different glasses can be related to each other as a series produced by fractional crystallization and differentiation of a single parent magma. In these cases, the most magnesian members of the suite define the composition of the parent magma. Delano (1986) discusses aspects of each variety in detail.

Volcanic glasses span a large range in TiO_2 contents, from 0.26 to 16.4 wt.%. However, most identified volcanic glasses are either very-low-Ti (<1.5 wt.% TiO_2) or high-Ti (>8 wt.% TiO_2), and only 3 of the 25 types fall in the range of most low-Ti basalts (2-5 wt.% TiO_2). The chief chemical distinction between volcanic glasses and mare basalts is the greater concentration of compatible elements (elements such as Mg and Ni that fit into olivine, pyroxene, and other common minerals of the lavas) in the glasses (Figs. 6.15 and 6.16). This relation suggests that the magmas that erupted to produce volcanic glasses underwent less crystallization (and removal of crystals) during their ascent to the lunar surface than did the magmas that gave rise to the mare basalt lavas.

Abundances of trace elements in most types of volcanic glasses have not been measured. Exceptions are the Apollo 15 green and yellow/brown glasses and Apollo 17 orange glass, for which there are extensive datasets (Tables A6.5, A6.6, and A6.7).

Apollo 17 orange glass has the same bow-shaped REE pattern that is characteristic of high-Ti mare basalts (Fig. 6.3), but it also has distinct enrichments in volatile elements, such as F, Cl, Zn, and Pb (see below). There are several chemically distinct groups of Apollo 15 green glass, all intermingled in a fragile clod composed of numerous glass spheres (sample 15426). The information in Table A6.6, therefore, is a grand average of all the Apollo 15 green glass groups, because the analyses were done on this green glass clod. The REE pattern (Figs. 6.3 and 6.17) is characterized by a negative slope from La to Sm and a positive slope from Gd to Lu, with a negative Eu anomaly. Like the Apollo 17 orange glass, Apollo 15 green glass is enriched in volatile elements. Trace element data are also listed for Apollo 15 yellow/brown volcanic glasses (Table A6.7). This glass type is much rarer than the green glass and it has not been studied in detail.

Textures and cooling rates. Lunar pyroclastic deposits are not composed entirely of glass droplets. Many of the spheres, which were erupted as droplets of molten lava, are now substantially crystalline. Subunits within the orange "glass" deposit from the rim of Shorty Crater at the Apollo 17 site, for example, are composed largely of black droplets because of the presence of very-fine-grained crystals of ilmenite, olivine, spinel, and metallic iron in the spheres. Many Apollo 15 green "glass" spheres also contain small crystals of olivine.

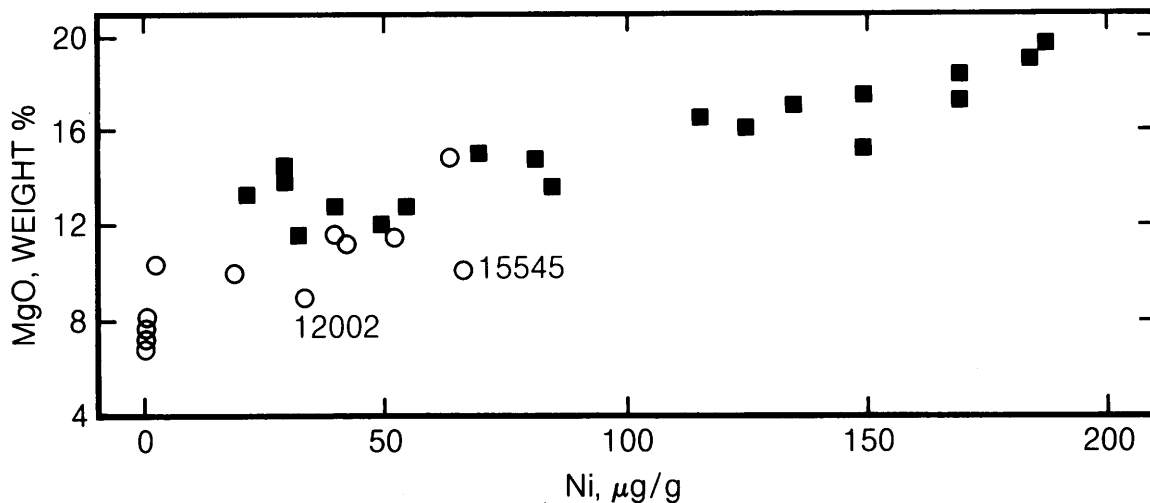


Fig. 6.15. Plot of Ni and MgO abundances in mare basalts (open circles) and in pristine lunar glasses (solid squares). The two elements are positively correlated with each other, and glasses tend to be richer in both Ni and Mg. Samples 12002 and 15545 (olivine basalts) are relatively Ni-rich for their MgO contents, relative to other basalts.

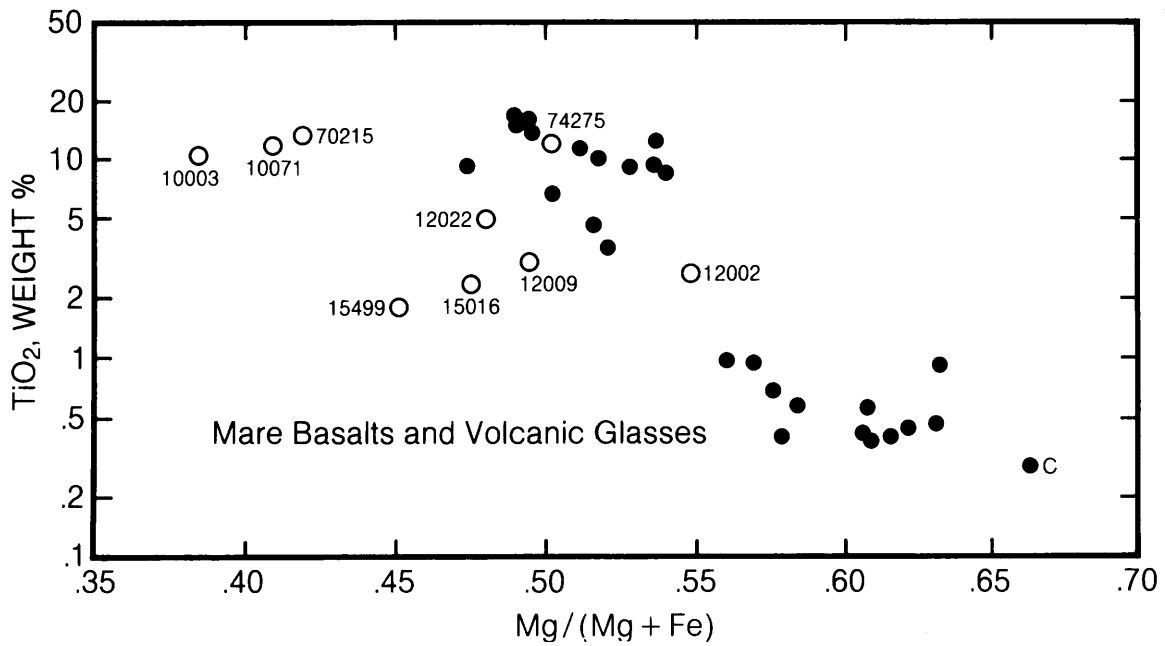


Fig. 6.16. Plot of TiO₂ against Mg/(Mg + Fe) mole ratios in mare basalts (numbered open symbols) and in pristine lunar glasses (solid circles). Each symbol represents a distinct magma type. For any given abundance of Ti, the pristine glasses commonly have higher Mg/(Mg + Fe) ratios than do the basalts. If the pristine glasses correspond to the initial compositions of comparable basalts, then the basalt lavas must have lost Mg (probably by the removal of olivine). The pristine glass labeled "C" in the lower right corner of this figure is the Apollo 15 green glass with the highest Mg/(Fe + Mg) ratio (Delano, 1979).

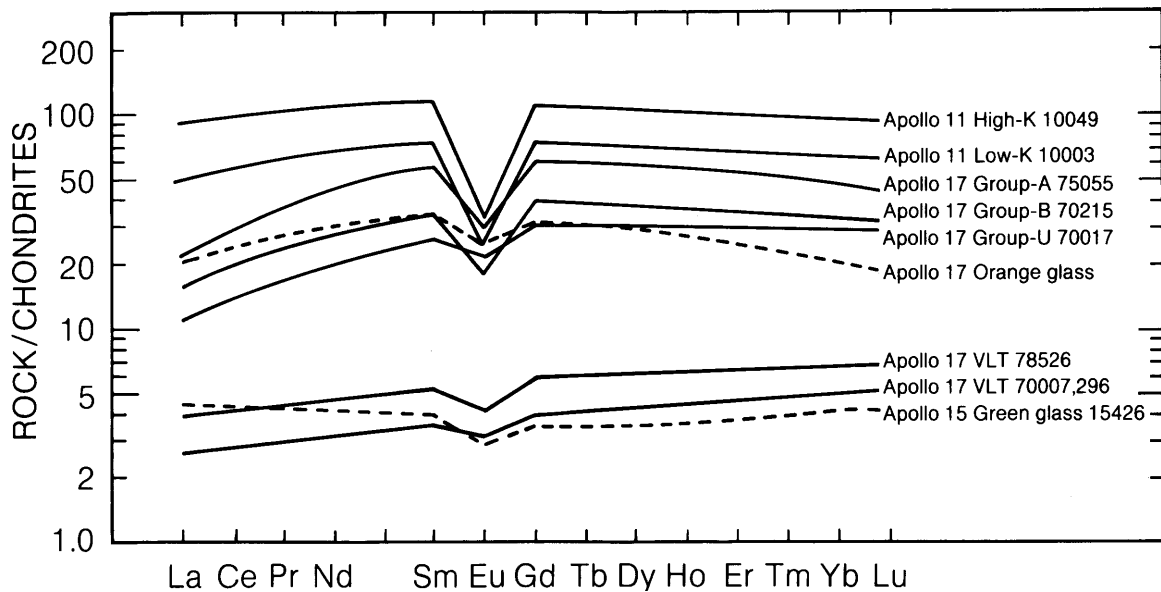


Fig. 6.17. REE contents, normalized to chondritic meteorites, in a range of mare basalts and related glasses. The Apollo 17 orange glass appears to be related to the high-Ti basalts plotted in the upper part of the diagram; it has the same REE contents, "bow-shaped" pattern, and negative Eu anomaly. Such similarities, however, do not prove a relationship. This figure is modified from BSVP (1981).

Experiments have shown that melt droplets with the composition of orange glass must cool faster than 10-60°C/sec to prevent crystallization (Uhlmann *et al.*, 1974). Similar droplets of noncrystalline green glass must have cooled even faster. Those spheres that contain crystallites obviously cooled more slowly.

Calculations of radiative cooling using a modified version of the Stefan-Boltzmann formula (Arndt *et al.*, 1979, 1984) indicate that the volcanic spheres containing crystallites must have cooled 10-1000 times more slowly than would isolated spheres erupted into the lunar vacuum. This result suggests that the spheres actually cooled in a hot, transient atmosphere of volcanic gas that accompanied the eruptions. The shapes of glass spheres (McKay *et al.*, 1973; Heiken and McKay, 1977; Clanton *et al.*, 1978) also indicate that the droplets were colliding repeatedly in a turbulent stream of gas. The spheres may have remained suspended in this gas for as long as 10 minutes (Arndt *et al.*, 1984), which is a long time compared to the ballistic flight-time of about 1 minute in the absence of a gas phase (McGetchin and Head, 1973).

Volatile elements associated with pyroclastic deposits. The most striking feature of the Apollo 15 and 17 pyroclastic deposits is their enrichment in volatile elements such as F, Cl, Zn, and Pb, when compared with other lunar materials (Table A6.8). These elements undoubtedly existed in the gas phase associated with the pyroclastic eruptions. The volatile elements tend to be concentrated on the surfaces of individual glass spheres. Other pyroclastic deposits on the Moon may show the same features, but our sampling of them is too limited to be sure.

The surface coatings of volatile elements on droplets of orange glass and green glass have been studied extensively; references are listed in Table A6.8. Key observations are listed below.

1. At least some of the elements listed in Table A6.8 were transported as fluorides, chlorides, or sulfides (Wasson *et al.*, 1976).

2. The elements Au, Sb, and Ge occur on the surfaces of both Apollo 15 green glass and Apollo 17 orange glass particles in the same ratios that are found in CI-type chondritic meteorites (Morgan and Wandless, 1984; Delano, 1980).

3. The volatile deposits on Apollo 17 orange glass particles possess an isotopic uranium/lead ratio, $^{238}\text{U}/^{204}\text{Pb}$, of <29 (Tera and Wasserburg, 1976), which is much lower than that found in both mare basalts and nonmare rocks. The Pb in the interior of green glass spheres is isotopically distinct from that on the surfaces, however (Tatsumoto *et al.*, 1987).

4. The U-Pb model age of the surface-correlated component on the Apollo 15 green glass and Apollo 17 orange glass is about 4.6 b.y. (Tera and Wasserburg, 1976; Meyer *et al.*, 1975). This result contrasts with the model ages determined for most nonmare lunar rocks, 4.3 b.y.

5. The formation ages measured for Apollo 15 pyroclastic fragments (-3.3 b.y.) and Apollo 17 pyroclastic fragments (3.75 b.y.) are nearly identical with the times of local mare volcanism at both sites. However, no crystalline equivalents (i.e., basalts) with the chemical compositions of these glasses have been identified.

6. Trapped noble gases occur in the Apollo 15 green glasses. Trapped Ne has an isotopic composition similar to that of solar Ne (Barraclough and Marti, 1985). However, this Ne was not implanted by the solar wind, because it is uniformly distributed through the green glass particles and not concentrated at grain surfaces.

6.1.8. Experimental Petrology and Phase Relations

The melting and crystallization relationships in synthetic melts of mare basalt composition have been extensively studied in the laboratory. Some dynamic crystallization experiments and their use in interpreting the textures in mare lavas are described in section 6.1.4. This section summarizes static (or near-equilibrium) experiments, which are used to interpret the temperatures at which different minerals crystallize rather than the textures that they form. Some experiments are carried out at low pressure (~1 bar), and the results bear on our understanding of basalt crystallization in lava flows erupted at the lunar surface. Other experiments are carried out at high pressures, ~5-25 kbar, appropriate to depths of 100 to 500 km (on the Moon, 1 kbar = a depth of 18 km). These are the depths at which formation and early crystallization of lunar magmas occurred. Reviews of experimental studies of mare basalts are given by Kesson and Lindsley (1976) and by BVSP (1981, their Tables 3.4.1 and 3.4.2).

Phase relations at low pressure. Low-pressure experiments attempt to duplicate the conditions in a continually cooling basaltic lava erupted at the lunar surface. Pressure is kept constant, the temperature is allowed to drop until crystallization occurs, and the temperatures at which different minerals appear are noted. The low-pressure equilibrium crystallization behavior of representative mare basalts is illustrated by the data in Tables 6.2, 6.3, and 6.4. The temperature at which each molten basalt begins to crystallize, called the *liquidus temperature*, ranges from 1150° C to almost 1400° C.

TABLE 6.2. Low-pressure (0-1 bar) equilibrium experimental results on high-Ti mare basalts.

Sample	Rock Type	Reference	Temp(°C)	Phases Present*
10072	high-Ti	<i>Walker et al. (1975)</i>	1195	liq
			1159	liq + Ol + armal + ilm
			1149	liq + Ol + ilm
			1145	liq + Ol + loCapx + ilm
			1140	liq + loCapx + ilm
			1130	liq + loCapx + hiCapx + ilm
			1122	liq + loCapx + hiCapx + ilm + plag
10020	low-K	<i>O'Hara et al. (1974)</i>	1170	liq
			1160	liq + Ol + sp
			1153	liq + Ol + sp
			1151	liq + Ol + sp + ilm
			1145	liq + Ol + sp + ilm + px + plag
			1133	liq + sp + ilm + pig + aug + plag
71569	very-high-Ti	<i>Walker et al. (1975)</i>	1192	liq
			1156	liq + Ol + armal + sp
			1146	liq + Ol + armal + sp
			1142	liq + Ol + hiCapx + armal + ilm
			1138	liq + Ol + hiCapx + ilm + plag
			1137	liq + hiCapx + loCapx + ilm + plag
			1127	liq + hiCapx + loCapx + ilm + plag
74220	orange glass	<i>Walker et al. (1975)</i>	1398	liq
			1302	liq + Ol
			1251	liq + Ol
			1195	liq + Ol + sp
			1159	liq + Ol + ilm + sp
			1149	liq + Ol + ilm + sp
			1145	liq + Ol + ilm
			1140	liq + Ol + ilm + sp
			1130	liq + Ol + pig + ilm

* "Phase" designates either mineral, liquid, or glass. In this table, liq = liquid; Ol = olivine; armal = armalcolite; ilm = ilmenite; sp = spinel; loCapx = low-Ca pyroxene; hiCapx = high-Ca pyroxene; pig = pigeonite; aug = augite; plag = plagioclase.

The basalts richest in FeO tend to have the lowest liquidus temperatures. The temperatures at which lavas of mare basalt composition become totally solid upon cooling (the *solidus temperatures*) have not been determined directly. Nevertheless, the lowest temperature listed for each basalt is probably close to the solidus temperature. The data imply that if solid mare basalts were heated they would begin to melt around 1050° C. This melting temperature is about 100° C higher than those of terrestrial basalts, chiefly because of the lack of H₂O in lunar basalts.

Phase relations at high pressures. Laboratory experiments at high pressures (5-25 kbar) are intended to examine a different problem, the formation of basaltic melts by partial melting of the lunar mantle at depths of perhaps 100-500 km. Such

partial melting rarely consumes more than a few percent of the original mantle rock in producing the basaltic melt, so that, until it moves, the newly-formed magma remains in chemical equilibrium with the minerals that make up the unmelted *residue* of the mantle. By experimentally applying high pressures and temperatures to solid basalts and their molten equivalents, it is possible to estimate (1) the pressure (and hence the depth) at which the magma formed and (2) the nature of the minerals in the original mantle with which the melt was in equilibrium.

In these experiments it is assumed that during melting at least two of the original mantle minerals remain in equilibrium with the newly-formed basaltic melt. Therefore, the depth of origin can be

TABLE 6.3. Low-pressure (0-1 bar) equilibrium experimental results on low-Ti mare basalts.

Sample	Rock Type	Reference	Temp(°C)	Phases Present*
12002	olivine	<i>Walker et al. (1976)</i>	1350	liq
			1328	liq + Ol
			1266	liq + Ol
			1232	liq + Ol + sp
			1201	liq + Ol + sp
			1176	liq + Ol + sp + px
			1164	liq + Ol + sp + px
			1150	liq + Ol + sp + px
15065	pigeonite	<i>Walker et al. (1977)</i>	1273	liq + Ol
			1249	liq + Ol
			1225	liq + Ol + sp + px
			1205	liq + Ol + sp + px
			1172	liq + Ol + sp + px
			1148	liq + sp + px + plag
			1129	liq + sp + px + plag
			1125	liq + Ol + sp + px + plag
14072	aluminous	<i>Walker et al. (1972)</i>	1285	liq
			1262	liq + Ol
			1212	liq + Ol
			1190	liq + Ol + sp
			1175	liq + Ol + sp + pig + plag
			1170	liq + Ol + sp + pig + plag
			1140	liq + Ol + sp + pig + aug

* "Phase" designates either mineral, liquid, or glass. In this table, liq = liquid; Ol = olivine; sp = spinel; px = pyroxene; pig = pigeonite; aug = augite; plag = plagioclase.

TABLE 6.4. Low-pressure (0-1 bar) equilibrium experimental results on very-low-Ti mare basalts.

	Rock Type	Reference	Temp(°C)	Phases Present*
Luna 24	average	<i>Grove and Vaniman (1978)</i>	1192	liq
			1189	liq
			1182	liq + plag
			1155	liq + plag + Ol + px
			1143	liq + plag + Ol + px
			1071	liq + plag + Ol + px
Apollo 15	green glass	<i>Grove and Vaniman (1978)</i>	1408	liq
			1392	liq + Ol
			1359	liq + Ol
			1221	liq + Ol
			1192	liq + Ol + px
			1163	liq + Ol + px
			1155	liq + Ol + px + plag
1143	liq + Ol + px + plag			
Apollo 14	VLT glass	<i>Chen et al. (1982)</i>	1390	liq
			1365	liq + Ol
			1210	liq + Ol
			1150	liq + Ol + px + plag

* "Phase" designates either mineral, liquid, or glass. In this table, liq = liquid; Ol = olivine; px = pyroxene; plag = plagioclase.

TABLE 6.5. High-pressure equilibrium experimental results on basaltic compositions thought to represent primary magmatic compositions.

	Basalt Type	Pressure*	Depth, km [†]	Phases [‡]	Olivine Fo [§]	Ref. [¶]
Apollo 15	red (high-Ti) glass	24	480	Ol, opx	75	a
Apollo 17	orange glass	20	400	Ol, opx	81	b
Apollo 14	VLT glass	19	380	Ol, pig	79	c
Apollo 17	VLT glass	18	360	Ol, pig	79	c
Apollo 15	green glass	15	300	Ol, opx	84	d, e
12002	low-Ti olivine	12.5	250	Ol, pig	78	f
74275	high-Ti	11	220	Ol, pig, aug	75	b
12009	olivine	7.5	150	Ol, pig	75	g
70215	high-Ti	6.5	130	Ol, aug	76	h

* Pressure (kbar) at which melt becomes saturated with two or more phases; errors are typically ± 2 kbar.

[†] Depths calculated from multiple-saturation pressures assuming a pressure gradient of 1 kbar/20 km; errors are typically ± 40 km.

[‡] Phases present at multiply-saturated liquidus: Ol = olivine; pig = pigeonite; opx = orthopyroxene; aug = augite.

[§] Fo = liquidus olivine forsterite [Mg/(Mg + Fe)] content at the multiple-saturation pressure.

[¶] (a) Delano (1980); (b) Green et al. (1975); (c) Chen et al. (1982); (d) Stolper (1974); (e) Green and Ringwood (1973); (f) Walker et al. (1976); (g) Green et al. (1971); (h) Longhi et al. (1974).

estimated by determining the pressure at which a given basalt melt first becomes *multiply saturated* (i.e., in equilibrium with two or more minerals). If the extent of original partial melting is so great that only one mantle mineral remains in the residue, then no unique pressure or depth can be determined.

In principle, these experiments involve keeping the temperature constant and increasing the pressure on a sample of basaltic melt until minerals form. For example, in some basalts olivine is the liquidus phase (i.e., as the magma cools, olivine crystallizes first and then coexists stably with the remaining magma), and olivine remains the only liquidus phase at pressures of one atmosphere up to several kilobars. At a higher pressure, olivine may be joined by pyroxene on the liquidus, i.e., the two minerals then coexist stably with the magma. This pressure is taken to be the pressure at which the basaltic magma was derived by partial melting. The compositions of the pyroxene and olivines formed are taken to represent those of the pyroxene and olivine present in the lunar mantle when the basaltic melt was first formed.

Such estimates of the depth of origin are also dependent on the extent to which the basaltic melt changed in composition as it migrated toward the surface. For the depth estimate to be accurate, the melt composition ought not to have changed at all. Such unchanged magmas are called *primary magmas*. In practice, formation and separation of crystals (*fractional crystallization*) will usually occur as the magma moves from the source region to the surface; this effect will cause the estimated depth of origin to be less than the real depth. Problems in

interpreting experimental data and in recognizing primary magma compositions are discussed at length by BVSP (1981) and succinctly by Delano (1980).

The pressures and depths estimated for the origin of several proposed primary magmas are listed in Table 6.5, along with the minerals with which they are saturated and the composition of the olivine present. The magma types are listed in order of decreasing inferred depth of origin. The data suggest vaguely that the basalts formed at greater depths have originated from rocks containing more Mg in the residual olivine. This trend could imply that variations in the Mg/Fe ratio with depth existed in the Moon during the time these mare basalts formed. However, the trend is weak, and more data are needed to test its validity.

6.1.9. Ages of Mare Basalts

Formation ages of numerous samples of mare basalts and related pyroclastic deposits have been determined by radioactive-isotope age-dating methods. (For summaries, see BVSP, 1981, their Table 7.3.1; Ryder and Spudis, 1980; and Taylor, 1982, his Table 6.6). Ages have also been estimated photo-geologically using the abundances of craters and the state of preservation of individual craters on mare surfaces. In these studies, images of the Apollo and Luna landing sites, where the ages are known, are used as calibration points. (For a summary, see Schultz and Spudis, 1983). Photogeologic ages are not as precise as radiometric ones, but they provide coverage of large areas of the Moon.

The high-Ti basalts from the Apollo 11 and Apollo 17 sites are relatively old, generally more than 3.5 b.y. The low-K, high-Ti basalts from the Apollo 11 site range in age from 3.55 to 3.86 b.y.; Apollo 11 high-K, high-Ti basalts appear generally younger, about 3.55 b.y. The Apollo 17 high-Ti basalts, though of similar age (3.59-3.79 b.y.), seem to have erupted over a shorter span of time than did those at the Apollo 11 site. However, the Apollo 17 orange glass is slightly younger (3.48 b.y.) than the crystalline Apollo 17 basalts.

It is not certain, however, that all high-Ti basalts are old. Photogeologic data indicate that some high-Ti basalts may have erupted onto the lunar surface as recently as about 1 b.y. ago; an area east of the crater Lichtenberg is one example of such relatively recent volcanism (see *Schultz and Spudis*, 1983).

Low-Ti mare basalt samples are generally younger; they range in age from 3.08 to 3.37 b.y. Those from the Apollo 12 site are slightly younger (3.08 to 3.29 b.y.) than those from the Apollo 15 site (3.21 to 3.37 b.y.). The ages of the Apollo 15 olivine and pigeonite basalts are not distinguishable from each other. The Apollo 15 green glass formed at about the same time as the Apollo 15 basalts (3.3 b.y. ago).

The aluminous, low-Ti mare basalts are the oldest mare basalts that have been dated directly. Clasts of these basalts in Apollo 14 breccias range in age from 3.9 to 4.2 b.y. (*Taylor et al.*, 1983). Photogeologic observations of the distribution of dark-halo craters, which have probably excavated mare basalt layers from beneath the ejecta of lunar basins, support the inference of widespread mare-type volcanism prior to 3.9 b.y. (*Schultz and Spudis*, 1983). However, fragments of aluminous mare basalts from other sites are not so ancient; an Apollo 12 fragment is 3.1 b.y. old, and one from the Luna 16 site is 3.4 b.y. old.

The ages of very-low-Ti basalts are uncertain because of the small number of samples, but they seem to span a considerable interval. One fragment of very-low-Ti mare basalt from the Luna 24 site has been dated; its age is 3.3 b.y. Very-low-Ti basalts found in Apollo 17 soils have not yet been dated directly, but those found as fragments in breccia 72235 must be older than the melt-rich matrix of the breccia, which crystallized 4.01 b.y. ago.

Measurements of isotopic compositions of basalts also give information about an earlier time when the source regions for the mare basalts were formed in the lunar mantle. These data suggest that the mare basalt source regions had formed by 4.4 b.y. ago. This age probably represents the end of the initial lunar differentiation during which the crust, mantle, and core formed (section 2.4).

6.2. EXTENDED MAPPING OF MARE LAVAS AND PYROCLASTIC DEPOSITS BY REMOTE SPECTRAL OBSERVATIONS

6.2.1. Techniques

A major limitation to understanding the nature and history of lunar mare volcanism is that the detailed data on compositions, formation ages, and properties of mare lavas are limited to the samples returned from only nine spots on the Moon. However, it has proved possible to extend this information to other areas of the Moon by making remote observations of the sites from which known samples have been returned and then making comparable observations of unsampled regions.

Imagery and photogeologic observations have already helped establish the nature and approximate ages of large areas of exposed mare lavas. An equally important and more specialized role is being played by remote spectral observations in the visible and infrared wavelengths, which can provide detailed information on the mineralogy and chemical composition of lunar basalts. By combining orbital information from the Apollo missions, Earth-based telescopic observations, and laboratory studies of returned samples, it has become possible to draw important conclusions about the chemistry, mineral composition, and origin of the lavas and glassy deposits that cover large areas of the Moon.

Earth-based spectral observations of the Moon are limited to the visible and near-infrared part of the electromagnetic spectrum. A lower wavelength limit of 0.3 μm is fixed by the absorption of shorter wavelengths by ozone in the Earth's atmosphere. The upper limit is set by thermal infrared radiation, which becomes significant beyond about 2.5 μm . Most reflectance data for mare regions were obtained in the late 1970s using visible and near-infrared spectrometers (0.3 to 1.1 μm). More recent measurements, made with more advanced sensors, have extended the spectral observations to 2.5 μm (see *Pieters*, 1978; *BVSP* 1981). These spectral observations have been supplemented by other remote measurements such as the γ -ray spectrometry done by the Apollo 15 and 16 missions, and by the critically important ground truth provided by Apollo and Luna samples.

The major silicate minerals in lunar basalts (pyroxene, plagioclase, and olivine) have characteristic absorption bands in the near-infrared spectral region. These individual absorption features do not combine in a simple linear fashion to produce a reflectance spectrum of basalt, because each mineral has a different overall opacity. Although the strength of an absorption band is dependent on the abundance of the absorbing species, detailed analytical

models of reflectance from soil particles are needed to determine the abundance of each component from raw spectral data (e.g., *Mustard and Pieters, 1987*).

The spectral character of lunar basalts tends to be dominated by the two strong absorption bands of Ca-rich clinopyroxene near 0.97–1.0 μm . This condition occurs in both laboratory samples of basalt powders (Fig. 6.18) and in telescopic spectra of young mare craters that have exposed fresh basalt bedrock (Fig. 6.19). Plagioclase influences the basalt spectrum (e.g., for rock 12063; Fig. 6.18) by producing a superimposed and weaker absorption band near 1.3 μm . These diagnostic features of mare basalt spectra are more subdued in spectra of older lunar soils that have few fresh fragments of basaltic bedrock.

Glasses of basaltic composition have spectra that are fundamentally different from those of crystalline basalts, chiefly because the specific absorption peaks produced by crystals of silicate minerals are absent. Reflectance spectra of three pyroclastic glass samples are shown in Fig. 6.20. For these glasses, the combined abundance of FeO and TiO₂ strongly affects the amount of absorption in the ultraviolet and blue portions of the spectrum (*Bell et al., 1976*). Although both contain abundant FeO, the TiO₂-rich orange glass (74220) is much more absorbing than the TiO₂-poor green glass (15401). The weak bands near 1.0 and 1.8 μm are caused by Fe⁺² in the slightly ordered atomic structure of glass. The black glass beads of sample 74001 are crystallized

equivalents of the orange glass 74220. They consist of abundant thin plates of ilmenite in an orange glass groundmass and produce a reflectance spectrum dominated by the spectral character of ilmenite (*Adams et al., 1974*).

6.2.2. Regional Distribution of Mare Basalts and Pyroclastic Glasses

Distribution of mare basalt types. Few dark mare basalts are seen on the lunar farside. An unknown, but possibly larger volume was erupted prior to the end of the intense meteorite bombardment of the Moon about 3.9 b.y. ago, and much of this is probably buried by ejecta from the large impacts that formed the mare basins. However, most of the visible maria occur on the nearside of the Moon. This concentration of maria on the nearside makes it possible to carry out Earth-based telescopic observations of the maria and to obtain important compositional information about mare basalts by measuring and analyzing their reflectance spectra. Actually, these observations measure the spectra of lunar soils that have developed on the mare lava flows.

The results of this spectral mapping are presented in detail in section 10.4. The maria exhibit great variety on a regional scale across the Moon. Stratigraphy derived from photogeological studies implies that a considerable heterogeneity also exists in the vertical dimension (see section 10.4). Of the basalts mapped on the lunar nearside, only about

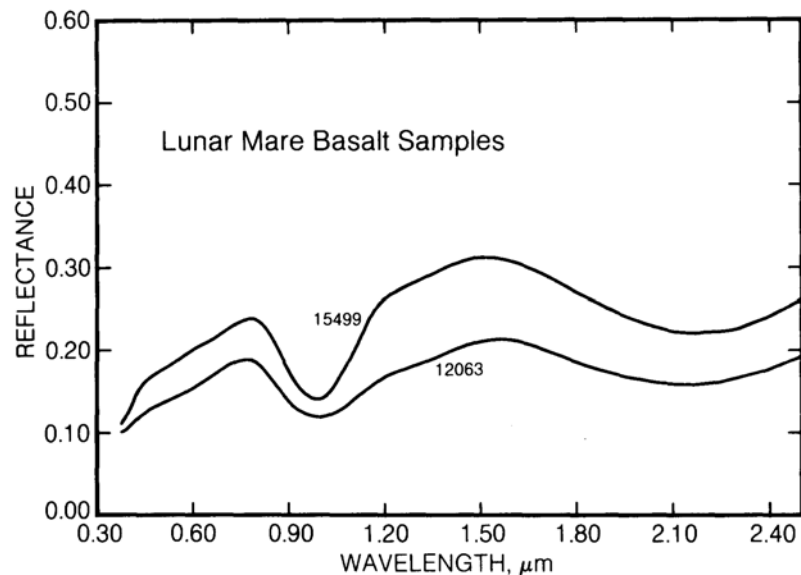


Fig. 6.18. Reflectance spectra in the visible and near-infrared, plotted as a function of wave-length for lunar mare basalt samples 12063 and 15499. The strong absorption band at 0.9–1.0 μm is diagnostic for pyroxenes in general and indicates the presence of Ca-pyroxene in this sample.

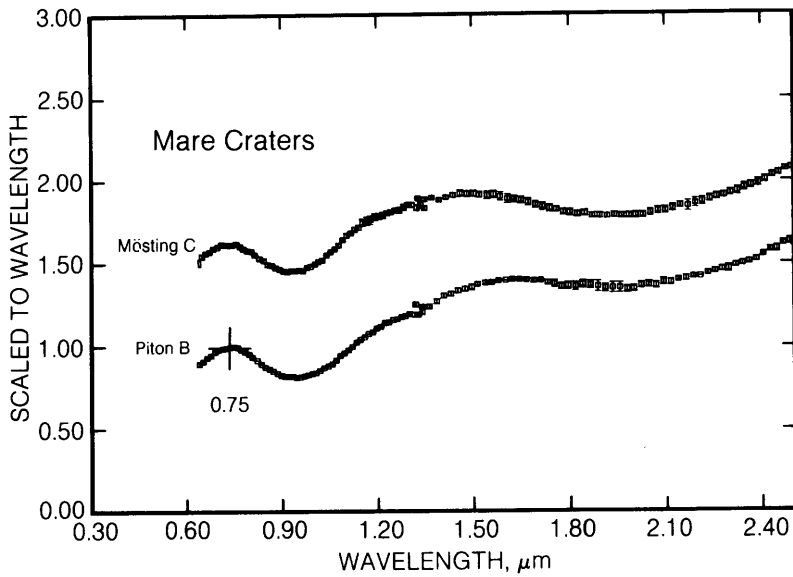


Fig. 6.19. Scaled visible and near-infrared reflectance spectra of lunar mare craters (Piton B, Mösting C) obtained with Earth-based telescopes. These spectra have been scaled to unity at 0.75 μm and offset vertically. The strong absorption at 0.9-1.0 μm indicates that Ca-pyroxene is abundant in the mare material excavated by these two young craters.

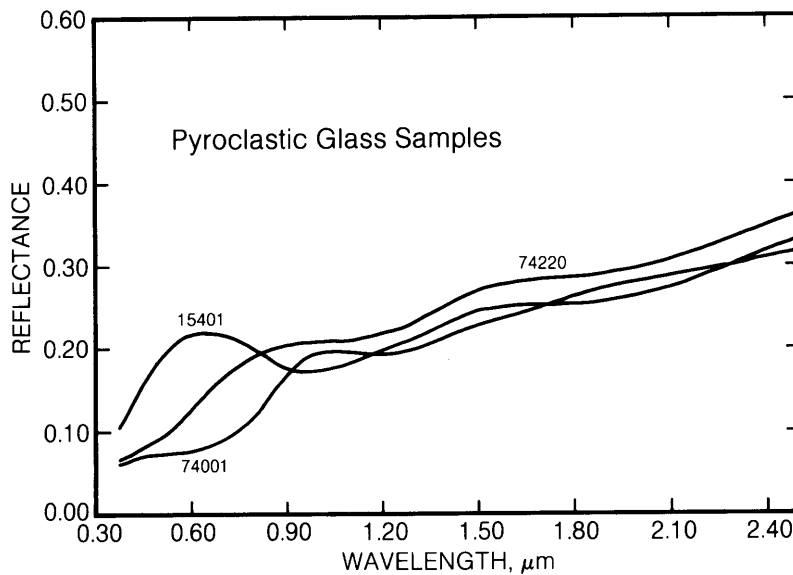


Fig. 6.20. Visible and near-infrared reflectance spectra of lunar volcanic glass samples 74220 (Apollo 17 orange glass), 74001 (Apollo 17 "black glass," the crystallized equivalent of orange glass), and 15401 (Apollo 15 green glass). The Ti-rich orange glass and black glass have greater absorption in the ultraviolet and blue regions of the spectrum (left side of graph, 0.3-0.4 μm).

one-third of them have compositions similar to the basalts sampled by Apollo and Luna missions. Our knowledge of mare volcanism is clearly incomplete.

Distribution of pyroclastic deposits. Remote-sensing data indicate that deposits of volcanic glasses (like those described in section 6.1.7) are fairly abundant on the Moon. Figure 6.21 shows the distribution of one type of possible pyroclastic unit, the dark-mantle deposits (see section 4.2), including the one sampled in the form of orange and black

glass by the Apollo 17 mission. Such pyroclastic deposits often occur on the edges of the maria and overlap onto the adjacent highland regions (see Fig. 10.10). As their name implies, these deposits have low albedos (they are poor reflectors of visible light) and so appear dark.

Other types of pyroclastic deposits may exist, however, and *Gaddis et al.* (1985) have shown that not all pyroclastic deposits are necessarily dark. They observed that thick dark mantle deposits exhibit low

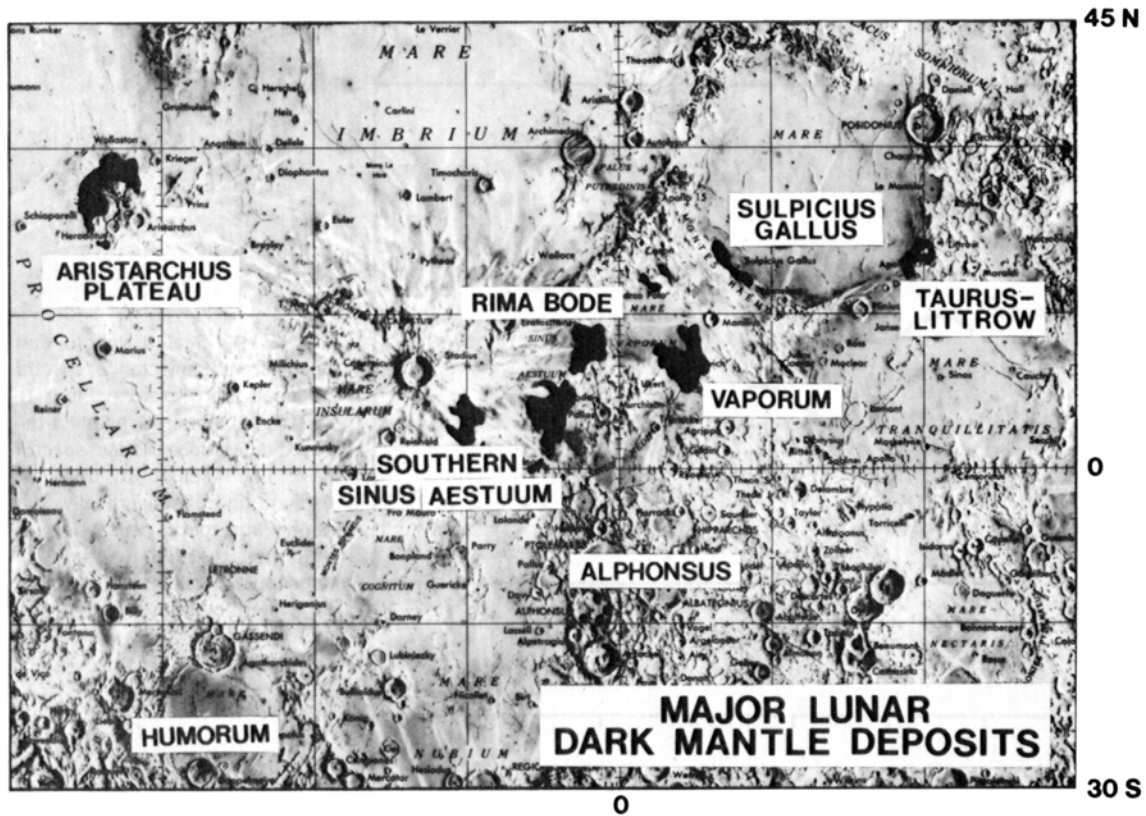


Fig. 6.21. Lunar map showing the distribution of major dark-mantle deposits (black) on the nearside northern hemisphere of the Moon (after Head, 1976a). These deposits are thought to be pyroclastic units ejected as a mixture of gas and lava droplets from volcanic vents.

intensities on depolarized 3.8-cm radar maps, indicating the absence of surface scatterers (such as boulders) in the 1 to 50 cm range. Gaddis *et al.* (1985) suggest that numerous other areas, with the same low radar scattering intensities, are likely to contain pyroclastic deposits. Some of these other pyroclastic units may be as large as the observed dark mantle deposits. If the dark mantle deposits and similar units are indeed pyroclastic, then they should be composed of relatively homogeneous glasses with concentrations of volatile elements on their surfaces, similar to Apollo 15 green glass and the Apollo 17 orange glass.

6.3 HIGHLAND PRISTINE ROCKS: IGNEOUS ROCKS AND MONOMICT BRECCIAS

The lunar crust onto which the mare basalts flowed, between about 4.0 and 3.1 b.y. ago, had itself formed within a few hundred million years of the origin of the Moon and the solar system (4.6 b.y. ago). As this crust formed, it suffered frequent large impacts as the violent process of planetary accretion

drew to a close. This heavy bombardment continued for ~500 to 600 m.y. after the crust formed. Many researchers contend that the end of this period was marked by a *terminal cataclysm* that accounts for most of the impact brecciation in the lunar crust.

These frequent and severe impacts transformed the upper few kilometers of the solid crust into a layer of fragmental and chaotically mixed impact debris, often referred to as *megaregolith*. In this manner, rocks of the upper crust were shattered, broken, and mixed down to submillimeter scales. The crustal rocks were also heated at the same time because a significant portion of the impact energy was converted into heat. As a result, virtually all of the highland rock samples collected by the Apollo missions are mixtures of diverse pulverized or shock-melted fragments of many different older rocks. These hybrid fragmental rocks, called *polymict breccias*, are the subject of the following section (section 6.4). In contrast, the present section describes rocks that, although shattered and deformed, have not been mixed together with other rocks. These *monomict breccias* are not hybrid mixtures.

A lunar monomict breccia is a rock that, although brecciated in texture and shattered into fragments, still represents a single original rock type. It has survived the meteoritic bombardment with no contamination, mixing, or other significant alteration of its original chemical composition. Because monomict breccias represent a single rock type rather than a mixture, they provide important clues to the makeup of the lunar crust.

Even rarer than monomict breccias are purely igneous highland rocks. These are crystalline rocks that have solidified from an original melt; they are not only monomict but also not brecciated. Together, monomict breccias and igneous rocks are often termed *pristine* highland rocks, using “pristine” in a chemical sense. They are rare among the lunar samples, but they are important because they are preserved components of the primary lunar crust. Among the Apollo samples, pristine highland rocks range in size from tiny clasts of less than 1 mg mass (i.e., only observable by chance in a thin section) to the fifth largest highland rock in the collection, the Apollo 16 ferroan anorthosite 60015 (5574 g, including a thin partial coating of impact glass).

In analyzing and interpreting a highland sample, it is essential to know whether it is a pristine rock (igneous rock or monomict breccia) or a polymict breccia. This distinction is especially important when interpreting chemical data. The bulk chemical composition of a polymict breccia represents an average of many older rocks that have been mixed together, but it does not correspond to any primary lunar rock type. If not recognized as mixtures, analyses of polymict breccias can convey a misleading impression that there is only a limited compositional diversity among highland rocks. Only by physically separating polymict breccias into their pristine components (or by doing equivalent mathematical separations on the resulting data) can we properly assess the compositional and genetic diversity of the highland crust.

How can pristine rocks be distinguished from polymict rocks? Sometimes the difference is obvious from microscopic examination of a thin section. A pristine rock may have a uniform coarse-grained, crystalline igneous texture throughout. In contrast, a polymict rock might be an obvious blend of fragments of different rocks.

Microscopic examinations may not always be adequate, however. Even pristine highland rocks are generally severely brecciated, obscuring their original textures. Some polymict rocks, formed by the cooling of impact-generated melts, have textures virtually indistinguishable from pristine igneous basaltic lavas. Electron microprobe analyses, which can determine the compositions of small areas of a crystal, can be

made on the different minerals to determine whether or not a particular breccia is monomict. In pristine rocks, the minerals tend to have a narrow range of compositions that reflects their formation together near chemical equilibrium. In contrast, polymict breccias tend to have minerals from different sources that have different compositions. This general distinction must be applied with caution, for pristine rocks from shallow levels in the crust can also have varied mineral compositions caused by disequilibrium in crystal growth.

Because textural and mineralogical data may be ambiguous, the most commonly used method for distinguishing between pristine and polymict rocks involves chemical analyses. The *siderophile* (i.e., geochemically associated with Fe metal) trace elements are especially useful discriminators. Compared with typical CI carbonaceous chondrite meteorites, pristine lunar igneous rocks are generally depleted in siderophile elements such as Au, Ge, Ir, Os, and Re, by factors of roughly 10,000 (section 8.6). Because large meteoroid impacts are primarily responsible for producing polymict breccias out of pristine rocks, the small amounts of meteoroid mixed into the resulting polymict breccia produce enhanced concentrations of siderophile elements. In general, a sample with a concentration of one of these siderophile elements >0.0003 times the concentration in CI carbonaceous chondrites is considered to be a polymict rock (Warren and Wasson, 1977); samples with less than this amount are considered pristine. This boundary is not an absolute discriminator; some monomict rocks have concentrations well above this limit (Warren *et al.*, 1987). However, a concentration below this value is usually a reliable indication that a sample is pristine. Other trace-element data may also assist in distinguishing pristine from polymict rocks.

In summary, there is no simple method for deciding whether a given lunar rock is pristine or polymict. In a few cases, all the available evidence is ambiguous, and the nature of the sample remains uncertain. For example, one entire category of possible pristine igneous rocks, the Apollo 15 KREEP basalts, may instead be coarse-grained impact-melt rocks (Taylor, 1982), simply because it is difficult to distinguish a pristine igneous texture from a relatively coarse-grained impact melt. In another example, the Apollo 14 sample 14310 has a texture (Lames, 1973) comparable to typical Apollo 15 KREEP basalts, and 14310 was therefore once presumed to be igneous (e.g., *Apollo Soil Survey*, 1971). The subsequent discovery of a clast of fine-grained polymict breccia in one thin section of 14310 (Carlson and Walton, 1978) eventually proved that 14310 is a polymict rock. Even before this conclusive

evidence was found, however, most petrologists had already concluded that 14310 is an impact-melt breccia, on the basis of its textural heterogeneity, high contents of meteoritic siderophile elements (Baedecker *et al.*, 1972; Morgan *et al.*, 1972a,b), and high plagioclase content, which is greater than expected for rocks formed by partial melting in the lunar interior (e.g., Green *et al.*, 1972).

6.3.1. Classification of Pristine Igneous Highland Rocks

Most petrologists distinguish three major classes of pristine igneous lunar highland rocks: KREEP rocks, ferroan anorthosites, and Mg-rich rocks. KREEP rocks have been found as small basaltic fragments in Apollo 15 and Apollo 17 breccia samples. The ferroan anorthosites and Mg-rich rocks are rarely found as plutonic (coarsely crystalline) rocks; most occur as monomict breccias. Volumetrically, KREEP rocks are far less important than ferroan anorthosites and Mg-rich rocks.

The KREEP rocks are named for their characteristically high contents of incompatible elements, especially K, rare earth elements (REE), and P, which always occur in virtually the same pattern of element:element ratios (see sections 2.4.4 and 8.4.2). In practice, because of their generally fine-grained crystalline textures, KREEP rocks are also considered to be basalts, crystallized on or just below the lunar surface.

A few other lunar rocks also show similar enrichments of the same elements, but do not show the same basaltic textures. One example is a quartz- and feldspar-rich lunar "granite" (Warren *et al.*, 1983b). The exact relationship between these coarse-grained KREEPy (or KREEP-like) rocks and the more common, fine-grained KREEP basalts remains a matter of debate and speculation.

A common synonym for KREEP rocks is "Fra Mauro basalt," because the highland rocks returned by the Apollo 14 mission, which landed on the Fra Mauro Formation, are almost exclusively KREEPy breccias or impact melts with major-element compositions (e.g., low silica) that approximate the compositions of basalts.

The other two types of common monomict highland rocks, *ferroan anorthosites* and *Mg-rich rocks*, are (or have been) derived from large igneous bodies rich in plagioclase feldspar. Earlier workers (e.g., Kell *et al.*, 1972) tended to combine them on the basis of mineral composition, with plagioclase-rich polymict rocks into a single category "ANT" (for Anorthosite-Norite-Troctolite rocks). However, evidence of a pristine character is now considered a more important criterion for classification than

mineralogy, and the pristine rocks in the earlier ANT series have been divided into two subgroups of roughly equal size. The ferroan anorthosite subgroup is chemically distinct from other highland rocks, as can be seen on plots of Mg/(Mg + Fe) against Na/(Na + Ca) (Fig. 6.22). Within typical large igneous bodies, which probably solidify with fractional crystallization and crystal separation, the Mg/(Mg + Fe) ratio tends to vary inversely with the Na/(Na + Ca) ratio. Typical ferroan anorthosites, however, do not show such a trend (Fig. 6.22).

The other subgroup, the Mg-rich rocks, contains less plagioclase and more Mg-rich minerals like olivine and pyroxene. Chemically, this group is distinguished from the ferroan anorthosites by showing the expected inverse variation between the Mg/(Mg + Fe) and Na/(Na + Ca) ratios that would be produced by crystal separation during cooling and crystallization.

These two groups of rocks are probably genetically distinct; chemically, they show no overlap on plots such as Mg/(Mg + Fe) vs. Na/(Na + Ca). Further-more, the ferroan anorthosites tend to have much higher plagioclase contents (generally >95 vol.%) than Mg-rich rocks (generally 40-80 vol.%).

Other pristine lunar highland rock types include high silica granites and alkali (Na-rich) anorthosites. These rocks may have been produced by extreme chemical differentiation from an Mg-rich rock, from a KREEP rock, or from both. Many petrologists also make a distinction, first proposed by James and Flohr (1983), between the Mg-rich rocks that contain abundant high-Ca pyroxene (*Mg-gabbronorites*) and the majority of Mg-rich rocks, which have little or no high-Ca pyroxene.

Another lunar rock type, "very-high-alumina basalt" or "highland basalt," was first believed to be an important monomict highland rock that occurred chiefly as lava flows. However, most petrologists soon agreed that "VHA basalt" was not a truly igneous rock type. Most, if not all, VHA basalts are actually polymict impact-melt rocks that formed as mixtures of other "pristine" rock types such as anorthosites, KREEP basalts, etc. (Dowry *et al.*, 1974c).

The naming and classification of lunar highland rocks can be confusing, even for petrologists. The nomenclature is largely based on mineralogy, the essence of which can be summarized on a diagram (Fig. 6.23) showing the relative abundances of the major mineral constituents: feldspar, pyroxene, and either olivine or a silica mineral. Magnesian olivine and a silica mineral cannot occur together in equilibrium (they react to form pyroxene), so each rock type can be represented in either the feldspar-pyroxene-olivine or the feldspar-pyroxene-silica

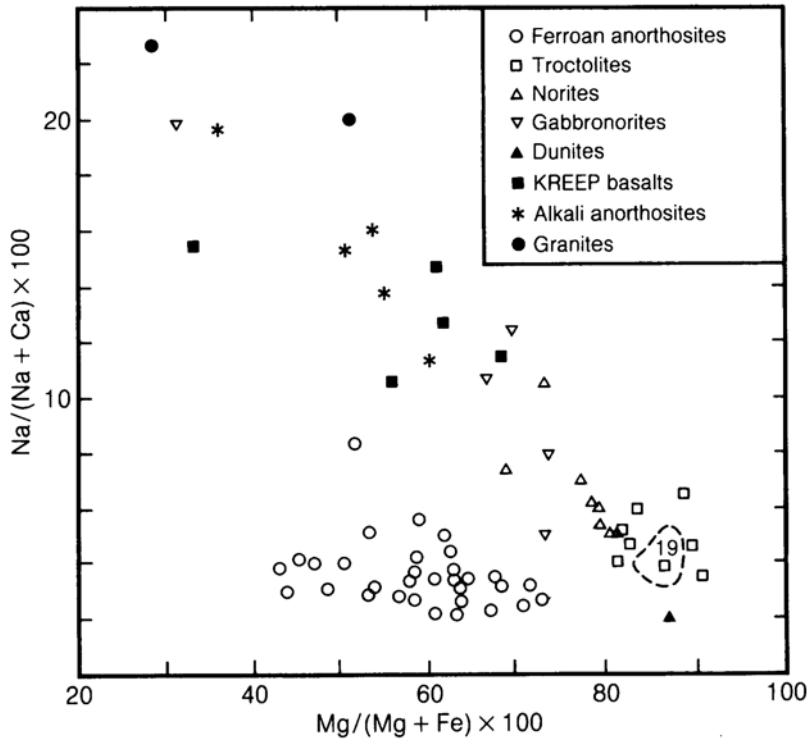


Fig. 6.22. Bulk-rock Na/(Na + Ca) vs. Mg/(Mg + Fe), mole ratios, for a variety of pristine highland igneous rocks (after Warren, 1986). Dashed field (lower right) encompasses 19 troctolites. The ferroan anorthosites (lower center) have distinctive, low Mg/(Mg + Fe), low Na/(Na + Ca) compositions.

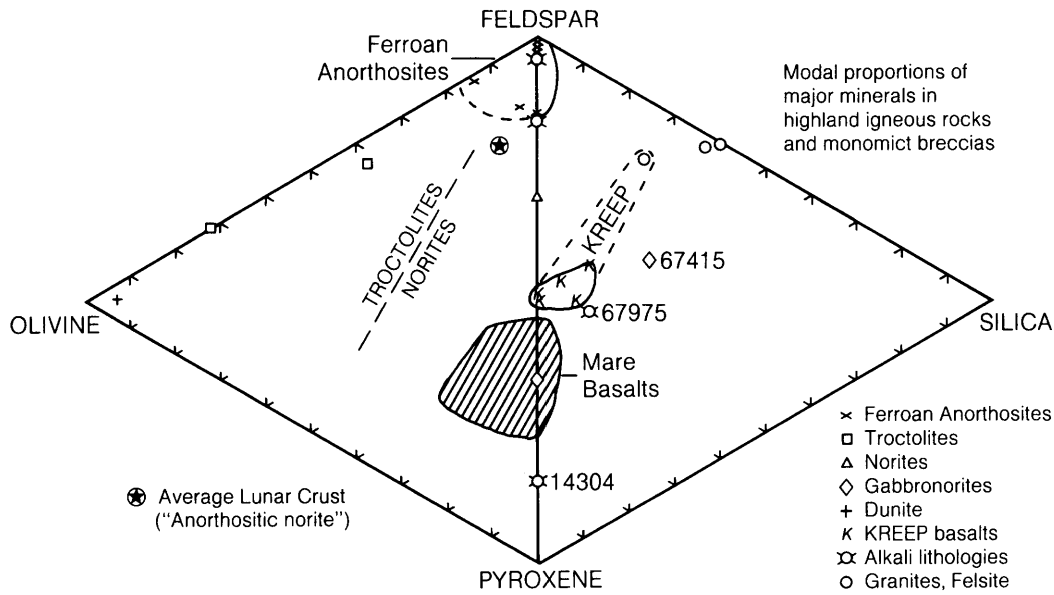


Fig. 6.23. Modal (volume) proportions of the four major minerals in highland pristine igneous rocks and monomict breccias (Tables 6.6, 6.7, 6.8, and 6.10). Gabbronorites include the sodic ferrogabbro 67415; alkali lithologies include two alkali anorthosites (with abundant feldspar), alkali norite 14304, and alkali granite 67975. The general area of mare basalt composition (BVSP, 1981) is shown for comparison (ruled area). The KREEP basalts have higher amounts of feldspar and silica minerals. The boundary between norite and troctolite is defined by the line representing a 1:1 olivine-to-pyroxene ratio (Stöffler *et al.*, 1980).

system. This diagram is also a good indication of the major mineral components that could be obtained for processing if the rocks shown were disaggregated. Other important variations are described in the text and in the tables.

6.3.2. KREEP Rocks

Even though KREEP is known to be a major chemical component of the upper lunar crust at the Apollo 12 and 14 landing sites, actual fragments of pristine KREEP rocks have only rarely been recognized in samples from any mission other than Apollo 15. Igneous-textured KREEP rocks are mainly basalts; the KREEPy granite and quartz monzodiorite types are much less common (Fig. 6.23; section 6.3.5).

The precise locations of KREEP bedrock are not known. The Apennine Bench Formation, exposed about 70 km west of the Apollo 15 landing site, is

thought to extend under the younger plains of mare basalts near the landing site itself and to be the source of the Apollo 15 KREEP basalts (*Spudis and Ryder, 1985*). The two largest samples of KREEP rocks are the Apollo 15 basalt samples 15382 and 15386 (3.2 and 7.5 g, respectively). Pristine KREEP rocks from other Apollo sites include a series of basalt clasts in Apollo 17 breccia 72275 (*Ryder et al., 1977; Salpas et al., 1987*) and a single tiny clast, not definitely pristine, of basalt in Apollo 16 breccia 67749 (*Ryder and Norman, 1980*). A thoroughly brecciated olivine norite clast from the Apollo 14 breccia 14318 may be related to KREEP, but this clast is neither definitely monomict, nor of typical Apollo 14 KREEP composition (*Warren et al., 1986*).

Figure 6.24 illustrates several examples of textures in igneous, unbrecciated KREEP rocks. Most igneous KREEP rocks are basalts; they are generally subophitic to intersertal in texture (see section 6.1.3 for

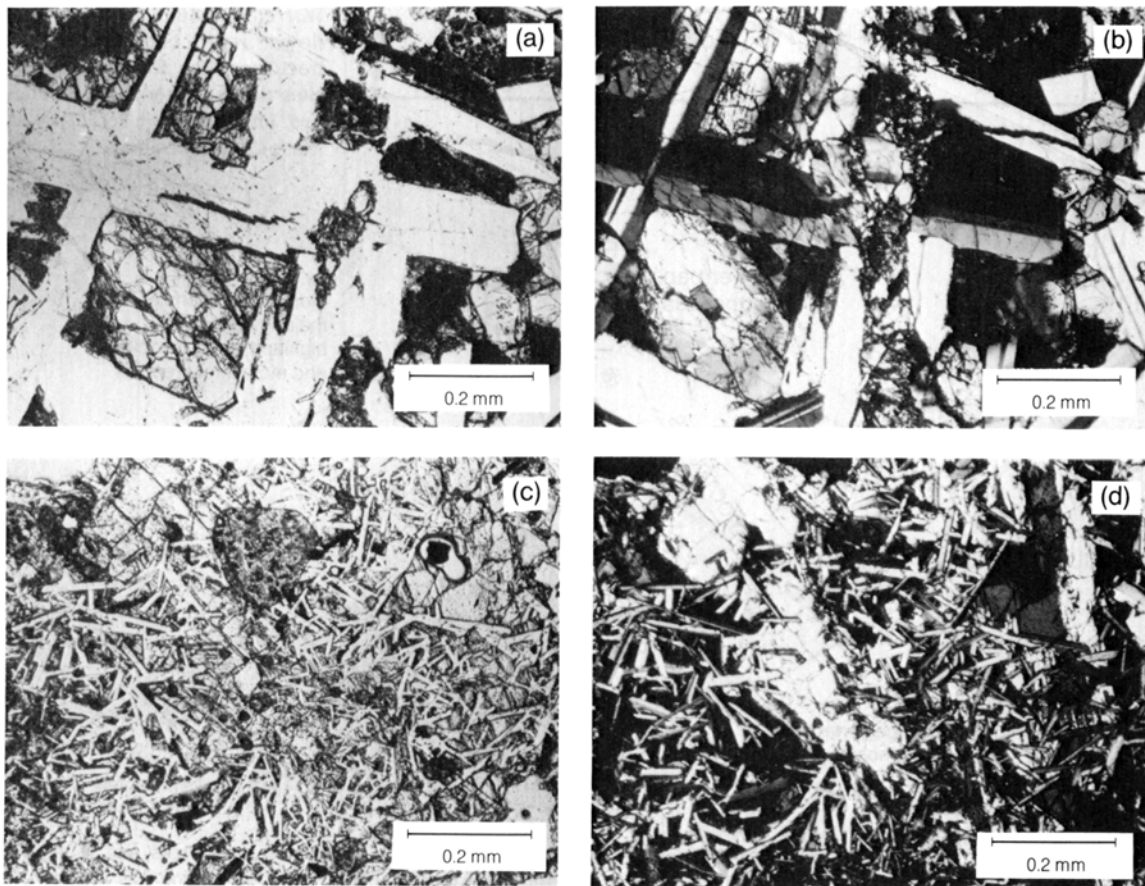


Fig. 6.24. Photomicrographs of small fragments of KREEP basalts collected from the Apollo 15 core sample 15007. Image (a) shows subophitic texture in plane-polarized light and (b) shows the same texture in cross-polarized light; (c) shows intersertal texture in plane-polarized light and (d) shows the same texture in cross-polarized light.

TABLE 6.6. Modal mineral composition (in vol.%) of some monomict KREEP rocks.

	14303c	A15KF*	15382	15386	15405c	72275 c
Plagioclase	33	41	43	43	35	40
Olivine	tr	—	—	—	—	tr
Orthopyroxene	—	P	9	P	—	P
Pigeonite	—	P	32	P	18	P
High-Ca pyroxene	11	P	P	P	18	P
Total pyroxene	-11	35	-41	43	-36	40
Ilmenite	1	—	P	3	1.6	P
FeNi metal	tr	tr	tr	tr	0.2	tr
Troilite (FeS)	tr	tr	tr	tr	tr	tr
Total opaque minerals	-1	3	6 [†]	-3	-2	—
Quartz	23	—	—	—	11	—
Cristobalite	—	4	P	8	—	P
Total SiO ₂ minerals	-23	-4	—	-8	-11	—
Zircon	tr	—	—	—	0.6	tr
K-feldspar	32	—	—	tr	15	tr
Apatite	tr	—	tr	—	—	—
Whitlockite	—	—	tr	tr	0.8	tr
Glassy mesostasis	—	17	8	P	—	20

* A15KF indicates the "typical" mode reported for six small fragments (coarse soil particles) of Apollo 15 KREEP basalt (Powell et al., 1973).

† Total opaque phases reported for 15382 include minor Cr,Fe-spinel, armalcolite, baddeleyite, tranquillityite, and zirconolite.

Abbreviations: P = present, "tr" = trace.

Additional references: "granite" 14303c, Warren et al. (1983b); basalt 15382, Dowty et al. (1976), Hollister and Crawford (1974); basalt 15386, Steele et al. (1972), Simonds et al. (1975), Takeda et al. (1984); quartz-monzodiorite 15405c, G. J. Taylor et al. (1980); basalt 72275c, Ryder et al. (1977).

a discussion of textural terms). Some coarser varieties have porphyritic textures. In these rocks, the phenocrysts are usually euhedral or subhedral prismatic crystals of orthopyroxene (containing almost no Ca), with smaller, lathlike (sometimes skeletal) plagioclase, normally intergrown with low-Ca pyroxene (pigeonite) rims. These textures indicate an origin as volcanic lavas (Ryder, 1987). However, several KREEP rocks have coarser, more equigranular textures that imply slower cooling and suggest an intrusive origin.

The higher-silica KREEPy rocks, quartz monzodiorite and granite, which occur as clasts in Apollo 15 breccia 15405, are themselves brecciated, but their original textures appear to have been "coarse basaltic, with plagioclase laths" (Ryder, 1976, 1985). Unlike typical KREEP basalts, these clasts contain intergrowths of silica and K-feldspar. These clasts also have unusually high incompatible element contents, even by KREEP standards. Another KREEP-like granite clast, from the Apollo 14 breccia 14303, is a thoroughly brecciated sample of a coarse, equigranular rock with abundant intergrowths of silica and K-feldspar (Warren et al., 1983b).

Table 6.6 illustrates the range in modal composition (mineral abundances by volume percent) among pristine KREEP rocks. Olivine is uniformly rare. Among the KREEP basalts, pyroxenes show a characteristically wide range in composition from the earliest-formed orthopyroxenes with Mg/(Mg + Fe) = 0.8 and essentially no Ca, to the later low-Ca, lower-Mg (pigeonite) and high-Ca (augite) varieties (Fig. 6.25). However, pyroxenes in the small clast in sample 67749 do not include any of the orthopyroxene, or even the low-Ca, high-Mg pigeonite, found in all other KREEP basalts (Ryder and Norman, 1980). Plagioclase feldspar in KREEP basalts (e.g., 15382) typically has normal zonation, from 95% Ca-feldspar (anorthite) in the crystal center to 80% or less at the edges (see section 5.1.2 and Dowty et al., 1976). There is also strong enrichment in K (the orthoclase component), as Ca (the anorthite component) decreases in the plagioclase; this is illustrated in Fig. 6.26 for the 72275 clasts (Ryder et al., 1977).

In many respects, the chemical compositions of igneous KREEP basalts (Table A6.9; Figs. 6.27 and 6.28) are remarkably uniform. The diagram in Fig. 6.27 is based on melting and crystallization

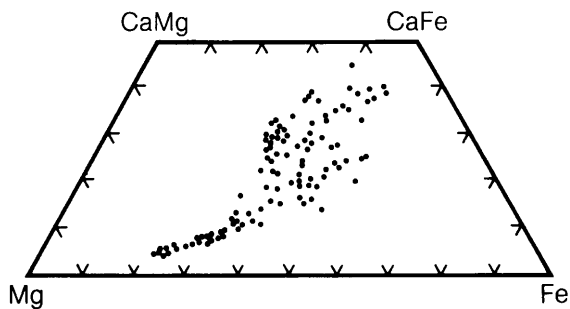


Fig. 6.25. Compositions (Mg:Fe:Ca atomic proportions) of zoned pyroxene crystals from Apollo 17 KREEP basalt 72275c. The first crystals to form were high-Mg orthopyroxenes (lower left). Formation of these crystals changed the composition of the remaining liquid, causing Fe- and Ca-rich rims (center and upper right) to form on the original Mg-rich cores. Data from *Ryder et al.* (1977).

experiments using actual lunar basalt compositions (*Walker et al.*, 1973a,b), and incorporating the five major oxides in the highland crust (Al_2O_3 , CaO, FeO, MgO, and SiO_2). The experimental results define stability fields for the three most abundant minerals in the highland crust: plagioclase feldspar, low-Ca pyroxene, and olivine. The compositions of KREEP basalts tend to cluster near the curve that represents melts that are saturated with (and therefore crystallizing) both plagioclase and low-Ca pyroxene. In particular, the KREEP compositions cluster near the high-temperature (low- SiO_2) end of the curve, where melts are cosaturated with plagioclase, low-Ca pyroxene, and olivine.

Although the KREEP rocks show relatively constant ratios between individual incompatible elements (Fig. 6.28), they have a considerable range in total incompatible element enrichments. As a result,

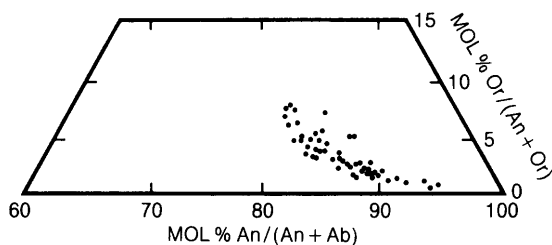


Fig. 6.26. Compositions of zoned plagioclase crystals from Apollo 17 KREEP basalt 72275c, showing molecular proportions of Ca-feldspar (An), Na-feldspar (Ab), and K-feldspar (Or). The earlier-formed crystals are Ca-rich (high An). As the An content decreased in the later-formed crystals (and in the rims on earlier-formed crystals), the Or content also increased. Data from *Ryder et al.* (1977).

the KREEP rocks can be divided into subgroups on the basis of their incompatible element contents. Potassium (K) is a convenient discriminator and is used to distinguish "low-K," "medium-K," and "high-K" KREEP types. Typical low-K KREEP is divided from medium-K KREEP at $\text{K}_2\text{O} = 0.35$ wt.% (corresponding to La = $46 \mu\text{g/g}$, Lu = $2.1 \mu\text{g/g}$, etc.). Medium-K KREEP is divided from high-K KREEP at $\text{K}_2\text{O} = 0.7$ wt.% (or La = $93 \mu\text{g/g}$, Lu = $4.2 \mu\text{g/g}$, etc.).

With the exception of the quartz monzodiorite clast in sample 15405, all known pristine KREEP rocks are medium-K KREEP; samples of low-K KREEP and volcanic high-K KREEP have been found only as polymict breccias. There is, in fact, even considerable doubt as to whether significant volumes of pristine igneous low-K KREEP ever existed, because this composition could easily result from impact-induced mixing of medium-K or high-K KREEP with typical nonKREEPy highland rocks. An average composition for high-K KREEP polymict breccias is included in Table A6.9.

Table A6.10 lists the ratios of incompatible elements used to define the characteristics of KREEP rocks. These incompatible element ratios are nearly constant among rocks with a wide range of overall incompatible-element enrichments. Despite their high incompatible-element contents (which would normally be produced by a high degree of igneous fractionation, in which the Mg/Fe ratio should decrease) typical KREEP rocks have moderately high Mg/(Mg + Fe) ratios (Fig. 6.29).

Radioactive age dating of KREEP basalts indicates that they formed at about 3.8-4.0 b.y. ago, either just before the oldest mare basaltic lavas or perhaps contemporaneously with them. Ages determined for Apollo 15 igneous KREEP basalt 15382 range from 3.82 b.y. (Rb-Sr system; *Papanastassiou and Wasserburg*, 1976), to 3.90-3.91 b.y. (^{40}Ar - ^{39}Ar system; *Stettler et al.*, 1973; *Turner et al.*, 1973). A similar basalt, 15386, yielded a Rb-Sr age of $3.86 \pm .04$ b.y. (*Nyquist*, 1977) and a Sm-Nd age of $3.85 \pm .08$ b.y. (*Carlson and Lugmair*, 1979). Initial $^{87}\text{Sr}/^{86}\text{Sr}$ ratios (a measure related to the evolution of the melted mantle source) reported for these rocks are 0.700241 and 0.70038 ± 10 , respectively. Another probable igneous Apollo 15 KREEP basalt, 15434,73, yielded a similar Rb-Sr age of $3.83 \pm .04$ b.y., but an initial $^{87}\text{Sr}/^{86}\text{Sr}$ ratio of 0.70070 ± 10 (*Nyquist*, 1977). The Apollo 17 KREEP basalt 72275 yielded a Rb-Sr age of $3.93 \pm .04$ b.y. and an initial $^{87}\text{Sr}/^{86}\text{Sr}$ ratio of 0.69957 ± 14 (*Compston et al.*, 1975). Model ages calculated for the source regions that produced the monomict Apollo 15 KREEP basalts are typically 4.2-4.4 b.y. (*Nyquist*, 1977; *Carlson and Lugmair*, 1979); however, *Nyquist* (1977) calculated a model age of 4.00-4.06 b.y. for the source of KREEP basalt 72275.

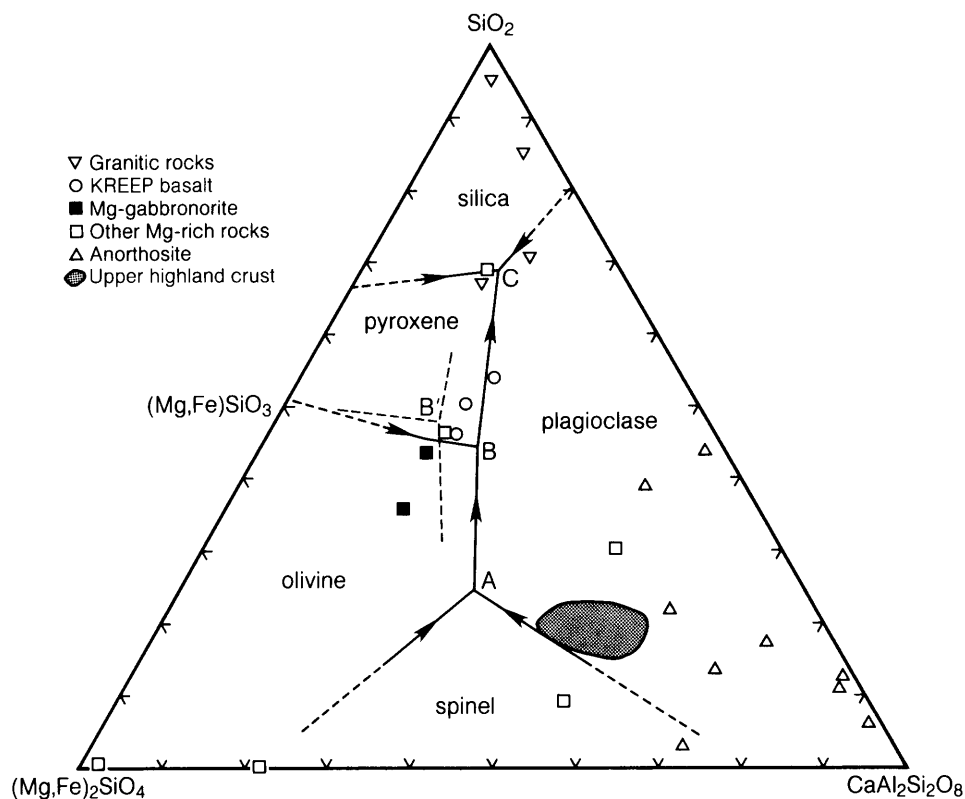


Fig. 6.27. Three-component (ternary) diagram for the system $(\text{Mg,Fe})_2\text{SiO}_4\text{-CaAl}_2\text{Si}_2\text{O}_8\text{-SiO}_2$, representing olivine—Ca-feldspar—silica, based on crystallization experiments by *Walker et al.* (1973a,b). The triangular plot is divided into several regions; melt compositions within each region will crystallize out the indicated mineral upon cooling. For the natural lunar compositions used to infer the boundary locations, the $\text{Mg}/(\text{Mg} + \text{Fe})$ ratio varies from 0.51 (at point C), to 0.64 (at point B), to 0.76 (at point A). The diagram is “pseudo” ternary because spinel is actually an oxide mineral, not a mixture of $(\text{Mg,Fe})_2\text{SiO}_4$ and $\text{CaAl}_2\text{Si}_2\text{O}_8$. The light-dashed curves show the equivalent crystallization-field boundaries determined by *Stolper* (1977) for similar but more FeO-rich compositions; the $\text{Mg}/(\text{Mg} + \text{Fe})$ ratio at point B' is 0.385. *Longhi and Pan* (1986) provide further data on shifts of these boundary curves as a function of bulk composition. Any Na in Ca-feldspar of anorthosites pulls these points (triangles) toward the SiO_2 apex because the diagram ignores the Na but not its associated SiO_2 . Compositions of monomict highland rocks (Tables A6.9, A6.11, A6.12, and A6.13) are shown. Also shown for comparison (shaded field) is a range of compositions for typical highland regolith samples, including three lunar meteorites (all regolith breccias), the Luna 20 soil, and average Apollo 16 soil (*Warren and Kallemeyn*, 1987). The average composition of the upper highland crust presumably plots within this field.

Age measurements on other KREEP-related rocks are less clear cut. The quartz monzodiorite clast in sample 15405 has been the subject of numerous isotopic studies. Unfortunately, it has been heavily shocked and the impact effects have severely disturbed the isotopic systems used for age dating. In one study, *Nyquist et al.* (1977) attempted to correct for Rb loss during shock by assuming an original Rb ratio similar to that of typical Apollo 15 KREEP; they concluded that the Rb-Sr age of the quartz monzodiorite is about 4.1 b.y., with an

initial $^{87}\text{Sr}/^{86}\text{Sr}$ ratio of 0.699. *Compston et al.* (1984b) used a high-resolution ion microprobe to obtain data for the U, Th, and Pb isotopes contained in four zircon grains from the quartz monzodiorite. Their results suggest that these zircons originally crystallized $4.365 \pm .030$ b.y. ago. *Compston et al.* (1984a) also obtained similar results for the 14303 granite clast; its zircon apparently crystallized 4.33-4.40 b.y. ago. Evidently the volcanic KREEP basaltic lavas tend to be younger than the coarser-grained, higher-silica KREEP-rich rocks.

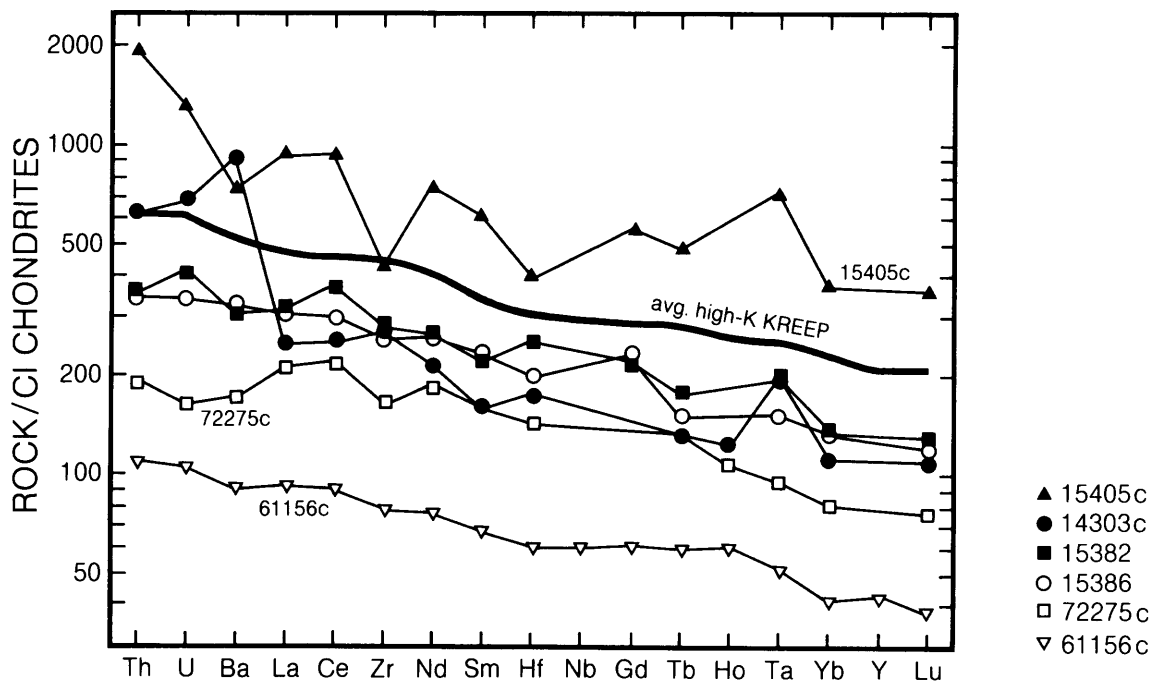


Fig. 6.28. Contents of various *incompatible elements* (i.e., elements not taken up by the common minerals in a crystallizing basalt) in KREEP-rich samples and related rocks. A lower-case “c” after the sample number indicates that a clast from within the sample was separated and analyzed. Higher incompatible-element contents correspond to higher KREEP content. The heavy line labeled “average high-K KREEP” represents polymict breccias of that composition. Sample 61156 is a VHA (very-high-alumina) “basalt” that is actually a type of polymict melt breccia. This sample is shown for comparison with the pristine KREEP rocks. Data for relatively coarse-grained rocks (samples 15405, 14303, and 15382) are plotted as solid symbols; these samples may be especially subject to errors caused by small sample sizes (e.g., major changes in Zr and Hf contents resulting from chance distribution of the mineral zircon). Data are from Table A6.9, normalized to element abundances in CI carbonaceous chondrites (Anders and Ebihara, 1982).

The fact that KREEP rocks tend to occur as volcanic lavas makes it difficult to use the Apollo data to estimate their overall abundance in the lunar crust. By assuming that (1) the lunar surface rocks are representative of the entire thickness of lunar crust and (2) most pristine KREEP occurs in the low-K form, Taylor (1975) produced a model lunar crust with 20 wt.% KREEP. However, if most of the KREEP rocks are broad, thin lava flows on the lunar surface, then the crust as a whole may be considerably less KREEP-rich than the outer surface. Warren and Wasson (1979a) estimate that, assuming that most monomict KREEP is of the “high-K” variety, KREEP rocks constitute only about 2 wt.% of the crust.

Recent analyses of meteorites from the Moon that have been collected in Antarctica (e.g., Warren and Kallemeyn, 1987) also suggest that the lunar crust as a whole is relatively poor in KREEP except for the

small region near the center of the Moon’s nearside that includes the Apollo and Luna sampling sites. This region covers 4.7% of the lunar surface. In other words, the post-Apollo lunar meteorite data also favor a reduction from earlier estimates of the overall crustal inventory of KREEP.

6.3.3. Ferroan Anorthosites

The single most common type of pristine highland rock is *ferroan anorthosite* (Fig. 6.23). It is distinguished from all other highland rocks by the peculiar combination of low-Na plagioclase feldspar with low-Mg pyroxene, with or without olivine. The majority of monomict rock types identified from the Apollo 16 site, the only sampled location in a typical highland region, are ferroan anorthosites. Among the lunar meteorites found since 1979 in Antarctica, the majority of pristine rock types identified as clasts

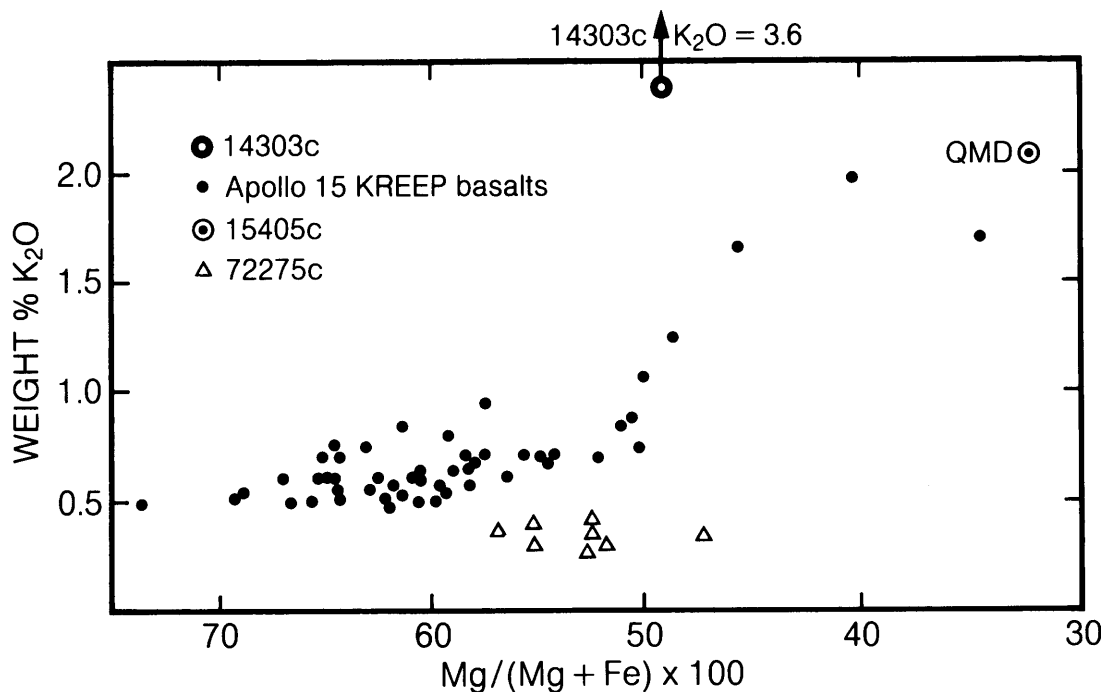


Fig. 6.29. Plot of mole $\text{Mg}/(\text{Mg} + \text{Fe})$ ratios against K_2O for pristine KREEP rocks. This plot illustrates a paradoxical characteristic of KREEP rocks: the combination of high $\text{Mg}/(\text{Mg} + \text{Fe})$ ratios (normally found in early-crystallized materials), with high K_2O contents (normally found in late-crystallized materials). Data are from Irving (1977), except for 14303c (a KREEP-like granite clast), which is from Warren *et al.* (1983b). These data have been obtained mainly from defocused-beam electron microprobe analyses, which are less reliable than most other types of major-element analyses of rocks. Note: QMD = quartz monzodiorite.

have similar ferroan (Fe-rich, Na-poor) mineral compositions. If the available Apollo pristine samples are representative, roughly 50% of the outer highland crust consists of ferroan anorthosite (the remainder is mainly Mg-rich rocks; see section 6.3.4).

The lunar ferroan anorthosites evidently formed as coarse-grained igneous rocks. The coarse grain size suggests that they are *intrusive* rocks, formed during slow cooling deep below the surface. The high concentration of plagioclase feldspar suggests that they are also *cumulate* rocks, produced by the separation of just-formed crystals (in this case, plagioclase feldspar) from the remaining melt. Although the vast majority of ferroan anorthosites are severely brecciated (Fig. 6.30), the few samples that show vestiges of their former igneous texture tend to be coarse-grained, with large subhedral to euhedral plagioclase crystals surrounded by smaller anhedral pyroxene or olivine (Fig. 6.31). For example, the anorthosite portion (about 100 g) of Apollo 16 breccia 60135 has remnants of original blocky

plagioclase crystals up to 4.4 mm across, which separated from the melt (*cumulus* plagioclase), surrounded by pyroxene that grew from the remaining melt (*adcumulus* or *orthocumulus* pyroxene). The pyroxene crystals are as much as 5.0 mm across. Although these vestiges of the original igneous texture have survived, 60135 is a severely shocked rock in which most mineral grains have been shock-melted *in situ* (Warren *et al.*, 1983c). Other examples of ferroan anorthosites that retain vestiges of former coarse igneous (*cumulate*) textures include samples 60025 (Ryder, 1982), 62236 (Nord and Wandless, 1983), and 62237 (Dymek *et al.*, 1975a).

The Apollo 15 "Genesis rock" (15415), which is by far the largest (269 g) ferroan anorthosite from a site other than Apollo 16, has a unique texture (Ryder, 1985). Plagioclase makes up about 99% of the rock and occurs as extremely coarse (up to 3 cm across) anhedral or polygonal grains. This unusual texture may have been produced by thermal metamorphism at least a few kilometers deep in the crust after the

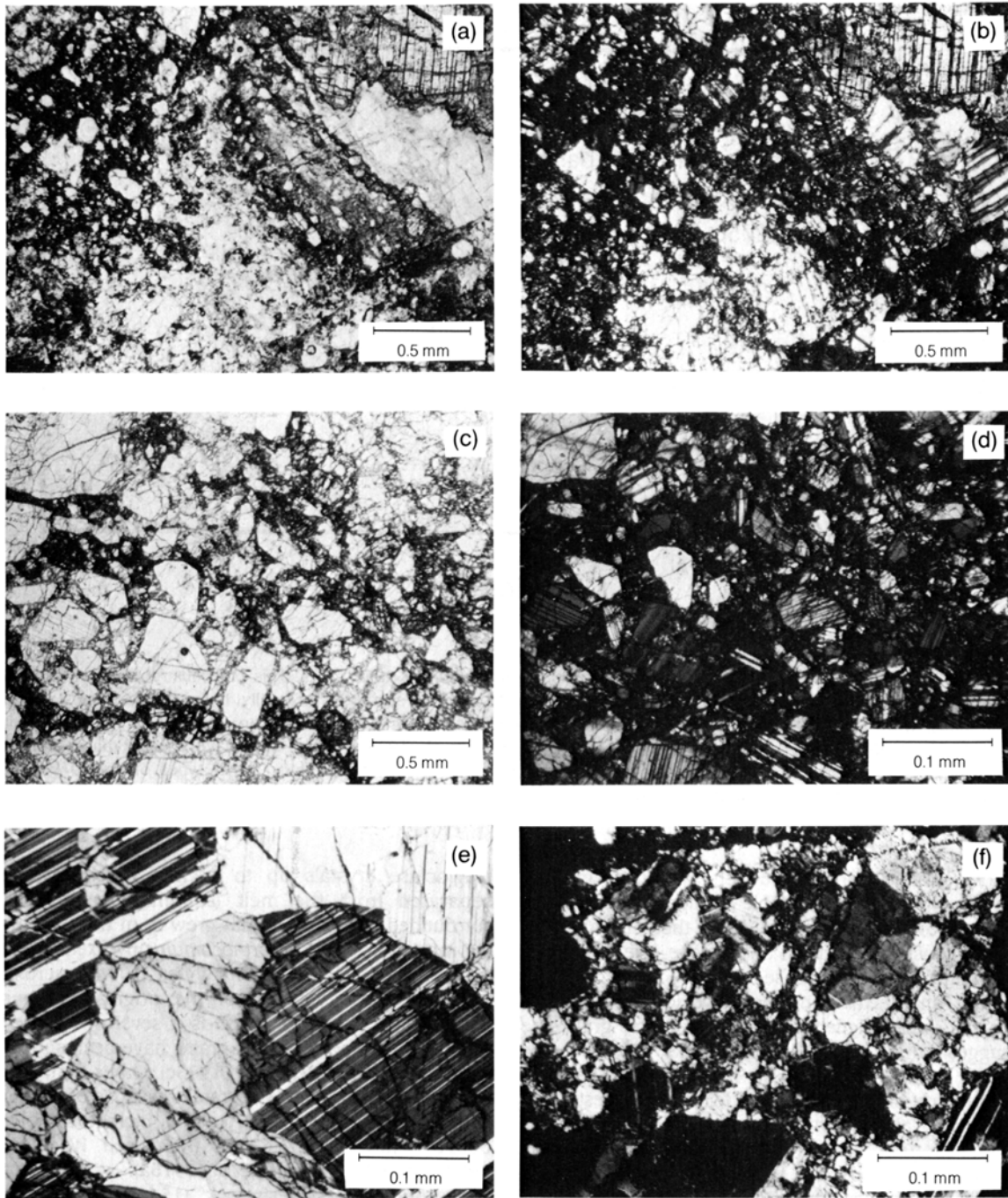


Fig. 6.30. Photomicrographs of typical ferroan and other anorthosites: **(a)** and **(b)**, severely brecciated and crushed areas in ferroan anorthosite 62236 [note relatively unbrecciated, pyroxene-rich area (gray) in lower left]; **(c)** and **(d)**, ferroan anorthosite 62237, showing “stringers” of pulverized mafic silicates (gray) among larger plagioclase fragments (white); **(e)** ferroan anorthosite 15415, showing coarsely crystalline texture; **(f)** alkali anorthosite 12073c, showing texture resulting from severe crushing followed by thermal annealing. All views in transmitted light and crossed polarizers, except **(a)** and **(c)**, which are with uncrossed polarizers.

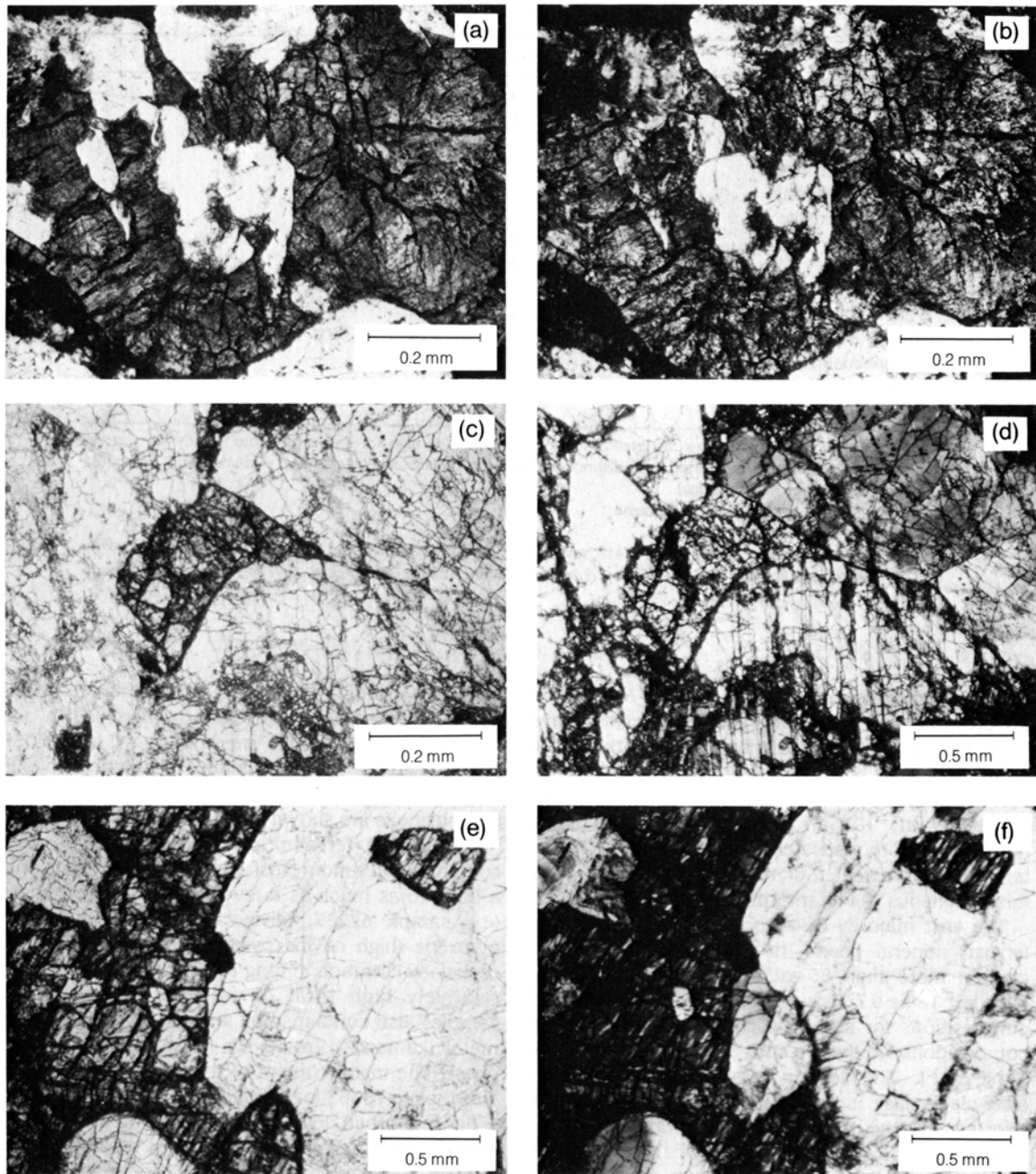


Fig. 6.31. Photomicrographs of areas of ferrous anorthosite samples containing *mafic* minerals (olivine and pyroxene). These minerals show relict *cumulate* textures produced by accumulation of crystals from a melt, most notably the smooth, arcuate boundaries between coarse pyroxenes (dark gray) and plagioclase. Images **(a)** and **(b)** show a small clast composed of augite, plagioclase, and low-Ca-pyroxene from the lunar meteorite ALHA81005. Based on its “ferrous” composition, this clast is thought to be an atypically pyroxene-rich fragment of an anorthosite. Images **(c)** and **(d)** show part of sample 62237, in which small pyroxenes are surrounded by large plagioclase crystals. Images **(e)** and **(f)** show another clast, composed of plagioclase and low-Ca pyroxene, which is also presumed to be an atypically pyroxene-rich fragment of an anorthosite, from sample 66035. Note that exsolution lamellae in the dark-gray pyroxene are visible as light, discontinuous diagonal bands in **(f)**. Images **(a,c,e)** were photographed with uncrossed polarizers; **(b,d,f)** are the same views, but photographed with crossed polarizers.

TABLE 6.7. Modal mineralogy (in vol.%) of some monomict ferroan anorthosites.

	15363	15415	60015	62236	62237	65315
Plagioclase	85	99	98.6	85	85	98.5
Olivine	tr	tr?	—	4	14	tr
Primary (?) hypersthene	12	tr	—	—	—	—
Inverted pigeonite*	—	tr?	1.3	10	1	1.4
Pigeonite lamellae†	—	tr	—	—	—	—
Primary (?) augite	2	tr	tr	1	tr	tr
Total pyroxene	-14	(tr)	-1.3	-11	-1	-1.4
Ilmenite	—	tr	tr	tr	tr	—
Cr-spinel	—	—	tr	tr	tr	—
FeNi metal	0.4	tr	tr	—	—	—
Troilite (FeS)	0.1	—	tr	tr	tr	—
Total opaque minerals	—	—	0.35	—	—	0.3
SiO ₂ mineral(s)	—	tr	—	—	—	—
Apatite	—	tr?	—	—	—	—

* Primary igneous pigeonite now inverted into orthopyroxene + high-Ca pyroxene. Note: nearly all ferroan anorthosites are severely brecciated, and distinctions between brecciated (hypersthene + augite) and brecciated inverted pigeonite are problematical.

† Pigeonite lamellae within high-Ca pyroxene.

References: 15363, *Warren et al.* (1987); 15415, review by *Ryder* (1985); 60015 and 65315, *Dixon and Papike* (1975); 62236, *Warren and Wasson* (1978), *Nord and Wandless* (1983); 62237, *Dymek et al.* (1975a), *Warren and Wasson* (1978).

rock had originally solidified (*Stewart*, 1975). Similar textures, although involving smaller grains, have been observed in individual clasts found within more normal-textured but brecciated ferroan anorthosites such as 62236 (*Nord and Wandless*, 1983) and 62237 (*Dymek et al.*, 1975a). Most ferroan anorthosites, however, are too severely brecciated to preserve textures that reveal much information about their former igneous or metamorphic histories (Fig. 6.30)

The vast majority of large (i.e., >10 g) rocks with ferroan mineral chemistries are anorthosites that contain more than 85 vol.% of Ca-rich plagioclase feldspar. Table 6.7 shows a range of modal mineral compositions for several rock types. The chemical compositions of these same samples are listed in Table A6.11. The second most abundant mineral, after plagioclase, is usually pyroxene. In most ferroan anorthosites, the pyroxene is mainly original low-Ca pigeonite that has, since crystallizing from the igneous melt, exsolved to form two pyroxenes: an orthopyroxene host crystal with almost no Ca, containing blebs or lamellae of high-Ca augite (e.g., samples 60025, 62236, 66035; see Fig. 6.31). However, typical ferroan anorthosites are so severely brecciated that it may be impossible to determine the precise origin of the scattered pyroxene fragments they contain; some orthopyroxenes may be primary igneous minerals. In a few cases (e.g., sample 15415), the pyroxene in the ferroan anor-

thosite is predominantly augite. A small clast of cumulate-textured ferroan gabbro, identified in one of the lunar Antarctic meteorites (ALHA81005), contains augite that is definitely of primary igneous origin (*Warren et al.*, 1983d). Typical pyroxene compositions are shown in Fig. 6.32.

Most large ferroan anorthosite samples also contain small amounts of olivine, ranging from only a trace to as much as a few percent. In a few cases (e.g., sample 62237), olivine is more abundant than pyroxene (high olivine/pyroxene ratios seem to be especially common among ferroan anorthosites with relatively high total olivine + pyroxene). Many samples also contain small amounts of ilmenite, Fe-metal (kamacite), troilite, Cr-Fe-spinel, and a silica phase. The metal content of the small (0.5 g) ferroan anorthosite 15363 is exceptionally high (Table 6.7).

Far more than any other rock type, the widespread abundance of ferroan anorthosite is responsible for (and is a reflection of) extreme enrichment of the lunar crust in plagioclase feldspar. Many petrologists think that the ferroan anorthosites are cumulate rocks that formed by the extensive flotation of plagioclase on top of a primordial Moonwide "magma ocean," an outer layer that was molten (or partially molten) to a depth of several hundred kilometers, from about 4.4 to 4.6 b.y. ago (section 2.4.3). In this view, the ferroan anorthosites should have formation ages that fall within this

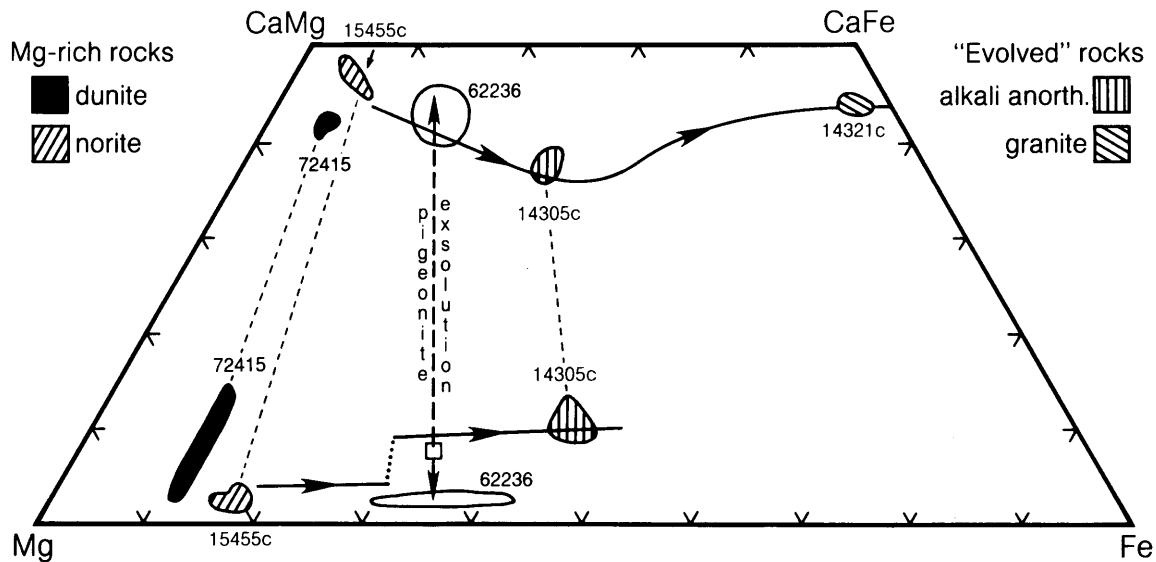


Fig. 6.32. Compositions (Mg:Fe:Ca atomic proportions) of pyroxenes from selected pristine highland intrusive rocks: dunitite 72415 (*Dymek et al.*, 1975a), anorthositic norite 15455c (*Ryder and Bower*, 1977), ferroan noritic anorthosite 62236 (*Nord and Wandless*, 1983), alkali anorthosite 14305c (*Warren et al.*, 1983c), and granite 14321c (*Warren et al.*, 1983b). Square symbol indicates estimated composition of typical 62236 pyroxene (pigeonite) prior to its exsolution into orthopyroxene (lower in Ca) and augite (higher in Ca). Note that the compositions of most of these lunar pyroxenes closely match positions on the pyroxene evolution trends (solid lines with arrows) observed for terrestrial pyroxenes formed by crystal settling in a single large igneous body, the Skaergaard intrusion, Greenland (*Deer et al.*, 1978).

time interval. Unfortunately, few if any reliable crystallization ages have been obtained for ferroan anorthosites, mainly because their extremely low abundances of Rb and REE make it difficult to apply standard age-dating techniques based on the Rb-Sr and Sm-Nd systems. The severe brecciation suffered by most ferroan anorthosites (and indeed, by nearly all monomict highland rocks) also hampers efforts to measure crystallization ages. Most of the "isotopic clocks" used in age dating involve elements (e.g., K, Rb, Ar) that are easily mobilized and expelled by shock and heating associated with impact events, and ages derived from these isotopic systems tend to reflect the time of the last severe shock suffered by the rock rather than its original crystallization age (*Unruh et al.*, 1977; *Nyquist*, 1982).

However, some age measurements are at least consistent with the magma ocean model. Ferroan anorthosites tend to have extremely low $^{87}\text{Sr}/^{86}\text{Sr}$ ratios (*Nyquist*, 1977), implying that they have been separated from any significant concentrations of Rb for a length of time that is comparable with the age of the Moon. More recently, *Lugmair* (1987) has reported a Sm-Nd age of $4.44 \pm .02$ b.y. for a ferroan anorthosite, sample 60025. *Hanan and Tilton* (1987)

reported a Pb-Pb model age of $4.51 \pm .01$ b.y. for the same sample. Any age for a plutonic lunar rock such as 60025 should be interpreted with caution, because rather than dating igneous crystallization it might date isotopic closure during prolonged global cooling of a primordial "magma ocean."

6.3.4. Mg-rich Rocks

The precise compositional range of the Mg-rich rock group is not well defined. Rocks in this group range from olivine-rich rocks (*dunitite*) all the way to rocks composed of pyroxene and Na-rich plagioclase (*sodic ferrogabbro*) (Fig. 6.23). As originally applied, the term "Mg-rich" covered all coarse-grained highland rocks that could be distinguished from the ferroan anorthosites by such chemical indicators as higher $\text{Mg}/(\text{Mg}+\text{Fe})$ and/or $\text{Na}/(\text{Na}+\text{Ca})$ ratios (*J. Warner et al.*, 1976a). Subsequently, many petrologists have come to suspect that there are fundamental genetic distinctions even within this group, and that different rocks have been produced by separate and dissimilar magmas (e.g., *James and Flohr*, 1983). For these reasons, some extreme highland rock types such as dunitite, gabbro-norite,

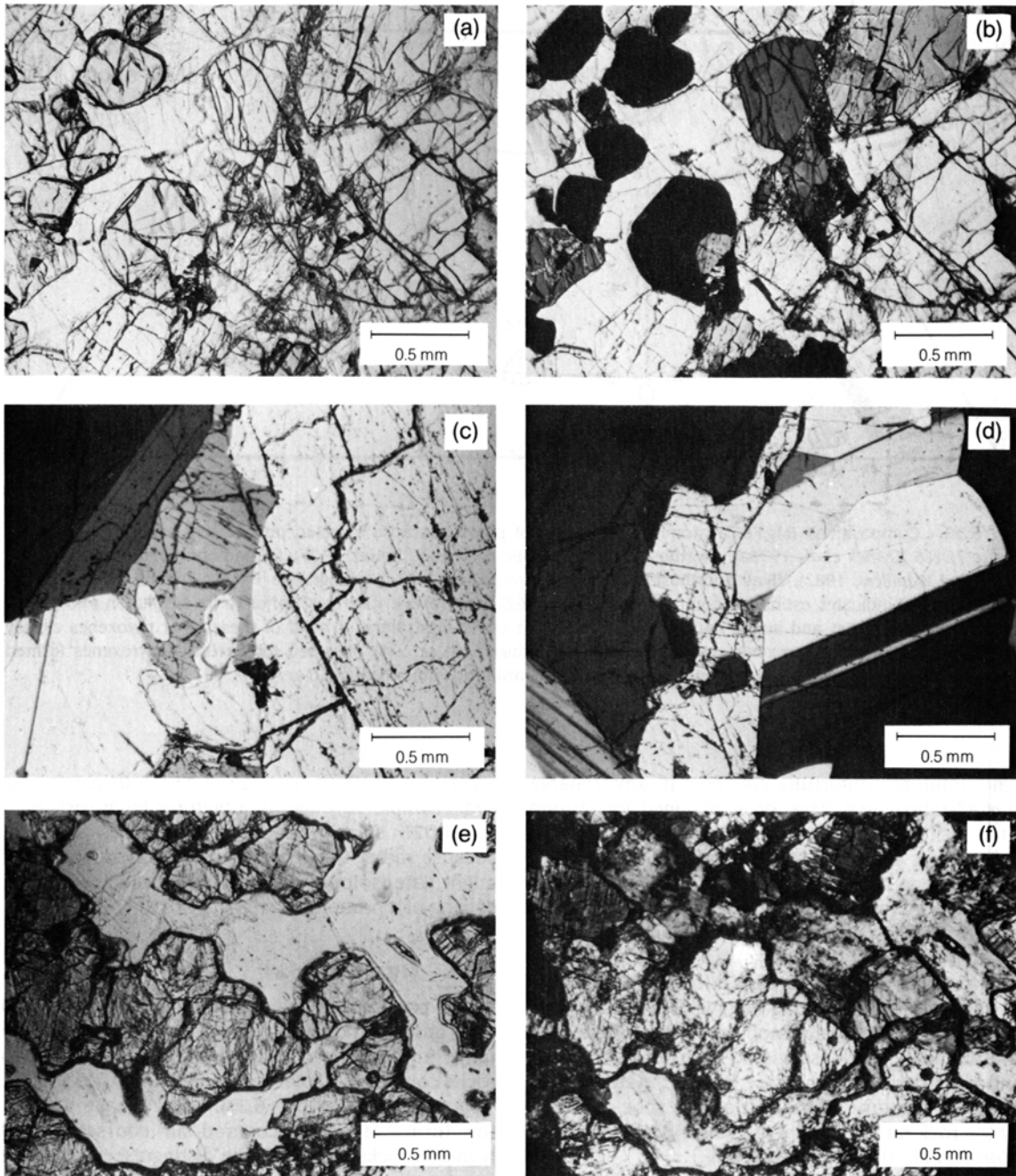


Fig. 6.33. Photomicrographs of Mg-rich pristine highland rocks: **(a)** and **(b)**, olivine-plagioclase-spinel cumulate clast from sample 67435. The plagioclase (white) is a single crystal that poikilitically encloses near-euhedral olivine (gray) and spinel (black in **(b)**). Note small crush zone that cuts diagonally across the field of view. Images **(c)** and **(d)** show troctolite 76535, composed mainly of plagioclase and olivine, which has a coarse granulitic texture. These views show some of the numerous small grains of trace minerals found in interstitial areas, which *Dymek et al* (1975a) interpret as the result of crystallization of residual trapped melt after deposition of the olivine-plagioclase cumulate. Images **(e)** and **(f)** show a gabbro fragment from sample 61224 (*Marvin and Warren, 1980*). Plagioclase (white in **(e)**) has recrystallized to feathery aggregates of tiny crystallites.

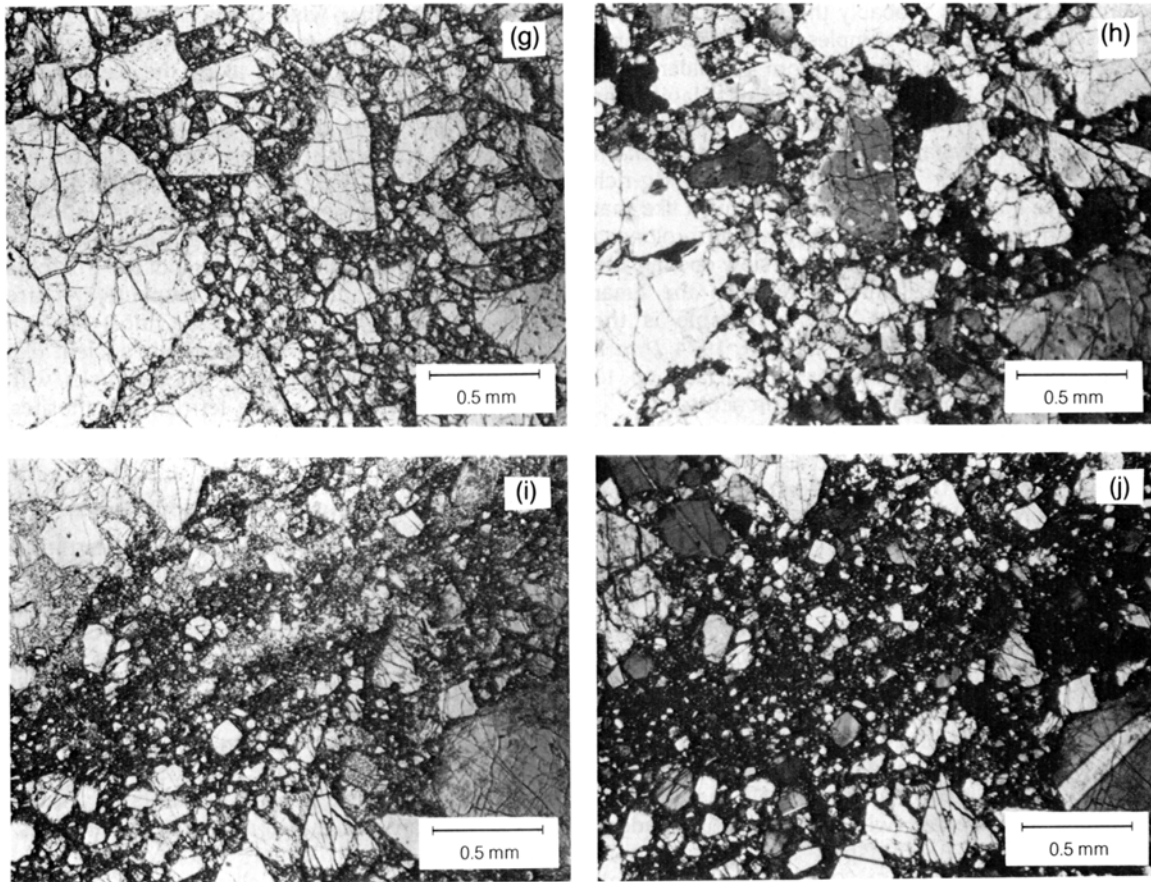


Fig. 6.33. (continued) Images **(g)** and **(h)** show the nearly monomineralic, brecciated dunite 72415, with various degrees of comminution of original extremely coarse olivine crystals. Images **(i)** and **(j)** show a clast of norite, composed of plagioclase and low-Ca pyroxene, from sample 77035, with a similarly cataclastic (crushed) texture. All pictures were taken in transmitted light. Images **(a,c,e,g,i)** are with uncrossed polarizers; images **(b,d,f,h,j)** are the same views, photographed under cross-polarized light, except for **(d)**, which shows a cross-polarized view different from **(c)**.

alkali anorthosite, and especially granite are sometimes excluded from the Mg-rich category. However, given the genetic implications sometimes attached to the term Mg-rich, and the rudimentary nature of current knowledge about highland petrogenesis, we have included both dunite and gabbro norite (which may be related) in the Mg-rich group. We consider alkali anorthosite and granite in the category of “other rock types” (section 6.3.5).

Most Mg-rich rocks are either highly magnesian *anorthositic troctolites* (plutonic rocks composed dominantly of plagioclase and olivine) or moderately magnesian *norites* (plutonic rocks composed dominantly of plagioclase and low-Ca pyroxene). The third most common type of Mg-rich rock is *gabbro norite*, which differs from norite by having much high-Ca pyroxene instead of (or in addition to) the

normal low-Ca pyroxene (*lames and Flohr*, 1983). Two of the larger samples of Mg-rich rocks are *ultramafic*, i.e., composed dominantly of olivine and/or pyroxene. One, the dunite (sample 72415), is a nearly monomineralic olivine cumulate (*Dymek et al.*, 1975a). The other, a *feldspathic lherzolite* (sample 67667) (*Warren and Wasson*, 1979b; *Hansen et al.*, 1980), is rich in high-Ca pyroxene and is therefore a type of gabbro norite.

Mg-rich rocks are common at all Apollo sites where many fragments of pristine highland rocks have been found. Like the ferroan anorthosites, most Mg-rich rocks are brecciated, but those that are relatively uncrushed tend to preserve textures that strongly suggest that these rocks have also originated as igneous cumulates (Fig. 6.33). The coarsest-grained lunar rock with clear vestiges of an igneous

cumulate texture is probably the norite represented by a series of Apollo 17 samples (the largest, sample 78235, weighs 199 g) collected from a boulder about 2/3 m in size. This norite contains plagioclase crystals up to 10 mm across, accompanied by orthopyroxene crystals up to 7 mm across (*Jackson et al.*, 1975; *Dymek et al.*, 1975a). A few Mg-rich rocks have a coarse granular texture, much like that of ferroan anorthosite 15415, suggesting prolonged thermal metamorphism (or at least slow cooling and equilibration) many kilometers deep in the lunar crust (*Stewart*, 1975). A prime example is the Apollo 17 troctolite 76535 (*Gooley et al.*, 1974; *Dymek et al.*, 1975a), which contains plagioclase up to 10 mm across and olivine up to 8 mm across.

Table 6.8 shows the mineral abundances in several Mg-rich rocks. The major minerals in Mg-rich rocks are the same as those in ferroan anorthosites. A combination of plagioclase feldspar, pyroxene, and olivine usually makes up more than 99% of the rock. However, in the Mg-rich rocks, plagioclase is frequently more Na-rich, the mafic silicates are generally more magnesian and more abundant, and the Ca-poor pyroxene tends to be primary orthopyroxene rather than pigeonite. Figure 6.32 shows typical pyroxene compositions. A wider variety of trace minerals occurs in the Mg-rich rocks than in the ferroan anorthosites. Troctolite 76535 alone contains Cr-Fe spinel, Fe-Ni metal (both kamacite and taenite), whitlockite, apatite, baddeleyite (ZrO_2), K-Ba-feldspar, and “pyrochlore” $[(Na,Ca)_2(Nb,Ta)_2O_6(OH,F)]$; *Dymek et al.*, 1975a]. Other accessory minerals observed in Mg-rich rocks include Mg-Al spinel (which may form up to 15% of the rock, e.g., the 67435 troctolite clast shown in Figs. 6.33a,b), ilmenite (which may form several percent of the rock), troilite, farringtonite $[Mg_3(PO_4)_2]$, armalcolite, zircon, zirconolite, and silica minerals (*Prinz and Keil*, 1977; *Ryder and Norman*, 1979; *James*, 1980).

Mg-rich rocks have a greater diversity in bulk composition than do the KREEP rocks or the ferroan anorthosites (Fig. 6.27; Table A6.12). One interesting aspect of this diversity is the observation that the Mg-rich troctolitic rocks from Apollo 14, whose major-element compositions are similar to the Mg-rich troctolitic rocks collected during other missions (e.g., Apollo 17), tend to have radically higher contents of incompatible trace elements (*Warren et al.*, 1981). The scatter of compositions shown in Fig. 6.27 probably reflects the removal or concentration of different minerals that are forming from melt(s) as they undergo fractional crystallization. For example, the troctolites presumably accumulated as crystals formed from melts evolving along the boundary where plagioclase and olivine were

crystallizing together, while the norites accumulated from more silica-rich melts (or possibly from the same melt at a later stage), along the plagioclase-pyroxene boundary (Fig. 6.27).

Isotopic age measurements for Mg-rich rocks are summarized in Table 6.9. These measurements are extremely difficult because of the limited sample sizes and the severe shock-produced brecciation of most samples. Often the results are equivocal; the Rb-Sr and Sm-Nd results for the age of the troctolite 76535 (4.51 b.y. and 4.26 b.y., respectively) are surprisingly discrepant. In any case, most Mg-rich rocks—including 76535—are extremely ancient (i.e., more than 4.2 b.y. old). No older igneous rocks, with the probable exception of the ferroan anorthosites, are known from either the Moon or the Earth.

6.3.5. Other Pristine Highland Rock Types

More exotic rock types, such as alkali anorthosite and granite, are rarely observed in highland samples. Despite their rarity, they are of considerable interest because they greatly extend the range of chemical composition observed in lunar rocks and require more complex theories to explain their origin. These rocks display a wide range in composition, from anorthosite to norite to granite (Fig. 6.23). Because the anorthositic and noritic varieties tend to be uncommonly enriched in alkali elements (e.g., Na, K, Rb, Cs), they are designated as “alkali anorthosites,” “alkali norites,” etc.

In terms of total volume, all these rock types are only minor components of the lunar crust. Alkali anorthosite and granite tend to be disproportionately abundant among the rocks returned by the Apollo 12 and 14 missions (although Apollo 12 returned few highland rocks). These two missions landed only about 180 km from one another, but over 1000 km from the next closest sampling site (Apollo 16; see Fig. 2.1). Surface spectra obtained from orbit (see section 10.2) indicate that the Apollo 12-Apollo 14 region has exceptionally high surface concentrations of incompatible trace elements (i.e., KREEP). It is therefore not surprising that these two missions yielded unusually high proportions of such “evolved” rock types as alkali anorthosite and granite. Even in this region, however, simple mixing-model calculations based on the observed compositions of returned polymict breccias indicate that alkali anorthosite and granite are only minor components of the crust. They are vastly outweighed by other rock types such as KREEP and troctolite.

Like the ferroan anorthosites, alkali anorthosites typically contain more than 85% plagioclase feldspar; the remainder is mainly pyroxene (Table 6.10). The key difference between the two types of anorthosite

TABLE 6.8. Modal mineralogy (in vol.%) of some monomict Mg-rich rocks.

	15455c	61224,6	67435c	67915c	72415	76535
Plagioclase	70	35	26	42	4	57
Olivine	—	—	69	—	93	37
Orthopyroxene	30	22	—	—	2	5
Pigeonite	—	—	—	5	—	—
High-Ca pyroxene	tr	43	—	23	1	tr
Mg-spinel	—	—	5	—	—	—
Cr,Fe-spinel	tr	tr	—	—	0.2	tr
Armalcolite	tr	—	—	—	tr	—
Ilmenite	tr	—	—	6	—	—
Rutile	tr	—	—	—	—	—
Pyrochlore	—	—	—	—	—	tr
Baddeleyite	tr	—	—	—	—	tr
Zirconolite	—	—	—	—	—	tr
FeNi metal	tr	tr	tr	tr	0.1	tr
Troilite (FeS)	tr	tr	tr	0.4	tr	tr
Unspecified SiO ₂ minerals	tr	—	—	23	—	—
K-feldspar	tr	—	—	1.2	—	tr
Zircon	tr	—	—	—	—	tr
Apatite	—	—	—	—	—	tr
Whitlockite	—	—	—	—	tr	tr
Unspecified phosphates	tr	—	—	0.2	—	—

References: 15455c (norite), *Ryder and Bower (1977), James and Flohr (1983)*; 61224,6 (gabbro), *Marvin and Warren (1980)*; 67435c (spinel troctolite with obvious cumulate texture), *Prinz et al. (1973)*; 67915c (sodic ferrogabbro), *G. J. Taylor et al. (1980)*; 76535 (dunite), *Dymek et al. (1975a)*; 76535 (troctolite), *Brown et al. (1974), Gooley et al. (1974), Dymek et al. (1975a)*. For a good compilation of additional modes, see *James and Flohr (1983)*.

TABLE 6.9. Sm-Nd and Rb-Sr isotopic age data (b.y.) for monomict highland rocks.

Sample	Lithology	Sm-Nd age	Rb-Sr age	Initial ⁸⁷ Sr/ ⁸⁶ Sr
15386	KREEP basalt	3.85 ± .08	3.86 ± .04	0.70038 ± 10
Range	KREEP basalts (8)	—	3.83 - 3.93	0.6994 - 0.7006
14321c	granite	4.11 ± .20	4.00 ± .1 1	0.703 ± 8
15455c	Mg-rich norite	4.48 (?)	4.48 ± .12	0.698960 ± 30
67667	Mg-rich lherzolite	4.18 ± .07	4.18 (?)	0.699050 (?)
72255c	Mg-rich notire	no data	4.08 ± .05	0.699130 ± 70
72417	Mg-rich dunite	no data	4.45 ± .10	0.699000 ± 70
73255c	Mg-rich norite	4.23 ± .05	no data	no data
76535	Mg-rich troctolite	4.26 ± .06	4.51 ± .07	0.699000 ± 30
77215	Mg-rich norite	4.37 ± .07	4.33 ± .04	0.699010 ± 70
78236	Mg-rich norite	4.34 ± 4.43	4.29 ± .02	0.699010 ± 20
Avg.	Ferroan anorthosites (5)	4.44 ± .02	—	0.698949 ± 10*

* Least-squares-weighted mean and uncertainty of mean, based on 16 measurements for 15415, 60015, 60025, 61016c, and 64423,13,1. The listed mean does not include four values from *Nunes et al. (1974a)*, which would drive it down to 0.698925 ± 10.

Data sources: *Carlson and Lugmair (1988), Shih et al. (1985)*, and reviews by *Nyquist (1977, 1982)*. The time constant for decay of ⁸⁷Rb is assumed to be 0.0142/b.y. (ages reported based on 0.0139/b.y. are adjusted × 0.979).

TABLE 6.10. Modal mineralogy (in vol.%) of some monomict "evolved" lithologies.

	Felsite 12033;507	Alk. A 14047c	Alk. N 14304c	Alk. A 14305c	Granite 14321c	Alk. GN 67975c
Plagioclase	6	84	14	95	—	—
Ca-rich ternary feldspar	—	—	tr	—	—	41
Fayalitic olivine	1	—	—	—	tr	—
Orthopyroxene	—	—	*	—	—	32
Pigeonite	—	16	75*	2	—	—
High-Ca pyroxene	1	—	*	1	tr	13
Ilmenite	1	tr	—	tr	tr	1
FeNi metal	—	tr	tr	tr	tr	tr
Troilite (FeS)	tr	—	tr	tr	—	tr
Quartz	—	—	—	—	40	—
Unspecified SiO ₂ minerals	33	—	tr	tr	—	11
K-feldspar	49	tr	tr	tr	60	tr
Zircon	—	—	—	—	—	0.3
Apatite	—	—	P	—	—	0.5
Whitlockite	—	—	P	2	—	tr
Unspecified Ca-phosphates	tr	—	2	—	—	—
Brownish glass	9	—	tr	—	—	—

* Pigeonite that has inverted into orthopyroxene + high-Ca pyroxene.

Abbreviations: Alk. = alkali; A = anorthosite; N = norite; GN = gabbro-norite; "tr" = trace; P = present.

References: Mostly compiled by *James et al.* (1987), which is the original source for 67975c. For 12033,507, *Warren et al.* (1987).

is that the plagioclase in alkali anorthosites is Na-rich, whereas plagioclase in ferroan anorthosites is uniformly Na-poor. Alkali anorthosites also have much higher contents of K, Rb, Cs, and other incompatible trace elements such as REE than do ferroan anorthosites (Fig. 6.34; Table A6.13).

Pyroxenes in alkali anorthosites are either low-Ca (pigeonite) or high-Ca (augite), or both. They tend to be Fe-rich, similar to the pyroxenes found in recrystallized ferroan anorthosites. The pyroxene crystals usually consist of a single mineral; exsolution to form inclusions of a second pyroxene is only rarely observed and is seldom extensive. *Hubbard et al.* (1971) describe a small sample of "high-K" anorthosite (12033,85c) that contains 1% olivine (70% forsterite) and no pyroxene at all. Several samples also contain 2-3% of the phosphate mineral whitlockite (*Warren et al.*, 1983c).

The alkali anorthosites appear related to a group of more mafic (lower-plagioclase) rocks with similar mineral compositions; examples are *alkali norite* (*Goodrich et al.*, 1986) and *alkali gabbro-norite* (*James et al.*, 1987). The latter rock contains plagioclase feldspar with a remarkably high K/Ca ratio (11-22% K-feldspar component within Ca-feldspar; see sections 5.1.2 and 5.1.5).

Typical mineral abundances for these rocks are listed in Table 6.10. Other minerals found in trace amounts among these alkali-rich rocks include ilmenite, zircon, apatite, K-Ba-feldspar, SiO₂ mineral(s), troilite, and Fe-metal.

By far the largest sample of an alkali-suite rock is a 1.6-g clast from breccia 14047; it contains 84% plagioclase and 16% pyroxene (*Warren et al.*, 1983a). The microscopic textures in this sample and in other samples of alkali lithologies typically reflect severe shock and/or thermal metamorphism (Fig. 6.35). The most "pristine" (or unaltered) texture observed among alkali lithologies is that of a small clast from breccia 12073 (*Warren et al.*, 1981); this texture resembles—and could easily be mistaken for—the monomict-breccia texture of a typical ferroan anorthosite (Fig. 6.30). Considering the small fragment sizes of the alkali rocks, it is conceivable that all of them are poorly representative and highly selective samples from a group of closely similar rocks with plagioclase contents of roughly 70-80%.

Lunar granites, and their finer-grained equivalents known as *felsites*, are much richer in K-feldspar and SiO₂ minerals than are other lunar rocks. Rocks intermediate in composition between granites and the anorthosite-norite-troctolite-gabbro group (e.g.,

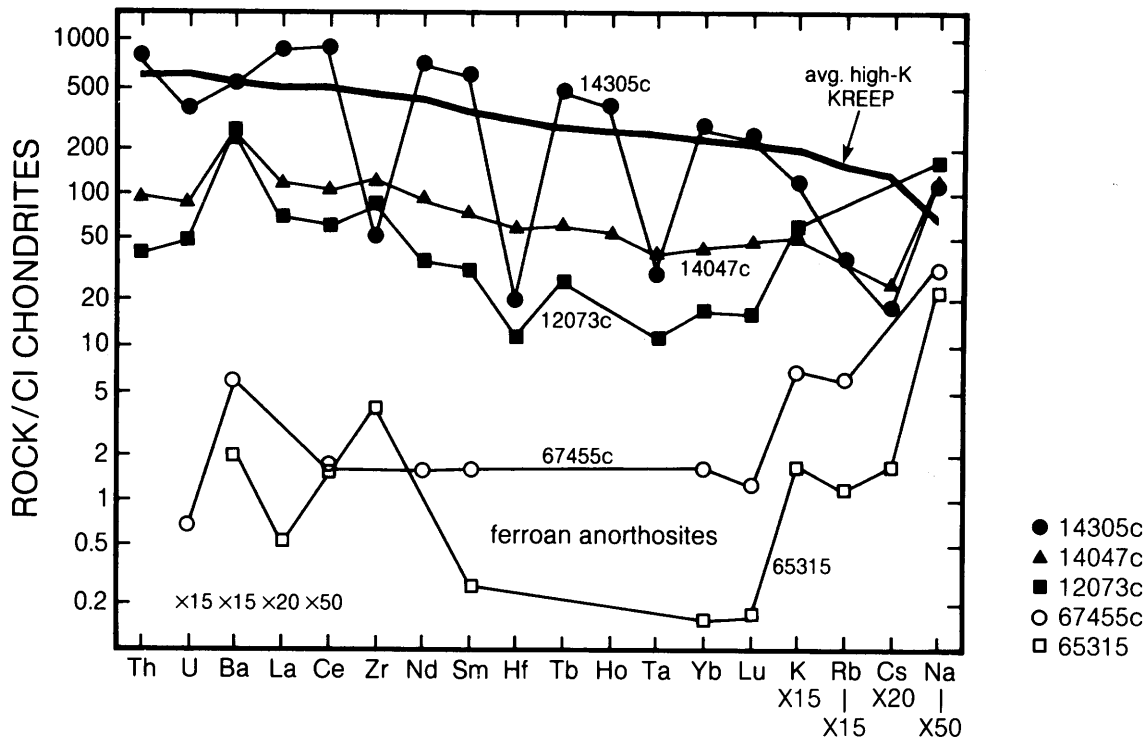


Fig. 6.34. Plots of incompatible-element contents in monomict alkali and ferroan anorthosite breccias. Element abundances are normalized to CI chondrite meteorites (Anders and Ebihara, 1982). Alkali anorthosites (filled symbols) have higher incompatible-element abundances than ferroan anorthosites (open symbols). Alkali anorthosite data: 12073c and 14047c from Table A6.13; 14305c from Warren *et al.* (1983c). Data for the two ferroan anorthosites (open symbols) are from Table A6.11 and encompass, at least for the REE, virtually the entire range of compositions observed among ferroan anorthosites. A lower-case “c” after the sample number indicates that a clast from within the sample was separated and analyzed.

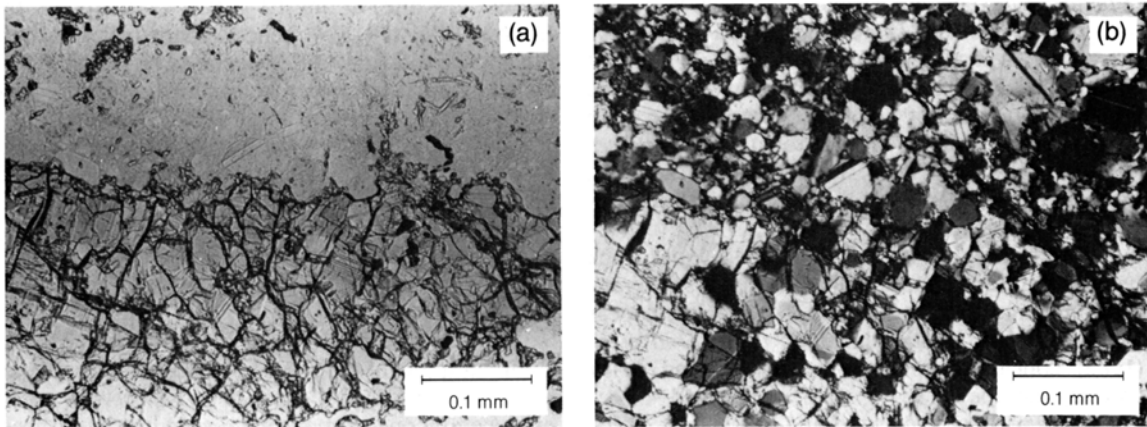


Fig. 6.35. Photomicrographs of alkali anorthosite 14047c. (a) The top half of this view shows an area typical of this sample; the bottom half shows the shattered, recrystallized remains of a single former large low-Ca pyroxene crystal (transmitted light). (b) Same view under cross-polarized transmitted light, showing the slightly granulitic texture and variable orientation of fragments of the shattered pyroxene.

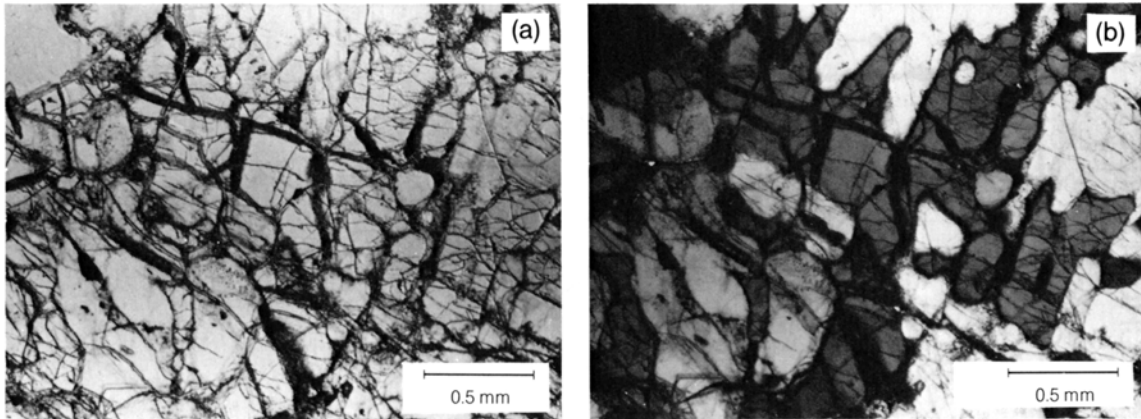


Fig. 6.36. Photomicrographs of an unusually well-preserved area of the brecciated “large” (1.8 g) granite clast from sample 14321. **(a)** “Graphic” intergrowth of quartz (dark grey) and K-feldspar (light grey and white; transmitted light). **(b)** Same view in transmitted light with crossed polarizers.

such terrestrial rocks as diorite, andesite, syenite, tonalite, etc.) are virtually unknown from the Moon. One possible intermediate variety, the “quartz monzodiorite,” observed only as clasts in breccia 15405, seems to be a coarse-grained variety of KREEP (see above).

Mineral compositions for typical granites and felsites are shown in Table 6.10. The granites, and even the finer-grained felsites, typically consist mostly of graphic intergrowths of K-feldspar and a silica phase (Shervais *et al.*, 1983). The largest granite, a 1.8-g clast from breccia 14321 (Warren *et al.*, 1983b) is a typical example (Fig. 6.36). The mafic minerals (pyroxenes or olivine) are simply more Fe-rich members of the same types found in the Mg-rich rocks. As in all lunar rocks, and in sharp contrast to terrestrial granites, lunar granites have no hydrous minerals (e.g., mica or amphibole). The felsites often consist largely of thin veins of brownish glass (James and Hammarstrom, 1977; Nord and James, 1978; Warren *et al.*, 1987). Typical bulk chemical compositions are listed in Table A6.13.

The ultimate origins of these odd lunar rock types—alkali anorthosites, alkali norites, and granites—are still poorly understood. The granites appear to be young for pristine highland rocks. Shih *et al.* (1985) concluded from Rb-Sr, Sm-Nd, and Ar-Ar studies that the 14321 granite crystallized 4.1 b.y. ago and was later excavated and brecciated 3.9 b.y. ago. Most other granites and felsites are either too small to analyze or not pristine (e.g., the felsite component of the 82-g polymict breccia 12013). However, Rb-Sr measurements on a relatively

undisturbed felsite clast from breccia 73215 indicate that 4.05 b.y. is a reasonable upper limit for its age (Compston *et al.*, 1977).

The granites and felsites are suspected to be the results of two processes: fractional crystallization accompanied by liquid immiscibility. If so, they could have formed as minor, late-stage components in subsurface igneous bodies that were producing larger volumes of more mafic rocks, i.e., Mg-rich rocks (Shih *et al.*, 1985; Warren *et al.*, 1987). No isotopic age measurements have yet been obtained on samples of the “alkali” lithologies, except for the high bulk-rock $^{87}\text{Sr}/^{86}\text{Sr}$ ratio (0.69963 ± 10) determined for one Apollo 12 alkali anorthosite by Hubbard *et al.* (1971). A genetic connection between the alkali rocks and KREEP seems firmly established by their similar trace-element patterns (e.g., Hubbard *et al.*, 1971; Warren *et al.*, 1983a; Shervais *et al.*, 1984b; James *et al.*, 1987), as well as by geographic association. One of the original names for alkali anorthosite (Hubbard *et al.*, 1971) was, in fact, “KREEP anorthosite.”

6.4. HIGHLAND POLYMICT BRECCIAS

All but a few of the samples collected in the lunar highlands are *polymict breccias* or *impact-melt rocks* produced by one or more meteoroid impacts. These rocks are mixtures of materials derived from different locations and different kinds of lunar bedrock. They contain varying proportions of two components: (1) broken or *clastic* rock fragments

(*clasts*), and (2) material melted by meteoroid impacts (*impact melt*). The latter material may occur in a range of forms from completely glassy to completely crystalline rocks. *Polymict breccias* consist chiefly of older rock fragments. *Impact-melt rocks* consist chiefly of the products of impact-produced melting, both glassy and crystalline.

The constituents of both fragmental polymict breccias and impact-melt rocks are derived from preexisting highland igneous rocks, plus a little meteoroid debris. However, the multiple impacts to which these components have been subjected have destroyed much of the direct evidence for what these precursors were, and all that remains are small rock fragments, mineral fragments, or molten mixtures. Some of the individual fragments in breccia samples are themselves fragments of older breccias and impact-produced melt rocks. Age determinations for these rocks can be very complex, and are discussed separately for each type of polymict breccia described in this section. [Note that all radiometric ages described in this section have been recalculated using the following decay constants: (^{87}Rb) = $1.42 \times 10^{-11}/\text{yr}$; (^{40}K) = $(0.581 + 4.962) \times 10^{-10}/\text{yr}$.]

As with all lunar samples, in no case do we have any polymict samples collected directly from bedrock. Many specimens of polymict rocks were collected as isolated samples from the lunar surface, and therefore nothing is known directly about their parent units. Other samples were chipped from displaced boulders of polymict breccia, where at least some local stratigraphic context is available from astronaut observations and photographs.

Polymict rocks show a wide diversity of textures, grain sizes, and chemical compositions. These features reflect the original nature and history of the individual components, the effects of the last impact that assembled the components, and the results of such subsequent processes as *lithification* (conversion of loose material into solid rock) and metamorphism (recrystallization). Lithification can result from the same impact that assembled the fragments if enough interstitial molten material is included, or by the application of heat and pressure at some later time. In many cases, lithification is so weak that the sample is very friable and falls to pieces with little handling.

Breccias consist of two textural components: (1) the *clasts* (individual fragments) and (2) the *matrix* that contains them. Clasts may be a wide variety of materials: fragments of igneous rocks or older breccias, or the shock-metamorphosed or melted derivatives of either. Generally, but not always, the clasts are internally at least as consolidated as the matrix and often more so.

The matrix material forms the host for the fragments and is finer grained. Three kinds of matrix are distinguished: solidified *melt* (crystalline or glassy), *clastic* (fragmental), or a *metamorphosed* clastic/melt mixture. A melt matrix consists of material that is entirely distinct from the clasts, although it may have formed in the same impact. Clastic and metamorphosed matrices are arbitrarily defined on the basis of grain size (usually as having grain sizes less than 25 μm). Breccias with these matrices generally have a wide range of fragment sizes, and the matrix fragments have populations and histories similar to those of the larger clasts.

A single large meteoroid impact can produce a variety of polymict rocks that range from totally molten and crystalline materials to masses of unconsolidated fragments. These materials may then be reworked by later impacts and incorporated into new breccias, many of which are therefore polygenetic. It is therefore almost impossible to trace a breccia sample, or one of its fragments, to a particular impact or a specific parent crater. The exceptions are some samples collected from rather small craters, e.g., glass-lined craters at the Apollo 15 landing site.

6.4.1. Nomenclature and Classification

At the time of the Apollo missions, little work had been done on terrestrial impact craters, so a ready-made and generally accepted classification for impact-produced polymict rocks did not exist. As a result, the nomenclature for lunar polymict rocks, most of which are fragmental or crystalline breccias, was built up rapidly during the Apollo missions on a piecemeal basis, without benefit of much prepublication discussion between different workers. Consequently the nomenclature and classification of lunar polymict rocks is confusing, duplicative (many different names are applied by different workers to the same samples) and often irrational (many terms are neither inclusive nor exclusive). Furthermore, the nomenclature changed as genetic interpretations developed and were modified. At first, there was a general impression that ejecta blankets were deposited hot, which gave rise to the incorrect belief that many crystalline samples were metamorphosed because of contact with, or burial in, layers of hot ejecta. Hence, the term "recrystallized breccia" was originally applied to rocks we now consider to have been formed instead by the crystallization of impact melts produced in a single impact event.

Stöffler *et al.* (1980) attempted to produce a more consistent, unified classification and nomenclature for lunar highland rocks, including polymict rocks, incorporating the recommendations of a Nomenclature Committee established by the Lunar and

TABLE 6.11. Classification, characteristics, and examples of highland polymict breccias (adapted from *Stöffler et al.*, 1980).

Class	Main Characteristics	Examples
Fragmental breccia	Angular clasts in a porous, clastic matrix of rock, mineral, and rare glass debris. Some melt clasts may be cogenetic with assembly (suevite). Most are friable.	14063, 67015, 67455
Glassy melt breccia and impact glass	Coherent glassy or devitrified glass matrix with (melt breccia) or without (impact glass) clasts.	60115, 68815, 60095, 79175
Crystalline melt breccia (impact melt breccia)	Rock or mineral clasts or both in an igneous (extrusive)-textured matrix (ophitic, subophitic, poikilitic, dendritic, etc.). May be fine- or coarse-grained, and clast-rich to clast-poor.	15455, 62295, 76015
Clast-poor impact melt	Igneous (extrusive)-textured rocks but containing meteoritic siderophile contamination. Textures can be slightly more heterogeneous than igneous rocks, and rare clasts may be present. Compositions can be unlike possible igneous-generated ones.	14310, 68415
Granulitic breccia and granulite	Rock or mineral clasts or both in an equilibrated, granoblastic to poikiloblastic matrix. Clasts may not be obvious, and poikilitic textures may mimic (or even be) siderophile contamination.	79215, 77017, 67955, 78155
Dimict breccia	Veined texture of intrusive dark fine-grained crystalline melt breccia with coarser-grained light-colored breccia consisting of plutonic or metamorphic fragments or both. In some cases the dark-light relationship is mutually intrusive.	61015, 62255, 64475
Regolith (soil) breccia	Lithified regolith. Regolith fragments including impact glass and volcanic debris with a glassy matrix. Commonly retain some solar wind gases through lithification process.	14318, 15299, 60019, ALHA 81005

Planetary Sample Team. These recommendations have been widely adopted, and their classification for polymict rocks is used here with slight modifications (Table 6.11). Table 6.12 is a list of the many previous names used (also adapted from *Stöffler et al.*, 1980).

The present classification leans heavily on more recent information from terrestrial impact craters; individual terms are based largely on observed textures and other objective features rather than on genetic or other interpretations. Additional characteristics (composition, detailed texture, grain size, visible shock effects) can be used as modifiers. While this system is a major improvement over the original state of affairs, it still represents a compromise between purely nongenetic and commonly used genetic terms, and it is therefore not entirely inclusive or exclusive.

The composite (and often reworked) nature of polymict lunar rocks makes their classification to some extent dependent upon the size of a sample. For instance, small samples of a fragmental breccia

might consist of individual pieces of metamorphosed crystalline rock, impact melt rock, or plutonic igneous rock. Several representative breccia samples are shown in hand-sample (macroscopic) photographs (Fig. 6.37) and in thin-section (microscopic) photographs (Fig. 6.38).

This descriptive classification is not entirely independent of the genesis of a sample. In particular, a distinction is made between the mechanical *assembly* of the components of a breccia and their *lithification* into coherent rocks. These processes may or may not take place in a single impact event. Figure 6.39, adapted from a concept of *Simonds et al.* (1976), shows the relationships for those breccias in which the same impact event produces both assembly and lithification. In these breccias, lithification is promoted mainly by the large amount of melt produced by shock-heating during impact. Such a breccia is a mixture of impact-produced melt (hot) and clastic material (cooler). When mixed, these materials thermally equilibrate in a short time (less

TABLE 6.12. Some of the more common previous names for polymict rocks (much simplified after Stöffler *et al.*, 1980).

Present Class	Previous Names	References
Fragmental breccia	Light matrix breccia (LMB)	<i>J. Warner et al. (1973)</i>
	Feldspathic breccia	<i>Chao et al. (1972a)</i>
	Clastic breccia	<i>Stöffler et al. (1979)</i>
Glassy melt breccia	Agglutinate	<i>Vaniman et al. (1976)</i>
	Glassy breccia	<i>R. Warner et al. (1976c)</i>
	Vitric matrix breccia	<i>Stöffler et al. (1979)</i>
Crystalline melt breccia	Annealed Fra Mauro breccia	<i>Chao et al. (1972a)</i>
	Metamorphosed breccia	<i>J. Warner et al. (1973)</i>
	Recrystallized noritic breccia	<i>Vaniman et al. (1976)</i>
	Crystalline matrix breccia	<i>Phinney et al. (1977)</i>
	Thermally metamorphosed breccia	<i>James (1977)</i>
Clast-poor impact melt	Pyroxene poikiloblastic breccia	<i>Delano et al. (1973)</i>
	High-alumina basalt	<i>Kushiro et al. (1972)</i>
	Fra Mauro basalt	<i>Ridley et al. (1972)</i>
Granulitic breccia	Basaltic impact melt	<i>Ryder and Norman (1980)</i>
	Polymict metamorphic breccia	<i>Stöffler et al. (1974)</i>
	Granulitic impactite	<i>J. Warner et al. (1977)</i>
Dimict breccia	Recrystallized ANT rocks	<i>R. Warner et al. (1978a)</i>
	Partially molten breccia	<i>LSPET (1973a)</i>
	Black and white rock	<i>J. Warner et al. (1973)</i>
Regolith breccia	Dike breccia	<i>Stöffler et al. (1979)</i>
	Dark matrix breccia (DMB)	<i>Wilshire and Jackson (1972)</i>
	Vitric matrix breccia	<i>Stöffler et al. (1974)</i>
	Soil breccia	<i>R. Warner et al. (1978a)</i>

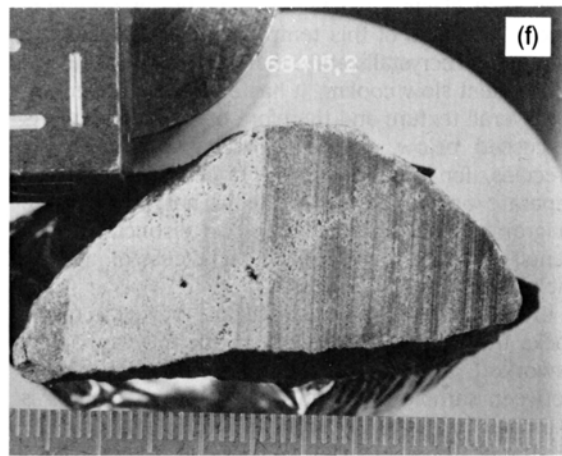
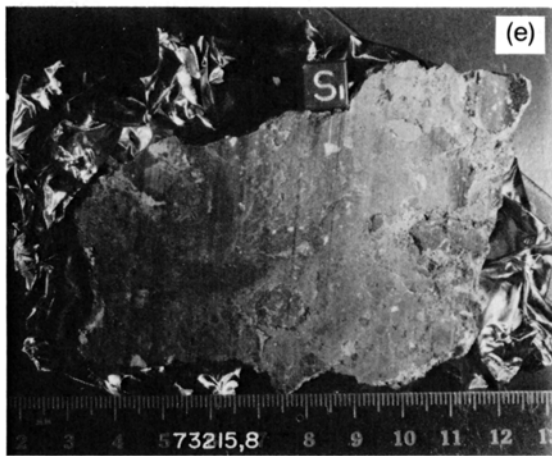
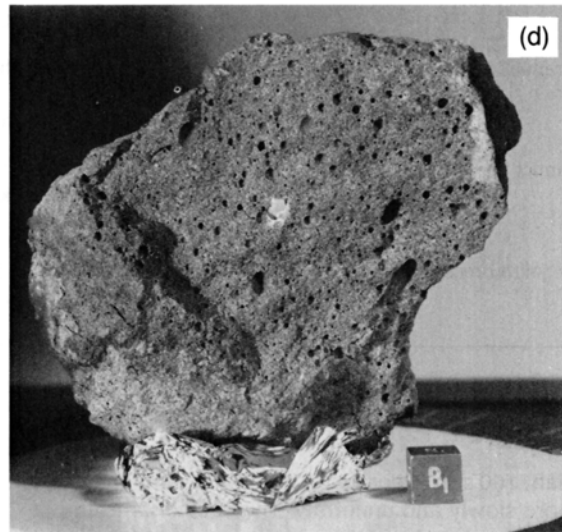
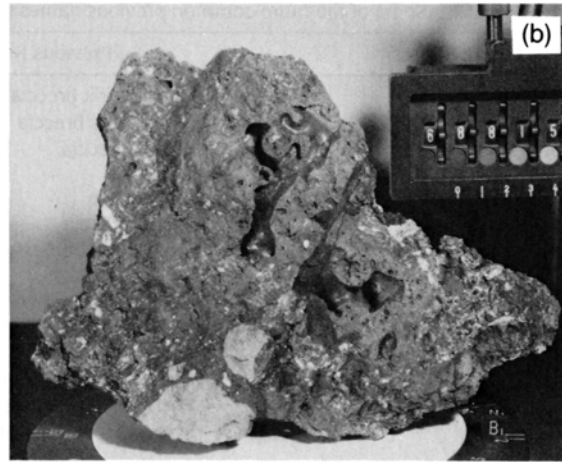
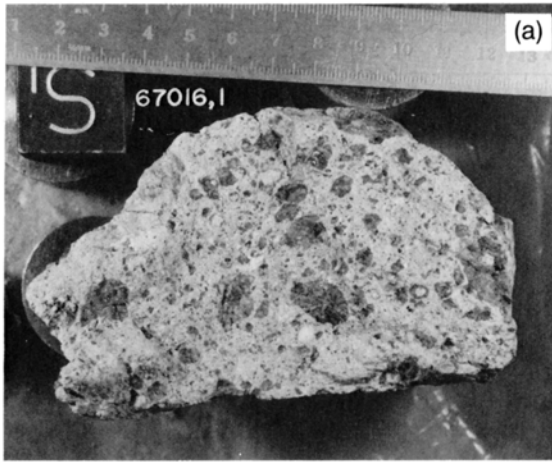
than 100 sec; *Onorato et al.*, 1976) and then cool more slowly and uniformly. The equilibrium temperature produced after mixing is largely a function of the melt/clast ratio; breccias with more hot melt than cold clasts have higher equilibrium temperatures. The value of this temperature determines the amount of recrystallization that will occur during the subsequent slow cooling; it has a dominant effect on the overall texture and therefore on classification. As discussed below, regolith breccias and granulitic breccias, for which assembly and lithification are separate and distinct events, do not plot on the diagram. *Dimict breccias* (with two distinct components) might be considered a special case of impact-melt breccias.

Craters in the lunar highlands are formed in target rocks that have previously been multiply impacted, reworked, and mixed together. The relationship between sample type and impact-crater features is sketched in Fig. 6.40. Multiple impacts cause the highland polymict rocks produced by the later

impacts to contain rocks and chemical components derived from a broad spectrum of lunar surface materials. This feature is illustrated by the comparative rare earth element concentration diagrams in Fig. 6.41. There is a wide and overlapping range of chemical compositions between fragmental breccias, glassy breccias, and melt rocks.

6.4.2. Fragmental Breccias

Polymict fragmental or *clastic* breccias are almost entirely composed of discrete fragments. Some monomict breccias are also fragmental (see section 6.3). Many specimens are porous and tend to fall apart very easily. Fragmental breccias consist of a variety of angular fragments of rocks or single mineral crystals embedded in a matrix of finely-comminuted similar materials (Fig. 6.37a). The individual fragments are bonded together only at limited points of contact, probably by a very thin layer of glass (*Nord et al.*, 1975). Deformation during lithification of these breccias has been minor; such



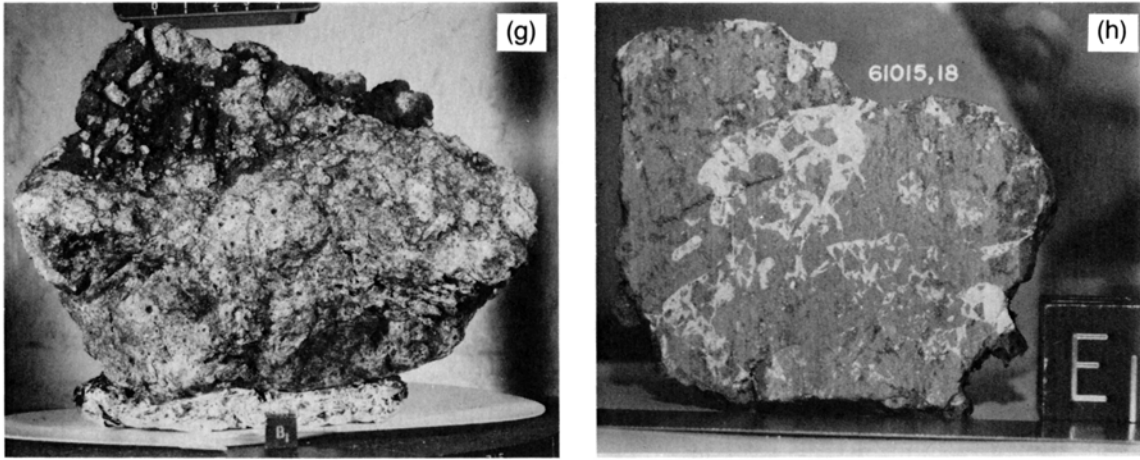


Fig. 6.37. Macroscopic views of lunar polymict breccias, showing the range of textures in this group of rocks. **(a)** Fragmental breccia 67016, sawn face, showing dark and light clasts in a finer fragmental matrix. Cube is 2 cm (NASA Photo S-75-32783). **(b)** Irregular glassy breccia 68815, broken face, showing clasts and irregular gas channels. Cube is 1 cm (NASA Photo S-72-37155). **(c)** Glass sphere 60095, showing broken surface and internal gas-produced vesicles. Cube is 1 cm (NASA Photo S-72-39424). **(d)** Crystalline melt breccia 77135, broken surface, showing numerous gas-produced vesicles and a lack of large conspicuous clasts. Cube is 1 cm (NASA Photo S-72-56391). **(e)** Fine-grained, schlieren-rich crystalline melt breccia 73215. Cube is 1 cm (NASA Photo S-73-38455). **(f)** Clast-free impact melt 68415, sawn surface showing a lack of prominent clasts but containing numerous very small vesicles. Slab is about 5 cm long (NASA Photo S-75-32778). **(g)** Granulitic (poikiloblastic) breccia 77017, showing adhering and intruding dark glass. Cube is 1 cm (NASA Photo S-73-17772). **(h)** Dimict breccia 61015, sawn face, showing mutually intrusive relationships of dark fine-grained melt and white cataclastic anorthosite. Slab is about 3.5 cm wide (NASA Photo S-75-20878).

delicate features as *deformation twins* (twin-crystal structures produced by pressure) are frequently preserved. The matrices, and many individual clasts, are contaminated with meteoritic siderophile elements (see section 6.3).

By definition, fragmental breccias do not preserve any physical features normally associated with the near-surface lunar regolith (see Chapter 7). Such features as glass-mineral agglutinate particles, glass spheres, or solar-flare tracks (e.g., *MacDougall et al.*, 1973) are absent.

Most known fragmental breccias were collected at the Apollo 16 landing site, but some prominent examples were collected from the Apollo 14 and Apollo 17 sites as well. The Apollo 16 fragmental breccias are highly enriched in plagioclase feldspar and, as a result, they contain more than 30% Al_2O_3 . Nearly all the specimens were collected from the rim of North Ray Crater, and they are probably derived from a subsurface unit in the North Ray area. Some samples were chipped from boulders of essentially similar rock. At the Apollo 14 site, a few fragmental

breccias collected from the rim of Cone Crater are less feldspathic. At the Apollo 17 site, a fragmental breccia makes up the matrix of Boulder 1 at Station 2. It therefore seems likely that a large part of the upper highland crust consists of deposits of fragmental breccia, which vary in composition between different regions.

Petrography and chemistry of fragmental breccias. Fragmental breccias consist of clasts of a variety of materials—other breccias, igneous rocks, and single mineral grains (Figs. 6.37a and 6.38a,b). Glass is present in some specimens, but most are glass-poor. The clasts are generally angular; they range in size from submicroscopic to several centimeters across, and they have varying intensities of shock metamorphism. *Stöffler et al.* (1980) distinguished two subclasses of fragmental breccias, according to the presence or absence of glassy melt particles with the same composition as the bulk rock, which were presumed to have been generated in the same impact that formed the breccia. This distinction has not often been attempted; *Norman*

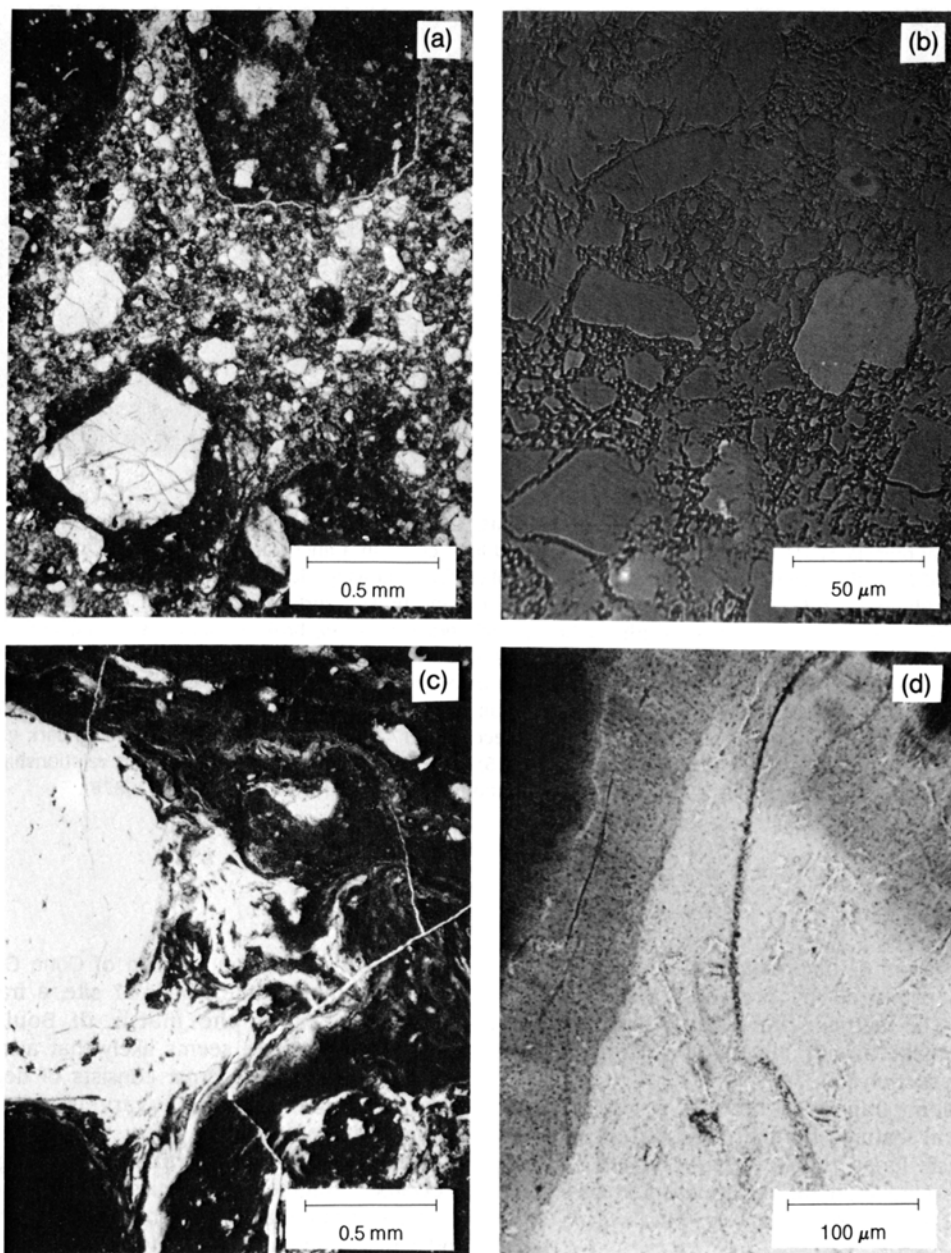


Fig. 6.38. Photomicrographs of lunar polymict breccias, showing the range of microscopic textures developed in this group of rocks. **(a)** Fragmental breccia 67016 in transmitted, plane-polarized light, showing dark melt clasts and mineral fragments. **(b)** Fragmental breccia 67016, the same sample as in **(a)**, photographed in reflected light, showing the fragmental and porous nature of the matrix, which is mainly plagioclase fragments (dark gray) with less abundant mafic grains (pyroxene and olivine, lighter gray). **(c)** Glassy breccia 68815 in transmitted, plane-polarized light, showing the irregular swirled texture produced by flow structure in the glass and occasional clasts. Clear glass is clast-free and undevitrified; dark areas of glass are clast-rich, and the glass is at least partly devitrified or crystallized. **(d)** Glassy crystallization front in breccia 66095 in transmitted, plane-polarized light. Clear areas are undevitrified glass; darkest areas are massive, spherulitic, devitrified glass. The intermediate zone shows a fibrous texture with crystals perpendicular to the contacts.

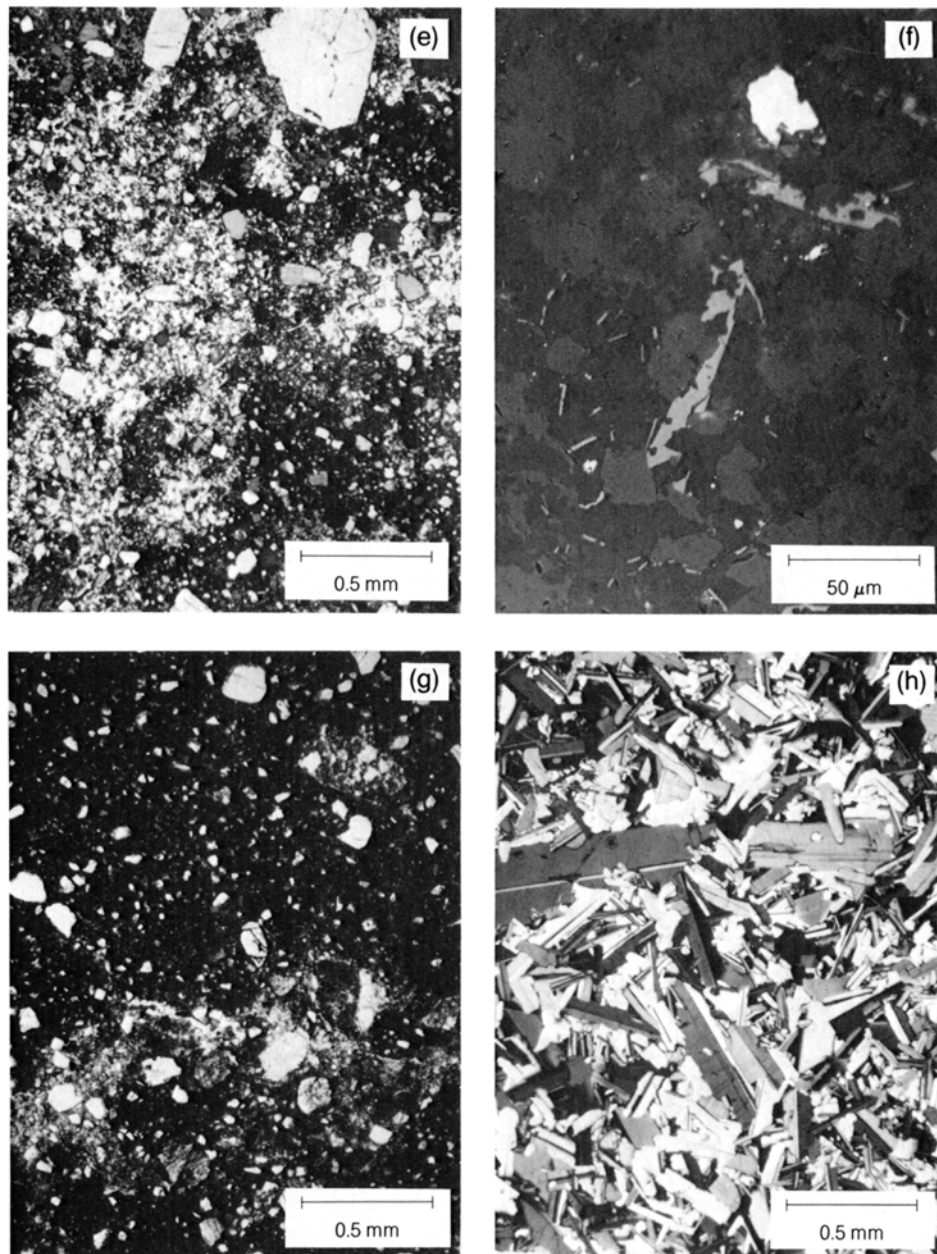


Fig. 6.38. (continued) **(e)** Poikilitic crystalline melt breccia (impact melt) 65015 in transmitted light with crossed polarizers. Distinct small clasts, mainly plagioclase, are common. Millimeter-sized zones of constant color (white, gray, black) are large pyroxene crystals (oikocrysts) in which numerous smaller crystals are embedded. **(f)** Intergranular area (*mesostasis*) of poikilitic melt particle 15423,40 in reflected light, showing late-stage crystallization products. Tiny very dark gray areas (mainly triangular) are interstitial residual silicic glass; dark gray is plagioclase; medium gray is pyroxene; tiny to moderate-sized very pale gray crystals are ilmenite; white bleb near top is Fe-Ni metal. **(g)** Very fine-grained (*aphanitic*) impact melt 73215 in transmitted, plane-polarized light. Flow lines of heterogeneous glass (*schlieren*) occur lower in the photo, and rounded mineral clasts are common. Individual groundmass crystals are too small to be distinguished at this scale, and the groundmass therefore appears massive and dark. **(h)** Crystalline (subophitic/ophitic) clast-poor impact melt 68415 in transmitted light with crossed polarizers. Lath-shaped (striped) crystals are plagioclase; the most abundant interstitial mineral is olivine.

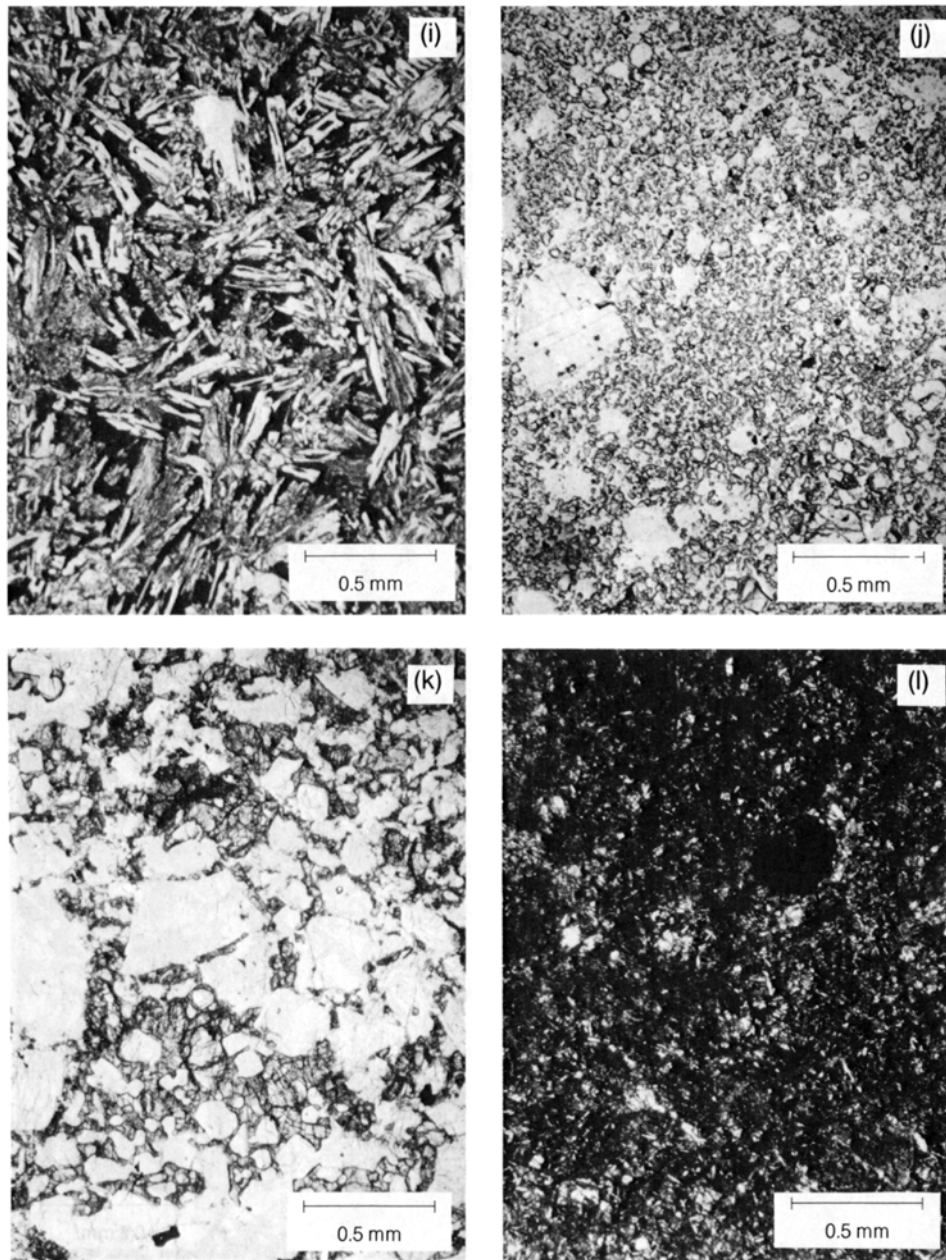


Fig. 6.38. (continued) **(i)** Crystals in glass (*vitrophyre*): Clast-poor impact melt 62295 in transmitted, plane-polarized light. Skeletal (hollow) olivine crystals are embedded in a glassy groundmass (black). Clasts are very rare. **(j)** Recrystallized (*granulitic*) breccia 79215 in transmitted, plane-polarized light. Sample is a fine-grained variety. The tiny grains are mainly olivine and pyroxene, and the bulk of the sample (including most of the obvious mineral clasts) is made up of plagioclase. **(k)** Recrystallized (*granulitic*) breccia 77017 in transmitted, plane-polarized light. The texture formed by small stubby plagioclase crystals (white) embedded in larger pyroxene crystals (gray) is *poikiloblastic*. More than one episode of brecciation can be recognized in this specimen. **(l)** Melt-rich component (dark-colored) of dimict breccia 61015 in transmitted, plane-polarized light. Melt is very fine-grained (tiny plagioclase laths are visible) and glassy (dark groundmass), and contains some vesicles. Clasts are visible in this view, but they make up only a small proportion of the rock.

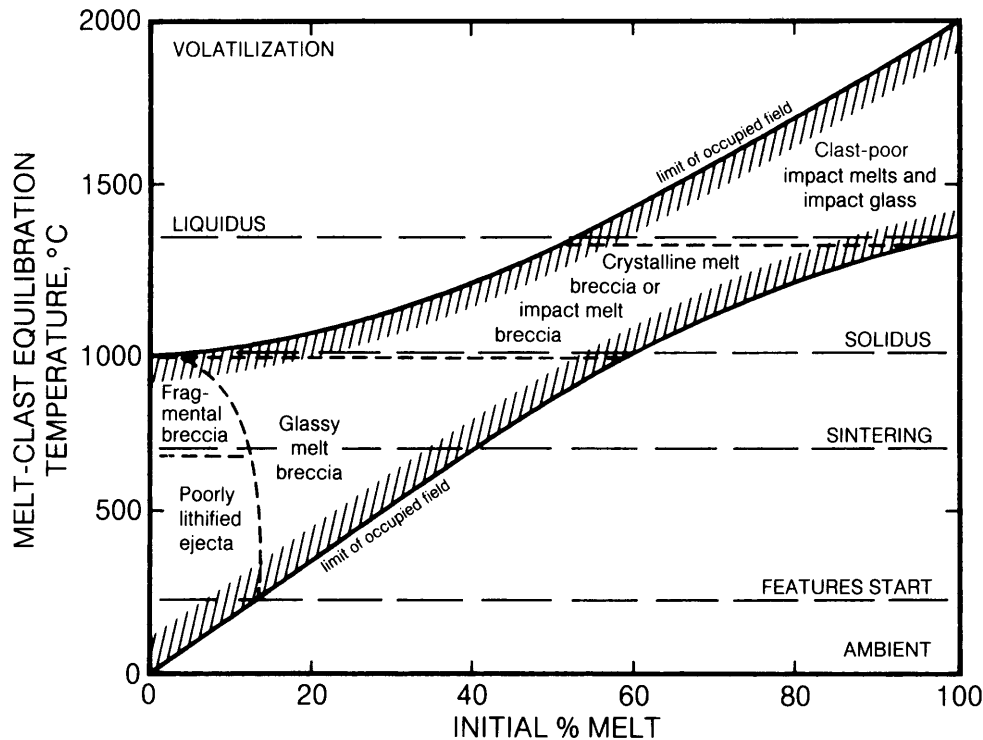


Fig. 6.39. Generalized scheme showing the relations between petrographically distinct impact breccias produced and lithified in a single impact event as a function of the amount of melt originally present and the equilibrium temperature attained between clasts and melt (figure modified from *Simonds et al.*, 1976). The textures of resulting breccias are assumed to be controlled by the initial process of rapid thermal equilibration between clasts and the enclosing melt. Subsequent cooling rates will have some, but much less, effect on matrix textures. Fields in which different breccias occur on the diagram are approximate, and the locations of liquidus, solidus, and other transformation boundaries will vary with bulk composition. Dimict breccias, granulitic breccias, and regolith breccias do not plot as classes on this diagram. Regolith breccias could be classified as glassy melt breccias or fragmental breccias, but they differ in that they are commonly lithified from loose fragments of lunar soil by an impact event that is separate from (and later than) those that produced the assemblage of fragments. Similarly, lithification of granulitic breccias is usually the result of recrystallization long after assembly of the fragments. Dimict breccias can be considered a special case of crystalline melt breccias.

(1981) identified such genetically-related melt fragments in breccia 67016, as did *Marvin et al.* (1987) in breccia 67015.

The Apollo 16 fragmental breccias consist mainly of plagioclase feldspar. They contain three dominant types of rock fragments: (1) cataclastic anorthosite, (2) granulitic breccia, and (3) fragment-rich feldspathic impact-melt rocks (*James*, 1981; *Stöffler et al.*, 1981, 1985; *R. Warner et al.*, 1976a; and others). The impact-melt clasts are dark, while the anorthosites and granulites are light colored.

The impact-melt clasts have significant variations in mineral and chemical composition. In sample 67455, a fairly typical specimen, half the mineral grains larger than 40 μm are plagioclase and about

10% are olivine and pyroxene (*Minkin et al.*, 1977). Fragments of cataclastic anorthosite make up about 12% of this rock, granulites about 8%, and impact melts about 8%.

However, the Apollo 16 fragmental breccias are not all the same. Sample 67015 contains a more diverse assemblage of fragments, including (1) anorthositic norites that are related to ferroan anorthosites and (2) less aluminous KREEPy impact melts (*Marvin and Lindstrom*, 1983; *Marvin et al.*, 1987; see section 6.3). *Stöffler et al.* (1985) studied the modal and textural characteristics of many of these Apollo 16 fragmental breccias from North Ray Crater and found that the relative proportions of different rock types in the lithic fragments vary

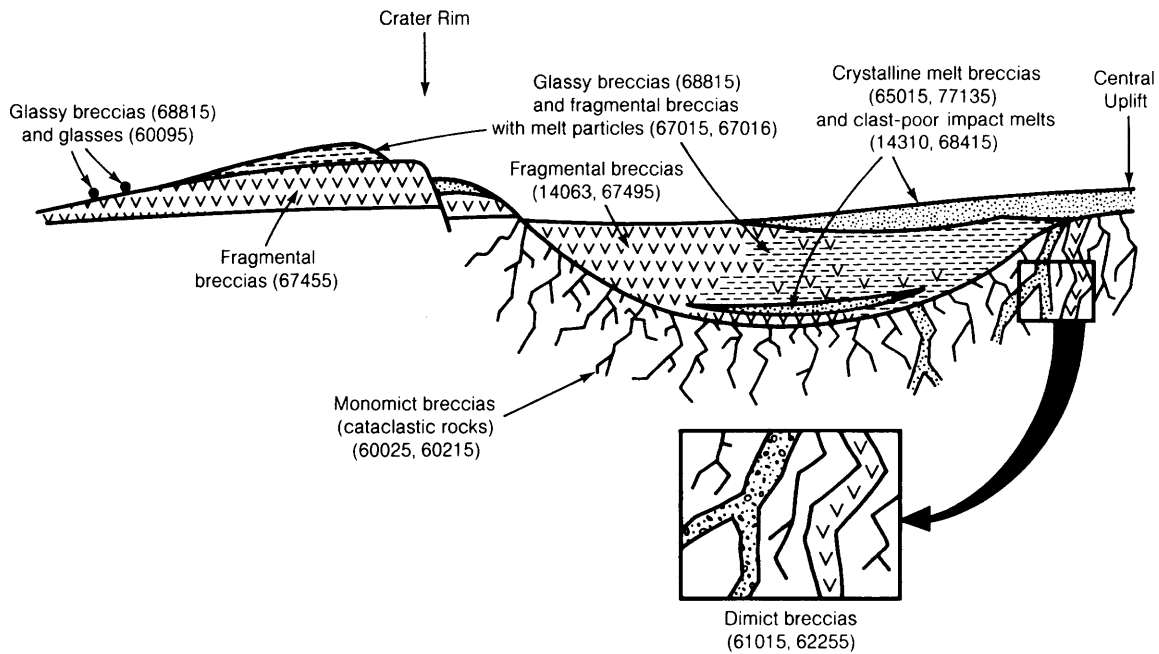


Fig. 6.40. Cross-section of an ideal lunar crater showing the relations of different polymict breccia types and possible monomict breccias to the geological environment of the crater (adapted from *Stöffler*, 1981). Numbers indicate actual lunar samples that are examples of the different breccia types. In reality, most lunar polymict breccias are the result of a series of impacts, and in almost all cases the target for each new breccia-producing impact is already a polymict breccia.

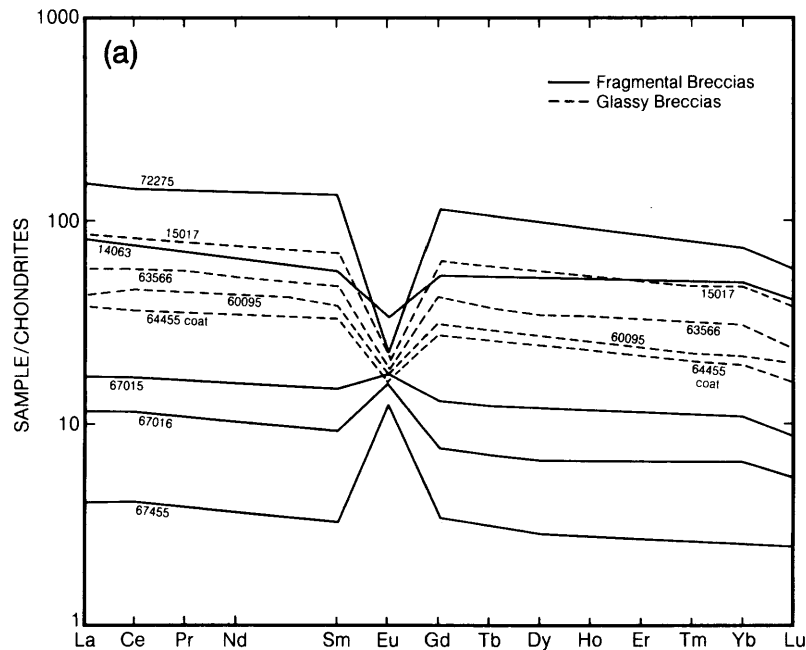


Fig. 6.41. Representative rare earth element (REE) distribution diagrams for lunar polymict breccias: (a) fragmental and glassy breccias.

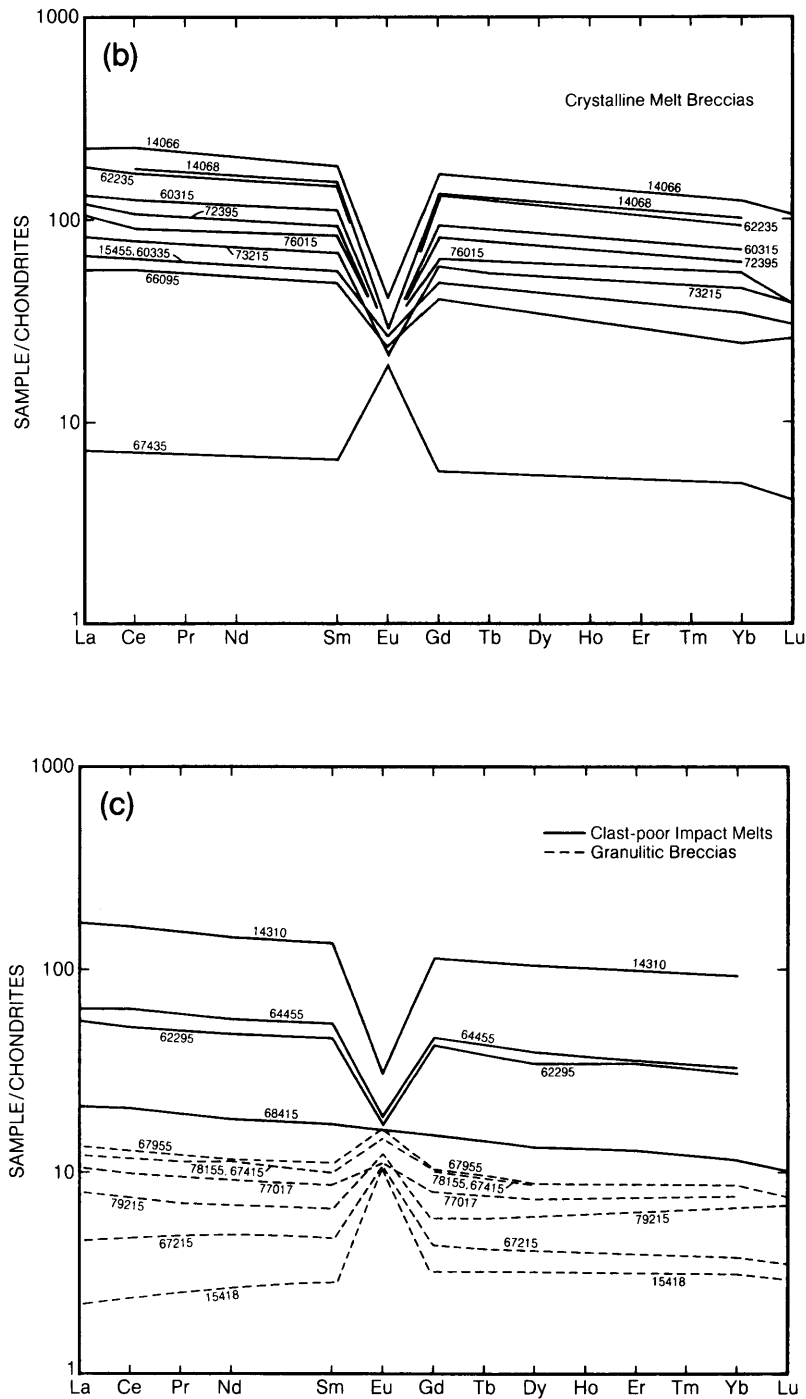


Fig. 6.41. (continued) **(b)** Crystalline melt breccias; **(c)** clast-poor impact melts and granulitic breccias. REE abundances are normalized to chondritic meteorites and are plotted on a logarithmic scale. The distributions show a general enrichment in light REE (curves are higher at the left side of the diagram) with either positive or negative Eu anomalies. In a few cases, the Eu point is omitted and the connecting lines have not been completed because their inclusion would clutter the diagram.

TABLE 6.13. Frequency % of lithic clasts (grain size: 0.05-4 mm) in Apollo 16 Stations 11 and 13 fragmental breccias measured by sectioned area in thin sections (Stöffler *et al.*, 1985).

Sample	n	1	2	3	4	5	6	7	8	9	10	11
63588,4	90	15.3	34.6	1.3	—	22.7	—	3.1	—	1.8	21.1	—
63595,4	88	22.5	13.9	20.8	0.6	6.5	3.8	2.8	—	—	29.0	—
67455,57	111	10.9	35.9	33.2	—	5.4	—	0.6	10.5	—	3.5	—
67455,61	139	5.2	63.4	24.4	—	—	—	2.8	1.4	—	2.8	—
67495,3	93	18.9	27.4	44.9	—	3.5	—	1.1	—	—	4.2	—
67517,3	156	5.4	86.9	6.3	—	—	—	—	—	1.4	—	—
67526,4	79	5.2	87.2	7.6	—	—	—	—	—	—	—	—
67527,1	30	1.8	85.0	13.2	—	—	—	—	—	—	—	—
67528,1	68	21.2	56.5	11.7	—	1.3	—	—	—	—	4.7	4.7
67545,4	36	—	90.2	9.8	—	—	—	—	—	—	—	—
67457,1	65	46.0	5.5	41.5	—	—	—	—	—	—	7.0	—
67549,5a	57	—	2.6	59.1	0.9	10.2	—	—	—	—	—	27.2
67549,5b	79	—	3.8	39.0	3.4	14.5	—	—	—	—	—	39.4
67639,2	121	18.2	15.4	62.6	—	—	—	3.7	—	—	—	—
67645,3	79	20.1	18.1	55.8	—	—	—	2.5	—	—	3.4	—
67647,2	79	1.3	3.8	88.4	—	—	—	5.7	—	—	0.8	—
67649,5	35	—	20.0	74.1	—	—	—	—	—	—	5.9	—
67655,1	55	14.1	63.6	—	—	—	—	20.8	—	0.1	0.8	0.7
67656,3	31	19.1	18.5	62.4	—	—	—	—	—	—	—	—
67657,7	58	51.5	40.9	7.6	—	—	—	—	—	—	—	—
67669,27	24	—	47.4	50.2	—	—	—	2.3	—	—	—	—
67706,2	121	7.9	15.6	73.1	0.3	—	—	0.3	—	—	2.4	0.4
67707,17	96	24.8	13.9	61.0	—	—	—	0.3	—	—	—	—
67768,3	65	24.6	42.5	32.0	—	—	—	—	—	—	0.9	—
67975,80,13	358	16.4	29.3	0.9	51.2	0.9	—	0.8	—	—	0.6	—
		2213										
Weighted average		14.4	35.7	30.6	8.4	2.6	0.15	1.7	0.6	0.2	3.4	2.3
Error (95% confidence):		±1.6	2.0	2.0	1.2	0.5	~0.07	0.4	~0.2	0.08	0.7	0.5

n = number of analyzed clasts; 1 = granulitic rocks and breccias; 2 = recrystallized cataclastic anorthosite; 3 = feldspathic microporphyritic melt breccia (MB); 4 = mafic microporphyritic MB; 5 = intergranular MB; 6 = micropoikilitic MB; 7 = fine-grained subophitic-ophitic-intersertal MB; 8 = coarse-grained subophitic-ophitic-intersertal MB; 9 = vitric or partly devitrified (impact) glass; 10 = devitrified (variolithic) glass; 11 = unrecrystallized cataclastic anorthosite. Weighted average (bottom) is based on n.

considerably from sample to sample (Table 6.13). However, it is obvious that the heterogeneity and the coarse fragment size in these samples produce variations even among determinations on the same sample. Stöffler *et al.* (1985) also found differences in the compositions of metal grains in the matrices of different samples.

The Apollo 16 fragmental breccias are all highly aluminous and have similar, but not identical, chemical compositions (Tables A6.14-A6.16). The Mg/Fe ratios vary substantially, although all the samples are rather ferroan when compared to the full range of lunar highland samples. The bulk composition of the Apollo 16 breccias seems to be dominated by ferroan anorthosites and other ferroan plutonic highland rocks (e.g., Stöffler *et al.*, 1985). Most of the incompatible elements are provided by a small component of KREEPy and magnesian impact melts.

The Apollo 14 fragmental breccias (samples 14063, 14064, and 14082/14083) contain much less plagioclase and hence have lower alumina contents than do the Apollo 16 samples (Table A6.14). These samples have been described briefly by Warner (1972), Steele and Smith (1976), and Ryder and Bower (1976). They contain a wide range of fragment types; fine-grained KREEPy impact melts and troctolitic breccias are prominent. Other fragment types include fine-grained or glassy melt rocks, granulites, norites, anorthosites, and rare mare basalts.

The only large fragmental breccia (sample 72275) recognized among Apollo 17 samples formed the matrix of Boulder 1 at Station 2. It is a highly complex rock that appears to be the crushed remnants of a mixture of KREEPy basalt and fine-grained KREEPy impact melts, which make up other parts (and samples) of a single boulder (Ryder *et al.*, 1975). Some fragments have melt rinds, a feature

that could have been produced by inflight agglomeration of the fragment and melt during ejection from the impact crater. A few other clasts, norites and granulites, are also present. The dominance of the KREEPy basalts in this sample is reflected in its chemical composition (Tables A6.14-A6.16).

The fragments of single minerals in the fragmental breccias range widely in composition, both within and between individual samples. This situation demonstrates the diverse nature of the source materials and the polymict origin of the rock. It also shows that the rocks have not been thermally metamorphosed since their assembly; intense metamorphism at high temperatures would tend to homogenize the different mineral grains to a single equilibrium composition. The mineral fragments generally resemble crystals in the coarser-grained rock fragments such as ferroan anorthosites. In some cases, they suggest unsampled rock types. For example, the Apollo 14 fragmental breccias contain some coarsely-exsolved pyroxenes apparently derived from slowly-cooled plutonic norites; however, no fragments or other samples of the parental norites themselves have been discovered.

Ages of fragmental breccias. Fragmental breccias consist of discrete fragments with diverse origins and ages; some of them have been dated by radiogenic isotope methods. None are younger than 3.9 b.y. and some are older. Interpretation of these results is complicated by the fact that a fragmental breccia may have two different "ages": One is the time that the fragments were assembled, the other is the time when the fragments were lithified (solidified into a rock). These two events may be simultaneous or they may be separated by a significant interval of time. To make things more complicated, neither event can generally be dated by radiogenic isotope methods because heating during either event is generally not intense enough to reset the original isotopic systems to the new time.

However, the ages of these events can sometimes be dated. *Malvin et al.* (1987) identified some melt clasts in Apollo 16 breccia 67015 that had been hot and plastic during assembly and were therefore produced by the impact that assembled the breccia. These clasts were dated at 3.9 b.y. (^{40}Ar - ^{39}Ar method), an age that is common for melt fragments in these and other rocks. Because no fragments younger than 3.9 b.y. have been identified among Apollo 16 fragmental breccias, it has been assumed that these breccias were assembled by a major impact 3.9 b.y. ago.

Coatings of glass are observed on some breccia samples, apparently splashed onto them by later impacts in the vicinity of the sample. Because these coatings cannot be older than the time when the

breccias were lithified (and may be much younger), they could provide minimum age estimates for the time of lithification. Unfortunately, little reliable information on the age of these coatings is available.

There are few age data for rock fragments in the Apollo 14 fragmental breccias. The KREEPy melt clasts that dominate these breccias are 3.8 b.y. old (*Bernatowicz et al.*, 1978), not significantly different from ages of other Apollo 14 rocks, and there is no compelling reason to believe that their chronology is significantly different from that of other highland rocks. The age of the fragmental breccia that forms the matrix of Boulder 1 at Station 2 at the Apollo 17 site is at present known only to be younger than its clasts, which have been dated at 3.9 b.y. (*Leich et al.*, 1975; *Compston et al.*, 1975).

Origins of fragmental breccias. Fragmental breccias were assembled and lithified while cool, in most cases about 3.9 b.y. ago. Because they do not contain any near-surface (regolith) components, their components must have been derived from considerable depth during the formation of substantial craters that penetrated the regolith, and the breccias themselves were assembled as large, blanket-like deposits around these craters.

The composition and characteristics of the Apollo 16 fragmental breccias have led many workers to believe that many of them represent material from the Descartes Formation, which is, in turn, thought to be a large deposit of ejecta from the Nectaris Basin (e.g., *Stöffler et al.*, 1985; *James*, 1981; *Norman*, 1981). This interpretation is consistent with orbital geochemical data. However, the KREEP-bearing Apollo 16 breccias may be derived from the younger Cayley Plains unit, which may be ejecta from the Imbrium Basin (*Stöffler et al.*, 1985; see section 10.6.5). The mild lithification observed in both breccia types could have taken place immediately after deposition or it may have been produced much later, possibly during their excavation by the formation of North Ray Crater in the immediate vicinity (e.g., *Nord et al.*, 1975). Because large basin-forming impacts such as the Imbrium and Nectaris events were common during the intense lunar bombardment that waned about 3.9 b.y. ago, and because the bulk of ejecta from any impact crater is deposited cold, it seems quite likely that a major portion of the upper part of the lunar crust consists of material similar to the Apollo 16 feldspathic fragmental breccias.

The origin of the Apollo 14 fragmental breccias is much less clear, mainly because their bulk chemistry is less well established and the context of the samples at the site is less well known. The Apollo 14 breccias contain some fragments of deeper crustal rock types as well as KREEPy melts, and their overall

bulk compositions may not be too different from those of the local, near-surface regoliths. The breccias suggest that there may be remnants of the upper lunar crust in the Fra Mauro region, from which both the regoliths and Apollo 14 impact melts were made.

The Apollo 17 fragmental breccia (the Boulder 1, Station 2 matrix) appears to have been produced by a much smaller impact than that which formed the Apollo 16 fragmental breccias, because it is dominated by materials (basalt and impact melt) that originally crystallized at the lunar surface.

6.4.3. Glassy Melt Breccias and Impact Glasses

Glassy materials produced by meteoroid impacts vary widely, depending on the amount of glass present. These materials range from extremely clast-rich breccias with glassy matrices (*glassy melt breccias*) to glass-rich bodies that are clast-poor or clast-free (*impact glasses*). Glassy melt breccias are polymict; they show a wide range of fragment types and there may be more than one generation of glass involved in their formation and lithification. The shapes of samples of glassy melt breccias are generally irregular and some are slaggy (Figs. 6.37b and 6.38c). Impact glasses appear to have formed and cooled in single impacts. Many samples are ovoid and some are hollow. A distinctive feature of most impact glasses is the presence of a free melt surface (Fig. 6.37c), in contrast with most breccias, including glassy melt breccias, which have mechanically broken surfaces.

The distinction between glassy melt breccias and impact glasses on the one hand, and crystalline melt breccias or clast-poor impact melts (which are also formed by meteoroid impact) on the other (sections 6.4.4 and 6.4.5), is the degree of crystallization of the melt. Impact melts that have been slowly cooled are largely crystalline, and they show textures indicating that their crystals formed in equilibrium with the melt at high temperatures. The glassy melt breccias and impact glasses can be considered as impact melts that were cooled too rapidly for crystallization to occur. *Devitrified glasses*, in which microscopic crystals have formed in the solidified glass, are also included in the category of glassy rocks.

There are several ways to distinguish between impact-produced glasses and glasses formed by volcanic processes. Volcanic glasses contain only rare broken rock and mineral fragments and are homogeneous. They also lack the high contents of siderophile elements that indicate meteoritic contamination (see section 6.1.7 and Chapter 8). An

additional, simple distinction is that all sampled lunar glass particles more than a few millimeters across are impact-produced, not volcanic. Examples of impact glasses that form coatings on chemically unrelated rocks are common. In these cases, the impact glass has been splashed onto nearby exposed rocks or the rock was entrained during flight of the melt.

Petrography and chemistry of glassy breccias and impact glasses. These rocks form a diverse group whose members share the common characteristic of a glassy (vitric) groundmass. In impact glasses, this groundmass may constitute virtually the entire rock.

Glassy melt breccias contain fragmental minerals and rocks; *schlieren* (flow layering) and vesicles are common in the glassy groundmass. Some samples are slaggy or cindery. Glassy melt breccias can be distinguished from *regolith breccias* formed near the surface because they have little or no surface-produced agglutinates (section 7.1.3), solar wind gases, or glass spheres. However, such distinctions are difficult in some cases. The groundmass glass can be heterogeneous and may have several different generations, but many samples have a dominant "latest" glass groundmass. These groundmass glasses form veins and protrusions throughout the rock.

Few detailed studies of glassy breccias have been made. One sample (68815, weighing 1789 g), which was chipped from a boulder at the Apollo 16 landing site, consists of many lobes of glass (Fig. 6.37b). *Brown et al.* (1973) described it as a "fluidized lithic breccia." The glasses vary in composition, color, and banding. The clasts in 68815 are commonly angular and consist dominantly of fine-grained impact melts that are much less aluminous (about 22% Al_2O_3 ; *Brown et al.*, 1973) than either the glass (26-30% Al_2O_3) or the average composition of the rock (about 27% Al_2O_3 ; Table A6.17). Two larger clasts are apparently *granulitic* breccias. The overall chemical composition of this breccia is similar to that of local soils at the Apollo 16 site.

Impact glasses occur as relatively small particles, generally less than a few centimeters across. They characteristically have at least one surface where the glass was chilled. Impact glasses are rarely optically homogeneous on scales of more than a few millimeters; heterogeneous and *schlieren-rich* glasses dominate. In shape, impact glasses range from spheres to ovoids to angular, blocky fragments with vesicles. Some occur as individual pieces resembling volcanic "bombs."

Most impact glasses have been found as coatings or drapings on rocks. These impact glasses have been found at most Apollo sites, and those from the

Apollo 16 site have been the most studied (See *et al.*, 1986; *Morris et al.*, 1986; *Borchardt et al.*, 1986). The glass drapings have sharp boundaries against the host rock, and differ from the host rock in chemical composition. These coatings were clearly not formed by fusion of the rock (i.e., they are not analogous to the fusion crusts found on meteorites). Instead, the glass seems to have been splashed onto the rocks, probably from nearby meteoroid impacts.

The presence of distinct crystallization fronts (Fig. 6.38d) in both glass bombs and melt splashes indicates that devitrification (subsolidus crystallization) has occurred (See *et al.*, 1986). Other samples have intersertal textures (with interstitial glass), indicating crystallization from a melt. In some samples, such textures may perhaps even be dominant, implying that the specimen should be classified as an impact melt. However, the outwardly glassy appearance of the samples and the presence of smooth exterior surfaces make it more convenient to include them with the impact glasses.

Rock and mineral fragments are common as inclusions in impact glasses. Among such inclusions, mineral fragments, particularly plagioclase, are most abundant (>80%), and various types of anorthosite predominate among the lithic clasts. Some fragments of earlier-formed impact-melt rocks and polymict breccias are also present, but the inclusion population is biased toward plagioclase. Most crystals have textures indicating that they are either unshocked or only moderately shocked and heated (<30 GPa; <300° C).

At the Apollo 15 landing site, glass coatings and some glass spheres are common. A few glass samples were collected from the glassy linings of small craters about a meter or two in diameter. These samples have not been studied in detail, but preliminary examination shows that they have petrographic characteristics similar to those of the Apollo 16 glasses. At both the Apollo 15 and 17 landing sites, neither the glassy breccias nor the impact glasses can be considered as purely highland samples. Most samples, both petrographically and chemically, have a major mare basalt component, and many were collected from the mare plain itself. Large (5-10 cm) samples of impact glasses are uncommon from the Apollo 11-14 missions, and the few specimens have not been well characterized.

Chemical compositions of some glassy melt breccias and impact glasses are listed in Tables A6.17-6.19. The Apollo 16 impact glasses are fairly homogeneous individually, but there is considerable chemical variation among samples (24-30% Al₂O₃; 2-6% FeO; See *et al.*, 1986) (Fig. 6.42). Most of the samples form a group that is chemically unlike local regoliths in having higher Mg/Fe ratios and

lower Al₂O₃ contents. These samples appear to be mixtures of anorthosite and a low-Sc type of very-high-alumina (VHA) impact melt (for a discussion of VHA, see section 6.4.4). A second group of samples is rather like the local regoliths and is comparatively enriched in a higher-Sc type of VHA impact melt or anorthositic norite. They also contain a minor high-Ti component (mare basalt?), which is absent from the first group (*Morris et al.*, 1986). All the glassy specimens, regardless of their chemical composition, are very enriched in meteoroid material, averaging over 7%, as indicated by their siderophile element abundances, which is higher than most regoliths or other breccias (Table A6.19). This meteoroid component apparently comes from chondritic meteoroids (*Morris et al.*, 1986). Impact glasses from the Apollo 15 site are chemically similar to the local regoliths and also have high meteoroid siderophile contamination. Their chemical composition indicates that most of the Apollo 15 glasses have a significant amount of mare basalt in them.

Ages of glassy melt breccias and impact glasses. Virtually no age-measurement data have been obtained for glassy melt breccias, and their ages of formation can only be constrained loosely from their surface exposure ages (see section 7.3) and from the ages of the clasts they contain. Most samples appear to be less than 1 b.y. old.

Impact glasses collected from the surface at the Apollo 16 landing site appear to be late additions; they have been on the lunar surface for less than 107 years, as estimated from micrometeoroid erosion rates and from the preservation of thin glass coatings on them (*Hörz et al.*, 1975). The dominant group of impact glass samples from the Apollo 16 site has surface exposure ages of 1.5 to 2 m.y. The other group, with regolith-like chemical compositions, has exposure ages of about 50 m.y. (*Morris et al.*, 1986). *Borchardt et al.* (1986) dated several samples from North Ray Crater using ⁴⁰Ar-³⁹Ar techniques, and found them all to be younger than the 3.9 b.y. age estimated for the Cayley Formation, from which they were presumably derived. Their formation ages ranged from 0.37 up to 3.8 b.y., but their surface exposure ages were restricted to 40-50 m.y.

Chronological data for other glasses are virtually nonexistent. However, the presence of mare components in the Apollo 15 samples, as well as the geological constraints, limit them to less than 3 b.y. old. The surface exposure ages are much younger than that, e.g., the glass coating on sample 15205 is about 1 m.y. old (see summary in *Ryder*, 1985).

Origins of glassy breccias and impact glasses. The production of glass, rather than crystalline materials, from a melt requires rapid

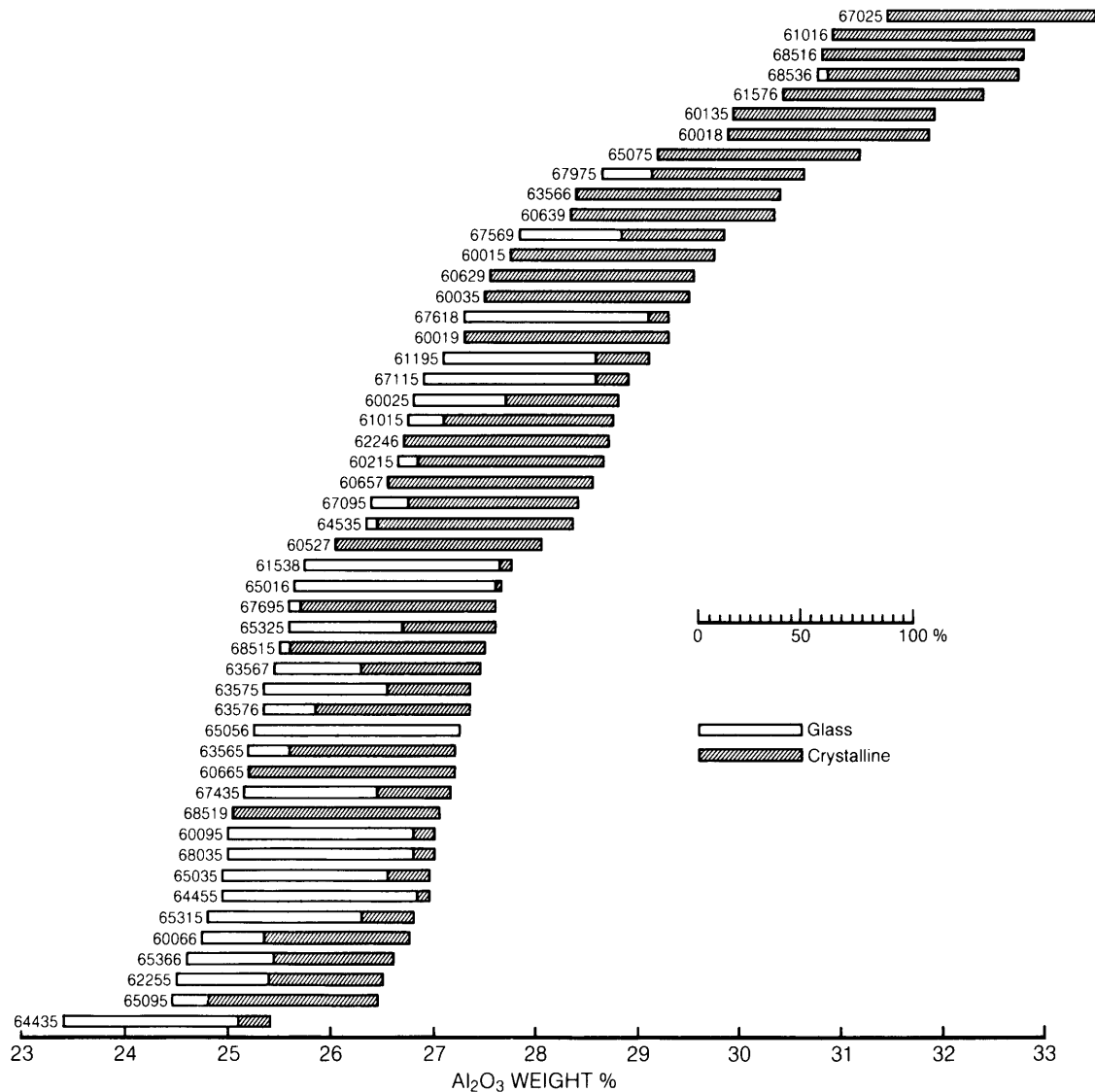


Fig. 6.42. Diagram showing alumina contents of impact glasses from the Apollo 16 site (See *et al.*, 1986), comparing Al₂O₃ contents of the crystalline and completely glassy (*holohyaline*) portions of the samples. The midpoint of each bar represents the bulk Al₂O₃ content of the sample. Impact glasses with more alumina (e.g., >30%; upper right) are generally more crystalline than those with less alumina (e.g., <25%).

cooling. Rapid cooling can be achieved in small cooling units, i.e., small volumes of original melt. Many glasses in the glassy polymict samples are smaller than a few centimeters in size, although some may be much larger. Such small, and therefore rapidly cooled, volumes of impact melt could be produced either in small impacts or in the most distant (distal) or uppermost portions of the ejecta blankets from larger impact craters.

Too little is known of the chemistry and petrology of most samples of glassy melt breccias and impact glasses to be sure of the origin of any particular sample. However, most samples show strong chemical similarities to the local regolith, suggesting that they have been produced by fairly small-scale craters that did not penetrate the existing regolith. These samples do not seem to be totally exotic to their collection sites. At the Apollo 15 site, the

impact glasses are chemically identical to local regolith. Others were collected as linings from small craters, so their origin is not in doubt.

In samples from all the Apollo sites, the glass coatings differ in composition from the coated host rocks, and they were therefore not derived from them. Furthermore, many of the glassy coatings on lunar rocks occur on several sides of the host rock, indicating that they were not splashed onto one side of a passive surface rock at some distance from the crater. Instead, most of the glasses were deposited onto their hosts inside growing crater cavities or during ballistic flight, so that more than one side of the rock was coated. The glass coatings were then "piggy-backed" on the rocks to their collection sites (See *et al.*, 1986).

The surface exposure ages of the Apollo 16 impact glass samples fall into two groups: about 2 m.y. and about 50 m.y. They seem to have been produced or exposed by the South Ray Crater and the North Ray Crater events, respectively (See *et al.*, 1986; Morris *et al.*, 1986; Borchardt *et al.*, 1986). Additional age data (e.g., Borchardt *et al.*, 1986) show that not all the glasses were produced by the North Ray Crater event; some are older than 50 m.y. The South Ray Crater group, however, might have been produced from that event itself (See *et al.*, 1986), since all of them have exposure ages of about 2 m.y. Chemical analysis indicates that most of these Apollo 16 glasses are not identical with the local regolith, but they appear to be dominated by subregolith materials of the Cayley Plains (Morris *et al.*, 1986; Borchardt *et al.*, 1986). This is consistent with the observation that they lack materials (agglutinates, glass droplets, etc.) formed and reworked at the lunar surface. However, these glasses were still formed by relatively small (<2 km diameter) craters in post-Imbrian times (section 4.4).

6.4.4. Crystalline Melt Breccias or Impact-Melt Breccias

Crystalline melt breccias are coherent rocks that contain obvious clastic material in a finer-grained groundmass that has formed by the crystallization of a silicate melt. The clasts range from a few percent to more than half the rock (Table 6.14); as the amount of clastic debris increases, the ground-mass tends to be more glassy and these samples grade somewhat arbitrarily into the glassy melt breccia group.

Many of the clasts show evidence of shock metamorphism or of resorption by the melt. The melt breccias invariably have high siderophile element contents resulting from meteoroid contam-

ination. Vesicles are abundant in some samples. In short, these breccias have clearly been produced by the crystallization of clast-laden, impact-produced melts (Simonds *et al.*, 1976; Onorato *et al.*, 1976), although the older literature commonly refers to them as recrystallized or metamorphic breccias.

The chemical compositions of crystalline melt breccias span virtually the entire range of compositions observed in highland samples, with about 15% to 30% Al₂O₃ (Table A6.20). Crystalline melt breccias are common at all the lunar highland sites and they have also been found among the regolith particles of highland origin in the Apollo 11 and 12 samples (e.g., the Type-A norites of Marvin *et al.*, 1971).

Petrography and chemistry of crystalline melt breccias. Many samples of crystalline melt breccias have a grossly homogeneous appearance and show a generally even distribution of clasts (Fig. 6.37d). The textures of the crystalline ground-mass in such samples tend to be poikilitic to subophitic. Only rarely is anything approaching a porphyritic texture observed, and then only in the most feldspathic samples. The crystalline ground-mass is generally fine- to medium-grained, with poikilitic pyroxenes typically no larger than a millimeter across (Fig. 6.38e,f). Other samples are more heterogeneous, with clasts occurring as *schlieren* in the groundmass (Fig. 6.37e). These heterogeneous samples tend to be finer-grained than homogeneous samples and may even be partly glassy (Fig. 6.38g). They may also have a higher percentage of clasts. Many descriptions of crystalline melt breccias have been published (e.g., Dymek *et al.*, 1976; Simonds, 1975; Simonds *et al.*, 1976; James, 1976; Ryder and Bower, 1976). Vaniman and Papike (1980) reviewed the mineralogy and chemistry of highland melt rocks, including crystalline melt breccias.

In most samples of crystalline melt breccias, the clasts are predominantly of plagioclase; pyroxene, olivine, and rock fragments are present in lesser amounts. The chemical composition of the clasts is more refractory than that of equivalent minerals in the groundmass that have crystallized from the melt. Plagioclase clasts are more calcic and the mafic mineral clasts more magnesian than the groundmass minerals (Fig. 6.43). In samples with a coarser-grained groundmass, the amount of clastic material tends to be less abundant, more refractory, and contains fewer rock (lithic) fragments. For example, the aphanitic (fine-grained) melt breccias at the Apollo 17 site contain abundant clasts of a diverse rock population. The coarser poikilitic-subophitic melt breccias contain few clasts and, among these, lithic fragments are scarce (Spudis and Ryder, 1981).

TABLE 6.14. Mineral modes (vol. %) of crystalline melt breccias (impact melt breccias).

Phase	14066	60315	60335	62235	66095	73215	77135
<i>Melt</i>	(84)	(96)	(84.2)	(86.5)	(88.5)	(68.1)	(87.9)
Feldspar	—	43.2	56.5	34.1	45.0	—	41.1
Hi-Ca px	—	4.9	13.4	6.0	{ 30.6 }	—	{ 30 }
Low-Ca px	—	39.0	0.6	36.3			
Olivine	—	6.1	9.0	6.0	10.2	—	15.1
Silica	—	—	—	—	—	—	—
Ilmenite	—	2.1	0.3	2.8	—	—	1.4
Ulvöspinel	—	—	—	—	—	—	—
Mg, Al-spinel	—	—	—	—	—	—	—
Fe-Ni metal	—	0.7	0.1	1.2	1.2	—	0.2
Troilite	—	—	0.8	0.1	0.1	—	0.1
Phosphate	—	—	<0.1	—	—	—	—
Mesostatis	—	—	3.6	—	—	—	—
Glass	—	—	—	—	1.4	—	—
<i>Clasts</i>	(16)	(4)	(15.8)	(13.5)	(11.5)	(31.9)	(12.1)
Feldspar	6.0	3.0	15.0	9.0	8.5	23.7	6.2
Olivine	0.7	1.0	—	—	—	{ 8.2 }	—
Pyroxene	2	—	—	0.5	0.1		
Lithic	7	—	0.8	4.0	2.9	0	3.9

14066: Juan et al. (1972); 60315, 60335, 62235, 66095, 77135: Vaniman and Papike (1980); 73215: James (1976).

In general, the crystallized groundmass of these breccias consists dominantly of plagioclase and a low-Ca pyroxene. Depending on the bulk chemistry and crystallization conditions, olivine and a variety of accessory minerals may also be present (Table 6.14). Small amounts of ilmenite or ulvöspinel are almost universally present. Globules of Fe-Ni metal and sulfide are also common (Fig. 6.38f). In the more common poikilitic groundmass, plagioclase crystals tend to be small (less than a few tenths of a millimeter) and stubby, and dozens of them may be embedded in the larger pyroxene (normally pigeonite, less commonly augite) or olivine crystals. In the subophitic textures, the plagioclase crystals form grains that are more comparable in size to the pyroxene or olivine crystals. Ilmenite crystals tend to be lath-like, rather than anhedral as in metamorphic (recrystallized) lunar rocks. A glassy mesostasis is observed between the larger crystals in some groundmasses, especially in the more KREEP-rich samples. This mesostasis may contain Fe-rich mafic minerals, a silica phase, and minor minerals such as zircon (Fig. 6.38f).

Chemically, the crystalline impact-melt breccias tend to have abundances and patterns of incompatible element (e.g., REEs) that indicate the presence of a significant amount of KREEP component (Table A6.21 and Fig. 6.41). In some crystalline impact-melt breccias, KREEP is particularly abundant, e.g., in the Apollo 12 and Apollo 14 samples. In these samples, the KREEP abundance is roughly

inversely related to alumina content, which is derived from the highland plutonic component. Therefore, in the more feldspathic varieties from the Apollo 16 site, KREEP is a relatively minor component. All samples are contaminated with meteoritic siderophile elements (Table A6.22).

Crystalline melt breccias and clast-poor impact melts (section 6.4.5) fall into distinct compositional groups. Four main groups have been recognized among the Apollo 16 melts. Very tightly-clustered compositional groups may represent samples derived from single impacts. Informal designations and acronyms have been applied in a nonrigorous fashion to different groups (BVSP, 1981). The LKFM (low-K Fra Mauro) group is a common one; the term is applied to samples that contain about 15-19% Al_2O_3 and have abundances of light REEs that are about 100-150× those in chondritic meteorites. Increasing REE and K contents give rise to the IKFM (intermediate-) and HKFM (high-) groups. More aluminous compositions (20-25% Al_2O_3) with lower REE contents have been called VHA (very-high-alumina) "basalts" (although they are not truly basalts in the traditional sense of lavas extruded from the planetary interior).

Ages of crystalline melt breccias. A large proportion of the material in crystalline melt breccias has been totally melted or degassed during formation. Under these extreme conditions, the isotopic systems used for age dating can be completely "reset," and meaningful crystallization ages can be

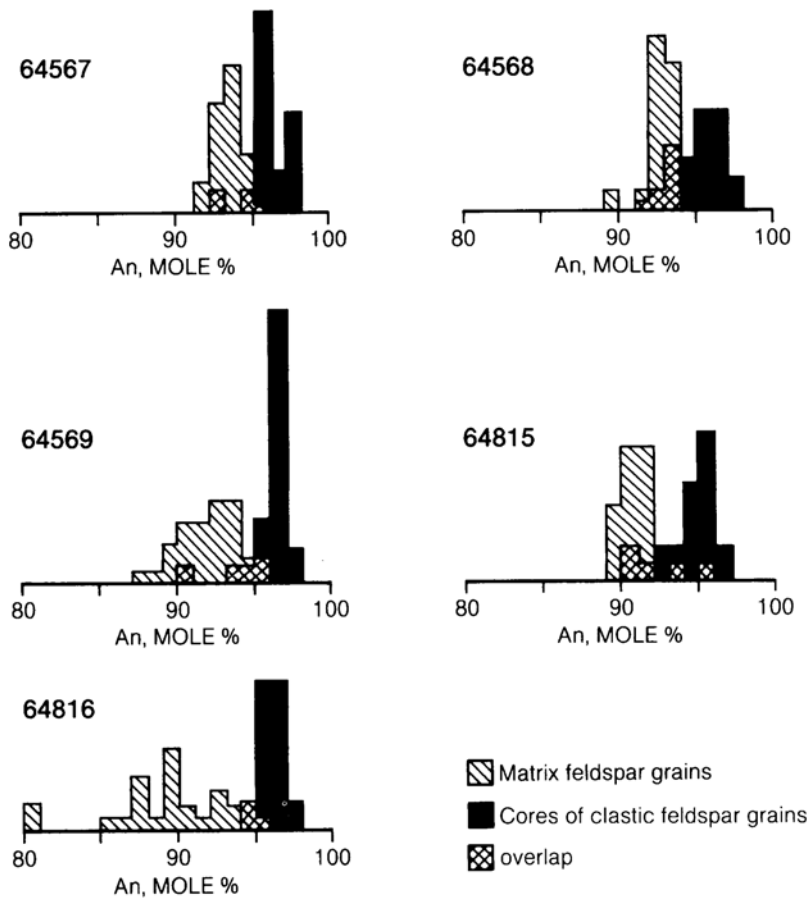


Fig. 6.43. Histograms of plagioclase compositions (mol.% anorthite, An) in Apollo 16 crystalline melt breccias. The included fragments of feldspar crystals from impact-shattered bedrock (clastic plagioclase; black bars) are more refractory (more Ca-rich) than groundmass plagioclases (diagonal ruling), which have crystallized from an impact-produced melt. Overlap of populations is shown by the criss-cross pattern. From *Simonds et al.* (1973).

obtained, particularly for the coarser-grained examples, which contain few original clasts. Dating the clast-rich varieties is more difficult. The clasts themselves, being relatively cold when mixed with the melt, act to cool the melt quickly. As a result, the crystalline groundmass is fine grained, and the necessary mineral separations are difficult or impossible. Furthermore, the clasts tend to be poorly reset or incompletely degassed, leading to inaccurate measurements. To minimize these complications, the ^{40}Ar - ^{39}Ar dating method is more commonly used than the Rb-Sr method for these rocks. There is some indication that the Rb-Sr systems in at least some of the melt rocks were open during impact melting, so that Rb could migrate in and out of the rock (e.g., *Reimold et al.*, 1985), a condition that would make Rb-Sr measurements even more unreliable.

Representative ages for crystalline melt breccias are listed in Table 6.15; the table also lists Al_2O_3 as a rough guide to composition. Most samples, irrespective of chemical composition, have ages

around 3.9 b.y., which is a common age for highland breccias in general. No sample is very far out of this range, implying that the available samples all formed during the period of large impacts that produced the mare basins. Even though such large young impact craters as Copernicus, Tycho, and King must have produced large volumes of crystalline melt breccias at much later times, these materials are not represented in the Apollo collections.

Origin of crystalline melt breccias. Crystalline melt breccias are of impact-melt origin as shown by their clasts, their nonigneous chemical compositions, and the presence of meteoroid contamination (see also section 6.3). Studies of large terrestrial impact craters (*Simonds et al.*, 1976) indicate that a large volume of completely melted rock forms near the point of impact, where the shock pressures are highest. This melt immediately moves outward across the developing crater, picking up cold debris (clasts) as it moves, and eventually forming a sheet within the crater or even spilling outside it (section 4.1.2 has a detailed discussion of this process).

TABLE 6.15. Representative crystallization ages (b.y. ago) of crystalline melt breccias.

Sample	~%Al ₂ O ₃	⁴⁰ Ar/ ³⁹ Ar whole rock	Ref.	Rb-Sr isochron	Ref.
14068	13	3.80±.01	9		
15455	17	3.87±.04	5		
60315	17	3.97±.03	1		
		3.86±.01	2		
64567	21	3.86±.05	8		
65015	20	3.92*	3	3.85±.02	4
		3.96±.04	1		
67715	30	4.09±.01	7		
73235	21	3.88±.04	10		
76315	18	3.92±.04	8		
76055	16	3.99±.07	11	3.78±.04	6
		3.92±.05	12		
		3.91±.04	13		

* Plagioclase, not whole rock.

(1) *Kirsten et al.* (1973); (2) *Schaeffer et al.* (1976); (3) *Jessberger et al.* (1974); (4) *Papanastassiou and Wasserberg* (1972); (5) *Alexander and Kahl* (1974); (6) *Tera et al.* (1974); (7) *Jessberger* (1983); (8) *Turner and Cadogen* (1975); (9) *Heusser* (1985); (10) *D. Phinney et al.* (1975); (11) *Kirsten and Horn* (1974); (12) *Turner et al.* (1973); (13) *Huneke et al.* (1973).

In this mixture, the hot melt and colder clasts come to an equilibrium temperature at which some clasts are preserved and the melt crystallizes into different minerals (often fine-grained) rather than chilling into a glass. In many cases it is difficult to distinguish a crystalline groundmass that has formed from a melt from one that has formed by later devitrification of solid glass. This difficulty makes the distinction of a crystalline melt breccia from a glassy melt breccia arbitrary in some cases (see also section 6.4.3).

Some crystalline melt breccias have compositions similar to upper-crustal or local compositions, implying origin from near-surface rocks involved in relatively small impacts. However, several groups, particularly those with basaltic compositions and moderate KREEP contents (e.g., the LKFM group), do not. The origin of these latter melts has not been fully explained. Part of the problem is that, while terrestrial crystalline impact-melt rocks can be chemically modeled by mixing compositions corresponding to the observed clasts, the lunar ones commonly cannot. This condition implies that these melts contain a chemical component not represented by the observed clasts.

A strong case can be made that at least some of these samples represent melts generated in large basin-forming impacts, which involved deeper levels of the lunar crust. Possible examples are (1) samples

15445 and 15455 (from Imbrium?; *Ryder and Bower*, 1977; *Ryder and Wood*, 1977), (2) the Apollo 17 poikilitic melts (from Serenitatis?; *Ryder and Wood*, 1977), which definitely represent an important part of the local massifs at the Apollo 17 site, and (3) perhaps the Apollo 16 poikilitic melts as well.

6.4.5. Clast-poor Impact Melts

Clast-poor impact melts are coherent. They contain very few, if any, clasts, so that their textures are almost wholly igneous. Most samples are fine-grained and resemble conventional volcanic rocks. They are much less common than melt breccias. Their chemical compositions span almost the entire range observed in highland rocks that contain more than about 15% Al₂O₃.

Because both clast-poor impact melts and conventional volcanic rocks crystallize from a silicate melt, it is not always easy to distinguish between them. Clast-poor impact-melt rocks have been identified by some workers (e.g., *Kushiro et al.*, 1972; *Crawford and Hollister*, 1974) as conventional, internally-generated igneous rocks; in these descriptions the rare included fragments were described as xenocrysts. The distinction between such impact melts and conventional igneous rocks produced by partial melting of the interior of the Moon is especially important when attempting to understand lunar petrogenesis. In general, a distinction can be made on the basis of siderophile-element abundances that indicate meteoroid contamination in the impact melts (see also section 6.3), although even that criterion has been questioned (*Crawford and Hollister*, 1974; *Delano and Ringwood*, 1978). The microscopic textures in impact melts are rather more heterogeneous and nonuniform than those of internally-generated igneous rocks. Chemically, most lunar impact melts have compositions that are unlike melts that could be expected to be produced by partial melting of the lunar interior; in particular, the impact melts tend to be more aluminous than internally-derived melts. Because most impact melts are fine-grained, this high aluminum content cannot easily be attributed to the accumulation of large plagioclase crystals during crystallization of an earlier and less-aluminous magma.

Petrography and chemistry of clast-poor impact melts. *Vaniman and Papike* (1980) reviewed highland melt rocks, including clast-poor impact melts. Clast-poor impact melts tend to have a range of fine-grained crystalline textures that are generally ophitic, and rarely vitrophyric or intersertal (Figs. 6.38h,i). Some impact-melt rocks have a slightly porphyritic texture with larger plagioclase crystals. The textures of impact-melt rocks are more

TABLE 6.16 Mineral modes (vol.%) of clast-poor impact melts.

Phase	14276	14310	62295	64455	65055	67747	67559	68415
Feldspar	64.6	59.0	35.5	59.9	68.5	67.2	83.1	82.2
High-Ca px	4.0	6.1	—	{32.7}	{27.6}	{8.0}	{13.8}	4.4
Low-Ca px	25.0	26.8	—	—	—	—	—	7.5
Olivine	—	—	28.3	6.5	—	16.3	—	3.1
Silica	—	—	—	—	—	—	—	—
Ilmenite	1.2	1.8	—	—	0.8*	0.7*	0.1	—
Ulvöspinel	<0.1	<0.1	—	—	0.7	—	—	—
Mg, Al-spinel	—	—	6.5	—	—	—	—	—
Fe-Ni	0.3	0.1	<0.1	0.2	0.7	0.3	0.1	0.2
Troilite	<0.1	<0.1	—	0.3	0.4	0.4	0.3	—
Phosphate	0.5	0.3	—	—	—	—	—	—
Mesostasis	3.5	4.4	—	0.4	2.0	7.0	2.0	2.1
Glass	—	—	30	—	0.2	—	—	—
Accessories (<0.1 %)	schreibersite armalcolite tranquillitite K-Ba feldspar	schreibersite armalcolite tranquillitite	schreibersite	schreibersite akaganeite				

* Includes armalcolite.

14276, 14310, 68415: *Gancarz et al.* (1972); 62295: *Walker et al.* (1973a); 64455 *BVSP* (1981); 67747, 67559: *Reimold et al.* (1985); 65055 *Vaniman and Papike* (1980).

heterogeneous than those in normal igneous rocks. In particular, impact-melt rocks have a much wider range in grain size within a single thin section, ranging from ragged plagioclase phenocrysts to irregular granular clots. Small, open, crystal-lined cavities (*vugs*) are common.

The minerals in clast-poor impact-melt rocks are virtually the same as those that make up normal, internally-derived lunar igneous rocks. Nearly all impact-melt rocks contain plagioclase and pyroxene (normally a low-Ca variety), and olivine is present in some samples. Minor minerals vary with the bulk chemistry. A common feature (shared with clast-bearing impact melts but not with volcanic basalts) is the presence of Ni-Fe metal/sulfide globules. Modal (mineral %) data for selected samples are given in Table 6.16; these data reflect the variety of compositions shown by the chemical data (Tables A6.23-A6.25).

A single bulk chemical composition may be represented by more than one sample. For instance, the only clast-poor melt composition among the Apollo 14 samples is represented by several different specimens, including 14310 and 14276. Sample 14310 was originally thought to be an igneous KREEP basalt, but its textures are more heterogeneous than those of a basaltic lava, it is not in fact clast-free, and it is enriched in meteoroid siderophile elements. This cluster of similar samples has a composition in which incompatible-element abun-

dances are only slightly lower than Apollo 14 regolith samples and the Mg/Fe ratio is similar. However, these samples differ from the regolith in having higher Al_2O_3 and lower FeO and MgO.

At the Apollo 16 site, several samples from separate locations (e.g., samples 67559 and 60635) have compositions similar to samples 68415 and 68416, which were chipped from a single boulder. This composition appears to be similar to that of the regolith from the nearby Descartes Highlands, and it is much more aluminous than the Apollo 14 samples. Other Apollo 16 impact-melt samples, such as 64455 and the distinctive 62295, differ from each other, from the 68415 sample group, and from the local regolith compositions.

Ages of clast-poor impact melts. During formation, virtually all the components of clast-poor impact melts were totally molten and/or degassed, resetting the isotopic systems used for age-dating measurements. Thus, it is comparatively easy (especially in comparison with other highland breccias) to acquire consistent, meaningful crystallization ages by a variety of radioactive isotopic systems. Several such determinations have been made, and often duplicated, in different laboratories. Some of these ages are compiled in Table 6.17, which includes Al_2O_3 contents as a general guide to the chemistry of the sample. Most impact melts correspond closely to the 3.9-b.y. ages for glassy breccias. This correspondence suggests that the

TABLE 6.17. Representative crystallization ages (b.y. ago) of clast-poor impact melts.

Sample	$\sim\%Al_2O_3$	$^{40}Ar/^{39}Ar$	Ref.	Rb-Sr isochron	Ref.
			whole rock		
14276	21			3.80±04	1
14310	20	3.82±06	2	3.79±04	1
		3.83±04	6	3.85±06	11
		3.85±05	4	3.86±03	5
		3.85±05	4	3.86±03	12
62295	21	3.84±05	6	3.92±06	5
67747	26			3.94±05	7
67559	28			3.84±05	7
60635	28			3.83±03	8
68415	28	3.75±04	2	3.76±01	9
		3.80±06	10		
		3.80±04	13		
65795	28			3.89±04	8

(1) Papanastassiou and Wasserburg (1971); (2) Stettler et al. (1973); (3) Schaeffer et al. (1976); (4) York et al. (1972); (5) Mark et al. (1974); (6) Turner et al. (1973); (7) Reinhold et al. (1985); (8) Deutsch and Stöffler (1987); (9) Papanastassiou and Wasserburg (1972); (10) Kirsten et al. (1973); (11) Murthy et al. (1972); (12) Compston et al. (1972a,b); (13) Huneke et al. (1973).

impact melts were also formed during the period of large, basin-forming impacts. However, some impact melts are around 3.85 b.y. old, almost as "young" as the 3.75-b.y.-old 68415 sample group. Relict clasts in the melts, even if not petrographically detectable, still cause problems with the isotopic systems because they may not be completely melted or outgassed. Relict plagioclase fragments, in particular, can preserve ages of older events.

Origin of clast-poor impact melts. Clast-poor impact melts evidently crystallized from impact-produced silicate liquids that were once entirely above their liquidus temperatures ($\sim 1300^{\circ}$ - 1200° C). Either these melts contained no clastic debris to start with, or virtually all the clastic material present dissolved into the melt before the melt had cooled below the liquidus temperature and had started to crystallize. The slightly heterogeneous textures (resulting from relict, heterogeneously-distributed nucleation sites), the common nonmagmatic chemical compositions (some of which are similar to brecciated rocks and regoliths in the highlands), and the presence of meteoroid siderophile elements precludes a normal magmatic origin and is consistent with an impact-melt origin.

Many impact melts evidently crystallized in units about the size of typical lava flows, because their crystal sizes (and therefore the inferred cooling rates) are similar. Similar clast-poor impact melt rocks are

found in some of the larger terrestrial impact craters, where they typically occur with clast-bearing impact-melt rocks stratigraphically above and below them.

Production of an impact-melt sheet more than a few meters thick requires a crater at least a few kilometers in diameter. The correspondence between the chemical composition of lunar impact melts and the compositions of upper crustal rocks or even regoliths suggests that at least some of the impact-melt samples we have are not derived from basin-scale impact melts, but from melts produced in smaller craters. The Apollo 16 group that includes sample 68415, in particular, appears to mimic very closely the composition of upper crustal materials presumed to be present in the Descartes Formation (see section 10.6.5).

6.4.6. Granulitic Breccias and Granulites

Granulitic breccias and *granulites* are coherent crystalline rocks that have apparently been derived by the recrystallization of other rock types by heating at temperatures over 1000° C for long periods of time. The recrystallization textures are characterized by rounded polyhedral grain shapes (i.e., *granoblastic* texture) or presence of small bead-like crystals within larger crystals (*poikiloblastic* texture), and an absence of typical volcanic textures (Warner et al., 1977; Lindstrom and Lindstrom, 1986).

Granulitic breccias contain obvious mineral or rock clasts or relicts of clasts, whereas granulites do not. The granulites are much less abundant. Both rock types commonly consist of a mosaic of grains whose boundaries meet at angles of about 120° , a texture produced by thorough recrystallization (Stewart, 1975). Mineral compositions are also uniform and equilibrated. All samples are aluminous (>25 - 29% Al_2O_3); they have a range of Mg/Fe ratios, and they have very low abundances of the incompatible elements that are indicative of a KREEP component. All granulitic breccias and granulites are contaminated with meteoroid siderophile elements, indicating that they were produced in meteoroid impact melts before they were recrystallized.

Both granulitic breccias and granulites have been found at all the Apollo and Luna landing sites. They are also present among the lunar meteorites recovered from Antarctica. Among the Apollo samples, they are generally found as small individual rocks, as clasts in other breccias, or as isolated regolith particles. A small number of larger samples, in the range of 5-10 cm, have also been returned. Their bulk chemical compositions are feldspathic and their incompatible-element concentrations are low. In these respects, they strongly resemble

estimates of the average lunar upper-crustal composition and, for that reason, they may have a greater significance in lunar history than their apparent scarcity would suggest.

Petrography and chemistry of granulitic breccias and granulites. The textures of granulitic breccias and granulites are extremely varied, ranging from granoblastic to poikiloblastic, from homogeneous to heterogeneous, and from coarse- to fine-grained (Figs. 6.38j,k). Granulitic breccias tend to have fine-grained matrices, whereas poikiloblastic breccias tend to be coarse-grained throughout. Generally, the clasts are as recrystallized as the matrices. The distinction between poikiloblastic textures (metamorphic, recrystallized) and poikilitic textures (primary igneous) on the basis of texture alone is all but impossible, and several workers have interpreted some of these samples as igneous (67955: *Hollister*, 1973; 77017: *Ashwal*, 1975).

The granoblastic rocks are dominated by anhedral and equant plagioclase (70-80%); smaller pyroxenes (15-25%) and small anhedral olivines (absent to a few percent) occur within and between the larger plagioclase crystals. The poikiloblastic rocks tend to have blocky plagioclase grains, partially enclosed in larger pyroxene crystals (*oikocrysts*). Ilmenite is rare and generally subhedral. Olivine inclusions commonly form strings or "necklaces" inside large plagioclase crystals; the strings possibly indicate the location of premetamorphic grain boundaries. In most samples, pyroxene and olivine grains are of nearly constant composition and are unzoned (e.g., *McCallum et al.*, 1974; *Ashwal*, 1975; *Bickel et al.*, 1977; *Ryder and Blair*, 1982; *Lindstrom and Lindstrom*, 1986). In contrast, *Norman* (1981) found that the granulitic clasts in fragmental breccia 67016 have ranges of mineral compositions within individual clasts. Among granulitic breccias, the pyroxene and olivine grains have Mg/(Mg + Fe) ratios ranging from less than 0.50 to more than 0.85 (review in *Lindstrom and Lindstrom*, 1986).

Most of the granulitic breccias and granulites, including the poikiloblastic varieties, have major-element chemical compositions similar to anorthositic norites (Fig. 6.23; *Warner et al.*, 1977; *Lindstrom and Lindstrom*, 1986). They have low abundances of the KREEP incompatible elements, and are contaminated with meteoroid siderophile elements. There are small but important differences in the major elements, as well as larger variations in the trace elements (Tables A6.26-A6.28). *Lindstrom and Lindstrom* (1986) divided the range of compositions into two groups: ferroan [Mg/(Mg + Fe) < 0.7] and magnesian [Mg/(Mg + Fe) > 0.7]. Although the major-element data do not show a clear break between the two groups, the element Sc appears to

define the groups more precisely. Ferroan granulites have about twice as much Sc as do magnesian granulites. Ferroan granulites also tend to have lower abundances of the incompatible elements. There is no correlation of microscopic texture with composition.

Ages of granulites and granulitic breccias. There are few data on the ages of granulitic rocks. Most age measurements are based on the ^{40}Ar - ^{39}Ar system applied to whole-rock samples because the rocks are too fine-grained to permit the mineral separations necessary for Rb-Sr or Sm-Nd internal-isochron age determinations. The available data suggest that the granulitic rocks formed as much as 4.3 b.y. ago, and that for some samples, the ^{40}Ar - ^{39}Ar system was reset by heating at around 3.9 b.y. ago (review in *Warner et al.*, 1977). The lack of the KREEP component in the breccias suggests that they were assembled before KREEP became widely dispersed on the lunar nearside, an event or a series of events that had taken place by 3.9 b.y. ago. Granulitic rocks are also common components of feldspathic fragmental breccias, some of which are interpreted to have been assembled by 3.9 b.y. ago (section 6.4.2). The chronological data are much too sparse to establish any systematic differences in age between ferroan and magnesian granulitic rocks.

Origins of granulites and granulitic breccias. The clast-matrix structure of the granulitic breccias and the meteoroid contamination detected in most granulitic rocks demonstrates that they were derived from even older breccias. These older breccias were metamorphosed and recrystallized by prolonged heating to temperatures of more than 1000° C (*Stewart*, 1975; *Bickel et al.*, 1977; *McCallum et al.*, 1974). They appear to have been formed from KREEP-free or KREEP-poor precursor rocks that were present early in lunar history. The prolonged heating necessary to produce the observed textures is different from the effects produced by the intense bombardment about 3.9 b.y. ago, in which prolonged heating is not evident. The effects in the granulitic breccias could have resulted from burial at a depth of several kilometers, possibly during an earlier period of even higher impact flux, accompanied by increased heat flow from the lunar interior (*Warner et al.*, 1977). The younger ages, about 3.9 b.y., might represent cooling (i.e., "freezing in" of the isotopic systems) by excavation from depth during the 3.9-b.y. bombardment period.

The chemical and textural characteristics suggest that some of the granulites may have been derived from distinctive anorthositic norite precursors; most, however, are clearly polymict (*Lindstrom and Lindstrom*, 1986). The bulk chemical compositions of granulites are similar to the average lunar surface

compositions estimated from remotely-sensed data (Taylor, 1982), even more so than the Apollo 16 fragmental breccias. There appears to be no difference in regional distribution between the ferroan and magnesian granulitic rocks, but the available orbital measurements are not adequate to preclude regional differences.

6.4.7. Dimict Breccias

Dimict breccias are a relatively rare lunar rock type. They consist of two distinct lithologies combined into a single rock. In most examples, the two lithologies are mutually intrusive, i.e., neither one can be defined as the host rock. The samples generally resemble complex veins or dikes of dark and light components. The dark material is a fine-grained crystalline melt breccia or a nearly clast-free impact melt. The light-colored material is, in most cases, an anorthositic breccia whose main constituents are crushed and shattered (*cataclastic*) anorthosite fragments. Dimict breccias cannot be recognized in samples less than a few centimeters across, because the scale of mutual intrusion is on that order.

All of the few recognized dimict breccias are from the Apollo 16 site. (In an older classification as "black-and-white rocks," some similar Apollo 15 samples were included with them.) The dark crystalline melt breccia is similar in all samples and contains about 21% Al_2O_3 (McKinley *et al.*, 1984). The white portion varies from nearly pure cataclastic ferroan anorthosite to less aluminous breccias (nearly all containing more than 30% Al_2O_3 ; McKinley *et al.*, 1984; James *et al.*, 1984). They are estimated to be about 3.9 b.y. old, and they may have formed during the period of major bombardment. In these large impact events the melt could have been created and the older anorthositic breccia could have been shattered and remobilized at the same time. Available surface exposure ages suggest that all the dimict breccia samples were ejected about 2 m.y. ago by the South Ray Crater event. Several samples have glass coats.

Petrography and chemistry of dimict breccias. Detailed petrographic and chemical studies, reviewed by McKinley *et al.* (1984) and James *et al.* (1984), provide the basis for characterizing dimict breccias. The mutually intrusive character is best displayed by sample 61015 (Fig. 6.37h). Most of the contacts between the two lithologies are smoothly curving surfaces; some are shear planes. Not all samples can be shown to be mutually intrusive, and in some specimens the melt phase is perhaps more clearly the host.

The dark-colored impact melt lithology is a crystalline melt breccia such as those described in section 6.4.4. In most cases, the melt contains less

than 5% of clastic material. The melt is fine-grained and consists of lath-shaped plagioclase crystals, generally equant olivine grains, and pyroxene. A glassy mesostasis, producing an intersertal texture, commonly occurs between the crystals (Fig. 6.381). The few clasts are mainly plagioclase, and lithic clasts are very rare. The melt composition is consistent at about 21% Al_2O_3 with light-REE incompatible-element contents of about 80-90x that of chondritic meteorites. This composition is remarkably constant and is similar to most impact melts found at the Apollo 16 site (Tables A6.20-A6.22). The dimict breccias, however, form a tighter compositional cluster than do the other impact melts of roughly similar composition. In addition, the Apollo 16 dimict breccias have Mg/(Mg + Fe) ratios of about 70, and all those analyzed show evidence of contamination from meteoroid siderophile elements.

The light-colored lithology is composed dominantly of cataclastic anorthosite, containing more than 95% plagioclase. Low-Ca pyroxene is more common than olivine or high-Ca pyroxene. In their chemistry and mineralogy, these anorthosites are similar to the pristine igneous anorthosites described in section 6.3.3. In dimict breccias, the compositional range of the mafic minerals (pyroxene, olivine) extends to more magnesian compositions, however, and this greater range suggests that these light portions are actually polymict. The textures of these anorthosites have been extensively modified by impact processes. The clasts are shattered, and the individual crystals are granulated and have undulatory (strain) extinction under polarized light. The anorthosites have typical low rare earth abundances and lack meteoroid contamination.

Ages of dimict breccias. There are no ages available for the dark crystalline melt breccia phase of dimict breccias, the lithology that offers the best possibilities for age dating. However, by analogy with chemically similar melts, they are presumably about 3.9 b.y. old. Two ^{40}Ar - ^{39}Ar determinations for the anorthosites give good ages of $3.92 \pm .02$ b.y. and $3.91 \pm .01$ b.y. (Jessberger *et al.*, 1977). These ages probably date the intense heating and deformation of the anorthosites, i.e., the impact event. The original crystallization of the anorthosites presumably took place much earlier.

Origin of dimict breccias. Terrestrial analogs for lunar dimict breccias occur in the basement rocks below large impact craters, where impact-produced melt was injected into hot shocked rock to form complex dike-like bodies (e.g., Stöffler *et al.*, 1979). Such melt-rich dikes have been referred to as *pseudotachylite*, although this term has been loosely applied to a variety of superficially similar lithologies

in both impact and nonimpact settings. The lunar dimict breccias were probably created in the same way.

The tight chemical clustering of the Apollo 16 dimict breccias suggests that they formed in a single impact (McKinley *et al.*, 1984), but the crater of origin cannot yet be identified. Although the samples appear to be associated with South Ray Crater, this crater is too young and too small to be their source. The South Ray Crater event merely excavated them and scattered them around. James *et al.* (1984) suggested that they were produced in a crater of about 50-150 km in diameter. However, Spudis (1984) noted that their composition is not that of the local crust and advocated an origin in the Nectaris basin-forming event.

6.4.8. Regolith Breccias

Regolith breccias form at or very near the lunar surface as the result of impacts into regolith (see section 7.6). Such breccias contain identifiable regolith components, such as solar wind gases, glass spherules, or agglutinates (section 7.1.3). They range from friable clods to coherent, glass-bonded breccias. They may represent ancient regoliths, rather than the visible regolith developing at the surface today. Many of them are not merely the lithified equivalents of ordinary regolith. Their agglutinate content is low, and some appear to be coarser-grained than modern lunar soil. They are also less mature than most modern regoliths.

Most regolith breccias were collected from mare surfaces or contain a mare component. These samples are probably younger than 3.9 b.y. old (the earliest time of widespread mare volcanism) and they are not strictly highland samples. However; some regolith breccias contain only or mostly highland material, including 18 specimens from the Apollo 16 landing site (McKay *et al.*, 1986) and several from the Apollo 14 landing site (e.g., 14318, Kurat *et al.*, 1974). Pure highland regolith breccias are rare at other Apollo landing sites, but four examples collected as lunar meteorites in Antarctica (summarized in Ryder, 1987) contain only minor mare components.

6.5. SPECTRAL PROPERTIES OF HIGHLAND ROCKS

The dominant mineral in lunar highland rocks is Ca-rich feldspar (anorthite). Pyroxene is usually present in varying amounts and olivine and oxide minerals are minor components. All these mineral components of highland rocks have diagnostic absorption features in the near-infrared. The few highland rock and breccia spectra measured in the laboratory (e.g., Charette and Adams, 1977) all have absorption bands due to the presence of low-Ca pyroxene in varying amounts (exceptions are pristine samples of anorthosite, troctolite, and dunite). Several rocks also have distinct feldspar absorption features.

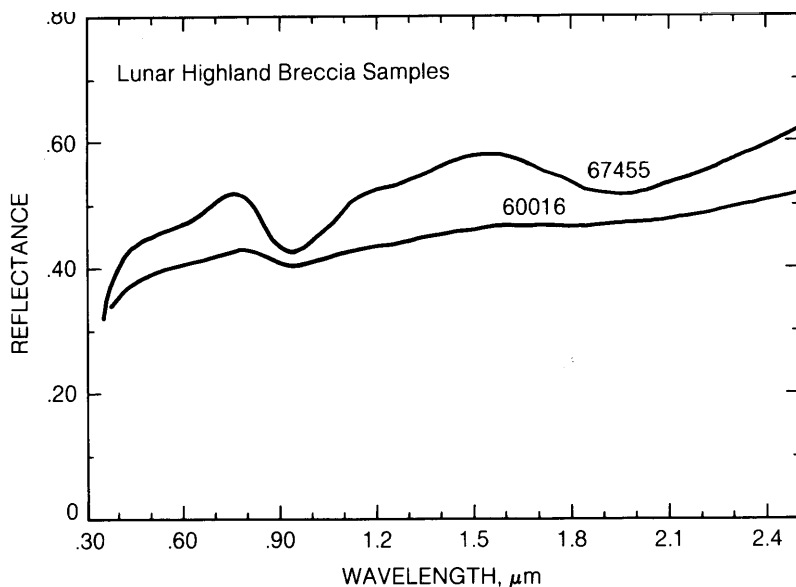


Fig. 6.44. Reflectance spectra as a function of wavelength for two lunar highland breccia samples, fragmental breccia 67455 (upper curve) and regolith breccia 60016 (lower curve). The absorption "valley" at about 0.93 μm reflects the presence of low-Ca pyroxene in the samples. Peaks in the regolith breccia are subdued. A very weak absorption feature at about 1.3 μm is due to crystalline feldspar.

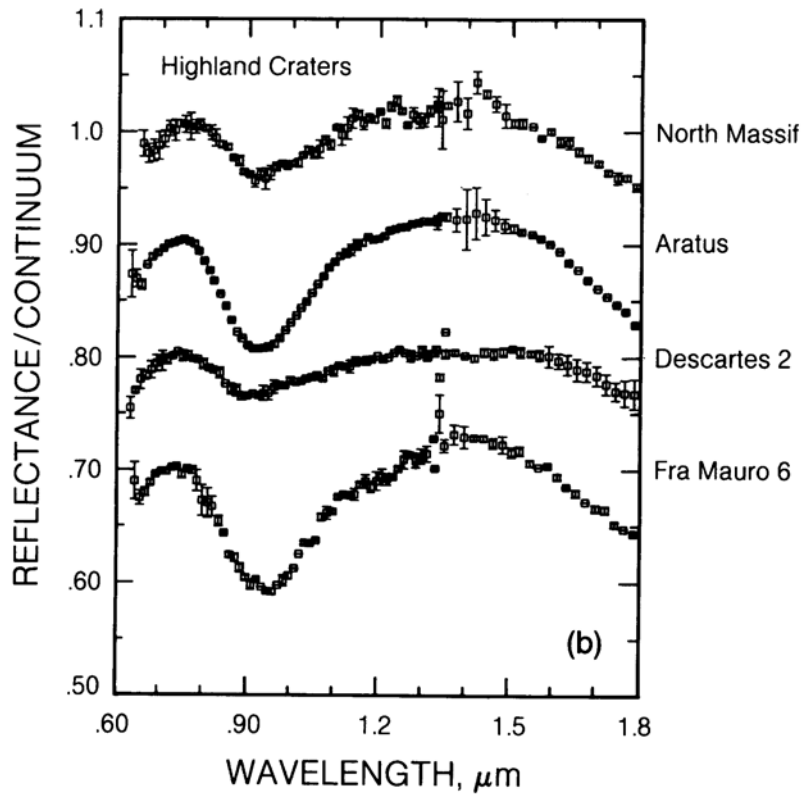
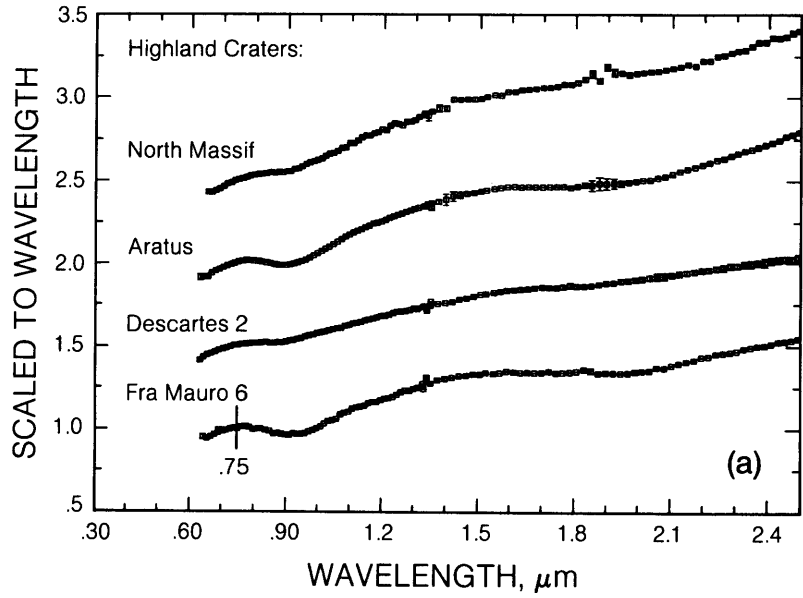


Fig. 6.45. (a) Scaled reflectance spectra, obtained with Earth-based telescopes, for small, fresh lunar highland craters or mountain regions. (b) Plots of residual absorption features of the spectra in (a) after removal of the sloping background continuum. (The continuum was approximated by a straight line tangent to the spectrum around the 1.0-mm absorption feature). Note the varying amounts of low-Ca pyroxene indicated by the varying depths of the 0.93-mm absorption feature. A similar variability can be (barely) distinguished in the 1.3-mm feature produced by crystal-line feldspar.

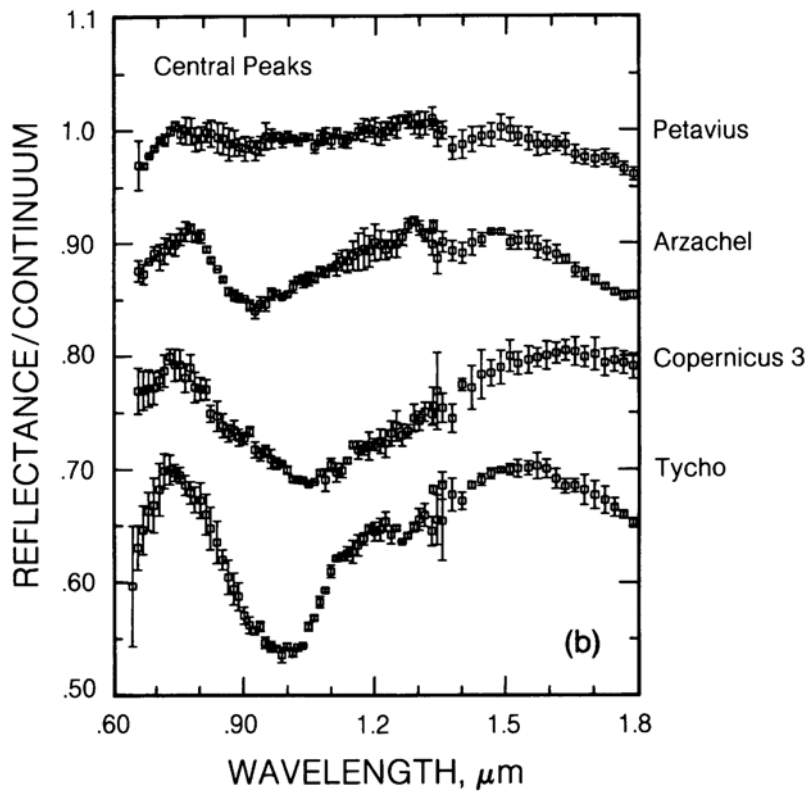
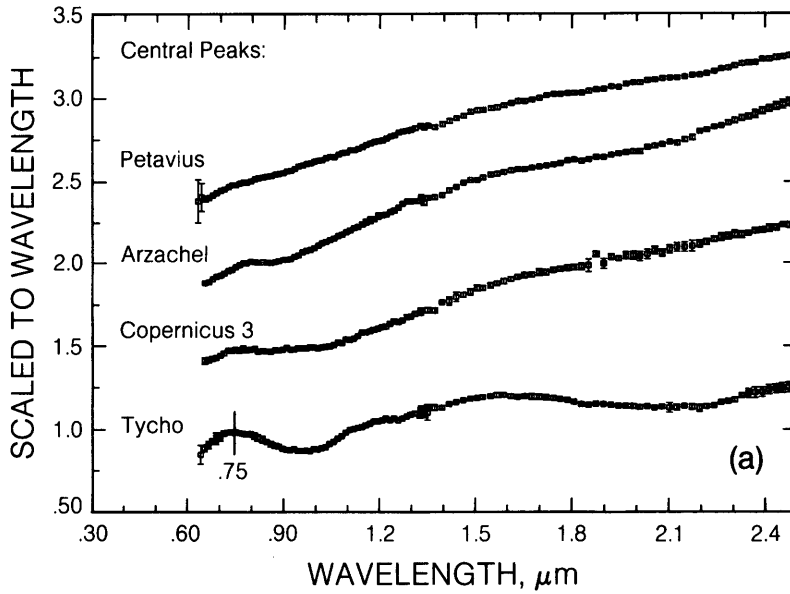


Fig. 6.46. (a) Scaled reflectance, obtained with Earth-based telescopes, of the central peaks of large lunar craters. (b) Residual absorption features of the spectra in (a) after removal of the sloping background continuum. The diverse spectra indicate that a wide range of different rocks have been uplifted from the deeper lunar crust to form the central peaks. The identified rock types and the major mafic (Fe, Mg-rich) silicate minerals that account for the spectral properties are, from top to bottom: anorthosite in Petavius (plagioclase with few mafic silicates); norite in Arzachel (abundant low-Ca pyroxene); troctolite in Copernicus 3 (abundant olivine); and gabbro in Tycho (abundant high-Ca pyroxene).

In principle, the strength of an infrared absorption band is a function of the abundance of the absorbing mineral, and the spectra can be used to estimate mineral percentages. However, in practice, the absorption bands of various mineral components of highland rocks do not combine in a linear fashion, and the more absorbing pyroxene tends to dominate the spectral character of a highland rock. Furthermore, feldspar that has been shocked to high pressure (e.g., ≥ 250 kbar), as is frequently the case in impact-produced breccias, has a featureless spectrum in the near-infrared (Adams *et al.*, 1979), quite unlike the spectrum of normal unshocked feldspar. The reflectance spectra of typical highland breccias are shown in Fig. 6.44. The bandcenters of the pyroxene features (e.g., the 0.93- μm band) result from the presence of low-Ca pyroxene as the major mafic mineral in these samples. The weaker feature near 1.3 μm is due to the crystalline feldspar component.

A complete survey of the spectral character of lunar samples has not been performed, so that the range of spectral types represented in the Apollo collection is still unknown. However, ground-based observations of the Moon, particularly of areas where fresh materials have been exposed by young impact craters, indicate that lunar materials are very heterogeneous on a large scale (Pieters, 1986). Figures 6.45 and 6.46 show near-infrared reflectance spectra (acquired with Earth-based telescopes) of small, fresh lunar craters (3-10 km in diameter) and of the central peaks in larger lunar craters. The small craters (representing excavation of the upper 1-2 km of lunar crust) yield spectra indicative of breccias containing varying amounts of low-Ca pyroxene and feldspar (compare Fig. 6.45b with 6.44). More deep-seated materials (from 5-10-km depth), which have been uplifted to form the central peaks of large craters, have diagnostic features indicating a diverse range of rock types on a regional scale.

APPENDIX: CHEMICAL DATA FOR LUNAR ROCKS

TABLE A6.1. Major-element concentrations in representative lunar mare basalts (wt.%).

	High-Ti				Low-Ti				
	Apollo 11 High-K 10049	Apollo 11 Low-K 10003	Apollo 17 70215	Apollo 17 Orange Gl. 74220	Apollo 12 Pigeonite 12064	Apollo 12 Olivine 12002	Apollo 12 Ilmenite 12051	Apollo 15 Pigeonite 15597	Apollo 15 Olivine 15545
SiO ₂	41.0	39.8	37.8	38.6	46.3	43.6	45.3	48.0	45.2
TiO ₂	11.3	10.5	13.0	8.8	4.0	2.6	4.7	1.8	2.4
Al ₂ O ₃	9.5	10.4	8.8	6.3	10.7	7.9	10.0	9.4	8.6
Cr ₂ O ₃	0.32	0.25	0.41	0.75	0.37	0.96	0.31	0.48	0.68
FeO	18.7	19.8	19.7	22.0	19.9	21.7	20.2	20.2	22.1
MnO	0.25	0.30	0.27	—	0.27	0.28	0.28	0.30	0.30
MgO	7.03	6.7	8.4	14.4	6.5	14.9	7.0	8.7	10.3
CaO	11.0	11.1	10.7	7.7	11.8	8.3	11.4	10.4	9.8
Na ₂ O	0.51	0.40	0.36	0.36	0.28	0.23	0.29	0.32	0.31
K ₂ O	0.36	0.06	0.05	0.09	0.07	0.05	0.06	0.06	0.04
Total	99.97	99.31	99.49	99.00	100.19	100.52	99.54	99.66	99.73
Ref.	a	a	a	a	a	a	a	a	a

	Low-Ti, aluminous					Very-low-Ti				
	Luna 16 21013,8	Apollo 14 14321 Gp. 5	Apollo 14 14053	Apollo 14 14321 Gp. 1	Apollo 14 VHK 14305,390	Apollo 17 70007,296	Apollo 17 78526	Luna 24 24174,7	Luna 24 24109,78	Apollo 15 Green Gl. 15426
SiO ₂	—	—	46.4	—	—	—	—	46.0	—	44.1
TiO ₂	5.1	2.6	2.6	2.2	2.2	0.4	0.9	1.1	1.3	0.37
Al ₂ O ₃	13.3	11.8	13.6	12.7	13.0	10.3	11.0	12.1	11.6	7.8
Cr ₂ O ₃	0.20	0.46	—	0.37	0.59	0.64	0.83	0.30	0.38	0.33
FeO	19.1	17.5	16.8	16.2	16.0	17.0	17.5	22.1	22.4	21.0
MnO	0.26	0.24	0.26	0.22	0.20	0.26	0.27	0.28	0.26	—
MgO	6.0	10.3	8.5	7.9	9.9	12.0	11.0	6.0	7.0	16.7
CaO	11.7	10.8	11.2	11.2	11.6	9.7	9.9	11.6	12.3	8.4
Na ₂ O	0.55	0.39	—	0.60	0.41	0.15	0.15	0.26	0.29	0.13
K ₂ O	0.21	0.01	0.10	0.16	0.80	0.01	0.02	0.02	0.02	0.03
Total	—	—	99.0	—	—	—	—	100.00	—	99.00
Ref.	b	c	a	c	d	e	e	g	f	a

References: (a) BVSP (1981); (b) Ma et al. (1979); (c) Dickinson et al. (1985); (d) Shervais et al. (1985b); (e) Wentworth et al. (1979); (f) Ma et al. (1978); (g) Laul et al. (1978b).

TABLE A6.2. (continued).

	Low-Ti, Aluminous					Very-low-Ti				
	Luna 16 21013,8	Apollo 14 14321 Gp.5	A-14 14053	A-14 14321 Gp.1	A-14 VHK 14305,390	A-17 70007,296	A-17 78526	Luna 24 24174,7	Luna 24 24109,78	A-15 Green Gl. 15426
Sc	61	62	55	59	55	54	50	57	47	—
V	62	121	—	102	120	202	226	140	177	—
Ni	—	—	14	—	70	—	—	30	80	—
Rb	—	—	2.19	—	—	—	—	—	—	0.58
Sr	—	—	98	—	—	—	—	110	—	41
Ba	320	53	146	159	500	—	—	50	—	18
La	19.8	3.4	13.0	25	12.0	0.88	1.2	2.87	2.0	—
Ce	56	8	34.5	65	31	—	—	8.6	—	3.8
Nd	48	6.3	21.9	40	20	—	—	7.0	—	2.2
Sm	15.4	2.3	6.56	12.5	6.10	0.70	1.0	2.10	1.9	0.76
Eu	3.74	0.71	1.21	1.45	0.90	0.24	0.28	0.83	0.58	0.21
Gd	—	—	8.59	—	—	—	—	—	—	0.91
Tb	2.8	0.67	—	2.5	1.4	0.20	0.28	0.45	0.44	—
Dy	18	4.5	10.5	14.9	—	1.5	1.9	2.9	2.8	1.1
Ho	—	—	—	—	—	—	—	0.71	—	—
Er	—	—	6.51	—	—	—	—	—	—	0.8
Tm	—	—	—	—	0.75	—	—	—	—	—
Yb	9.1	3.2	6	8.3	5.35	1.1	1.4	2.00	1.9	0.93
Lu	1.28	0.61	—	1.21	0.82	0.19	0.23	0.31	0.29	0.14
Hf	11.6	1.9	9.8	8.7	3.7	0.62	0.6	1.4	1.1	—
Zr	—	70	215	320	—	—	—	50	—	—
Th	1.9	0.4	2.1	2.3	1.6	—	—	0.20	—	—
U	—	—	0.59	—	—	—	—	—	—	—
Ref	b	c	a	c	d	e	e	g	f	a

References: (a) BVSP (1981); (b) Ma et al. (1979); (c) Dickinson et al. (1985); (d) Shervais et al. (1985b); (e) Wentworth et al. (1979); (f) Ma et al. (1978); (g) Laul et al. (1978b).

TABLE A6.3. Composition (wt.%) of varieties of pristine lunar glasses arranged in sequence of increasing Ti-abundance.*

	1	2	3	4	5	6	7	8	9	10	11	12	13
SiO ₂	48.0	45.5	43.9	46.0	45.1	45.2	44.8	46.0	43.7	45.3	44.3	44.1	42.9
TiO ₂	0.26	0.38	0.39	0.40	0.41	0.43	0.45	0.55	0.57	0.66	0.91	0.97	3.48
Al ₂ O ₃	7.74	7.75	7.83	7.92	7.43	7.44	7.14	9.30	7.96	9.60	6.89	6.71	8.30
Cr ₂ O ₃	0.57	0.56	0.39	0.55	0.55	0.54	0.54	0.58	0.46	0.40	n.a.	0.56	0.59
FeO	16.5	19.7	21.9	19.1	20.3	19.8	19.8	18.2	21.5	19.6	20.2	23.1	22.1
MnO	0.19	0.22	0.24	n.a.	0.22	0.22	0.24	0.21	n.a.	0.26	0.23	0.28	0.27
MgO	18.2	17.2	16.9	17.2	17.6	18.3	19.1	15.9	17.0	15.0	19.5	16.6	13.5
CaO	8.57	8.65	8.44	8.75	8.43	8.15	8.03	9.24	8.44	9.40	7.40	7.94	8.50
Na ₂ O	n.d.	n.d.	n.d.	n.d.	n.d.	n.d.	0.06	0.11	n.d.	0.27	0.10	n.d.	0.45
K ₂ O	n.d.	n.d.	n.d.	n.d.	n.d.	n.d.	0.03	0.07	n.d.	0.04	n.d.	n.d.	n.d.
	14	15	16	17	18	19	20	21	22	23	24	25	
SiO ₂	40.8	40.5	39.4	38.5	37.9	38.8	37.3	37.2	35.6	35.6	34.0	33.4	
TiO ₂	4.58	6.90	8.63	9.12	9.12	9.30	10.0	12.5	13.8	15.3	16.4	16.4	
Al ₂ O ₃	6.16	8.05	6.21	5.79	5.63	7.62	5.68	5.69	7.15	4.81	4.6	4.6	
Cr ₂ O ₃	0.41	0.63	0.67	0.69	0.65	0.66	0.63	0.86	0.77	n.a.	0.92	0.84	
FeO	24.7	22.3	22.2	22.9	23.7	22.9	23.7	22.2	21.9	23.7	24.5	23.9	
MnO	0.30	0.25	0.28	n.a.	n.a.	0.29	n.a.	0.31	0.25	n.a.	0.31	0.30	
MgO	14.8	12.6	14.7	14.9	14.9	11.6	14.3	14.5	12.1	13.0	13.3	13.0	
CaO	7.74	8.64	7.53	7.40	7.41	8.55	7.62	7.04	7.89	6.49	6.9	6.27	
Na ₂ O	0.42	0.39	0.41	0.38	0.36	0.39	0.31	0.28	0.49	0.50	0.23	0.05	
K ₂ O	0.10	n.d.	0.04	n.d.	n.d.	n.d.	n.d.	0.29	0.12	n.d.	0.16	0.12	

* These are the most primitive compositions within each of the groups (Delano, 1986).

n.a. = not analyzed; n.d. = not detected.

(1) Apollo 15 green C; (2) Apollo 15 green A; (3) Apollo 16 green; (4) Apollo 15 green B; (5) Apollo 15 green D; (6) Apollo 15 green E; (7) Apollo 14 green B; (8) Apollo 14 VLT; (9) Apollo 11 green; (10) Apollo 17 VLT (R.D. Warner et al., 1979b); (11) Apollo 17 green (preliminary); (12) Apollo 14 green A; (13) Apollo 15 yellow; (14) Apollo 14 yellow; (15) Apollo 17 yellow; (16) Apollo 17 orange; (17) Apollo 17 orange (74220-type); (18) Apollo 15 orange; (19) Apollo 17 orange; (20) Apollo 11 orange; (21) Apollo 14 orange; (22) Apollo 15 red; (23) Apollo 14 red (preliminary); (24) Apollo 14 black; (25) Apollo 12 red (Marvin and Walker, 1978).

TABLE A6.4. Abundances of Ni ($\mu\text{g/g}$) and MgO (wt.%) in pristine lunar glasses demarcated according to their TiO_2 abundances* (after *Delano*, 1986).

	Ni($\mu\text{g/g}$)	MgO (wt.%)	Ni/Mg ($\times 10^3$)
<i>(TiO₂ ≤ 1.0 wt.%)</i>			
Apollo 15 green A	170	17.2	1.64
Apollo 15 green B	150	17.2	1.45
Apollo 15 green E	170	18.3	1.54
Apollo 14 green B	185	19.1	1.61
Apollo 14 VLT	125	15.9	1.30
Apollo 11 green	135	17.0	1.32
Apollo 17 VLT	150	15.0	1.66
Apollo 17 green	188	19.5	1.60
Apollo 14 green A	115	16.6	1.15
Apollo 15 green C	90	18.2	0.82
<i>(TiO₂ ≥ 3.5 wt.%)[†]</i>			
Apollo 15 yellow	85	13.5	1.04
Apollo 14 yellow	82	14.8	0.92
Apollo 17 yellow	55	12.6	0.72
Apollo 17 orange	46	14.7	0.52
Apollo 17 orange (74220)	70	14.9	0.78
Apollo 17 orange	33	11.6	0.47
Apollo 11 orange	30	14.3	0.35
Apollo 14 orange	30	14.5	0.34
Apollo 15 red	<50	12.1	<0.69
Apollo 14 black	≤22	13.3	≤0.27

* Precision for Ni is typically $\pm 10 \mu\text{g/g}$ with a detection limit of about $20 \mu\text{g/g}$.

[†] No volcanic glasses have been found having TiO_2 abundances between 1.0 wt.% and 3.5 wt.%.

TABLE A6.5. Abundances of trace elements in the Apollo 17 pristine orange glass.

Element	Abundance	Reference	Element	Abundance	Reference
Li	12 $\mu\text{g/g}$	1,2,3,4	Ba	78 $\mu\text{g/g}$	3,4,6,15
F	60 $\mu\text{g/g}$	1,5	La	6.2 $\mu\text{g/g}$	1,4,8,9,15
P	200 $\mu\text{g/g}$	1,6	Ce	19 $\mu\text{g/g}$	1,3,4,9,15
S	725 $\mu\text{g/g}$	4,6,7	Pr	2.5 $\mu\text{g/g}$	1
Cl	20.2 $\mu\text{g/g}$	1	Nd	17.5 $\mu\text{g/g}$	1,3,4,15
K	625 $\mu\text{g/g}$	1,3,4,6	Sm	6.7 $\mu\text{g/g}$	1,3,4,8,9,15
Sc	46 $\mu\text{g/g}$	1,8,9	Eu	1.85 $\mu\text{g/g}$	1,3,4,9,15
V	131 $\mu\text{g/g}$	1,6	Gd	8.8 $\mu\text{g/g}$	1,3,4,15
Co	61 $\mu\text{g/g}$	1,6,8,9	Tb	1.6 $\mu\text{g/g}$	1,9
Ni	72 $\mu\text{g/g}$	1,4,6,9,10,11	Dy	9.3 $\mu\text{g/g}$	1,3,4,15
Cu	26 $\mu\text{g/g}$	1,6	Ho	1.9 $\mu\text{g/g}$	1
Zn	210 $\mu\text{g/g}$	1,4,6,8,10,11,12	Er	5.1 $\mu\text{g/g}$	1,3,4,15
Ga	16 $\mu\text{g/g}$	1,12	Yb	4.2 $\mu\text{g/g}$	1,3,4,8,9,15
Ge	230 ng/g	1,8,10,11,12	Lu	0.60 $\mu\text{g/g}$	1,3,4,9,15
As	15 ng/g	1	Hf	5.8 $\mu\text{g/g}$	1,9,13,14
Se	430 ng/g	10,11	Ta	1.2 $\mu\text{g/g}$	1,9
Br	88 ng/g	10	W	83 ng/g	1
Rb	1.2 $\mu\text{g/g}$	1,3,4,6,10	Re	0.04 ng/g	10,11
Sr	195 $\mu\text{g/g}$	1,3,4,6,	Os	0.04 ng/g	11
Y	46 $\mu\text{g/g}$	1,4,6	Ir	0.03 ng/g	8,11
Zr	185 $\mu\text{g/g}$	1,3,4,6,13,14	Au	1.1 ng/g	1,8,10,11,12
Nb	14 $\mu\text{g/g}$	1,4,6	Hg	7 ng/g	2,8
Pd	1.4 ng/g	11	Tl	9 ng/g	10,11
Ag	83 ng/g	10,11	Pb	2.5 $\mu\text{g/g}$	16
Cd	150 \pm 100 ng/g	8,10,11,12	Bi	1 ng/g	10,11
In	20 ng/g	8,11,12	Th	480 ng/g	9,16
Te	60 ng/g	8,10	U	135 ng/g	1,2,4,8,10,11,16,17
Cs	60 ng/g	1,10			

References: (1) *Wänke et al.* (1973); (2) *Jovanovic and Reed* (1974); (3) *Philpotts et al.* (1974); (4) *Rhodes et al.* (1974); (5) *Goldberg et al.* (1976); (6) *Duncan et al.* (1974); (7) *Gibson and Andrawes* (1978a); (8) *Kröhenbühl* (1980); (9) *Blanchard and Budahn* (1978); (10) *Morgan et al.* (1974); (11) *Morgan and Wandless* (1979); (12) *Wasson et al.* (1976); (13) *Ehmann and Chyi* (1974); (14) *Hughes and Schmitt* (1985); (15) *Masuda et al.* (1974); (16) *Tatsumoto et al.* (1973); (17) *Fleischer and Hart* (1974).

TABLE A6.6. Abundances of trace elements in the Apollo 15 pristine green glasses.

Element	Abundance	Reference	Element	Abundance	Reference
F	42 ± 21 µg/g	1	Ba	17 µg/g	4,7
S	330 µg/g	2	La	1.3 µg/g	3,4,7
K	145 µg/g	7	Ce	4.0 µg/g	4,7
Sc	39 µg/g	3,4,6	Pr	0.58 µg/g	4
V	163 µg/g	3,4	Nd	2.4 µg/g	4,7
Co	77 µg/g	3,4,5,6	Sm	0.82 µg/g	3,4,7
Ni*	170 µg/g	3,4,6	Eu	0.24 µg/g	3,4,7
Cu	5.4 µg/g	4	Gd	1.2 µg/g	4,7
Zn	16 µg/g	5,6	Tb	0.19 µg/g	3,4
Ga	4.2 µg/g	4,6	Dy	1.4 µg/g	4,7
Ge	58 ng/g	5,6	Ho	0.29 µg/g	4
Se	69 ng/g	5	Er	0.9 µg/g	4,7
Br	40 ng/g	5	Tm	0.15 µg/g	4
Rb	0.40 µg/g	4,5	Yb	0.97 µg/g	3,4,7
Sr	28 µg/g	8	Lu	0.15 µg/g	3,4,7
Y	8.7 µg/g	4	Hf	0.6 µg/g	3,4,7
Zr	24 µg/g	4,7	W	0.14 µg/g	4
Nb	1.8 µg/g	4	Re	0.02 ng/g	5
Ag	8.9 ng/g	5	Ir	0.29 ng/g	5,6
Cd	58 ng/g	5,6	Au	0.4 ng/g	5,6
In	1.1 ng/g	5,6	Tl	1.13 ng/g	5
Sn	0.13 µg/g	4	Pb	1.0 µg/g	4
Sb	0.12 ng/g	5	Bi	0.38 ng/g	5
Te	3.3 ng/g	5	Th	0.2 µg/g	4
Cs	24 ng/g	5	U	44 ± 7 ng/g	8

* Ni varies among the Apollo 15 green glasses. The variation is a result of magmatic fractionation processes. Refer to Table A6.4 for additional information.

References: (1) Goldberg et al. (1976); (2) Gibson and Andrawes (1978a); (3) Ma et al. (1981b); (4) S.R. Taylor et al. (1973a); (5) Ganapathy et al. (1973); (6) Chou et al. (1975); (7) Wiesmann and Hubbard (1975); (8) Fleischer and Hart (1974).

TABLE A6.7. Abundances of trace elements ($\mu\text{g/g}$) in the Apollo 15 pristine yellow/brown glass from two INAA investigations conducted at Oregon State University by R.A. Schmitt and coworkers.

Element	Ma et al. (1981b)	Delano (1986)
Sc	43.5 \pm 0.2	41.5 \pm 3.3
V	116 \pm 2	118 \pm 4
Co	65 \pm 2	64 \pm 5
La	9.4 \pm 0.8	7.9 \pm 0.9
Ce	—	23 \pm 6
Sm	6.8 \pm 0.4	6.0 \pm 0.2
Eu	1.51 \pm 0.02	1.51 \pm 0.15
Tb	1.40 \pm 0.06	—
Yb	4.6 \pm 0.1	2.9 \pm 0.5
Lu	0.62 \pm 0.03	—
Hf	5.0 \pm 0.3	4.8 \pm 1.1
Ta	0.69 \pm 0.05	0.70 \pm 0.11

TABLE A6.8. References for surface-correlated volatile elements enriched in pristine lunar glasses.

B (1)	Br (3,12,16)
C (20)	Ag (6,12,19)
N (23)	Cd (6-8,12,14,18,19)
F (2-5)	In (6,7,14,19)
Na (6-8,18,21)	Sb (6,19)
S (2,8-10,18,21)	Te (14,19)
Cl (2,3,18,21,24)	I (16)
Ar (11,23)	Xe (16)
K (6,24)	Ir (14)
Cu (2,5)	Au (6,7,14,19)
Zn (2,5-9,12-14,18,19,21)	Hg (14,17)
Ga (2,5,7)	Ti (2,12,13,19,22)
Ge (6,7,14,19)	Pb (2,8,13,15,22)
Se (19)	Bi (6)

References: (1) Meyer and Schonfeld (1977); (2) Meyer et al. (1975); (3) Jovanovic and Reed (1974); (4) Goldberg et al. (1975, 1976); (5) Wänke et al. (1973); (6) Chou et al. (1975); (7) Wasson et al. (1976); (8) Cirlin et al. (1978); (9) Butler and Meyer (1976), Butler (1978); (10) Grant et al. (1974), Thode and Rees (1976), Gibson and Andrawes (1978a), Ding et al. (1983); (11) Alexander et al. (1980); Chou et al. (1973, 1974), Eberhardt et al. (1973), Eugster et al. (1980), Huneke (1978), Podosek and Huneke (1973), Schaeffer and Husain (1973), Lakatos et al. (1973); (12) Morgan et al. (1974); (13) Allen et al. (1975); (14) Krähenbühl (1980); (15) Nunes et al. (1974b); Silver (1974a,b), Tatsumoto et al. (1973), Tera and Wasserburg (1976), Cirlin and Housley (1977); (16) Eugster et al. (1980); (17) Jovanovic and Reed (1979); (18) Cirlin and Housley (1979); (19) Morgan and Wandless (1979, 1984); (20) Epstein and Taylor (1973), Gibson and Moore (1973c), Sato (1979), Wszolek et al. (1973); (21) Clanton et al. (1978); (22) Reed et al. (1977); (23) Barraclough and Marti (1985); (24) Carusi et al. (1972).

TABLE A6.9. Bulk compositions of some monomict KREEP rocks, the KREEP-like 14303 granite clast, a typical VHA basalt (probably not really a basalt, but an impact melt breccia), and an average composition for high-K KREEP breccias.

	Na ₂ O (wt.%)	MgO (wt.%)	Al ₂ O ₃ (wt.%)	SiO ₂ (wt.%)	K ₂ O (wt.%)	CaO (wt.%)	TiO ₂ (wt.%)	FeO* (wt.%)	Li (μg/g)	P (μg/g)	S (μg/g)	Sc (μg/g)
15382 basalt	0.87	7.83	16.9	52.5	0.53	9.43	1.90	9.02	—	2400	—	19
15386 basalt	0.77	9.34	15	50.8	0.61	9.60	2.06	10.4	27.2	3054	900	22
15405 QMD clasts	0.89	3.60	12.6	56.4	2.06	8.10	1.85	13.5	40.9	1700	—	30
14303 'granite' clast	1.25	3.30	18.5	58	3.6	8.8	0.75	5.57	—	—	—	10.7
72275 basalt clasts	0.42	8.42	14.3	49.2	0.33	10.4	1.10	14.0	—	—	—	50
High-K KREEP breccias	0.86	10.6	16.6	47.9	0.83	9.51	1.67	10.6	56	3400	1100	23
61156 VHA (basalt ??)	0.40	9.59	23	45	0.108	13.4	0.63	7.83	10.5	960	1200	9.4

	V (μg/g)	Cr (μg/g)	Mn (μg/g)	Co (μg/g)	Ni (μg/g)	Cu (μg/g)	Zn (μg/g)	Ga (μg/g)	Ge (ng/g)	As (ng/g)	Se (ng/g)	Br (ng/g)
15382	60	1780	940	17	23	—	2.6	—	47	—	72	142
15386	62	2280	1200	23	12.5	—	3.5	6.2	61	—	—	—
15405	33	1370	1400	7.9	<2	—	5.6	—	250	—	96.5	170
14303	23	550	480	14.1	<60	—	—	9.2	—	—	—	—
72275	120	2940	1630	35	60	—	4	3.14	—	—	—	—
High-K KREEP	43	1300	1080	33	20	20	3.6	7.5	40	—	—	—
61156 (VHA)	—	917	780	59	690	6.6	5.0	4.5	1750	370	—	—

	Rb (μg/g)	Sr (μg/g)	Y (μg/g)	Zr (μg/g)	Nb (μg/g)	Ru (ng/g)	Pd (ng/g)	Ag (ng/g)	Cd (ng/g)	In (ng/g)	Sb (ng/g)	Te (ng/g)
15382	15.4	189	—	1068	—	—	<0.6	0.44	87	2.66	0.17	1.0
15386	16.2	187	—	970	—	—	—	—	10	1.8	—	—
15405	34	172	—	1620	—	—	<0.9	2.33	14	23	0.88	5.7
14303	113	230	—	1020	—	—	—	—	—	—	—	—
72275	13	85.6	—	623	—	—	—	—	—	—	—	—
High-K KREEP	22	200	300	1700	80	500	—	—	15	1.2	—	—
61156 (VHA)	2.43	153	62.3	299	16.3	—	59	—	—	—	—	—

TABLE A6.9. (continued)

	Cs (ng/g)	Ba (μg/g)	La (μg/g)	Ce (μg/g)	Nd (μg/g)	Sm (μg/g)	Eu (μg/g)	Gd (μg/g)	Tb (μg/g)	Ho (μg/g)	Yb (μg/g)	Lu (μg/g)
15382	725	702	73.8	215	115	31.4	2.75	42.9	6.2	—	21.6	3.07
15386	800	744	70.8	179	114	33	2.56	45.4	5.3	—	21.3	2.84
15405	1055	1695	217	558	328	87.5	2.65	110	17.3	—	60.4	8.42
14303	2200	2080	57	147	93	22.8	3.30	—	4.7	6.7	18	2.6
72275	450	398	49	130	81.8	22.8	1.61	—	4.7	5.8	13	1.8
High-K KREEP	1200	1200	110	270	180	49	3.0	57	10.0	14	36	5.0
61156 (VHA)	150	207	21.5	53.4	33.1	9.6	1.32	11.9	2.10	3.3	6.65	0.90
	Hf (μg/g)	Ta (μg/g)	W (μg/g)	Re (ng/g)	Os (ng/g)	Ir (ng/g)	Au (ng/g)	Tl (ng/g)	Pb (μg/g)	Bi (ng/g)	Th (μg/g)	U (μg/g)
15382	29.9	3.1	—	0.0089	0.018	0.0132	0.0033	3.2	5.94	290	10.3	3.37
15386	23.6	2.4	—	—	—	0.061	0.22	—	—	—	10.0	2.80
15405	47.9	11.6	—	0.0525	0.007	0.175	0.15	4.8	14	260	56.1	11.0
14303	21	3.1	—	—	—	<2.8	—	—	—	—	17.9	5.6
72275	17.0	1.51	—	—	—	<2.0	—	—	—	—	5.6	1.35
High-K KREEP	37	4.0	2.0	—	—	0.1	0.1	—	—	—	18	5.0
61156 (VHA)	7.3	0.83	0.56	2.6	—	23	22	—	2.1	—	3.24	0.86

* All Fe is reported as FeO, albeit a small proportion may actually be Fe-metal.

References: 15382, 15386 and 15405, literature compilations of *Ryder* (1985); 14303, *Warren et al.* (1983b); 72275, *Stoeser et al.* (1974), *Blanchard et al.* (1975a), *Ryder et al.* (1977), *Salpas et al.* (1987); high-K KREEP, *Warren and Wasson* (1979a), except see *Warren et al.* (1983c) regarding Cs; 61156, numerous references, all cited in *Ryder and Norman* (1980). Note: except for a few REE, if an element is not in this table, no data have been published for that element in these particular samples.

TABLE A6.10. Selected ratios between incompatible elements, which are characteristically enriched, in approximately these proportions, in KREEP.

	K	P	Rb	Zr	Cs	Ba	La	Gd	Tb	Lu	Hf	Ta	U
Be	880	440	2.8	220	0.15	150	14	7.3	1.3	0.64	4.7	0.51	0.64
Li	190	94	0.61	47	0.033	33	3.1	1.6	0.28	0.14	1.0	0.11	0.14
K	1	0.49	0.0032	0.25	0.00017	0.17	0.016	0.0083	0.0014	0.00072	0.0054	0.00058	0.00072
P	2.0	1	0.0065	0.50	0.00035	0.35	0.032	0.017	0.0029	0.0015	0.011	0.0012	0.0015
Rb	310	150	1	77	0.055	55	5.0	2.6	0.45	0.23	1.7	0.18	0.23
Y	23	11	0.073	5.7	0.0040	4.0	0.37	0.19	0.033	0.017	0.12	0.013	0.017
Zr	4.1	2	0.013	1	0.00071	0.71	0.065	0.034	0.0059	0.0029	0.022	0.0024	0.0029
Nb	86	43	0.28	21	0.015	15	1.4	0.71	0.13	0.063	0.46	0.050	0.063
Cs	5800	2800	18	1400	1	1000	92	48	8.3	4.2	31	3.3	4.2
Ba	5.8	2.8	0.018	1.4	0.0010	1	0.092	0.048	0.0083	0.0042	0.031	0.0033	0.0042
La	63	31	0.20	15	0.011	10.9	1	0.52	0.091	0.045	0.34	0.036	0.045
Ce	26	13	0.082	6.3	0.0044	4.4	0.41	0.21	0.037	0.019	0.14	0.015	0.019
Nd	38	19	0.12	9.4	0.0067	6.7	0.61	0.32	0.056	0.028	0.21	0.022	0.028
Sm	140	69	0.45	35	0.024	24	2.2	1.2	0.20	0.102	0.76	0.082	0.102
Gd	120	60	0.39	30	0.021	21	1.9	1	0.18	0.088	0.65	0.070	0.088
Tb	690	340	2.2	170	0.12	120	11	5.7	1	0.50	3.7	0.40	0.50
Ho	490	240	1.6	120	0.086	86	7.9	4.1	0.71	0.36	2.6	0.29	0.36
Yb	190	94	0.61	47	0.033	33	3.1	1.6	0.28	0.14	1.0	0.11	0.14
Lu	1380	680	4.4	340	0.24	240	22	11.4	2.0	1	7.4	0.80	1.00
Hf	190	92	0.59	46	0.032	32	3.0	1.5	0.27	0.14	1	0.11	0.14
Ta	1700	850	5.5	420	0.30	300	28	14	2.5	1.3	9.3	1	1.25
W	3400	1700	11	850	0.60	600	55	29	5.0	2.5	19	2.0	2.5
Th	380	190	1.2	94	0.067	67	6.1	3.2	0.56	0.28	2.1	0.22	0.28
U	1400	680	4.4	340	0.24	240	22	11	2.0	1.0	7.4	0.80	1

To read table, find element for numerator along top row, and denominator element along leftmost column; e.g., the K/Be ratio is 880. Ratios involving Be are based on *Wänke et al. (1977)*. All other ratios are based on average high-K KREEP (Table A6.9).

TABLE A6.11. Bulk compositions of some monomict ferroan anorthosites.

	Na ₂ O (wt.%)	MgO (wt.%)	Al ₂ O ₃ (wt.%)	SiO ₂ (wt.%)	CaO (wt.%)	FeO* (wt.%)	Li (μg/g)	C (μg/g)	N (μg/g)	F (μg/g)	P (μg/g)	S (μg/g)	K (μg/g)
15363	0.288	3.85	28.0	45.3	16.8	4.76	—	—	—	—	—	—	107
15415	0.364	0.26	35.6	44.5	20.4	0.21	—	9	—	—	40	<100	122
60015	0.392	0.53	35.0	43.9	19.0	0.33	<6	20	23	18	65	27	54
62236	0.215	3.55	30.1	44.2	17.6	3.67	—	—	—	—	—	—	111
62237	0.205	5.11	29.6	41.9	16.3	5.89	—	—	—	—	—	—	104
65315	0.303	0.25	34.9	44.3	19.1	0.31	—	—	—	14	40	—	58
67455c	0.42	1.31	32.3	44.9	18.1	2.62	3.47	—	—	—	<100	—	235
	Cl (μg/g)	Sc (μg/g)	Ti (μg/g)	V (μg/g)	Cr (μg/g)	Mn (μg/g)	Co (μg/g)	Ni (μg/g)	Cu (μg/g)	Zn (μg/g)	Ga (μg/g)	Ge (ng/g)	As (ng/g)
15363	—	9.3	700	—	650	520	6.0	9	—	6.6	4.5	—	—
15415	150	0.42	120	—	20	45	0.21	9	58	0.26	3.1	1.2	4.1
60015	<8	0.60	100	4.7	38	75	0.8	—	0.5	—	—	—	—
62236	—	5.8	290	—	490	430	7.9	4.0	—	1.7	2.9	10	—
62237	—	4.1	100	—	400	540	12.2	6	—	1.6	2.8	3.3	—
65315	104	0.39	72	—	20	59	0.58	1.4	2.1	93	3.25	—	2
67455c	—	—	780	—	100	300	—	2.5	—	2.7	—	1.8	—
	Se (ng/g)	Br (ng/g)	Rb (μg/g)	Sr (μg/g)	Y (μg/g)	Zr (μg/g)	Nb (μg/g)	Pd (ng/g)	Ag (ng/g)	Cd (ng/g)	In (ng/g)	I (ng/g)	Sb (ng/g)
15363	—	—	<6	140	—	<100	—	—	—	—	—	—	—
15415	0.23	2.3	0.17	188	—	—	—	—	1.73	0.57	0.18	—	0.067
60015	—	<0.09	0.12	173	0.4	0.11	0.2	—	—	—	—	—	—
62236	—	—	—	145	—	—	—	—	—	0.79	1.2	—	—
62237	—	—	—	133	—	—	—	—	—	3.9	<1.1	—	—
65315	—	930	0.17	167	<0.3	15	<0.2	—	—	—	—	47	—
67455c	56	48	0.88	116	—	—	—	<0.31	0.41	1.45	0.73	—	0.11

TABLE A6.11. (continued).

	Te (ng/g)	Cs (ng/g)	Ba (μ g/g)	La (μ g/g)	Ce (μ g/g)	Nd (μ g/g)	Sm (μ g/g)	Eu (μ g/g)	Gd (μ g/g)	Tb (μ g/g)	Dy (μ g/g)	Yb (μ g/g)	Lu (μ g/g)
15363	—	<200	<60	0.31	0.52	—	0.131	0.88	—	0.042	—	0.28	0.045
15415	2.1	26	6.2	0.15	0.33	0.19	0.053	0.81	0.056	0.0085	0.054	0.034	0.0043
60015	—	—	9	0.13	0.63	0.35	0.07	0.82	0.06	—	—	0.02	0.003
62236	—	—	<60	0.18	0.68	—	0.093	0.61	—	—	—	0.15	0.022
62237	—	—	6	0.19	0.47	0.28	0.078	0.61	—	0.017	—	0.101	0.016
65315	—	15	4.8	0.12	—	—	0.04	0.74	—	—	0.056	0.026	0.004
67455c	<0.24	56	13.6	—	0.92	0.67	0.228	0.80	0.324	—	0.394	0.260	0.030
	Hf (μ g/g)	Ta (μ g/g)	W (μ g/g)	Re (ng/g)	Os (ng/g)	Ir (ng/g)	Au (ng/g)	Tl (ng/g)	Pb (μ g/g)	Bi (ng/g)	Th (ng/g)	U (ng/g)	
15363	<0.15	<0.12	—	0.057	0.95	1.03	0.061	—	—	—	<100	—	
15415	0.014	—	0.026	0.00084	—	<0.010	0.117	0.09	0.23	0.097	4	2	
60015	0.011	<0.01	—	—	—	—	—	—	0.19	—	3.7	1.3	
62236	—	—	—	0.007	—	0.02	0.006	—	—	—	<10	<40	
62237	0.035	—	—	—	—	0.07	0.08	—	—	—	<12	4.3	
65315	0.49	—	0.019	—	—	—	—	—	—	—	—	<0.6	
67455c	—	—	—	<0.0003	<0.012	0.001	0.0025	0.32	—	0.25	—	5.7	

* All Fe is reported as FeO, albeit a small proportion may actually be Fe-metal.

References: 15363, Warren *et al.* (1987); 15415, compilation by Ryder (1985); 60015, 62236 and 62237, references listed by Ryder and Norman (1980), plus, for 62237, Haskin *et al.* (1981); 65315, Wänke *et al.* (1974); 67455c (clast 67455,32), Lindstrom *et al.* (1977a) and Hertogen *et al.* (1977).

TABLE A6.12. Bulk compositions of some monomict Mg-rich rocks.

	Na ₂ O (wt.%)	MgO (wt.%)	Al ₂ O ₃ (wt.%)	SiO ₂ (wt.%)	CaO (wt.%)	TiO ₂ (wt.%)	FeO* (wt.%)	Li (μg/g)	F (μg/g)	P (μg/g)	S (μg/g)
15455c	0.44	6.9	27.0	47.7	14.8	0.10	2.91	7.2	—	220	—
61224,6	0.91	12.8	13.2	50.7	11.6	0.40	9.91	—	—	—	—
67435c	0.14	31.7	18.3	37.5	6.7	0.05	5.55	—	—	—	—
67915c	1.25	3.0	11.8	56.0	9.2	5.1	12.3	—	—	[40]	—
72415	0.13	44.8	1.3	40.3	1.1	0.03	11.7	—	—	200	44
76535	0.23	20.0	19.9	43.0	10.8	0.05	5.0	3.0	9	100	<100
77215	0.40	12.5	15.0	51.1	9.1	0.33	9.9	12.3	—	480	—
	K (μg/g)	Cl (μg/g)	Sc (μg/g)	V (μg/g)	Cr (μg/g)	Mn (μg/g)	Co (μg/g)	Ni (μg/g)	Zn (μg/g)	Ga (μg/g)	Ge (ng/g)
15455c	540	—	5.3	—	1180	376	27.2	21	1.4	—	33
61224,6	140	—	20.8	—	1990	1230	23.6	8.3	4.0	3.0	4.3
67435c	110	—	1.9	101	510	800	57	1230	—	—	—
67915c	4500	—	32	3	200	1240	6.6	—	—	—	—
72415	24	<6	4.3	50	2300	940	55	200	5	—	150
76535	233	<0.8	1.94	—	730	500	27.6	44	1.2	—	1.7
77215	1440	—	15.6	—	2470	1270	28.0	2	3.1	4.4	15.2
	Se (ng/g)	Br (ng/g)	Rb (μg/g)	Sr (μg/g)	Y (μg/g)	Zr (μg/g)	Nb (μg/g)	Ag (ng/g)	Cd (ng/g)	In (ng/g)	I (ng/g)
15455c	8.3	35	1.1	131	—	70	—	1.7	1.0	0.05	—
61224,6	—	—	—	160	—	[170]	—	—	4.1	<0.6	—
67435c	—	—	—	—	—	—	—	—	—	—	—
67915c	—	—	—	260	—	300	—	—	—	—	—
72415	5.0	18	0.036	10	1.1	2.6	0.3	15	0.6	—	0.9
76535	4.1	3.2	0.22	114	—	17	—	0.12	0.60	—	1.1
77215	77	42	4.38	104	—	175	—	0.62	4.9	0.30	—

TABLE A6.12. (continued).

	Sb (ng/g)	Te (ng/g)	Cs (ng/g)	Ba (μg/g)	La (μg/g)	Ce (μg/g)	Nd (μg/g)	Sm (μg/g)	Eu (μg/g)	Gd (μg/g)	Tb (μg/g)	Dy (μg/g)
15455c	0.079	2.6	126	90	4.8	11.2	6.8	1.81	1.21	2.21	0.35	2.59
61224,6	—	—	—	32	1.47	4.3	<9	0.87	1.43	—	0.22	—
67435c	—	—	—	18	1.3	—	—	0.63	0.33	—	0.10	0.6
67915c	—	—	—	340	22.7	54	37	11.0	2.42	—	2.2	15
72415	1.6	0.3	14	4.1	0.15	0.37	—	0.08	0.061	—	0.017	0.11
76535	0.014	0.28	14	33	1.51	3.8	2.3	0.61	0.70	0.73	—	0.80
77215	0.121	1.0	180	176	8.5	24.6	14.2	4.0	1.05	6.6	0.89	7.1
	Yb (μg/g)	Lu (μg/g)	Hf (μg/g)	Ta (μg/g)	Re (ng/g)	Ir (ng/g)	Au (ng/g)	Tl (ng/g)	Pb (μg/g)	Bi (ng/g)	Th (ng/g)	U (ng/g)
15455c	1.43	0.216	0.67	0.14	0.004	0.01	0.016	0.054	0.59	0.14	630	170
61224,6	1.06	0.16	0.55	0.16	0.013	0.148	0.079	—	—	—	190	<600
67435c	0.38	0.053	0.37	[0.02]	—	—	—	—	—	—	—	—
67915c	8.5	1.27	8.6	2.2	—	—	—	—	—	—	3900	1000
72415	0.074	0.012	0.10	—	0.05	1.6	1.4	0.041	—	0.8	<150	5
76535	0.56	0.079	0.41	—	0.0012	0.0054	0.0025	0.012	—	0.037	190	54
77215	4.5	0.68	3.4	0.37	0.008	0.071	0.045	0.61	1.08	0.13	1840	600

* All Fe is reported as FeO, although a small proportion may actually be Fe-metal.

References: 15455c (norite), references compiled by *Ryder* (1985); 61224,6 (gabbro), *Marvin and Warren* (1980); 67435c (spinel troctolite), *Prinz et al.* (1973), *Ma et al.* (1981a); 67915c (sodic ferrogabbro), *Taylor et al.* (1980); 72415 (dunite), references compiled by *Ryder and Norman* (1979) — principally *Laul and Schmitt* (1975b) and *Higuchi and Morgan* (1975); 76535 (troctolite), references compiled by *Ryder and Norman* (1979), plus *Garg and Ehmann* (1976); 77215 (norite), references compiled by *Ryder and Norman* (1979), including those for 77075 and 77077, which are pieces of the same norite as 77215.

TABLE A6.13. Bulk compositions of some monomict "evolved" lithologies.

	Na ₂ O (wt.%)	MgO (wt.%)	Al ₂ O ₃ (wt.%)	SiO ₂ (wt.%)	K ₂ O (wt.%)	CaO (wt.%)	TiO ₂ (wt.%)	FeO* (wt.%)
12033;507	1.9	0.3	12.1	73	5.6	1.6	0.7	3.2
12073c	2.14	0.35	32.3	48.3	0.25	15.8	0.13	1.1
14047c	1.56	2.77	28.1	48.1	0.21	14.8	0.42	4.2
14321c	0.52	0.07	12.5	74.2	8.1	8.8	0.33	5.6
67975c	0.39	9.8	11.3	—	1.1	13.4	3.53	14.5
	Sc (μg/g)	V (μg/g)	Cr (μg/g)	Mn (μg/g)	Co (μg/g)	Ni (μg/g)	Zn (μg/g)	Ga (μg/g)
12033;507	—	—	<600	<500	<8	<21	—	7
12073c	1.97	—	98	140	7.1	71	1.16	17
14047c	9.2	—	274	480	6.7	9.5	3.2	12
14321c	3.0	—	17	175	0.94	4.9	1.9	9.0
67975c	38.8	58	1770	1710	14.8	<80	—	—
	Ge (ng/g)	Br (ng/g)	Rb (μg/g)	Sr (μg/g)	Zr (μg/g)	Cd (ng/g)	Cs (ng/g)	Ba (μg/g)
12033;507	—	—	—	—	—	—	—	8000
12073c	32	<1200	—	750	310	—	—	620
14047c	67	—	—	380	470	9.6	220	600
14321c	87	—	167	64	660	34	5700	2160
67975c	—	—	25	159	—	—	410	1200
	La (μg/g)	Ce (μg/g)	Nd (μg/g)	Sm (μg/g)	Eu (μg/g)	Tb (μg/g)	Dy (μg/g)	Yb (μg/g)
12033;507	—	—	—	—	—	—	—	—
12073c	16.2	35	16	4.6	8.4	0.87	5.8	2.7
14047c	27.7	64	40	10.7	5.9	2.17	11.3	7.2
14321c	44.3	117	59	17.3	1.17	4.3	31.5	32.2
67975c	88	240	—	45	—	—	—	—
	Lu (μg/g)	Hf (μg/g)	Ta (μg/g)	Re (ng/g)	Ir (ng/g)	Au (ng/g)	Th (ng/g)	U (ng/g)
12033;507	—	—	—	—	—	—	—	—
12073c	0.37	1.4	0.18	0.037	0.11	—	1.2	0.4
14047c	1.13	6.8	0.64	0.061	0.76	0.074	2.8	0.71
14321c	5.1	13.9	8.3	<0.018	0.047	0.035	65	23.4
67975c	—	—	—	—	—	—	—	—

* All Fe is reported as FeO, although a small proportion may actually be Fe-metal.

References: 12033,507 (felsite), *Warren et al.* (1987); 12073c (alkali anorthosite), *Reed et al.* (1971b), *Warren et al.* (1981); 14047c (alkali anorthosite), *Warren et al.* (1983a); 14321c (granite), *Warren et al.* (1983b); 67975c (alkali gabbroanorthite), *James et al.* (1987).

TABLE A6.14. Major element oxides of the bulk average of matrix samples of fragmental breccias (wt.%).

	Bulk Avg.	67015(i)	67015(ii)	67016(i)	67016(ii)	67115	67455(i)	67455(ii)	72275	14063(i)	14063(ii)
SiO ₂	45.1	(44.8)	46.0	45.3	44.8	44.8	44.5	45.2	48.3	—	45.0
TiO ₂	0.32	0.51	0.50	0.44	0.35	0.24	0.21	0.20	1.0	1.5	1.64
Al ₂ O ₃	30.4	29.0	29.5	30.01	28.2	31.2	30.8	30.6	16.3	22.0	21.6
Cr ₂ O ₃	0.06	0.08	0.06	—	0.08	0.06	0.05	0.05	0.35	0.18	0.19
FeO	3.34	4.26	3.65	3.57	3.94	2.60	3.58	4.37	11.9	7.0	6.9
MnO	0.05	—	0.05	0.05	0.05	0.04	0.05	0.06	0.17	0.08	0.09
MgO	3.14	5.1	3.9	3.5	4.4	3.0	2.83	3.4	10.3	—	10.7
CaO	17.0	15.7	15.4	16.9	16.7	17.8	17.1	18.1	11.0	13.1	12.6
Na ₂ O	0.48	0.51	0.52	0.48	0.49	0.51	0.44	0.38	0.44	0.84	0.86
K ₂ O	0.04	—	0.08	0.06	0.04	0.08	0.02	0.03	0.25	0.17	0.17
P ₂ O ₅	—	—	—	0.07	0.02	0.02	0.03	0.01	—	—	0.25
Σ	99.9	(100)	99.7	100.4	99.1	100.4	99.6	102.4	100.0	—	100.0
Mg/(Mg+Fe) atom ratio	0.63	0.68	0.66	0.64	0.67	0.67	0.58	0.58	0.61	—	0.73

Bulk average: James (1981); 67015(i): Marvin et al. (1987); 67015(ii): Wänke et al. (1975); 67016(i): Duncan et al. (1973); 67016(ii): Wänke et al. (1976); 67115: Rose et al. (1973a); 67455(i): Lindstrom et al. (1977a); 67455(ii): Wänke et al. (1973); 72275: Blanchard et al. (1975a); 14063(i): Laul et al. (1972a); 14063(ii): average of 3 chips, Rose et al. (1972).

TABLE A6.15. Sr, incompatible elements, and transition metals in matrix samples of fragmental breccias (μg/g).

	67015(i)	67015(ii)	67016(i)	67016(ii)	67115	67455(i)	67455(ii)	72275	14063(i)	14063(ii)
Li	—	—	—	—	4.8	4.0	—	—	—	23
Rb	—	1.42	1.1	—	1.2	0.38	—	—	—	5.0
Sr	189	195	191	162	180	174	130	—	—	208
Zr	—	55	62.5	46	22	—	17	—	—	300
Hf	2.18	1.67	—	1.16	—	—	0.40	16.5	—	—
Ba	83	86.2	67	60	50	23.6	40	—	360	315
Th	1.07	0.7	—	0.53	—	—	—	6.1	—	—
U	0.28	0.22	—	—	—	—	0.053	—	1.1	—
Ta	0.34	0.21	—	0.18	—	—	0.40	1.7	—	—
La	5.83	4.90	—	3.76	—	—	1.35	50.5	26.5	28
Ce	15.7	11.6	—	10.1	—	3.32	3.7	130	—	—
Nd	—	7.9	—	7.6	—	2.08	—	—	—	—
Sm	2.71	2.14	—	1.64	—	0.64	0.60	24.6	10.6	—
Eu	1.18	1.16	—	1.06	—	0.91	0.84	1.57	2.4	—
Gd	—	2.6	—	—	—	—	0.90	—	—	—
Tb	0.58	0.47	—	0.33	—	—	—	4.9	—	—
Dy	—	3.1	—	2.11	—	1.11	0.92	—	—	—
Ho	—	0.7	—	—	—	—	0.2	—	—	—
Er	—	1.9	—	—	—	0.68	0.63	—	—	—
Tm	—	—	—	—	—	—	—	—	—	—
Yb	2.19	1.79	—	1.35	0.6	0.60	0.52	15.0	10	8.2
Lu	0.305	0.24	—	0.19	—	0.08	0.085	2.01	1.4	—
Sc	6.7	7.5	—	6.6	23	—	6.8	44.7	13.6	15.3
Cr	—	483	—	540	—	—	420	—	—	—
Co	16.9	9.7	—	10.4	6.2	—	10.0	30.4	20	16
Ni	187	110	36.7	100	62	—	28	75	—	110
Mn	—	392	—	—	—	—	420	—	—	—

67015(i): Marvin et al. (1987); 67015(ii): Wänke et al. (1975); 67016(i): Duncan et al. (1973); 67016(ii): Wänke et al. (1975); 67115: Rose et al. (1973a); 67455(i): Lindstrom et al. (1977a); 67455(ii): Wänke et al. (1973); 72275: Blanchard et al. (1975a); 14063(i): Laul et al. (1972a); 14063(ii): average of three chips, Rose et al. (1972).

TABLE A6.16. Volatile and siderophile elements in matrix samples of fragmental breccias (ng/g).

	67015	67016(i)	67016(ii)	67115	67455(i)	67455(ii)	72275	14064
Zn	3600		9100	4200	5000	8500	2700	3100
Ga	4100	—				3400	406	—
Ge	30	—	11.6	18.7	17.4	—		32.9
Cd	—	—	0.56	2.31	1.37		13	16.7
In	—	—	0.46	0.22	1.09			—
Ir	—	10	2.31	1.59	1.08	4	2.26	1.63
Au	1.1	4.8	0.455	0.164	0.355	1	0.82	0.128

67015: *Wänke et al. (1975)*; 67016(i): *Wänke et al. (1976)*; 67016(ii): *Hertogen et al. (1977)*; 67455(i): *Hertogen et al. (1977)*; 67115: *Hertogen et al. (1977)*; 67455(ii): *Wänke et al. (1973)*; 72275: *Morgan et al. (1975)*; 14064: *Gros et al. (1976)*.

TABLE A6.17. Major oxides in glassy melt breccias and impact glasses (wt.%).

	60095 sphere	64455 coat	63566 glass with clasts	68815 breccia matrix	15017 shell	15255 coat
SiO ₂	44.8	44.8	45.1	45.1	49.9*	46.4
TiO ₂	0.48	0.44	0.22	0.49	—	1.80
Al ₂ O ₃	25.9	25.8	29.2	27.2	14.9	14.1
Cr ₂ O ₃	—	0.15	0.09	0.10	0.44	0.44
FeO	5.7	5.6	4.7	4.8	14.3	14.7
MnO	—	0.06	0.06	0.06	0.20	0.22
MgO	7.9	8.1	4.6	5.9	10.7	11.1
CaO	14.6	14.3	16.0	15.5	9.7	10.7
Na ₂ O	0.32	0.36	0.57	0.42	0.44	0.38
K ₂ O	0.12	0.13	0.06	0.14	0.21	0.16
P ₂ O ₅	—	—	—	0.18	—	0.11
Σ	99.8	99.7	100.6	99.9	—	100.1
Mg/(Mg+Fe) atom ratio	0.71	0.72	0.64	0.69	0.57	0.57

* This SiO₂ value suspiciously high.

60095, 63566, 64455: *See et al. (1986)*; 68815: *LSPET (1973a)*; 15017: *Wänke et al. (1972)*; 15255: *Nava et al. (1977)*.

TABLE A6.18. Incompatible elements and transition metals in glassy melt breccias and impact glasses ($\mu\text{g/g}$).

	63566	64455 coat	15017 shell	15255 rind	60095
Li	—	—	—	18.0	—
Rb	4.7	3.1	—	7.49	—
Sr	200	—	135	134	—
Zr	260	—	437	501	—
Nb	—	—	—	—	—
Hf	6.37	4.3	10.3	—	4.90
Ba	—	—	300	383	200
Th	2.72	—	3.93	—	2.60
U	0.78	—	—	—	0.99
Pb	—	—	—	—	—
Ta	0.74	—	—	—	0.68
La	19.2	12.6	28.2	—	14.4
Ce	51.2	32.1	77.7	71.5	41.7
Nd	32.5	21.0	56	53.9	—
Sm	8.5	5.9	12.7	15.0	7.0
Eu	1.19	1.11	1.42	1.67	1.22
Gd	10.5	7.4	—	—	—
Tb	1.76	1.14	2.79	—	1.27
Dy	11.0	7.5	16.8	20.0	—
Ho	2.48	1.6	3.7	—	—
Er	6.6	4.5	—	12.2	—
Tm	0.97	—	—	—	—
Yb	6.04	3.92	9.49	11.0	4.3
Lu	0.80	0.56	1.32	1.54	0.71
Sc	7.7	7.0	29.9	—	7.1
Cr	830	1000	3000	—	780
Co	53.0	48.2	40.6	—	40
Ni	990	760	260	—	412
Mn	578	—	1530	—	—

63566: Borchardt et al. (1986); 64455: Haskin et al. (1973); 15017: Ganapathy et al. (1973); 15255: Nava et al. (1977); 60095: Morris et al. (1986).

TABLE A6.19. Volatile and siderophile elements in glassy melt breccias and impact glasses.

	60095	64455 coat	15017 shell
$\mu\text{g/g}$			
Cs	64	144	273
Zn	1550	2400	5800
ng/g			
Ge	306	500	241
Cd	1.8	5.2	4.2
Ir	25.4	40.6	9.1
Au	7.11	12.7	2.9

64455 coat, 60095: Ganapathy et al. (1974); 15017: Ganapathy et al. (1973).

TABLE A6.20. Major element oxides in crystalline melt breccias (impact melt breccias) (wt.%).

	14066	14068	15445	60315	60335	62235	66095	67475	73215	72395	77135	76015
SiO ₂	49.2	47.2	44.6	46.8	46.3	47.1	44.9	44.4	46.4	46.9	46.2	46.4
TiO ₂	1.0	1.39	1.47	1.38	0.57	1.19	0.72	0.36	0.70	1.75	1.53	1.53
Al ₂ O ₃	15.9	13.3	16.7	17.1	25.0	18.9	23.7	30.9	20.6	18.1	17.8	17.8
Cr ₂ O ₃	0.17	—	—	0.24	0.15	—	—	0.03	0.25	0.20	0.21	—
FeO	10.1	10.0	9.8	8.6	4.6	9.5	7.5	2.9	7.3	9.3	9.1	9.1
MnO	0.12	0.13	0.14	0.11	0.08	0.13	0.08	0.04	0.10	0.12	0.13	0.12
MgO	11.4	17.6	16.0	13.4	7.7	10.2	8.9	2.6	11.6	12.0	12.4	12.7
CaO	10.1	8.38	10.0	10.5	14.2	11.6	13.5	17.2	11.9	1.3	11.1	11.1
Na ₂ O	0.84	0.75	—	0.61	0.62	0.42	0.45	0.60	0.50	0.69	0.69	0.69
K ₂ O	0.94	0.59	—	0.49	0.27	0.33	0.16	0.04	0.20	0.29	0.27	0.26
P ₂ O ₅	—	0.55	0.21	0.48	0.21	0.39	0.25	<0.02	—	0.33	0.30	0.29
Σ	98.8	99.8	99.0	99.7	99.7	99.8	100.2	99.1	99.6	101.0	99.7	100.0
Mg/ (Mg+Fe) atom ratio	0.67	0.76	0.74	0.74	0.75	0.66	0.68	0.62	0.74	0.70	0.71	0.71

14066: Wänke et al. (1972); 14068: Hubbard et al. (1972a); 15445: Ridley et al. (1973); 60315, 60335: Rose et al. (1973a,b); 62235: Hubbard et al. (1973); 66095: Duncan et al. (1973); 67475: Lindstrom et al. (1977a); 73215: Blanchard et al. (1976); 72395: Wänke et al. (1975); 77135: Rhodes et al. (1974); 76015: Simonds (1975).

TABLE A6.21. Incompatible and transition metal trace elements in crystalline melt breccias (impact melt breccias) ($\mu\text{g/g}$).

	14066	14068	15445	60315	60335	62235	66095	67475	73215	72395	77135	76015
Li			14.1					5.33		24.8		21.6
Rb		14.5	3.56	9.80	7.1	9.32	11.0	0.672		6.21	6.2	6.57
Sr		139	160	156		161		216		167	174	177
Zr			315							570	508	507
Hf	30		10.5		7.0		5.0		9.5	13.7		—
Ba		780	237	445		568	150	48.5		386		358
Th							2.2		4.1	6.05		5.56
U		3.47	0.800	2.05		2.53	1.0			2.06		1.96
Ta	3.6						0.44		1.4	1.82		—
La	75	—	22.1	45.5	22.0	60.1	18.5	—	27.0	39.7		33.4
Ce	200	157	57.6	113	58.0	153	50.0	6.66	70	95		84.9
Nd		93.4	35.7	71.3	36.4	94.3		4.22		61		54.0
Sm		28.1	10.1	20.1	10.0	27.1	8.8	1.21	12.5	16.8		15.2
Eu	2.76	2.01	1.85	1.89	1.38	2.03	1.63	1.28	1.43	1.93		1.99
Gd		29.1	11.9	23.8		32.2		1.43		21.1		18.9
Tb	7.8				2.03		1.3		2.6	3.7		—
Dy	39	35.1	13.2	26.3	13.9	35.0	9.4	1.68		23.2		19.9
Ho					2.9		1.3			5.1		—
Er			7.71	15.5		21.2	4.1	1.06		13.9		11.7
Tm							—					—
Yb	25.1	20.0	6.90	14.0	6.88	18.7	4.9	1.01	9.1	12.4		10.8
Lu	3.6		1.02		0.95		0.90	0.140	1.30	1.88		1.30
Sc	20				7.9		6.8	—	14.7	18.7		—
Cr	1190		1750	1477	910	1309	860	200	1700	1400		1188
Co	30				16		44		25.3	31.1		
Ni	—				300		710		65	260	62	135
Mn	920		1085		550		550	300	800	930		950

14066: Wänke et al. (1972); 14068: Hubbard et al. (1972a); 15445: Ridley et al. (1973); 60315, 62235: Hubbard et al. (1973); 60335: Haskin et al. (1973); 66095: Brunfelt et al. (1973a,b); 67475, Lindstrom et al. (1977a); 73215: Blanchard et al. (1976); 72395: Wänke et al. (1977); 77135: Rhodes et al. (1974); 76015: Simonds (1975).

TABLE A6.22. Volatile, chalcophile, and siderophile elements in crystalline melt breccias (impact melt breccias) (ng/g).

	15445	65015	62295	66095	73215	77135	76315
Cs	177	405	530	160	161	250	250
Zn	2.5	0.48	16.5	50.5	2.0	3.3	3.1
Se	91	245	186	314	72	144	100
Te	4.7	3.25	12.5	20	5.9	8.84	4.04
Ge	630	380	642	2140	175	618	346
Cd	5.3	9.25	4.9	328	18	3.5	5.0
Br	96	22	60	825	26	45	48
Ir	6.21	11.6	3.58	16.6	4.9	10.5	5.42
Re	0.668	1.16	0.336	2.13	0.37	1.06	0.507
Au	6.02	10.2	3.10	17.9	2.7	6.45	3.21

15445: Gros et al. (1976); 65015, 62295, 66095: Krähenbühl et al. (1973); 73215: Higuchi and Morgan (1975); 77135, 76315: Morgan et al. (1974).

TABLE A6.23. Major element oxides in clast-poor impact melts (wt.%).

	14276	14310(i)	14310 (ii)	62295	64455	68415(i)	68415(ii)
SiO ₂	47.6	47.2	47.8	44.7	48.5	45.4	45.3
TiO ₂	1.20	1.24	1.11	0.68	0.65	0.32	0.29
Al ₂ O ₃	21.3	20.1	21.5	20.3	22.4	28.6	28.7
Cr ₂ O ₃	0.26	0.18	0.25		0.16	—	0.14
FeO	7.9	8.4	7.6	6.3	5.5	4.3	4.1
MnO	0.12	0.11	0.10	0.10	0.07	0.06	0.05
MgO	7.1	7.9	7.5	15.1	9.3	4.4	4.4
CaO	13.2	12.3	12.9	11.8	13.4	16.4	16.2
Na ₂ O	0.72	0.63	0.68	0.43	0.57	0.41	0.50
K ₂ O	0.48	0.49	0.48	0.08	0.245	0.06	0.09
P ₂ O ₅	0.40	0.34	0.43	0.13	—	0.07	0.06
Σ	100.3	98.9	100.4	99.6	100.8	100.0	99.8
Mg/(Mg + Fe) atom ratio	0.62	0.63	0.64	0.81	0.75	0.65	0.66

14276, 14310(ii): Rose et al. (1972); 14310(i): Hubbard et al. (1972a); 62295: Hubbard et al. (1973); 64455: Haskin et al. (1973); 68415(i) LSPET (1973a); 68415(ii) Rose et al. (1973a,b).

TABLE A6.24. Incompatible and transition metal trace elements in clast-poor impact melts (µg/g).

	14276	14310(i)	14310(ii)	62295	64455	68415(i)	68415(ii)
Li	21		23			5.1	5.1
Rb	13	13	15	4.6	6.0	1.704	1.9
Sr	165	193	175	139		182.4	140
Zr	20	842	610			97.5	72
Hf					7.8	2.4	
Ba	700	617	780	187		76.2	70
Th		11				1.26	
U				0.882		0.32	
La	59	56.4	59	18.6	21.1	6.8	
Ce		144		45.9	56.0	18.3	
Nd		87.0		29.0	34.0	10.9	
Sm		24.0		8.30	9.8	3.09	
Eu		2.15		1.18	1.23	1.11	
Gd		2.81		10.1	—	3.78	
Tb		—		—	1.97	—	
Dy		32.7		10.8	12.2	4.18	
Ho		—		—	2.7	—	
Er		19.7		6.85	6.7	2.57	
Tm		—		—	—	—	
Yb	16	18.4	16	6.06	6.6	2.29	2.0
Lu				0.879	0.96	0.34	
Sc	20		25		7.8		8.2
Cr				773	1110	599	
Co	9.0		17.0		31.1		11
Ni	113	64	120		540		184

14276, 14310(ii): Rose et al. (1972); 14310(i): Hubbard et al. (1972a); 62295: Hubbard et al. (1973); 64455: Haskin et al. (1973); 68415(i) Hubbard et al. (1974); 68415(ii): Rose et al. (1973a,b).

TABLE A6.25. Volatile, chalcophile, and siderophile elements in clast-poor impact melts (ng/g).

	14310(i)	14310(ii)	62295	64455	68415
Cs	540	—	530	280	80
Zn	2300	1500	1650	2200	1450
Se	120	—	186	190	98
Te	4	—	12.5	2.5	4.7
Ge	130	90	642	62	73
Cd	2.6	8.4	4.9	5.3	0.85
Br	235	—	50	1200	140
Ir	10.6	7.8	3.6	2.25	4.58
Re	1.02	—	0.336	0.284	0.434
Au	4.31	—	3.10	1.56	2.65

14310(i): *Morgan et al. (1972b)*; 14310(ii): *Baedecker et al. (1972)*; 62295, 68415: *Kr̄denbühl et al. (1973)*; 64455: *Ganapathy et al. (1974)*.

TABLE A6.26. Major element oxides in granulitic breccias and granulites (wt.%).

	67955	67415	79215	67215	77017	78155	15418
SiO ₂	45.0	44.6	44.8	—	44.1	45.6	44.2
TiO ₂	0.27	0.32	0.5	0.33	0.41	0.27	0.27
Al ₂ O ₃	27.7	26.0	27.4	27.4	26.6	25.9	26.6
Cr ₂ O ₃	0.11	0.08	0.11	0.11	0.13	0.14	—
FeO	3.8	4.6	4.9	6.4	6.2	5.8	6.7
MnO	0.05	0.06	0.06	—	0.08	0.10	0.10
MgO	7.7	7.8	7.4	5.3	6.1	6.3	5.1
CaO	15.5	15.1	14.4	16.2	15.4	15.2	16.0
Na ₂ O	0.40	0.52	0.58	0.30	0.30	0.33	0.27
K ₂ O	0.05	0.04	0.12	—	0.06	0.08	0.02
P ₂ O ₅	0.03	0.03	—	—	0.03	0.04	0.03
Σ	100.6	99.2	100.3	—	99.4	99.8	99.3
Mg/(Mg+Fe) atom ratio	0.78	0.75	0.73	0.60	0.64	0.66	0.58

67955, 77017, 78155, 15418: *Hubbard et al. (1974)*; 67415: *Lindstrom et al. (1977a)*; 79215: *Blanchard et al. (1972)*; 67215: *Lindstrom and Lindstrom (1986)*.

TABLE A6.27. Incompatible and transition metal elements in granulitic breccias and granulites ($\mu\text{g/g}$).

	67955	67415	79215	67215	77017	78155	15418
Li	5.1	6.06	—	—	4.4	5.2	—
Rb	0.884	0.964	—	—	1.31	2.06	—
Sr	169.1	177	—	150	141.5	146.7	150
Zr	124	—	—	25	59.1	—	<50
Hf	3.1	—	1.2	0.80	1.6	—	0.40
Ba	61.9	61.2	—	16	49.0	58.8	15
Th	1.03	—	0.32	0.96	—	1.013	0.049
U	0.38	—	—	0.032	0.22	0.284	<0.10
Ta	—	—	0.125	—	—	—	0.031
La	4.45	—	2.65	1.58	3.48	4.02	0.756
Ce	11.3	9.62	6.8	4.3	8.90	10.2	2.05
Nd	7.09	6.23	—	3.0	5.56	6.29	1.6
Sm	2.02	1.84	1.19	0.855	1.60	1.81	0.499
Eu	0.973	1.11	0.84	0.726	0.79	0.874	0.698
Gd	2.57	—	—	—	2.01	2.32	—
Tb	—	—	0.28	0.199	—	—	0.149
Dy	2.81	2.75	—	—	2.35	2.64	—
Ho	—	—	—	—	—	—	—
Er	1.79	1.77	—	—	1.50	1.69	—
Tm	—	—	—	—	—	—	—
Yb	1.74	1.75	1.37	0.752	1.50	1.73	0.628
Lu	0.25	0.255	0.24	0.125	—	0.259	0.102
Sc	—	—	8.14	12.8	—	—	13.4
Cr	659	—	740	755	881	1008	870
Co	—	—	18.9	12.0	—	—	13.5
Ni	—	—	126	26	—	—	65
Mn	387	465	496	—	620	—	—

67955, 77017, 78155: Hubbard et al. (1974); 67415: Lindstrom et al. (1977a); 79215: Blanchard et al. (1977); 67215, 15418: Lindstrom and Lindstrom (1986).

TABLE A6.28. Volatiles and siderophiles in granulitic breccias and granulites (ng/g).

	67955(i)	67955(ii)	67415	78155	77017	15418
Zn	5000	6700	5800	2300	2500	490
Ga	4100	—	—	—	—	—
Ge	120	59	11.2	27	110	17
Cd	≤ 10	4.3	1.93	63	9.0	2.4
In	≤ 1.6	—	1.38	—	—	—
Ir	8	5.56	2.04	3.32	17.0	2.2
Au	2.1	1.60	1.02	0.66	5.65	0.26

67955(i): Wasson et al. (1977); 67955(ii) Ganapathy et al. (1974); 67415 Hertogen et al. (1977); 78155, 77017: Morgan et al. (1974); 15418: Ganapathy et al. (1973).

THE LUNAR REGOLITH

*David S. McKay, Grant Heiken, Abhijit Basu, George Blanford,
Steven Simon, Robert Reedy, Bevan M. French, and James Papike*

Regolith is a terrestrial term, also used for the Moon. It has been defined as “a general term for the layer or mantle of fragmental and unconsolidated rock material, whether residual or transported and of highly varied character, that nearly everywhere forms the surface of the land and overlies or covers bedrock. It includes rock debris of all kinds, [including] volcanic ash . . .” (*Bates and Jackson*, 1980). All the lunar landings and all photographic investigations show that the entire lunar surface consists of a regolith layer that completely covers the underlying bedrock, except perhaps on some very steep-sided crater walls and lava channels, where there may be exposed bedrock.

The regoliths developed on the Earth are produced by processes that are uniquely terrestrial—the presence of oxygen, the influences of wind and water, and the activities of life. In contrast, on the airless, lifeless Moon, the lunar regolith results from uniquely different processes—the continuous impact of large and small meteoroids and the steady bombardment of the lunar surface by charged atomic particles from the sun and the stars.

Exposed rocks on the lunar surface are covered with impact craters whose diameters range from more than 1000 km to less than 1 μm . The corresponding impacting objects range from asteroids tens of kilometers in diameter to particles of cosmic dust a few hundred angstroms across, a range of more than 12 orders of magnitude. Despite the size disparity, the effects on bedrock are similar at both

ends of the size spectrum—excavation of a crater, accompanied by shattering, pulverization, melting, mixing, and dispersal of the original coherent bedrock to new locations in and around the crater.

The moment that fresh bedrock is exposed on the Moon (e.g., by the eruption of a lava flow), meteoroid bombardment begins to destroy it. As the impacts continue, the original bedrock is covered by a fragmental layer of broken, melted, and otherwise altered debris from innumerable superimposed craters. This layer is the *lunar regolith*.

Studies of returned samples have shown that the bulk of this lunar regolith (informally called the lunar soil) consists of particles <1 cm in size although larger cobbles and boulders, some as much as several meters across, are commonly found at the surface. Because the impact cratering events produce shock overpressures and heat, much of the pulverized material is melted and welded together to produce *breccias* (fragmental rocks) and *impact melt rocks*, which make up a significant portion of the regolith and add to its complexity.

The processes of regolith formation can be divided roughly into two stages. During the early stage, shortly after bedrock is first exposed and the regolith is still relatively thin (less than a few centimeters), both large and small impacts can penetrate the regolith and excavate fresh bedrock. The regolith layer builds up rapidly. As time goes on and the thickness increases (to a meter or more), only the larger (and far less frequent) impacts penetrate the

regolith and bring up new bedrock. In this later stage, the smaller (and more numerous) impacts only disturb and mix (garden) the regolith layer already present, and the regolith thickness increases more slowly.

Since about 4 b.y. ago, the impact flux on the lunar surface has been relatively low, and a regolith only a few meters thick is adequate to shield the underlying bedrock almost indefinitely. For this reason, the regolith thickness rarely exceeds 10 to 20 m. Regolith thicknesses on the maria are typically only a few meters (*Langevin and Arnold, 1977; Taylor, 1982*). Astronauts have drilled to a depth of approximately 3 m in the regoliths at Apollo sites, and estimates based on grain-size distributions suggest that the maximum thickness of the regolith may not exceed 20 m, at least in these locations (*McKay et al., 1974*). Early estimates of regolith thicknesses by *Oberbeck and Quaide (1968)*, based on crater-shape models, ranged from 3.3 m on Oceanus Procellarum to 16 m for the inner wall of the crater Hipparchus. At the four Surveyor mare sites, apparent regolith thicknesses range from 1 to 10 m (*Shoemaker et al., 1968*).

The current consensus is that the regolith is generally about 4–5 m thick in the mare areas but may average about 10–15 m in older highland regions. Beneath this true regolith is a complex zone that probably consists of large-scale ejecta and impact-fractured, brecciated bedrock (based on orbital radar data and modeling; *Peeples et al., 1978; Langevin, 1982*). This layer of fractured bedrock has been called the *megaregolith* and may consist of large (>1 m) blocks. Some of the inferred properties of this megaregolith are different from those of the unconsolidated surficial material that has been sampled (see Fig. 4.22). However, the detailed properties of the megaregolith are essentially unknown, and we shall not consider it further in this section.

The formation and evolution of the lunar regolith is a complex process. At any given spot, the nature and history of the regolith is determined by two completely random mechanisms. One is destructive—the excavation of existing regolith by impact craters. The other is constructive—the addition of layers of new material (either from bedrock or older regolith) that is excavated from either near (small) or distant (large) impact craters. Superimposed on these mechanical processes are the effects of solar and cosmic particles that strike the lunar surface. At the very surface, dust particles form microcraters, and solar-wind atomic particles are trapped in the outer layers of regolith grains, while high-energy particles produce distinctive nuclear reactions to depths of several meters.

These simultaneous processes combine to produce a regolith whose structure, stratigraphy, and history may vary widely, even between locations only a few meters apart. Surface layers can be buried and then reexposed. Single layers, or slabs containing multiple layers, can be transported, overturned, or buried. Deciphering these complications is a major challenge that requires the application of a wide range of analytical techniques—petrologic studies, gas analyses, measurements of radioactivity, stable isotope studies, trace element geochemistry, magnetic measurements, and statistical modeling—to have any hope of success.

Importance of the lunar regolith. The lunar regolith is the actual boundary layer between the solid Moon and the matter and energy that fill the solar system. It contains critical information about both of these regions, and the complexities of studying the regolith are exceeded only by its importance to understanding the Moon and the space environment around it.

The regolith is the source of virtually all our information about the Moon. All direct measurements of physical and chemical properties of lunar material have been made on samples, both rocks and soils, collected from the regolith. Experiments, whether conducted by astronauts on the Moon or remotely monitored from the Earth, were done on or in the regolith layer. For example, heat flow measurements were made with sensors that were emplaced in the regolith; estimates of heat flow from the rocks below were made only by inference from the regolith data. Even seismic data were obtained from seismometers that were implanted on or in the regolith and were not coupled to bedrock. Remotely sensed X-ray fluorescence, infrared spectra, and gamma-ray signals come from the very top of the lunar regolith; in fact, from depths of no more than 20 μm , 1 mm, and 10–20 cm respectively (*Morris, 1985; Pieters, 1983; Adler et al., 1973; Metzger et al., 1973*). At the resolution of these methods (>1 km²), the lunar surface appears totally covered with regolith. Thus, all the remotely sensed chemical data, even on a regional scale, have also come from the regolith. Finally, because of its surficial, unconsolidated, and fine-grained nature, it is likely that the regolith will be the raw material used for lunar base construction, mining, road building, and resource extraction when permanent lunar bases are established in the twenty-first century (*Mendell, 1985*). In other words, the economic importance of the lunar regolith is far greater than that of the underlying bedrock, at least in the foreseeable future.

The lunar regolith also preserves information from beyond the Moon. Trapped in the solid fragments that make up the regolith are atoms from the sun

and cosmic-ray particles from beyond the solar system. In the regolith, data about the nature and evolution of the Moon are mixed with other records. These records include the composition and early history of the sun, and the nature and history of cosmic rays. The regolith also contains information about the rate at which meteoroids and cosmic dust have bombarded the Moon—and, by inference, the Earth. Unscrambling these intertwined histories is a major challenge—and a major reward—of lunar research.

Data sources. The principal source of data about the regolith is, of course, the samples returned by both manned and unmanned missions to the Moon. The relatively large (e.g., >1 cm) fragments of pebbles, cobbles, and boulders are treated as separate rock samples (see section 7.6 for a discussion of regolith breccias). On the other hand, all scoop samples and drill cores are true regolith samples (for cataloging purposes, an arbitrary definition of a lunar soil is the “unconsolidated portion of regolith with particle sizes of less than 1 cm”). Therefore, all the Soviet Luna samples, as well as the U.S. collections (Apollo samples) are actually regolith.

Regolith samples returned from the Moon during the Apollo missions were handled in many different ways, and the sample handling protocols evolved from mission to mission (Morris *et al.*, 1983). When evaluating grain-size studies of these samples, one must look carefully at the sample’s history from the time it was collected on the lunar surface to the time when the research results were published. Nearly all regolith samples in the Apollo collection have been sieved into size fractions of >1 cm, 1 cm–4 mm, 4–2 mm, 2–1 mm, and <1 mm at the Johnson Space Center curatorial facilities (see section 2.3). Most of the detailed regolith studies have been performed on the <1-mm-sized fractions, also called the “fine fines.” It is important to note that the >1-mm fractions (coarse fines) have not been studied in such a way that their data can be easily integrated with results from the fine fines. In addition, no data from the >1-mm fraction have been included in attempts to infer the bulk properties of the regolith. Most of the laboratory data on lunar regolith have been obtained from the <1-mm fractions; although these fractions make up the bulk of the regolith (>90% of most regolith samples), some caution should be used in applying the results to the regolith as a whole.

The regolith, being at the Moon’s surface, has been continuously bombarded by meteoroid impacts for at least 3–4 b.y. Some of these impacts were large enough to reconsolidate and lithify parts of the regolith into coherent fragmental rocks, called *regolith breccias* (section 7.6). These breccias make

up some of the large individual rocks picked up by astronauts. The ages of assembly or “closure” of some of these breccias, measured by radiometric age-dating techniques, may be more than 4 b.y. (McKay *et al.*, 1986), and many regolith breccias were lithified more than 1 b.y. ago. Studies of the regolith breccias provide critical data about the Moon’s ancient regolith and also add to the general database for the modern regolith.

In addition to laboratory studies of returned soils, cores, and regolith breccias, data on the lunar regolith have been obtained from a variety of other sources. Many physical and mechanical properties were directly measured during experiments on the Moon itself. For example, the penetration depth of the landing gear of the lunar module provided an estimate of regolith compressibility. Such geotechnical properties, extremely important for any engineering venture, are discussed in detail in Chapter 9. Photogeology and other remote-sensing methods also reveal many large-scale regolith properties.

The underlying assumption in most lunar studies is that the regolith cover adequately represents local bedrock and, in general, represents the Moon’s crust in a given region. To test this assumption, it is especially important to measure regolith properties that can be used to infer the extent of lateral transport and regolith mixing on the lunar surface. It now appears that lateral transport of primary ejecta from impact craters has been restricted to relatively short distances, i.e., a few crater radii, although a small fraction of primary ejecta may be present in crater rays that have traveled halfway round the Moon from large impacts such as the ones that formed larger craters like Copernicus and Tycho. Similarly, the sharp contrasts in color and chemical compositions at highland-mare contacts, inferred from optical observations and orbital X-ray fluorescence data on the regolith, imply that lateral transport and mixing could not have been extensive, even over more than 3 b.y.

7.1. LUNAR SOIL

The lunar science community has generally used the word “soil” in an engineering geology sense. Although “lunar soil” is lexicographically synonymous with “lunar regolith” (Bates and Jackson, 1980), “lunar soil” usually refers to the finer-grained fraction of the unconsolidated material (*regolith*) at the lunar surface. In this discussion *we define lunar soil as the subcentimeter fraction of the lunar regolith.*

7.1.1. General Description

The lunar soil is a somewhat cohesive, dark grey to light grey, very-fine-grained, loose, clastic material derived primarily from the mechanical disintegration

of basaltic and anorthositic rocks. The mean grain size of analyzed soils ranges from about 40 μm to about 800 μm and averages between 60 and 80 μm . Individual lunar soil particles are mostly glass-bonded aggregates (*agglutinates*), as well as various rock and mineral fragments. The soils range in composition from basaltic to anorthositic, and they include a small (<2%) meteoritic component. Although the chemical compositions of lunar soils show considerable variation, physical properties such as grain size, density, packing, and compressibility are rather uniform (see Chapter 9). One manifestation of such uniform physical properties is that seismic velocities in regolith materials at both mare and highland sites are quite similar, varying between 92 m/sec and 114 m/sec (Cooper *et al.*, 1974).

7.1.2. Petrography

Petrographic studies of regolith samples make it possible to characterize the material in two complementary ways: by the relative proportions of different kinds of fragments and by the chemical and mineral compositions of individual rock and mineral fragments. These studies are done by examining thin sections of regolith samples with an optical microscope or by studying individual regolith particles with a scanning electron microscope (SEM).

Optical studies of regolith samples make it possible to conduct a census of the relative amounts (by volume) of different particles—rocks, mineral and glass fragments, and other components—in each sample. This determination of relative volumes of components, a process called *modal analysis*, can be expanded to estimate the chemical composition of the soil as well if chemical data for individual mineral, rock, and glass components can be summed. (Usually, the chemical data for fragments are determined directly with an electron microprobe.) The bulk chemical composition, reconstructed in this way, can be compared with destructive “whole rock” chemical analyses. The chemical analyses can be used to interpret the sources for particles, origin, and evolution of the soil sample.

These studies show that five basic particle types make up the lunar soils: mineral fragments, pristine crystalline rock fragments, breccia fragments, glasses of various kinds, and the unique lunar constructional particles called *agglutinates*. These diverse particles can also be divided into two groups: regolith derived and bedrock derived. All agglutinates, fragments of regolith breccias, and heterogeneous glasses have been formed by the action of meteorite impacts

(chiefly impact melting) on regolith targets. These particles are sometimes called the *fused soil component*. The remaining fragments are pieces of igneous rocks, monomict breccias, and polymict breccias, which make up the bedrock-derived component.

Except for a few igneous rock fragments, the average size of rock clasts in the regolith is <250 μm . In general, it is difficult to identify the rock type in particles <250 μm , and most rock fragments in lunar soils are even smaller. For this reason, the chemistry of individual mineral grains in the fragments has been used instead for identifying the parent rock.

A further complication in studying the bedrock-derived component is that the relative abundance of particle types depends on the particle size. Polymineralic and lithic (rock) fragments dominate the coarser size fractions. In contrast, the finer soil fractions are enriched in feldspars and glassy phases. The glasses come from two sources—the noncrystalline material in the groundmass of basaltic rocks and the glassy bonding material originally present in breccias and agglutinates (Table 7.1).

Modal analyses commonly provide an adequate picture of the relations between the composition of the local bedrock and that of the regolith developed on it. All lunar soils have a minor exotic component derived from some distance away, but most of these soils appear to have been derived largely from bedrock in their immediate vicinity. The modal compositions of a regolith reference suite (Papike *et al.*, 1982) illustrate the local influence well (Table 7.2; Fig. 7.1). The Apollo 11, Apollo 12, Luna 16, and Luna 24 missions landed well inside mare basalt regions. The soil samples from these sites contain abundant mare-derived basaltic rock fragments and their mafic minerals like pyroxene and olivine. The Apollo 16 and Luna 20 missions landed in highland regions, and Apollo 14 landed on a ridge apparently formed by material ejected from the Imbrium Basin. Soils from these missions show a preponderance of highland-derived lithic fragments (anorthositic rocks) and plagioclase feldspar. Apollo 15 and 17 landings were made in areas where highland hills meet the mare plains. Soil samples collected during these missions are intermediate in character between those from the mare and highland regions, and they contain rock and mineral fragments derived from both.

Even within a single landing site, there can be remarkable variation between sampling locations. For example, soil 15221 (Table 7.2), collected from the slopes of the Apennine Front (Fig. 7.1), contains significant amounts of both highland and mare material. On the other hand, soil 15601 (Table 7.3),

TABLE 7.1. Petrography of grain size fractions from 71061,1 (a typical Apollo 17 mare soil) and 72441,7 (a typical South Massif soil) (*Heiken, 1975*).

Components	Petrographic Description, vol.%							% Visual Estimate in Lunar Receiving Laboratory			
	<20 μm	20-45 μm	45-75 μm	75-90 μm	90-150 μm	150-250 μm	250-500 μm	0.5-1 mm	1-2 mm	2-4 mm	4-10 mm
<i>Soil 71061,1*</i>											
Agglutinates	17.0	17.3	13.0	17.3	9.3	11.8	10.0	10.0	—	—	—
Basalt, equigranular			9.0	15.0	30.9	—	—	—	—	—	—
Basalt, variolitic			0.6	1.6	19.6	3.4	51.5	65.0	100.0	100.0	100.0
Breccia											
Low grade, brown			1.0	4.0	3.6	5.1	6.9	—	—	—	—
Low grade, colorless			0.3	1.3	0.6	—	—	5.0	—	—	—
Medium, high grade			1.0	1.3	1.6	2.8	1.5	—	—	—	—
Anorthosite			—	—	0.3	—	—	—	—	—	—
Cataclastic anorthosite			1.0	—	—	—	—	—	—	—	—
Norite			—	—	—	—	—	—	—	—	—
Gabbro			—	—	—	—	0.5	5.0	—	—	—
Plagioclase			16.3	7.0	17.3	9.0	8.5	—	—	—	—
Clinopyroxene			21.3	26.3	21.0	17.4	10.8	—	—	—	—
Orthopyroxene			—	—	—	—	—	—	—	—	—
Olivine			—	—	—	0.6	—	—	—	—	—
Ilmenite			6.0	3.3	4.6	3.3	2.3	—	—	—	—
Glass											
Orange			7.6	5.0	6.3	4.5	0.8	—	—	—	—
"Black"			18.7	10.6	9.6	5.1	6.1	5.0	—	—	—
Colorless			1.0	1.0	1.3	—	1.5	—	—	—	—
Brown			0.3	5.2	4.6	3.3	—	—	—	—	—
Gray, ropy			0.7	0.6	—	1.7	—	10.0	—	—	—
Other			2.0	—	—	1.0	—	—	—	—	—
Total number of grains counted	300	161	300	300	300	178	130	20	100	?	?
Wt.% of total sample for each size fraction	17.98	12.21	8.39	3.0	8.66	7.04	7.08	3.44	6.15	6.74	10.16

TABLE 7.1. (continued)

Components	Petrographic Description, vol.%							% Visual Estimate in Lunar Receiving Laboratory			
	<20 μm	20-45 μm	45-75 μm	75-90 μm	90-150 μm	150-250 μm	250-500 μm	0.5-1 mm	1-2 mm	2-4 mm	4-10 mm
<i>Soil 72441,7†</i>											
Agglutinates	21.0	50.0	39.3	45.5	41.7	54.6	30.5	x	20.0	25.0	25.0
Basalt, equigranular			0.6	1.5	1.3	1.3	—	x	—	—	—
Basalt, variolitic			0.3	—	1.3	—	1.0	x	—	—	—
Breccia											
Low grade, brown			9.3	6.6	9.3	10.7	9.4	x	—	—	—
Low grade, colorless			2.7	2.3	6.3	0.7	6.3		80.0	74.0	75.0
Medium high grade			22.7	29.0	19.3	20.0	30.5	x	—	—	—
Anorthosite			—	—	1.0	—	—	x	—	1.0	—
Cataclastic anorthosite			0.7	1.2	1.3	0.7	2.1	x	—	—	—
Norite			—	—	0.7	0.7	1.0	x	—	—	—
Gabbro			—	—	—	—	—	x	—	—	—
Plagioclase			10.7	1.2	6.7	3.3	7.3	x	—	—	—
Clinopyroxene			6.0	3.9	3.0	2.7	2.1	x	—	—	—
Orthopyroxene			1.0	—	3.3	—	—	x	—	—	—
Olivine			—	1.2	0.7	—	2.1	x	—	—	—
Ilmenite			—	—	0.3	—	—	x	—	—	—
Glass											
Orange			0.3	1.2	0.3	—	—	x	—	—	—
"Black"			1.3	1.5	0.3	—	1.0	x	—	—	—
Colorless			1.0	1.5	1.3	—	—	x	—	—	—
Brown			3.3	3.0	1.0	5.3	4.2	x	—	—	—
Gray, ropy			—	—	0.3	—	1.0	x	—	—	—
Other			—	—	0.3	0.7	1.0	x	—	—	—
Total number of grains counted	300	162	249	259	300	150	95	x	—	—	—
Wt.% of total sample for each size fraction	25.84	18.79	12.0	4.01	11.02	8.37	8.55	x	3.67	2.76	1.01

Sample 71061,1 was collected at Station 1 on the mare surface. Agglutinate vs. nonagglutinate grains were identified by using a scanning electron microscope in size ranges of <20 and 20-45 μm. The >10-mm fraction made up 9.42% of the sample. "Black" glass is partly crystalline orange glass. Sample 72441,7 was collected at the base of the South Massif, on the "light mantle" deposit (from *Heiken and McKay, 1974*). Agglutinate vs. nonagglutinate grains were identified by using a scanning electron microscope in size ranges of <20 and 20-45 μm. x = Data for the 0.5-1.0 mm fraction of 72441,7 were not available.

* The <20-μm fraction is 83% nonagglutinate; the 20- to 45-μm fraction is 82.7% nonagglutinate.

†The <20-μm fraction is 79.0% nonagglutinate; the 20- to 45-μm fraction is 50.0% nonagglutinate.

TABLE 7.2. Modal (vol.%) abundance data for particles in the 1000–90 μm size fraction of representative soils from each mission (*Simon et al.*, 1981).

	10084	12001	12033	14163	15221	15271	64501	67461	72501	76501	78221	21000	22001*	24999
Mineral Fragments														
Pyroxene + Olivine	4.2	18.3	26.3	2.6	16.1	13.5	1.0	0.5	5.2	17.3	9.8	6.4	8.9	40.2
Plagioclase	1.9	3.9	9.9	5.1	13.1	7.4	32.1	12.2	10.9	15.2	9.9	1.1	14.7	10.6
Opaque	1.1	0.2	1.3	—	0.1	0.3	—	1.1	0.1	2.8	0.4	—	0.1	0.2
Lithic Fragments														
Mare basalts	24.0	12.9	7.5	2.2	3.1	3.2	0.3	0.5	2.9	9.2	5.7	18.3	1.7	6.9
ANT [†]	0.4	1.0	1.3	2.9	2.6	2.2	5.0	21.7	5.2	0.5	2.2	0.8	9.7	3.5
LMB [‡]	0.8	0.1	0.3	0.3	0.6	0.4	2.1	30.7	2.4	6.3	2.3	0.3	2.8	0.5
Feldspathic Basalt (KREEPY)	1.1	0.5	—	0.6	0.4	1.9	1.6	1.6	0.2	0.2	0.2	1.4	0.8	1.4
RNB/POIK [§]	—	2.3	3.7	10.9	2.7	2.8	8.3	7.9	9.7	8.1	4.4	2.8	10.9	2.2
Fused Soil Component														
DMB	7.5	9.5	11.9	19.3	13.3	12.9	13.9	11.1	22.6	4.2	12.0	15.0	15.0	10.6
Agglutinate	52.0	40.1	17.0	45.7	36.9	37.0	29.1	8.5	37.6	29.2	46.6	42.8	28.7	16.6
Glass Fragments														
Orange/Black	2.7	0.5	1.5	—	0.4	1.6	0.7	0.5	1.7	1.6	1.6	1.4	0.2	—
Yellow/Green	0.8	2.8	0.2	2.9	4.5	7.0	1.2	—	0.1	1.3	1.3	1.7	0.7	0.9
Brown	—	1.5	7.8	—	0.3	0.3	—	—	0.2	—	—	—	—	0.2
Clear	1.3	1.0	—	1.3	1.5	3.8	1.4	—	0.2	0.8	1.0	2.5	1.1	0.6
Miscellaneous														
Devitrified Glass	1.8	5.0	10.8	6.1	4.1	5.6	3.4	3.2	0.4	2.2	1.9	4.4	4.6	5.4
Others	0.3	0.5	0.5	—	0.3	0.2	—	0.5	0.4	1.1	0.7	1.1	0.1	0.3
Total	99.9	100.1	100.0	99.9	100.0	100.1	100.1	100.0	99.8	100.0	100.0	100.0	100.0	100.1
Number of points	625	823	666	311	1000	1008	942	189	801	820	1266	360	1333	634

* 500–90 μm fraction.

[†] ANT = anorthosite, norite, troctolite.

[‡] LMB = Light matrix breccia.

[§] RNB/POIK = Recrystallized noritic breccia/poikilitic breccia.

COMPARATIVE MODAL PETROLOGY (1000 - 90 μm)

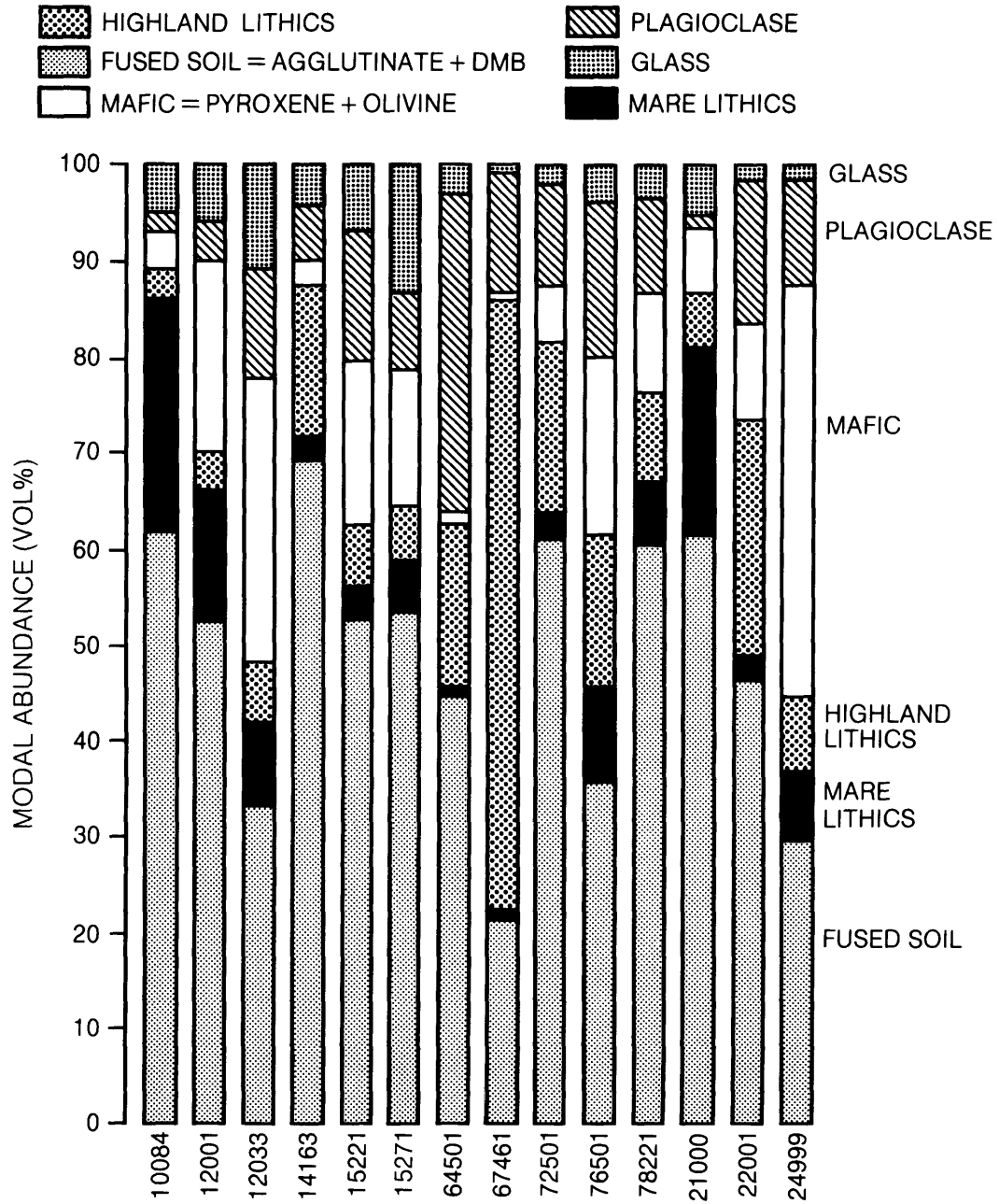


Fig. 7.1. Bar graphs showing modal (volume) abundances of principal particle types in 14 lunar soil samples (Simon et al., 1981). This diagram distinguishes between rock fragments (mare lithics, highland lithics), single mineral and glass fragments (pyroxene and olivine, plagioclase, glass), and fused soil (agglutinates and dmb—Dark Matrix Breccia). Soil samples are from Apollo 11 (10084), Apollo 12 (12xxx), Apollo 14 (14163), Apollo 15 (15xxx), Apollo 16 (6xxxx), Apollo 17 (7xxxx), Luna 16 (21000 and 22001), and Luna 24 (24999).

TABLE 7.3. Modal (volume) abundances of particles in six size fractions of lunar soil 15601,96.

Size (μm) Wt.%	250-500	150-250	90-150	75-90	45-75	20-45	15601,96 avg. (%)	Error %
	11.91	13.13	15.99	5.48	14.45	17.37	78.33	
Monomineralic	21.4	35.4	39.7	53.3	47.6	52.5	41.5	1.2
Plagioclase	1.3	4.2	7.5	6.0	6.1	8.8	5.9	0.5
Pyroxene	17.6	28.3	27.2	43.9	37.4	37.8	31.3	1.1
Olivine	2.5	2.9	4.3	2.2	2.8	2.5	3.0	0.4
Opaque Minerals	—	—	(0.7)	(1.2)	(1.6)	(3.4)	(1.3)	
Oxides	—	—	0.7	1.2	1.6	2.2	1.0	
Metal, sulphide	—	—	—	—	—	1.2	0.3	
Silica phase	—	—	—	—	—	—	0.0	
Crystalline lithic clasts	34.0	24.1	15.7	14.6	11.4	11.7	18.1	0.9
ANT suite	(1.3)	(0.6)	(0.3)	(0.0)	(0.0)	(0.0)	(0.4)	
Anorthositic	1.3	0.6	—	—	—	—	0.3	
Gabbroic	—	—	0.3	—	—	—	0.1	
Mare basalt	(29.0)	(17.7)	(8.6)	(10.8)	(9.8)	(8.3)	(13.5)	1.2
Olivine-bearing	14.5	7.1	3.6	2.5	1.2	1.2	4.8	0.5
Olivine-free	(17.7)	(4.8)	(2.7)	(2.7)	(2.4)	(0.9)	(3.8)	0.4
Microgabbroic	1.9	1.0	0.7	0.9	0.6	0.6	0.9	
Porphyritic, etc.	6.9	2.9	1.3	0.3	0.3	0.3	2.0	
Ophitic, etc.	1.9	0.6	0.7	0.9	0.6	—	0.7	
Intersertal/granular	—	0.3	—	0.9	0.6	—	0.2	
Other	3.8	5.8	2.3	5.6	6.2	6.2	4.9	0.5
Nonmare basalt	(0.6)	(1.6)	(0.7)	(1.3)	(0.0)	(0.6)	(0.7)	
Feldspathic	—	—	—	—	—	—	0.0	
KREEPy	0.6	1.6	0.7	1.3	—	0.6	0.7	
Plagioclase-phyric	—	—	—	—	—	—	0.0	
Indeterminate	3.1	4.2	6.2	2.5	1.6	2.8	3.5	0.4
Breccias	5.7	6.1	4.9	5.6	6.2	4.7	5.5	0.6
Vitric	(4.4)	(5.8)	(4.6)	(3.4)	(5.6)	(4.4)	(4.8)	0.5
Dark matrix	4.4	5.5	4.3	3.4	4.7	4.1	4.5	0.5
Light matrix	—	0.3	0.3	—	0.9	0.3	0.3	
Crystalline	(1.3)	(0.3)	(0.3)	(2.2)	(0.6)	(0.3)	(0.6)	
Poikilitic	—	—	—	—	—	—	0.0	
Melt matrix	1.3	—	—	1.9	0.6	0.3	0.5	
Other	—	0.3	0.3	0.3	—	—	0.1	
Agglutinate	32.1	28.0	32.1	19.7	26.5	25.9	28.1	1.1
Glass	6.3	6.4	7.5	6.6	8.1	4.9	6.6	0.6
Ropy/Clast-laden	3.1	2.9	2.0	1.9	2.5	1.2	2.2	0.2
Quench-crystal (vitrophyres)	(0.6)	(1.6)	(1.6)	(0.6)	(0.9)	(0.0)	(0.9)	
Green glass	—	0.3	0.3	0.3	0.6	—	0.2	
Other	0.6	1.3	1.3	0.3	0.3	—	0.7	
Devitrified	1.3	1.3	2.3	1.6	1.9	0.9	1.5	
Homogeneous	(1.3)	(0.6)	(2.0)	(2.5)	(2.8)	(2.8)	(2.0)	0.2
Green	1.3	0.3	1.0	1.6	2.5	1.6	1.4	
Yellow	—	—	1.0	0.3	—	—	0.2	
Gray, colorless	—	—	—	0.3	—	0.3	0.1	
Brown, black, etc.	—	0.3	—	0.3	0.3	0.9	0.3	
Miscellaneous	0.6	—	—	—	—	—	0.1	
No. of particles	159	311	305	319	321	320	1735	

A weighted average is calculated for the bulk sample and is given in the far right column. The errors (1σ) are based on counting statistics at 95% confidence level; error statistics are not valid for concentrations less than 2% (Basu *et al.*, 1981). Subtotals are in parentheses.

collected from the edge of a lava rille and 3.5 km downslope from the Apennine Front sampling site, is made up of about 90% mare material.

Several complications arise in trying to identify the bedrock components that make up a lunar soil. One problem is the fine grain size of the soil itself. The average grain size of lunar soils is only about 60 μm . Thus, the presence of recognizable, polymineralic rock fragments in the smaller size fractions is a function of the mineral grain size in the parent rocks. Rocks composed of minerals $>60 \mu\text{m}$ in size will, when crushed, produce mostly single mineral fragments and it will be difficult to identify the original source rock. However, many basalts in the Apollo 11 collection are very fine grained; crystal size in these basalts averages only about 40–100 μm . Many of these fragments in Apollo 11 soils contain several mineral grains and can be identified as basaltic rocks. On the other hand, many basalts from the Luna 24 site are fairly coarse grained; crystal sizes range from 100–500 μm . As a result, and as expected, many more monomineralic particles are found in Luna 24 soils than in the Apollo 11 soils, although more than 90% of both soils was derived from mare basalts. Similar complications have been observed in studies of terrestrial clastic sediments (e.g., sandstones and siltstones), in which simple modal data also do not necessarily provide direct information about the source rocks.

An additional complication is introduced by the fact that lunar soils show variations in *maturity*, a quantity roughly equivalent to age. Lunar soils change significantly as they develop over time, and a highly mature soil, with an increased degree of comminution and melting, may significantly obscure parent rock compositions (for a discussion of maturity and its effects, see section 7.3).

Even in finely comminuted or mature soils, considerable information about the parent bedrock can be obtained from the chemical composition of individual mineral fragments. These compositions can be measured with an electron microprobe on fragments as small as 10 μm in size. Several studies (*Bence and Papike, 1972; J. V. Smith, 1974; Smith and Steele, 1976; Steele and Smith, 1975*) have shown that the chemical compositions of a few common rock-forming minerals, especially their minor element abundances and ratios, provide clues to the nature of their source rocks. With these data it is possible to infer the parent rocks from which individual mineral grains in lunar soils were derived. For some elements, the compositional ranges of pyroxenes derived from mare basalts are distinctly different from pyroxenes derived from highland rocks. Unfortunately, a large range also exists in which the compositions of pyroxenes from different parent

rocks overlap. In addition, different basalts show different chemical trends in pyroxene composition during progressive crystallization (section 5.1.1), so that a range of pyroxene compositions can be obtained from a single lava flow.

The magnesium (or forsterite molecule) content of olivine and the calcium (or anorthite molecule) content of plagioclase can also be used to discriminate between individual grains from different parent rocks. *Vaniman et al. (1979)* made a detailed study of chemical compositions of monomineralic pyroxene grains in soil layers from the Apollo 17 deep drill core. They were able to infer the relative proportions of monomineralic pyroxene grains that were contributed by a variety of bedrock types—high-Ti mare basalts, noritic rocks, and anorthositic gabbros (Table 7.4). Earlier, *Basu and Bower (1977)* used a similar approach to confirm the identification of two different sources for KREEP rocks and mare basalt lavas for the pyroxene grains in Apollo 15 soils. Chemical compositions of monomineralic olivine and plagioclase particles from the Luna 24 soils suggest that a significant fraction of these soil particles was derived from distant sources, including highland rocks (3%) and a mafic cumulate (10%) (*Basu et al., 1978*).

Completely glassy fragments (glasses without either crystal or rock inclusions) of both impact and volcanic origin are present in all sampled lunar soils. The origins of these glasses, whether impact melting or volcanic eruptions, can often be inferred from their chemical compositions (see section 6.1.7). Because the volcanic glasses are derived from eruptions on the maria, this information provides an additional clue to the proportions of highland and mare materials in lunar soils.

Mature (old) and immature (young) soils from the same area may also have different mineralogical compositions (*Papike et al., 1982; Greene et al., 1975; Engelhardt et al., 1976; McKay et al., 1972*). In general, mature soils are finer grained. The mineral grains

TABLE 7.4. Modal (vol.%) classification of pyroxene fragments in Apollo 17 deep drill core 70002–70009 by lithic origin (*Vaniman et al., 1979*).

	High-Ti Mare	Noritic	Anorthositic Gabbro	Total Highland
Unit E	0.66	0.01	0.32	0.33
Unit D	0.92	0.02	0.06	0.08
Unit C	0.61	0.20	0.19	0.39
Unit B	0.57	0.21	0.22	0.43
Unit A	0.63	0.19	0.18	0.37

TABLE 7.5. Particle types and relative abundances (vol.%) in size fractions of soil 64501 (Houck, 1982a).

Size (μm) Wt.%	500-250	250-150	150-90	90-75	75-45	45-20	Σ 500-20
	8.9	8.2	10.0	3.5	10.0	15.6	56.2
<i>Monomineralic</i>	29.0	35.3	25.3	30.9	45.0	44.0	36.4
Plagioclase	29.0	34.0	25.0	28.6	43.1	34.2	33.0
Pyroxene	—	1.3	0.3	2.3	1.6	6.5	2.5
Olivine	—	—	—	1.0	0.3	2.0	0.3
Opagues, Oxides, etc.	—	—	—	—	—	1.3	0.4
SiO ₂ Phases	—	—	—	—	—	—	—
<i>Crystalline Lithic Clasts</i>	5.8	0.3	—	0.3	—	—	1.0
Anorth., Nor., Troct.	(5.8)	(0.3)	—	(0.3)	—	—	(1.0)
Anorthositic	5.8	0.3	—	0.3	—	—	1.0
Noritic-troctolitic	—	—	—	—	—	—	—
Mare Basalt	—	—	—	—	—	—	—
KREEP Basalt	—	—	—	—	—	—	—
Indeterminate/Other	—	—	—	—	—	—	—
<i>Breccias</i>	31.4	32.7	26.2	24.0	21.6	22.9	26.1
Fragmental/Vitric Matrix	(7.0)	(8.9)	(8.3)	(5.3)	(6.5)	(5.9)	(7.0)
Regolithic/Vitric Matrix	(6.2)	(5.9)	(5.0)	(4.3)	(5.2)	(4.9)	(5.3)
Porous	—	1.3	3.0	1.0	0.3	1.0	1.1
Compact	6.2	4.6	2.0	3.3	4.9	3.9	4.2
Feldspathic/Vitric Matrix	(0.4)	(0.7)	(1.3)	(0.7)	(0.3)	—	(0.5)
Porous	—	—	1.0	0.7	0.3	—	0.8
Compact	0.4	0.7	0.3	—	—	—	0.2
Fragmental Matrix	(0.4)	(2.3)	(2.0)	(0.3)	(1.0)	(1.0)	(1.2)
Unshocked clasts >50%	—	—	—	0.3	0.3	—	0.6
Shocked clasts >50%	0.4	2.3	2.0	—	0.7	1.0	1.2
Crystalline Matrix	(24.4)	(23.8)	(17.9)	(18.7)	(15.1)	(17.0)	(2.7)
Poikilitic	(4.5)	(5.0)	(4.0)	(3.9)	(2.6)	(0.6)	(3.0)
Equant Plagioclase	3.6	4.3	2.3	1.6	2.3	0.3	2.2
Acicular Plagioclase	0.9	0.7	1.7	2.3	0.3	0.3	0.8
Basaltic-Textured	(9.3)	(5.6)	(7.9)	(5.3)	(2.3)	(1.4)	(4.8)
Variolitic	1.3	—	0.3	0.3	—	—	0.3
Subophitic	3.6	4.0	3.3	1.0	0.7	0.7	3.9
Intergranular	1.3	0.3	1.7	0.7	0.6	—	0.7
Intersertal	—	—	0.3	—	—	—	0.1
Porphyritic	—	—	—	—	—	—	—
Other/Indeterminate	3.1	1.3	2.3	3.3	1.6	0.7	1.8
Granulitic	0.4	1.3	0.3	1.6	0.7	0.3	0.6
Other/Indeterminate	11.2	11.9	5.7	7.9	9.5	14.7	10.8
<i>Agglutinates</i>	28.1	27.1	44.0	34.5	25.7	22.5	29.2
<i>Glass</i>	4.3	4.7	4.9	9.2	7.5	9.4	6.8
Clast Laden/Ropy	2.2	2.3	2.3	3.0	2.3	2.3	2.3
Vitrophyric/Quench Crystal	0.4	0.7	0.7	0.3	0.3	1.1	0.7
Cryptocrystalline	0.9	0.3	0.3	2.6	1.3	0.3	0.7
Clast and Crystal Free	(0.8)	(1.4)	(2.3)	(2.9)	(3.6)	(6.5)	(3.4)
Green	0.3	0.1	—	—	—	—	0.1
Yellow	0.4	0.7	0.7	1.0	0.7	0.7	0.7
Colorless/Gray, etc.	0.4	0.7	1.3	1.6	2.3	3.9	2.0
Black/Orange, etc.	—	—	0.3	0.3	0.3	2.9	0.9
<i>Miscellaneous</i>	—	—	—	—	—	0.3	0.1
No. of particles	224	303	300	304	304	307	1742

Subtotals are in parentheses.

that are fine grained in the parent rocks, as well as minerals with good cleavage (e.g., plagioclase) that are easily broken, tend to be concentrated in the finer soil fractions. This concentration is especially pronounced in the extremely fine (<10- μ m) fraction (*Devine et al.*, 1982). Experimental studies also support the theory that such differential comminution of mineral grains is an important process in forming lunar soils (*Hörz et al.*, 1984). Examples of plagioclase concentration in the finest-size fractions of actual lunar soil samples are shown in Tables 7.3 and 7.5 (*Basu et al.*, 1981; *Houck*, 1982a; see also *McKay et al.*, 1978b).

7.1.3. Agglutinates

Agglutinates are individual particles that are aggregates of smaller lunar soil particles (mineral grains, glasses, and even older agglutinates) bonded together by vesicular, flow-banded glass. Agglutinate particles (Fig. 7.2a) are small (usually <1 mm) and contain minute droplets of Fe metal (much of which is very fine-grained, single domain Fe⁰), and troilite (FeS). They have probably formed by the melting and mixing produced by micrometeoritic bombardment of the lunar regolith.

Agglutinates were one of the most interesting features observed in the first returned lunar soil samples. These somewhat unexpected, abundant, heterogeneous, clast-rich particles are made of soil grains (clasts) bonded together by impact-melted glass (*Duke et al.*, 1970a; *McKay et al.*, 1970, 1972; *Heiken*, 1975). In some mature soils agglutinates are

the major constituent, and they may make up as much as 60% of the soil by volume. Agglutinates are unique to soils developed on terrestrial planets lacking an atmosphere, such as the Moon and Mercury.

The formation of agglutinates requires (1) a rain of high-velocity micrometeoroids onto the surface of an airless planet and (2) a target consisting of a regolith produced by prior bombardment. Therefore, agglutinates are not found at all on the Earth, even in association with terrestrial impact craters. Although some meteorites may have been derived from regolith-like deposits on some asteroids, no true agglutinates have been observed in them. So far, we have found true agglutinates only in lunar soils.

Figure 7.2 shows a series of scanning electron micrographs of agglutinates. They are typically irregular in shape and often have branching or dendritic morphologies. In thin section (Fig. 7.2d), agglutinates are usually heterogeneous in appearance, with clasts and glass intermixed in varying proportions. Vesicles are present in most agglutinates. Metallic iron droplets are also common and, under high-power reflected-light microscopy, clouds of very fine metallic iron droplets are often visible. Agglutinates frequently display mounds and trains of metallic iron (Fig. 7.2e), as well as attached mineral grains and small lithic fragments. Vesicles are also common on agglutinate surfaces.

Unique properties. Agglutinates differ from other lunar impact glasses and from terrestrial impact glasses in several important respects. First, they always contain Fe metal droplets. Analysis of

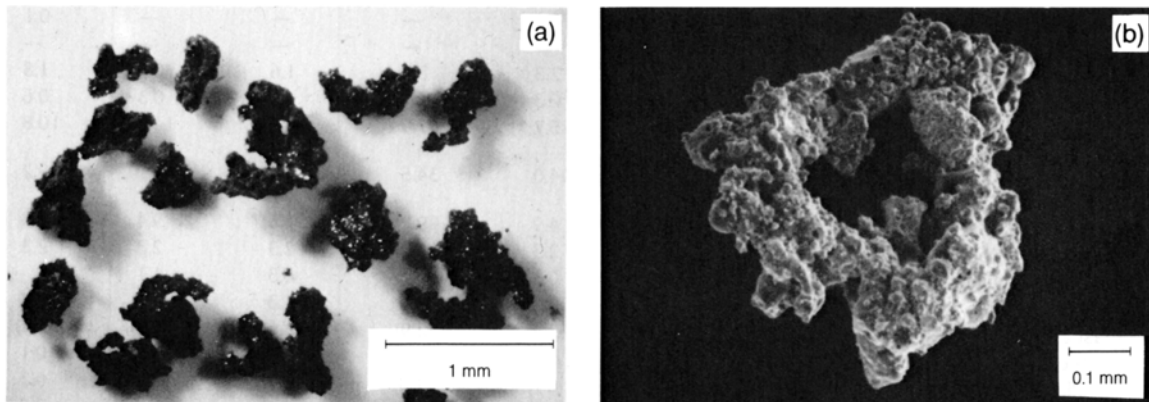


Fig. 7.2. Typical lunar soil agglutinates. **(a)** Optical microscope photograph of a number of agglutinates separated from Apollo 11 soil sample 10084, showing a variety of irregular agglutinate shapes (NASA Photo S69-54827). **(b)** Scanning electron photomicrograph of a doughnut-shaped agglutinate. This agglutinate, removed from soil 10084, has a glassy surface that is extensively coated with small soil fragments. A few larger vesicles are also visible (NASA Photo S87-38812).

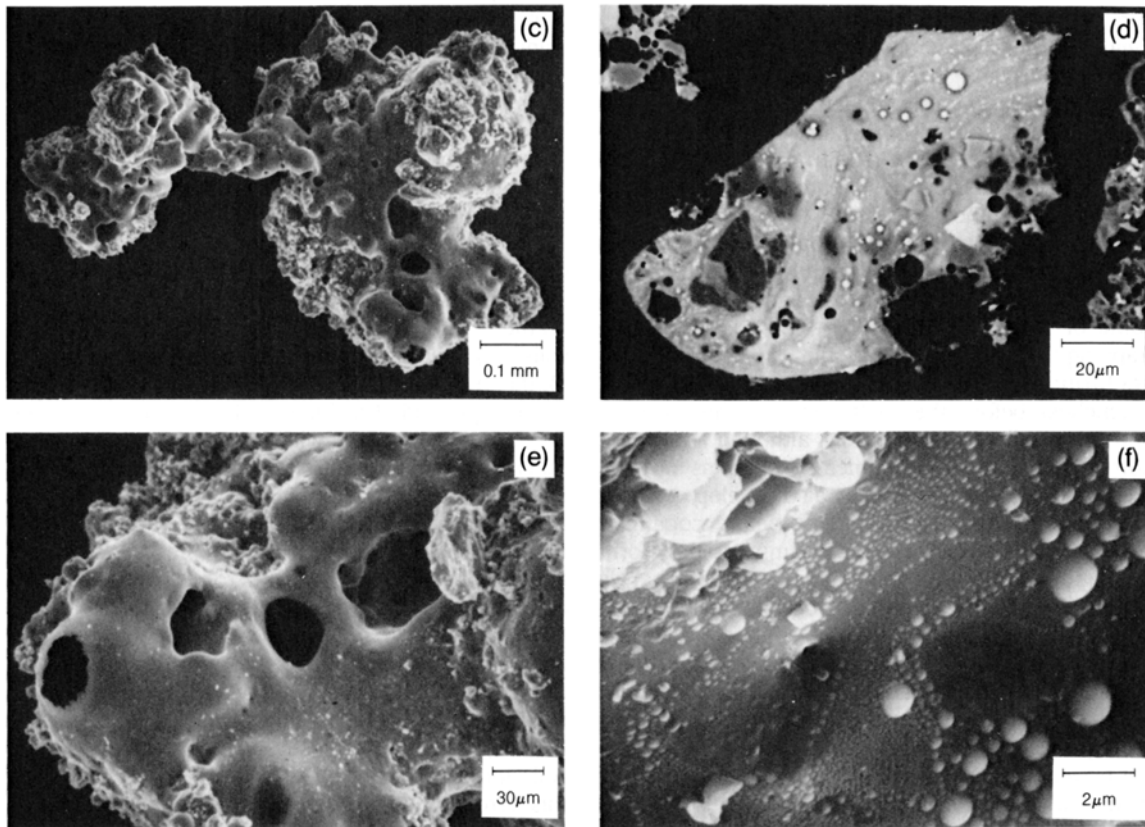


Fig. 7.2. (continued) **(c)** Scanning electron photomicrograph of an irregular agglutinate from soil 10084, showing some vesicular, glassy, fragment-free surfaces adjacent to fragment-laden surfaces. Some agglutinates are very delicate and display narrow bridges, necks, and dendrite-like arms (NASA Photo S87-38811). **(d)** Scanning electron photomicrograph of a polished thin section of an agglutinate using back-scattered electrons. The agglutinate particle contains a variety of vesicles, with circular, elongate, and irregular shapes. Irregular mineral fragments in the glass include plagioclase (darker), pyroxene, and ilmenite (brighter). The bright circular features are metallic Fe, which occurs as isolated droplets, and trains and swirls of small droplets ($<5 \mu\text{m}$). The metallic Fe has apparently been formed by reduction of FeO in the glass. It is not confined to surfaces, but is present throughout the volume of most agglutinates (NASA Photo S87-38816). **(e)** Closer SEM view of a glassy agglutinate surface, showing vesicular structure. Small mounds and trains of metallic Fe are visible as bright spots that occur over the entire glassy surface (NASA Photo S87-39605). **(f)** Closeup SEM view of a glassy agglutinate surface from sample 10084, showing clusters of Fe mounds, together with groups and trains of smaller Fe mounds ($20\text{-}\text{\AA}$ to $1\text{-}\mu\text{m}$ diameters). Most, if not all, of this Fe has presumably been formed by reduction of the lunar glass by implanted H (and possibly C) during the high-temperature pulse from the micrometeorite impact that created the agglutinate (NASA Photo S87-38846).

this metal shows that it is usually relatively pure Fe, lacking the significant Ni and Co present in meteoritic metal. Second, most of the metal droplets are extremely fine-grained. Ferromagnetic analysis shows that most of the metal is in the single-domain size range ($30\text{--}100 \text{\AA}$), and this material is therefore not always visible using an optical microscope (Morris, 1976; Pearce *et al.*, 1975). Third, agglutinates always contain solar-wind gases, including He and

H (DesMarais *et al.*, 1974; Housley *et al.*, 1973b). The abundances of these gases in agglutinates are usually higher than in any other grains of equivalent size in the soil.

The properties of agglutinates are best explained by a model in which agglutinates are formed by impacts of micrometeoroids into a lunar soil that contains previously implanted solar-wind elements, mainly H and He. During the impact event, several

complex processes occur. Some of the soil grains are melted, forming glass and liberating their implanted solar-wind H and He. The liberated H reacts with FeO in the glass, partly reducing it to metallic iron and producing some H₂O, which escapes from the glass (Housley *et al.*, 1973a,b). The vesicles are formed in the glass by the liberated solar-wind gases and possibly by the generated H₂O as well.

After the impact, the iron droplets are formed by the reduction process. The melted glass also engulfs small soil grains before it cools, and it may liberate some of their implanted solar-wind gases, possibly trapping them immediately within the newly-formed agglutinate. The agglutinate generally cools (quenches) before the melt can fully homogenize both physically and chemically, although somewhat homogenized smaller volumes or domains may be present. The reduced iron may also develop complex forms on the agglutinate surface before cooling is complete. Some micrometeoroid impacts may form a single agglutinate, especially if the target is coherent and the impacting body is small, and agglutinates in the form of bowl-shaped craters are not uncommon. Other impacts may form many agglutinates as the impact-produced melt pulls apart and is ejected from the impact site through neighboring soil masses. Most agglutinates probably do not travel far from the site of the impact that formed them, but few data exist on this point.

The importance of agglutinates. Agglutinates make up a high proportion of lunar soils, about 25–30% on average, although their abundances may range from a rare 5% to about 65%. At high abundances, the agglutinates, which have been produced in the regolith itself, obscure the percentages of the comminuted bedrock fragments in lunar soils. Furthermore, agglutinates contain an appreciable amount of metallic Fe⁰ in their glass, which has formed by the reduction of Fe-silicates in the soils. Both the Fe⁰ metal and the glass in the lunar soil obscure and modify infrared and X-ray fluorescence signals from the other soil phases, thereby complicating the mapping of the lunar surface, especially with orbital and Earth-based remote sensing. Finally, because agglutinates are continuously produced by micrometeoroid bombardment at the surface of the regolith, the agglutinate abundance in a soil increases with time and is directly proportional to its cumulative exposure age. Thus, the percentage of agglutinates in a lunar soil is one of the most useful indicators of its maturity.

Agglutinate petrography. Agglutinates are small and, like most other lunar soil grains, can be observed adequately only with a scanning electron microscope (SEM) or in polished thin sections under a petrographic microscope equipped with both

transmitted and reflected light. They are best studied using ion-etched thin sections and the backscatter-electron mode of an SEM (Figs. 7.2b–f). Using these tools, agglutinates appear as heterogeneous swirls or bands of glass that contain rock, mineral, and glass fragments of all sizes; irregular lines of fine-grained iron are scattered throughout the glass. There are also fragments stuck to glassy agglutinate surfaces.

The presence of very-fine-grained (300 Å), single-domain Fe⁰ metal is a characteristic feature of agglutinates. Production of this Fe is dependent on (1) the availability of Fe compounds in the target soils, (2) melting by micrometeoritic impacts, and (3) the availability of a reducing agent like solar-wind-implanted H in lunar soils. Because the latter two variables increase with increasing exposure age, other factors remaining constant, the abundance of fine-grained, single-domain Fe⁰ in a soil should be a good indicator of soil maturity. The ratio of single-domain Fe⁰ to original FeO increases as a soil matures because repeated micrometeoroid impacts continuously reduce the FeO-bearing silicates to Fe⁰. It has been shown that the intensity of ferromagnetic resonance of lunar soils (I_s on an arbitrary scale) is caused by this fine-grained, single-domain Fe⁰. Thus, the ratio I_s/FeO (with total iron in a soil expressed as FeO) is a good measure of maturity of a lunar soil, and agglutinate glass is the physical carrier of this ferromagnetic resonance (see section 7.3).

Agglutinate chemistry. Agglutinates consist of soil grains bonded by glass, and the glass itself is produced by melting the lunar soil. For these reasons, agglutinates tend to mimic the composition of the soils from which they formed. However, an agglutinate can only incorporate smaller particles than itself. Therefore, agglutinates can only be representative of that fraction of a soil whose grain size is smaller than that of the agglutinates. However, agglutinates can range up to >1 mm in size, and it is reasonable to expect that the average composition of agglutinates will be generally similar to that of the bulk soil. The only anomaly expected should be a higher concentration of Fe in the agglutinates because of the production of metallic Fe from original FeO in the soil. Indeed, analyses of agglutinate-rich magnetic concentrates from soils (Adams *et al.*, 1975; Rhodes *et al.*, 1975; Blanchard *et al.*, 1975b) indicate the presence of such an enrichment of Fe in the agglutinates over the respective bulk soils.

Although the chemical composition of whole agglutinates may be soil-like, the composition of the agglutinate glass is not. The glass that forms the binder in the agglutinate particle is, in contrast, a product of several complex processes. Primarily the glass is a melt from the very small volume of soil

that was directly impacted by a micrometeoroid. This small volume may not have been representative of the total soil. Furthermore, small compositional changes must have occurred during melting, such as the escape (at least in part) of volatile elements, or the extraction of metallic Fe^o from silicate melts, leaving the melt slightly depleted in Fe. Additional effects could have been produced by the character of the mineral grains involved. Shocked grains with high internal strain energy and those with high surface-to-volume ratios (i.e., small grains), permit easier heat transfer and are likely to melt preferentially.

This last possibility led *Papike et al.* (1981) to propose that fusion of the finest fraction of soils (F³ model) is the chief process that produces agglutinitic glass. The best test of this model has been provided by studies of Luna 24 soils, which are extremely immature, relatively pure mare soils (*Basu et al.*, 1978). In these samples, the ratio of agglutinitic glass composition (*Hu and Taylor*, 1978) to the bulk soil composition is quite similar to the ratio of the <10- μ m fraction composition (*Laul et al.*, 1981) to that of the bulk soil. In particular, the enrichment and depletion patterns of specific elements in both agglutinates and in the <10- μ m fraction are quite similar (*Walker and Papike*, 1981; Fig. 7.3). This study provides a large-scale demonstration that the chemical composition of agglutinitic glass is indeed biased toward that of the <10- μ m fraction of the original soil.

Furthermore, closer examination of the composition of individual agglutinates suggests that the composition of the agglutinate glass is determined by the initial shock-induced melting and is not modified by incorporation (assimilation) of unmelted grains into the glass. Seemingly pure glass is actually riddled with many submicrometer-sized vesicles and clasts. Analyses by *Basu and McKay* (1985) of the "pure" glass, both adjacent to and away from such clasts, both large and small, show no differences in chemical composition between different areas. This observation suggests that assimilation of the clasts by the primary impact melt has not been a major process modifying the final composition of the glass in different areas.

However, special problems are produced by large agglutinates, which may be the result of several generations of impact events. These large multigenerational agglutinates contain small glassy areas that are remarkably homogeneous in chemical composition. These areas are different in different agglutinates, or even within single multigenerational agglutinates, and they show no systematic chemical relationship to the composition of either bulk soils or their finest fractions (Fig. 7.4). These homogene-

ous glassy areas within agglutinate grains may represent the melt from single impact events, and their homogeneity could reflect total melting of the target (rather than just melting of the finest fraction) upon micrometeoroid bombardment (*Gibbons et al.*, 1976; *Hu and Taylor*, 1978). It seems likely that, when micrometeoroids strike random small targets in lunar soils (i.e., mineral grains approximately 100 μ m in size or less), the impacts can produce only extremely small volumes of melt that are not representative of the bulk soil.

Agglutinates, formed as the result of surface exposure, are themselves subsequently exposed to further surface processes, especially to bombardment by extralunar charged particles from the solar wind, solar flares, and cosmic rays. Solar-wind ions implant themselves in a thin outer rind of any soil target (e.g., an agglutinate particle), with varying

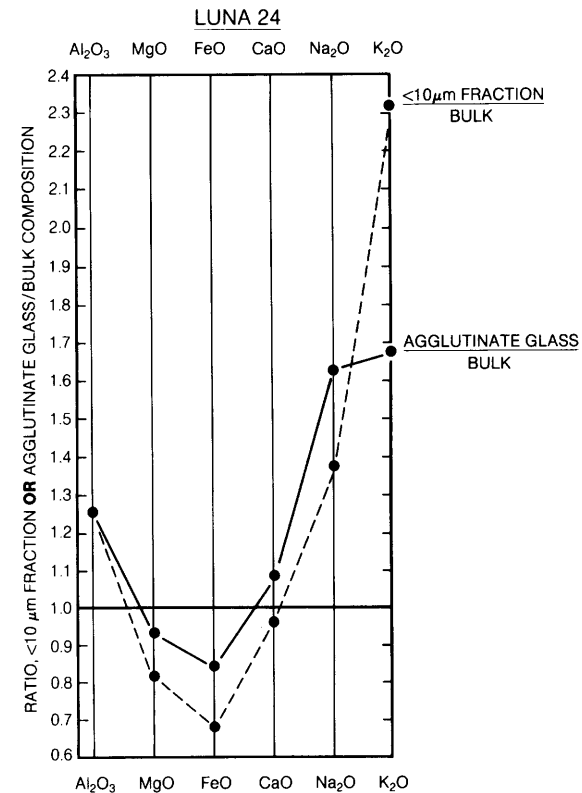


Fig. 7.3. Plot showing similarities in chemical composition between agglutinate glass from the Luna 24 soils and the <10- μ m fraction of Luna 24 soils (*Papike et al.*, 1982). The plot shows ratios of key oxides in both the agglutinates and the <10- μ m fraction, normalized to the same oxide in the total bulk soil.

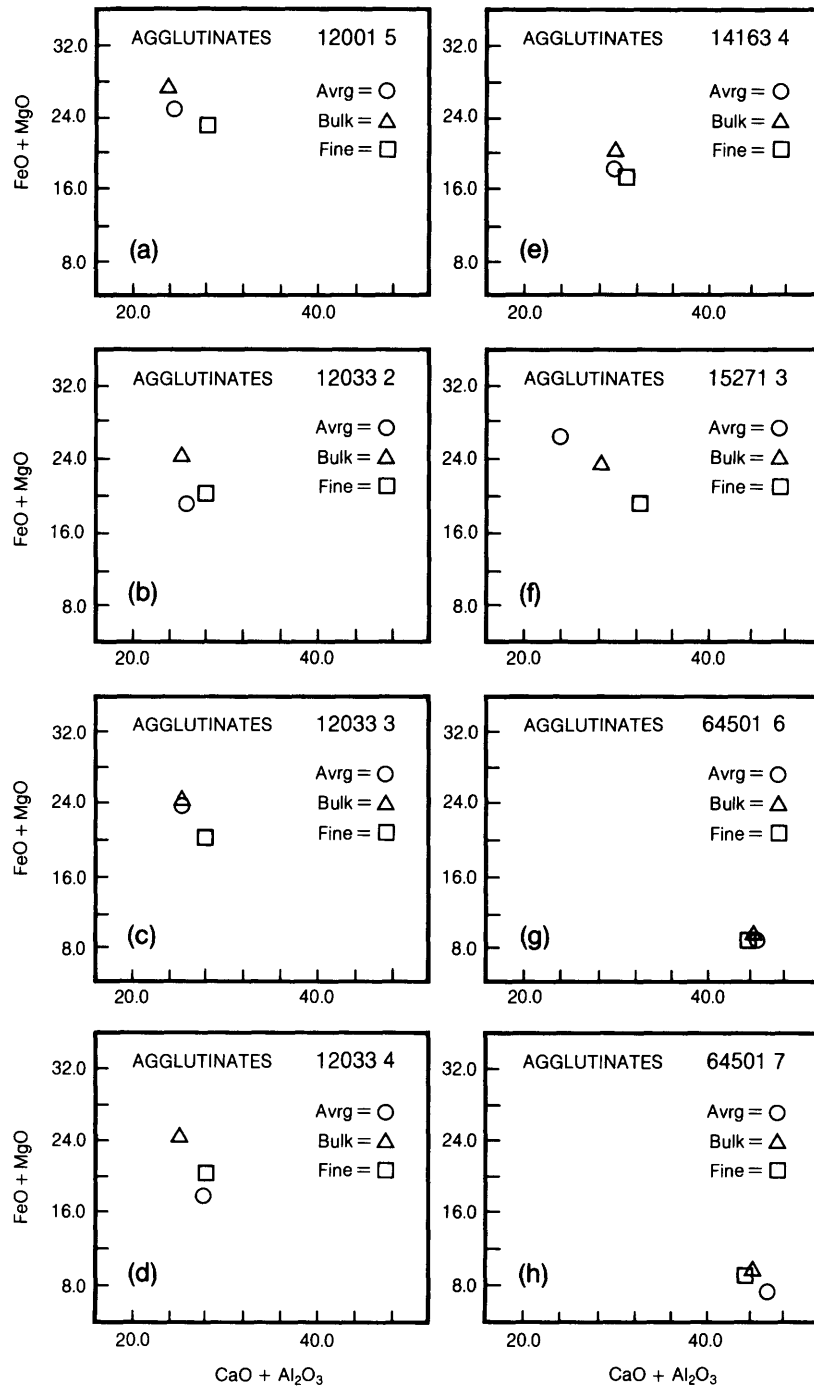


Fig. 7.4. Plots of (FeO + MgO) vs. (CaO + Al₂O₃) for isolated glassy areas in large single agglutinates. Note the tight clustering of the agglutinate glass compositions. Data plotted for comparison are the average compositions of agglutinate glass from the soil sample (Avrg), the bulk composition of the soil sample (Bulk), and the composition of the finest fraction (<10 μm) of the soil (Fine). The composition of any single domain of agglutinate glass shows no systematic relation to either the bulk composition of the parent soil or to that of the finest soil fraction (*Basu and McKay, 1985*).

TABLE 7.6. Concentrations of solar-wind elements (in cm³STP/g) in magnetic agglutinate fractions separated from soil 15601.

Isotope	Range of grain size [μm]								Repurified				
	20-30	30-40	40-53	53-75	75-106	106-150	150-250	250-1000	10-20	20-30	30-40	40-53	53-75
³ He[10 ⁻⁵]	2.02	2.08	1.57	1.10	1.04	0.845	0.778	0.854	2.62	2.34	1.90	1.71	1.25
					0.996			0.663					
⁴ He[10 ⁻²]	5.21	5.28	3.99	2.88	2.64	2.20	2.01	2.23	6.62	5.94	4.91	4.33	3.23
						2.58			1.60				
²⁰ Ne[10 ⁻⁵]	142	149	110	88.9	85.8	75.5	65.9	76.7	183	161	136	122	95.9
					83.3			58.0					
²¹ Ne[10 ⁻⁵]	0.390	0.417	0.325	0.258	0.262	0.231	0.209	0.240	0.491	0.449	0.381	0.344	0.28
					0.254			0.193					
²² Ne[10 ⁻⁵]	11.4	11.8	8.96	7.19	6.96	6.07	5.38	6.19	14.8	13.0	11.0	9.94	7.85
					6.74			4.61					
³⁶ Ar[10 ⁻⁵]	41.4	38.4	29.4	25.9	21.8	19.7	17.6	19.3	52.1	42.0	36.4	31.7	26.3
					22.7			14.6					
³⁸ Ar[10 ⁻⁵]	7.81	7.22	5.51	4.88	4.16	3.71	3.32	3.65	9.87	7.91	6.93	5.97	4.98
					4.24			2.71					
⁴⁰ Ar[10 ⁻⁵]	36.2	33.5	26.7	23.1	19.2	18.7	17.7	16.9	45.1	35.7	30.5	27.1	23.2
					20.2			13.1					
⁸⁴ Kr[10 ⁻⁸]	25.7	22.7	19.5	17.0	13.7	13.2	12.5	12.2	35.8	28.7	25.2	22.0	18.7
					14.8			9.9					
¹³² Xe[10 ⁻⁸]	4.27	3.36	2.83	2.69	2.01	2.14	1.90	1.79	5.29	4.38	3.69	3.34	2.80
					2.18			1.50					

The weight of the samples analyzed varied between 0.45 and 2.1 mg. Included are also “repurified” agglutinate separates, samples that were received after three sequential magnetic separations to make sure that no nonmagnetic material was left (Schultz *et al.*, 1977).

degrees of efficiency; the penetration depth for an element is no more than a few hundred angstroms. For all practical purposes, therefore, the solar-wind atoms, implanted after the agglutinate formed, can be considered to reside at the surface of the agglutinate. However, older solar-wind particles occur inside agglutinates in the small soil particles contained within the agglutinates. These soil particles had been irradiated by the solar wind for various lengths of time before they were incorporated into the newly formed agglutinates.

Measurements of the isotopes of common solar-wind elements, such as noble gases, in agglutinate concentrates from soil grain-size fractions, clearly show an enrichment in the finer sizes (Table 7.6). The data show a good fit to the equation

$$C = S(d/r)^{-n} + V$$

where C is the concentration of an isotope of a solar-wind element in the grain-size fraction, which has average diameter d; r is an arbitrary reference grain size with a concentration of S of the same trapped isotope; the exponent n corresponds to the negative slope in a plot of log grain size vs. log concentration; and V is the grain-size-independent volume-correlated component (Schultz *et al.*, 1977). These volume-correlated components of solar-wind-implanted noble gas isotopes for a typical lunar soil (sample 15601) are given in Table 7.7. Similar systematic variations are also found for other solar-wind elements such as H and C (Basu *et al.*, 1975). Because agglutinates trap samples of the solar wind at different times, understanding the agglutination process is an essential part of using solar-wind-element systematics in lunar soils for any investigations of the past history of the sun.

TABLE 7.7. Surface and volume correlated concentrations of solar-wind elements (in cm³STP/g) in agglutinates from soil 15601.

Element	S	V
⁴ He[10 ⁻⁴]	106 ± 13	131 ± 20
²⁰ Ne[10 ⁻⁴]	2.46 ± 0.25	5.45 ± 0.40
³⁶ Ar[10 ⁻⁴]	0.72 ± 0.06	1.44 ± 0.13
⁸⁴ Kr[10 ⁻⁸]	4.12 ± 0.22	10.4 ± 0.5
¹³² Xe[10 ⁻⁸]	0.68 ± 0.04	1.52 ± 0.09

S is the concentration in the fraction of 100 diameter. V is the grain size independent volume correlated component. (Uncertainties given correspond to 1 sigma error of the fit.)

7.1.4. Other Unusual Soil Components

Impact glasses. A significant portion of all lunar soils (~3–5%) consists of small beads or irregular pieces of glass that lack any clastic inclusions. Most of these glass particles were produced by impact melting of preexisting regolith. Chemical analyses of large numbers of these glasses show that some of their compositions form clusters that correspond to the compositions of some rock types identified in larger samples. However, the compositions of many of these glasses represent mixtures of rock types and not primary rocks.

An additional complication in comparing the compositions of regolith glasses and lunar bedrock is that chemical fractionation processes that may accompany impact melting, such as selective volatilization of Si, have given rise to new glass compositions that do not correspond to any lunar bedrock. One such group is the high-alumina, silica-poor (HASP) glasses that have been identified from several areas of the Moon (Naney *et al.*, 1976; Vaniman, 1990).

The impact-glass beads in the submillimeter fraction of lunar soils are generally free from inclusions or crystals, but a small population of larger glassy objects, usually >1 mm in size and containing significant numbers of inclusions, has now been identified. Studies indicate that these heterogeneous objects probably formed by the splashing of molten impact melt onto exposed regolith. The impacts responsible for these splashes appear to have been much smaller than those that produced large numbers of the clear glass beads.

Ropy glasses. A set of distinctive, twisted glasses occur as broken pieces in all lunar soils. They contain fine dusty soil grains as inclusions, and some of them even contain skeletal crystals that grew during cooling and solidification of the glass itself (Fig. 7.5). These glasses exhibit a wide variety of chemical compositions, and they are believed to be products of impacts that were intermediate in size between those responsible for producing the impact-melt splashes and those that form large melt sheets, and similar in origin to the glassy impact bombs of the Ries Crater in Germany (Fruiland *et al.*, 1977; also see sections 2.3 and 6.4).

Shocked minerals. Lunar soils are generated by the impact-produced comminution and melting of bedrock. Therefore, these soils abound in shock-metamorphosed materials that have been altered by the intense shock waves produced by the impact. A large part of this material is made up of shocked mineral fragments. A complete range of shock effects (reflecting shock waves of different intensities) is observed in both feldspars and pyroxenes. For

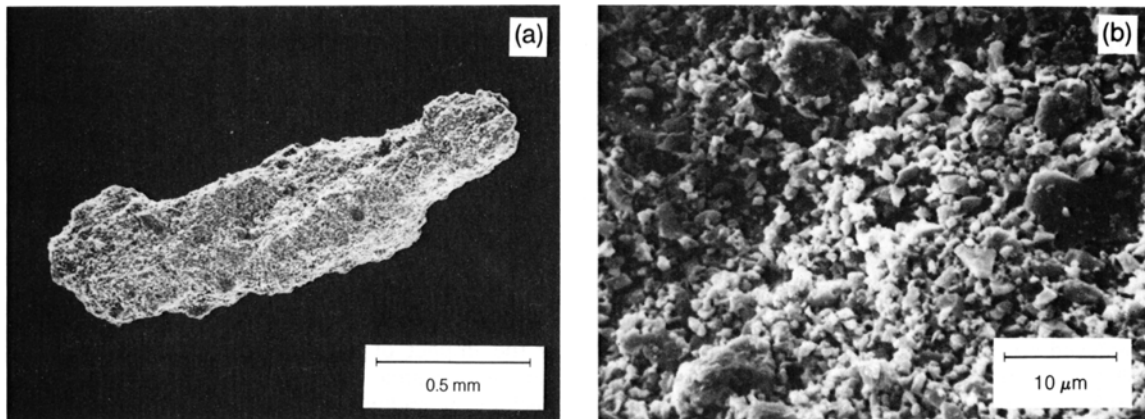


Fig. 7.5. Scanning electron micrograph of typical ropy glass particle from Apollo 12 sample 12033. **(a)** The twisted form (NASA Photo S71-24593), and **(b)** the tightly welded coating of fine fragmental material (NASA Photo S71-24586), are characteristic of many ropy glass fragments. These particles have been interpreted as impact products, which were possibly ejected to great distances as ray material.

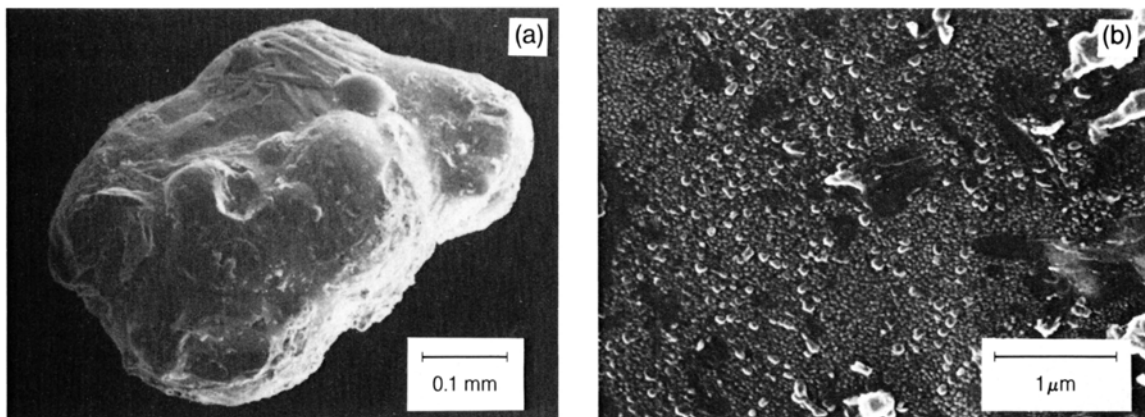


Fig. 7.6. Scanning electron micrograph of a composite volcanic glass droplet from Apollo 17 core 74001/2 (the “orange soil”). **(a)** This grain is composed of multiple droplets that collided in an eruption column while still molten. **(b)** The surfaces of such beads are usually partly coated with complex deposits of material that were possibly formed by sublimation from volcanic gases onto the bead during the volcanic eruption.

example, some plagioclase crystals show no effect of shock, whereas many show various degrees of strained and undulose optical extinction, and others exhibit total solid-state vitrification to a glass (maskelynite). A detailed discussion is provided in section 4.1.2.

Volcanic glasses. Volcanic glass particles in lunar soils are recognized by their uniformity in chemical composition, the presence of a surface coating of condensates of volatile elements, and the

absence of any enrichment of siderophile elements derived from impacting meteoroids. The most abundant glasses of this type are green and orange glass spherules (Fig. 7.6), which are inferred to have formed in volcanic fire-fountain eruptions. Many different volcanic glass types have been identified in lunar soils (e.g., *Delano*, 1986). These glasses (mostly droplets and fragments) are probably the only primary lunar materials that have become part of the lunar regolith without any ballistic transport from

impact craters. When erupted, these glass pyroclasts may form layers of pyroclastic debris, such as the orange soil near Shorty Crater at the Apollo 17 site. In particular, this orange soil has grain sizes and other properties that are clearly different from those of the common impact-produced soils on the Moon (*Heiken et al.*, 1974). Section 6.1 covers lunar volcanic glasses in detail.

7.1.5. Grain Shapes and Surfaces

The effects of the interaction between the space environment and the lunar surface are commonly preserved on the exposed surfaces of grains of lunar soil. The resulting alteration features are small in scale and are observable only with a scanning electron microscope. A freshly broken soil grain, newly exposed to the space environment, has characteristic surface fractures, regardless of whether the original grain is crystalline or glassy. With continued exposure at the lunar surface, however, the grain surface characteristics gradually change. The changes are of principally two kinds: (1) the surface may acquire material in the form of added splashes and coatings of glass, or (2) the surface may lose material through erosion. Each of

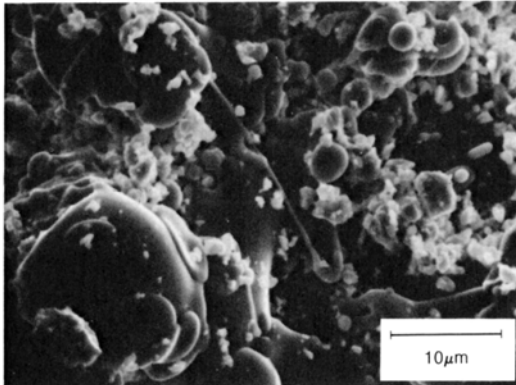


Fig. 7.7. Scanning electron micrograph of a plagioclase grain from lunar soil sample 10084, showing a variety of complex depositional features on the surface of the grain. These depositional features include irregular glass splashes, glass beads, circular “pancake” glass splashes, and adhering fine-grained fragments of crystals and glass. These features indicate that the grain was exposed at the lunar surface, where it was struck by melt ejected from nearby impact craters. Other features possibly present, but not obvious in the photograph, may include vapor-deposited coatings. Such complex surface features tend to build up on individual grains with increasing exposure time at the lunar surface.

these two changes may also have a continuum of variations. In addition, the processes responsible for these changes operate simultaneously and in opposition, so that a grain may reach a steady state balanced between growth and destruction.

The depositional features on grain surfaces are principally coatings or splashes of impact-melted material that may or may not have come from the same grain (Fig. 7.7).

Erosion of exposed lunar soil grains is caused chiefly by two microscopic processes: (1) the removal of surface material at the atomic level (*sputtering*) by the impact of high-energy ions from the solar wind and cosmic rays (see Chapter 3), and (2) the mechanical melting and ejection of material from microcraters (*zap pits*) (Fig. 7.8) produced by the high-velocity impact of cosmic dust particles (see Chapter 4).

7.1.6. Grain-size Characteristics

The grain-size characteristics of any unconsolidated fragmental material are mostly controlled by the mechanical processes responsible for its formation. Because of the unique and complex processes responsible for the formation of the lunar soil, it is

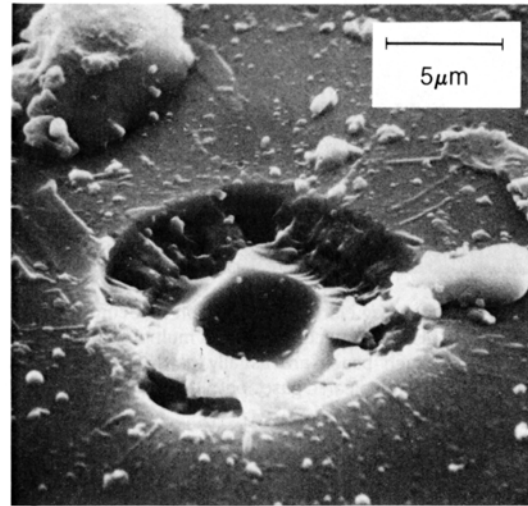


Fig. 7.8. Micrometeoroid impact crater on the surface of a lunar soil particle. This crater consists of a 5- μm -diameter crater (center), surrounded by a 5- μm -wide spall zone. Streamers and droplets of glass (melt) radiate from the crater center. Although material is deposited as shown in Fig. 7.7, competing processes work to remove material from exposed surfaces, including sputter erosion and erosion from micrometeoroid impacts that can remove material by spallation and by melt ejection or vaporization.

TABLE 7.8. The range of mean or median grain sizes for lunar soils.

	Number of Analyses	Medians [*]	Means [†]	References
Apollo 11	13	4.40 ϕ (48 μm) to 3.25 ϕ (105 μm)		<i>Carrier</i> (1973)
Apollo 12	55	4.58 ϕ (42 μm) to 3.40 ϕ (94 μm)		<i>Carrier</i> (1973)
Apollo 14	8	3.74 ϕ (75 μm) to 0.32 ϕ (802 μm)		<i>McKay et al.</i> (1972)
Apollo 15	19	4.3 ϕ (51 μm) to 3.22 ϕ (108 μm)		<i>Carrier</i> (1973)
Apollo 16	14		3.29 ϕ (101 μm) to 1.89 ϕ (268 μm)	<i>Heiken et al.</i> (1973)
Apollo 17	42		4.59 ϕ (41.5 μm) to 2.59 ϕ (166 μm)	<i>McKay et al.</i> (1974)
Luna 16	4	3.8 ϕ (70 μm) to 3.05 ϕ (120 μm) to		<i>Vinogradov</i> (1971)
Luna 20		~3.8 ϕ (70 μm) to 3.62 ϕ (80 μm)		<i>Vinogradov</i> (1973)

^{*} Median, half of the particles are coarser than the median and half are finer; corresponds to the 50% mark on a cumulative curve.

[†] Mean (M_z), the graphic mean is based on three points on a cumulative curve (see *Folk*, 1968).

Phi units (ϕ), grade scale for granular sediment $\phi = -\log_2 \xi$ (ξ equals the diameter in millimeters).

not surprising that the grain-size distributions of lunar soil samples do not match those of terrestrial sediments that have been deposited by wind or water. Nor do lunar soil samples match the expected size distribution for impact-comminuted rock debris.

The process of lunar soil formation is obviously more complicated than simple impact comminution. Although meteoroid and micrometeoroid bombardment reduces lunar rocks and their debris to fine particles, the micrometeoroid bombardment of the soil itself produces, with each impact, small amounts of melt that adhere to nearby soil particles, bonding them together to produce the larger constructional particles called *agglutinates*. At the same time, bombardment by larger meteoroids churns (gardens) the lunar regolith and mixes together different soils produced under many different conditions. Thus, lunar soil grain size is controlled by three principal processes: comminution (which reduces the grain size), agglutination (which increases the grain size), and mixing.

Many comprehensive grain-size analyses of lunar soils have been made at the NASA Johnson Space Center (e.g., *McKay et al.*, 1974). Data from this laboratory have been reported mostly in terms of a few standard parameters (mean grain size, median grain size, sorting, etc.) that were calculated using procedures developed by *Folk and Ward* (1957) for terrestrial sediments. Most lunar soils fit a log-normal grain-size distribution, so that their grain-size-frequency data are plotted on a logarithmic

scale, using a phi scale [$\phi = -\log_2$ (grain size, mm)], in which they approximate a Gaussian distribution. It has also been claimed that they more closely follow a Rosin's size-frequency distribution (*King and Butler*, 1977). However, in either case the approximations using parameters of *Folk and Ward* (1957; described in section 9.1) are still valid.

In general, for a given site, both the grain size of the finest-grained soil collected, as well as the average mean grain size of all soil samples collected, are different from those at any other site. This result appears to be related to the regolith thicknesses at each landing site. Thicker regoliths imply longer exposure ages and longer periods of meteoroid bombardment. The exposure age thus determines how the grain-size distribution will reflect the combined processes of mixing, comminution, and agglutination. This same relation between mean grain size and regolith thickness is also observed in lunar soil samples from a single mission, but which were collected at different locations within one landing site.

Mean grain size and sorting. With no wind or water on the Moon it is difficult to apply grain-size parameters that have been developed on Earth for a full range of clastic sediments (deposited by wind and water). However, some statistical descriptions can be made. The mean grain size of lunar soils ranges from 40 to 800 μm , with most means falling between 45 and 100 μm (Tables 7.8 and A9.1). Using conventional terrestrial descriptions, most lunar

regolith samples would correspond to pebble- or cobble-bearing silty sands (Fig. 7.9). Sorting values (the standard deviation of Folk, 1968) range from 1.99 to 3.73 ϕ ; in other words, the lunar soils are poorly to very poorly sorted. There is also an inverse correlation between mean grain size and sorting (standard deviation); the coarsest samples are the most poorly sorted (Fig. 7.9). Soils from all the Apollo sites are nearly symmetrically to coarsely skewed (skewness = 0 to 0.3).

Exceptions to these generalizations are the green-glass and the dark-mantle deposits sampled at the Apollo 15 and 17 sites, respectively. These pyroclastic deposits are finer-grained (mean grain sizes of 40.0 and 37.9 μm) and better sorted ($\sigma = 1.57$ and 1.69 ϕ), than any of the sampled lunar soils. These deposits have been interpreted as deposits of volcanic ash and are not true impact-produced soils (see section 6.1.7 on lunar pyroclastic deposits). When these glass spheres become mixed into neighboring layers of ordinary lunar soil, their presence significantly lowers the mean grain size of the soil.

Attempts to estimate the grain-size distribution of lunar soils from photographs and electronic images have not been successful. On the basis of a comparison between Surveyor 3 television images, obtained in 1967, and soils sampled nearby during the Apollo 12 mission in 1969, Carrier (1973) determined that accurate estimation of grain-size

distribution from the television images was not possible. Jaffe *et al.* (1968), using the Surveyor images, had predicted that the lunar soil at the Apollo 12 site was composed of particles between 2 and 60 μm in size. In fact, the mean grain size of soils collected from the Apollo 12 site (<1-mm fraction) ranged from 70 to 220 μm . This difficulty of estimating regolith grain size using televised images should be kept in mind when planning future unmanned missions on the lunar surface.

7.1.7. Chemical Composition of Lunar Soils

The chemical compositions of lunar soils reflect their mixed origins. All regolith samples brought back from the Moon contain some components exotic to the collection site. Although Apollo 11 landed in the middle of a mare basalt plain, the soils do not have compositions equivalent to 100% mare basalt. There is chemical evidence for the presence of additional rock and mineral fragments from the anorthositic highlands, rare KREEP-bearing material, and a small meteoroid component.

Certain minerals, including potassium feldspar, apatite, whitlockite, and zircon, are rare in the lunar soil, but they carry the bulk of such important trace elements such as K, the rare earth elements (REE), P, and Zr. The abundance of major elements can be used to indicate roughly the proportions of highland anorthositic (Ca,Al-rich) and mare basaltic (Fe,Ti-rich) rocks that are present in the soil (see section 8.3). The trace elements K, REE, and P can be used to estimate the percentage of KREEPy source rocks in a soil (see section 8.4).

The proportions of different petrologic components in a soil vary with grain size, and therefore the bulk chemical compositions will also vary with grain size. Minerals that were originally present as small crystals in parent rocks may dominate the composition of the finest-grained sizes of a lunar soil, even though they made up only a small percentage of the parent rock.

Multivariate analysis of a large array of chemical elements can provide insights into the variety of rock types represented in any lunar soil. Laul and Papike (1980) chose several common lunar rock types as end-members, and then carried out mixing-model calculations based upon 35-element analyses of lunar soils. The results can be used to interpret the chemical composition of any lunar soil in terms of the principal rock types present in the immediate area, and can provide estimates of the amount and nature of exotic material introduced into the soil from beyond the landing site.

This chemical-statistical approach is especially useful because most lunar soils have abundant fused material, making petrographic identification of

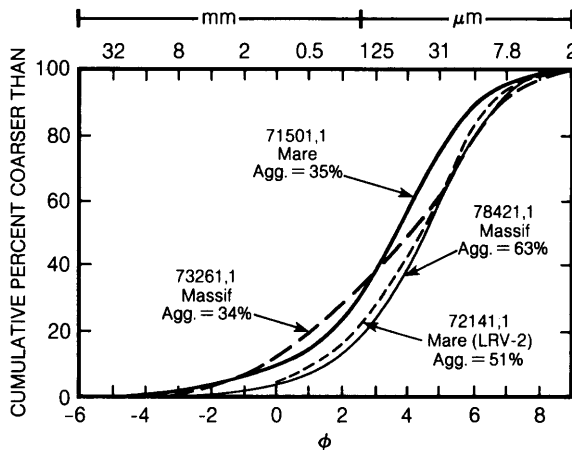


Fig. 7.9. Cumulative size-frequency diagram for typical lunar surface soil samples. Data are shown as cumulative percent by weight greater than a given particle size. Particle sizes are given in both mm and μm and 41 classes (see text for discussion). "Agg" refers to the agglutinate content of individual soil samples.

source rock types difficult. For example, the Apollo 11 soils contain 60% agglutinates and 20% dark-matrix breccias, leaving only a small part of the sample composed of easily identified rock fragments and mineral grains. *Laul and Papike* (1980) determined, from their chemical analyses and mixing calculations, that the source rocks for these soils are (1) high-K mare basalt (10%); (2) low-K mare basalt (62%); (3) anorthosite, norite, and troctolite (ANT rocks) (14%); and (4) low-K KREEP (13%).

Determination of the abundances of K, Rb, Sr, and Ba in nine grain-size fractions of Apollo 17 mare soil 71501 showed that these incompatible elements are systematically enriched in the finer-grained fractions. *Korotev* (1976) and *Haskin and Korotev* (1977) show that this enrichment is produced by the differential comminution of feldspathic and mesostasis portions of the original bedrock. These materials, which carry the bulk of the incompatible elements in the bedrock, are both finer grained and more easily broken than the other bedrock components, which accounts for their preferential incorporation into the finer size fractions. A more quantitative treatment of soil chemistry is provided in Chapter 8.

7.2. SPECTRAL PROPERTIES OF THE LUNAR REGOLITH

Although diagnostic absorption bands are present in the visible and infrared spectra of lunar rocks (sections 6.2 and 6.5) and in their mineral constituents, these bands are subdued in the reflectance spectra from the regolith because of the regolith's high content of dark, absorbing agglutinates. The reflectance spectral properties of mature soils from each of the Apollo sites are shown in Fig. 7.10. In particular, the complex multicomponent agglutinates, which are the products of prolonged exposure to the space environment, are also responsible for the characteristic slope in the spectra, which increases toward longer wavelengths.

Superimposed on this sloping continuum are the weak but diagnostic absorption bands characteristic of the mineral fragments present in the soil. These weak features are seen more clearly in the residual spectra of Fig. 7.10, which are obtained by normalizing to remove the effects of the continuum. The absorption band near 1.0 μm largely reflects the presence of different varieties of the mineral pyroxene (section 5.1.1). Soils with abundant orthopyroxene exhibit a band centered near 0.91 μm , and soils with abundant clinopyroxene exhibit a band centered at longer wavelengths, near 1.0 μm .

The reflectance spectra of immature regoliths, whose agglutinate content is lower, have more prominent absorption features. As the agglutinate

abundance decreases, the spectra of these regoliths become comparable to those of fresh samples of lavas, plutonic rocks, and breccias (sections 6.2 and 6.5). Areas of immature regoliths on the Moon can readily be identified by Earth-based telescopic observations. The special spectral character of these regoliths can be easily seen in the spectra obtained from small areas of the Moon (5–10 km in diameter) shown in Fig. 7.11.

In the blue and ultraviolet wavelengths, the slope of the reflectance spectrum is notably less steep for the darker, more TiO_2 -rich mature mare soils (*Charette et al.*, 1974). This property has been useful for mapping the spatial extent of different mare soil types on the Moon (*Pieters*, 1978).

7.3. REGOLITH EVOLUTION AND MATURITY

The lunar regolith is produced by meteoroid impacts that shatter exposed lunar bedrock, which may consist of a wide variety of rock types—lavas, coarse crystalline rocks, and fragmental breccias (see Chapter 6). When this process begins, the resulting regolith material is both fresh and young. If the newly formed regolith is exposed at the lunar surface, it continues to be progressively modified by micrometeoroid impacts and by high-energy solar and cosmic charged particles. This modification process, described below, is called *maturation*, and regolith exposed to these processes for long periods of time becomes *mature*. If the fresh, young regolith soon becomes deeply buried (e.g., by ejecta from a nearby impact crater), it is not exposed to these surface processes, and it therefore remains fresh or *immature*.

However, such buried regoliths may not remain buried indefinitely. Subsequent impacts may turn the regolith over (gardening) and bring young, buried regolith to the surface. At this point, it again becomes subjected to micrometeoroids and charged particles, and the maturation process continues.

This potential for alternate burial and exposure of lunar regolith gives rise to the concept of *surface exposure age*. This age is defined as the cumulative length of time that a given lunar soil has been exposed at (or near) the surface, as measured by the effects of some alteration process—micrometeoroid impact pits, solar-wind implantation, or the effects of high-energy cosmic rays. The effects of solar-wind, solar-flare, and galactic-cosmic-ray exposure are summarized in Table 7.9.

To estimate surface exposure ages, it is generally assumed that the lunar surface environment has remained constant over the time span in question. Even so, calculations of exposure ages are compli-

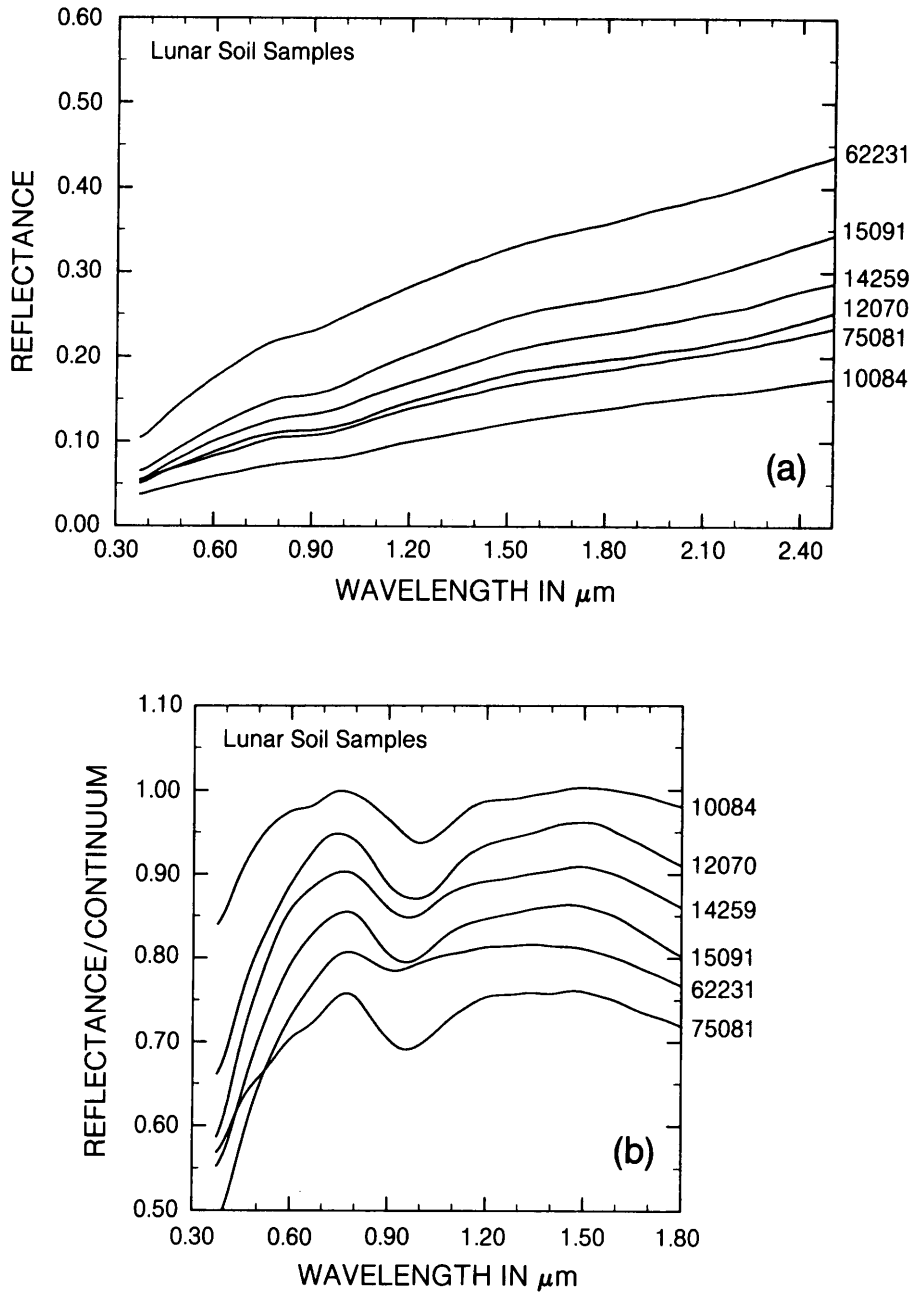


Fig. 7.10. Spectral properties of lunar soils in the ultraviolet and near-infrared, as measured in the laboratory. **(a)** Reflectance spectra, shown as the ratio of total radiant flux reflected by the soil to the total incident on the surface, of lunar soil samples 10084 (mature mare regolith), 12070 (submature mare regolith), 14259 (mature soil developed on breccias), 15091 (mature soil at a highland-mare boundary), 62231 (mature highland soil), and 75081 (submature mare soil). **(b)** Residual absorption features of the spectra in **(a)** after removal of the steeply sloped continuum reflectance.

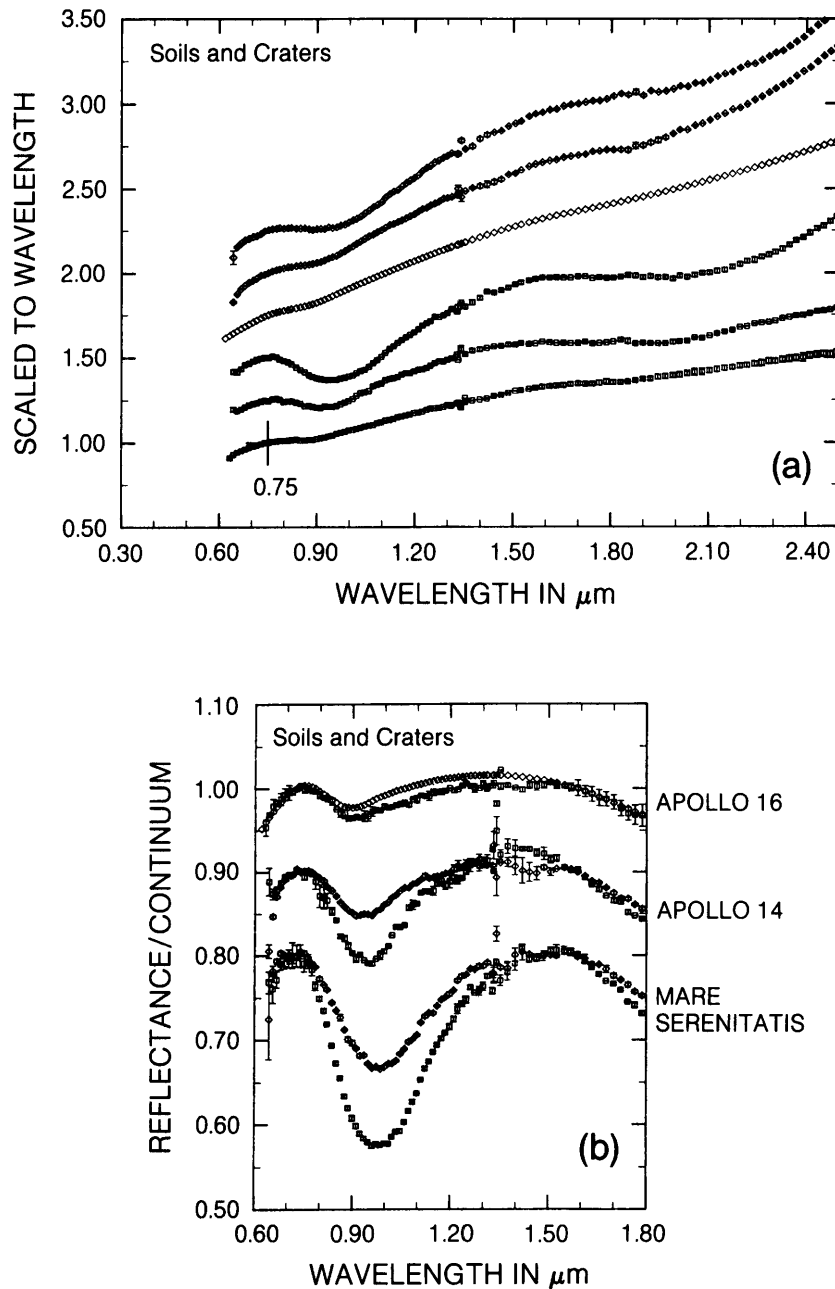


Fig. 7.11. (a) Reflectance spectra of mature and immature lunar soils obtained remotely (using instruments on Earth-based telescopes). The areas measured on the lunar surface are 5–10 km across. All spectra are normalized to unity at 0.75 μm and are offset vertically for comparison. (b) Residual absorption features of the spectra in (a) after removal of the steeply sloped continuum reflectance. Residual absorption curves for mature soils and immature soils (fresh crater ejecta) from the same geologic region are superimposed; absorption features tend to be subdued in the more mature soils. The location of mineral absorption features, e.g., the deep absorption at 0.8–1.0 μm , varies from region to region (e.g., between the Apollo 14 and 16 highland sites), consistent with observed changes in geology and geochemistry. However, when mature and immature soils from the same site are compared, the chief variation is in the intensity of the reflectance rather than in the location of absorption features.

TABLE 7.9. Nuclear particle effects in extraterrestrial materials (from Walker, 1980).

Radiation Source	Energy and Characteristic	
	Penetration Distance	Major Observable Effects
Solar wind	1 keV/amu several hundred angstroms	Direct implantation (e.g., surface-correlated rare gases) Reimplantation of lunar-atmospheric species (e.g., ^{40}Ar excess in lunar soils) Radiation damage (e.g., amorphous layers on lunar dust grains)
Solar flares	<1 MeV/amu to ≥ 100 MeV/amu millimeters to centimeters many more low-energy than high-energy particles	Radionuclide production (e.g., ^{26}Al , ^{53}Mn) Track production (principally tracks produced by slowing down VH nuclei) Electronic defects (e.g., thermoluminescence)
Galactic cosmic rays	≥ 100 MeV/amu typically ~ 3 geV/amu centimeters to meters	Radionuclide production Stable isotope production (e.g., ^{21}Ne , ^{15}N) Nuclear effects due to buildup of nuclear cascades with depth (e.g., N-capture in Gd) Tracks (spallation recoils in addition to slowing down heavy nuclei)

cated by the fact that different alteration processes operate at different depths within the regolith. Micrometeoroid craters (zap pits) and solar-wind-ion implantation occur at the very surface, and regolith particles that show these effects have been exposed to free space. The radioactive transformations produced in the lunar regolith by high-energy solar-flare and cosmic-ray particles develop at depths of a few centimeters to a few meters and indicate exposure near (but not necessarily at) the surface. These complications produce a situation in which the resulting exposure age is depth dependent.

In addition to exposure ages, lunar soils can be distinguished on the basis of different degrees of maturity (usually *immature*, *submature*, and *mature*) by measuring how greatly the soil is altered on average by some particular external process.

This view of the maturation of the lunar regolith is necessarily oversimplified. In fact, regolith formation, surface exposure ages, and observed degree of maturity are inextricably mixed. Nevertheless, a simple perspective, in which maturity and exposure ages are treated separately, is useful for describing

lunar regolith processes, because most regolith was deposited early in the history of the Moon, before ~ 3.5 b.y. ago. At this time, the impact flux was higher, large impacts were more frequent, and exposure times were short because of the high probability of subsequent burial. As meteoroid impacts subsequently became less frequent, the more gradual maturation processes active today became more important in producing and modifying the presently observed regolith.

7.3.1. Maturation by Meteoroid Bombardment

Bombardment by meteoroids, both large and small, produces the most significant changes in lunar soils:

1. Large particles are broken down into smaller ones.
2. Large impacts shock-indurate the regolith, producing coherent regolith breccias.
3. Micrometeoroid impacts produce small amounts of melt at the point of impact; the melt then cements nearby small grains to make agglutinates.

4. Impacts of all sizes may produce vaporized projectile and target material that is dispersed from the impact site and deposited on the exposed surfaces of regolith particles.

5. With moderate to large impacts that form craters more than a few meters in diameter, the ejected regolith material forms a layer that covers up neighboring soils. Such impacts may also excavate previously buried regolith soils, reexposing them to surface processes.

6. Continued bombardment produces a continuous churning of the regolith, thus mixing soils together at random.

7. Large impacts, which penetrate the regolith layer, also eject deep-seated bedrock fragments, often to significant distances, where they form the exotic component of the regolith at that site. These impacts may also generate a sheet of impact melt that covers regolith in and around the crater.

8. Finally, material ejected from a large crater may also produce secondary craters when it lands. These craters produce additional ejecta, and many other effects of the primary impacts, although at decreasing energy levels.

Therefore, meteoroid bombardment controls the maturation of the lunar soil in several different ways. It produces physical and chemical changes in the soil itself—comminution, vapor fractionation, the formation of aggregates (agglutinates and regolith breccias), and the addition of a meteoritic component. In addition, impacts produce other and more widespread changes—breaking up bedrock and adding it to the regolith, mixing together layers of soil that were originally discrete, introducing exotic rock components from distant sites, and turning over or reworking the exposed soil to depths that depend on the meteoroid size-frequency distribution and impact flux rate (see Chapter 4). Meteoroid impact also determines what volumes of the regolith are brought to or near the lunar surface, where they can be affected—and matured—by other processes.

Production of new particles. Meteoroid impacts control the maturation of the regolith by regulating its excavation and exposure to near-surface processes, but they also produce their own maturation effects. Micrometeoroids comminute soil particles, a process that changes the distribution of particle sizes by producing smaller particles and removing larger ones. Therefore, the mean grain size of the <250- μ m soil fraction is an index of maturity; finer-grained soils are more mature.

Meteoroid impacts also produce agglutinates, bits of welded soil fragments, glasses, and mineral and rock fragments (see sections 7.1.3 and 7.1.4). Agglutinate content is one index of soil maturity; higher

agglutinate contents imply more mature soils. This index conflicts to some extent with the previous one because agglutinate formation results from the welding of smaller particles into larger ones, and therefore acts to increase the overall grain size.

Vapor fractionation. The intense and transient shock-wave heating produced by a meteoroid impact has several distinctive effects. Volatile elements are vaporized from the regolith and bedrock targets. Because the gravity of the Moon is low, some of these vaporized elements can escape the Moon's gravitational field. As a result, the lunar soils can become progressively depleted in these elements with increasing maturity.

In addition, volatile elements that do not escape exhibit a measurable mass fractionation of their isotopes, probably produced during this vaporization process. Analyses of O and Si isotopic ratios in lunar rocks and soils indicate that lunar soils are enriched in the isotopes ^{18}O and ^{30}Si relative to the crystalline rocks (*Epstein and Taylor, 1972*). These workers also found that these large enrichments of the heavy isotopes of O and Si in lunar soils are directly related to the amount of solar-wind-derived H present. Successive partial fluorinations of soil grains, a technique that enables the extraction of Si and O from successively deeper layers in the grains, show that the enrichment of ^{18}O and ^{30}Si is essentially *surface-correlated* (i.e., restricted to the grain surface) (*Epstein and Taylor, 1972; Table 7.10*). These measurements also show that this apparent vaporization of the light isotopes, ^{16}O and ^{28}Si (or, conversely, a fractional condensation of the heavy isotopes, ^{18}O and ^{30}Si) is accompanied by a reduction of the bulk O/Si ratio; it is therefore likely that more O than Si escapes during the fractional vaporization process.

The concentrations of other volatile elements (e.g., Zn, Ga, Ge, Cd, Sb, Te, and Hg) in different grain-size fractions of lunar soil samples also show a negative correlation with grain size, indicating that these elements are enriched in the finer fractions. Because the small grains have higher surface-to-volume ratios than do larger ones, these results indicated that these elements have been deposited on grain surfaces (*Krähenbühl et al., 1977; Tables 7.1.1 and 7.1.2*). Calculations by *Boynton et al. (1975)* suggest that, even with the maximum possible introduction of some of these elements into the lunar regolith from meteoroids, there is still an excess of volatile elements on the surfaces of lunar soil grains. Lunar volcanism has been suggested also as the source of this excess (*Boynton et al., 1976a*). (Establishment of a volcanic source for these condensable volatiles would be of special significance in understanding the formation of the volcanic glass spherules that are

TABLE 7.10. Isotopic compositions of oxygen and silicon extracted by successive partial fluorination of Apollo 14 and Apollo 15 lunar samples (*Epstein and Taylor, 1972*).

Sample	Cum. $\mu\text{mole O}_2$ mg original sample	δO^{18}	$\mu\text{mole O}_2$	δSi^{30}	$\mu\text{mole SiF}_4$	Ratio O_2/SiF_4
14298,14 fines (0.772 g)						
a. 30 min/80°C	0.036	+57.7	28	+24.8	28	1.00
b. 60 min/121°C	0.049	+34.9	9.5	+7.65	7.5	1.27
c. 30 min/143°C	0.070	+30.9	16.5	+4.20	39	1.39
d. 30 min/197°C	0.118	+23.8	37			
e. 30 min/209°C	0.177	+15.66	46			
f. 30 min/247°C	0.303	+11.93	<u>97</u>	+1.31	<u>65</u>	<u>1.49</u>
Total			234		170.5	1.37
14422 12 fines (1.265 g)						
a. 20 min/87°C	0.020	+56.6	25	+23.2	25	1.00
b. 60 min/121°C	0.033	+30.0	16.5	+6.51	30	1.48
c. 45 min/146°C	0.055	+26.7	28			
d. 25 min/190°C	0.113	+20.6	73			
e. 25 min/217°C	0.177	+15.40	82	+2.87	55	1.49
f. 30 min/247°C	0.336	+11.29	201	+0.47	154	1.31
g. 30 min/279°C	0.559	+8.24	281		167	1.68
h. 30 min/299°C	0.774	+8.13	277		175	1.58
i. 30 min/345°C	1.097	+7.38	<u>404</u>		<u>258</u>	<u>1.57</u>
Total			1387.5		919	1.51
14148,7 trench fines, top (0.6639 g)						
a. 30 min/77°C	0.035	+51.4	23	+22.3	23	1.00
b. 30 min/120°C	0.049	+27.6	9.5	+5.97	15	1.37
c. 30 min/145°C	0.066	+28.9	11			
d. 30 min/200°C	0.132	+19.8	44			
e. 30 min/247°C	0.341	+11.31	139	+2.62	93	1.49
f. 50 min/266°C	0.645	+8.40	202		138	1.46
g. 30 min/296°C	0.935	+7.01	192		127	1.51
h. 30 min/303°C	1.186	+6.63	<u>167</u>		<u>111</u>	<u>1.50</u>
Total			787.5		536	1.47
14156,4 trench fines, middle (0.6273 g)						
a. 30 min/77°C	0.021	+56.3	13	+26.4	12	1.17
b. 30 min/121°C	0.040	+33.3	12	+8.97	12	1.00
c. 30 min/147°C						
d. 30 min/198°C	0.096	+26.3	<u>35</u>	<u>+4.50</u>	<u>24</u>	<u>1.46</u>
Total			60		48	1.25

TABLE 7.10. (continued)

Sample	Cum. $\mu\text{mole O}_2$ mg original sample	δO^{18}	$\mu\text{mole O}_2$	δSi^{30}	$\mu\text{mole SiF}_4$	Ratio O_2/SiF_4
14149,23 trench fines, bottom (0.7696 g)						
a. 30 min/77°C	0.017	+42.4	13	+20.6	12	1.08
b. 30 min/121°C	0.038	+25.9	16	+8.91	10	1.60
c. 30 min/147°C	0.064	+24.4	20	+6.36	9	2.22
d. 30 min/200°C	0.146	+15.47	63		45	1.4
e. 30 min/247°C	0.326	+10.31	139		96	1.45
f. 50 min/266°C	0.585	+7.79	199		138	1.44
g. 30 min/297°C	0.823	+6.95	183		130	1.41
h. 30 min/303°C	1.046	+6.73	<u>172</u>		<u>114</u>	<u>1.51</u>
Total			805		554	1.45
14321,59 rock breccia (0.963 g)						
a. 30 min/80°C	0.021	+7.81	20	+1.48	11	1.82
b. 30 min/123°C	0.032	+9.12	11			
c. 30 min/156°C	0.042	+8.90	9.5	-0.13	17	1.21
d. 30 min/202°C	0.066	+7.78	<u>23</u>	-1.32	<u>17</u>	<u>1.35</u>
Total			63.5		45	1.41
15021,25 fines (0.8811 g)						
a. 30 min/80°C	0.040	+49.7	35	+24.5	29	1.07
b. 60 min/118°C						
c. 45 min/144°C	0.042	+24.6	20			
d. 25 min/190°C	0.085	+26.0	20	+7.74	24	1.17
e. 25 min/217°C	0.125	+18.64	35	+4.15	23	1.35
f. 30 min/247°C	0.187	+15.16	55	+2.17	40	1.38
g. 30 min/294°C	0.439	+8.33	222	-0.02	166	1.34
h. 30 min/303°C	0.691	+6.32	222	-0.74	168	1.32
i. 30 min/311°C	0.928	+5.28	209	-0.92	129	1.62
j. 30 min/342°C	1.239	+5.07	274	-0.37	175	1.57
k. 30 min/371°C	1.546	+6.25	<u>270</u>	-0.20	<u>141</u>	<u>1.91</u>
Total			1362		895	1.52
15251,24 fines (0.8847 g)						
a. 30 min/67°C	0.020	+51.8	18	+25.4	12	1.50
b. 60 min/119°C	0.037	+37.0	15	+12.9	8	1.88
c. 45 min/144°C	0.052	+35.0	13	+8.87	6	2.17
d. 25 min/190°C	0.094	+26.7	37	+6.24	31	1.19
e. 25 min/216°C	0.144	+18.2	44	+2.66	36	1.22
f. 25 min/259°C	0.270	+12.40	112	+1.04	80	1.40
g. 30 min/291°C	0.527	+8.01	227	-0.06	154	1.50
h. 30 min/303°C	0.729	+6.86	179	-0.24	139	1.32
i. 35 min/319°C	0.931	+6.13	179	-0.41	143	1.28
j. 30 min/343°C	1.241	+5.06	274	-0.33	152	1.83
k. 30 min/369°C	1.552	+5.66	<u>275</u>	-0.10	<u>141</u>	<u>1.98</u>
Total			1373		902	1.52

TABLE 7.11. Weight distribution of grain-size fractions in samples 72501 and 72461 and results for the volatile elements determined by radiochemical procedures (Krähenbühl *et al.*, 1977).

Grain-size Size interval (μm)	Mean (μm)	Weight mg	Cd ppb	Ge ppb	Hg ppb	In ppb	Sb ppb	Te ppb	Zn ppm
72501									
1000-350	540	47.5	28±2	250±25	1.0±0.1	4.1±0.5	1.3±0.3		7.3±0.7
350-149	250	54.8	31±3	665±65	1.9±0.2	2.1±0.3	2.9±0.7		9.8±0.9
149-74	110	51.7	41±3	350±35	1.6±0.2	2.1±0.3	2.8±0.65		12 ±1.1
74-45	60	55.45	37±3	250±25	2.4±0.3	2.0±0.3	2.1±0.5		14 ±1.3
45-30	36	49.2	34±3	280±30	2.5±0.3	2.0±0.3	2.1±0.5		20 ±1.8
30-15	22	33.5	40±3	290±30	4.8±0.5	1.9±0.3	4.1±1		20 ±1.8
15-7	11	34.1	72±6	375±40	6.3±0.7	3.4±0.4	2.9±0.7		33 ±3
7-2*	3	36.5	59±5	435±45	8.3±0.9	4.7±0.5	4.5±1		36 ±3.2
<2*	1.25	6.7	106±8	520±50	22 ±2	6.0±0.7	7.7±2		54 ±5
Mean†	—		42±3	368±40	3.6±0.3	2.8±0.4	2.8±0.7		18.2±1.6
Bulk		82.3	39±3	400±45	3.1±0.3	2.1±0.2	2.5±0.5		17 ±1.5
72461									
1000-350	540	31.4	25±2	235±27	4.5±0.5	4.0±0.5	1.2±0.3	14 ±3	6.0±0.5
350-149	250	45.4	33±3	510±58	1.3±0.1	1.3±0.2	2.0±0.5	14 ±3	8.5±0.7
149-74	110	36.8	35±3	485±55	1.3±0.1	2.0±0.2	1.6±0.4	17 ±3	11.5±1
74-45	60	49.7	53±4	320±37	2.0±0.2	1.9±0.2	1.5±0.4	20 ±4	13 ±1
45-30	36	40.1	43±3	260±30	2.5±0.3	1.8±0.2	1.7±0.5	24 ±5	18 ±2
30-15	22	37.7	34±3	315±36	6.6±0.7	4.3±0.5	2.9±0.7	22 ±4	17 ±2
15-7	11	47.9	49±4	365±42	4.8±0.5	3.1±0.3	1.9±0.4	33 ±7	26 ±2
7-2*	3	17.3	65±5	370±42	7.4±0.7	4.0±0.4	4.0±1.0	42.5±8	35 ±3
<2*	1.25	6.2	130±10	510±58	12.5±1	10.7±1.2	1.5±0.4	101 ±20	54 ±5
Mean†	—		43±3	364±42	3.6±0.4	2.8±0.3	2.0±0.5	24 ±5	16.5±2
Bulk		47.8	44±3	295±34	3.6±0.4	2.0±0.2	4.0±0.8	22 ±4	17.5±2

* Obtained by sedimentation.

† Taking in account weight of fractions.

TABLE 7.12. Estimated percentages of volatile elements contributed to Apollo 16 lunar soils by lunar bedrock, the known flux of extralunar particles (C1 chondrite composition), and "excess" volatiles possibly due to volcanism (mean and standard deviation; Boynton *et al.*, 1976a).

	From Lunar Rocks				Extralunar*				Excess			
	Zn	Ga	Cd	In	Zn	Ga	Cd	In	Zn	Ga	Cd	In
60002	3.3	66.5	2.2	3.2	73.6	11.1	32.7	32.1	23.1	22.4	65.1	64.7
	± 0.2	± 5.5	± 0.4	± 0.5	± 6.9	± 0.2	± 4.5	± 3.4	± 6.9	± 5.2	± 4.8	± 3.8
Stations 1,2,13	3.2	63.9	2.0	2.6	35.1	4.7	15.6	12.2	61.7	31.4	82.4	85.2
	± 0.6	± 2.6	± 0.3	± 0.9	± 6.5	± 1.0	± 5.3	± 2.2	± 6.7	± 2.7	± 5.6	± 3.1
Station 11	5.1	75.8	3.2	9.7	34.1	2.5	16.2	28.8	60.8	21.7	80.6	61.5
	± 1.0	± 0.6	± 0.8	± 1.2	± 16.4	± 0.9	± 8.7	± 11.3	± 17.5	± 0.6	± 9.5	± 12.3

*The extralunar contribution is an upper limit.

found in lunar soils, because we still do not know which gases drove explosive volcanic eruptions on the Moon.)

Impact-produced heating also releases the solar-wind H that has been trapped in the outermost surfaces of lunar soil grains. This release produces an important additional effect. Hydrogen is a strong reducing agent, and it reacts with FeO in the impact melt to form micrometer-sized grains of native Fe metal (see sections 5.4 and 7.1.3). This is the mechanism proposed to produce the amounts of single-domain Fe particles that generate the ferromagnetic resonance observed in lunar soils (*Tsay et al.*, 1971; *Housley et al.*, 1973b). With increasing exposure to micrometeoroids, the amount of single-domain Fe in the soil increases, and so does the ferromagnetic intensity. The ratio of ferromagnetic resonance intensity (I_s) to the total Fe content (expressed as FeO, written as I_s/FeO), is an additional index of soil maturity (*Morris*, 1976).

7.3.2. Maturation by Ionizing Radiation

Ionizing radiation on the Moon comes in the form of atomic particles from the solar wind, solar flares, and extrasolar high-energy cosmic rays. Each source contains a wide variety of atomic particles, mostly protons accompanied by an approximately "cosmic" distribution of heavier atoms. Particles from different sources differ essentially in the magnitude of their energy distribution, which determines their depth of penetration into lunar materials. In addition to penetrating into lunar surface particles, the charged extralunar particles can ionize atoms of gas in the tenuous lunar atmosphere. The gas ions can then be accelerated by magnetic fields associated with the solar wind and implanted onto regolith grains (*Manka and Michel*, 1971). Table 7.9 (after *Walker*, 1980) summarizes the effects of ionizing radiation on lunar materials. A more detailed discussion of ionizing radiation can be found in section 3.11.

Solar wind. Solar-wind particles, which have an average energy of 1 keV/amu, penetrate to about 150 nm (0.15 μm) in lunar materials. The particles interact with the atoms in the target grains to create an amorphous outer layer in dielectric crystals, especially in grains of lunar plagioclase (Fig. 7.12; *Dran et al.*, 1970). These trapped solar-wind elements gradually accumulate in exposed grains. It is estimated that a saturation value for such trapped elements, balanced between implantation and loss by sputtering, is reached in approximately 100 yr (*Borg et al.*, 1980). The accumulation of solar-wind H is especially important because it enables the subsequent chemical reduction of FeO in lunar materials involved in micrometeoroid impacts. The

accumulation of solar-wind elements, especially H, He, and other noble gases, is a measurable parameter of surface maturity, and more mature soils have higher contents of these elements.

A second effect of the solar wind is destructive; the ions act to sputter off the outer micrometer or so of exposed lunar soil particles (cf. section 7.1.5). This effect is most significant and easily observed on micrometer-sized particles, which are usually rounded in lunar soils.

Solar flares. Solar-flare particles, with energies from 10^4 to 10^8 eV/amu, penetrate on the order of a few millimeters to several centimeters into lunar rocks and soil particles. Their flux is much lower than that of solar-wind particles, and their accumulation is negligible by comparison. Being more energetic, however, heavy solar-wind particles (atomic number, $Z > 20$) form trails of ionization damage in dielectric materials (crystals and glass). These damage trails can be etched into visible tracks (*particle tracks*) with suitable reagents (Fig. 7.12; *Fleischer et al.*, 1975). The density of the tracks provides an indicator of the exposure age of the sample, i.e., the length of time that it resided within a few centimeters of the surface. The track length can be used to estimate the composition (atomic number, Z) of the particles that produced them.

Cosmic rays. Cosmic-ray protons and neutrons are sufficiently energetic (>1 GeV/amu) that they penetrate into lunar materials to depths of about 1 m. These particles produce nuclear reactions, and the products of these reactions can be used to measure the incoming flux, the exposure age of the sample, and the depth of the sample in the regolith. In the laboratory, stable products, such as spallogenic noble gas isotopes and neutron-induced isotopes of Gd and Sm, can be measured by mass spectrometry. Radioactive products, such as the isotopes ^{26}Al and ^{53}Mn , can be measured by sensitive detectors. The cosmic-ray production curves for spallogenic isotopes as a function of penetration depth have been calculated by *Reedy and Arnold* (1972) and *Hohenberg et al.* (1978); the production curves for neutron-induced isotopes, with depth, have been calculated by *Lingenfelter et al.* (1972). If these cosmogenic isotopic profiles can be measured in the lunar regolith, then the experimentally-determined profiles can be used to calculate surface exposure ages from the measured production profiles. This approach is valid, however, only when the thickness of the regolith layer is at least a significant fraction of a meter.

Both solar flares and cosmic rays produce particle tracks in lunar soil grains. At depths of less than about 1 cm the lower-energy solar-flare particles dominate track production because the low-energy

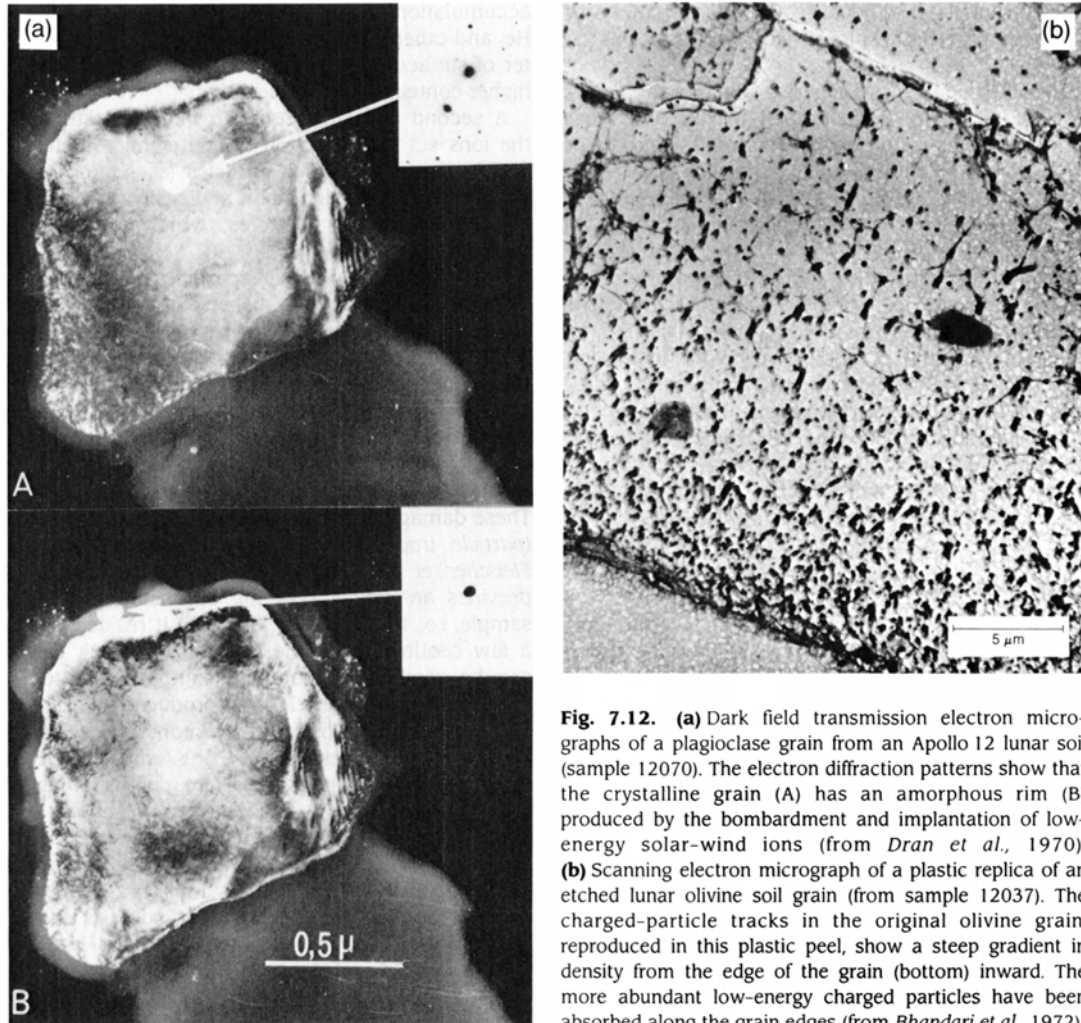


Fig. 7.12. (a) Dark field transmission electron micrographs of a plagioclase grain from an Apollo 12 lunar soil (sample 12070). The electron diffraction patterns show that the crystalline grain (A) has an amorphous rim (B) produced by the bombardment and implantation of low-energy solar-wind ions (from *Dran et al.*, 1970). (b) Scanning electron micrograph of a plastic replica of an etched lunar olivine soil grain (from sample 12037). The charged-particle tracks in the original olivine grain, reproduced in this plastic peel, show a steep gradient in density from the edge of the grain (bottom) inward. The more abundant low-energy charged particles have been absorbed along the grain edges (from *Bhandari et al.*, 1972).

cosmic-ray particles that would be stopped at these depths have been already modulated out of the solar system by solar magnetic fields. The production of particle tracks in lunar materials as a function of depth has been measured by a number of groups; results are shown in Fig. 7.13. The track production rates follow a negative power law that depends on depth, so that the production rate for tracks drops off rapidly with increasing depth. The quality of these measurements is reviewed by *Zinner* (1980), who concluded that the production curve of *Blanford et al.* (1975) (64455 in Fig. 7.13) is probably within a factor of 2 of the recent long-term flux.

Particle-track densities in individual grains can be used to measure the exposure age of the sample in which they are found. If a soil sample has a significant fraction of fresh grains, then these grains will have the minimum track density possible for any of the soil grains from the sample. If the depth at which the sample was collected can be determined or estimated, this measured minimum-track density can be used to calculate a maximum exposure age for the sample (*Crozaz et al.*, 1970). Lunar soil grains exposed within millimeters of the surface, i.e., to solar-flare particles, accumulate particle tracks rapidly, and in only 10^3 to 10^4 yr have track densities

in excess of $10^9/\text{cm}^2$. In sharp contrast, soil grains exposed deeper than about 1 cm (i.e., only to cosmic rays), will rarely have track densities in excess of $10^8/\text{cm}^2$. Consequently, mature soils or mature soil components, which have been exposed for longer periods of time and whose upper parts are relatively well-mixed, will have large numbers of grains with track densities $>10^9/\text{cm}^2$, while immature and submature soils or soil components will have large numbers of grains with track densities below $10^8/$

cm^2 . The percentage of soil grains with track densities greater than $10^9/\text{cm}^2$ is called the *track maturity index*, and it increases as the maturity of the soil increases.

7.3.3. Maturity Indices and Their Use

The physical processes caused by exposure of lunar regolith at or near the lunar surface (section 7.3.2) have been used to define a number of maturity indices: I_s/FeO , mean grain size, the

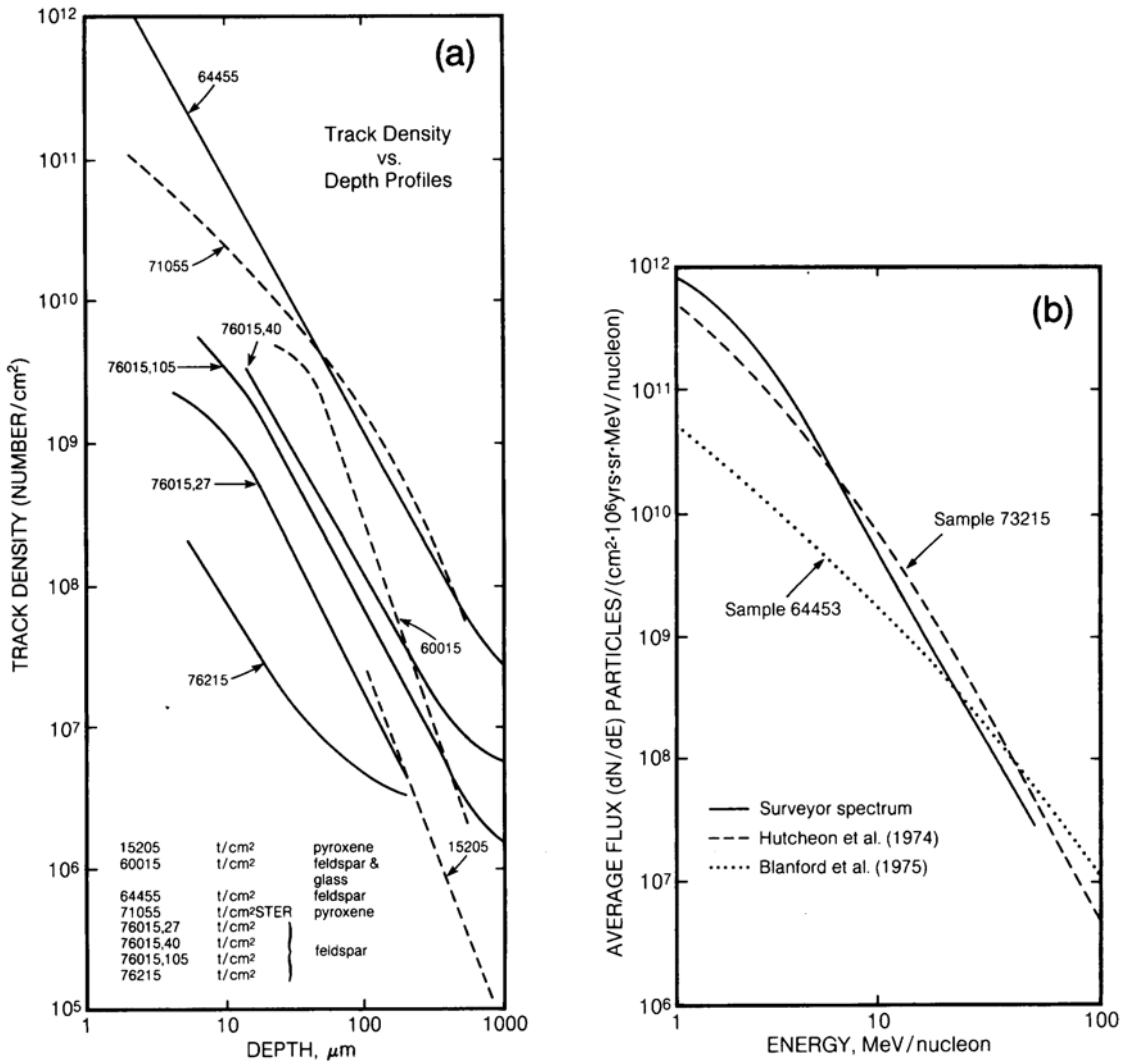


Fig. 7.13. (a) Profiles of solar-flare track densities as a function of depth, measured in single mineral and glass grains from several soil samples (Zinner, 1980). Track densities are given either as t/cm^2 or as $t/\text{cm}^2\text{-steradian}$, as indicated in the figure, depending on the original orientation of the soil grain. Different line types are only for clarity. **(b)** Energy-flux spectra for Fe-group solar flare particles, measured over 2.6 yr between 1967 and 1969 (Surveyor lunar lander spectrum) and from lunar rocks 64455 and 73215 (from Zinner, 1980).

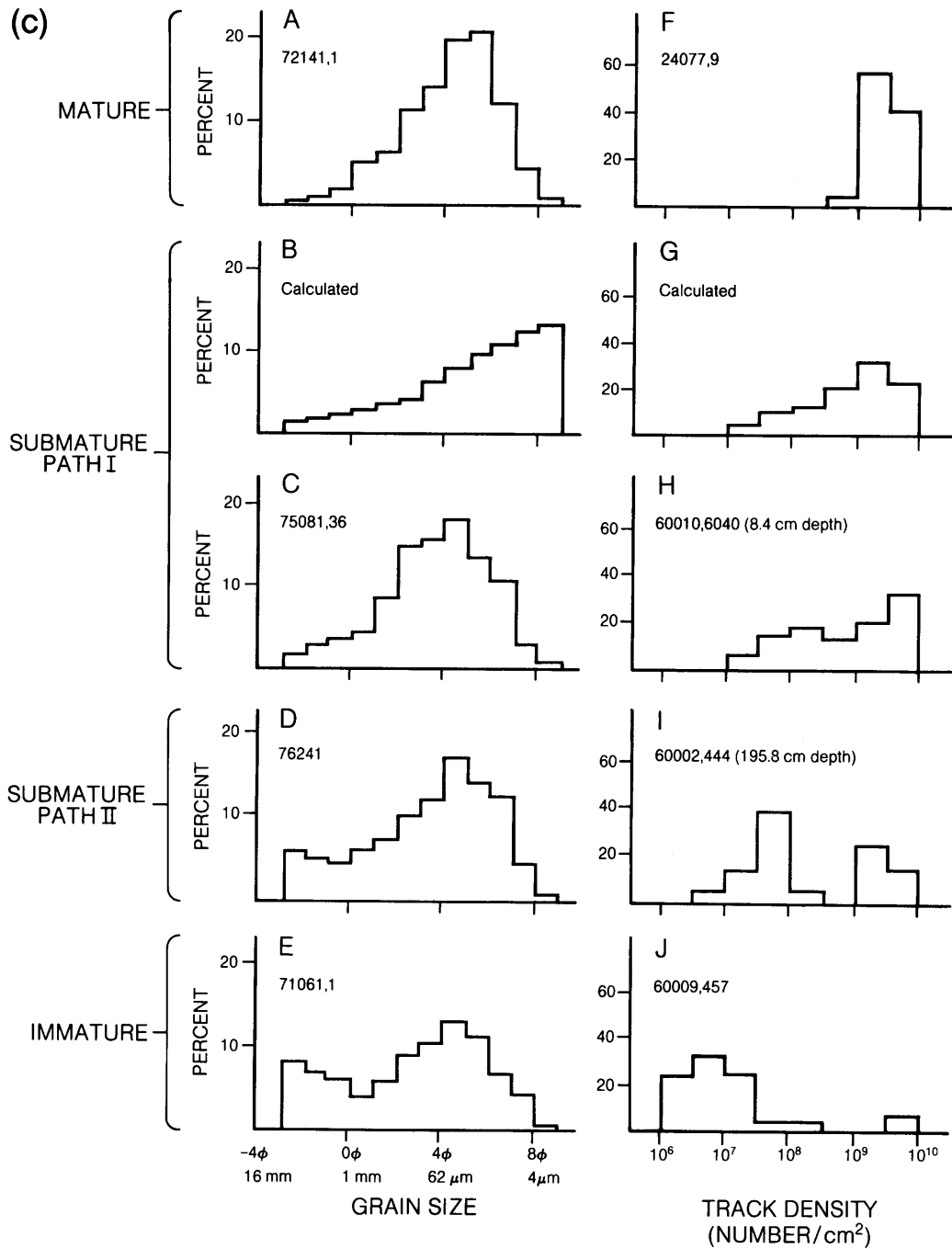


Fig. 7.13. (continued) **(c)** Histograms showing frequency distributions of grain sizes and track densities for lunar soils that show a range of maturities. Ordinates in percent. *Mature* soils (A and F) show a concentration of grain sizes and track densities into single peaks (Blanford *et al.*, 1979), while *immature* soils (E and J) show a wider, bimodal distribution. Two types of *submature* soils can be distinguished: those matured in place (path I; C and H), which show a single broad distribution, and those matured by mixing (path II; D and I) (McKay *et al.*, 1974), which show a bimodal distribution. Calculated distributions for submature path I soils (B and G) are from Shoemaker (1971) and Duraud *et al.* (1975).

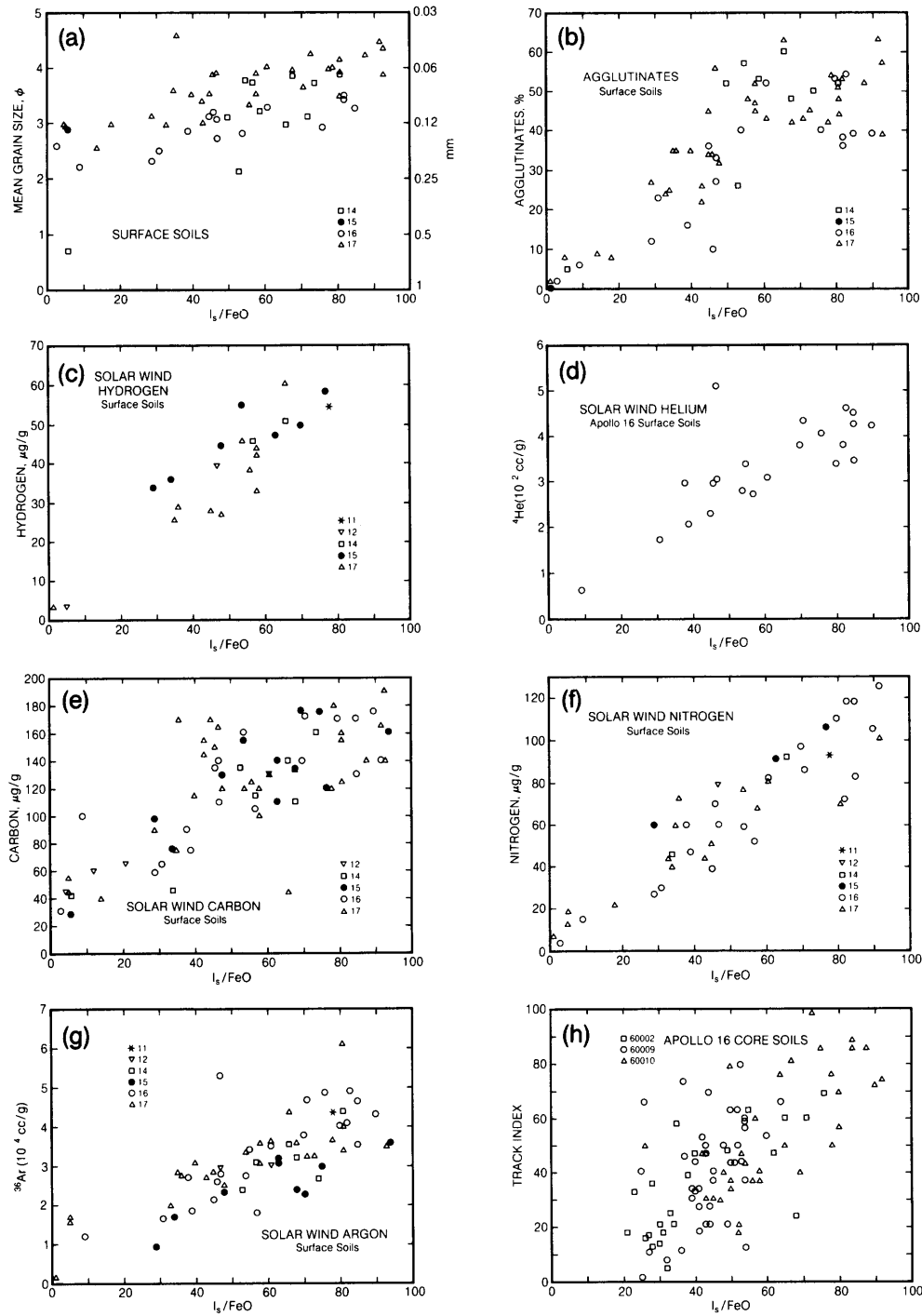


Fig. 7.14. Diagrams showing correlations between I_s/FeO and other maturity indices in lunar surface soils and core soil samples. **(a)** Mean grain size, in ϕ and mm; **(b)** percentages of petrographic agglutinates. Several solar-wind elements, including **(c)** H, **(d)** He, **(e)** C, **(f)** N, **(g)** Ar; and **(h)** the percentage of grains with track densities $>10^9/cm^2$. Data are from Morris (1976), except for **(c)** from E. K. Gibson (personal communication, 1985) and **(h)** from Morris and Gose (1976) and Blanford *et al.* (1979). Numbers for different symbols indicate different Apollo missions.

TABLE 7.13. Concentrations of metallic iron (in equivalent wt.%) contributed by three metal particle diameter ranges for 79 lunar soils (from *Morris*, 1980).

Soil	FeO (wt.%)	I _s /FeO (arb.) <250 μm	Equivalent wt.% Fe ⁰			Soil	FeO (wt.%)	I _s /FeO (arb.) <250 μm	Equivalent wt.% Fe ⁰		
			Fe _A ⁰	Fe _B ⁰	Fe _C ⁰				Fe _A ⁰	Fe _B ⁰	Fe _C ⁰
10084,853	15.8	78.0	0.34	0.61	0.81	67960,30	4.6	20.0	0.030	0.069	0.13
12001,7	16.8	56.0	0.28	0.47	0.67	69921,11	5.6	90.0	0.19	0.43	0.65
12003,11	15.4	57.0	0.22	0.37	0.55	70251,1	16.6	43.0	0.22	0.39	0.61
12024,46	14.6	30.0	0.14	0.27	0.49	70271,4	16.2	56.0	0.28	0.47	0.71
12030,122	14.3	14.0	0.072	0.11	0.31	70311,3	17.5	39.0	0.21	0.36	0.68
12033,45	14.2	4.6	0.022	0.13	0.27	71131,8	18.2	33.0	0.20	0.34	0.68
12037,23	17.3	21.0	0.13	0.22	0.34	71151,2	18.0	34.0	0.20	0.34	0.59
12042,24	16.8	61.0	0.32	0.54	0.69	71501,18	18.3	35.0	0.21	0.39	0.60
12044,12	15.7	57.0	0.27	0.45	0.69	72131,4	17.2	60.0	0.29	0.51	0.72
12070,104	16.5	47.0	0.24	0.40	0.64	72701,24	8.8	61.0	0.20	0.33	0.59
15041,34	14.3	94.0	0.41	0.61	0.78	72161,61	14.9	87.0	0.41	0.66	0.83
15071,19	16.4	52.0	0.27	0.40	0.54	72221,2	9.6	58.0	0.18	0.28	0.58
15091,34	11.6	74.0	0.28	0.42	0.57	72241,2	9.1	64.0	0.18	0.29	0.47
15101,179	11.6	70.0	0.27	0.40	0.61	72261,5	9.6	59.0	0.20	0.34	0.50
15211,56	11.8	54.0	0.25	0.37	0.56	72431,1	9.8	63.0	0.21	0.33	0.53
15221,36	11.5	63.0	0.25	0.38	0.55	73131,2	6.8	16.0	0.044	0.090	0.23
15231,51	11.6	71.0	0.27	0.40	0.51	73151,4	9.3	68.0	0.21	0.32	0.58
15251,56	12.0	75.0	0.27	0.40	0.60	73211,1	9.4	39.0	0.13	0.21	0.38
15271,115	12.2	63.0	0.29	0.43	0.54	74111,1	10.2	31.0	0.11	0.19	0.47
15301,120	14.0	53.0	0.24	0.36	0.62	74220	22.0	1.0	0.013	0.043	0.07
15401,14	16.6	5.6	0.044	0.083	0.18	76031,4	11.7	64.0	0.23	0.36	0.55
15431,17	11.9	39.0	0.14	0.23	0.35	76121,10	15.2	71.0	0.33	0.54	0.75
15471,18	16.4	34.0	0.21	0.33	0.47	76131,4	12.3	70.0	0.24	0.35	0.57
15501,41	16.6	51.0	0.28	0.45	0.58	76221,7	10.9	66.0	0.22	0.37	0.53
15531,48	20.2	27.0	0.16	0.27	0.31	77511,4	12.3	80.0	0.31	0.50	0.73
15601,103	19.2	29.0	0.21	0.34	0.44	78121,3	14.2	68.0	0.30	0.51	0.69
60601,9	5.5	85.0	0.14	0.27	0.57	78221,7	11.7	93.0	0.32	0.53	0.76
61141,57	5.3	56.0	0.096	0.18	0.66	78231,4	13.1	81.0	0.35	0.59	0.76
61121,12	4.9	9.2	0.018	0.059	0.29	78441,45	12.4	77.0	0.30	0.51	0.77
61241,14	5.4	47.0	0.087	0.20	0.45	78481,61	13.1	82.0	0.32	0.56	0.87
61501,103	5.6	53.0	0.10	0.20	0.60	79121,10	16.5	57.0	0.32	0.56	0.80
62231,3	5.1	91.0	0.16	0.29	0.58	79241,30	15.6	51.0	0.26	0.45	0.63
64501,11	5.2	61.0	0.10	0.18	0.50	79511,55	15.3	61.0	0.28	0.49	0.73
64801,35	5.2	71.0	0.15	0.28	0.56	24077,7	19.9	39.0	0.20	0.32	0.51
64811,84	5.6	54.0	0.11	0.23	0.58	24109,14	20.6	31.0	0.18	0.29	0.46
65701,8	5.7	106.0	0.21	0.39	0.73	24149,16	20.3	21.0	0.11	0.20	0.33
65901,104	5.8	99.0	0.18	0.33	0.71	24174,17	20.9	27.0	0.11	0.19	0.37
66031,8	5.5	102.0	0.17	0.32	0.65	24182,12	20.2	19.0	0.077	0.14	0.30
67461,103	4.3	25.0	0.037	0.065	0.13	24210,10	21.1	19.0	0.15	0.19	0.33
67511,11	4.2	8.8	0.012	0.024	0.076			Average	0.20	0.33	0.54
								Std. Dev.	0.10	0.15	0.18

The values of FeO and I_s/FeO were obtained from *Morris* (1978b). I_s/FeO was measured for the <250-μm size fraction. Diameter range of metallic iron particles: Fe_A⁰ = 40-330 Å; Fe_B⁰ = 40 - >330 Å; Fe_C⁰ = ~20 - >1000 Å.

percentage of grains with high track densities (>10⁹/cm²), agglutinate content, content of solar-wind elements, depletion of volatiles, and the presence and degree of isotopic mass fractionation.

Many of the maturity indices are of limited value for estimating soil maturity because, after a period of initial increase, they tend to saturate and become constant with time. For example, mean grain size will reach some equilibrium value as comminution

is balanced by agglutinate formation. Similarly, the concentration of implanted solar-wind elements tends toward a saturation level at which implantation of new atoms is balanced by the removal of the particle surface—and the solar-wind atoms it contains—by sputtering.

However, the value of I_s/FeO appears to increase steadily with increasing maturity and shows no tendency to saturate with time (*Morris*, 1976).

Consequently, I_s/FeO has become widely used to establish a soil's maturity level, and the quantity has been measured for every lunar soil. These data are catalogued in the *Handbook of Lunar Soils* (Morris *et al.*, 1983).

Figure 7.14 shows typical correlation plots of I_s/FeO with other maturity indices; Table 7.13 gives numerical I_s/FeO values for a set of lunar soils. There is considerable scatter in these plots, indicating that determination of the maturity level of a soil should be based on more than one maturity index. For example, *McKay et al.* (1974) have effectively used grain size, sorting, and agglutinate content to define immature, submature, and mature soil groups at the Apollo 17 site (Fig. 7.15).

7.3.4. Regolith Processes and Maturity

Regolith turnover by meteoroid impacts does not simply take a volume of lunar soil with a given maturity and then expose or bury it; impacts also mix discrete volumes of soil together. This soil mixing is a complex process, but most measures of soil maturity make no distinction between soils

matured *in situ* (i.e., which underwent very small-scale mixing) and those subjected to large-scale mixing. However, if soil mixing is sufficiently gross, and the mixed components have sufficiently different levels of maturity, then grain-size and track-density frequency distributions can demonstrate that a soil has been mixed. Submature soils can thus be distinguished on the basis of whether they matured by small-scale or large-scale mixing.

McKay et al. (1974) designated the two processes for producing submature soils as path I (matured *in situ* with only small-scale mixing) and path II (matured with large-scale mixing).

7.4. VARIATION OF SOILS WITH DEPTH: THE LUNAR CORE SAMPLES

7.4.1. General Characteristics of Lunar Regolith Core Samples

Core samples of the lunar regolith have provided the most dependable information about the evolution of the regolith and about its textural and structural complexities. Identification of individual soil layers within the core samples has been based mostly on discrete changes in grain size and particle proportions from layer to layer. Depths of regolith sampled by coring range from 10 cm (Apollo 11) to 298.6 cm (Apollo 17). At the time of this writing, about 85% of the cores have been studied. (See sections 2.2 and A2.1 for a description of cores and drive tubes.)

Core studies (and some observations of shallow trenches dug by Surveyor spacecraft and later by astronauts) indicate that the lunar regolith is made up of discrete layers of material ejected from both large and small impact craters. Within a single layer, the observed grain size is related to the depth of catering in the excavated material, and the duration of subsequent exposure to micrometeoroid bombardment at the lunar surface. With a high percentage of bedrock in the ejecta layer, the material is coarsest grained; conversely, the finest-grained regoliths have a smaller bedrock component. The relationship between grain size and regolith thickness—that thicker regoliths have generally finer grain sizes—has been well-documented by *McKay et al.* (1980).

Throughout a section of multilayered regolith, however, the grain size varies randomly from layer to layer. Exposure to micrometeoroid bombardment at the lunar surface further comminutes fragments in the regolith, but also builds up an increasing volume of agglutinates with time. Eventually, a

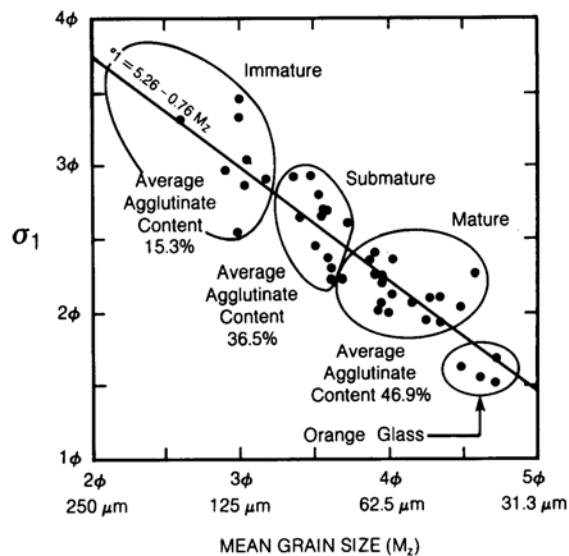


Fig. 7.15. Diagram showing the relationship between grain size, sorting, and agglutinate content for 42 Apollo 17 soils (*McKay et al.*, 1974). Mean grain size (M_z , abscissa) is shown in both millimeter and ϕ scales; smaller grain sizes are to the right. Sorting (ordinate) is expressed as the inclusive graphic standard deviation σ_1 , in ϕ . Better-sorted soils are toward the bottom. The diagram shows that increasingly mature soils become progressively finer-grained, better-sorted, and composed of a greater proportion of agglutinates.

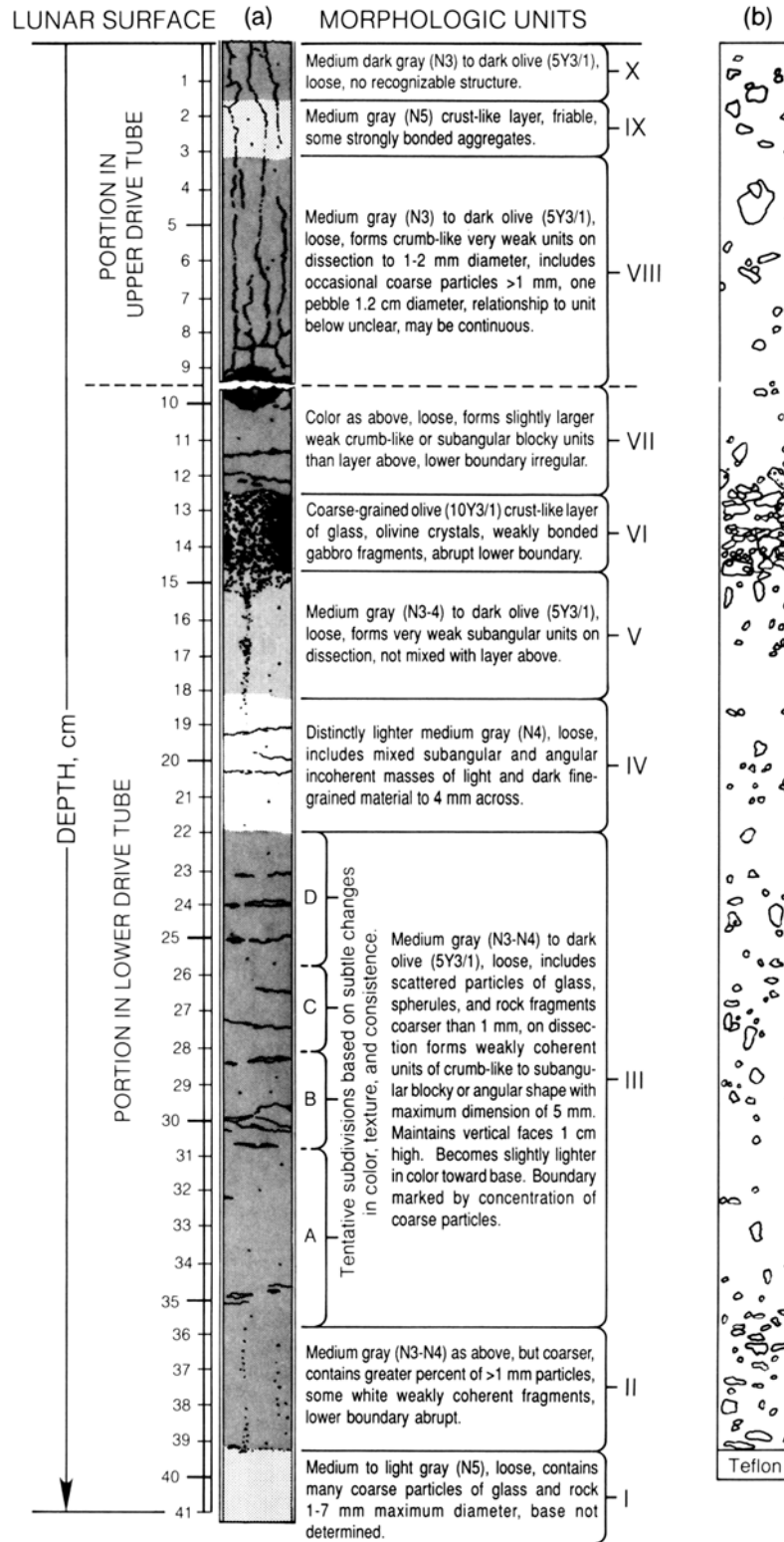


Fig. 7.16. Drawing of the Apollo 12 double drive-tube core (samples 12025-12028). **(a)** Within the core, 10 discrete layers have been identified, mostly on the basis of sharp changes in grain size and grading between adjacent layers (stratigraphic diagram by R. Fryxell; *Fryxell and Heiken*, 1974). Color designations are according to the Munsell standard. **(b)** Location of coarser lithic fragments.

steady-state grain size develops as the agglutinate content increases and balances comminution (Morris, 1976; Fig. 7.14a,b).

In studying the core samples, similar grain-size measurement techniques have been used, but different workers have preferred to use slightly different statistical parameters to describe and compare the grain sizes of individual layers. Some investigators have preferred to designate the average grain size by the *median* (half the particles by weight are coarser than the median sizes, and half are finer). Others have used the *mean*, a quantity calculated or determined graphically by measuring the percentage of particles corresponding to three points on a cumulative size-frequency curve, summing the weights at 16%, 50%, and 84% and dividing by three (Folk, 1968). These parameters are discussed in more detail in section 9.1.1.

The first cores from lunar regolith were collected at the Apollo 11 site, using hollow drive tubes that were hammered into the soil. These drive tubes were short (about 30 cm) and the incomplete sections they secured gave little indication of the textural complexity that is characteristic of the regolith sampled more deeply at other Apollo and Luna landing sites. A double drive-tube core sample (sample 12025/12028), collected at the Apollo 12 site on the rim of a 10-m-diameter crater, provided the first evidence that lunar regolith is layered. This 42-cm regolith sample is composed of ten discrete layers; the median grain sizes of the soils from the individual layers range from 61 μm to 595 μm (Fig. 7.16).

A more complete view of the textural characteristics of the regolith, layer by layer, has been obtained from analyses of regoliths sampled by drilling at the Apollo 15, 16, and 17 sites. The 236-cm-deep section sampled by a core drill at the Apollo 15 site (no. 15001-15006) consists of 42 distinct textural units, with median grain sizes from 44 μm to 89 μm ; all the layers are poorly sorted (Heiken *et al.*, 1973, 1976). Most of the samples from these layers form a tight grouping around a median grain size of 50 μm .

At the same Apollo 15 landing site, a shorter drive tube, inserted only 20 m from the edge of Hadley Rille, penetrated the upper 60 cm of a 1-m-thick immature regolith (lunar core sample 15010/11; McKay *et al.*, 1980). Because of this sample's close proximity to bedrock, together with the process of continuous mass wasting of regolith material into the rille, the regolith at this location is coarser grained than regolith samples collected elsewhere; it has an average mean grain size (average of several samples) of 85 μm (Fig. 7.17) (McKay *et al.*, 1980 used mean rather than median grain size).

At the Apollo 16 site on the Cayley Plains, a 221-cm-thick section of highland regolith was sampled by drilling (Allton and Waltz, 1980). In this core, three major subdivisions were recognized by Meyer and McCallister (1977) and 46 textural units by Duke and Nagle (1974). Only samples from the individual layers in the upper 20 cm of the core have been sieved; median grain sizes for the <1-mm fraction range from 56 to 72 μm , and all are poorly sorted. A systematic study of changes in grain size with depth (to 65 cm) was made by McKay *et al.* (1977) for another Apollo 16 sample, core 60009/60010. In this core, there is a general increase in mean grain size with depth, with the exception of a layer at the bottom of the core, from 85 μm at the surface to 200 μm at a depth of 55 cm (Fig. 7.18). The upper 12 cm of the core shows the highest degree of *in situ* maturation and reworking, and it is the finest-grained unit sampled in this regolith section.

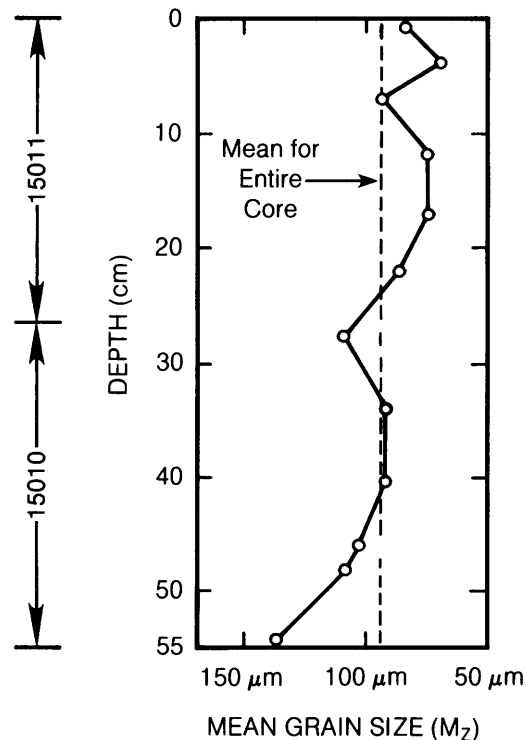


Fig. 7.17. Plot of data from the Apollo 15 drive-tube core 15010/11, showing sample locations and mean grain sizes for individual samples. This core was collected close to the rim of Hadley Rille, where regolith is thin and immature, as indicated by the relatively large mean grain size (about 100 μm) for all portions of the core.

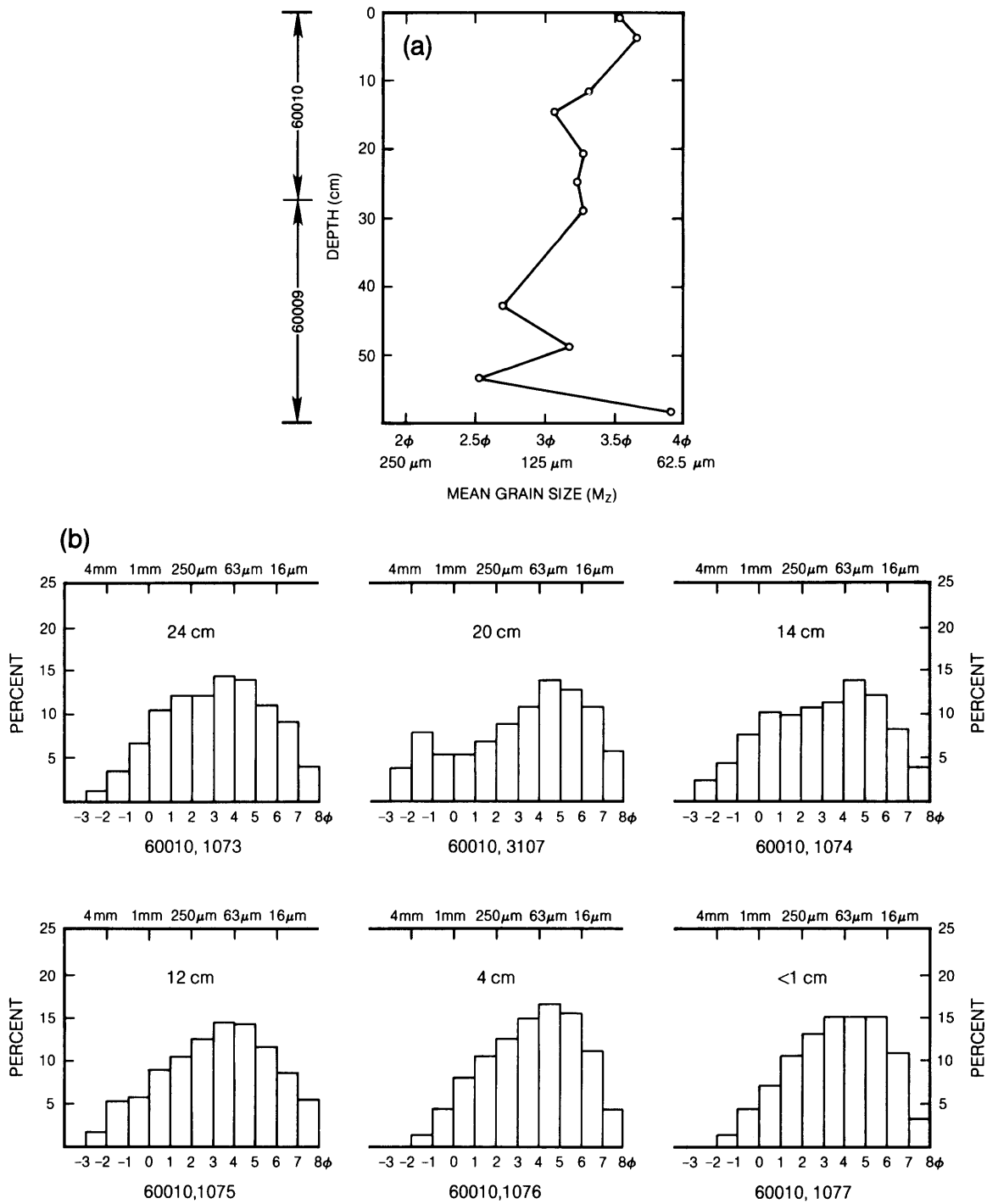


Fig. 7.18. Variation with depth of grain size characteristics of lunar soil samples from the Apollo 16 core 60009/10. **(a)** Variation in mean grain size as a function of depth in the core. **(b)** Histograms of grain-size distribution for six soil samples (depths given in centimeters) from core 60010 **(a)**. The samples show a gradual increase in mean grain size with increasing depth, except at the bottom of the core, where a new layer may have been penetrated. The upper core layers tend to be finer-grained and slightly better sorted than the lower ones.

The showpiece of regolith core samples was collected by deep drilling at the Apollo 17 site. Sampling a total regolith thickness of 284 cm, drill core 70009–70002 was collected between two 650-m-diameter craters. *Vaniman et al.* (1979) identified five stratigraphic units, and *Taylor et al.* (1979) identified eight stratigraphic units in this core, based upon textural (grain size) and petrographic differences. Detailed grain-size analyses of the individual depositional units have not been completed; however, maturity indices such as I_s/FeO (*Morris et al.*, 1979) and core descriptions indicate that a wide range of grain size and sorting is present from layer to layer (*Duke and Nagle*, 1974).

A unique core sample (sample no. 74001/2) was collected on the rim of an impact crater (Shorty Crater) at the Apollo 17 site; it sampled not a true lunar soil, but a deposit of volcanic ash (the “orange and black soils”) in the overturned rim flap of the impact crater. This deposit has a mean grain size of 40 μm . Variations of grain size (Fig. 7.19; *McKay et al.*, 1977) and sorting appear to have been controlled by eruption processes and do not reflect comminution by meteoroid impact processes after the material was deposited.

In a study of the Luna 24 regolith sample from Mare Crisium, *McKay et al.* (1978b) determined that the individual layers are composed of mixtures of

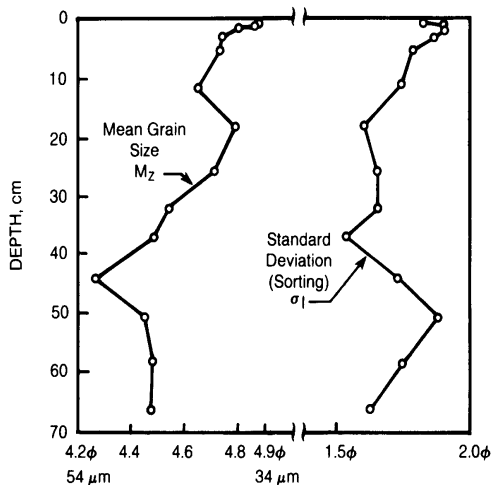


Fig. 7.19. Variations of mean grain size (M_z) and sorting (σ_1) within Apollo 17 core 74001/2, the orange “soil” from the rim of Shorty Crater. The deposit is not a lunar soil, but a pyroclastic (volcanic ash) deposit, and the grain size and sorting reflect eruption processes rather than maturation processes within a lunar soil (*McKay et al.*, 1974).

coarse-grained, immature components, together with finer-grained, more mature components. The grain-size distributions are thus bimodal, with peaks at 1 mm and 100 μm (Fig. 7.20). Within the regolith sampled, there appears to be a general decrease in mean grain size with depth, from 139 μm at the surface to 72 μm at an approximate depth (distance along the core tube) of 200 cm. This result is the reverse of the trend observed in the Apollo 16 core samples.

In summary, the analysis of regolith core samples has shown that regolith properties vary in a complex and not entirely predictable way with depth. A trend to coarser-grained samples with depth is present in some of the cores (e.g., Apollo 16), but there are exceptions (e.g., Luna 24).

7.4.2. Variations with Depth in Regolith Core Samples

Drilling of the Earth has often supplied the valuable third dimension needed to interpret its history and structural complexity. Even though the mechanism (meteoroid impact) that produces most of the layered deposits on the Moon is not a major process on Earth, core samples of the lunar regolith have the same potential to provide a chronology of the depositional and erosional events that have been responsible for the Moon’s formation.

Cores have been retrieved from seven landing sites on the Moon; the deepest core reached a depth of 298.6 cm. Not all of these cores have yet been studied (Table 7.14), but most have been examined for variations in physical, chemical, and geologic properties with depth. These variations have been used to identify discrete layers (strata) and to infer maturation rates.

Unfortunately, despite the detailed study of the Apollo cores, it has not been possible to identify any single layer as ejecta from a known impact crater at the landing site. A tenuous correlation has been made at the Apollo 17 site between Camelot Crater and a coarse-grained, immature layer in the drill core.

Study of the lunar cores has confirmed that our general understanding of cratering mechanics and regolith formation seems to be correct. However, we still do not completely understand the interconnections of different stratigraphic features, such as grain size, sorting, the presence or absence of graded bedding, and the identification of former surface horizons.

A wide range of stratigraphic data have been measured in the cores: visual color and texture, bulk chemistry, petrography, various maturity indices (section 7.3), the amounts of cosmogenic nuclides and particle tracks (which can be related to exposure

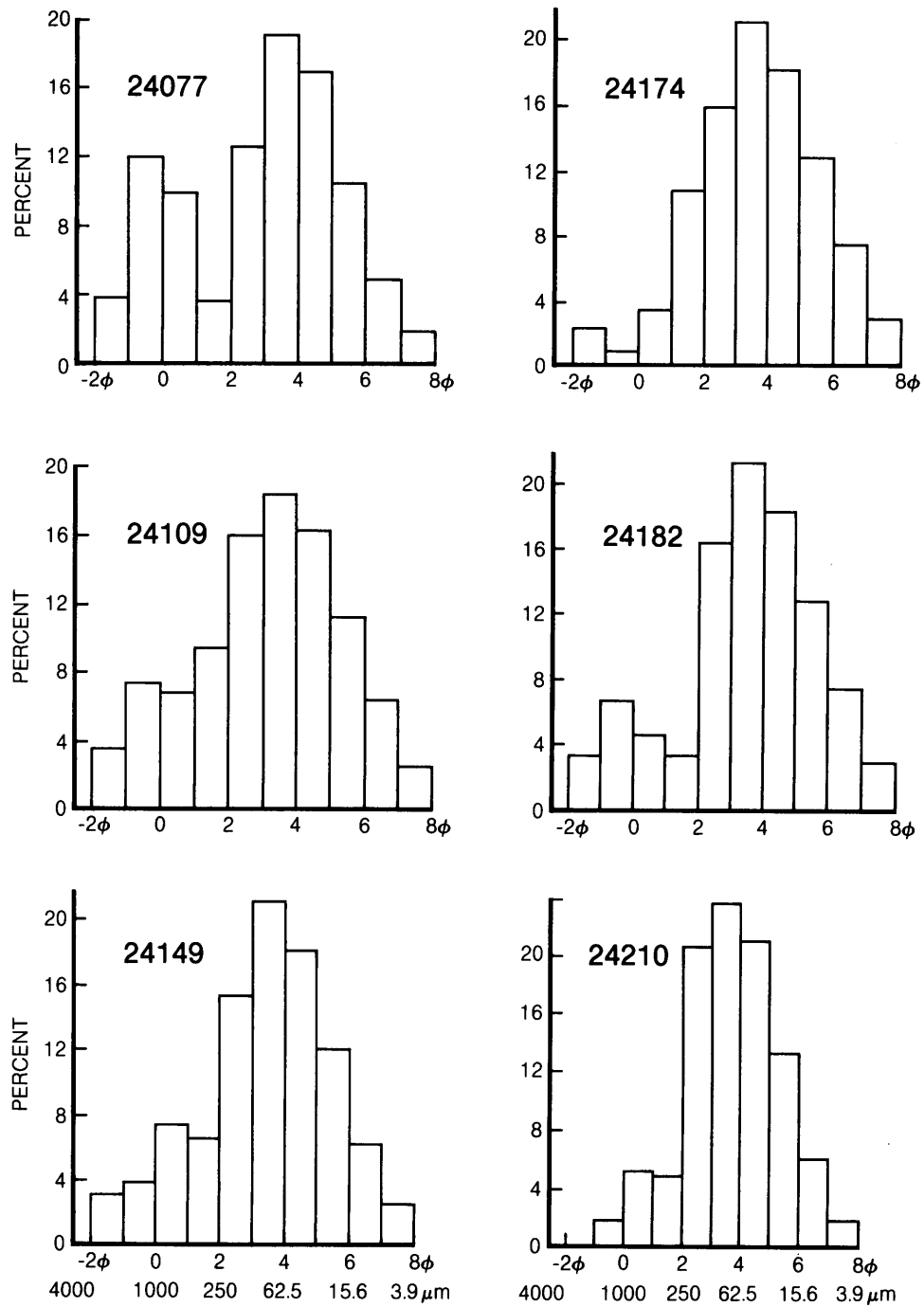


Fig. 7.20. Histograms of grain-size distributions for Luna 24 core samples (McKay *et al.*, 1978b). The grain-size distributions are generally bimodal, with peaks at 1 mm and 100 μm. Approximate sample depths: 24077 (10 cm), 24109 (110 cm), 24149 (150 cm), 24174 (175 cm), 24182 (180 cm), and 24210 (220 cm). There is a general increase in mean grain size with depth.

TABLE 7.14. Core samples collected by the Apollo missions and current status of investigation.

Core Number	Station	Landmark	Diameter and Type	Approximate Dissection Date	Depth (cm)	Dissection Length (cm)	Bulk Density (g/cm ³)	Peel	Epoxy Impreg- nation	Thin Section	Spectral Reflec- tance	Comments
10004	LM		2 cm Drive	3/78	<32	13.5	1.59	N	N	N	N	
10005	LM		2 cm Drive	3/78	>25	10.5	1.71	N	N	N	N	
12025		Halo Crater	2 cm Drive	12/69	*	9.5	1.98	N	N	N	N	Upper tube - paired with 12028
12026	LM		2 cm Drive	11/69	37	19.3	1.74	N	N	N	N	
12027		Sharp Crater	2 cm Drive	1/80	~37	17.0	—	Y	Y	Y	Y	
12028		Halo Crater	2 cm Drive	12/69	9.5*	31.6	1.96	N	N	N	N	Lower tube - paired with 12025
14210	A	Weird Crater	2 cm Drive	1/79	} ~64	32	1.75	Y	Y	Y	Y	Lower tube - paired with 14211
14211	A	Weird Crater	2 cm Drive	11/78		7.7	1.73	Y	Y	Y	Y	Upper tube - paired with 14210
14220	G	Triplet	2 cm Drive	5/79	<36	16.0	1.60	Y	Y	Y	Y	
14230	G	Triplet/Cone	2 cm Drive	7/71	45	12.5	—	Y	Y	N	N	Core driven twice
15001	8		2 cm Drill	4/72	} 236	36.9	1.93	Y	Y	Y	N	6 of 6
15002	8		2 cm Drill	1/72		39.2	1.64	Y	Y	Y	N	5 of 6
15003	8		2 cm Drill	8/72		39.3	1.74	Y	Y	Y	N	4 of 6
15004	8		2 cm Drill	3/72		40.1	1.74	Y	Y	N	N	3 of 6
15005	8		2 cm Drill	1/72		41.0	1.78	Y	Y	N	N	2 of 6
15006	8		2 cm Drill	4/72		40.7	1.58	Y	Y	N	N	1 of 6
15007	2	St George Crater	4 cm Drive	10/80	} 70.1	34.1	1.69	Y	Y	Y	N	Lower tube - paired with 15008
15008	2	St George Crater	4 cm Drive	4/80		23.1	1.36	Y	Y	Y	Y	Upper tube - paired with 15007
15009	6	Appenine Front	4 cm Drive	12/87	34.6	29.3	1.30	Y	Y	Y	N	
15010	9A	Hadley Rille	4 cm Drive	9/78	} 67.6	29.9	1.91	Y	Y	Y	N	Lower tube - paired with 15011
15011	9A	Hadley Rille	4 cm Drive	2/79		26.4	1.69	Y	Y	Y	N	Upper tube - paired with 15010
60001	LM		2 cm Drill	5/72	} 223	5.5	1.67	N	N	N	N	7 of 7
60002	LM		2 cm Drill	7/74		35.8	1.81	Y	Y	Y	N	6 of 7
60003	LM		2 cm Drill	8/76		39.5	1.67	Y	Y	Y	N	5 of 7
60004	LM		2 cm Drill	11/72		38.3	1.62	Y	Y	Y	N	4 of 7
60005	LM		2 cm Drill	11/74		14.6	1.62	N	N	N	N	3 of 7
60006	LM		2 cm Drill	10/72		32.0	1.58	Y	Y	Y	N	2 of 7
60007	LM		2 cm Drill	2/74	22.4	1.44	Y	Y	Y	N	1 of 7	
60009	LM		4 cm Drive	6/76	} 71	31.5	1.72	Y	Y	Y	N	Lower tube - paired with 60010
60010	LM		4 cm Drive	12/76		27.3	1.47	Y	Y	Y	N	Upper tube - paired with 60009
60013	LM		4 cm Drive	Unopened	} 70.5	—	1.63	N	N	N	N	Lower tube - paired with 60014
60014	LM		4 cm Drive	Unopened		—	1.48	N	N	N	N	Upper tube - paired with 60013
64001	4	Stone Mountain	4 cm Drive	7/81	} 65.5	34.1	1.66	Y	Y	Y	N	Lower tube - paired with 64002
64002	4	Stone Mountain	4 cm Drive	7/81		26.4	1.40	Y	Y	Y	N	Upper tube - paired with 64001

TABLE 7.14. (continued).

Core Number	Station	Landmark	Diameter and Type	Approximate Dissection Date	Depth (cm)	Dissection Length (cm)	Bulk Density (g/cm ³)	Peel	Epoxy Impreg- nation	Thin Section	Spectral Reflec- tance	Comments	
68001	8	South Ray Crater	4 cm Drive	Unopened	68.6	—	1.80	N	N	N	N	Lower tube - paired with 68002	
68002	8	South Ray Crater	4 cm Drive	Unopened		—	1.59	N	N	N	N		Upper tube - paired with 68001
69001	9	South Ray Crater	4 cm Drive	Unopened		27.5	—	—	N	N	N	N	
70001	LM	Camelot Crater	2 cm Drill	1/73	~300	5.5	1.66	N	N	N	N	9 of 9	
70002	LM	Camelot Crater	2 cm Drill	2/77		34.5	1.84	Y	Y	Y	Y	N	8 of 9
70003	LM	Camelot Crater	2 cm Drill	3/78		39.5	1.84	Y	Y	Y	Y	N	7 of 9
70004	LM	Camelot Crater	2 cm Drill	4/76		39.2	1.86	Y	Y	Y	Y	N	6 of 9
70005	LM	Camelot Crater	2 cm Drill	8/77		40.3	1.83	Y	Y	Y	Y	N	5 of 9
70006	LM	Camelot Crater	2 cm Drill	5/77		38.0	1.85	Y	Y	Y	Y	N	4 of 9
70007	LM	Camelot Crater	2 cm Drill	10/75		30.5	1.80	Y	Y	Y	Y	N	3 of 9
70008	LM	Camelot Crater	2 cm Drill	3/73		37.8	2.07	Y	Y	Y	Y	N	2 of 9
70009	LM	Camelot Crater	2 cm Drill	5/75		25.1	1.75	Y	Y	Y	Y	N	1 of 9
70012	LM		4 cm Drive	Unopened	28	—	1.77	N	N	N	N		
73001	3	Lara Crater	4 cm Drive	Unopened	70.6	—	1.73	N	N	N	N	Lower tube - paired with 73002	
73002	3	Lara Crater	4 cm Drive	Unopened		—	1.60	N	N	N	N	N	Upper tube - paired with 73001
74001	4	Shorty Crater	4 cm Drive	1/77	71	34.3	2.29	Y	Y	Y	Y	Lower tube - paired with 74002	
74002	4	Shorty Crater	4 cm Drive	1/77		32.0	2.04	Y	Y	Y	Y	Y	Upper tube - paired with 74001
76001	6	North Massif	4 cm Drive	10/78	37.1	31.4	1.57	Y	Y	Y	Y		
79001	9	Van Serg Crater	4 cm Drive	4/87	71	29.3	1.74	Y	Y	Y	N	Lower tube - paired with 79002	
79002	9	Van Serg Crater	4 cm Drive	10/86		17.4	1.67	Y	Y	Y	Y	N	Upper tube - paired with 79001

A *peel* is prepared by pouring a thin coating of epoxy onto a flat, dissection surface of the core. See *Fryxell and Heiken (1974)* for a description of the technique.

* 12025 and 12028 were a double drive tube.

ages), and their variations with depth. The most intensively studied cores are the Apollo 15 deep drill core (15001–15006), the Apollo 16 double drive tube 60009/60010, and the Apollo 17 deep drill core (70001–70009). The results obtained for these cores are summarized below.

Petrographic variations. One of the simplest and most valuable techniques for understanding the nature and history of a section of regolith is to determine the variations, with depth, of the relative amounts of the different *petrographic components* of the lunar soil, i.e., the particles that can be identified using an optical (petrographic) microscope or a scanning electron microscope. These components are principally of two kinds: (1) those derived from bedrock, such as rock and mineral fragments; and (2) those produced as the result of exposure at the lunar surface—agglutinates, regolith breccias, and impact-produced glasses (sections 7.1 and 7.3). Petrographic variations with depth have helped to identify different layers in the lunar regolith at every station where a core has been collected. In particular, abrupt changes in the petrographic components have made it possible to locate the boundaries between discrete layers. Where such boundaries also coincide with breaks in the chemical and maturity profiles, a significant break in the history of regolith development may be inferred.

Agglutinates are a petrographic component formed during surface exposure, and the variation of agglutinate abundances in all lunar cores closely follows the profiles of other maturity indexes. This effect is seen in all lunar cores; an example is the covariance seen in the depth profiles of I_s/FeO and agglutinate content in the Apollo 16 core 60009/60010 (Fig. 7.22a; *McKay et al.*, 1977).

The variation of other petrographic constituents—rock and mineral fragments—with depth in the lunar regolith depends essentially on the extent to which these bedrock-derived materials are introduced from both local and distant bedrock, and especially on the relative contributions of highland and mare sources (Fig. 7.21). As shown above (see also *Papike et al.*, 1982) it has not proved possible to correlate different stratigraphic layers, sampled by coring and identified on the basis of the variety of rock fragments, over any distance on the Moon. Therefore, the petrographic variations of the lunar regolith with depth can only be understood in terms of the mixing together of different lithologic components.

Two of the Apollo 16 cores have been studied in considerable detail. *McKay et al.* (1977) showed that the content of mineral and rock fragments in core 60009/60010 can be successfully modeled by mixtures of nearly pure anorthositic plagioclase feldspar and crystalline breccias (metamorphosed

breccia plus poikilitic breccia) (Fig. 7.22c), with modification by subsequent maturation. In a study of the core 64001/64002, *Houck* (1982b) and *Basu and McKay* (1984) showed that a more complex situation existed. These cores contain a significant amount of mare basalt fragments. Although their abundance is low (mare basalts being exotic to the Apollo 16 site), there is a positive correlation between mare basalt fragments and monomineralic pyroxene fragments that may have been derived from the mare basalts (Fig. 7.23). The variation of other constituents, such as monomineralic plagioclase grains, crystalline-matrix breccias, and glass show negative correlations with the exotic mare basalts, which is consistent with mixing of local components (anorthosites and breccias) and exotic components (mare basalts). In a separate chemical investigation of this core, *Korotev et al.* (1984) discovered the presence of a mafic (basaltic) component at depths of 5.5 cm and 42 cm. *Basu and McKay* (1984) suggest that this mafic component is probably present as regolith breccias rather than as fragments of mare basalt bedrock.

Another very-well-studied core is the Apollo 17 deep drill core 70001–70009, which sampled a 298-cm-thick section of regolith and is the deepest core from the Moon. Detailed petrographic and mineral chemistry investigations are reported by *Vaniman and Papike* (1977a,b), *Vaniman et al.* (1979), and *Taylor et al.* (1979). These studies show that the core is composed of several stratigraphic units, each of which had a complex history of mixing and emplacement. The conclusion that at least three different rock types contributed pyroxene crystals to these soils in various proportions (*Vaniman et al.*, 1979) indicates both the power of petrographic techniques and the complexity of regolith formation.

Chemical variations. Because the lunar regolith is a mechanical mixture of several kinds of broken and melted rocks, variations in the chemical composition of the regolith with depth also provide a record of the influx and mixing of these materials through time. The chemical variations go in tandem with petrologic variations, but they have the advantage of including data from the fine-grained soil fractions that cannot be examined with petrographic methods. Variations in trace-element abundances also record the input of different parent rocks and the mixing process.

Analyses of 36 soil samples from various depths of the Apollo 16 core 60009/60010 by *Ali and Ehmman* (1977) show that Al and Ca dominate over Mg and Fe, reflecting the dominance of plagioclase feldspar over such mafic minerals as olivine and pyroxene. Although Mg and Fe are lower in abundance, there is a weak positive correlation between

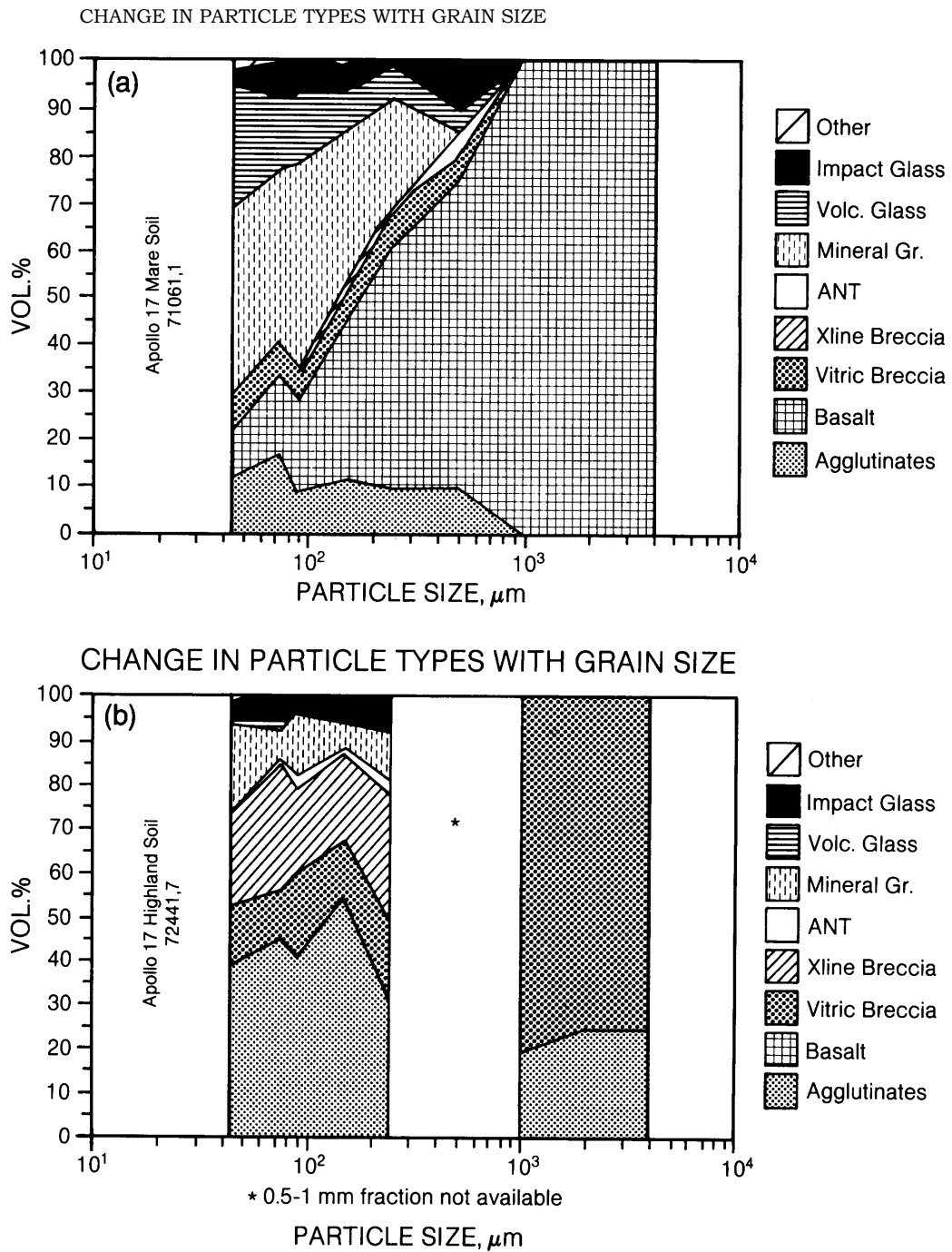


Fig. 7.21. Diagrams showing variations between grain size and relative percentages of different particle types in two Apollo 17 surface soils, **(a)** sample 71061 (mare surface) and **(b)** sample 72441 (highland surface). The two soils show wide variations in the amount of different particles (agglutinates, breccias, basalt and anorthosite fragments, and mineral and glass fragments) present in different grain-size fractions. The main differences reflect the different bedrock sources (mare basalts and highland rocks, respectively) from which the two soils have been derived (Xline = crystalline; ANT = anorthosite-norite-troctolite rock; gr = grain; volc = volcanic).

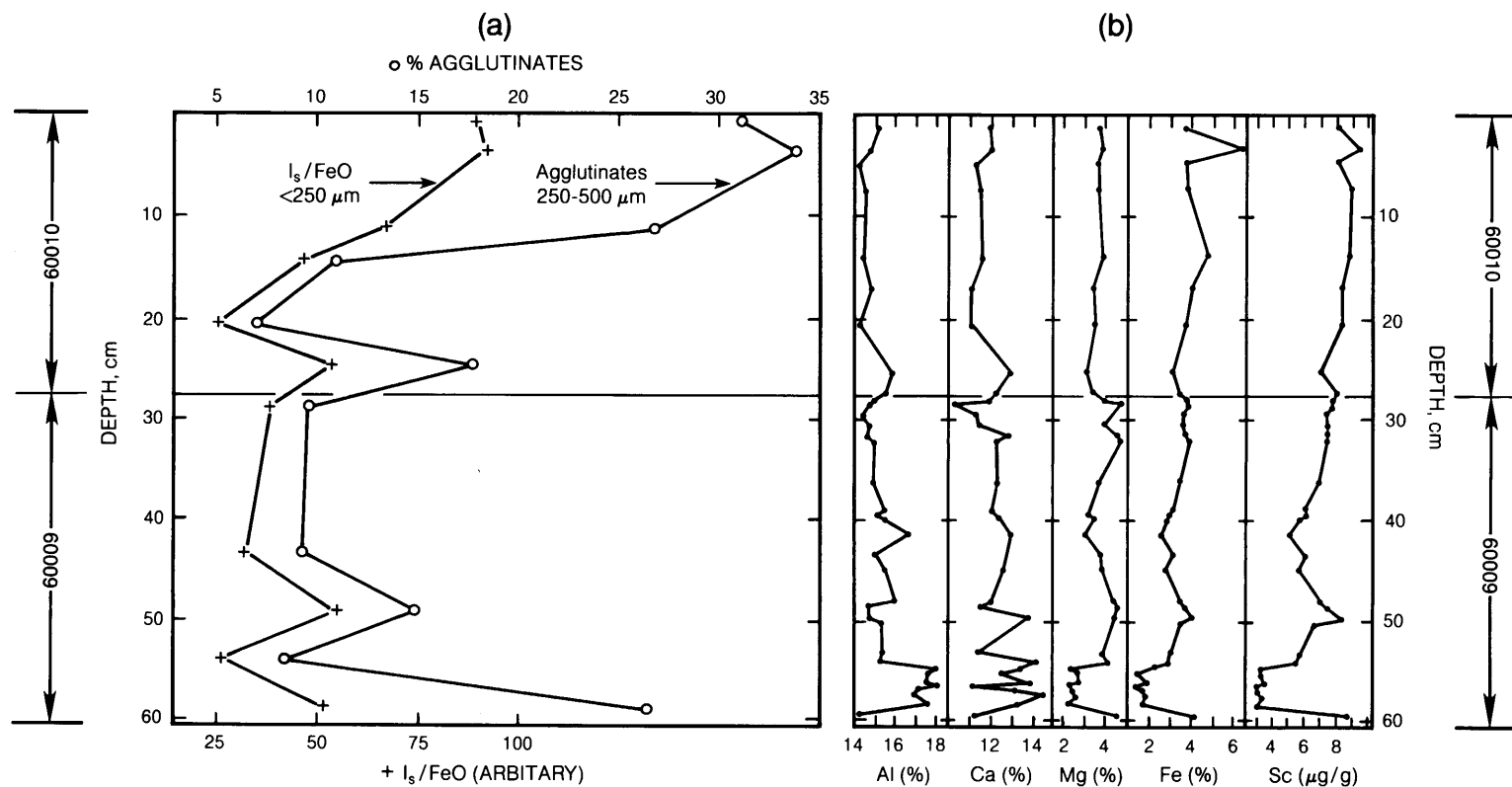


Fig. 7.22. (a) Variation with depth (in centimeters) of two maturity indices: I_s/FeO in the $<250\text{-}\mu\text{m}$ size fraction, and agglutinate abundances in the $250\text{-}500\text{-}\mu\text{m}$ size fraction of the Apollo 16 drive core 60009/10 (McKay *et al.*, 1977). The two indices correlate closely, despite the irregular variations in both throughout the core. Note the mature zone in the upper 15 cm of the core. **(b)** Variations in chemical composition, plotted for Al, Ca, Mg, Fe, and Sc as a function of depth in the Apollo 16 drive core 60009/10 (from Ali and Ehmann, 1977). The vertical scales give depth in centimeters. Significant chemical variations occur over depths of only a few centimeters, especially in the lower part of the core.

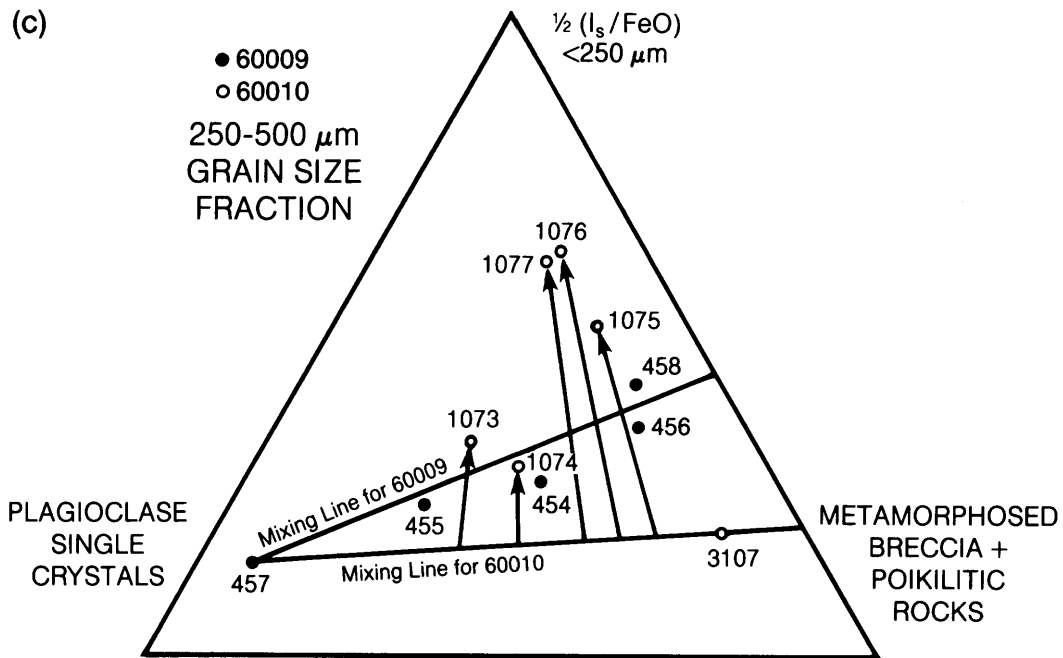


Fig. 7.22. (continued) (c) Triangular plot showing the dual effects of lithological mixing and maturation for samples from the Apollo 16 drive core 60009/10. Lithological mixing lines for the two cores lie approximately between the lower corners of the diagram, which represent the two most common rock components, plagioclase single crystals (left) and metamorphosed and poikilitic rocks (right). Most 60010 samples (1073, 1074, 1075, 1076, 1077, and 3107) show considerable displacement from the 60010 mixing line in the direction of increasing maturity (i.e., toward the I_s/FeO apex), indicating that maturation occurred after the samples were mixed together. In contrast, the 60009 samples (454, 455, 456, 457, and 458) have no systematic displacement from the mixing line toward the I_s/FeO apex, and therefore show no evidence of postmixing maturation.

them, and there is a strong positive correlation between Fe and Sc, which indicates that they are both present in mare basalt components (Fig. 7.22b).

Korotev *et al.* (1984) analyzed samples of the lower half of a different Apollo 16 core (sample 64001/64002) at 5-mm intervals. They found that Fe, Cr, and Sc (indicators of mare basalt) are strongly correlated, indicating that a mare basalt component is present. Abundances of Na, Eu, and Ba show a fair correlation (Fig. 7.24). Although all three of the latter group of elements occur together in plagioclase, they are also found in the late crystallizing phases—K-feldspar and glass—of mare basalts. Because they are found in two unmelted components, their covariance is weaker than those of the former group.

Laul and Papike (1980) analyzed 3 grain-size fractions of soil samples from 30 levels of the Apollo 17 deep drill core 70001–70009, and their data show the same systematic variations mentioned above. In addition, they carried out mixing calculations using 25 chemical elements (allowing a

10% uncertainty for each), attempting to duplicate the lunar soil compositions with four components that represent common rock types identified at the Apollo 17 site. Their results show that the chemical compositions of each of the 30 soils analyzed can be adequately expressed in terms of contributions from these four end members (Fig. 7.25). These chemical results are also consistent with the five stratigraphic units that have been recognized on the basis of petrologic work (Vaniman *et al.*, 1979), and this consistency between the two techniques strengthens the identification of these layers as discrete depositional units.

Finally, these studies show that certain elements record the effects of soil maturation processes on the Moon. Comparison of the I_s/FeO profile in the Apollo 17 deep drill core with the abundance of Zn, a volatile element, clearly shows a strong negative correlation (Fig. 7.26; Laul and Papike, 1980), implying that Zn has been progressively lost, probably by impact vaporization, as the soil matured.

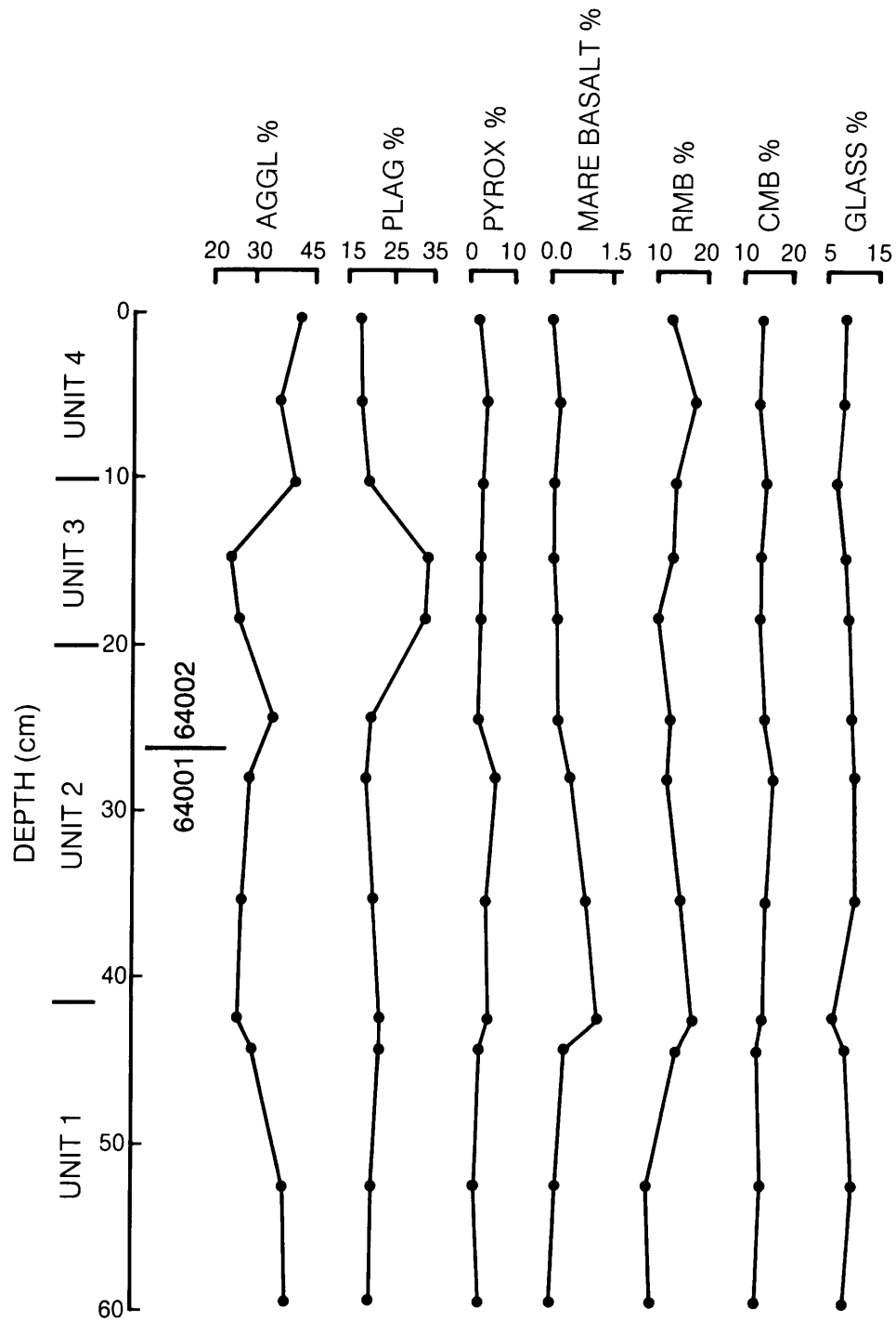


Fig. 7.23. Variations in the abundance of particle types with depth in the Apollo 16 core 64001/2 (Basu and McKay, 1984; Houck, 1982b). Scale at left shows the depth, sample locations, and boundaries between four distinct layers. Aggl = agglutinate, Plag = plagioclase, Pyrox = pyroxene, RMB = regolith matrix breccia, and CMB = crystalline matrix breccia.

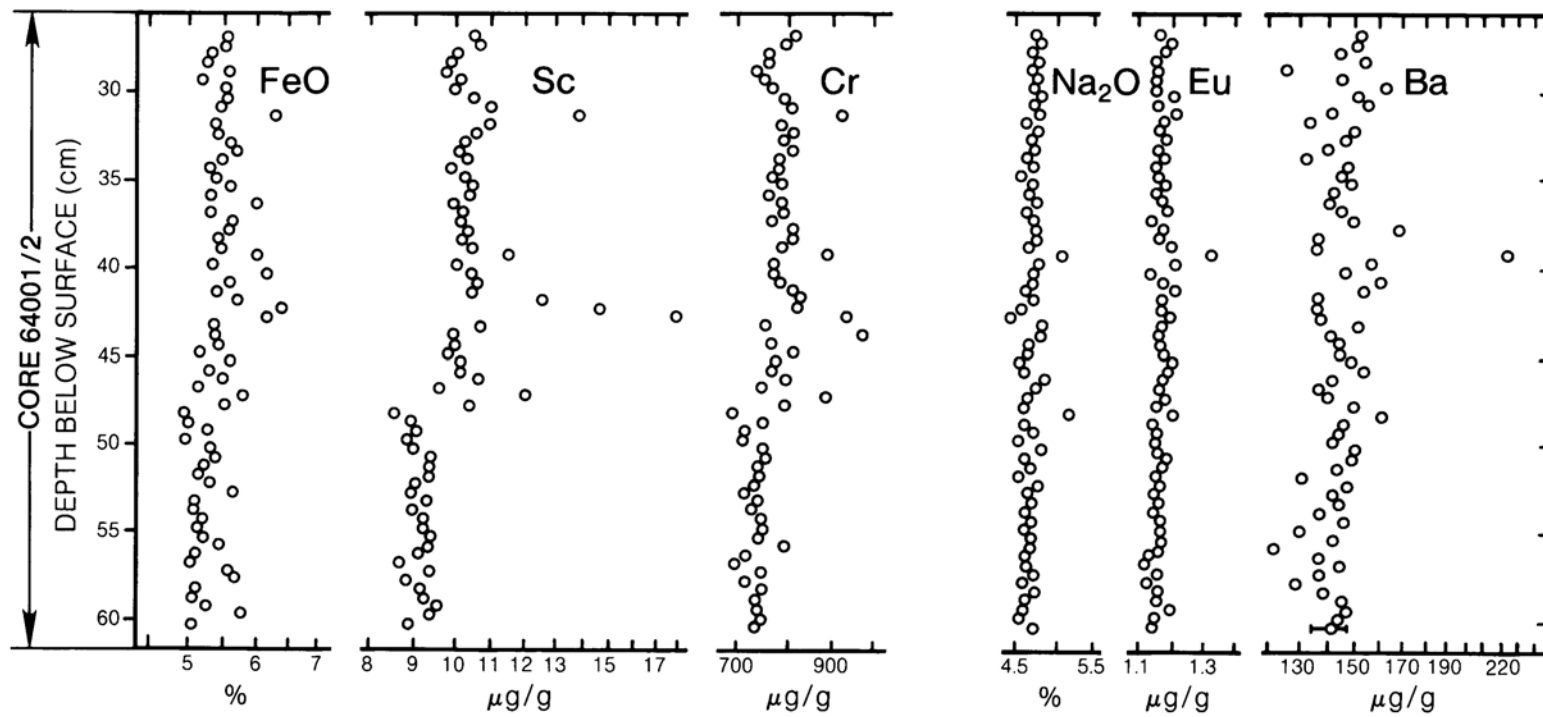


Fig. 7.24. Variations, with depth, of specific elements associated with ferromagnesian minerals (Fe, Sc, and Cr), and with plagioclase feldspar (Na, Eu, and Ba) in soil samples from the Apollo 16 core 64001/2 (Korotev *et al.*, 1984). Variations in these elements correlate approximately with the relative abundances of mare and highland materials, respectively, in the soil.

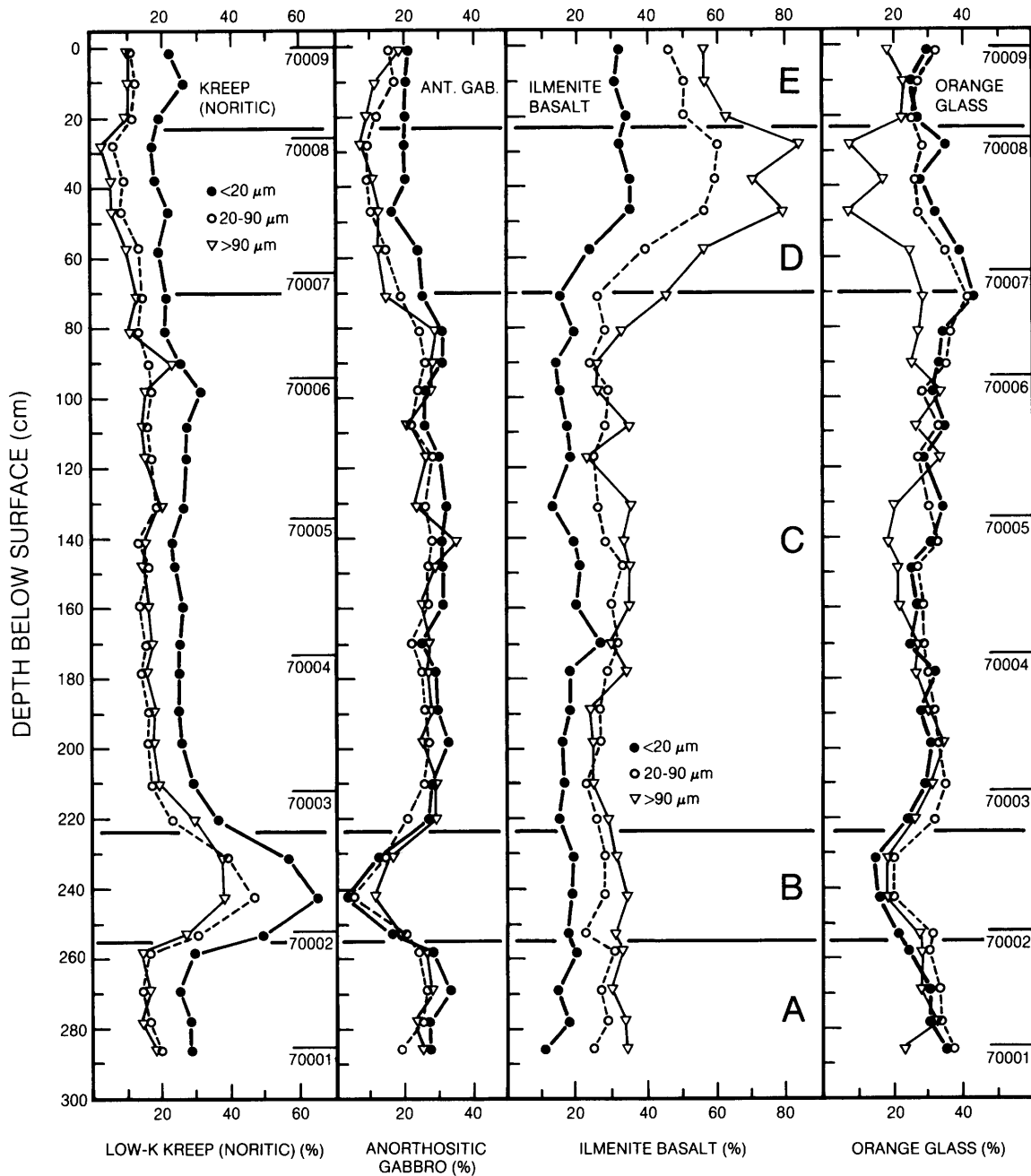


Fig. 7.25. Calculated percentages of different lithologic components as a function of depth for soil samples from the Apollo 17 core 70001–70009 (Papike et al., 1982). For each sample data represent analyses for 25 chemical elements in each of 3 size fractions: $<20 \mu\text{m}$, $20-90 \mu\text{m}$, and $>90 \mu\text{m}$. Mixing models then use the chemical data to determine the best match for the amounts of four rock types present: low-K noritic KREEP, anorthositic gabbro, ilmenite basalt, and orange glass. Vertical axis gives depth in core; horizontal axes give percentages for each component. Note that the boundaries (horizontal lines) of the five stratigraphic units (A–E) identified on the basis of petrographic studies coincide with significant variations in the abundances of different components.

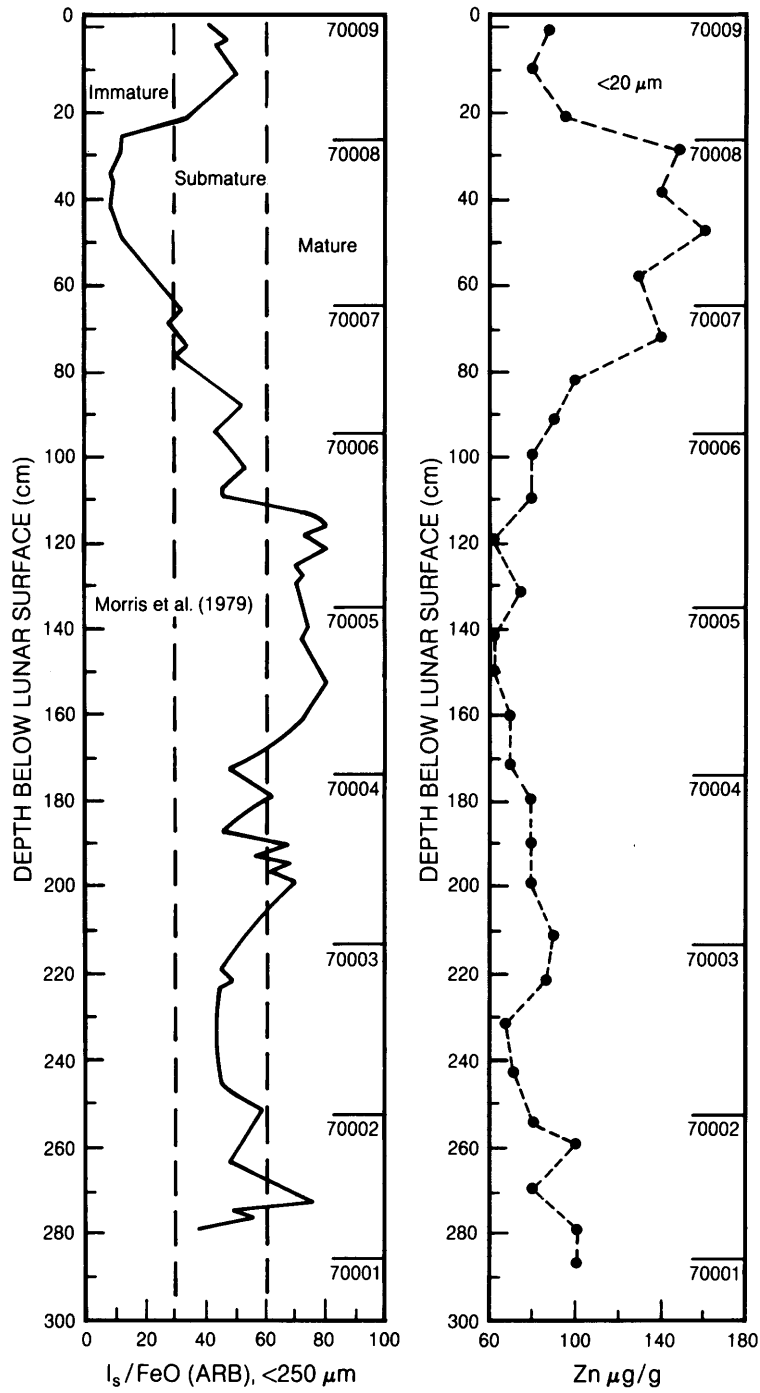


Fig. 7.26. Depth profiles of the abundance of Zn, a volatile element, and I_s/FeO , a maturity index, in the <20- μm size fraction of soil samples from the Apollo 17 drill core 70001–70009. These two quantities show a strong negative correlation, especially in the upper part of the core. This relationship suggests that Zn may be depleted in mature lunar soils, possibly having been expelled by vaporization during agglutinate production (Laul and Papike, 1980).

7.4.3. Regolith Stratigraphy

Nature of the regolith sections. The study of layered lunar regolith has many of the same goals as terrestrial stratigraphy—to determine the composition, formation, historical sequence, and correlation of a series of layered deposits. However, the lunar regolith presents special complications. Simply viewed, the regolith is built up as a series of layers of material ejected from individual meteorite craters over a period of time, and interbedded lava flows and pyroclastic deposits. At the same time, however, other large impacts may destroy, overturn, or bury a layered sequence. Furthermore, the near-surface part of the regolith, which is subjected to more frequent small impacts, tends to become uniformly mixed (gardened) and to lose many of the characteristics of the original discrete layers.

At any given time, the regolith ideally consists of two zones: (1) a near-surface *reworked* or *gardened* zone, typically a few centimeters to tens of centimeters thick, in which all layers have been homogenized or mixed together; and (2) an underlying *slab* or sequence of slabs in which the original layering is still undisturbed. The lowest section of regolith may grade downward into highly fractured bedrock into which regolith has been mixed or has seeped into the fractures.

In the reworked zone or layer, observed maturity indices have nearly constant values from top to bottom. (The term “layer” can be used, even though the zone described may have originally included more than one layer of ejecta. Mixing has been so complete that no trace of the original layering remains.) The soils from such a reworked layer are mature, and their maturity indices (with the exception of I_s/FeO) tend to be saturated.

Reworked zones are developed at or near the surface, where impacts are small and frequent. The resulting mixing and turnover of this zone occurs often enough to expose most of the soil particles to the near-surface environment for periods of time that are longer than needed to saturate such exposure indicators as solar-flare track densities and trapped solar-wind gases. The time needed to saturate solar-wind and solar-flare effects is less than a few thousand years.

The uppermost part of any lunar core should consist of such a reworked layer, unless the core has been drilled into fresh ejecta from a young crater. With prolonged surface exposure, more large impacts affect the exposed regolith, and the thickness of the reworked layer gradually increases. In the returned Apollo cores, the thickness of this uppermost reworked layer varies between about 10 cm and 50 cm.

Beneath the reworked layer may be layers of material that have remained unmixed since they were deposited. These *slabs* may consist of several layers that still preserve their original depositional relationship to each other. The slabs are shielded by the overlying zone of reworked regolith from near-surface effects such as solar-wind implantation and solar-flare tracks, but more energetic particles (solar-flare protons and cosmic rays) may penetrate the slabs and produce distinctive effects to depths of several meters. Because these effects vary with depth, distinctive *in-situ exposure profiles* develop within the slabs. In core samples, the presence of such profiles indicates that the overall slab, no matter how complexly layered, has remained in place and undisturbed for a significant period of time.

Large impacts excavate and deposit thick ejecta layers. Because the impacts may excavate a significant thickness of layered regolith, much of the material in the resulting ejecta may have been previously exposed, and this material brings the records of that exposure with it into the new ejecta layer. Near the crater, the ejecta layer is thick, and the original regolith layers may be preserved (often overturned) in the new ejecta deposit. Further from the crater, the ejecta layer is thin, and the preimpact regolith components, with their different exposure histories, may be mixed together.

Figure 7.27 shows depth profiles of several maturity indices and indicators of surface (or near-surface) exposure for the Apollo 15 deep drill core, the Apollo 16 double drive tube 60009/60010, and the Apollo 17 deep drill core. The parameters that are plotted, I_s/FeO , the track maturity index, agglutinate content, solar-wind gases, cosmogenic isotopes, and minimum track densities, are discussed in section 7.3. These are the basic data upon which many of the interpretations of lunar regolith stratigraphy have been based.

It would be difficult to resolve such complexities in detail, even with a large number of carefully collected samples. With the relatively few Apollo core samples available, it is not surprising that there is no general consensus on how to interpret the stratigraphic data contained in the lunar regolith cores. The sections below provide general stratigraphic interpretations for three core samples and attempt to account for all of the observations. The interpretations here are not always the same as those presented by the scientists who made specific measurements. The references cited in the sections below and in Fig. 7.27 should be consulted to obtain other points of view.

Apollo 15 deep drill core (sample numbers 15001–15006; 242 cm long). The upper 40-

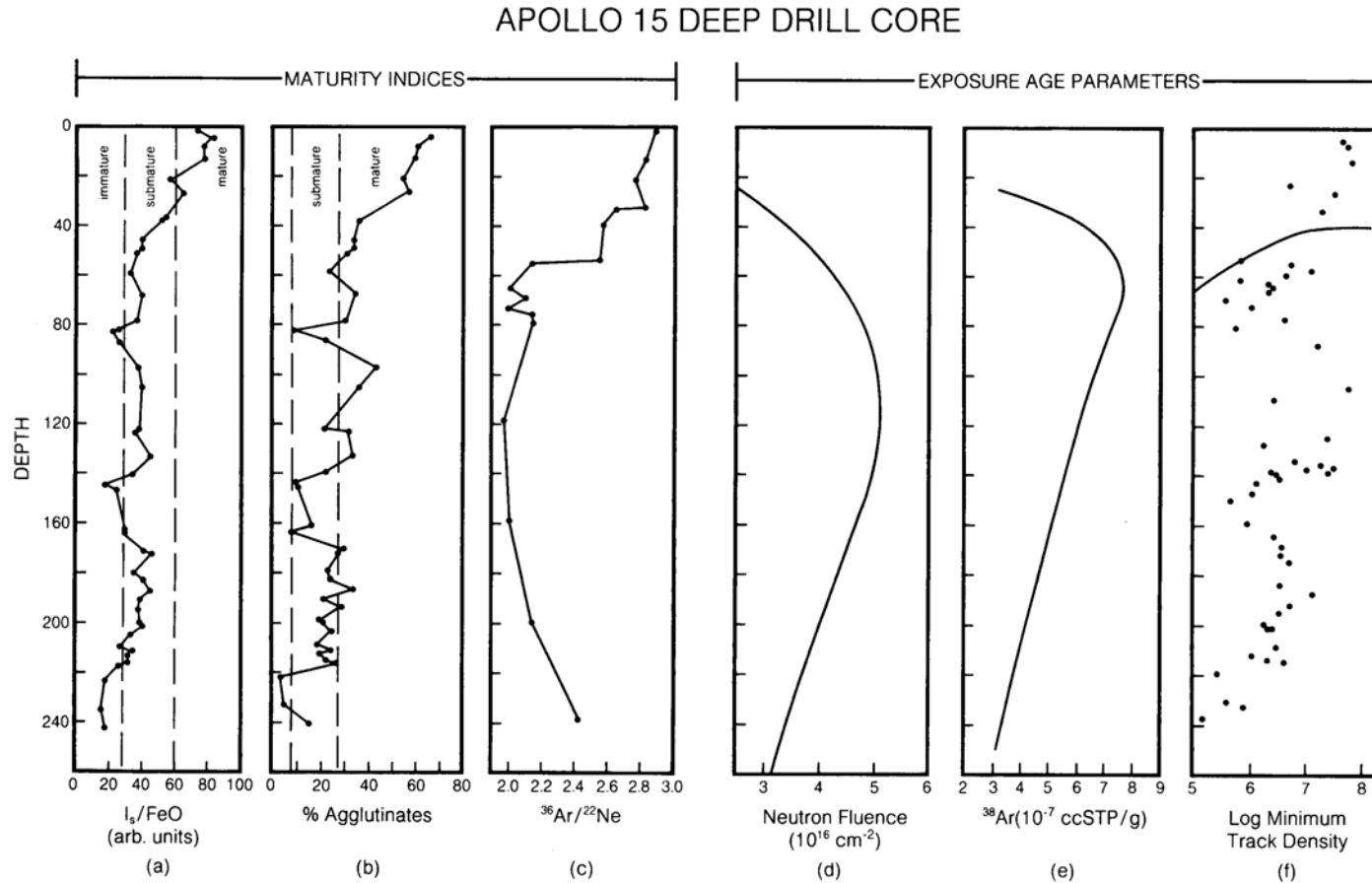


Fig. 7.27. Depth profiles of maturity indices and exposure age parameters for the Apollo 15 deep drill core 15001–15006, Apollo 16 core 60009/10, and the Apollo 17 deep drill core 70001–70009. In general the maturity indices shown (I_s/FeO , agglutinate percentages, and trapped solar-wind noble gases) show a gradual increase upward in the regolith and are highest within a few tens of centimeters of the surface. In contrast, some exposure age parameters (neutron fluence, ^{38}Ar content, and track densities) reflect charged-particle interactions or nuclear reactions that reach a maximum at depths of 50–200 cm in the regolith, where the incoming primary charged particles have been slowed by absorption. *Apollo 15—15001–15006: (a) I_s/FeO , and (b) petrographic agglutinate percentages, after Heiken et al. (1976); (c) solar-wind rare-gas data after Bogard and Hirsch (1975); (d) neutron fluences after Curtis and Wasserburg (1977); (e) spallogenic argon (^{38}Ar), after Pepin et al. (1974); and (f) minimum track densities (number/cm²) after Goswami and Lal (1977).*

APOLLO 16 CORE 60009/10

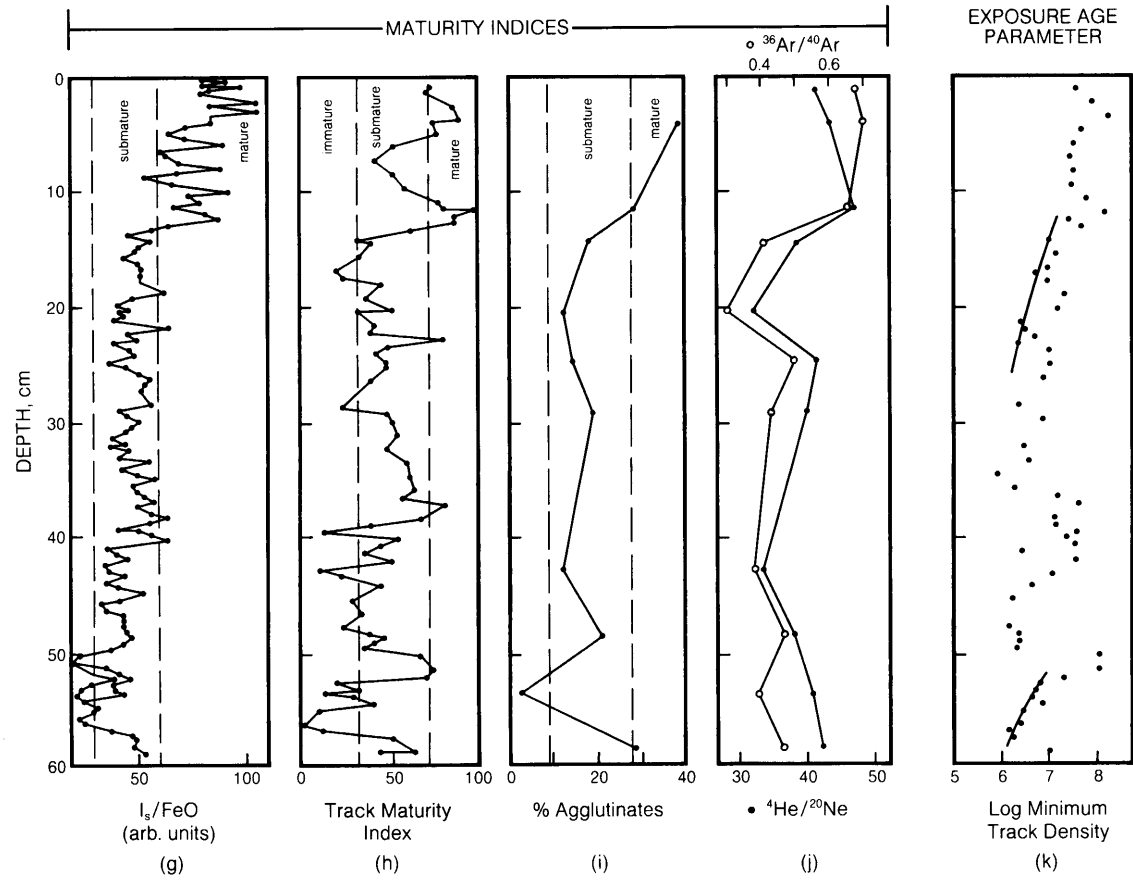


Fig. 7.27. (continued) Apollo 16—60009/10: **(g)** I_s/FeO after *Morris and Gose* (1976); **(h)** track maturity index after *Blanford et al.* (1979) (track maturity index = % grains with track densities $>10^9/\text{cm}^2$); **(i)** petrographic agglutinate percentages, after *McKay et al.* (1977); **(j)** solar-wind rare gases after *Bogard and Hirsch* (1977); and **(k)** minimum track density after *Blanford et al.* (1979).

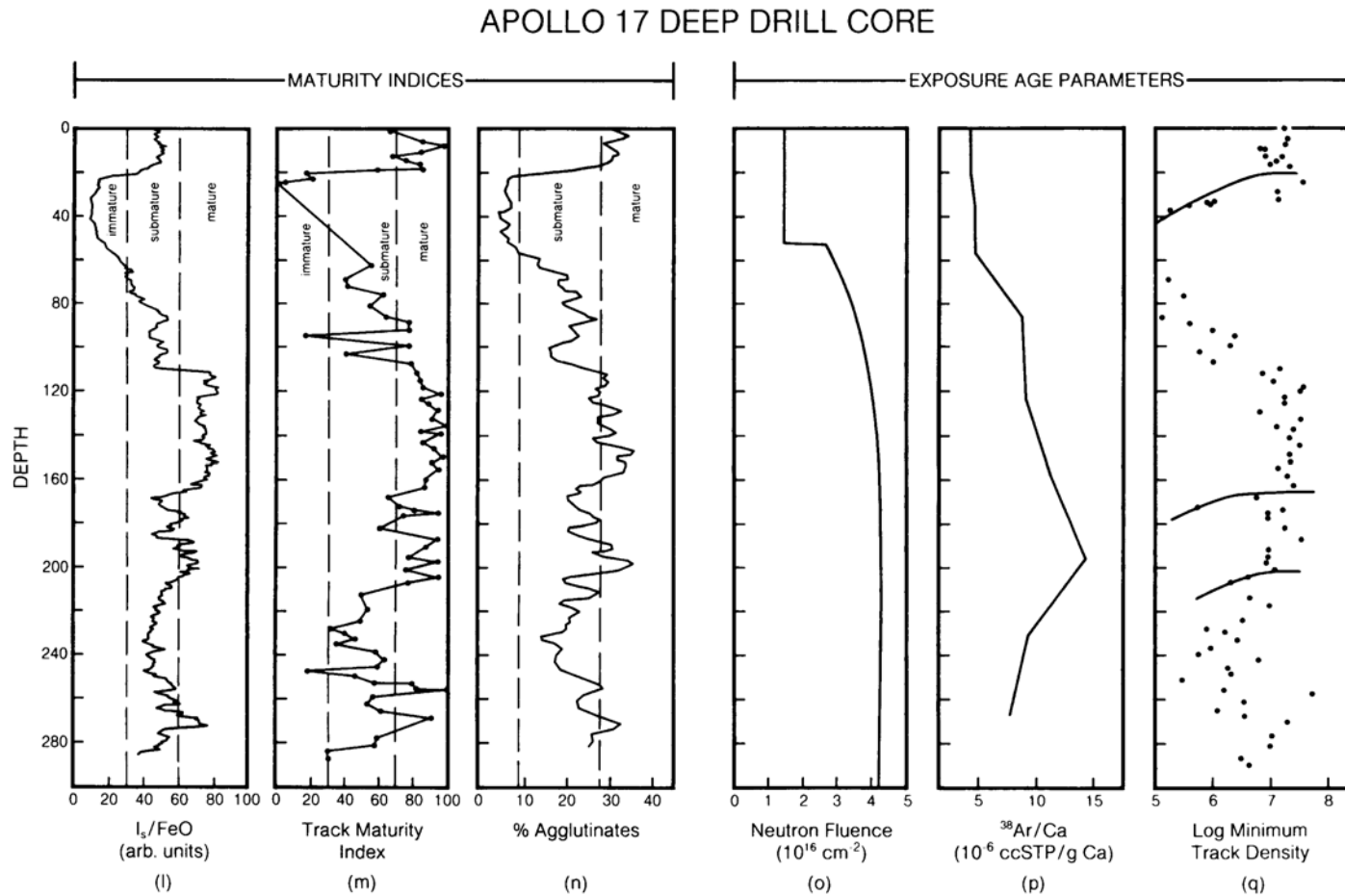


Fig. 7.27. (continued) *Apollo 17—70001–70009*: **(l)** I_s/FeO after *Morris et al.* (1979); **(m)** track maturity index after *Goswami and Lal* (1979); **(n)** petrographic agglutinate percentages, after *Taylor et al.* (1979); **(o)** neutron fluence after *Curtis and Wasserburg* (1977); **(p)** spallogenic argon (^{38}Ar) after *Pepin et al.* (1975); and **(q)** minimum track density after *Goswami and Lal* (1979). The track densities, in numbers/cm², show at least three levels where soils were buried by fresh ejecta (curved lines); these correlate also with changes in maturity indices.

45 cm of the Apollo 15 deep drill core has been identified as a reworked zone. Below this zone, the remainder of the core (200 cm) has lain undisturbed *in situ* for $\sim 4.2 \times 10^8$ yr. The upper reworked zone is distinguished by the fact that all the maturity indices in this part of the core reach equilibrium values, which persist from the surface to a depth of ~ 40 cm (Fig. 7.27a–c). Petrographic and chemical variability, still preserved within this zone, reflect the lithologic heterogeneity of the site.

The remainder of the core below a depth of 40 cm must have been undisturbed *in situ* because the deeper profiles of cosmogenic nuclides are well-formed and well-preserved (Fig. 7.27d–e). These profiles have scale lengths on the order of a meter, and sizable variations on scales smaller than this would produce highly variable profiles, which, in fact, are seen in all other measured lunar cores.

The emplacement of this slab on the lunar surface was an ancient event. The measured exposure ages of the slab are 4.2×10^8 yr (Pepin *et al.*, 1974), 4.5×10^8 yr (Curtis and Wasserburg, 1977), and 4.0×10^8 yr (Blanford, 1980). This slab can be divided into several distinct layers, which show great heterogeneity in track densities, surface correlated gases, petrographic characteristics, and chemistry. These variations reflect the heterogeneities within the soil at the time of emplacement. In fact, the inherited track densities at the time of deposition were so high that there are no meaningful track profiles, reflecting later irradiation, which can be distinguished (Fig. 7.27f).

Apollo 16 core (sample numbers 60009/60010; 65.4 cm long). Examination of the I_s/FeO profile for this core (Figs. 7.27g–k) reveals that a reworked zone is present from the surface to a depth of ~ 12 cm. The track maturity index shows some variation from the ideal uniform profile at a depth of ~ 2 cm, implying some nonuniform disturbance, but no well-developed track profile can be established below this point because the inherited track densities are too high.

If this zone at ~ 2 cm depth did result from some specific lunar event, the thickness and location of the zone suggest an event about 10^6 yr ago. At the Apollo 16 site, South Ray Crater (0.5 km in diameter, located 6 km south of the core sample) has been dated at 2.0×10^6 yr (Drozd *et al.*, 1974). The track maturity index in the core sample may have been sufficiently sensitive to respond to this event, and to the sudden deposition of the resulting ejecta, but the data provide only suggestive support for this interpretation.

The track profile that developed in the regolith below a depth of 12 cm corresponds to an exposure age of $< 1.2 \times 10^8$ yr (Bogard and Hirsch, 1977) or $5\text{--}14 \times 10^7$ yr (Blanford *et al.*, 1979). This age is about

the same as that of North Ray Crater (0.8 km in diameter, located 5 km north of the core sample) (5×10^7 yr; Drozd *et al.*, 1974). This connection is problematical, however. The track data require that the impact ejecta must be at least as thick as the reworked zone (12 cm) and possibly as thick as 39 cm. These are minimum estimates that neglect any overburden that may have originally been present and then subsequently removed. In contrast, the impact ejecta from North Ray Crater are estimated to be only ~ 1 cm deep at the lunar module site where core 60009/60010 was collected (Stöffler *et al.*, 1974).

There are no clearly defined strata in this core from ~ 24 cm to ~ 50 cm. From 12 to 50 cm, all maturity indexes indicate that the material is a submature soil that shows little variation with depth. Because there are no clear reworking zones in this interval, it is probable that this zone was emplaced as a unit in a single impact event. At 50 cm depth, a reworking zone, ~ 2 cm thick, has been identified; the zone can be seen clearly in both the I_s/FeO and track profiles (Fig. 7.27g,h).

Below this thin reworked zone, there is a slab of material that shows a well-developed track density exposure profile from 52–58 cm deep. This profile corresponds to an exposure age of $4.5\text{--}9 \times 10^6$ yr (Blanford *et al.*, 1979), implying that the slab was deposited by a nearby impact at that time. However, any small crater corresponding to this event has probably been severely modified or eroded away by smaller subsequent impacts.

The bottom centimeter of the Apollo 16 60009/60010 core appears to be composed of more mature soil than the material above it, and this lowermost zone may represent a new stratum, but not enough of it was penetrated to conclusively state anything about the exposure history of this soil.

Apollo 17 deep drill core (sample numbers 70001–70009; 298.6 cm long). The upper 20 cm of the Apollo 17 deep drill core is a reworked zone. Immediately below the reworked zone is a slab, 40 cm thick, composed of the freshest lunar soil recovered in the Apollo program. The boundary between the two layers is clearly marked by every observable property of lunar soil (Figs. 7.271–q). The lower, 40-cm-thick layer, which is extremely coarse-grained, has remained undisturbed since its deposition, and the exposure profiles for cosmogenic nuclides are well developed. The exposure ages estimated for the time of deposition of this layer are $> 3 \times 10^7$ yr (Crozzaz and Plachy, 1976); $< 8 \times 10^7$ yr (Curtis and Wasserburg, 1977); 1.1×10^8 yr (Drozd *et al.*, 1977); and 7×10^7 yr (Blanford, 1980).

Below this layer, the core has not been studied (with particle-track techniques) in sufficient detail to

give a full history for the entire core. The $^{137}\text{Cs}/^{56}\text{FeO}$ profile (Fig. 7.271) suggests that there may be several distinct strata in this section, deposited at different times. However, *Curtis and Wasserburg* (1977) prefer an interpretation involving rapid emplacement of the entire section sampled by the core. The maturity index profiles (Figs. 7.271-n) suggest that reworked zones exist below the coarse layer at depths of approximately 112–166 cm and 188–203 cm. Profiles of cosmogenic nuclides have not been made with sufficiently close sampling to establish whether this interpretation is correct. However, unpublished spallogenic rare gas profiles and related calculations of neutron fluence based on this interpretation are consistent with the available data (*Pepin et al.*, 1975; *Curtis and Wasserburg*, 1977).

If this view is correct, the lower part of the core contains two more undisturbed slabs at about 40–112 cm and 166–188 cm, separated by reworked zones, and the *in situ* exposure-age estimates are $3\text{--}10 \times 10^7$ yr for the second undisturbed slab (40–112 cm deep), and $6\text{--}60 \times 10^7$ yr for the third undisturbed slab (166–188 cm deep). The cumulative *in situ* residence time of the lowest portion of the core (188–298 cm deep) would be $1.8\text{--}8.2 \times 10^8$ yr, with the true age more probably near the lower limit, a value that is consistent with the $1\text{--}2 \times 10^8$ yr age reported by *Curtis and Wasserburg* (1977).

7.5. MODELS FOR REGOLITH FORMATION

7.5.1. Regolith Dynamics

The movement of regolith materials across the lunar surface, either as individual grains or as large slabs, has built up the present lunar surface and is responsible for the layers observed in lunar core samples. Data from these cores make it possible to model regolith dynamics and to determine the rate constants for the different processes responsible for regolith formation and evolution. Some Apollo core samples were collected from considerable slopes or near rilles; at these locations, mass-wasting processes occur more rapidly, and data from these cores are particularly useful in the development of dynamic models for regolith evolution.

The most important parameters for models of regolith development are the mass and velocity distributions of impacting meteoroids, the impact flux rate, and the relation between the mass and velocity of an impacting object and the diameter, depth, and volume of the resulting crater. The present meteoroid fluxes are well known (see section 4.1.3), although significant uncertainties still exist. Cratering mechanics have been studied in detail on Earth and the application of the results to the Moon has been carried out with considerable

success (see section 4.1.2). These two datasets—impact flux rates and lunar cratering mechanics—have been used to develop models for regolith development and turnover on the Moon. These models have been very successful. They show general agreement with the measured buildup rates of the regolith and with erosion rates measured on individual lunar rocks, and, on larger scales, they agree with the cratering history of the Moon. Models that have proven particularly appropriate for measurements of regolith development are reviewed in detail by *Langevin and Arnold* (1977). In particular, the models derived from meteoroid flux data by *Gault et al.* (1974), *Arnold* (1975), and *Duraud et al.* (1975) have been the most useful.

The differences between models reflect the choice of different input parameters—meteoroid mass, flux rate, and the depths and diameters of the resulting craters. Other differences arise from different calculational methods. The model of *Gault et al.* (1974) assumes that the number of crater excavations to a given depth is a Poisson distribution that is functionally dependent on the input parameters. This model cannot predict the exposure ages indicated by different lunar soil characteristics. However, the critical factor that it can predict is the probability of turning the regolith over to a given depth as a function of time (see section 4.1.4).

The models of *Arnold* (1975) and *Duraud et al.* (1975) are more random Monte Carlo models. Particle mass and impact location are chosen from their respective distributions with pseudorandom numbers. A “run” consists of a continuous series of such choices until some predetermined endpoint is reached, e.g., the regolith is turned over to a specific depth. The statistical effects on different maturity parameters in the soil are determined by examining many such “runs.”

In further work, *Arnold* (1975) developed a model to describe the evolutionary history of a section of lunar regolith, while *Duraud et al.* (1975) developed a model to determine the burial history of individual lunar soil grains. When identical input parameters are used, both models produce remarkably close predictions for specific lunar observations such as track densities and cosmogenic nuclide distributions (*Langevin and Arnold*, 1977) within the regolith. In particular, these models can successfully predict levels of exposure developed in individual grains and can provide estimates of when they became saturated. In their models, *Gault et al.* (1974) predicted the turnover rate for the lunar regolith. These different models have subsequently been tested against the data from the Apollo core samples. *Morris* (1978a) assumed that the measured depths of surface reworked zones was equivalent to the *in*

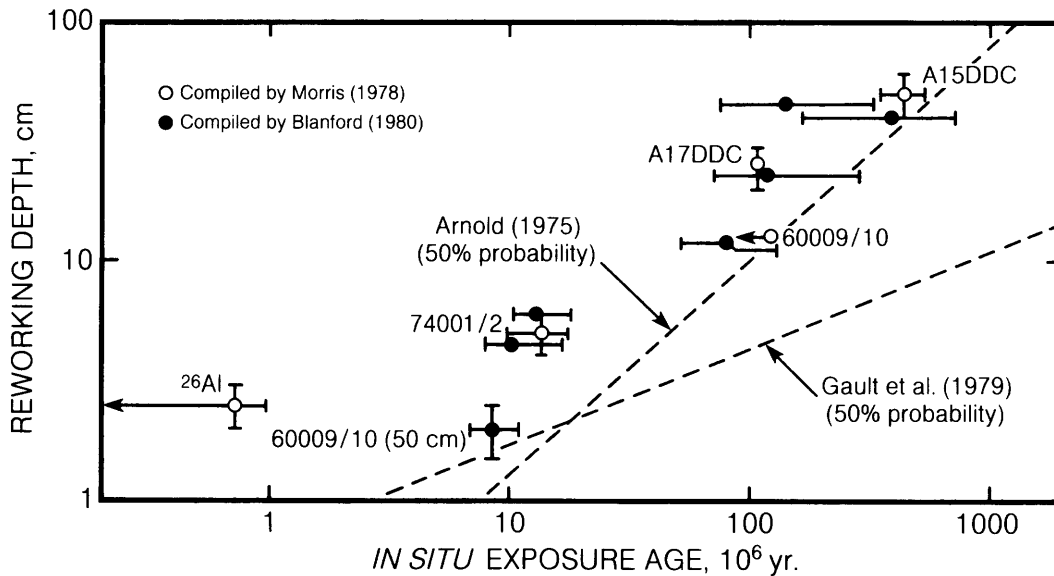


Fig. 7.28. Diagram showing calculated and measured relationships between near-surface exposure ages of lunar soil samples and reworking depths in the regolith layer. Samples represent several landing sites: Apollo 15 (A15 deep drill core), Apollo 16 (core 60009/10), and Apollo 17 (A17 deep drill core; core 74001/2). Horizontal axis shows surface exposure ages, measured with a variety of techniques; vertical axis shows reworking depth as determined from I_s/FeO values and ^{26}Al average profiles. Data are from *Morris* (1978a) and *Arnold* (1975). The experimentally determined points lie on a power-law trend that follows the *Arnold* (1975) model closely.

situ turnover of the cores and compared these depths with measured exposure ages for the cores. These data are shown in Fig. 7.28, together with additional data obtained from track densities. Because the regolith turnover is produced by stochastic (random) meteoroid impacts, the observed ages and depths can be compared with those predicted by different models. From the cores that have been measured so far, it appears that the experimental points agree with the *Arnold* (1975) model for exposure ages longer than $1\text{--}2 \times 10^7$ yr, while the *Gault et al.* (1974) model predicts reworking depths that are too shallow at all times.

7.5.2. Grain-size Distributions

McKay et al. (1974) have developed a steady-state model for the evolution of grain-size distributions in the lunar regolith that is in qualitative agreement with observed grain-size distributions of lunar soils. This model consists of three mechanisms. The first is the continuous pulverization of large particles to make smaller particles. The second mechanism, operating in reverse to the first, is the formation of agglutinates from multiple small particles. If these two mechanisms were the only ones operating, then any lunar soil would reach an equilibrium state in

which there were no large particles and all the small particles were comminuted agglutinates. However, this is not the distribution found in lunar soils, and a third mechanism is required, one which continually adds large particles directly from bedrock or from exhumed deposits of coarse material produced earlier from bedrock. This third mechanism consists of occasional large meteoroid impacts that penetrate the deeper layers of the regolith or penetrate the entire regolith, excavating fresh bedrock and scattering the fragments across the surface. It is the inclusion of this third mechanism—occasional large meteoroid impacts—that distinguishes the steady-state model from equilibrium soil models.

A comprehensive steady-state model must also allow for the slow and steady addition of exotic fine-grained material, transported ballistically from distant impacts, directly to the small particle component of the soil. Such a comprehensive model predicts that a definite relationship should exist between the mean grain size of the finest soils and the thickness of the regolith in which they are found. Finer size fractions also begin to appear, and become progressively more important, as the soil matures. Because regolith thickness is related to age, mean grain size of the finest-grained soil will also

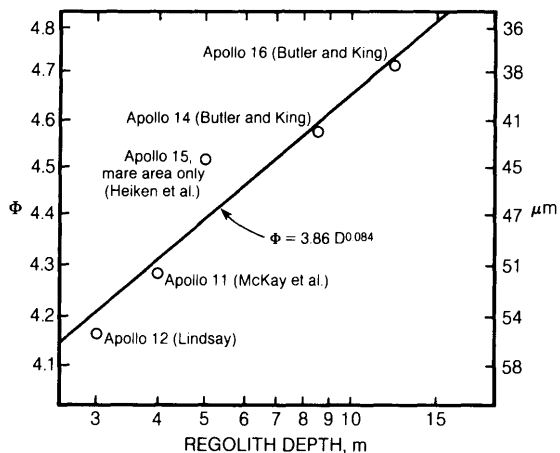


Fig. 7.29. A plot of mean grain size of the most fine-grained soil sample at several Apollo sites as a function of the regolith depth at that site (after McKay et al., 1974), showing a clear relation between the two quantities. Finer-grained soils (higher ϕ values) are associated with thicker, deeper regolith. From Butler and King (1974); Heiken et al. (1973); McKay et al. (1970); and Lindsay (1973).

be indirectly related to the age of the site. The actual data for Apollo soil samples shown in Fig. 7.29 demonstrate that the mean grain size of the finest-grained soil samples does, in fact, correlate with regolith thickness.

7.5.3. Differential Comminution

The Moon is randomly bombarded by large and small impacts that fracture lunar rocks, comminute smaller particles, and then redistribute and mix the resulting lunar soils (section 7.3.1). Therefore, it would be reasonable to expect that all lunar rocks and minerals would be crushed, abraded, and eroded at approximately the same rate. The data from Apollo lunar soil samples show a more complex pattern. In particular, the rates of abrasion and erosion are also dependent on the grain sizes of the target material. In addition, we find that different minerals in lunar soils are apparently comminuted at different rates.

In terrestrial sediments, feldspars are broken down into finer sizes much faster and more efficiently than quartz; the explanation given is that the excellent cleavage in feldspars promotes fracturing and facilitates its breakdown relative to quartz, which has very poor cleavage (Basu, 1976; Basu et al., 1975). Measurements of the chemical compositions of different size fractions of lunar soils also show a general enrichment of feldspar components in the

finer sizes over other minerals (Devine et al., 1982; Papike et al., 1982) (Fig. 7.30). It is likely that the cleavage in feldspars is the cause of this preferential fragmentation in both lunar and terrestrial samples, a conclusion that is supported by experimental shock studies (Hörz et al., 1984).

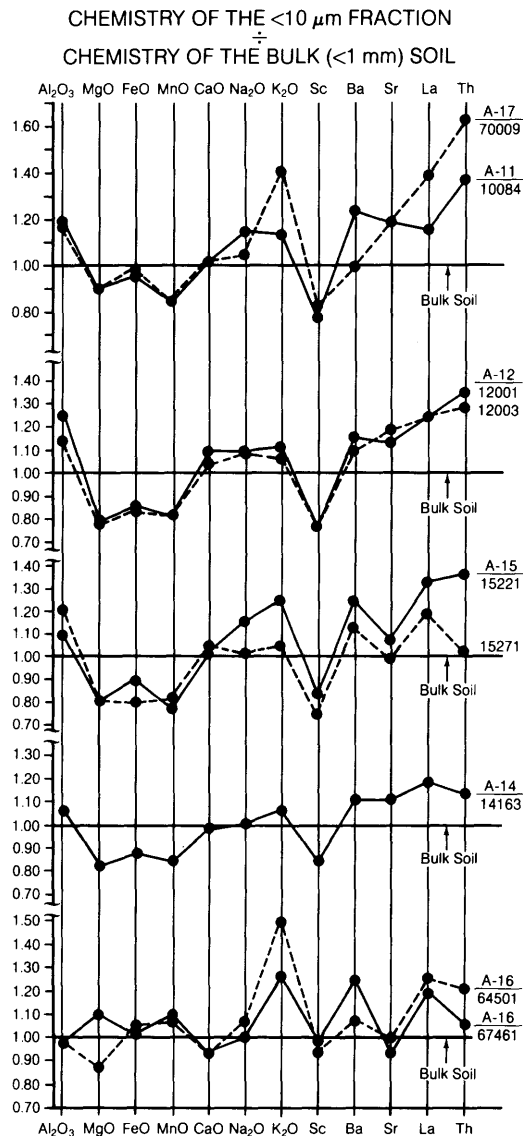


Fig. 7.30. Diagrams showing the ratios of chemical composition of the <10- μ m fraction of nine lunar soils to the composition of the bulk soils (Papike et al., 1982). The data show a general enrichment of feldspar components (Al_2O_3 and Na_2O) and rock mesostasis components (K_2O , Ba, Sr, La, and Th; see section 8.4) in the fine-grain-size fraction relative to the bulk soils from the same samples (normalized to 1).

These studies have also demonstrated that minerals that occur as very small grains in the original parent rocks (e.g., mesostasis minerals in mare basalts, or small olivine “beads” in granulitic breccias) are concentrated into the finer soil fractions (e.g., *Laul et al.*, 1981). It is therefore probable that comminution of lunar rocks occurs, at least partly, along grain boundaries, a phenomenon also observed in terrestrial rocks.

In summary, the grain-size distributions of lunar soils are controlled primarily by random meteoroid impacts, but the distribution of individual minerals in different grain-size fractions also reflects other variables like mineral cleavage and original grain sizes.

7.5.4. Comparison of Soil Chemistry With Bedrock Chemistry

Significant insights into the formation of the lunar regolith can be obtained by comparing the chemical compositions of soils from different landing sites (or from geologically distinct areas within a single site) with the compositions of common lunar rocks. These comparisons are one way to evaluate the degrees to which local, regional, and distant sources of different rock types have contributed to the lunar regolith at any single point. The complexity of regolith formation is indicated by the fact that no lunar soil, or any average composition of several soils from any region, is compositionally identical to any single lunar rock type. Average soil compositions from all lunar sample return missions are given in Table 7.15. Compositions of common rocks in the lunar crust are discussed in Chapter 6.

The most common crustal rock type from the Moon, based on sample returns and chemical measurements made from orbit, is anorthositic gabbro, as represented by samples 15455, 60335 and 66095 (*Taylor*, 1982; *Vaniman and Papike*, 1980). The Apollo 16 and Luna 20 landing sites are well within highland areas, and these sites provide our best samples of the premare lunar crust.

The Apollo 16 soils come closest to being similar to anorthositic gabbros. The average Apollo 16 soil is only slightly enriched in Al and Ca, but is substantially depleted in Mg, in comparison with sample 60335, a typical anorthositic gabbro. It appears that some contribution from relatively pure anorthosite to the average Apollo 16 soil is responsible for these differences in major element abundances. Apollo 16 soils are also slightly depleted in the KREEP component relative to sample 60335, and they have a lower abundances of K, La, U, and Th. In contrast to the Apollo 16 soils, the highland soils

from the Luna 20 site are even less similar to anorthositic gabbro, or, for that matter, to any other lunar crustal rock.

In contrast, the Apollo 11, Luna 16, and Luna 24 soils have been collected from mare areas far from any exposed highland material. Despite their apparent derivation entirely from mare basalt lavas, the soils from these sites differ significantly from samples of mare basalts returned as large rocks. In general, the soils are considerably enriched in Si relative to high-Ti basalts, depleted in Al relative to high-Al basalts, or enriched in Mg relative to low-Ti basalts. The Luna 24 soils and the Apollo 15 soil 15601 (from the edge of Hadley Rille) are the two most mare-basalt-rich soils from the Moon. Except for substantial Mg enrichment, Luna 24 soils are compositionally closest to the very-low-Ti basalts; they are, however, more enriched in the KREEP component.

The differences between these soils and the dominant local bedrock are explained by the addition to the soil of material from a high-Mg gabbroic rock to account for the Mg enrichment (*Basu et al.*, 1978) and by the concentration of mare basalt mesostasis, which is always enriched in the KREEP component and other large-ion lithophile elements, into the finer soil fractions as a result of differential comminution. The Apollo 15 rille-margin soil (sample 15601) is compositionally similar to the Apollo 15 pigeonite basalt sample 15597, except that the soil is depleted in Si and enriched in Mg. In addition, this soil is relatively enriched in KREEP components such as K and La (Tables 7.16 and 7.17). The addition of fragments of local olivine basalt appears able to account for the differences in Si and Mg; preferential concentration of mesostasis, together with some KREEP basalt clasts, into the finer fractions produces the observed trace element differences.

The examples mentioned above, in which soil compositions can be easily related to a few local bedrock sources, actually represent the few exceptions among returned soil samples. Most other lunar soils are compositionally far removed from known lunar rocks.

7.5.5. Variation of Soil Chemistry Within Sites

Extended traverses by astronauts during the Apollo 15, Apollo 16, and Apollo 17 missions provided a collection of soil samples that is large enough to be used to examine variations of soil composition within single landing sites. These landing sites all share a common geomorphic feature: They are located at the boundary between

TABLE 7.15. Chemical compositions (wt.%) of average soils at lunar landing sites and in selected regions at the Apollo 15, Apollo 16, Apollo 17, Luna 16, Luna 20, and Luna 24 sites.

	11	12	14	15a	15b	15c	15	16a	16b	16c	16	17a	17b	17c	17d	17	L16	L20	L24	
SiO ₂	42.2	46.3	48.1	46.7	46.6	47.1	46.8	45.0	44.9	45.1	45.0	40.6	45.1	43.5	43.7	43.2	41.7	45.1	43.9	
TiO ₂	7.8	3.0	1.7	1.7	1.4	1.0	1.4	0.56	0.47	0.60	0.54	8.4	1.7	3.4	3.5	4.2	3.4	0.55	1.3	
Al ₂ O ₃	13.6	12.9	17.4	13.2	17.1	13.4	14.6	27.1	28.0	26.8	27.3	12.0	20.7	18.0	17.4	17.1	15.3	22.3	12.5	
Cr ₂ O ₃	0.30	0.34	0.23	0.44	0.27	0.37	0.36	0.34	0.54	0.11	0.33	0.45	0.25	0.28	0.32	0.33	0.28	–	0.32	
FeO	15.3	15.1	10.4	16.3	11.7	14.9	14.3	5.2	4.7	5.4	5.1	16.7	8.8	10.9	12.2	12.2	16.7	7.0	19.8	
MnO	0.20	0.22	0.14	0.21	0.16	0.19	0.19	0.41	0.27	0.22	0.30	0.23	0.12	0.16	0.16	0.17	0.23	0.13	0.25	
MgO	7.8	9.3	9.4	10.9	10.5	13.0	11.5	5.8	5.6	5.7	5.7	9.9	9.8	10.7	11.1	10.4	8.8	9.8	9.4	
CaO	11.9	10.7	10.7	10.4	11.6	10.3	10.8	15.8	15.7	15.6	15.7	10.9	12.8	12.12	11.3	11.8	12.5	15.1	12.3	
Na ₂ O	0.47	0.54	0.70	0.38	0.45	0.33	0.39	0.46	0.50	0.43	0.46	0.35	0.42	0.42	0.42	0.40	0.34	0.50	0.31	
K ₂ O	0.16	0.31	0.55	0.23	0.20	0.19	0.21	0.13	0.23	0.14	0.17	0.16	0.16	0.12	0.09	0.13	0.10	0.10	0.04	
P ₂ O ₃	0.05	0.4	0.51	0.16	0.19	0.19	0.18	0.13	0.10	0.10	0.11	0.14	0.15	0.09	0.08	0.12	0.12	0.16	0.11	
S	0.12	–	–	0.07	0.08	0.04	0.06	0.07	0.05	0.09	0.07	0.12	0.09	0.07	0.09	0.09	0.21	0.08	0.14	
Total	99.9	99.6	99.8	100.6	100.2	100.9	100.8	100.9	100.9	100.4	100.8	100.1	100.0	99.8	99.9	100.5	99.7	100.8	100.4	
ppm																				
Sc	60	38	23	30	22	24	25.3	9.0	8.0	9.0	8.7	63	17	31	37	37	37	16	34	
U	0.5	1.7	1.5	1.3	–	0.9	0.73	0.53	0.45	0.61	0.53	0.29	0.90	0.44	–	0.41	0.25	0.29	0.26	
Th	1.9	6.4	6.7	3.8	–	3.0	2.3	1.9	1.4	2.8	2.0	0.53	2.7	2.7	1.5	1.9	0.8	0.85	1.1	
La	16	39	70	23	32	24	26.3	11	8	13	10.7	8	15	11	–	8.5	13	5	5	

11 Composition of soil 10002 from Apollo 11 site.

12 Average composition of selected soils (12001, 12023, 12030, 12032, 12033, 12037, 12041, 12042, 12044, 12070) from the Apollo 12 site.

14 Average composition of selected soils (14003, 14148, 14149, 14156) from the Apollo 14 site.

15a Average composition of selected mare soils (15012, 15013, 15020, 15030, 15040, 15070, 15080, 15470, 15500, 15530, 15600) from the Apollo 15 site.

15b Average composition of selected Apennine Front soils (15090, 15100, 15210, 15221, 15230, 15250, 15270, 15290) from the Apollo 15 site.

15c Average composition of selected green-glass-rich soils (15300, 15400, 15410, 15403) from the Apollo 15 site.

15 Average composition of Apollo 15 soils.

16a Average composition of Cayley Plain soil (60050, 60500, 61140, 61161, 61180, 61220, 61240, 61500, 62240, 62280) from the Apollo 16 site.

16b Average composition of selected North Ray soils (63320, 63340, 63500, 67460, 67480, 67600, 67700, 67710, 68500, 68820, 69920, 69940) from the Apollo 16 site.

16c Average composition of selected Stone Mountain and South Ray soils (64420, 64500, 64800, 65500, 65700, 66040, 66080) from the Apollo 16 site.

16 Average composition of Apollo 16 soils.

17a Average composition of selected mare soils (70011, 70160, 70180, 71040, 71060, 71500, 72160, 75060, 75080, 79220, 79240) from the Apollo 17 site.

17b Average composition of selected South Massif and light mantle soils (72320, 72440, 72460, 72500, 73120, 73140, 73220, 73280, 74120) from the Apollo 17 site.

17c Average composition of selected North Massif soils (76246, 76260, 76280, 76320, 76500, 77530) from the Apollo 17 site.

17d Average composition of selected Sculptured Hill soils (78220, 78420, 78440, 78460, 78480) from the Apollo 17 site.

17 Average composition of Apollo 17 soils.

L16 Average composition of Luna 16 soils (Russian data).

L20 Average composition of Luna 20 soils (Russian data; Sc from *Laul and Papike*, 1980).

L24 Average composition of Luna 24 soils (Russian data).

Data Source: *Baedecker et al.* (1974); *Barisal et al.* (1972); *Boynton et al.* (1975, 1976a); *Brunfelt et al.* (1972a,b, 1973a,b); *Carron et al.* (1972); *Christian et al.* (1976); *Compston et al.* (1973); *Cuttitta et al.* (1971); *Duncan et al.* (1973, 1975); *Finkelman et al.* (1975); *Frondel et al.* (1971); *Fruchter et al.* (1974a,b); *Goles et al.* (1971); *Haskin et al.* (1971, 1973); *Korotev* (1976, 1981, 1982); *Krähenbühl et al.* (1973); *Laul and Papike* (1980); *Laul and Schmitt* (1973b); *Laul et al.* (1972, 1974); *Lindstrom et al.* (1972); *LSPET* (1972, 1973a,b); *Mason et al.* (1973); *Masuda et al.* (1972); *Müller et al.* (1974); *Morgan et al.* (1972); *Philpotts et al.* (1972, 1974); *Rhodes et al.* (1974); *Rose et al.* (1972, 1973, 1974, 1975); *Schnetzler and Philpotts* (1971); *Simkin et al.* (1973); *Tarasov et al.* (1977); *Taylor et al.* (1973); *Vinogradov et al.* (1973); *Wakita et al.* (1971); *Wänke et al.* (1973; 1974; 1975); *Warren et al.* (1978); *Willis et al.* (1972); *Woodcock and Pillinger* (1978).

TABLE 7.16. Major and minor element abundances (wt.%) in bulk soils and separated size fractions of "reference suite" lunar soils and sample 15601 (*Papike et al.*, 1982; *LSPET*, 1972).

Sample	Size, μm	SiO ₂	TiO ₂	Al ₂ O ₃	FeO	MgO	CaO	Na ₂ O	K ₂ O	MnO	Cr ₂ O ₃	Total
10084,1591	Bulk	41.3	7.5	13.7	15.8	8.0	12.5	0.41	0.14	0.213	0.290	99.8
	>90	41.6	7.4	13.1	16.1	8.0	12.5	0.42	0.14	0.205	0.300	99.9
	20-90	41.0	7.3	12.8	16.2	9.2	12.4	0.38	0.15	0.220	0.305	99.9
	10-20	41.5	7.3	14.6	15.8	7.5	11.4	0.43	0.15	0.200	0.295	99.2
	<10	41.3	7.3	16.3	15.1	7.2	12.7	0.47	0.16	0.180	0.290	101.0
12001.599	Bulk	46.0	2.8	12.5	17.2	10.4	10.9	0.48	0.26	0.220	0.410	101.1
	>90	45.8	2.5	11.8	17.7	11.2	10.0	0.46	0.25	0.219	0.414	100.3
	20-90	45.8	2.7	11.7	17.7	10.7	10.3	0.44	0.22	0.230	0.420	100.2
	10-20	45.7	3.1	13.2	17.2	9.9	10.7	0.50	0.26	0.200	0.460	101.2
	<10	45.0	3.0	15.6	14.8	8.2	12.0	0.53	0.29	0.180	0.410	100.0
12033.464	Bulk	46.9	2.3	14.2	15.4	9.2	11.1	0.67	0.41	0.195	0.387	100.8
	>90	48.0	2.4	13.5	14.5	10.2	10.2	0.71	0.44	0.200	0.360	100.5
	20-90	45.9	2.6	12.5	16.9	9.8	10.6	0.62	0.33	0.220	0.385	99.9
	10-20	46.6	2.5	14.8	15.0	9.7	11.1	0.65	0.39	0.190	0.350	101.2
	<10	47.3	2.6	16.2	13.0	7.2	11.5	0.73	0.44	0.160	0.330	99.5
14163.778	Bulk	47.3	1.6	17.8	10.5	9.6	11.4	0.70	0.55	0.135	0.200	99.8
	>90	48.0	1.6	17.3	10.4	10.7	11.3	0.71	0.58	0.140	0.190	100.9
	20-90	46.2	1.6	17.1	11.1	10.7	11.5	0.68	0.52	0.143	0.205	99.8
	10-20	48.0	1.5	17.5	10.2	9.8	10.9	0.69	0.54	0.135	0.190	99.5
	<10	48.5	1.7	19.0	9.2	8.0	11.3	0.71	0.59	0.115	0.190	99.3
15221,29	Bulk	46.0	1.1	18.0	11.3	10.7	12.3	0.43	0.16	0.154	0.325	100.5
	>90	46.4	1.0	17.5	12.0	11.0	11.7	0.46	0.19	0.159	0.305	100.7
	20-90	46.5	1.1	16.7	12.1	11.4	11.3	0.42	0.16	0.162	0.335	100.2
	10-20	47.0	1.1	18.0	11.4	9.6	11.7	0.42	0.19	0.145	0.318	100.0
	<10	46.5	1.2	19.8	10.2	8.6	12.6	0.50	0.20	0.120	0.305	100.0
15271,27	Bulk	46.0	1.5	16.4	12.8	10.8	11.7	0.49	0.22	0.162	0.350	100.4
	>90	47.0	1.3	15.5	13.2	11.7	10.8	0.50	0.22	0.167	0.370	100.7
	20-90	45.9	1.4	15.3	13.8	11.8	11.0	0.49	0.20	0.175	0.381	100.4
	10-20	45.7	1.4	17.1	12.4	10.0	11.7	0.50	0.20	0.157	0.360	99.5
	<10	46.0	1.5	19.8	10.3	8.7	12.3	0.50	0.23	0.133	0.300	99.8
64501.122	Bulk	45.3	0.37	27.7	4.2	4.9	17.2	0.44	0.10	0.056	0.090	100.3
	>90	45.5	0.45	27.9	4.5	4.4	16.8	0.40	0.090	0.060	0.085	100.2
	20-90	44.8	0.33	27.2	4.3	5.1	16.8	0.43	0.099	0.055	0.090	99.2
	10-20	45.2	0.38	27.9	4.4	5.0	16.1	0.44	0.11	0.060	0.090	99.7
	<10	45.6	0.45	27.4	4.4	4.3	16.1	0.47	0.15	0.060	0.100	99.0
67461,74	Bulk	45.0	0.29	29.2	4.2	3.9	17.6	0.43	0.055	0.055	0.075	100.8
	>90	45.3	0.29	28.7	4.3	3.9	17.2	0.42	0.050	0.060	0.080	100.3
	20-90	44.4	0.40	28.8	4.5	4.6	17.2	0.43	0.055	0.062	0.084	100.5
	10-20	44.3	0.40	29.3	4.4	4.0	17.6	0.42	0.062	0.065	0.087	100.6
	<10	45.1	0.29	28.6	4.3	4.3	16.5	0.43	0.070	0.060	0.088	99.7
72501,15	Bulk	45.2	1.4	20.1	9.50	10.0	12.5	0.44	0.17	0.120	0.230	99.7
	>90	45.9	1.1	20.2	8.80	10.3	13.4	0.51	0.17	0.110	0.220	100.7
	20-90	45.2	1.6	19.4	10.0	11.0	12.9	0.43	0.14	0.120	0.250	101.0
	10-20	45.1	1.6	20.6	9.10	10.4	12.7	0.44	0.16	0.100	0.230	100.4
	<10	—	1.4	20.6	8.60	8.5	12.2	0.43	0.17	0.096	0.230	—

TABLE 7.16. (continued).

Sample	Size, μm	SiO ₂	TiO ₂	Al ₂ O ₃	FeO	MgO	CaO	Na ₂ O	K ₂ O	MnO	Cr ₂ O ₃	Total
76501,48	Bulk	43.4	3.2	18.1	10.8	12.0	12.8	0.38	0.10	0.145	0.270	101.2
	>90	43.7	3.1	18.5	10.3	12.3	12.8	0.38	0.10	0.130	0.260	101.5
	20-90	42.7	3.5	16.7	12.0	12.7	11.4	0.37	0.10	0.150	0.300	99.9
	10-20	41.8	3.4	18.7	11.6	11.1	13.0	0.38	0.10	0.147	0.290	100.5
	<10	41.6	3.2	20.2	10.6	9.8	12.7	0.40	0.12	0.130	0.280	99.0
78221,71	Bulk	43.0	4.2	17.0	12.6	11.0	12.4	0.37	0.10	0.163	0.350	101.1
	>90	42.0	4.1	16.5	12.7	11.9	11.9	0.39	0.10	0.154	0.360	100.1
	20-90	43.4	4.2	16.0	13.7	11.8	11.9	0.37	0.090	0.168	0.360	101.9
	10-20	41.8	4.2	17.3	12.2	10.7	11.9	0.36	0.10	0.160	0.325	99.5
	<10	43.9	3.9	19.0	11.9	9.3	12.4	0.40	0.12	0.135	0.320	101.4
Luna 16 21000,5	Bulk	—	3.5	15.5	16.5	8.1	11.8	0.38	0.11	0.230	0.300	—
	>90	—	3.4	15.5	16.4	8.1	12.4	0.41	0.12	0.230	0.300	—
	20-90	—	3.2	14.0	17.6	9.0	11.4	0.37	0.10	0.220	0.323	—
	10-20	—	3.8	14.0	16.6	8.5	11.4	0.36	0.11	0.219	0.320	—
	<10	—	3.0	16.7	13.0	6.6	11.5	0.40	0.13	0.170	0.280	—
Luna 20 22001,35	Bulk	—	0.48	23.5	7.27	9.7	14.1	0.35	0.068	0.100	0.180	—
	>90	—	0.43	21.2	6.68	8.8	13.7	0.34	0.066	0.090	0.170	—
	20-90	—	0.50	22.8	8.00	9.6	14.4	0.32	0.063	0.120	0.210	—
	10-20	—	0.46	20.5	8.00	9.5	12.3	0.34	0.065	0.107	0.210	—
	<10	—	0.50	25.0	6.25	7.2	14.9	0.36	0.078	0.070	0.170	—
Luna 24 24999,6	Bulk	—	1.0	11.7	20.2	9.7	11.1	0.27	0.027	0.270	0.467	—
	>90	—	0.97	10.6	20.5	10.8	10.7	0.23	0.017	0.280	0.410	—
	20-90	—	1.1	11.4	20.8	10.3	10.8	0.25	0.024	0.290	0.450	—
	10-20	—	1.3	11.7	19.5	9.0	10.8	0.30	0.040	0.229	0.510	—
	<10	—	1.0	14.7	13.8	8.0	10.7	0.37	0.066	0.162	0.400	—
Apollo 15 15601	Bulk	45.05	1.98	10.2	19.8	10.9	9.9	0.29	0.10	0.26	0.56	—

the bottom of a hill and the edge of a plain. At the Apollo 15 and Apollo 17 sites, the plains consist of mare basalt flows; at the Apollo 16 site, the plain consists mainly of fragmental highland rocks. The hills at all these sites are composed of highland material that may have been ejected from the interiors of large impact basins (*Head, 1976b, 1977*).

Apollo 17. At the Apollo 17 landing site, strong contrasts are observed between soils from the mare plain and from the adjoining South Massif light mantle deposit (analyses 17a and 17b in Table 7.15). Soils from the plain were derived largely from mare basalts. The massif soils were derived mostly from highland material, and are enriched in the feldspar components CaO and Al₂O₃. These differences indicate that the soil compositions are controlled mostly by local bedrock compositions; the sharp contrast in albedo between these two adjacent areas also supports this conclusion. Small differences in

soil compositions between the South Massif and the North Massif suggest that the South Massif is a little more anorthositic (Ca- and Al-rich) than the North Massif, the latter being more enriched in gabbroic components Mg and Fe. It is interesting to note that a model soil composition, produced by mixing together equal quantities of soil from all of the four distinct geomorphic areas of the Apollo 17 site, is nearly identical to that of the soil sampled in the Sculptured Hills area (see Fig. 10.28).

Apollo 15. Variations in soil compositions are also seen in the different geomorphic areas at the Apollo 15 site. The relatively flat, bay-like area below the Apennine Front and adjacent to Hadley Rille is apparently composed of thin mare basalt lava flows that range in composition from higher SiO₂ (quartz-normative) to lower SiO₂ (olivine-normative). Some pyroclastic deposits and KREEP basalt flows are also intercalated with the basalt flows (*Spudis and Ryder,*

TABLE 7.17. Trace element abundances (parts per million) in bulk soils and separated size fractions of “reference suite” lunar soils and sample 15601 (*Papike et al.*, 1982; *Brunfelt et al.*, 1972a).

Sample	Size, μm	V	Co	Ba	Sr	La	Ce	Nd	Sm	Eu	Tb	Dy	Ho	Tm	Yb	Lu	Hf	Ta	Th	U	Ni*
10084,1591	Bulk	60.2	7028.0	170160	15.8	43	37	11.4	1.60	2.917	4.1	1.6	10.0	1.39	9.00	1.25	1.90	0.5	200		
	>90	64.7	7030.5	160160	15.4	44	36	11.8	1.65	3.018	4.3	1.6	10.3	1.47	8.90	1.20	2.00	0.5	230		
	20–90	66.4	8028.4	150160	14.9	42	36	11.9	1.60	3.018	4.3	1.6	10.6	1.53	8.95	1.20	1.90	0.5	190		
	10–20	55.3	7030.3	180180	15.4	44	37	11.4	1.70	2.918	4.2	1.5	10.0	1.43	9.32	1.30	2.00	0.5	290		
	<10	46.9	7037.4	210190	18.3	52	40	12.8	1.95	2.918	4.2	1.5	10.1	1.43	9.60	1.40	2.60	0.7	450		
12001,599	Bulk	40.2	11042.5	430140	35.6	85	57	17.3	1.85	3.722	5.0	1.8	13.0	1.85	11.8	1.50	5.40	—	190		
	>90	42.0	12043.0	420130	34.7	87	57	16.7	1.85	3.822	4.8	2.0	12.6	1.80	11.8	1.60	5.70	1.7	150		
	20–90	42.0	12045.2	380120	31.1	78	54	15.2	1.70	3.420	4.8	1.9	11.9	1.70	11.6	1.50	5.10	1.4	210		
	10–20	38.0	11046.2	410130	36.3	95	63	17.5	1.95	3.521	5.0	2.1	13.0	1.85	13.3	1.65	6.40	1.7	400		
	<10	31.0	10041.0	500160	44.6	112	75	21.4	2.15	4.326	6.2	2.3	14.5	2.05	12.8	1.75	7.30	2.0	600		
12033,464	Bulk	36.4	10034.3	600160	50.0	133	85	22.8	2.45	4.930	7.2	2.6	17.3	2.45	16.6	2.20	8.50	2.4	130		
	>90	34.6	10031.3	670160	60.7	150	95	27.7	2.60	5.634	7.8	3.2	20.8	2.96	21.2	2.60	10.2	2.6	110		
	20–90	40.7	10039.5	530150	43.6	112	74	20.5	2.20	4.326	6.5	2.3	16.2	2.40	17.0	2.10	7.50	2.2	190		
	10–20	34.5	10032.3	540170	43.0	120	76	19.0	2.30	4.425	6.4	2.5	15.5	2.20	17.0	2.10	8.40	2.1	220		
	<10	28.2	9032.0	660190	62.4	170	105	28.4	2.70	5.733	8.0	3.0	19.2	2.70	15.2	2.30	10.8	2.7	600		
14163,778	Bulk	21.7	4533.0	800170	66.7	170	100	29.1	2.45	5.936	8.6	3.2	21.2	3.00	22.5	2.90	13.3	3.5	350		
	>90	21.1	3532.5	800180	73.0	185	110	30.2	2.40	6.340	9.4	3.6	23.4	3.20	23.5	2.90	14.7	3.5	380		
	20–90	23.5	5035.5	730160	60.6	154	95	25.2	2.30	5.435	8.6	3.2	20.5	2.90	22.0	2.80	12.4	3.1	380		
	10–20	21.3	4530.5	780160	63.4	160	103	26.4	2.30	5.536	8.6	3.2	20.2	2.85	22.0	2.90	12.4	3.3	480		
	<10	18.5	4031.0	890190	79.1	200	120	33.7	2.65	6.541	10	3.6	22.4	3.16	20.2	3.10	15.2	4.0	690		
15221,29	Bulk	21.2	8041.0	240120	20.5	54	36	9.70	1.30	2.012	2.9	1.1	6.90	0.97	6.70	0.93	3.00	—	360		
	>90	22.7	7034.5	250140	22.6	58	40	10.8	1.50	2.113	3.1	1.2	8.10	1.15	7.50	0.96	3.30	1.0	220		
	20–90	22.7	8537.0	210120	20.0	50	32	9.56	1.20	2.012	2.9	1.1	7.10	1.00	6.60	0.90	3.10	0.9	220		
	10–20	20.8	7035.5	250130	22.1	59	36	10.7	1.40	2.213	3.2	1.2	7.60	1.10	7.60	1.00	3.75	1.0	290		
	<10	17.8	7536.0	300130	27.2	69	44	12.5	1.60	2.615	3.7	1.2	8.20	1.15	7.60	1.10	4.10	1.3	640		
15271,27	Bulk	24.3	8040.5	300130	25.8	70	45	12.0	1.50	2.615	3.9	1.4	8.54	1.20	8.60	1.20	4.60	1.2	230		
	>90	26.1	8539.0	280130	27.1	70	44	12.6	1.60	2.715	3.9	1.3	9.00	1.27	9.00	1.10	4.30	1.3	200		
	20–90	26.5	8041.0	280130	25.7	66	43	12.2	1.50	2.615	3.9	1.4	9.00	1.27	9.30	1.20	4.10	1.1	200		
	10–20	23.4	8039.0	280130	25.9	70	46	12.3	1.50	2.515	3.9	1.3	8.75	1.25	9.40	1.20	4.30	1.2	370		
	<10	18.3	7036.4	340130	31.0	82	54	14.4	1.70	2.716	3.9	1.4	9.20	1.30	8.20	1.30	4.72	1.2	700		
64501,122	Bulk	8.0	2019.5	130170	10.8	28	19	4.79	1.05	1.0	6.0	1.40	0.55	3.40	0.49	3.30	0.45	1.85	0.4	300	
	>90	8.9	2021.0	120160	10.6	27	18	4.70	1.10	1.060	1.40	0.60	3.60	0.51	3.50	0.43	1.70	0.5	340		
	20–90	7.8	1520.1	120160	10.8	27	18	4.70	1.10	1.064	1.50	0.56	3.50	0.50	3.50	0.45	1.80	0.5	320		
	10–20	8.2	2017.9	130160	11.5	30	20	5.20	1.05	1.1	6.5	1.60	0.60	3.90	0.55	3.80	0.47	1.85	0.5	400	
	<10	7.6	2022.5	140170	13.6	34	22	5.83	1.15	1.2	7.5	1.80	0.65	4.00	0.54	4.00	0.54	2.25	0.55	850	

TABLE 7.17. (continued).

Sample	Size, μm	Sc	V	Co	Ba	Sr	La	Ce	Nd	Sm	Eu	Tb	Dy	Ho	Tm	Yb	Lu	Hf	Ta	Th	U	Ni*
67461,74	Bulk	7.8	20	9.0	60	170	4.67	12	7.2	2.00	1.00	0.45	2.8	—	0.25	1.60	0.22	1.60	0.24	0.83	—	80
	>90	8.4	20	10	60	160	4.40	11	7.0	2.00	0.95	0.43	2.9	—	0.24	1.55	0.21	1.30	0.20	0.82	—	100
	20-90	8.1	20	14	70	170	4.78	12	7.7	2.17	0.98	0.47	3.0	—	0.27	1.73	0.26	1.50	0.24	0.81	—	170
	10-20	8.1	20	9.2	70	170	4.85	12	8.3	2.20	0.98	0.44	3.0	—	0.28	1.76	0.25	1.70	0.22	0.83	—	200
	<10	7.7	15	9.5	75	160	5.60	15	10	2.44	1.00	0.56	3.2	—	0.33	1.80	0.26	1.95	0.25	0.89	—	540
72501,15	Bulk	20.0	45	33.0	210	160	16.2	46	29	8.00	1.30	1.6	10.0	—	0.84	5.90	0.82	6.00	0.90	3.00	1.0	260
	>90	18.6	45	27.0	230	180	18.6	49	30	8.75	1.40	1.7	11.7	—	0.98	6.50	0.93	6.50	0.90	3.50	1.0	240
	20-90	21.5	50	31.0	210	170	15.1	40	27	7.70	1.25	1.6	10.7	—	0.84	6.00	0.90	6.40	0.85	3.00	1.0	260
	10-20	19.4	50	28.7	210	180	15.5	42	26	7.63	1.30	1.6	10.5	—	0.89	5.70	0.80	6.00	0.80	2.80	0.8	340
	<10	17.2	45	30.0	210	190	17.5	46	30	8.10	1.30	1.6	10.5	—	0.86	5.70	0.79	5.60	0.95	3.20	0.9	700
76501,48	Bulk	28.0	65	30.4	120	160	8.30	23	16	5.30	1.20	1.2	8.3	—	0.71	4.60	0.66	4.20	0.70	1.60	0.4	190
	>90	27.7	50	32.6	130	160	8.30	22	17	5.30	1.20	1.2	8.0	—	0.70	4.40	0.64	4.20	0.72	1.50	0.4	220
	20-90	32.5	70	32.5	120	160	8.20	23	16	5.40	1.25	1.3	8.2	—	0.71	4.70	0.72	4.60	0.80	1.60	0.4	220
	10-20	28.9	60	31.0	120	160	8.80	26	18	5.75	1.25	1.3	8.3	—	0.69	4.60	0.66	4.80	0.80	1.75	0.4	300
	<10	24.5	60	32.0	150	190	10.4	29	20	6.30	1.35	1.4	8.6	—	0.71	4.70	0.68	4.70	0.80	2.00	0.5	600
78221,71	Bulk	36.3	70	40.0	120	160	8.10	24	16	5.46	1.25	1.3	8.4	—	0.72	4.70	0.70	4.70	0.86	1.60	0.4	200
	>90	39.8	70	37.0	140	160	8.00	23	17	5.55	1.25	1.3	8.7	—	0.71	4.90	0.73	4.60	0.85	1.40	0.4	250
	20-90	39.5	75	35.0	110	160	8.30	24	18	5.75	1.30	1.3	8.5	—	0.74	5.10	0.75	4.90	0.85	1.40	0.4	230
	10-20	33.2	75	34.5	120	160	8.90	26	18	5.80	1.30	1.3	9.1	—	0.75	4.90	0.74	5.10	1.00	1.60	0.4	350
	<10	29.3	65	36.5	170	170	11.4	30	22	6.90	1.50	1.5	10.0	—	0.81	5.40	0.79	5.00	0.93	1.85	0.4	600
Luna 16 21000,5	Bulk	52.0	80	29.6	180	260	11.6	33	26	8.25	2.15	1.7	11	—	0.90	5.70	0.80	7.04	0.50	1.39	0.4	200
	>90	52.0	85	29.4	170	270	12.5	35	27	8.70	2.30	1.7	11	—	0.85	5.80	0.80	7.50	0.53	1.33	0.4	190
	20-90	58.0	85	28.9	180	220	11.0	33	24	7.80	2.10	1.6	11	—	0.80	5.40	0.76	7.00	0.51	1.25	0.4	600
	10-20	50.5	80	30.7	300	220	11.1	31	26	7.95	1.90	1.6	11	—	0.86	5.50	0.81	6.90	0.49	1.27	0.4	1000
	<10	35.0	60	36.6	330	290	11.7	32	25	7.30	2.10	1.5	10	—	0.75	4.70	0.73	6.30	0.55	1.52	0.4	2700
Luna 20 22001,35	>125	15.4	40	31.6	100	130	7.20	17	12	3.20	0.90	0.65	4.2	—	0.37	2.55	0.35	2.30	0.28	1.32	—	300
	90-125	15.2	35	26.2	80	120	6.50	16	10	2.80	0.82	0.61	4.3	—	0.36	2.45	0.34	2.00	0.23	1.20	—	300
	20-90	18.6	50	26.0	80	120	6.60	17	10	2.80	0.85	0.62	4.4	—	0.38	2.45	0.33	2.15	0.28	1.20	—	390
	10-20	16.9	40	31.7	80	110	6.30	15	11	2.70	0.85	0.62	4.5	—	0.40	2.40	0.35	2.50	0.31	0.90	—	1000
	<10	12.3	40	30.7	130	130	7.60	19	12	3.30	0.92	0.66	4.6	—	0.37	2.40	0.34	2.40	0.38	1.45	—	1000
Luna 24 24999,6	Bulk	44.0	150	47.0	40	80	2.40	6.1	5.0	1.70	0.59	0.43	2.7	—	—	1.75	0.27	1.20	0.17	0.40	—	110
	>90	43.5	150	50.0	30	70	1.90	4.9	4	1.30	0.55	0.3	2.2	—	—	1.40	0.22	1.00	0.11	0.16	—	140
	20-90	43.7	140	50.0	40	80	2.75	7.3	6.0	1.90	0.62	0.5	3.0	—	—	2.00	0.29	1.30	0.18	0.38	—	170
	10-20	37.2	130	50.5	80	80	3.40	9.0	6.0	2.20	0.70	0.53	3.2	—	—	2.10	0.32	1.70	0.30	0.50	—	1500
	<10	24.0	90	36.1	100	80	5.30	13	10	2.70	0.80	0.60	3.8	—	0.36	2.10	0.30	2.00	0.28	0.91	—	1700
Apollo 15 15601	Bulk	35.1	200	48.9	135	—	11.3	29	—	6.3	1.01	1.33	9.7	—	—	5.2	0.9	4.9	0.60	1.52	0.46	170

* The Ni values are suspect of contamination from the Rh-plated Ni sieves.

* The Ni values are suspect of contamination from the Rh-plated Ni sieves.

1985; Figs. 10.21 and 10.22). The average soil compositions from this embayment are unlike that of any single rock type; instead they are intermediate between the compositions of the three different basalt types.

The average composition of the soils from the Apennine Front, including those ejected from Elbow Crater, is distinctly different from that of the embayment soils. Significant differences also exist on the Apennine Front itself. The average composition of the soils near Spur Crater, which are rich in green glass deposits, are clearly distinct from other Apennine Front soils. Spur Crater soils are significantly more magnesian than average Apollo 15 soils because of the abundance of the high-Mg green glasses.

It appears that there has been more mixing of fragments from the local bedrock into the soil over larger areas at the Apollo 15 site than at the Apollo 17 site. Albedo and other remotely sensed properties measured at the Apollo 15 site do not clearly define geologic units, in sharp contrast to the Apollo 17 site, where specific units could be readily distinguished. This result suggests that the boundaries between surficial units at the Apollo 15 site are more gradational than at the Apollo 17 site, implying a higher degree of mixing and transport of surface materials. In addition, compositional variations among soils from different areas of the Apollo 15 site are also less pronounced than at the Apollo 17 site.

Apollo 16. In comparison with the Apollo 15 and Apollo 17 sites, the Apollo 16 site is remarkably uniform. At this location there are only small variations in albedo, other remotely sensed properties, and the compositions of large rocks. The important geomorphic features are the hills north and south of the Cayley Plain, on which the lunar module landed (see Fig. 10.25). The average compositions of soils collected from the bases of these two hills and from the plains between them are remarkably similar. Only minor differences exist between the soils collected near Smoky Mountain, in the north, and those collected from Stone Mountain, in the south. The northern soils are slightly less magnesian, more enriched in Al and Cr, and somewhat depleted in U, Th, and La, although K is more abundant in the northern soils. The average composition of soils from the Cayley Plain, between the two hills, is intermediate between those of the northern and southern soils. However, the differences between the averages are small, and firm conclusions regarding mixing cannot be made.

The bedrock at the Apollo 16 site is composed of anorthositic gabbros and anorthosites, both of which are found in a highly shattered (cataclastic) state. The largest rock samples are generally crystalline breccias. It is likely that these breccias, which are

themselves mixtures of several rock types (see sections 6.3 and 6.4), control the bulk of soil compositions at the Apollo 16 site and account for the apparent overall uniformity. A similar situation may exist at all highland areas of the Moon in which similar breccias are probably the dominant rock types.

Local control of regolith chemistry. The chemical variations observed between different soil samples at the three landing sites suggest that the primary factors controlling soil composition are the compositions of the local bedrock and the proportions of different bedrock types in a given soil sample. If soil compositions were completely controlled by the regional compositions of rock types, the soils within a single landing site would be uniform, a situation that is not observed.

7.5.6. Variation of Soil Chemistry Between Sites

Because the average soil compositions are primarily controlled by local bedrock, the variations of soil composition from site to site should reflect the variation of the average bedrock compositions at each site. If this is correct, then there are significant differences in lunar bedrock compositions, not only between maria and highland regions, but at different areas within these regions.

Both the Apollo 16 and Luna 20 sites are in similar-appearing highland regions, but the average composition of Luna 20 soils is much more mafic than those at the Apollo 16 site (Table 7.15). The Luna 20 site is located in a highland region relatively close to Mare Fecunditatis, and it is possible that there has been an appreciable contribution of material from the mare to the Luna 20 site. However, this explanation seems unlikely; the boundary between mare and highlands in this region is sharp, as indicated by both topography and albedo changes, implying that there has been little lateral migration of surface material. It is more likely that the composition of Luna 20 soils reflects the addition of an unknown mafic highland rock present near the site itself.

The Apollo 11, Apollo 12, Luna 16, and Luna 24 missions all landed on areas of mare basalt flows fairly far away from any highlands; despite this, the soil compositions from these missions are quite distinct from each other. The Apollo 11 soils are rich in Ti, Luna 16 soils have the highest Al of sampled mare soils, and Luna 24 soils are enriched in Fe. Apollo 11 soils have the highest abundance of Sc; Apollo 12 soils are significantly enriched in K, U, Th, and La; Luna 16 and Luna 24 soils are depleted in U, Th, and La. These variations and related differences have also been observed with Earth-based

telescopic spectral studies and in measurements of gamma-ray and X-ray intensities made from lunar orbit during the later Apollo missions. In addition, the average compositions of mare soils from the Apollo 15 and Apollo 17 sites each have their own distinctive character.

The chemical data from lunar soils therefore suggest that the nine different regions of the Moon from which we have soil samples are composed of significantly different rock types. These rocks have been shattered, pulverized, differentially comminuted, and mixed to produce soils with a wide range of different compositions. The soils therefore reflect the local bedrock. Even though small amounts of exotic and distant materials are found in the soils from all missions, usually in the finer grain-size fractions, these occur in such small amounts that bulk soil compositions are not significantly affected.

7.6. REGOLITH BRECCIAS

Ancient regolith. Ballistic ejection from impact craters, together with gravitational creep, tend to emplace newer soils on top of older soils, burying them. However, even deeply buried soils may subsequently be ejected by larger meteoroid impacts and reexposed at the lunar surface. The irradiation histories deduced from discrete soil layers in some regolith cores reveal that such processes of burial and reexposure have, in fact, been operative at the surface of the Moon. It is therefore theoretically possible that some shallow cores can actually penetrate and sample layers of very old (i.e., >4.0 b.y.) regolith, which has been excavated and reexposed at or near the lunar surface. However, a more definite source of samples of such ancient regolith has already been provided in the form of a group of samples called *regolith breccias*.

Characteristics of regolith breccias. Regolith breccias are polymict breccias that contain rock, mineral, and glass fragments in a glassy matrix (see also section 6.4.8). The presence of glass fragments and agglutinates within these breccias shows clearly that they have formed from earlier regolith deposits (Stöffler *et al.*, 1980).

Regolith breccias are abundant among the samples returned by the Apollo 11 astronauts, and early studies showed that they were formed from the local regolith. There was considerable early debate about the process that had indurated the originally loose regolith particles into a more or less coherent rock. Most investigators (e.g., King *et al.*, 1970; Quaide and Bunch, 1970) concluded that the breccias were *shock-lithified*, i.e., compacted and indurated by the

action of shock waves passing through the regolith, generated by nearby meteoroid impacts. McKay *et al.* (1970) and Duke *et al.* (1970b) disagreed and said that the breccias were more analogous to hot welded deposits of volcanic ash. In particular, McKay *et al.* (1970) stated that the breccias were too porous and the materials in them not shocked enough to be consistent with shock lithification.

However, subsequent experimental studies have shown that the lunar regolith can be shock-lithified at pressures as low as 170 kbar (Schaal and Hörz, 1980; Simon *et al.*, 1986b). This result reflects the fact that the lunar soil is porous, and the pores collapse rapidly during passage of the compressive phase of the shock wave. During this collapse, the fine soil particles are efficiently melted by the resulting frictional heat. The small-scale melts then quickly cool to glass, bonding the unmelted soil particles to form a coherent rock. The materials used in shock-wave experiments did not retain any of their original porosity. It is therefore possible that some regolith breccias, which still retain considerable porosity, have formed at even lower shock pressures. This possibility has yet to be confirmed experimentally.

In a survey of Apollo 11 and Apollo 12 regolith breccias, Chao *et al.* (1971) distinguished four groups on the basis of texture: (1) porous and unshocked, (2) shock-compressed but still porous, (3) glass-welded, and (4) thermally metamorphosed and recrystallized. The coherence of these samples varies from extremely friable (crumbly) to very coherent. These characteristics reflect not only the intensity of the events that formed the breccias, but also their postformation histories. For example, porous breccias were probably formed at low shock pressure without suffering any later impacts, whereas the more compressed or welded breccias probably formed by more intense shock waves (closer to the impact) or were shocked again by later impacts.

These regolith breccias are important because they represent samples of old regolith that have been protected from the processes of maturation and mixing since the breccia formed. Some of the breccias are ancient, having formed between 500 and 1500 m.y. ago. Over these long periods of time, further maturation and mixing of the original regolith will produce significant changes in the composition and properties between the regolith and the ancient material preserved in these breccias. Even over long periods of time, these differences are subtle, and detailed petrologic and chemical data are needed to identify them. Such data already exist for soils (Papike *et al.*, 1982), and similar data have recently been collected for some regolith breccias, using the members of the regolith breccia reference suite selected by Fruland (1983).

Results for Apollo 11 regolith breccias (*Simon et al.*, 1984) show that they were formed locally; their compositions can be modeled closely by using appropriate proportions of local bedrock and soils. However, the breccias contain different populations of glass and plagioclase feldspar than the present-day soils, and they also have a higher ratio of high-K basalt to low-K basaltic components than do the soils. Although the exposed soil has been open to the addition of exotic materials much longer than have the breccias, both the present-day soil and the ancient breccias have similar amounts of highland components, indicating that little or no addition of highland material to the Apollo 11 site has occurred since the formation of the breccias.

By contrast, only five of the eleven Apollo 12 regolith breccias studied (*Simon et al.*, 1985) could be modeled by using the compositions of present-day Apollo 12 soils. One breccia (sample 12034) that could not be modeled was extremely KREEP-rich and clearly originated in a very different source regolith. Two other breccia samples were formed from anorthositic soils representing either a source exotic to the Apollo 12 site or perhaps the local premare regolith, present before eruption of the mare basalt lavas.

The Apollo 15 site is geologically diverse, with a highland-mare contact to the south and the deep Hadley Rille to the west. There are gradients with distance in the compositions of the regolith in both directions from the highland-mare contact (*Basu and McKay*, 1979). Mare components become more abundant toward the mare, and highland components increase toward the highlands. The Apollo 15 regolith breccias appear to have formed from local materials at the site (*Bogard et al.*, 1985; *Korotev*, 1985; *Simon et al.*, 1986a), and they can therefore provide information on local regolith dynamics and evolution.

Simon et al. (1986a) showed that most of the breccias collected at the Apollo 15 site had not traveled far from where they were formed. Except for an anomalously KREEPy breccia (sample 15205) and one (sample 15306) with less green volcanic glass than the corresponding soil, each breccia is compositionally similar to the regolith at the spot (station) where it was collected. Comparison of the rock and mineral components of breccias and soils from the same station yields insights into regolith evolution over the whole site. For example, breccias collected at the edge of Hadley Rille contain slightly higher highland components than the soil there. This effect can be explained by the location; there is a continuous loss of regolith particles by gravitational creep into the rille, and the lost material is steadily replaced by material excavated from the mare

bedrock under the thin regolith. Thus, any basalt particles lost into Hadley Rille are efficiently replaced by local mare material, but highland fragments are not, because the sources of highland material are more distant. As time passed, the regolith became progressively richer in mare basalt components, while the breccias stayed the same, and the regolith has evolved to a point where the difference is detectable.

On the other hand, soils from the highland stations at the Apollo 15 site are slightly richer in highland components than are the corresponding regolith breccias. This observation can also be explained by the morphology of the site. The highland samples were collected at the base of the Apennine Front, a mountain of highland rock that rises above the mare plain. With time, loose material from higher up on the mountain creeps or rolls down to collect at the base, enriching the soils there in highland materials while the breccias, which were formed much earlier, do not evolve. The fact that we can observe and explain such contrasts between breccias and soils demonstrates that both the geology and morphology of the Apollo 15 site has remained essentially the same since the mare basalts were erupted there more than 3×10^9 yr ago.

A multidisciplinary study of Apollo 16 regolith breccias that included petrography, chemistry, texture analysis, and attempts at age-dating the individual breccia components has been completed by *McKay et al.* (1986). They found, as did *Simon et al.* (1988), that the breccias are generally similar to the soils, except that agglutinate contents are higher in the soils. Although the Apollo 16 regolith breccias were apparently formed locally, their compositions do not correlate closely with the compositions of soils collected at the same stations.

McKay et al. (1986) disaggregated two breccias, measured surface irradiation parameters, and found them to be very low, indicating that they had been buried at least a few meters deep in the regolith since they formed. They also found relatively high $^{40}\text{Ar}/^{36}\text{Ar}$ ratios in most of the breccias, indicating that the materials making up the breccias may have been exposed and irradiated at the lunar surface as early as 4×10^9 yr ago. *McKay et al.* (1986) concluded that the Apollo 16 breccias contain ancient regolith that was only briefly exposed at the surface and is unlike any of the sampled Apollo 16 soils.

Finally, a characteristic of all regolith breccias studied thus far is a very low content of fused soil components (agglutinates and fragments of older regolith breccias) compared to present lunar soils. There are two possible explanations for this situation. Either the breccias were formed from an extremely immature regolith (unlike any present-day

regolith that was sampled) that contained very little fused soil, or agglutinates were present in the source material and were destroyed in the breccia-forming process. Because intact agglutinates and glass beads are observed in the Apollo 11 breccias, implying that they can survive moderate shock, *Simon et al.* (1984) preferred an origin from immature regolith. However, experimental studies (*Simon et al.*, 1986b) have shown that agglutinates are easily destroyed by shock, although they can survive mild shock (<200 kbar). *Simon et al.* (1986a) then suggested that formation of regolith breccias from an immature regolith source can be inferred only for the unshocked, porous regolith breccias. Agglutinates originally present in more intensely shock-compressed (or higher-grade) regolith breccias would probably be destroyed, and the absence of agglutinates in such breccias cannot be used as evidence for an immature source. Nonetheless, the virtual absence of agglutinates in unshocked regolith breccias is consistent with the idea that they are very ancient rocks that formed at a time of much more intense meteoroid bombardment, ~4 b.y. ago (*McKay et al.*, 1986). At that time, when both large and small impacts were frequent, agglutinates should have been rare due to the youth of the regolith, the higher turnover rates, and shorter exposure times. The results of *McKay et al.* (1986) suggest such an origin for Apollo 16 regolith breccias. Many other types of breccias seem to have formed at about that time as well (see section 6.4).

7.7. THE RECORD OF SOLAR HISTORY PRESERVED IN THE LUNAR REGOLITH

The Moon has virtually no atmosphere or magnetic field, and a relatively quiet and passive surface. Because of these features, the Moon has little ability to deflect or attenuate the energetic solar particles that constantly bombard it. Many studies have attempted to examine these particles or the products of their impact into the lunar regolith in order to unravel the history of solar radiation. This topic is of considerable importance for the near-term and long-term history of solar activity and has direct implications for climate, atmosphere, and life on Earth.

7.7.1. A Summary of Historical Results

In order to read the “fossil” evidence of solar particles in the lunar regolith, it is necessary to know (1) the timespan over which the regolith sample studied was exposed at the lunar surface and (2) the antiquity of the sample, i.e., the interval or intervals in history during which the sample was exposed. It

is possible to generate models for these parameters that suit the “average” regolith (section 7.5.1), but specific soil samples must be studied carefully to unravel their actual exposure history (section 7.4.2). Although quiet, the lunar surface is impact gardened—mixed and overturned—on a timescale that is brief (Fig. 7.28) relative to the age of the sun (4.7 b.y.). Ideally, the soil presently at the lunar surface is the most readily studied, because it might be assumed to have been in place for a measurable timespan leading up to the present. It is common, however, for the regolith at the lunar surface to have been recycled and mixed, including some fraction of material that has been at the lunar surface more than once. Thus it is critical to examine several types of solar exposure measures with differing effects to help unravel the regolith sample’s history.

Materials in the top centimeter of the lunar soil are churned back into the deeper regolith with such regularity that they seldom provide exposure records extending back in time more than 1 m.y., and almost never more than 10 m.y. Large rocks in the regolith at the lunar surface can provide a more durable surface, with practical in-place exposure ages up to ~50 m.y. (*Walker*, 1980).

The effects of energetic particles from the sun on the lunar surface are related mainly to bombardment energy. Solar-wind particles are typically ionized atoms (mostly H, He, C, N) with energies of ~1000 electron volts per nuclear particle (i.e., ~1 keV/amu; see section 3.11.1). This energy is sufficient to implant these particles several hundred angstroms (about 10^{-4} mm) into the surfaces of exposed mineral grains. The energies of particles accelerated by solar flares range from <1 MeV/amu to >100 MeV/amu, and these particles penetrate several millimeters to several centimeters to produce nuclear reactions with some elements (e.g., conversion of Si, Fe, and ^{27}Al to ^{26}Al or ^{21}Ne , and conversion of Fe to ^{53}Mn or ^{54}Mn). These particles also produce lattice damage tracks and trapped-electron anomalies in crystals.

Despite the problems in obtaining lunar samples with decipherable surface exposure histories, the effort expended to date has shown that, within a factor of about 2 or 3, the solar-wind composition has remained constant over most of the lifetime of the sun (*Pepin*, 1980). This result is consistent with current astronomical theories in which the sun, slightly less than 5 b.y. old, is regarded as a main-sequence star about halfway through a long stable period that began shortly after its formation and that should last for about another 5 b.y.

Studies of lunar samples have also been able to examine different solar processes on a number of different timescales. First-order stability in the sun is

indicated by the presence of a solar wind at least 4.2 b.y. ago; solar-wind elements from this era have been identified in meteorites (Croaz, 1980; Goswami *et al.*, 1980). However, there is evidence that both the intensity and the composition of the solar wind have changed with time.

The evidence for relative solar stability should not be read to imply that the sun has not changed at all over the last 4 b.y. The most striking example of possible change is an apparent systematic increase in the ratio $^{15}\text{N}/^{14}\text{N}$ over this timespan (Kerridge, 1975, 1989). Although this change is not readily explained by theories of solar activity, it has been equally difficult to explain away the variation by other causes. If caused by the internal operations of the sun, the significance of this timewise change is still unknown.

At the time of the Apollo missions, it was hoped that vertical core samples throughout the regolith might be sufficient to provide a readily datable stratigraphy, from which a well-constrained record of solar activity might be reconstructed. This ideal was not realized because of the complex nature of lunar regolith processes and the difficulty of distinguishing between the *antiquity* of an exposed sample (*when* it was exposed) and its *maturity* (*how long* it was exposed) (Kerridge, 1980). However, based on what we now know, it may be possible to seek other situations in which regolith samples may be collected with well-known duration and timing of exposure. For example, it should be possible to collect regoliths that were developed on one mare lava flow and then covered by another, allowing both the age and duration of the regolith exposure to be precisely obtained by dating the lava flows above and below.

7.7.2. Solar-Wind History

The sun has been generating solar wind for most of its lifetime. Samples of ancient solar wind are found in the oldest solar-system materials available for analysis—meteorites whose individual components were assembled more than 4.2 b.y. ago (Croaz, 1980; Goswami *et al.*, 1980). These studies suggest that this ancient solar wind was not greatly different from the modern solar wind in intensity or composition.

Lunar samples provide a shorter record of ancient solar wind than do meteorites because of the complex dynamics of the lunar surface. In particular, the erosion of exposed lunar rock fragments, which takes place at a rate of several millimeters per million years, removes the surface layers containing solar wind and limits the solar-wind record in exposed samples to less than 1 m.y. However, buried lunar materials preserve samples of more ancient

solar wind. The deep (3-m) cores contain single grains that accumulated solar wind about 1 b.y. ago, while soil breccias contain solar wind from up to 3.5 b.y. ago.

The suite of solar-wind elements available for analysis is limited to the volatile elements (e.g., H, He, Ne, Ar, Kr, Xe, C, and N) because lunar materials have very low volatile contents, and the solar-wind contributions can easily be recognized. However, these elements can be measured to establish the character of the solar wind over a considerable fraction of the sun's lifetime.

Analyses of lunar samples have established that the solar wind has been generally constant (within a factor of 2) over at least the last 2.5 b.y. (Pepin, 1980). However, significant changes in specific characteristics have been detected between ancient and modern solar winds. In the area of physical changes, analyses of solar-wind Xe (Geiss, 1973; Kerridge, 1989) suggested that the flux was higher (2–3 \times) in the ancient solar wind. This conclusion is model-dependent and not definitely established, but it is supported by independent measurements of solar-wind N (Clayton and Thiemans, 1980; Kerridge, 1980). In addition, a more energetic solar wind in the past has been proposed to explain the erosion and rounding of small mineral grains in the lunar soil (Borg *et al.*, 1980).

The earliest studies of returned lunar samples provided evidence that some compositional characteristics of ancient and modern solar winds were significantly different. An early conclusion was that the relative amount of Ar had decreased with time (Geiss, 1973). Despite a general constancy in the ratios of isotopes of Ar, Kr, and Xe over time, a significant decrease in the ratio $^4\text{He}/^3\text{He}$ was noted (Eberhardt *et al.*, 1972; Kerridge, 1980; Becker and Pepin, 1989); the change amounted to a decrease of 23% over the age of the regolith. There is also evidence for a roughly 50% decrease in the proportions of He and Xe, relative to N or Kr (Kerridge, 1980; Becker and Pepin, 1989). A possible decrease in the ratio $^{22}\text{Ne}/^{20}\text{Ne}$ over the same time was also indicated, but is less definite (Pepin, 1980; Becker and Pepin, 1989).

The strongest and most definite change in solar wind composition with time is a pronounced *increase* in the $^{15}\text{N}/^{14}\text{N}$ ratio with time (Kerridge, 1975, 1989; Clayton and Thiemans, 1980). Careful isotopic measurements of the N extracted from recently exposed soils and from a series of old regolith breccias, which trapped solar wind as much as 3.5 b.y. ago, show an increase in the $^{15}\text{N}/^{14}\text{N}$ ratio of about 50% or about 15% per billion years. This result, which has been reinforced by more recent measurements, is still not explained (Kerridge, 1989).

A variety of lunar-related mechanisms have been proposed: meteoroid contamination, infall of interstellar material, and N outgassing from the Moon. For various reasons none of these is satisfactory. A solar mechanism seems necessary to explain the change, though its nature is not clear at this time (Kerridge, 1989).

7.7.3. Solar-Flare History

Evidence for the existence of solar-flare activity more than 4 b.y. ago is present as particle tracks in grains of chondritic meteorites (Croaz, 1980; Goswami *et al.*, 1980). Solar-flare effects in lunar rocks and soil are relatively shallow (less than a few centimeters), and the erosion of exposed lunar rocks limits the available solar-flare record to about 10^7 yr. However, because of the continual stirring of the regolith, individual grains in deep lunar cores may provide solar-flare records from as much as 10^9 yr ago.

Within these time limits, the record of solar-flare behavior is approximately constant, with no deviations $\geq 3\times$ noted in the distant past. There is no evidence that the average intensity of solar flares was higher in the past 10^7 yr. A maximum intensity for past solar flares may be no more than 10^{10} particles/cm² per flare (Lingenfelter and Hudson, 1980), but it possible that larger flares could have occurred.

Several specific studies have provided other indicators of long-term constancy. The overall solar proton flux, as indicated by the radioactive elements ²⁶Al and ⁵³Mn produced in lunar samples, has been constant over the last 1–10 m.y. and is similar to the modern flux (Reedy, 1980; Russ and Emerson, 1980). The enrichment in the ratio of VVH (atomic number, $Z > 30$) to VH ($Z = 20\text{--}28$) atoms, observed at particle energies of less than 20 MeV, is present in both ancient and modern solar-flare particles. The ratio Fe/H in flare particles appears to have been constant over the last 2 m.y. (Zinner, 1980), and is still about $20\times$ the solar ratio (Croaz, 1980; Goswami *et al.*, 1980).

However, some lunar sample studies have provided indications that modern solar-flare activity may be different from that in the past. Studies of particle tracks developed in the glass linings of

microcraters on lunar rocks suggest that the flux of solar flare particles was higher about 20,000 yr ago (Zook, 1980), but these estimates are both model-dependent and controversial. A higher flux over the last $10^4\text{--}10^5$ yr is also suggested by ⁸¹Kr and ¹⁴C activities (Reedy, 1980). However, Fireman (1980) has argued that the latter effect arises from ¹⁴C carried to the Moon in the solar wind and that the record from ³⁹Ar and ³H activities shows constancy in both the ancient and modern solar wind.

7.7.4. Galactic-Cosmic-Ray History

The history of galactic cosmic rays (GCR) preserved in lunar materials has been explored by two main methods and over two different timescales. Single grains rich in GCR-produced particle tracks have been recovered from deep lunar regolith cores; these grains preserve records of exposure to GCR during the last $10^8\text{--}10^9$ yr. The levels of GCR-produced radionuclides in most lunar rocks or soil provide younger records of GCR behavior over the last $10^6\text{--}10^8$ yr.

The records so far deciphered show that the flux and composition of GCR have been constant (within about a factor of 2) and similar to the present flux, over all the timescales studied. The ratio of VVH/VH particles has been constant at about $(1.3 \pm 0.6) \times 10^{-3}$ for the last $10^8\text{--}10^9$ yr (Bhandari and Padia, 1974a,b).

Studies of the GCR-produced radionuclides developed in exposed lunar rocks indicate that the same constancy has existed on shorter timescales (Croaz, 1980). Rocks with simple exposure histories indicate constancy over exposure ages of 2 m.y. to 50 m.y. (Walker and Yuhas, 1973; Yuhas and Walker, 1973). Other samples show a similar constancy over periods from 60 yr to about 10^4 yr (Fireman, 1980).

Studies of both lunar samples and recently fallen meteorites have detected the modulation in GCR flux that is produced by variations in the sun's magnetic field during the 11-yr solar cycle (Reedy, 1987). Activities of such GCR-produced radionuclides as ⁵⁴Mn, ⁴⁶Sc, and ²²Na in these samples vary by about a factor of 2, and the timing of these variations is closely correlated with solar activity and the strength of the sun's magnetic field.

LUNAR CHEMISTRY

Larry Haskin and Paul Warren

To understand a planet it is essential to determine its chemistry. Our understanding of the Earth, its history, and its evolution has grown steadily with our ability to analyze its rocks. The whole discipline of geochemistry, about a century old, has been devoted to determining the chemistry of terrestrial materials, understanding the way that the different chemical elements behave in geological processes, and using the chemical information to decipher the nature of the processes themselves. The same need for chemical data is equally true for the Moon. Before we could obtain direct chemical measurements, our knowledge of the Moon was limited, and our theories about it were vague and unconstrained.

The Apollo missions provided chemical data in abundance. The returned lunar samples are probably the most intensively analyzed geological materials ever collected, and new analyses are still being made. Sophisticated instruments have made it possible to analyze virtually all the known chemical elements, while the analytical sensitivity has made it possible to obtain results on samples no more than a few milligrams in weight, often without destroying the sample.

As a result, the number of individual major-element, minor-element, trace-element, and isotopic ratios measured on lunar materials is probably in the millions. This information has been determined for the full variety of returned lunar materials—mare volcanic rocks, highland rocks of great variety,

breccias, and soils from all sampling sites. Analyses on new samples continue today, through collection and study of meteorites from the Moon that have been found in Antarctica (section 2.2). Added to this laboratory information are the remote measurements of lunar surface chemistry made from orbit during the Apollo missions (see section 10.2), which allow scientists to extend the data from individual landing sites to wider areas of the Moon.

This immense amount of new chemical information has increased understanding about the Moon to a level from which it is possible to understand the Moon's place in the solar system and its special relationship to the Earth. With chemical data, scientists can now quantitatively probe major topics that, before the Apollo program, could not have even been subject to more than speculation. What is the origin of the Moon? How is the origin of the Moon related to the origin of the Earth and the solar system? How closely is the Moon related to the Earth? What is the history of the Moon's crustal regions and what are the processes by which they separated from the bulk Moon? How did the mare lavas form, and when did they erupt? What are the origins of lunar breccias and the lunar soil layers? What was the original chemical composition of the Moon? Was the Moon initially homogeneous? What chemical components have been introduced to the Moon by impacting meteoroids? What chemical species have been carried into the Moon from the

sun in the solar wind? What is the economic potential of the Moon, and how can lunar materials support future human activities in space?

The Moon and the Earth

All the chemical elements that make up the Earth are also found on the Moon. On scales both large and small, however, the abundances and distributions of the elements differ greatly between the two planets. The Moon lacks a large iron core. It has no appreciable atmosphere and therefore does not undergo chemical weathering of the type found on planets with atmospheres. A key difference is that the Moon's interior and surface have virtually no water or other gases. Without oceans, rivers, and rainfall, and without groundwaters and deep crustal waters, the entire realm of aqueous geochemistry that is so critical on Earth is absent on the Moon.

Most geochemical processes on the Earth, and nearly all those that concentrate chemical elements into ores, require water and therefore have never operated on the Moon. Nevertheless, the evidence from samples of lunar rocks and soils is that the Moon did undergo extensive nonaqueous chemical separations, which produced—among other things—the Moon's thick outer crust. Many chemical elements were concentrated into portions of that crust, and there may be ores for more elements than we presently realize.

This chapter briefly describes what is known about the concentrations and chemical states of the elements found on the Moon's surface. Rather than merely listing these states and concentrations, this chapter provides an overview (section 8.2) of how planetary materials attain their varied compositions; this will assist the reader in developing an intuitive feeling for the nature of lunar geochemical processes and a sense for what lunar resources might be available.

Definitions and Conventions

The basis for geochemical exploration of the Moon was provided by over a century of terrestrial geochemical investigations. Some of the definitions and conventions developed for the Earth have been applicable to the Moon; others have not, and new ones had to be developed.

In studying the Earth, geochemists recognized early that different chemical elements behave in different ways in geological processes. These differences in behavior are, in fact, the clues to deciphering the processes themselves. From studies of chondritic meteorites and terrestrial materials, geochemists have grouped the chemical elements

according to their associations with major types of minerals. These groupings are useful because they generally reflect the results of major geochemical processes.

Lithophile (rock-loving) elements are those concentrated in the silicate rocks of the Earth's crust, including major elements such as Si, O, Al, Mg, Ca, and Mg, together with lesser elements such as Na, K, Rb, Cs, U, Th, and rare earth elements (REE; La to Lu).

Siderophile (iron-loving) elements are more closely associated with Fe, meteoritic metal, and the Earth's metallic core, e.g., Ni, Co, and the Pt-group metals.

Chalcophile (copper-loving) elements include Cu and related metals (Zn, As, Sb, etc.) that are usually associated with S in sulfide minerals.

The Moon, even more than the Earth, has not been a closed chemical system since it formed. Both planets receive meteoroid and cometary debris from space, but the Moon lacks Earth's magnetic field to deflect the ions (section 3.11) that sweep through space. Such particles, coming mostly from the sun as "solar wind," are a small but important part of the lunar surface. In order to understand the chemical nature and evolution of the Moon, it is necessary to distinguish clearly between chemical components that are indigenous to the Moon and components that have been added later by impacting meteoroids or by the solar wind. Because the basic chemical data come from lunar samples, it is necessary to know the proportions of lunar and exotic chemical components in a given sample. This distinction is not always easy (see sections 6.3 and 6.4). However, two kinds of lunar samples appear to be fundamental samples of the Moon, with no significant additions from the outside. These are mare basalts and certain crystalline highland rocks (sections 6.1 to 6.3). These rocks are called *pristine*, to indicate that they represent lunar material that has not been contaminated by additions from outside the Moon or by impact mixture with other lunar rock types. Many mare basalts are *pristine*, but the lunar highlands have been so severely impacted that few highland samples are *pristine*. *Pristine* rocks may still be brecciated, but such shattered yet not impact-mixed rocks are called *monomict*, as distinct from the majority of lunar impact-scrambled samples, which are *polymict* (see section 6.4).

Meteoroids and meteorites are important to lunar chemistry in two ways. Meteoroids provide the major source of exotic materials to the lunar surface by impact, and they change the chemistry of the resulting breccias and lunar soils. In addition, meteorites (i.e., meteoroids collected on Earth) serve as a chemical standard for discussing the chemistry of both the Moon and the Earth. One group of

meteorites, the *chondrites*, and especially the *CI carbonaceous chondrites*, corresponds closely to the composition of the sun (minus H and He) and is therefore used as a first approximation to the material out of which the Moon and the other terrestrial planets formed. Commonly, chemical compositions of lunar and terrestrial materials are normalized to CI compositions to provide a common basis for comparison.

The terms *major*, *minor*, and *trace* are commonly and loosely used to designate approximate or relative amounts of chemical elements in samples or amounts of minerals in rocks. These terms have no firm boundaries, and their use is complicated by the fact that a minor element in one rock may be a trace or even a major element in another. For chemical elements, it will be convenient (although not always accurate) to use the following very rough definitions: major elements >1 wt.%, minor elements >0.1–<1 wt.%, and trace elements <0.1 wt.%. For mineral percentages in rocks, a similar general scale can be used: major minerals >10 vol.%, minor minerals >1–<10 vol.%, trace minerals <1 vol.%.

8.1. WHERE TO FIND A PARTICULAR ELEMENT DISCUSSED

8.1.1. Organization of the Data

This chapter divides the chemical elements into six geochemical groups: *major elements*, *incompatible trace elements*, *minor elements*, *siderophile elements*, *vapor-mobilized elements*, and *solar-wind-implanted elements*. These groups are based mainly on the relative abundances of the elements and the nature of the lunar materials in which they occur. In such a grouping, the elements do not correlate in a simple way with their positions in the periodic table, although there is, of course, some relationship. The rationale for the classification according to these six groups is discussed below (section 8.2). The same classification is used in presenting the data on elemental concentrations.

To locate information quickly about a chemical element, find the element in the periodic table (Fig. 8.1). The figure caption indicates the group the element is in and the section of the chapter where it is discussed. Some elements actually fall into more than one group. For example, Co occurs in elemental form in ferrous alloys (a siderophile association), but Co is also concentrated as a divalent ion in the minerals olivine and pyroxene (a lithophile association). Nevertheless, because of its affinity with Fe, information on Co is found in the section on siderophile elements.

This chapter indicates in a broad sense what lunar materials contain what elements in what concentrations. To do this, lunar materials are divided into four categories: *mare basalts*, *highland monomict rocks*, *soils and regolith breccias*, and *polymict breccias* (see Chapter 6). Chemical data are presented graphically, by sample location, to show the range of concentrations for each element in each of these general categories. The data reflect samples obtained from at least ten locations on the Moon: six Apollo landing sites, three Luna landing sites, and several (unknown) source regions for the Antarctic lunar meteorites (section 2.2).

The appendix to this chapter provides a more detailed statistical summary of elemental concentrations in subclasses of various lunar materials. The appendix presents averages, standard deviations, maxima, and minima for those groups of materials for which enough analytical data have been compiled and for which the magnitude of the standard deviations does not exceed about one-third of the mean value. It is important to note that for some elements, which are not routinely analyzed (e.g., Cs, Ga, Mo, In, and Kr), nearly all the available analyses have been compiled to make the tables and graphs for this chapter, but for other elements (including most of the major elements) only a fraction of the many analytical data are used. In addition, most of the available data for relatively rare samples (e.g., soils and fragments from the Luna missions, Antarctic lunar meteorites, and rare rock types such as quartz monzodiorite) have been compiled, but only part of the data for the common Apollo mare basalts, soils, and breccias have been used. For this reason, the number of points for a given landing site shown on a graph does not reflect proportionally the relative amounts of different materials at that landing site or in the overall sample collection.

8.1.2. Types of Lunar Materials Considered

The first category of lunar materials considered is *mare basalts*. Compositions of mare basalts differ from each other on the size scale of the individual samples allocated for analysis (typically 1 g, or about 0.2–0.4 cm). Compositionally distinct types of mare basalts generally occur at a single landing site (e.g., Apollo 11 low-K and high-K types). Basalt types also differ significantly between landing sites (for details, see sections 6.1 and 6.2).

The second category of materials consists of the igneous rocks that are part of the lunar highland crust. Most of the igneous rocks that formed the early highland crust have undergone extensive shattering or melting from meteoroid impacts. The bulk of the highland rocks near the lunar surface

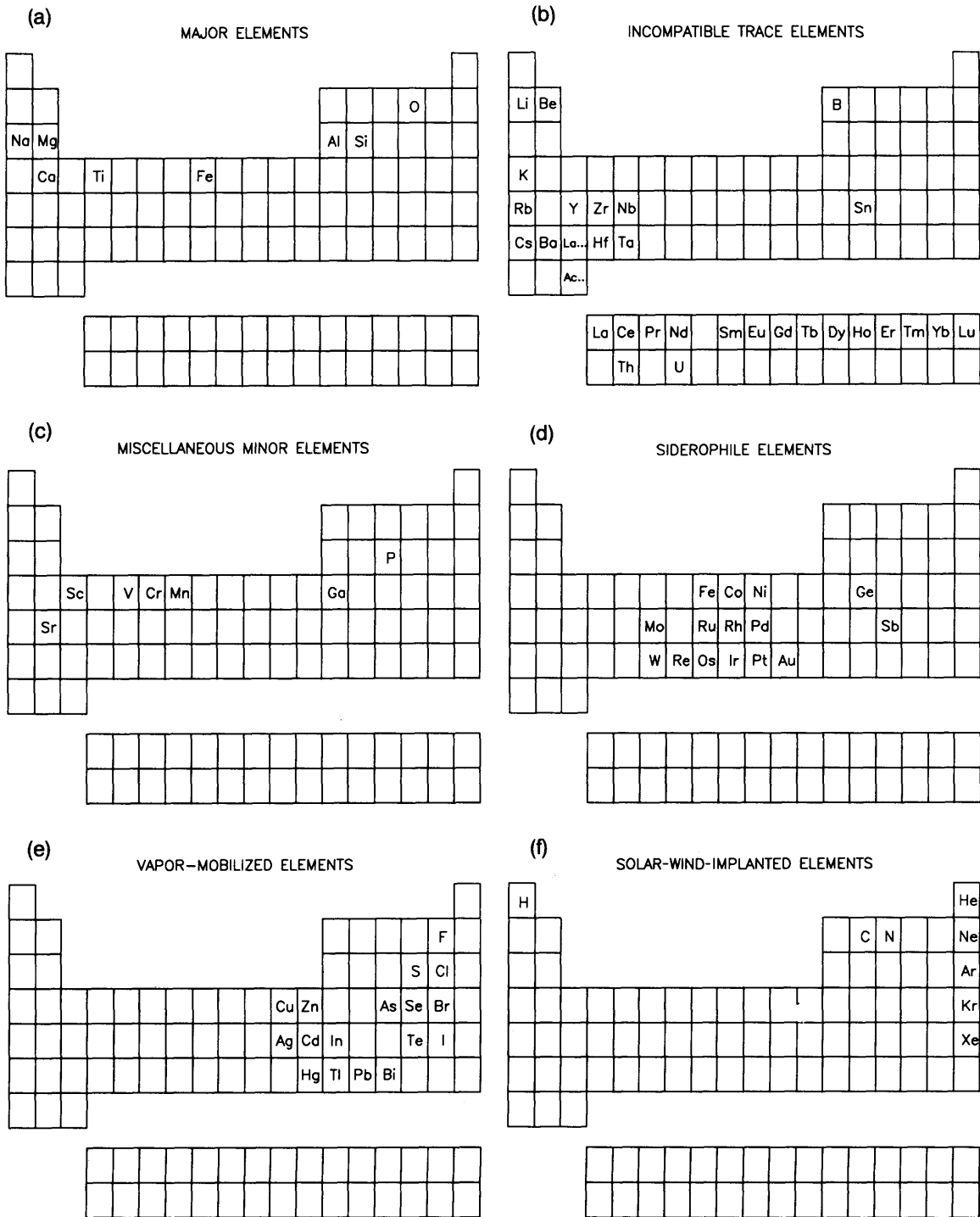


Fig. 8.1. Diagrams of the Periodic Table of the Elements, showing the identity and locations of elements discussed in the various sections of this chapter: **(a)** major elements (section 8.3); **(b)** incompatible trace elements (section 8.4); **(c)** miscellaneous minor elements (section 8.5); **(d)** siderophile elements (section 8.6); **(e)** vapor-mobilized elements (section 8.7); **(f)** solar-wind-implanted elements (section 8.8).

have been broken up and mixed into soils and breccias. Relatively few have survived to the extent that we can now identify them unambiguously and determine their original compositions. We call these few surviving specimens *highland monomict rocks*, indicating that while most or all of them are actually fragments of breccias, we can make the case that they are breccias from a single rock formation or lithology (therefore monomict) as opposed to mixtures of rocks from more than one formation or lithology (polymict). The spread of chemical compositions is greater in highland monomict rocks than in mare basalts. The basalts stem primarily from a single process (mantle melting), which leads to a somewhat limited range of basalt types. In contrast, highland rocks range in character from almost monomineralic to polymineralic rocks, many of which were produced by more complex processes, including processes that operated during the initial formation of the lunar crust and mantle.

The third category is *soils and regolith breccias*. Lunar *soils* are the <1-cm fraction of loose debris on the lunar surface (see Chapter 7). This debris is the ultimate in polymict material, being a mixture of pulverized mare rocks, highland rocks, and older soils plus a small proportion of meteoroid material from the various impacting objects that produced this debris. Some soils (e.g., from the Apollo 11 site and from the Apollo 15 site near Hadley Rille) are derived mainly from local mare basalts, but they include small amounts of highland material excavated from beneath the younger lava flows. Other soils (e.g., those from the Apollo 16 site and from Station 2 of the Apollo 17 site) are derived almost exclusively from highland materials (section 7.5.5). Some early soils have been sintered into clods known as *regolith breccias* (section 7.6). In this chapter, regolith breccias are included with the soils because of their similar origins and compositions. Compositions are given by landing site, usually without detailed discussion of the nature of the soils within a site (see section 7.5.5 for details). Nevertheless, some graphs show the distinctions between soils of mainly mare origin and those of mainly highland origin.

The fourth category, *polymict breccias*, contains everything not included in the other three categories. Polymict breccias make up the bulk of the highland samples collected. They range in character from materials that are nearly as complex as soils and regolith breccias to materials that deviate only slightly from being monomict. They are not a coherent group in terms of compositional similarity, and they tend to show the same ranges of elemental concentrations that the highland monomict rocks show.

8.1.3. Cautions on Data Use

The statistical data in the appendix are useful for summary purposes, but they should be used with caution. For example, average elemental concentrations for breccias are not meaningful for most elements. Exceptions are elements such as O, whose concentrations are nearly the same in all types of lunar material. Similarly, an average composition for highland monomict rocks in general is not meaningful, but averages for individual types of highland monomict rocks are. Average compositions for mare basalts are most meaningful if there is one dominant type of basalt at the landing site (e.g., Apollo sites 12, 15, and 17). Averages for soils may be meaningful if all the soils collected at a given landing site are similar in composition (e.g., the Apollo 16 soils, except for those near North Ray Crater), but such averages may be misleading if some of the soils at a landing site are derived mostly from mare material and others mainly from highland material (e.g., Apollo 17 soils). For those elements whose principal source is either meteoroids or the solar wind, concentrations are nearly independent of whether the source of the soil was mainly highlands or mainly mare, and generally depend more on the timespan over which the soil was exposed at the lunar surface.

The significance of averages depends on our knowledge of the extent of chemical heterogeneity at a particular landing site. We know, for example, that the composition of Apollo 16 soils is nearly constant over an area of several square kilometers. The compositions of soils from the U.S.S.R. Luna sites represent material collected by only a single core at each site. Finally, we do not know which source sites are represented by the individual Antarctic lunar meteorites. The reader should remember these cautions when considering the averages given in the tables, and realize that the best use of these tables is in conjunction with the figures that display compositional information for each element.

8.2. OVERVIEW OF PLANETARY SEPARATION PROCESSES

Each planet has a unique chemical character that reflects the chemical and physical conditions in the region of the original solar nebula where the planet formed. It is generally believed that the solar system formed from a mixture of original galactic H, with lesser amounts of other gases and previously-formed solid grains of dust. Astronomical observations indicate that not all star systems have the same composition.

This cloud of gas and dust collapsed inward under its own gravity. As it did so, its center was intensely compressed and heated, and a luminous protosun was formed. Material not pulled into the center formed a disk (*nebula*) surrounding the protosun. Original dust grains near the sun were probably vaporized during this process; condensation of new grains occurred as the temperature of the nebula decreased.

The small terrestrial planets formed nearer the sun, where temperatures were higher, and they condensed from relatively refractory chemical elements and compounds. Consequently, these planets (including the Earth and Moon) have low concentrations of the principal constituents of the solar system, the gases H and He, and other volatile elements. These inner planets are also far denser than the outer gaseous planets, which formed in colder regions of the nebula and accumulated larger amounts of H, He, and other volatile elements.

The inner planets are not all alike; for example, the density of the Earth (5.52 g/cm³) greatly exceeds that of the Moon (3.34 g/cm³). However, the major elemental constituents of all the inner, or terrestrial, planets are the same—O, Fe, Si, Al, Mg, Ca, Na—simply because those were overwhelmingly the most abundant elements in the solar nebula that could condense at high temperatures. These elements are not present in the same relative proportions in all the planets, however. These elements, plus Ti, make up the *major elements* discussed in section 8.3.

A planet consisting primarily of nonvolatile elements may melt as it forms or, if not, heating in its interior will cause partial melting. The composition of the first-melted portion will differ from the average composition of the planet in accord with the thermodynamic relationships between the melt components and the residual, more refractory solid phases. If the melt is denser than the bulk material of the planet, it will sink toward the center; the Earth's iron-rich core presumably formed in this way. Such a core arises if the planet contains Fe in excess of oxygen available to react with it. Thus, the Earth's metallic core consists mainly of Fe, and it is believed to contain most of the Earth's supply of *siderophile elements* (section 8.6), which include Ni, Co, and the noble metals (Pt, Au, Pd, Rh, etc.).

In contrast, the Moon's moment of inertia and low density indicate that the Moon cannot have a very large metallic core, and present evidence is ambiguous about whether it has any such core at all. Nevertheless, the noble metals are found in extremely low concentrations in lunar crustal rocks. However, they are present in greater concentrations in the pulverized surface of the Moon than in the underlying crust, indicating that they have been

added to the surface debris by impacting meteoroids.

If the melt is less dense than the refractory residual material, it will migrate toward the surface and solidify to form a crust. The refractory residues in planetary interiors from which such melts separate are enriched in Mg, Fe, Si, and O. They make up the planet's mantle. The melts also contain these elements, but are relatively enriched in Ca, Na, and Al. Solidification of the melts, when they reach the surface to form parts of the outer crust, produces minerals such as plagioclase feldspar, which is a Ca-Na-Al silicate, together with pyroxene and olivine, which are Mg-Fe silicates. Once an initial crust has formed, portions of melt from the interior that flow onto it are called *lavas*. Portions of melt that intrude into a planet's crust, but do not breach it, solidify within the crust as *plutons*. Some plutonic rocks may be excavated and brought to the crustal surface by meteoroid bombardment.

On both the Earth and the Moon, the crusts are richer in Si and Al than the bulk planets, and they are correspondingly poorer in Fe and Mg. Some specific ideas about how this separation may have occurred are discussed in section 2.4.3. Of the less abundant elements in a planet's interior, most enter the melts and are carried upward to the planet's crust, where they enrich the crust over the bulk planet's composition. The elements that make up this large group do not fit well into the crystal structures of the principal crustal minerals, and are thus called *incompatible trace elements* (section 8.4). Examples include K, Rb, Th, U, and REE (rare earth elements).

Several elements, for example, Sc, V, Cr, and Mn, mainly remain in the refractory Fe- and Mg-rich residual minerals, with whose crystal structures they are compatible. Others, for example, Sr and Ga, concentrate into plagioclase feldspar as it forms. These, plus P, which is incompatible with major mineral structures but reaches high concentrations as melts solidify to produce its own minerals (apatite and whitlockite), constitute the group we call the *miscellaneous minor elements* (section 8.5).

Some elements that are incompatible are also relatively volatile. This is evidence that these particular elements have been partially evaporated from lunar surface materials when they were heated by meteoroid impacts. In the text that follows, they are called the *vapor-mobilized elements* (section 8.7).

Elements that are even more volatile, such as H, C (in compounds), N, and the noble gases (He, Ar, Kr, etc.), do not even appear to have been incorporated into the Moon in appreciable quantities when it formed. However, they are present in significant amounts in the grains of surface soils because these grains have trapped them as atoms and ions from

the solar wind. These are the *solar-wind-implanted elements* (section 8.8).

8.3. MAJOR ELEMENTS

8.3.1. Concentrations of Major Elements in the Moon

It may seem incongruous for a planet that has no atmosphere, but O is overwhelmingly the most abundant element in lunar surface materials. More than 60% of the atoms are O, but all of them are tightly bound chemically to other elements. The second most abundant element is Si, which contributes another 16–17% of the atoms. Aluminum is third most abundant, contributing about 10% of the atoms in the highlands, but only about 4.5% of those in the thin layers of mare basalts that cover 20% of the Moon's nearside. Calcium and Mg are about equally abundant, each contributing some 5% of the atoms; Ca is less abundant in the maria (about 4.5%). Iron contributes approximately 2.5% of the atoms in the highlands but 6% of those in the maria. Titanium and Na atoms make up the remaining percent or so.

We call these elements that make up the bulk of common lunar materials the *major elements*. Conversion of their abundances in lunar surface materials from an atom-percent to a weight-percent basis changes their order of abundance somewhat. Oxygen is still the most abundant major element, at about 45% (by weight). Silicon is still second, at 21%. Aluminum is third at about 13% for the highlands, although only about 5% for the maria. Calcium is next, at about 10% for the highlands and 8% for the maria. Iron contributes about 6% to the highlands, but 15% to the maria. Magnesium comes next at 5.5% for both types of material. Titanium and Na each contribute a fraction of a percent in the highlands, but the average Ti concentration exceeds 1% and may be as high as ~5% in the maria.

Traditionally, concentrations of major elements are not reported as elemental percentages. Instead, their chemical combination with O is acknowledged and the available O is partitioned among them as if each were present as a simple oxide. We follow this practice in Fig. 8.2, where the concentrations of each major element are plotted for lunar materials from each sampling site, and in Table A8.1, where some averages and extents of variation are given. Concentrations are shown on a logarithmic ordinate in Fig. 8.2; thus, a factor of 2 difference in concentrations between two materials covers the same linear vertical distance independently of the concentration level. Concentrations for all major elements are plotted on the same scale, so that the concentration range for each element can be readily

compared with those for the other elements. (The order of relative abundances by weight of the oxides for the materials considered here is the same as that of the elements themselves.) We include concentrations for O as a “stand-alone” element in Fig. 8.2 and Table A8.1, in contrast to our treatment of the other major elements. Oxygen concentrations are nearly constant at about 45% (by weight) in all common lunar materials.

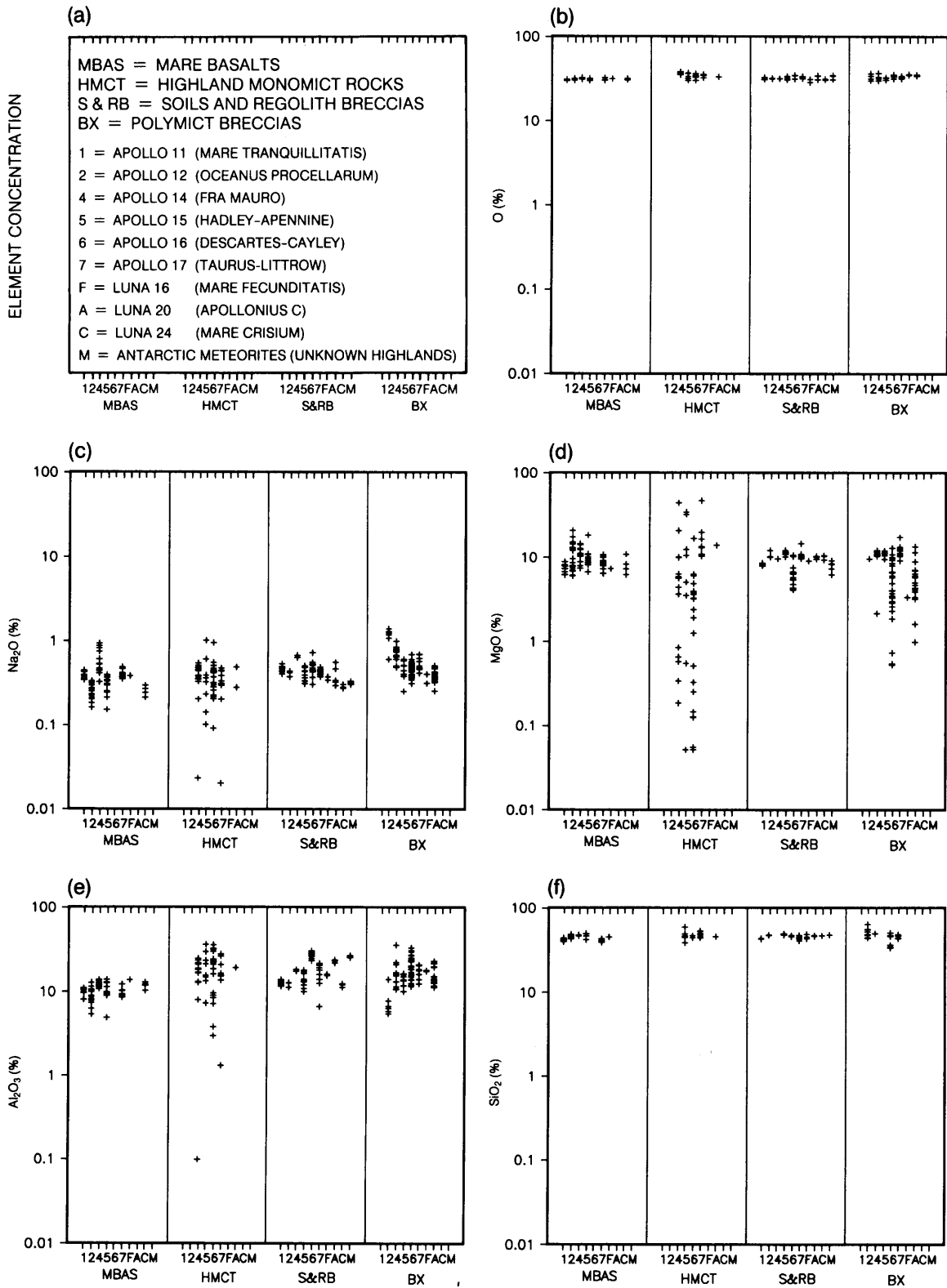
8.3.2. Minerals and Rocks Formed by Major Elements

Although all major-element cations are in some manner combined chemically with O, they are not present as simple oxides, as might be inferred from the type of compositional information given here. Rather, most major elements are in cation sites of compositionally complex silicate or oxide minerals (Chapter 5) or in glasses that have been produced by impact melting of rocks containing those minerals. Most of these minerals are actually solid solutions of simpler silicate endmember compounds.

The relationships among major-element concentrations in most lunar materials can be generally understood in terms of the minerals that make up lunar rocks. Both highland and mare rocks contain plagioclase feldspar, which is a solid solution consisting mainly of two components. *Anorthite* ($\text{CaAl}_2\text{Si}_2\text{O}_8$) is dominant, while *albite* ($\text{NaAlSi}_3\text{O}_8$) constitutes only a few percent. Plagioclase is the carrier of nearly all the Al in the lunar crust. The proportion of plagioclase in the highlands is greater than that in the maria, consistent with the higher concentrations of Al detected by orbital remote sensing in the highlands and observed in the analyses of highland samples. That higher proportion of plagioclase, which is white in color, also helps explain the lighter color of the highlands, in contrast to the darker maria.

The most abundant dark mineral at the lunar surface is pyroxene, which occurs in two general varieties—high-Ca and low-Ca. The high-Ca variety consists of solid solutions of $\text{Ca}_2\text{Si}_2\text{O}_6$, $\text{Mg}_2\text{Si}_2\text{O}_6$, and $\text{Fe}_2\text{Si}_2\text{O}_6$. From a mineralogical point of view, high-Ca pyroxene consists mostly of solid solutions of the chemical components *diopside* ($\text{CaMgSi}_2\text{O}_6$) and *hedenbergite* ($\text{CaFeSi}_2\text{O}_6$). In the low-Ca pyroxene, the solid solution is primarily between *enstatite* ($\text{Mg}_2\text{Si}_2\text{O}_6$) and *ferrosilite* ($\text{Fe}_2\text{Si}_2\text{O}_6$) (see Fig. 5.3). Another dark mineral found in lunar rocks is *olivine*, which consists of solid solutions of *forsterite* (Mg_2SiO_4) and *fayalite* (Fe_2SiO_4). Titanium mainly forms *ilmenite* (FeTiO_3) and related minerals.

The highlands consist principally of plagioclase-rich rocks such as *anorthosite* (>90% plagioclase), *norite* (roughly equal proportions of plagioclase and



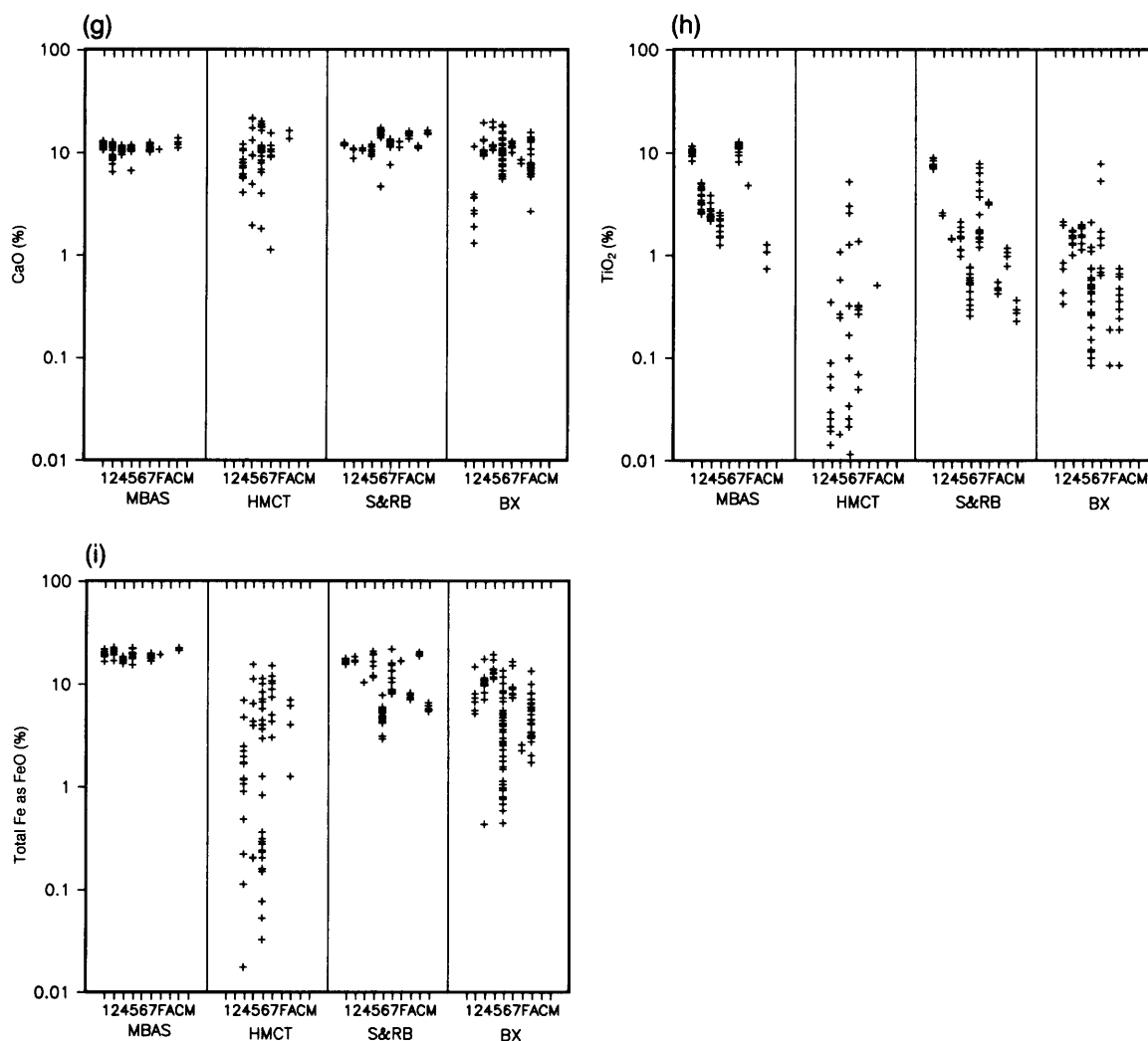


Fig. 8.2. Concentration ranges of major elements in various lunar materials: mare basalts (MBAS), highland monomictic rocks (HMCT), soils and regolith breccias (S&RB), and polymictic breccias (BX). Horizontal axis shows sample types, separated according to individual missions. Vertical axis shows concentrations in weight percent. **(a)** Graphical key to the plots and abbreviations. Data are presented for: **(b)** O; **(c)** Na₂O; **(d)** MgO; **(e)** Al₂O₃; **(f)** SiO₂; **(g)** CaO; **(h)** TiO₂; **(i)** total Fe as FeO. Statistical data for these plots are summarized in Table A8.1.

low-Ca pyroxene), and *troctolite* (plagioclase and lesser amounts of olivine). Some investigators regard anorthosite as the principal rock type of the early highland crust. Others suggest that a plagioclase-enriched norite (*leuconorite*, mainly plagioclase feldspar plus low-Ca pyroxene) was the principal rock type; its composition more closely matches that of the present average highland surface. A few samples of *dunite*, a rock type that consists almost

entirely of olivine, are present in highland breccias. Minor amounts of *gabbro* (mainly plagioclase feldspar and high-Ca pyroxene) and *granite* (which contains K-feldspar) are also present. Many highland rocks and soils contain ilmenite and related Ti-rich oxides, but usually in minor quantities.

Our present knowledge of the composition of the lunar highland surface is restricted by the limited amount and quality of remote-sensing data. Data

from remote sensing (e.g., the Apollo 15 and 16 orbital gamma-ray and X-ray data, and Earth-based infrared spectra, discussed in section 10.2) are for surface materials, mainly regolith. It is difficult to relate the types of bedrock in remotely sensed areas to the “ground truth” provided by the Apollo and Luna sample collections. To make this connection, it is necessary to interpret the chemical compositions of polymict highland soils in terms of their parental rock types.

Several types of igneous highland rocks have been identified and characterized. These are the highland monomict rocks. However, it has not been possible to explain the compositions of the polymict breccias and soils by simply mixing together these highland monomict rocks. One difficulty is that we have not yet identified all the highland rock types on the Moon. The bulk of the material sampled in the highlands is polymict; monomict highland samples are rare. One indication that other rock types must be present is that the Mg value [the molar ratio of MgO to (MgO + FeO)] of the highland soils ranges from about 0.67 to 0.71. Most of the monomict highland rocks, especially the norites and troctolites, contain pyroxene and olivine with higher Mg values, 0.75–0.85. The more common *ferroan anorthosites* (section 6.3.3) have suitably low Mg values, but their total concentrations of MgO and FeO are too low to balance the contribution from norites and troctolites.

Similar polymict materials make up the bulk of the Apollo and Luna collections and the Antarctic lunar meteorites as well. Our failure to account for the compositions of polymict soils and breccias in terms of the primary lunar rock types we have identified so far is a good reminder of how limited our understanding of lunar rocks still is.

In contrast to the lunar highland rocks, the mare basalts have lower proportions of plagioclase and higher proportions of pyroxene, and their pyroxene is mainly the high-Ca type. Many mare basalts also contain olivine. The pyroxenes and olivines in the mare basalts are more ferroan than in the highland rocks (i.e., the pyroxenes and olivines have lower Mg values). This situation explains the high Fe concentrations of mare basalts and of the soils derived from them. Mare basalts contain ilmenite and related Fe,Ti-oxide minerals in proportions that vary from low (about 1 % oxide minerals) to surprisingly high (>20% oxide minerals; see listing of “opaque” oxide minerals in Table 6.1). The Fe,Ti-oxide minerals also contribute to the high Fe concentrations of mare basalts. Mare soils collected so far contain at least a few percent of highland material, presumably excavated by meteoroid impact from beneath the relatively thin lava flows unless mountainous highlands are nearby to shed debris over the lavas.

8.3.3. Abundances and Correlations Among Major Elements

Abundances (Fig. 8.2). Much of the chemical data in Fig. 8.2 can be understood in terms of the principal minerals that make up the samples and the known compositional differences between highland and mare rocks. In the case of TiO₂, the Apollo 11 and 17 high-Ti mare basalts stand out relative to lower-Ti basalts and from most other lunar materials analyzed. The contribution of the Apollo 11 high-Ti basalts is strongly reflected in the high TiO₂ concentrations of all of the Apollo 11 soils. In contrast, some Apollo 17 soils have relatively low concentrations of TiO₂ because they are composed mainly of low-Ti highland material. The highest TiO₂ concentrations are in soils consisting of (or containing high proportions of) orange glass spherules. These spherules are essentially mare volcanic ash (*pyroclastic* deposits; see section 6.1.7), but they are included with the soils because of their physical form. The lowest concentrations of TiO₂ are in the highland monomict rocks, particularly in the anorthosites and dunites.

Iron-oxide concentrations are highest in the mare basalts. In polymict breccias and soils, FeO concentrations vary depending on the relative proportions of mare basalt and mafic highland materials. Concentrations of FeO in feldspathic highland rocks are also low to very low. Concentrations of MgO are greater in some highland rocks (especially the dunites and spinel troctolites) than in most mare basalts. The mare basalts from the Apollo 12 site stand out, probably because they formed under circumstances that enriched some of them in Fe- and Mg-rich olivine. Plagioclase-rich highland rocks and the Apollo 16 soils have low MgO concentrations.

Concentrations of Al₂O₃ are highest in the anorthositic rocks of the highlands. They are lowest in the dunites and are intermediate in the mare basalts. Calcium-oxide concentrations for all lunar rocks fall within a relatively narrow range. The greatest CaO variation is among the highland monomict rocks; dunites and spinel troctolites have the lowest concentrations. Sodium concentrations are low in all lunar materials, but they cover a substantial range in mare basalts. Some of that range may reflect the presence of variable amounts of Na-rich, late-stage melt (*mesostasis*; see section 8.4) within the individual small samples analyzed. This Na-rich material is heterogeneously distributed on a centimeter-distance scale in some basalt specimens.

Correlations between Al₂O₃-FeO and Al₂O₃-(FeO + MgO) (Figs. 8.3a,b). The contrasts between highland and mare compositions, as well as

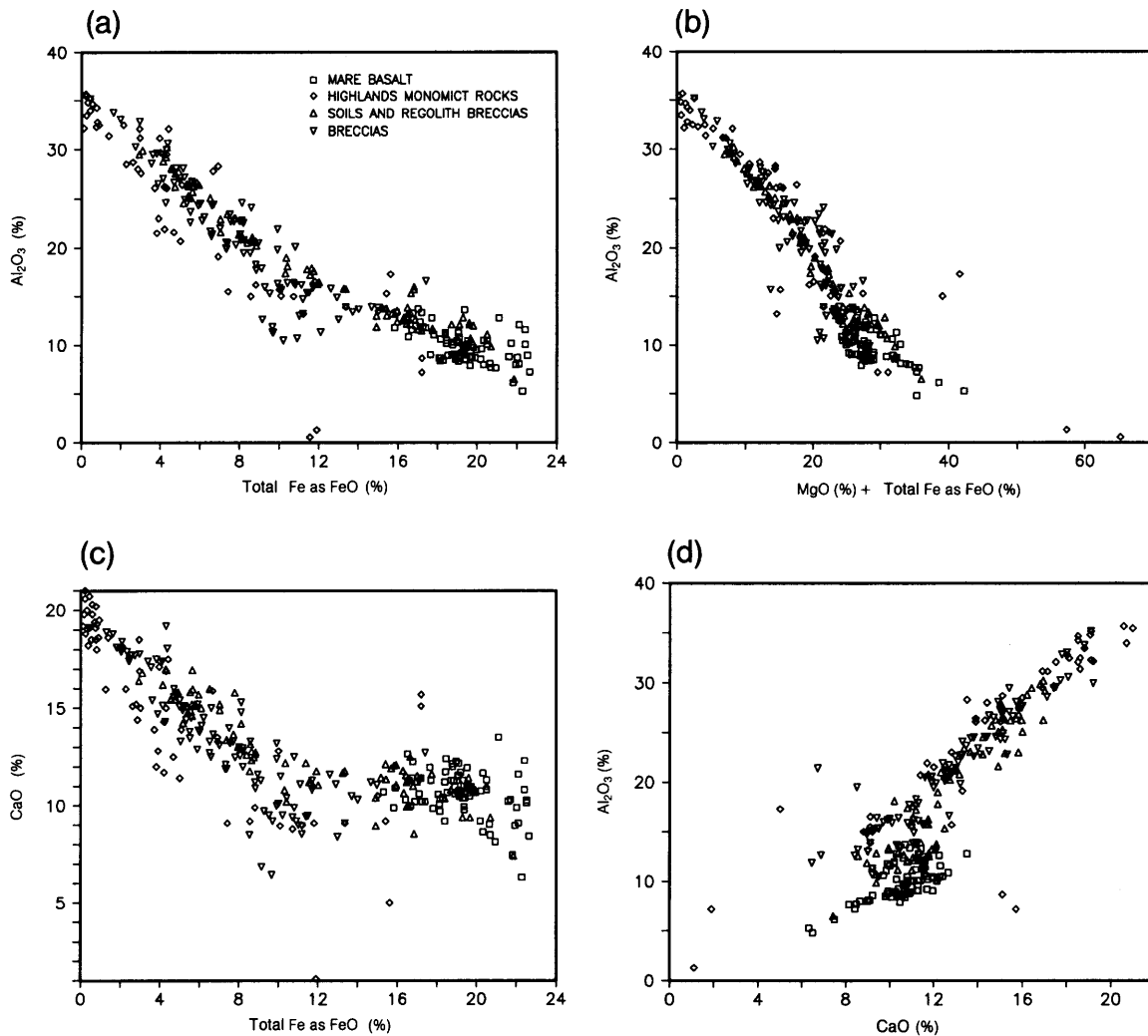


Fig. 8.3. Correlation plots of different major-element concentrations (in wt.% oxide) in lunar materials, showing the effects of different mineral proportions on major-element compositions. **(a)** Plot of Al_2O_3 vs. total Fe as FeO. These two elements show a strong negative correlation. In lunar highland materials (for which $\text{FeO} < 10\%$), the Al_2O_3 concentration decreases as the proportion of Al-bearing plagioclase feldspar decreases and the proportions of Fe-bearing olivine and pyroxene increase. **(b)** Plot of Al_2O_3 vs. (MgO plus total Fe as FeO) for both highland and mare materials. The slope of the line is steeper for mare ($< 15\% \text{Al}_2\text{O}_3$) than for highland materials because of the presence of high-Ca pyroxene in the mare materials, and the higher ratio of Ca-Fe-Mg pyroxene to plagioclase than in the highland rocks. **(c)** Plot of CaO vs. total Fe as FeO for both highland and mare materials. The highland materials ($\text{FeO} < 10\%$) have a steep slope because of their high proportion of plagioclase to mafic minerals. The mare materials ($\text{FeO} > 10\%$) show no decrease in CaO, because in mare materials both pyroxene and plagioclase contain significant Ca, and changes in their relative proportions do not affect the CaO value greatly. **(d)** Plot of Al_2O_3 vs. CaO for both highland and mare materials. The strong positive correlation in highland rocks ($\text{CaO} > 12\%$) is due to the presence of both elements in the mineral plagioclase. The effect is not seen in mare materials ($\text{CaO} < 12\%$) because Ca is present in both plagioclase and pyroxene.

the effects of the variable amounts of different minerals in the samples, become clearer if we examine correlations and anticorrelations among the major elements. For example, there is a well-developed anticorrelation between FeO and Al₂O₃ (Fig. 8.3a). The principal mineral components of most lunar rocks are plagioclase and mafic minerals (pyroxene and olivine). The higher the proportion of plagioclase, the higher the Al₂O₃ concentration is. Rocks with higher proportions of plagioclase necessarily contain lower proportions of mafic minerals, which makes their FeO concentrations lower. Thus, to a first approximation, this anticorrelation simply reflects the varying proportions of plagioclase and mafic minerals.

However, a variety of materials plot on the low-Al₂O₃ side of this trend. These include the magnesian troctolites (diamond-shaped symbols at about 4–5% FeO), magnesian norites (diamonds at about 7–9% FeO), magnesian dunites (diamonds at about 12% FeO), and granitic materials from sample 12013 (inverted triangles at about 9–12% FeO). Furthermore, there is a break in slope at about 8–10% FeO. This break arises because most materials with concentrations of FeO greater than 10% are either mare basalts or soils containing a substantial proportion of mare basalt. Most materials containing <8% FeO are mainly of highland origin. The mare basalts are more ferroan and also richer in ilmenite than most highland materials. If we use the sum of FeO and MgO as the abscissa (Fig. 8.3b), then the slope of the trend to the right of about 12% (FeO + MgO) becomes more steeply negative than when FeO alone is used. This reflects the mineralogic properties of the mare basalts, e.g., the presence of high-Ca rather than low-Ca pyroxene despite the higher proportion of Mg,Fe-silicate minerals and ilmenite to plagioclase as compared to highland materials.

Correlations between CaO-FeO and Al₂O₃-CaO (Figs. 8.3c,d). The negative slope for mainly highland materials (<8% FeO) in Fig. 8.3c reflects the higher relative proportion of plagioclase to mafic minerals, as described above. As in the case of Al₂O₃, the CaO values for magnesian highland monomict rocks (diamonds) also fall below the main trend, as do the values for some granitic materials from sample 12013. Highland alkali gabbronorites (diamonds at about 17% FeO) fall to the high-CaO side of the mare basalts. For mare basalts and mare-rich soils, the CaO concentrations are essentially independent of FeO concentrations. This is because the pyroxenes in the mare basalts are the high-Ca variety; their presence dilutes the Al₂O₃ contribution from the feldspars but also provides compensating amounts of Ca to keep the CaO content constant.

The same effect can also be seen in Fig. 8.3d, where the mare materials plot in a broad cluster at ~10% CaO and ~10% Al₂O₃.

Correlations between Na₂O-FeO, Na₂O-CaO, and Al₂O₃-Na₂O (Figs. 8.4a–c). Sodium, which occurs in the plagioclase end member *albite*, might be expected to show a negative correlation with FeO, as do Al₂O₃ and CaO. Actually, only a weak correlation is evident in the mare basalts, and no correlation at all appears in the highland materials with <8% FeO (Fig. 8.4a). In highland samples, or in samples rich in highland components, Na₂O concentrations span a substantial range and are independent of FeO concentrations. Concentrations of Na₂O are highest (up to about 1%) in granitic materials, e.g., the quartz monzodiorite from sample 15405 (diamond at about 12% FeO) and granitic breccia fragments from sample 12013 (inverted triangles at about 9–12% FeO), which lie well above the main group of Na₂O concentrations. Nor is there any correlation between Na₂O and CaO (Fig. 8.4b) or between Na₂O and Al₂O₃ (Fig. 8.4c), as might be expected if plagioclase were the main carrier of both elements. A plausible explanation of this lack of correlation is that varieties of plagioclase richer in Na than those in most of the highland monomict rocks may be more important in the lunar highlands than we currently realize. These data also indicate that some granitic material is also present in highland breccias and soils. Sodium enrichment can also occur in the maria. Some clasts of relatively alkali-rich Apollo 14 mare basalts have Na₂O values well above the main trend for most mare basalts. The highland dunites, which consist almost entirely of olivine, have the lowest Na concentrations.

Correlations between SiO₂-FeO (Fig. 8.4d). There is a slight positive correlation between FeO and SiO₂ for most highland materials (Fig. 8.4d). This probably occurs because most pyroxenes have more SiO₂ (56% to 44%) than anorthite (43%). Therefore, as the proportion of pyroxene increases, the concentrations of FeO and SiO₂ increase together. Silicon-dioxide concentrations are highest in granitic materials, such as quartz monzodiorite and the felsite fragments from sample 12013 (see section 6.3.5), and the SiO₂-FeO data for the highland magnesian norites show Si concentrations that lie above the main trend of the data (diamonds at 8–12% FeO). This relation reflects the larger amount of Mg-bearing enstatite component (which is also higher in Si than the Fe-bearing ferrosilite component) in the pyroxenes in these rocks.

On the same plot, the mare basalts divide into high-Ti and low-Ti groups. The low-Ti group has higher SiO₂ than does the high-Ti group; in the latter group, SiO₂ concentrations are diluted by the greater

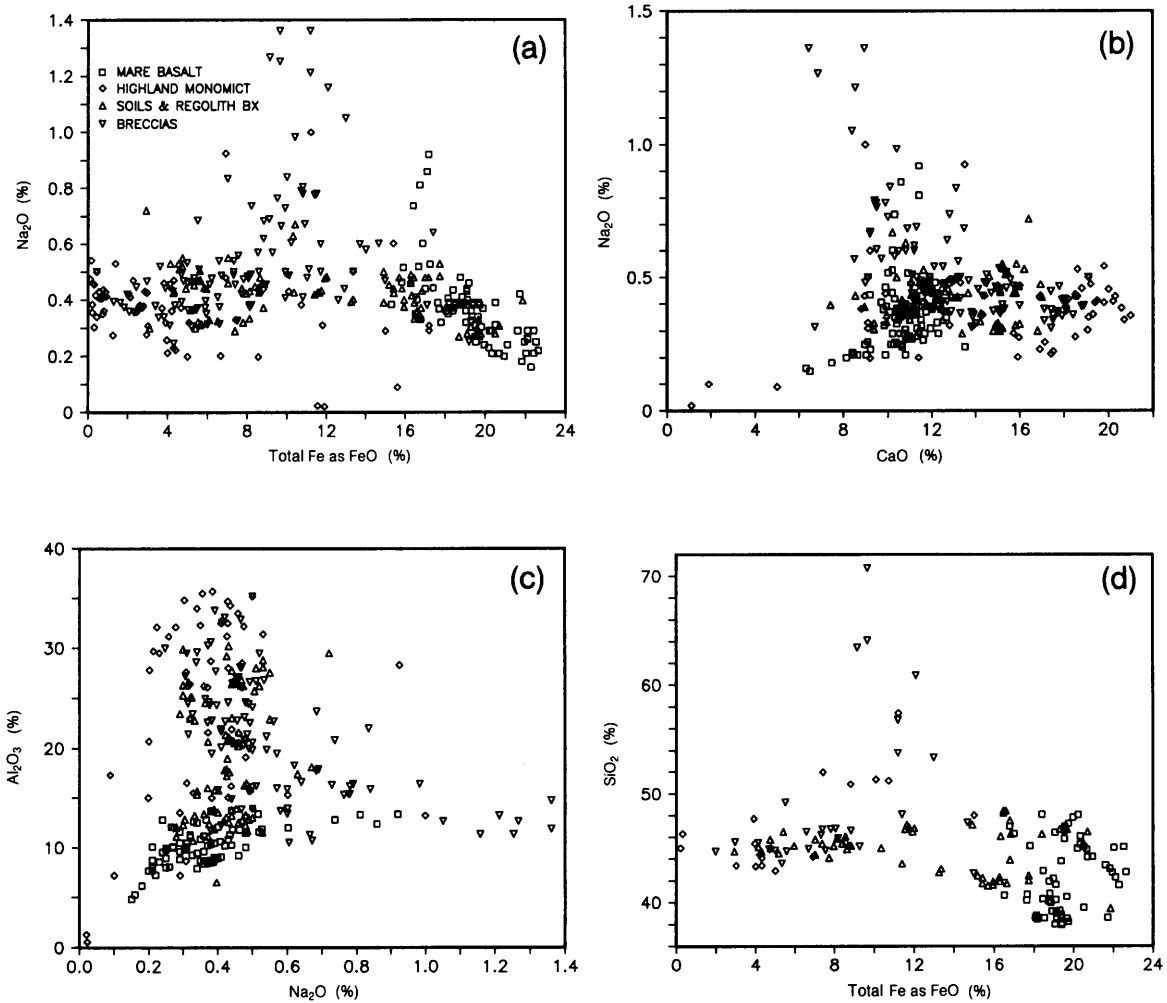
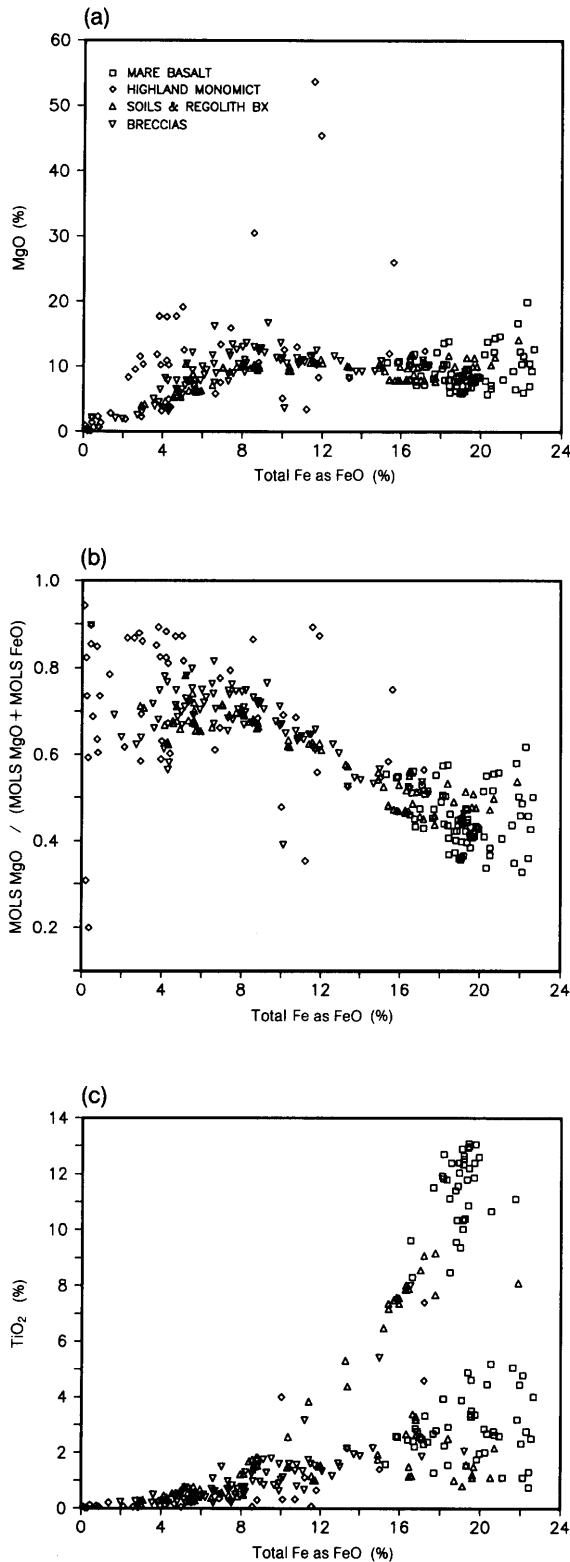


Fig. 8.4. Correlation plots of different major-element concentrations (in wt.% oxide) in lunar materials, showing effects (or lack of effects) of mineral proportions on the chemical composition. **(a)** Plot of Na_2O vs. total Fe as FeO. Unlike CaO (Fig. 8.3c), Na_2O concentrations do not vary with changes in relative proportions of major minerals in highland materials ($\text{FeO} < 10\%$), indicating that plagioclase feldspar is not the only carrier of Na_2O in these materials. **(b)** Plot of Na_2O vs. CaO; **(c)** Plot of Al_2O_3 vs. Na_2O . For the same reasons, no simple correlation is present in either of these plots. **(d)** Plot of SiO_2 vs. total Fe as FeO. For highland materials ($\text{FeO} < 10\%$), SiO_2 concentrations increase slightly with increasing FeO because the SiO_2 concentration in low-Ca pyroxene, which becomes a significant component in higher-Fe highland materials, is slightly higher than in plagioclase, which becomes less abundant as the Fe content increases. However, for mare basalts ($\text{FeO} > 10\%$), SiO_2 decreases with increasing Fe because the pyroxene in such rocks is the high-Ca variety, which has a lower SiO_2 concentration than the low-Ca pyroxene present in highland materials. The two trends visible in the mare basalt region correspond to high-Ti basalts (lower SiO_2 data) and low-Ti basalts.

amounts of ilmenite (FeTiO_3) present.

Correlations between MgO - FeO and $\text{Mg}'\text{-FeO}$ (Figs. 8.5a,b). For highland materials with $\text{FeO} < 8\%$ there is a rough correlation between MgO and FeO (Fig. 8.5a) that reflects the varying proportions of mafic minerals (which carry both the Mg and Fe) to plagioclase. The highland troctolites (diamonds at

$2\% < \text{FeO} < 6\%$, plus one at 9% FeO) display a separate trend because they contain mafic minerals (chiefly olivine) that are more magnesium than those of the polymict soils and breccias. The MgO concentrations are highest in the dunites, which consist almost entirely of magnesian olivine. Another rock type, highland spinel troctolite (diamond at



about 16% FeO), lies well above the main trend. Between about 9% FeO and the cluster of points for mare basalts, the polymict breccias and soils show a slightly decreasing ratio of Mg to Fe, as the proportion of Fe-rich mare basalts increases.

Among the mare basalts themselves, there is a considerable spread caused by wide variations in the amount of ilmenite. A high proportion of ilmenite produces a high FeO/MgO ratio (equivalent to the low MgO/FeO ratio shown). A low proportion of ilmenite is equivalent to a higher proportion of mafic silicate minerals, which have higher MgO/FeO ratios, and this set of points therefore has a positive slope.

Some of these features can also be seen in a plot of Mg' , the molar proportion of MgO to that of (MgO + FeO) (Fig. 8.5b). The lowest values of Mg' are for anorthosite 15415; these fall below most values for anorthosites. The highest values of Mg' are found in the magnesian troctolites and in the two dunites. Data points for the quartz monzodiorite (diamond at about 12% FeO) and for two alkali gabbros (a diamond and an inverted triangle at 10% FeO) fall well below the trend. The values of Mg' cover a wide range for highland materials (<8% FeO), then decrease for samples representing mixtures of highland and mare basalts to the generally lower values for the mare basalts.

Fig. 8.5. Correlation plots of different major-element concentrations (molar or wt.% oxide) in lunar materials, showing effects of mineral proportions on the chemical composition. **(a)** Plot of MgO vs. total Fe as FeO. MgO concentrations reflect the relative proportions of plagioclase vs. Fe- and Mg-bearing mafic minerals. Data points for some unusual highland rock types, the *dunites* and *troctolites* (see section 6.3.4), lie well above the main trend of the data. The spread of FeO concentrations in mare materials (FeO > 10%) within a limited range of MgO concentrations reflects variations in the proportion of ilmenite as well as plagioclase and pyroxene. **(b)** Plot of the molar ratio of [MgO/(MgO + FeO)] vs. total Fe as FeO. The higher values for highland data points (FeO < 10%) indicate that the proportion of Mg in cation sites in highland minerals is higher than in the same minerals from mare basalts (FeO > 10%). **(c)** Plot of TiO₂ vs. total Fe as FeO. For highland materials (FeO < 10%), there is only a gradual increase in TiO₂ concentrations with FeO, because the proportion of ilmenite and related Ti-bearing minerals that are associated with mafic minerals in highland rocks is small. For mare basalt materials (FeO > 10%), there is a steep, well-defined increase with FeO for the high-Ti basalts and a lower cluster for the low-Ti and very-low-Ti basalts.

Correlations between TiO_2 -FeO (Fig. 8.5c).

Concentrations of TiO_2 increase slightly with FeO in highland materials, then increase significantly for polymict materials containing appreciable proportions of mare basalt with high TiO_2 content. The distinctions between high-Ti and low-Ti mare basalt are clearly displayed in this diagram.

8.3.4. Ores of Major Elements

The lunar minerals that contain the major elements are generally not the same minerals that would be used on Earth as economical sources for those elements. For example, Al is generally extracted from bauxite on Earth, whereas the likeliest source of Al on the Moon would be plagioclase. The common lunar rocks and minerals are therefore unlikely ores in a terrestrial sense. However, the general definition of ore is any material whose use is economical. If resources are to be sought from the Moon, then these rocks and minerals are the chemical forms that we can expect to serve as lunar ores. A more detailed description of some possible lunar major-element ores is provided in section A11.2; some more general considerations are discussed below.

The minerals in lunar rocks are generally tightly intergrown and are difficult to separate from each other. Nevertheless, minerals are the primary entities that can be separated and concentrated by strictly mechanical means, i.e., with no chemical processing, to provide material enriched in a particular chemical element. For some purposes, some of the necessary processing has already been done by nature. There is a great abundance of pulverized rock, the lunar regolith, that forms a surface layer several meters deep. In the regolith, some grains of all lunar minerals occur as single fragments, not interlocked with crystals of other minerals as in the original rocks. Unfortunately, most of the regolith is made up not of such grains but of small rock fragments and glassy agglutinates. Single-mineral grains make up only a small fraction of most lunar soils, so that mineral separations from large volumes of soil would be needed to provide significant quantities of individual minerals.

Any further concentration beyond mechanical mineral separation requires chemical destruction of the mineral or glass containing the element by some process such as dissolution, melting, or evaporation. Such destruction does not necessarily require prior separation of a mineral concentrate, but without some mechanical concentration, the chemical processing will have to be done on a larger quantity of starting material. For this reason, any schemes to

obtain a particular element from a lunar mineral should take into account the methods and economics of mechanically extracting that mineral from bulk rock or soil.

It is almost certain that the bulk raw material for any lunar resource will be a complicated mixture of rocks, minerals, or glasses. Such polymict materials make up most of the Apollo and Luna sample collections and the Antarctic lunar meteorites. Future lunar explorers will surely encounter similar polymict materials at the surface over the whole Moon. In addition to the complex soils, most rocks found at the surface in the lunar highlands will be polymict breccias. Few regions consisting of nearly monomineralic highland igneous rocks such as anorthosite or dunite have been discovered so far by Earth-based spectroscopic mapping of the Moon (section 10.2). Most regions of the highlands for which we have orbital gamma-ray data indicate the presence of significant concentrations of Th and Fe. Some investigators interpret these results as indicating the presence of anorthosite "contaminated" by small proportions of KREEP (see section 8.4). Others who have chemically analyzed polymict lunar samples in the laboratory interpret some data as indicating the presence of plutonic igneous rocks that contain significant amounts of mafic minerals in addition to plagioclase. In this interpretation the compositions may represent igneous precursors (plagioclase-enriched norites or gabbros) that were mixtures of mafic minerals and plagioclase, or they may represent mechanical mixtures of anorthosite with dunite or other igneous rocks rich in mafic minerals. There may be substantial bodies of anorthosite and dunite buried at shallow depths beneath the surface soils seen by remote sensing, but we have no independent evidence for their presence.

A special feature of the Moon is the ubiquitous occurrence of Fe metal as a trace mineral in lunar samples. On Earth, nearly all lavas and intrusive igneous rocks have part of their Fe in the divalent (2+) oxidation state, but at least a few percent is in the trivalent (3+) state. Furthermore, Fe oxidizes readily at the Earth's surface. In contrast, lunar igneous rocks have no measurable trivalent Fe, but they commonly contain small amounts of Fe metal, a result of the much more chemically reducing conditions on the Moon than on the Earth. The lunar surface, as well as the lunar interior, is a highly reducing environment. Meteoroids that have struck the lunar surface have introduced small amounts (a fraction of a percent in most soils) of metallic Fe-Ni alloy into the surface soils, and have liberated similar metals from lunar soils by reduction of FeO (see section 5.4.3). These alloys could be concentrated by simple magnetic methods. However, much

of the metal is incorporated into glassy agglutinates and microbreccia fragments, so a clean separate of pure metal cannot be easily obtained.

8.4. INCOMPATIBLE TRACE ELEMENTS

A large group of chemical elements does not fit readily into crystal sites of major minerals. Because of this behavior, they are called *incompatible trace elements*. Being unable to enter the crystal lattices of common minerals in large amounts, they tend to enter the liquid phase preferentially when rocks and minerals begin to melt, and they tend to remain in the liquid phase when it begins to crystallize. If they become sufficiently concentrated in a liquid after extensive crystallization has taken place, some of these elements form minerals of their own. For example, the mineral *zircon* ($ZrSiO_4$) forms if the concentration of Zr becomes high enough. Such trace minerals, as well as trace-to-minor minerals such as *whitlockite* [$Ca_3(PO_4)_2$], which may form if the concentration of P becomes high enough, serve as hosts for many incompatible trace elements such as Hf, Y, and the REE (see Tables A5.11a and A5.18).

The behavior of the REE in a cooling basaltic lava provides a good demonstration of the processes affecting incompatible elements. The REE (except Eu) are typical incompatible trace elements. The major basaltic minerals plagioclase and pyroxene are considered to “exclude” REE; actually, those minerals will accept them, but they do not compete effectively for the REE because their crystal sites are energetically less favorable for REE ions than are the sites in the coexisting silicate liquid. The REE are thus said to be “incompatible” with respect to the mineral phases forming from the melt, and they tend to stay in the melt as crystallization proceeds. As the last portions of remaining melt crystallize, the bulk of the REE may enter late-forming phosphate minerals such as apatite or whitlockite, in which they are compatible minor elements, or they may form trace amounts of a rare earth mineral such as *monazite* [(REE,Y,Th)(PO_4)], which is extremely rare on the Moon but in which the REE are essential components. Late-forming materials rich in incompatible elements thus develop in trace quantities in the interstices between earlier-formed crystals of major minerals, forming a complex mixture of fine-grained minerals and glass collectively known as *mesostasis*.

Figure 8.6 shows the abundances of the REE in the major minerals and in the mesostasis of a lunar basalt, sample 70135 (*Haskin and Korotev, 1977*), illustrating how the REE distribute, or *partition*, themselves among solid and liquid phases. The highest REE concentrations are in the final liquid or

mesostasis, for which the ratios of concentration to those of the whole rock are greater than 1. Ratios of elemental concentrations in the major minerals to those of the whole rock are almost all less than 1, with ilmenite and pyroxene preferentially including the heavier and smaller REE (Tb-Lu) over the lighter REE, and with plagioclase favoring the lighter REE (especially Eu). Partitioning such as this, which occurs both wholesale during planetary differentiation and on smaller scales of local melting or crystallization, is responsible for the variable distributions among all the incompatible trace elements.

8.4.1. Abundances of Incompatible Trace Elements in Lunar Crustal Materials

The incompatible trace elements form a large group that includes many reactive, cation-forming elements whose cosmic relative abundances are low. When planets form, the concentrations of these elements in the planets are too low to produce major minerals. During the early chemical differentiation of the Moon, these incompatible trace elements partially separated as a group from the other chemical elements. They became particularly concentrated in early silicate melts of noritic or gabbroic composition called KREEP (discussed below and in sections 2.4 and 6.3.2). Even though this concentration mechanism has enriched the incompatible trace elements in some lunar surface materials to levels three orders of magnitude above their abundances in meteorites or in the bulk Moon, they remain trace elements (i.e., <0.1 wt.%) in virtually all known types of lunar rocks.

Figure 8.7 shows concentrations of most of the incompatible trace elements in a variety of lunar materials. Table A8.2 provides some statistics of their concentrations in these materials. Many of these elements have been studied extensively by geochemists, because they indicate the types of igneous processes that formed lunar (or terrestrial) rocks and to what extent those processes operated. For example, the concentrations of these elements and their abundances relative to each other can be used to infer the compositions of the source regions that produced the silicate melts now present as igneous rocks of the lunar crust.

For many incompatible trace elements, analytical data from lunar materials are abundant (e.g., K, Rb, and La; Figs. 8.7e,f,m). For others, relatively few analyses are available; such elements are determined infrequently by geochemists, usually because accurate analyses for them are difficult or time consuming. Examples of elements for which relatively few data are available are Pr, Ho, and Tm. Concentrations

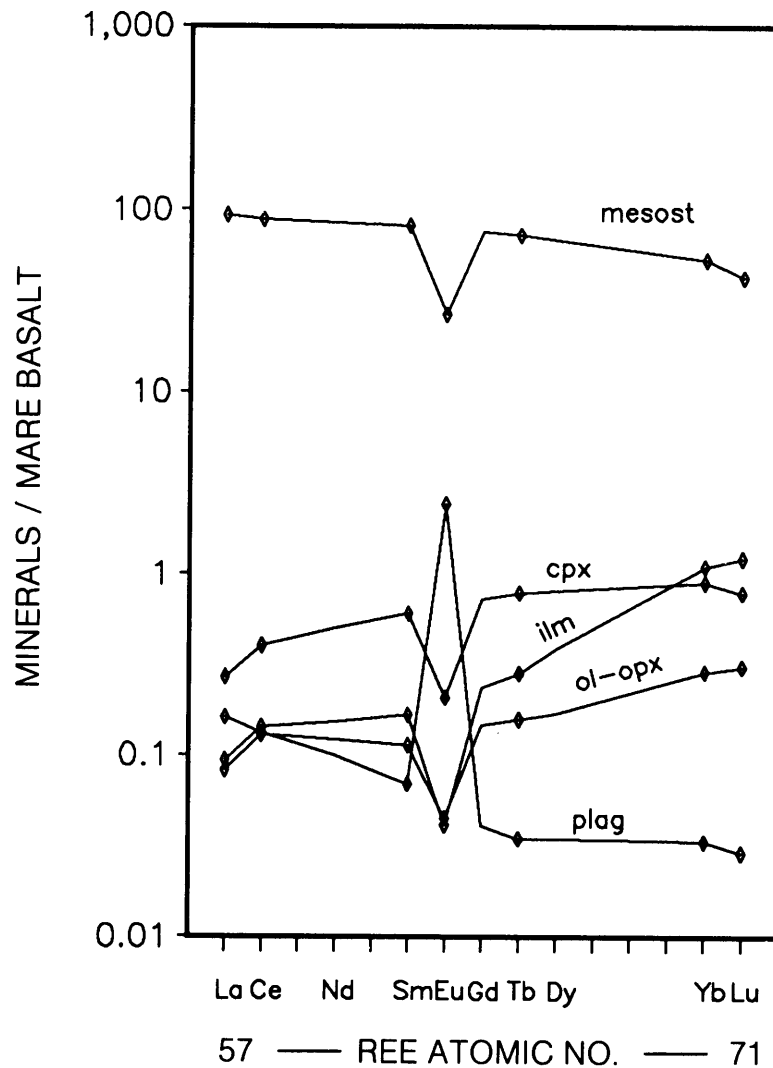


Fig. 8.6. Concentrations of REE in mare basalt sample 70135, showing partitioning of the REE between different minerals and the late-crystallizing *mesostasis* relative to the bulk mare basalt melt. Horizontal axis shows REE in order of increasing atomic number. Vertical axis shows value of the *partition coefficient* or the ratio of the concentration in the mineral to the concentration in the bulk melt (mare basalt). Data are presented for several minerals: plagioclase (plag), olivine and low-Ca orthopyroxene (ol-opx), ilmenite (ilm), high-Ca pyroxene (cpx), and mesostasis (mesost). Values of the distribution coefficient differ widely between different minerals, indicating that such partitioning is an important separation mechanism for incompatible trace elements. During crystallization of the initially liquid lava, the minerals grew and their composition evolved as the extent of crystallization increased (*Haskin and Korotev, 1977*). In partitioning between the minerals and the chemically evolving melt, all REE except Eu tend to remain with the melt (coefficients <1), which is a distinguishing characteristic of all incompatible trace elements. Only a small fraction of each available REE enters the major minerals. The fraction entering plagioclase has a higher proportion of lighter REE than of heavier REE, while the fractions entering Fe- and Mg-rich minerals (olivine, pyroxene) have higher proportions of heavier REE. The mesostasis consists of several minerals and glass that formed from the highly-evolved, last several percent of the original liquid to crystallize on cooling. It has higher REE concentrations than the other minerals, and its negative Eu anomaly shows the effect of the compatibility of Eu with plagioclase (positive Eu anomaly), which has depleted the melt in Eu as plagioclase crystallized.

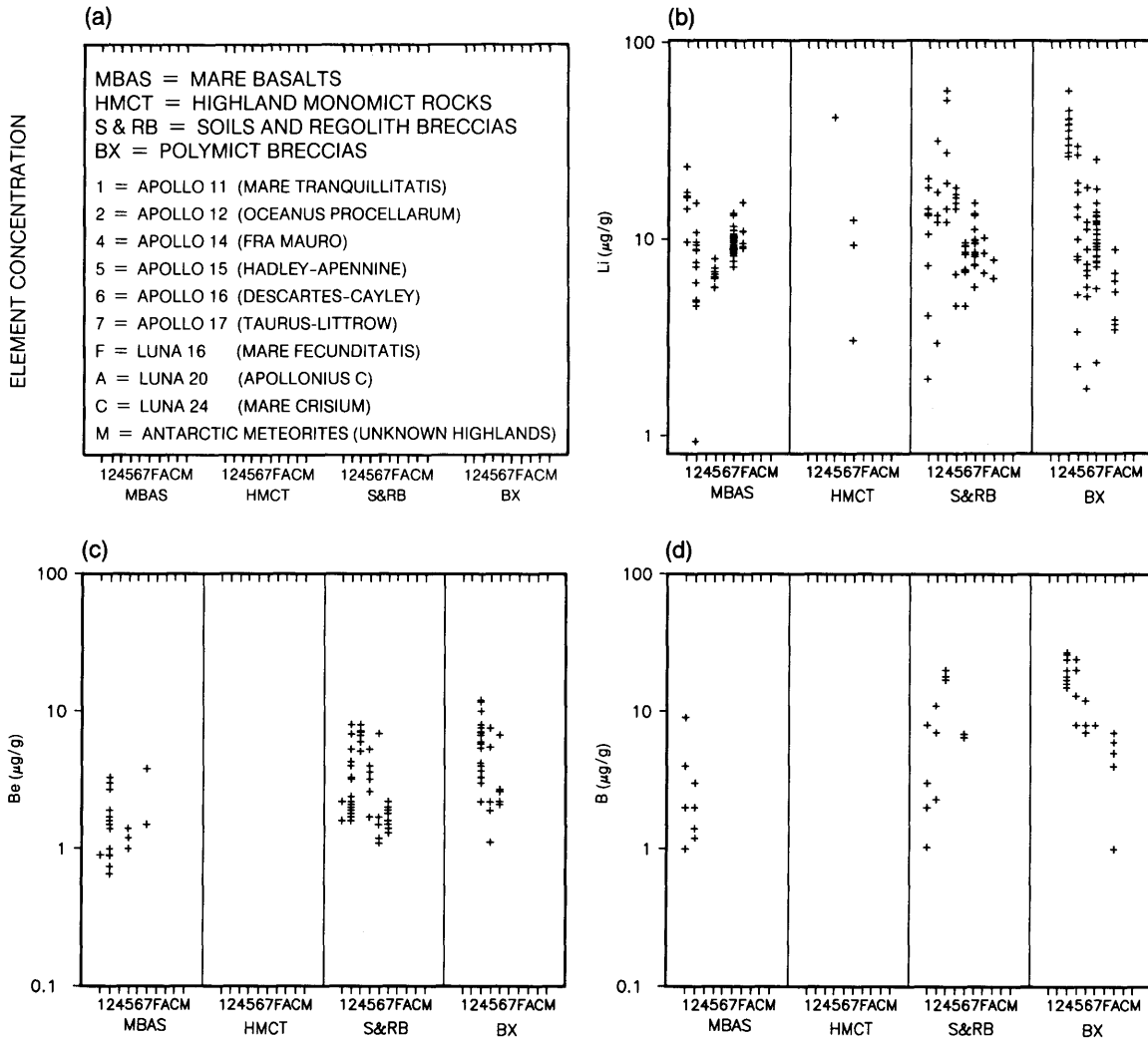


Fig. 8.7. Concentration ranges of incompatible trace elements in various lunar materials: mare basalts (MBAS), highland monomict rocks (HMCT), soils and regolith breccias (S&RB), and polymict breccias (BX). Horizontal axis shows sample types, separated according to individual missions. Vertical axis shows elemental concentrations (in $\mu\text{g/g}$). **(a)** Graphical key to the plots and abbreviations. Data are presented for: **(b)** lithium, Li; **(c)** beryllium, Be; **(d)** boron, B; **(e)** potassium, K; **(f)** rubidium, Rb; **(g)** yttrium, Y; **(h)** zirconium, Zr; **(i)** niobium, Nb; **(j)** tin, Sn; **(k)** cesium, Cs; **(l)** barium, Ba; **(m)** lanthanum, La; **(n)** cerium, Ce; **(o)** samarium, Sm; **(p)** europium, Eu; **(q)** ytterbium, Yb; **(r)** hafnium, Hf; **(s)** tantalum, Ta; **(t)** thorium, Th; **(u)** uranium, U. Most measurements were made by either mass spectrometry with isotope dilution or by neutron activation analysis. Statistical data for most of these plots are given in Table A8.2. The data shown here are a relatively small sampling of the total available for this widely studied element group. They include most of the analyses of Wänke and coworkers, who provided reliable data for a large number of elements in each sample analyzed. Such multiple data from a single sample are important in deciphering the correlations in behavior among different elements. The data also include measurements by other investigators.

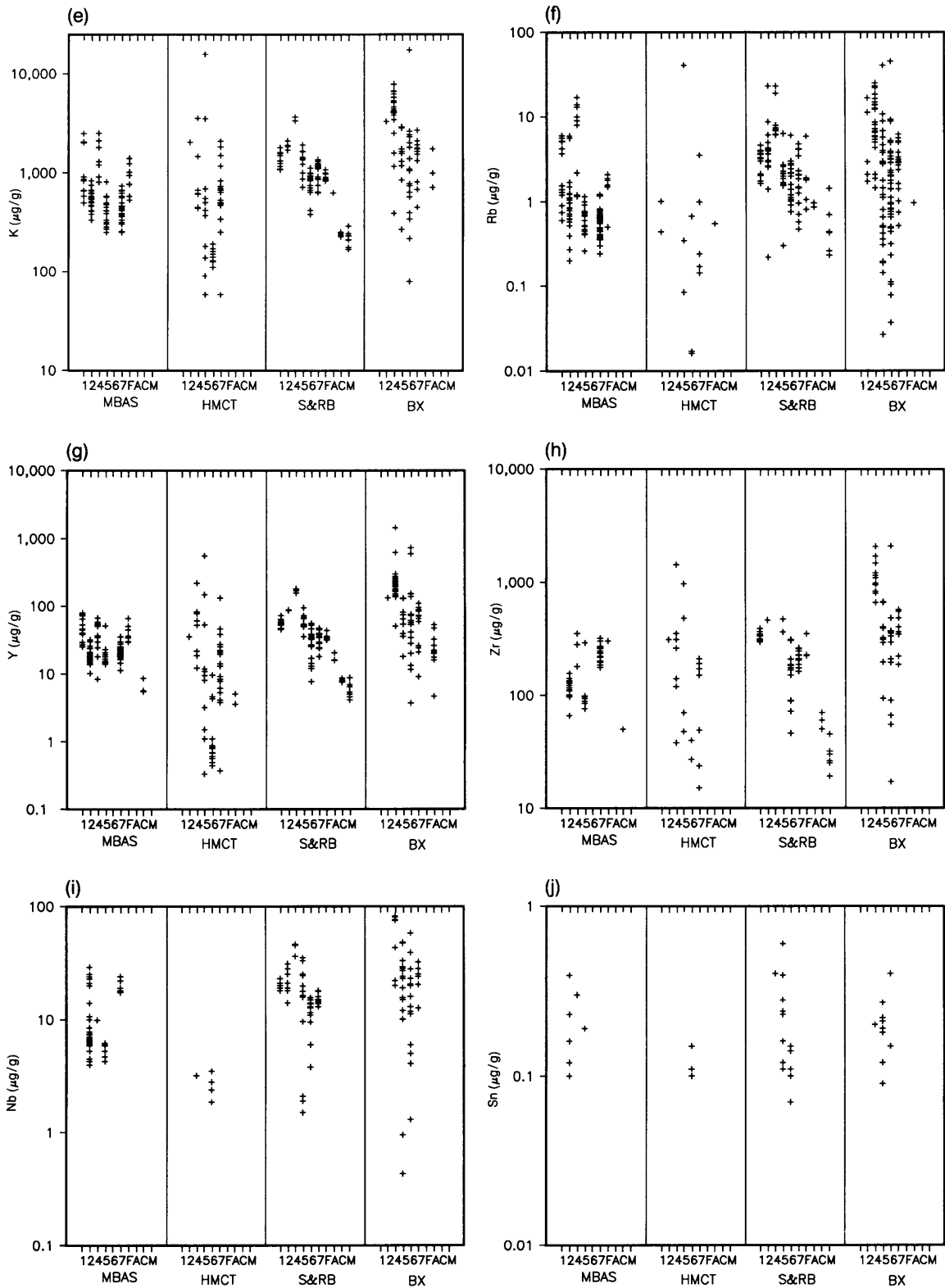


Fig. 8.7. (continued).

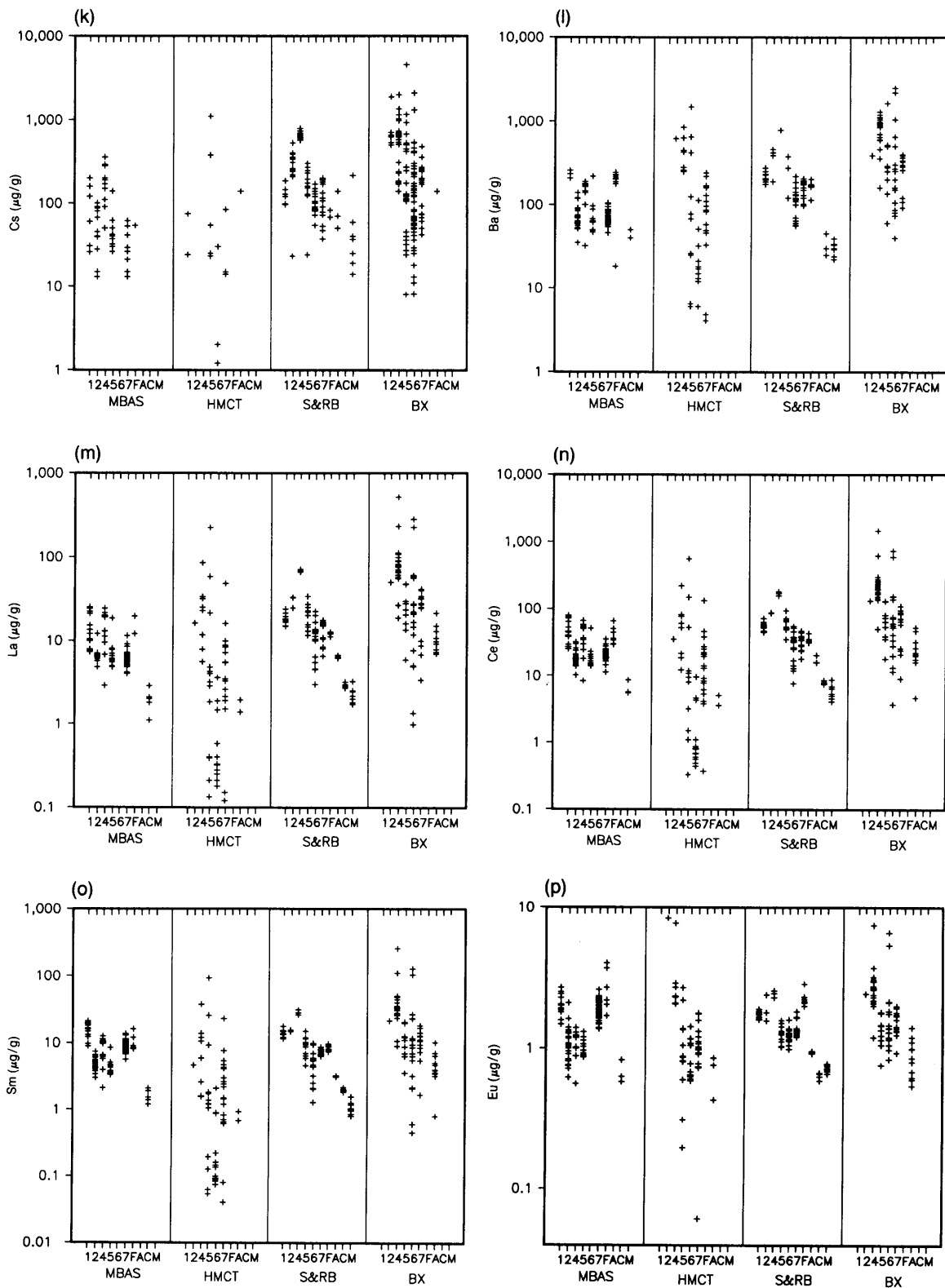


Fig. 8.7. (continued).

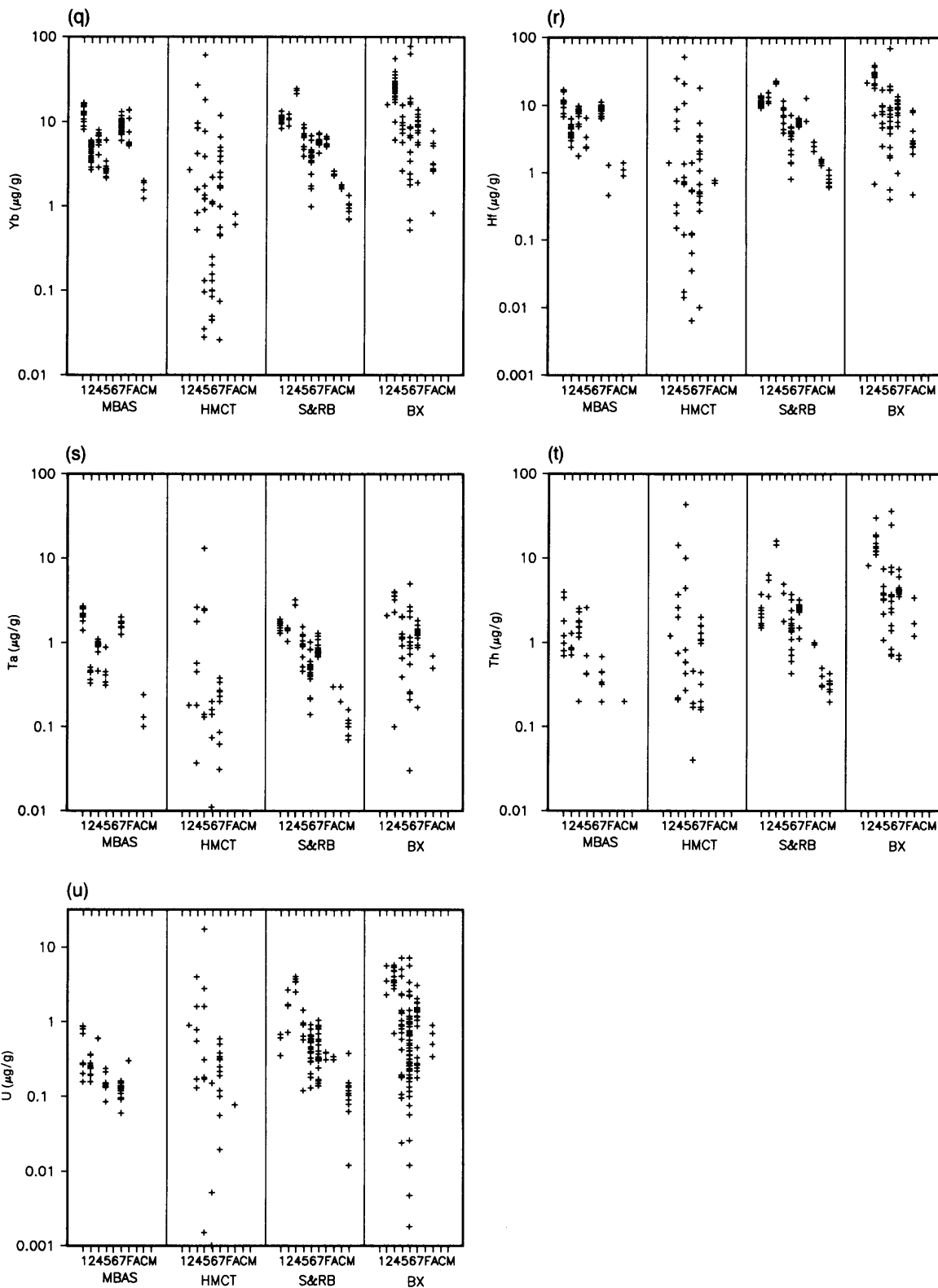


Fig. 8.7. (continued).

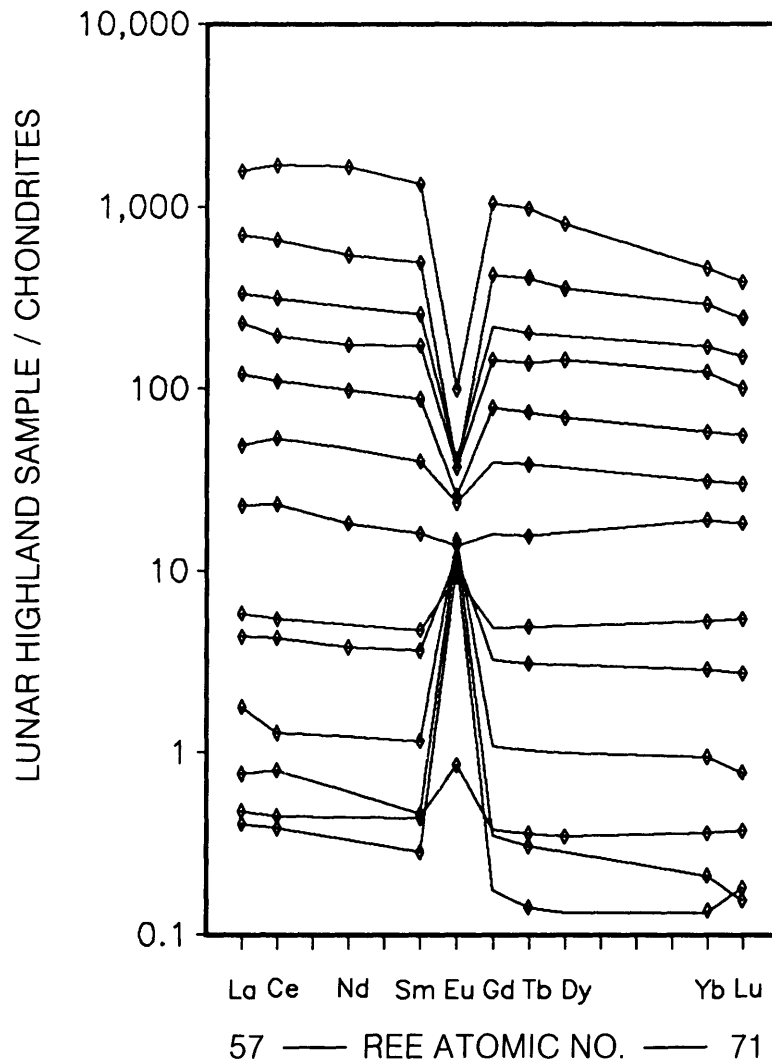


Fig. 8.8. Concentrations of REE in a series of samples from the lunar highlands. Horizontal axis shows the REE in order of increasing atomic number. Vertical axis shows the REE concentration in the sample, which has been normalized by dividing it by the concentration in chondritic meteorites (Table 8.1), a procedure that provides a common reference standard. There is a smooth transition between samples with very high REE concentrations (at top) to samples with low REE concentrations (at bottom). The highest concentrations are from a phosphate-rich anorthosite, the second-highest from typical Apollo 14 KREEP. The lowest concentrations are from ferroan anorthosites, except for the sample with very low Eu concentration, which is a dunite. The sharp negative Eu anomalies (upper curves) and positive Eu anomalies (lower curves) are produced by the entry of Eu into plagioclase feldspar, which has been concentrated in the REE-poor anorthositic highland samples and has been depleted in the REE-rich highland samples. The compatibility of Eu^{2+} with plagioclase makes the compositional range of Eu much lower than that of other REE, or of incompatible trace elements in general.

for these and most other REE are not included in Fig. 8.7. However, because of the general chemical similarities among REE, concentrations for those REE (except Eu) that are not illustrated can be estimated from the data for La, Ce, Sm, and Yb, which are shown (Figs. 8.7m,n,o,q). For example, the concentration of one REE can be estimated from that of a REE of adjacent atomic number by using the ratio of the two REE concentrations determined for a similar material, e.g., KREEP or chondritic meteorites. A better estimate can be made by dividing the concentrations of the analyzed REE in the sample of interest by those for KREEP or chondritic meteorites, and plotting the ratios against REE atomic number, as in Fig. 8.8. The value of the ratio for an undetermined REE can then be estimated by interpolation on the graph and multiplied by the concentration in KREEP or chondritic meteorites (whichever was used as the standard to make the graph) to give the desired REE concentration. On such diagrams, when REE concentrations in ordinary chondritic meteorites are used as a standard, the ratios yield smooth curves (except for Eu, which is preferentially incorporated in plagioclase and excluded from most other phases; see Fig. 8.6). These estimates of REE concentration can be quite reliable. For lunar samples, a good alternative to ordinary chondrites as a standard is the REE concentrations in KREEP (e.g., Warren and Wasson, 1979a). Rare earth element concentrations in chondrites and KREEP are given in Table 8.1 (data averaged from several compilations).

Such graphical estimates are reliable for the REE (except Eu), which form a geochemically coherent group, but for other elements it is more risky to estimate the concentration of one incompatible trace element from the concentration of another. However, even for other elements, estimates within a factor of 2 of the correct value can usually be obtained, particularly for samples that have high overall incompatible-element concentrations. In many highland materials, correlations among all elements in the group are strong, and such estimates can be quite reliable.

However, such estimates for elements other than the REE should not be used for comparing widely different lunar materials. Even for the chemically coherent pair Zr-Hf, there is evidence for separation of Zr from Hf in lunar materials. The Zr/Hf ratio in typical highland materials rich in incompatible elements is about 42, but ratios for mare basalts average about 33, which is close to the value of 32 for chondritic meteorites (e.g., Wasson, 1985). Hughes and Schmitt (1984, 1985) have confirmed this difference by careful analytical work and have also found consistent differences in values of Zr/Hf among separate groups of mare basalts.

TABLE 8.1. Concentrations of rare earth elements (REE) in chondritic meteorites and in KREEP, the two most-used standards for REE values in lunar materials.

	Chondrites *	KREEP †
La	0.319 ± 0.012	115
Ce	0.836 ± 0.043	283
Pr	0.113 ± 0.007	35.8
Nd	0.602 ± 0.019	181
Sm	0.186 ± 0.005	48.7
Eu	0.0724 ± 0.0035	3.1
Gd	0.259 ± 0.012	57.0
Tb	0.0483 ± 0.0022	10.1
Dy	0.324 ± 0.013	64.8
Ho	0.0725 ± 0.0032	14.0
Er	0.21 ± 0.011	39.3
Tm	0.0315 ± 0.0013	5.67
Yb	0.208 ± 0.009	35.8
Lu	0.0328 ± 0.0013	5.48

All values are in µg/g.

* Average of values from Haskin *et al.* (1968), Nakamura (1974), Leedy chondrite/1.225 (Masuda *et al.*, 1973), and CI chondrite avg./0.796 (Evensen *et al.*, 1978).

† Apollo 14 KREEP, adapted from Warren and Wasson (1979a).

The data in Fig. 8.7 provide first-order information on abundances and ranges of concentrations of the incompatible trace elements in a wide variety of lunar materials. Figure 8.7 contains only a small fraction of the available data for REE, Hf, Y, Cs, Zr, Ba, P, K, Rb, Ta, and U in lunar materials, but it contains most of the available data for these elements in certain types of rocks (especially the highland monomict rocks). It also contains most of the available data for Nb, Sn, Li, Be, B, and W in all types of rocks and soils.

Because of the general geochemical coherence of the incompatible trace elements, this group should show about the same relative range of variation as observed for Sm (~10⁴). However, some elements do not show as broad a range in Fig. 8.7 because their analytical detection limits were too high to allow measurement at their lowest concentrations. Compilation of a complete database for the most commonly analyzed elements is beyond the scope of this work, but anyone interested in concentrations of the more commonly determined incompatible trace elements will find a large and growing supply of high quality data in the Lunar and Planetary Science Conference Proceedings (e.g., Wänke *et al.*, 1977).

The broadest range of concentrations for most incompatible trace elements is found among the highland monomict rocks. Most of these rocks are

fragments obtained from lunar breccias, but on the size scale taken for chemical analysis they have not been mixed with other lunar materials. These igneous rocks are survivors from the early highlands, and their compositions were strongly differentiated from that of the bulk Moon (section 2.4.3). Many of these rocks also have compositions that are strongly fractionated compared to compositions of partial melts of bulk lunar material.

Highland monomict rocks are the dominant components of some breccias, and they are responsible for the fact that these breccias have a substantial range of concentrations for most elements. Although the soils also consist of mixtures of rock types, they have smaller ranges of concentrations than either the breccias or the highland monomict rocks. This situation occurs because the soils are mixtures of a sufficient variety of different materials to average out the compositional differences introduced by the igneous rocks. Among mare basalts, those from the Apollo 11 and 17 sites have significantly higher concentrations of incompatible trace elements than those from the Apollo 12, Apollo 15, and Luna 24 sites. The magnitude of the range of concentrations for incompatible trace elements in mare basalts is about the same as that for all lunar soils.

No rocks with ore-grade concentrations of the incompatible trace elements are yet known. However, these elements are so enriched in some rock types, particularly those that bear phosphate minerals, that in extreme cases the geochemical processes that concentrated them into phosphates may have produced ores.

8.4.2. Incompatible Trace Elements in Lunar Highland Materials: KREEP

In considering the incompatible trace elements, it is useful to discuss highland rocks and soils separately from those of the maria. This is because the concentrations of these elements in highland breccias and soils are so strongly dominated by *KREEP* that the incompatible trace elements correlate well with each other over a wide range of surface materials.

The nature of *KREEP*. “*KREEP*” is a name originally given to an incompatible-trace-element-rich glass (rich in K, REE, and P) that was first discovered among Apollo 12 soil fragments (*Hubbard et al.*, 1971). The term *KREEP*, originally applied to fragments of glass with this particular composition, is now commonly used as an adjective or as a general term (“*KREEP*” or “*KREEPy*”) to refer to any lunar material with the same characteristic set of relative abundances of incompatible trace elements

first found in *KREEP*. Relative abundances for the REE in Apollo 14 *KREEP* are shown as the next-to-highest curve in Fig. 8.8, where they are compared with the abundances in chondritic meteorites, whose relative REE abundances are considered to represent the average for planetary starting materials. This figure can be compared with Fig. 2.6, in which the REE of Apollo 14 *KREEP* are compared to a model whole-Moon composition with REE contents $\sim 2.8 \times$ those of chondritic meteorites. The use of the term *KREEP* as a noun does not imply a specific major-element composition for a rock or soil. However, most materials having the *KREEPy* set of relative trace-element abundances also have major-element abundances in the range for the rock type known as *norite* (a rock with abundant plagioclase and low-Ca pyroxene).

The ultimate origin of the characteristic *KREEPy* trace-element signature is unknown. A few small samples of “*KREEP* basalt,” i.e., fine-grained igneous rocks of noritic composition, have been found in the Apollo collection, primarily from the Apollo 15 site (see section 6.3.2). However, other materials enriched in the incompatible trace elements, some with *KREEPy* relative abundances, have been found in higher concentrations in some highland breccias than in the *KREEP* basalts. *KREEP* is thus a material, or a trace-element composition, associated with the lunar highlands, and it is a key feature in understanding their origin and evolution.

KREEP may have originated when the highlands formed, as incompatible trace elements became concentrated relative to the more abundant major elements, by remaining in the original residual liquids while the more abundant elements crystallized (see *Warren and Wasson*, 1979a, for a review of ideas on the origin of *KREEP*). Alternatively, *KREEP* may have partitioned selectively into liquids formed during the early stages of subsequent partial melting. In either case, the *KREEPy* abundances probably represent the results of selective extraction processes operating in the lunar crust or upper mantle.

Some investigators regard the characteristic trace-element pattern of *KREEP* (next-to-highest curve in Fig. 8.8) to be a general characteristic produced by the Moon’s major differentiation into a crust and mantle. In this view, *KREEP* represents the relative distribution of incompatible trace elements in the lunar crust in a general sense, rather than being the consequence of a specific concentration mechanism or production of a specific rock type. The orbital detection of relatively high intensities of gamma rays from the Th radioactive decay series provides evidence for the presence of substantial areas of *KREEP* on the Moon’s surface, especially in the vicinity of Mare Imbrium and near several other large

craters (see the map of gamma-ray Th intensities, Plate 10.1).

The smooth transition from KREEPy relative abundances and high concentrations of the incompatible trace elements to the more varied relative abundances and lower concentrations for a series of typical lunar highland materials is illustrated in Fig. 8.8. The relative REE abundances, compared here to those of chondritic meteorites (assumed to represent the average relative abundances in solar-system matter), change only gradually over most of the range between the highest and lowest REE concentrations. For some polymict materials, this smooth transition occurs because many of the highland materials that contain high concentrations of incompatible trace elements (i.e., >10 times the concentration in chondrites) are mixtures of the characteristic KREEPy materials, rich in incompatible trace elements, with materials having much lower concentrations of incompatible trace elements.

Concentrations of Eu have a far smaller range than the other REE. This is because Eu is present partly in the 2+ oxidation state under lunar rock-forming conditions and, owing to the different chemical properties of Eu²⁺ compared with those of Eu³⁺ and the other REE³⁺ ions, some of the Eu separates from the rest of REE. In particular, Eu²⁺ becomes enriched relative to the trivalent REE in plagioclase minerals, in which it easily substitutes for Ca²⁺.

Ranges of incompatible-trace-element concentrations in highland materials. The lowest concentrations of incompatible trace elements are found in some of the lunar highland monomict rocks (Fig. 8.7; see section 6.3), especially the anorthosites and dunites. Lunar soils have a range of concentrations. Among polymict samples, the KREEP-rich Apollo 14 soils from Cone Crater and certain breccia fragments (those rich in phosphate minerals) show the highest incompatible-element concentrations. Breccias with high concentrations of incompatible trace elements are discussed in sections 6.3 and 6.4; concentrations of some of these elements in lunar soils are summarized in Tables 7.15 and 7.17. Some entire breccias are relatively rich in incompatible trace elements, e.g., "granitic" breccia 12013, quartz monzodiorites, and phosphate-rich anorthosites. Figure 8.8 shows the relationships between various lunar highland materials in terms of concentration of incompatible REE.

Correlations between incompatible trace elements in highland materials. As mentioned above, the incompatible trace elements are strongly correlated with each other in most sampled highland materials. Typical relationships between concentrations of incompatible trace elements are shown in Fig. 8.9, in which concentrations of La, Hf, Th, and

Ba are plotted against Sm for a variety of highland soils and breccias. Samarium is arbitrarily chosen as a useful element for this comparison because it has been determined with good accuracy over a wide range of concentrations and in many samples. To cover all the incompatible trace elements, correlation coefficients for the regression lines for element pairs are listed in Table 8.2.

Because lunar breccias are heterogeneous on a small scale, accurate determination of correlations requires careful analyses of single breccia fragments for a large number of elements. The correlations described in Table 8.2 are derived mainly from analyses by Wänke and coworkers (see citations for Wanke et al. in the reference section). Their data have been supplemented by data from other researchers to confirm the accuracy of their results, to extend the range of concentrations measured for some elements, and to provide data for elements not analyzed by them. In all cases, only pairs of elements from the same analysis were used in determining the parameters of the correlation lines. In no case was an analysis for one element in one sample of a rock used along with that for the second element determined on a different sample of the same rock. The slopes, intercepts, uncertainties, and correlation coefficients are given for the correlation of concentrations of each incompatible trace element with Sm. The range of concentrations over which each correlation line is considered valid is discussed below. Although parameters are given only for correlation lines with Sm as the abscissa, values for correlation lines between any pair of elements can be obtained by solving the corresponding equations for Sm and equating them to each other.

The values given in Table 8.2 were obtained in several steps. First, values were estimated for the intercepts and slopes of the correlation lines for pairs of elements by making an ordinary least-squares fit to the data from a selected suite of highland samples of reliable analytical quality. (A linear fit was used rather than one based on logarithmic axes as shown in Fig. 8.9.) Then, the distance between the observed concentration in each sample for an element plotted on the ordinate and the concentration predicted by the least-squares line was compared to the standard deviation from the line at the corresponding concentration level for Sm, based on the quality of the least-squares fit. If the concentration of the element deviated by more than 2.7 standard deviations from the line, its sample was eliminated, and a new least-squares line was determined for the remaining samples. This process was repeated until no further samples were eliminated.

The purpose of this iteration was to give the best estimate of the overall correlation. The eliminated

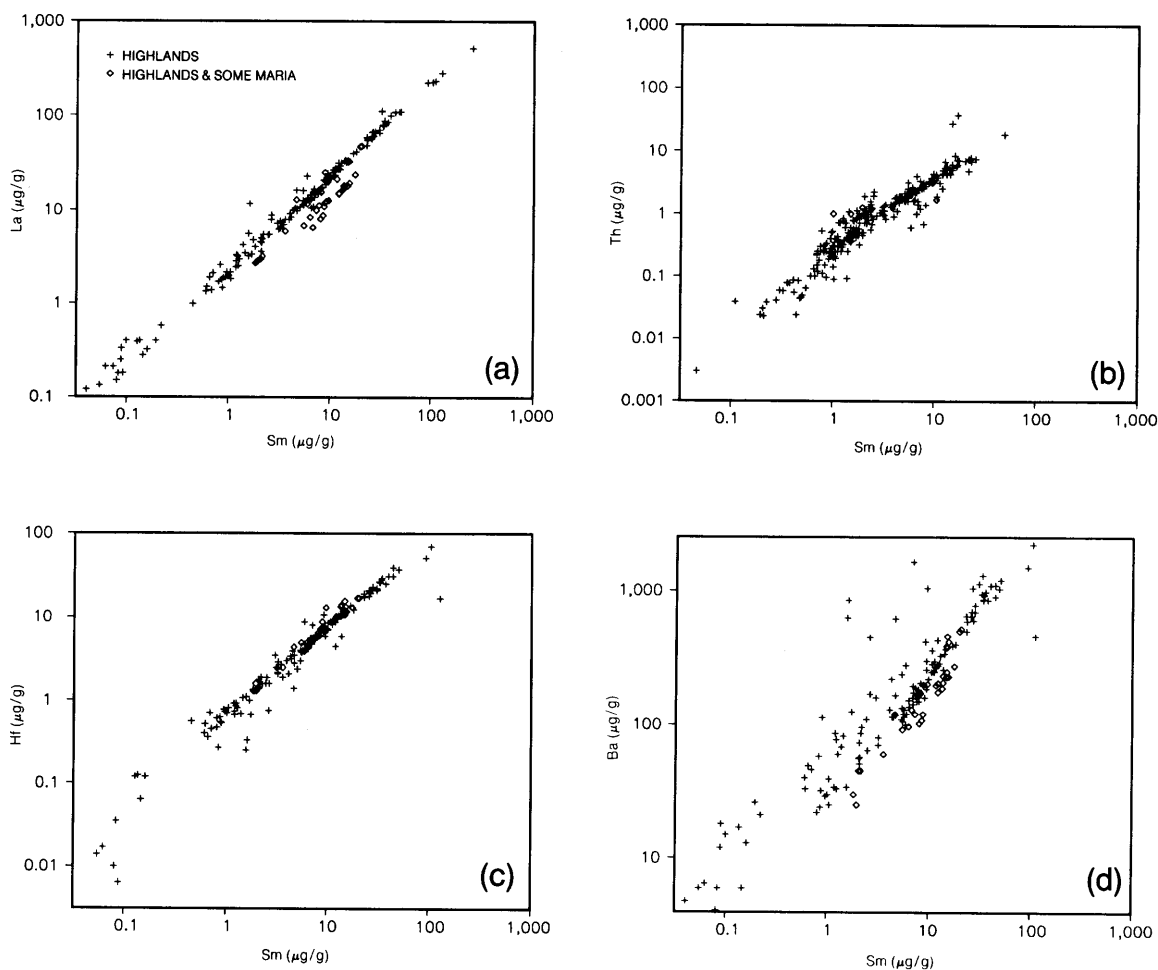


Fig. 8.9. Correlation plots for various incompatible trace elements in lunar (mostly highland) materials, plotted against the concentration of Sm, a typical incompatible trace element. Horizontal and vertical axes are both logarithmic and show elemental concentrations in $\mu\text{g/g}$. **(a)** La vs. Sm; **(b)** Th vs. Sm; **(c)** Hf vs. Sm; **(d)** Ba vs. Sm. The good correlations produced in all these plots demonstrate the strong coherence of this group of elements in a wide range of highland materials. The strength of the correlations with Sm decreases in the order La, Hf, Th, Ba.

points were not necessarily erroneous; they simply did not fit the correlation. The correlations are in fact not valid for all lunar samples, and they are therefore not as strong as suggested by the data of Table 8.2. The table lists the number of samples for each element for which data were retained in calculating the correlation lines, as well as the number of data points eliminated because they fell too far away from the final line.

For the correlation with Eu, data for Sm $< 2.5 \mu\text{g/g}$ were eliminated because the correlation line did not extend to lower Sm concentrations. For Zr, Cs, Dy,

Yb, and Lu, no data were used for Sm $< 0.08 \mu\text{g/g}$, because the correlation clearly ended at about that Sm concentration. For Hf, no data were used for Sm $< 0.3 \mu\text{g/g}$ for the same reason. For these elements, the correlations are not valid for samples with Sm concentrations below those levels.

For the elements Li, P, Y, Nb, and W the correlations may appear to be stronger than they actually are because relatively few samples were analyzed for both these elements and Sm. For Na, K, Rb, Cs, REE, and U the fraction of samples whose data do not fit the correlations is 5–15%. Some of these discrepan-

TABLE 8.2. Correlations between individual incompatible trace elements and samarium (Sm) in highland rocks.

	r	Slope (a)	Intercept (b)	N*	Rej.*	% Rej.*
Li	0.980	1.010 ± 0.0520	3.100 ± 0.800	21	1	4.5
P	0.980	79.000 ± 3.0000	50.000 ± 20.000	36	1	2.7
K	0.980	130.000 ± 1.0000	150.000 ± 30.000	119	18	13.1
Rb	0.960	0.440 ± 0.0200	0.500 ± 0.300	38	4	9.5
Y	0.980	7.800 ± 0.2000	-3.800 ± 1.900	40	0	0.0
Zr	0.995	31.600 ± 0.4000	3.000 ± 4.000	65	16	19.8
Nb	0.960	1.760 ± 0.0700	2.600 ± 0.700	67	3	4.3
Sn	0.880	0.0118 ± 0.0014	0.082 ± 0.017	22	1	4.3
Cs	0.920	13.200 ± 1.0000	45.000 ± 10.000	34	4	10.5
Ba	0.990	23.700 ± 0.4000	11.000 ± 4.000	105	20	16.0
La	0.999	2.300 ± 0.0100	-0.200 ± 0.100	139	21	13.1
Ce	0.998	5.830 ± 0.0400	0.000 ± 0.400	144	14	8.9
Nd	0.998	3.670 ± 0.0300	0.200 ± 0.400	74	10	11.9
Eu	0.970	0.051 ± 0.0014	0.880 ± 0.020	91	16	15.0
Gd	0.998	1.168 ± 0.0120	0.480 ± 0.190	43	2	4.4
Tb	0.998	0.212 ± 0.0014	-0.013 ± 0.012	127	12	8.6
Dy	0.998	1.380 ± 0.0100	-0.020 ± 0.130	88	8	8.3
Yb	0.997	0.721 ± 0.0050	0.140 ± 0.050	141	19	11.9
Lu	0.997	0.102 ± 0.0007	0.021 ± 0.008	145	15	9.4
Hf	0.998	0.807 ± 0.0050	-0.290 ± 0.050	125	16	11.3
Ta	0.994	0.101 ± 0.0011	-0.020 ± 0.011	90	17	15.9
W	0.760	0.050 ± 0.0070	-0.090 ± 0.110	35	1	2.8
Th	0.990	0.390 ± 0.0060	-0.270 ± 0.060	103	7	6.4
U	0.980	0.109 ± 0.0020	-0.150 ± 0.020	72	9	11.1
Na ₂ O	0.840	0.013 ± 0.0008	0.344 ± 0.009	105	8	7.1

Data have been fitted to a correlation line corresponding to the equation $y = ax + b$, where y = concentration of element, x = concentration of Sm. Original data (see Fig. 8.7) are all in $\mu\text{g/g}$, except for Na_2O , which is in wt.%.

* N = number of analyses, a = slope of correlation line, b = intercept, r = residual, rej. = number rejected by program, % rej. = percent rejected.

cies reflect analytical error; however, there is also a significant number of samples whose compositions indicate actual partial separation among the members of the incompatible-trace-element group. This separation also occurs for Zr, Ba, and Ta, but for these elements analytical uncertainty plays a larger role, at least for data obtained by neutron activation analysis. Europium behaves partly as an incompatible trace element in the 3+ state, but also partly as a miscellaneous minor element compatible with plagioclase (in the 2+ state). Because of this unique behavior, the Eu correlation with Sm is less rigorous than those for most other rare earth elements, and 15% of the Eu data had to be excluded in developing the final regression lines.

For many incompatible trace elements the correlations are quite strong, and few or no samples deviate from them. Examples of such tight correlations are the individual REE with each other, e.g., Sm and La as shown in Fig. 8.9a. Some pairs of chemically less closely related elements (e.g., Sm and Hf,

Fig. 8.9c) show similarly close correlations. For other elements there is more scatter, mainly at the lowest and the highest levels of concentration (e.g., Sm and Ba, Fig. 8.9d). Such scatter is even more evident on diagrams with linear, rather than logarithmic axes. The scatter at low concentrations is not caused by poor analyses. The reason for most of this scatter centers around the existence of several different rock types that consist predominantly of different single minerals with low but distinctive trace-element concentrations. At the highest concentrations, individual incompatible trace elements show evidence of partial separation from each other in comparison to their relative abundances in KREEP. This tendency is reflected in the slight change in slope of the data with highest trace-element contents ("super-KREEP") in Fig. 8.9.

Separations between incompatible trace elements in highland materials. Partial separations are expected between those incompatible trace elements that become concentrated into minor- and

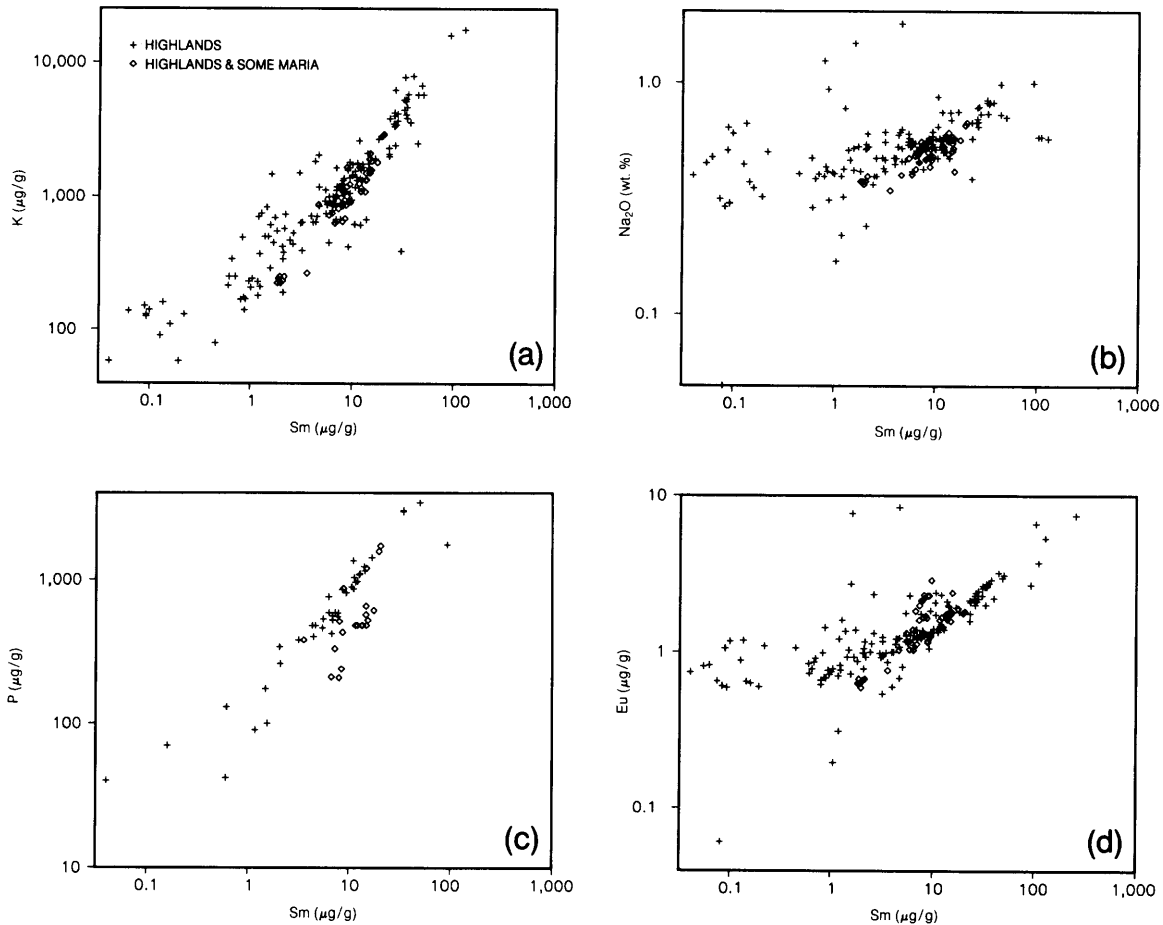


Fig. 8.10. Correlation plots for Na (a major element) and three incompatible trace elements (K, P, and Eu) in lunar (mostly highland) materials, plotted against the concentration of Sm, a typical incompatible trace element. Horizontal and vertical axes are both logarithmic and show elemental concentrations in $\mu\text{g/g}$, except for Na, which is in oxide wt.%. **(a)** K vs. Sm; **(b)** Na_2O vs. Sm; **(c)** P vs. Sm; **(d)** Eu vs. Sm. Good positive correlations with Sm are present for both K and P, but those for Na and Eu are poor.

trace-mineral phases and those that do not. That is, members of the incompatible trace element group can behave as “trace-mineral major elements” if concentrations of these elements become high enough to stabilize such minerals. For example, Zr becomes a major element in the trace mineral zircon, where Hf accompanies it as a minor element. In addition, the REE can be concentrated in the minor phosphate minerals apatite and whitlockite. Individual analyzed samples from some rocks show the presence of “excess” whitlockite or zircon (e.g., Lindstrom, 1984). Values for P show a better

correlation with Sm at higher concentrations than at lower concentrations; presumably, this reflects the close association of the REE with whitlockite.

Potassium, a major element in many terrestrial crustal rocks, is scarce on the Moon, where it is an incompatible trace element (<0.1%) in most lunar crustal rocks (see Sm and K data, Fig. 8.10a, and K data in Table A8.2). At high concentrations, there is also some correlation between Sm and the major-element oxide Na_2O (Fig. 8.10b) and between Sm and Eu (Fig. 8.10d). However, these correlations break down at low concentrations because Na and Eu are

compatible with the mineral plagioclase while Sm is not. In fact, a significant fraction of the Eu in the lunar highlands is present in plagioclase. There is nevertheless a strong tendency for Eu to correlate with the rest of the REE, because only a fraction of the Eu is in the 2+ oxidation state; the rest is in the 3+ state typical of the other REE, and this remainder behaves coherently with the other REE. Other divalent cations have varying degrees of correlation with Sm. For Sr, a 2+ ion that is also compatible with plagioclase, the correlation is much weaker than for Eu because all the Sr is in the 2+ oxidation state. Other 2+ ions such as Ba deviate from Sm only at high concentrations, in contrast to Sr, which deviates most at low concentrations. This is because Ba is too large to fit readily into the Ca sites of plagioclase and, unlike Sr, does not separate into that mineral preferentially to the REE. Barium does enter potassium feldspar readily, and potassium feldspar is present in some lunar rocks. Separation of potassium feldspar from other minerals, e.g., during late-stage crystallization of a melt, would separate Sm from Ba and K. Such processes may contribute to the scatter of Ba-Sm data in Fig. 8.9d.

There is significant scatter over the entire concentration range for Sm and Na₂O (Fig. 8.10b), which probably reflects the combined results of differing degrees of separation of the incompatible trace elements from feldspar in different regions of the Moon. In addition, there may be a tendency for Na to separate from the incompatible trace elements in the impact-produced vapor phase during formation of some breccia fragments.

In most sampled lunar highland soils, the incompatible trace elements are associated with *impact glasses*, *impact-melt breccias*, and *clast-poor impact melts* (sections 6.4.3 to 6.4.5). These rock types are quenched or frozen products of impact melting with variable contributions from KREEP-bearing target materials. Most highland soils are mixtures of rock and mineral fragments, earlier soils, and the products of melting of earlier soils. The mixing process has been continuous and thorough. Few end members for the compositional trends observed in highland soils are themselves pure minerals or single types of igneous rock; most end members are in fact other types of soils (Korotev, 1981, 1987b).

The element concentrations for soils shown in the figures in this chapter, unless otherwise specified, are for the <1-mm size fraction of sieved soils. Compositions of individual soils are not constant for all grain sizes, however (see sections 7.1.7 and 7.5.3, as well as Table 7.17). In several studies, soils from different landing sites have been sieved into four or more grain-size fractions and analyzed for major elements and incompatible trace elements (e.g.,

Papike et al., 1982). The different size fractions have different compositions. In particular, the finest (<20 μm) grain-size fractions of many soils are enriched in Al, Ca, Na, K, the lighter REE, and Th, and they are depleted in Mg, Fe, Mn, and Sc relative to the soil's bulk composition. In such soils, the components enriched in the finest fraction are those associated with plagioclase and with the fine-grained mesostasis found in many basalts.

For most soils, the extent of enrichment or depletion in the finest size fraction is from a few percent to about 10%; for some soils it is as great as 30%. These variations become even more extreme when very fine material (e.g., <2 μm) is analyzed. The <2-μm size fraction of the Luna 24 soil, relative to the 200–370-μm size fraction, is enriched by 2 times in Al and by more than 3 times in La; it is depleted to 0.4 times in Sc (Laul *et al.*, 1987).

Korotev (1976) discussed possible causes of such enrichments in the finer fraction; he concluded that the principal reason for this effect in four Apollo 17 soils from the primarily basaltic valley floor was the mixing of fine-grained, somewhat KREEPy highland material with comminuted mare basalt. However, *Papike et al.* (1982) attribute this effect in the soils that they analyzed to differential comminution that preferentially reduces the grain size of plagioclase and of the friable mesostasis, relative to mafic minerals, thus enriching the finest fractions in Al, Ca, Na, and the incompatible trace elements. No compelling criteria to determine the relative importance of mixing vs. differential comminution have yet been developed.

Possible highland ores of incompatible trace elements. Because the incompatible trace elements generally occur in extremely low amounts (<0.1 wt.%) in most highland materials, special concentration mechanisms would be required to produce ore-grade deposits. One such mechanism could be the natural concentration of trace and minor minerals (such as whitlockite or zircon) that are enriched in incompatible trace elements. These concentrations would have to occur on scales greater than any so far observed.

There is as yet no definite evidence that such concentration mechanisms have ever been effective on the Moon, but there are indications that the products of such processes might be present. High concentrations of whitlockite have been found in some anorthositic rocks, e.g., in a white clast in Apollo 14 breccia 14313 (*Haskin et al.*, 1973), which is also the sample with the highest REE concentrations shown in Fig. 8.8. Remote-sensing data from the Apollo 15 and 16 orbiting gamma-ray experiments (section 10.2) show that surface soils in the vicinity of the Apollo 14 landing site are relatively

rich in Th. To the extent that the chemical correlations shown here are valid globally, this high Th content indicates that the other incompatible trace elements would be concentrated in this general area as well.

It is reasonable to assume that the chemical correlations derived from the lunar highland samples hold for much of the lunar nearside. This view is strengthened by the fact that the same correlations hold even for small fragments of many lunar highland soils and breccias. However, the detailed systematics of incompatible-trace-element concentrations on the lunar farside may not follow the correlations given in Table 8.2. On the farside, orbital remote-sensing data (Plate 10.1) indicate that Th concentrations fall below the limit of validity of the correlation in Table 8.2.

At least some elements of the vapor-mobilized element group (see section 8.7) also correlate to a substantial extent with the incompatible trace elements. During separations of crystals from liquid, most or all of the vapor-mobilized elements probably remain in the liquid with the incompatible trace elements. However, when vapor phases can separate from the liquids, elements of the two groups can separate from each other.

8.4.3. Incompatible Trace Elements in the Lunar Maria

Concentrations of incompatible trace elements in mare basalts do not correlate as closely with each other as they do among highland rocks. However, there is still a strong tendency for all incompatible trace elements to be concentrated together in mare materials.

Figure 8.11 shows REE comparison diagrams for typical mare basalts from the Apollo and Luna missions. A more detailed set of similar diagrams can be seen in Figs. 6.3 to 6.5. For the majority of incompatible trace elements, the range of concentrations observed in lunar mare basalts (e.g., 1 to 21 $\mu\text{g/g}$ for Sm) is much smaller than that for highland samples (0.04 to 260 $\mu\text{g/g}$). This difference is also evident in Fig. 8.7 for most but not all elements. Exceptions include Eu, which, because of its occurrence with 2+ as well as 3+ valence, is not totally an incompatible trace element, and Sn, for which few analytical data are available, but whose concentrations may actually vary over a shorter range than other elements of this group.

Mare basalts as guides to lunar mantle compositions. Despite the narrower range of REE concentrations in mare basalts as compared to highland materials, the relative abundances of the REE to each other are more variable in the mare

basalts, and they are systematically different from those of highland materials. Most mare basalt REE distributions have lower chondrite-normalized relative abundances of the lighter REE (La, Ce) than of the somewhat heavier REE (Nd, Sm, Tb) (see Fig. 8.11). This tendency is also seen in the most common terrestrial basalts, those from the Earth's ocean floors (see section 5.1.6 and Figs. 5.14 to 5.16). In terrestrial ocean-floor basalts, this pattern is attributed to production of the basalts in regions of the Earth's mantle that had undergone partial extraction of incompatible trace elements (especially the light REE) prior to the formation of terrestrial ocean-floor basalts (e.g., *Gast*, 1968; *Schnetzer and Philpotts*, 1970). An analogous explanation may also apply to the REE distributions in lunar mare basalts. The mare basalts thus appear to represent melts from the lunar mantle that were produced after the separation and formation of much of the highland crust.

This explanation may be incomplete, however. The mare basalts still have concentrations of incompatible trace elements that are higher than the average concentrations for the bulk Moon. Partial melting within the lunar mantle and possibly the lower crust, required for producing the parent magmas of the mare basalts. Within the mantle, this melting extracted those elements that do not readily fit into the major element sites in the principal minerals. These partial melts were an efficient mechanism for extracting incompatible trace elements from the residual solids and carrying these elements to the lunar surface. Some mare basalts, e.g., those found as small clasts in some Apollo 14 breccias, may also have assimilated some KREEP elements during their rise through the lunar crust (e.g., *Shervais et al.*, 1985a,b).

The concentrations of the incompatible trace elements remaining in the residual solid mantle after such a partial melting episode will be lower than before the extraction. A series of such partial melting episodes will lower the concentrations of incompatible trace elements even further. Any partial melting that occurred soon after the mare basalt source regions formed in the lunar mantle (~4.4 b.y. ago; see section 6.1.9) may have depleted the mantle regions most enriched in incompatible trace elements. Subsequent melting events, which gave rise to the mare basalts we have sampled, would have occurred in a mantle from which any anomalously high concentrations of incompatible trace elements had been extracted. This process, plus physical limits on the extent of subsequent partial melting (probably limited to a few percent of the mantle), resulted in a smaller range of concentrations and a substantially altered set of relative abundances of the incompatible-

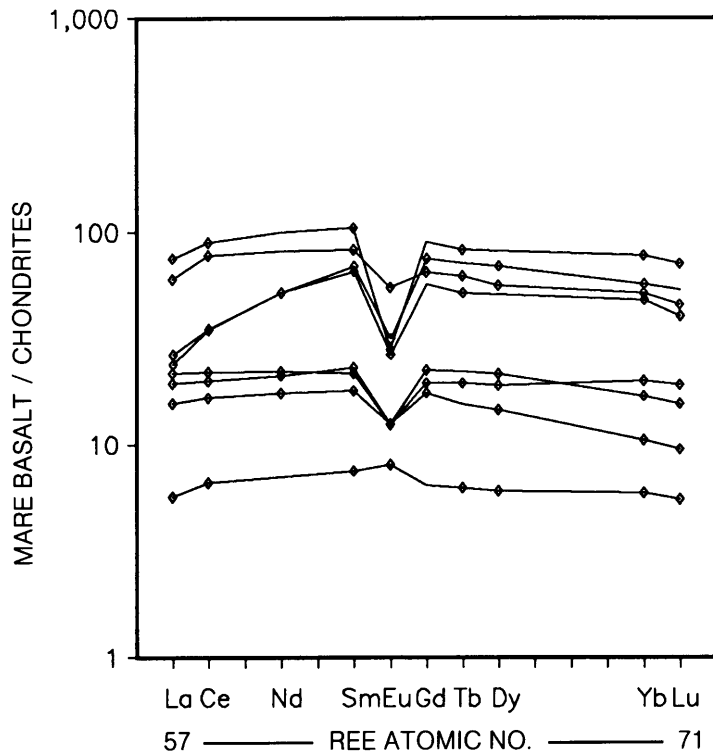


Fig. 8.11. Concentrations of REE in a series of mare basalt samples. Horizontal axis shows the REE in order of increasing atomic number. Vertical axis shows the REE concentration in the sample, which has been normalized by dividing it by the concentration in chondritic meteorites (Table 8.1), a procedure that provides a common reference standard. There is a smooth transition between samples with very high REE concentrations (at top) to samples with low REE concentrations (at bottom). However, the range of REE concentrations is less in mare basalts than in highland samples (Fig. 8.8). Furthermore, the relative depletion in heavy REE seen in highland samples (Fig. 8.8) is less prominent in the mare basalts.

ible trace elements in products of subsequent melting, in this case the mare basalts, most of which were collected from the uppermost (i.e., youngest) flows within mare basins.

Limited correlations between incompatible trace elements in mare basalts. It seems clear that the characteristics of the source regions for individual mare basalts and the processes that produced the basalts were significantly different from the sources and processes that generated the highland crust. The consequences of these differences are evident when pairs of incompatible trace elements from mare samples are plotted against each other (Figs. 8.12 and 8.13). No simple correlations are visible between Sm and most other incompatible trace elements in data that include all mare basalts. There are, however, some crude correlations. For example, high Sm concentrations

are accompanied by high La or Ba concentrations. This tendency is somewhat stronger among basalts of a given type, or from a particular mission, than among mare basalts in general. Divergent correlations are evident for basalts from different sampling sites when Sm is plotted against other incompatible trace elements (Fig. 8.12).

In mare basalts, the greater the geochemical coherence between two elements, the closer the correlations between them. For example, Sm in mare basalts correlates much more closely with Yb than with La. All three elements are REE, but the geochemical behavior of Sm in most rock-forming systems more nearly matches that of Yb than that of La. In general, those elements that correlate fairly well with Sm do so because no step in the melting or crystallization processes that formed the mare basalts separated those elements from Sm. In most

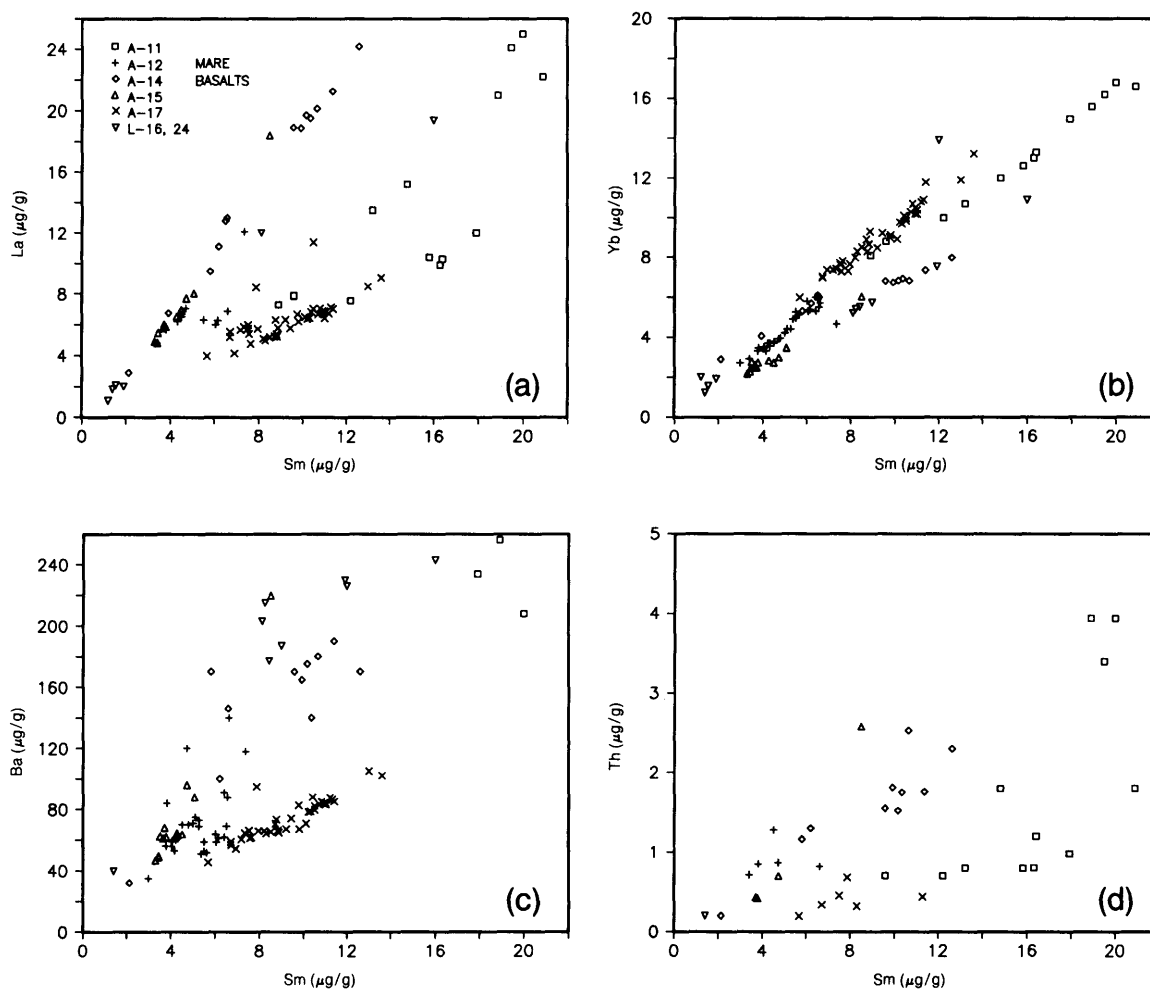


Fig. 8.12. Correlation plots for four incompatible trace elements (La, Yb, Ba, and Th) in lunar mare basalts, plotted against the concentration of Sm, a typical incompatible trace element. Because of the lower range of concentrations of these elements in basalts, relative to the KREEP-rich highland samples with negative Eu anomalies (Fig. 8.8), the horizontal and vertical axes are both linear; elemental concentrations are shown in $\mu\text{g/g}$. There is also more compositional scatter for the basalts than for the highland samples. **(a)** Plot of La vs. Sm. The data show a good correlation between La and Sm, but samples from each Apollo landing site form a different correlation line, unlike the single correlation line for highland samples (Fig. 8.9a). **(b)** Yb vs. Sm; **(c)** Ba vs. Sm; **(d)** Th vs. Sm. In all plots, data for the Apollo 11 low-K basalts overlie those for the Apollo 17 basalts.

cases, the ratios of those elements to Sm in mare basalts are similar to the corresponding ratios for highland materials. However, the correlations between Sm and K, P, Eu, and Na that are present in the highland samples (Fig. 8.10) are very poor or simply not present among the mare basalts (Fig. 8.13). Except for Eu, such correlations are weak or absent for individual types of basalts as well.

Possible maria ores of incompatible trace elements. It is possible that pools of mare basalt, perhaps in relatively small impact craters, might cool slowly enough to allow accumulation of high concentrations of minerals such as ilmenite or chromite (see section 5.2). These accumulations would concentrate such major and minor elements as Fe, Ti, and Cr. However, it is not evident that this

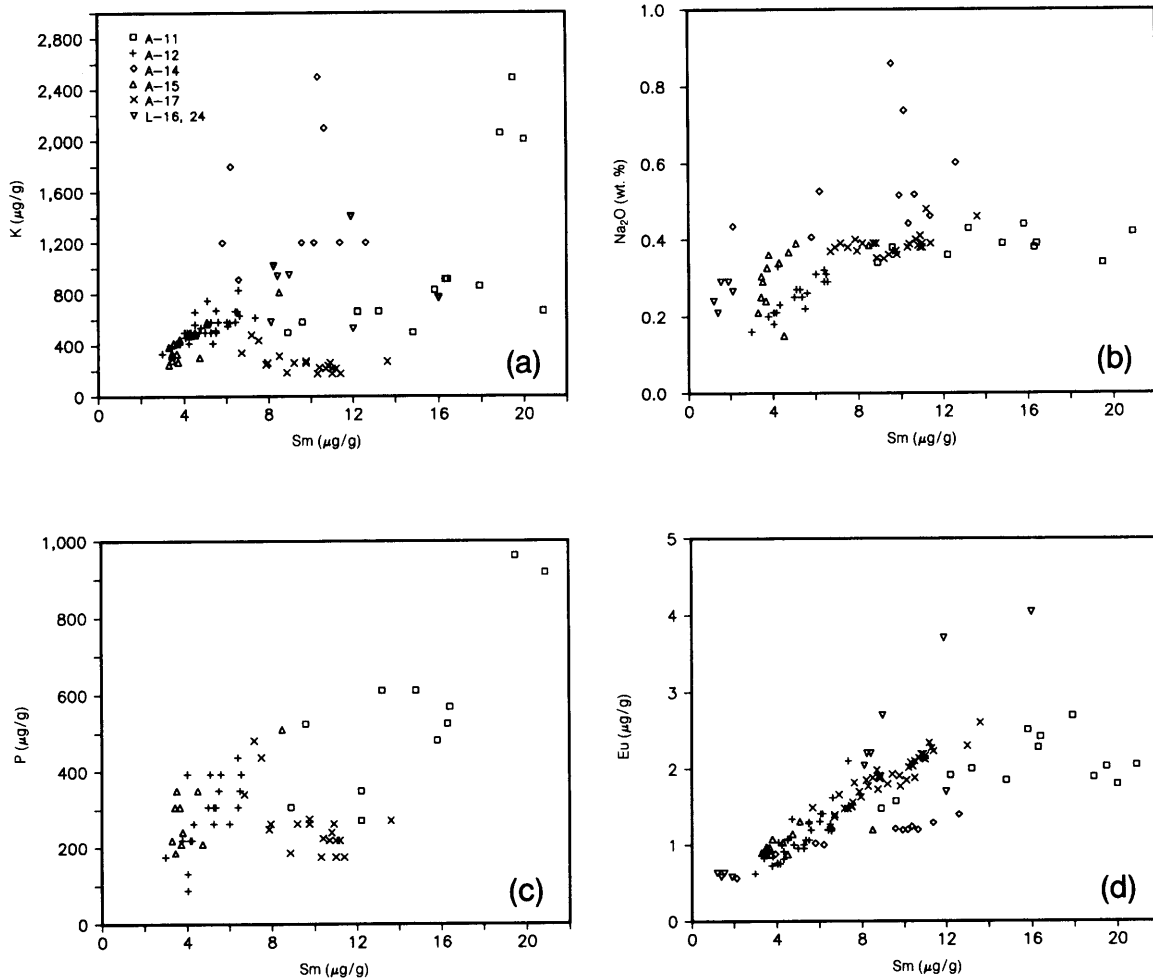


Fig. 8.13. Correlation plots for Na (a major element) and three incompatible trace elements (K, P, and Eu) in lunar mare basalt samples, plotted against the concentration of Sm, a typical incompatible trace element. Horizontal and vertical axes are both linear and show elemental concentrations in $\mu\text{g/g}$, except for Na, which is in oxide wt.%. **(a)** K vs. Sm; **(b)** Na₂O vs. Sm; **(c)** P vs. Sm; **(d)** Eu vs. Sm. In mare basalts, correlations between these elements are generally poor, but a fair correlation exists between Eu and Sm at low concentrations.

type of concentration would produce an ore of any incompatible trace element. In fact, the reverse process might occur. Accumulation of heavy minerals toward the bottom of a slowly-cooling magma pool might lead to basalt-derived pyroxene- or olivine-rich materials with even lower incompatible-trace-element concentrations than those observed so far, because these elements would tend to remain with the liquid phase.

During partial melting of any single source region in the lunar mantle, smaller percentages of melting will lead to higher abundances of incompatible trace

elements in the melt. Conversely, melts produced by relatively large amounts of partial melting will have lower concentrations of incompatible trace elements. For example, the green glass found at the Apollo 15 landing site, with its low incompatible-trace-element concentrations, indicates a relatively high degree of partial melting of its source region. However, the history of the magma after melting is also important. Once formed by partial melting, a rising magma may reside for significant periods of time in intermediate storage regions (called *magma chambers*) prior to eruption onto the surface. If appreciable cooling and

crystallization occur while the magma is in the chamber, the incompatible trace elements may become significantly enriched in the residual liquid before it erupts onto the surface.

The concentrations of incompatible trace elements in mare basalts do not seem related to differences in major-mineral content among different types of basalts. However, the concentrations reported for individual samples of mare basalt may reflect the specific suite of minerals in the particular sample chosen for analysis; this effect has been observed in the small samples of lunar rocks available for analysis. Figure 8.6 shows the concentrations of REE in the separated mesostasis and minerals of a mare basalt. It is evident that differences in the amount of mesostasis in different samples can strongly affect the concentrations of REE measured by chemical analysis. In one careful study of this effect, it was shown that a series of small samples of a single Apollo 17 basalt (basalt 70135; *Haskin and Korotev, 1977*) produced about the same range of REE concentrations that was observed for the samples analyzed from a large suite of different Apollo 17 basalts.

Although the combined effects of small amounts of melting in the lunar mantle, subsequent crystallization to produce enriched residual liquids, and late concentration of mesostasis might enrich the incompatible trace elements in mare basalts, it is unlikely that extreme concentrations of these elements will ever be found in the mare as a result of such events. From the point of view of ores for the incompatible trace elements, the mare basalts do not offer as much promise as highland materials, chiefly because of the far greater concentrations of these elements observed in phosphates and other minor minerals that are more abundant in some highland rocks.

8.5. MISCELLANEOUS MINOR ELEMENTS

The elements discussed in this section (P, Sc, V, Cr, Mn, Ga, and Sr) generally do not conform to any of the major categories (incompatible, siderophile, etc.) into which geochemists like to pigeonhole minor and trace elements. Some of these "miscellaneous minor elements" (e.g., Ga, Sr) partition indifferently between silicate melts and common lunar minerals (i.e., their crystal/melt distribution coefficients are ~ 1). As a result, there is remarkably little sample-to-sample variation in their concentration. This section includes some minor or trace elements that geochemically resemble certain major elements (e.g., Mn, which is akin to the major element Fe) to such a degree that chemical pro-

cesses such as igneous differentiation seldom have much effect on the ratio of the minor element to its major relative. Other elements discussed here (e.g., P) have little or no tendency to enter any major lunar minerals; instead, they tend to form essential components of specific minor minerals (e.g., phosphates; section 5.5).

8.5.1. Data Sources

The miscellaneous minor elements generally do not pose extraordinary analytical challenges. Published data, especially relatively recent (post-1974) data, are almost uniformly accurate and, at least for most purposes, adequately precise. Table A8.3 summarizes the main sources used to compile our database for these elements in lunar samples. Element concentrations are shown in Fig. 8.14.

In all cases, the sources we have selected represent only a subset of the entire literature database. The main sources selected for Table A8.3 are not necessarily the most precise available data. However, the sources used are generally reliable and all of them have two important advantages: (1) The elements of interest were determined simultaneously with numerous other elements, allowing the determination of some interesting correlations (e.g., P correlates with incompatible elements such as La). (2) The elements of interest were all determined by the same laboratory, thus providing an internally consistent database for a wide variety of rock and soil samples from a large number of sites. Scandium, Cr, and Mn are particularly easy to determine in lunar samples with the popular instrumental neutron activation analysis (INAA) technique. Vanadium is only slightly harder to determine by INAA. Gallium and Sr were once difficult to determine by INAA, but can generally be measured without much trouble using current techniques. Strontium is often determined with extreme precision using isotope dilution techniques in conjunction with age determinations, but such studies seldom determine enough other elements to allow the Sr concentration data to be unambiguously interpreted, given the small sample masses typically used. Phosphorus is generally determined by the XRF spectrometry technique, which is excellent for relatively high concentrations, but it is not quite sensitive enough for a few unusually P-poor lunar samples.

8.5.2. Phosphorus, Potassium, and Barium

The elements P, K, and Ba are not significant components in most lunar minerals. However, a highly differentiated or evolved igneous melt may produce minerals in which P, K, and Ba may be

major or even essential elements (e.g., K-feldspar or phosphates; Tables A5.11a and A5.18). On the Moon P, K, and Ba behave primarily as incompatible elements (section 8.4).

Phosphorus is infrequently determined in lunar samples. However, the database for P included here probably contains well over half of all the reliable published analyses (Fig. 8.14 and Table A8.3). There is a strong correlation between P and La (Fig. 8.15a), and, for many purposes, the P content of a lunar sample can be satisfactorily estimated from the measured concentration of La (or of some other highly incompatible element), assuming a constant ratio, e.g., P/La = 31.

This method of estimation will be least accurate for samples with extraordinarily high or low concentrations of other incompatible elements. For example, the monomict quartz monzodiorite fragment from Apollo 15 highland breccia 15405 appears to have an exceptionally low P/La ratio, although the P content has only been imprecisely determined from thin-section studies (see *Ryder*, 1985).

In general, P behaves as an incompatible element akin to La (Fig. 8.15a). Like most lunar incompatible trace elements, P tends to be most concentrated in samples with major-element compositions resembling basalts, e.g., those with Al contents close to 9 wt.% (Fig. 8.15b), presumably because P was originally emplaced in the lunar crust primarily as some type of KREEP basalt (section 6.3.2). In samples with high concentrations of incompatible trace elements, most of the P is present as phosphate minerals, typically apatite or whitlockite. The phosphide *schreibersite*, (Fe,Ni,Co)₃P, has also been reported as a trace mineral in some highland rocks (e.g., *Gooley et al.*, 1973). In rocks with extremely high contents of incompatible trace elements, the phosphate content is high and the mineral grains may be coarse and heterogeneously distributed. Some of the phosphates may even be present as *cumulus* crystals (crystals that accumulated during the main phase of differentiation in a large magma body). Fractionation of phosphate minerals probably contributed to the genesis of the extraordinary REE patterns found among evolved lunar rocks such as granites (*Warren et al.*, 1983b; *Shih et al.*, 1985; see section 6.3.5).

The lunar distribution patterns of K and Ba (discussed in more detail in section 8.4) are in most ways analogous to those of P, except that the mineral concentrating K and Ba is K,Ba-feldspar instead of a phosphate mineral. Only a few volumetrically insignificant lunar rock types, most notably the granites, contain more than trace amounts of K,Ba-feldspar. Thus K and Ba also tend to correlate well with incompatible elements such as La, although K and Ba (but not P) are also partially

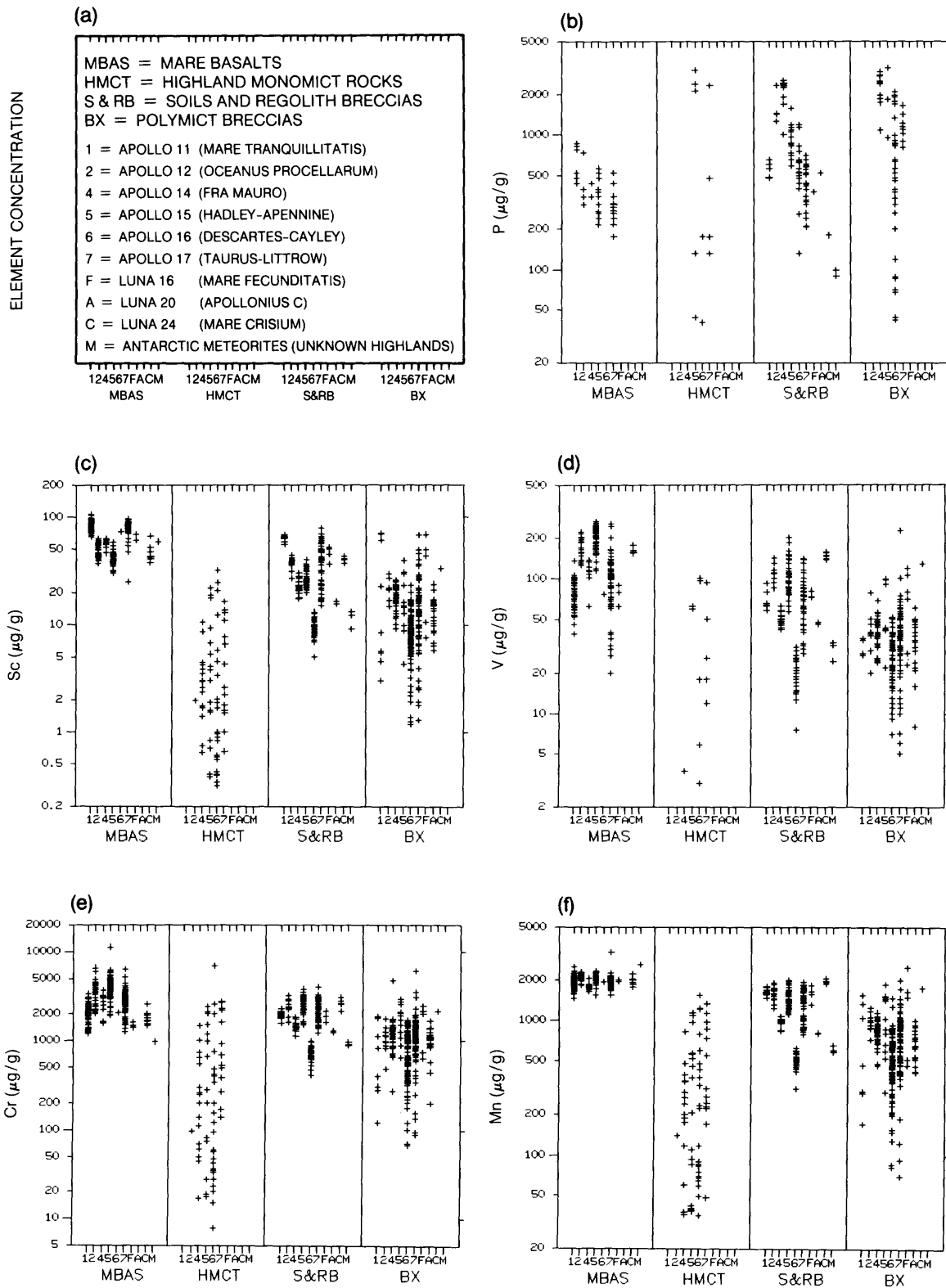
compatible with a major crustal mineral, plagioclase feldspar (*Weill and McKay*, 1975; *G. A. McKay and Weill*, 1976, 1977). From the standpoint of lunar resources, it is important to recognize that, thanks to phosphates and K,Ba-feldspar, lunar rocks with extremely high concentrations (>1 wt.%) of P, K, and Ba probably do exist, although they are not volumetrically abundant.

When lunar regolith samples are analyzed after being sieved into different grain-size fractions (e.g., *Laul et al.*, 1981, 1983, 1987; *Boynton et al.*, 1976b; *Boynton and Wasson*, 1977), concentrations of K, Ba, and all other incompatible elements (and thus, by implication, also P) usually have strong inverse correlations with grain size (section 7.5.3 and Table 7.17). The enrichment of these elements in the finer grain sizes seems particularly strong in the soil from the Luna 24 (Mare Crisium) site (*Laul et al.*, 1983, 1987). In these soils the <10- μ m fraction is enriched over the bulk soil in K by a factor of ~2.6, and in Ba by a factor of ~2.5.

8.5.3. Scandium, Vanadium, Chromium, and Manganese

These four transition-metal elements, which occur in trace to minor amounts, might be termed "ferrophile" in lunar materials, because during elemental separations they all tend to follow, at least loosely, the major element Fe where it occurs in the ferrous (Fe²⁺) state in common minerals. They also have weak correlations with Mg and another transition element, Ti, which tend to concentrate in the same major minerals as Fe does. Crystal/liquid distribution coefficients have been determined experimentally for most possible combinations of these elements between major lunar minerals and melts of typical lunar composition (Table 8.3). Vanadium, Cr, and Mn are prone to assume a variety of valence states, although their valences under lunar conditions are most commonly 2+ or 3+. Oxygen fugacity (fO₂; see section 5.2) has a major effect on the distribution coefficients for these elements. Table 8.3 shows only the experimental results obtained under Moon-like, extremely low fO₂.

In equilibria involving the four most common minerals of the lunar crust (plagioclase feldspar, low-Ca pyroxene, high-Ca pyroxene, and olivine), the elements Sc, V, Cr, and Mn are all incompatible with plagioclase, and they are mildly incompatible to compatible (crystal/liquid distribution coefficients of the order 0.3–3) with the three mafic silicates (olivine, low-Ca pyroxene, and high-Ca pyroxene). The first-order constraint on the lunar distributions of these elements (Figs. 8.14c,d,e,f; Table A8.3) is that they are depleted in anorthositic (i.e., typical



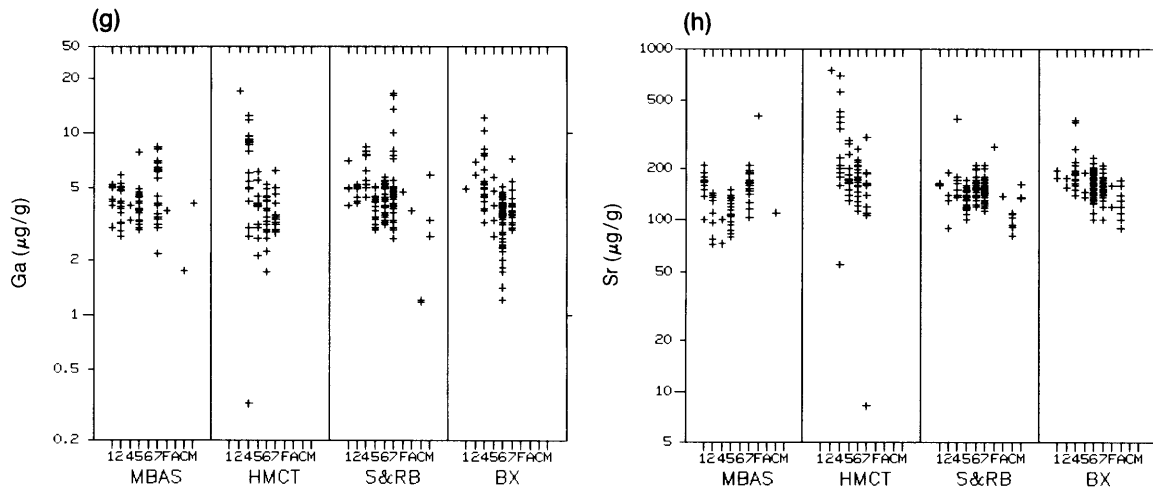


Fig. 8.14. Concentration ranges of miscellaneous minor elements in various lunar materials: mare basalts (MBAS), highland monomict rocks (HMCT), soils and regolith breccias (S&RB), and polymict breccias (BX). Horizontal axis shows sample types, separated according to individual missions. Vertical axis shows elemental concentrations (in $\mu\text{g/g}$). **(a)** Graphical key to the plots and abbreviations. Data are presented for: **(b)** phosphorus, P; **(c)** scandium, Sc; **(d)** vanadium, V; **(e)** chromium, Cr; **(f)** manganese, Mn; **(g)** gallium, Ga; **(h)** strontium, Sr. Statistical summaries for most of these plots are provided in Table A8.3.

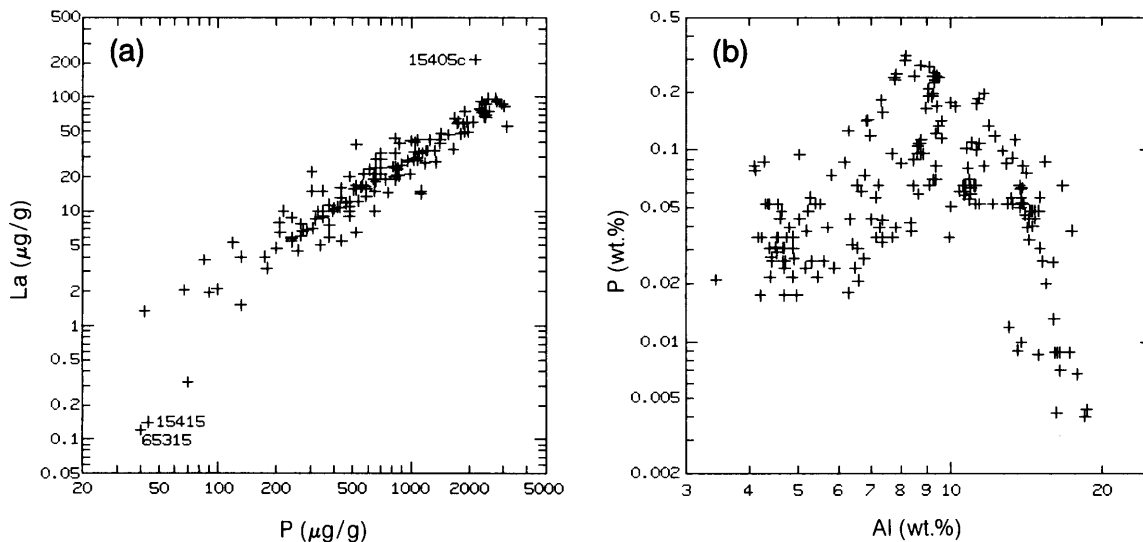


Fig. 8.15. Correlation plots for miscellaneous minor elements in lunar samples. **(a)** Plot of La vs. P. Horizontal and vertical axes, which are both logarithmic, show elemental concentrations in $\mu\text{g/g}$. A strong correlation exists between the two elements, indicating that P tends to behave as an incompatible trace element (like La) in most lunar samples. **(b)** Plot of P vs. Al (a major element). Horizontal and vertical axes, both logarithmic, show elemental concentrations in wt.%. The correlation is poor, although P is clearly present at lower concentration in Al-rich (anorthositic) highland rocks.

TABLE 8.3. Experimentally measured crystal/liquid distribution coefficients (D) for Sc, V, Cr, Mn, Ga, and Sr between six common lunar minerals and melts compositionally similar to typical lunar basalts [$D = (\text{concentration in mineral})/(\text{concentration in melt})$].

	Sc	V	Cr	Mn	Ga	Sr
Plagioclase	0.02-0.07	n.d.<1)	n.d.<1)	0.05	0.79-0.96	1.5-1.9
Low-Ca pyroxene	0.5-1.4	2.8-3.4	2-5	0.7-0.8	n.d.<1)	0.01-0.02
Olivine	0.27-0.37	0.04-1.3	0.6-1.2	0.8-1.6	0.02	0.003
High-Ca pyroxene	0.4-8.8	2-3	1-2	0.4-1.2	0.14-0.24	0.06-0.4
Ilmenite	n.d.	12	6-12	1.2	n.d.	n.d.
Mg-Al spinel	0.048	38	77	n.d.	3.7-4.9	n.d.
References	1,2,3	1,4,5	1,4,6-9	1,5,10,11	12	2,6,7,13

Abbreviation: n.d. = not determined.

References: **1.** Lindstrom (1976), as cited in review of Irving (1978); **2.** McKay and Weill (1977); **3.** Nagasawa et al. (1976), as cited in review of Irving (1978); **4.** Ringwood (1970); **5.** Duke (1976); **6.** McKay and Weill (1976); **7.** Weill and McKay (1975); **8.** Huebner et al. (1976); **9.** Irving et al. (1978); **10.** Bird (1971), as cited in review of Irving (1978); **11.** Longhi et al. (1978); **12.** Malvin and Drake (1987); regarding plagioclase see also Goodman (1972); **13.** regarding D for Sr into high-Ca pyroxene, see review by Irving (1978).

highland) rocks, and relatively enriched in basalts and Fe-rich cumulates (i.e., all mare rocks and a few highland rocks). This pattern extends to soils as well; the anorthosite-rich Apollo 16, Luna 20 (Apollonius), and Antarctic lunar meteorite regolith samples have low Sc, V, Cr, and Mn concentrations in comparison to other, more basalt-rich regoliths.

A second-order effect, presumably due to ilmenite fractionation, is that Sc tends to be more concentrated in high-Ti mare basalts (typical of the Apollo 11 and 17 sites) than in low-Ti mare basalts (typical of the Apollo 12, 14, and 15 sites). The relations are reversed for V and Cr, which do not concentrate as strongly in ilmenite as they do in spinel, the more common oxide mineral in low-Ti basalts (Table 8.3 and Figs. 8.14c,d,e; section 5.2.2).

Correlations with Fe. Correlations between these elements and Fe are shown in Fig. 8.16. The Sc/Fe ratio is generally between 0.0002 and 0.0005. A few olivine-rich cumulate rocks, such as an "olivine clast" from sample 60035 (Fig. 8.16a; Ma and Schmitt, 1982) and a monomict spinel troctolite clast from sample 67435 (Ma et al., 1981a), have exceptionally low Sc/Fe ratios. The correlation between V and Fe is relatively weak (Fig. 8.16b). The monomict fragments of sodic ferrogabbro found in the Apollo 16 highland breccia 67915 (Marti et al., 1983) have exceptionally low V/Fe ratios. Among the highest-Fe samples (i.e., mare basalts), V/Fe ratios scatter widely, probably as a result of fractionation of ilmenite (note the moderately high ilmenite/melt distribution coefficient for V, Table 8.3).

The correlation between Cr and Fe (Fig. 8.16c) also tends to fade at high Fe concentrations, presumably due to ilmenite fractionation [note that the ilmenite/melt distribution coefficient for Cr (Table 8.3) is only slightly less than that for V]. Even so, bulk-sample Cr/Fe ratios are generally within the range 0.001-0.003. A clast of olivine-rich mare basalt from Apollo 15 breccia 15299 (Warren et al., 1987), a troctolite clast from breccia 67435, and possibly (although the Cr data seem suspect) a monomict ferroan anorthosite clast from Apollo 16 breccia 60215 (Rose et al., 1975) all have exceptionally high Cr/Fe ratios. Low Cr/Fe ratios are found in several samples: an Fe-rich gabbroic (possibly mare) clast from the Yamato-791197 Antarctic meteorite (labelled "Y79" in Fig. 8.16c; Warren and Kallemeyn, 1987), a sodic ferrogabbro clast from breccia 67915, and a monomict granite clast from Apollo 14 breccia 14321 (Warren et al., 1983b). In contrast to the variations shown by the other elements in this group, the correlation between Mn and Fe (Fig. 8.16d) is excellent. The Fe/Mn ratio is so nearly constant ($\sim 75 \pm 5$) in bulk samples from the Moon that it is frequently used as a key test for meteorites suspected to be of lunar origin (the only otherwise-comparable meteorites have Fe/Mn ratios closer to 40).

Limited correlations with Mg and Al. Despite their generally strong correlations with Fe, the elements Sc, Cr, V, and Mn all have only faint correlations with Mg (the best correlations are shown by Cr). The feeble correlations that do exist

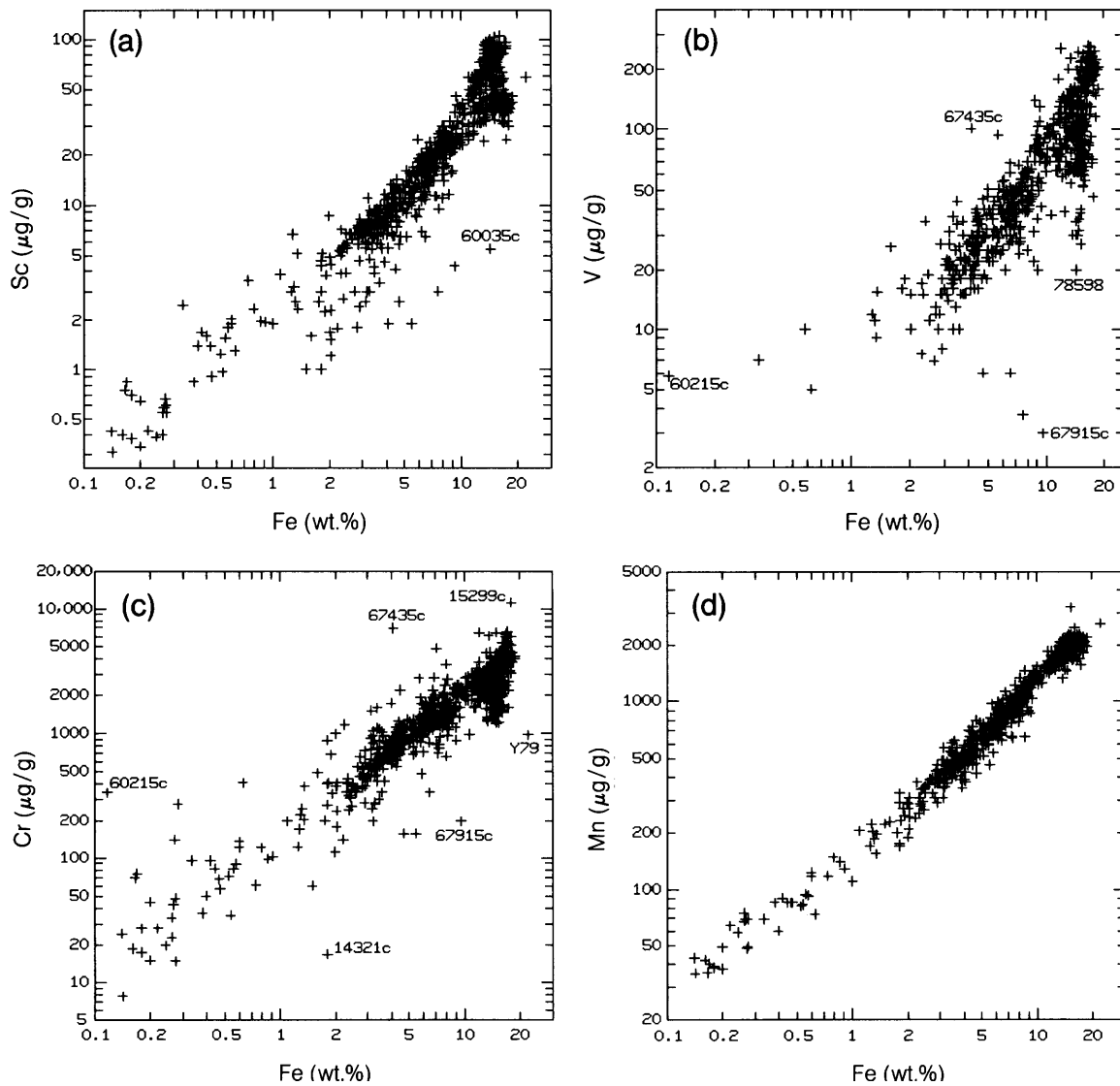


Fig. 8.16. Correlation plots for four miscellaneous minor elements (Sc, V, Cr, and Mn) against Fe (a major element) for a range of lunar sample materials. Horizontal and vertical axes, both logarithmic, show elemental concentrations (in $\mu\text{g/g}$ against wt.% Fe). **(a)** Sc vs. Fe; **(b)** V vs. Fe; **(c)** Cr vs. Fe; **(d)** Mn vs. Fe. Moderate to strong positive correlations exist between all four elements and Fe, indicating that this group of miscellaneous minor elements is strongly associated with FeO in lunar materials.

hold only for low Mg concentrations, up to about 3 wt.% Mg. The inverse correlations that exist between these elements and Al are far more impressive (Fig. 8.17). Even with Al, however, there are notable exceptions. Despite its moderate Al content, the granite clast from breccia 14321 is exceptionally low in Sc, Cr, Mn, and probably in V (not determined) as well. Paradoxically, several dunites, the “olivine” clast from breccia 60035, and

the dunite 72417 (Laul and Schmitt, 1975a), also plot on the low-Cr, low-V, low-Mn, and especially low-Sc sides of trends extrapolated from those shown in Fig. 8.17. This figure also illustrates the uniquely high Mn concentration reported by Murali *et al.* (1977) for the Apollo 17 high-Ti mare basalt 71535.

Correlations among the “ferrophile” transition elements. Examples of the coherence between pairs of “ferrophile” transition elements in lunar

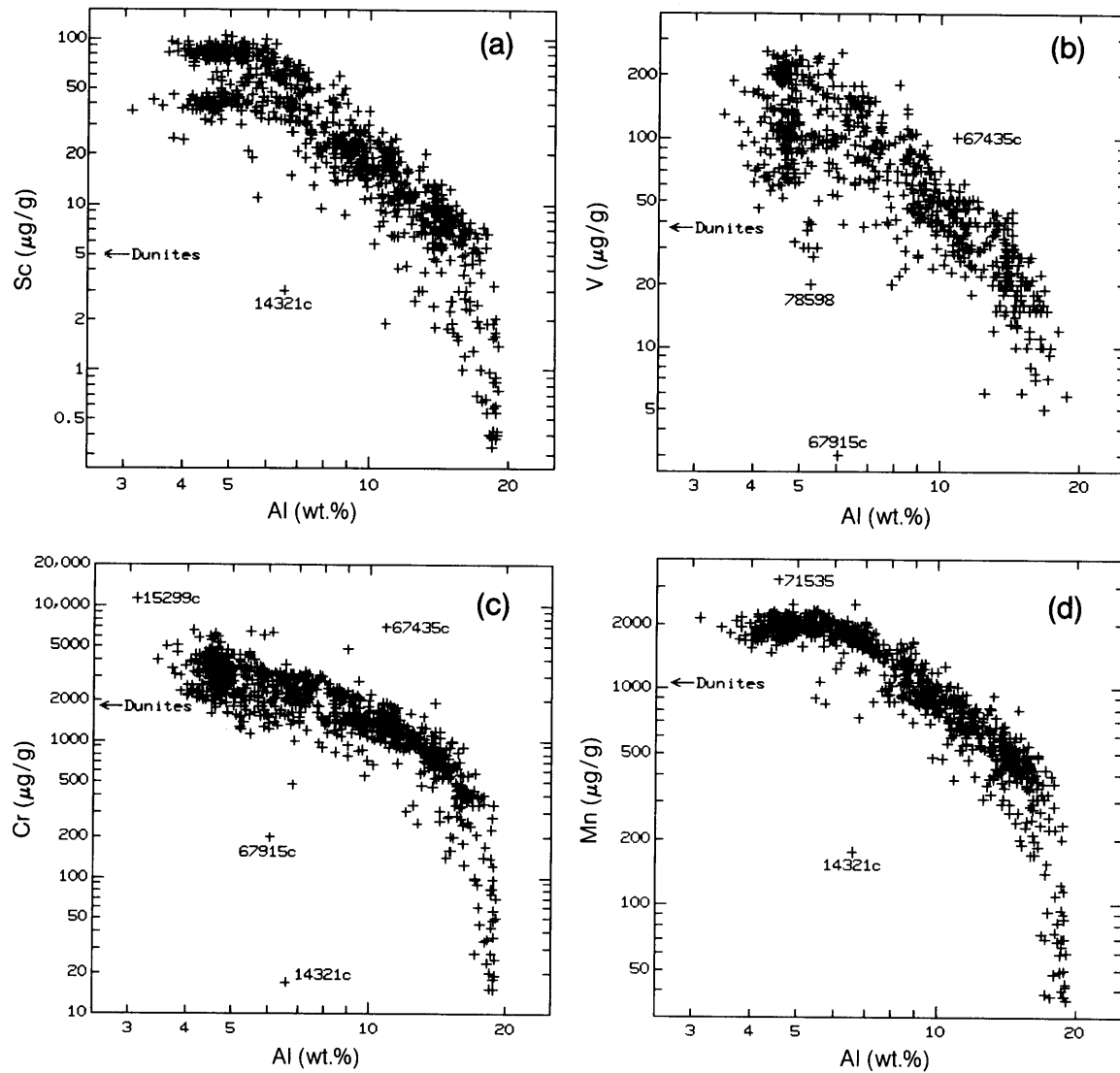


Fig. 8.17. Correlation plots for four miscellaneous minor elements (Sc, V, Cr, and Mn) against Al (a major element) for a range of lunar sample materials. Horizontal and vertical axes, both logarithmic, show elemental concentrations (in $\mu\text{g/g}$ against wt.% Al). **(a)** Sc vs. Al; **(b)** V vs. Al; **(c)** Cr vs. Al; **(d)** Mn vs. Al. Moderate to strong negative correlations exist between all four elements and Al, indicating that the concentration of all elements decreases in Al-rich anorthositic highland rocks.

samples are shown in Fig. 8.18. (Plots for Mn vs. Sc, Cr, and V are not shown because they mirror the analogous plots in Fig. 8.16 for Fe vs. Sc, Cr, and V.) Most of the scatter in Fig. 8.18 is produced by unusual highland monomict rocks, e.g., a granite clast from breccia 14321 (Warren *et al.*, 1983b). The samples with unusual Cr/V ratios include a dunite clast from Apollo 14 breccia 14304 (Warren *et al.*, 1987), a KREEPy clast of "pure dark matter" from Apollo 14 breccia 14083 (Laul *et al.*, 1972a), numer-

ous samples of very-low-Ti (VLT) basalt from Luna 24, and a small ferroan anorthosite (possibly monomict) from Apollo 17 (a clast from soil 70007,298; Ma and Schmitt, 1980). Kinks at the high-V and high-Cr ends of these diagrams result from the fractionation of ilmenite during crystallization of the mare basalt samples.

Chromium is usually considered a minor (if not a trace) element, but in a typical lunar rock much of the Cr resides in a trace or minor mineral in which

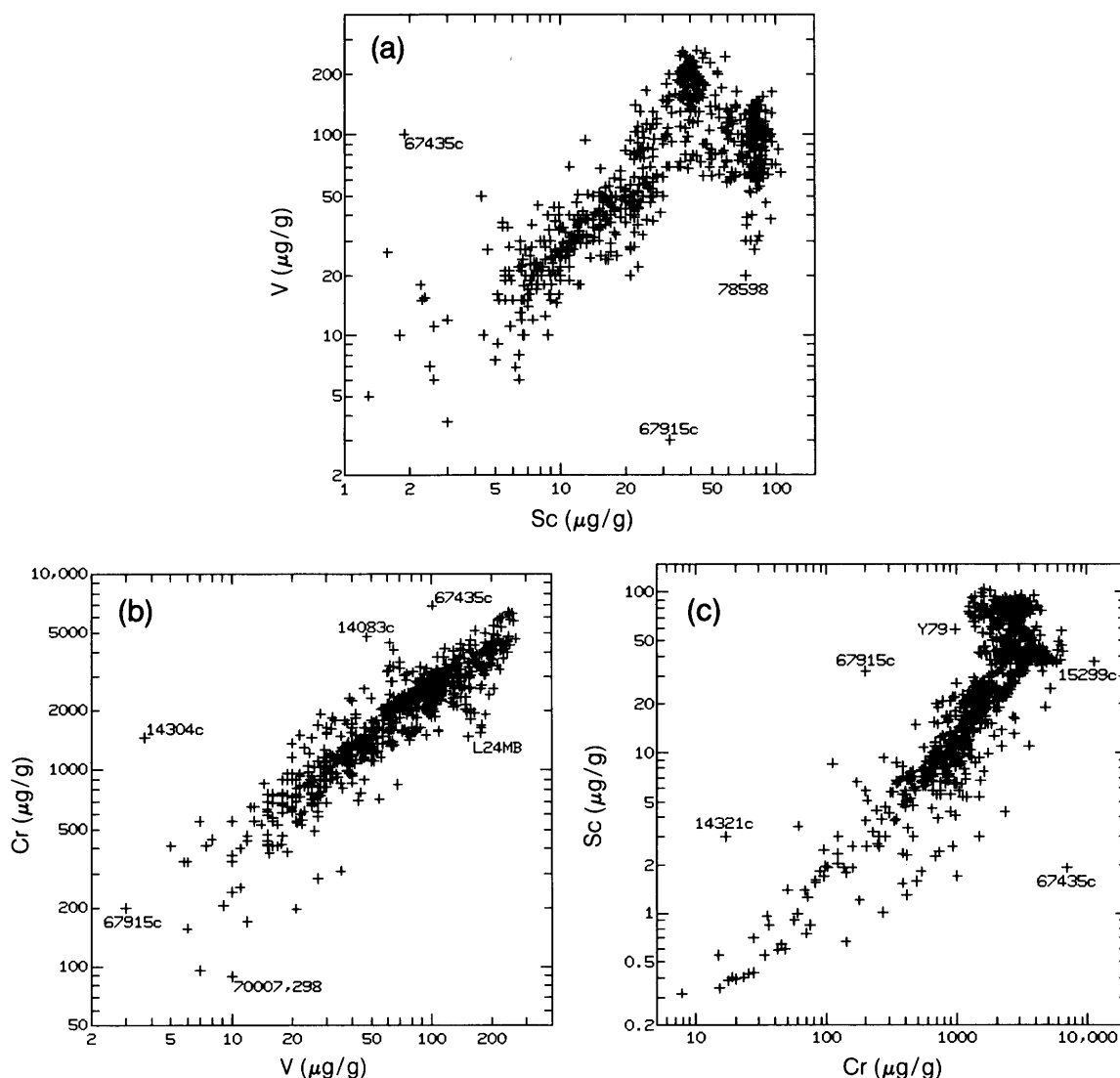


Fig. 8.18. Correlation plots for several pairs of “ferrophile” miscellaneous minor elements (V, Sc, and Cr) against each other for a range of lunar sample materials. Horizontal and vertical axes, both logarithmic, show elemental concentrations (in $\mu\text{g/g}$). **(a)** V vs. Sc; **(b)** Cr vs. V; **(c)** Sc vs. Cr. Good correlations are present between all three pairs of these “ferrophile” elements, indicating that they behave chemically as a coherent group. In addition to the sample numbers shown, “L24MB” represents the Luna 24 very-low-Ti basalt, and “Y79” represents the Antarctic lunar meteorite Yamato 791197.

it is a major element: Cr,Fe-spinel (chromite; section 5.2.2). Although no extremely Cr-rich rocks are known among the limited suite of lunar samples so far collected, the fact that Cr is highly concentrated into a single mineral raises the possibility that Cr-rich cumulate rocks, formed by the separation and concentration of the mineral chromite, may be found among the roughly $2 \times 10^9 \text{ km}^3$ of plutonic rocks that make up the lunar highland crust (see section 5.2). On the basis of typical Cr,Fe-spinel

compositions (Table A5.13), such a cumulate rock would probably also be rich in V.

Grain-size distributions in soils. When lunar regolith samples are analyzed after being sieved into different grain-size fractions (e.g., *Laul et al.*, 1981, 1983, 1987; *Boynton et al.*, 1976b; *Boynton and Wasson*, 1977), the Fe concentrations of the fractions are consistently found to be correlated with grain size (the Fe concentration of the $<10\text{-}\mu\text{m}$ fraction is typically about 0.8 times the bulk-soil Fe concentra-

tion). Scandium, V, Cr, and Mn usually have similar grain-size dependencies, but Cr is the most frequent exception to this rule. Particularly pronounced grain-size fractionations have been reported by *Laul et al.* (1981, 1987) for sieve fractions of the Luna 24 (Mare Crisium) soil. *Laul et al.* (1981) report that the concentrations of these elements in the <10- μ m fraction, normalized to the bulk soil, are as follows: Fe = 0.68, Sc = 0.55, V = 0.62, Cr ~ 0.89, and Mn = 0.59. Apollo 17 soil 72461 appears to be a glaring exception to this general pattern. According to the results of *Krähenbühl et al.* (1977), the finest sieve fractions of soil sample 72461 have higher Fe, Sc, V, and Mn than does the bulk soil (Cr was not determined).

8.5.4. Sulfur, Cobalt, and Nickel

In the lunar environment, S is primarily a vapor-mobilized element (section 8.7.7). However, in one respect, its distribution behavior resembles that of Cr. As with Cr, much of the S in a typical lunar rock resides in a trace or minor mineral in which S is a major element: troilite (FeS; section 5.3.1). The elements Co and Ni can behave, under certain circumstances, as though they were partially lithophile and not siderophile (section 8.6). Under these chemical conditions, Co and Ni are closely correlated with Fe and behave much like the four “ferrophile” transition elements described in the preceding section.

8.5.5. Gallium and Strontium

The trace elements Ga and Sr have been termed “plagiophile” among lunar materials (*Warren and Kallemeyn*, 1984). Although they tend to be only indifferently accommodated by plagioclase, they are thoroughly excluded by all other common lunar minerals (Table 8.3). Because plagioclase is ubiquitous in the lunar crust, concentrations of Ga and Sr among bulk lunar samples (Figs. 8.14g,h; Table A8.3) tend to be remarkably constant. However, an anomalously high Sr concentration is found in Luna 16 (Mare Fecunditatis) mare basalts (*Albee et al.*, 1972; *Philpotts et al.*, 1972; *Vinogradov*, 1971, 1973).

Concentrations of both Ga and Sr are low among dunites, which are rare and have little or no plagioclase. These elements are enriched among alkali anorthosites, which are also rare but occur as fragments of highland monomict rocks at the Apollo 12 and 14 sites (*Warren and Kallemeyn*, 1984). However, geochemical correlations between Ga and Sr and other elements are practically nonexistent among lunar samples. Even Al, which on the Moon

is slightly more “plagiophile” than Ga and Sr, shows little or no correlation with Sr (Fig. 8.19a) or with Ga. The plagioclase/melt distribution coefficient for Al is sensitive to overall melt composition, but in most cases it is about 2–3 (*Warren and Kallemeyn*, 1984), which is 2–3 times higher than the corresponding distribution coefficients for Sr and Ga. Apparently even this relatively slight difference in distribution coefficients is enough to preclude correlations among Al, Ga, and Sr. A feeble correlation does exist between Ga and Sr (Fig. 8.19b). In this plot, some of the spread in Ga contents is caused by the enrichment of Ga in the volatile coatings found on the surfaces of the pyroclastic glasses that make up the bulk of the Apollo 17 orange-soil samples (marked as “742xx” in Fig. 8.19b, e.g., 74220; see section 6.1.7).

Nevertheless, the Ga and Sr concentrations of lunar rocks are not totally unrelated. Among highland monomict rocks, except for the ferroan anorthosites (which appear genetically distinct from all other highland rocks), a good correlation exists between the ratio Ga/Al and the ratio Mg/(Mg + Fe), which is a standard index for the degree of igneous differentiation of a rock. The ratio Sr/Al also shows some correlation with Mg/(Mg + Fe) (*Warren and Kallemeyn*, 1984). However, the element that most closely mimics the correlation of Ga with Mg/(Mg + Fe) is not Sr but Eu (section 8.4). This similarity in behavior between Sr and Eu is not surprising in light of the similarity (in the lunar environment) between the various mineral/melt distribution coefficients for Ga (Table 8.3) and for Eu (*McKay and Weill*, 1976, 1977), most notably between the mineral/melt distribution coefficients for Eu into plagioclase (1.1–1.2) and for Ga into plagioclase (0.79–0.96).

In their sieving experiments on five Apollo 15 and 16 soils, *Boynton et al.* (1976b) and *Boynton and Wasson* (1977) found Ga to be enriched in the finest grain-size fraction relative to the bulk soil. In one case (soil 63500), the <5- μ m fraction was found to be enriched in Ga by a factor of ~4. Likewise, *Laul et al.* (e.g., 1981, 1983, 1987) found that the finest fractions of lunar soils are enriched in Sr, although the Sr enrichments tend to be relatively slight (generally the <10- μ m fraction contains ~1.1–1.3 times as much Sr as the bulk soil does).

8.5.6. Possible Lunar Ores of the Miscellaneous Minor Elements

Phosphate minerals such as apatite or whitlockite could be the principal highland hosts for ores of the incompatible trace elements; this possibility is discussed at the end of section 8.4.2. In general, any

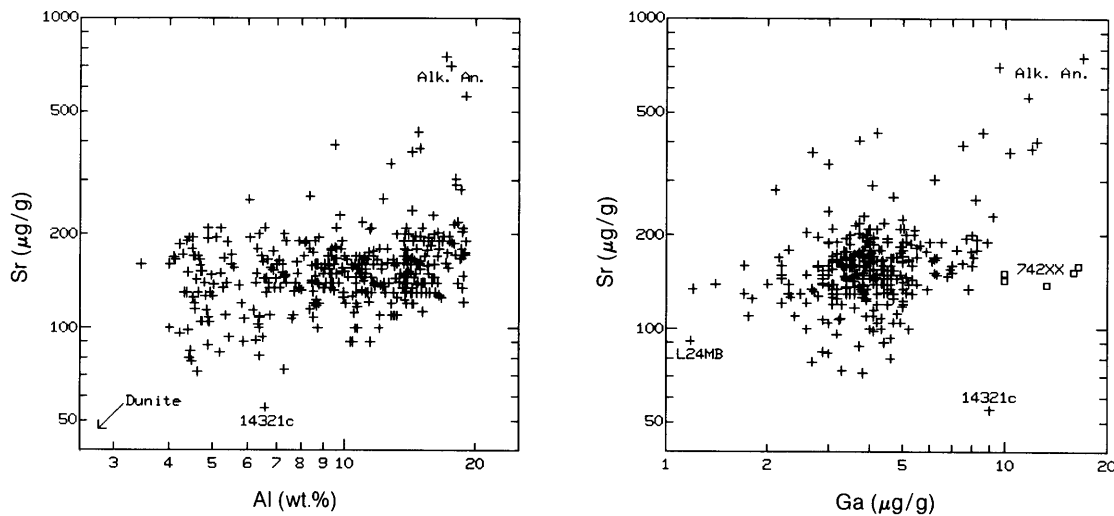


Fig. 8.19. Correlation plots for two miscellaneous minor elements (Sr and Ga) and Al (a major element) for a range of lunar sample materials. Horizontal and vertical axes, both logarithmic, show elemental concentrations (in $\mu\text{g/g}$, except Al in wt.%). **(a)** Sr vs. Al; **(b)** Sr vs. Ga, a “plagiophile” element concentrated in plagioclase. The lack of good correlations between Sr and either Al or Ga indicates that Sr is not entirely concentrated in plagioclase or plagioclase-rich rocks. In addition to the sample numbers shown, “L24MB” represents the Luna 24 very-low-Ti basalt, “Alk. An.” represents alkali anorthosite, and “742xx” represents the Apollo 17 orange-glass pyroclastic deposits.

lunar ore body rich in KREEP would contain abundant P (which is, after all, the P in KREEP). Among the transition metals that are miscellaneous minor elements, Cr is most likely to form ores as the mineral chromite; concentrations of heavy spinel minerals such as chromite are possible in thick bodies of low-Ti mare basalt, where the low viscosity of the lava would allow gravitational settling and accumulation of the chromite (see section 5.2). Chromite accumulations could also occur in some highland plutonic rocks (see section 8.5.3). Concentrations of phosphate or chromite ore in the highlands and chromite ore in the mare, however, are still speculative.

8.6. SIDEROPHILE ELEMENTS

Siderophile means “iron-loving.” The elements discussed in this section (Fe, Co, Ni, Mo, W, Ge, Sb, and such Pt-group elements as Pt, Ir, Os, and Au; Fig. 8.1d) are easily reduced to the metallic state, and they therefore tend to concentrate into alloys with metallic Fe. In lunar samples, Fe metal is generally alloyed with a few percent of Ni. This FeNi alloy most frequently occurs as the mineral *kamacite* with 0–6 wt.% Ni; *taenite* with 6–50 wt.% Ni also occurs, but *tetrataenite* (tetragonal structure with ~50 wt.% Ni) is rare (see section 5.4). Generally, any FeNi alloy in lunar samples is referred to simply as “metal.”

The behavior of siderophile elements is conveniently examined by the degree to which they concentrate in the metal phase, as opposed to the coexisting silicate minerals. Table 8.4 shows metal/silicate distribution coefficients ($D_{m/s}$) for several siderophile elements. These coefficients are defined as the equilibrium weight concentration of an element in metal, divided by weight concentration of the element in coexisting silicate minerals. Distribution coefficients were determined either directly from experiments (Table 8.4, refs. 1, 2, 3, 4, and 7) or estimated from the observed distributions of the elements among the metal and silicate minerals of meteorites or lunar igneous rocks (Table 8.4, refs. 4, 5, and 6). These distribution coefficients are probably highly sensitive to chemical variables (especially to O fugacity and S concentration) and to the temperature of equilibration, but the values in Table 8.4 do indicate at least the relative magnitudes of the fractionations that will result when metal is segregated from molten metal/silicate systems.

Compared to the crust of the Moon (or for that matter, to the crust of the Earth), most meteorites are extremely metal-rich. A typical chondrite meteorite has about 20 wt.% metal, and many meteorites are virtually pure metal. In contrast, a typical lunar basalt has <1 wt.% metal (section 5.4.2). Consequently, meteorites also tend to have far higher concentrations of siderophile elements than do lunar

TABLE 8.4. Experimentally determined and estimated metal/silicate distribution coefficients ($D_{m/s}$) for siderophile elements [$D_{m/s}$ = (concentration in metal)/(concentration in silicate)].

Element	$D_{m/s}$	References
Fe	roughly 10	*
Co	200	1,2
Ni	5000 [†]	1,2
Ge	>>100, comparable to Ir	3,4
Mo	2000	1,2
Ru	comparable to Ir	5
Rh	comparable to Ir	5
Pd	similar to Re, Ir and Au	6
Sb	>15, but $\ll D_{m/s}$ for Ir	6,5
W	roughly 10	1,7
Re	2000, >>2000	1,3
Os	comparable to Ir	5
Ir	20,000, approx. 100,000	1,3
Pt	comparable to Ir	5
Au	10,000, >20,000	1,3

References: **1.** Jones and Drake (1986). **2.** Newsom (1986). **3.** Wolf and Anders (1980). **4.** Jones and Drake (1982). **5.** Mason (1979). **6.** Fouche and Smales (1967). **7.** Rammensee and Wänke (1977).

* $D_{m/s}$ for Fe is a strong function of oxygen fugacity.

[†]Despite this high $D_{m/s}$ (determined from laboratory experiments), lunar crustal rocks frequently contain considerable Ni of indigenous (nonmeteoroid) origin, albeit the exact magnitude of the indigenous Ni content of the highland crust is controversial (see text).

igneous rocks; the degree of this siderophile-element enrichment in meteorites tends to follow the $D_{m/s}$ values in Table 8.4. Concentrations of siderophile elements are shown in Fig. 8.20, and statistics for siderophile elements are given in Table A8.4. The list of data sources in Table A8.4 is intended to be comprehensive for reliable data on bulk lunar samples, except for the much more voluminous literature on frequently determined siderophile elements (Fe, Co, and to a lesser extent Ni, Ir, and Au).

The entire siderophile element contents of mare rocks (section 6.1) and of pristine highland rocks (section 6.3) are derived from magmas indigenous to

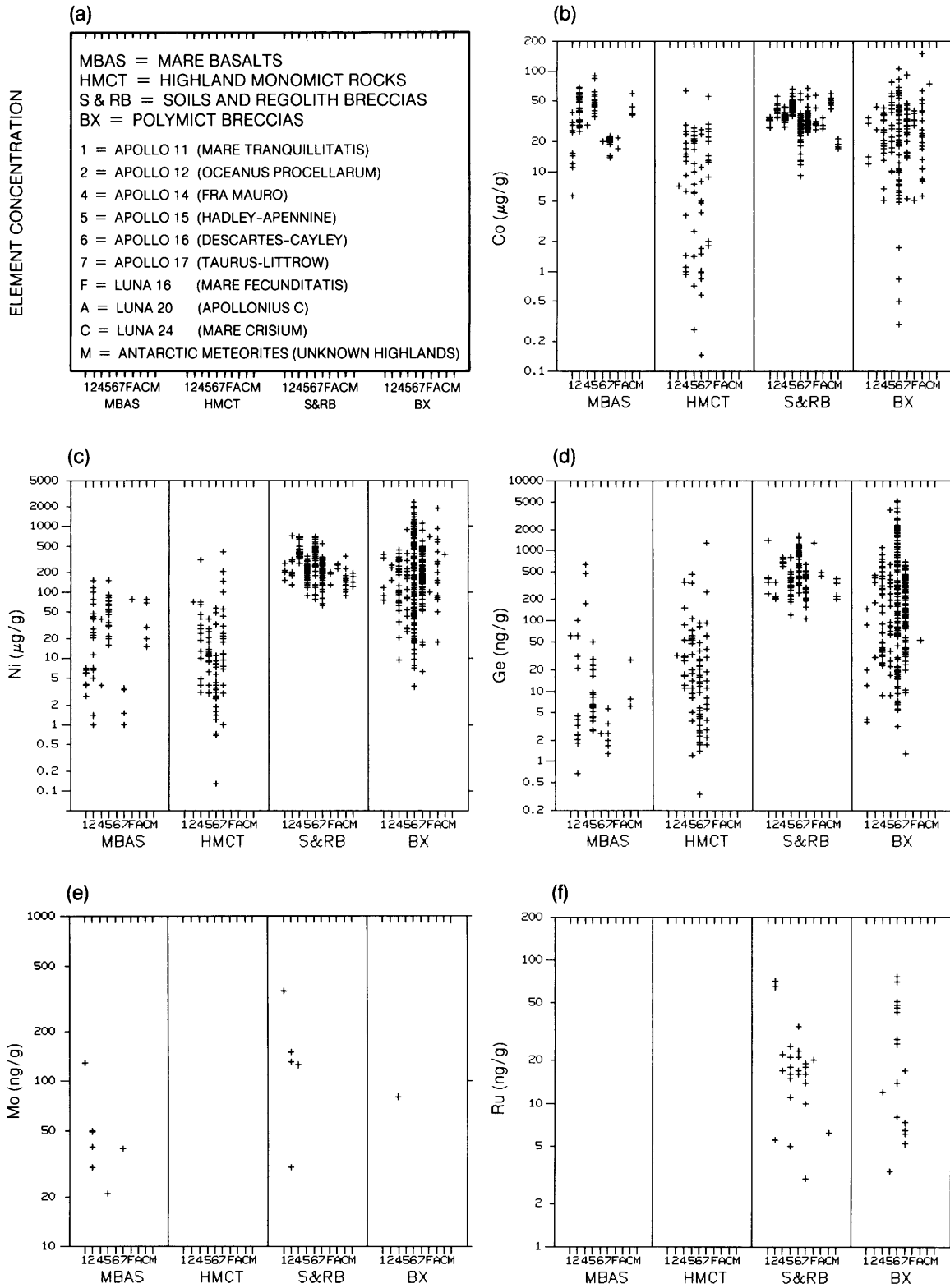
the Moon. These rock types are chemically *pristine* in the sense that they are not impact mixtures that have lost the chemical purity of indigenous lunar magmas (see section 6.3). Although almost all the highland pristine samples are breccias, they are only shattered, not mixed with other rocks and soils (i.e., they are *monomict*). From a chemical perspective, the terms *pristine* and *monomict* can be used interchangeably. All monomict samples discussed in this section are clearly monomict, based on textural and mineralogic criteria independent of their siderophile-element contents. The monomict samples are shown in the two lefthand columns, for mare basalts (*MBAS*) and highland monomict rocks (*HMCT*), in Fig. 8.20 and in all similar figures in this chapter.

In contrast, the siderophile element concentrations in nearly all *polymict* samples have been significantly enhanced by the addition of varying amounts of meteoroid debris. This is true for most polymict breccias (*BX* in Fig. 8.20), and is true for all lunar soils and regolith breccias (*S&RB* in Fig. 8.20). In fact, it is a common practice to estimate the percentage of meteoroid material in a lunar soil by comparing the concentration of a highly siderophile element (e.g., Ir) in the soil to the concentration of the same element in typical chondritic meteorites. The indigenous Ir content of the soil is assumed to be negligible; the meteoroid component is assumed to be the result of so many meteoroid impacts that its aggregate composition is essentially that of the average for known meteorites.

8.6.1. Analytical Difficulties

Typical lunar igneous rocks are depleted in siderophile elements relative to average meteorites. The exact patterns and origins of these depletions have been, and continue to be, a source of controversy. Resolution of this controversy is important for testing various theories for the origin of the Moon. The depletion of siderophile elements in indigenous lunar materials presumably reflects some period of metal/silicate fractionation before or during formation of the Moon. The exact nature of these depletions could thus provide a crucial test of the various models for the origin of the Moon. Many models involve a metal/silicate fractionation that

Fig. 8.20. Concentration ranges of siderophile elements in various lunar materials: mare basalts (MBAS), highland monomict rocks (HMCT), soils and regolith breccias (S&RB), and polymict breccias (BX). Horizontal axis shows sample types, separated according to individual missions. Vertical axis shows elemental concentrations (in $\mu\text{g/g}$ or ng/g). **(a)** Graphical key to the plots and abbreviations. Data are presented for **(b)** cobalt, Co; **(c)** nickel, Ni; **(d)** germanium, Ge; **(e)** molybdenum, Mo; **(f)** ruthenium, Ru; **(g)** palladium, Pd; **(h)** antimony, Sb; **(i)** tungsten, W; **(j)** rhenium, Re; **(k)** osmium, Os; **(l)** iridium, Ir; **(m)** gold, Au. Statistical summaries for most of these plots are provided in Table A8.4. Most of these analyses have been obtained by RNAA. The assistance of E. Anders (University of Chicago) is gratefully acknowledged for providing many unpublished analyses from the University of Chicago RNAA laboratory.



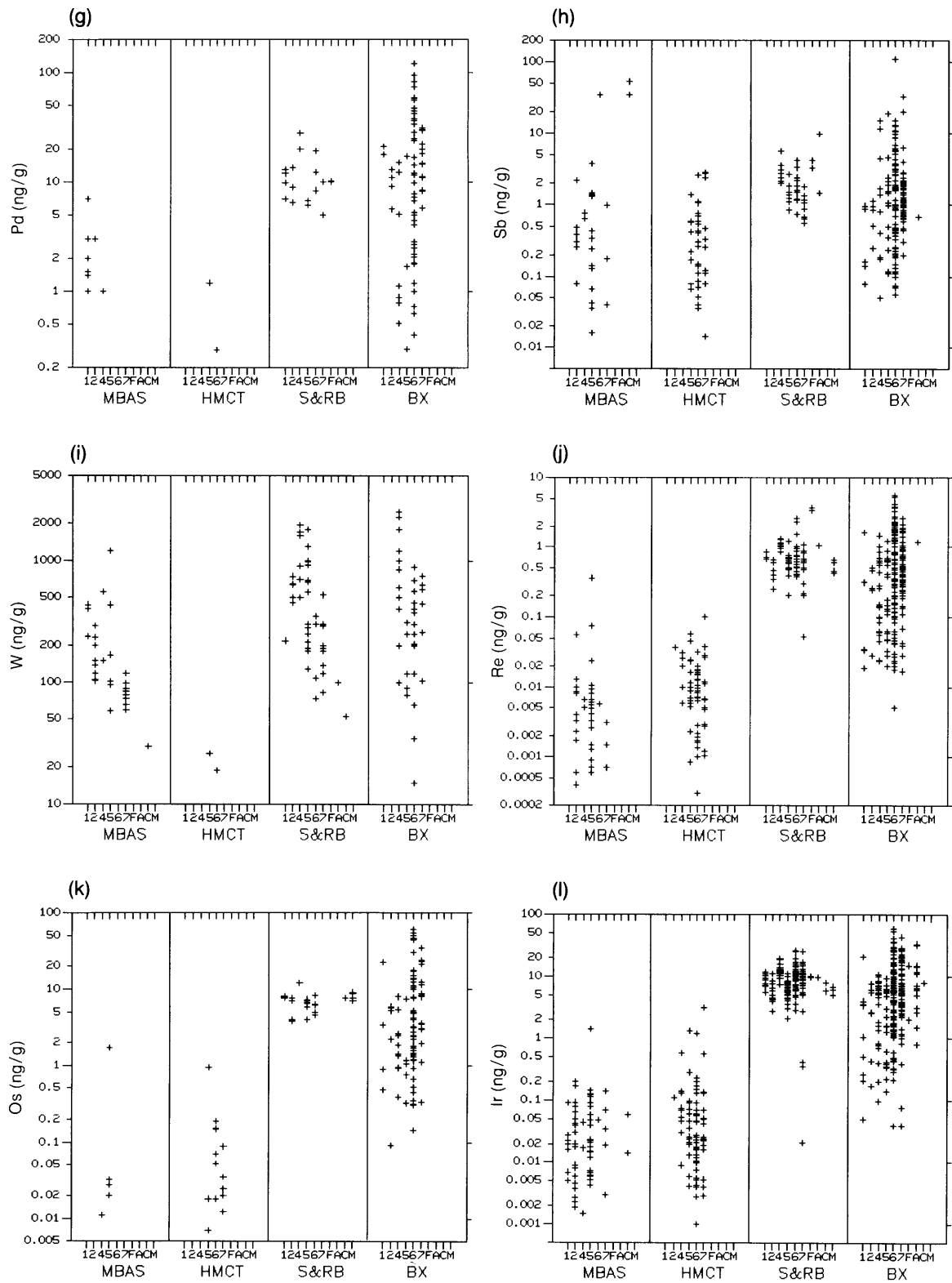


Fig. 8.20. (continued).

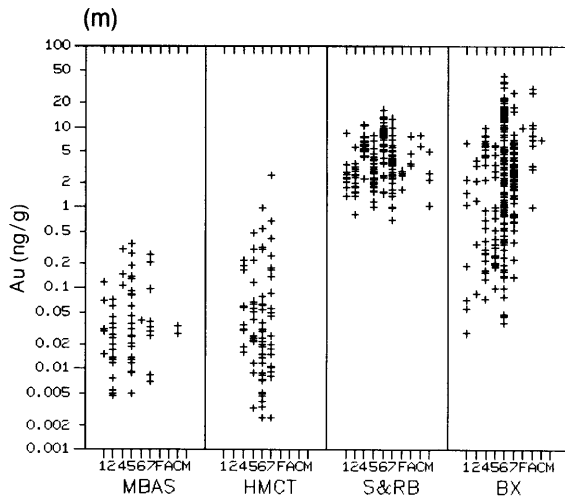


Fig. 8.20. (continued).

occurred on some other body (in most models, the Earth) before the Moon itself formed. Other models relate the observed depletion of siderophile elements to chemical differentiation within the Moon, possibly involving formation of a small metal core. One problem in resolving these questions is the difficulty of obtaining reliable analyses of siderophile elements, especially for the monomict mare and highland rocks, in order to determine what the original siderophile abundances in the Moon really were.

Of the elements discussed in this chapter, only Fe, Co, and (in a few laboratories) W are easily and reliably measured in virtually all lunar samples. The main problem in measuring the others is their extremely low concentrations [typically measured in nanograms per gram (ng/g), compared to micrograms per gram ($\mu\text{g/g}$) for most other trace elements]. The widely-used technique of INAA can accurately determine Ni in all but a few percent of lunar rocks, including, under optimum conditions of mass and other analytical factors, many monomict varieties. This same technique can also detect Ir and Au in most lunar polymict rocks and soils, but almost never in any type of monomict rock. For most other siderophile elements (the main exception is Mo), the only published data have been determined by the more laborious technique of radiochemical neutron activation analysis (RNAA). Most siderophile-element concentrations reported for mare basalts in the early 1970s are suspiciously high in comparison to data acquired since about 1974, when most of the relatively few analysts still studying lunar rocks came to appreciate the enormous potential for laboratory contamination and to take increased precautions to avoid it (Wolf *et al.*, 1979; Warren *et al.*, 1986).

For highland monomict rocks, there is also a severe sampling problem. Many of these rocks occur as fragments in breccias, and only a few of them are large enough to permit taking splits of even a few hundred milligrams for analysis. In fact, most samples of highland monomict rocks have masses of only a few hundred milligrams. From such samples, only a few tens of milligrams (if any) can be used for destructive analyses. Even for the few kilogram-sized samples, the largest subsamples consumed for analysis never weigh more than a few hundred milligrams.

In any lunar rock, the siderophile elements are concentrated into a few tiny, randomly distributed grains of metal or other opaque minerals. Even for a highly siderophile element such as Ir, replicate analyses of mare basalts, using samples of roughly 200 mg, frequently differ by factors of >3 (Warren *et al.*, 1986; Anders *et al.*, 1971). Highland monomict rocks tend to be coarser grained and more mineralogically heterogeneous than mare basalts. Thus, even the relatively few highland monomict samples with reliable siderophile data are not clearly representative of any large volume of the lunar crust.

In addition to these problems, the general difficulty of determining most of the siderophile elements (the main exceptions are Fe, Co, and W) inevitably produces a bias toward higher concentrations in the database. Many siderophile analyses provide only upper bounds (determined by the analytical detection limits) on concentration. In some tabulations, no result may be reported for a siderophile-poor sample even though the same author may report data for the same element in similar but more siderophile-rich samples. There is no clear way to compensate for these complexities when calculating average

siderophile concentrations for any particular set of samples. This problem tends to be most acute for the elements with strongest siderophile character (e.g., Re and Os), which are most depleted in lunar samples.

For highland monomict rocks, another factor may bias the database for siderophile elements toward lower contents. One of the prime means for distinguishing whether a highland rock is monomict or polymict is to compare its concentrations of highly siderophile elements (e.g., Ir, Ni, Re, or Os) to those in meteorites. Since many highland monomict rocks (unlike mare basalts) are so thoroughly brecciated that the evidence from texture and mineralogy may be ambiguous, there could be cases where samples are identified as polymict mainly on grounds of high siderophile contents, when in fact they might simply be uncommonly siderophile-rich monomict rocks.

8.6.2. Iridium: The "Type" Siderophile Element

Iridium is one of the most extremely siderophile elements (Table 8.4). It is also one of the most frequently and most reliably determined elements among the siderophile group. Iridium thus represents a good standard for comparison, particularly for siderophile elements that are often determined simultaneously with Ir. Most of the following general observations about Ir concentrations in lunar materials seem to apply equally well to other comparably siderophile elements (see Table 8.4). The main exception to this generalization is Ni, which is apparently not as Ir-like in its behavior as its $D_{m/s}$ in Table 8.4 would suggest. In addition, the distributions of Au and Ge may be significantly affected by their greater volatility (see discussions of individual elements in section 8.6.3).

Mature lunar soils derive virtually all their Ir from introduced meteoroid debris; apparently, the indigenous contribution of Ir from lunar bedrock is virtually negligible. This conclusion is strongly supported by the general observation that all reliable analyses of presumed monomict rocks (mare basalts as well as numerous undamaged—and clearly recognizable—highland monomict rocks) yield extremely low Ir concentrations in comparison to soils and regolith breccias (Fig. 8.201). Since the aggregate composition of all the analyzed monomict rocks from any given site is roughly the same composition as the local soils, the soils evidently receive their Ir from a component (or components) that make up only a few percent of the mass of the soils.

Lunar soils are produced by the disaggregation and crushing of rocks by meteoroid impacts, and it is clear that the average meteoroid contains several

orders of magnitude more Ir than any known lunar monomict rock. Therefore, the obvious source for the Ir-rich component in lunar soils is meteoroid debris. This conclusion is corroborated by studies of the metal grains separated from lunar soils. The larger metal grains generally have compositions and textures that may have formed within a meteoroid host (Wlotzka *et al.*, 1973; Goldstein *et al.*, 1972), although commonly the metal grains appear to have been metamorphosed during an earlier residence in polymict breccias before entering the soil.

Wänke *et al.* (1971) and Wlotzka *et al.* (1972) used mass-balance calculations on their data for metal grains from soils and for the bulk soils (including total Fe-metal contents) to estimate that meteoroid metal grains contribute about 53–62% of the total Ir in two Apollo soils (12001 and 14163; Table A8.4). The same approach, applied to Apollo 11 soil 10084, yielded a bogus meteoroid metal-grain Ir contribution of 226%, but Wänke *et al.* (1972) explained this discrepancy as a consequence of their having analyzed only the coarsest metal grains in sample 10084, whereas for samples 12001 and 14163 metal grains of all sizes were analyzed.

The data from samples 12001 and 14163 suggest that much of the Ir added to the soil comes from meteoroids similar to carbonaceous chondrites, which are common, primitive, volatile-rich meteorites that have roughly the same concentrations of Ir (and other nonvolatile elements) as an average meteorite. However, carbonaceous chondrites contain little or no Fe metal, and their Ir is believed to reside in the ultrafine-grained, amorphous matrix material that constitutes a major fraction of these meteorites. Comets and micrometeoroids, which are also likely objects to collide with the Moon, are believed to be generally similar to carbonaceous chondrites in this regard.

Table A8.4 includes statistics for concentrations of Ir and other frequently determined siderophile elements in two types of lunar samples: mare basalts (monomict samples from the lunar mantle) and soils and regolith breccias (polymict samples). The contrast in Ir contents between monomict mare basalts on the one hand and polymict soils and regolith breccias on the other is probably even more pronounced than this table and Fig. 8.201 would suggest because of the analytical problems discussed above. The sensitivity of the RNAA technique for Ir is so great that Ir has been detected about 90% of the times that RNAA has been applied to mare basalts (e.g., Wolf *et al.*, 1979; Warren *et al.*, 1986, 1987), a far better success rate than for most other siderophile elements. However, even these data may be complicated by occasional failures to detect Ir in extremely low-Ir samples, and there may also be

(even in a selective literature compilation) a significant number of spuriously high values arising from laboratory contamination.

Despite these problems, several relatively high-Ir data points for highland monomict breccias (Fig. 8.20l) seem to be reliable. The high value among the Apollo 15 highland monomict breccias is from an apparently pristine anorthosite (15363) containing an observed high proportion of Fe metal (1.0 wt.% in a corresponding thin section; Warren *et al.*, 1987). The highest Ir concentration among all the highland monomict breccias is from an Apollo 17 dunite (sample 72417) that is also exceptionally rich in Co, Ni, and other siderophile elements (Higuchi and Morgan, 1975; Laul and Schmitt, 1975a). The relatively constant Ir concentrations of regolith samples, their varied major element compositions notwithstanding, are consistent with the hypothesis that essentially all the Ir is of extralunar (meteoroid) origin. Based on the mass balance for Ir in the soils, assuming that an average meteoroid has about the same Ir concentration as CI carbonaceous chondrites (i.e., 480 ng/g; Anders and Ebihara, 1982), typical lunar soils appear to contain roughly 1–4 wt.% of meteoroid debris. The outstanding low-Ir values in the S&RB column of Fig. 8.20l are not typical soils, but the pyroclastic deposits of orange glass at the Apollo 17 site. Since these are in fact extensive deposits of mare basalt magma particles, rather than true soils, it is not surprising that they are the only data in the S&RB column that plot as if they should be in the MBAS column. The orange glass deposit is essentially pristine; it is diluted by as little as 1% of soil-like materials, and thus has only a trace of meteoroid contamination (Heiken *et al.*, 1974; Jerde *et al.*, 1987).

Virtually all the Ir found in polymict breccias is probably also of meteoroid origin. In fact, lunar soils and polymict breccias (both regolith breccias and other types of polymict breccias; see section 6.4) have similar average Ir concentrations. (Note that on the logarithmic scale of Fig. 8.20l, the actual mean of a group of data points is far higher than appears at first glance because the value of the spacing between data points is much greater at higher concentrations.) The breccias show much greater dispersion than do the soils, especially toward low Ir concentrations; this behavior probably reflects their generally simpler mixing history in comparison to even the most immature soils.

Among regolith samples, those from the purely highland Apollo 16 site and from the preponderantly highland Apollo 14 site tend to have relatively high Ir concentrations (Fig. 8.20l). However, highland soils do not necessarily contain more Ir than do mare soils. The Apollo 17 soils (from a mixed highland-

mare site) have similar Ir concentrations, but there is no correlation between the Ir concentrations of Apollo 17 soils and the ratios of highland components to mare components in the soils. (This ratio is easily estimated from an element such as Fe, which is highly enriched in mare materials.) In addition, the Antarctic lunar meteorites and to a lesser degree the Luna 20 soil, all from highland regoliths, have only moderate Ir concentrations.

There are few relationships between Ir concentrations and those of nonsiderophile elements in lunar samples. The available data scarcely permit any predictions about Ir concentrations in monomict rocks, except that Ir concentrations in mare basalts are generally 0.001–0.2 ng/g, and in monomict highland rocks most Ir concentrations are 0.001–3 ng/g (Fig. 8.20l). For other, less strongly siderophile elements, there are some correlations with nonsiderophile elements. For example, Ni and especially Co have indistinct but significant correlations with Mg, and W has an excellent correlation with a host of incompatible trace elements such as La (regarding such correlations, see discussions of these individual elements in section 8.6.3). Iridium shows no such predictability (Fig. 8.21), although it may not be an accident that the highest Ir concentration among all monomict rocks occurs in a dunite with 27 wt.% Mg (Fig. 8.21a).

The scatter among the Ir data in Figs. 8.20l and 8.21 greatly exceeds the analytical precision of the measurements (generally about ± 10 –20%). Apparently, the Ir concentrations of the small chips of lunar igneous rocks that are analyzed are related to Ir concentrations of their parent melts only by the vagaries of obscure, highly localized processes such as nucleation of minute FeNi metal grains. Presumably, analyses of larger samples could at least slightly reduce the scatter, thereby concentrating the data points closer to the means, which are roughly 0.05 ng/g for mare basalts and 0.1 ng/g for monomict highland rocks.

8.6.3. Other Siderophile Elements

The remaining siderophile elements are discussed below in an estimated sequence of decreasing siderophile behavior (i.e., decreasing $D_{m/s}$ in Table 8.4). Unfortunately, for many elements there are no precise constraints on $D_{m/s}$. For a large set of elements, $D_{m/s}$ is only known to be roughly comparable to the $D_{m/s}$ of Ir. These elements, Ni, Ge, Ru, Rh, Pd, Re, Os, Pt, and Au, are discussed below in order of decreasing atomic number. It is likely, at least in a general way, that $D_{m/s}$ is positively correlated with atomic number. Other siderophile, or

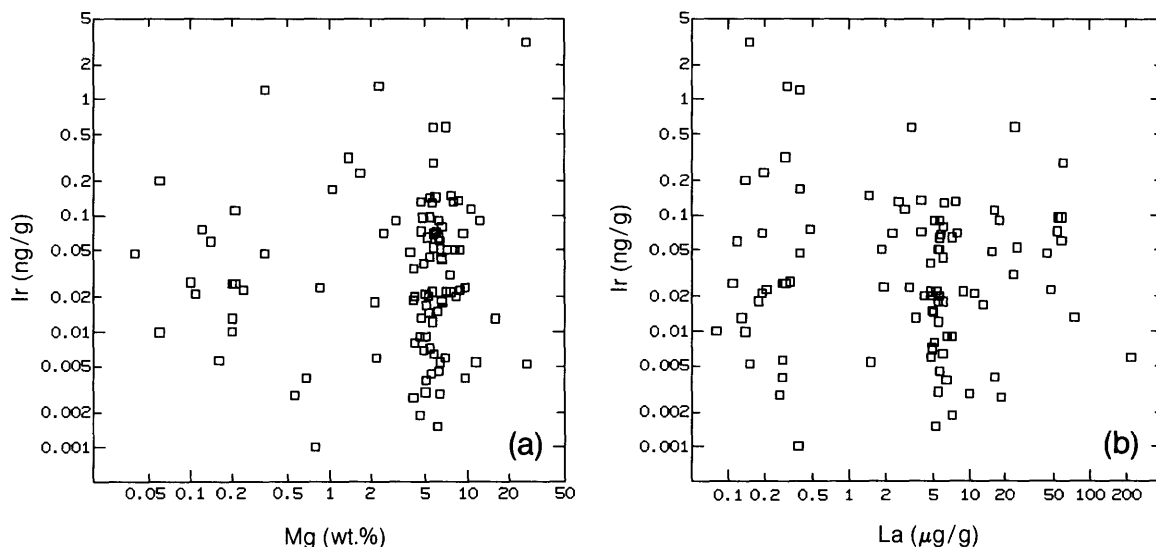


Fig. 8.21. Correlation plots for the “type” siderophile element Ir with Mg (a major element) and La (an incompatible trace element): **(a)** Ir vs. Mg; **(b)** Ir vs. La. Horizontal and vertical axes, both logarithmic, show elemental concentrations (Ir in ng/g, Mg in wt.%, and La in $\mu\text{g/g}$). Data points are only for samples free of meteoroid contamination, i.e., mare basalts and monomict highland rocks. There is no correlation between Ir and either Mg or La, indicating that Ir behaves neither like a major element nor like an incompatible trace element.

partly siderophile, elements (Mo, Sb, W, and Fe) are discussed at the end of this section.

Gold. As in the case of Ir, most of the Au in lunar samples is extralunar in origin. The main factor governing Au concentrations appears to be the extent to which the samples have been contaminated with meteoroid debris. Mare basalts and monomict highland rocks have far lower Au concentrations (generally <1 ng/g) than soils and polymict breccias (up to 50 ng/g; Fig. 8.20m). Neutron activation analysis is so sensitive for Au that it is almost always detected in RNAA. However, because gold objects are common in the human environment, the potential for laboratory contamination is greater for Au than for any other siderophile element. Nevertheless, the principal “outlier” data point in Fig. 8.20m, the high Au value (about 3 ng/g) for one of the monomict highland rocks, is almost certainly real. It represents an Apollo 17 dunite (72417) that has been analyzed for Au by two different laboratories and is also exceptionally rich in Ir, Ni, and other siderophile elements (Higuchi and Morgan, 1975; Laul and Schmitt, 1975a).

Like Ir, Au has practically no correlation with any other chemical element except those that are also associated with meteoroid contamination. Gold concentrations correlate well with Ir concentrations

(Fig. 8.22a). In this plot, most of the scatter at the low-Au end of the trend is in the direction of higher Au/Ir ratios. This effect could be caused by a higher potential for laboratory contamination in Au-poor samples, but it is more likely an indication that, in the lunar environment, Au may not be quite as siderophile as Ir.

In most environments Au would hardly be considered volatile, but it does condense at lower temperatures than more typical siderophile elements such as Ir (e.g., Wasson, 1985). This difference has led to speculations that a significant fraction of the Au enrichments observed in some highland soils and breccias may be related to a tendency for Au to become mobilized in fumarolic or perhaps very rare hydrothermal fluids (Hughes *et al.*, 1973; Delano and Ringwood, 1978; Wänke *et al.*, 1978).

In Fig. 8.22a, even the highest values for Au tend to fall well above the line representing the Au/Ir ratio in CI-carbonaceous chondrites, which are the presumed source of both elements. This discrepancy is not easy to explain, because only relatively few meteorites have Au/Ir ratios more than about 1.4 times the CI ratio (Mason, 1979). In order to account for the high Au/Ir ratios commonly found among Apollo 16 samples, Korotev (1987a,b) suggested that an ancient impact by an unusual giant meteorite

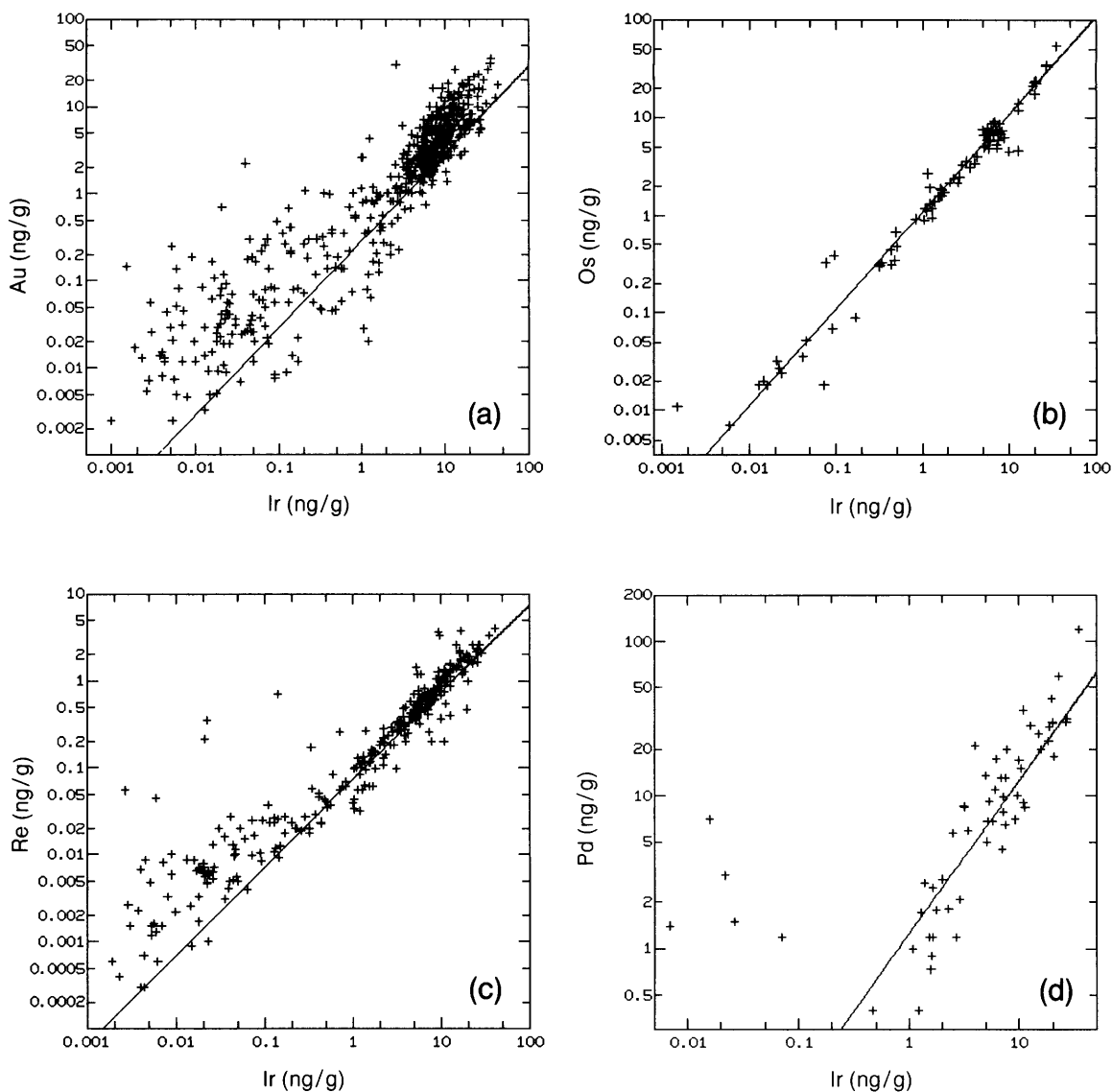


Fig. 8.22. Correlation plots for the “type” siderophile element Ir with other siderophile elements (Au, Os, Re, and Pd) for a range of lunar sample materials. **(a)** Au vs. Ir; **(b)** Os vs. Ir; **(c)** Re vs. Ir; **(d)** Pd vs. Ir. Horizontal and vertical axes, both logarithmic, show elemental concentrations (in ng/g). Data points are for all types of lunar materials, monomict and polymict. The diagonal line indicates the “standard” elemental ratios characteristic of CI-type carbonaceous chondrites (*Anders and Ebihara, 1982*). Iridium shows good correlations with all the other siderophile elements (especially with Os), indicating that they behave as a chemically coherent group. The Ir-Au, Ir-Re, and Ir-Pd correlations deviate from the CI line at low Ir concentrations, trending to higher Au, Re, and Pd values above the CI line. This may be because of the tendency for these elements to be less siderophile than Ir during lunar igneous processes.

(with a high Au/Ir ratio, similar to the rare Emsland iron meteorite) enriched the breccias near the Apollo 16 site in Au relative to Ir.

It is also possible, however, that our knowledge of Au distributions in all rocks of the lunar highlands is still too limited to determine the real cause of the lunar Au/Ir ratios. Euclitic meteorites, which are basaltic rocks that generally have siderophile-element concentrations (and many other compositional features) similar to those of monomict mafic lunar rocks, are known to have relatively high Au concentrations, e.g., 4.6 ng/g in the Lakangaon meteorite (Warren and Jerde, 1987), 7 ng/g in Juvinas (Morgan *et al.*, 1978), and 9 ng/g in Cachari (Palme *et al.*, 1978). Thus, the evidence from the few small monomict rocks that have been analyzed (Fig. 8.20m) notwithstanding, it remains conceivable that the lunar highland crust contains abundant monomict rocks with Au concentrations $\gg 1$ ng/g.

Platinum. Very few data have been reported for Pt because of difficulty in analyzing for it. Vinogradov (1973) reported a Pt concentration of ~ 50 ng/g for Luna 16 soil. Kolesov and Surkov (1980) reported values of 6–7 ng/g (average 6.7 ng/g) for Luna 24 soil. Considering that the Pt/Ir ratios of meteorites are generally in the range 1.7–3.0 (Mason, 1979), these Pt data, especially for the Luna 24 soil, are quite plausible. However, the Pt data reported by Kolesov and Surkov (1980) for Luna 24 mare basalts (7–8 ng/g) are probably spuriously high. Palme *et al.* (1978) determined the Pt contents of two uncommonly Ir-rich highland polymict breccias to be 60 and 130 ng/g, with an estimated precision of 40% relative. Based on this scanty database, the distribution of Pt among lunar samples appears similar to that of Ir, except that Pt concentrations tend to be roughly 2 times higher.

Osmium. Osmium is another element that is difficult to detect in lunar samples, even using RNAA. Consequently, the database for Os is sparse (Fig. 8.20k). Nevertheless, Os clearly tends to follow the same distribution pattern as Ir, and Os concentrations in mare basalts and monomict highland rocks are far lower than those in soils and polymict breccias. The correlation between Os and Ir is excellent (Fig. 8.22b). The most striking outlier in the Os data (Fig. 8.20k, column HMCT), a concentration of 0.95 ng/g for an Apollo 15 monomict rock, is probably reliable. This point represents the anorthosite sample discussed above (sample 15363; section 8.6.2), which has extraordinarily high concentrations of Fe-metal, Ir, and other siderophile elements. For monomict rocks, the Os data shown in Fig. 8.20k are potentially misleading because they represent the only monomict rocks in which the Os concentration was measured. Seventeen samples for

which only Os upper limits could be established were omitted. These include 12 mare basalts, mostly low-Ti varieties from the Apollo 12 and 15 sites, in which Os upper limits range from <0.01 to <0.06 ng/g, and 5 monomict highland rocks, in which Os upper limits range from <0.003 to <0.03 ng/g, all reported by Wolf *et al.* (1979).

Rhenium. Rhenium also shows a distribution pattern much like that of Ir, and Re concentrations in mare basalts and monomict highland rocks are also far lower than in meteoroid-“contaminated” soils and polymict breccias (Fig. 8.20j). The correlation between Re and Ir is good, especially for samples with more than about 0.1 ng/g Ir (Fig. 8.22c). The high-Re mare basalt and highland monomict rock outliers in Fig. 8.20j call for special attention. The data point for the high-Re Apollo 15 mare basalt (representing sample 15536) is suspiciously higher than all other mare basalt data, but this analysis is recent (Warren *et al.*, 1987) and considered reliable. The highest Re value for a monomict highland rock represents the same Apollo 17 dunite (72417) for which high but reliable Ir and Au values have been determined, as noted above. The exceptionally low Re value among the Apollo 17 S&RB data represents the orange-glass pyroclastic deposit, which is actually not a soil but a mare eruptive unit, with low concentrations of most meteoroid-derived siderophile elements. The two Re data points for Luna 16 soil are surprisingly high, particularly in view of the only moderate Ir and Au contents of the same analyzed samples (Figs. 8.20l,m), but these data (Laul *et al.*, 1972b) are also believed reliable.

Like Ir, Re has virtually no correlation with any nonsiderophile element in monomict lunar rocks. In particular, there is no correlation between Re and the incompatible trace element La among monomict rocks. Gros *et al.* (1976) claimed to detect a weak correlation between Re and Cs among 18 monomict highland rocks, but they omitted the Apollo 17 dunite (72417) from their data; restoring this one high-Re, moderate-Cs datum destroys the apparent correlation. Plots of Re vs. such major elements as Al, Mg, or Fe in mare basalts and monomict highland rocks likewise yield only random distributions.

In Fig. 8.20j, the highland monomict rocks seem to have generally higher Re concentrations than mare basalts. However, this pattern is at least partly the result of higher detection limits (i.e., failures to detect Re) among monomict highland rocks than among mare basalts. This situation in turn reflects the fact that different laboratories (using different nuclear reactors for RNAA) have focused their efforts on different rock types. Considering this source of bias, the data show little indication of any real difference

between the mean Re concentrations of mare basalts and the mean Re concentrations of monomict highland rocks.

Palladium. Palladium is also difficult to detect in lunar samples, even using RNAA. Consequently, the database is sparse (Fig. 8.20g). Nevertheless, Pd appears to follow the same distribution pattern as Ir, and Pd concentrations in mare basalts and monomict highland rocks are far lower than those in soils and polymict breccias. Except for a few early measurements on Apollo 11 mare basalts (*Ganapathy et al.*, 1970), the correlation between Pd and Ir values is excellent (Fig. 8.22d). Even if these early low-Ir analyses are accurate, the range of Pd values shown for mare basalts in Fig. 8.20g is almost certainly atypically high, as a result of the tendency for this element to be detected only in relatively Pd-rich samples. Upper limits reported by *Wolf et al.* (1979) for Pd in 12 mare basalts (mostly low-Ti types from the Apollo 12 and 15 sites) range from <0.25 to <1.3 ng/g; most are between <0.25 and <0.5 ng/g.

Rhodium. According to *Vinogradov* (1971), the Luna 16 soil has a Rh concentration of 3.7 ng/g; this value is reasonable when compared to its Ir content (~9.7 ng/g; Table A8.4) and the tendency for typical meteorites to have Rh/Ir ratios of about 0.3 (*Mason*, 1979). This Rh value appears to be the sole reliable analysis of Rh in a lunar sample. By analogy with Ir and other siderophile elements, the Rh data reported for Apollo 12 samples by *Bouchet et al.* (1971) seem far too high. (*Bouchet et al.* also report data that appear too high for Mo, Ru, and Ge.) It seems reasonable to assume that the distribution of Rh among lunar samples is similar to that of Ir, with Rh concentrations roughly 3 times lower than Ir concentrations.

Ruthenium. Ruthenium is also difficult to detect, even by RNAA, and it has been determined reliably only for lunar soils and polymict breccias (Fig. 8.20f). Three Ru concentrations measured from Apollo 12 soils (*Reed and Jovanovic*, 1971) show an inexplicably wide range that perhaps reflects the commonly poorer accuracy and precision of older data. The Apollo 17 S&RB sample with an exceptionally low Ru content is in fact not a soil, but the orange-glass pyroclastic deposit that is similarly low (as are other mare basaltic samples) in most meteoroid-added siderophile elements. Even lower Ru concentrations in the orange-glass pyroclastic deposits are implied by two upper limits of <1 ng/g reported by *Jovanovic and Reed* (1974).

Ruthenium measurements for Apollo 16 breccias may be somewhat unrepresentative. All analyses but one are from a single paper reporting only data above a detection limit of roughly 5 ng/g for a set of samples deliberately selected for their unusually

high Mg concentrations (*Wasson et al.*, 1977). Considering the generally low precision of most Ru data, these Ru values have a reasonably good correlation with Ir.

The only reliable constraints on Ru contents of monomict rocks are a few upper limits: <0.5 ng/g for Apollo 15 anorthosite 15415 (*Reed et al.*, 1972), <0.7 ng/g for Apollo 16 troctolitic anorthosite 62237 (*P. H. Warren*, unpublished data), <3 ng/g for the Apollo 17 dunite (72417), and less than roughly 1 ng/g for Apollo 17 troctolite 76535 (*Jovanovic and Reed*, 1974). Also, the low Ru concentrations in the Apollo 17 orange-glass pyroclastic samples imply that the Ru concentrations for pure high-Ti mare basalts, without any soil component, are even lower. The distribution pattern for Ru among lunar samples is presumably similar to that of Ir, except that, in part by analogy with meteorites (*Mason*, 1979), Ru concentrations are considered to be roughly 1.7 times higher.

Germanium. Geochemists accustomed to the limited variation of Ge concentrations in terrestrial igneous rocks find the erratic distribution of Ge among lunar rocks truly remarkable. Germanium does not appear to be quite as siderophile in its behavior as Ir does. The disparity between the lower Ge contents of monomict rocks and the higher Ge contents of typical soils is less pronounced than for Ir, Au, and the other siderophile elements previously discussed. A few monomict rocks even have Ge concentrations that overlap the range of Ge in typical soils, and these data appear reliable. Three of the four highest Ge concentrations found in highland monomict rocks are from KREEP samples (72275,91 = 1290 ng/g, *Morgan et al.*, 1975; 15007,293 = 460 ng/g, *Warren et al.*, 1983c; 15405,86 = 345 ng/g, *Gros et al.*, 1976). The three highest Ge values from mare basalts are in samples from the Apollo 14 site. For this site, *Dickinson et al.* (1985) have inferred that assimilation of a KREEP component greatly influenced the final magma compositions.

Anders (1978) has argued that there is a correlation between Ge and incompatible elements such as Cs in monomict highland rocks, but the correlation is tenuous. *Anders* excluded several samples from his database for reasons stated in his original paper (*Anders*, 1978, p. 180). Restoring just one of these samples, the low-Cs, high-Ge dunite 72417 (originally excluded on grounds of being a mantle sample, an assumption that has since been proved incorrect; *Ryder*, 1984), practically destroys the correlation.

Another correlation, between Ge and Ir (Fig. 8.23a), all but disappears at Ge concentrations below roughly 200 ng/g. In this plot, the points at the low-Ge end of the trend are scattered in the direction of

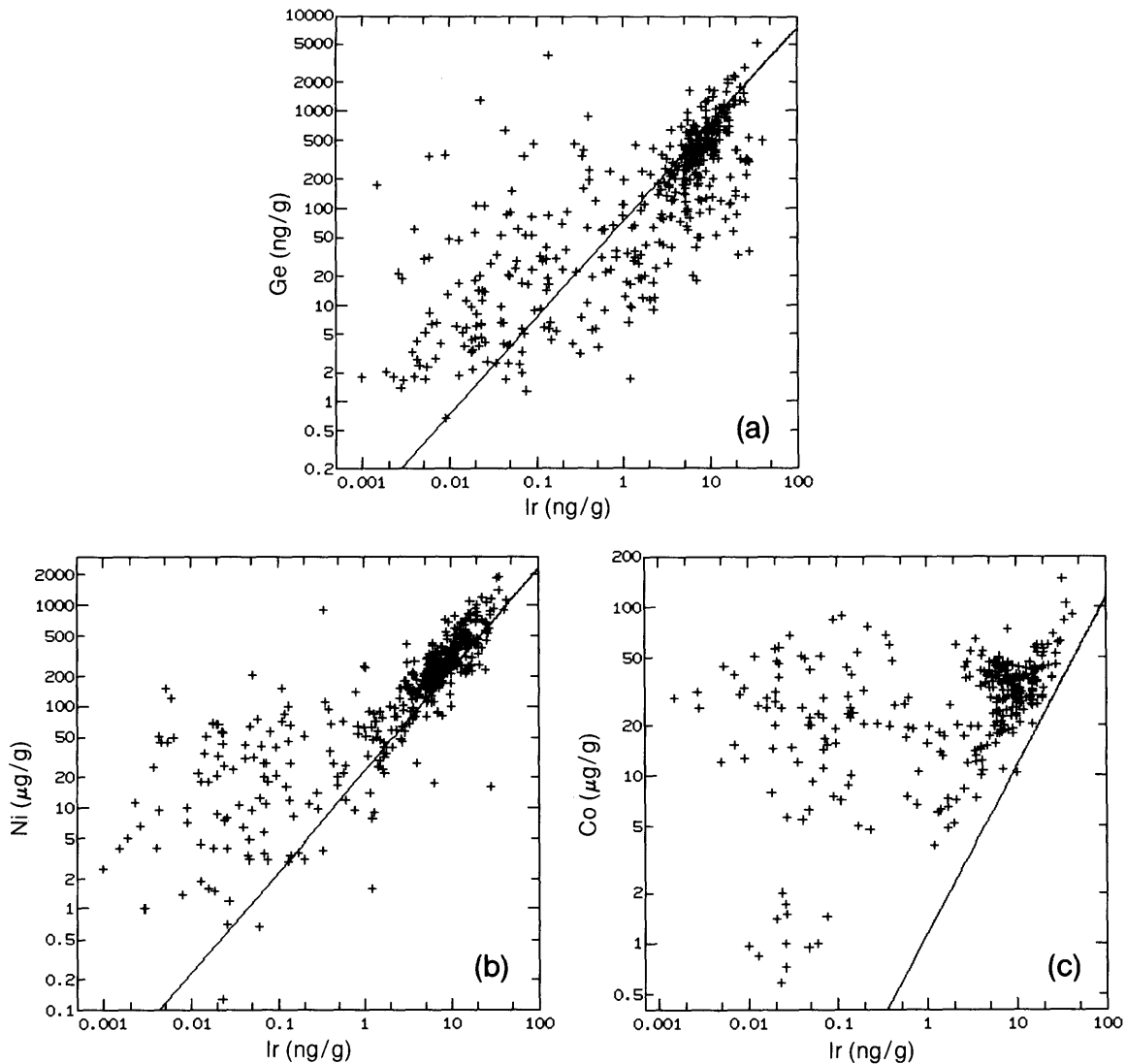


Fig. 8.23. Correlation plots for the “type” siderophile element Ir with other siderophile elements (Ge, Ni, and Co) for all types of lunar materials, monomict and polymict. **(a)** Ge vs. Ir; **(b)** Ni vs. Ir; **(c)** Co vs. Ir. Horizontal and vertical axes, both logarithmic, show elemental concentrations (Ir and Ge in ng/g, Ni and Co in µg/g). The diagonal line indicates the elemental ratios characteristic of CI-type carbonaceous chondrites (Anders and Ebihara, 1982). Correlations within this group of elements range from fair (Ni) to poor (Co). A large number of data points, especially for Ni and Co, lie on the high-Ni and high-Co sides of the CI lines because these elements are less siderophile than Ir.

higher Ge/Ir ratios, another indication that, in the lunar environment, Ge is not as perfectly siderophile as Ir.

Germanium is one of the most volatile siderophile elements, considerably more volatile than Au (Wasson, 1985). For this reason, many workers have concluded that the distribution of Ge among monomict highland rocks is controlled largely by transport of Ge in volcanic vapors, or by redistribu-

tion of volatiles generated in large meteoroid impact events (e.g., Wasson *et al.*, 1975a; Delano and Ringwood, 1978; Wolf *et al.*, 1979). Nevertheless, the Ge data for monomict highland rocks show no convincing evidence for any correlation between Ge and such vapor-mobilized elements as Tl. The correlation between Ge and Au is only slightly better than that between Ge and Ir. In short, Ge concentrations of monomict lunar rocks are virtually as

erratic as their Ir concentrations. Probably the best way to estimate the Ge concentration of a monomict rock would be to determine Au (or one of the other extremely siderophile elements) and then assume that the Ge/Au ratio is between 5 and 500.

Nickel. Nickel does not appear to be quite as siderophile in the lunar crust as its high value of $D_{m/s}$ (Table 8.4) would suggest. However, as with other siderophile elements, the contrast in Ni concentrations between monomict rock types and soils is substantial (Fig. 8.20c). As for many other highly siderophile elements, the Ni database is potentially misleading because the concentrations of Ni in many monomict rocks are below analytical detection limits. In order to include as many reliable determinations of Ni in Apollo 11 mare basalts as possible, our usual database (Table A8.4) was expanded to include the early analyses of *Annell and Helz* (1970) and *G. M. Brown et al.* (1970). Most monomict rocks have Ni concentrations within about a factor of 20 of typical soil concentrations. In fact, several monomict highland rocks (dunites) have higher Ni concentrations than most soils, reflecting the fact that in solid-melt equilibria, mafic silicate minerals (such as the olivine that makes up the dunite) are receptive hosts for Ni. The crystal/melt distribution coefficients measured for Ni have a strong inverse correlation with temperature, but at a typical magmatic temperature of 1200°C they are about 10–20 for olivine and roughly 5 for both low-Ca and high-Ca pyroxene (*Irving, 1978*).

There is a correlation between Ni and Ir (Fig. 8.23b), but it breaks down at Ni concentrations lower than about 50–100 µg/g. Below these values, the data points scatter almost entirely in the direction of higher Ni/Ir ratios. Data points showing this “surplus” Ni are mostly from monomict rocks with Mg contents greater than about 5 wt.%. The overall Ni-Mg correlation for monomict rocks (Fig. 8.24a) is weak, although better than the random distributions displayed by Ir and the other comparably siderophile elements. The high-Ti mare basalts common at the Apollo 11 and 17 sites have lower Ni concentrations than do the low-Ti mare basalts that predominate at the other sampled sites.

The average Ni concentration of the original lunar crust has been a topic of great controversy. E. A. Ringwood, H. Wänke, and their coworkers (e.g., *Delano and Ringwood, 1978; Wänke et al., 1978; Ringwood et al., 1987*) have speculated that the existing suite of monomict highland rock samples, for which Ni concentrations are mostly <100 µg/g, may be grossly unrepresentative for Ni. Instead, they argue that the average pristine Ni concentration of the highland crust (i.e., the average Ni concentration that would be found for a representative suite of

monomict highland rocks) may be several hundred micrograms per gram. In support of this idea, these authors have cited the high Ni concentrations, and especially the high Ni/Ir ratios, found in many Apollo 16 polymict breccias (Fig. 8.23b). However, their model for interpreting these enrichments is far from universally accepted (for contrasting views, see *Warren et al., 1989; Anders, 1978; Warren and Wasson, 1978; Wolf et al., 1979; Ryder, 1979; Korotev, 1987a,b*). As the data in Table A8.4 indicate, the high Ni concentrations (and Ni/Ir ratios) typical of Apollo 16 soils are not matched by other highland regolith samples, e.g., those from the Luna 20 highland site or from the (unknown) site(s) that produced the Antarctic lunar meteorites, almost all of which are nearly pure highland regoliths with major-element compositions similar to those of Apollo 16 soils.

Cobalt. Cobalt is decidedly less siderophile than any of the elements discussed above (see Table 8.4). Mare basalts, which are monomict rocks, have a range of Co concentrations little different from those of mare soils (Fig. 8.20b). The Co concentrations of monomict highland rocks tend to be much lower, but the two exceptionally high values in Fig. 8.20b are definitely reliable. These two values represent the same dunites that have anomalously high contents of Ni (see discussion of Ni above).

Cobalt is not closely correlated with other siderophile elements. Only among soils and breccias with very high Ir concentrations can any correlation between Co and Ir be discerned (Fig. 8.23c). There is a better, but inverse, correlation between Co and Al in monomict samples, except at high Al concentrations (Fig. 8.24b), similar to the correlation with Al shown by the miscellaneous minor elements Sc, V, Cr, and Mn (Fig. 8.17). There are reasonably strong correlations between Co and both Mg and Fe, and these mainly reflect the tendency for Co to partition into Fe- and Mg-rich minerals during igneous differentiation. There are no significant correlations between Co and incompatible trace elements such as La. As with Ni, the high-Ti mare basalts common at the Apollo 11 and 17 sites have lower Co concentrations than do the low-Ti mare basalts that predominate at the other sampled sites.

Molybdenum. Molybdenum is an element that is only seldom, and with great difficulty, determined for lunar samples. As discussed by *Newsom* (1986), more than half of all the published data for Mo in lunar samples appear to be unreliable. The few reliable data show little difference between mare basalts (which are monomict samples) and mare soils (Fig. 8.20e). Based on analogy with terrestrial rocks, *Newsom* (1986) suggested that Mo concentrations of lunar samples (which seldom contain more

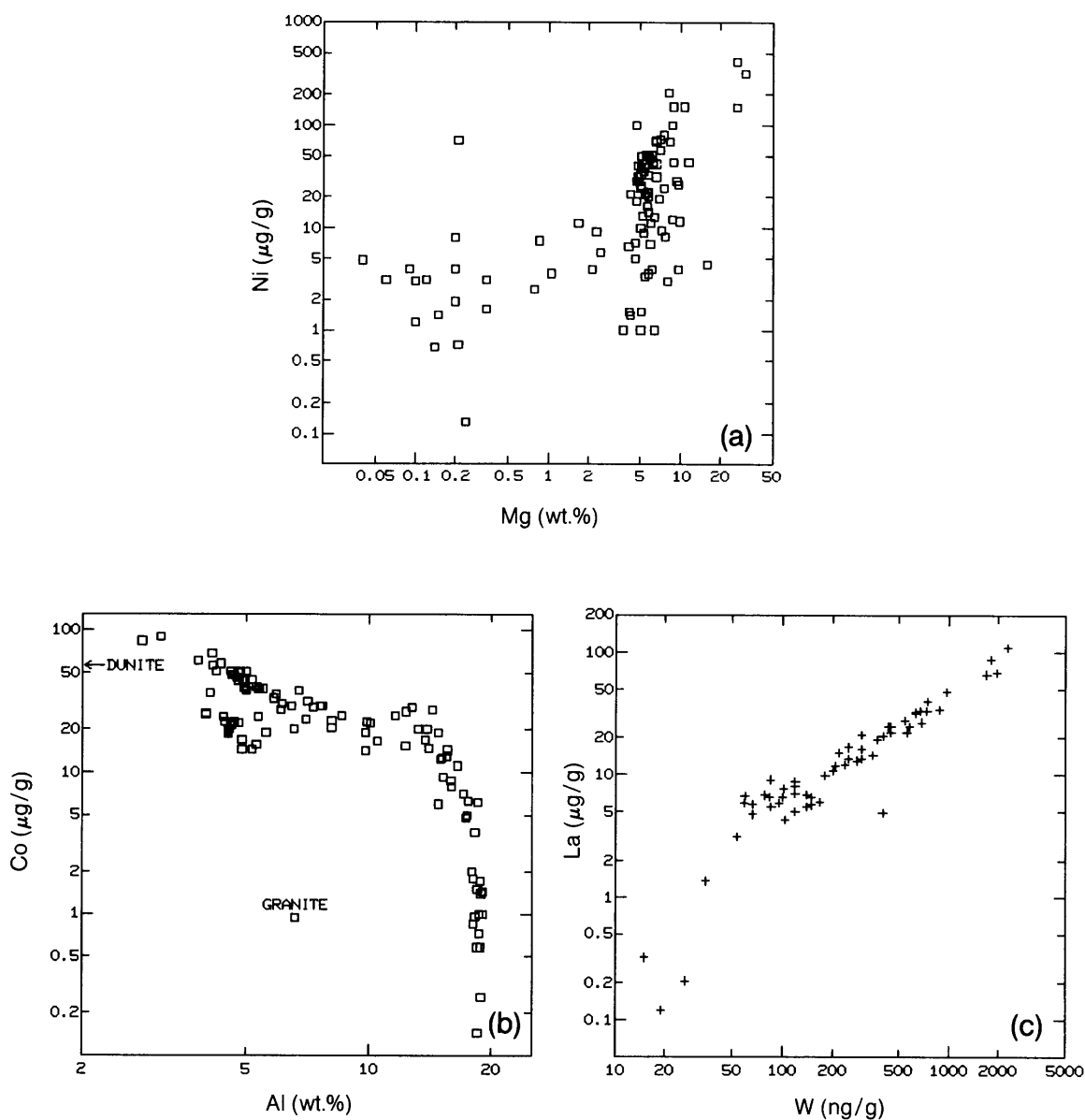


Fig. 8.24. Correlation plots for selected siderophile elements (Ni, Co, and W) with selected lithophile elements (Mg, Al, and La) for a range of lunar sample materials. **(a)** Ni vs. Mg; **(b)** Co vs. Al; **(c)** La vs. W. Horizontal and vertical axes, both logarithmic, show elemental concentrations (W in ng/g; Ni, Co, and La in $\mu\text{g/g}$; Mg and Al in wt.%). The Ni-Mg and Co-Al plots show only samples free of meteorite contamination, i.e., mare basalts and monomict highland rocks. [The Al concentration of dunite 72417 is off the diagram **(b)** at 0.7 wt.%.] The La-W diagram includes data from all types of lunar samples, monomict and polymict. Only a weak positive correlation exists between Ni and Mg. A stronger negative correlation exists between Co and Al, indicating that Co is strongly depleted in plagioclase-rich anorthositic rocks. A very strong positive correlation is present between La and W, indicating that, in the lunar environment, W also behaves as an incompatible trace element.

than traces of a metal phase) are controlled mainly by a tendency for Mo to behave as if it were an incompatible *lithophile* element (see section on W, below). The available data show no significant correlation between Mo and any incompatible trace elements (see Fig. 2 in *Newsom*, 1986), but this result may be due to scatter caused by the great imprecision of the few available data. Molybdenum is an element for which additional reliable data would be extremely valuable.

Antimony. Antimony appears to be only moderately siderophile (Table 8.4). It is also among the most volatile of the siderophile elements, more volatile than Au and comparable in volatility to Ge (*Wasson*, 1985). There is only a feeble correlation between Sb and Ir, even among soils, and the Sb data show considerable overlap between monomict rocks and soils (Fig. 8.20h). The mare basalt with an anomalously high Sb concentration is a clast from highland breccia 60639 (*Wolf et al.*, 1979) that may have acquired its high Sb by exposure to impact-generated vapors during the breccia-forming process.

Tungsten. Tungsten has only a mild siderophile affinity (Table 8.4), and its tendency to behave, at least in part, as an incompatible trace element is far more important in establishing its distribution among lunar samples than is its mild tendency toward siderophile behavior. Only about 40% of the W in lunar soils resides in Fe-metal. Furthermore, in contrast to more siderophile elements, there is little difference in W concentrations between monomict rocks (MBAS and HMCT) and soils (Fig. 8.20i). The two highland monomict rocks for which W data are available are definitely unrepresentative. Both are nearly monomineralic anorthosites with extraordinarily low contents of incompatible trace elements.

There is virtually no correlation between W and Ir. However, W shows excellent correlations with incompatible elements such as La (Fig. 8.24c). (See section 8.4 for discussion of W as an incompatible trace element.)

Iron. Even in the extremely reducing environment of the lunar crust, Fe is paradoxically the least siderophile of all the iron-loving elements. Of the total Fe in lunar soils, only about 2–5% of the amount present is Fe metal (*Housley et al.*, 1972, 1973b; *Wänke et al.*, 1971; *Wlotzka et al.*, 1972). The ratio of metallic Fe to total Fe is even lower for most lunar rocks. Mature lunar soils contain more reduced Fe than do otherwise similar immature soils, apparently because much of the Fe metal in soils originates through reduction of Fe-silicate minerals by adsorbed solar-wind gases during micrometeoroid impacts (section 5.4.3). (See section 8.3 for discussion of Fe as a major element.)

8.6.4. Siderophile-Element Fractionations Related to Grain Size in Lunar Soils

Although Fe-metal particles constitute only a fraction of a percent of lunar soils, they contain much—if not most—of the bulk soils' siderophile elements (Table 8.5). It is difficult in many cases to differentiate indigenous lunar metal from introduced meteoroid metal, especially if the distinction is based only on Co and Ni content of the metal (see section 5.4). Nevertheless, Fe metal is the most important recognizable meteoroid debris in lunar soils. It might be expected that there would be a direct connection between meteoroid metal sizes and the distribution of siderophile elements in size fractions of lunar soils, but this connection is complicated by soil formation processes.

The abundances of most chemical elements in lunar soils vary with grain size (see section 7.5.3 and Fig. 7.30). In some of the early work on returned lunar samples, *Ganapathy et al.* (1970) found Ir concentrations to be 1.7 times greater in the <44- μm fraction of Apollo 11 mare soil 10084 than in two coarser fractions of the same soil. *Boynton and Wasson* (1977) confirmed this pattern with data for Apollo 15 mare soil 15100. They found that Ir concentrations are relatively constant in size fractions greater than about 40 μm , but the Ir values rise in the finer fractions, reaching 2.4 times the bulk soil value in the <7- μm fraction. Other siderophile elements such as Ni, Ge, and Au show a similar pattern, but Co does not. *Duncan et al.* (1974) also found that Ni concentrations increase with decreasing grain size in the Apollo 17 soil 75081.

Boynton et al. (1976b) and *Boynton and Wasson* (1977) found that four Apollo 16 highland soils have more complex and less uniform relationships between Ir content and grain size. In one sample (soil 66080) Ir is enriched in the finest fraction (<7 μm) to about 1.5 times the bulk-soil concentration. In another sample (soil 61220), the Ir concentrations of the finest size fractions are only about half that of the bulk soil. In the two other samples (soils 65500 and 63500) the Ir concentrations of the finest fractions are similar to those of the bulk soils. However, in all these soils Ir, Co, Ni, Ge, Au, and (in the one case where it was determined) Ru all show a peak in concentration (typically up to about 1.5 times the bulk-soil composition) at grain sizes of roughly 100–300 μm . *Krähenbühl et al.* (1977) found the same pattern for Ge in Apollo 17 highland soils. A study of Ni and Co (as well as other elements) in eleven Apollo 16 soils, involving subdivisions of each soil into 2 or 3 size fractions, revealed little systematic relationship between grain size and

TABLE 8.5. Estimated chemical contribution from Fe-metal particles to bulk compositions of three lunar soils.

	Co	Ni	Ge	Pd	W	Ir	Au
	µg/g	µg/g	ng/g	ng/g	ng/g	ng/g	ng/g
12001, Fe-metal = 0.124 wt.%							
Bulk soil composition	38	314	200	9	630	11	2.6
Avg. composition of metal	6,500	64,000	—	—	110,000	5500	1000
Contribution of metal, %	21	25	—	—	22	62	48
14163, Fe-metal = 0.5 wt.%							
Bulk soil composition	43	400	720	28	1,950	19	6.1
Avg. composition of metal	5,500	57,400	138,000	2800	223,000	2000	1 100
Contribution of metal, %	64	72	96	50	57	53	90
15601, Fe-metal = 0.35 wt.%							
Bulk soil composition	51	157	2006.2		2804.1		1.6
Avg. composition of metal	10,350	48,500	—	—	25,000	—	350
Contribution of metal, %	71	108	—	—	31	—	77

Data from Wänke *et al.* (1971), Wänke *et al.* (1972), and Wlotzka *et al.* (1972), except Ge for bulk 14163 is from Baedecker *et al.* (1972), Ni for bulk 15601 is from Chou *et al.* (1974)—the Ni datum of 90 µg/g reported by Wänke *et al.* (1972) is far lower than any of several literature data.

* Housley *et al.* (1972) report a significantly lower total ferromagnetic Fe content for 14163: 0.34 ± 0.03 wt.%.

siderophile element concentration (Finkelman *et al.*, 1975).

Boynton and Wasson (1977) attribute the tendency for siderophile elements to be richest in the 100–300-µm size fraction primarily to the presence in this size range of welded aggregates of fine-grained metal condensates, originally vaporized by meteoroid impacts. The curious lack of any such pattern for the mare soil 15100 is attributed, in this model, to the lesser extent of impact welding of metal grains in soils from this relatively young mare terrain.

Boynton and Wasson (1977) also suggested that agglutinates, which are most abundant in about the 100–300-µm size range (D. S. McKay *et al.*, 1974), make a secondary contribution to the siderophile element enrichment of this size fraction. Laul *et al.* (1984) report data indicating that Ni tends to be enriched in agglutinates over the bulk soil, by a factor of roughly 2, in Apollo 17 mare soils.

8.6.5. Possible Lunar Ores of Siderophile Elements

The discussion above emphasizes the fact that trace siderophile elements are extremely rare in indigenous (monomict) lunar rocks; virtually all the trace siderophile elements are introduced as meteoroid materials. For this reason, ores of the siderophile elements are most unlikely to be found in any native lunar materials. However, it is conceivable that the meteoroid debris itself might be mined. On a small

scale, the FeNi metal particles in the lunar soil are not abundant, but they are ubiquitous, and might be concentrated magnetically and then refined by carbonyl extraction to produce pure Fe and Ni metals (Lewis *et al.*, 1988). Iron meteorite fragments up to ~60 tonnes mass have been found on Earth, and the ejecta blankets around lunar craters of modest (~1–10 km) diameter might be explored for comparable materials. On a much larger but very speculative scale, it is worth noting that siderophile-element ores of the Sudbury structure in Ontario, Canada, have been suggested to be derived from meteorite contributions (Dietz, 1964). This suggestion is not widely accepted, but it is much more likely that such possibilities will be rigorously tested on the Moon than on Earth.

8.7. VAPOR-MOBILIZED ELEMENTS

8.7.1. Concentration Levels

Before the return of the first lunar samples in 1969, several geochemists had been analyzing meteorites in order to determine the sequence in which the various chemical elements had condensed from the original solar nebula as it cooled. In their investigations they concentrated on a group of relatively volatile elements—Cu, Zn, As, Se, Ag, Cd, In, Te, Hg, Tl, Pb, Bi, and the halogens F, Cl, Br, and I. When lunar samples became available, the same scientists, joined by new workers, analyzed them in detail for this group of elements.

Although most of these elements are not gases under normal conditions, they are more easily volatilized than most elements in meteorites and lunar rocks. In much of the literature, these elements have been called "volatile elements" or simply "volatiles." To avoid confusion with more conventionally volatile species (H, He, other noble gases, C, and N), the group of elements described in this section is called the *vapor-mobilized elements* because they tend to be transferred from solid materials into a coexisting vapor phase at relatively moderate temperatures.

Before lunar samples were available, geochemists had determined that the Earth, the differentiated (*achondritic*) meteorites, and most types of chondritic meteorites were depleted in these vapor-mobilized elements relative to such standards of original solar-system composition as the atmosphere of the sun and the most primitive (e.g., type CI) carbonaceous meteorites.

For lunar materials, it is convenient to treat these elements as a single group. However, this group includes chemically diverse elements, and their chemical behavior is not as coherent as that of the *lithophile* and *siderophile* element groups. The only characteristics common to all the elements of this group (and to the alkali metals Na, K, Rb, and Cs) are relative volatility and consequent low abundance in the Moon. Under some circumstances, the behavior of most of the vapor-mobilized elements resembles that of siderophile elements; in other cases they behave like lithophile elements; and in still other cases the vapor-mobilized elements simply do not behave as a coherent group.

Figure 8.25 shows the concentrations of vapor-mobilized elements in lunar samples. Statistical summaries of the data are given in Table A8.5. The low concentrations of vapor-mobilized elements in all lunar materials (Fig. 8.25) were immediately apparent when the first lunar samples were analyzed. For example, *Keays et al.* (1970) reported that concentrations of Cs, Cd, Ag, Bi, Tl, and Br were below 1 $\mu\text{g/g}$ in Apollo 11 mare basalts and those of Zn, Cu, and Rb were not more than a few micrograms per gram, values that were extremely low relative to typical terrestrial basalts. In addition, they found that concentrations of those elements in polymict samples (soils and regolith breccias) were higher than in the monomict mare basalts from the same site by factors ranging from about 1.5 to 20. This pattern of higher concentrations of vapor-mobilized elements in lunar soils than in the local crystalline rocks was eventually found in samples from all lunar sites.

This apparent depletion of vapor-mobilized elements in all lunar rocks was a discovery that had

major implications for understanding the origin of the Moon. Initially, several questions were asked: Did the Moon have significantly higher amounts of vapor-mobilized elements when it formed? Might not these elements have been subsequently lost from the lunar surface as vapors accompanying ordinary volcanic eruptions when fluid lavas spread across the surface and cooled in the lunar vacuum? Or could they have been lost by the heating and vaporization produced by large impact events, especially those that stirred the lunar crust to depths of tens of kilometers?

A strong argument against all such later losses as the principal reason for the low lunar concentrations of vapor-mobilized elements comes from study of the isotopes of the element Sr. One of its isotopes, ^{87}Sr , is produced by the decay of a long-lived radioisotope of one of the volatile (vapor-mobilized) elements, ^{87}Rb , and this process is used extensively by geochemists to measure the ages of rocks. From numerous studies, particularly of meteorites, we know that the initial ratio of the isotopes $^{87}\text{Sr}/^{86}\text{Sr}$ for common solar-system materials was about 0.699. As time passed, this ratio has increased because the decay of any ^{87}Rb present in the planets has added ^{87}Sr to them. Many lunar rocks, especially anorthosites, have $^{87}\text{Sr}/^{86}\text{Sr}$ ratios that approach the solar system initial ratio; a few rocks even retain this initial ratio, indicating that virtually no ^{87}Sr has been added to them by ^{87}Rb decay since the Moon formed. The small amount of change in the ratio $^{87}\text{Sr}/^{86}\text{Sr}$ in lunar rocks overall indicates that throughout their history the rocks were never exposed to concentrations of ^{87}Rb significantly higher than their present values.

Another argument for originally low concentrations of lunar vapor-mobilized elements is the low ratio of Na to Ca in plagioclase feldspars from samples representative of the bulk of the lunar highlands. If Na, which is a relatively volatile element, had been as abundant in relation to Ca on the Moon as it is on Earth, lunar plagioclase would be more sodic. It is unlikely that the Na could have evaporated from an anorthosite (with composition essentially equivalent to pure feldspar) or from mare lavas without leaving excess silica or especially excess alumina, which we do not observe except in extreme cases of impact-volatilized glasses (*Naney et al.*, 1976; *Vaniman*, 1990). These results indicate that the Moon's relative concentrations of Rb, Na, and (by inference) other alkali elements have always been low. The volatility of these elements, leading to losses during high-temperature episodes in the formation of the Moon, seems to be the reason for their relative absence on the Moon. If the volatile alkali elements are depleted in the Moon, it follows

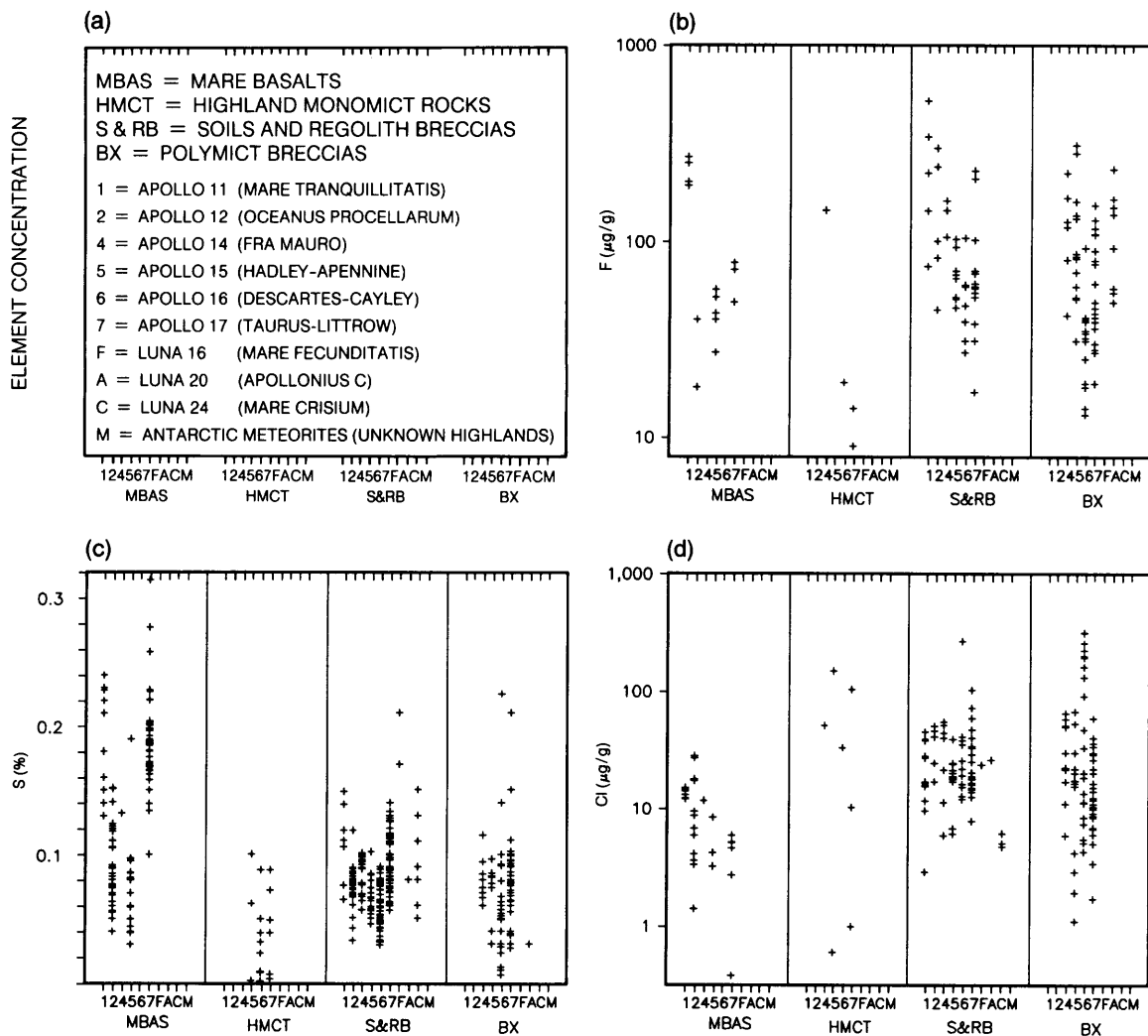


Fig. 8.25. Concentration ranges of vapor-mobilized elements in various lunar materials: mare basalts (MBAS), highland monomict rocks (HMCT), soils and regolith breccias (S&RB), and polymict breccias (BX). Horizontal axis shows sample types, separated according to individual missions. Vertical axis shows elemental concentrations (in ng/g, $\mu\text{g/g}$, or wt.%). Note that all vertical axes are logarithmic except for S. **(a)** Graphical key to the plots and abbreviations. Data are presented for **(b)** fluorine, F; **(c)** sulfur, S; **(d)** chlorine, Cl; **(e)** copper, Cu; **(f)** zinc, Zn; **(g)** arsenic, As; **(h)** selenium, Se; **(i)** bromine, Br; **(j)** silver, Ag; **(k)** cadmium, Cd; **(l)** indium, In; **(m)** tellurium, Te; **(n)** iodine, I; **(o)** mercury, Hg; **(p)** thallium, Tl; **(q)** lead, Pb; **(r)** bismuth, Bi. Statistical summaries for most of these plots are provided in Table A8.5. The values for I **(n)** are only lower limits because most of the measurements have been made only on leachable I rather than on total I.

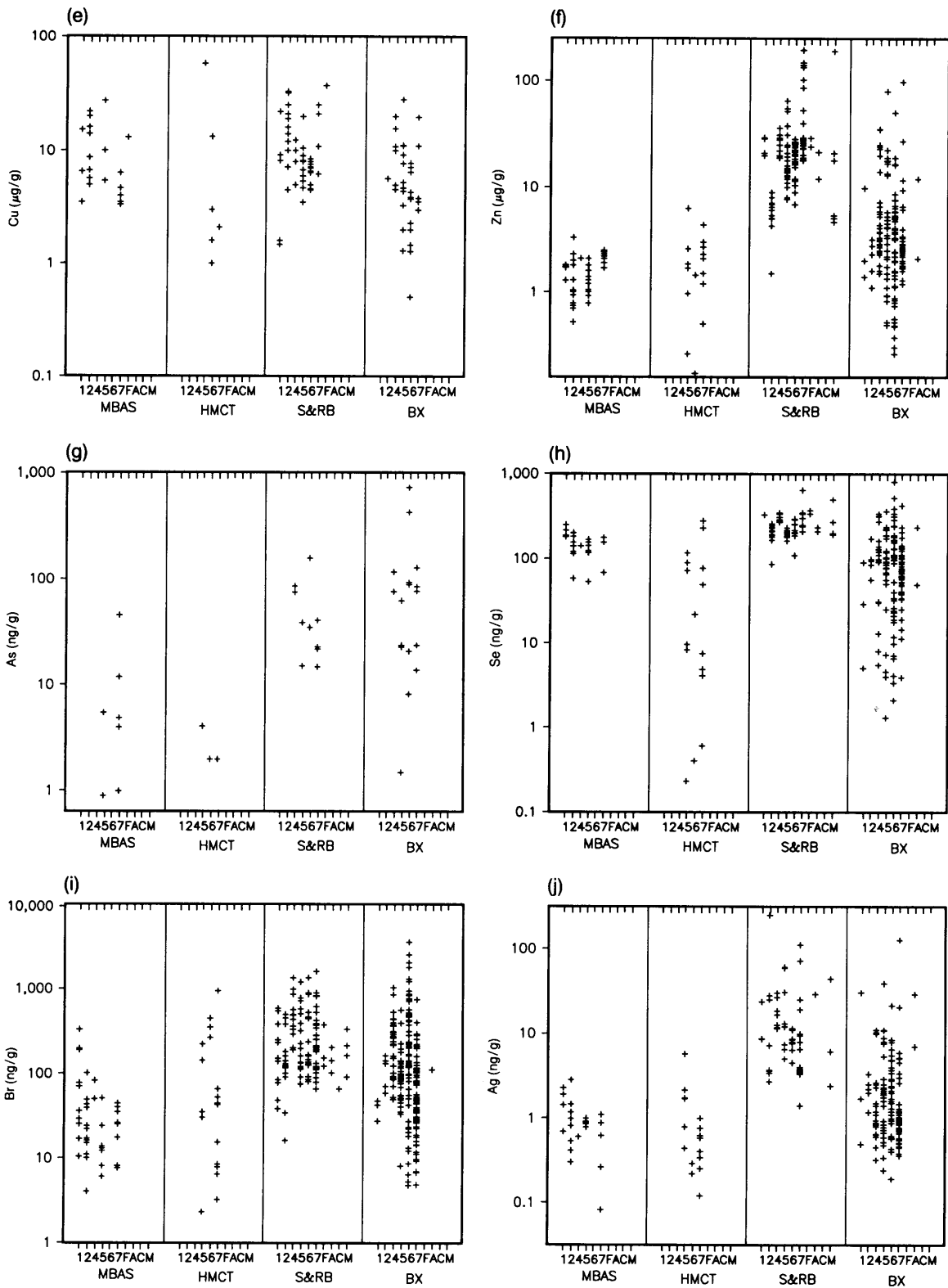


Fig. 8.25. (continued).

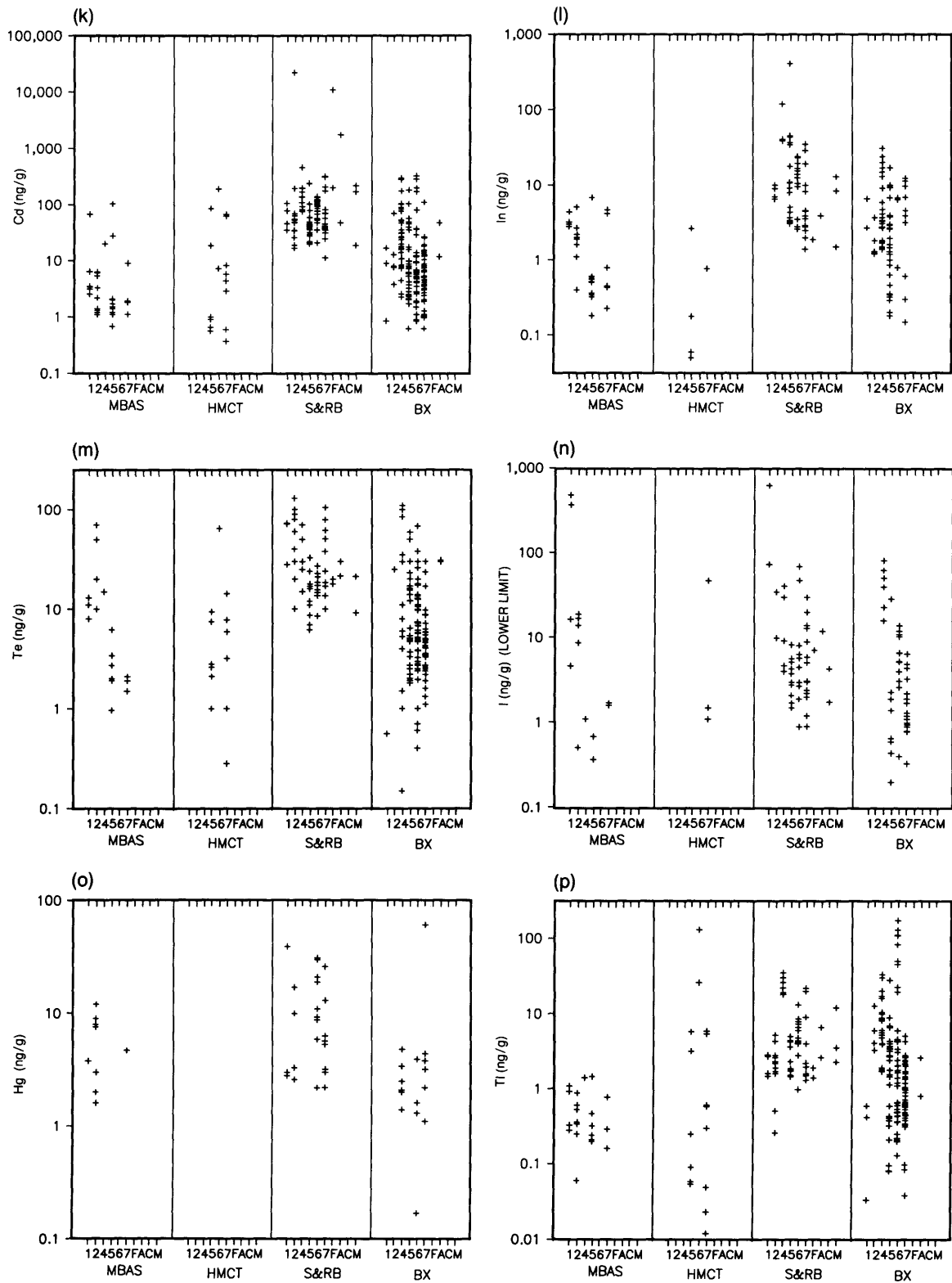


Fig. 8.25. (continued).

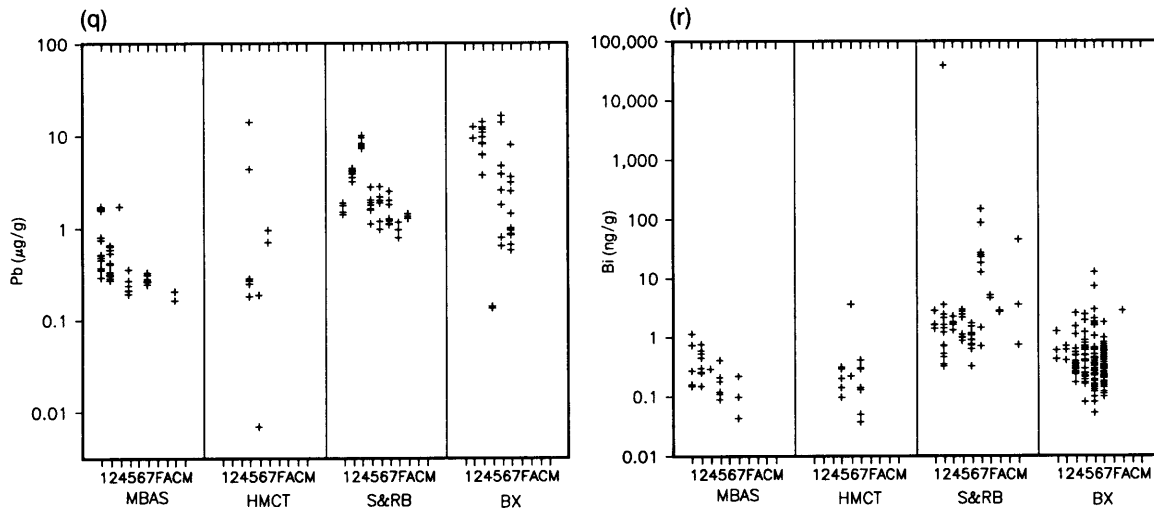


Fig. 8.25. (continued).

that the vapor-mobilized elements should have low concentrations as well.

The different degrees of depletion in vapor-mobilized elements between the Earth and Moon provide clues to their different origins (see *Ganapathy et al.*, 1974). The Moon accreted a lower proportion of material rich in vapor-mobilized elements than did the Earth. *Baedecker et al.* (1971) suggested that, as the Earth and Moon were accreting, there was a late addition of relatively volatile material to the Earth that the Moon did not capture as efficiently (e.g., *Anders*, 1968; see also *Krähenbühl et al.*, 1973). *Morgan et al.* (1972a) noted that the ratios of certain key elements to each other in lunar materials are essentially constant (e.g., $Tl/Cs \sim 1.2 \times 10^{-2}$, $Cs/U \sim 0.23$) and are unlike the ratios in either meteorites or terrestrial basalts. Even more than most elements, the vapor-mobilized elements (such as Tl) reveal that the combination of accretion plus chemical differentiation processes that went on in the Moon were different from those in the Earth. Apparently the Moon had a higher effective "accretion temperature" than the Earth, as indicated by the fact that the Moon has a lower ratio of the more volatile element Tl to the less volatile Cs.

8.7.2. Meteoroid Additions to the Regolith

The vapor-mobilized elements, like the siderophile elements, are more concentrated in lunar soils than in primary igneous rocks (section 8.6). As with the siderophile elements, the addition of vapor-mobilized elements from meteoroids is the main reason for their higher concentrations in the soils. However, unlike the siderophile elements, substantial

amounts of vapor-mobilized elements of indigenous lunar origin are also present in some lunar materials (e.g., *Baedecker et al.*, 1972; *Morgan et al.*, 1972a); these indigenous contributions will be discussed in section 8.7.3. Analyses of the vapor-mobilized elements in lunar rocks and soils provide the raw data for two important areas of investigation. First, any excess of these elements makes it possible to roughly estimate the amount of meteoroid material present in the sample (if corrections can be made for the indigenous component). Second, the pattern of relative abundances makes it possible to identify the chemical variety of meteoroid responsible for the excess.

Nature of the meteoroid component. In most lunar soils of relatively recent age, the meteoroid component most closely matches the CI-type carbonaceous chondrite, a variety of meteorite also believed to represent the original composition of the solid matter of the solar system. Comparisons between lunar materials and CI chondrites are shown in Fig. 8.26, which presents, for 10 vapor-mobilized elements, the ratio between the concentration of the element in lunar materials and the concentration in CI chondrites. The data represent 79 samples of mare basalts (MBAS) and 140 samples of soils, normalized to the standard concentrations in CI carbonaceous meteorites (*Mason*, 1971). Also shown are concentrations of Au, Ir, and Sb (representative siderophile elements), U (a representative refractory element), and the less-refractory trace elements Rb and Cs.

If all the elements shown in Fig. 8.26 were present in the soils in the same concentrations as in CI chondrites, the tops of all the bars would fall along

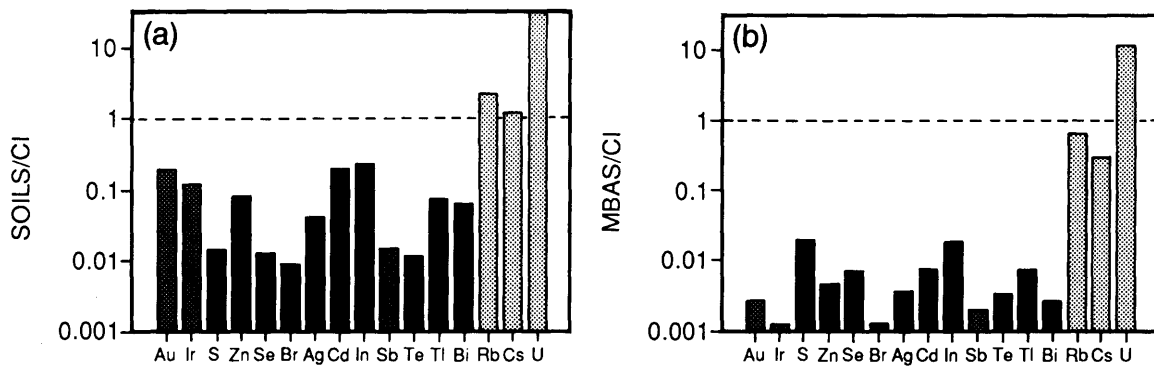


Fig. 8.26. Histograms showing ratios of vapor-mobilized elements in lunar materials, relative to those in standard CI-type carbonaceous chondrites. Data for three siderophile elements (Au, Ir, and Sb) and three incompatible trace elements (Rb, Cs, and U) are included for comparison. **(a)** Data for lunar soils; **(b)** data for mare basalt lavas (MBAS). The soils show consistently higher amounts of vapor-mobilized elements than do the mare basalts, indicating that the bulk of vapor-mobilized elements in the soils has been introduced by impacting meteorites rather than derived from the lunar interior. The relative abundances of vapor-mobilized elements in both soils and basalts do not match those in CI chondrites; in general, they are depleted by factors of 10–100. However, the lunar abundances are closer to CI chondrites than to any other meteorite type. Concentrations of the incompatible trace elements (Rb, Cs, and U) in lunar materials are either close to or greater than the CI values. Refractory U shows the strongest enrichments in lunar materials, followed by the heavy alkali elements Rb and Cs. In general, both the incompatible trace elements and the vapor-mobilized elements are enriched in lunar crustal rocks relative to the whole Moon as a result of the igneous differentiation processes that formed the lunar crust.

the horizontal line at unity. If they were present in the same concentrations relative to each other as in CI chondrites, the tops of all the bars would also fall along a horizontal line, but not necessarily at unity.

For soils, concentrations of Au, Ir, and most of the vapor-mobilized elements range between about 10^{-2} and 10^{-1} times those in CI meteorites. In the mare basalts, they range in concentration between about 10^{-3} and 10^{-2} times the concentrations in CI meteorites. The relative abundances in the soils are clearly not the same as in CI chondrites, because the ratios vary over more than an order of magnitude. However, the relative abundances of vapor-mobilized elements in lunar soils are much more similar to those of CI chondrites than they are to those of ordinary chondrite meteorites or the even more fractionated types of meteorites (e.g., *Laul et al.*, 1971).

In Fig. 8.26a, the elemental concentrations in the soils have not been corrected for contributions from the endogenous monomict lunar rocks. In contrast to the siderophile elements, most of whose abundances in monomict rocks can be neglected, corrections are required for vapor-mobilized elements of indigenous origin in order to make quantitative comparisons with CI chondrites (e.g., *Gros et al.*, 1976). However, such corrections do not change the

main conclusion, which is that the relative elemental abundances in the added meteoroid material are roughly similar to those found in the carbonaceous meteorites.

Variations in the meteoroid component with time. Several researchers have tried to use siderophile or vapor-mobilized elements to unravel the gross variations in meteoroid compositions that impacted the Moon over time. Some of the inferences based on siderophile elements made early on relied heavily on the Apollo 16 highland samples, which now appear to be anomalous in comparison to data from the Antarctic lunar meteorites (see *Wasson et al.*, 1975b; *Warren et al.*, 1989). Although the hypotheses of meteoroid variation with time have been difficult to prove, the concept is important for understanding the evolution of the inner solar system. A three-stage model of meteoroid variation is summarized below.

Anders et al. (1973) suggested three classes of meteoroid additions to the lunar regolith: (1) large planetesimals that produced the major impact basins; (2) smaller objects that formed younger and smaller craters; and (3) a recent flux of even smaller bodies and micrometeoroids that have played a major role in the formation and continuing evolution of the lunar regolith. The earliest additives were the

planetesimals, generally tens of kilometers in diameter, that excavated the major lunar basins such as Imbrium and Nectaris more than 3.9 b.y. ago (see section 4.4). A solid highland crust was already established when these major basins formed. The impact that produced each basin excavated enormous amounts of crust, and these combined basin-forming events largely shaped the present lunar highlands. During these impacts, materials from the projectiles were mixed with much larger volumes of the shattered and melted lunar target rocks to form deposits of melt and breccias. Evidence for this ancient projectile material is seen in the relatively high siderophile-element contents of some highland materials. Distinctive siderophile-element ratios are found within the interiors of ancient breccia fragments in the highland regolith, and especially within melt rocks.

This ancient meteoroid material apparently has no component of vapor-mobilized elements associated with it. One explanation for this observation is that these elements were not a significant part of the original projectiles. This idea is supported by data suggesting that the ancient meteoroid component at the Apollo 16 site has siderophile-element ratios similar to those of some iron meteorites (Korotev, 1987a,b). Another possibility is that the vapor-mobilized elements were so effectively decoupled from the siderophile elements during basin formation (e.g., by vaporization during the impact) that no connection is preserved. In any event, the concentrations of vapor-mobilized elements in highland clast-poor impact-melt rocks are very low, even in samples that show enrichments in the siderophile elements. (The values for Au and Ir shown in Fig. 8.26a are significantly enhanced by the contribution of this ancient component, which is the principal contributor of those elements to most highland soils.)

A second and younger meteoroid addition to lunar soils may come from projectiles up to a few kilometers in diameter that produced the plethora of large visible craters, many of which have rays that extend over large distances. These meteoroids have been accumulated over a long period of time, from about 3.9 b.y. to <1 b.y. ago. However, the extent of this contribution to total meteoroid input is difficult to specify. Anders *et al.* (1973) estimate it at 5–20% of the meteoroid total, but they were able to say little about its chemical character.

The third and youngest meteoroid component consists of numerous objects ranging from small meter-scale meteoroids to micrometeoroids less than 1 mm in diameter (see section 3.10). This component could be responsible for the relatively high concentrations of vapor-mobilized elements in

the soils and regolith breccias (Anders *et al.*, 1973). This conclusion arises from three lines of evidence: (1) the ubiquity of vapor-mobilized elements in about the same proportions in all lunar soils; (2) the closest similarity of volatile-element abundance patterns of lunar soils to those in carbonaceous meteorites; and (3) indications that carbonaceous meteorites are the most abundant type of material that has impacted both the Earth and Moon, now and perhaps over the past 3 b.y. or more. The bulk of the vapor-mobilized elements in lunar soils appears to be associated with grain surfaces, rather than with grain interiors, as would be expected if the impacting objects vaporized on impact and then condensed onto the granular materials that the impact had disturbed.

Amount of added meteoroid component. The quantity of meteoroid material added to lunar soils and regolith breccias can be estimated by ignoring the ancient component present in older highland rocks and assuming that the added meteoroid material was like CI chondrites (e.g., Keays *et al.*, 1970). The concentration of each siderophile or vapor-mobilized element in the soil, after correction for contributions from the indigenous lunar rocks, is divided by the concentration of that element in the CI chondrites. The results from mature soils are similar for most siderophile and vapor-mobilized elements and correspond to about 1.5–2 wt.% CI equivalent.

Furthermore, if the vapor-mobilized elements come mainly from micrometeoroids impacting the upper regolith (i.e., from meteoroids too small to excavate deep into the regolith), then the concentrations of vapor-mobilized elements should correlate with other measures of regolith surface exposure (see sections 7.3 and 8.8.2). Ganapathy *et al.* (1974) found a good correlation between the concentrations of Bi and Te in Apollo 16 soils and the measured cosmic ray exposure ages for the same soils. The correlation between Bi and exposure age is shown in Fig. 8.27. From the slope of the line, Ganapathy *et al.* derived an influx rate for CI meteorites of about 2.4×10^{-9} wt.% CI-equivalent/year for surface-exposed soils, a figure that is within the broad range of estimates based on terrestrial meteorite observations.

Comparisons between uranium and volatile elements. In contrast to the generally low concentrations of vapor-mobilized elements in lunar soils, the concentrations of U in most soils are tens of times higher than in CI meteorites. This difference is due to two factors. First, the average whole-Moon concentrations of U and other refractory incompatible trace elements are at least as high as in carbonaceous chondrites. Second, crustal con-

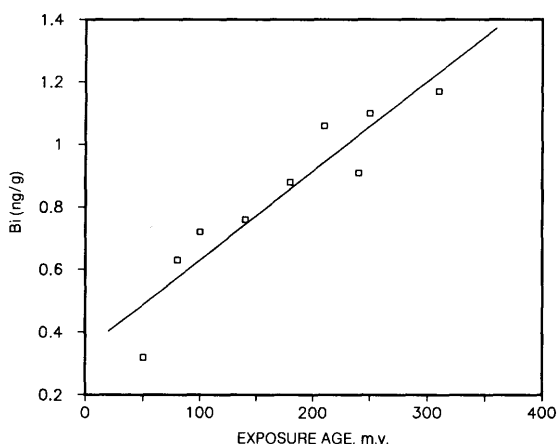


Fig. 8.27. Plot of bismuth (Bi) concentrations in Apollo 16 soils, as a function of exposure ages for the soils determined from cosmogenic ^{21}Ne content (after Ganapathy *et al.*, 1974). Horizontal axis shows estimated exposure age in millions of years; vertical axis shows Bi concentration in ng/g. The Bi concentrations show a good positive correlation with exposure age, indicating that Bi (and other vapor-mobilized elements) in lunar soils have been derived chiefly from infalling meteoroids.

concentrations of these elements are enhanced over the bulk-Moon values as a result of the preferential concentration of incompatible trace elements in the melt during the melting and separation processes occurring in the lunar mantle, followed by the transport of these elements into the crust by rising magma bodies. In contrast to U, the concentrations of the volatile incompatible trace elements Rb and Cs in lunar soils are about the same as in CI-carbonaceous meteorites (see Fig. 8.26a). This result indicates that the bulk Moon has concentrations of alkali elements that are *lower* than those in CI-carbonaceous meteorites because the large-ion alkali metals (Na, K, Rb, and Cs), like U, are incompatible trace elements and have likewise been concentrated into the lunar crust. Since U is substantially more concentrated (relative to CI chondrites) in lunar soils than are Rb and Cs (and Na and K), then the alkali elements must be depleted in the whole Moon, relative to CI chondrites. This depletion is believed to be a consequence of their relative volatility, which may have led to their loss during a period of high temperature prior to or during formation of the Moon.

Solar-wind contributions. In addition to impacting solid bodies, the other extralunar sources of vapor-mobilized elements are the solar wind and the more energetic solar cosmic rays associated with

solar flares (see discussion of the solar wind and solar cosmic rays, section 3.11). Ganapathy *et al.* (1970) were able to demonstrate that the solar wind is not a major contributor of vapor-mobilized elements to the regolith because of the relatively low solar-wind and solar-cosmic-ray abundances of these heavy atoms (Table 3.5). They estimated that the solar wind contributes only 0.16 ng/g of the Ir in lunar soil, compared with about 7 ng/g of Ir measured in the Apollo 11 regolith. The solar wind contribution thus amounts to about 2% of the Ir present in soils. Similar calculations for vapor-mobilized elements indicate that the solar wind contribution probably does not exceed 5%, even for relatively light and volatile elements such as Se.

8.7.3. Vapor-Mobilized Elements as Incompatible Trace Elements: Indigenous Concentrations in Lunar Materials

Most of the vapor-mobilized elements except the halogens (F, Cl, Br, and I) are *chalcophile* in behavior (i.e., they tend to concentrate in sulfide minerals). Sulfide minerals make up only a tiny fraction of lunar rocks and occur mainly as late-stage crystallization products. There is no evidence to suggest that sulfide minerals could have retained the more chalcophile of the vapor-mobilized elements deep within the lunar mantle. This view is supported by the observation that the ratio of S to other chalcophile elements is higher in lunar basalts than in terrestrial basalts, making it unlikely that there was extensive sulfide removal from the lunar mantle before the mare basalts were formed.

Without dense sulfide minerals retained deep in the Moon, ions of the vapor-mobilized elements would presumably partition into the rising liquid during the melting and crystallization processes that separated the lunar crust from the mantle (see section 2.4). Under these conditions, the vapor-mobilized elements should behave as incompatible lithophile trace elements. Because of their behavior as incompatible trace elements (section 8.4), it is likely that the vapor-mobilized elements would also have their highest concentrations in those materials that have the highest concentrations of Rb, Cs, U, and other incompatible trace elements.

The most common lunar material concentrating incompatible trace elements is KREEP, a component rich in K, the rare earth elements (REE), and P (section 8.4.2). As expected, KREEP-rich materials do have higher concentrations of vapor-mobilized elements than other lunar rocks. Among lunar soil samples, those from Apollo 14 soils have the highest concentrations of incompatible trace elements (Fig. 8.7). These soils also have the highest concen-

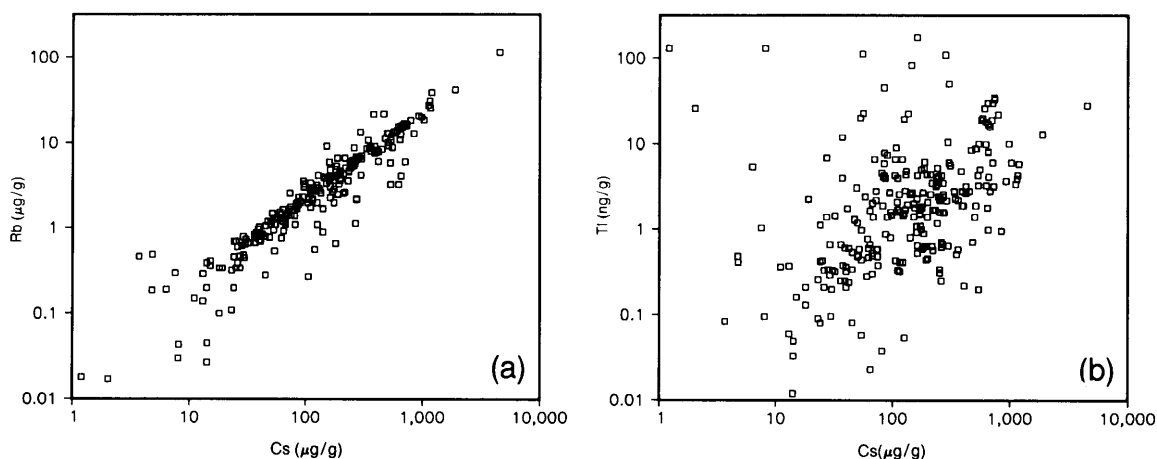


Fig. 8.28. Correlation plots for rubidium (Rb) (an incompatible trace element) and thallium (Tl) (a vapor-mobilized element) against cesium (Cs) (an incompatible trace element) in polymict highland breccias: **(a)** Rb vs. Cs; **(b)** Tl vs. Cs. Horizontal and vertical axes, both logarithmic, show elemental concentrations (Tl in ng/g; Rb and Cs in µg/g). The use of a logarithmic scale enhances the scatter present at low concentrations and compresses it at high concentrations, where greater deviations should be expected because of the extreme chemical separation processes required to produce such differences. Despite this effect, Rb and Cs **(a)** still show a very strong correlation because they are both incompatible trace elements and they behave coherently in chemical processes. In contrast, the Tl-Cs data **(b)** show a slight tendency for higher Tl concentrations to be accompanied by higher Cs concentrations, but there is considerable scatter. Thallium, like Rb and Cs, behaves as an incompatible trace element in magmatic processes, but the lack of correlation with Cs probably reflects the fact that, unlike Rb, Cs, and U, only a small proportion of lunar Tl comes from the lunar interior; most Tl has been introduced by incoming meteoroids.

tration of Tl (Fig. 8.25p). However, Apollo 15 and 17 soils have the highest concentrations of Zn (Fig. 8.25f), Se (Fig. 8.25h), Br (Fig. 8.25i), and In (Fig. 8.25l) because of pyroclastic contributions (see section 8.7.5). The highest concentrations of Te (Fig. 8.25m) are found in Apollo 12 soils. An anomalous Apollo 12 soil sample (12028,55; *Laul et al.*, 1971) has exceptionally high concentrations of Bi, Cd, and Ag, but does not have high concentrations of incompatible trace elements.

There is a strong correlation between concentrations of the relatively volatile alkali elements Cs and Rb in highland breccias (Fig. 8.28a). The correlation is probably better than shown, because at least some deviations from the correlation line probably reflect analytical error. The correlation results from the fact that the principal sources of Rb and Cs are indigenous to the Moon, and, because these two elements are so similar, no major separation between them was produced by the chemical differentiation processes that formed the lunar crust. There are also correlations between Tl and Cs (and Rb) in the same breccias, but many samples show substantial deviations from these trends (Fig. 8.28b). The scatter may arise because there is more than one source of Tl (a meteoroid source as well as an indigenous

lunar one), and some separation process (impact vaporization?) may have operated to cause additional decoupling of concentrations of Tl from those of the large-ion alkali elements.

Gros et al. (1976) investigated the behavior of vapor-mobilized elements as incompatible trace elements by examining the correlations between vapor-mobilized elements and Rb and Cs in samples with very low concentrations of siderophile elements. The low siderophile-element content indicates that this group of samples is monomict, with little or no added meteoroid component, and therefore free of any vapor-mobilized elements from nonlunar sources. Figure 8.29a shows the relationship between concentrations of Zn and a large-ion alkali element, Cs, for 19 monomict samples, together with the regression line determined by *Gros et al.* The strong correlation in Fig. 8.29a affirms the behavior of indigenous lunar Zn as an incompatible trace element. Similar correlations hold for other vapor-mobilized elements, although there is substantial scatter for some of them.

From such correlations between the vapor-mobilized elements and Rb and Cs, *Gros et al.* (1976) developed logarithmic equations relating the indigenous concentrations of vapor-mobilized elements

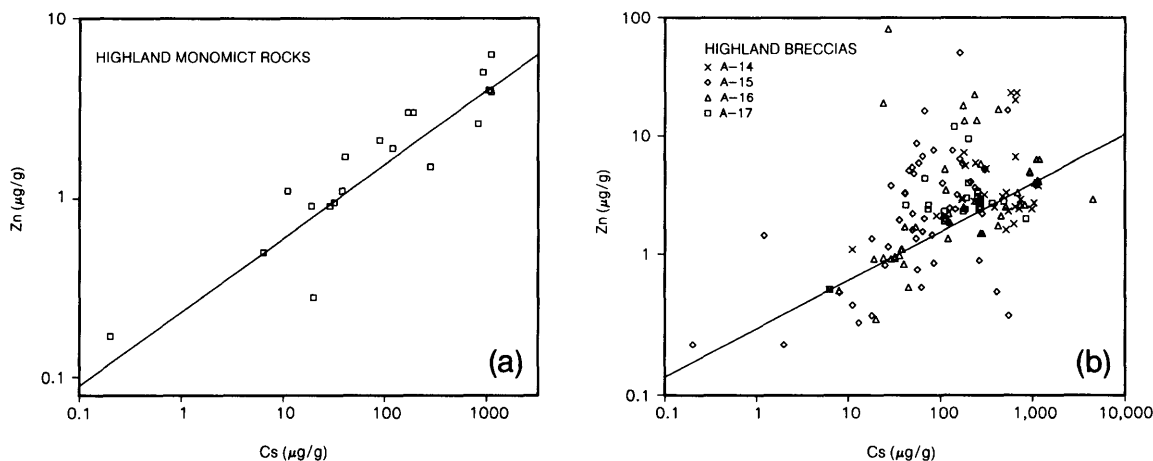


Fig. 8.29. Correlation plots for zinc (Zn) (a vapor-mobilized element) and cesium (Cs) (an alkali incompatible trace element) for highland monomict rocks and polymict breccias. **(a)** Zn vs. Cs in highland monomict rocks, which do not show significant contamination from meteoroids (after Gros *et al.*, 1976); **(b)** Zn vs. Cs in highland polymict breccias, which contain an added meteoroid component. The diagonal line in **(b)** is the same as the correlation line in **(a)**. Horizontal and vertical axes, both logarithmic, show elemental concentrations (in $\mu\text{g/g}$). In the monomict rocks **(a)**, Zn and Cs are strongly correlated, implying an internal lunar source for both elements. In contrast, in the highland breccias **(b)**, no correlation is evident, either among the whole group of breccias or among breccias from a single mission, implying that most of the Zn in these rocks has been added from meteoroids and not derived from internal lunar processes.

to the concentrations of Rb and Cs. The parameters for these equations are shown in Table 8.6. Although these equations were developed from data obtained only from monomict highland samples, they can be used to predict concentrations of vapor-mobilized elements in mare basalts (which have about $1 \mu\text{g/g}$ Rb) that are roughly similar (within a factor of ± 2) to those actually observed. Gros *et al.* (1976) argue that this consistency implies a single lunar source of vapor-mobilized elements for endogenous (monomict) rocks of both the maria and the highlands.

In principle, the equations in Table 8.6 can be used to estimate the original whole-Moon concentrations of the vapor-mobilized elements. These estimates are subject to two assumptions: (1) that the vapor-mobilized elements, as well as Rb and Cs, are well-behaved incompatible trace elements, and (2) that the whole-Moon concentration of Rb or Cs is known. Unfortunately, these values are not well known, but the Rb value is probably between 0.1 and $1 \mu\text{g/g}$. For an estimated value of $0.28 \mu\text{g/g}$ (S. R. Taylor, 1982), the concentrations of the vapor-mobilized elements equal the antilogarithms of the intercept constants in Table 8.6. These calculations produce concentrations between 0.1 and 1 ng/g for Sb, Ag, Cd, Bi, and Tl; between 1 and 10 ng/g for Se and Te; between 10 and 100 ng/g for Br; and about 750 ng/g for Zn. These concentrations are equivalent to a content of

CI carbonaceous meteorites between 0.03% and 0.2% for the whole Moon. These values also suggest that the vapor-mobilized elements could have been incorporated into the primitive Moon in relative concentrations that are the same (within an order of magnitude) as those in the primitive CI chondrites.

It is probably unwise to push these estimates too far. Estimated values for whole-Moon concentrations of vapor-mobilized elements are not well grounded. They depend on the correlations observed between vapor-mobilized elements and refractory lithophile elements in one set of highland samples. This correlation surely reflects, and is valid for, the magmatic processes that produced the particular materials of the lunar crust. However, additional processes such as those leading to gas-rich pyroclastic eruptions (section 6.1.7) may also have removed substantial amounts of vapor-mobilized elements from the lunar interior. The estimates for the whole Moon based on correlations with incompatible trace elements in highland rocks are thus only lower limits.

8.7.4. Vapor-Phase Transport of Vapor-Mobilized Elements

Analyses of numerous lunar samples have established that additions of extralunar meteoroid debris have provided most of the vapor-mobilized elements

TABLE 8.6. Regression coefficients for concentrations of vapor-mobilized elements against concentrations of Rb and Cs.

Element	Regression against Rb (in $\mu\text{g/g}$)			Regression against Cs (in $\mu\text{g/g}$)		
	a (slope)	b (const.)	r	a (slope)	b (const.)	r
Zn ($\mu\text{g/g}$)	0.42 ± 0.04	0.11	0.94	0.41 ± 0.04	-0.63	0.916
Se ($\mu\text{g/g}$)	0.67 ± 0.16	-1.77	0.71	0.64 ± 0.18	-0.99	0.646
Br ($\mu\text{g/g}$)	0.56 ± 0.08	-1.58	0.85	0.67 ± 0.09	-0.80	0.858
Ag (ng/g)	0.26 ± 0.06	-0.17	0.69	0.26 ± 0.06	0.15	0.691
Cd (ng/g)	0.57 ± 0.08	0.32	0.90	0.69 ± 0.11	1.09	0.863
Te (ng/g)	0.16 ± 0.10	0.20	0.40	0.18 ± 0.10	0.42	0.423
Tl (ng/g)	0.80 ± 0.13	-0.47	0.83	0.99 ± 0.16	0.65	0.83
Bi (ng/g)	0.17 ± 0.08	-0.81	0.52	0.20 ± 0.09	-0.58	0.506
Rb ($\mu\text{g/g}$)	—	—	—	0.94 ± 0.07	1.17	0.95
Cs ($\mu\text{g/g}$)	0.96 ± 0.07	-1.25	0.95	—	—	—
U ($\mu\text{g/g}$)	1.13 ± 0.05	-0.80	0.99	1.07 ± 0.08	0.56	0.959

Data are from Table 2 of *Gros et al.* (1976).

Regression lines developed from the equation $\log y = a \log x + b$, where y = concentration of element, x = concentration of Rb (or Cs), r = residual to least-squares fit, a = slope of regression line, b = intercept of regression line.

now found in lunar surface materials. Nevertheless, the observed patterns of concentrations of vapor-mobilized elements cannot be explained, even to a first approximation, by the simple mixing of indigenous lunar material (whose concentrations of vapor-mobilized elements are well correlated with those of incompatible trace elements) with meteoroid material similar to CI-carbonaceous chondrites. To explain the relations described in detail below, there must also have been substantial chemical separations, additional sources of vapor-mobilized elements, or both, to account for the complex patterns of concentrations observed.

A typical instance of these complications involves the elements Zn and Cs. Figure 8.29b shows a plot of Zn vs. Cs concentrations for samples of highland breccias. The line on the graph corresponds to the correlation between Cs and Zn determined for the low-siderophile monomict samples discussed above, in which virtually all the vapor-mobilized samples have an indigenous lunar source. As a group, these highland breccias show no correlation between Zn and Cs. Most values fall on the high-Zn side of the correlation line, which would be expected if there were inclusions of micrometeoroid material (containing Zn but not Cs) in the breccias. Some values fall below this line, however, suggesting the loss of Zn by some process from some breccia fragments. Many of the most striking excesses and deficiencies in Zn concentrations are found in samples from the same mission, Apollo 16. Some strong Zn excesses are also present in samples from the Apollo 14, 15, and 17 sites.

If the vapor-mobilized elements found in highland breccias and soils come mainly from two sources, the average meteoroid and the average lunar crust, and if no additional separation processes have affected them, their concentrations should be mutually correlated. Figures 8.30 and 8.31 show concentration plots for different pairs of vapor-mobilized elements. Correlations with Zn are shown in Fig. 8.30 for Apollo 16 soils and breccias (Figs. 8.30a,b), and for highland and mare materials from all missions (Figs. 8.30c,d). There is a rough correlation between Zn and Ag in the Apollo 16 soils and breccias (Fig. 8.30a). The soils have the highest concentrations, probably reflecting micrometeoroid additions to the exposed regolith after most of the breccias formed, or possibly because the breccias were formed from materials at such depths that they did not receive appreciable meteoroid additions. There is a similar crude correlation between Zn and Ag for both mare and highland material from all sampling sites (Fig. 8.30c). Concentrations of both elements in mare materials are relatively low; the bulk of these elements in the soils must therefore come from meteoroid additions and admixed KREEP. The amount of indigenous lunar vapor-mobilized elements in these samples can be estimated from the correlations with Rb and Cs (Table 8.6). The maximum possible lunar contribution can be calculated by using the Rb concentration in the highly enriched quartz monzodiorite (sample 15405, with Rb = 40 $\mu\text{g/g}$). With this value of Rb, the highest possible indigenous contributions of Zn and Ag in highland materials are about 6 $\mu\text{g/g}$ and 2 ng/g,

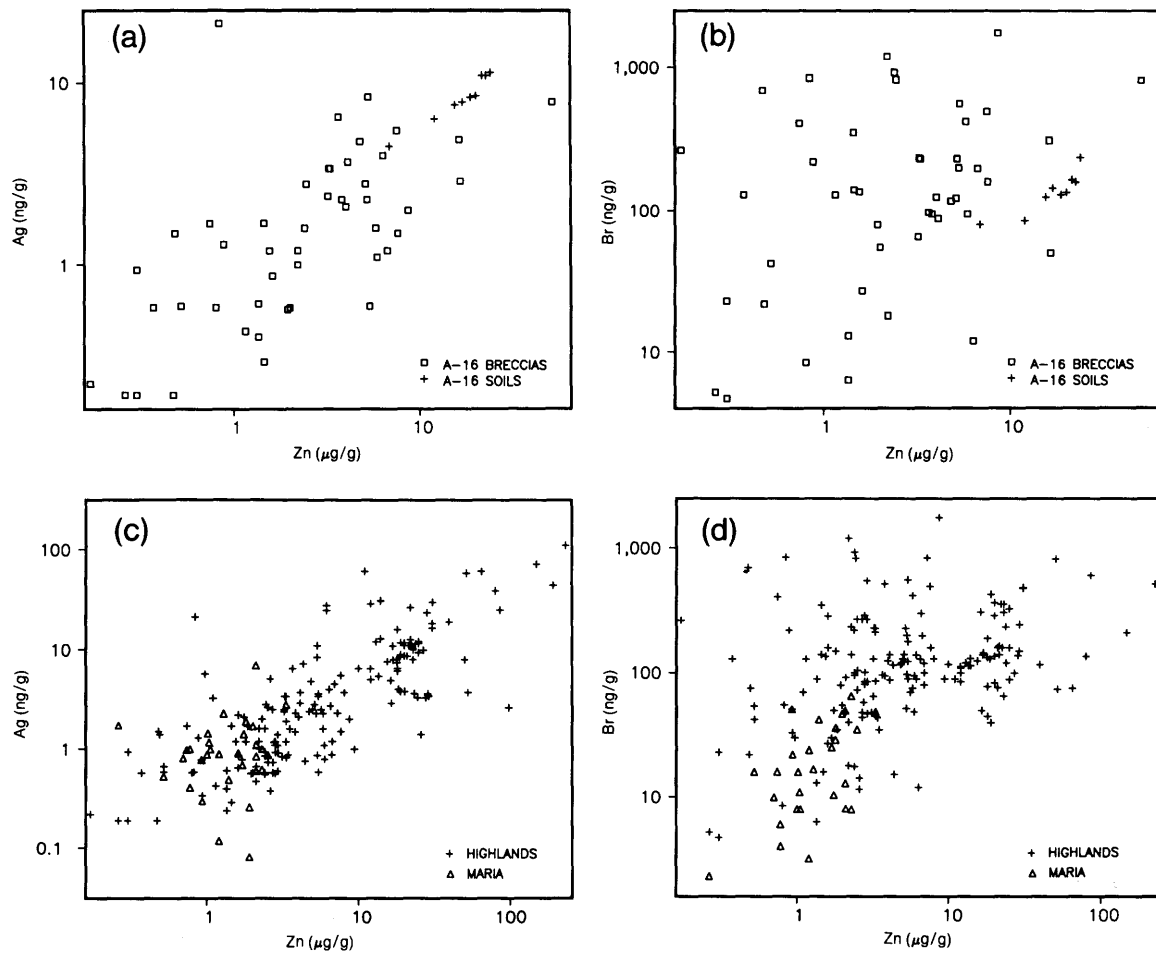


Fig. 8.30. Correlation plots for three vapor-mobilized elements (Ag, Br, and Zn) against each other for a range of lunar materials. **(a)** Ag vs. Zn in Apollo 16 highland breccias and soils, which contain an added meteoroid component; **(b)** Br vs. Zn in Apollo 16 highland breccias and soils; **(c)** Ag vs. Zn in all types of samples; **(d)** Br vs. Zn in all types of samples. Horizontal and vertical axes, both logarithmic, show elemental concentrations (Ag and Br in ng/g; Zn in $\mu\text{g/g}$). The Apollo 16 highland materials show a rough correlation between Ag and Zn **(a)** and no correlation between Br and Zn **(b)**. The more complete suite of lunar materials shows a similar rough correlation between Ag and Zn **(c)** and little or no correlation between Br and Zn **(d)**.

respectively. These values are far below the highest observed concentrations, which exceed 100 $\mu\text{g/g}$ and 100 ng/g. These Zn and Ag concentrations appear too high to be produced by a combination of meteoroid and lunar sources. Values of 100 $\mu\text{g/g}$ for Zn and 100 ng/g for Ag would require >25% CI meteorite equivalent to be present in the samples with the highest concentrations, an excessive amount that would be unlikely in so many samples.

Data for other vapor-mobilized elements also indicate that the simple introduction of even 25% CI-type meteoroid material cannot be the cause of the

high Zn and Ag concentrations in the highland breccias and soils. Clear evidence for the absence of a large meteoroid component is the lack of any corresponding correlation between Zn and Br in Apollo 16 materials (Fig. 8.30b). There is at best only a rough correlation between concentrations of Zn and Br in rocks and soils from all sites (Fig. 8.30d). Furthermore, the highest Br concentrations (about 1000 ng/g) correspond to the addition of only about 5% CI-type meteoroid. There is no correlation between Se and Br (Figs. 8.31a,c); the highest Se concentrations correspond to <5% CI equivalent

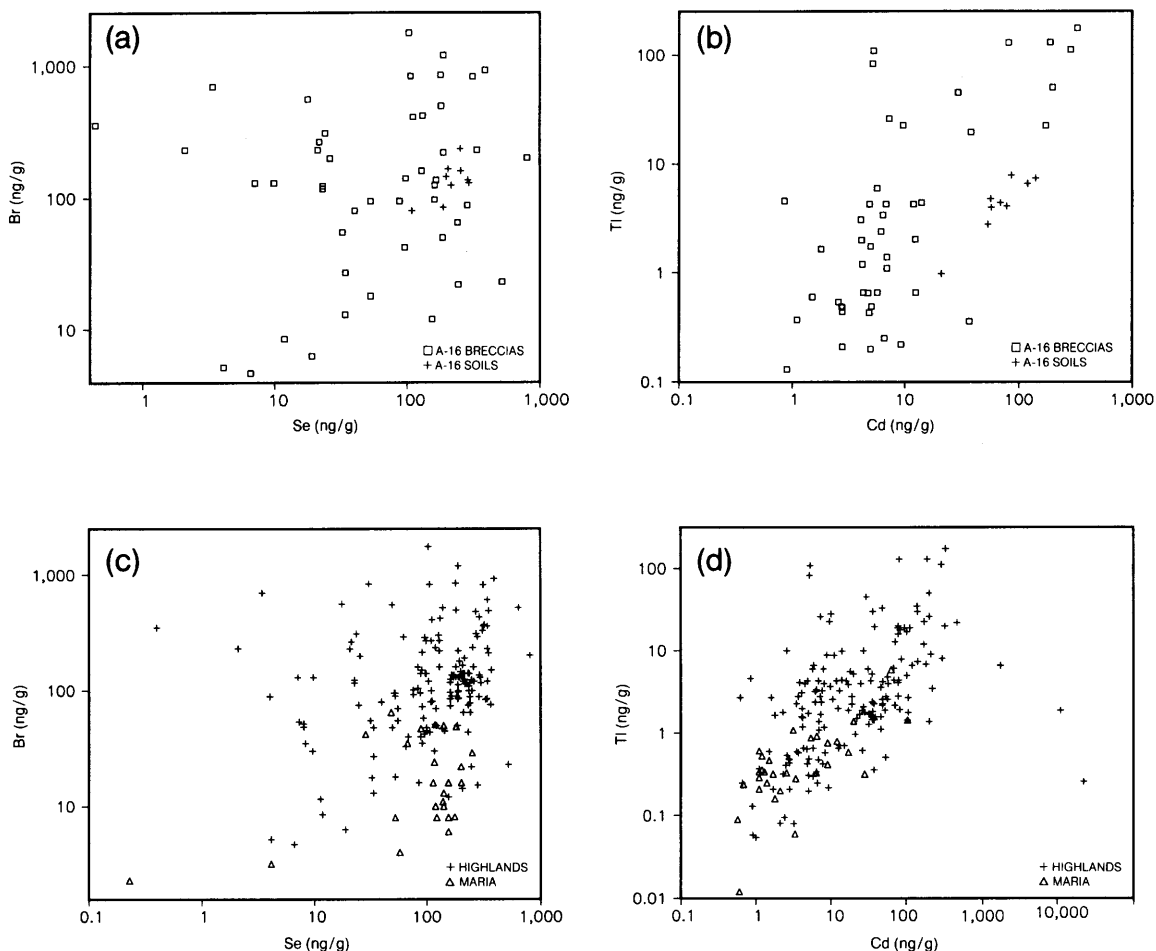


Fig. 8.31. Correlation plots for four vapor-mobilized elements (Br, Se, Tl, and Cd) against each other for a range of lunar sample materials. **(a)** Br vs. Se in Apollo 16 highland breccias and soils, which contain an added meteoritic component; **(b)** Tl vs. Cd in Apollo 16 highland soils and breccias; **(c)** Br vs. Se in all types of samples; **(d)** Tl vs. Cd in all types of samples. Horizontal and vertical axes, both logarithmic, show elemental concentrations (in ng/g). In the Apollo 16 highland samples, the Br-Se plot **(a)** shows no correlation, and the Tl-Cd plot **(b)** shows only a rough correlation. Similarly, in the plots for all sample types, the Tl-Cd data show only a rough correlation **(d)**, while the Br-Se data show no correlation **(c)**.

added. There is a rough correlation between Cd and Ti, both for Apollo 16 samples (Fig. 8.31b) and for rocks and soils from all sites (Fig. 8.31d), but there are also large deviations. Curiously, concentrations of both Tl and Br in some Apollo 16 breccias lie well above the concentrations found in the soils.

8.7.5. Pyroclastic Volcanic Emissions as an Indigenous Source of Vapor-Mobilized Elements

Discovery of the rust-colored (orange-glass) pyroclastic deposit near Shorty Crater at the Apollo 17 site (see section 10.6.6 and Fig. 10.28)

briefly raised the exciting possibility that oxidizing, hydrous gases might have vented there to produce, among other things, Fe rust. Such a discovery would have been the first firm evidence for the presence of highly volatile materials (especially water) in the lunar interior.

This possibility was quickly eliminated when samples of the pyroclastic deposit were analyzed back on Earth. The orange color is produced by a titaniferous, very dry glass of mare basalt composition, present in the form of small glass spheres (section 6.1.7).

The pyroclastic glass spheres are products of gas-driven volcanic eruptions, and they are coated with vapor-mobilized elements that were condensed from the volcanic gas. These deposits provide direct evidence that vapor-mobilized elements can separate from incompatible trace elements in the lunar interior, and concentrate to drive volcanic eruptions. Similar coatings of vapor-mobilized elements are also found on the green pyroclastic glass spheres from the Apollo 15 site (section 6.1.7).

It is of interest to compare the concentrations of vapor-mobilized elements in these samples with those in mare basalts (e.g., *Baedecker et al.*, 1974) because the concentrations of major elements and incompatible trace elements in these glass spheres are the same as expected for mare basalts with similarly high concentrations of MgO and FeO. Figure 8.32a plots the ratios of concentrations of a group of vapor-mobilized elements (together with Au, Ir, Sb, Rb, Cs, and U) in the orange glass (sample 74220) to the average concentrations in 79 mare basalts. Ratios for the siderophile elements (Au, Ir, and Sb) and for Rb, Cs, and U all fall near the line at unity, indicating that their concentrations are similar in both materials. However, the concentrations of the vapor-mobilized elements Zn, Br, Ag, Cd, and Tl are 1-2 orders of magnitude higher in the orange glass than in the mare basalt average. This contrast demonstrates that some vapor-mobilized elements separated from the other elements during the magmatic and volcanic events that produced the pyroclastic glasses. The processes responsible for these separations are not known. However, the high ratios of the more volatile vapor-mobilized elements (Zn, Br, Ag, Cd, and Tl) to Rb and Cs suggest that there was a general expulsion of excess amounts of the more volatile elements relative to those behaving simply as incompatible trace elements.

The relative concentrations of vapor-mobilized elements to each other in green pyroclastic glasses are similar to those of the orange glasses, although the patterns in the two glasses are distinguishable from each other. The similarities and differences between these two types of pyroclastic glasses are summarized in a comparative plot of the ratios of the element concentrations in the green-glass-rich sample 15426,35 (*Ganapathy et al.*, 1973) and the orange glass (Fig. 8.32b). Concentrations of the vapor-mobilized elements (but not Rb, Cs, U, and some siderophile elements) are 0.06 to 0.6 times lower in the sample containing the green glass than in the orange-glass sample. The compounds containing the vapor-mobilized elements apparently do not coat the surfaces of the spherules uniformly, and the data in Fig. 8.32b may reflect the fact that there are more gaps in the coatings on the green-glass spherules

than in the coatings of the orange-glass spherules (*Butler and Meyer*, 1976). In addition, the green-glass sample is in fact a recycled mixture of several loosely related pyroclastic glass types, unlike the much more extensive and homogeneous orange glass sample from the Apollo 17 site (see section 6.1.7).

Several studies have confirmed that the vapor-mobilized elements associated with the pyroclastic glasses are surface coatings and are only present in much smaller amounts within the glass spheres. For example, *Goldberg et al.* (1976) demonstrated that F, one of the more abundant vapor-mobilized elements, is concentrated to the level of $\sim 1.5 \times 10^{15}$ atoms/cm² at the surface of individual orange glass spherules but only to the level of $< 0.3 \times 10^{15}$ atoms/cm² at depths between 0.1 and 1.2 μm within the spheres. This surface concentration corresponds roughly to a monolayer of F atoms on the sphere surface. They also found approximately the same surface concentrations of F on spherules of green glass, but not as uniformly distributed over the surface. In studying mare basalt samples by the same technique, they found slightly high F concentrations on the surfaces of vesicles (bubbles) in mare basalt samples, relative to concentrations within the basalts. Concentrations of F on the vesicle walls of basalt samples were only one-fifth as high as on the surfaces of the glass spheres, but the bulk F concentrations in the basalts were higher than those inside the glass spheres. There is still some controversy about how labile the F in these samples is to leaching. *Jovanovic and Reed* (1974) reported that 40% of the F could be leached from the orange glass at pH 5, but *Goldberg et al.* (1976) found the same surface concentration both before and after leaching.

The orange-glass spheres at the Apollo 17 site are closely associated with black spheres, which are essentially the same material, only darkened by crystallization of the glass. *Butler and Meyer* (1976) and *Cirlin et al.* (1978) confirmed that high concentrations of S, Zn, Cd, and Pb are associated with both orange and black spheres from the Apollo 17, Station 4 core tubes, which sampled the pyroclastic deposit near Shorty Crater. From thermal release patterns, they concluded that the Zn was mainly on the surfaces of the spheres. *Wasson et al.* (1976) cited the observations of high concentrations of Zn and Pb in samples of orange- and green-glass spheres as evidence for an endogenous origin for the spherules. Of particular importance are the unusually high values of the isotopic ratios $^{204}\text{Pb}/^{206}\text{Pb}$ and $^{204}\text{Pb}/^{207}\text{Pb}$ measured by *Nunes et al.* (1974b,c), which indicate that the Pb (and, by association, the other vapor-mobilized elements) in the spheres come from an isolated source whose U and Th were mainly lost early in lunar history, thus preventing the

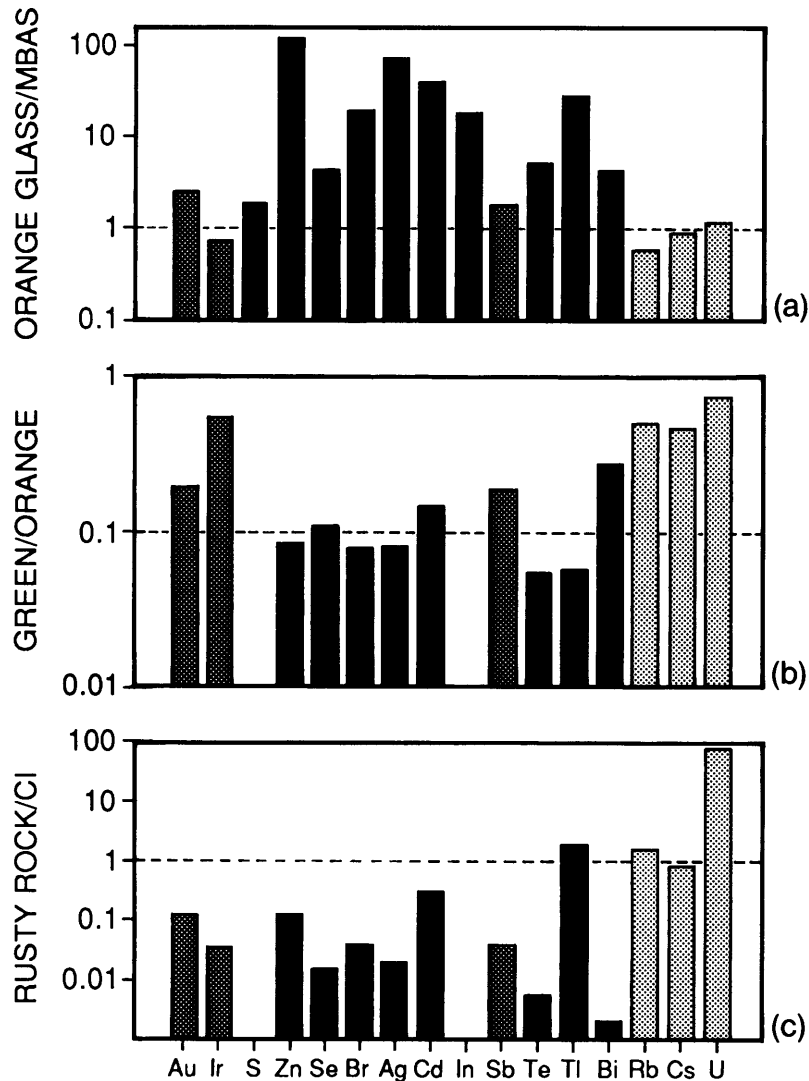


Fig. 8.32. Histograms showing ratios of vapor-mobilized elements in various lunar materials ("rusty rock" 66095, the Apollo 17 orange glass, the Apollo 15 green glass, and mare basalts), relative to each other and to standard CI-type carbonaceous chondrites. Data for three siderophile elements (Au, Ir, and Sb) and three incompatible trace elements (Rb, Cs, and U) are included for comparison. **(a)** Concentration ratios of Apollo 17 orange glass (ORANGE GLASS) relative to average mare basalts (MBAS) from all missions. The orange glass, despite its general chemical similarity to high-Ti mare basalts, is highly enriched in vapor-mobilized elements. **(b)** Concentration ratios of Apollo 15 green glass (GREEN) relative to Apollo 17 orange glass (ORANGE). There is a close match between concentrations of the vapor-mobilized elements in both glasses, although the patterns are distinctively different. **(c)** Concentration ratios for "rusty rock" 66095 (RUSTY ROCK) relative to CI meteorites. Concentrations of vapor-mobilized elements in "rusty rock" 66095 are depleted by factors of 10–100 relative to CI meteorites, but their relative abundances agree more closely with CI meteorites than with other meteorite types.

development of significant amounts of radiogenic ^{206}Pb and ^{207}Pb . In other words, the isotopic signature of the Pb from the glass spheres indicates that they did not form by impact melting of evolved lunar crust, which would have more radiogenic Pb.

8.7.6. Surface Mobility of Vapor-Mobilized Elements

Some large samples of Apollo 16 breccias, when first examined in the Lunar Receiving Laboratory back on Earth, were found to have spots of rust (e.g., "rusty rock" 66095). The rust had been produced by the action of water of probable terrestrial origin (from the spacecraft cabin atmosphere, the Lunar Receiving Laboratory, or both) with a reactive mineral, perhaps lawrencite (FeCl_2), present in the breccia (e.g., *L. A. Taylor et al.*, 1973a). This mineral had apparently condensed from a vapor phase onto the surfaces of the rock fragments incorporated into the breccias. The samples showing rust also contain abnormally high concentrations of vapor-mobilized elements. Figure 8.32c shows the ratio of concentrations of vapor-mobilized elements (plus Au, Ir, Sb, Rb, Cs, and U) in "rusty rock" 66095 to those in CI-chondrite meteorites; in general, the volatile elements in sample 66095 do not occur in chondritic relative abundances.

In addition to the volcanic gas emissions from deep in the Moon, there are lunar surface processes that can concentrate vapor-mobilized elements as a group and fractionate some of them away from the others. These processes can concentrate vapor-mobilized elements by several orders of magnitude relative to their concentrations in bulk lunar material. For example, surprisingly high concentrations of Ag (301 ng/g), Cd (22,000 ng/g), and Bi (38,500 ng/g) were reported for a sample of soil from an Apollo 12 drive tube (12028,66) by *Laul et al.* (1971), who believe that these values are not a consequence of inadvertent contamination of the soil with terrestrial material.

The mechanisms that produce such unusual enrichments of vapor-mobilized elements in near-surface lunar materials have not been definitely identified. However, processes based on thermal vaporization are one reasonable possibility. Most of the vapor-mobilized elements in lunar soils are found to be surface-correlated in the soils that contain them; i.e., their abundances are greatest in the smallest grain-size fractions, which have the most surface area per unit volume. This relationship suggests vapor transport and condensation.

The normal daytime surface temperature of the Moon ($>100^\circ\text{C}$) is high enough to cause some materials we normally regard as stable to volatilize but, even in direct sunlight, the daytime tempera-

tures are too low to distill FeCl_2 efficiently (mp $\sim 670^\circ\text{C}$). Meteoroid impacts of substantial size, however, can vaporize even silicate minerals, generate pools of silicate melt, and trap large bodies of hot impact debris beneath insulating blankets of ejecta, thus insuring slow heat loss and the preservation of high temperatures for long periods of time.

The short- and long-term heat effects associated with meteoroid impacts can be expected to distill vapor-mobilized elements, perhaps in a manner analogous to the hydrothermal circulation within the Earth's crust that concentrates trace elements into ores. However, in the lunar environment, any such system would have to operate without water. On the Moon, C-O-S compounds of various forms might serve as circulating fluids. Under such conditions, fractional distillation, sublimation, or extraction processes could separate individual vapor-mobilized elements from each other. Such processes may account for the irregular patterns of relative abundances among the vapor-mobilized elements that are observed from sample to sample.

Isotopic evidence from Pb supports the idea that the vapor-mobilized elements can be selectively moved by heating. Most of the Pb in lunar samples is produced by radioactive decay of U and Th, and it consists chiefly of the isotopes ^{206}Pb (from ^{238}U), ^{207}Pb (from ^{235}U), and ^{208}Pb (from ^{232}Th). Most lunar rocks are very old in comparison to geologic time, and their Pb concentrations have been enhanced substantially over time at the expense of their original U and Th concentrations. The concentration of original (nonradiogenic) Pb in a lunar sample can be estimated from the concentration of ^{204}Pb present, because that isotope is not produced by any radioactive decay process. To a first approximation, a lunar rock or soil (if soils are assumed, for simplicity, to be mechanical mixtures of rocks) should have concentrations of radiogenic Pb isotopes (^{206}Pb , ^{207}Pb , and ^{208}Pb) that correlate with the concentrations of U and Th present. Deviations from those correlations between Pb isotopes, U, and Th would indicate that some chemical separation or addition process had occurred.

The U-Th-Pb relations based on radioactive decay are the basis of a fundamental method for measuring the ages of terrestrial rocks and of meteorites, and the same techniques were applied to returned lunar samples. Precise determinations of U, Th, and Pb isotopes were made to measure the ages of individual rocks and to determine the timescales for lunar processes. The results indicate that the concentrations of Pb often deviate from what would be expected based on concentrations of U and Th, indicating that Pb separation or addition has occurred.

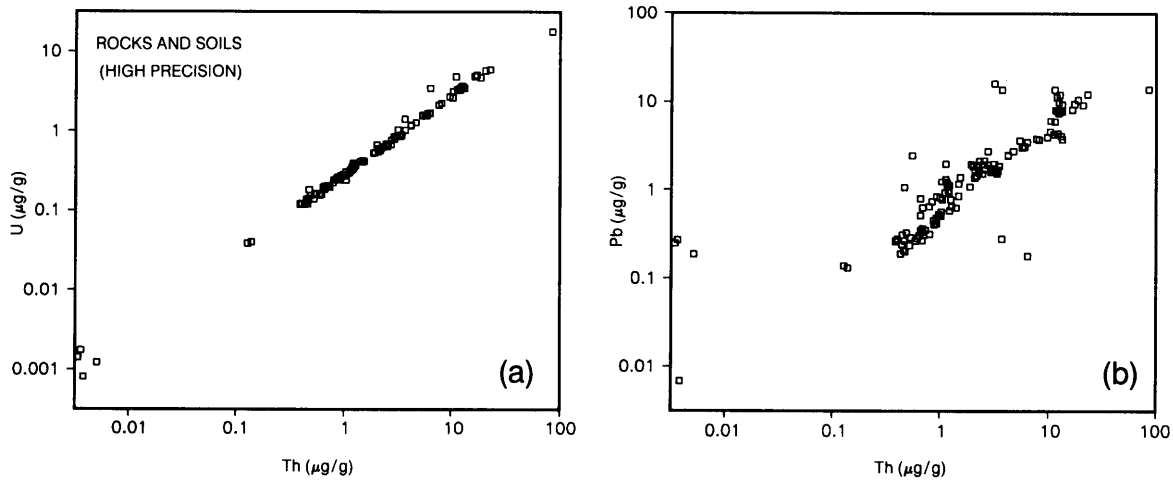


Fig. 8.33. Correlation plots for uranium (U), thorium (Th) (both refractory incompatible trace elements), and lead (Pb) (a vapor-mobilized element) in lunar samples analyzed by high-precision mass spectrometry in connection with radiometric age measurements. **(a)** U vs. Th; **(b)** Pb vs. Th. Horizontal and vertical axes, both logarithmic, show elemental concentrations (in µg/g). The U-Th plot **(a)** shows an excellent correlation between these two elements, indicating their chemically coherent behavior under lunar conditions. The Pb-Th plot **(b)** also shows a definite correlation, which reflects the fact that most of the Pb in lunar samples has been produced by the radioactive decay of Th and U. The greater scatter in the Pb-Th plot is partly due to vapor loss and transport of the relatively volatile Pb as a result of heating by meteoroid impacts.

Figure 8.33a shows the excellent correlation between concentrations of the nonvolatile incompatible elements U and Th in lunar rocks and soils. Figure 8.33b shows the significant, but less coherent correlation between Th and Pb. There are two reasons why Pb should, at least to a first approximation, correlate with Th and U. First, all three elements behave as incompatible trace elements during magmatic processes and do not separate from each other unless those processes operate to extremes. Second, the Moon is highly depleted in Pb relative to meteorites, having apparently lost Pb with the other volatile elements when it formed. As a result, most of the Pb in lunar rocks and soils has been produced by the decay of some of the Th and U originally present, and since many lunar rocks cluster in age at ~3.9 b.y., the ratio of Pb to U or Th tends to be relatively constant. Deviations in concentration from the general trend of Pb coherence (Fig. 8.33b) thus indicate a separation of Pb from Th and U.

Analyses of lunar samples provide clear evidence that such separations do occur on the Moon. *Silver* (1970) pointed out that the Apollo 11 soils contained higher concentrations of radiogenic Pb than could have been produced by the decay of the amount of original U and Th corresponding to their present concentrations. He suggested that volatilization

produced by meteoroid impacts might have mobilized Pb selectively into soils. However, this process, if it occurs, is not ubiquitous. Some soils and breccias are relatively deficient in Pb relative to U and Th.

A striking example of such selective movement of Pb is "rusty rock" 66095 (*Tatsumoto*, 1973). In typical lunar mare basalts, the ratio of the most abundant isotope of U (^{238}U) to nonradiogenic Pb (^{204}Pb) is 400 to 600, with U and Pb concentrations of <1 µg/g. In KREEPy materials, the $^{238}\text{U}/^{204}\text{Pb}$ ratio is 1000 to 3000, with concentrations of total U < 3 and of total Pb < 5 µg/g. In sharp contrast, the U and Pb concentrations in samples of 66095 are about 1.0 and 15 µg/g, respectively, and the $^{238}\text{U}/^{204}\text{Pb}$ ratio is only 36. In sample 66095, nonradiogenic Pb (^{204}Pb) is greatly enriched relative to what would be expected from the concentrations of Th and U. Furthermore, the radiogenic Pb (^{206}Pb , ^{207}Pb , and ^{208}Pb) is also enriched beyond the amounts that could have been produced by the decay of initial U and Th corresponding to the concentrations still remaining in the rock. Clearly, some process mobilizes Pb, both original and radiogenic, at or near the lunar surface.

Before the Apollo missions, it was already known that daytime temperatures on the Moon exceed 100°C. Under such conditions, vaporization, vapor

transport, and condensation were considered to be possible lunar surface processes, and experiments were carried out on the Apollo missions to determine whether they occurred. Samples were skimmed from the uppermost parts of soils that were permanently shaded by boulders, and were therefore presumably cold. Identical samples were skimmed from nearby unshaded soils that received the full diurnal heating and cooling typical of the lunar surface. Analyses of these shadowed soils and of the nearby control soils showed no differences in concentration for most elements (e.g., *Laul et al.*, 1974; *Morgan et al.*, 1974), but the Hg and Cd contents were both higher in the shadowed soils. The differences for Cd (e.g., *Baedecker et al.*, 1974; *Morgan et al.*, 1974; *von Gunten et al.*, 1982) were small and were not found in all shadowed samples. However, the differences for Hg were substantial (e.g., *Reed and Jovanovic*, 1970; *Reed et al.*, 1971a) and were found consistently by several investigators (see review by *von Gunten et al.*, 1982).

Jovanovic and Reed (1979) analyzed Hg in soil samples obtained with drive tubes and drill cores from the Apollo 14, 15, 16, and 17 sites. Except in deep drill sample 15006, they found a substantial decrease of the weakly-bound Hg (that which can be vaporized from the sample on heating to 130°C) in the uppermost 3–8 cm in all cores. They interpreted this decrease as the result of the diurnal heating of the uppermost soils, which causes the weakly bound Hg to migrate downward to cooler intervals (*Reed and Jovanovic*, 1979). Deep drill sample 15006 shows a similar increase in Hg concentrations with depth, but also shows an unexplained high value in the uppermost centimeter. At depths greater than 4–8 cm, the Hg concentrations are more scattered.

Jovanovic and Reed (1979) interpret deeper variations in Hg concentration as the product of fossil thermal gradients of surface regolith, frozen in as the surface on which they formed was covered with new layers of regolith that were thick enough to provide thermal shielding against further diurnal disturbance. If this interpretation is correct, then the Hg concentrations provide an interesting index of surface exposure that is not a cumulative one like solar-wind exposure or cosmic-ray-produced nuclides (see section 7.3).

Jovanovic and Reed (1979) also noted that a portion of the halogen Br is also released at low temperature, and that Br, like Hg, may respond to the lunar diurnal temperature gradient. However, there is no obvious correlation between their reported concentrations of weakly-bound Hg and those of Br released at low temperatures. Furthermore, in contrast to Hg, there is no evident gradient

of low-temperature Br concentrations with depth. In conclusion, evidence for redistribution of vapor-mobilized elements in the upper regolith, as a result of solar heating, is strongest for Hg, weaker for Cd, and questionable for Br.

8.7.7. Sulfur

Sulfur has seldom been studied in conjunction with other vapor-mobilized elements because the required analytical techniques are different (S is commonly determined by spectrometry following acid hydrolysis or O₂ combustion to extract the S; neutron activation does not work for S). Nevertheless, S clearly shows at least some of the behavior characteristic of vapor-mobilized elements. Sulfur concentrations are shown in Fig. 8.25c, where values are given in *weight percent* on a *linear* scale (unlike the other plots in the same figure, where the vertical scale is logarithmic and values are in micrograms per gram or nanograms per gram). Some analysts argue that S values obtained by some techniques are systematically too high, by perhaps as much as 20%. Unfortunately, the suspected techniques were used to provide most of the S analyses for lunar samples. If this concern is valid, then the majority of the data points in Fig. 8.25c are too high.

The relatively restricted range of S concentrations in most lunar igneous rocks indicates that S is associated with a common mineral that occurs in most samples and controls its abundance. This mineral is *troilite* (FeS), though other sulfide minerals also occur in lunar samples (section 5.3). The lowest S concentrations are found in highland monomictic plutonic rocks such as ferroan anorthosites, some of which have concentrations as low as 0.001%. The highest S concentrations are found in mare basalts, and the high-Ti lavas from the Apollo 11 and 17 sites have, on average, higher concentrations (~0.2%) than do the low-Ti lavas from the Apollo 12 and 15 sites (~0.1%). In comparison, S concentrations in the most common terrestrial lavas (ocean-floor basalts) are generally <0.08%. As indicated by the data on mare basalts, S concentrations tend to be higher in basalts with higher TiO₂. This is true not only between the general classes of high-Ti vs. low-Ti basalts from different landing sites, but also within the more closely related basalts of a single site (e.g., Apollo 12 basalts; *Gibson et al.*, 1977).

The partial pressure of S in lunar basalts, and the mechanisms controlling it, are not well understood. Early analyses suggested the pressure was high because of equilibria between S and FeS (troilite) in basaltic magmas. An inverse correlation between concentrations of S and those of metallic iron (Fe⁰) was initially reported for Apollo 17 basalts; however, an expanded dataset shows that the correlation is

poor (correlation coefficient $r = -0.59$). The initial result was interpreted as indicating that the Fe° metal was produced by the loss of sulfur from FeS during volatilization (see *Gibson et al.*, 1976, and *Brett*, 1976, for discussions). However, no such correlation between S and Fe° was found in Apollo 12 basalts (*Gibson et al.*, 1977), and there is no reason to think that a S-volatilization mechanism produced the Fe° in those rocks. On the basis of the initial interpretation of loss of S by volatilization, which implied a high and uniform concentration of S in initial Apollo 17 magmas, *Brett* (1976) concluded that the Apollo 11 and 17 lavas were saturated in S (relative to immiscible FeS) at the time of their eruption, and that the Apollo 12 and 15 lavas, which have significantly lower S concentrations, were not saturated. However, the vapor pressure of S that would be required for equilibrium with lunar basaltic magma is some 8 orders of magnitude greater than the estimated confining pressure on erupted lavas (*Nash and Hansel*, 1973).

In lunar soils, the S concentrations reflect the type of terrain, mare or highland, from which the soils are derived. *Kerridge et al.* (1975a,b) found a strong positive correlation between total Fe and S concentrations in highland soils from the Apollo 16 site, strongly indicating a common source for both elements in highland materials. The S concentrations in these soils approximately match those calculated from mixing together the various types of igneous rocks from which the soils are derived, using the S values determined for them. Unfortunately, this apparent agreement from a simple mass balance is deceiving (e.g., *Kerridge et al.*, 1975a,b) because such a simple model is ruled out by isotopic measurements.

Sulfur isotopes have low enough atomic masses (32–36 amu) to exhibit measurable mass fractionation as a result of chemical separation processes. Indigenous lunar S, as determined from analyses of lunar igneous rocks, has nearly the same relative abundances of the various S isotopes as does S from meteorites. The $^{34}\text{S}/^{32}\text{S}$ ratio in lunar igneous rocks is only 0.05% different from the ratio in troilite (FeS) from the Canyon Diablo iron meteorite. However, in lunar soils, the difference in the ratio, which represents mass fractionation of the two isotopes, is higher. In mature bulk lunar soils the fractionation is as high as 1.2% and for the smallest grain size fraction of such soils as high as 1.7%. This difference between lunar rocks and the soils derived from them could result from addition to the soils of an extralunar component enriched in S. However, the most likely extralunar components are common types of meteorites, and these are not enriched in S. The S abundance in the solar wind is too low

to affect the isotopic composition of lunar soil.

The relative changes observed for the S isotopes ^{33}S and ^{36}S (e.g., *Rees and Thode*, 1972) are proportional to those for ^{34}S , indicating that the cause of the isotopic differences is some process that results in mass fractionation. One obvious process that would fractionate S isotopes in this manner is the loss of S by vaporization following meteoroid impacts (e.g., *Clayton et al.*, 1974). This process would also produce a negative correlation between the amount of enrichment in ^{34}S and the total S concentration, because the light isotopes will be preferentially vaporized and, as the extent of S loss by vaporization increases, the small amounts of residual S will become increasingly enriched in the heavier isotopes such as ^{34}S . Surprisingly, the reverse seems to be the case. *Kerridge et al.* (1975a,b) found a good positive correlation between the degree of ^{34}S enrichment and the total concentration of S in Apollo 16 highland soils. They also found a good positive correlation between the extent of ^{34}S enrichment and the N concentration. Because N is introduced into exposed lunar soils from the solar wind (section 8.8.3), the N concentration increases with exposure age, and these results indicate that enrichment in S heavy isotopes increases with the exposure age of the soils.

To reconcile these results with the fact that any S loss by vaporization would leave behind a residue enriched in ^{34}S , and to account for the positive correlation between ^{34}S enrichment and total S concentration, *Kerridge et al.* (1975a,b) suggested that their results reflect the combined operation of two processes: (1) loss of S through vaporization or ion sputtering to produce the observed ^{34}S enrichment; and (2) addition of new meteoroid material at a rate that slightly exceeds the total S loss.

Kerridge et al. (1975a) further demonstrated that the S loss from a mature highland soil amounts to several tens of percent of the amount originally present. This estimate is consistent with that of *Cripe and Moore* (1976), which was based on the mass balance of S between possible parent materials of the soils (*Schonfeld and Meyer*, 1972) and the actual analyzed S values for the soils. The meteoroid inputs of S required to balance this loss are consistent with those inferred from the concentrations of other vapor-mobilized elements in these soils (section 8.7.2). However, other mechanisms besides vaporization may contribute to the loss of S from lunar soils. *Kerridge and Kaplan* (1978) favored sputtering over thermal vaporization as the mechanism to account for isotopic fractionation, not only of S, but also of Si and O, at soil surfaces.

Sulfur is the principal vapor-mobilized element in the volatile-rich coatings on glass spheres produced

by lunar pyroclastic fire-fountain eruptions (*Butler and Meyer, 1976*; see sections 6.1.7 and 8.7.5). The Apollo 17 orange and black pyroclastic spheres and the Apollo 15 green pyroclastic spheres have clear affinities with mare basalts in their contents of major elements and incompatible trace elements. It might be expected that the spheres, which have mare basalt chemical affinities and also have S-rich coatings, would have anomalously high overall S concentrations. Indeed, the overall concentrations of other vapor-mobilized elements in these soils are substantially greater than in mare basalts, as pointed out above. However, this is not the case for S. The mean S concentration in the orange-glass sample 74220 is between 0.07 and 0.08 wt.%, well below the median, and even the range, for Apollo 17 mare basalts (Fig. 8.25c). The low S concentrations of the pyroclastic deposits may indicate that S, if present in relatively high concentrations in the vapor as inferred for the other vapor-mobilized elements, was in a chemical form too volatile to condense onto the spherules.

Several investigators have argued that it is unlikely that the S in the coatings was deposited as free S, mainly because temperatures on the glass surfaces were too high during eruption (e.g., *Butler and Meyer, 1976*; *Wasson et al., 1976*). However, analyses of the surface coatings appear to show that more S is present than would be needed to combine with the measured amounts of such cations as Fe^{2+} and Zn^{2+} to form minerals such as troilite (FeS) or *sphalerite* [(Zn,Fe)S] (see *Butler and Meyer, 1976*). Proof that elemental S did condense onto the spherule surfaces would provide important constraints on the composition of the vapor phase in these volcanic eruptions, its cooling rate, and the conditions under which it cooled.

Not all the movement of S on the lunar surface is caused by simple evaporation and condensation. In a few breccias, small veins of troilite are observed, and pyroxenes in the breccias have undergone partial replacement by some reaction that left troilite in their place. This form of sulfide metamorphism may be analogous to the formation of sulfide ore bodies on Earth, in which the movement of fluid phases through large volumes of terrestrial rocks results in extraction of trace elements from the rocks and their concentration into ores. On the Moon, the heat present in large ejecta blankets around major impact craters may produce substantial migration of S and extraction of the chalcophile elements.

8.7.8. Halogens

The halogens have been studied as a group in lunar materials mainly by Reed and Jovanovic (e.g., *Reed and Jovanovic, 1971, 1972, 1973a,b*) using

neutron and photon activation analysis. These investigators found that a substantial fraction (about 50% to 90%) of the Cl and Br in most lunar materials, but especially in soils and breccias, could be leached out with hot water (e.g., *Jovanovic and Reed, 1973, 1974*). Iodine was also leached out, but the fraction so leached was not determined because the I concentrations of the residues were not measured. The values for I in Figs. 8.25n and 8.34c are therefore lower limits.

The halogens are not an especially coherent geochemical group, nor would they necessarily be expected to show strongly correlated behavior. Figure 8.34 shows concentrations of F, Br, and I plotted against Cl for a wide variety of lunar rocks and soils. The Cl and Br concentrations are only roughly correlated. The calculated correlation coefficient (after the deletion of data points that lie more than 2.7 standard deviations from the regression line) is 0.79. The slope of the calculated correlation line is 3.47 ± 0.24 , which is only about four standard deviations lower than the range of 4.4–5.1 for cosmic abundances (*Anders and Ebihara, 1982*) and for average values of Cl chondrites (*Mason, 1971*).

Based on the available data, it appears that concentrations of Cl and F are not correlated (Fig. 8.34b). Concentrations of whole-rock Cl and I (leachable I, in most cases) are also not correlated (Fig. 8.34c), but there may be a crude correlation between leachable Cl and leachable I in many samples, mainly soils and breccias (Fig. 8.34d). There are no apparent correlations among the halogen data for samples from a single mission or of a given sample type, e.g., highland breccias from Apollo 17. In part, this lack of apparent relationship may result from analytical scatter, for replicate analyses by Jovanovic and Reed show scatter of tens of percent for the amounts of all analyzed halogens. The lack of correlation may also reflect the small number of samples analyzed for any single mission or rock type. However, the data more likely reflect a genuine incoherence of behavior between any pair of halogens.

The exact mineral locations of the halogen elements in lunar samples are not well known. On Earth, the phosphate mineral apatite (see section 5.5) normally contains one atom of F or Cl (or an OH^-) in its formula unit, with F being more common than Cl, particularly in apatite from igneous rocks thought to have formed under dry conditions. If the F and Cl in lunar samples are located in phosphate minerals (apatite or whitlockite), then the concentrations of F and Cl should correlate with the P contents of the samples. However, there is little evidence for a correlation between F and P in lunar materials and

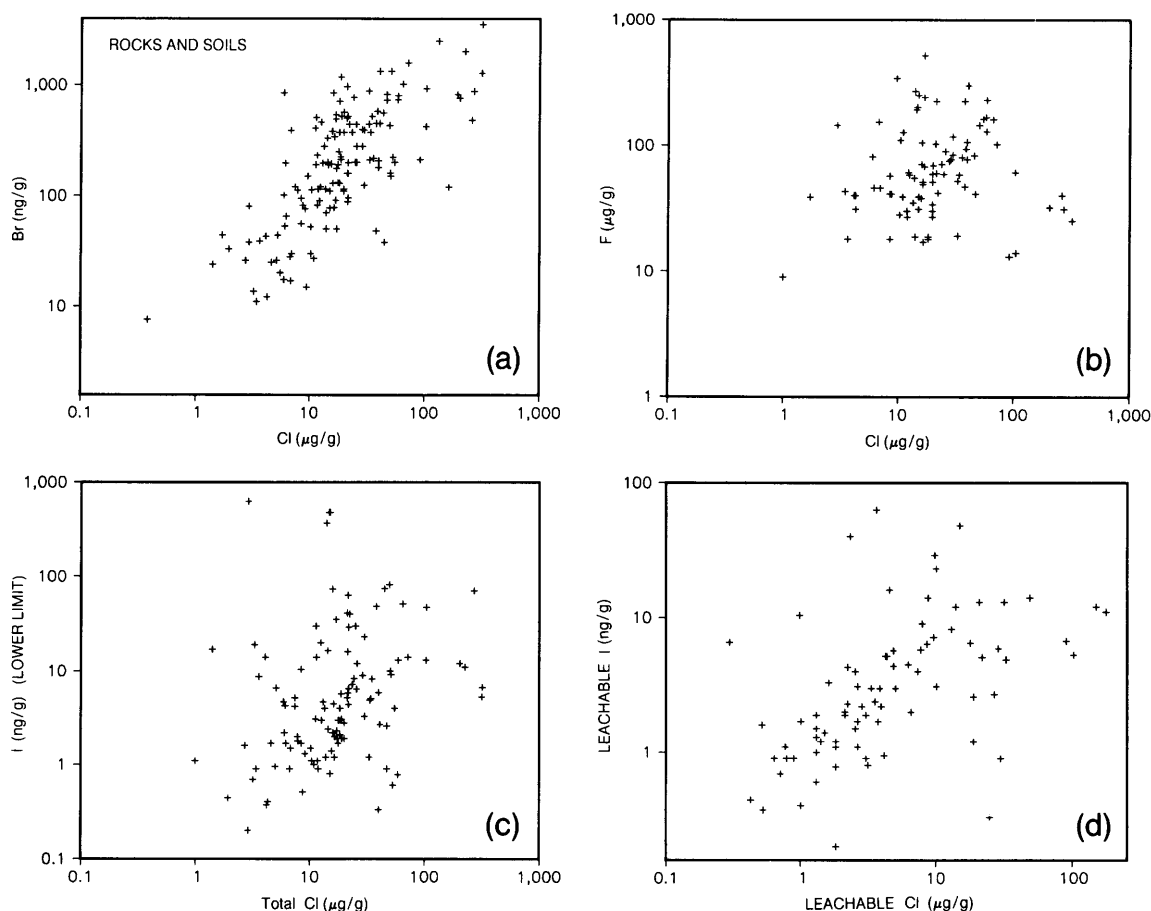


Fig. 8.34. Correlation plots for four vapor-mobilized halogen elements (Br, F, I, and Cl) in a range of lunar samples of all types. **(a)** Br vs. Cl; **(b)** F vs. Cl; **(c)** I (“lower limits”) vs. Cl; **(d)** “leachable” I vs. “leachable” Cl (Jovanovic and Reed, 1973, 1974, 1976a,b, 1980a,b). Horizontal and vertical axes, both logarithmic, show elemental concentrations (Br and I in ng/g, F and Cl in μg/g). Most of the I values represent “leachable” I leached from the samples **(d)**, and the I data **(c)** therefore represent only lower limits. Despite the chemical similarity of the halogen elements to each other, there are no strong correlations between their concentrations in lunar materials. The Br-Cl data **(a)** show a weak positive correlation, and a weaker positive correlation may exist between the “leachable” I and “leachable” Cl **(d)**. However, the F-Cl data **(b)** and the I-Cl data **(c)** show no correlation.

none at all for a correlation between Cl and P. Jovanovic and Reed (e.g., 1976, 1980) have grouped the rocks they analyzed according to the Cl/P₂O₅ ratio, and they have suggested that each different group represents a different mantle source. However, it is difficult to reconcile their suggestion with other geochemical information (e.g., Taylor and Hunter, 1981). It is also possible that some correlation between halogens and P could be produced during lunar magmatic processes, regardless of the source of the magma, because in such situations the vapor-mobilized elements behave as incompatible trace elements, whose concentrations do correlate with P.

8.7.9. Possible Lunar Ores of Vapor-Mobilized Elements

The chemical forms in which the vapor-mobilized elements occur in lunar materials have not been thoroughly characterized. Overall, the most abundant element of this group is S. Concentrations of S in lunar lavas are even higher than those in terrestrial basalts. The reasons for this difference are not known. It may be related to the extremely reducing conditions under which lunar magmas form. Another possibility is that terrestrial basalts have low S contents because gravitational separa-

tion of a dense sulfide phase deep in the Earth removed S from the Earth's mantle where basalts subsequently formed.

The surface coatings of volatile materials on pyroclastic spheres, such as those from the orange-glass deposit 74220 and similar pyroclastic deposits (section 8.7.5), may be too thin to serve as an economic source of these elements. For example, a tonne of such spheres contains only 200 g of Zn and 700 g of S. Instead, the surface coatings may be more important in demonstrating that chemical separation during vapor transport has occurred in conjunction with volcanic eruptions on the Moon. In exceptional cases, this process may have been carried far enough to produce ore-grade concentrations of these otherwise rare elements.

Vapor mobilization in the regolith, due to the heat produced in meteoroid impacts, also might produce ores. The highly enriched, albeit small, soil sample from the Apollo 12 drive tube (12028, *Laul et al.*, 1971) apparently contains a minor particle that is highly enriched in some vapor-mobilized elements (Ag, Cd, and Bi; see section 8.7.6). This indicates that, at least on a small scale, very high concentrations (>20 $\mu\text{g/g}$) of elements such as Cd and Bi can be produced. Perhaps some soils will be rich in such particles. The formation of sulfide veins and the replacement of pyroxene by sulfide minerals in some breccias are other indications that vapor mobilization can concentrate these elements.

Large amounts of vapor-mobilized elements may have been concentrated in large craters at the lunar poles (section 3.8), where permanently shaded crater floors can act as long-term cold traps for volatile substances. These elements could reach the lunar surface either by outgassing of the lunar interior or as materials vaporized from meteoroids and comets that have struck the Moon. These polar craters have not yet been examined by any type of remote sensing, including imaging.

Whether or not the Moon has ores of vapor-mobilized elements, it is already clear that these elements are not abundant on the Moon. Their concentrations in pristine lunar rocks are generally low, and they are typically more abundant in the regolith, where their abundances have been augmented by material from meteoroids and micrometeoroids, whose vapor-mobilized elements vaporized on impact and subsequently condensed onto the surfaces of soil grains.

However, the overall low lunar concentrations of vapor-mobilized elements should not discourage further consideration of the possibility of ore-grade concentrations. The occurrence of such concentrations will depend on the interplay between processes that concentrate vapor-mobilized elements and

processes that destroy the ores that have formed. Such ores exist on Earth, even though both the whole Earth and its crust are also depleted in vapor-mobilized elements, although generally not as depleted as the Moon (e.g., *Krähenbühl et al.*, 1973).

8.8. SOLAR-WIND-IMPLANTED ELEMENTS

It is no wonder that the search for biogenic materials (H, C, and N compounds) in the Apollo samples proved to be extremely difficult. Concentrations of H, C, and N in lunar samples are in the 100- $\mu\text{g/g}$ range or below. Concentrations of the noble gases (He, Ne, Ar, Kr, and Xe) are even lower. The Moon apparently never accreted significant amounts of these elements when it formed, just as it apparently never accreted much of the vapor-mobilized elements. As with the vapor-mobilized elements, the lunar soils are richer in the biogenic elements (H, C, and N) and noble gases than are the lunar igneous rocks. However, unlike the vapor-mobilized elements, the principal source of the biogenic elements and noble gases in lunar soils is the solar wind, and not meteoroids. For this reason, this group of elements (H, C, N, and the noble gases) are designated the *solar-wind-implanted elements*.

8.8.1. The Solar Wind

The solar wind (see section 3.11.1) is a plasma of chemical elements, expelled as ionized atoms from the atmosphere of the sun. It bombards all objects in the solar system. Earth's magnetic field and atmosphere deflect and absorb the solar wind and prevent it from reaching the Earth's surface and interacting with it. The Moon has no such protection; ions from the solar wind strike the lunar surface with kinetic energies of about 1 keV per nucleon and embed themselves to depths of up to a few hundredths of a micrometer in exposed materials. Solar cosmic rays (associated with solar flares) consist of similar particles with mega-electron volt and higher energies, which penetrate farther (Table 3.5). The solar wind, however, supplies about 2 orders of magnitude more particles than solar cosmic rays, and is therefore the more significant source of solar-wind-implanted elements.

The principal component of the solar wind is H, and there is relatively less deuterium (D) present in the solar wind than in the Earth. The solar-wind isotopic ratio D/H is at least 3 orders of magnitude less than the terrestrial value (1.5×10^{-4}), and for practical purposes is essentially zero because D that may have originally been present in the sun has been destroyed by nuclear reactions there. The second most abundant component of the solar wind is He, with an isotopic ratio of ${}^3\text{He}/{}^4\text{He} = 4 \times 10^{-4}$. This

ratio is substantially higher than the value for terrestrial atmospheric He (1.4×10^{-6}), which has been strongly affected by addition of ^4He from the radioactive decay of U- and Th-series elements within the Earth. Next most abundant in the solar wind are C, N, and O, with concentrations an order of magnitude lower than that of He. Heavier elements are also present, most at concentrations too low to observe in lunar soil grains.

8.8.2. Noble Gases (He, Ne, Ar, Kr, and Xe)

The fundamental character of the solar-wind-implanted elements is evident in the concentrations and behavior of the noble gases He, Ne, Ar, Kr, and Xe. These gases, and their various isotopes, can be measured in incredibly small amounts with very high precision by mass spectrometry. These measurements provide unique and extensive information about a broad range of fundamental questions: the chronology of earliest solar-system development; the surface exposure and radiation histories of lunar rocks and soils; the outgassing histories of planets; the nature of the solar wind; and the composition of the sun. The importance of this information and the interest in obtaining it has generated such an extensive literature on noble gases as to create the impression that these gases must be far more abundant in lunar materials than is actually the case.

Concentrations and sources. Concentrations of noble gases in lunar materials are shown in Fig. 8.35. Statistical summaries of the data are given in Table A8.6. In accordance with the convention used for other trace elements in this chapter, these data are presented in weight proportions, i.e., micrograms per gram or nanograms per gram. However, in most of the literature noble gas concentrations are reported as atomic abundances, which have been converted to their equivalent volumes in cubic centimeters of gas at STP ($T = 25^\circ\text{C}$, $P = 1 \text{ atm}$) per gram of sample. These values are usually multiplied for convenience by some factor such as 10^8 (because the volumes are on the order of $10^{-8} \text{ cm}^3/\text{g}$). Using micrograms per gram or nanograms per gram instead of atomic percentages for noble gas concentrations partly masks the wide differences in atomic abundance among the noble gases, because the higher atomic weights of the heavier gases (e.g., Kr and Xe) compensate in part for their lower atomic abundances.

There is a consistent pattern to noble gas concentrations in lunar materials: soils have the highest concentrations and igneous rocks the lowest (Fig. 8.35). Igneous rocks with low noble gas contents may be either monomict samples from the lunar interior (MBAS and HMCT columns in Fig. 8.35) or

they may be polymict materials that were completely melted and outgassed during meteoroid impacts (low values in the BX column of Fig. 8.35, representing mostly clast-poor impact melts; see section 6.4.5). Breccia samples span a range that extends from concentrations as high as those found in soils (for breccias consisting of indurated soils) to as low as those in igneous rocks.

Noble gases in lunar materials can be expected to come from five different sources: (1) an original accretional component trapped in the lunar interior when the Moon formed; (2) radioactive decay within the Moon, involving (a) ^{40}K , which produces ^{40}Ar by *beta decay*, (b) U- and Th-series elements, which produce ^4He by *alpha decay*, and (c) ^{235}U , ^{238}U , and ^{244}Pu , which produce heavy noble gases (Kr and Xe) by *spontaneous fission*; (3) the solar wind; (4) impacting meteoroids; and (5) *spallation reactions* produced in lunar materials by energetic solar and galactic cosmic rays (see section 3.11 and ^{38}Ar data in Fig. 7.27e). The relative contributions from each source can be determined from the isotopic ratios of the various noble gases, which vary substantially from sample to sample. For example, Fig. 8.36 shows the atomic ratios $^4\text{He}/^3\text{He}$, $^{22}\text{Ne}/^{21}\text{Ne}$, $^{40}\text{Ar}/^{36}\text{Ar}$, and $^{36}\text{Ar}/^{38}\text{Ar}$ for various rock types and soils.

Examination of the various noble gas isotopic ratios shows that the contribution from primordial noble gases trapped in the lunar interior is negligible, except perhaps for Xe, a component of which has been attributed either to indigenous lunar Xe or to an early solar wind component (Eugster, 1986; Eugster and Niedermann, 1987). The contribution from meteoroids and comets impacting the lunar surface is also negligible (e.g., Ozima and Podosek, 1983). However, the contribution from the solar wind is important for all noble gases and in fact accounts for the bulk of the noble gases contained in the lunar regolith. Isotopic ratios of solar wind gases fall close to the soil and regolith breccia (S&RB) values shown in Fig. 8.36; more detailed summaries of solar-wind isotopes can be found in Eberhardt *et al.* (1970) and the monograph by Ozima and Podosek (1983).

The major contribution of the solar wind to the contents of all noble gases produces a large number of good correlations between various noble gases across a wide range of concentrations (Fig. 8.37). These correlations reflect the fact that the data points in Fig. 8.37 include two sources: soils that are rich in noble gases introduced by the solar wind, and lunar igneous rocks, which have little noble gases of any kind. The correlations are tightest between Ne, Kr, and Xe, because these elements do not contain any component produced by radioactive decay within the Moon. The substantial scatter in correlation diagrams based on pairs of these elements

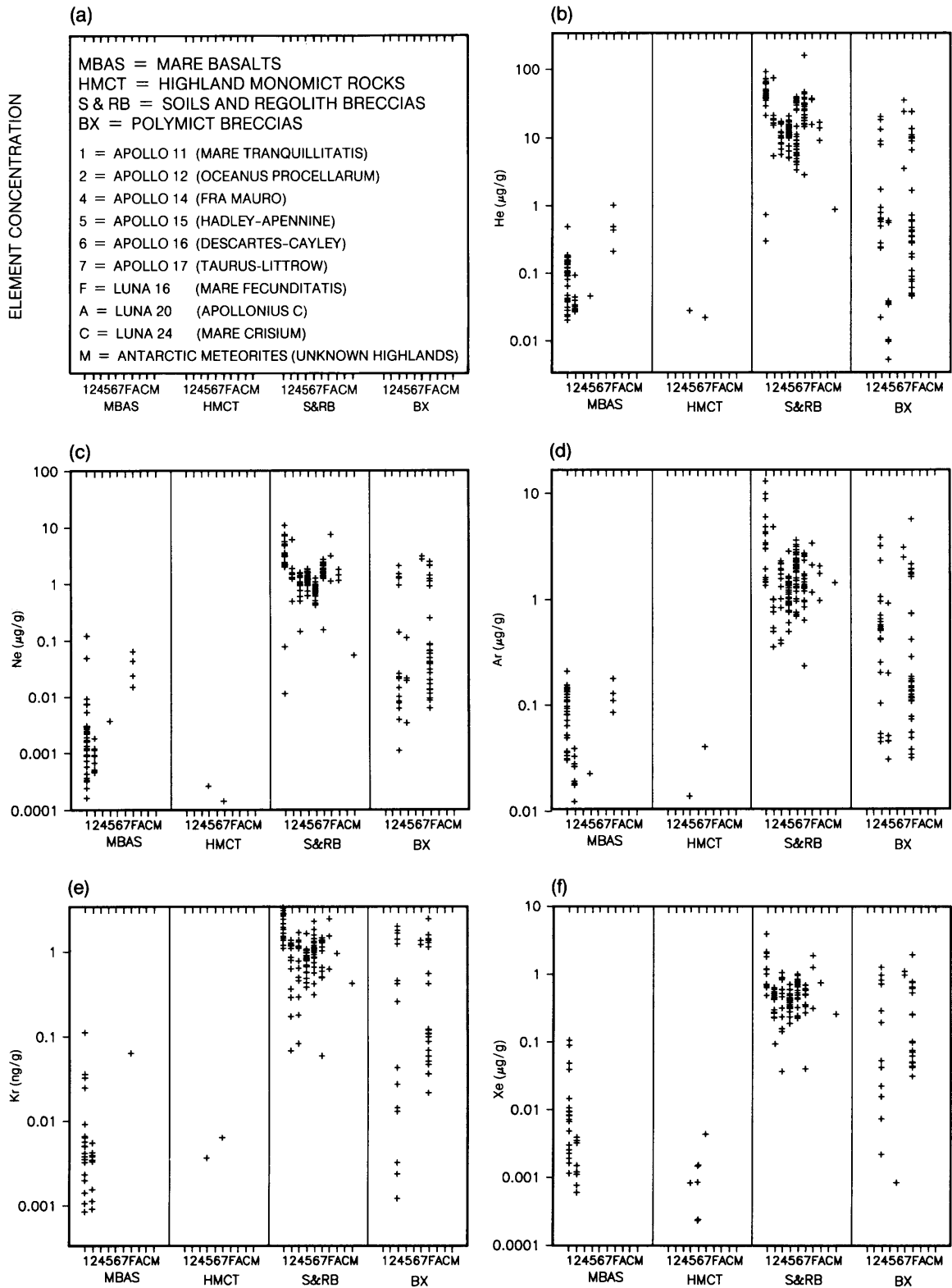


Fig. 8.35. Concentration ranges of solar-wind-implanted noble-gas elements (He, Ne, Ar, Kr, and Xe) in various lunar materials: mare basalts (MBAS), highland monomict rocks (HMCT), soils and regolith breccias (S&RB), and polymict breccias (BX). Horizontal axes show sample types, separated according to individual missions. Vertical axes show elemental concentrations (Kr and Xe in ng/g; He, Ne, and Ar in $\mu\text{g/g}$). **(a)** Graphical key to the plots and abbreviations. Data are presented for **(b)** helium, He; **(c)** neon, Ne; **(d)** argon, Ar; **(e)** krypton, Kr; **(f)** xenon, Xe. Statistical summaries for most of these plots are provided in Table A8.6.

arises in part from different rates of loss by diffusion for the individual noble gases from soil grains.

Solar-wind contributions. The influence of the solar wind is also evident in all four of the isotopic ratios plotted in Fig. 8.36. For lunar soils (S&RB), these lie in a narrow range, at or near the highest or the lowest values observed for all samples, because the solar wind is the principal source for those elements in most soils. Deviant values occur for some soils because they are *immature* (i.e., they have not been exposed near the surface long enough to attain the high concentrations of noble gases present in most other soils). The noble gas concentrations and isotopic ratios have been used to determine the average exposure ages of lunar soils (e.g., Ozima and Podosek, 1983).

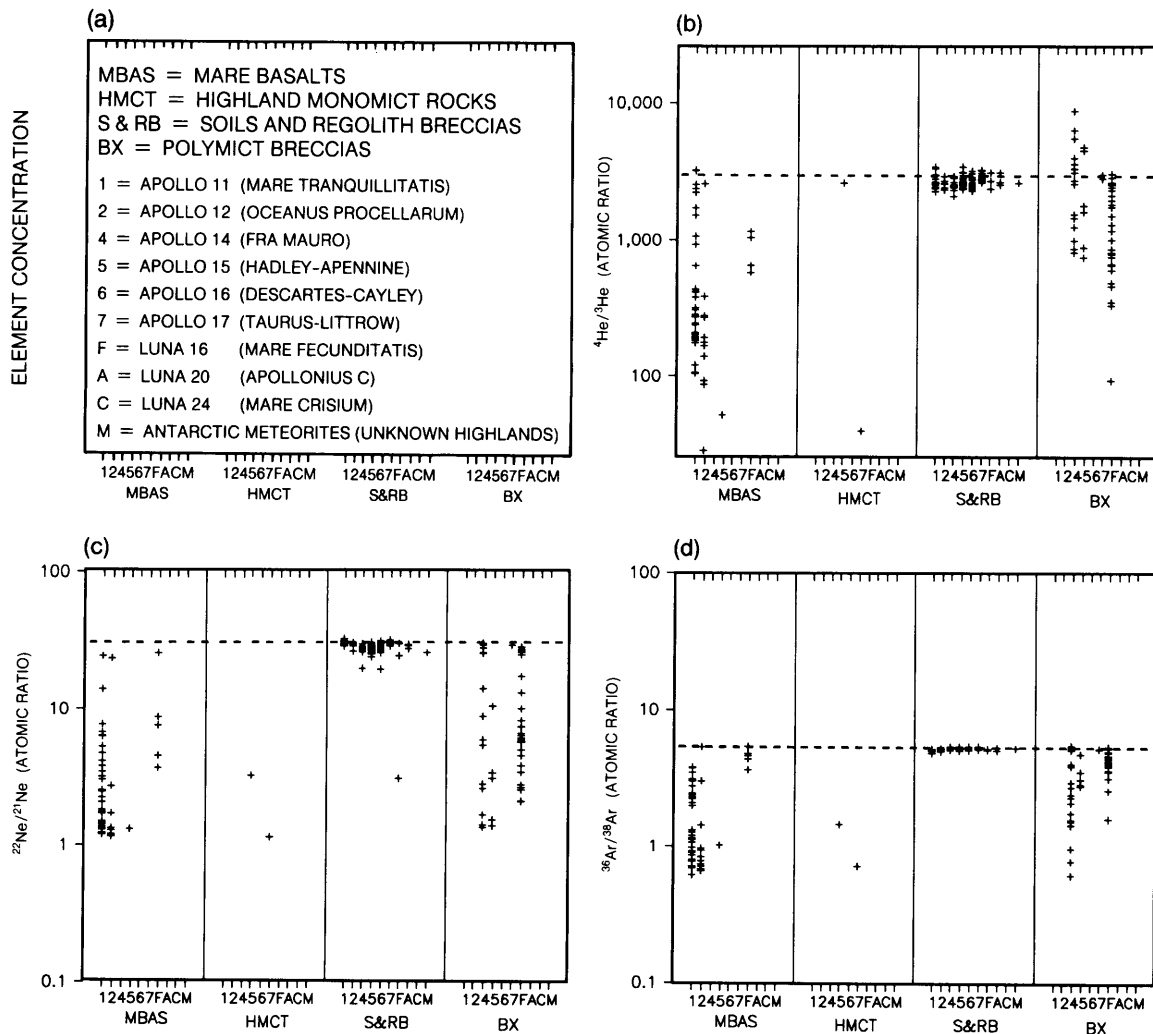
The high soil and regolith breccia values for $^{22}\text{Ne}/^{21}\text{Ne}$ (Fig. 8.36c) and $^{36}\text{Ar}/^{38}\text{Ar}$ (Fig. 8.36d) reflect the relatively high solar wind values for those isotopic ratios. In addition, the $^{22}\text{Ne}/^{21}\text{Ne}$ ratio is particularly sensitive to Ne produced by spallation reactions (e.g., Ozima and Podosek, 1983). The mixing of spallation-produced isotopes of Ne, Ar, and other noble gases with the noble-gas isotopes from the solar wind is responsible for the spread in values for the $^{22}\text{Ne}/^{21}\text{Ne}$ and the slight variability in $^{36}\text{Ar}/^{38}\text{Ar}$ ratios (Figs. 8.36c,d), and is partly responsible for the spread in the other isotopic ratios shown in Fig. 8.36. The $^{40}\text{Ar}/^{36}\text{Ar}$ isotopic ratio for lunar soils lies at the low extreme for all lunar materials. This is because the principal source of ^{40}Ar in lunar materials is ^{40}K , which decays to produce ^{40}Ar . ^{36}Ar , which is not produced by radioactive decay but is introduced mostly from the solar wind, can be used as a standard of comparison. The radioactive decay of ^{40}K raises the $^{40}\text{Ar}/^{36}\text{Ar}$ isotope ratios of the rocks (Fig. 8.36e), in which the total Ar concentrations are low (Fig. 8.35d). However, the low K concentrations of most lunar rocks do not generate enough ^{40}Ar to make a significant contribution to the higher Ar concentrations found in most soils, much of which has been introduced by the solar wind. Therefore, materials with high $^{40}\text{Ar}/^{36}\text{Ar}$ ratios tend to be those that are low in total Ar, i.e., the lunar rocks.

It might seem that the $^4\text{He}/^3\text{He}$ ratio (Fig. 8.36b) would also be low in lunar soils because of the similarity to $^{40}\text{Ar}/^{36}\text{Ar}$ in that there is a substantial contribution of ^4He from radioactive decay within the

Moon, as there is of ^{40}Ar . However, this is not the case, and the difference lies in the amount of He produced by galactic and solar cosmic rays in spallation reactions. Lunar materials with low $^4\text{He}/^3\text{He}$ ratios are also those with low overall concentrations of He and other noble gases, and their $^4\text{He}/^3\text{He}$ should be the most affected by ^4He added from radioactive decay. However, this effect is overwhelmed by the very low $^4\text{He}/^3\text{He}$ ratios for spallation products (~ 5 , Ozima and Podosek, 1983). No samples of lunar igneous rocks have yet shown a combination of low He concentrations and very high $^4\text{He}/^3\text{He}$ ratios. Any such rock would have had to have an extremely short residence time near the lunar surface, so there would have been little time to form He by spallation, and the rock's He content would be dominated by the ^4He produced through radioactive decay.

Spallation reactions also affect the isotopic ratios of other noble gases. For Kr and Xe, the relative proportions of the lightest and least abundant isotopes are most affected by contributions from spallation. Additional scatter for Kr and Xe is produced by contributions of these heavy noble gases from spontaneous fission of such heavy atoms as ^{244}Pu and ^{235}U ; these fission contributions have been observed in some lunar samples (e.g., Bematowicz *et al.*, 1977).

The lunar atmosphere. Some of the ^{40}Ar and ^4He produced in the lunar interior by radioactive decay is carried to the lunar surface by volcanic eruptions, some leaks to the lunar surface by diffusion through fractures in the crust, and some is released from near-surface soils and rocks by heating and vaporization during meteoroid impacts. Much of this gas is lost to space because of the Moon's low escape velocity (2.38 km/sec) and because of accelerations due to ionization by the solar wind (section 3.9). Surprisingly, a significant proportion of it is recaptured and trapped in the lunar surface. This effect is particularly evident for ^{40}Ar , which has much higher concentrations relative to the other Ar isotopes in lunar soils than can be explained by contributions from the solar wind, in which the value of $^{40}\text{Ar}/^{36}\text{Ar}$ is negligibly low ($<10^{-4}$; Clayton, 1968). It appears that a significant fraction of the ^{40}Ar atoms that reach the lunar atmosphere and become ionized are accelerated not into space



but back toward the Moon, where they become implanted in regolith grains just like gases of the solar wind itself (Manka and Michel, 1971). The same is true of the other noble gases and, indeed, of atoms of any element, whether their original source is lunar, meteoritic, or solar, once they enter the lunar atmosphere. Manka and Michel estimate that the steady-state ${}^{40}\text{Ar}$ concentration of the lunar atmosphere may be as high as 10^2 to 10^3 atoms/cm³ (see Table 3.4).

Solar-wind noble gases and soil grains. The solar wind strikes exposed rocks and grains of lunar soil, and the solar wind ions are implanted in the outermost surfaces of the rock fragments and soil grains. The concentrations of solar-wind gases therefore tend to be correlated with the surface area,

and not the volume, of the grains containing them. Small soil grains have, on the average, higher concentrations of noble gases than do larger grains. This effect is illustrated for the noble gas isotopes in Fig. 8.38. The volume concentrations of all solar-wind-implanted elements increase with decreasing grain size in a manner consistent with surface saturation or near-saturation.

The continued solar-wind bombardment of the same exposed material produces radiation damage and erodes the surfaces of the grains by ionic sputtering. Consequently, a saturation level for concentrations of solar-wind-implanted elements on grain surfaces can be reached in a few tens of years of exposure (e.g., Warhau et al., 1979; see section 7.3.2).

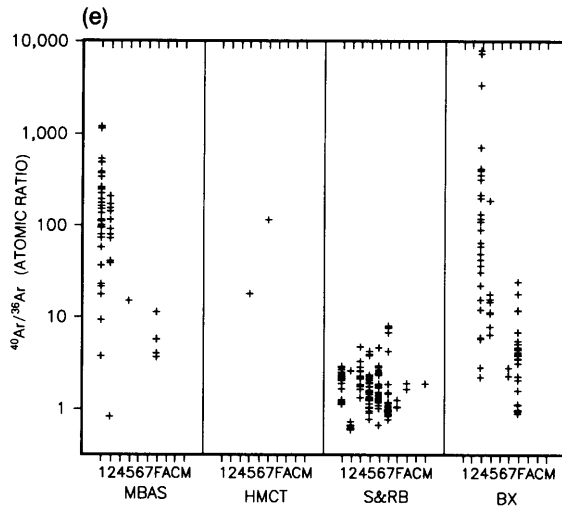


Fig. 8.36. Isotopic abundance ratios for selected solar-wind-implanted noble-gas elements (He, Ne, and Ar) in various lunar materials: mare basalts (MBAS), highland monomictic rocks (HMCT), soils and regolith breccias (S&RB), and polymict breccias (BX). Horizontal axes show sample types, separated according to individual missions. Vertical axes show atomic ratios of the indicated isotopes. **(a)** Graphical key to the plots and abbreviations. Data are presented for **(b)** $^4\text{He}/^3\text{He}$; **(c)** $^{22}\text{Ne}/^{21}\text{Ne}$; **(d)** $^{36}\text{Ar}/^{38}\text{Ar}$; **(e)** $^{40}\text{Ar}/^{36}\text{Ar}$. The value of each ratio measured in the solar wind is indicated by a horizontal dashed line, except for $^{40}\text{Ar}/^{36}\text{Ar}$ **(e)** where the solar-wind ratio is 1 (off scale). The solar-wind value for $^4\text{He}/^3\text{He}$ is variable, but close to the dashed line in **(b)**. The soils and regolith breccias (S&RB) show tightly clustered values of isotopic ratios (especially of $^4\text{He}/^3\text{He}$, $^{22}\text{Ne}/^{21}\text{Ne}$, and $^{38}\text{Ar}/^{36}\text{Ar}$) **(b,c,d)**, which correspond closely to those measured for the solar wind, indicating that the solar wind is the source of virtually all the noble gases in exposed lunar materials. However, $^{40}\text{Ar}/^{36}\text{Ar}$ ratios **(e)** for the same materials (S&RB) are more scattered and have been complicated by the addition of lunar-derived ^{40}Ar produced by radioactive decay within the Moon. The isotopic ratios for lunar rocks, especially for mare basalts (MBAS) and breccias (BX), are also complicated by ^4He and ^{40}Ar produced by internal radioactive decay. However, many of these samples show lower $^4\text{He}/^3\text{He}$ ratios **(b)** than expected because cosmic-ray-induced spallation reactions produce He with a low $^4\text{He}/^3\text{He}$ ratio, and this component may overwhelm the ^4He produced by radioactive decay. The highest values of the $^{22}\text{Ne}/^{21}\text{Ne}$ **(c)** and $^{36}\text{Ar}/^{38}\text{Ar}$ **(d)** ratios are also found in lunar soils, and spallation reactions are also responsible for the lower values seen in mare basalts and some breccias. Values for the $^{40}\text{Ar}/^{36}\text{Ar}$ ratio **(e)** are lowest in soils; the higher values in mare basalts (MBAS) and some breccias (BX) arise from the presence of ^{40}Ar produced by the decay of radioactive ^{40}K .

The principal factor controlling the maximum surface concentration corresponding to this saturation level appears to be the resistance of individual exposed mineral grains to the radiation damage produced by solar X-rays. Ilmenite (FeTiO_3 ; see section 5.2.1) is regarded as the most resistant of the abundant lunar minerals (e.g., Eberhardt *et al.*, 1972). (Actually, the same resistance seems to be shared by a variety of oxide minerals, not just true ilmenite, and the term “ilmenite” is used loosely in these studies to refer to all of them.) Of all lunar materials analyzed, the Ti-rich Apollo 11 soils have the highest concentrations of He and Ne, presumably because of their high proportions of ilmenite (Figs. 8.35b,c).

Both solar and galactic cosmic rays produce linear regions of crystal damage (*particle tracks*) in near-

surface lunar materials (section 7.3.2). Examination of soils collected from a range of depths in the regolith shows that many grains have high densities of particle tracks, indicating that they have spent some time at the lunar surface (e.g., Crozaz *et al.*, 1974). However, the density of particle tracks varies over more than 2 orders of magnitude among different grains from a single sample of soil, and there is no simple relationship between the average track density of grains in a soil sample and the depth from which the sample came. There is apparently sufficient gardening of the lunar soil by meteoroid impacts to continually mix fresh material from depth with material that has been at the surface (see section 7.5.1). Analyses of soils for solar-windimplanted elements provide additional evidence that

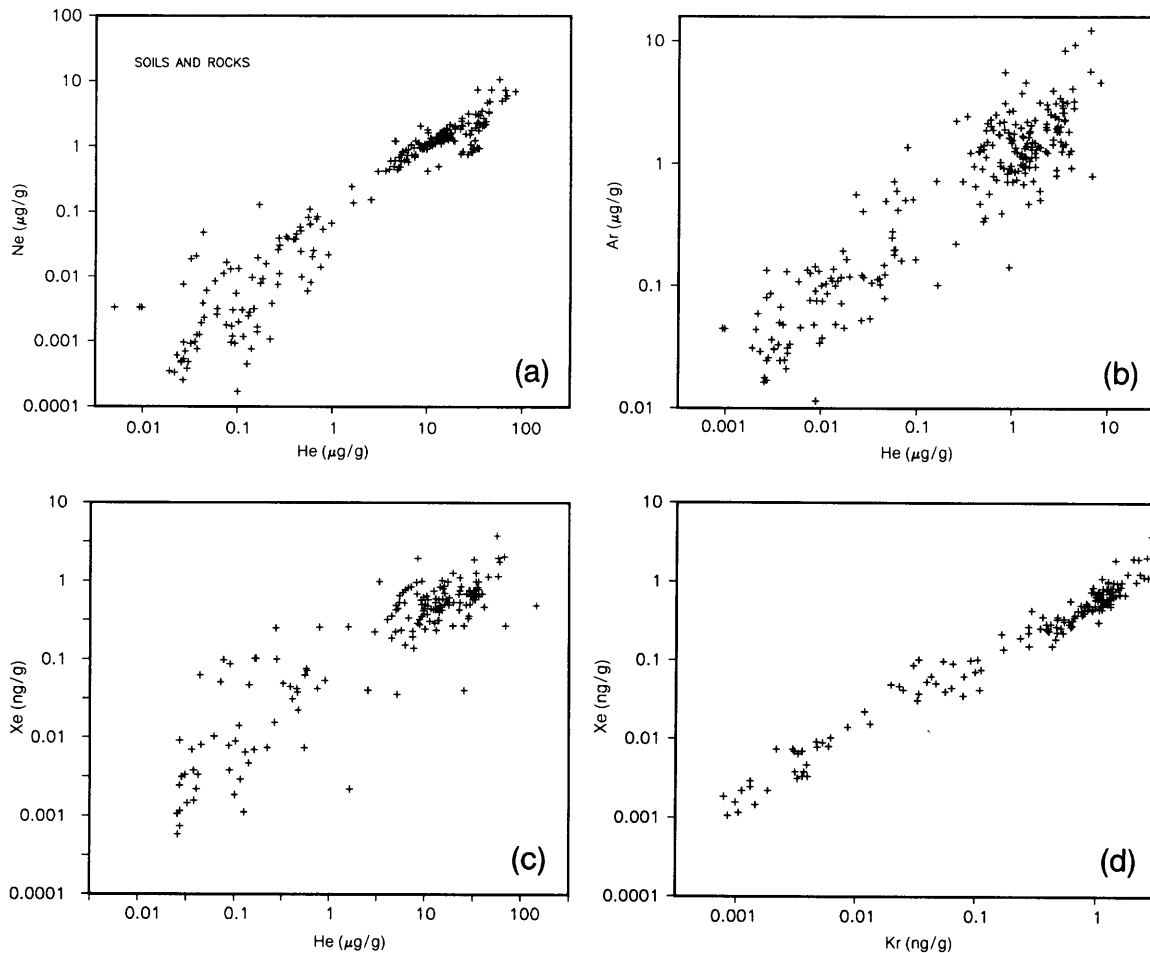


Fig. 8.37. Correlation plots for solar-wind-implanted noble-gas elements (He, Ne, Ar, Kr, and Xe) in a range of lunar sample materials. **(a)** Ne vs. He; **(b)** Ar vs. He; **(c)** Xe vs. He; **(d)** Xe vs. Kr. Horizontal and vertical axes, both logarithmic, show elemental concentrations (in $\mu\text{g/g}$, except Kr and Xe in ng/g). Data are the same as shown in Fig. 8.35. The various noble-gas pairs show positive correlations that range from weak [Xe-He, **(c)**] to strong [Xe-Kr, **(d)**]. The correlations tend to be better between pairs of heavier noble gases [Xe-Kr, **(d)**] because these have similar (and lower) diffusion coefficients and come mainly from a single source, the solar wind. Much of the scatter is due to differential loss by diffusion for different elements, to significant contributions of some isotopes from other sources (e.g., ^4He and ^{40}Ar from radioactive decay), or to both.

soils at all depths contain materials that were once exposed at the lunar surface. Soils collected from as deep as the bottoms of the Apollo deep-drill cores (2–3 m down) contain essentially the same bulk concentrations of solar-wind-implanted elements as do soils collected from the surface (e.g., *Pepin et al.*, 1975).

There is some evidence for significant variations in the strength of the solar wind or in the rate at which solar-wind-implanted elements have been added to the Moon over geologic time; this evidence

is summarized in section 7.7.2. In general, ancient soils exposed at the lunar surface about 4 b.y. ago contain approximately the same concentrations of solar-wind-implanted elements as are found in much younger soils. However, some soils are deficient in solar-wind-implanted elements and in other features produced by long surface exposure. Such soils are either associated with young craters, which have excavated and exposed material that has had little or no previous exposure to the surface, or they occur within thick layers of similar materials,

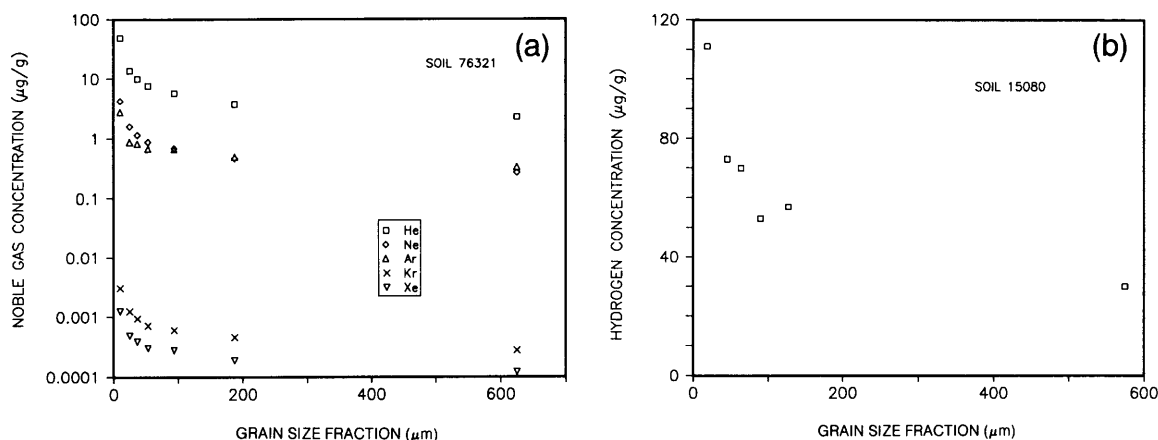


Fig. 8.38. Concentrations of different solar-wind-implanted gases as a function of grain size in two lunar soil samples. **(a)** Noble-gas measurements were made on a sample of soil 76321 that had been sieved into separate grain-size fractions (Bogard *et al.*, 1974); **(b)** H concentrations vs. grain size for soil 15080 (DesMarais *et al.*, 1974). Horizontal axes show grain size (in μm); vertical axes show gas content (in $\mu\text{g/g}$). For all solar-wind-implanted gases, there is a definite increase in concentration with decreasing grain size, indicating that the amount of noble gas present is closely correlated with the surfaces of the grains and not with the volumes.

indicating that they were buried shortly after their exposure on the surface and have been protected from gardening ever since. The concentrations of solar-wind-implanted elements in lunar soils generally correlate with other indices of soil maturity, such as I_s/FeO and agglutinate content (see Fig. 7.14).

8.8.3. Biogenic Elements (H, C, and N)

Concentrations and contamination. Concentrations of total H, total C, and total N in lunar materials are shown in Fig. 8.39. The analyses plotted have been carefully selected from the literature, and many analyses, especially early ones, have been omitted for a variety of reasons, discussed below.

Many early analyses of lunar rocks (both mare basalts and highland monomict rocks) have been omitted. These samples were probably contaminated with N_2 , H_2O , and CO_2 from the Earth's atmosphere before being placed in the curatorial processing cabinets, and they were probably contaminated further with N_2 from the atmospheres within the cabinets themselves (e.g., Becker *et al.*, 1976). Epstein and Taylor (1972), on the basis of release temperatures and isotopic compositions, suggest that about half the H in early analyses of lunar soils is from terrestrial water contamination. More recently obtained measurements support this view (e.g., Gibson and Bustin, 1987). Lunar soils have a small but significant adsorptive capacity for water ($\sim 1500 \mu\text{g H}_2\text{O/g}$ soil) and other gases, although

they have almost no adsorptive capacity (e.g., Cadenhead *et al.*, 1972; Fuller *et al.*, 1971; see section 3.9.1).

Contamination by H, C, and N gases is plausible in view of the collection and transport histories of the lunar samples. When collected on the lunar surface, the samples were placed in teflon bags, in which they were transported to Earth. Unfortunately, these bags allowed some of the outside atmospheric gas to enter by diffusion, and the samples were therefore exposed to the Apollo spacecraft atmosphere and then to the atmosphere of the Lunar Receiving Laboratory for various lengths of time before they were finally stored in ultrapure nitrogen gas.

Hydrogen concentrations in monomict lunar rocks are probably less than $1 \mu\text{g/g}$, and those of N and C may also be that low. These measurements of H, C, and N were made on interior rock fragments, after the samples had been warmed to high enough temperatures to insure that all terrestrial contamination had been removed. However, even these low amounts may not be indigenous to the Moon, because the measured gases may include a component produced by cosmic-ray-induced spallation reactions. Because of this complication, the true indigenous levels of H, C, and N in lunar monomict rocks are only known to be very low, and their isotopic ratios are uncertain.

In selecting soil analyses, if results from more than one analysis of a single sample were available, and one result was substantially higher than the rest, only

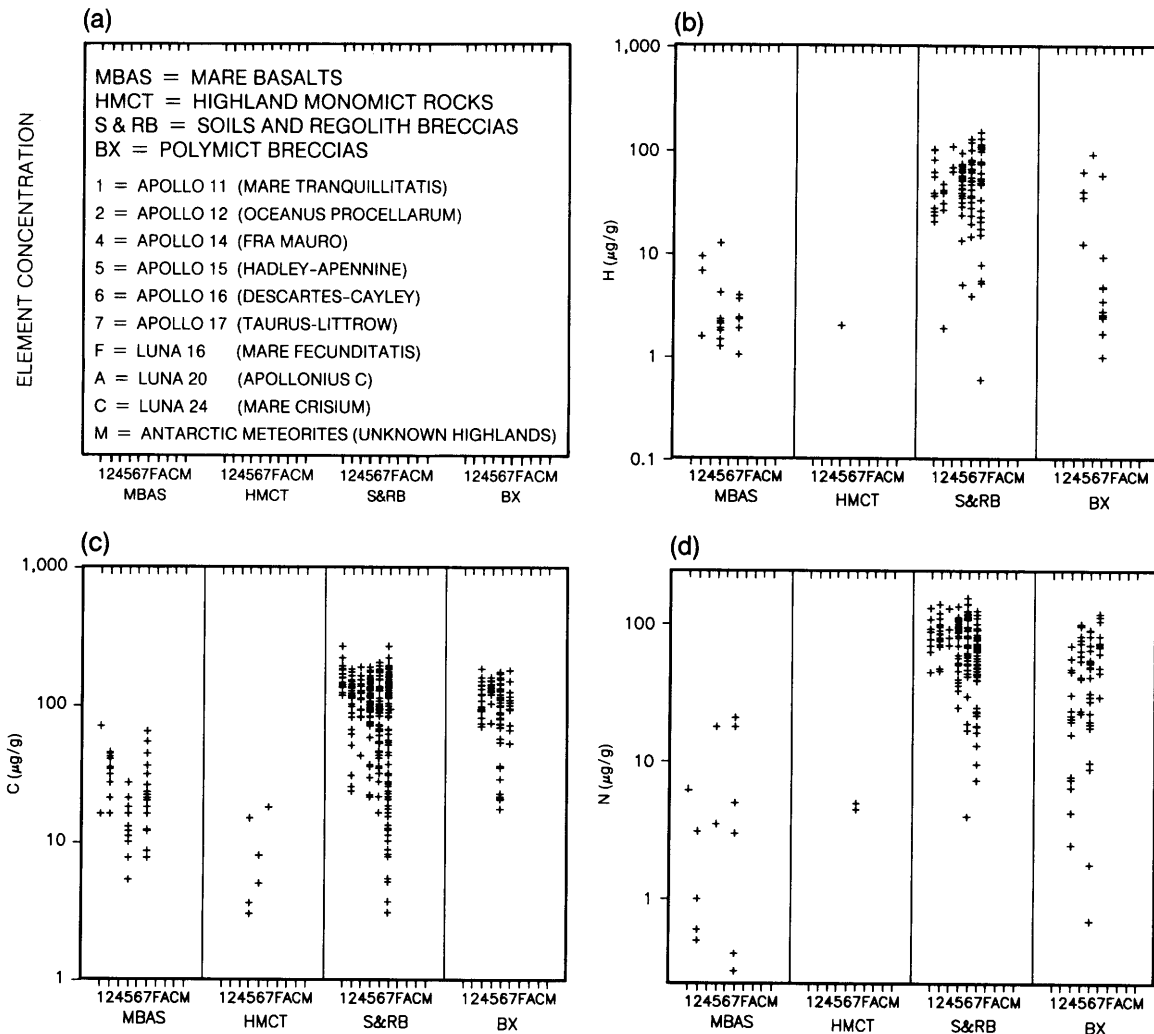


Fig. 8.39. Concentration ranges of solar-wind-implanted biogenic elements (H, C, and N) in various lunar materials: mare basalts (MBAS), highland monomict rocks (HMCT), soils and regolith breccias (S&RB), and polymict breccias (BX). Horizontal axis shows sample types, separated according to individual missions. Vertical axis shows elemental concentrations (in $\mu\text{g/g}$). (a) Graphical key to the plots and abbreviations. Data are presented for (b) hydrogen, H; (c) carbon, C; (d) nitrogen, N. Values generally range between 1 and 100 $\mu\text{g/g}$. Statistical summaries for most of these plots are provided in Table A8.6.

the lower values were included in Fig. 8.39. For other soil samples, some values that include contaminating terrestrial H, C, and N were undoubtedly retained. (This problem is even more serious among the breccias, for which few duplicate analyses are available. In fact, for many breccias, true duplication of an analysis is impossible because of the small-scale heterogeneity within breccias.)

The H concentrations in most mature soils are about 50 $\mu\text{g/g}$, and N concentrations are about the

same (Figs. 8.39b,d). Some soils may have concentrations of C exceeding 100 $\mu\text{g/g}$ (Fig. 8.39c) and comparable N concentrations. Similarly, some breccias may have concentrations higher than 100 $\mu\text{g/g}$ for C or N, but such high values are open to question in view of the ease with which contamination can occur. In summary, despite an attempt to select the most accurate data, Fig. 8.39 probably contains some values for soils, and surely contains some for breccias, that are too high because of

terrestrial contamination.

In any case, concentrations of H, C, and N are uniformly low in all lunar materials. As with the vapor-mobilized elements and the noble gases, the biogenic elements are more abundant in lunar soils than in lunar rocks. In fact, many soils and some breccias that contain former soils have H, C, and N concentrations some 2 orders of magnitude higher than those of mare basalts and highland monomict rocks. However, some breccia fragments also have very low concentrations, indicating that they are either (1) fragments of mare basalts or of highland monomict rocks that are uncontaminated by solar wind or (2) impact-melt rocks that have been so thoroughly outgassed that they no longer contain volatile elements. It is not known how many of the breccia samples plotted in Fig. 8.39 contain a combination of solar-wind gas and terrestrial contaminants. The data for breccias are the least well screened against contamination of any group of samples.

Solar-wind contributions. The solar-wind origin for most of the H, C, and N found in lunar surface materials is well established. Therefore, the ratios of H, C, and N concentrations, especially in soils and breccias, should correspond to the ratios in the solar wind, much as in the case for the noble gases. Correlations between H, C, and N concentrations in lunar soils are shown in Figs. 8.40a,b. Although the elemental ratios in lunar soils are close to those in the solar wind, the data show substantial scatter. Some of this scatter may reflect analytical error, and some may reflect actual differences in the retentivity of different elements in the lunar soil, but much of the scatter probably reflects terrestrial contamination.

Soils from the Apollo 17 drill core (see section 7.4.3) have H concentrations that correlate reasonably well with He, and their H/He ratios are close to those of the solar wind (Stoerner *et al.*, 1974). In contrast, samples of soils from the Apollo 16 drill core (section 7.4.3) analyzed by the same investigators have H/He ratios a factor of 2 higher. The higher H/He ratios in these Apollo 16 soils presumably arise from preferential loss of He by diffusion. This process would occur to a lesser extent in the Apollo 17 samples, because they have higher proportions of the mineral ilmenite, which retains He better than other minerals.

In evaluating the accuracy of measured concentrations of H, C, and N in lunar soils and rocks, the occurrence of these elements in solar-wind proportions, together with strong mutual correlations between their concentrations in a suite of related samples, provide the best evidence that the measured quantities are true, uncontaminated lunar

concentrations. A good discussion of correlations between H, C, N, and He as related to a solar-wind source is given by Becker (1980); Fig. 8.40c shows the correlation between C and He. Thiemens and Clayton (1980) demonstrated, for soils from the Apollo 15 and 17 drill cores, that there is a good correlation between N concentrations and measures of soil maturity such as I_s/FeO (e.g., Housley *et al.*, 1973a,b; Morris, 1976) (Fig. 8.40d; see also Fig. 7.14f for N- I_s/FeO correlations in surface soils).

Meteoroid contributions of biogenic elements to the "lunar atmosphere." In addition to the major contributions of H, C, and N from the solar wind, appreciable amounts of water and carbonaceous materials have been introduced into the lunar environment by the impact of carbonaceous meteoroids, asteroids, and comets. Much of this material must have been vaporized by impact-produced heating and evaporated into space. Volatile materials such as water and light hydrocarbons, once released into the lunar atmosphere, undergo photoionization, and once ionized they are accelerated by the electrical fields associated with the solar wind. These ionized species become entrained in the flow of the solar wind and are either swept away into space, or accelerated toward the Moon and into the regolith, as discussed above (section 8.8.2). This process, combined with continued solar heating of the lunar surface and repeated gardening of the regolith, would cause most of the volatile materials introduced by impacting objects to be lost into space. Nevertheless, our direct exploration of the Moon is still limited, and it is possible that polar lunar craters with permanently shaded floors might contain substantial quantities of water and carbonaceous material that has been cold-trapped there from the temporary atmospheres that formed when comets, carbonaceous meteoroids, or other volatile-rich bodies collided with the Moon (e.g., Arnold, 1979; Hodges, 1980; Lanzerotti and Brown, 1981; see section 3.8).

Bibring *et al.* (1974a) considered the probability that C and its compounds, which had been released temporarily into the lunar atmosphere from any solid sources, could be reimplanted in the lunar soil. They concluded that such a source was negligible relative to the C from trapped solar wind.

Despite the possibility of reimplantation in the lunar regolith of volatile materials brought to the Moon in impacting objects, little if any actual contribution of H, C, or N to the lunar regolith from cometary or meteoritic sources can be confirmed. Epstein and Taylor (1973) and Wszolek *et al.* (1973) discussed meteoroid sources, and Gibson and Moore (1973b) suggested a cometary origin for C in Apollo 16 soil 61221 on the basis of gas-release

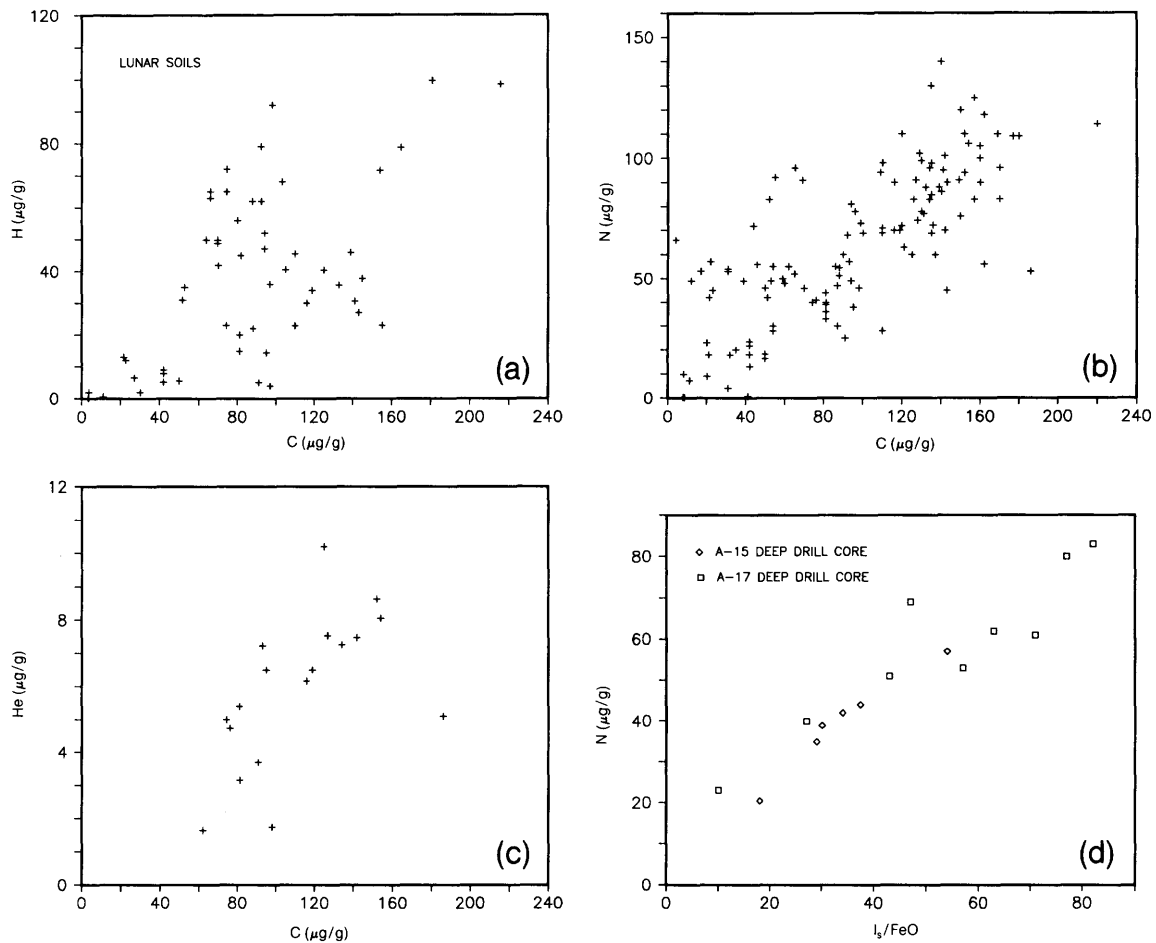


Fig. 8.40. Correlations between solar-wind-implanted biogenic elements (H-C and N-C), and relative to He (a solar-wind-implanted noble gas) and I_s/FeO (a measure of metallic Fe that is an index of soil maturity) in a range of lunar sample materials. **(a)** H vs. C; **(b)** N vs. C; **(c)** He vs. C; **(d)** N vs. I_s/FeO . Horizontal and vertical axes, both linear, show elemental concentrations (in $\mu\text{g/g}$, except I_s/FeO in arbitrary units). Although the H-C correlations **(a)** are poor, the N-C correlations **(b)** and He-C correlations **(c)** are better, indicating that the principal source for both the biogenic elements and He is the solar wind. Concentrations of these elements, especially N, correlate closely with indices of soil maturity, such as I_s/FeO , indicating (as would be expected) that solar-wind-implanted gases are more abundant in soils that have been exposed at the lunar surface for longer periods of time. Data for the N- I_s/FeO plot **(d)** are from *Thiemens and Clayton* (1980). Data points for the other elements are from the same dataset used in Fig. 8.39.

patterns. *Thiemens and Clayton* (1980), however, found no evidence to require any other source than the solar wind for lunar H, C, and N. They point out that soil 61221 actually has relatively low concentrations of solar-wind-implanted elements; it is not a mature soil, so its exposure on the lunar surface has not been long. They note that the special property of 61221 that makes it appear rich in H, C, and N is the ease with which its volatiles are released on pyrolysis. This characteristic may

actually be a consequence of the soil's immaturity, because the proportion of glassy, impact-produced agglutinates is so low that only a small fraction of the H, C, and N has been embedded in the more retentive glass. In soil 61221, these elements still reside near the boundaries of grains of mineral and lithic fragments, from which they are easily released during pyrolysis.

The most promising samples in which to look for higher concentrations of H, C, and N, either of

primordial lunar origin or from later meteoroid or cometary additions, may be the Apollo 16 breccias that have high contents of vapor-mobilized elements and that show signs of Fe oxides, e.g., "Rusty Rock" sample 66095 (see section 8.7.6). However, *Epstein and Taylor* (1974) concluded, on the basis of D/H ratios and the low temperatures of release for most of the H in samples of this rock (20% of the H released at 25°C, and nearly all by 200°C), that the H in sample 66095 comes from reaction of lunar chlorides (probably *lawrencite*, FeCl₂) with terrestrial water. The possibility that significant indigenous water is present in lunar materials is not improved by the very low O fugacities observed for lunar basalts (<10⁻¹⁵ to 10⁻¹²; *Sato et al.*, 1973), indicating the virtually total absence of water that would dissociate to produce O during their crystallization.

Various experiments show that the bulk of the H, C, and N in lunar soils is either located near the surfaces of rock and mineral grains or is rather uniformly distributed within agglutinates, in which many grains are embedded intact in a glassy matrix. *Des Marais et al.* (1975) indicate, from analyses on different grain size fractions, that about half the C in a typical soil is surface-correlated (i.e., enriched in the finer grain sizes), but a higher proportion is near the grain surfaces in immature soils. *Filler et al.* (1978) found about a third to half of the C to be in the outer 0.5 μm of grains. Stripping experiments, in which the outer portions of the grains are progressively dissolved (e.g., by HF leaching) and the released gases analyzed, confirm this proportion (e.g., *Becker et al.*, 1976).

To explain these results, *Warhant et al.* (1979) provided a model involving the production of traps within grains, combined with rates of surface erosion of grains by radiation damage, to account for the observed profiles of solar-wind-implanted elements as a function of depth within lunar soil grains. Those soil processes that are constructive (i.e., processes like agglutinate formation and shock lithification that produce larger particles from smaller ones) trap these elements within glassy agglutinates and lightly-heated breccias.

Many of the solar-wind-implanted elements trapped in lunar soil grains have reacted to form molecules, and these molecules have been partially characterized. Ions of H, C, and N in the incoming solar wind are implanted in lunar soil grains with kinetic energies that significantly exceed the energies typical of chemical reactions. The kinetic energies of the incoming ions disrupt the crystal structure in the vicinity of the implanted ions and enable the ions to react aggressively with the O in the crystal lattice.

Pyrolysis of lunar soils releases CO, CO₂, H₂O, and other, less abundant species (e.g., *Simoneit et al.*,

1973). Nitrogen is released as N₂ gas; any N oxides present before analysis are probably destroyed during pyrolysis. The products of pyrolysis of lunar soils appear over a range of temperatures, but most of the H, C, and N compounds are removed at temperatures in the vicinity of 700°C or higher (e.g., *Simoneit et al.*, 1973), and complete melting of the soils is required to extract a substantial high-temperature fraction.

Despite the tendency of H, C, and N molecular species to be released only at high temperatures during pyrolysis, much additional information about them has been obtained at lower temperatures, especially in experiments that involve crushing, grinding, and leaching. Only a small fraction of these compounds is released on crushing of the samples (e.g., *Gibson and Andrawes*, 1978b). *Graham et al.* (1979) showed that grinding of a basalt in air results in strong adsorption of N₂ and CO₂ from air onto the pulverized basalt, and they demonstrated that these adsorbed gases are released at high temperatures (principally in two releases, at ~700°C and 1050°C) that are comparable to the temperatures required for release of the same gases from mature lunar soils. Leaching of soils with deuterated acid produces small amounts of C₂H₂, CH₄, HCN, and their deuterated counterparts, as well as CO₂ and N₂. *Bibring et al.* (1974b) implanted D, C, and N ions into feldspar grains and were able to simulate many of the thermal release and leaching patterns of lunar soils. *Pillinger et al.* (1974) argued that their leaching and hydrolysis patterns indicated the presence of C in the form of carbide.

Because D is converted to ³He by nuclear reactions in stars, the original D in the sun has been largely consumed. As a result, the D/H ratio in the solar wind is so low that any D released from lunar samples must come from some other source (e.g., *Epstein and Taylor*, 1970; *Hintenberger et al.*, 1970). Small amounts of D not associated with terrestrial contamination and released at high temperature have been definitely identified in lunar rocks. This D may have been produced in the rocks by cosmic-ray-induced spallation.

Solar nitrogen anomalies. *Thiemens and Clayton* (1980) found that the old, immature soils in the Apollo 17 deep-drill core have ¹⁵N/¹⁴N ratios some 7% lower than that of the present terrestrial atmosphere, while the young, mature soils have values closely approaching the terrestrial value. Such isotopic anomalies for N have been tentatively interpreted as the result of a secular increase in the ¹⁵N/¹⁴N ratio of solar-wind N (e.g., *Kerridge*, 1980; *Clayton and Thiemens*, 1980; see also *Becker*, 1980) (see also section 7.7.2, where evidence for an ~15%/b.y. increase in ¹⁵N/¹⁴N ratio is summarized).

8.8.4. Solar-Wind-Implanted Elements as Lunar Resources

Concentrations of H, noble gases, N, and C, are extremely low, usually <100 µg/g, in lunar soils. However, with only moderate heating (up to 700°C), the cumulate amounts of these gases in mature soils are adequate to generate pressures of up to 10 atm; most of this evolved gas would be H₂. Such high gas pressures would facilitate extraction of the gases from the soil, thus compensating to some extent for the large quantities of soil that would have to be heated to obtain significant amounts of gas.

Such gas extraction on the Moon might prove economical if it could produce H₂ with a high enough efficiency to be used as a rocket fuel, principally for near-Earth space activities. Such a use would be even more efficient if the H₂ could be combined with lunar-produced O₂. Oxygen is abundant in combined form in all lunar rocks and soils, from which it might be extracted by several processes (see section A11.2.5). An additional use of lunar-derived H₂ and O₂ would be in life support (water and oxygen) for long-term human activities on the Moon.

A relatively fine-grained fraction of any lunar soil, perhaps an ilmenite-rich one, would be the best ore for solar-wind-implanted elements. However, the extra cost of separating individual size fractions from

the already fine-grained and highly cohesive (section 9.1.7) lunar soil might offset the advantage obtained by enriching the soil feedstock.

Recently, an intriguing proposal has been made to mine lunar ³He from the regolith for use as fuel in power-generating fusion reactors on Earth (*Wittenberg et al.*, 1987). Helium-3 has several advantages over tritium (³H; the commonly considered fuel) for large-scale energy production by fusion. In the standard ³H fusion schemes, a byproduct of the power-generating fusion reaction is abundant high-energy neutrons, which can cause extensive radiation damage to the fusion reactors. In contrast, very few neutrons are produced by the ³He reaction, in which high-energy protons are generated rather than neutrons. These protons create no long-term radioactivity from the containment system. In addition, ³H itself is radioactive and therefore a health hazard. Helium-3 is not.

Unfortunately, most of the He available on Earth is ⁴He that has been produced by radioactive decay, and the amount of ³He available from terrestrial resources is meager. In contrast, the quantities of ³He in the upper meter of the lunar regolith, where it has been introduced by the solar wind for billions of years, are sufficient to supply the energy needs of the Earth for hundreds of years.

APPENDIX: STATISTICAL SUMMARIES OF LUNAR CHEMISTRY

TABLE A8.1. Statistical data for concentrations of major elements (values in weight percent) (see section 8.3, Fig. 8.2).

	SiO ₂	TiO ₂	Al ₂ O ₃	FeO	MgO	CaO	Na ₂ O
Apollo 11 MBAS							
N	11	11	11	11	11	11	11
Average	40.46	10.41	10.08	19.22	7.01	11.54	0.38
Std. dev.	1.37	1.02	0.84	1.28	0.87	0.82	0.04
Minimum	38.59	8.47	7.91	16.51	5.91	10.30	0.34
Maximum	42.89	11.87	10.87	21.71	8.52	12.65	0.44
Apollo 12 MBAS							
N	20	20	20	20	20	20	20
Average	44.88	3.62	8.93	20.48	10.64	9.81	0.25
Std. dev.	1.76	0.87	1.78	1.38	3.99	1.66	0.05
Minimum	41.56	2.59	5.30	16.78	5.75	6.31	0.16
Maximum	47.27	5.20	12.63	22.64	19.97	12.25	0.33
Apollo 15 MBAS							
N	9	14	14	14	15	14	15
Average	46.68	1.97	10.21	19.87	8.76	10.63	0.30
Std. dev.	1.53	0.39	1.64	2.05	1.17	0.49	0.06
Minimum	45.02	1.28	8.77	15.30	6.45	9.89	0.21
Maximum	48.10	2.51	13.70	22.52	10.60	11.50	0.39
Apollo 17 MBAS							
N	19	26	25	25	25	26	26
Average	39.03	11.94	9.00	18.82	8.54	10.82	0.39
Std. dev.	1.03	1.11	0.78	0.73	1.13	0.59	0.03
Minimum	37.93	8.30	8.38	16.60	6.15	9.79	0.35
Maximum	41.92	13.08	12.10	19.90	10.36	12.15	0.48
Luna 16 MBAS							
N	3	6	6	9	6	9	9
Average	44.0	4.77	13.83	18.7	6.40	11.82	0.53
Std. dev.	1.4	0.49	0.81	0.7	0.51	0.81	0.13
Minimum	42.8	4.0	13.3	17.8	5.95	10.4	0.28
Maximum	45.5	5.3	15.4	19.9	7.05	13.0	0.70
Luna 24 MBAS							
N	2	6	6	7	6	6	7
Average	46.00	1.02	12.20	21.58	7.40	12.20	0.23
Std. dev.		0.19	1.30	0.87	1.60	0.90	0.06
Minimum	45.20	0.75	10.10	20.46	6.00	10.80	0.10
Maximum	46.80	1.30	13.80	22.40	10.50	13.50	0.29
Anorthosite							
N	3	7	12	21	13	21	21
Average	45.57	0.08	33.4	1.00	1.21	19.1	0.40
Std. dev.	0.66	0.07	1.6	1.1	1.20	1.1	0.06
Minimum	45	0.01	31	0.16	0.05	16.9	0.26
Maximum	46	0.23	36	4.0	3.7	21	0.54
Norite							
N	11	17	23	23	23	24	24
Average	50.6	0.30	17.0	8.2	12.5	9.9	0.38
Std. dev.	1.6	0.02	3.1	2.5	2.1	1.5	0.05
Minimum	47.7	0.27	15	3.9	10.2	8.8	0.32
Maximum	52	0.33	23	10.7	15.9	12.8	0.44
Troctolite							
N	2	8	11	12	11	12	12
Average	43.5	0.18	24.0	4.1	15.1	13.4	0.37
Std. dev.		0.22	4.3	1.7	6.4	2.0	0.09
Minimum	42.9	0.04	15.02	2.26	8.3	9.2	0.20
Maximum	44.1	0.69	28.7	8.55	30.5	16	0.47

TABLE A8.1. (continued).

	SiO ₂	TiO ₂	Al ₂ O ₃	FeO	MgO	CaO	Na ₂ O
Apollo 11 S&RB							
N	8	13	13	13	13	13	13
Average	41.99	7.94	12.58	16.40	7.93	11.74	0.47
Std. dev.	0.31	0.62	0.80	0.79	0.17	0.25	0.03
Minimum	41.50	7.17	11.47	15.41	7.67	11.34	0.40
Maximum	42.43	9.17	13.77	17.74	8.33	12.12	0.53
Apollo 12 S&RB							
N	3	3	3	3	3	3	3
Average	46.21	2.61	12.13	17.19	10.42	9.85	0.41
Std. dev.	0.12	0.10	0.86	1.07	1.07	1.14	0.03
Minimum	46.07	2.50	11.14	16.33	9.73	8.54	0.37
Maximum	46.29	2.67	12.69	18.39	11.65	10.64	0.43
Apollo 15 S&RB							
N	12	14	14	14	14	14	14
Average	47.19	1.46	14.32	14.98	10.95	10.47	0.40
Std. dev.	0.74	0.34	2.62	3.30	0.53	0.96	0.07
Minimum	46.50	1.00	9.86	11.55	9.80	8.96	0.30
Maximum	48.43	2.17	17.91	20.70	11.67	11.76	0.50
Apollo 16 S&RB							
N	8	18	19	19	19	19	19
Average	44.89	0.53	27.23	4.98	6.00	14.56	0.47
Std. dev.	0.51	0.14	1.84	1.08	1.76	3.64	0.08
Minimum	44.10	0.26	23.04	2.91	3.97	4.54	0.30
Maximum	45.80	0.78	30.22	7.73	10.32	17.00	0.72
Apollo 17 S&RB							
N	15	16	16	16	16	16	16
Average	44.47	2.84	18.93	10.29	9.95	12.29	0.43
Std. dev.	1.41	2.01	2.89	2.67	0.30	0.61	0.03
Minimum	41.57	1.22	12.43	7.95	9.32	11.06	0.37
Maximum	46.07	7.35	21.38	15.94	10.55	13.16	0.48
Luna 16 S&RB							
N	3	3	3	3	1	3	3
Average	44.37	3.30	15.68	16.75	8.78	11.50	0.35
Std. dev.	2.93	0.10	0.34	0.09		0.86	0.02
Minimum	41.70	3.20	15.33	16.64		11.00	0.34
Maximum	47.50	3.39	16.00	16.80		12.49	0.37
Luna 20 S&RB							
N	3	5	5	5	4	5	5
Average	45.2	0.50	22.75	7.46	9.69	14.70	0.39
Std. dev.	0.72	0.06	0.69	0.47	0.35	0.93	0.11
Minimum	44.4	0.43	21.6	7.02	9.19	13.38	0.29
Maximum	45.8	0.56	23.44	8.1	10	15.8	0.55
Luna 24 S&RB							
N	1	5	6	6	6	6	6
Average	45.40	1.04	11.95	19.55	9.87	11.07	0.28
Std. dev.		0.15	0.43	0.62	0.43	0.25	0.01
Minimum		0.80	11.10	18.70	9.00	10.80	0.27
Maximum		1.20	12.30	20.50	10.20	11.40	0.30
AMET S&RB							
N	1	7	7	8	6	8	8
Average	46.50	0.28	25.69	5.72	7.67	15.13	0.32
Std. dev.		0.05	0.68	0.38	0.98	0.38	0.01
Minimum		0.23	25.10	5.40	6.00	14.80	0.30
Maximum		0.37	26.60	6.50	8.80	16.00	0.33

TABLE A8.1. (continued).

	SiO ₂	TiO ₂	Al ₂ O ₃	FeO	MgO	CaO	Na ₂ O
Apollo 14 BX							
N	1	10	15	16	10	15	16
Average	48.09	1.51	16.72	9.53	10.18	10.67	0.73
Std. dev.		0.23	6.04	2.69	2.88	2.64	0.13
Minimum		1.03	10.50	0.43	2.08	9.00	0.48
Maximum		1.80	35.20	11.50	11.70	19.10	0.98
Apollo 15 BX							
N		8	8	8	8	8	8
Average		1.68	13.96	14.04	10.25	12.78	0.46
Std. dev.		0.32	2.26	2.77	0.95	3.39	0.11
Minimum		1.16	9.90	11.10	9.20	10.30	0.25
Maximum		2.05	16.20	19.20	11.60	19.20	0.60
Apollo 16 BX							
N	13	26	32	41	32	41	41
Average	45.48	0.64	25.11	5.08	7.24	15.14	0.45
Std. dev.	1.35	0.45	5.01	2.84	3.24	2.72	0.08
Minimum	43.60	0.20	13.90	1.29	1.94	8.50	0.31
Maximum	49.20	2.15	33.80	13.35	13.00	18.90	0.68
Apollo 17 BX							
N	7	10	10	10	10	10	10
Average	45.21	2.23	17.82	9.80	11.55	11.42	0.53
Std. dev.	2.14	2.47	2.99	3.22	2.20	0.84	0.10
Minimum	41.79	0.65	12.26	7.30	8.80	9.72	0.41
Maximum	46.80	7.98	20.82	16.50	16.72	12.56	0.69
Luna 20 BX							
N		19	19	27	19	23	24
Average		0.49	23.18	7.11	10.46	13.75	0.42
Std. dev.		0.22	2.78	2.05	3.24	2.25	0.20
Minimum		0.20	19.50	3.80	3.10	6.70	0.25
Maximum		0.90	30.00	13.30	16.20	19.20	1.32

Note that standard deviations are not given for those categories where the number of analyses (N) is <3. N = number of analyses, Std. dev. = standard deviation, MBAS = mare basalts, S&RB = soils and regolith breccias, BX = polymict breccias, AMET = Antarctic lunar meteorites. Highland monomict rocks (HMCT in Fig. 8.2) are listed by individual rock type name (anorthosite, norite, and troctolite; see section 6.3).

References: *Blanchard et al.* (1974, 1975a, 1978); *Compston et al.* (1972a); *Dymek et al.* (1975a,b); *Gillum et al.* (1972); *Haskin et al.* (1973, 1974, 1981); *Helmke et al.* (1973); *Hubbard et al.* (1973); *James et al.* (1984); *Jerome and Phillipot* (1973); *Kallemeyn and Warren* (1983); *Korotev* (1981); *Korotev et al.* (1983); *Laul and Schmitt* (1973a,b); *Laul et al.* (1977, 1983); *M. Lindstrom* (1984); *M. Lindstrom et al.* (1984, 1986); *Lunatic Asylum* (1970); *Ma et al.* (1977); *D. S. McKay et al.* (1986); *Nava and Philpotts* (1973); *Ostertag et al.* (1986); *Palme et al.* (1978, 1983); *Rhodes and Blanchard* (1980, 1981); *Rhodes and Hubbard* (1973); *Rhodes et al.* (1974, 1976, 1977); *Ryder and Norman* (1978, 1979); *Shervais et al.* (1985a,b); *Vinogradov* (1971, 1973); *Wänke et al.* (1970a, 1971, 1972, 1973, 1974, 1975, 1976, 1977); *Warren and Kallemeyn* (1986); *Warren and Wasson* (1979b, 1980); *Winzer et al.* (1974).

TABLE A8.2. Statistical data for concentrations of incompatible trace elements (values are in $\mu\text{g/g}$) (see section 8.4, Fig. 8.7).

	Li	Be	K	Rb	Y	Zr	Nb	Sn	Cs	Ba	La	Ce	Nd	Sm	Eu
Apollo 11 MBAS															
N	2	1	15	16	8				7	3	14	14		14	14
Average	18.5	0.9			123					232				15.5	2.03
Std. dev.					27					24				3.8	0.34
Minimum	14		500	0.6	87				26	208	7.3	25		8.9	1.48
Maximum	23		2500	6.0	166				200	260	25	79		21	2.7
Apollo 12 MBAS															
N	8	18	37	36	41	29	32	5	12	31	11	31	7	39	32
Average	7.0		540			119				70	6.8	18.9	15.7	5.3	1.09
Std. dev.	2.4		100			24				22	1.9	4.5	3.9	1.3	0.30
Minimum	4.5	0.65	330	0.29	28	66	4	0.10	13	35	4.8	10.2	11.9	3.0	0.62
Maximum	10.6	3.3	830	6.0	168	186	29	0.39	100	140	12.1	32	24	9.4	2.1
Apollo 14 MBAS															
N			1	3			1	1	1	1	3	3	3	4	3
Average			912	1.83			9.9	0.3	90	146	10.8	30	19.0	5.3	1.11
Std. dev.				0.54							3.5	10	5.2	1.4	0.20
Minimum				1.21							6.7	17.9	13	3.9	0.88
Maximum				2.2							13	36	22	6.6	1.23
Apollo 15 MBAS															
N	8	3	23	26	16	17	10	1	11	23	20	23	7	24	23
Average	6.38	1.2	409	0.76	25.9		5.41	0.19					12.2	4.0	0.99
Std. dev.	0.73	0.2	131	0.19	2.8		0.75						2.3	1.1	0.13
Minimum	5.6	1	249	0.39	21	64	4.3		26	47	4.8	13.9	9.9	3.3	0.87
Maximum	7.8	1.4	810	1.15	29	290	6.2		140	220	18.4	51	16.3	8.5	1.31
Apollo 17 MBAS															
N	35	2	39	43	9	22	7		9	42	42	42	16	42	42
Average	9.3	2.7	440		81	250	20.5			74	6.3	21.2	21.5	9.3	1.89
Std. dev.	1.2		120		15	77	2.8			13	1.3	4.1	4.6	1.8	0.29
Minimum	7.1	1.5	250	0.30	58	176	17.4		13	46	4.0	11.3	13.2	5.7	1.37
Maximum	13.3	3.8	740	1.34	105	540	24		61	105	11.4	35	32	13.6	2.6

TABLE A8.2. (continued).

	Li	Be	K	Rb	Y	Zr	Nb	Sn	Cs	Ba	La	Ce	Nd	Sm	Eu
Luna 16 MBAS															
N	9		14	9	1	1			1	14	8	13	11	13	13
Average	10.3		970	1.65	58	300			54	230	15.8	43	34.1	11.0	2.85
Std. dev.	2.0		310	0.49						84	5.0	14	9.4	3.4	0.96
Minimum	8.8		530	0.5						62	4.6	12.8	11	3.1	0.78
Maximum	15.1		1410	2.1						470	20	66	48	16	4.0
Luna 24 MBAS															
N						1				2	5	3		5	5
Average						50				45	1.97	6.6		1.62	0.65
Std. dev.											0.63	1.7		0.37	0.10
Minimum										40	1.1	5.5		1.2	0.58
Maximum										50	2.87	8.6		2.1	0.83
Anorthosite															
N			9	7		4	4	3	6	11	13	11		13	13
Average			123				2.65					0.73			0.87
Std. dev.			33				0.69					0.24			0.22
Minimum			58	0.017		15	1.87	0.1	2	4.8	0.12	0.33		0.04	0.59
Maximum			160	0.9		48	3.5	0.15	30	21	0.58	1.1		0.22	1.18
Norite															
N	1		13	1		6				10	11	13	5	13	13
Average	12.3			3.54											1.10
Std. dev.															0.29
Minimum			140			49				32	1.47	4.3	5.4	0.87	0.68
Maximum			1830			480				420	21	53	16.8	9.2	1.75
Troctolite															
N	1		12	2		7	1		1	13	13	13	4	14	13
Average	3		520	0.220			3.2		14						
Std. dev.			160												
Minimum			250	0.2		23.6				33	1.51	3.8	2.3	0.61	0.73
Maximum			830	0.24		350				630	33.2	82	52	13.8	2.72

TABLE A8.2. (continued).

	Li	Be	K	Rb	Y	Zr	Nb	Sn	Cs	Ba	La	Ce	Nd	Sm	Eu
Apollo 11 S&RB															
N	6	2	16	19	10	10	10		9	12	16	16	2	16	16
Average	11.4	1.90	1370	3.80	110	330	20.1		130	220	18.0	55.2	54	13.8	1.71
Std. dev.	1.5		210	0.82	10	28	1.7		27	30	2.3	8.5		1.5	0.08
Minimum	10.4	1.6	1080	3	97	290	18		96	176	14.9	45	47	11.6	1.6
Maximum	13.3	2.2	1800	6.6	131	390	23		186	280	24	72	60	17.6	1.9
Apollo 12 S&RB															
N	1	17	6	27	19	9	11	1	16	4	4	3	2	3	4
Average	12		2100		128	560	21.5	0.3	310	360	30.7	87	67.0	15.1	1.89
Std. dev.			470		42	134	5.1		114	120	4.2	1		0.40	0.36
Minimum		1.6	1700	0.32	81	410	14		23	190	24	86	62	14.7	1.57
Maximum		8	3010	23	245	790	31		530	460	33	88	72	15.5	2.4
Apollo 14 S&RB															
N	1	7	2	10	8	6	4	1	10	1	3	3	3	7	3
Average	14	6.6	3500	16.5	267	810	43.0	0.4	660	780	68.1	170	117	28.7	2.43
Std. dev.		1.0		3.0	29	100	4.7		74		2.2	12	15	4.1	0.14
Minimum		5.1	3300	13.5	220	640	36		570		66	157	101	23	2.3
Maximum		8	3700	23	300	930	46		790		70	180	130	36	2.6
Apollo 15 S&RB															
N	1	8	14	23	9	9	12	5	25	3	14	10	9	23	14
Average	16.6	3.4	1300	3.8	84	320			170		21.1	61	51		1.27
Std. dev.		1.0	360	1.2	15	68			62		6.7	16	29		0.19
Minimum		1.7	720	0.46	69	240	1.5	0.24	24	120	11.6	35	33	0.76	1.03
Maximum		5.3	1920	6.3	115	470	35	0.6	300	380	34	94	124	15.1	1.58
Apollo 16 S&RB															
N	2	7	17	19	23	25	15	5	17	19	19	19	9	26	19
Average	5.7		800		38	160	11.8	0.11	107	115		30			1.23
Std. dev.			200		12	66	3.3	0.03	33	44		13			0.13
Minimum	4.5	1.1	380	1.2	8.9	46	3.8	0.07	54	56	3.0	7.7	8	1.28	0.99
Maximum	6.9	6.9	1120	6	60.5	310	15.6	0.15	170	220	22	55	33	9.8	1.60

TABLE A8.2. (continued).

	Li	Be	K	Rb	Y	Zr	Nb	Sn	Cs	Ba	La	Ce	Nd	Sm	Eu
Apollo 17 S&RB															
N	5	15	17	16	29	29	12		16	14	17	17	3	17	17
Average	11.2	1.69	1050		60	230	14.9		119	158	13.6	34.9	25.0	7.48	1.38
Std. dev.	2.8	0.28	220		12	48	1.6		58	35	3.6	7.9	7.9	0.68	0.18
Minimum	8.4	1.3	630	0.76	44	133	13		37	97	6.5	18	16	6.3	1.21
Maximum	15	2.2	1360	4.8	91	350	18		200	210	17.6	47	31	8.7	1.83
Luna 16 S&RB															
N	3		9	11	1	3			4	8	4	7	6	9	9
Average	8.9		920	2.2	17.3	270			75.0	167	12.08	34.3	25.7	8.29	2.26
Std. dev.	1.0		81	1.3		70			8.1	25	0.65	4.1	1.3	0.75	0.25
Minimum	8.3		830	1.4		220			68	114	11.2	31	24	7.3	1.99
Maximum	10		1080	5.9		350			82	200	12.7	43	27	9.6	2.9
Luna 20 S&RB															
N			1	2					3		3	3	2	3	3
Average			630	1.60							6.43	17.4	10.80	3.177	0.94
Std. dev.											0.25	2.5		0.068	0.02
Minimum				1.5					50		6.2	15.8	10.5	3.1	0.92
Maximum				1.7					140		6.7	20	11.1	3.2	0.96
Luna 24 S&RB															
N			6			5				4	6	6	5	6	6
Average			238			56.0				36	2.91	8.02	6.44	1.96	0.642
Std. dev.			11			8.9				10	0.17	0.47	0.38	0.12	0.031
Minimum			220			50				25	2.7	7.5	6	1.83	0.59
Maximum			250			70				45	3.2	8.6	7	2.1	0.67
AMET S&RB															
N			8	7		8			11	9	9	9	9	9	9
Average			219			29.0				29.9	2.21	5.6	3.48	1.05	0.719
Std. dev.			39			7.6				5.7	0.49	1.5	0.81	0.24	0.040
Minimum			168	0.34		19			14	22	1.71	4.1	2.8	0.79	0.66
Maximum			290	2.7		45			220	39	3.2	8.8	5.2	1.56	0.78

TABLE A8.2. (continued).

	Li	Be	K	Rb	Y	Zr	Nb	Sn	Cs	Ba	La	Ce	Nd	Sm	Eu
Apollo 14 BX															
N	10	20	25	29	18	26	8	1	25	24	29	28	22	32	29
Average	36.8				227			0.2		850					
Std. dev.	8.9				72					280					
Minimum	25.8	2.2	390	2.7	94	260	20		140	160	18.7	50	32	9	1.2
Maximum	56	12	7900	31	340	2100	82		2000	1300	520	1460	1030	260	7.5
Apollo 15 BX															
N	10	10	15	28	12	16	18	9	28	15	9	9	7	20	9
Average															1.34
Std. dev.															0.33
Minimum	2.2	0.8	270	0.03	27	40	0.43	0.09	8	26	5.9	18	11.1	0.43	0.76
Maximum	29	7.6	4600	114	176	740	48	0.27	1400	1640	47	130	47	20	1.81
Apollo 16 BX															
N	3	6	18	54	15	19	14	2	55	17	18	18	13	24	18
Average	7.0														
Std. dev.	1.6														
Minimum	5.6	0.9	80	0.043	4.4	17	1.3	0.15	8.1	40	0.99	3.7	7.7	0.08	0.84
Maximum	8.7	6.7	17500	45	140	2100	58	0.4	2100	2500	280	730	460	127	6.6
Apollo 17 BX															
N	9	1	13	20	7	10	6		23	12	13	13	8	13	13
Average		1.2			77		23.7								1.56
Std. dev.					27		6.7								0.32
Minimum	7.5		450	0.84	39	162	12.6		42	92	3.4	9	16	1.67	0.93
Maximum	25		2700	11.3	112	570	32		480	400	41	109	65	18.1	1.99
Luna 20 BX															
N	5	3	8	1		4			1	4	10	11	3	11	11
Average	4.5			1.7		60			140	50					0.89
Std. dev.	1.4					15				13					0.28
Minimum	3.4	0.2	106			44				38	7	4.7	11.2	0.8	0.54
Maximum	6.6	1.6	1740			75				67	21.4	53	30	10.1	1.41

TABLE A8.2. (continued).

	Gd	Tb	Dy	Yb	Lu	Hf	Ta	W	Th	U
Apollo 11 MBAS										
N		14		14	14	14	14	3	13	9
Average		3.50		12.8	1.84	12.0	2.14	0.36		
Std. dev.		0.95		3.0	0.36	3.3	0.35	0.10		
Minimum		2.1		8.1	1.22	6.8	1.4	0.24	0.7	0.156
Maximum		5		16.8	2.4	16.9	2.7	0.43	3.9	0.87
Apollo 12 MBAS										
N	7	25	14	34	34	25	7	4	5	12
Average	7.4	1.37	8.3	4.3	0.63	4.2	0.430	0.140	0.91	0.252
Std. dev.	1.5	0.42	1.8	0.9	0.13	1.0	0.062	0.014	0.21	0.061
Minimum	5.5	0.77	5.7	2.7	0.4	2.4	0.33	0.12	0.71	0.157
Maximum	9.3	2.6	10.6	6	0.89	6.4	0.51	0.15	1.28	0.36
Apollo 14 MBAS										
N	3	2	3	3	2	2		1		2
Average	7.1	1.30	9.2	5.4	0.75	8.4		0.2		0.60
Std. dev.	2.5		2.8	1.2						
Minimum	4.2	0.98	6	4.0	0.61	6.9				0.59
Maximum	8.6	1.62	11.1	6.1	0.89	9.8				0.60
Apollo 15 MBAS										
N	6	5	7	23	14	5	5		4	9
Average	5.4	1.09	5.63	2.78	0.38					0.154
Std. dev.	0.9	0.43	0.82	0.79	0.14					0.045
Minimum	4.5	0.79	4.7	2.2	0.31	2.3	0.31		0.42	0.085
Maximum	6.8	1.85	7.3	6.0	0.86	6.5	0.88		2.6	0.24
Apollo 17 MBAS										
N	17	8	17	42	25	25	8	1	6	24
Average	13.6	2.54	15.9	9.1	1.33	8.6	1.63	0.06		0.123
Std. dev.	2.7	0.60	3.1	1.5	0.21	1.2	0.23			0.022
Minimum	9.0	1.8	10.7	6.0	0.95	6.3	1.25		0.198	0.06
Maximum	19.6	3.8	23	13.2	1.88	11.2	2.0		0.68	0.16
Luna 16 MBAS										
N		7	7	14	13	8	5		5	4
Average		2.3	13.7	7.9	1.07					
Std. dev.		0.7	4.5	3.0	0.34					
Minimum		0.72	8.8	3.3	0.50	0.46	0.29		0.37	0.03
Maximum		3.1	21	13.9	1.8	11.8	1.2		2.4	0.3

TABLE A8.2. (continued).

	Gd	Tb	Dy	Yb	Lu	Hf	Ta	W	Th	U
Luna 24 MBAS										
N		3		5	5	5	4		2	
Average				1.734	0.234	1.08	0.143		0.2	
Std. dev.				0.34	0.069	0.20	0.067			
Minimum		0.34		1.22	0.15	0.9	0.1		0.2	
Maximum		2.9		2.0	0.31	1.4	0.24		0.2	
Anorthosite										
N	1	6	3	13	13	9	2		1	5
Average	0.3						0.043		0.04	
Std. dev.										
Minimum		0.007	0.054	0.026	0.004	0.0064	0.011			0.001
Maximum		0.047	0.33	0.25	0.04	0.49	0.074			0.0052
Norite										
N	1	11	2	13	13	11	10		10	7
Average	6.6		4.7							
Std. dev.										
Minimum		0.22	2.3	0.98	0.13	0.53	0.086		0.17	0.15
Maximum		2.0	7.1	7.7	1.01	10.7	2.5		4.4	1.6
Troctolite										
N	1	12	3	13	13	13	10	1	12	11
Average	0.73							0.1		
Std. dev.										
Minimum		0.13	0.8	0.44	0.051	0.25	0.031		0.17	0.0194
Maximum		2.6	15.7	8.4	1.19	5.9	0.57		3.7	0.78
Apollo 11 S&RB										
N	1	16	1	16	16	15	16	2	13	5
Average	18	3.21	17	10.8	1.59	11.6	1.59	0.22	2.34	0.52
Std. dev.		0.62		1.3	0.19	1.6	0.20		0.72	0.16
Minimum		2.5		8.3	1.3	9.2	1.3	0.22	1.5	0.35
Maximum		4.2		13.4	2.0	14	1.9	0.22	3.7	0.67
Apollo 12 S&RB										
N	3	4	3	4	4	4	4	3	4	6
Average	17.0	3.60	20.2	10.7	1.54	12.8	1.35	0.61	5.2	1.68
Std. dev.	2.1	0.36	2.4	1.4	0.16	2.1	0.22	0.15	1.2	0.62
Minimum	15.7	3.2	17.8	8.9	1.35	10.9	1.04	0.45	3.52	0.82
Maximum	19.4	4	23	12.4	1.74	15.6	1.5	0.74	6.3	2.7

TABLE A8.2. (continued).

	Gd	Tb	Dy	Yb	Lu	Hf	Ta	W	Th	U
Apollo 14 S&RB										
N	3	3	3	3	3	3	2	4	2	5
Average	35	6.43	41.0	23.2	2.85	22	3.00	0.68	15.1	3.46
Std. dev.	1	0.15	3.5	1.6	0.27	1		0.17		0.58
Minimum	34	6.3	38	22	2.7	21	2.8	0.5	14.3	2.5
Maximum	36	6.6	45	25	3.2	23	3.2	0.9	15.9	4.07
Apollo 15 S&RB										
N	2	12	14	13	14	14	14	5	3	7
Average	15.6	2.10	13.0	6.6	0.98	7.1	0.90			
Std. dev.		0.47	3.6	1.7	0.25	2.2	0.32			
Minimum	12.6	1.6	8	3.9	0.67	3.9	0.46	0.14	1.8	0.12
Maximum	18.7	3.3	18.3	9.2	1.54	11.8	1.55	0.68	4.9	1.43
Apollo 16 S&RB										
N	4	19	11	19	19	19	19	4	17	27
Average			7.2							
Std. dev.			2.7							
Minimum	2.8	0.29	2.5	0.98	0.141	0.81	0.14	0.074	0.43	0.13
Maximum	12.1	2.1	13.3	6.8	0.9	7.3	1.02	0.56	3.7	0.92
Apollo 17 S&RB										
N	5	17	12	17	17	17	17	4	13	28
Average	10.1	1.68	10.7	5.81	0.83	5.76	0.88		2.44	
Std. dev.	0.9	0.13	1.3	0.66	0.10	0.50	0.19		0.56	
Minimum	9.1	1.5	9.5	4.2	0.58	4.9	0.68	0.083	1.12	0.139
Maximum	11.1	1.9	14	7.3	1.02	6.5	1.3	0.3	3.2	1.05
Luna 16 S&RB										
N	5	1	7	9	4	2				3
Average	10.6	1.9	10.8	5.69	0.901	9.4				0.360
Std. dev.	0.9		1.2	0.56	0.081					0.044
Minimum	9.6		9.8	5.0	0.82	5.9				0.31
Maximum	12		13.5	6.7	0.98	13				0.39
Luna 20 S&RB										
N	1	3	2	3	3	3	1		2	2
Average	4.4	0.657	4.25	2.42	0.383	2.5	0.3		0.975	0.325
Std. dev.		0.025		0.16	0.041	0.4				
Minimum		0.63	4	2.3	0.35	2.1			0.95	0.31
Maximum		0.68	4.5	2.6	0.43	2.9			1	0.34

TABLE A8.2. (continued).

	Gd	Tb	Dy	Yb	Lu	Hf	Ta	W	Th	U
Luna 24 S&RB										
N		6	5	6	6	6	3		6	
Average		0.438	2.94	1.68	0.250	1.40	0.233		0.40	
Std. dev.		0.032	0.17	0.07	0.017	0.13	0.057		0.09	
Minimum		0.41	2.8	1.6	0.23	1.3	0.2		0.3	
Maximum		0.49	3.2	1.8	0.28	1.6	0.3		0.5	
AMET S&RB										
N	4	9	7	9	9	9	9		9	16
Average	1.16	0.237	1.51	0.93	0.138	0.78	0.101		0.301	
Std. dev.	0.23	0.050	0.36	0.22	0.027	0.17	0.028		0.076	
Minimum	0.96	0.17	1.15	0.69	0.106	0.61	0.07		0.198	0.012
Maximum	1.4	0.33	2.2	1.34	0.190	1.11	0.16		0.43	0.38
Apollo 14 BX										
N	12	21	20	29	29	20	10	9	12	17
Average									15.8	3.9
Std. dev.									5.2	1.2
Minimum	27	2.1	32	6.1	0.94	0.68	0.1	0.2	11	0.7
Maximum	280	49	270	99	13.1	39	4	2.6	30	5.8
Apollo 15 BX										
N	4	9	8	9	9	9	9	12	9	22
Average										
Std. dev.										
Minimum	4.9	0.79	5.4	2.6	0.37	2.5	0.39	0.08	1.08	0.024
Maximum	26	4.5	27	15.8	2.2	17	2.0	0.98	7.5	7.2
Apollo 16 BX										
N	7	17	15	18	18	18	16	6	16	64
Average										
Std. dev.										
Minimum	2.6	0.13	0.92	0.52	0.085	0.4	0.03	0.12	0.7	0.0018
Maximum	33	27	38	77	10.9	69	5.0	0.69	36	7.2

TABLE A8.2. (continued).

	Gd	Tb	Dy	Yb	Lu	Hf	Ta	W	Th	U
Apollo 17 BX										
N	8	13	12	13	13	13	13	6	11	28
Average	14.6	2.5	15.6	8.7	1.23	8.7	1.19			1.11
Std. dev.	3.8	0.9	5.9	3.2	0.45	3.4	0.41			0.71
Minimum	9.5	0.45	3.8	1.9	0.34	0.99	0.17	0.12	0.64	0.178
Maximum	21.1	4	24	13.9	2	13.7	1.82	0.75	7.4	3.1
Luna 20 BX										
N	3	6	6	11	11	10	3		3	4
Average										
Std. dev.										
Minimum	5	0.72	4.5	0.82	0.15	0.47	0.5		1.2	0.34
Maximum	7	1.6	9.8	7.8	1.13	8.5	0.7		3.4	0.9

Note that standard deviations are not given for those categories where the number of analyses (N) is <3. Wherever N is >1 but no average or standard deviation is given, this was done because of either (1) extreme scatter in the data, where the relative standard deviation was >30%, or (2) data from mixed samples, such as highland and mare soils, where averages would be misleading. N = number of analyses, Std. dev. = standard deviation, MBAS = mare basalts, S&RB = soils and regolith breccias, BX = polymict breccias, AMET = Antarctic lunar meteorites. Highland monomict rocks (HMCT in Fig. 8.7) are listed by individual rock type name (anorthosite, norite, and troctolite; see section 6.3).

Main sources for data used in Fig. 8.7 and this table: **Li**: refs. 1, 12, 17, 18, 21, 27, 29, 30; **Be**: refs. 8, 9, 18, 30, 32; **B**: refs. 5, 8, 18, 19, 24, 30; **K**: refs. 1, 4, 10, 11, 12, 15, 17, 18, 20, 27, 29, 30, 31, 32; **Rb**: refs. 1, 2, 6, 7, 8, 11, 12, 14, 15, 17, 20, 21, 23, 27, 28, 29, 30, 31, 32; **Y**: refs. 4, 8, 12, 18, 24, 29, 30, 32; **Zr**: refs. 4, 8, 11, 12, 15, 16, 18, 21, 23, 29, 30, 31, 32; **Nb**: refs. 4, 8, 12, 26, 30; **Sn**: ref. 26; **Cs**: refs. 1, 2, 6, 11, 14, 15, 23, 27, 28, 30, 31; **Ba**: refs. 1, 4, 11, 12, 15, 16, 17, 18, 20, 21, 22, 23, 27, 29, 30, 31; **REE (La to Lu)**: refs. 4, 10, 11, 12, 13, 15, 16, 17, 20, 21, 22, 23, 27, 30, 31; **Hf**: refs. 4, 11, 12, 13, 15, 16, 21, 23, 30, 31; **Ta**: refs. 4, 11, 15, 16, 20, 22, 23, 30, 31; **W**: refs. 13, 26, 30; **Th**: refs. 4, 11, 12, 13, 15, 16, 20, 23, 30, 31; **U**: refs. 1, 2, 6, 11, 12, 15, 16, 23, 25, 28, 30, 31.

References: **1.** Albee *et al.* (1972); **2.** E. Anders, R. Ganapathy, J. W. Morgan, U. Krähenbühl, and coworkers; **3.** S. R. Taylor and coworkers; **4.** D. P. Blanchard, J. M. Rhodes, and coworkers; **5.** Bouchet *et al.* (1971); **6.** Boynton and Hill (1983); **7.** Compston *et al.* (1970, 1972a,b); **8.** F. Cuttitta, H. J. Rose, C. S. Annell, and coworkers; **9.** K. J. Eisentraut, R. E. Sievers, and coworkers; **10.** Gillum *et al.* (1972); **11.** L. A. Haskin, P. A. Helmke, R. L. Korotev, M. M. Lindstrom, and coworkers; **12.** N. J. Hubbard, C.-Y. Shih, L. E. Nyquist, J. M. Rhodes, and coworkers; **13.** Jerome *et al.* (1972); **14.** Kaczaral *et al.* (1986); **15.** J. C. Laul and coworkers; **16.** D. S. McKay *et al.* (1986); **17.** G. A. McKay *et al.* (1979); **18.** Meyer (1978); **19.** Morrison *et al.* (1970, 1971, 1973); **20.** Ostertag *et al.* (1986); **21.** J. A. Philpotts, C. S. Schnetzler, D. F. Nava, and coworkers; **22.** R. A. Schmitt, M.-S. Ma, and coworkers; **23.** Shervais *et al.* (1985a,b); **24.** Strasheim *et al.* (1972); **25.** M. Tatsumoto, P. Nunes, and coworkers; **26.** S. R. Taylor and coworkers; **27.** Tera *et al.* (1970); **28.** Verkouteren *et al.* (1983); **29.** Vinogradov (1971, 1973); **30.** H. Wänke, H. Palme, and coworkers; **31.** P. W. Warren, J. T. Wasson, G. W. Kallemeyn, and coworkers; **32.** Willis *et al.* (1971).

TABLE A8.3. Statistical summary of the database for concentrations of seven "miscellaneous minor elements" in mare basalts (MBAS) and in soils and regolith breccias (S&RB); all values are in $\mu\text{g/g}$ (see section 8.5, Fig. 8.14).

	P	Sc	V	Cr	Mn	Ga	Sr
Apollo 11 MBAS							
N	7	64	62	76	79	11	10
Average	636	83.5	78.2	2090	1919	4.1	163
Std. dev.	171	8.0	18.7	473	193	0.8	28
Minimum	436	65	38.5	1220	1480	3.0	100
Maximum	873	105	136	3381	2490	5.2	209
Apollo 12 MBAS							
N	5	32	19	32	32	23	8
Average	427	48.3	170.1	3641	2082	4.1	113
Std. dev.	160	7.2	30.3	1097	107	0.9	27
Minimum	305	37	126	2025	1845	2.7	72
Maximum	742	63	221	6570	2290	5.9	145
Apollo 14 MBAS							
N	2	17	14	17	17	2	2
Average	393	56.5	111.8	2673	1795	3.7	87
Std. dev.		5.0	22.7	705	98		
Minimum	349	46	63	1574	1650	3.3	73
Maximum	436	63	139	3724	2070	4.0	100
Apollo 15 MBAS							
N	19	72	66	72	72	23	21
Average	363	40.4	198.9	4027	2077	4.2	113
Std. dev.	116	4.6	32.7	1223	128	1.0	20
Minimum	218	30	116	1917	1541	2.9	80
Maximum	567	58	266	11300	2310	7.8	150
Apollo 16 MBAS (clast in breccia 60639)							
N		1	1	1	1		
Average		73	78	2053	1952		
Apollo 17 MBAS							
N	16	114	109	114	114	20	21
Average	288	78.6	104.3	2983	1925	5.1	163
Std. dev.	92	8.7	37.0	808	166	1.8	28
Minimum	175	25	20	1273	1557	2.2	104
Maximum	524	96	256	6420	3230	8.3	209
Luna 16 MBAS							
N		3	3	3	3	1	1
Average		66.3	76.7	1506	1996	3.7	404
Std. dev.		3.8	11.1	93	31		
Minimum		61	62	1403	1952		
Maximum		69	89	1629	2022		
Luna 24 MBAS							
N		8	8	8	8	1	1
Average		46.3	167.9	1845	1938	1.8	110
Std. dev.		8.5	10.2	341	131		
Minimum		38	154	1478	1774		
Maximum		66	179	2608	2208		
Apollo 11 S&RB							
N	5	7	7	14	14	5	6
Average	560	62.4	69.6	1986	1662	5.0	163
Std. dev.	68	3.9	11.1	173	80	1.1	2
Minimum	480	55	58	1574	1487	4.0	160
Maximum	654	68	92	2300	1815	7	165

TABLE A8.3. (continued).

	P	Sc	V.	Cr	Mn	Ga	Sr
Apollo 12 S&RB							
N	4	15	10	15	15	8	5
Average	1616	37.1	114.4	2468	1600	4.7	138
Std. dev.	420	3.9	17.6	397	178	0.4	32
Minimum	1265	27	85	1610	1247	4.1	90
Maximum	2334	44	143	3230	1910	5.2	190
Apollo 14 S&RB							
N	8	16	15	17	17	10	9
Average	2073	23.1	51.1	1496	1009	6.2	184
Std. dev.	482	3.5	6.7	198	75	1.4	74
Minimum	1003	17.8	41.8	1136	840	4.4	135
Maximum	2531	30	62	1848	1084	8.3	390
Apollo 15 S&RB							
N	22	52	40	54	54	21	26
Average	908	27.1	110.4	2530	1445	4.0	138
Std. dev.	228	4.9	32.6	529	228	0.7	19
Minimum	590	20	57.5	1506	1120	2.9	100
Maximum	1570	39.9	200	3810	2014	5.1	170
Apollo 16 S&RB							
N	23	53	35	51	48	35	33
Average	570	9.3	21.1	728	511	4.3	154
Std. dev.	229	1.5	5.3	121	58	0.8	22
Minimum	131	5.0	7.5	411	310	3.1	120
Maximum	1180	13.2	31.0	980	620	5.7	210
Apollo 17 S&RB							
N	30	64	50	64	63	35	43
Average	453	37.0	71.0	2220	1252	5.8	153
Std. dev.	146	18.2	27.4	667	363	3.4	21
Minimum	208	15	28	1230	798	2.6	112
Maximum	698	78	140	4030	1950	16.5	210
Luna 16 S&RB							
N	1	4	4	4	4	1	1
Average	380	45.8	37.2	1953	1600	4.7	266
Std. dev.		6.3	3.7	232	183		
Minimum		40	36	1595	1325		
Maximum		40	52.3	2160	1836		
Luna 20 S&RB							
N	1	2	2	2	2	1	1
Average	520	16.2	46.5	1259	813	3.7	138
Std. dev.							
Minimum		15.8	46	1230	806		
Maximum		16.5	47	1287	821		

TABLE A8.3. (continued).

	P	Sc	V.	Cr	Mn	Ga	Sr
Luna 24 S&RB							
N	1	7	7	7	7	1	6
Average	179	40.3	149.7	2657	1962	1.2	97
Std. dev.		1.7	7.7	249	54		10
Minimum		37	139	2163	1898		81
Maximum		43	159	3053	2068		109
AMET S&RB							
N	2	3	3	3	3	3	3
Average	95	11.5	30.0	917	611	4.0	144
Std. dev.		1.8	3.9	31	35	1.4	13
Minimum	90	9.1	24.6	890	580	2.7	134
Maximum	100	13.3	33.5	960	660	5.9	162

Note that only the mare basalts (MBAS) and the soils and regolith breccias (S&RB) are included in this table. The data for highland monomict rocks (HMCT) and polymict breccias (BX) show so much scatter that statistics are practically meaningless. For the data listed, standard deviations are not given in those categories where the number of analyses (N) is <3. Abbreviations: N = number of analyses, Std. dev. = standard deviation, MBAS = mare basalts, S&RB = soils and regolith breccias, AMET = Antarctic lunar meteorites.

Main sources of data used for this table: **P**: refs. 1*, 2; **Sc**: refs. 1, 2, 3, 4, 5; **V**: refs. 1, 2, 3[†], 4, 5; **Cr**: refs. 1, 2, 3, 4, 5; **Mn**: refs. 1, 2, 3, 4, 5; **Ga**: refs. 1, 2, 3, 4; **Sr**: refs. 1[‡], 2, 3, 4[§].

References: **1.** H. J. Rose and coworkers (a series of 9 papers published in the *Proceedings of the Lunar Science Conference*, beginning with *Rose et al.*, 1970, and ending with *Rose et al.*, 1975 and *Christian et al.*, 1976): data from XRF spectrometry (P, Cr, Mn) or one of several techniques based on "wet" chemistry followed by spectrographic analysis (P, Cr, Mn, Sc, V, Ga, Sr). **2.** H. Wänke and coworkers (a series of 9 papers published in the *Proceedings of the Lunar and Planetary Science Conference*, beginning with *Wänke et al.*, 1970a, and ending with *Palme et al.*, 1984, and *Ostertag et al.*, 1987): data from XRF (P, Cr, Mn) or INAA (Cr, Mn, Sc, V, Ga, Sr). **3.** *Brunfelt et al.* (1971, 1972a,b, 1973a,b, 1974a,b); data from INAA. **4.** P. H. Warren and coworkers (a series of 14 papers published in the *Proceedings of the Lunar Science Conference*, beginning with *Boynton et al.*, 1976b, and ending with *Jerde et al.*, 1987, and *Warren et al.*, 1987): data from INAA. **5.** R. A. Schmitt and coworkers (a series of 23 papers published in the *Proceedings* or in the abstracts of the Lunar and Planetary Science Conference, beginning with *Wakita et al.*, 1970, and ending with *Delano et al.*, 1986): data from INAA. In addition to these references, data for a broad range of miscellaneous minor elements were obtained from *Laul et al.* (1972a,b), *Laul and Schmitt* (1973a), and *Ma et al.* (1978). Some of the data plotted but not tabulated for highland monomict rocks are from *Ryder and Norman* (1979); additional P data for Apollo 11 MBAS are from *Compston et al.* (1970). For samples from the U.S.S.R. Luna missions, sources used in addition to those enumerated above are *Albee et al.* (1972), *Bakos et al.* (1977), *Bansal et al.* (1972), *Barsukov et al.* (1980), *Blanchard et al.* (1978), *Bobrov et al.* (1980), *Cimbalnikova et al.* (1977), *Gangadharan et al.* (1974), *Gillum et al.* (1972), *Helmke and Haskin* (1972a,b), *Helmke et al.* (1973), *Hubbard et al.* (1972b, 1977), *Jerome and Philippot* (1973), *Jerome et al.* (1972), *Jovanovic et al.* (1978), *Kolesov and Surkov* (1980), *Kuznetsov et al.* (1979), *Lau! et al.* (1978b, 1981), *Murali et al.* (1979), *Nava and Philpotts* (1973), *Nyquist et al.* (1978), *Philpotts et al.* (1972), *Surkov and Kolesov* (1979), and *Vinogradov* (1971, 1973). Essentially all these data were obtained using INAA. For the Antarctic lunar meteorites, *Koebel et al.* (1989) and *Warren et al.* (1989) list all the published sources used, which are generally based on INAA.

* The P data reported by Rose and coworkers appear unreliable at concentrations below roughly 0.04 wt. %.

† The V data reported by Brunfelt and coworkers for Apollo 16 samples appear unreliable (too high).

‡ The Sr data reported by Rose and coworkers for Apollo 12 samples appear unreliable (too low).

§ Schmitt and coworkers also report Sr data in some of their most recent papers.

TABLE A8.4. Statistical summary of the database for concentrations of frequently determined siderophile elements in mare basalts (MBAS) and in soils and regolith breccias (S&RB) (see section 8.6, Fig. 8.20).

	Fe wt.%	Co μg/g	Ni μg/g	Ge ng/g	Mo ng/g	W ng/g	Re ng/g	Os ng/g	Ir ng/g	Au ng/g
Apollo 11 MBAS										
N	79	10		2	1	3			7	6
Average	15.2	20.6		60	129	357			0.027	0.056
Std. dev.	1.0	9.9				83			0.027	0.035
Minimum	12.8	5.7		60		240			0.005	0.015
Maximum	16.8	38.5		60		430			0.090	0.120
Apollo 12 MBAS										
N	21	31	23	17	4	11	11		29	17
Average	15.7	45.3	46.7	31.8	42.5	161	0.0098		0.060	0.024
Std. dev.	1.0	12.9	39.7	40.5	8.3	55	0.0151		0.051	0.019
Minimum	13.4	25	1	0.7	30	104	0.0004		0.0019	0.0046
Maximum	17.2	69	150	100	50	290	0.056		0.20	0.072
Apollo 14 MBAS										
N	3	2	2	3		2	2	1	3	3
Average	12.8	28.9	21.5	428		350	0.0058	0.011	0.021	0.186
Std. dev.	0.8			192					0.018	0.082
Minimum	12.1	28.7	4	175		150	0.0051		0.0015	0.11
Maximum	13.9	29.0	39	640		550	0.0066		0.044	0.30
Apollo 15 MBAS										
N	14	22	23	28	1	6	23	3	29	29
Average	15.9	49.6	57.5	11.0	21	342	0.022	0.026	0.043	0.073
Std. dev.	1.7	13.5	28.5	10.2		403	0.072	0.005	0.044	0.082
Minimum	12.9	34.4	16	2.8		59	0.0006	0.020	0.0043	0.005
Maximum	18.8	89	150	50		1200	0.36	0.032	0.144	0.36
Apollo 16 MBAS (clast in breccia 60639)										
N	1	1		1			1		1	1
Average	15.55	20		2.53			0.0057		0.048	0.04
Std. dev.										
Minimum										
Maximum										
Apollo 17 MBAS										
N	15	15	6	6	1	10	3		5	9
Average	14.5	19.7	2.0	2.78	39	83.4	0.0018		0.053	0.079
Std. dev.	0.7	2.9	1.1	1.49		16.2	0.0010		0.049	0.088
Minimum	12.6	13.7	1.0	1.27		60	0.0007		0.003	0.007
Maximum	15.5	22.5	3.6	5.7		120	0.0031		0.140	0.26
Luna 16 MBAS										
N	4	4	1							
Average	14.7	18.2	79							
Std. dev.	0.6	2.0								
Minimum	14.0	17.0								
Maximum	15.7	21.7								
Luna 24 MBAS										
N	12	12	5			1				
Average	16.3	40.7	43.0			30				
Std. dev.	0.9	6.3	26.8							
Minimum	14.7	36.0	15							
Maximum	17.4	59.3	80							

TABLE A8.4. (continued).

	Co μg/g	Ni μg/g	Ge ng/g	Sb ng/g	W ng/g	Ru ng/g	Pd ng/g	Re ng/g	Os ng/g	Ir ng/g	Au ng/g
Apollo 11 S&RB											
N	7	5	7		1		4	4	3	9	11
Average	31.0	199	511		220		10.5	0.74	7.83	8.6	2.9
Std. dev.	3.0	48	367				2.3	0.07	0.21	1.9	1.9
Minimum	27.2	150	240				7	0.67	7.6	5.4	1.4
Maximum	34.8	280	1400				13	0.85	8.1	11.6	8.5
Apollo 12 S&RB											
N	21	10	4		5	3	3	7	5	15	18
Average	40.8	260	247		592	47	9.7	0.44	5.2	5.6	2.4
Std. dev.	4.4	165	63		104	30	2.9	0.13	1.6	2.1	1.1
Minimum	34	130	200		450	5.5	6.5	0.25	3.8	2.7	0.82
Maximum	55	730	355		740	71	13.5	0.67	7.5	11	5.7
Apollo 14 S&RB											
N	25	29	8	8	8	2	2	12	1	19	18
Average	34.6	411	671	3.01	1331	19.5	24	1.13	12.0	12.5	6.2
Std. dev.	3.3	101	68	1.13	509			0.14		2.8	2.0
Minimum	27.5	273	590	2	500	17	20	0.86		7.3	2.3
Maximum	43.5	700	790	5.7	1950	22	28	1.34		19	11
Apollo 15 S&RB											
N	51	52	27	8	15	7	2	18	8	38	36
Average	44.6	216	340	1.67	628	15.9	6.5	0.61	6.3	6.4	3.0
Std. dev.	6.5	52	127	0.66	473	6.1	0.3	0.20	1.0	1.8	1.5
Minimum	35.4	90	120	0.85	130	5	6.2	0.2	4.0	2.1	1.0
Maximum	66	360	790	2.7	1800	25	6.8	1.2	7.3	11	8
Apollo 16 S&RB											
N	40	44	33	9	4	8	3	18	6	50	51
Average	27	378	763	1.93	209	18.1	13.3	0.9	5.9	11.6	7.8
Std. dev.	10	151	364	0.94	119	7.4	4.7	0.6	1.4	4.9	3.5
Minimum	9	80	245	0.73	74	9	8.4	0.37	4.5	2.8	1.5
Maximum	59	693	1630	4.23	350	34	19.6	2.6	8.5	26	16.6
Apollo 17 S&RB											
N	69	68	23	8	13	6	3	14		47	59
Average	33.8	211	346	0.93	203	13.3	8.3	0.56		9.7	4.1
Std. dev.	6.7	83	133	0.39	110	5.5	2.4	0.28		4.5	2.5
Minimum	24.5	64	105	0.55	88	3	5	0.052		0.021	0.7
Maximum	68	550	625	1.81	520	19	10	1.07		25	13
Luna 16 S&RB											
N	7	3	2	2		1	1	2		2	4
Average	35.2	174	1300	3.8		20	10.2	3.6		9.7	2.5
Std. dev.	10.3	30									0.5
Minimum	26	132	1300	3.3				3.4		9.6	1.7
Maximum	57.3	200	1300	4.2				3.7		9.8	2.9
Luna 20 S&RB											
N	3	3	3	2	1			2		3	5
Average	30.0	252	448	5.7	100			1.04		9.51	5.4
Std. dev.	2.9	16	26							0.01	2.0
Minimum	27	230	430	1.5				1.04		9.5	3.29
Maximum	34	267	485	9.8				1.04		9.52	7.8

TABLE A8.4. (continued).

	P	Sc	V.	Cr	Mn	Ga	Sr
Luna 24 S&RB							
N	1	7	7	7	7	1	6
Average	179	40.3	149.7	2657	1962	1.2	97
Std. dev.		1.7	7.7	249	54		10
Minimum		37	139	2163	1898		81
Maximum		43	159	3053	2068		109
AMET S&RB							
N	2	3	3	3	3	3	3
Average	95	11.5	30.0	917	611	4.0	144
Std. dev.		1.8	3.9	31	35	1.4	13
Minimum	90	9.1	24.6	890	580	2.7	134
Maximum	100	13.3	33.5	960	660	5.9	162

Note that data for the highland monomict rocks (HMCT) and polymict breccias (BX) show so much scatter that statistics are practically meaningless. Even among the MBAS and S&RB categories, standard deviations are often very large, and statistical data should be used with caution. For the data listed, standard deviations are not given in those categories where the number of analyses (N) is <3. Abbreviations: $\mu\text{g/g}$ = micrograms per gram (parts per million), ng/g = nanograms per gram (parts per billion), N = number of samples, Std. dev. = standard deviation, MBAS = mare basalts, S&RB = soil and regolith breccias, AMET = Antarctic lunar meteorites.

Main sources for data for siderophile element concentrations of rocks (including breccia clasts) and bulk-soil samples: **Fe**: refs. 1, 2, 3, 4, 5, 6, 7; **Co**: refs. 1, 2, 3, 4, 5, 6, 8; **Ni**: refs. 1, 2, 3, 4, 5, 6, 8; **Ge**: refs. 1, 2, 8; **Mo**: refs. 4, 7, 9; **Ru**: refs. 1, 10*; **Rh**: see text; **Pd**: refs. 2, 8; **Sb**: refs. 8; **W**: refs. 2, 4, 5, 11*; **Re**: refs. 1, 2, 8, 11*, 12*; **Os**: refs. 1, 8, 12*; **Ir**: refs. 1, 2†, 3†, 8, 12*; **Pt**: ref. 2; **Au**: refs. 1, 2†, 3†, 5†, 6*, 8, 12*.

References: **1.** J. T. Wasson, P. H. Warren and coworkers (a series of 17 papers published in the *Proceedings of the Lunar Science Conference*, beginning with *Wasson and Baedecker*, 1970, and ending with *Warren et al.*, 1987; also several papers published elsewhere: *Wasson et al.*, 1973, 1975a; *Boynton et al.*, 1976a; *Boynton and Wasson*, 1977); data mostly from INAA and RNAA. **2.** H. Wänke and coworkers; data mostly from INAA and RNAA. **3.** R. A. Schmitt and coworkers (same publications cited in the footnotes to Table A8.3); data mostly from INAA. **4.** S. R. Taylor et al. (1971, 1972, 1973a,b); data from spark source mass spectrometry. **5.** *Brunfelt et al.* (1971, 1972a,b, 1973a,b, 1974a,b); data mostly from INAA and RNAA. **6.** H. J. Rose and coworkers (same publications cited in the footnotes to Table A8.3); data mostly from XRF spectrometry. **7.** *Turekian and Kharkar* (1970) and *Kharkar and Turekian* (1971); data mostly from INAA and RNAA. **8.** E. Anders, J. W. Morgan and coworkers (a series of 15 papers published in the *Proceedings of the Lunar Science Conference*, beginning with *Ganapathy et al.*, 1970, and ending with *Wolf et al.*, 1979; also the data of *Morgan et al.*, 1979, published elsewhere); data from RNAA. **9.** *Newsom* (1986), data from RNAA. **10.** *Reed and Jovanovic* (1971, 1972), *Reed et al.* (1972), *Jovanovic and Reed* (1973, 1974), and *Jovanovic et al.* (1978); data from RNAA. **11.** *Michel et al.* (1972), data from RNAA. **12.** *Lovering and Hughes* (1971) and *T. C. Hughes et al.* (1973); data from RNAA. For samples from the U.S.S.R. Luna missions, sources used in addition to those enumerated above are *Barsukov et al.* (1980), *Blanchard et al.* (1978), *Bobrov et al.* (1980), *Cimbalnikova et al.* (1977), *Gangadharan et al.* (1974), *Gillum et al.* (1972), *Helmke and Haskin* (1972a,b), *Helmke et al.* (1973), *Hubbard et al.* (1977), *Jerome and Philippot* (1973), *Jerome et al.* (1972), *Kolesov and Surkov* (1980), *Kuznetsov et al.* (1979), *Laul and Schmitt* (1973a), *Laul et al.* (1978b, 1981), *Surkov and Kolesov* (1979), and *Vinogradov* (1971, 1973). Essentially all these data were obtained using either INAA or RNAA. For the Antarctic lunar meteorites, *Koebel et al.* (1989) and *Warren et al.* (1989) list all the published sources used, which are based on INAA and RNAA analysis.

*Only data for soils and regolith breccias were used (data for other types of samples, where reported, frequently appear suspiciously high).

†Only data for soils, regolith breccias, and polymict breccias were used (data for mare basalts and monomict highland rocks, where reported, frequently appear suspiciously high).

TABLE A8.5. Statistical data for concentrations of vapor-mobilized elements (see section 8.7, Fig. 8.25).

	S	F	Cl	Cu	Zn	As	Se	Br	Ag	Cd	In	Te	Tl	Bi	Pb
	μg/g	μg/g	μg/g	μg/g	μg/g	ng/g	ng/g	ng/g	ng/g	ng/g	ng/g	ng/g	ng/g	ng/g	μg/g
Apollo 11 MBAS															
N	11	4	7	3	9		5	12	5	8	4	3	7	6	16
Average	1930	229	13.6				203				3.35	10.7			
Std. Dev.	320	38	1.2				30				0.72	2.5			
Minimum	1500	193	12	3.5	1.29		181	10.4	0.69	2.6	2.8	8	0.28	0.15	0.29
Maximum	2300	271	15	15.2	18		250	330	16	68	4.4	13	6.16	1.15	1.71
Apollo 12 MBAS															
N	30	2	13		14		10	16	9	13	12	6	9	8	12
Average	910	29					145								0.42
Std. dev.	320						43								0.14
Minimum	400	18	1.4		0.52		58	4	0.3	1.1	0.4	10	0.06	0.15	0.27
Maximum	1520	40	28		3.3		201	101	2.8	6.4	5.1	70	0.88	0.76	0.65
Apollo 15 MBAS															
N	5	3	3		11	2	7	8	7	11	11	7	7	7	6
Average	820	50			1.28		125		0.903						0.24
Std. dev.	130	9			0.41		37		0.079						0.06
Minimum	600	40	3.2		0.78	0.9	53	6	0.78	0.68	0.18	0.96	0.2	0.089	0.191
Maximum	970	57	8.4		2.1	5.5	167	51	1	104	6.8	6.2	1.45	0.41	0.35
Apollo 17 MBAS															
N	6		6		10	5	3	10	5	6	7	3	3	3	7
Average	1890				2.14		133					1.83			0.278
Std. dev.	160				0.25		57					0.31			0.030
Minimum	1590		0.38		1.7	1	68	7.6	0.082	1.1	0.23	1.5	0.16	0.043	0.24
Maximum	2000		5.9		2.5	50	176	44	1.1	9	4.7	2.1	0.77	0.22	0.36
Apollo 11 S&RB															
N	5	5	15	4	4		1	12	3	4		3	4	4	4
Average	1240				24.7		330						2.15	1.845	1.61
Std. dev.	360				4.9								0.71	0.64	0.22
Minimum	660	75	2.9	1.47	20			38	8.6	35		28	1.47	1.37	1.39
Maximum	1500	520	45	22	29			580	24	106		73	2.8	2.8	1.86

TABLE A8.5. (continued).

	S μg/g	F μg/g	Cl μg/g	Cu μg/g	Zn μg/g	As ng/g	Se ng/g	Br ng/g	Ag ng/g	Cd ng/g	In ng/g	Te ng/g	Tl ng/g	Bi ng/g	Pb μg/g
Apollo 12 S&RB															
N	8	5	5		15		13	18	8	15	4	11	13	13	8
Average	820				6.0		200				8.1				3.90
Std. dev.	240				1.7		44				1.7				0.41
Minimum	620	9	0.6		1.5		86	2.3	2.7	17	6.5	10	0.26	0.32	3.2
Maximum	1200	520	150		8.9		260	930	301	22000	10	130	5.2	38500	4.4
Apollo 14 S&RB															
N	8	3	9		11	2	8	13	8	11	3	7	8	8	7
Average	870	138			26.7	85	316						23.5	1.68	8.3
Std. dev.	117	29			5.5		32						6.3	0.29	1.0
Minimum	706	106	5.9		19	80	270	190	11.5	77	39	15	18	1.3	7.2
Maximum	1000	162	55		36	90	350	1330	30	460	120	70	35	2.2	10.0
Apollo 15 S&RB															
N	5	8	13		31	2	10	20	9	31	20	10	10	10	7
Average	624	69					193								1.81
Std. dev.	79	21					22								0.51
Minimum	520	46	6.1		7.7	15	162	74	5	20	3.1	6.2	1.46	0.87	1.10
Maximum	710	103	39		65	40	230	1183	61	240	410	33	5	2.9	2.8
Apollo 16 S&RB															
N	5	7	12		25	2	9	20	9	21	12	9	13	12	10
Average	543				19.1		224		8.5	83		17.7			1.90
Std. dev.	74				6.2		58		2.3	33		5.5			0.51
Minimum	470	27	12		6.9	35	109	80	4.5	21	2.6	8.5	0.98	0.32	0.96
Maximum	640	105	270		28	170	300	1330	11.4	140	24	27	13.2	1.7	2.8
Apollo 17 S&RB															
N		16	29		25		8	36	19	24	16	12	9	9	9
Average															1.47
Std. dev.															0.50
Minimum		17	7.8		18		210	65	1.4	11.4	1.4	10	1.3	0.7	1.08
Maximum		230	103		230		640	1580	111	320	35	105	22	148	2.5

TABLE A8.5. (continued).

	S	F	Cl	Cu	Zn	As	Se	Br	Ag	Cd	In	Te	Tl	Bi	Pb
	$\mu\text{g/g}$	$\mu\text{g/g}$	$\mu\text{g/g}$	$\mu\text{g/g}$	$\mu\text{g/g}$	ng/g	$\mu\text{g/g}$								
Luna 16 S&RB															
N			1		2		2	3		2	1	2	2	2	3
Average			23.6		27		355				19	1.9	1.7	4.9	0.96
Std. dev.															0.18
Minimum					24		340	120		200		18	1.4	4.6	0.78
Maximum					29		370	370		10900		20	1.9	5.1	1.14
Luna 20 S&RB															
N			2		2		2	4	1	2	1	2	2	2	
Average			26		17		220	160	29		3.9	26		2.7	
Std. dev.								49							
Minimum			26		12		209	100		48		22	2.6	2.63	
Maximum			26		22		230	200		1740		30	6.6	2.8	
AMET S&RB															
N					6		4	8	3	3	3	3	3	3	
Average															
Std. dev.															
Minimum					4.7		190	90	2.4	19	1.5	9.2	2.3	0.73	
Maximum					189		500	330	44	220	13	230	12	45	
Apollo 14 BX															
N	1	6	12		34	2	23	31	22	34	25	15	23	22	10
Average	990	127				100									9.0
Std. dev.		64													3.2
Minimum		42	5.9		1.5	80	5.5	49	0.32	2.3	1.4	0.15	1.7	0.17	3.7
Maximum		225	64.9		35	120	340	1020	11	300	31	110	33	2.5	13.9
Apollo 15 BX															
N		13	13		32	4	29	37	29	31	30	28	29	28	
Average															
Std. dev.															
Minimum		31	1.1		0.49	1.6	1.3	8	0.24	0.62	0.18	1.8	0.08	0.08	
Maximum		310	67		80	70	360	550	39	183	17	59	28	2.4	

TABLE A8.5. (continued).

	S	F	Cl	Cu	Zn	As	Se	Br	Ag	Cd	In	Te	Tl	Bi	Pb
	μg/g	μg/g	μg/g	μg/g	μg/g	ng/g	ng/g	μg/g							
Apollo 16 BX															
N		13	29		49	8	45	78	45	48	3	44	46	46	10
Average															
Std. dev.															
Minimum		13	4.3		0.26	9	2.1	4.7	0.19	0.85	0.63	0.4	0.13	0.052	0.63
Maximum		93	319		50	750	800	3500	21	330	6.8	68	280	12.6	16.3
Apollo 17 BX															
N	1	23	29		58	5	56	76	56	58	10	46	56	52	14
Average	2000														
Std. dev.															
Minimum		18.8	1.7		1.2	14	3.9	4.8	0.36	0.63	0.15	1.1	0.038	0.098	0.57
Maximum		154	58.8		98	140	420	732	127	112	12.4	30	5.0	1.76	7.9

Note that data for the highland monomict rocks (HMCT) are not given because the concentrations in the HMCT scatter so much that statistics would be meaningless. For the data from other sample types, wherever the number of analyses (N) is >1 but no average or standard deviation is given, this was done because of either (1) extreme scatter in the data, where the relative standard deviation was >30%, or (2) data from mixed samples, such as highland and mare soils, where averages would be meaningless. Standard deviations are also not listed where N is <3. N = number of analyses, Std. dev. = standard deviation, MBAS = mare basalts, S&RB = soils and regolith breccias, BX = polymict breccias, AMET = Antarctic lunar meteorites.

Main sources for data used in this table: **F**: refs. 37–41, 56, 69, 71–73, 99, 101–103; **S**: refs. 1, 9, 15–19, 22–24, 28–32, 35, 47–49, 55, 57, 58, 70, 75–80, 83, 96, 106; **Cl**: refs. 36–44, 69, 72–74, 97–103; **Cu**: refs. 4, 15, 25, 53, 69, 88–90, 98–103; **Zn**: refs. 2, 3, 5–8, 10–14, 25–27, 33, 34, 45, 46, 51–53, 59–63, 95, 104, 105; **As**: refs. 69, 99–103; **Se**: refs. 3, 10, 26, 27, 33, 34, 45, 51, 53, 59–63, 95; **Br**: refs. 3, 14, 25–27, 33, 36–44, 46, 50, 51, 53, 54, 60–63, 69, 71–74, 101, 102, 104; **Ag**: refs. 3, 8, 25–27, 33, 34, 45, 51, 53, 59–63, 95; **Cd**: refs. 3, 5–8, 11–14, 25–27, 33, 34, 45, 51–53, 59–63, 95, 105; **In**: refs. 3, 5–8, 11–14, 25, 26, 33, 45, 52, 60, 61, 95, 105; **Te**: refs. 2, 3, 25–27, 33, 34, 45, 51–53, 60–63, 95; **I**: refs. 37–43, 71, 72, 74, 101; **Tl**: refs. 2, 3, 25–27, 33, 34, 45, 51, 53, 59–63, 95; **Bi**: refs. 2, 3, 25–27, 33, 34, 45, 51, 53, 59–63, 95; **Pb**: refs. 21, 64–68, 81, 82, 84–87, 91–94.

References: **1.** Agrell et al. (1970a); **2.** Allen et al. (1974); **3.** Anders et al. (1971); **4.** Ansell and Helz (1970); **5.** Baedecker et al. (1971); **6.** Baedecker et al. (1972); **7.** Baedecker et al. (1973); **8.** Baedecker et al. (1974); **9.** Barsukov et al. (1977); **10.** Boynton and Hill (1983); **11.** Boynton et al. (1975); **12.** Boynton et al. (1976a); **13.** Chou et al. (1974); **14.** Chou et al. (1975); **15.** Compston et al. (1970); **16.** Compston et al. (1971); **17.** Cripe and Moore (1974); **18.** Cripe and Moore (1975); **19.** Cripe and Moore (1976); **20.** Des Marais (1978); **21.** Doe and Tatsumoto (1972); **22.** Duncan et al. (1973); **23.** Duncan et al. (1974); **24.** Engel and Engel (1970a,b); **25.** Ganapathy et al. (1970); **26.** Ganapathy et al. (1973); **27.** Ganapathy et al. (1974); **28.** Gibson and Moore (1973a,b); **29.** Gibson and Moore (1974); **30.** Gibson et al. (1975); **31.** Gibson et al. (1976); **32.** Gibson et al. (1977); **33.** Gros et al. (1976); **34.** Higuchi and Morgan (1975); **35.** Hubbard et al. (1974); **36.** Jovanovic and Reed (1980a); **37.** Jovanovic and Reed (1973); **38.** Jovanovic and Reed (1974); **39.** Jovanovic and Reed (1975); **40.** Jovanovic and Reed (1976a); **41.** Jovanovic and Reed (1977); **42.** Jovanovic and Reed (1978a); **43.** Jovanovic and Reed (1978b); **44.** Jovanovic and Reed (1981); **45.** Kaczaral et al. (1986); **46.** Kallemeyn and Warren (1983); **47.** Kaplan and Petrowski (1971); **48.** Kaplan et al. (1970); **49.** Kerridge et al. (1975a,b); **50.** Korotev et al. (1983); **51.** Krähenbühl et al. (1973); **52.** Krähenbühl (1980); **53.** Laul et al. (1971); **54.** Lindstrom et al. (1986); **55.** Maxwell et al. (1970); **56.** Meyer (1978); **57.** Moore et al. (1972); **58.** Moore et al. (1974); **59.** Morgan and Petrie (1979); **60.** Morgan et al. (1972a); **61.** Morgan et al. (1972b); **62.** Morgan et al. (1973); **63.** Morgan et al. (1974); **64.** Nunes and Tatsumoto (1973); **65.** Nunes et al. (1973); **66.** Nunes et al. (1974a); **67.** Nunes et al. (1974b); **68.** Nunes et al. (1975); **69.** Palme et al. (1978); **70.** Petrowski et al. (1974); **71.** Reed and Jovanovic (1970); **72.** Reed and Jovanovic (1971); **73.** Reed and Jovanovic (1973a); **74.** Reed et al. (1972); **75.** Rees and Thode (1972); **76.** Rees and Thode (1974); **77.** Rhodes and Hubbard (1973); **78.** Rhodes et al. (1974); **79.** Scoon (1971); **80.** Scoon (1972); **81.** Silver (1970); **82.** Silver (1972); **83.** J. W. Smith et al. (1973); **84.** Tatsumoto (1970); **85.** Tatsumoto et al. (1971); **86.** Tatsumoto et al. (1972a); **87.** Tatsumoto et al. (1972b); **88.** S. R. Taylor et al. (1971); **89.** S. R. Taylor et al. (1972); **90.** S. R. Taylor et al. (1973a,b); **91.** Tera and Wasserburg (1972a); **92.** Tera and Wasserburg (1972b); **93.** Tera et al. (1972); **94.** Unruh and Tatsumoto (1978); **95.** Verkouteren et al. (1983); **96.** Vinogradov (1973); **97.** Wänke et al. (1970a); **98.** Wänke et al. (1971); **99.** Wänke et al. (1972); **100.** Wänke et al. (1973); **101.** Wänke et al. (1974); **102.** Wänke et al. (1975); **103.** Wänke et al. (1977); **104.** Warren and Kallemeyn (1986); **105.** Wasson et al. (1976); **106.** Willis et al. (1972).

TABLE A8.6. Statistical data for concentrations of solar-wind-implanted elements
(see section 8.8, Figs. 8.35 and 8.39).

	H $\mu\text{g/g}$	C $\mu\text{g/g}$	N $\mu\text{g/g}$	He $\mu\text{g/g}$	Ne $\mu\text{g/g}$	Ar $\mu\text{g/g}$	Kr ng/g	Xe ng/g
Apollo 11 MBAS								
N				33	33	32	21	20
Average								
Std. dev.								
Minimum				0.0192	0.00017	0.0280	0.00079	0.00111
Maximum				0.47	0.1270	0.194	0.104	0.102
Apollo 12 MBAS								
N	3	11	6	10	10	10	9	10
Average		33				0.0227		
Std. dev.		11.0				0.0073		
Minimum	1.5	5.3	0.6	0.026	0.00047	0.0114	0.00086	0.00058
Maximum	9	45	44	0.089	0.00191	0.036	0.0051	0.0038
Apollo 15 MBAS								
N	11	13	3					
Average								
Std. dev.								
Minimum	1.2	7.7	3.5					
Maximum	12	22	125					
Apollo 17 MBAS								
N	6	25	12					
Average								
Std. dev.								
Minimum	1	3	0					
Maximum	3.8	80	105					
Luna 20 MBAS								
N				4	4	4	1	
Average							0.059	
Std. dev.								
Minimum				0.199	0.0157	0.079		
Maximum				0.97	0.067	0.165		
Apollo 11 S&RB								
N	11	16	7	30	23	17	25	16
Average		154	78	46			1.95	
Std. dev.		38	21	14			0.66	
Minimum	20	96	45	19.6	1.93	1.28	1.05	0.47
Maximum	100	216	110	84	10.7	12.3	3.2	3.8
Apollo 12 S&RB								
N	7	33	19	7	7	7	14	16
Average		115	89					0.42
Std. dev.		42	24					0.15
Minimum	1.9	23	46	14.0	1.20	0.47	0.065	0.090
Maximum	106	170	140	68	6.0	4.6	1.32	0.62

TABLE A8.6. (continued).

	H μg/g	C μg/g	N μg/g	He μg/g	Ne μg/g	Ar μg/g	Kr ng/g	Xe ng/g
Apollo 14 S&RB								
N	3	25	5	13	13	13	14	14
Average	80	131	91	10.6				
Std. dev.	24	42	23	3.6				
Minimum	67	42	25	5.2	0.141	0.36	0.079	0.036
Maximum	105	225	130	15.9	1.55	2.2	1.60	1.02
Apollo 15 S&RB								
N	24	90	46	33	33	33	22	22
Average		109	86	11.2	1.24	1.10	0.76	0.41
Std. dev.		35	26	3.4	0.31	0.39	0.25	0.12
Minimum	13	21	33	4.5	0.61	0.47	0.36	0.187
Maximum	125	186	135	18.7	1.80	2.7	1.56	0.70
Apollo 16 S&RB								
N	26	58	52	39	37	39	30	31
Average		112			0.78		1.04	0.63
Std. dev.		49			0.21		0.37	0.21
Minimum	3.9	31	4	3.0	0.41	0.65	0.29	0.22
Maximum	146	280	209	36	1.23	3.4	2.2	1.00
Apollo 17 S&RB								
N	24	63	40	28	22	22	19	20
Average				23.9	1.76	1.44		0.45
Std. dev.				7.9	0.39	0.57		0.17
Minimum	0.1	3.5	7.3	13.0	1.21	0.60	0.056	0.040
Maximum	106	200	94	41	2.7	2.6	1.39	0.69
Luna 20 S&RB								
N				3	3	3	1	1
Average				11.8	1.41	1.51	0.91	0.74
Std. dev.				3.4	0.31	0.52		
Minimum				8.1	1.12	0.92		
Maximum				14.9	1.74	1.95		
Apollo 14 BX								
N		15	17	17	16	24	15	15
Average								
Std. dev.								
Minimum		21	2.5	0.021	0.0011	0.0107	0.00111	0.0022
Maximum		170	99	19.5	2.0	3.75	1.82	1.27
Apollo 15 BX								
N	4	20	14					
Average								
Std. dev.								
Minimum	12	11	23					
Maximum	60	210	102					

TABLE A8.6. (continued).

	H μg/g	C μg/g	N μg/g	He μg/g	Ne μg/g	Ar μg/g	Kr ng/g	Xe ng/g
Apollo 16 BX								
N	1	49	28					
Average	89							
Std. dev.								
Minimum		2	0.7					
Maximum		385	135					
Apollo 17 BX								
N	11	24	13					
Average			72					
Std. dev.			27					
Minimum	1	12	30					
Maximum	56	157	120					

Note that data for the highland monomict rocks (HMCT) are not given because the HMCT have very low concentrations of solar-wind-implanted elements, and the few data available show a great deal of scatter. For the data from other sample types, wherever the number of analyses (N) is >1 but no average or standard deviation is given, this was done because of extreme scatter in the data (relative standard deviation >40%). Standard deviations are also not listed where N is <3. N = number of analyses, Std. dev. = standard deviation, MBAS = mare basalts, S&RB = soils and regolith breccias, BX = polymict breccias.

Main sources for data used in this table: **H**: refs. 2, 10, 12, 16–20, 23, 25, 26, 43, 56, 57; **He**: refs. 3, 8, 9, 21, 22, 24, 29–31, 33, 38, 41–43, 53, 54, 56, 57; **C**: refs. 2, 6, 11–20, 23, 34–37, 44–48, 52, 54–56; **N**: refs. 3–6, 11–13, 27, 28, 34, 37, 39, 46, 48–52, 54, 56, 58; **Ne**: refs. 7, 9, 21, 22, 24, 29–33, 38, 41, 42, 53; **Ar**: refs. 8, 9, 21, 22, 24, 29–33, 38, 41, 42, 53; **Kr**: refs. 1, 9, 24, 29–31, 33, 38, 41, 42; **Xe**: refs. 1, 9, 24, 29–31, 33, 40, 41, 42.

References: **1.** Basford *et al.* (1973); **2.** Becker (1980); **3.** Becker and Clayton (1975); **4.** Becker and Clayton (1977); **5.** Becker *et al.* (1976); **6.** Becker and Epstein (1981); **7.** Behrmann *et al.* (1973); **8.** Bogard *et al.* (1974); **9.** Bogard and Nyquist (1973); **10.** Bustin *et al.* (1984); **11.** Chang *et al.* (1974a); **12.** Chang *et al.* (1974b); **13.** Des Marais (1978); **14.** DesMarais *et al.* (1975); **15.** Des Marais *et al.* (1973); **16.** Des Marais *et al.* (1974); **17.** Epstein and Taylor (1970); **18.** Epstein and Taylor (1971); **19.** Epstein and Taylor (1973); **20.** Epstein and Taylor (1975); **21.** Eugster *et al.* (1975); **22.** Frick *et al.* (1973); **23.** Friedman *et al.* (1971); **24.** Funkhouser *et al.* (1970); **25.** Gibson and Bustin (1987); **26.** Gibson *et al.* (1987); **27.** Goel and Kothari (1972); **28.** Goel *et al.* (1975); **29.** Hintenberger *et al.* (1975); **30.** Hintenberger *et al.* (1974); **31.** Hintenberger *et al.* (1970); **32.** Hübner *et al.* (1975); **33.** Husain *et al.* (1972); **34.** Kaplan *et al.* (1976); **35.** Kaplan and Petrowski (1971); **36.** Kaplan *et al.* (1970); **37.** Kerridge *et al.* (1975b); **38.** Kirsten *et al.* (1973); **39.** Kothari and Goel (1973); **40.** Lightner and Marti (1974); **41.** Lugmair *et al.* (1976); **42.** Marti *et al.* (1970); **43.** Merlivat *et al.* (1974); **44.** Moore and Lewis (1976); **45.** C. B. Moore *et al.* (1974); **46.** Moore *et al.* (1972); **47.** Moore *et al.* (1973); **48.** Moore *et al.* (1971); **49.** Muller (1972); **50.** Muller (1973); **51.** Mailer (1974); **52.** Norris *et al.* (1983); **53.** Pepin *et al.* (1970); **54.** Petrowski *et al.* (1974); **55.** Pillinger *et al.* (1974); **56.** J. W. Smith *et al.* (1973); **57.** Stoenner *et al.* (1974); **58.** Thiemens and Clayton (1980).

PHYSICAL PROPERTIES OF THE LUNAR SURFACE

W. David Carrier III, Gary R. Olhoeft, and Wendell Mendell

This chapter discusses the physical properties of the lunar surface, determined at depths varying from a few micrometers to a few tens of meters. The properties considered include *geotechnical* properties (those properties of a planetary surface needed to evaluate engineering problems, including the mechanical properties of soil and rock), electrical and electromagnetic properties, and the reflection and emission of radiation.

The lunar surface material (*regolith* or “lunar soil”) is a complex mixture of five basic particle types: crystalline rock fragments, mineral fragments, breccias, agglutinates, and glasses. The relative proportion of each particle type varies from place to place and is dependent on the mineralogy of the source rocks and the geologic processes that the rocks have undergone (see Chapters 4 and 7 for more details).

The lunar regolith is distinctly different from terrestrial materials. For one thing, its mineral composition is limited. Fewer than a hundred minerals have been found on the Moon, compared to several thousand on Earth (see Chapter 5). Furthermore, continuous meteoroid impact has converted the lunar surface materials into a well-graded silty sand that has reached a “steady state” in thickness, particle size distribution, and other properties at most locations on the Moon. Hence, the limited particle types and sizes, the absence of a lunar atmosphere, and the lack of water and organic material in the regolith constrain the physical properties of the lunar surface material to relatively narrow, well-defined ranges. The primary factors that affect the physical properties are bulk density, relative density, and temperature.

The physical properties of lunar soils and rocks have been measured *in situ* by robots and astronauts, in the laboratory on returned samples, and by remote sensing from the Earth’s surface and from lunar orbit. The results of these measurements are presented in the following sections.

9.1. GEOTECHNICAL PROPERTIES

“I’m at the foot of the ladder. The LM [Lunar Module] footpads are only depressed in the surface about 1 or 2 inches, although the surface appears to be very, very fine-grained, as you get close to it, it’s almost like a powder; down there, it’s very fine ... I’m going to step off the LM now. That’s one small step for (a) man. One giant leap for mankind. As the—The surface is fine and powdery. I can—I can pick it up loosely with my toe. It does adhere in fine layers like powdered charcoal to the sole and sides of my boots. I only go in a small fraction of an inch. Maybe an eighth of an inch, but I can see the footprints of my boots and the treads in the fine sandy particles.”

*Neil A. Armstrong Tranquillity Base (Apollo 11),
July 20, 1969*

Prior to the Luna, Surveyor, and Apollo soft landings on the Moon, various theories had been proposed regarding the nature of the lunar surface. One theory was that the lunar craters were volcanic in origin and that the surface was mostly lava and hence very hard. The other popular theory was that the craters had been formed by meteoroid impact

and that the surface was a regolith or soil with diverse particle sizes. In short, the lunar surface might be either very hard or very soft. The “hard soil” advocates believed that the ultrahigh vacuum conditions on the Moon would produce “cold welding” between the soil particles. This phenomenon is known to occur if two carefully cleaned surfaces (e.g., of aluminum) are brought together in a vacuum. The lack of water and organic molecules in the lunar vacuum would allow the surfaces to bond atomically or weld. Experiments had also shown that the mineral mica could be cleaved and pressed back together in a vacuum. Thus, the lunar surface was thought to be porous and yet rock-hard, like pumice. At the other extreme, it was believed that the combination of low gravity, vacuum, and electrostatic charges on the soil particles would produce a “fairy-castle” structure, with a consistency similar to sifted flour.

Because of the long lead time required, the design of the Apollo Lunar Module (LM) landing gear had to be completed in the mid-1960s, before there were any direct tactile data available about the lunar surface. Because of the different theories that were being hotly debated at that time, the engineers chose a landing gear that could accommodate a wide range of conditions. To accommodate the “soft” extreme of possible lunar surface properties, the LM landing pad was sized so that it could sink as much as 60 cm into the soil and would have a bearing pressure on the Moon of only approximately 4.6 kPa. This value is only about one-fifth of the stress that a typical person exerts when standing on one foot on Earth. To accommodate the “hard” extreme, a shock absorber system was built into the LM landing struts; this system would allow a safe landing on concrete at a vertical velocity of up to 3 m/sec, which is equivalent to free-fall from a height of 2.9 m in lunar gravity. This shock absorber consisted of a honeycomb material that would crush as the landing struts were forced into it during touchdown, thereby dissipating the energy of impact. Unlike the normal hydraulic shock absorber system in an aircraft, the landing gear on the LM only had to work once and could therefore use the crushable design, which was both simpler and lighter.

The landing pads of the pre-Apollo Surveyor spacecraft were sized for a bearing pressure of 2.2 kPa, and when these unmanned probes were successfully soft-landed on the Moon during 1966-1968, the design of the Apollo LM pads was confirmed as conservative. In spite of this evidence, some scientists were still concerned about the bearing capacity of the lunar surface and recommended that the astronauts have snowshoes and that the LM be equipped with a long radio antenna

in case it disappeared into the soft dust at touchdown (Cooper, 1969, 1970). Just a few months before the flight of Apollo 11, it was seriously suggested that, when Astronaut Armstrong took his first steps on the lunar surface, the soil would jump onto his spacesuit because of the electrostatic attraction. The resulting coating of soil covering his suit was expected to be so thick that he would not be able to see and might not be able to move. Then, if he were able to stagger back into the LM, there was concern that the highly reduced soil would burst into flames when the cabin was repressurized with pure oxygen. Even after several successful Apollo missions to the Moon, some scientists were still convinced that the lunar soil was like fresh snow and that an astronaut could push a rod into it to almost any desired depth.

We now know that the lunar surface is neither so soft, nor so hard, as was once imagined. We also know that the astronauts can land a spacecraft far more gently than the designed 3 m/sec. In fact, the landing struts were stroked only slightly on all of the six Apollo landings. Furthermore, we know that the ranges of geotechnical properties of lunar materials are less than those that occur in surficial materials on Earth. This is because of the following factors:

1. The familiar terrestrial geologic processes of chemical weathering, running water, wind, and glaciation are absent on the Moon. These processes tend to produce well-sorted sediments with uniform grain sizes. The primary lunar soil-forming process is meteoroid impact, which produces a heterogeneous and well-graded (poorly-sorted) soil.

2. The three main constituents most likely to produce unusual or “problem” soils on Earth are absent on the Moon; there is no water, and there are no clay minerals or organic materials.

3. As discussed in Chapters 5 and 7, the variety of minerals in lunar soil is much less than that found on Earth. In fact, many soil particles are simply fragments of rocks, minerals, and glass stuck together with glass (agglutinates).

As a result, the geotechnical properties of lunar soil tend to fall in a fairly narrow range, and the most significant variable is the *relative density*, defined in section 9.1.5. To a certain extent, relative density also controls the other physical properties discussed in this chapter.

To set the stage for discussion of the effects of relative density, other properties will be described first: particle size distribution, particle shapes, specific gravity, bulk density, and porosity. Relative density will then be described. After that, the influence of these properties on compressibility, shear strength, permeability, bearing capacity, slope stability, and trafficability will be considered.

9.1.1. Particle Size Distribution

The particle size distribution in an unconsolidated material, such as lunar soil, is a variable that controls to various degrees the strength and compressibility of the material, as well as its optical, thermal, and seismic properties (Carrier, 1973). Particle size analyses of terrestrial *clastic* sediments (sediments that are composed of broken fragments from preexisting rocks and minerals that have been transported some distance, e.g., sandstone) are the basic descriptive element for any clastic material (Tucker, 1981) and also provide information on their origin and the depositional processes affecting them. The *phi* (ϕ) scale used commonly for measuring particle size is not linear but is a logarithmic transformation of a geometric scale such that $\phi = -\log_2 d$, where d is the particle diameter in millimeters (Folk, 1968; Pettijohn *et al.*, 1973).

The principal method of determining the particle size distribution of an unconsolidated material is sieving, which is generally effective for particle sizes greater than about 10 μm . Scanning electron microscope (SEM) image analysis or Coulter counter methods are usually applied for measuring particle sizes that are smaller than 10 μm (Butler and King, 1974; McKay *et al.*, 1974; Heiken, 1975). The particle size distribution can be presented graphically as histograms (as shown in Fig. 7.18b) or as cumulative curves, usually on log-probability plots (Fig. 9.1). Alternatively, the distribution may be characterized by parameters such as mean particle size, median particle size, sorting, skewness, and kurtosis, which are standard statistical measures for any grouped population (Folk, 1968; Koch and Link, 1970).

Morris *et al.* (1983) have produced a compendium of available data on lunar soils that includes the mean and the median particle sizes. Data on a select set of lunar soils are given in Table 9.1. The selection is based on availability of data, inclusion of representatives of a standard suite of soils as defined by Papike *et al.* (1982), and an intent to represent soils from all Apollo missions. The table provides the gross distribution of weights in different size fractions of the samples collected, together with the mean size (M_z) for the subcentimeter and submillimeter fractions. In addition, a complete dataset for Apollo 17 soils is included (Table A9.1), which provides all of the statistical parameters defined in the following section. (Table numbers preceded by an "A" are found in the appendices at the end of this chapter.)

Definitions of particle size distribution parameters. Rigorous definitions of the statistical parameters for particle size distribution are obtained by computing the moment functions from the

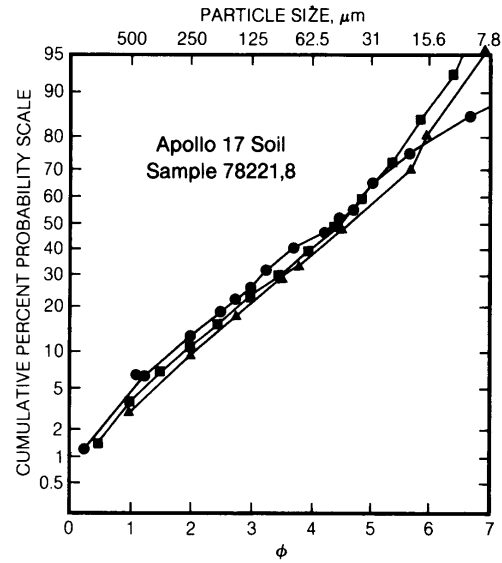


Fig. 9.1. Distribution of particle sizes in separate splits of Apollo 17 lunar soil 78221,8, analyzed by three different laboratories. Lower horizontal axis shows particle size as (ϕ), where (ϕ) = $-\log_2 d$ and d is the particle diameter in millimeters. Upper horizontal axis shows particle size in micrometers. Vertical axis plots cumulative percent on a probability scale. The three curves are close but not identical; the largest differences are present at the smallest particle sizes. All information from unpublished data (after Butler and King 1974).

percent function of weights or numbers in each size class. Approximate values of these parameters may also be obtained by reading selected percentile sizes from a cumulative frequency plot on a log-probability sheet. The convention of defining a percentile is such that, at the n -th percentile, $n\%$ of the sample is coarser than the n -th percentile particle size. In practice, a size class is really a size interval; let the midpoint of any size class be m (ϕ) in phi units, p the percent fraction in that size interval, and (ϕ) the n -th percentile size; then

$$\text{Mean } (\bar{x}) = \frac{\sum p m \phi}{100} \approx \frac{\phi_{16} + \phi_{50} + \phi_{84}}{3} = M_z$$

$$\text{Median} = \phi_{50} = M d_\phi$$

$$\text{Sorting } (\sigma) = \sqrt{\frac{\sum p (m \phi - \bar{x})^2}{100}} \approx \frac{\phi_{84} - \phi_{16}}{4} + \frac{\phi_{95} - \phi_5}{6.6} = \sigma_1$$

TABLE 9.1. Weight distribution in size fractions of representative scooped surface soils (from Morris *et al.*, 1983; data emphasize coarser fractions).

Soil	Size Fraction					Mean Size, M_z	
	>1 cm	4-10 mm (weights in grams)	2-4 mm	1-2 mm	<1 mm	<1 cm (μm)	<1 mm (μm)
10002*	18.5	7.6	11.0	14.7	424.5	—	52
12001		UNAVAILABLE				—	60
14003	23.0	33.0	31.8	42.1	947.9	129	99
14141	0.0	7.4	6.7	5.4	28.5	616	123
14163*	0.0	196.5	197.1	288.7	4444.0	76	56
15220	0.0	7.0	5.8	2.4	290.0	—	43
15270*	0.0	4.4	13.7	20.7	798.3	—	94
15400	513.1	7.9	6.1	4.8	86.4	330	61
61180	0.0	6.1	6.2	9.4	156.2	94	64
61220	5.1	10.6	9.6	6.4	61.0	216	68
62280	12.0	14.3	13.1	21.7	218.5	134	70
64500*	31.2	24.2	24.1	28.4	495.7	104	65
68500	1.3	17.3	25.1	37.8	521.1	106	68
70180	466.6	1.7	3.1	4.6	157.1	67	58
71500	52.3	13.1	17.6	22.7	600.9	83	65
72140	1.3	2.7	1.9	5.3	225.9	57	50
72500*	3.1	8.0	12.9	24.1	687.2	67	57
73240	1.6	22.3	14.4	14.9	192.7	127	51
74220†	0.0	0.98	0.17	0.68	7.77	—	41
78220*	0.0	1.5	2.7	5.2	227.1	50	45
78500	109.3	19.2	16.1	21.4	718.7	46	41

* Reference suite soil (Papike *et al.*, 1982).

† Orange soil; this is not a typical soil but likely represents fire fountain deposits on the Moon (see section 6.1.7).

$$\text{Skewness } (\alpha_3) = \frac{\sum p (\phi - \bar{x})^3}{100\sigma^3}$$

$$\approx \frac{\phi_{16} + \phi_{84} - 2\phi_{50}}{2(\phi_{84} - \phi_{16})} + \frac{\phi_5 + \phi_{95} - 2\phi_{50}}{2(\phi_{95} - \phi_5)} = SK_1$$

$$\text{Kurtosis} = \frac{\sum p (\phi - \bar{x})^4 - 3\sum p (\phi - \bar{x})^2}{100}$$

$$\approx \frac{\phi_{95} - \phi_5}{2.44(\phi_{75} - \phi_{25})} = K_G$$

Typical particle size distribution. The majority of lunar soil samples fall in a fairly narrow range of particle-size distributions (Carrier, 1973). In general, the soil is a well-graded (or poorly sorted), silty sand to sandy silt: SW-SM to ML in the Unified Soil Classification System (ASTM D 2487, 1987; Lambe and Whitman, 1969). The median particle size is 40 to 130 μm , with an average of 70 μm ; i.e., approximately half of the soil by weight is finer than the human eye can resolve. Roughly 10% to 20% of the soil is finer than 20 μm , and a thin layer of dust

adheres electrostatically to everything that comes in contact with the soil: spacesuits, tools, equipment, and lenses. Housekeeping is a major challenge for operations on the lunar surface.

9.1.2. Particle Shapes

The shapes of individual lunar soil particles are highly variable, ranging from spherical to extremely angular (Tables A9.2, A9.3, and A9.4; Fig. 7.2). In general, the particles are somewhat elongated and are subangular to angular. Because of the elongation, the particles tend to pack together with a preferred orientation of the long axes. This effect has been observed in lunar core tube samples and laboratory simulations, and the orientation has been found to be dependent on the mode of deposition (Mahmood *et al.*, 1974a). Because of this preferred particle orientation, the physical properties of the lunar soil *in situ* are expected to be anisotropic. For example, the thermal conductivity in the horizontal direction should be different from that in the vertical direction. Furthermore, many of the particles are not compact, but have irregular, often reentrant surfaces. These particle surface irregularities especially affect the compressibility and shear strength of the soil, as discussed in more detail in sections 9.1.6 and 9.1.7.

TABLE 9.2. Average particle shapes of lunar soil.

Parameter	Average Value	Description	References
Elongation	1.35	Somewhat elongated	<i>Heywood (1971); Mahmood et al. (1974b)</i>
Aspect ratio	0.55	Slightly-to-medium elongated	<i>Görz et al. (1971, 1972)</i>
Roundness			
Silhouette	0.21	Subangular	<i>Mahmood et al. (1974b)</i>
Direct light	0.22	Angular	
Volume coefficient	0.3	Elongated	<i>Heywood (1971)</i>
Specific surface area	0.5 m ² /g	Irregular, reentrant	<i>Cadenhead et al. (1977)</i>

Thus, particle shape has a significant influence on bulk physical properties. Although shape is difficult to quantify, a number of measurements have been made, and the results are summarized in Table 9.2. The various shape parameters are discussed in the following sections.

Elongation. Elongation is defined as the ratio of the major to intermediate axes of the particle, or length to width. Particles with values of the ratio <1.3 are considered equant, and particles whose ratio is >1.3 are elongate.

Mahmood et al. (1974b) measured elongations of 1136 particles from three lunar soil samples (14163,148, 14259,3, and 15601,82). Individual particle sizes ranged from 2300 to <44 μm. The weighted average elongation ranged from 1.31 to 1.39. More details are given in Table A9.2.

Heywood (1971) measured elongation on 30 particles with a nominal size of 700 μm, all taken from one soil sample (12057,72). His values ranged from 1.32 to 1.38. Heywood also measured six other shape coefficients for these same particles: flatness, area ratio, volume coefficient, rugosity coefficient, specific circularity of profile, and specific circularity including the effect of rugosity. More details are given in Table A9.2.

Aspect ratio. In geotechnical studies, aspect ratio is inversely related to elongation; it is defined as the ratio of the minor axis to the major axis of an ellipse fitted to the particle by a least-squares approximation. *Görz et al. (1971, 1972)* measured aspect ratios on 2066 particles from seven lunar samples; particle sizes ranged from 1.25 to 30 μm. Values of the aspect ratios varied from 1.0 (equant) to <0.1 (very elongate), with most values falling in the range 0.4 to 0.7 (slightly-to-moderately elongated). *Görz et al. (1972)* also measured the shape complexity factor for most of these same particles. More details are given in Table A9.3.

Roundness. Roundness is defined as the ratio of the average of the radii of the corners of the particle image to the radius of the maximum inscribed circle. *Mahmood et al. (1974b)* measured roundness on silhouettes of the same 1136 particles for which they had measured elongation. The weighted average roundness values varied from 0.19 to 0.26, corresponding to subangular particle shapes. They also measured roundness in direct light on 641 particles from the same three lunar samples and found that the weighted average value varied from 0.20 to 0.25, corresponding to angular particles. More details are given in Table A9.4.

Volume coefficient. Volume coefficient is defined as the volume of a particle divided by the cube of the diameter of the circle that encloses the same area as the particle profile. *Heywood (1971)* determined the volume coefficient of 6755 particles taken from one Apollo 12 sample (12057,72); particle sizes ranged from 733 to 60 μm, which represents roughly the coarser half of a typical lunar soil sample. The results are plotted in Fig. 9.2, where it can be seen that the volume coefficient varies from 0.24 to 0.37, with an average value of about 0.3; this value corresponds approximately to a prolate spheroid with a major-to-minor axis ratio of 3 to 1.

The volume coefficient for a sphere is greater than 0.52, well above the measured values shown in Fig. 9.2. Heywood found that the glass spherules represent only about 1 in 500 particles in the coarse fraction of this Apollo 12 sample, and hence their effect on geotechnical properties is negligible. [Immediately after the Apollo 11 mission, some scientists had speculated that the “slipperiness” of the lunar soil reported by the astronauts was caused by the presence of a large proportion of such glass beads. This was even commented upon in the September 1969 issue of *Scientific American*. The observed amounts of such beads in most lunar soils

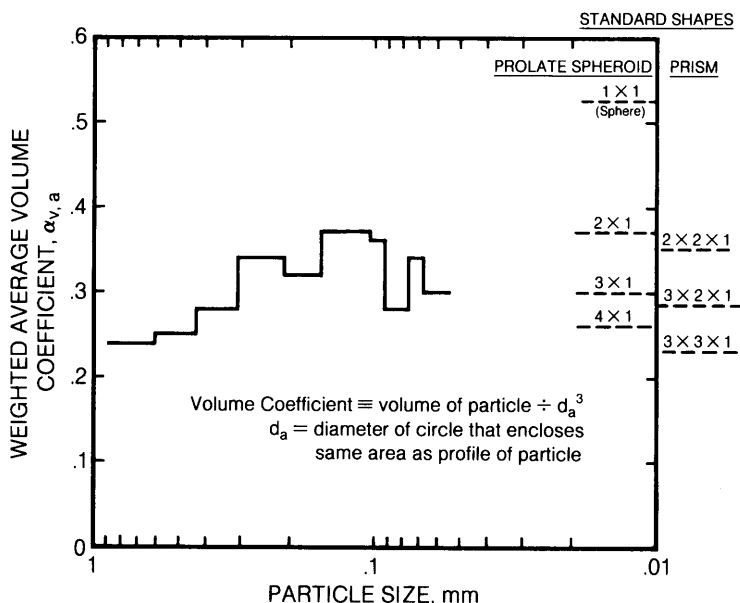


Fig. 9.2. Distribution of volume coefficient for lunar soil particles as a function of particle size (in millimeters) for sample 12057,72 (after Heywood, 1971). Theoretical volume coefficients for a range of standard prismatic and ellipsoidal particle shapes are shown on the right vertical axis for comparison.

(<1%) are too low to produce any such mechanical effects.]

Fourier analysis. Particle shape can also be quantified from the two-dimensional image of a particle. Commonly, a two-dimensional image is the only “sample” available for shape analysis when working with thin sections of grain mounts. The outline of a two-dimensional image is digitized using a polar coordinate system with the center of the image as the origin. The measurements are expressed in the form of a Fourier expansion series (Ehrlich and Weinberg, 1970). Briefly, an image is expressed as

$$R(\theta) = R_0 + \sum_{n=1}^{\infty} R_n \cos(n\theta - \phi_n)$$

where θ = polar angle; R_0 = average radius, n = harmonic order, R_n = harmonic amplitude, and ϕ = phase angle. The shape of the grain thus becomes represented as the sum of the radii, expressed as a function of polar angles and phase angles, ideally for every point on the outline of the image. In essence, each harmonic may be viewed as a system of flowers with two petals (harmonic 2), three petals (harmonic 3), four petals (harmonic 4), . . . n petals (harmonic n). The amplitude of each harmonic is the contribution of that harmonic to the shape (in this case the outline of the image) of the particle. Comparison between samples is achieved by amplitude spectral analysis and/or by analyzing the amplitude frequency distribution at selected harmonics. Kordesh et al. (1982) and Kordesh (1983a,b)

measured the shapes of monomineralic silicate mineral fragments in a lunar soil breccia (10065), in lunar drill-core soils (15003,6059), and in brecciated achondrites (meteorites). Results show that the general shapes of lunar soil particles and those of clasts in meteoritic breccias are similar (Fig. A9.1). The shapes of these particles are different from those that have undergone abrasion in water and wind on Earth.

Specific surface area. Specific surface area is defined as the surface area of a particle divided by its mass, usually expressed in square meters per gram. It is a measure of both the size and the shape of the particle. For a spherical particle, the specific surface area (SSA) is inversely proportional to the diameter, and is given by

$$SSA = \frac{6}{d G \rho_w} \text{ (m}^2\text{/g)}$$

where d is the diameter of the sphere in micrometers; G is the specific gravity; and ρ_w is the density of water, 1 g/cm³.

For example, uniform, solid spheres with a specific gravity of 3.1 (typical for lunar soils, see section 9.1.3) would have the following specific surface areas:

Diameter (μm)	Specific Surface Area (m ² /g)
1000	0.0019
100	0.019
10	0.19
1	1.9

A "soil" consisting of spheres with the same submillimeter particle size distribution as lunar soil would have a SSA of about 0.065 m²/g. This SSA value corresponds to an equivalent diameter of approximately 30 μm, which is less than the average particle size by weight of lunar soils (~65 μm). Because of the reciprocal relationship shown above, the smaller particles in a soil tend to contribute most to the bulk SSA value.

By comparison, terrestrial clay minerals have much higher SSA values, owing to their very small size and platy shape:

Clay	Specific Surface Area (m ² /g)
Kaolinite	10 - 20
Illite	65 - 100
Montmorillonite	50 - 800

(after Mitchell, 1976)

The results of 17 measurements of the SSA of lunar soils are tabulated in Table A9.5 (Cadenhead *et al.*, 1977). All these measurements were performed on the submillimeter soil fraction by means of nitrogen gas adsorption. The SSA values range from 0.02 to 0.78 m²/g, with a typical value of 0.5 m²/g, which corresponds to an equivalent spherical diameter of 3.9 μm. Hence, the SSA of lunar soil is much less than that of terrestrial clay minerals, and yet it is significantly greater than can be accounted for by small particle sizes alone. Rather, the relatively large SSA of lunar soils is indicative of the extremely irregular, reentrant particle shapes.

These considerations suggest in turn the definition for a new shape parameter that is independent of the particle size, which is called the *equivalent surface area ratio* (ESAR)

$$ESAR = \frac{d_s}{d_e} = \frac{SSA_e}{SSA_s}$$

where d_s = equivalent diameter of spheres with the same particle size distribution as the soil being tested and d_e = equivalent spherical diameter of the soil, as calculated from the specific surface area.

For a typical lunar soil, the equivalent surface area ratio would be nearly 8; that is, the soil would have eight times as much surface area as would an assemblage of spheres with the equivalent particle size distribution.

9.1.3. Specific Gravity

The *specific gravity*, G , of a soil particle is defined as the ratio of its mass to the mass of an equal volume of water at 4°C. Many terrestrial soils have a specific gravity of 2.7; that is, the density of the individual particles is 2.7 g/cm³, or 2.7 times that of water (1 g/cm³).

In order to determine the specific gravity of a soil, a portion of the material is first weighed, and then immersed in a fluid to measure the volume that it displaces. Various fluids can be used, including water, air, or helium. The specific gravity of lunar soils, breccias, and individual rock fragments has been measured by various investigators, and the results are summarized in Table 9.3. Values for lunar soils range from 2.3 to >3.2; we recommend a value of 3.1 for general scientific and engineering analyses of lunar soils.

The average specific gravity of a given lunar soil is related to the relative proportions of different particle types; i.e., basalts, mineral fragments, breccias, agglutinates, and glasses (Fig. 7.1). However, the interpretation of the specific gravity is complicated by the porosity of the particles. As illustrated in Fig. 9.3, the porosity may be divided into three categories: (1) *intergranular* porosity, or the volume of space between individual particles;

(2) *intragranular* porosity, or the volume of reentrant surfaces on the exterior of the particles; and

(3) *subgranular* porosity, or the volume of enclosed voids within the interior of particles.

When the soil particles are immersed in a fluid, the intergranular and intragranular space is filled, but not the subgranular space. Thus, the measured specific gravity is not solely an index of particle mineralogy, but also includes the effect of enclosed voids. By suspending the soil particles in a density gradient, produced by varying the proportions of a mixture of methylene iodine and dimethyl formamide, Duke *et al.* (1970b) found the following values of specific gravity:

Agglutinate and glass particles	1.0 to >3.32
Basalt particles	>3.32
Breccia particles	2.9 to 3.10

The enclosed voids in a lunar soil particle with a specific gravity of 1.0 occupy two-thirds of the total volume of the particle. Thus, the average specific gravity of the particles would be even greater if there were no enclosed voids. For example, if the lunar soil were ground into a fine powder (in which the resulting particles were smaller than the enclosed voids), these voids would be destroyed, and the specific gravity would be increased. The actual subgranular porosity of individual lunar soil particles is only poorly known, and additional measurements of subgranular porosity are needed.

The intragranular porosity has a strong effect on the bulk density of the lunar soil, whereas the intergranular porosity affects both the bulk density and the relative density. These relations will be discussed in more detail in the following sections.

TABLE 9.3. Specific gravity of lunar soils and rock fragments.

Sample Number	Sample Weight (grams)	Specific Gravity, G	Test Technique	References
10004 and 10005	49.1	3.1*	Nitrogen pycnometry	<i>Costes et al. (1970a)</i>
10020,44	5.94	3.25†	Water pycnometry	<i>Horai and Winkler (1980)</i>
10065,23	4.48	3.12†	Water pycnometry	<i>Horai and Winkler (1980)</i>
10084	1.5	3.01	Suspension in density gradient	<i>Duke et al. (1970a)</i>
Apollo 12 (unnumbered)	56.9	3.1*	Air pycnometry	<i>Carrier (1970)</i>
12002,85	2.32	2.31†	Water pycnometry	<i>Horai and Winkler (1975)</i>
12029,8	1.10	2.9	Nitrogen pycnometry	R. F. Scott (personal communication, 1988)
12057,72		2.9	Unknown	<i>Heywood (1971)</i>
14163,111	0.65	2.9 ± 0.1	Helium pycnometry	<i>Cadenhead et al. (1972)</i>
14163,148	0.97	2.90 ± 0.05	Water pycnometry	<i>Carrier et al. (1973a, b)</i>
14259,3	1.26	2.93 ± 0.05	Water pycnometry	<i>Carrier et al. (1973a, b)</i>
14321,74		3.2 ± 0.1†	Helium pycnometry	<i>Cadenhead et al. (1972)</i>
14321,156		3.2 ± 0.1†	Helium pycnometry	<i>Cadenhead et al. (1972)</i>
15015,29		3.0 ± 0.1†	Helium pycnometry	<i>Cadenhead et al. (1974); Cadenhead and Stetter (1975)</i>
15101,68		3.1 ± 0.1	Helium pycnometry	<i>Cadenhead and Jones (1972)</i>
15601,82	0.96	3.24 ± 0.05	Water pycnometry	<i>Carrier et al. (1973a, b)</i>
70017,77	2.55	3.51†	Water pycnometry	<i>Horai and Winkler (1976)</i>
70215,18	4.84	3.44†	Water pycnometry	<i>Horai and Winkler (1976)</i>
72395,14	3.66	3.07†	Water pycnometry	<i>Horai and Winkler (1976)</i>
77035,44	3.68	3.05†	Water pycnometry	<i>Horai and Winkler (1976)</i>

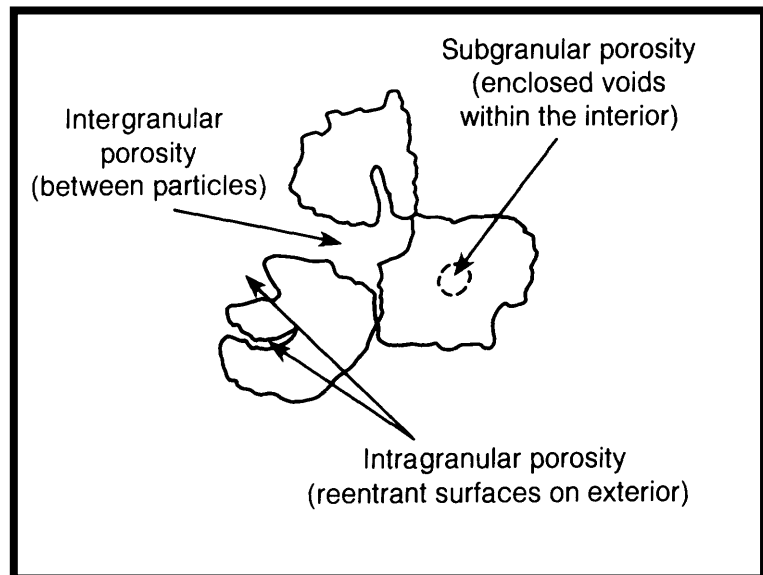
Recommended typical specific gravity of lunar soil: 3.1

* Total soil sample; others were performed on submillimeter fraction.

† Single basalt fragment.

‡ Single breccia fragment.

Fig. 9.3. Schematic diagram showing the different types of soil porosity produced in the lunar soil by soil particles: (1) intergranular porosity, produced by open spaces between different particles; (2) intragranular porosity, produced by reentrant surfaces on individual irregular particles; (3) subgranular porosity, produced by completely enclosed voids within single particles.



9.1.4. Bulk Density and Porosity

The *bulk density*, ρ , of soil is defined as the mass of the material contained within a given volume, usually expressed in grams per cubic centimeter. The *porosity*, n , is defined as the volume of void space between the particles divided by the total volume. Bulk density, porosity, and specific gravity are interrelated as

$$\rho = G\rho_w(1 - n)$$

where G = specific gravity (including subgranular porosity; section 9.1.3); ρ_w = density of water = 1 g/cm³; and n = porosity, expressed as a decimal (combining both inter- and intragranular porosity).

It is convenient in geotechnical engineering to also define another parameter, the *void ratio*, which is equal to the volume of void space between the particles divided by the volume of the "solid" particles (again, including the subgranular porosity). Void ratio, e , and porosity are interrelated as

$$e = \frac{n}{1 - n} \text{ or } n = \frac{e}{1 + e}$$

The *in situ* bulk density of lunar soil is a fundamental property. It influences bearing capacity, slope stability, seismic velocity, thermal conductivity, electrical resistivity, and the depth of penetration of ionizing radiation. Consequently, considerable effort has been expended over the years in obtaining estimates of this important parameter.

Prior to the soft landings on the Moon, remote-sensing techniques were used to infer the bulk density of the lunar soil. These techniques included passive measurements of optical, infrared, and microwave emissivity and active measurements of radar reflectivity. With the Surveyor and Luna unmanned landings, direct measurements were possible at discrete points. In addition, correlations with laboratory tests on simulated lunar soil permitted extrapolation over wider areas. Finally, beginning with Apollo, core tube samples of lunar soil were returned that permitted unambiguous measurements of the *in situ* bulk density. At present, the best estimate for the average bulk density of the top 15 cm of lunar soil is 1.50 ± 0.05 g/cm³, and of the top 60 cm, 1.66 ± 0.05 g/cm³ (Mitchell et al., 1974).

A summary of estimated lunar bulk densities is presented in Table 9.4, together with recommended typical values. The various estimating and measuring techniques are described in the following sections.

Early inferred values of bulk density based on remote sensing. As shown in Table 9.4, a very low density of 0.3 g/cm³ was assumed by Jaffe (1964,

1965) in an effort to estimate lower-bound bearing capacities. Halajian (1964) also assumed a very low density of 0.4 g/cm³, but believed that the strength of the lunar surface was similar to that of pumice.

Robotic measurements of bulk density on the lunar surface. When Surveyor 1 landed on the Moon in June 1966, a much higher density of 1.5 g/cm³ was deduced by Christensen et al. (1967), using records of the interaction between the lunar soil and the spacecraft footpads, combined with analysis of the television images, to determine the particle size distribution. Shortly thereafter, the first *in situ* measurement of lunar soil density was made by the U.S.S.R. probe, Luna 13, using a gamma-ray device. The calibration curve for this device was double-valued, and the data obtained were consistent with two density values: 0.8 and 2.1 g/cm³; Cherkasov et al. (1968) chose the lesser value. Based on the results from the soil mechanics surface sampler experiments on Surveyor 3 and 7, Scott and Roberson (1967, 1968a,b) confirmed the Surveyor 1 value of 1.5 g/cm³, and Scott (1968) suggested that the Soviet investigators had chosen the wrong portion of their calibration curve. Just before the Apollo 11 landing, Jaffe (1969) reevaluated the Surveyor data and proposed that the bulk density was 1.1 g/cm³ at the surface and increased linearly to 1.6 g/cm³ at a depth of 5 cm.

Later, during the early 1970s, the U.S.S.R. unmanned roving vehicles Lunokhod 1 and Lunokhod 2 traversed a total of 47 km on the lunar surface. These vehicles performed approximately 1000 cone-vane penetrometer tests to depths of 10 cm (see section 9.1.7). Leonovich et al. (1974a, 1975) correlated the lunar surface penetration resistance with measurements on returned lunar samples from Luna 16 and Luna 20, and they deduced an average surficial bulk density of about 1.5 g/cm³.

Inferred values of bulk density based on correlations with simulated lunar soil. The *in situ* bulk density of lunar soil has also been estimated from analyses of astronaut bootprints, vehicle tracks, boulder tracks, and penetration resistance. The results are summarized in Table 9.4. Mitchell et al. (1974) found that the astronaut bootprints indicated a density of approximately 1.45 to 1.59 g/cm³, representative of the top 15 cm of the lunar surface in the intercrater areas. The soils on crater rims were found to be slightly less dense: 1.34 to 1.57 g/cm³. Analysis of vehicle tracks made by the Modular Equipment Transporter (Apollo 14) and the Lunar Roving Vehicle (Apollo 15, 16, and 17) indicated values of 1.40 to 1.56 g/cm³, also representative of the top 15 cm. The tracks left by boulders that had rolled downslope at the Apollo 17 site indicated a density of 1.38 to 1.68 g/cm³,

TABLE 9.4. Estimates of lunar soil *in situ* bulk density.

Source	Bulk Density, (g/cm ³)	References
<i>Remote Sensing</i>	0.3 0.4	Jaffe (1964, 1965) Halajian (1964)
<i>Robotic Measurements on Surface</i>		
Surveyor 1	1.5	Christensen et al. (1967)
Luna 13	0.8	Cherkasov et al. (1968)
Surveyor 1, 3, and 7	1.5	Scott and Roberson (1967, 1968a,b); Scott (1968)
Surveyor	1.1 at surface; 1.6 at 5 cm	Jaffe (1969)
Lunokhod 1/Luna 16	1.5-1.7	Leonovich et al. (1971, 1972)
Surveyor 3	1.7	Jaffe (1973)
Lunokhod 1 and 2/Luna 16 and 20	1.5	Leonovich et al. (1974a, 1975)
<i>Correlations with Simulated Lunar Soil</i>		
<i>Astronaut Bootprints</i>		
Intercrater area	1.45 - 1.59	Mitchell et al. (1974)
Crater rims (depth 0-15 cm)	1.34 - 1.57	Mitchell et al. (1974)
<i>Vehicle Tracks</i>		
MET and LRV (depth 0-15 cm)	1.40 - 1.56	Mitchell et al. (1974)
Boulder Tracks (depth 0-300 to 400 cm)	1.38 - 1.68	Mitchell et al. (1974)
<i>Penetration Resistance</i>		
Apollo 11	< 1.81 - 1.92	Costes et al. (1971)
Apollo 12	< 1.80 - 1.84	Costes et al. (1971)
Lunokhod 1 and Apollo 14-16 (depth 0-60 cm)	1.58 - 1.76	Mitchell et al. (1974)
<i>Returned Core Samples</i>		
Apollo 11	1.54 - 1.75 0.75 ->1.75	Costes and Mitchell (1970) Scott et al. (1971)
Apollo 12	1.6 - 2.0 1.55 - 1.90 1.7 - 1.9	Scott et al. (1971) Houston and Mitchell (1971) Carrier et al. (1971)
Luna 16	1.2	Vinogradov (1971)
Apollo 14	1.45 - 1.6	Carrier et al. (1972a)
Apollo 15		
Core Tubes	1.36 - 1.85	Carrier et al. (1972a); Mitchell et al. (1972a)
Drill Cores	1.62 - 1.93	Carrier (1974); Mitchell et al. (1972a)
Luna 20	1.1 - 1.8	Vinogradov (1972)
Apollo 16		
Core Tubes	1.40 - 1.80	Mitchell et al. (1972b)
Drill Cores	1.47 - 1.75	Carrier (1974)
Apollo 17		
Core Tubes	1.57 - 2.29	Mitchell et al. (1973a)
Drill Core	1.74 - 1.99	Carrier (1974)
Luna 24	1.6 - 2.1	Florensky et al. (1977); Barsukov (1977)
<i>Best Estimates: Typical Average Values (Intercrater Areas)</i>		Mitchell et al. (1974)
<i>Depth Range (cm)</i>		
0 - 15	1.45 - 1.55	
0 - 30	1.53 - 1.63	
30 - 60	1.69 - 1.79	
0 - 60	1.61 - 1.71	

representative of the top 300 to 400 cm of the regolith (Mitchell *et al.*, 1974). Costes *et al.* (1971) analyzed the resistance of the soil to penetration by the flagpole, the Solar Wind Composition Experiment staff, and other tools at the Apollo 11 and 12 sites; they deduced upper limits for the densities of 1.81 to 1.92 g/cm³ and 1.80 to 1.84 g/cm³, respectively. Finally, Mitchell *et al.* (1974) found that penetrometer measurements made by Lunokhod 1 and on the Apollo 14, 15, and 16 missions indicated densities of 1.58 to 1.76 g/cm³, representative of the top 60 cm.

In each of the above analyses, it was necessary to assume that the lunar soil behaves approximately the same as a simulant of crushed basaltic lava with a similar particle size distribution, after correction for the effect of gravity. These correlations were developed by normalizing with respect to relative density (see section 9.1.5). During the early Apollo missions, when very little data were available, it was necessary to assume that both the specific gravity and maximum and minimum porosity values for lunar soil were the same as for the simulant. Later, it became clear that this was not the case. Hence, these interpretive methods are better estimators of relative density than of bulk density, and will be discussed in more detail in section 9.1.5.

Measurements of bulk density on returned core samples. Beginning with the Apollo 11 mission, core tube samples of lunar soil were collected and returned from all of the Apollo sites and three of the Luna sites. Such cores are important because they provide a more or less continuous section into the uppermost lunar regolith, to depths up to 3 m.

Two different types of coring tools were used to sample the regolith: *Drive core tubes* were hollow tubes hammered vertically into the regolith by an astronaut to depths of less than a meter. *Rotary drill core tubes* were drilled into the surface to depths of several meters.

Altogether, nearly 16 kg of drive core tube materials have been recovered, using core tubes driven to depths of approximately 70 cm into the lunar surface. In addition, more than 4 kg of rotary drill

core tube samples have been recovered, from depths of up to 3 m. Density data for these samples are summarized in Tables A9.6 and A9.7, respectively.

The drive core tube sampler used on the Apollo 11 mission is shown in Fig. 9.4, and a photograph of Astronaut Aldrin hammering one of the core tubes into the lunar surface is shown in Fig. 9.5. Two core tube samples were recovered on Apollo 11, and densities measured on the returned samples were 1.59 and 1.71 g/cm³ (see Table A9.6). The Apollo 11 drive core tube utilized a reverse-flare bit, as indicated schematically in Fig. 9.6. Thus, if the surface soil were initially loose, the shape of the bit would tend to compress the soil as it entered the core tube, thereby leading to an overestimation of the *in situ* bulk density. On the other hand, if the soil were initially dense, the shearing action of the bit would tend to loosen the soil, leading to an underestimation of the *in situ* density. As a result of this ambiguity, Scott *et al.* (1971) could only conclude that the value of the *in situ* density was somewhere between 0.75 and >1.75 g/cm³. A photograph of one of the Apollo 11 core tube samples as returned to the Lunar Receiving Laboratory is shown in Fig. 9.7.

The drive core tube bit used on the Apollo 12 and 14 missions did not have a reverse flare, as shown in Fig. 9.6. However, the wall thickness of the bit still caused significant disturbance to the soil sample. The *in situ* density at the Apollo 12 site was initially estimated to be from 1.6 to 2 g/cm³ (Scott *et al.*, 1971). Core tube simulations performed later by Houston and Mitchell (1971) and Carrier *et al.* (1971) yielded additional estimates of 1.55 to 1.9 g/cm³ and 1.7 to 1.9 g/cm³, respectively.

Vinogradov (1971) estimated a value of 1.2 g/cm³ for a 101-g rotary drill sample returned by Luna 16 (Fig. 9.8), and Carrier *et al.* (1972a) estimated *in situ* densities of 1.45 to 1.6 g/cm³ for the Apollo 14 core tube samples.

The shapes of the drive core tube bits used on the Apollo 11, 12, and 14 missions not only affected the measurements of the *in situ* soil density, they also complicated the interpretation of the relationships

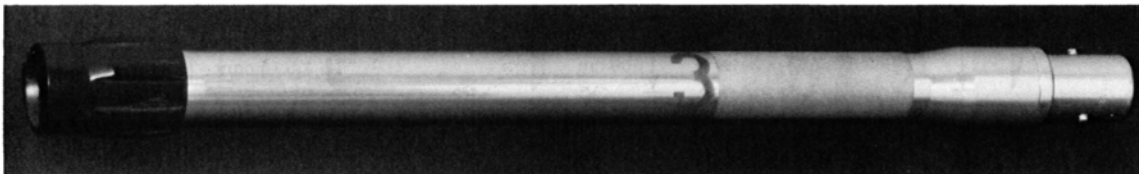


Fig. 9.4. Core tube sampler used to obtain cores of lunar soil during the Apollo 11 mission. Separate tubes, each 2.8 cm in diameter (outside diameter) and 39.9 cm long, could be connected into a single tube that was progressively hammered into the lunar surface by an astronaut. (NASA Photo S69-31856.)

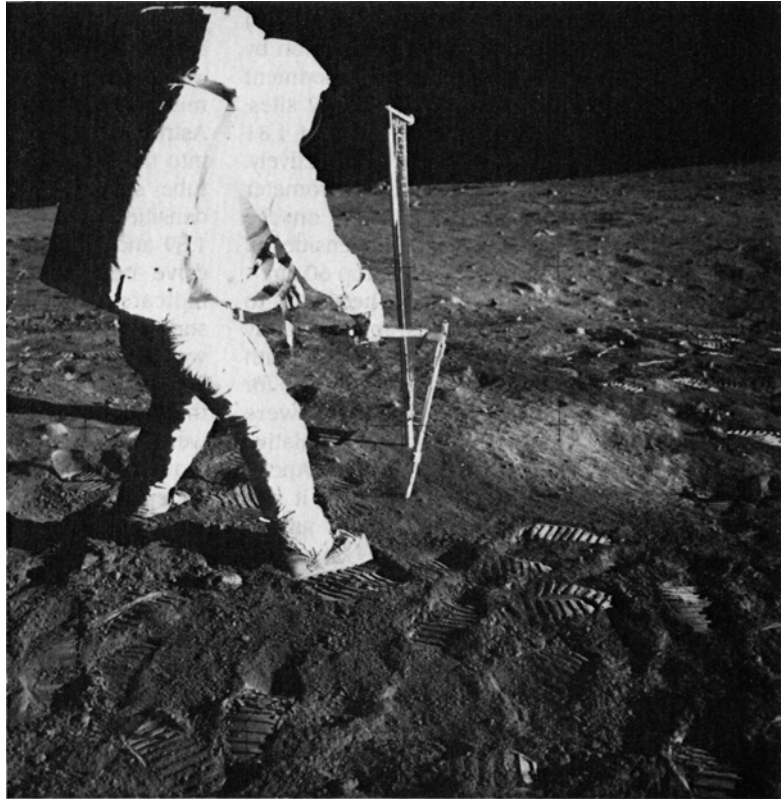


Fig. 9.5. Astronaut Edwin Aldrin driving the core tube sampler into the lunar surface at the Apollo 11 landing site (Tranquillity Base). A short extension handle is attached to the core tube and is being driven with a hammer. The aluminum sheet of the Solar Wind Composition Experiment stands vertically in the background. (NASA Photo AS-11-40-5964.)

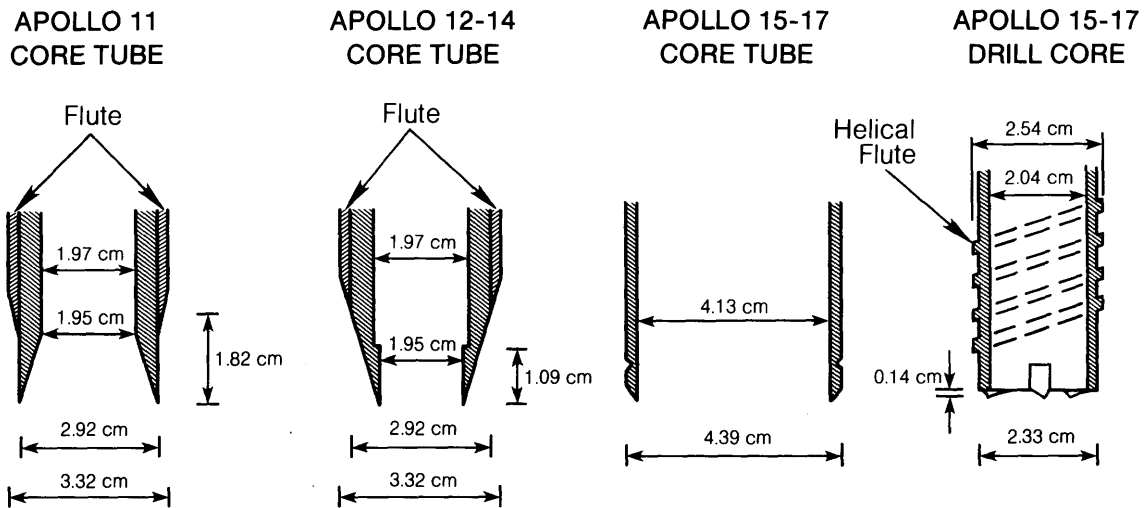


Fig. 9.6. Comparative cross-sections with dimensions (in centimeters) of the tips of the core tubes and drill bits used to collect core samples of lunar soil on the various Apollo missions.

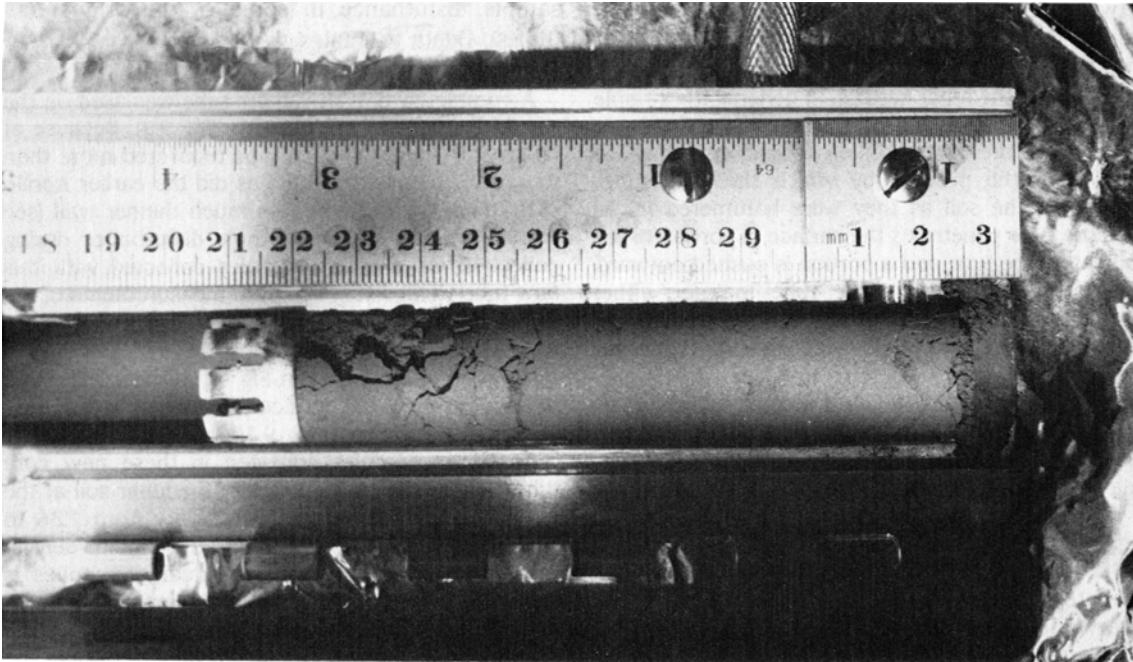


Fig. 9.7. Photograph of Apollo 11 core tube sample 10005 (S/N 2007), immediately after opening of the tube in the Lunar Receiving Laboratory at the NASA Johnson Space Center in 1969. The core was opened by extruding the liner, which consisted of two hemicylindrical, thin aluminum sleeves held together by teflon shrink tubing. The teflon was cut off and the upper half of the aluminum sleeve lifted off without disturbing the core inside. The lunar soil material densely fills the core tube, but some cracking and disintegration are visible in the middle of the portion of the core shown. The white plug is a teflon stopper inserted into the core tube. Metal bar at top gives scales in inches and centimeters. (NASA Photo S-69-45048.)

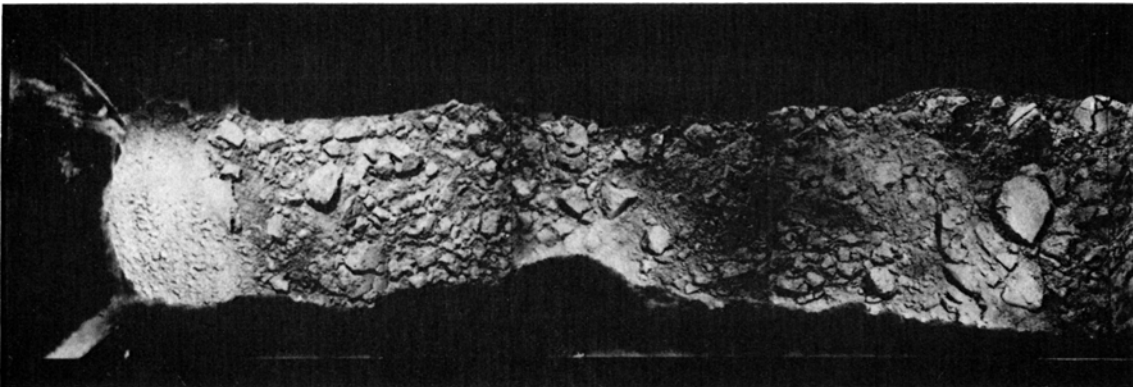


Fig. 9.8. Photograph of the U.S.S.R. Luna 16 drill core sample collected and returned by a robot lander in 1970. The returned core, about 35 cm long and collected in a flexible tube, was extruded out into a metal tray for examination. This picture shows a section of the core about 40 cm long (after being shaken into the tray); the material in the tray is about 3 cm across. Upper part of the core is at the top (left); coarse rock fragments can be seen in the lower part of the picture (bottom; right). (Photograph from *Vinogradov*, 1971.)

between density and depth. The problem arises from the fact that a depth of, e.g., 50 cm in an early Apollo core tube sample does not correspond to the same depth below the lunar surface. In general, the sample lengths in the core tube are less than the depths to which the cores were driven. These discrepancies arise from the process by which the core tubes penetrated the soil as they were hammered in. As the core tube penetrates the surface, a portion of the soil enters the tube and a portion is pushed outward; the portion that enters the tube may be either compressed or loosened. As the depth increases, the portion entering the tube progressively decreases until no more sample is recovered; the tube is now plugged, and the deeper soil is simply pushed aside. Detailed laboratory simulations were performed with the Apollo 11, 12, and 14 core tubes, and approximate depth calibrations were developed by *Carrier et al.* (1971, 1972a). The results are summarized in Fig. A9.2.

The same types of laboratory simulations were used to evaluate the depth relationships for the rotary drill cores used on the Apollo 15, 16, and 17 missions. In some of these returned core samples, the interpretation was complicated by obvious

sample disturbance in some of the drill stems (tubes). Depth estimates were developed by *Carrier* (1974) and are summarized in Fig. A9.3.

A completely new drive core tube was used on the Apollo 15, 16, and 17 missions (Fig. 9.9). Because of its greater diameter, each tube recovered more than four times as much sample as did the earlier Apollo core tubes. Furthermore, the much thinner wall (see Fig. 9.6) greatly reduced sample disturbance during collection. As a result, samples collected with this new tube yielded very accurate measurements of the *in situ* bulk density. Sampling with a double core tube at Station 9A at the Apollo 15 site is shown in a series of photographs in Fig. 9.10. The neat, round hole left in the lunar surface after the core tube was withdrawn is shown in Fig. 9.10d.

Based on samples collected in these new core tubes, the *in situ* bulk density of the lunar soil at the Apollo 15 site was estimated to vary from 1.36 to 1.85 g/cm³ (*Carrier et al.*, 1972a). A plot of density vs. depth for each of the individual core tubes is shown in Fig. 9.11; the bands indicate the small uncertainty associated with measurements of the returned bulk density. The *in situ* bulk density at the Apollo 16 site was estimated to vary from 1.40 to

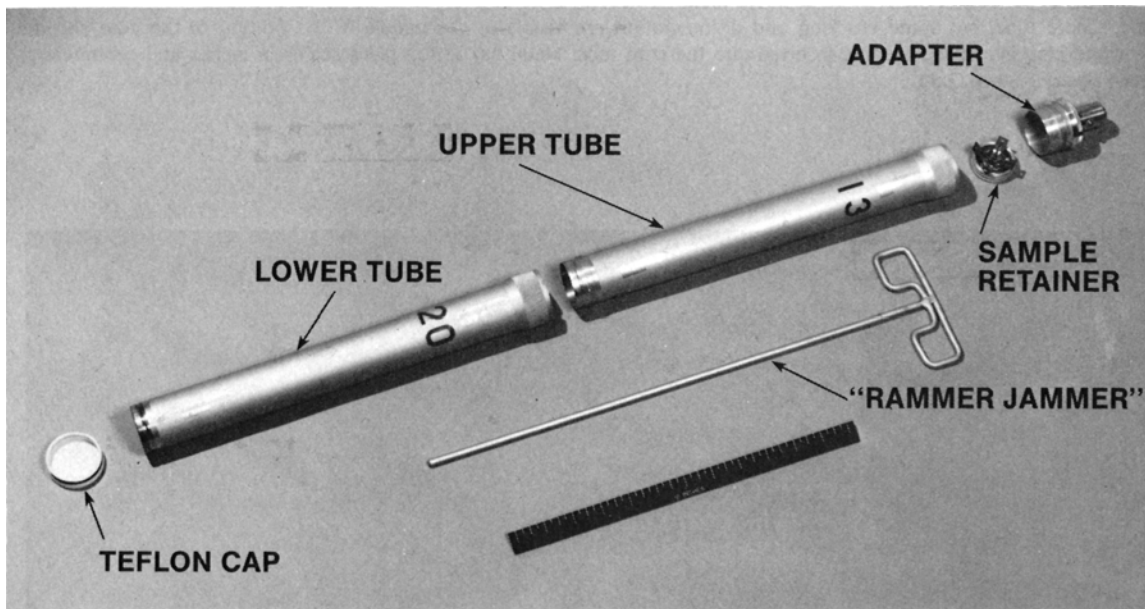


Fig. 9.9. Photograph of the core tube sampler used on the Apollo 15-17 missions. The unit consists of two single tubes, each 4 cm in (inside) diameter and 42 cm long, that can be connected to form a double tube. The “rammer jammer” was used to insert and seat the sample retainer before the core was pulled from the ground. The larger diameter and thinner tube walls on this sampler made possible the recovery of larger and less disturbed samples than had been collected with core samplers used on earlier Apollo missions.

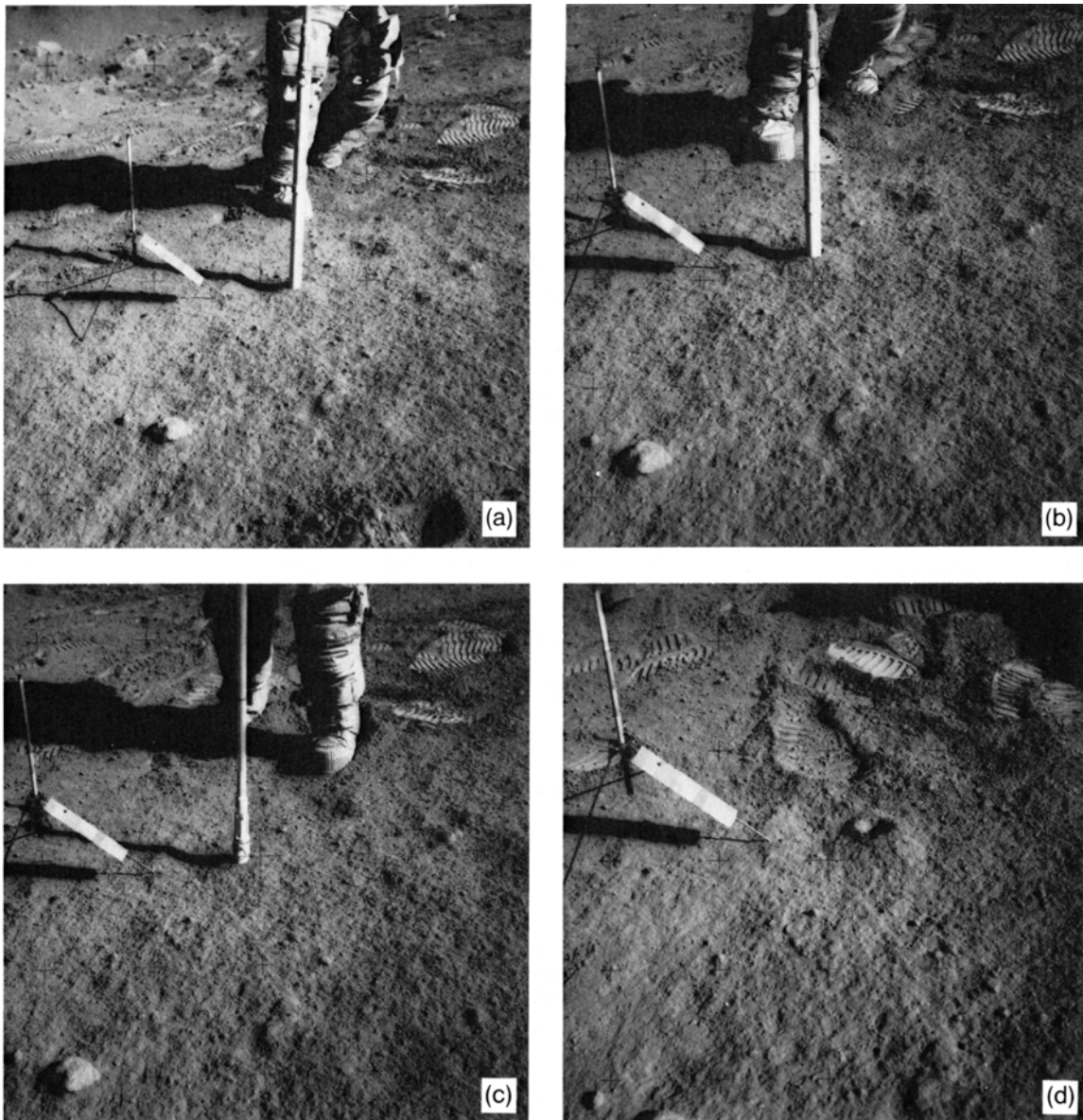


Fig. 9.10. Sequential photographs showing collection of a deep core sample of lunar soil on the Apollo 15 mission (Station 9A), using the new double core tube sampler. The core tube barrel is 4.4 cm in diameter. The tripod-like device at the left is a gnomon that measures the sun angle and local vertical and also contains a comparative color chart. **(a)** Core tube in position, ready for penetration (NASA Photo AS-15-82-11160); **(b)** core tube pushed to a depth of about 22 cm (NASA Photo AS-15-82-11161); **(c)** core tube driven to a final depth of 68 cm after approximately 50 hammer blows (NASA Photo AS-15-82-11162); **(d)** open hole remaining in lunar surface material after withdrawal of the core tube (NASA Photo AS-15-82-11163). Note the numerous well-molded footprints of the astronaut's boots in the lunar surface surrounding the hole.

Fig. 9.11. Plot of the *in situ* bulk density of lunar soil as a function of depth below the surface at the Apollo 15 landing site (Hadley Rille), as determined from several core tube samples collected over a range of depths (after *Carrier et al.*, 1972a; *Mitchell et al.*, 1972a). The soil density clearly increases at depths below about 20 cm. S/N refers to the core serial numbers listed in Table A9.6.

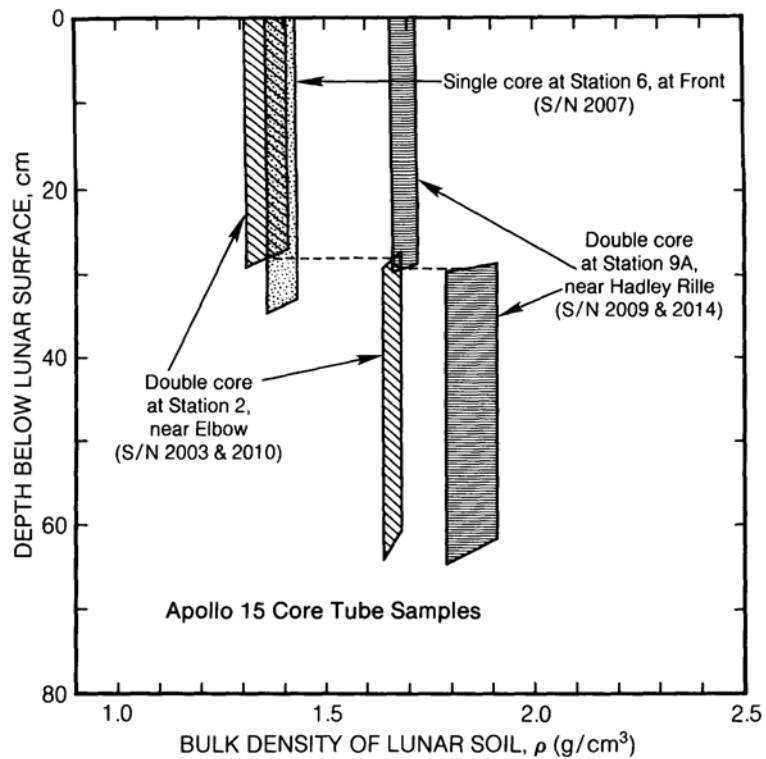
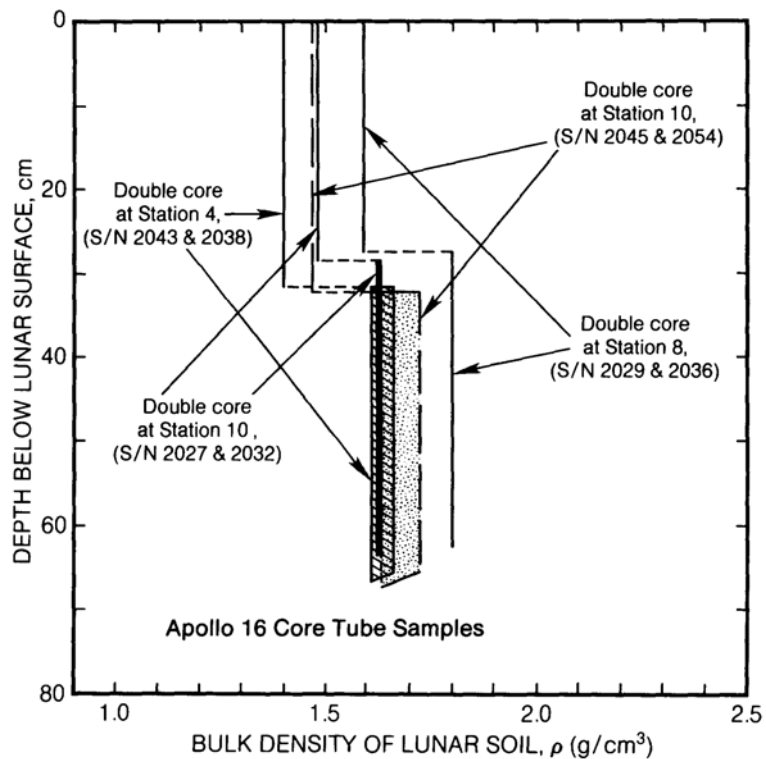


Fig. 9.12. Plot of the *in situ* bulk density of lunar soil as a function of depth below the surface at the Apollo 16 landing site (Descartes), as determined from several core tube samples collected over a range of depths (after *Mitchell et al.*, 1972b). The soil density clearly increases at depths below about 20 cm. (See also Table A9.6.)



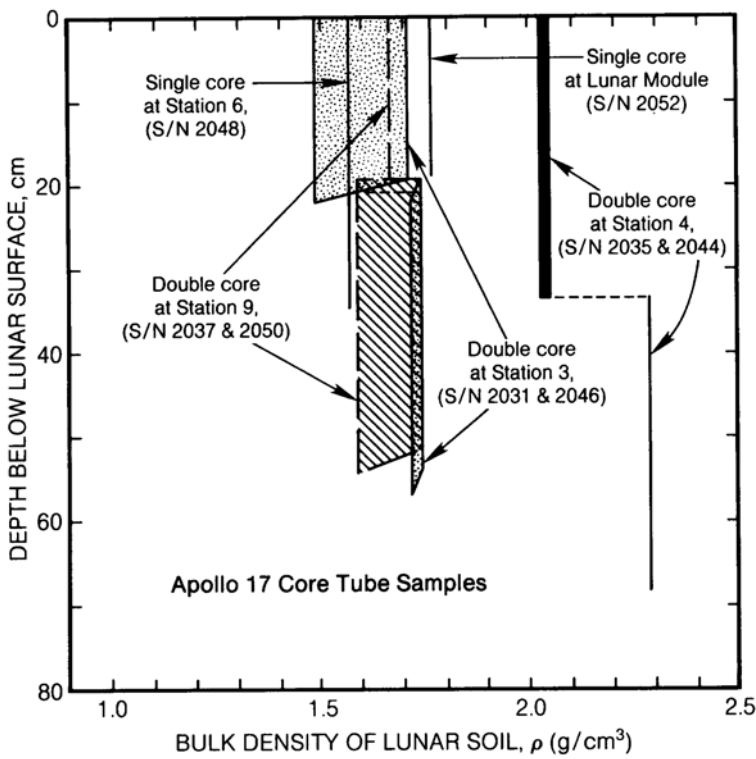


Fig. 9.13. Plot of the *in situ* bulk density of lunar soil as a function of depth below the surface at the Apollo 17 landing site (Taurus-Littrow), as determined from several core tube samples collected at a range of depths (after Mitchell *et al.*, 1973a). As at the Apollo 15 and 16 sites, the soil density clearly increases at depths below about 20 cm. Note that the anomalously dense core sample (serial numbers 2035 and 2044) was obtained in the pyroclastic deposits near Shorty Crater (samples 74001, 74002). (See also Table A9.6.)

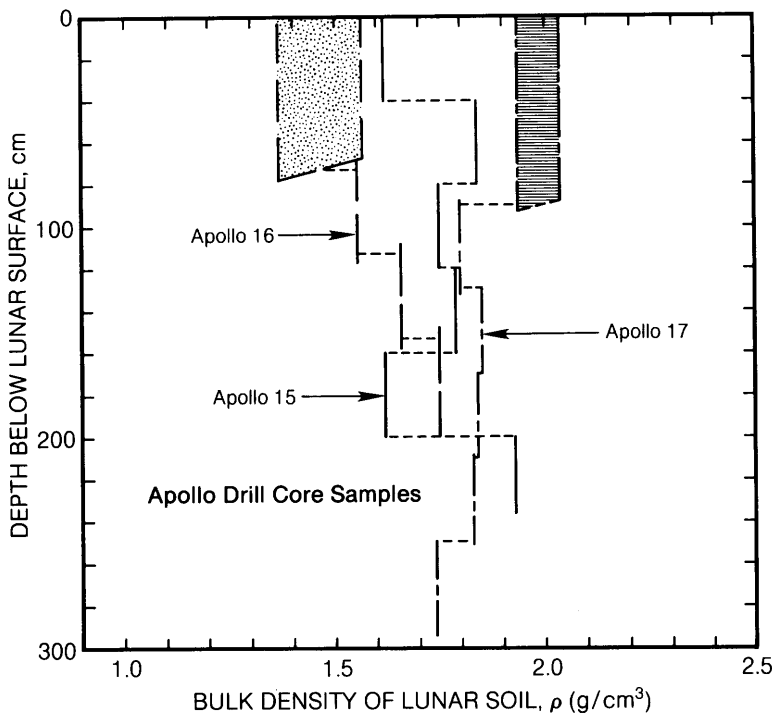


Fig. 9.14. General plot of the *in situ* bulk density of lunar soil as a function of depth below the surface, as determined from drill core samples collected on the Apollo 15, 16, and 17 missions (after Carrier, 1974; Mitchell *et al.*, 1972a,b, 1973a). Lightly stippled area (top) indicates range of densities for the upper portion of the Apollo 16 drill core, and the horizontally ruled area (top) indicates the range of densities for the upper Apollo 17 drill core. An abundance of coarse basalts in the upper part of the Apollo 17 drill core makes this interval exceptionally dense (see Fig. 7.25). (See also Table A9.7.)

TABLE 9.5. Best estimates of lunar soil *in situ* porosity (inter- and intragranular porosity combined).

Depth Range (cm)	Average Porosity, n (%)	Average Void Ratio, e
0 - 15	52 ± 2	1.07 ± 0.07
0 - 30	49 ± 2	0.96 ± 0.07
30 - 60	44 ± 2	0.78 ± 0.07
0 - 60	46 ± 2	0.87 ± 0.07

1.80 g/cm³ (Mitchell *et al.*, 1972b); the individual core densities are shown in Fig. 9.12. The density at the Apollo 17 site varied from 1.57 to 2.29 g/cm³ (Mitchell *et al.*, 1973a); the core densities are shown in Fig. 9.13.

Rotary drill cores were also recovered at the Apollo 15, 16, and 17 sites. As shown in Fig. 9.6, the diameter of the rotary drill core sample was only slightly greater than that of the Apollo 11-14 core tube samples. However, the thickness of the drill core wall is much less, and the bulk densities of returned core samples are believed to be reasonably representative of the *in situ* conditions, with the exception of certain corrections mentioned above. Carrier (1974) found that the *in situ* bulk density of the soil at the drill core location at the Apollo 15 site varied from 1.62 to 1.93 g/cm³; at the Apollo 16 site, from 1.47 to 1.75 g/cm³; and at the Apollo 17 site, from 1.74 to 1.99 g/cm³. Density values as a function of depth for these three sites are presented in Fig. 9.14.

The samples from the drive core tubes and from the rotary drill cores obtained on the Apollo 15, 16, and 17 missions provide the most accurate measurement of *in situ* bulk density of lunar soil at different discrete locations. By examining Figs. 9.11 through 9.14, it can be seen that the density is highly variable, not only from site to site, but also from station to station, and even with depth in a single core. In general, the density increases steadily from the surface to a depth of about 70 cm; below that depth, the density profile is erratic. These variations are related to differences in (1) specific gravity (i.e., chemical composition, mineralogy, and/or subgranular porosity), (2) particle shape (intragranular porosity), (3) particle size distribution (intergranular porosity), and (4) relative density (intergranular porosity), all of which reflect different geologic sources and processes.

Best estimates of bulk density. Taking into account all the measurements, approximations, analyses, qualifications, and uncertainties described in the preceding sections, Mitchell *et al.* (1974) have recommended the following best estimates for the average bulk density of the lunar soil in the intercrater areas of the lunar surface:

Average Bulk Density (g/cm ³)	Depth Range (cm)
1.50 ± 0.05	0 - 15
1.58 ± 0.05	0 - 30
1.74 ± 0.05	30 - 60
1.66 ± 0.05	0 - 60

Porosity of lunar soil. The *in situ* porosity (n) of lunar soil is calculated by combining the best estimates of bulk density (above) and specific gravity (section 9.1.3)

$$n = 1 - \frac{\rho}{G\rho_w} = 1 - \frac{\rho}{(3.1)(1)} = 1 - \frac{\rho}{3.1}$$

The results are shown in Table 9.5, together with the corresponding void ratios. For example, the average porosity in the top 30 cm of the lunar surface is 49%. This value combines both inter- and intragranular porosity. An approximate way to distinguish between the two porosities will be described in section 9.1.5.

Density vs. depth: Some speculation. As shown in Table 9.4, the typical average bulk density of the lunar soil is 1.50 ± 0.05 g/cm³ for the top 15 cm, and 1.66 ± 0.05 g/cm³ for the top 60 cm. However, we really do not know the fine details of how the density varies with depth, particularly very near the surface.

During the Apollo 11 mission, numerous photographs were taken of astronaut bootprints in the lunar soil. Where there was lateral movement of the astronaut's foot, the upper few millimeters of soil adjacent to the footprint broke away as delicate, irregular plates. These observations were confirmed by analysis of the Apollo Lunar Surface Closeup Camera (ALSCC) photographs from the Apollo 11 and 12 missions. Greenwood *et al.* (1971) concluded that "the soil is weakly coherent and has a thin crust" (duricrust). Heiken and Carrier (1971) also stated that the regolith has a thin, fine-grained crust. The crust cohesion and strength may be related to finer mean grain size and better sorting in the uppermost few millimeters of the lunar soil as the result of continuous micrometeoroid impacts.

Another hypothesis is that the uppermost soil layer is sorted during the process of thermal solifluction (Shoemaker *et al.*, 1968).

The presence of a thin soil crust was questioned by Jaffe (1971b), who had observed similar features on the regolith surface around the Surveyor landers. He proposed that the thin plates were artifacts produced by the lighting angle at which the pictures were taken and that the "lunar duricrust" does not exist. However, the ALSCC photographs confirm the presence of such a crust at the Apollo 11 and 12 sites. Furthermore, during dissection of the Apollo core tubes, thin, blocky "clods" were observed, each being slightly more cohesive and finer-grained than the surrounding soil. It is possible that these clods are remnants of lunar duricrust, broken by micrometeoroid impacts and mixed into the underlying regolith.

Below the top few millimeters of lunar soil, the Apollo drive core tube and rotary drill core data presented in Figs. 9.11 through 9.14 can be used to establish certain constraints on the density profile:

First, the *integrated mass depth*, d_m , is calculated for each drive core tube and drill core sample by summing the average densities, ρ_{ave} , multiplied by the corresponding depth intervals, Δz

$$d_m = \sum_i \rho_{ave} \Delta z_i$$

This has been done and is shown in Fig. 9.15. For example, at a depth of 291 cm, the mass depth for the Apollo 17 drill core is 544 g/cm².

Second, a simple linear curve can be fit to the data in Fig. 9.15 with the following form

$$d_m = 1.68 z$$

The derivative of this expression yields the density at any depth

$$\frac{d}{dz} d_m = \rho = 1.68 \text{ g/cm}^3$$

which is shown in Fig. 9.16. This linear best-fit curve implies a constant value of density that is obviously too high at the surface and too low at depth.

Third, a simple power-law relationship can be fit to the data, i.e.

$$d_m = 1.32 z^{1.056}$$

For this relation, the density is given by

$$\rho = 1.39 z^{0.056}$$

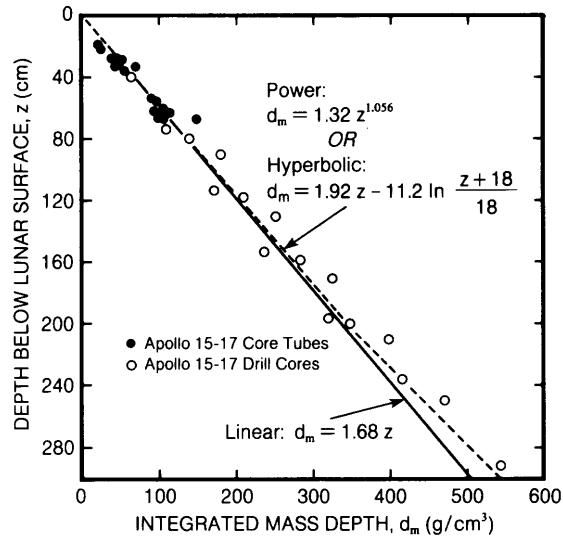


Fig. 9.15. Plot of integrated mass depth in the lunar soil layer as a function of depth below the surface. Data points are derived from measurements on core samples (obtained with both rotary drill tubes and drive tubes) collected on the Apollo 15, 16, and 17 missions (Figs. 9.11-9.14). The data are approximated by a linear fit (solid line) and a power-law or hyperbolic fit (dashed line).

as shown in Fig. 9.16. Unfortunately, this power-law relationship is not wholly satisfactory either. It implies a zero value of density at the surface ($z = 0$) and an unlimited density for large values of z . However, this relationship does show that, if the surface density is low, then ρ must increase very rapidly in the first 5-10 cm in order to be compatible with the core tube data. This condition was also discussed by Carrier *et al.* (1973a,b).

In addition, analyses of the heat flow experiments emplaced on the Apollo 15 and 17 missions indicated that the bulk density must be approximately 1.3 g/cm³ at the surface and must rise steeply in the upper few centimeters, in order to accommodate the nighttime surface temperatures (Keihm *et al.*, 1973; Keihm and Langseth, 1973, 1975a; Langseth *et al.*, 1976) (see also sections 3.5, 3.6, and 9.2.4).

To accommodate all these factors, a hyperbolic relationship between density and depth is proposed in which

$$\rho = 1.92 \frac{z + 12.2}{z + 18}$$

Thus, at $z = 0$, the surface density is 1.30 g/cm³, and as z increases indefinitely, the maximum density approaches 1.92 g/cm³, which appears to be a

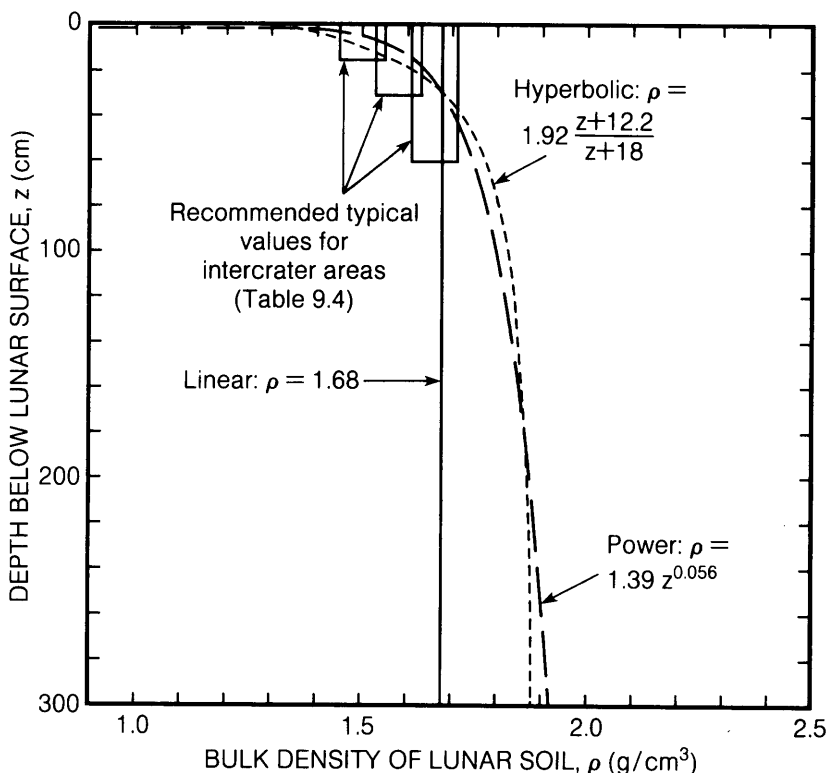


Fig. 9.16. Calculated *in situ* bulk density in the lunar soil layer as a function of depth below the surface, derived from data shown in Fig. 9.15. Three calculated density-depth relations are presented: linear (solid line), power-law (heavy dashed line), and hyperbolic (light dashed line). Boxes at the top of the plot show recommended near-surface bulk density values for intercrater areas.

reasonable upper limit. The integrated mass depth for this density relationship is then given by

$$d_m = 1.92 z - 11.2 \ln \left(\frac{z + 18}{18} \right)$$

which coincides almost exactly with the power function, as shown in Fig. 9.15, but has the advantage that d_m becomes linear for large z .

This hyperbolic density relationship falls within the bounds established by *Mitchell et al.* (1974) to a depth of 60 cm, and it is probably fairly reasonable to a depth of 3 m, which is the limit reached by the Apollo drill core samples.

Below 3 m, we have no direct tactile data about the density of the lunar regolith. But we do know that the density approaches a maximum value at about 50 cm depth (see section 9.1.5) and increases very slowly beyond that (see section 9.1.6). By assuming that the thermal and electrical properties are also uniform below that depth, *Keihm and Langseth*

(1975a,b) reanalyzed lunar microwave emission data and concluded that the soil layer may be 10 to 30 m thick over a large portion of the Moon. This should be considered a tentative prediction until more data are obtained (see also Fig. 4.21).

9.1.5. Relative Density

The bulk density of a given soil can vary over a wide range, depending on how the particles are assembled. For example, a soil consisting of uniform spheres could be arranged in face-centered cubic packing, as shown in Fig. 9.17a. Such a packing is the loosest possible stable arrangement. Under these conditions, the porosity of the soil would be 47.6% and the void ratio would be 0.92. If the specific gravity of the spheres were 3.1, the bulk density of the soil would be 1.61 g/cm³. On the other hand, the spheres could be arranged in hexagonal close packing as shown in Fig. 9.17b. This is the densest possible arrangement, without deforming or breaking the particles, and requires 30% less volume. The

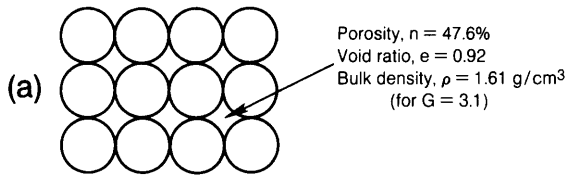
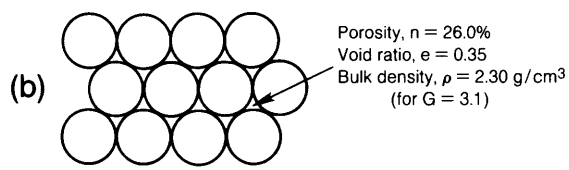
RELATIVE DENSITY, $D_R = 0\%$ RELATIVE DENSITY, $D_R = 100\%$ 

Fig. 9.17. Diagrams showing packing of ideal uniform spheres into two extreme configurations, together with the resulting values of porosity, void ratio, bulk density, and relative density for each. **(a)** Face-centered cubic packing, the loosest possible arrangement of uniform spheres. **(b)** Hexagonal close packing, the densest possible arrangement of uniform spheres.

porosity would now be 26.0%, the void ratio would be 0.35, and the bulk density would be 2.30 g/cm³. Hence, this ideal soil could exist in a stable condition anywhere between these two extremes. In real materials, these limits vary from soil to soil, depending on particle size distribution, shape, texture, orientation, and specific gravity.

For a granular soil, such as lunar soil, it is common to express the degree of particle packing by means of the *relative density*, D_R , which is defined as

$$D_R = \frac{e_{\max} - e}{e_{\max} - e_{\min}} \times 100\%$$

where e = the void ratio of the soil sample or deposit as it presently exists (corresponding to the porosity, n , or bulk density, ρ); e_{\max} = the maximum void ratio at which the soil can be placed (corresponding to the maximum porosity, n_{\max} , or minimum bulk density, ρ_{\min}); e_{\min} = the minimum void ratio at which the soil can be placed (corresponding to the minimum porosity, n_{\min} , or maximum bulk density, ρ_{\max}).

Because of the relationships among void ratio, porosity, and bulk density described in section 9.1.4, the relative density can also be expressed as

$$D_R = \frac{1 - n_{\min}}{1 - n} \times \frac{n_{\max} - n}{n_{\max} - n_{\min}} \times 100\%$$

or

$$D_R = \frac{\rho_{\max}}{\rho} \times \frac{\rho - \rho_{\min}}{\rho_{\max} - \rho_{\min}} \times 100\%$$

Thus, if $\rho = \rho_{\min}$, then $D_R = 0\%$; and if $\rho = \rho_{\max}$, $D_R = 100\%$. In conventional terms, the relative density of a soil deposit can typically be described as (cf. *Lambe and Whitman*, 1969):

Relative Density (%)	Description
0 - 15	Very loose
15 - 35	Loose
35 - 65	Medium
65 - 85	Dense
85 - 100	Very dense

Physical properties such as thermal conductivity, seismic velocity, shear strength, compressibility, and dielectric constant are all dependent on the *in situ* relative density as well as the absolute bulk density. Some of these properties may vary several orders of magnitude between relative density values of 0% and 100%. Two soils with the same bulk densities may have quite different relative densities, and as a result will show very dissimilar behavior. Conversely, two soils can have the same relative density and different bulk densities, but still exhibit similar behavior.

The *in situ* relative density of lunar soil has been found to be about 65% (medium to dense) in the top 15 cm, increasing to more than 90% (very dense) below a depth of 30 cm. Such high relative densities at such shallow depths were unexpected prior to the Apollo missions. These lunar soil values are even more remarkable when it is considered that a relative density of 65-75% is the practical limit for field compaction of terrestrial soils, even using heavy construction equipment. Obviously, the lunar soil has not been gently "sifted" into place, but rather has been extensively shaken and densified, probably by the shock waves generated by impacts of innumerable meteoroids.

The high relative density of lunar soils actually became a problem during the Apollo 15 mission, when astronauts David Scott and James Irwin attempted to Deploy the Heat Flow Experiment (see Fig. 3.7). This experiment consisted of two 3.0-m-long, closed-end, hollow-stem augers that were to

be drilled into the lunar soil (Langseth *et al.*, 1972). Each auger tube had a smooth interior, with a helical structure on the outside of the tube to do the actual drilling. A long probe containing sensors and electronics was then to be inserted into each hollow stem for measurements of thermal conductivity and temperature gradients in the surrounding soil.

Each hollow stem consisted of six 0.5-m-long sections for ease of assembly by the astronaut. Because of scientific requirements, the stem was made entirely of a low-thermal-conductivity material, boron-fiberglass; consequently, the sections were connected by a press-fit joint, rather than being screwed together. As a result, the helical auger on the exterior of the stem was discontinuous at each joint.

When the Apollo 15 astronauts attempted to drill the hollow stems into the lunar surface, they were only able to reach a depth of approximately 1.5 m with each stem. As the drill cuttings rode up the helical auger on the outside of the tube, the soil particles encountered the joints and could travel no further upward. They had no place to go except into the surrounding soil. Because of the high relative density of the soil, not all the soil particles in the drill cuttings could be pressed into the wall of the boring, and the stem became bound to such an extent that the safety clutch in the drill powerhead slipped. (In drillers' terms, the auger flight could not be cleared and the bore stem became stuck in the ground.) So much heat was generated by the friction between the fiberglass stem and the soil that one of the joints is suspected to have collapsed.

Prior to the Apollo 15 mission, all the drilling tests had been made with lightly compacted soils, and this kind of binding failure had never been experienced. Immediately after the mission, tests were run with heavily compacted basaltic lunar soil simulant, and the same problems developed that had occurred on the Moon. The heat flow stems were promptly redesigned with titanium inserts so that the joints could be screwed together to form a continuous auger. The inclusion of a high thermal conductivity metal in the hollow stem was, of course, a compromise between science and engineering requirements (Crouch, 1971). With the new design, full penetration depth was achieved on the Apollo 16 and 17 missions.

A summary of estimated lunar soil relative densities is presented in Table 9.6, together with typical average values. The various estimating and measuring techniques are described in the following sections.

Laboratory measurements of minimum and maximum density. Values for minimum and maximum density of lunar soils are presented in

Table 9.7. In those cases where the specific gravity is also known, the corresponding maximum and minimum void ratios have also been calculated.

The Apollo 11 minimum and maximum densities reported by Costes *et al.* (1970a,b) were determined as part of a study of penetration resistance. Cremers and his colleagues (Cremers, 1972; Cremers and Birkebak, 1971; Cremers and Hsia, 1973; Cremers *et al.*, 1970) found only minimum densities for Apollo 11-15 samples as part of their investigation of thermal conductivity. The densities determined by Jaffe (1971a) were for a sample returned inside the scoop of the Surveyor 3 spacecraft and were part of a study on penetration resistance. Carrier *et al.* (1973a,b) made measurements of relative density on one Apollo 15 and two Apollo 14 samples. The densities of a Luna 16 sample were determined by Gromov *et al.* (1972) in connection with penetrometer, compressibility, and shear strength tests. Later, Leonovich *et al.* (1974a, 1975) also reported similar test results for samples from the Luna 16 and 20 missions.

The maximum and minimum void ratios for the Apollo 11, 14, and 15 samples shown in Table 9.7 are plotted in Fig. 9.18. Also shown for comparison are the results for uniform spheres and for a basaltic simulant with a particle size distribution similar to that of the lunar soils. The minimum void ratio of the simulant is 0.45, corresponding to an intergranular porosity of 31%. However, the minimum void ratios of natural lunar soils are significantly higher. The value for the Apollo 15 sample is 0.71, or 0.26 greater than that of the simulant. This difference is a function of the intragranular void ratio, which represents approximately one-third of the total minimum void ratio of the Apollo 15 sample and corresponds to an intragranular porosity of about 21%.

Similar relations are seen in lunar soils from other missions. The minimum void ratio of the two Apollo 14 samples is approximately 0.46 greater than that of the simulant. This value represents approximately one-half of the total minimum void ratio of the Apollo 14 samples, corresponding to an intragranular porosity of about 32%. The intragranular porosity of the Apollo 11 sample appears to be similar to that of the Apollo 15 sample, but the slope of the line in Fig. 9.18 suggests that the maximum void ratio (minimum density) is in error.

Measurement of the minimum void ratio of a lunar soil can thus be used to estimate its intragranular porosity. The resulting porosity values of 21% to 32% are large compared to typical terrestrial granular soils, and this result is another indication of the significance of the irregular, reentrant shapes of lunar soil particles. The higher values for Apollo 14

TABLE 9.6. Estimates of lunar soil *in situ* relative density (after Mitchell et al., 1974 and Houston et al., 1974).

Source	Depth Range (cm)	Relative Density (%)	Standard Deviation (%)	References
Apollo 15-17 Core Tube Samples	0-15	64*		<i>Carrier et al. (1972a); Mitchell et al. (1972a,b, 1973a)</i>
	0-30	74*		
	30-60	92*		
	0-60	83*		
Apollo 15, Station 9A	0-30	84		<i>Carrier et al. (1973a,b)</i>
	30-65	97		
Astronaut Bootprints Intercrater areas	0-15	66	10	<i>Houston et al. (1972); Mitchell et al. (1973a,b)</i>
	0-15	56	17	
Vehicle Tracks (MET, LRV, and Lunokhod 1) Intercrater areas Crater rims	0-15	48-71		<i>Mitchell et al. (1971, 1972a, b, c, 1973a); Costes (1973)</i>
	0-15	30-38		
		(minimum)		
Boulder Tracks	0-400	61	24	<i>Houston et al. (1972); Hovland and Mitchell (1973)</i>
Penetration Resistance Lunokhod 1; Apollo 14-16 Lunokhod 1 and 2	0-60	83-84	>10	<i>Mitchell et al. (1974); Leonovich et al. (1974a, 1975)</i>
	0-5	70†	6†	
Best Estimates: Typical Average Values Intercrater areas	0-15	65 ± 3		<i>Mitchell et al. (1974); Houston et al. (1974)</i>
	0-30	74 ± 3		
	30-60	92 ± 3		
	0-60	83 ± 3		

* Calculated, based on average $G = 3.1$, $e_{max} = 1.7$, and $e_{min} = 0.7$.

† Estimated.

TABLE 9.7. Measured minimum and maximum densities of lunar soils (after Carrier et al., 1973a,b).

Mission	Sample Number	Sample* Weight (g)	Density		Specific Gravity, G (Table 9.3)	Void Ratio		References
			ρ_{min} (g/cm ³)	ρ_{max} (g/cm ³)		e_{max}	e_{min}	
Apollo 11	10084	565	1.36†	1.80	3.01	1.21†	0.67	<i>Costes et al. (1970a,b); Cremers et al. (1970)</i>
	10084,68	5	1.26		3.01	1.39		
Apollo 12	12001,19	6	1.30					<i>Cremers and Birkebak (1971); Jaffe (1971a)</i>
	12029,3	6.5	1.15	1.93				
Apollo 14	14163,133	5	1.10		2.9 ± 0.1	1.64		<i>Cremers (1972); Carrier et al. (1973a,b); Carrier et al. (1973a,b)</i>
	14163,148	0.97	0.89 ± 0.03	1.55 ± 0.03	2.90 ± 0.05	2.26	0.87	
	14259,3	1.26	0.87 ± 0.03	1.51 ± 0.03	2.93 ± 0.05	2.37	0.94	
Apollo 15	15031,38	5	<1.30					<i>Cremers and Hsia (1973); Carrier et al. (1973a,b)</i>
	15601,82	0.96	1.10 ± 0.03	1.89 ± 0.03	3.24 ± 0.05	1.94	0.71	
Luna 16	—	~10	1.12	1.79				<i>Gromov et al. (1972); Leonovich et al. (1974a, 1975)</i>
Luna 20	—	~6†	1.1-1.2	1.7-1.8				<i>Vinogradov (1972); Ivanov et al. (1973a,b); Leonovich et al. (1974a, 1975)</i>
	—	~10	1.04	1.80				

* All tests performed on <1 mm size fraction.

† May be in error; see Fig. 9.18.

† Unsieved sample.

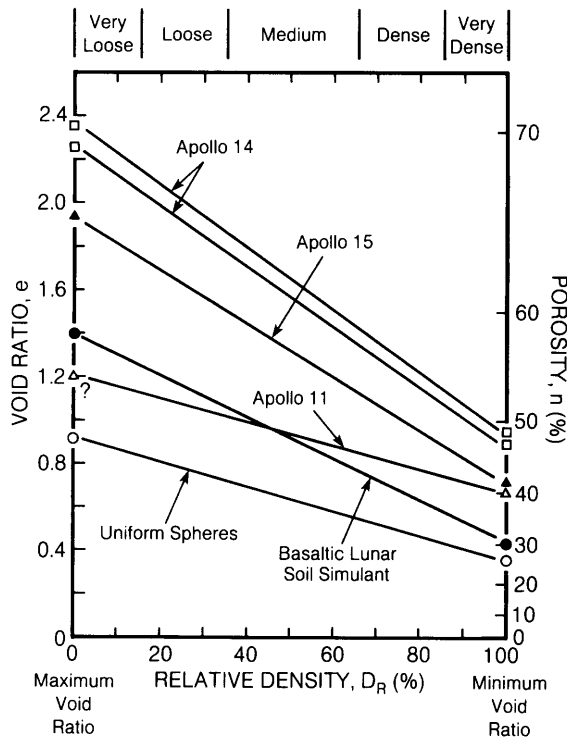


Fig. 9.18. Plots of void ratio (left vertical axis) and porosity (right vertical axis) as a function of relative density (horizontal axis) of lunar soil. Data shown are for samples from the Apollo 11, 14, and 15 missions, for a comparable basaltic lunar soil simulant, and for ideal, variably-packed uniform spheres. The curves for lunar soil samples vary among themselves, and all lunar soils are different from the basaltic simulant and the uniform spheres. Equivalent general terms for soils with different relative densities, ranging from “very loose” to “very dense,” are given at the top.

samples undoubtedly reflect the greater percentage of agglutinates and breccia clasts in these soils. Data presented later (section 9.1.7) show that the particle shapes and intragranular porosity have a profound influence on the shear strength of lunar soil.

Relative density based on returned core samples. To date, no direct measurement of relative density has been made on any returned lunar core samples. Instead, *Houston et al.* (1974) and *Mitchell et al.* (1974) assumed an average specific gravity of 3.1, $e_{\max} = 1.7$ ($\rho_{\min} = 1.15 \text{ g/cm}^3$), and $e_{\min} = 0.7$ ($\rho_{\max} = 1.82 \text{ g/cm}^3$) and converted the best estimates of bulk density shown in Table 9.4 into the relative densities shown in Table 9.6. For example, an

average bulk density of 1.5 g/cm^3 in the top 15 cm corresponds to

$$D_R = \frac{1.82}{1.5} \times \frac{1.5 - 1.15}{1.82 - 1.15} \times 100\% = 63\%$$

In Fig. 9.18, it can be seen that the assumptions regarding e_{\max} and e_{\min} tend to underestimate the actual relative density.

Additional comparative data were provided by sample 15601,82, which was taken less than 10 m away from the double core tube (15010/15011) recovered at Station 9A near the rim of Hadley Rille at the Apollo 15 site (see Fig. 9.10). *Carrier et al.* (1973a,b) compared the minimum and maximum densities for this sample (Table 9.7) with the bulk densities in the core tubes (Fig. 9.11). By assuming that the soils were similar, they calculated an average relative density of 84% for the top 30 cm and 97% for the next 35 cm. (A typographical error was made in the original references: The relative densities previously reported were 87% and 94%, respectively.) Both values indicated a very dense soil, a condition that had previously been predicted by *Mitchell et al.* (1972a) because approximately 50 hammer blows had been required to drive the core tube into the lunar surface and the soil surrounding the tube had heaved slightly during driving.

A hyperbolic curve can be fitted to the measured core tube densities (similar to the plot shown in Fig. 9.16), in which the surface bulk density is assumed to be equal to the minimum density for sample 15601,82 (1.10 g/cm^3) and the maximum density (1.89 g/cm^3) is approached asymptotically with increasing depth. The results are presented in Fig. 9.19; the relative density increases very rapidly from the surface, reaching 75% by a depth of 5 cm and 85% at 10 cm. Thus, although the surface soil may be loose and stirred up, it is very dense just 5 to 10 cm down. In fact, the relative density below 10 cm is much greater than can be accounted for by compression under self-weight, a condition that will be discussed in more detail in section 9.1.6.

Relative density based on astronaut boot-prints.

Detailed statistical analyses of the depths of 776 astronaut bootprints in the lunar surface have been reported by *Houston et al.* (1972) and *Mitchell et al.* (1973a,b, 1974). These analyses were based on a correlation with the relative density of a lunar soil simulant, and the results are summarized in Table 9.8. The average footprint depth in the intercrater areas at all of the Apollo landing sites was 0.7 cm, which corresponds to an average relative density of 66% for the top 15 cm. Each of the sites is very similar, with the exception of Apollo 16, where the average relative density is slightly less: 62%. More significantly, soils on the rims of craters

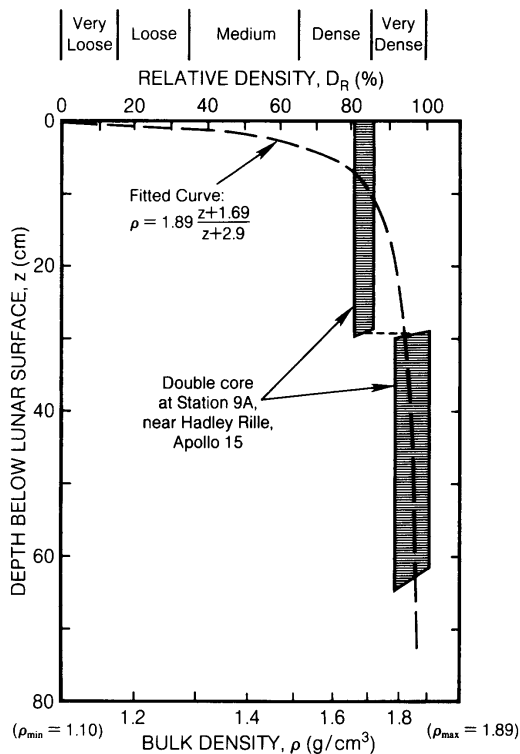


Fig. 9.19. Plots of *in situ* bulk density (bottom horizontal axis) and relative density (top horizontal axis) as a function of depth in the lunar soil layer at the Apollo 15 landing site (Hadley Rille), based on data from core tube samples (Fig. 9.11) and detailed studies of soil sample 15601,82 (Table 9.7) (after *Carrier et al.*, 1973a,b). The soil, although less dense near the surface (<10 cm deep), quickly becomes “dense” to “very dense” with depth (>20 cm).

tend to be softer than those in the intercrater areas. The average footprint depth in crater rims was 1.6 cm, which corresponds to a relative density of 56%; furthermore, the standard deviation of footprint depth is greater, indicating a wider variability in relative density on crater rims.

Frequency distributions of relative density based on bootprints are presented in Fig. A9.4.

Relative density based on vehicle tracks. Tracks made by manned and unmanned vehicles as they traversed the lunar surface can also be used to indicate the relative density in the top 15 cm. Analyses have been made of the tracks left by the Lunokhod 1 rover (Luna 17), the hand-hauled Mod-

ular Equipment Transporter (MET) (Apollo 14), and the manned Lunar Roving Vehicle (LRV) (Apollo 15-17). The results are reported by *Mitchell et al.* (1971, 1972a,b,c, 1973a, 1974) and *Costes* (1973).

The average depth of the LRV wheel tracks was approximately 1.25 cm, but the track depth varied from almost imperceptible to as much as 5 cm. The greater track depths occurred on the rims of small, fresh craters. Through correlations with lunar soil simulants, the relative density in the intercrater areas was estimated to be either 48-63% or 62-71%, depending on which of two different sets of assumptions was used. The minimum relative density on the crater rims was estimated to be 30-38%. These results were also consistent with analyses of tracks made by unmanned vehicles: the Lunokhod 1 rover and the MET.

Additional data are presented in Table A9.8.

Relative density based on boulder tracks. Tracks made by boulders that have rolled downhill have been observed in many locations on the Moon, mostly on lunar orbital photographs. The triggering mechanism that starts a boulder rolling is not known, but the resulting tracks can be very impressive. At the Apollo 17 site, for example, a 20-m-diameter boulder left a track 4 m deep, 16 m wide, and 800 m long.

Tracks from 69 boulders in 19 locations have been analyzed in detail by *Houston et al.* (1972), *Hovland and Mitchell* (1973), and *Mitchell et al.* (1974). Based on bearing capacity theory and correlations with lunar soil simulants, an average relative density of 61% was determined for the soils on which the tracks were formed. (The value reported in the original reference was 65%. However, an error was made in converting from average porosity to average relative density, because of the nonlinear relationship between these two parameters.) This value is representative of the top 400 cm, and the results indicate that the soils on slopes are significantly looser than those in the plains areas. This difference is probably caused by density reduction during downslope movements of the soil. Furthermore, the standard deviation of estimated soil densities is much larger for the slopes, suggesting that there are wide variations in conditions.

The frequency distribution of relative densities estimated from 69 boulder tracks is presented in Fig. A9.5. Preliminary analyses of 36 additional boulder tracks from the Apollo 17 site are included in *Mitchell et al.* (1973a).

Relative density based on penetration resistance. A variety of penetrometers, both manned and unmanned, have been poked into the lunar surface. These are discussed in more detail in section 9.1.7.

TABLE 9.8. Summary of statistical analyses of relative density based on astronaut footprint depth (depth range 0-15 cm) (after *Houston et al.*, 1972; *Mitchell et al.*, 1973a,b, 1974).

Location	Intercrater Areas			Crater Rims			Combined		
	N*	\bar{D}_R	S.D.	N	\bar{D}_R	S.D.	N	\bar{D}_R	S.D.
Apollo 11	30	67%	7%	3	48%	8%	33	66%	9%
Apollo 12	88	68%	12%	31	56%	19%	119	65%	13%
Apollo 14	38	67%	9%	4	42%	11%	42	65%	9%
Apollo 15	117	67%	11%	12	58%	17%	129	66%	12%
Apollo 16	273	62%	11%	36	57%	—	309	60%	12%
Apollo 17	141	67%	9%	3	67%	—	144	65%	9%
All Apollo Sites	687	66%	10%	89	56%	17%	776	65%	10%

* N = number of observations; \bar{D}_R = mean relative density; S.D. = standard deviation.

Mitchell et al. (1974) compared measurements of penetration resistance on the Lunokhod 1 and Apollo 14-16 missions, using correlations with lunar soil simulants. From these measurements, they deduced relative densities that varied from 63% to 95%, with an average value of 83-84%.

Leonovich et al. (1974a, 1975) analyzed the results of approximately 1000 cone penetrometer tests made by Lunokhod 1 and 2. They also presented the results of penetration measurements made on lunar soil returned by the Luna 16 and 20 missions. By comparing these measurements with the estimated values of minimum and maximum density in Table 9.7, the average relative density is calculated to be 70%. (In section 9.1.7, a somewhat lower value of relative density is deduced, based on a different analysis of the same data.) This value is representative of the top 5 cm of the lunar surface, over a combined traverse distance of 47 km. The frequency distribution of relative density based on the cone penetrometer tests on the Lunokhod 1 and 2 missions is presented in Fig. A9.6.

Best estimates of relative density. The *in situ* relative density of lunar soil has been estimated by a variety of methods, as described in the preceding sections. Despite differences in the values obtained from different data and by different methods, the following trends are apparent: (1) The relative density of lunar soil tends to be low on the rims of fresh craters, on slopes, and virtually everywhere within the top few centimeters of the surface. (2) However, in intercrater areas, the relative density is exceptionally high at depths of only 5-10 cm. (Shortly after the Apollo 11 mission, astronaut Edwin Aldrin walked and ran on a simulated lunar surface at the Johnson Space Center in Houston. The test facility consisted of a circular sand track, approximately 15 cm deep, 1 m wide, and 30 m in diameter; a special marionette rig supported five-sixths of Aldrin's weight, including his spacesuit. When asked how the test track

compared to the real lunar surface, Aldrin replied that the sand was too yielding. While walking on the Moon, he had noticed that although the lunar soil was soft at the surface, there was a firmer stratum at a shallow depth.)

This large and relatively sudden change in relative density with increasing depth has been attributed to the effects of continuing small meteoroid impacts, which evidently generate a loose, stirred-up surface but at the same time shake and densify the underlying soil (*Carrier et al.*, 1973a,b).

Best estimates of relative density vs. depth for the intercrater areas have been made by *Mitchell et al.* (1974) and *Houston et al.* (1974) as follows:

Depth Range (cm)	Relative Density (%)	Description
0 - 15	65 ± 3	Medium to dense
0 - 30	74 ± 3	Dense
30 - 60	92 ± 3	Very dense
0 - 60	83 ± 3	Dense

These values are presented graphically in Fig. 9.20.

9.1.6. Compressibility

The preceding sections have discussed the geotechnical index properties of lunar soil, e.g., density and porosity. The next three sections describe important engineering properties: compressibility, shear strength, and permeability.

Compressibility describes the volume change, or densification, that occurs when a confining stress is applied to soil. At low stress or low initial density, compression of the soil results from particle slippage and reorientation. At high stress or high initial density, particle deformation and breakage at

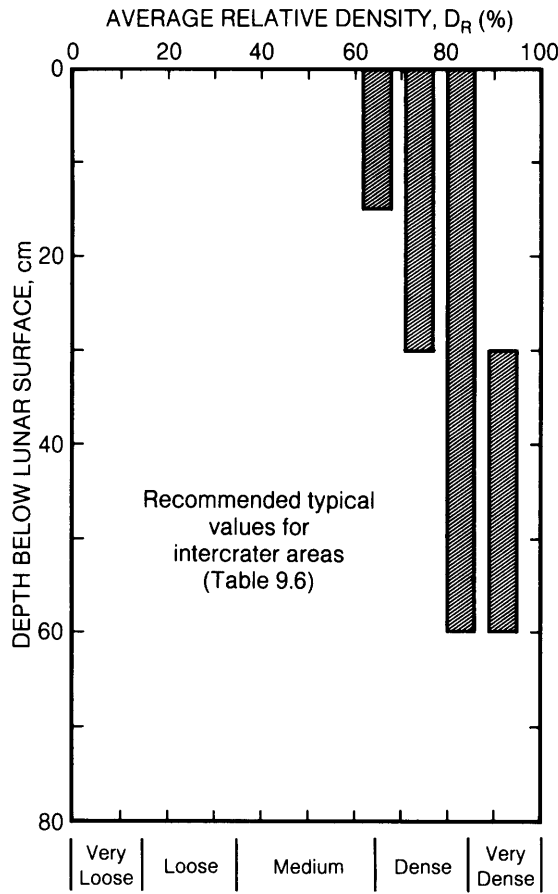


Fig. 9.20. Plot of typical average (“recommended”) values for relative density of lunar soils as a function of depth, using data collected from all Apollo missions (e.g., Fig. 9.19) (after Mitchell et al., 1974; Houston et al., 1974). With increasing depth, the lunar soil quickly becomes dense, reaching values of relative density equivalent to “dense” to “very dense” below about 20 cm.

the points of contact also occur. A summary of compressibility parameters is presented in Table 9.9 and discussed in the following sections.

Compression index. The *compression index*, C_c , is defined as the decrease in void ratio that occurs when the stress is increased by an order of magnitude

$$C_c = - \frac{\Delta e}{\Delta \log \sigma_v} = - \frac{de}{d \log \sigma_v}$$

where Δe = change in void ratio (negative) and $\Delta \log \sigma_v$ = change in logarithm of applied vertical stress.

TABLE 9.9. Compressibility parameters of lunar soil.

Parameter	Range	Recommended Typical Value
Compression Index, C_c		
Loose		0.3
Dense	0.01 - 0.11	0.05
Recompression Index, C_r	0.000 - 0.013	0.003
Maximum Past Pressure		Unknown
Coefficient of Lateral Stress, K_0		
Normally consolidated	0.4 - 0.5	0.45
Over-consolidated		Unknown
Recompacted		0.7

To measure C_c in the laboratory, the soil is placed in a rigid ring at a known density (void ratio) and then squeezed with a vertical piston; this is called a one-dimensional oedometer test. The void ratio is plotted vs. the logarithm of applied stress and the slope of the curve yields the value of C_c .

The compression index has been measured on soil samples from the Apollo 12 and Luna 16 and 20 missions (Table 9.10, Fig. 9.21). Carrier et al. (1972b, 1973c) performed compression and shear strength tests in vacuum on a 200-g sample of Apollo 12 soil and found that C_c varied from 0.01 to 0.11, depending on the initial density and the applied stress. Jaffe (1973) ran miniature compression and shear strength tests on a 1.3-g sample returned with the Surveyor 3 scoop by the Apollo 12 crew. Leonovich et al. (1974a, 1975) performed oedometer tests on two 10-g samples from the Luna 16 and 20 sites and found values of C_c varying from 0.02 to 0.9. However, these results are uncertain because no actual data points are presented, only a smooth curve with a curious shape. The end points of the curve appear reasonable; i.e., an initial void ratio of approximately 1.8 and a final void ratio of about 0.8 at an applied stress of nearly 100 kPa. These data correspond to an average C_c of about 0.3. Detailed compression data are tabulated in Table A9.9.

The compressibility of lunar soil in terms of relative density vs. the logarithm of applied stress is shown in Fig. 9.22. This interpretation is based on the minimum and maximum densities presented in Table 9.7. The Apollo 12 compression tests are based on data of Jaffe (1971a), and the Luna 16 and 20 sample results are based on data from Leonovich et al. (1974a, 1975). Although these results are rough approximations, it can be seen that the compression index is inversely related to the *initial relative density* (D_{Ri}): As D_{Ri} increases, C_c decreases.

The compressibility of lunar soil has been compared with that of basaltic simulants by Carrier et al. (1972b) and Mitchell et al. (1974). In both cases,

TABLE 9.10. Compression index of lunar soils.

Mission	Sample Number	Sample Weight (g)	Density Range (g/cm ³)	Stress Range (kPa)	C _c	References
Apollo 12	12002,119	200	1.67 - 1.82	0.08 - 67.5	0.04 - 0.11	<i>Carrier et al. (1972b, 1973c)</i>
			1.84 - 1.92	0.09 - 31.2	0.012 - 0.062	
			1.91 - 2.00	1.9 - 69.9	0.03 - 0.09	
Apollo 12	12029,8	1.3	1.29 - 1.60	0.12 - 28.0	0.21*	<i>Jaffe (1973)</i>
			1.4 - 1.64	0.14 - 28.0	0.11*	
			1.58 - 1.68	0.14 - 28.0	0.04*	
Luna 16	—	~10	1.03 - 1.51	0.05 - 98.0	0.3*	<i>Leonovich et al. (1974a, 1975); Gromov et al. (1972)</i>
Luna 20	—	~10	0.98 - 1.51	0.05 - 98.0	0.3*	<i>Leonovich et al. (1974a, 1975)</i>

* Estimated.

Fig. 9.21. Compressibility measurements on lunar soil samples from the Apollo 12 mission (circles and triangles) and the Luna 16 and 20 missions (solid and dashed lines), determined in one-dimensional oedometer experiments. The plot shows the resulting void ratio (vertical axis) produced as a function of applied vertical stress (horizontal axis). Apollo 12 sample data after *Carrier et al. (1972b, 1973c)*; Luna 16 and 20 data after *Leonovich et al. (1974a)*.

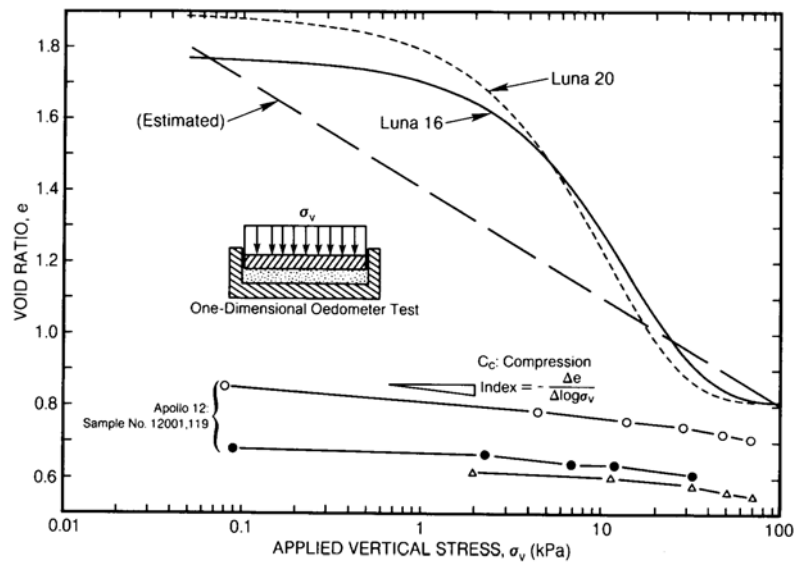
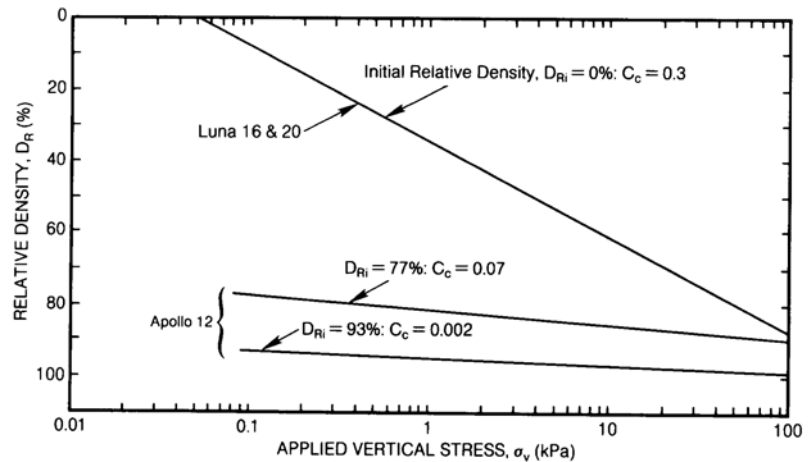


Fig. 9.22. Compressibility measurements on lunar soil samples from the Apollo 12 and Luna 16 and 20 missions, determined in one-dimensional oedometer experiments. The plot shows the resulting relative density (vertical axis) produced as a function of applied vertical stress (horizontal axis). Apollo 12 sample data after *Carrier et al. (1972b, 1973c)*; Luna 16 and 20 data after *Leonovich et al. (1974a)*.



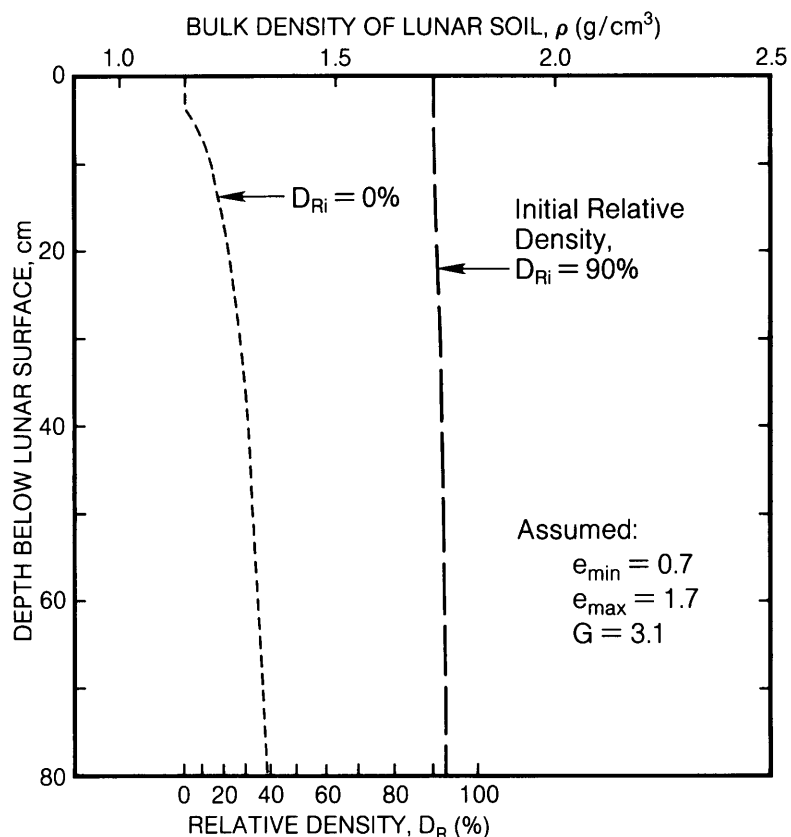


Fig. 9.23. Densification of lunar soil caused by self-weight compression in lunar gravity. The plot shows *in situ* bulk density (top horizontal axis) and relative density (bottom horizontal axis) as a function of depth below the surface (vertical axis). Self-compression of material with an initial relative density of 0% (light dashed curve, left) produces densities at depth that are much lower than those actually observed. Postdepositional vibration of the material (e.g., by seismic waves associated with meteorite impacts) could produce a material with an initial relative density of 90% or more (heavy dashed curve, right). The fact that lunar soil samples have relative densities of 60–100% (Fig. 9.20) indicates that such a vibration/compaction process has taken place. The steepness of both curves is related to the fact that the effects of self-compaction are limited because of the low lunar gravity.

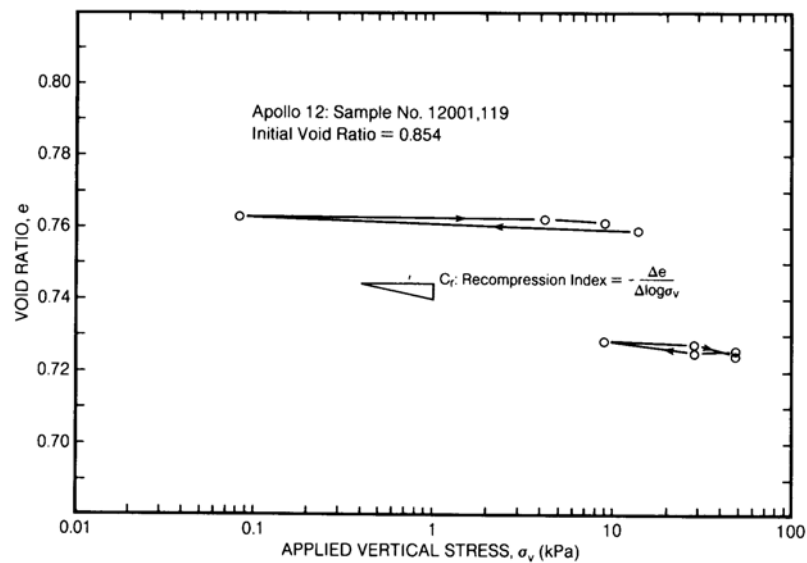
it was found that lunar soil is slightly more compressible than the simulant, regardless of whether the two soils are compared at the same void ratio or at the same relative density. Evidently, the irregular fragile particles in lunar soil, such as agglutinates, which have no equivalent in the basaltic simulant, crush under relatively low confining stress. Thus, the intragranular and subgranular porosities also influence the compressibility of lunar soil.

The compressibility curves for soils of different initial relative densities (Fig. 9.22) do not converge until the stress exceeds 100 kPa, which corresponds, on the Moon, to a depth of more than 30 m below the lunar surface. Thus, these oedometer data cover

a range of extreme practical interest. Furthermore, the stress produced by self-weight is not sufficient to squeeze the soil to such high relative densities at shallow depth. At some time after deposition, the *in situ* lunar soil has either been exposed to higher stresses, or compacted by vibration, or a combination of the two processes.

If lunar soil were sifted gently into place, with an initial relative density of 0%, the density profile developed by self-weight would be that shown in Fig. 9.23. This profile is obtained by integrating the compressibility curve for $D_{Ri} = 0\%$ in Fig. 9.22. Even though the compression index of loose soil is much higher than that of dense soil, the densification as a function of depth is small because of the low lunar

Fig. 9.24. Compressibility of Apollo 12 lunar soil sample 12001,119, shown in terms of rebound-reload behavior. The plot shows the resulting void ratio (vertical axis) produced as a function of applied vertical stress (horizontal axis). Arrows indicate behavior of the soil sample during release from the compressed state (left-pointing arrows) and on subsequent recompression (right-pointing arrows). Circles indicate two sets of 12001,119 sample data from Table A9.10 (after Carrier *et al.*, 1972b, 1973c). Triangular diagram (inset) shows the relationships from which the compression index is determined.



gravity. At a depth of 50 cm, the calculated bulk density produced by self-weight would be 1.30 g/cm³ and the relative density would be 32%, both of which are significantly less than the measured *in situ* values shown in Figs. 9.16 and 9.19. In fact, the actual *in situ* soil would have had to have been compressed to a pressure greater than 100 kPa, or more than 100 times its present stress, to account for the measured density. On the other hand, if the soil had been vibrated after being deposited (i.e., by meteoroid impacts), the relative density might be 90% or more, and the density profile would be virtually uniform, as shown in Fig. 9.23.

To explain the extreme changes in relative density that occur in the top 30 cm of lunar soil, there must be a mechanism that both stirs up the surface and densifies the immediately underlying soil. Both of these effects are presumably caused by repeated meteoroid impacts. However, we do not know yet whether such impacts have a greater tendency to vibrate the soil or to stress it; the observed increases in relative density with depth could reflect either or both processes.

Recompression index. When the applied stress is decreased after compression in an oedometer test, the soil sample swells slightly and rebounds elastically. When the same stress is applied again, the soil returns to approximately the same void ratio as in the previous compression with a small hysteresis. The slope of the rebound-reload curve is called the *recompression index*, C_r , and it is always much less than the compression index. Carrier *et al.* (1972b, 1973c) and Jaffe (1973) measured values of C_r

varying from 0 to 0.013 in lunar soils, with a typical value of 0.003. The data are presented in Fig. 9.24 and tabulated in Table A9.10.

Maximum past pressure. If a soil has been exposed to a higher stress than is presently imposed on it by self-weight, this higher stress is referred to as the *maximum past pressure*, and the soil is called *overconsolidated*. In such a case, the soil's currently-measured compressibility would correspond to the recompression index. In contrast, if the maximum past pressure is equal to the present stress, the soil is called *normally consolidated*, and its compressibility corresponds to the compression index.

As mentioned above, it is still not clear whether the lunar soil is normally consolidated or overconsolidated. From a practical point of view, this uncertainty does not matter; the discussion in section 9.1.9 shows that the predicted settlement of a typical structural footing in lunar soil would be small in either case.

However, future experiments in the laboratory or on the lunar surface could resolve the issue. In their vacuum oedometer tests of lunar sample 12001,119, Carrier *et al.* (1972b, 1973c) observed gas pressure bursts whenever the stress exceeded a previous maximum value (Fig. 9.25). The released gas consisted of 60% hydrogen, 35% helium, and 4.6% amu = 28, consistent with the composition of the solar wind. The gas bursts were attributed to the breakage of fragile particles such as agglutinates (section 7.1.3), which contain surface-correlated solar-wind gases. Thus, vacuum oedometer tests on undisturbed returned core tube samples could be

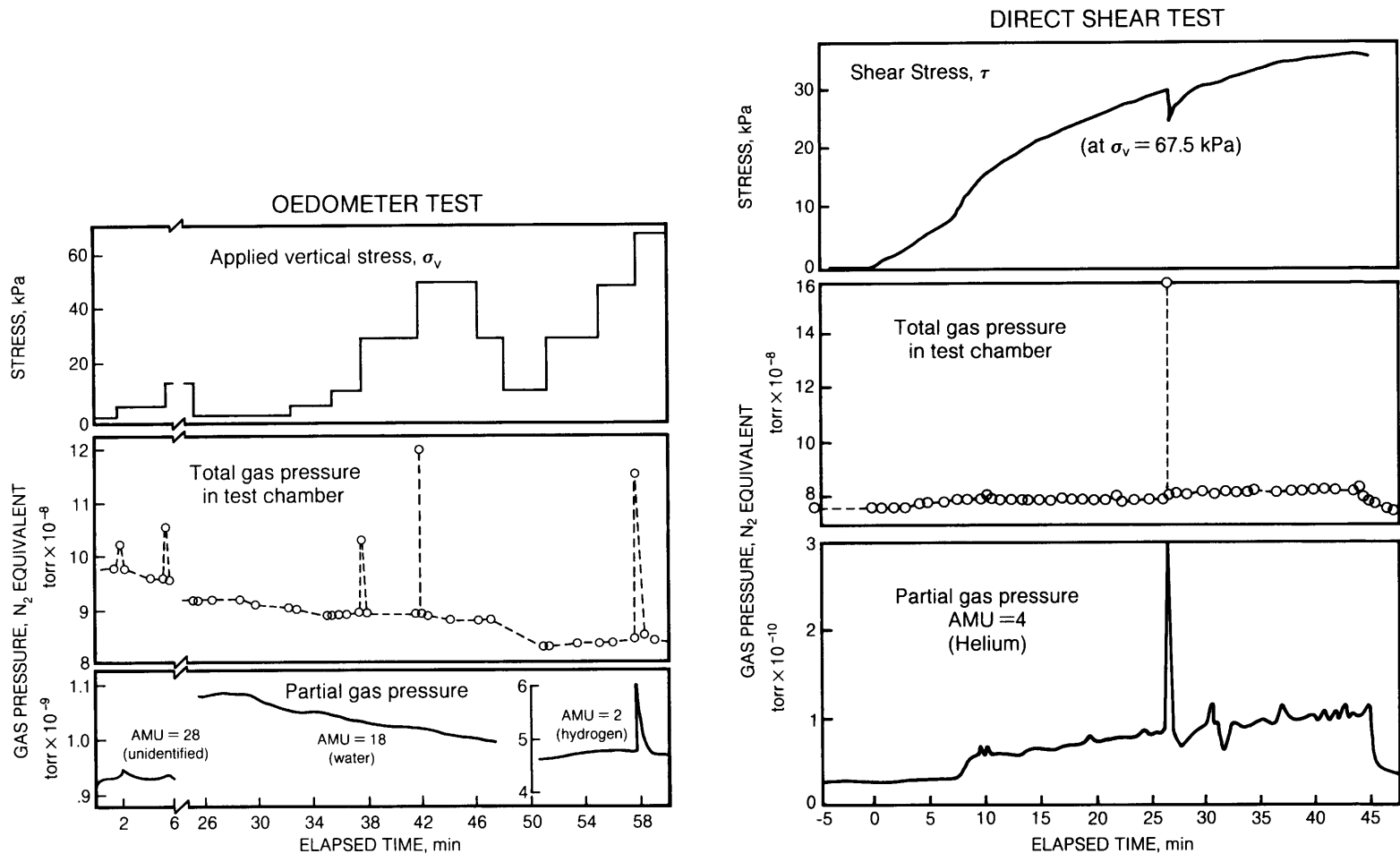


Fig. 9.25. Experimental data showing bursts of released gas pressure from lunar soil sample 12001,119 during compression (vacuum oedometer) and shear experiments (after *Carrier et al., 1973c*). Data are plotted as functions of elapsed time (horizontal axis) for applied vertical stress (top), N₂ equivalent in the released gas (center), and partial gas pressures for different observed masses (bottom). The peaks of gas release are closely correlated with periods of increasing stress, indicating that the gas is being released from individual soil particles as they are fractured and crushed. Note that gas pressures read from these graphs must be divided by the factors shown (e.g., the highest value shown for total gas pressure from the direct shear test is 16×10^{-8} torr).

used to measure maximum past pressure. Alternatively, loading tests on undisturbed soil could be performed *in situ* as part of future robotic or human missions to the Moon. Such studies would provide valuable information regarding the mechanics of regolith evolution and impact crater formation.

Coefficient of lateral stress. The coefficient of lateral stress, K_o , defines the ratio of horizontal stress, σ_h , to vertical stress, σ_v

$$K_o = \frac{\sigma_h}{\sigma_v}$$

No measurements of K_o have been made on lunar soils. But if the lunar soil is normally consolidated, K_o would be approximately 0.4 to 0.5. If the soil is over-consolidated, then K_o could be greater, depending on the ratio of the maximum past pressure to the present pressure. Below a depth of a few meters, the maximum possible value of K_o is probably 3-5. In the future, better estimates of the *in situ* K_o of lunar soils may be necessary for the design of tunnels in the lunar surface.

If the lunar soil were excavated and then recompact against the wall of a structure, a design value of $K_o = 0.7$ is recommended, based on terrestrial construction experience.

9.1.7. Shear Strength

The shear strength of a granular soil is typically defined in terms of the classic Mohr-Coulomb equation

$$\tau = c + \sigma \tan \phi$$

where τ = shear strength (kPa); σ = normal stress (kPa); c = cohesion (kPa); and ϕ = friction angle.

The shear strength therefore consists of two components: a cohesive component that is independent of the applied stress, and a frictional component that is directly proportional to the normal stress (i.e., the stress that is perpendicular to the failure surface).

The shear strength governs such important engineering properties as ultimate bearing capacity, slope stability, and trafficability. As a result, estimates of lunar soil cohesion and friction angle have been the object of intensive research, as summarized in Table 9.11. In retrospect, many of the early inferred values, and even some early estimates from the subsequent Surveyor landings, were wide of the mark. The best available estimates prior to the Apollo 11 mission (July 1969) were derived from the soil mechanics surface sampler on the Surveyor 3 and 7 spacecraft (Scott and Roberson, 1969):

Surveyor Model: Best Estimate

Cohesion, c = 0.35 to 0.70 kPa
Friction angle, ϕ = 35° to 37°

We now know that the Surveyor Model values are near the lower bounds of actual lunar soil shear strength. Based on a variety of data sources, including the manned Apollo missions, Mitchell *et al.* (1972d, 1974) have developed the Apollo Model:

Apollo Model: Best Estimate

Cohesion, c = 0.1 to 1 kPa
Friction angle, ϕ = 30° to 50°

The higher shear strength parameters correspond to higher values of relative density of the lunar soil.

We have plotted all the estimates of cohesion and friction angle made with data from the Apollo and Lunokhod missions in terms of shear strength vs. normal stress (Fig. 9.26). This figure also shows, for comparison, the shear strengths of a basaltic simulant at relative densities of 30% and 90%, which bracket the shear strengths of the *in situ* lunar soil. These latter curves are based on data from Mitchell *et al.* (1972d, 1974) (Fig. 9.27). All the variations in the estimates of cohesion and friction angle can be accounted for by differences in the *in situ* relative density.

The estimates and measurements underlying these results are described in the following sections. Recommended typical values are summarized in Table 9.12.

Apollo 11 and 12 measurements. The estimates of shear strength made from observations at the Apollo 11 and 12 sites were limited to analyses of physical interactions with the lunar surface, including the Lunar Module (LM) landing; astronauts walking on level ground and on crater slopes; and penetration into the soil by core tubes, the flag pole, and the Solar Wind Composition (SWC) shaft. Although crude, these estimates showed that the lunar surface was at least as strong as predicted by the Surveyor Model (Costes *et al.*, 1969).

Lunokhod 1. The first unmanned lunar rover, Lunokhod 1, was equipped with a cone penetrometer and a vane shear device. A total of 327 tests were performed in the lunar soil to depths of 10 cm along a 5-km traverse in the western part of Mare Imbrium. More details are given immediately below.

Apollo 14. Two experiments on the Apollo 14 mission were conducted specifically to evaluate the shear strength properties of lunar soils: (1) The astronauts excavated a shallow trench, and (2) they pushed a rod into the surface. The latter was called the Apollo Simple Penetrometer (ASP) because it had

TABLE 9.11. Estimates of lunar soil cohesion and friction angle (after *Mitchell et al.*, 1972d, 1974).

Source	Cohesion, <i>c</i> (kPa)	Friction Angle, ϕ (degrees)	References
EARLY INFERRED: REMOTE SENSING			
	24-240	0	<i>Halajian</i> (1964)
	>0.007	>28	<i>Jaffe</i> (1964)
	>0	>25	<i>Jaffe</i> (1965)
INFERRED: BOULDER TRACKS			
	0.35	33	<i>Nordmeyer</i> (1967)
	0.1	10-30	<i>Moore</i> (1970)
	0.5*	21-55 (39†)	<i>Hovland and Mitchell</i> (1971)
Apollo 17 - North, East and South Massifs	1*	26-50 (37†)	<i>Mitchell et al.</i> (1973a)
SURVEYOR: EARLY ESTIMATES			
1: TV and Landing Data	10	0	<i>Halajian</i> (1966)
TV and Landing Data	0.15-15	55	<i>Jaffe</i> (1967)
TV and Landing Data	0.4-0.13	30-40	<i>Christensen et al.</i> (1967)
3: Soil Mechanics Surface Sampler, TV, and Landing Data	0	>35	<i>Scott and Roberson</i> (1968a)
	10 for	45-60	<i>Christensen et al.</i> (1968a)
	>0.07 for	0	<i>Christensen et al.</i> (1968b)
6: Vernier Engine Attitude Jets	0.05-1.7	35	<i>Christensen et al.</i> (1968b)
3 and 7: Soil Mechanics Surface Sampler	0.35-0.70	35-37	<i>Scott and Roberson</i> (1969)
SURVEYOR MODEL: BEST ESTIMATE			
	0.35-0.70	35-37	<i>Scott and Roberson</i> (1969)
APOLLO 11			
LM Landing, Bootprints, Crater Slope Stability	Consistent with Surveyor Model		<i>Costes et al.</i> (1969)
Core Tube, Flag Pole, SWC Shaft Penetration	0.75-2.1	37-45	<i>Costes et al.</i> (1971)
APOLLO 12			
LM Landing, Bootprints, Crater Slope Stability	Consistent with Surveyor Model		<i>Scott et al.</i> (1970)
Core Tube, SWC Shaft Penetration	0.56-0.75	38-44	<i>Costes et al.</i> (1971)
LUNOKHOD I			
Vane Shear	3.9-4.9	N/A	<i>Leonovich et al.</i> (1971, 1972)
- Lowest	0.26-1.1	50-25	<i>Mitchell et al.</i> (1972d)
- Highest	1.2-4.8	50-25	
- Mode	0.64-2.6	50-25	
Cone Penetrometer			<i>Mitchell et al.</i> (1972d)
- Crater Wall (inner)	0.17-1.0	45-25	
- Crater Slope (outer)	0.52-2.7	45-25	
- Horizontal Ground	0.34-1.8	45-25	
APOLLO 14			
Soil Mechanics Trench	<0.03-0.1	35-45	<i>Mitchell et al.</i> (1971)
Apollo Simple Penetrometer	Equal to or greater than Surveyor Model		<i>Mitchell et al.</i> (1971)
MET Tracks		37-47	<i>Mitchell et al.</i> (1971)

TABLE 9.11. (continued).

Source	Cohesion, <i>c</i> (kPa)	Friction Angle, ϕ (degrees)	References
APOLLO 15			
SRP Data and Simulation Studies		47.5-51.5	<i>Mitchell et al. (1972a)</i>
SRP Data and Soil Mechanics Trench	1.0	50	<i>Mitchell et al. (1972a)</i>
APOLLO 16			
SRP: Station 4 (10-20 cm depth)	0.6	46.5	<i>Mitchell et al. (1972b)</i>
SRP: Station 10	0.37	49.5	<i>Mitchell et al. (1972b)</i>
SRP: Station 10	0.25-0.60	50-47	<i>Mitchell et al. (1972b)</i>
Drill Core Open Hole	1.3	46.5*	<i>Mitchell et al. (1972b)</i>
APOLLO 17			
Drill Core Open Hole (Neutron Flux Probe)	1.1-1.8	50-30	<i>Mitchell et al. (1973a)</i>
LRV	0.17	35	<i>Mitchell et al. (1973a)</i>
APOLLO MODEL: BEST ESTIMATE			
	0.1-1.0	30-50	<i>Mitchell et al. (1972d, 1974)</i>
LUNOKHOD 1 AND 2 (AVE.)			
	0.4 [§]	40 [§]	<i>Leonovich et al. (1974a, 1975)</i>
RETURNED LUNAR SAMPLES			
Apollo 11: Penetrometer	0.25-0.85	42-38	<i>Costes et al. (1969, 1970a,b); Costes and Mitchell (1970) Jaffe (1971a)</i>
Apollo 12: Penetrometer (Surveyor 3)		N/A	
Apollo 12: Vacuum Direct Shear	0-0.7	28-35	<i>Carrier et al. (1972b, 1973c)</i>
Apollo 12: Direct Shear (Surveyor 3)	0.1-3.1	13-56	<i>Jaffe (1973)</i>
Apollo 12: Triaxial Shear (Surveyor 3)	0-1	51-59	<i>Scott (1987; personal communication, 1988)</i>
Luna 16 and 20: Direct Shear and Coulomb Device	3.9-5.9	20-25	<i>Leonovich et al. (1974a, 1975); Gromov et al. (1972)</i>

* Assumed.

† Mean of 69 values.

‡ Mean of 25 values.

§ Estimated.

no moving parts. The depth of penetration was estimated by the astronaut calling out the exposed stripes on the rod, and the required force was estimated on the basis of measurements made with a spacesuited subject flying in an aircraft under $1/6$ -g conditions. Although approximate, these tests again confirmed the Surveyor Model (*Mitchell et al., 1971*).

Apollo 15 and 16. A more sophisticated Self-Recording Penetrometer (SRP) was operated by the astronauts on the Apollo 15 and 16 missions. A total of 17 tests were performed to depths of 74 cm. Details are given immediately below.

In addition, when the deep rotary drill core was successfully removed from the lunar surface during the Apollo 16 mission, Astronaut Charles Duke was

able to insert a "rammer-jammer" tool down the open hole to a depth of more than 2 m. Analysis indicated the cohesion would have to be 1.3 kPa for a friction angle of 46.5° to keep such an unsupported hole open (*Mitchell et al., 1972b*).

Apollo 17. At the Apollo 17 site, a thin, cylindrical Neutron Flux Probe was inserted into the open drill core hole, which was even deeper (3 m) than the similar hole at the Apollo 16 site. In this case, it was found that the cohesion would have to be 1.1 to 1.8 kPa for a wide range of friction angles (*Mitchell et al., 1973a*).

Cone penetrometer measurements. Cone penetrometer tests were made by astronauts on the Apollo 14, 15, and 16 missions and from the

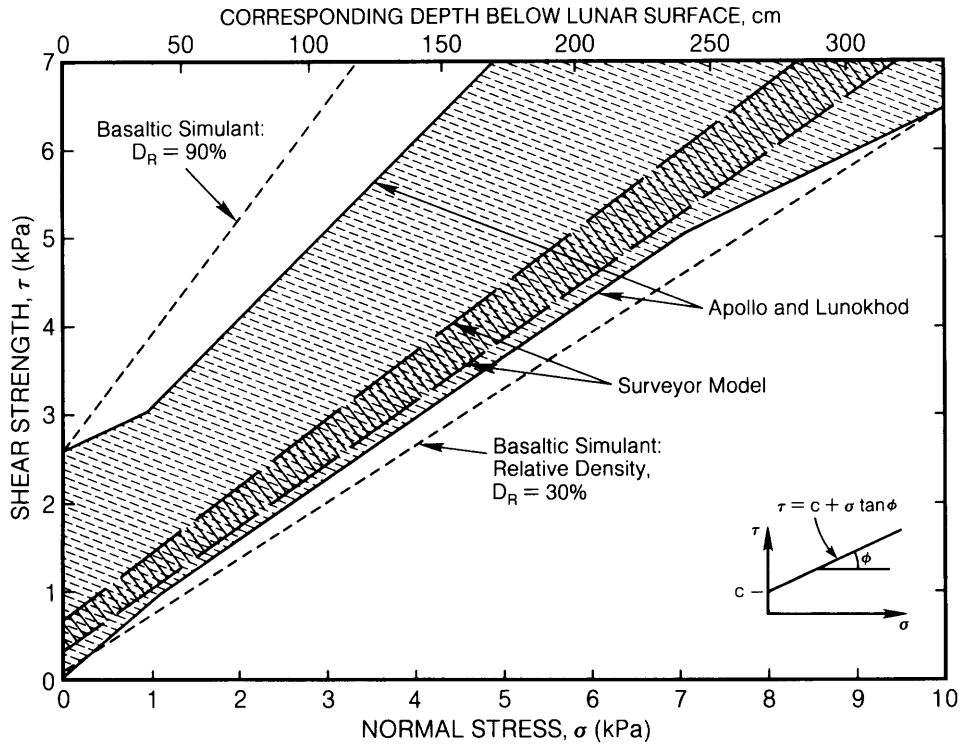


Fig. 9.26. Calculated *in situ* shear strengths of lunar soil (vertical axis), plotted as a function of normal stress (bottom horizontal axis) and corresponding depth below the lunar surface (top horizontal axis) (after Mitchell *et al.*, 1972d, 1974). Envelopes of shear strength are shown for Surveyor model data (oblique solid ruling), for Apollo and Lunokhod results (oblique dashed ruling), and for a basaltic simulant at relative densities of 30% and 90% (dashed lines).

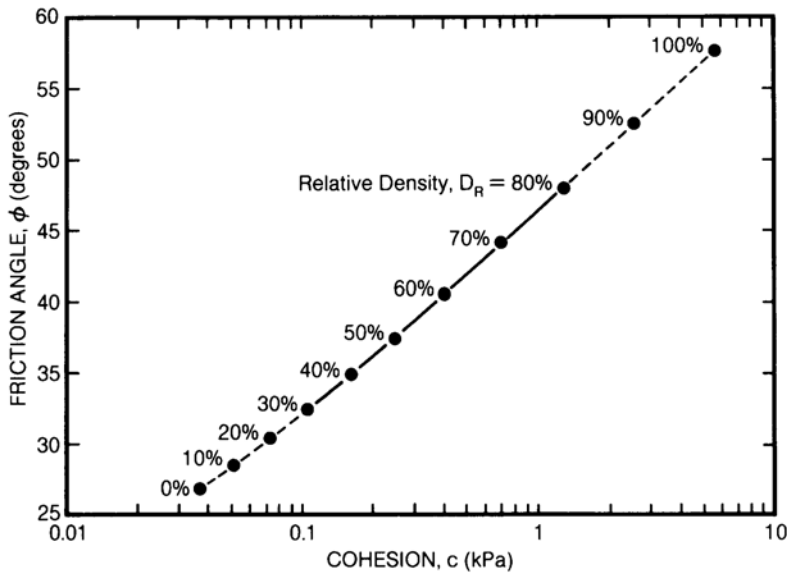
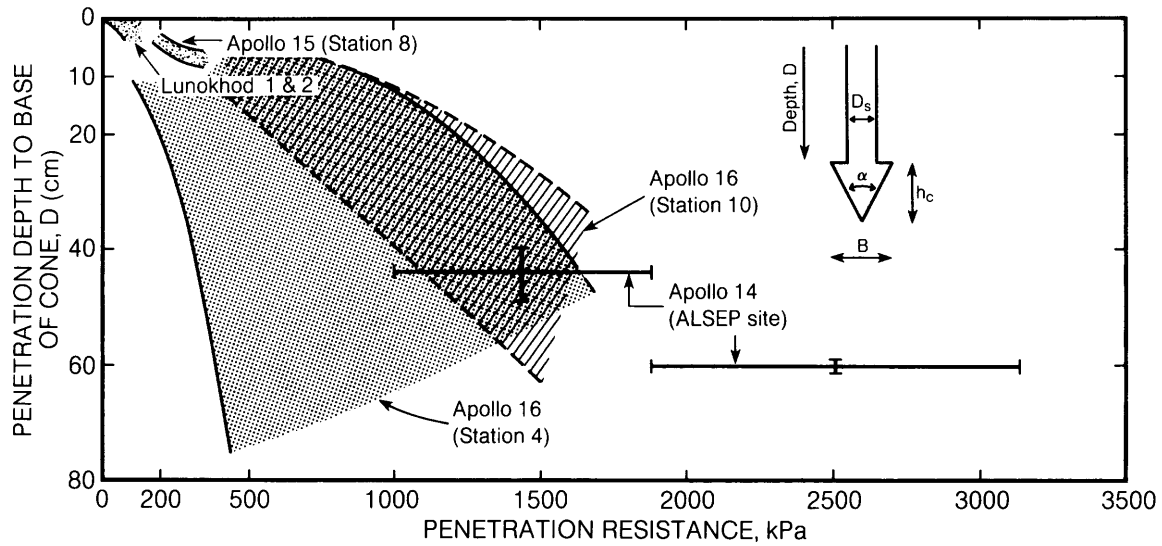


Fig. 9.27. Measured shear strengths of a basaltic simulant of lunar soil, showing the friction angle (vertical axis) and cohesion (horizontal axis) for different relative densities (after Mitchell *et al.*, 1972d, 1974).

TABLE 9.12. Recommended typical values of lunar soil cohesion and friction angle (intercrater areas).

Depth Range (cm)	Cohesion, c (kPa)		Friction Angle, ϕ (degrees)	
	Average	Range	Average	Range
0 - 15	0.52	0.44 - 0.62	42	41 - 43
0 - 30	0.90	0.74 - 1.1	46	44 - 47
30 - 60	3.0	2.4 - 3.8	54	52 - 55
0 - 60	1.6	1.3 - 1.9	49	48 - 51



Mission	No. of Tests	B (cm)	α	h_c (cm)	D_s (cm)
Apollo 14	3	0.95	30°	1.78	0.95
Lunokhod 1 and 2	~1000	5.0	60°	4.4	—
Apollo 15	2	2.03	30°	3.78	0.94
Apollo 16 (Station 4)	{ 1, 3	{ 2.03, 1.28	{ 30°, 30°	{ 3.78, 2.39	{ 0.94, 0.94
Apollo 16 (Station 10)	{ 1, 3	{ 2.03, 1.28	{ 30°, 30°	{ 3.78, 2.39	{ 0.94, 0.94

Fig. 9.28. Cone penetrometer resistance data measured for *in situ* lunar surface material, plotted as penetration depth (vertical axis) vs. penetration resistance (horizontal axis). Data were obtained from the Lunokhod 1 and 2 automated rovers and by astronauts on several Apollo missions. Inset (upper right) shows diagrammatically the shape of the cone penetrometer and the forces involved (after Mitchell *et al.*, 1973b, 1974).

Lunokhod 1 and 2 robotic roving vehicles (Fig. 9.28). These measurements are the most important source of *in situ* shear strength data for the lunar soil.

The Lunokhod roving vehicle carried a combination cone penetrometer and vane shear device. The two perpendicular blades of the vane were 7 cm long and 4.4 cm high. The cone had an apex angle of 60° with a base diameter of 5 cm and a height of 4.4 cm.

Typical cone penetrometer test results are shown in Fig. 9.29 (Leonovich *et al.*, 1971, 1972).

The base of the Lunokhod cone was level with the soil surface when the tip depth was 4.4 cm, as shown by the horizontal dashed line in Fig. 9.29. Using bearing capacity theory, Mitchell *et al.* (1972d) analyzed this case for curves 1, 2, and 3, with the results shown in Fig. 9.30. This bearing capacity

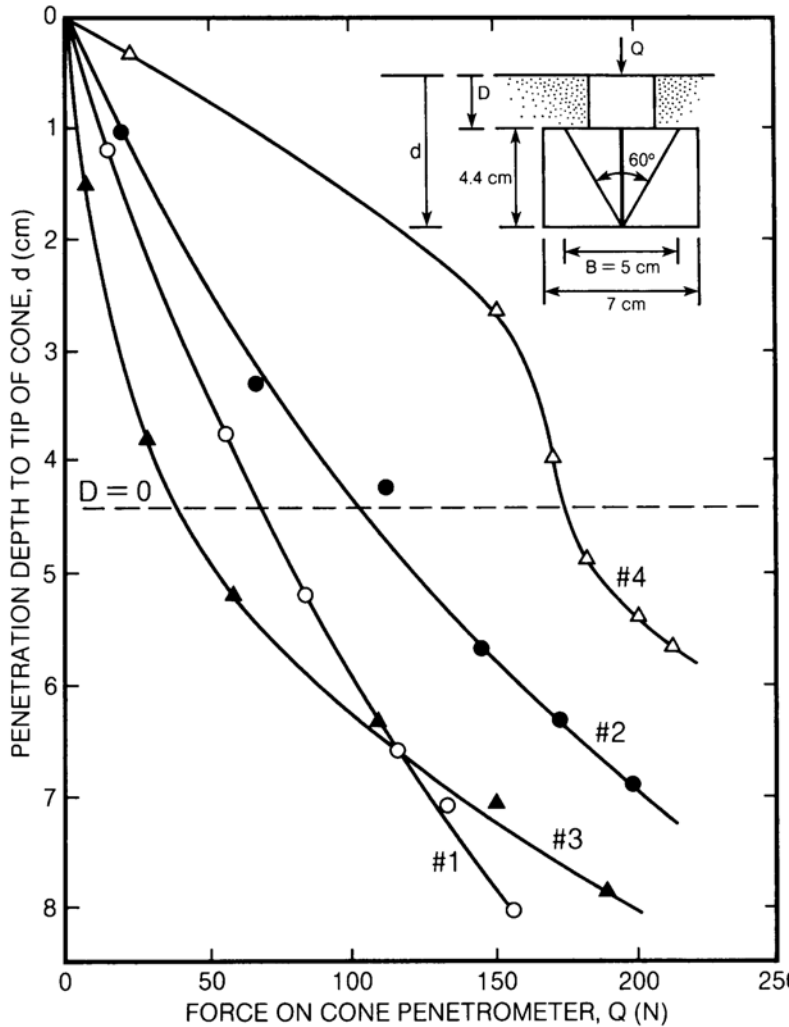


Fig. 9.29. Typical cone penetrometer resistance data, obtained by the Lunokhod 1 automated rover, for the lunar surface material in different areas of its landing site. Data are plotted as penetration depth to the tip of the cone (vertical axis) as a function of applied force (horizontal axis). Inset (upper right) diagrammatically shows the shape of the cone penetrometer and the forces involved. The base of the Lunokhod 1 cone was level with the surface when the tip depth was 4.4 cm (horizontal dashed line). Different curves were obtained for different types of lunar surface terrain: #1—level intercrater region (open circles); #2—crater slope (filled circles); #3—crater wall (filled triangles); #4—sector covered with small rocks (open triangles). Data from Leonovich *et al.* (1971, 1972) and Mitchell *et al.* (1972d).

theory was specifically developed for evaluating lunar cone penetrometer tests and is expressed as follows (Mitchell and Durgunoglu, 1973; Durgunoglu and Mitchell, 1975)

$$q = cN_c \xi_c + \rho g_m B N_{\gamma q} \xi_{\gamma q}$$

where q = cone penetration resistance; c = cohesion; ρ = density of lunar soil; g_m = acceleration of lunar gravity; B = penetrometer base width or diameter;

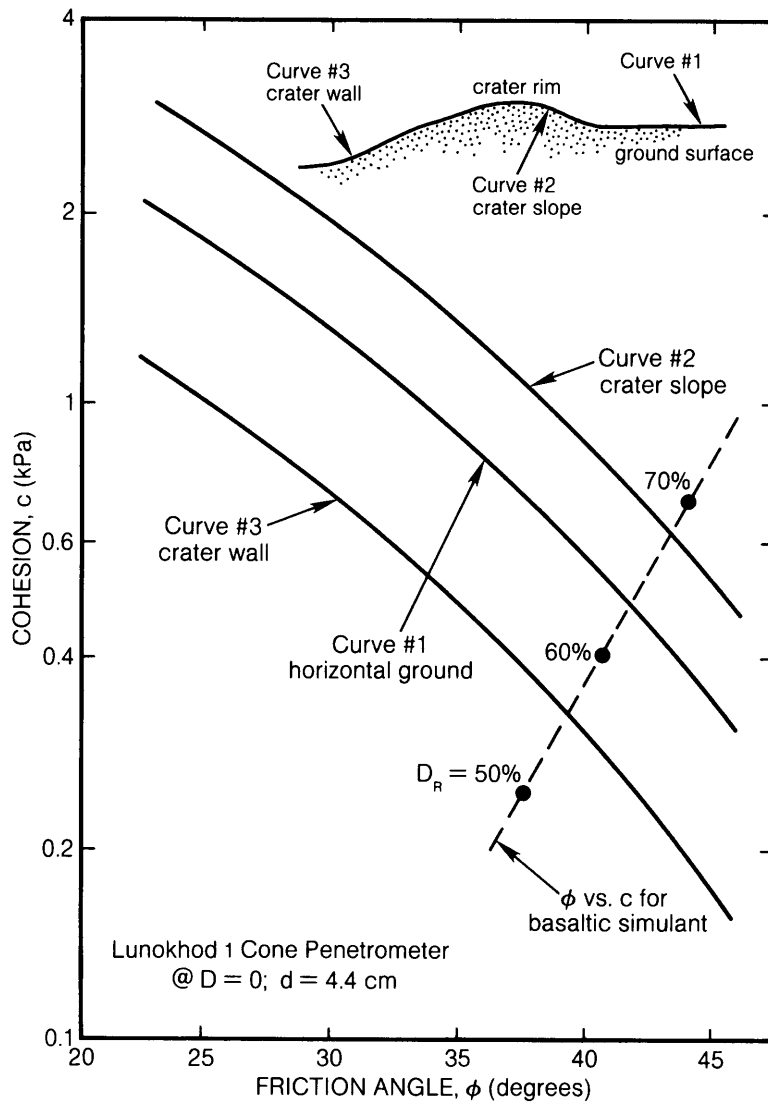
N_c , $N_{\gamma q}$ = bearing capacity factors (functions of friction angle, cone roughness, and coefficient of lateral stress); and ξ_c , $\xi_{\gamma q}$ = shape factors (functions of width, length, and depth).

There are five unknowns in this one equation: cohesion, friction angle, soil density, cone roughness, and coefficient of lateral stress. Reasonable values of

the latter three unknowns were assumed by Mitchell *et al.* (1972d); cohesion was then calculated for selected values of friction angle (Fig. 9.30). The calculated cohesion decreases as the friction angle increases: For example, on horizontal ground (curve 1), when $\phi = 25^\circ$, $c = 1.8$ kPa; and when $\phi = 45^\circ$, $c = 0.34$ kPa. The complete range of values is listed in Table 9.11.

The measured shear strength of the basaltic simulant (Fig. 9.27) is also plotted on Fig. 9.30 as the dashed curve, in which c and ϕ both increase as the relative density increases. Where the measured (dashed) curve crosses the theoretical curves (solid), a unique solution can be obtained: For example, on horizontal ground, $\phi = 42^\circ$ and $c = 0.5$ kPa. Furthermore, the corresponding relative density (D_R) is about 65%.

Fig. 9.30. Shear strength parameters for lunar soil, calculated from Lunokhod 1 cone penetrometer measurements (Fig. 9.29) (after Mitchell *et al.*, 1972d). Data are plotted in terms of cohesion (vertical axis) and friction angle (horizontal axis) for several types of terrain at the landing site (curves #1-#3). Inset (upper right) shows relation of measurement locations to the surface topography, which includes a small crater. Dashed line is based on data for a basalt simulant over a range of relative densities; where the dashed and solid curves are crossed, unique solutions are obtained.



In later papers, Leonovich *et al.* (1974a, 1975) presented statistical results for approximately 1000 cone penetrometer tests from Lunokhod 1 and 2, all at the same tip depth of 4.4 cm. A similar bearing capacity analysis to that above, performed on their data, yields the following average values: $\phi = 40^\circ$, $c = 0.40$ kPa, and $D_r = 59\%$. Frequency distributions for these data are presented in Fig. A9.7. This relative density is somewhat less than the value calculated in section 9.1.5 and Fig. A9.6 using the same Lunokhod data.

The Apollo Self-Recording Penetrometer (SRP) (Fig. 9.31) was equipped with three cones and one flat plate. Each cone had an apex angle of 30° , and

the base diameters varied from 1.28 cm to 2.86 cm. The plate was 2.54 cm wide and 12.7 cm long. The astronaut could attach the plate or one of the cones to the shaft as needed to perform a test. The record of each penetration test was scribed on a gold-plated, stainless-steel cylinder contained in the upper housing assembly (Fig. 9.32). After the test, this assembly was disconnected from the rest of the SRP and returned to Earth, while the cones and plate were discarded. The recording cylinder from the Apollo 16 SRP is shown in Fig. 9.33.

A total of 17 cone and plate tests were performed on the Apollo 15 and 16 missions (Mitchell *et al.*, 1974; Mitchell and Houston, 1974). With the smallest

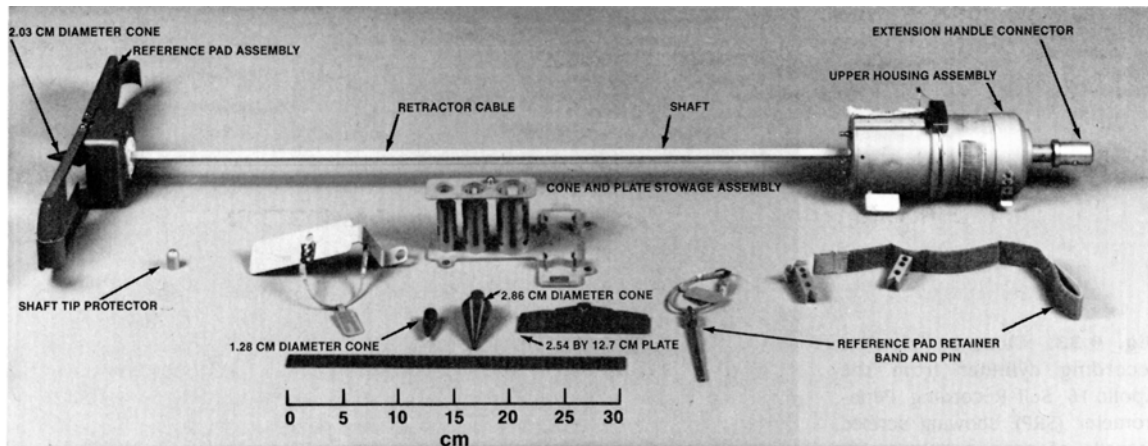


Fig. 9.31. Photograph and explanatory diagram of the Self-Recording Penetrometer (SRP) used on the Apollo 15 and 16 missions. When used, the SRP is held vertically, with the pad (left) placed flat on the soil surface. The astronaut holds the upper housing assembly (right) and pushes the cone into the surface. The depth of cone penetration is recorded by a scribe on a metal cylinder in the upper housing assembly (right). Three cones were available for testing, with diameters ranging from 1.28 to 2.86 cm (only the 1.28 and 2.03 were actually used, plus the 2.54 × 12.7-cm plate).

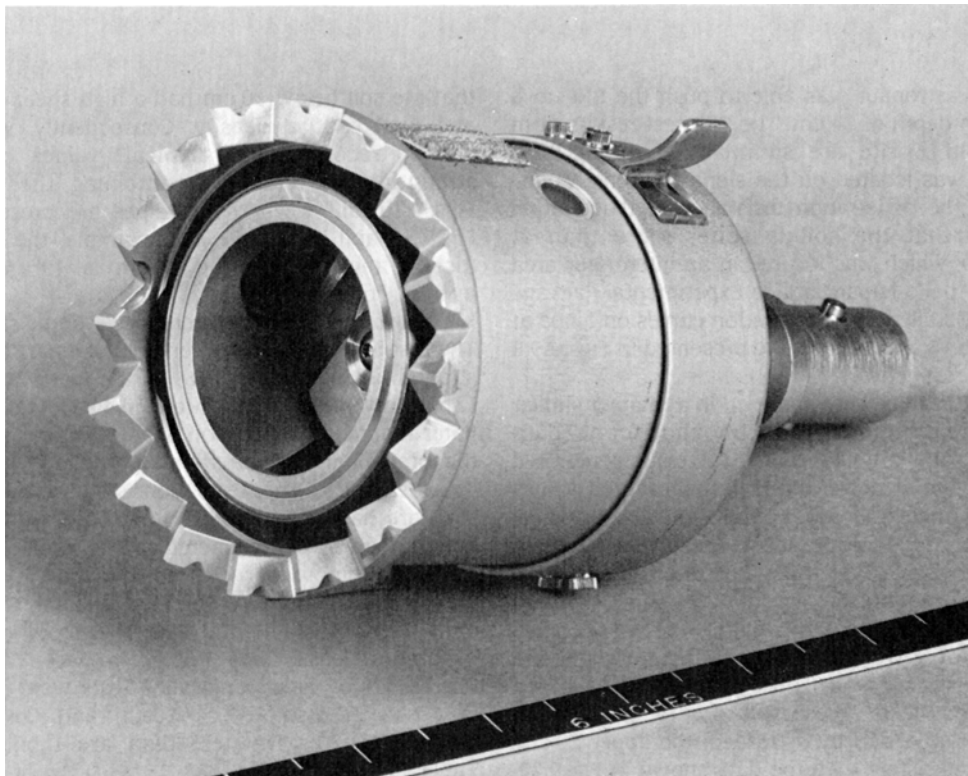
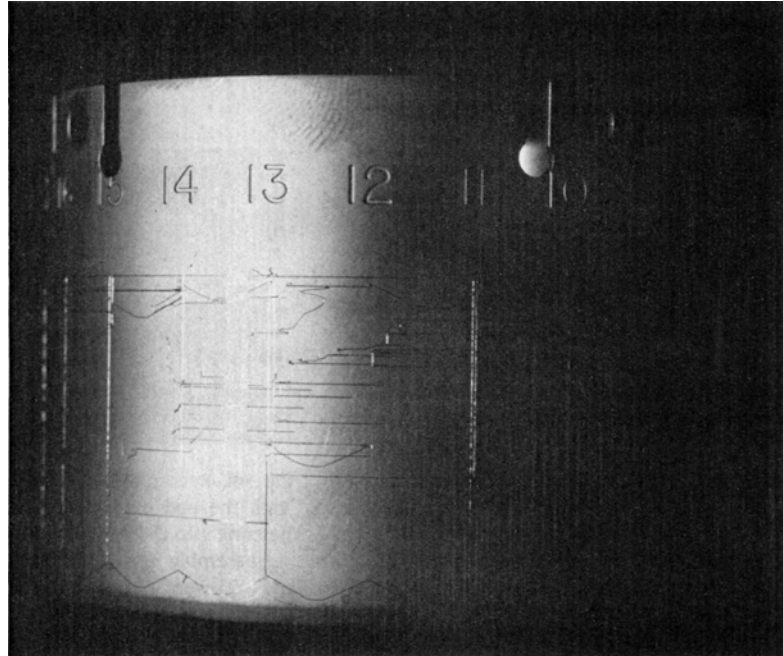


Fig. 9.32. Close-up view of upper housing assembly of Apollo Self-Recording Penetrometer (SRP) (see Fig. 9.31). Scale bar below housing is in inches. (NASA Photo S-71-39600.)

Fig. 9.33. Close-up view of recording cylinder from the Apollo 16 Self-Recording Penetrometer (SRP), showing scribed records of cone penetrometer tests of lunar surface material. The scratches under each number indicate the results of a single test measurement; a total of 17 measurements were made during the Apollo 15 and 16 missions. (Photo courtesy of W. D. Carrier III.)



cone, the astronaut was able to push the SRP to a maximum depth of 74 cm. The SRP test results from the Apollo 16 site are summarized in Fig. 9.34. Station 4 was located on the slope of Stone Mountain, and the penetration resistance at that station indicates that the soil is softer there than at Station 10, which was located in an intercrater area near the Apollo Lunar Surface Experimental Package (ALSEP). Detailed SRP penetration curves obtained at the Apollo 15 and 16 sites are presented in Figs. A9.8 and A9.9, respectively.

The SRP results were analyzed in a manner similar to the treatment of the Lunokhod cone data described above. Only eight SRP tests penetrated below 20 cm; of these, the lowest measured values of friction angle and cohesion are 41° and 0.45 kPa, respectively, found at Station 4. These values remain essentially constant to a depth of more than 60 cm at the same station.

In an intercrater region (Station 10, Apollo 16 site), at a depth of 20 cm, the average friction angle and cohesion are 46° and 0.95 kPa, respectively, based on only four tests. These values correspond to an average relative density of 75% for the upper 20 cm, which is consistent with the data shown in Fig. 9.20. To reach greater depths with the probe, the astronaut generally had to apply a force that exceeded the capacity of the recording mechanism, indicating

that the soil below 20 cm had a high shear strength and high relative density. Consequently, we have derived recommended "typical" values of shear strength parameters by combining the data in Figs. 9.20 and 9.27. These values are presented in Fig. 9.35 and Table 9.12. For example, the average friction angle in the top 60 cm is 49° , and the average cohesion is 1.6 kPa.

Laboratory measurements of shear strength. The first laboratory measurements of lunar soil shear strength were made in 1969 in the Lunar Receiving Laboratory at the NASA Manned Spacecraft Center (later renamed the Johnson Space Center) as part of the preliminary examination of Apollo 11 returned lunar samples. The tests consisted of pushing a standard hand-penetrometer (flat base) into several hundred grams of compacted soil. The soil had been sieved to remove particles coarser than 1 mm and was kept in a dry nitrogen atmosphere. The minimum density of the soil was 1.36 g/cm^3 and the maximum density was 1.80 g/cm^3 (see Table 9.7). The results of these penetration tests were reported in *Costes et al.* (1969, 1970a,b) and *Costes and Mitchell* (1970). The test data are tabulated in Table A9.1 1.

Reanalysis of the data for the bearing test performed on this Apollo 11 soil at the maximum density, utilizing the bearing capacity theory de-

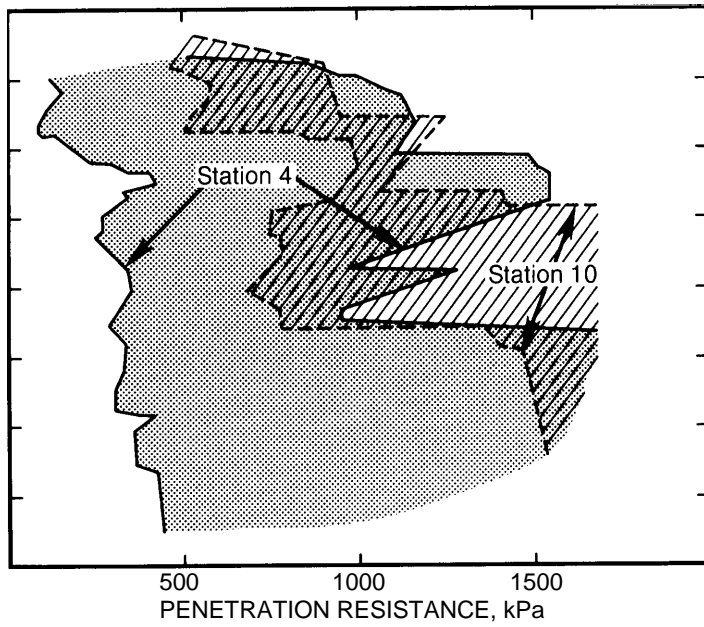


Fig. 9.34. Cone penetrometer resistance data obtained for lunar surface material at the Apollo 16 site, using the Self-Recording Penetrometer (SRP) (Fig. 9.31) (data after Mitchell *et al.*, 1973b). Data are plotted in terms of penetration depth (vertical axis) and penetration resistance (horizontal axis). Soil properties at Station 4 (stippled area) are bounded by the two curves designated "Station 4." A narrower range of soil properties at Station 10 (cross-hatched area) is bounded by two similar curves.

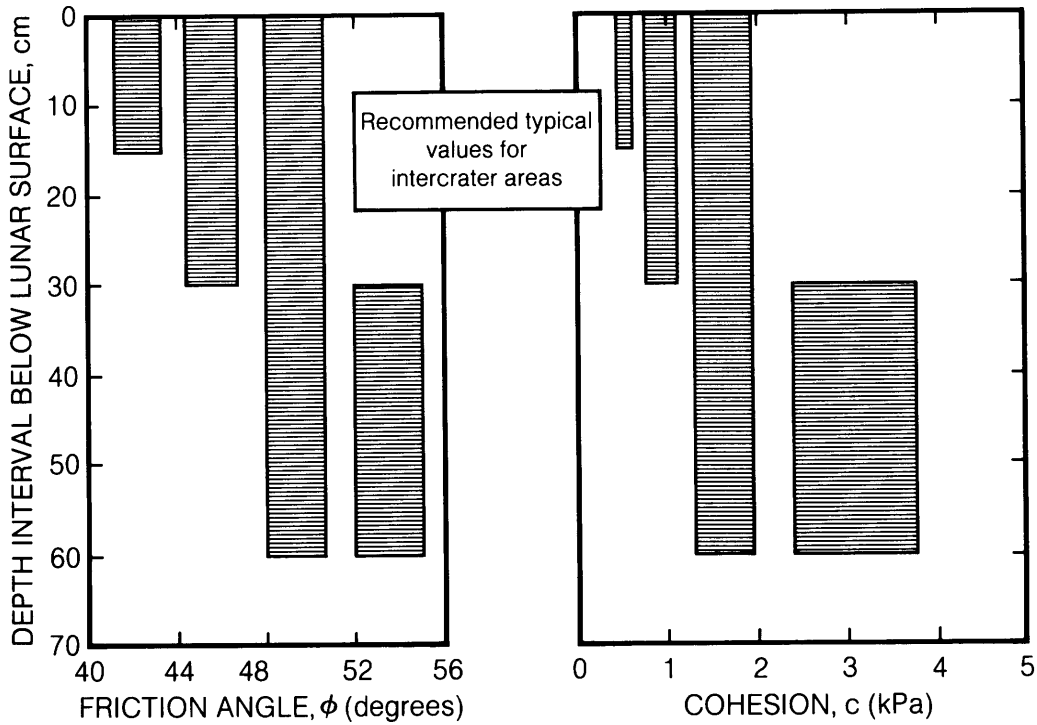


Fig. 9.35. Calculated average ("recommended") values of shear strength parameters (friction angle and cohesion) (horizontal axes) in the lunar surface material as a function of depth below the surface (vertical axis) (see also Table 9.12). Both parameters, particularly the cohesion, increase with depth.

scribed above (*Durgunoglu and Mitchell, 1975*) show that for a friction angle in the range from 42° to 38°, the cohesion would be 0.25 to 0.85 kPa.

Jaffe (1971a) performed similar penetrometer experiments on a 6.5-g soil sample contained in the Surveyor 3 scoop returned in October 1969 by the Apollo 12 astronauts. The test data are tabulated in Table A9.12.

Carrier et al. (1972b, 1973c) performed three direct shear tests in vacuum on a 200-g sample of Apollo 12 soil. For a range of cohesion from 0-0.7 kPa, the measured friction angle was 28°-35°. These values were significantly less than the shear strength of a basaltic simulant. This difference was attributed to the crushing of fragile particles such as agglutinates and breccias, which are unique to the lunar soil. A similar difference was observed during measurements of compressibility (section 9.1.6). Gas-pressure bursts, releasing a gas of solar-wind composition, also occurred during shear tests, as they had during compression tests (see Fig. 9.25). Complete test data are tabulated in Table A9.13.

Jaffe (1973) also performed miniature direct shear tests on 1.3 g of the soil returned with the Surveyor 3 scoop. The tests were performed in air, using soil samples with five initial bulk densities, ranging from 0.99 to 1.87 g/cm³. The measured values of cohesion varied from 0.1 to 3.1 kPa and the friction angle from 13° to 56°. *Jaffe* concluded that the test results were consistent with an *in situ* bulk density of about 1.7 g/cm³ (Table 9.4). He also concluded that exposure to air did not significantly alter the shear strength properties of lunar soil. The test results are tabulated in Table A9.14; most of the reported values of friction angle are significantly lower than those determined in other experiments.

Scott (1987, and personal communication, 1988) performed miniature triaxial shear tests on a 1.1-g sample of the soil returned with the Surveyor 3 scoop. The test results are tabulated in Table A9.15.

Leonovich et al. (1974a, 1975) performed direct shear and coulomb device tests on Luna 16 and 20 samples and reported a cohesion of 3.9 to 5.9 kPa and a friction angle of 20°-25°. Additional laboratory measurements of shear strength have been made by Soviet scientists, and they are reported (in Russian) in *Leonovich et al. (1974b)*, *Vedenin et al. (1974)*, *Douchowskoy et al. (1974, 1979)*, and *Gromov et al. (1979)*.

Lunar soil shear strength: Some speculation. All the laboratory tests on returned lunar soil samples suffer from the following limitations: (1) disturbance: the samples were sieved, remolded, and recompacted prior to testing; (2) size: the samples were small (to very small) by terrestrial testing standards; and (3) stress: unavoidably, the

confining stresses applied to the samples were one to two orders of magnitude greater than the *in situ* lunar stresses.

The last point appears to be especially significant. Under the low stresses present near the lunar surface, irregular and reentrant soil particles tend to interlock, producing an usually high shear strength. Even when the Lunokhod cone penetrometer was pushed into the soil with a tip pressure of 50 kPa, the average stress on the failure surface was only about 5 kPa. For the Apollo SRP, the average applied stress was even less because of the greater depth of penetration by the probe. On the other hand, when a returned soil sample is tested at laboratory stresses (30-70 kPa in the case of the vacuum direct shear tests), the fragile particles tend to crush, resulting in a lower measured shear strength.

As a result, *Carrier et al. (1972b, 1973c)*, *Mitchell et al. (1974)*, and *Leonovich et al. (1974a)* have all suggested that a curved Mohr-Coulomb equation would more appropriately describe the shear strength of lunar soil.

Instead of the normal Mohr-Coulomb equation, $\tau = c + \sigma \tan \phi$, *Carrier (1984)* has proposed that a better shear strength equation might be of the form

$$\tau = a\sigma^b$$

The apparent friction angle is then given by

$$\phi = \tan^{-1}(ab\sigma^{b-1})$$

and the apparent cohesion is given by

$$c = a(1-b)\sigma^b$$

Carrier has proposed preliminary values of $a = 1.83$ and $b = 0.73$, when the stresses are expressed in kilopascals. For example, at $\sigma = 5$ kPa, the shear strength, τ , would be 5.9 kPa, ϕ would be 41°, and c would be 1.60 kPa, all of which are consistent with the data in Fig. 9.26. In contrast, at $\sigma = 100$ kPa, τ would be 53 kPa, ϕ would be 21°, and c would be 14 kPa, which are close to the laboratory measurements of *Leonovich et al. (1974a, 1975)*.

For the present, the recommended shear strength parameters shown in Fig. 9.35 and Table 9.12 are sufficiently accurate for the design of near-surface lunar structures and construction activities. However, at later stages in the human development of the Moon, heavy structures or deep excavations will likely be constructed. At that point, a more complete understanding of the shear strength of lunar soil under higher stress conditions will be required.

Regolith seismic properties. P-wave velocities (α) measured in regolith at the Apollo landing sites are very low and uniform and range from 92 to

114 m/sec, with an average of 105 m/sec (Watkins and Kovach, 1973). The low velocities are interpreted as being related to brecciation and high porosity. The seismic Q ($\alpha Q/10^3$; loss of energy by absorption) of lunar regolith is ~ 200 at a velocity of 105 m/sec; for comparison, terrestrial analogues such as unconsolidated volcanic ash have seismic Qs of 1.5-3.0 at an $\alpha = 400$ m/sec (Watkins and Kovach 1973).

9.1.8 Permeability and Diffusivity

The coefficients of permeability and diffusivity are used to evaluate the movement of a fluid (gas or liquid) through a porous solid medium. No direct measurements of these parameters have been made on lunar soil. Approximate values are presented in the following sections.

Permeability. The *coefficient of permeability* defines the quantity of flow of a fluid through a porous medium in response to a pressure gradient.

In the simplest case of steady-state flow of an incompressible, nonreactive liquid, Darcy's Law states that

$$Q = K \frac{\rho g_m}{\mu} i A$$

where Q = flow rate (m^3/sec); K = absolute permeability (m^2); ρ = density of the liquid (kg/m^3); g_m = acceleration due to lunar gravity (m/sec^2); μ = viscosity of liquid ($\text{N}\cdot\text{sec}/\text{m}^2$); i = hydraulic gradient (m/m); and A = cross-sectional area normal to the flow (m^2). For a given arrangement of particles, the coefficient of absolute (or specific) permeability is controlled by the size and shape of the pore spaces, and it is independent of the properties of the liquid.

The transient flow of rocket-engine exhaust into the lunar surface material was studied extensively in order to estimate the amount of erosion that could occur when the accumulated gas pressure in the pores exceeded the weight of the overlying soil under different operating conditions (cf. Scott and Ko, 1968). Based on a test firing of the Surveyor 5 vernier engine on the lunar surface, the permeability of the soil to a depth of about 25 cm was deduced to be $1.7 \times 10^{-12} \text{ m}^2$ (Choate et al., 1968). This value was considered to be consistent with the fine-grained nature of the soil.

Diffusivity. The *gas diffusivity* defines the molecular flow of gas through a porous medium in response to a concentration gradient. The diffusivity depends on the gas composition, the pressure and temperature, and the particle size and shape distributions of the soil. Martin et al. (1973) measured the diffusivity of noble gases—He, Ar, and Kr—through a basaltic lunar soil simulant. The void ratio

in the soil was established at about 0.6, and the tests were run at room temperature under very low vacuum conditions, such that the mean free path length of the molecules was much greater than the pore dimensions. The measured results for gas diffusivity were 7.7, 2.3, and $1.8 \text{ cm}^2/\text{sec}$ for He, Ar, and Kr, respectively.

For these relatively nonreactive gases, the diffusivity is proportional to $(T/M)^{1/2}$, where T is the absolute temperature and M is the molecular weight of the gas. The "sticking time" of the gas molecules, or heat of absorption, becomes significant if the gas is more reactive or the temperature is reduced.

9.1.9. Bearing Capacity

The remaining three subsections of 9.1 discuss important practical consequences of the geotechnical index and engineering properties of the lunar regolith: bearing capacity, slope stability, and trafficability.

Bearing capacity describes the ability of a soil to support an applied load, such as a vehicle, a structure, or even an astronaut. Usually, the topic of bearing capacity is divided into two categories: ultimate bearing capacity and allowable bearing capacity; each of these are then subdivided further into static and dynamic quantities.

Ultimate bearing capacity defines the maximum possible load that can be applied without causing gross failure, such as the overturning of a structure. For a 1-m footing on the lunar surface, the ultimate bearing capacity is approximately 6000 kPa.

Allowable bearing capacity defines a lesser load that can be applied without exceeding a given amount of settlement. A settlement limit is usually imposed either for structural or operational requirements. For example, if the settlement of an experiment package placed on the lunar surface must be less than 1 cm, with a confidence level of 95%, and the width of the package is less than 0.5 m, then its allowable bearing pressure is just 2 kPa.

These topics are discussed in more detail in the following sections.

Ultimate bearing capacity: Static. The static ultimate bearing capacity, q_{ult} , can be estimated on the basis of plasticity theory and is given by (Durgunoglu and Mitchell, 1975)

$$q_{ult} = c N_c \xi_c + \rho g_m B N_{\gamma q} \xi_{\gamma q}$$

where ρ = density of soil; $g_m = 1.62 \text{ m}/\text{sec}^2$ (acceleration of gravity on the Moon); B = footing width; c = cohesion of soil; N_c , $N_{\gamma q}$ = bearing capacity factors, which are primarily dependent on the friction angle, ϕ , of the soil; and ξ_c , $\xi_{\gamma q}$ = shape factors (see section 9.1.7 for additional details).

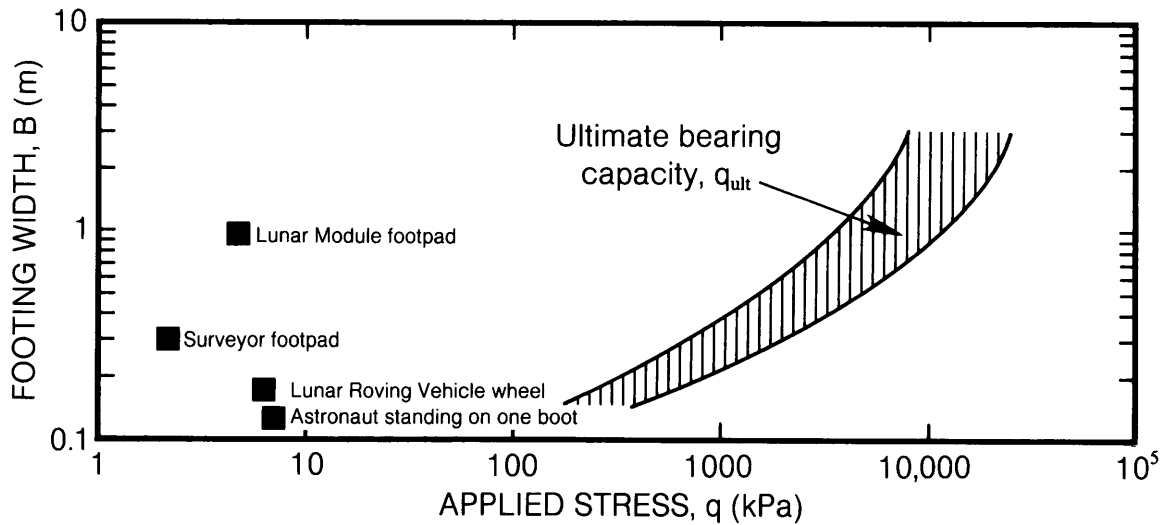


Fig. 9.36. Ultimate bearing capacity data for lunar surface material. Data are plotted in terms of the applied stress (horizontal axis) produced by an object on the lunar surface and the footing width (essentially the footpad size) of the object. Data (filled squares) are given for an astronaut standing on one boot, for an Apollo Lunar Roving Vehicle (LRV) wheel, and for the footpads of the robotic Surveyor spacecraft and the manned Lunar Module. The envelope of ultimate bearing capacity (right side, vertical ruling) lies at much higher applied stresses, indicating that the lunar surface can support virtually any type of conceivable spacecraft or structure.

The ultimate bearing capacity is therefore controlled by the soil density, its shear strength, and the size of the footing. Using the *in situ* bulk density estimates in section 9.1.4 and the *in situ* shear strength estimates in section 9.1.7, the ultimate bearing capacity vs. footing width can be calculated (Fig. 9.36). As an example, during the Apollo 11 landing, the Lunar Module (LM) footpad was nearly 1 m in diameter, and the ultimate bearing capacity of the lunar soil was approximately 3000 to 11,000 kPa. Because the stress actually applied by the footpad was only about 5 kPa, the factor of safety was 600 to 2200. Furthermore, for larger footings, the ultimate bearing capacity is roughly proportional to the width. That means that the ultimate load (stress \times area) for a circular or square footing is proportional to the cube of its width. Consequently, the ultimate bearing capacity of the lunar surface is more than sufficient to support virtually any conceivable structure.

Ultimate bearing capacity: Dynamic. The dynamic ultimate bearing capacity defines the maximum resistance to impact loading. This dynamic capacity is always greater than the static capacity because of the inertial resistance of the soil.

Even after the experience from several manned lunar landings, many scientists and engineers still believed that an astronaut could hammer a rod or

core tube into the lunar surface material to almost any depth. In fact, the practical limit of the Apollo 15-17 thin-walled core tubes (see Figs. 9.6 and 9.10) was only about 70 cm, and it typically required about 50 hammer blows to reach this depth. An analysis by *Carrier et al.* (1971) showed that if energy losses were neglected, the number of hammer blows required to reach a given depth would increase with the square of the depth; if energy losses were included, then there would be a depth beyond which no amount of hammering would drive a rod or core tube.

The same analysis (*Carrier et al.*, 1971) concluded that it would be impossible for the Apollo 17 astronauts to drive the long, cylindrical Lunar Neutron Probe Experiment (*Woolum et al.*, 1973) into the soil, as was originally planned. The probe had a diameter of about 2 cm, and it had to be inserted to a depth of 1-2 m. As a result of this analysis, it was decided that the Apollo 17 astronauts would attempt to drop the probe down the hole opened up by the drill to collect the deep core sample. Earlier studies (*Mitchell et al.*, 1972a) had predicted that the hole would remain open after the drill stem was withdrawn, and this effect had been demonstrated by the Apollo 16 astronauts (*Mitchell et al.*, 1972b). When this operation was attempted during the Apollo 17 mission, the probe fell into the drill core

hole without difficulty. The success of the predictions served to confirm the shear strength parameters of the lunar soil (section 9.1.7 and Tables 9.11-9.12).

Allowable bearing capacity: Static. The allowable bearing capacity is controlled by the compressibility of the soil and the acceptable amount of settlement for a given structure. For a load applied directly on the lunar surface, and a footing width of less than about 0.5 m, our best source of information about the behavior of the lunar soil is the astronaut footprint data discussed in section 9.1.5 and Fig. A9.4. With a known load and depth of footprint, the modulus of subgrade reaction, k , can be calculated statistically, as shown in Fig. 9.37. Then the allowable bearing capacity, q_{all} , is given by

$$q_{all} = k d_{acc}$$

where d_{acc} = the amount of acceptable settlement.

For example, the average value of $k = 8$ kPa/cm for a range of lunar locations, including the rims of fresh craters. If the acceptable settlement is 1 cm, then

$$q_{all} = (8) (1) = 8 \text{ kPa}$$

The data in Fig. 9.36 show that the allowable bearing capacity is significantly less than the ultimate bearing capacity; hence, the former always

controls the design of a foundation. If a 95% confidence level is required for acceptable settlement depth, then Fig. 9.37 indicates that a modulus value of $k = 2$ kPa/cm should be used

$$q_{all} = (2) (1) = 2 \text{ kPa}$$

The modulus of subgrade reaction (k) presented in Fig. 9.37 is sufficiently accurate to design many structures and experiment packages for emplacement on the lunar surface. However, for highly settlement-sensitive structures, such as telescopes, the lunar surface compressibility from point to point is too variable for a general approach. Founding such a structure directly on the surface could lead to unacceptably high differential settlements. These structures will more than likely have to be supported by spread footings set at a depth of at least 30 cm, and perhaps 1 m beneath the actual surface, in order to be below the depth of diurnal temperature fluctuations. The settlement d of such a footing is calculated on the basis of elasticity theory and is given by

$$d = \sum_{j=1}^n \frac{C_j}{1 + e_j} \Delta H_j \log \left(\frac{\sigma_{ij} + \Delta \sigma_j}{\sigma_{ij}} \right)$$

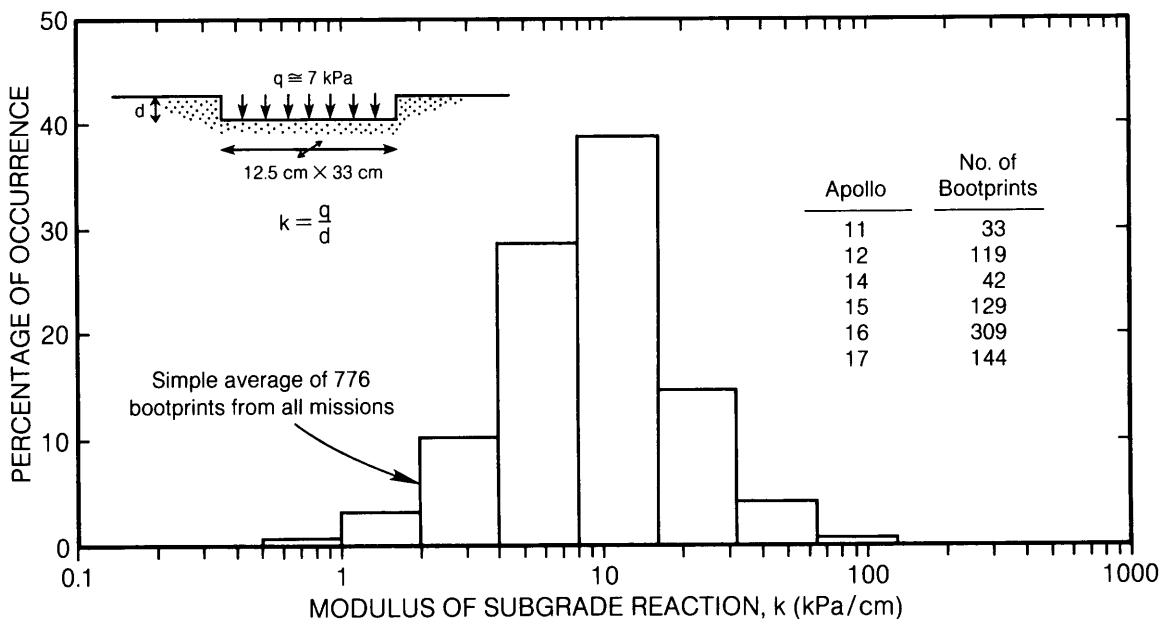
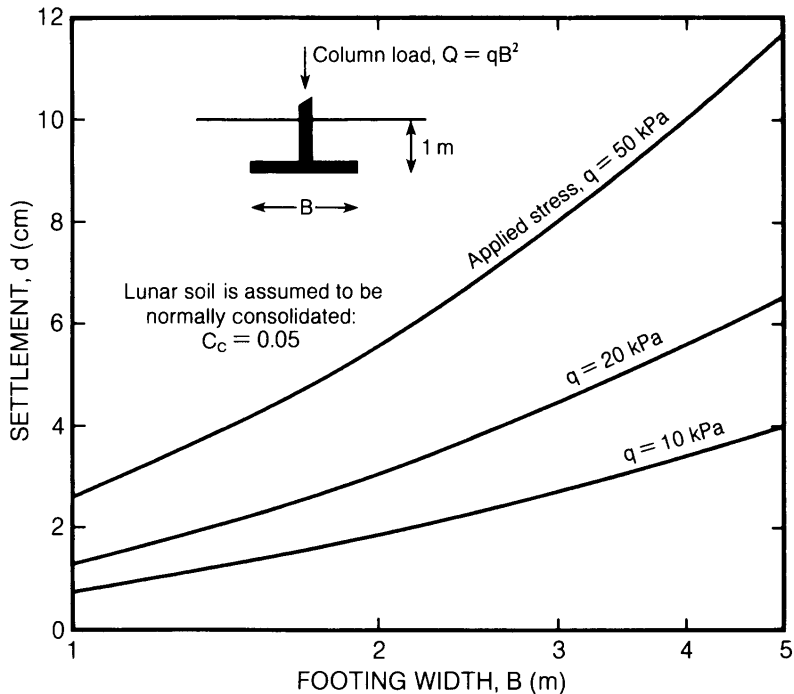


Fig. 9.37. Data for calculating the maximum allowable bearing capacity for lunar surface material. The plot shows a histogram of values of the modulus of subgrade reaction, determined from measurements of 776 astronaut bootprints made on all Apollo missions (data after Mitchell et al., 1974). Inset (upper left) shows a schematic cross-section of a footprint and the forces involved. The maximum allowable bearing capacity for any required minimum subsidence can be calculated from the determined values of the modulus (see text).

Fig. 9.38. Estimated depths of settlement for structures on the lunar surface, determined from estimates of bulk density vs. depth (Fig. 9.16) combined with measurements of compressibility (Table 9.9). Individual curves show the calculated settlement as a function of footing width for a single square footing, bedded at a depth of 1 m in the soil, carrying a range of applied stresses. Inset diagram (upper left) shows the footing and the forces involved. The estimated settlement depths are small, even for heavy loads, and they can be easily accommodated in the design and construction of actual lunar structures.



where C_j = compressibility of soil layer j (either compression index, C_c , or recompression index, C_r); e_j = initial void ratio of soil layer; ΔH_j = thickness of soil layer; σ_{ij} = initial vertical stress in soil layer (caused by overburden stress); and $\Delta\sigma_j$ = increment of vertical stress in soil layer (related to foundation load; estimated from elasticity theory).

A given soil profile can be subdivided into as many layers, n , as desired. The settlement of each layer is calculated, and the results are then summed to yield the total settlement of the foundation, d .

Typical settlement estimates for isolated spread footings are shown in Fig. 9.38. The calculations assume that the footings are square and are placed at a depth of 1 m. The initial void ratio and vertical stress distributions are based on the bulk density profile described in section 9.1.4. It is also assumed that the soil is normally consolidated and has a compression index, C_c , of 0.05 (Table 9.9). As shown in Fig. 9.38, the calculated settlement varies from a low of 0.7 cm for an applied stress of 10 kPa on a 1-m footing to 11.6 cm for an applied stress of 50 kPa on a 5-m footing. The footing sizes and applied stresses shown in Fig. 9.38 cover a wide range of possible conditions, and the calculated settlement values can be easily accommodated in the design of the structure. Because the relative

density of lunar soil has been found to be uniformly very high below a depth of 30 cm, the differential settlement between footings should be very small.

If the lunar soil is in fact over-consolidated (a question that remains to be answered; see section 9.1.6), the calculations of settlement for the same footings would be based instead on the recompression index, C_r , which is approximately 0.003 (Table 9.9). In this case, where the lunar soil is over-consolidated, the settlements would be only 1/17 of those shown in Fig. 9.38; such settlements are practically negligible.

Allowable bearing capacity: Dynamic. In the case of a slowly cyclical load, such as a rotating telescope, it is important to avoid differential settlements that produce rocking motions. The usual terrestrial practice is to require that the dynamic component of load be no greater than one-fourth of the static load.

In addition, if the structure contains rotating machinery, it is very important that resonances be avoided. Because of the low lunar gravity, the resonant frequency of a soil-supported structure will be less than that for a similar structure on Earth. Careful design will be required in order to eliminate annoying, or even detrimental, vibrations and settlements (cf. *Richart et al.*, 1970).

9.1.10. Slope Stability

In the past 100 years, literally dozens of numerical methods have been developed to evaluate the stability of a soil slope, i.e., its ability to stand without support. The most common methods are based on limit equilibrium analysis of circular potential slip surfaces. This approach is described in detail in numerous references (cf. *Taylor, 1937, 1948; Bishop, 1955; Lambe and Whitman, 1969*).

On the Moon, the absence of water greatly simplifies the analysis of slope stability. The factor of safety, F.S., against slope failure can be reduced to the following expression

$$F.S. = N \frac{\rho g_m h}{c}$$

where ρ = density of soil; c = cohesion of soil; g_m = acceleration of gravity on the Moon; h = height of slope; and N = stability number, which is a function of the friction angle, ϕ , of the soil and the slope angle, β .

Stability of constructed slopes. A constructed slope could be either an excavation, a compacted embankment, or a dumped pile (Fig. 9.39). The safe

depth (i.e., the depth up to which no slope failure will occur) of an excavation in an intercrater area can be calculated by combining values for the *in situ* density (section 9.1.4) with the *in situ* shear strength (section 9.1.7). Using a factor of safety of 1.5, which is more than adequate for design purposes, the calculations show that a vertical cut could be made in lunar soil to a depth of about 3 m (Fig. 9.39), and a slope of 60° could be maintained to a depth of about 10 m.

In order to construct an embankment, the soil must first be excavated, then transported, placed, spread, and compacted. As discussed above (section 9.1.5), the *in situ* lunar soil is very dense, with a greater density than could be produced with mechanical compaction equipment. The processes of handling and manipulating the lunar soil would loosen it considerably, and it would not then be possible to compact the soil back to its original, undisturbed density. As a result, the density of the soil in a compacted embankment would be lower than its original density, and the maximum possible slope angle of the embankment would be less than that of an excavation in undisturbed soil. Assuming a compacted relative density of 65–75%, a 10-m-

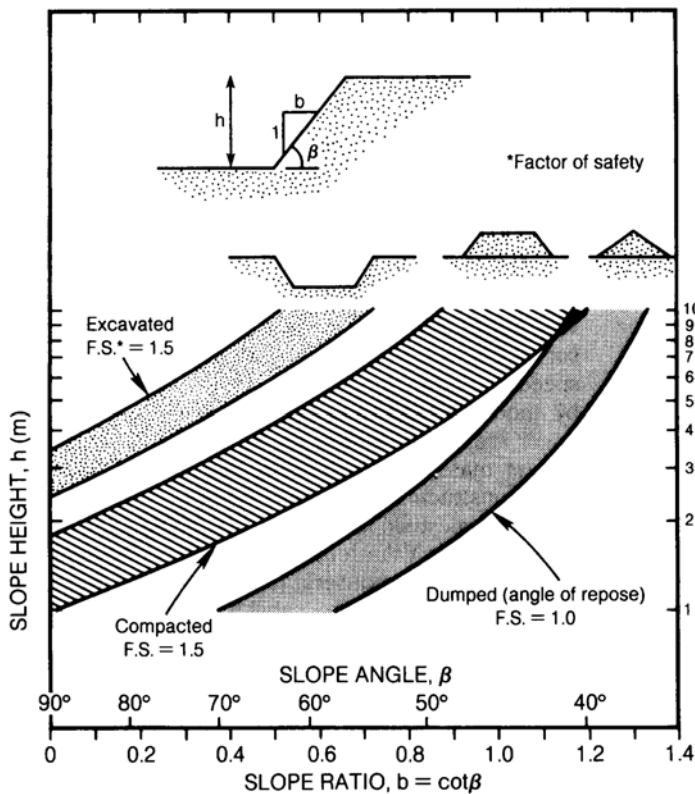


Fig. 9.39. Calculated stability of artificial slopes constructed in lunar surface material. Data are presented in terms of slope height (vertical axis) as a function of slope angle (or slope ratio) (horizontal axis). Inset (upper left) diagrammatically shows a slope and the quantities involved. Data are presented for three situations: (1) an excavation in lunar soil (stippled area); (2) a compacted pile of excavated lunar soil (ruled area); and (3) a dumped pile of lunar soil (shaded area). The data show that a vertical cut can safely be made in lunar soil to a depth of about 3 m, while an excavated slope of 60° can be maintained to a depth of about 10 m.

high slope could be constructed at an angle of about 45°, or one horizontal increment to one vertical increment (Fig. 9.39).

If lunar soil were simply dumped in a pile, it would attain a relative density of about 30–40% and the factor of safety (i.e., the “angle of repose”) would be 1.0. The pile could be raised to a height of 10 m at an angle of nearly 40°.

Stability of natural slopes. We really do not know very much about the stability of natural lunar slopes. In the early days, prior to any actual lunar landings, some scientists thought that the hills and mountains must be stronger than the mare basins, simply because the hills had slopes and the maria were relatively flat. However, the very limited cone penetrometer data obtained by both human and robotic missions have established that the soil on the slopes is actually somewhat weaker than the soil in the flatter intercrater areas, at least to a depth of 70 cm.

There is also considerable evidence, chiefly from orbital photography of the Moon, that slope failures have occurred on the lunar surface. In some cases, the resulting talus or landslide material has covered large areas and has traveled many kilometers. On Earth, slope failures are usually caused by fluctuations in the groundwater table, by erosion from running water, and occasionally by tectonic activity. On the Moon, the triggering mechanism is presumed to be the seismic vibrations produced by meteoroid impact, but explanations of how the talus has been able to move such long distances are very speculative.

Houston *et al.* (1973) attacked the question of lunar slope stability by analyzing the stability of lunar slopes under seismic conditions. They calculated that the cumulative downslope movement produced by more than 3.5 b.y. of meteoroid impacts was insignificant except on very steep slopes. They concluded that meteoroid impact could not account for the observed lunar slope degradation or “erosion.” On the other hand, Carrier *et al.* (1973c) suggested that outgassing during the shearing of lunar soil (see Fig. 9.25) could produce a fluidized flow condition, thereby resulting in large run-out distances for the transported material. Scott (1987) suggested an alternate mechanism based on numerical analyses by Campbell and Brennen (1985). He proposed that an intact soil layer could move at high velocity, suspended by the extremely dynamic motion of a few particles bouncing between the bottom of the soil layer and the underlying stable stratum. The bouncing soil particles would provide an equivalent pressure that would support the overlying layer in a pseudofluidized condition, even in the absence of an atmosphere, thus allowing the

layer to move with almost no frictional resistance. Finally, Florensky *et al.* (1978) analyzed the X-ray fluorescence spectroscopic data obtained from the Lunokhod 2 roving vehicle. They concluded that lateral movement of soil was occurring on slopes flatter than the angle of repose. While some of this movement could be attributed to meteoroid impacts, they proposed that a portion was caused by some kind of soil creep of “problematic origin.”

Clearly, many questions regarding the stability of natural lunar slopes remain unresolved.

9.1.11. Trafficability

Trafficability is defined as the capacity of a soil to support a vehicle and to provide sufficient traction for movement. Before actual landings on the Moon, it was believed that trafficability on the lunar surface would be poor and that the movement of vehicles would be very difficult. Consequently, all sorts of strange-looking walking machines were developed. From the experience of the Apollo and Lunokhod missions, we now know that almost any vehicle with round wheels will perform satisfactorily on the lunar surface, provided the ground contact pressure is no greater than about 7–10 kPa.

As a wheeled vehicle travels on a level lunar surface, the energy consumed in overcoming the combined effect of surface roughness and rolling resistance (soil compaction) is roughly equivalent to the energy expended in continuously climbing a smooth, rigid, 1½° slope. For the Apollo Lunar Roving Vehicle (LRV), which carried two astronauts, the combined surface roughness and rolling resistance accounted for only 15% of the total energy expended. The remainder was lost to mechanical linkages, inertia, instrumentation, etc.

The primary limitations on the trafficability of the lunar soil are speed and slope climbing. The normal cruise speed of the LRV was 6–7 km/hr. This speed was constrained by the irregularity of the cratered surface, coupled with the low lunar gravity. The speed of a future lunar vehicle can be increased only by modifying its dynamic response (e.g., by using larger diameter wheels, an increased wheel base, greater mass, or a softer suspension system), and/or by constructing permanent roads.

The steepest slope that the LRV could climb was 19°–23°. This value could be improved by adding variable-length grousers (cleats) to the wheels. Additional details on trafficability are provided in the following sections.

Lunar vehicles. To date, three types of wheeled vehicles have been operated on the lunar surface: the U.S.S.R. Lunokhod, the Apollo 14 Modular Equipment Transporter (MET), and the Apollo Lunar Roving Vehicle (LRV) (Figs. 9.40–9.42, respectively). The

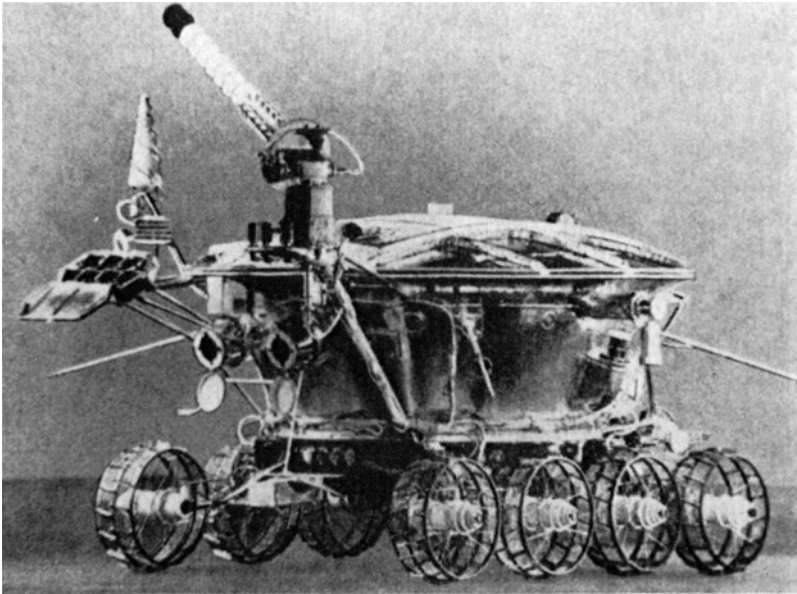


Fig. 9.40. Photograph showing a general view of the Lunokhod 1 robotic roving vehicle, which landed in Mare Imbrium in November 1970 and carried out exploratory traverses of the area around the landing site. The vehicle, which is driven by eight wire wheels, has a wheelbase of 1.7 m and is about 1 m wide. (Photograph from Alexandrov *et al.*, 1972.)

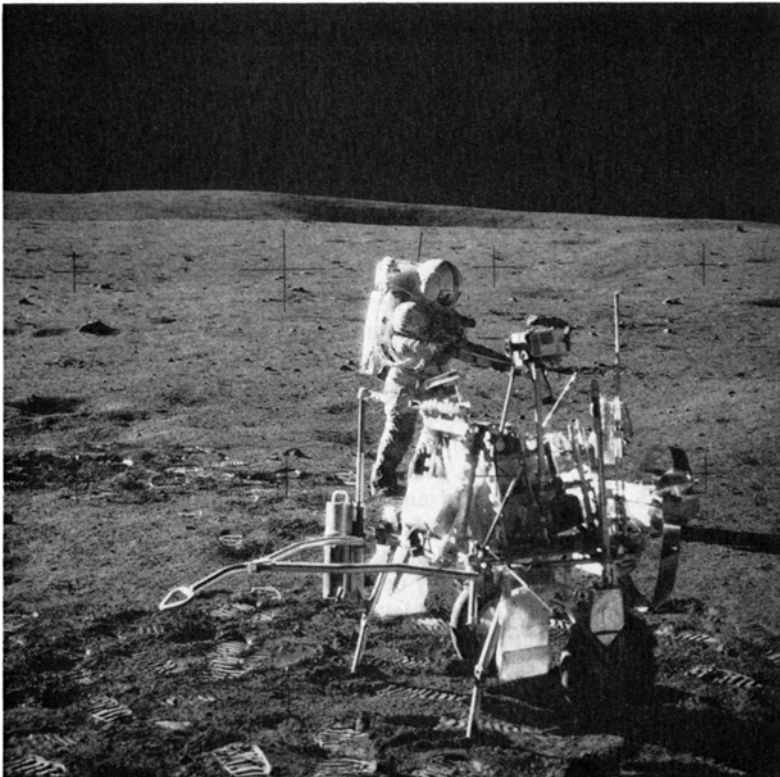
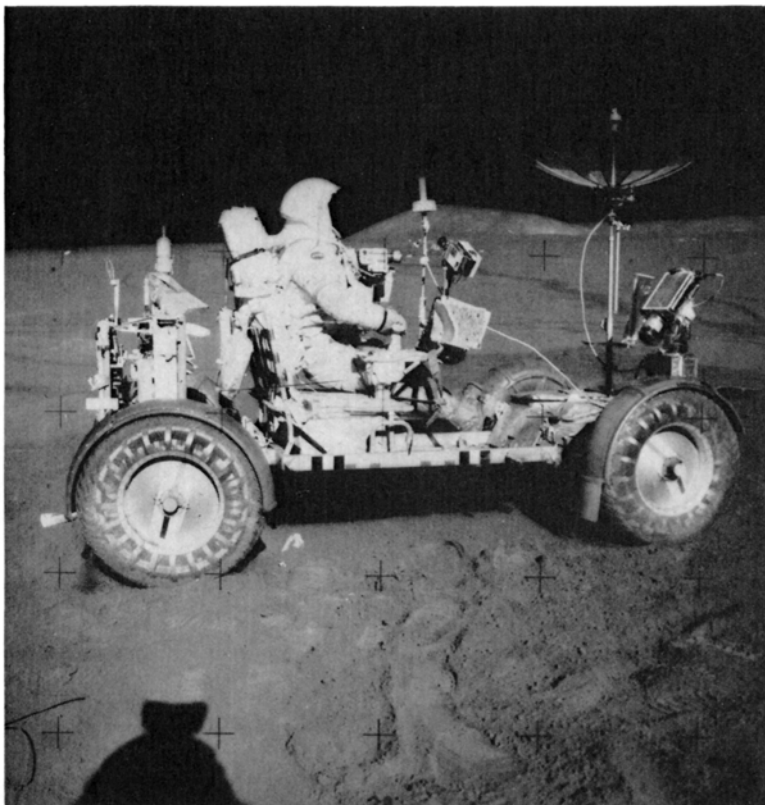


Fig. 9.41. Photograph of an Apollo 14 astronaut on the lunar surface with the Modularized Equipment Transporter (MET) (foreground). The MET was a hand-drawn, rickshaw-type carrier used to transport tools, instruments, and lunar samples on the Apollo 14 traverses. Mounted on two pneumatic tires, the MET was pulled by the astronaut. (NASA Photo AS-14-68-9404.)

Fig. 9.42. Photograph of the Apollo Lunar Roving Vehicle (LRV), or "Moon Buggy," being driven by an astronaut across the lunar surface at the Apollo 15 landing site. The LRV had an overall length of 310 cm (Fig. 9.44) and was electrically driven on four 82-cm-diameter wheels. Depending on the nature of the lunar surface being traversed, the LRV could be driven at speeds of 6–13 km/hr. (NASA Photo AS-15-85-11471.)



unmanned Lunokhod had a mass of 756 kg and rode on eight rigid, spoked wheels (Petrov, 1972; Alexandrov *et al.*, 1972). The rim of each wheel was constructed of metal mesh, reinforced with three hoops connected by transverse cleats. The diameter of the wheel was about 51 cm and the width about 20 cm. The MET was an unpowered two-wheeled, rickshaw-type vehicle used by the Apollo 14 astronauts to carry tools and samples on their geology traverses. Its loaded mass was about 75 kg. The wheels were pneumatic tires, each with a diameter of about 40 cm and a width of about 10 cm. The LRV, or Rover, was a four-wheeled, battery-powered vehicle driven by the astronauts on the Apollo 15, 16, and 17 missions. Its gross mass was 708 kg, more than half of which consisted of the two astronauts and their life support systems. The wheels were flexible and consisted of woven piano wire, with chevron-shaped titanium treads. The wheel diameter was about 82 cm, and the width was about 23 cm.

In addition, a fourth vehicle, the "Lunar Motorcycle," was designed at NASA's Manned Spacecraft Center during the Apollo program to serve as a backup in case the LRV was not ready in time for

Apollo 15. Figure 9.43 shows this two-wheeled, pneumatic-tired vehicle undergoing trafficability testing.

Performance characteristics of the LRV. The performance characteristics of the LRV are summarized in Table 9.13; vehicle dimensions are presented in Fig. 9.44. The payload mass of the LRV was 490 kg, more than twice the mass of the empty vehicle; the bulk of the payload was the two astronauts themselves. Each of the wheels was individually powered by an electric motor coupled to a harmonic-drive gear reduction unit. In case of a motor or gear failure, the wheel involved could be disengaged and allowed to roll free. Wheel-slip on the lunar surface was measured to be between only 2–3%, which allowed for reasonably accurate navigation by dead-reckoning. The maximum speed on a smooth, level surface was about 13 km/hr, but because it was necessary to slow down and turn to avoid small, hummocky craters and other obstacles, the cruise speed was limited to 6–7 km/hr. Hard turns of the LRV at speeds above 5 km/hr resulted in skidding. The maximum negotiable slope was 19°–23°, and such slope values were approached at

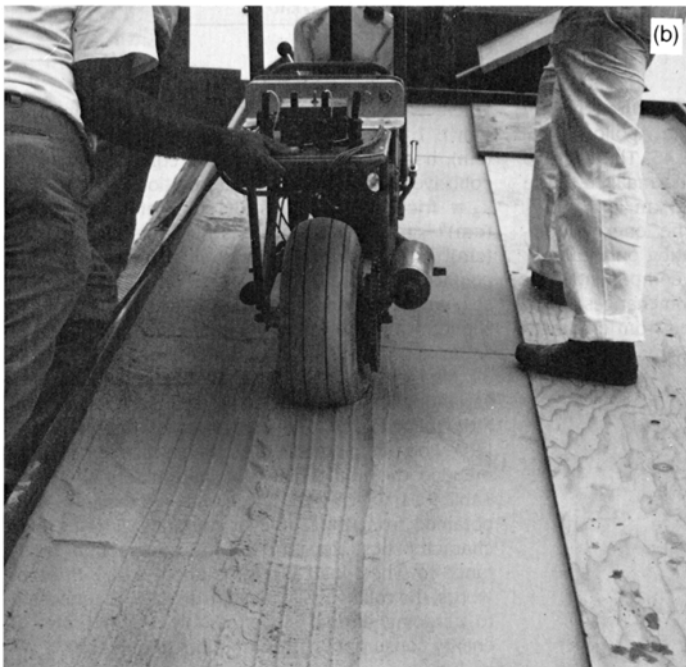
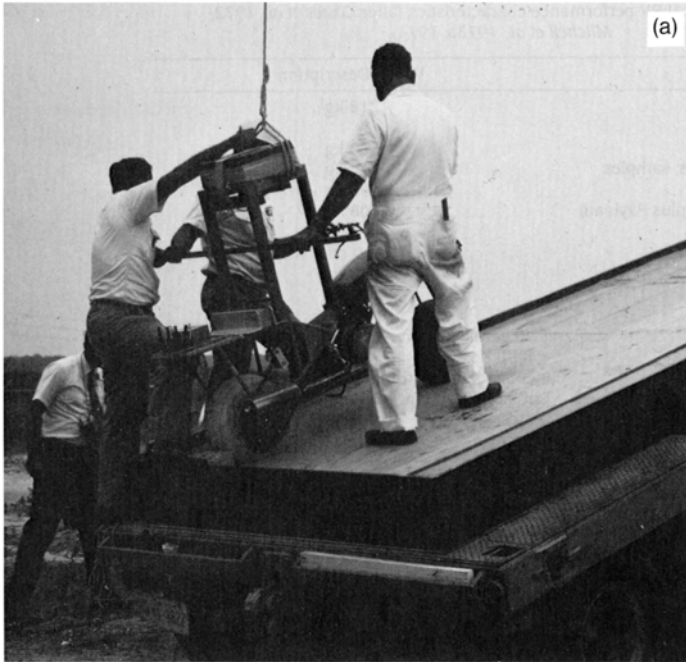


Fig. 9.43. Photographs showing testing of the “Lunar Motorcycle,” a two-wheeled vehicle developed as a backup for the Apollo 15 mission in 1971 in case the Lunar Roving Vehicle (LRV) was not ready in time. **(a)** Placing the vehicle onto an inclined surface; **(b)** operation of the vehicle on the inclined surface, showing the track produced by the pneumatic tires in the sandy material used to simulate the lunar surface. (Photos courtesy of W. D. Carrier III.)

TABLE 9.13. LRV performance characteristics (after Costes *et al.*, 1972; Mitchell *et al.*, 1973a, 1974).

Parameter	Value/Description
Empty Mass	218 kg
Payload Mass	
Two astronauts	363 kg
Experiments, tools, samples	<u>127 kg</u>
	490 kg
Gross Mass (Empty plus Payload)	708 kg
Dimensions	
Overall Length	310 cm
Wheelbase	229 cm
Overall Width	206 cm
Height	114 cm
Power Supply	Two parallel, nonrechargeable silver-zinc batteries (36V)
Drive	Independent electric motor on each wheel
Steering	Double Ackerman: Front and rear independent steering
Minimum Turning Radius	305 cm
Wheels	Woven zinc-coated piano wire; chevron-shaped titanium treads (50% coverage); inner titanium bump stop
Wheel-slip	2 - 3 %
Maximum speed (smooth, level surface)	13 km/hr
Normal Cruise Speed	6 - 7 km/hr
Maximum Slope	19° - 23°
Energy Consumption (smooth mare)	
Vehicle "Mileage"	35 - 56 W-hr/km
Mass "Mileage"	0.050 - 0.080 W-hr/km/kg

the Apollo 16 and 17 sites. The measured energy consumption of the LRV during the Apollo 15, 16, and 17 missions is shown in Fig. 9.45. The average "mileage" was 35-56 W-hr/km or, normalized to the gross mass, about 0.050-0.080 W-hr/km/kg.

Trafficability parameters. The energy consumed by a wheeled vehicle operating on the lunar surface can be divided into three components: soil compaction, roughness, and elevation changes.

Soil compaction can be estimated from empirical equations developed by Bekker (1969)

$$\text{Wheel Sinkage (cm)} \quad z = \left(\frac{W}{Ak} \right)^{\frac{1}{n}}$$

Gross Pull Per Wheel (N)

$$H = (Ac_b + W \tan \phi_b) \left[1 - \frac{K}{sL} \left(1 - e^{-\frac{sL}{K}} \right) \right]$$

Soil Compaction Resistance Per Wheel (N)

$$R_c = \left(\frac{bk}{n+1} \right) z^{n+1}$$

where W = wheel load (N); A = wheel footprint area (cm²); L = wheel chord length of ground contact (cm); b = wheel width of ground contact (cm); k_c = cohesive modulus of soil deformation [N/(cm)ⁿ⁺¹]; k_ϕ = frictional modulus of soil deformation [N/(cm)ⁿ⁺²]; $k = k_c/b + k_\phi$ = soil consistency [N/(cm)ⁿ⁺²]; n = exponent of soil deformation; c_b = coefficient of soil/wheel cohesion (N/cm²); ϕ_b = soil/wheel friction angle (deg); K = coefficient of soil slip (cm); and s = wheel slip (dimensionless).

Based on detailed wheel-soil interaction studies of 34 simulants, Costes *et al.* (1972) concluded that variations in the trafficability soil parameters had little influence on the energy consumption of the LRV. For planning the LRV traverses, they recommended the trafficability soil parameters shown in Table 9.14, which were based on soil mechanics data obtained from the Surveyor missions. For the LRV characteristics, the ratio of soil compaction resistance to wheel load (R_c/W) is about 0.016. In other words, the rolling resistance for the LRV is equivalent to climbing a rigid slope of only 1°. In terms of energy consumption, this amounts to only 0.0073 W-hr/km/kg.

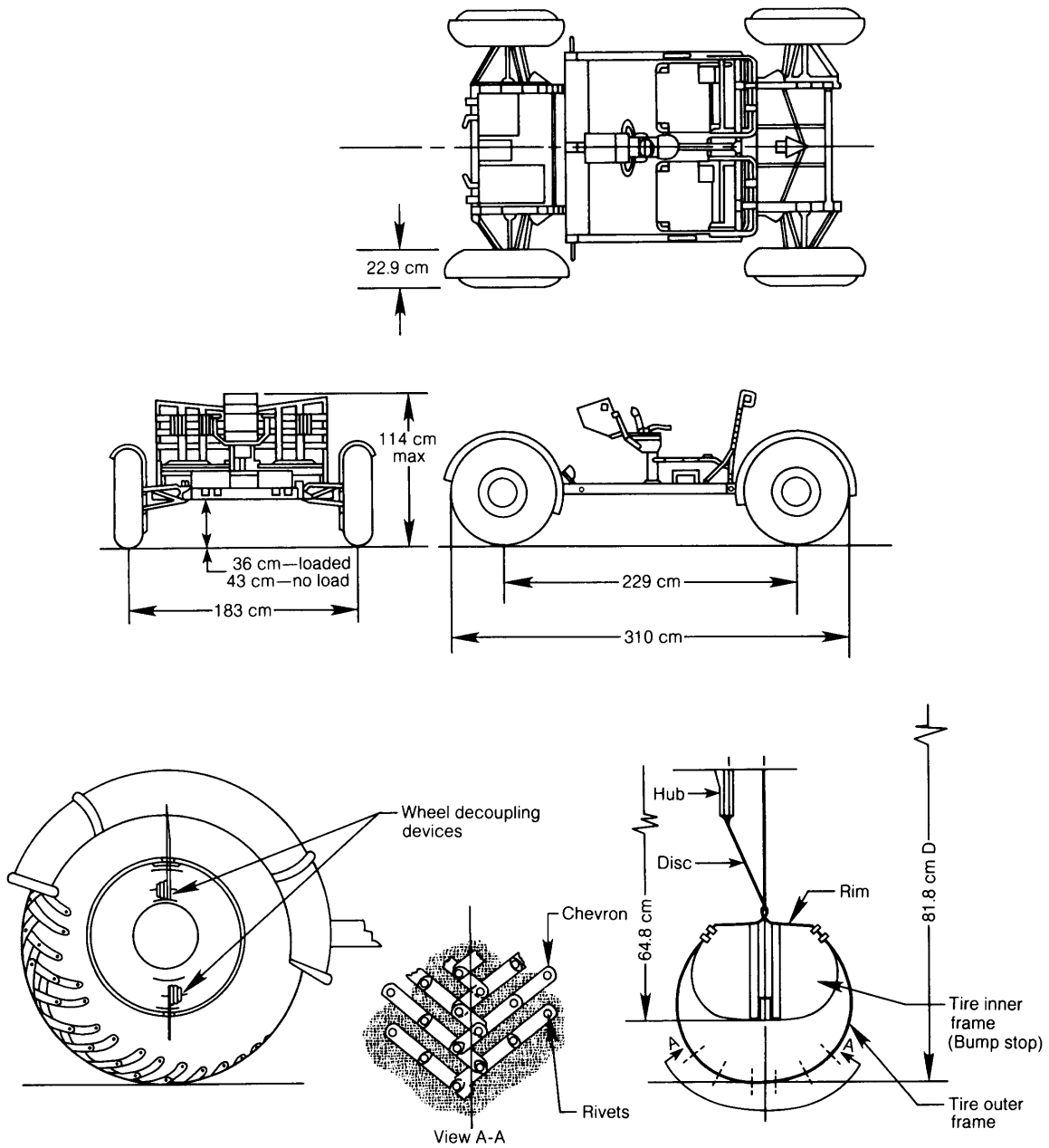


Fig. 9.44. Schematic three-way diagram of the Apollo Lunar Roving Vehicle (LRV) and its dimensions (after Costes *et al.*, 1972). Upper diagrams show entire LRV; lower diagrams show details of wheel and wheel assembly.

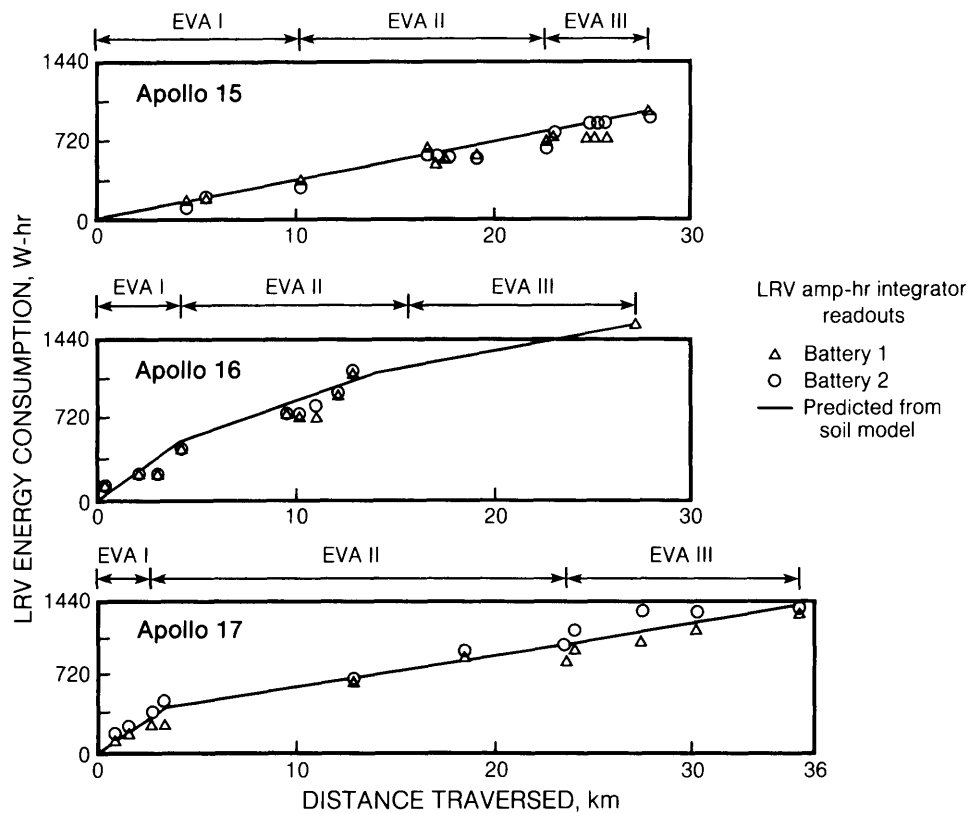


Fig. 9.45. Diagrams of cumulative energy consumption of the Apollo Lunar Roving Vehicle (LRV) as a function of distance traversed during the Apollo 15 (top), Apollo 16 (center), and Apollo 17 (bottom) missions. Durations of each Extravehicular Activity (EVA) are given at the top of each diagram. The agreement between actual measurements of battery levels (points) and the theoretical consumptions predicted from a soil model for each landing site (solid lines) is excellent. Average "mileage" for the LRV was about 35–56 W-hr/km altogether, or about 0.05–0.08 W-hr/kg for each kilogram of mass transported.

Surface roughness is usually described by a power spectral density curve, as shown in Fig. 9.46. For this type of analysis to apply, the wheel-chassis suspension system must be sufficiently "soft" to keep the vehicle on the surface in the low lunar gravity. All four wheels of the LRV can (and did) leave the ground at high speeds. For vehicle trafficability estimates, the energy loss caused by roughness over a given distance is proportional to the speed (*Costes et al.*, 1972). During the LRV traverses on Apollo 15–17, this component of energy consumption amounted to about 0.0027 W-hr/km/kg, which is equivalent to climbing a smooth slope of 0.4° . This value is probably a fairly reasonable estimate for designing future manned vehicles, even for travel in rougher areas, because the speed in such regions will necessarily be reduced. A lower energy consumption

could be attained if improved roads are constructed on the lunar surface; a value of practically zero could be used for a slow-moving unmanned vehicle.

The component of energy consumption lost during elevation change depends on the traverse. Over distances in excess of 100 km, the average lunar slope is typically less than 2° . In the case of the Apollo 15–17 LRV traverses, the net elevation change was zero, because they were all round trips, beginning and ending at the Lunar Module. As shown in Fig. 9.47, the up and down slopes on these traverses were essentially symmetrical.

Altogether, the LRV energy consumption caused by all lunar surface characteristics amounted to only about 0.01 W-hr/km/kg, or about 15% of the total "mileage" (Table 9.13). The remainder is the sum of energy losses in the traction drive system, the energy

TABLE 9.14. Trafficability soil parameters (after *Cosies et al.*, 1972; *Mitchell et al.*, 1973a, 1974).

k_c	Pressure sinkage characteristics under wheel load	0.14 N/cm ^{2*}
k_ϕ		0.82 N/cm ³
n		1
c_b	Cohesion	0.017 N/cm ²
ϕ_b	Soil friction angle	35°
K	Normalizing constant; shear strength and thrust at given wheel slip	1.8 cm*

* Incorrectly converted from English to SI units in *Mitchell et al.* (1973a, 1974).

needed to overcome inertia (acceleration), and the electrical energy consumed by navigation instruments, steering, data display, and the electrical cables themselves.

The steepest slope that a wheeled vehicle can climb is estimated from the Bekker equation above

$$\text{Slope} = \tan^{-1} \left(\frac{H - R_c}{W} \right)$$

Typically, the maximum pull is achieved at a wheel slip of about 20%. For the LRV characteristics, the steepest practicable slope is 19°–23° (*Mitchell et al.*, 1973a, 1974). The slope-climbing performance of a future roving vehicle could be improved by adding variable grousers (cleats) to the wheels. These grousers would be extended when climbing slopes and retracted for cruising on relatively flat areas. The driver would have to be able to operate the grousers without leaving his seat on the vehicle.

Critical conditions: Soft soil. The previous section summarized the average trafficability parameters required to design surface roving vehicles and to plan their missions. However, there are isolated areas of soft soil on the lunar surface that could immobilize a vehicle.

For example, the Apollo 15 LRV encountered loose soil at the ALSEP site and spun its wheels (*Costes et al.*, 1972). Fortunately, the empty LRV weighed only 360 N in the low lunar gravity, and the astronauts simply moved it to another location.

Similarly, when the Lunokhod 2 automated rover approached a crater, the soil became progressively softer, particularly on the inside wall; the most critical location is at the toe of the slope (*Florensky et al.*, 1978). Although the wheels of Lunokhod 2 sank only a few centimeters into the surface over most of its traverse, they sank more than 20 cm in

the vicinity of some craters. In fact, the unmanned vehicle had great difficulty in proceeding in these areas.

Clearly, future lunar surface vehicle design and operation will need to take into account such soft-soil areas and other impediments. For adverse conditions, a more flexible (i.e., variably-g geared) vehicle or multiple vehicles may be needed. There is an old rule for terrestrial four-wheel-drive vehicles that is equally applicable to the Moon: Use two-wheel drive until you get stuck, then use four-wheel drive to get unstuck. The corollary to this rule is that if you use four-wheel drive continuously, you will eventually get very stuck. That is when a winch and another vehicle come in handy.

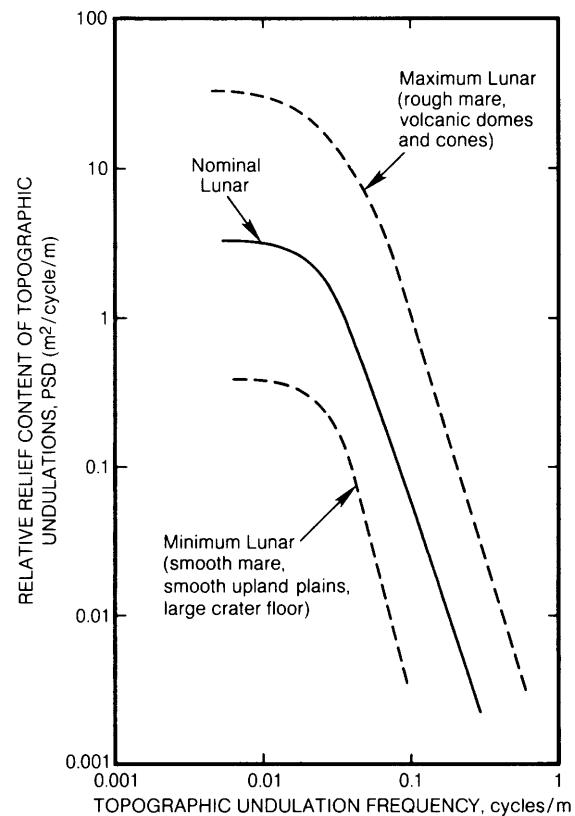


Fig. 9.46. Diagram of lunar surface roughness, presented in terms of a theoretical power spectral density of surface relief (vertical axis) and the topographic surface undulations (wave frequency) (horizontal axis) (after *Pike*, 1968; *Hutton and Evensen*, 1972). The theoretical “nominal lunar” curve (solid curve) falls between the extreme values (dashed curves) for the roughest and smoothest observed lunar areas.

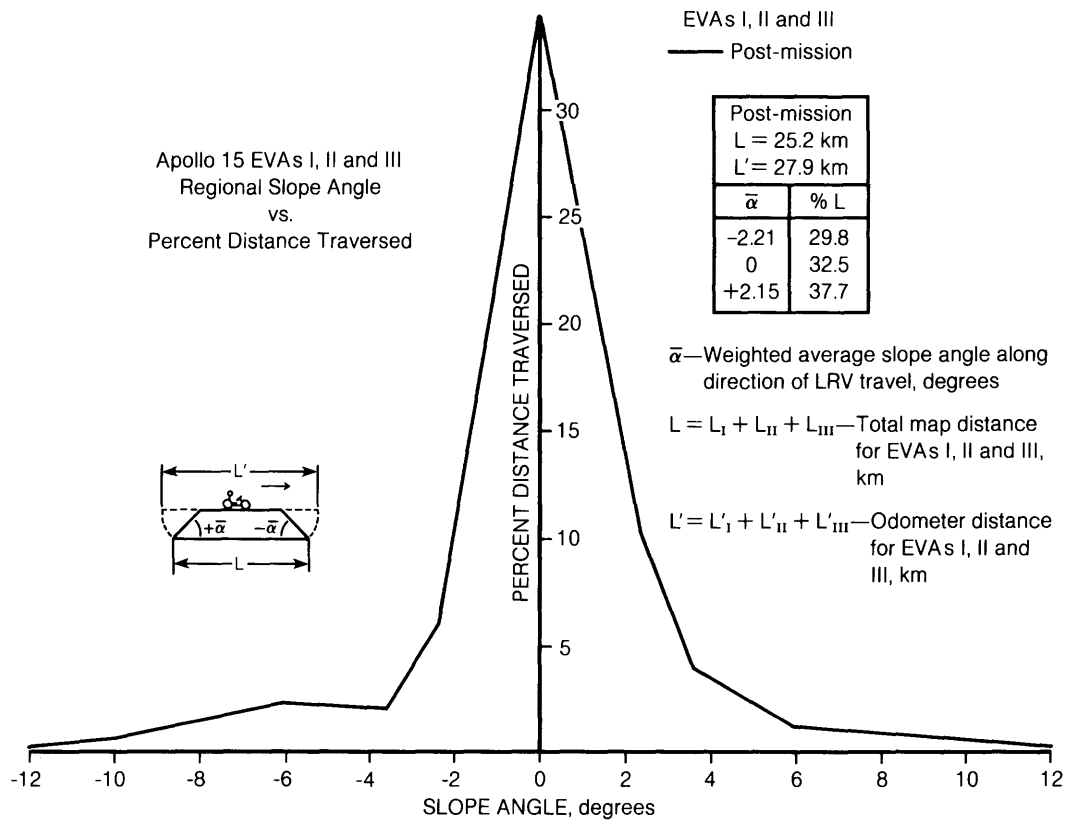


Fig. 9.47. Distribution of observed slope angles on the lunar surface, using data obtained from the three Apollo 15 Extravehicular Activities (EVAs) employing the Lunar Roving Vehicle (LRV) (after Costes *et al.*, 1972). The slopes encountered on this mission were typically <2°. All EVA traverses began and ended at the same point, the Lunar Module.

9.2. ELECTRICAL AND ELECTROMAGNETIC PROPERTIES

The electrical and electromagnetic properties of lunar samples describe how such materials respond to electrical current flow and how electromagnetic energy is diffused and propagated within them.

The bulk electromagnetic properties of the Moon have been determined to some extent by Earth-based radar scattering and by orbital measurements made during the Apollo Program and other missions. Interaction between the magnetic fields of the solar wind and the Moon have been used to obtain a profile of lunar electrical conductivity with depth from low-frequency electromagnetic induction (Sonett, 1982; Hood *et al.*, 1982a,b). This electrical conductivity profile has, in turn, been transformed into a profile of temperature vs. depth for the lunar interior (Hood, 1986), using laboratory studies of

electrical conductivity as a function of temperature (Schuerer *et al.*, 1974; Duba *et al.*, 1976; Huebner *et al.*, 1979).

Higher-frequency electromagnetic radar and radiometry measurements of the Moon have been made from the Earth (DeWitt and Stodola, 1949; Evans and Pettengill, 1963; Keihm and Langseth, 1975a,b; Schloerb *et al.*, 1976; Gary and Keihm, 1978; Pettengill, 1978; Thompson, 1979; Simpson and Tyler, 1982), from lunar orbit (Brown, 1972; Tyler and Howard, 1973; Elachi *et al.*, 1976; Peebles *et al.*, 1978; Sharpton and Head, 1982), and on the Moon's surface itself (Muhleman *et al.*, 1969; Strangway *et al.*, 1975; Kroupenio *et al.*, 1975). These experiments have been used to map topographic and subsurface stratigraphic features on the lunar surface to depths of a few meters.

Terrestrial applications of impulse ground-penetrating radar indicate that this technique would be ideal for subsurface profiling of the Moon to

depths of more than 100 m (Olhoeft, 1979, 1984; Wright *et al.*, 1984; Schaber *et al.*, 1986). The depth of investigation would not be limited by material intrinsic loss properties, but by the electromagnetic scattering, which would depend on the scale of heterogeneities in the subsurface.

The electrical properties of the Moon's surface materials are those of silicates characterized by extremely low loss and low electrical conductivity. In the total absence of water, the DC electrical conductivity ranges from 10^{-14} mho/m for lunar soils to 10^{-9} mho/m for lunar rocks at 300 K in darkness. Upon irradiation with sunlight, there is a $>10^6$ increase in electrical conductivity in both lunar soils and rocks. The relative dielectric permittivity for lunar materials is approximately

$$k = 1.9\rho \quad (\text{dimensionless})$$

where ρ = bulk density in g/cm^3 . The relative dielectric permittivity is dominantly controlled by bulk density and is independent of chemical or mineralogical composition, frequency variations above 1 MHz, and temperature variations within the range of lunar surface temperatures.

The high frequency electromagnetic loss is given by

$$\tan \delta = 10^{[0.038 (\%TiO_2 + \%FeO) + 0.312\rho - 3.260]}$$

where ρ = density and $\tan \delta$ = *loss tangent* (ratio of the imaginary to the real part of the complex dielectric permittivity). The loss is strongly dependent upon density and the (TiO₂ + FeO) content, and less dependent on frequency and temperature. Electromagnetic losses in the lunar soils have nearly negligible frequency and temperature dependence in comparison to the behavior of lunar rocks.

The extremely low electrical conductivities and low loss tangents indicate that lunar materials are very transparent to electromagnetic energy. For example, radio transmissions should readily penetrate through the lunar soils to depths of about 10 m. As a result, radio communications on the lunar surface need not be by direct line-of-sight, but may penetrate low hills; this situation partially compensates on the Moon for the inability to skip signals off an ionosphere for long distances as is done on Earth. The low conductivity and low loss are also responsible for the fact that lunar materials are readily chargeable and will remain electrically charged for long periods of time. The large photo-induced change in electrical conductivity at lunar sunrise and sunset can charge surface soil particles to the point that they will levitate and move (Alvarez, 1977a; De and Criswell, 1977; Criswell and De, 1977;

Rhee *et al.*, 1977; McDonnell, 1979; Ip, 1986). Such charged soils and mobile particles could readily coat surfaces and be hazardous to visibility and equipment operation during lunar night.

9.2.1. Electrical Conductivity

Electrical conductivity is a measure of how easily electrical current flows through a material, i.e., how easily electrical charge may be transported through it. High electrical conductivity means that the material easily carries electrical current and does not readily remain electrically charged. Low electrical conductivity means that the material does not easily transport charge and tends to remain electrically charged. The electrical conductivity of lunar materials at low frequencies (below 1 Hz) is essentially the same as of DC (0 Hz) conductivity, is extremely low (Table 9.15), and is dominantly controlled by temperature. A soil from the Apollo 15 site (sample 15301,38) exhibits a temperature dependence of conductivity (Fig. 9.48) of the form

$$\text{DC conductivity} = 6 \times 10^{-18} e^{0.0237T} \text{ mho/m}$$

where T = temperature (Kelvin) (Olhoeft *et al.*, 1974a). This type of temperature dependence is characteristic of amorphous materials and is typical of the heavily radiation-damaged lunar soil particles. The low-frequency electrical conductivity of lunar rocks is typical of terrestrial silicates in the total absence of water. The temperature dependence of one Apollo 16 rock (sample 65015,6) (Olhoeft *et al.*, 1973a) was similar in form to that of soil

$$\text{DC conductivity} = 3 \times 10^{-14} e^{0.0230T} \text{ mho/m}$$

However, the temperature dependence of the electrical conductivity measured on the remaining lunar rocks (Fig. 9.48) was found to be given by

$$\text{DC conductivity} = \sigma_0 e^{-E_0/kT} + \sigma_1 e^{-E_1/kT} \text{ mho/m}$$

where k = Boltzmann's constant = 8.6176×10^{-5} eV/K and T = temperature (Kelvin), and E_0 and E_1 are activation energies (Table 9.15). Because these lunar materials have very low conductivities, dielectric relaxation effects and displacement currents dominate at very low frequencies. Olhoeft *et al.* (1973a) and Schwerer *et al.* (1974) provide the best reviews of electrical conductivity of lunar rocks.

The electrical conductivities measured on lunar samples (Schwerer *et al.*, 1972, 1973, 1974; Olhoeft *et al.*, 1973a,b, 1974b) and related materials (Housley and Morin, 1972; Piwinski and Duba, 1975; Duba *et al.*, 1976, 1979; Huebner *et al.*, 1978, 1979; Schock *et al.*, 1980) are key parameters in using the data

TABLE 9.15. DC electrical conductivity of lunar rocks.

Lunar Sample	σ_0^* mho/m	E_0^\dagger eV	σ_1 mho/m	E_1 eV
10048	3.5	0.896	2.66×10^{-3}	0.559
12002,85	13	1.09	1.8×10^{-4}	0.48
15058	134	1.374	2.78×10^{-3}	0.593
15418	137	1.509	9.84×10^{-2}	0.971
15555	36.8	1.040	1.27×10^{-2}	0.604
68415	1.27×10^8	2.640	0	0
68815	14.2	1.366	0	0

* Conductivity.

† Activation energy.

Data for sample 12002 are from *Olhoeft et al. (1973)*; the rest are from *Schwerer et al. (1974)*.

obtained by deep electromagnetic induction sounding of the Moon to derive a *selenotherm*, i.e., a temperature profile within the Moon (*Dyal and Parkin, 1971; Schubert et al., 1973; Sonett and Duba, 1975; Dyal et al., 1976; Wiskerchen and Sonett, 1977; Dyal and Daily, 1979; Vanyan et al., 1979; Hobbs, 1980; Hood et al., 1982a,b. Sonett (1982) and Hood*

(1986) provide the best reviews of the problems of interpreting electrical conductivity profiles from the electromagnetic sounding data in order to further infer a selenotherm. Figure 9.49 illustrates a typical set of such interpretations from *Hood (1986)*.

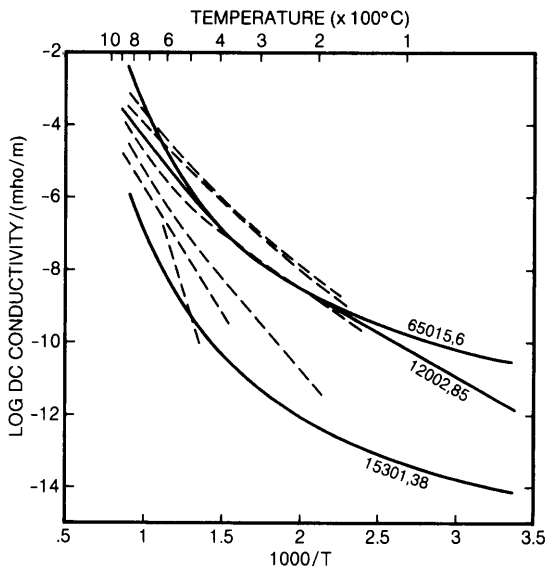


Fig. 9.48. Electrical conductivity of lunar samples. DC conductivity (vertical axis) is plotted as a function of inverse temperature in kelvins (bottom horizontal axis) and temperature (top horizontal axis), using the equations given in the text. In general, conductivity increases with increasing temperature for both lunar soil and rock samples. Dashed curves (from *Schwerer et al., 1974*) are for samples 10048, 15058, 15418, 15555, 68415, and 68815. Solid curves (*Olhoeft et al., 1973a*) give data for two soil samples (12002,85 and 15301,38) and one rock (65015,6).

9.2.2. Photoconductivity

Alvarez (1975, 1977b) measured the effects of ultraviolet (UV), visible, and infrared (IR) irradiation on the electrical conductivity of lunar samples, including lunar soils (Figs. 9.50 and 9.51). Relative to their surface electrical conductivity in darkness, the soils show about a 10^1 increase in conductivity in the IR and a 10^6 increase in the UV. The latter increase is comparable to that produced by an 800°C increase in temperature. These large changes in conductivity with irradiation can produce large movements of electrical charge across the solar terminator on the lunar surface.

9.2.3. Electrostatic Charging and Dust Migration

A large number of observations of *lunar transient events*, especially unexplained glows and obscurations, have been noted over two centuries of groundbased observations, continuing up to the present (*Cameron, 1974, 1978; see section 11.4.2*). These changes in lunar brightness may have rise times of <1 sec and range in color from reddish to bluish.

More recent reports of such phenomena include observations by the Apollo astronauts (*McCoy and Criswell, 1974a; McCoy, 1976a,b*). Although these observations have never been satisfactorily explained (for discussions, see *Cameron, 1974, 1978* and section 11.4.2), electrical phenomena in the lunar surface layers are one possible mechanism.

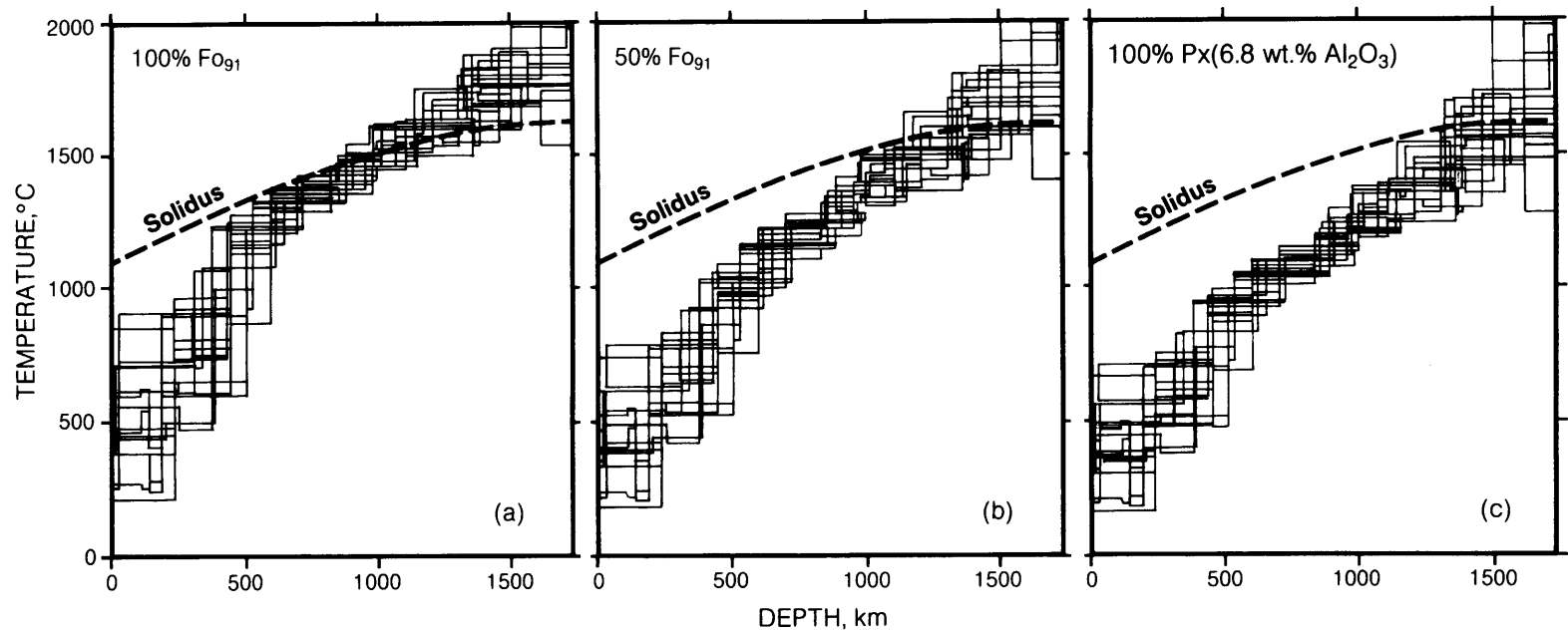


Fig. 9.49. Calculated temperature-depth profiles for the lunar interior, derived by combining laboratory measurements (conductivity vs. temperature) and spacecraft measurements of perturbations of the magnetic field around the Moon (conductivity vs. depth) (after Hood *et al.*, 1982a,b; Hood, 1986). Data are shown for temperature (vertical axis) as a function of depth (horizontal axis) for three assumed lunar materials: (1) 100% olivine (Fo_{91}) (left), (2) 50% olivine (Fo_{91}) plus 50% pyroxene (center); and (3) 100% pyroxene (right). For all three materials, the temperature-depth curve reaches the solidus (or lowest partial melting temperature) (dashed line) at a depth of 1000–1500 km, implying that a small portion of the innermost Moon could be in a partly molten state.

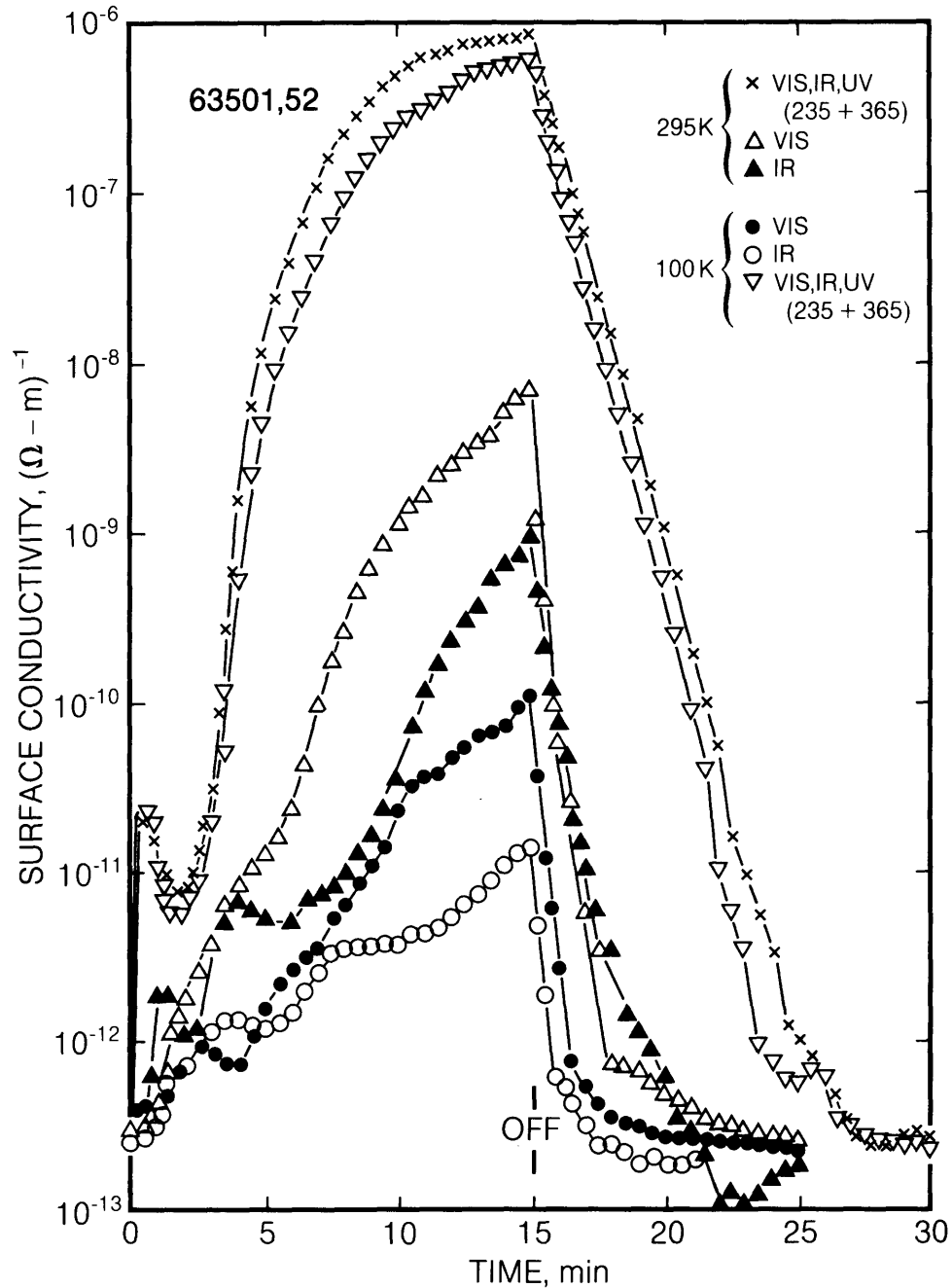


Fig. 9.50. Changes in surface electrical conductivity (vertical axis) of lunar soil 63501,52 produced as the result of irradiation by ultraviolet (UV; the sum of 235 nm + 365 nm wavelength irradiation), visible (VIS), and infrared (IR) radiation (after Alvarez, 1977b). Conductivity rises rapidly at the start of irradiation (time = 0 on horizontal axis), then drops rapidly when the irradiation ceases ("OFF"). The effect is greater at higher temperatures (295 K; upper curves) than at lower ones (100 K; lower curves). Note that the two highest curves were obtained with all three sources on (VIS, IR, UV).

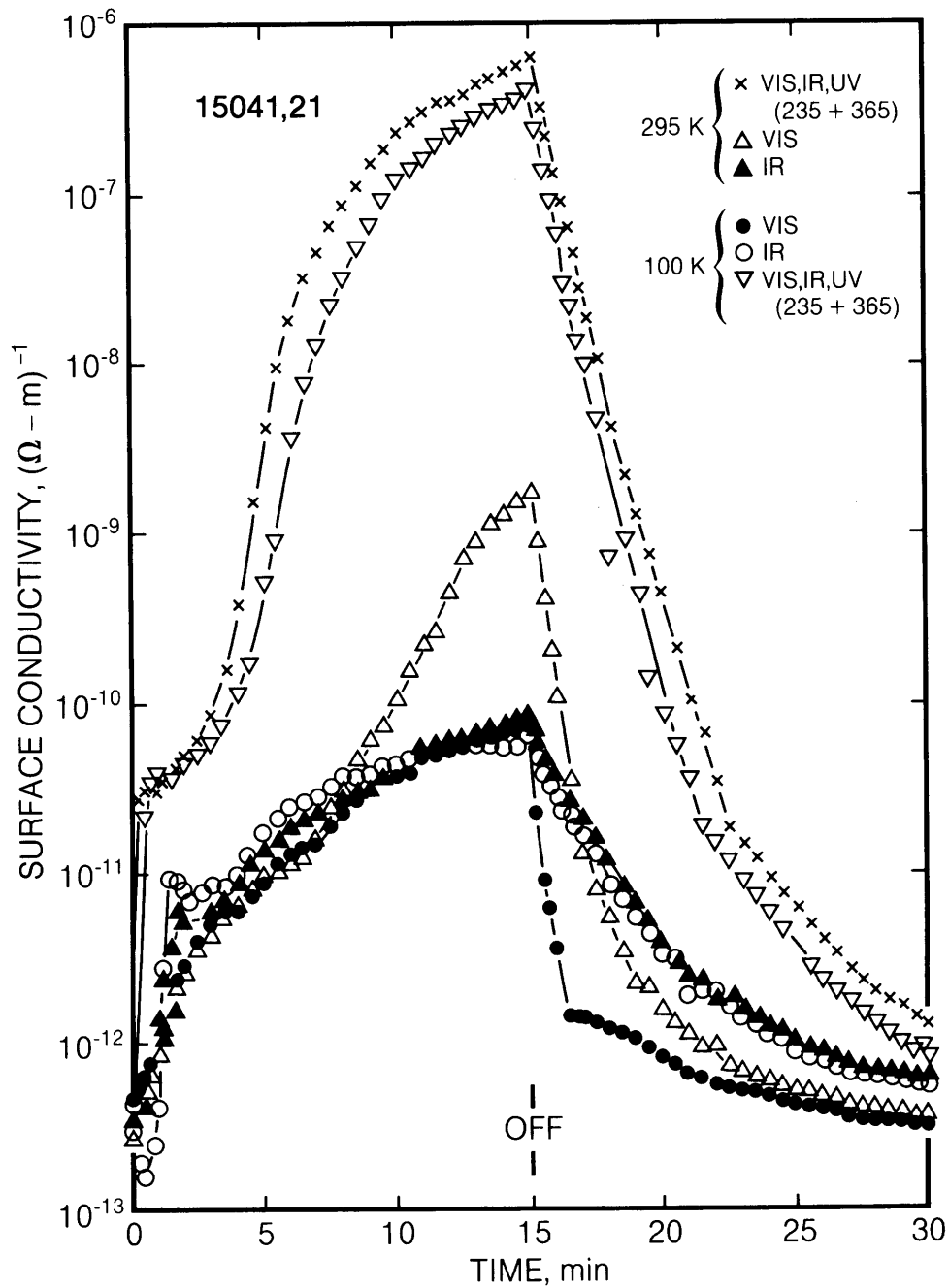


Fig. 9.51. Changes in surface electrical conductivity (vertical axis) of lunar soil 15041,21 produced as the result of irradiation by ultraviolet (UV; the sum of 235 nm + 365 nm wavelength irradiation), visible (VIS), and infrared (IR) radiation (after Alvarez, 1977b). Conductivity rises rapidly at the start of irradiation (time = 0 on horizontal axis), then drops rapidly when the irradiation ceases ("OFF"). The effect is greater at higher temperatures (295 K; upper curves) than at lower ones (100 K; lower curves). As in Fig. 9.50, the two highest curves were obtained with all three sources on (VIS, IR, UV).

The large electrical conductivity change with visible and UV irradiation (discussed above), combined with the very low electrical conductivity and dielectric losses of lunar materials, can produce an extremely efficient electrostatic charging mechanism between opposite sides of the lunar terminator. Across this moving boundary, charging of lunar soil particles could be sufficient to levitate them above the surface, producing a “dust storm” of particles that would follow the solar terminator around the Moon. *McDonnell and Flavill* (1977) and *McDonnell* (1979) have calculated that such electrostatic levitation would extend to 10 m above the lunar surface. However, if the dust could reach higher altitudes, such a phenomenon could explain some observations of the Apollo astronauts, who reported and drew pictures of “streamers” and bands of corona/zodiacal light (the results of light scattering by dust?) extending several kilometers above the lunar surface while approaching orbital sunrise (*McCoy*, 1976a,b).

The Apollo 17 Lunar Ejecta and Meteorites (LEAM) experiment (*Berg et al.*, 1973) found increased particle counts during the passage of the terminator over the instrument (*Berg et al.*, 1974), and the experimenters noted that “. . . all of the events recorded by the sensors during the terminator passages are essentially surface microparticles carrying a high electrostatic charge.” Other experimenters observed that “the particle event rate increases whenever the terminator passes over the instrument. This increase starts some 40 hours before sunrise and ends about 30 hours after it” (*Rhee et al.*, 1977). Such charged, levitating soil particles, moving across the lunar surface, could create visibility problems during passage through the terminator, and the particles would also readily adhere to surfaces, creating coatings. Because the electrical conductivity is lowest during lunar night, the soil will have the highest electrostatic charge-ability at night. Nighttime surface activities that disturb the lunar soil could generate dust that would thickly coat exposed surfaces. Upon lunar sunrise, the resultant photo-induced increase in electrical conductivity would cause most of the coatings to slough off, leaving only a thin residual coating behind.

During lunar night, the low conductivity of the soil will also create significant electrical charging hazards between mobile objects on the lunar surface, producing the well-known wintertime “spark” electrical discharge when the charged objects meet. The possible presence of a stabilizing lunar duricrust (*Greenwood et al.*, 1971; *Heiken and Carrier*, 1971; *Carrier and Heiken*, 1972) (see section 9.1.4) would tend to reduce the levitation

effects, but not the charge accumulations and discharge hazard. More detailed discussions of these effects are found in *Criswell* (1972, 1973, 1974), *Fenner et al.* (1973), *Gold and Williams* (1973, 1974), *Arrhenius* (1974), *Alvarez* (1974c, 1975, 1977a), *Cameron* (1974, 1978), *Freeman and Ibrahim* (1974), *Gold* (1974), *Goldstein* (1974), *McCoy and Criswell* (1974b), *Williams* (1974), *Rennilson and Criswell* (1974), *Reasoner* (1975), *Criswell and De* (1977), and *De and Criswell* (1977). Similar effects have also been suggested to exist on the surface of Mercury (*Ip*, 1986).

Another hypothesis to explain lunar transient phenomena is that they are associated with electrodynamic effects generated during rock fracturing (*Zito*, 1989). For other hypotheses, see section 11.4.2.

9.2.4. Dielectric Permittivity

Dielectric permittivity is a measure of the ability of a material to keep electrical charges physically separated by a distance, a process called *electrical polarization*. The *relative dielectric permittivity* is the ratio of the permittivity of a material to the permittivity of vacuum. The speed of electromagnetic propagation in a material is the speed of light in vacuum divided by the square root of the permittivity. Available measurements on lunar sample dielectric properties as a function of bulk density, frequency, and $\text{TiO}_2 + \text{FeO}$ content are summarized in Table A9.16. The same data are plotted in Figs. 9.52–9.55 in terms of relative dielectric permittivity and loss tangent vs. density. Data are presented for all lunar sample types in Table A9.16 and Fig. 9.52, for soils only (Fig. 9.53), for measurements at 450 MHz only (Fig. 9.54), and for the Apollo 15–17 samples only (Fig. 9.55). In Figs. 9.56–9.59 the data are plotted as a function of ($\text{TiO}_2 + \text{FeO}$) content for the same data groups.

In each of the permittivity plots in Figs. 9.52–9.59, the solid curve represents the rigorous Bruggeman-Hanai-Sen (BHS) mixing formula (*Sen et al.*, 1981), given as

$$\frac{([9.8 + i0.1] - k)}{([9.8 + i0.1] - 1)} (k)^{-1/3} = \rho/3.5$$

where ρ = bulk density in g/cm^3 ; k = the complex relative dielectric permittivity at the density, ρ ; i = square root of -1 ; and $[9.8 + i0.1]$ is the complex relative dielectric permittivity of a hypothetical zero-porosity lunar material with $\rho = 3.5 \text{ g/cm}^3$. The dashed curve in the same plot is the simpler formula proposed by *Olhoeft and Strangway* (1975), after regression analysis on the entire larger dataset of Table A9.16

$$k = 1.919\rho \text{ for all samples}$$

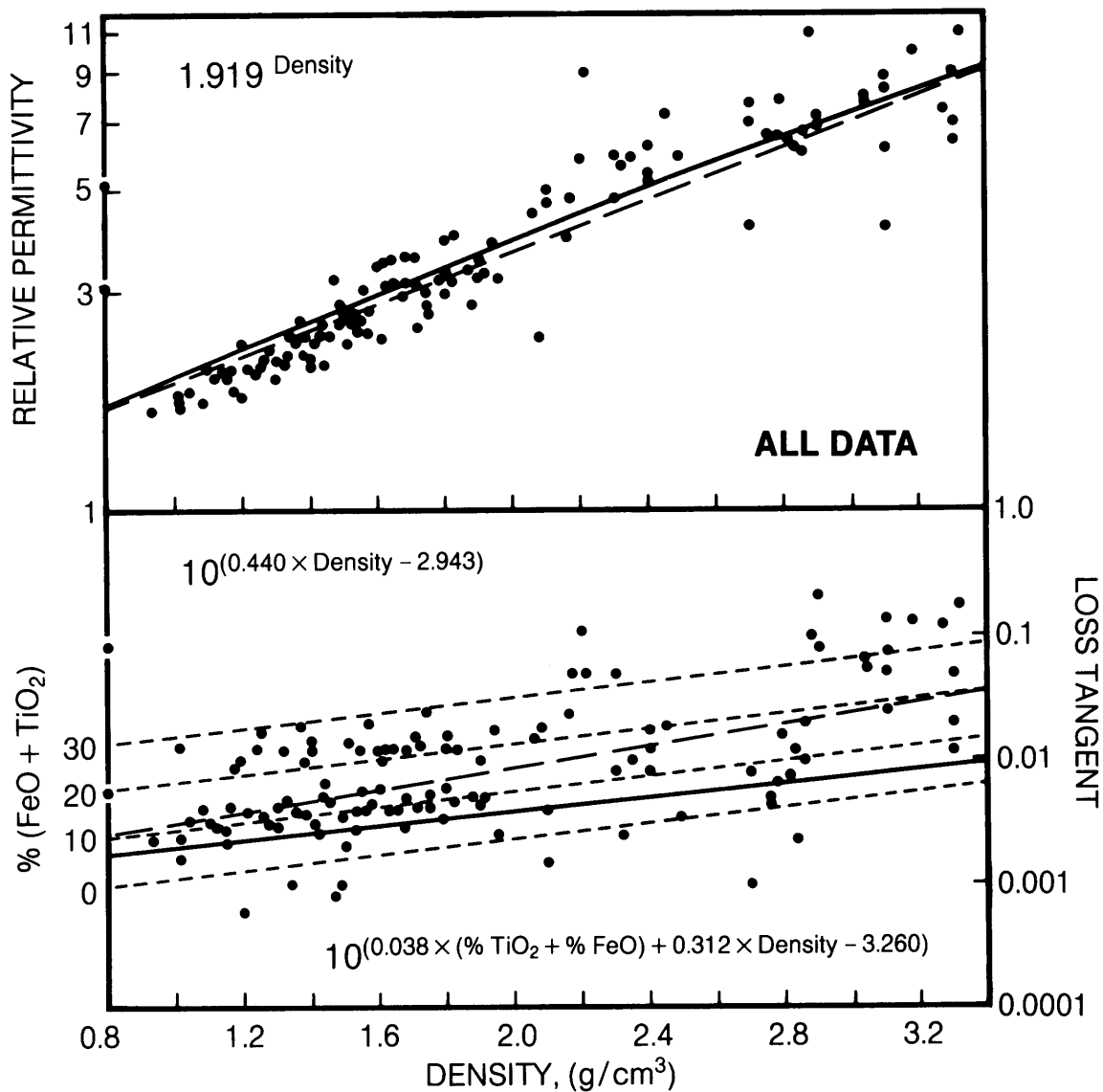


Fig. 9.52. Relative dielectric permittivity (upper vertical axis) and loss tangent (lower right vertical axis) for lunar materials as functions of bulk density (horizontal axis) and %($\text{TiO}_2 + \text{FeO}$). Data points represent all samples from Table A9.16. Both permittivity and loss tangent increase with increasing density. The permittivity plot (upper) shows two theoretical fits to the data points: the Bruggeman-Hanai-Sen (BHS) mixing formula (*Sen et al.*, 1981) (solid line; see text for details) and a least-squares power-law fit (*Olhoeft and Strangway*, 1975) (dashed line). The loss tangent plot (lower) shows three theoretical fits to the data: the equivalent BHS formula (solid line), the two-dimensional regression to the power-law formula (given in upper left) (dashed line), and three-dimensional regression (light dashed lines) of variance as a function of density and selected values of %($\text{TiO}_2 + \text{FeO}$) (light dashed curves for 0%, 10%, 20%, and 30%).

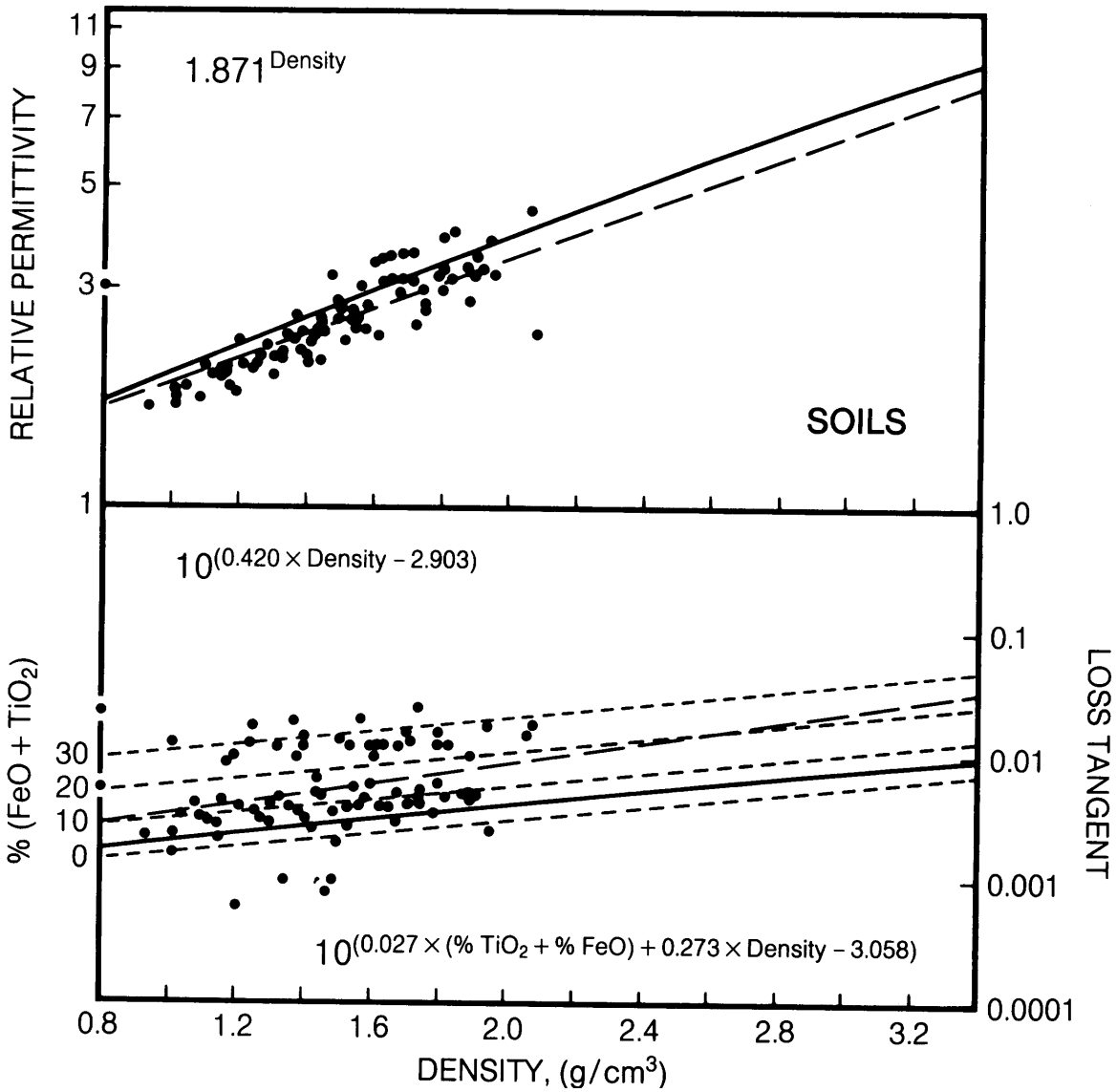


Fig. 9.53. Relative dielectric permittivity (upper vertical axis) and loss tangent (lower right vertical axis) for lunar materials as functions of bulk density (horizontal axis) and %TiO₂ + FeO). In contrast to Fig. 9.52, data points represent only soil samples from Table A9.16. Both permittivity and loss tangent increase with increasing density. Theoretical fitted curves and their derivation are the same as described in Fig. 9.52.

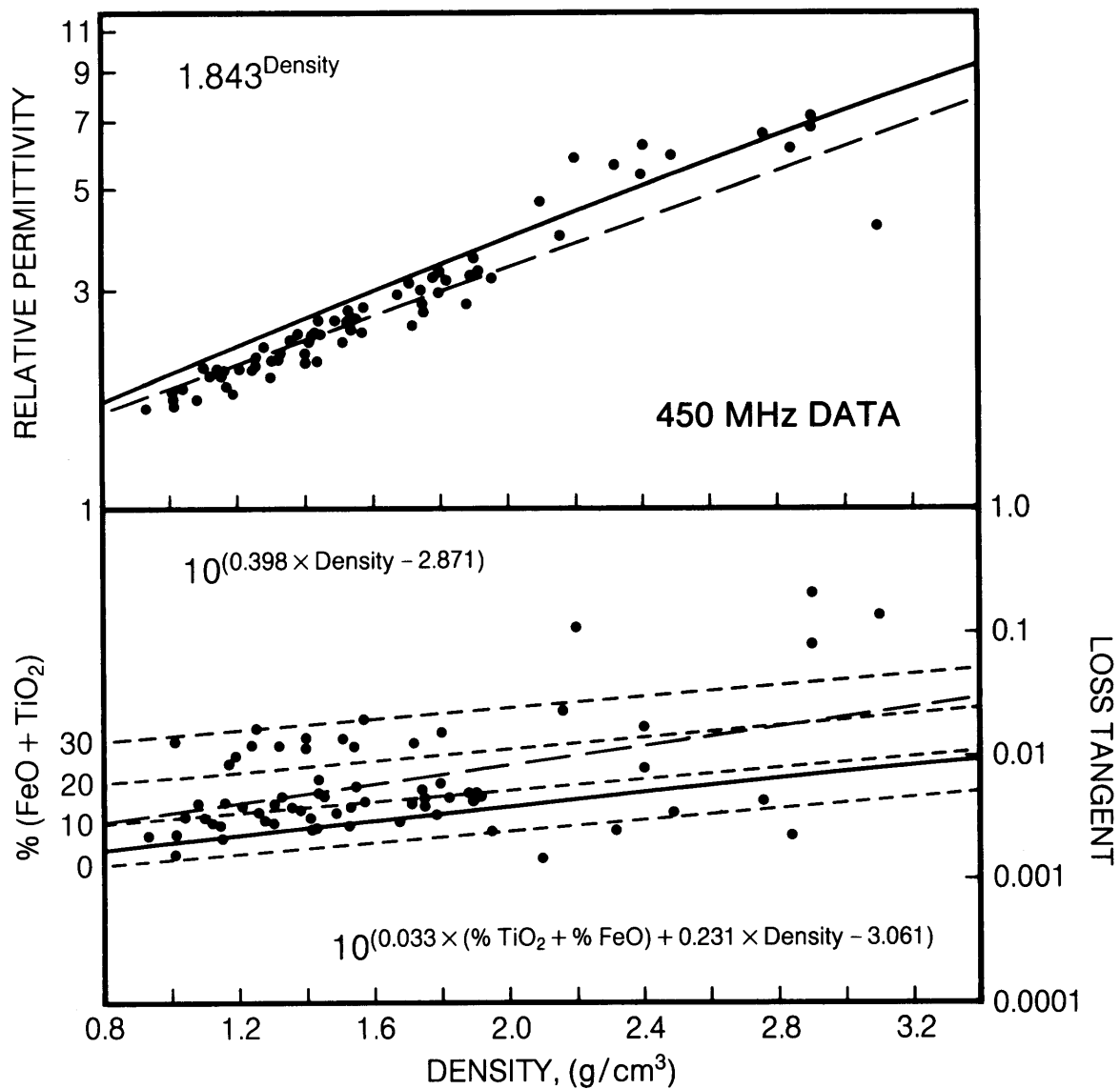


Fig. 9.54. Relative dielectric permittivity (upper vertical axis) and loss tangent (lower right vertical axis) for lunar materials as functions of bulk density (horizontal axis) and %TiO₂ + FeO). In contrast to Fig. 9.52, data points represent only measurements obtained at 450 MHz (from Table 19.16). Both permittivity and loss tangent increase with increasing density. Theoretical fitted curves and their derivation are the same as described in Fig. 9.52.

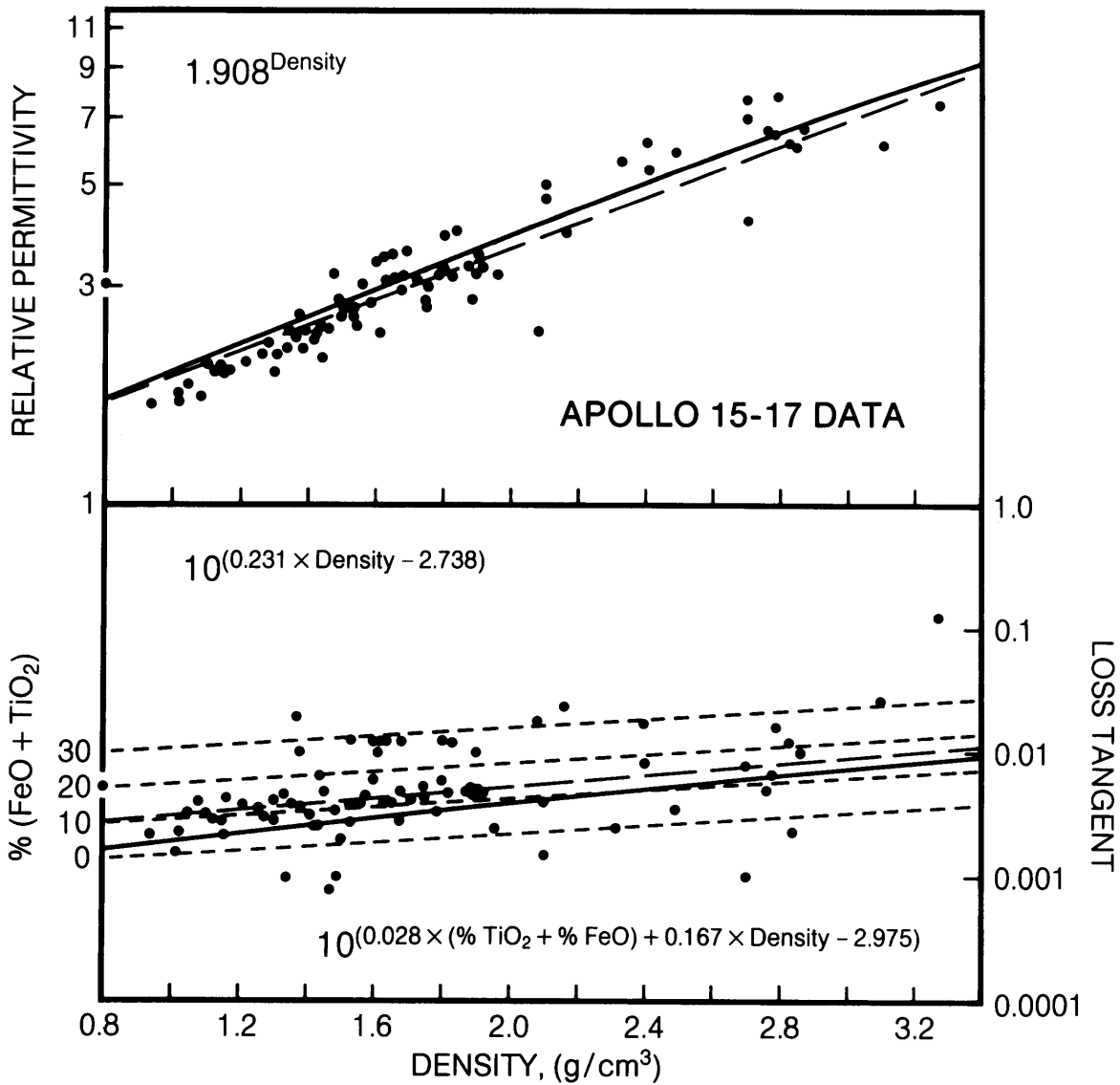


Fig. 9.55. Relative dielectric permittivity (upper vertical axis) and loss tangent (lower right vertical axis) for lunar materials as functions of bulk density (horizontal axis) and % (TiO₂ + FeO). In contrast to Fig. 9.52, data points represent only soil samples from the Apollo 15-17 missions (from Table A9.16). Both permittivity and loss tangent increase with increasing density. Theoretical fitted curves and their derivation are the same as described in Fig. 9.52.

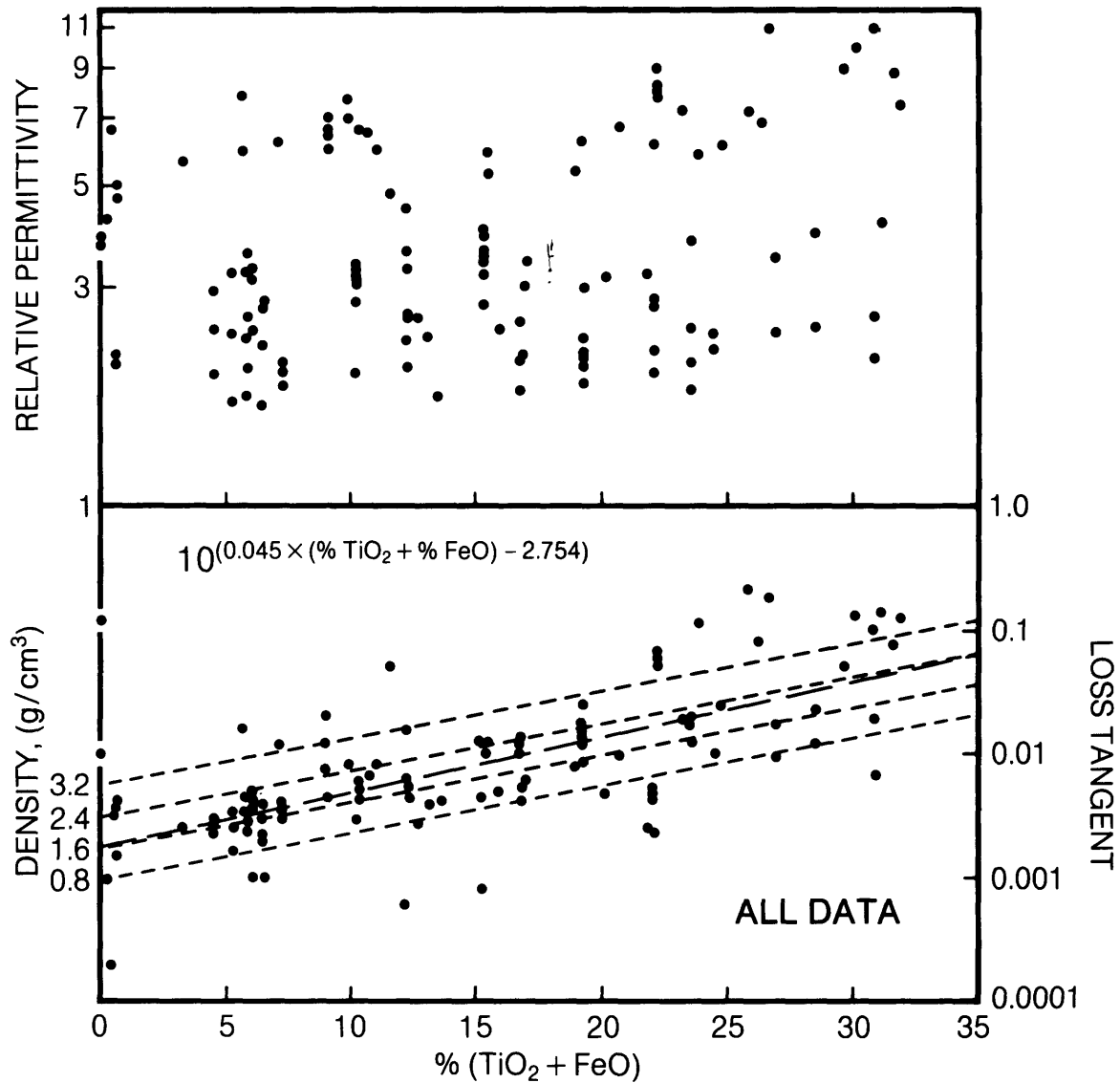


Fig. 9.56. Relative dielectric permittivity (upper vertical axis) and loss tangent (lower right vertical axis) of lunar materials as functions of $\%(\text{TiO}_2 + \text{FeO})$ (horizontal axis) and bulk density. Data points represent all samples from Table 19.16. The relative permittivity (upper) is apparently independent of chemistry, but the loss tangent increases with increasing $\%(\text{TiO}_2 + \text{FeO})$. Two theoretical fits to the loss-tangent data (lower) are shown: the two-dimensional least-squares power-law fit (*Olhoeft and Strangway, 1975*) (dashed line) and the same three-dimensional regression as in Fig. 9.52 (light dashed lines), plotted for four specific density values (0.8, 1.6, 2.4, and 3.2 g/cm^3).

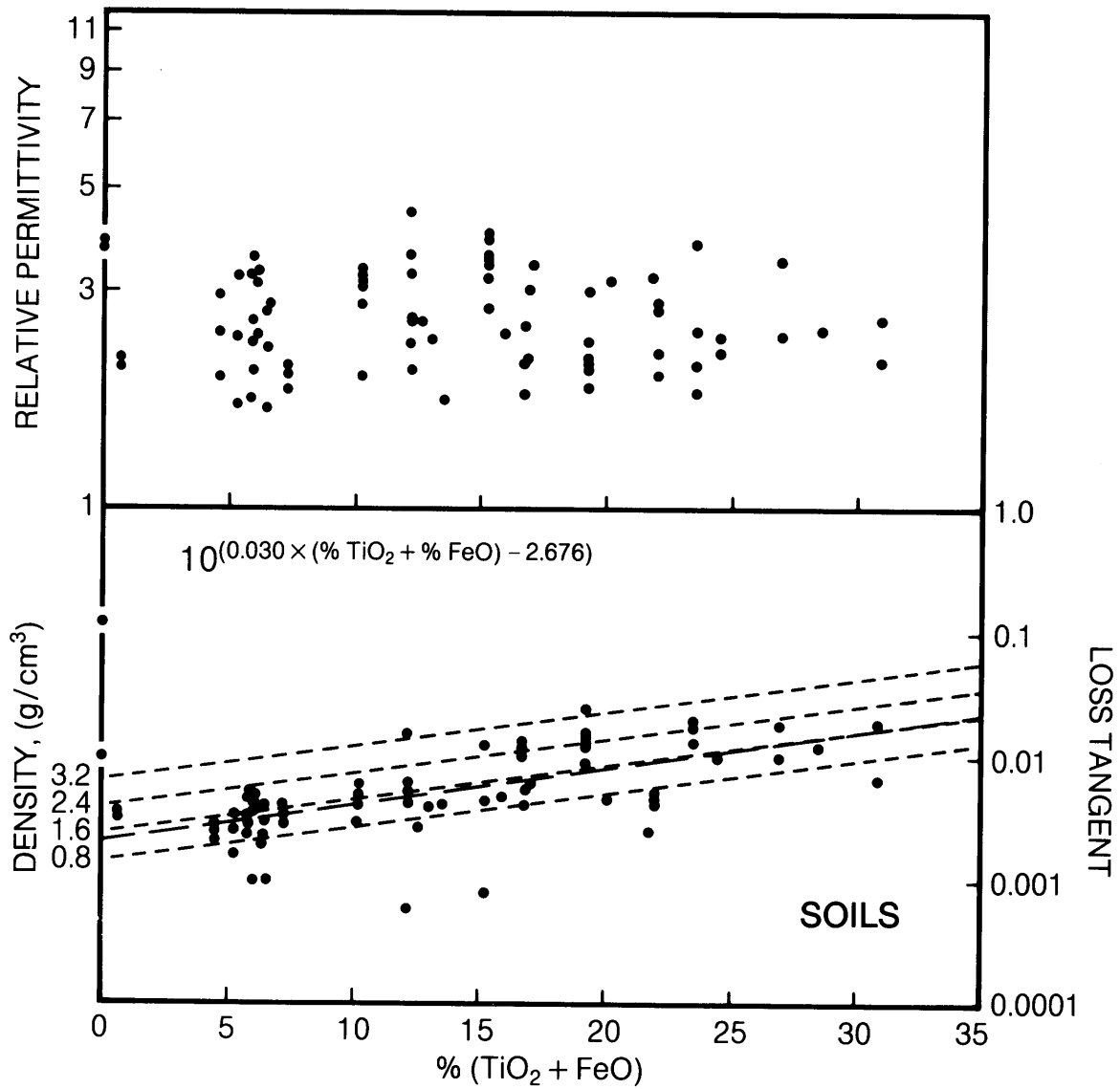


Fig. 9.57. Relative dielectric permittivity (upper vertical axis) and loss tangent (lower right vertical axis) for lunar materials as functions of $\%(\text{TiO}_2 + \text{FeO})$ (horizontal axis) and bulk density. In contrast to Fig. 9.56, data points represent only soil samples from Table A9.16. The relative permittivity (upper) is apparently independent of chemistry, but the loss tangent increases with increasing $\%(\text{TiO}_2 + \text{FeO})$. Theoretical fitted curves and their derivation are the same as described in Fig. 9.56.

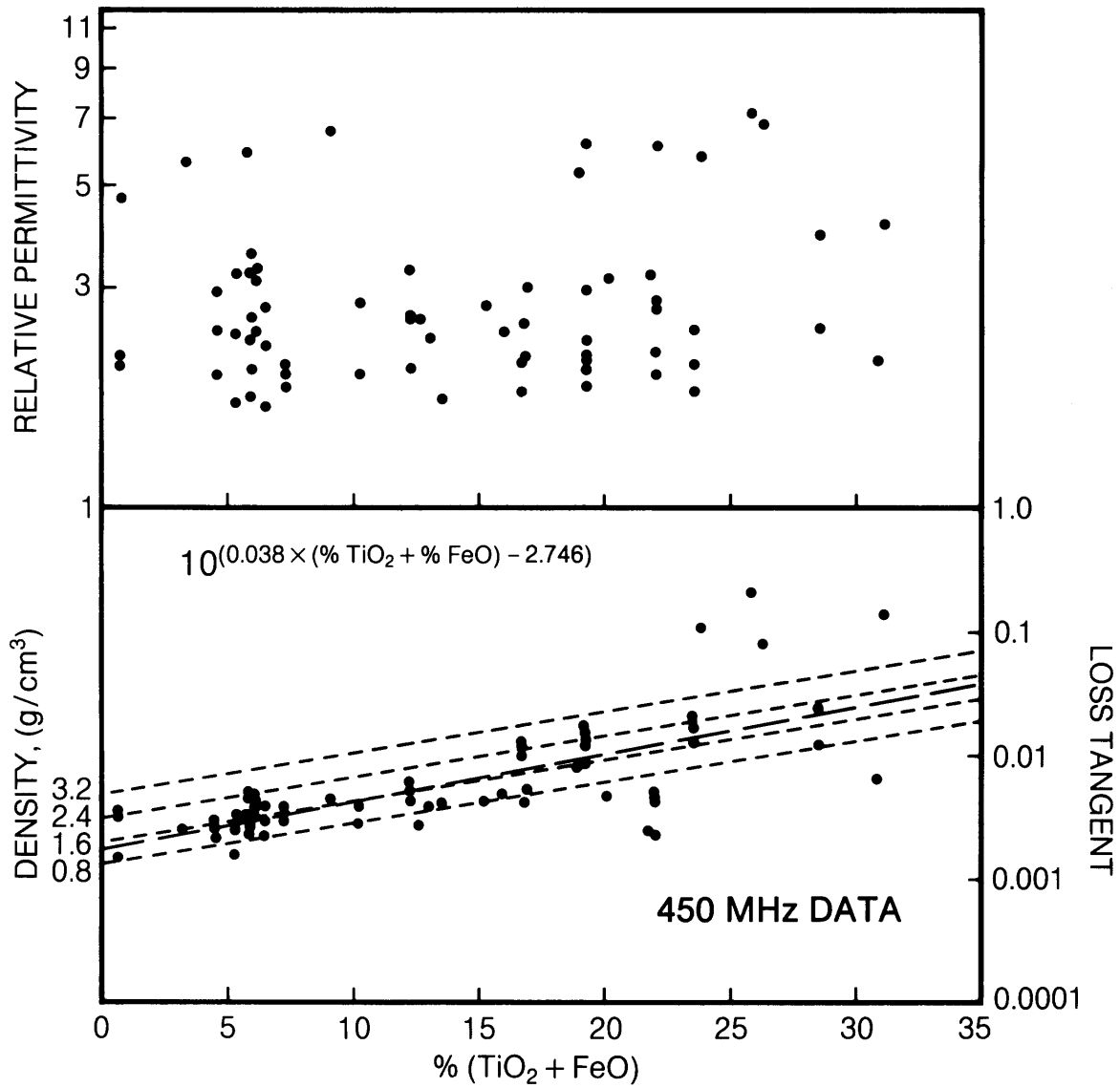


Fig. 9.58. Relative dielectric permittivity (upper vertical axis) and loss tangent (lower right vertical axis) for lunar materials as functions of $\%(\text{TiO}_2 + \text{FeO})$ (horizontal axis) and bulk density. In contrast to Fig. 9.56, data points represent only measurements at 450 MHz (from Table A9.16). The relative permittivity (upper) is apparently independent of chemistry, but the loss tangent increases with increasing $\%(\text{TiO}_2 + \text{FeO})$. Theoretical fitted curves and their derivation are the same as described in Fig. 9.56.

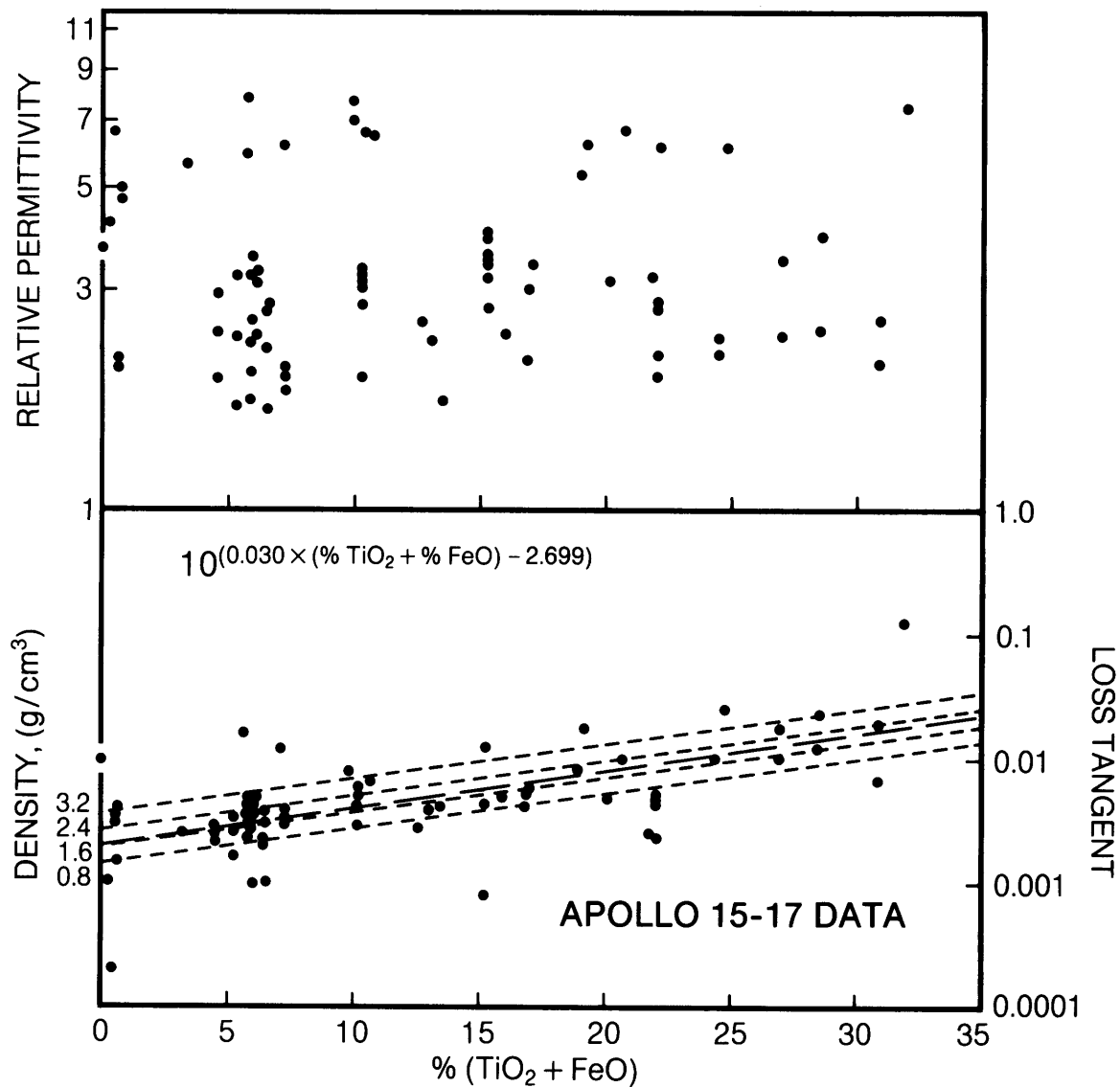


Fig. 9.59. Relative dielectric permittivity (upper vertical axis) and loss tangent (lower right vertical axis) for lunar materials as functions of $\%(\text{TiO}_2 + \text{FeO})$ (horizontal axis) and bulk density. In contrast to Fig. 9.56, data points represent only measurements on Apollo 15–17 samples (from Table A9.16). The relative permittivity (upper) is apparently independent of chemistry, but the loss tangent increases with increasing $\%(\text{TiO}_2 + \text{FeO})$. Theoretical fitted curves and their derivation are the same as described in Fig. 9.56.

(The parameters are the same as those above.) The value of the regression for each subset of the data is shown in the upper left corner of each plot.

In the plots of loss tangent as a function of density (Figs. 9.52–9.55), the solid lines shown are derived from the same BHS formula as above for the permittivity. The heavy dashed line is the two-dimensional regression to the formula (shown at the top of each loss tangent plot)

$$\text{loss tangent} = 10^{(0.440P - 2.943)} \text{ for all samples}$$

The light dashed line is a three-dimensional regression to the formula (shown at the bottom of each loss tangent plot)

$$\text{loss tangent} = 10^{(0.038(\%TiO_2 + \%FeO) + 0.312P - 3.260)}$$

for all samples, plotted at 0, 10, 20, and 30% (TiO₂ + FeO).

The plots of relative permittivity as a function of (TiO₂ + FeO) contents (Figs. 9.56–9.59) indicate that the permittivity shows no dependence on the (TiO₂ + FeO) content. The light dashed lines in the plots of loss tangent as a function of (TiO₂ + FeO) (Figs. 9.56–9.59) are the same as those in Figs. 9.52–9.55, but they are plotted at densities of 0.8, 1.6, 2.4 and 3.2 g/cm³; the heavy dashed line in these plots is the two-dimensional regression of the formula (shown at the top of the loss tangent plot)

$$\text{loss tangent} = 10^{(0.045(\%TiO_2 + \%FeO) - 2.754)}$$

for all samples. Figures 9.56–9.59 show a variety of presentations: all data from Table A9.16 (Fig. 9.56), the soil data only (Fig. 9.57), the 450 MHz data only (Fig. 9.58), and the Apollo 15–17 data only (Fig. 9.59).

There are detectable differences between the Apollo 11–14 samples and the Apollo 15–17 samples, and these differences reflect different procedures in the quarantine and curation of the sample sets after collection (see section A2.3). The Apollo 11–14 lunar samples were quarantined to protect the Earth from possible lunar life forms, and the procedures used produced some contamination of the samples by the Earth's atmosphere before measurement. The Apollo 15–17 samples collected after the quarantine procedures had been dropped were more carefully protected against the outside environment. As a result, the Apollo 15–17 samples showed slightly lower loss tangents and conductivities, because they had only minimal exposure to the effects of moisture (Olhoeft *et al.*, 1975).

The data in Figs. 9.52–9.59 show clearly that the relative dielectric permittivity is a function of bulk density but not of chemistry, and the loss tangent is a strong function of both density and chemistry.

The data in Figs. 9.60 and 9.61 (after *Strangway and Olhoeft*, 1977) illustrate the frequency dependence of the complex dielectric permittivity (shown as relative dielectric permittivity) (closed circles) and the loss tangent (open circles). Figure 9.60 shows data for soil sample 14163, reduced to a density of 1 g/cm³, at several different frequencies: <1 MHz (*Strangway et al.*, 1972), 450 MHz (*Gold et al.*, 1972), 9375 MHz (*Bassett and Shackelford*, 1972), and at 3.6 × 10⁷ MHz in the IR (*Perry et al.*, 1972). Figure 9.61 shows the frequency dependence of rock sample 14310 at similar frequencies: <1 MHz (*Chung et al.*, 1972), 450 MHz (*Gold et al.*, 1972), 9375 MHz (*Bassett and Shackelford*, 1972), and in the IR (*Perry et al.*, 1972).

In both samples, the dielectric permittivity (dotted line) shows little or no frequency dependence at frequencies below the IR, whereas the loss tangent (dashed line) is strongly frequency dependent. The apparent minimum seen in the loss tangent for the soil sample near 10 MHz (Fig. 9.60) would suggest that frequency to be the optimum choice for a deep penetrating radar (*Olhoeft*, 1984) or for long distance subhorizon radio communication through soils.

However, for the rock sample (Fig. 9.61), the appearance of a strong dielectric relaxation near 0.1 MHz moves the equivalent minimum in loss tangent up to 500 MHz for rocks. However, few rock samples exhibited such a relaxation effect.

The temperature dependence of the dielectric properties of lunar soil sample 15301,38 are illustrated in Figs. 9.62–9.65 (*Olhoeft et al.*, 1974b). The dielectric permittivity of the soil (Fig. 9.62) is independent of temperature at frequencies above 1 MHz, and both the permittivity (Fig. 9.64) and loss tangent (Fig. 9.65) are relatively independent of temperature below 200°C. Solid lines in Figs. 9.62–9.65 represent data for the model equation

$$k' - ik'' = k_1 + \frac{k_0 - k_1}{1 + (i\omega\tau_0 e^{E_0/kT})^{1-\alpha}}$$

where $k_0 = 6700$; $k_1 = 3.0$; ω = frequency in radians/sec; $\tau_0 = 2.56 \times 10^{-12}$ sec; $E_0 = 2.5$ eV; and α = the Cole-Cole frequency distribution parameter.

The frequency distribution parameter (α) was also found to be temperature-dependent, with the form

$$1 - \alpha = [1 + e^{0.0018(1000 - T)}] - 1$$

The loss tangent is given as

$$\text{loss tangent} = \frac{k''}{k'} + \frac{\sigma_{DC}}{\omega k' \epsilon_0}$$

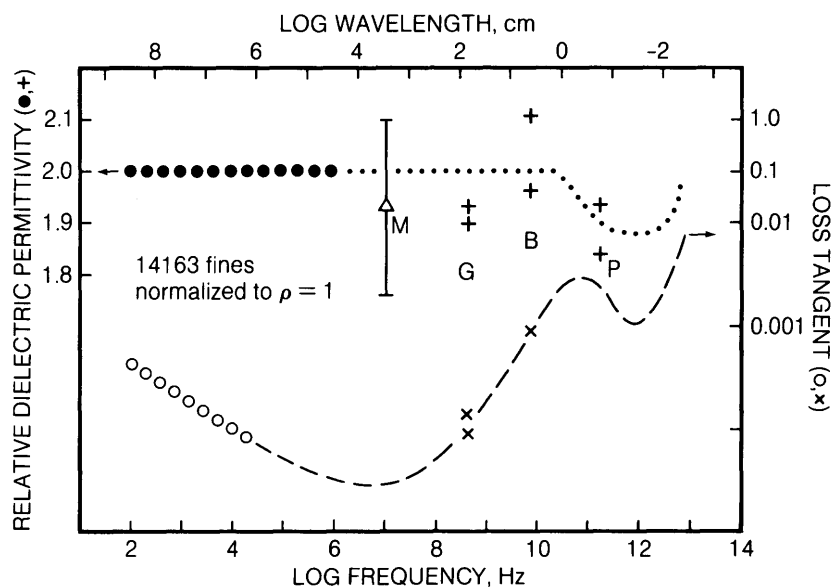


Fig. 9.60. Relative dielectric permittivity (left vertical axis) and loss tangent (right vertical axis) for a lunar soil sample (14163 fines) as a function of frequency (bottom horizontal axis) or wavelength (top horizontal axis) (after *Strangway and Olhoeft, 1977*). Data are normalized to a soil density of 1 gm/cm³. The diagram summarizes measurements made by several workers over a range of frequencies: <1 MHz (*Strangway et al., 1972*); 450 MHz (crosses labeled G; *Gold et al., 1972*); 9375 MHz (crosses labeled B; *Bassett and Shackleford, 1972*); and 3.6×10^7 MHz (in the infrared) (crosses labeled P; *Perry et al., 1972*). The value marked M is an overall mean permittivity for all lunar samples at 10^7 Hz.

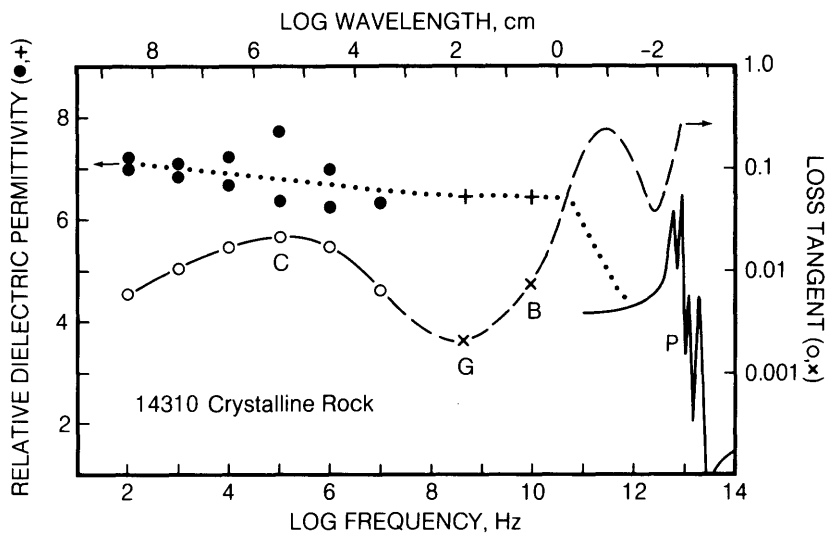


Fig. 9.61. Relative dielectric permittivity (left vertical axis) and loss tangent (right vertical axis) of a lunar rock (crystalline rock 14310) as a function of frequency (bottom horizontal axis) or wavelength (top horizontal axis) (after *Strangway and Olhoeft, 1977*). The diagram summarizes measurements made by several workers over a range of frequencies: <1 MHz (circles labeled C; *Chung et al., 1972*); 450 MHz (crosses labeled G; *Gold et al., 1972*); 9375 MHz (crosses labeled B; *Bassett and Shackleford, 1972*); and permittivity at $>3.6 \times 10^7$ MHz (in the infrared) (curve labeled P; *Perry et al., 1972*).

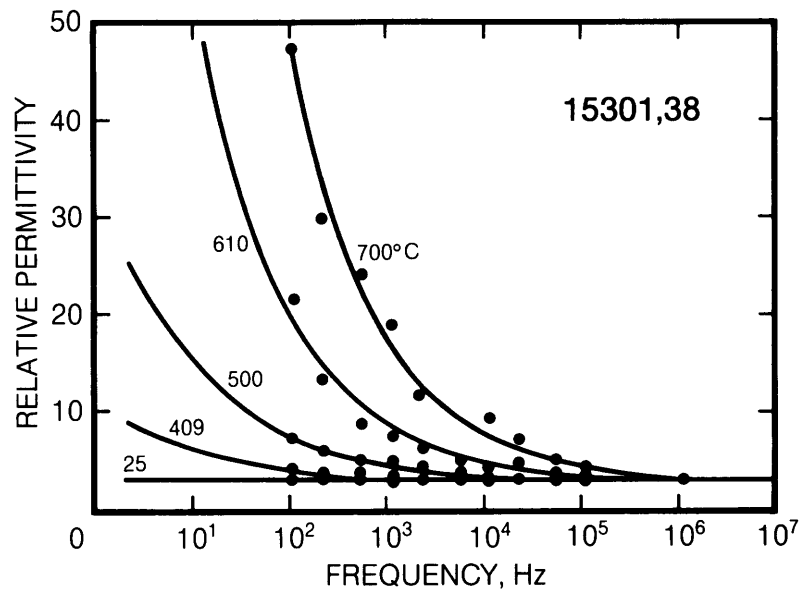


Fig. 9.62. Relative dielectric permittivity (vertical axis) of lunar soil sample 15301,38 as a function of frequency (horizontal axis) at several different temperatures (after *Olhoeft et al.*, 1974b). Theoretical curves (solid lines) fitted to the data points are derived from the model equation discussed in the text. The data indicate that the permittivity of the soil sample is largely independent of temperature at frequencies $>10^6$ Hz.

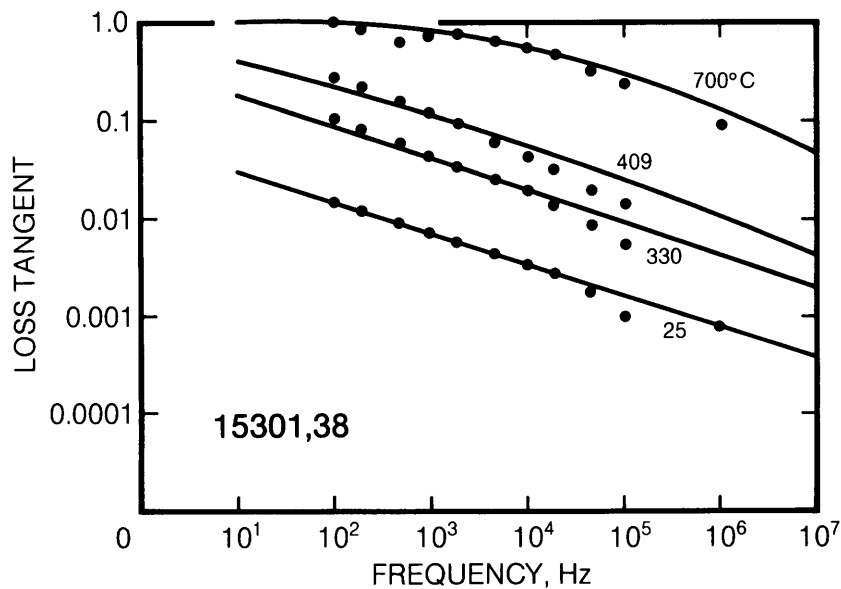


Fig. 9.63. Loss tangent (vertical axis) of lunar soil sample 15301,38 as a function of frequency (horizontal axis) at several different temperatures (after *Olhoeft et al.*, 1974b). Theoretical curves (solid lines) fitted to the data points are derived from the model equation discussed in the text. On this log-log plot, the loss tangent shows an approximately linear decrease with increasing frequency for temperatures between 25°C and 700°C.

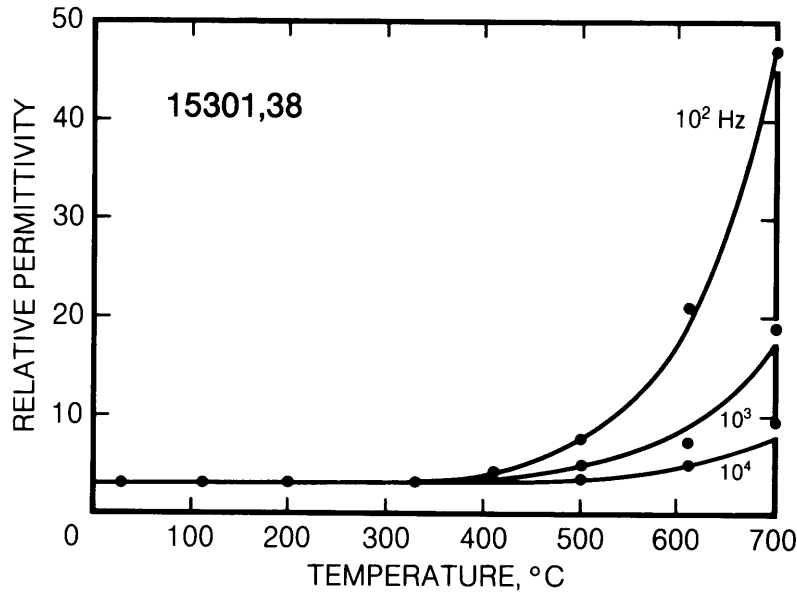


Fig. 9.64. Relative dielectric permittivity (vertical axis) of lunar soil sample 15301,38 as a function of temperature (horizontal axis) at several different frequencies (after *Olhoeft et al., 1974b*). Theoretical curves (solid lines) fitted to the data points are derived from the model equation discussed in the text. The data indicate that the permittivity of the soil sample is largely independent of both temperature and frequency at temperatures $<400^\circ\text{C}$, or essentially over the whole range of lunar surface temperatures.

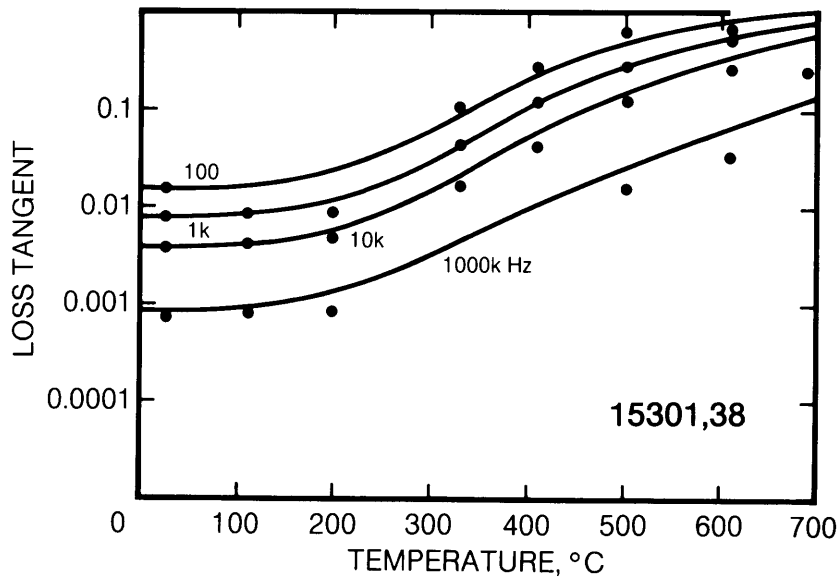


Fig. 9.65. Loss tangent (vertical axis) of lunar soil sample 15301,38 as a function of temperature (horizontal axis) at several different frequencies (after *Olhoeft et al., 1974b*). Theoretical curves (solid lines) fitted to the data points are derived from the model equation discussed in the text. The loss tangent of the soil sample is largely independent of temperature below about 200°C , or essentially over the whole range of lunar surface temperatures.

where σ_{DC} = DC electrical conductivity discussed above, and ϵ_0 = vacuum permittivity = 8.854185×10^{-12} Farad/m.

The temperature dependence of the dielectric properties of lunar rock is shown in Figs. 9.66–9.71 for several different samples: 12002,85 (Olhoeft *et al.*, 1973b), 14310,75 (Chung *et al.*, 1972), and 70215,14 (Alvarez, 1974a,b,c). The temperature dependence of the permittivity (Fig. 9.66) decreases with increasing frequency, but the temperature dependence of the loss tangent (Fig. 9.67) depends strongly on both temperature and frequency. Further studies of the effects of frequency and temperature on the dielectric permittivity and loss tangent are found in Chung *et al.* (1970, 1971, 1972), Katsube and Collett (1971, 1973b), Chung (1972), Strangway *et al.* (1972, 1975), Chung and Westphal (1973), Alvarez (1973a, 1974b), Olhoeft *et al.* (1973a, 1974a, 1975), and Bussey (1979).

Frisillo *et al.* (1975) added another variable to these investigations by studying the effects of frequency, temperature and vertical confining stress on the electromagnetic properties of lunar soils. The loss tangent showed no dependence upon stress. However, the relative dielectric permittivity increased rapidly from 6% to 20% between 0.04 and 0.4 bar stress. This rapid increase was followed by a linear

increase with further stress (at a rate of about 0.5%/bar), up to the maximum applied stress of 2 bar.

In summary, the relative dielectric permittivity of lunar rocks and soils is strongly dependent upon density and independent of chemistry; above 1 MHz, it is also independent of frequency and temperature over the lunar surface temperature range. The loss tangent is strongly dependent upon density, chemistry, temperature, and frequency, with a minimum loss near 10 MHz in soils. The best reviews of these properties and the related research are found in Olhoeft and Strangway (1975), Strangway and Olhoeft (1977), and Gary and Keihm (1978).

These data have been used to estimate the electromagnetic properties of the lunar surface materials to significant depths. Olhoeft and Strangway (1975) combined the density profiles of Carrier *et al.* (1972a, 1973b), Houston *et al.* (1974), and Mitchell *et al.* (1972d) with the formula for permittivity as a function of density to produce a profile of electrical properties with depth in the lunar surface to depths of 100 m. Using more recent statistical data and regressions, the formula for density vs. depth in the regolith (see Fig. 9.16)

$$\rho = 1.91 \frac{z + 12.2}{z + 18} \text{ g/cm}^3$$

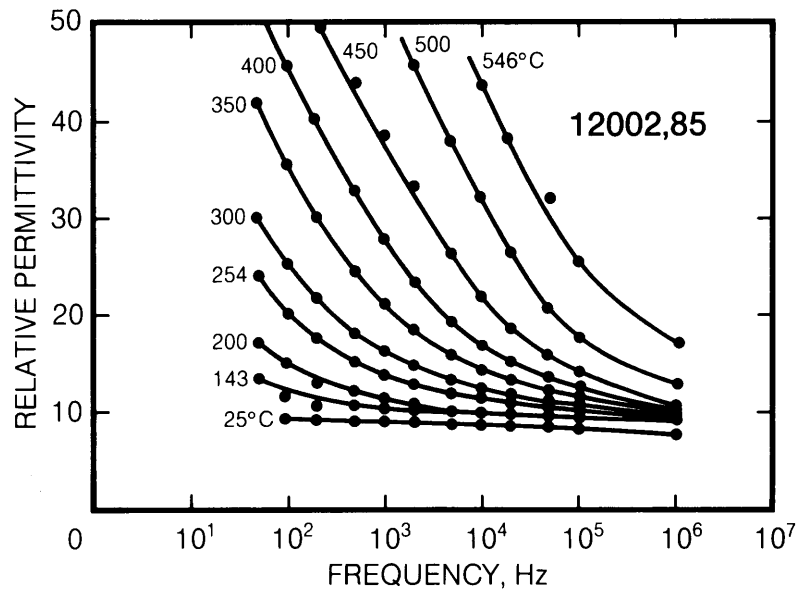


Fig. 9.66. Relative dielectric permittivity (vertical axis) of lunar rock sample 12002,85 as a function of frequency (horizontal axis) at several temperatures (after Olhoeft *et al.*, 1973a). The solid lines are smooth curves fitted to the data. Curves derived from the model equation described in the text are more complicated and are not shown here. At prevailing lunar surface temperatures (<200°C), the permittivity of the rock is virtually independent of frequency for frequencies >10³ Hz.

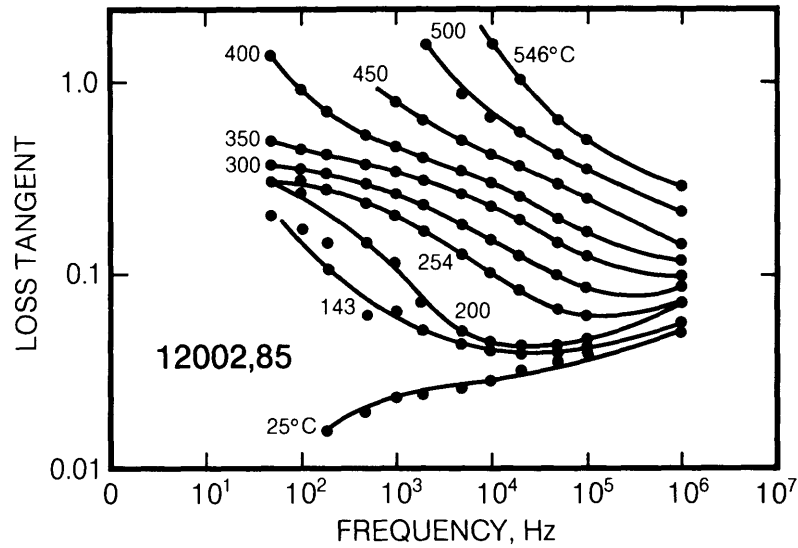


Fig. 9.67. Loss tangent (vertical axis) of lunar rock sample 12002,85 as a function of frequency (horizontal axis) at several temperatures (after *Olhoeft et al.*, 1973a). The solid lines are smooth curves fitted to the data. Curves derived from the model equation described in the text are more complicated and are not shown here. The measured loss tangent varies significantly with frequency over the full range of frequencies and temperatures measured, including temperatures corresponding to the lunar surface.

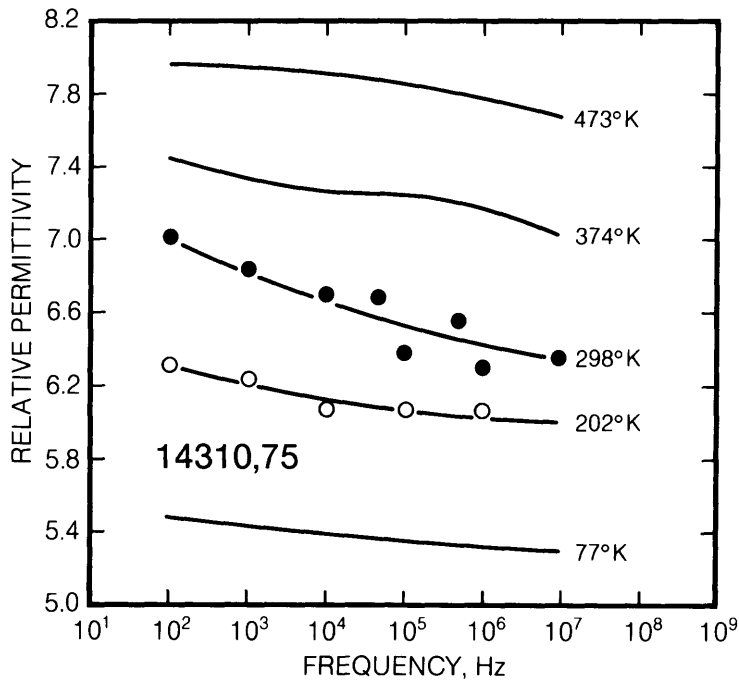


Fig. 9.68. Relative dielectric permittivity (vertical axis) of lunar rock sample 14310 as a function of frequency (horizontal axis) at several temperatures. The solid lines are smooth curves fitted to the data. Curves derived from the model equation described in the text (see *Chung et al.*, 1972) are more complicated and are not shown here. In contrast to rock 12002,85 (Fig. 9.66), the permittivity of rock 14310 varies significantly with frequency at all temperatures.

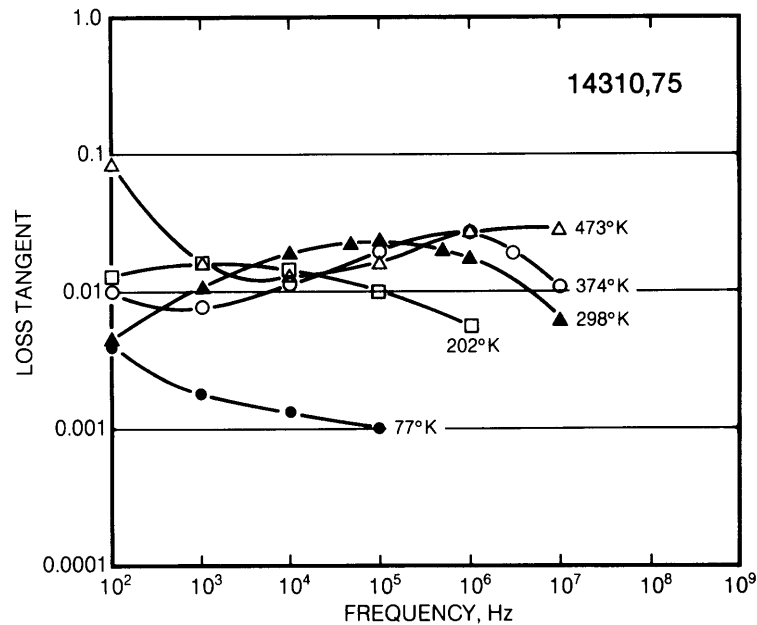


Fig. 9.69. Loss tangent (vertical axis) of lunar rock sample 14310 as a function of frequency (horizontal axis) at several temperatures. The solid lines are smooth curves fitted to the data. Curves derived from the model equation described in the text (see *Chung et al.*, 1972) are more complicated and are not shown here. In contrast to rock 12002,85, the measured loss tangent varies with frequency over the full range of frequencies and temperatures measured, including temperatures corresponding to the lunar surface. However, the value remains close to 0.01 for a wide range in both temperature and frequency.

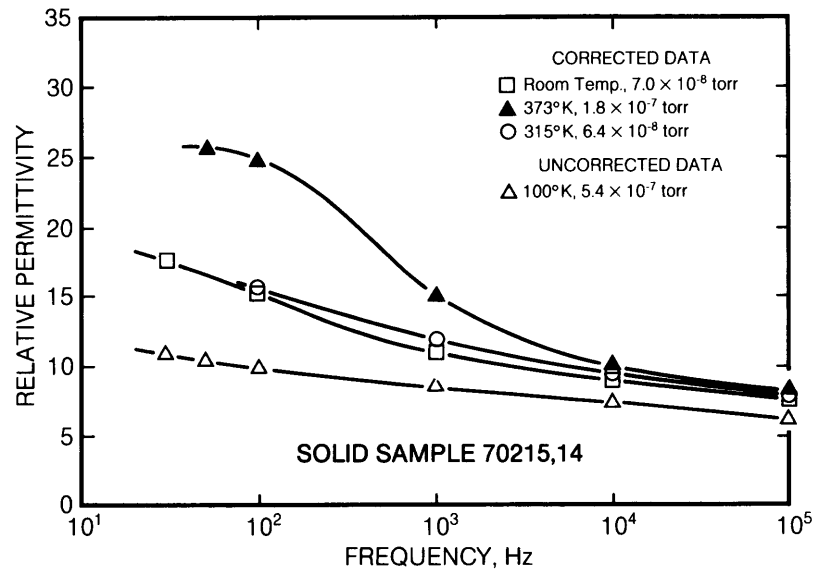


Fig. 9.70. Relative dielectric permittivity (vertical axis) of lunar rock sample 70215,14 as a function of frequency (horizontal axis) at several temperatures (after *Alvarez*, 1974b). The solid lines are smooth curves fitted to the data. The permittivity of this rock sample varies slightly with frequency at all temperatures, but the variation is lowest at lower temperatures.

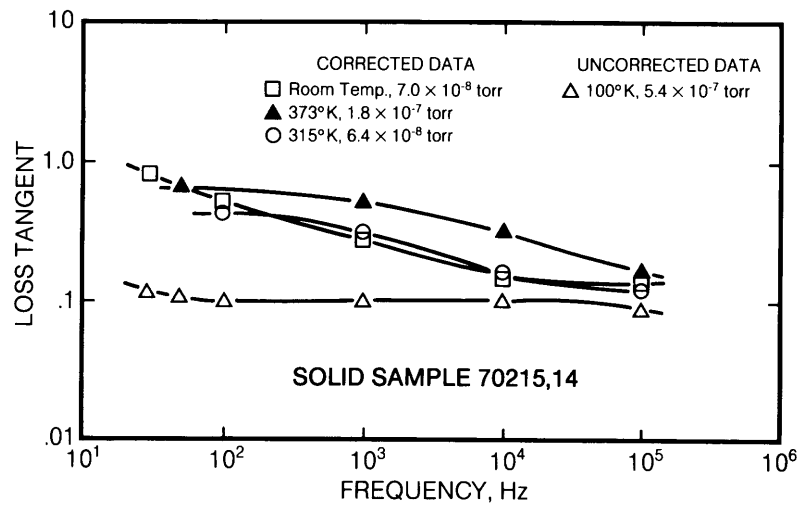


Fig. 9.71. Loss tangent (vertical axis) of lunar rock sample 70215,14 (basaltic lava) as a function of frequency (horizontal axis) at several temperatures (after Alvarez, 1974c). The solid lines are smooth curves fitted to the data. In contrast to other rock samples, the measured loss tangent varies with frequency at higher temperatures, but is relatively independent of frequency (and close to 0.1) at the low temperatures corresponding to the lunar surface (lower curve).

where z is depth in centimeters, may be combined with the formula for relative dielectric permittivity vs. density

$$k = 1.919\rho$$

to produce a profile for relative dielectric permittivity vs. depth, and a similar depth profile for the loss tangent. These combined formulas should be valid to regolith depths of at least tens of meters.

9.2.5. Electromagnetic Sounding

Electromagnetic sounding of the Moon can be accomplished in three different ways. The first technique is passive and uses the interaction between the Moon and the solar wind. This interaction produces low-frequency electromagnetic waves, which diffuse into the Moon, inducing eddy currents. These induced currents in the Moon then perturb the existing magnetic fields around the Moon. These perturbations may be monitored with magnetometers on the lunar surface or in orbit around it, as a function of frequency, to produce an electrical conductivity profile of the Moon. This concept was discussed earlier with regard to Fig. 9.49 (section 9.2.1), and it is best reviewed by Sonett (1982) and Hood (1986).

The second method of electromagnetic sounding uses the artificial propagation of high-frequency electromagnetic energy. This energy may be trans-

mitted and received by Earth-based radar systems (DeWitt and Stodola, 1949; Evans and Pettengill, 1963; Low and Davidson, 1965; Hagfors and Evans, 1968; Evans, 1969; Pettengill, 1978; Thompson, 1979; Ostro, 1983), by orbiting systems (Brown, 1972; Phillips et al., 1973a,b; Tyler and Howard, 1973; Porcello et al., 1974; Elachi et al., 1976; May, 1976; Peeples et al., 1978; Sharpton and Head, 1982; Sharpton, 1985), or by surface instruments (Brown, 1967; Brown et al., 1967; Muhleman et al., 1968a,b, 1969; Simmons et al., 1972, 1973; Kroupenio, 1973; Kroupenio et al., 1975; Rossiter, 1977).

A third method involves the passive Earth-based detection of microwave radiation associated with natural lunar thermal emissions (Krotikov and Troitsky, 1963; Gary et al., 1965; Hagfors, 1970; Muhleman, 1972; Keihm and Langseth, 1973, 1975b; Schloerb et al., 1976). Table 9.16 summarizes these dielectric sounding results, excluding the Earth-based measurements. Figure 9.72 summarizes the results of Earth-based observations. These data are in excellent agreement with the laboratory measurements on lunar samples discussed earlier.

In each of these methods, electromagnetic scattering is the largest loss mechanism, and this process causes the single largest uncertainty in interpretation. Electromagnetic scattering occurs when the wavelength of the electromagnetic energy being propagated in a material approaches the same size as the scale of heterogeneities in the material's electrical properties. Such scattering may occur

TABLE 9.16. Summary of dielectric sounding results.

System	Wavelength (m)	Relative Dielectric Permittivity	Loss Tangent	References
Surveyor				
Surveyor 1	0.023	2.40±0.50	—	Muhleman et al. (1969)
Surveyor 3	0.023	2.07±0.11	—	Muhleman et al. (1969)
Surveyor 5	0.023	2.00±0.16	—	Muhleman et al. (1969)
Surveyor 7	0.023	3.28±0.40	—	Muhleman et al. (1969)
Surveyor 3	0.023	3.7±0.5-1.0	(0.0257±0.005) ρ	Brown et al. (1967)
(where ρ is density)				
Apollo 17 SEP				
First 7±1 m depth		3.8±0.2	0.08±0.04	Strangway et al. (1975)
Next 100±10m		7.5±0.5	0.035±0.025	Strangway et al. (1975)
Remainder		9	—	Strangway et al. (1975)
Luna 9	0.17	2.7±0.9	—	Kroupenio (1971)
Luna 11		2.85±0.15	—	Kroupenio (1971)
Luna 13		4.4±2.1	—	Kroupenio (1971)
Luna 14	0.17	2.9±0.1	—	Kroupenio (1971)
Luna 16	0.031	2.15±0.35	—	Kroupenio (1973)
Luna 17	0.031	2.3±0.4	—	Kroupenio (1973)
Luna 19		2.35±0.65	—	Kroupenio et al. (1975)
Luna 19		3.2±0.2	—	Kroupenio et al. (1975)
Luna 20		1.7±0.2	—	Kroupenio et al. (1975)

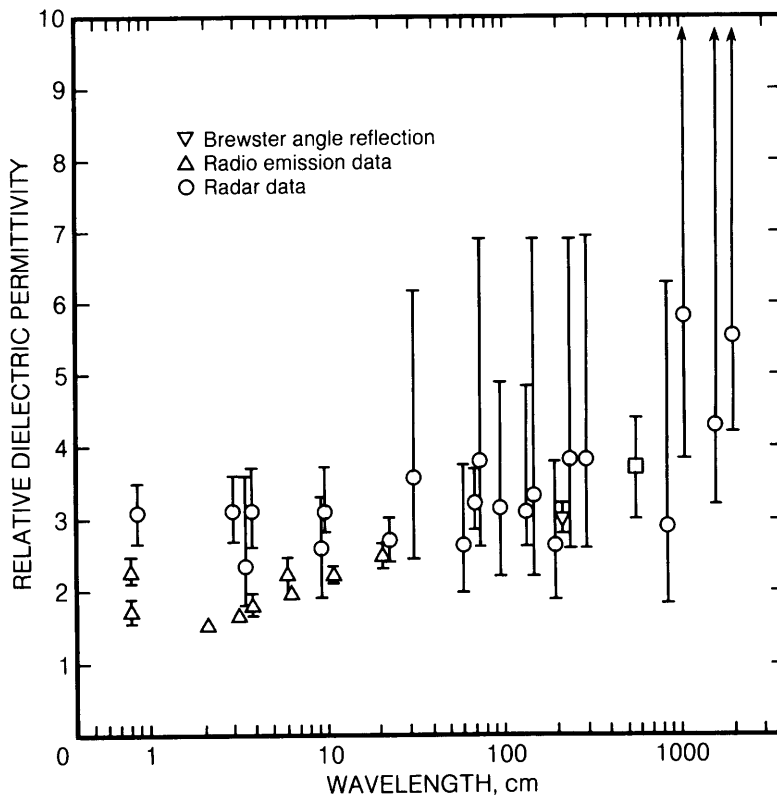


Fig. 9.72. Plot of relative dielectric permittivity (vertical axis) as a function of wavelength (lower axis) for the lunar surface material, based on the results of Earth-based active radar observations (after Lincoln Laboratory, 1970). The permittivity appears to increase gradually with increasing wavelength, although measurement uncertainties are also higher at the higher wavelengths.

TABLE 9.17. Earth-based radar cross-sections for the Moon (after *Evans and Pettengill*, 1963; *Pettengill*, 1978).

Wavelength (m)	Radar Cross-Section (Fraction of Physical Cross-Section)	References
19.20	0.16 ±0.08	<i>Davis and Rohlf</i> s (1964)
3.00	0.10 ±0.08	<i>Evans et al.</i> (1959)
0.70	0.074±0.02	<i>Fricker et al.</i> (1960)
0.23	0.065±0.01	<i>Evans and Hagfors</i> (1966)
0.035	0.070±0.02	<i>Hagfors and Evans</i> (1968)
0.0086	0.070±0.02	<i>Lynn et al.</i> (1964)

TABLE 9.18. Hagfors RMS slope for the Moon (after *Pettengill*, 1978).

Wavelength (m)	Hagfors RMS Slope (degrees)	References
19.20	4.1	<i>Beckmann and Klemperer</i> (1965)
1.16	6-8 Highlands	<i>Tyler and Howard</i> (1973)
	1-2 Mare	<i>Tyler and Howard</i> (1973)
0.70	5.9	<i>Hagfors</i> (1970)
0.23	7.1	<i>Hagfors</i> (1970)
0.13	6-8 Highlands	<i>Tyler and Howard</i> (1973)
	2-4 Mare	<i>Tyler and Howard</i> (1973)
0.35	9.1	<i>Evans</i> (1969)
0.031	11±1.5 Luna 16	<i>Kroupenio</i> (1973)
	7.5±1.0 Luna 17	<i>Kroupenio</i> (1973)
	10±1.0 Luna 19	<i>Kroupenio et al.</i> (1975)
	8.5±1.0 Luna 19	<i>Kroupenio et al.</i> (1975)
	9.5±1.5 Luna 20	<i>Kroupenio et al.</i> (1975)
0.0086	33	<i>Beckman and Klemperer</i> (1965)

within an otherwise uniform volume of material as *volume scattering* produced by appropriate-sized heterogeneities within the material. (The same effect on the scale of visible light waves prevents us from seeing through snow, although ice may be clear.) Scattering may also occur at the boundary between two different materials, such as the soil-vacuum interface at the Moon's surface or the regolith-bedrock interface below the surface. A similar effect prevents seeing through the surface of scratched ice or frosted glass. Fundamental references on the nature of the various scattering processes are *Evans and Pettengill* (1963), *Salomonovich and Losovskii* (1963), *Hagfors* (1964, 1967, 1968), *Burns* (1969), *Tyler et al.* (1971), *Pollack and Whitehill* (1972), *Parker and Tyler* (1973), *Pettengill et al.* (1974), *England* (1975), *Fisher and Staelin* (1977), *Strangway and Olhoft* (1977), *Ishimaru* (1978a,b), *Olhoft et al.* (1979), *Tyler* (1979), *Fung* (1982), *Simpson and Tyler* (1982), *Ulaby et al.* (1982), *Moore* (1983), and *Elachi et al.* (1984).

At the simplest level, the whole Moon scatters electromagnetic energy by reflection (*Evans and Pettengill*, 1963). Table 9.17 lists the total radar cross-section of the Moon as a function of wave-length, after *Pettengill* (1978). The *total radar cross-section* is the area of an isotropic scatterer (identical in all directions), perpendicular to the transmitted energy, that would yield the observed radar echo amplitude if it were located in place of the Moon. Table 9.18 lists the Hagfors root-mean-square (RMS) slope quantity (*Hagfors*, 1970), which is one measure of the angular dependence of scattering. Increasing Hagfors RMS slope values indicate increasing quasispecular (quasismooth) scattering. Small slopes correspond to smooth surfaces (like that of still water). Higher slopes indicate increasing roughness (like choppy or wavy water).

Several key quantities can be measured in radar returns from the Moon. These include the wave-length dependence of reflections, the changes in polarization of the radar beam, the Doppler shift of

the original frequency, and the angular dependence of the return energy amplitude. By analyzing these quantities, radar scattering measurements may be interpreted to determine the variations in surface topographic relief, hillslope angles, surface undulations, and boulder populations (roughness). These analyses and their interpretations are discussed in the above references and also in *Low and Davidson* (1965), *Thompson et al.* (1970, 1974), *Zisk* (1970, 1972a,b), *Hagfors and Campbell* (1973), *Linsky* (1973), *Thompson* (1974, 1979, 1986), *Ulich et al.* (1974), *Zisk et al.* (1974), *Schaber et al.* (1975), *Gary and Keihm* (1978), *Schaber et al.* (1986), and *Thompson and Saunders* (1986).

The results of some of these analyses are shown in Figs. 9.73–9.75. Figure 9.73 (after *Gary and Keihm*, 1978) shows an effective specific loss tangent derived from both laboratory studies on lunar samples (similar to results shown in Figs. 9.60 and 9.61) and Earth-based measurements, including the effects of scattering. Their model (Fig. 9.73) incorporates several factors: an intrinsic loss mechanism (slope -0.25), Rayleigh-type scattering from the soil

grain size distribution (slope -4), and scattering from a two-parameter model with stratified layers (long wavelength scattering; based upon the results of *Fisher*, 1977). Figures 9.74 and 9.75 (after *Strangway and Olhoeft*, 1977) illustrate two more measures of scattering for the Moon. Figure 9.74 illustrates scattering as a function of delay time at various wavelengths (after *Hagfors*, 1970). Figure 9.75 illustrates scattering from different regions of the Moon in terms of Hagfors RMS slope angle and shows comparisons with similar measurements of Mercury, Venus, and Mars.

The earlier Earth-based radar investigations of the Moon were used to help locate the Surveyor and Apollo landing sites. Similar Earth-based investigations of Mars were used to help select the landing sites for the Viking landers. Radar methods, both Earth-based and from the Pioneer Venus orbiting spacecraft, have produced the only topographic maps of the atmosphere-obscured surface of Venus. [Because of the strong absorption of radar waves by the water present in virtually all terrestrial surficial deposits, the only comparable terrestrial location

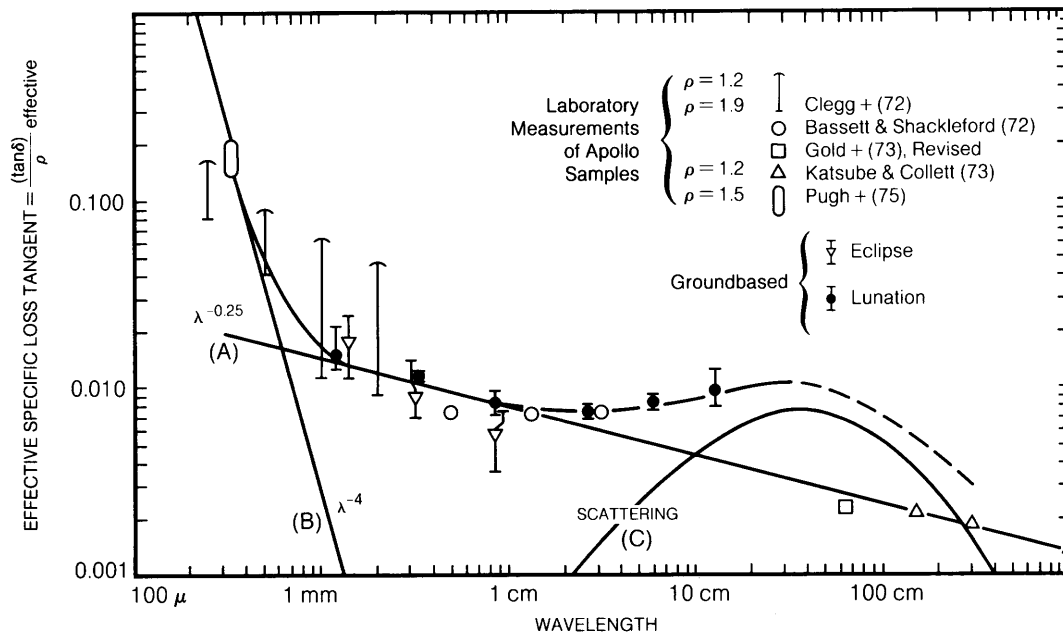


Fig. 9.73. Plot of effective specific loss tangent (vertical axis) as a function of wavelength (horizontal axis) for lunar surface material, based on the results of active radar experiments (after *Gary and Keihm*, 1978). The loss tangent appears to decrease with increasing wavelength in a nonuniform manner. The heavy solid line passing through most of the experimental points represents a model consisting of the three components shown as solid lines: (A) intrinsic loss (slope -0.25); (B) Rayleigh scattering from particle grains (slope -4); (C) scattering from stratified subsurface layers (peak at long wavelengths; after *Fisher*, 1977).

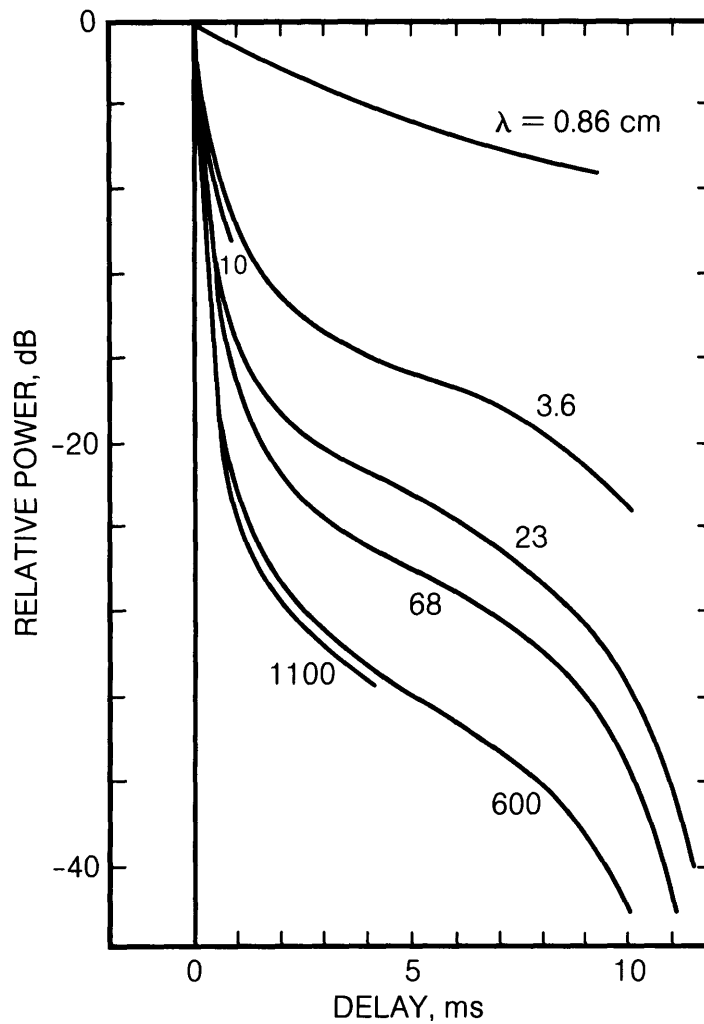


Fig. 9.74. Data on scattering from the Moon using Earth-based active radar observations at different wavelengths. Data are presented as a function of relative returned power (vertical axis) and delay time (horizontal axis) for different wavelengths (individual curves). Scattering by the lunar surface increases with increasing wavelength, causing the values of returned relative power (plotted here) to decrease. The decline of relative power with delay time for a given wavelength is called *limb-darkening*, i.e., the center of the Moon (the subradar point) is brighter than the edges. Data from *Hagfors* (1970) and *Strangway and Olhoeft* (1977).

where these methods can be applied is in mapping the subsurface of the extremely arid Western Desert in Egypt, where scattering, rather than water absorption, is the dominant loss mechanism (*Schaber et al.*, 1986).] Figure 9.76 illustrates a topographic contour map, obtained from radar studies, of a portion of the lunar surface. Table 9.19 lists some of the available images and maps derived from radar observations, two of which are shown in Figs. 10.8 and 10.9.

In summary, a variety of methods have used electromagnetic energy to probe both the interior and the surface of the Moon. Low-frequency electromagnetic induction sounding, using the solar wind and magnetometers, has been interpreted to produce a conductivity vs. depth profile for the lunar interior. Laboratory measurements of conductivity vs. temperature on lunar samples have then been combined with these profiles to infer a profile of temperature vs. depth (selenotherm). In addition to

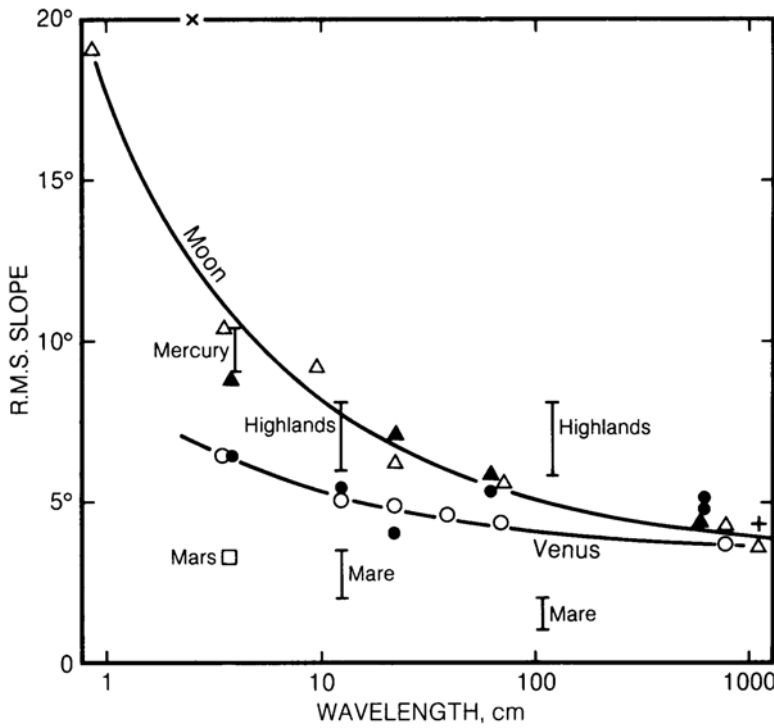


Fig. 9.75. Comparative data for radar scattering from the surfaces of the Moon and other planets (Mercury, Venus, and Mars) (after *Strangway and Olhoeft, 1977*). Data are plotted in terms of the Hagfors RMS slope (vertical axis) as a function of wavelength (horizontal axis); higher values of the RMS slope correspond to rougher surfaces. Of all the planets examined, the Moon exhibits the widest range of surfaces, from the smoothest (maria) to the roughest (highlands). Data sources for the Moon are *Kroupenio (1972)*, open triangles; *Evans (1969)*, solid triangles; *Muhleman et al. (1968a,b)*, cross at top; *Davis and Rohfs (1964)*, plus sign at right; *Tyler and Howard (1973)*, bars labeled "highlands" and "mare." Data sources for other planets are Mercury, *Evans (1969)*; bar; Mars, *Evans (1969)*; square; Venus, *Kroupenio (1972)*; open circle, *Evans (1969)*; closed circle).

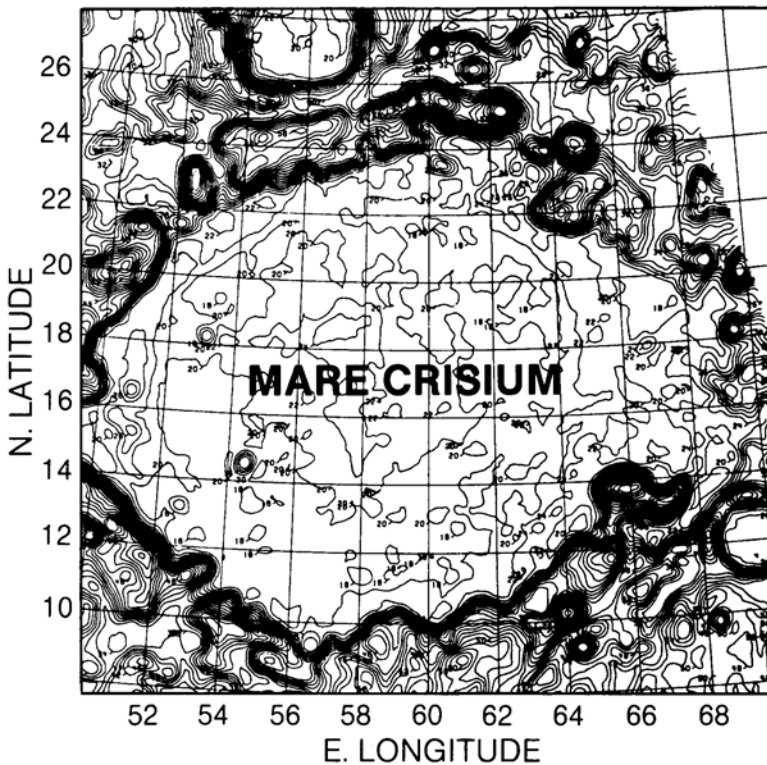


Fig. 9.76. Contour map of Mare Crisium topography based on Earth-based radar interferometer measurements. Contour interval is 200 m. Contours are in hundreds of meters, referred to a datum sphere of 1731.6 km radius (e.g., 18 = 1800 m above datum = 1733.4 km). From *Zisk (1978)*.

TABLE 9.19. Available maps and images of the Moon derived from radar observations.

Wavelength (m)	References
7.5	Thompson (1979)
0.70	Thompson (1974, 1986, 1987*)
0.23	Hagfors and Evans (1968)
0.038	Zisk (1970, 1972a, 1978†), Zisk et al. (1974‡)

* See Figs. 10.8 and 10.9.

† See Fig. 10.10.

‡ See Fig. 9.76.

the deep probing of the Moon, high-frequency electromagnetic propagation sounding has been used from Earth-based, orbital, and surface radar systems to map the topography, stratigraphy, roughness, and homogeneity of the upper 100 m of the lunar surface (see section 9.3.2 below).

9.3. REFLECTION AND EMISSION OF RADIATION FROM THE MOON

Much of what we know about the lunar surface comes from remote observations using optical or radio astronomical methods, either from Earth or from spacecraft orbiting above the Moon. In general, the astronomical instrumentation used in these studies is designed to detect various forms of electromagnetic radiation, which differ significantly in their wavelengths. Different kinds of detectors and telescope combinations are used, depending on the wavelength of the radiation.

The lunar radiation measured by these devices may have several different origins: (1) insolation (sunlight) reflected from the lunar surface, (2) manmade radiation reflected from the surface (e.g., radar), (3) thermal emission from the Moon itself, and (4) X-rays and gamma rays induced in the lunar surface material by solar or galactic radiation. In this section we will discuss only the first three, which are related to the optical and dielectric properties of the surface. More information on the fourth type is provided in Chapter 10.

9.3.1. Optical Astronomy

Galileo made the first recorded telescopic observations of the Moon, looking at it through a crude telescope that sensed visible-light radiation. Modern astronomy has expanded the use of telescopes with lenses and/or mirrors to detect "light" (e.g., IR and UV wavelengths) that may not be visible to the human eye. However, the properties of the lunar surface that determine how it reflects sunlight are

similar regardless of whether the incoming illumination is dominated by UV, visible, or IR wavelengths.

Visible light corresponds to electromagnetic radiation ranging in wavelength from about 0.4 μm (violet) to about 0.76 μm (red). For wavelengths longer than about 3 μm , however, lunar thermal emission begins to make up a significant proportion of the radiation received from the illuminated Moon, and at wavelengths longer than about 4 μm , this thermal radiation dominates. Other factors, including the optical transmission characteristics of the Earth's atmosphere, the onset of thermal emission, and the spectral response of common telescope detector systems combine to set an effective upper limit of about 2.5 μm for the wavelengths that can be detected in modern lunar reflectance observations. A lower limit of approximately 0.3 μm , between the visible and UV, is defined for similar reasons.

In considering the physics of moonlight, the Moon can be regarded as a sphere that is illuminated from a specific direction in space. The intensity of the radiation measured by an observer depends on what fraction of the incoming sunlight is reflected by an element of surface area (*albedo*) and how the reflected light is distributed into various directions (*photometric function*) (Minnaert, 1961). Since most solar system objects appear to be single points of light in the sky, the definitions in planetary photometry usually describe any planet as if it were a sphere with uniform surface properties, and these definitions are adequate for most purposes. However, the Moon's nearness allows us to observe its surface at relatively high spatial resolution, and the standard definitions of observational astronomy sometimes require modifications for the Moon.

Photometric function. The photometric function of a surface is a mathematical expression that relates the intensity of the radiation scattered into any one direction to the intensity of the incident radiation, which arrives from a different direction. The parameters in the function vary somewhat with wavelength, but the differences are small. Optical astronomers can usually discuss the scattering of sunlight from a planetary surface without reference to a specific wavelength.

The directions of the incident beam and the scattered beam are described in terms of the angles they make with the *surface normal*, which is a vector perpendicular to the local surface. A third angle is required to fully specify the geometrical relationships; in lunar photometry this is taken to be the *phase angle* between the incident and scattered (outgoing) beams. The incoming and outgoing beams define the *phase plane*, which contains the phase angle. Full Moon corresponds to (almost) zero phase angle; at new Moon, the phase angle is 180°.

(At a truly zero phase angle, the Earth lies exactly between the sun and the Moon, and we have a lunar eclipse.)

A hypothetical surface that reflects incident light uniformly into all directions is said to be *Lambertian*. Astronomers were puzzled for many years by the fact that the Moon is decidedly non-Lambertian in its reflectance. The lunar surface is highly *backscattering*, meaning that it preferentially reflects incoming light back in the direction of illumination. For this reason, the apparent brightness of the lunar surface increases as the phase angle decreases toward zero, and for phase angles of less than 5° the brightening is dramatic. This surge in surface brightness near zero phase angle is called the *opposition effect* (Gehrels *et al.*, 1964) or *heiligschein* (Willey and Pohn, 1969). This effect is also visible to observers on the lunar surface. Astronauts working on the Moon experience a loss of contrast and detail as they look at the surface with their backs to the sun, and ground that slopes away from the observer is just as bright as slopes facing an observer.

Minnaert (1961) provided an extensive review of the early observational work that defined the general scattering behavior of the lunar surface (Fedorets, 1952; van Diggelen, 1959). Phase curves for various features were determined by measuring their brightness on photographs of the Moon at different phases. Gehrels *et al.* (1964) measured such phase curves by using photomultipliers in the focal plane of a telescope and thus documented the reality of the opposition effect. Willey and Pohn (1964) also produced phase curves using photoelectric photometry, and they discounted the apparent results, obtained from early photographic work, that not all lunar features peaked in brightness at zero phase.

Because Earth-based measurement of the Moon's brightness cannot be made exactly at zero phase, measurements of the phase curve for nonzero angles must be extrapolated to the maximum value. The heiligenschein surge at low phase angles makes that extrapolation difficult. However, photography from the orbiting Apollo Command Module has captured the zero phase point in some instances. Photographic measurements of the brightness surge between phase angles of 1.5° and 0° (Pohn *et al.*, 1969; Willey and Pohn, 1969) show a variability, ranging from albedos of 7% at the Apollo 11 site to 19% at a site in highland terrain.

Saari and Shorthill (1967), also using a photomultiplier tube, scanned the image of the Moon in the focal plane of a telescope and produced digitized images of the illuminated Moon at successive phases throughout a lunation. In principle, this dataset can be used to produce phase curves for any visible lunar feature. Although this has been done for a limited

number of locations, the report is not widely available, and the method has not yet been widely applied.

Hapke (1963) developed the first theoretical model that adequately accounted for the lunar photometric function. A later reformulation of the theory (Hapke, 1981, 1984) is widely accepted as the definitive model for reflectance from planetary surfaces. Hapke (1963) bases his formulation on the two-stream solution of the radiative transfer equation, applied to a medium composed of widely dispersed particles externally illuminated by a beam of radiation. He corrected the obtained solution to account for actual contiguity of the particles on a real surface and the resultant shadowing of deeper particles by particles in the upper layers. He also utilized an observation by Irvine (1966) that photons penetrating the medium to illuminate a particle can always escape unattenuated if they happen to scatter back along the path of incidence. These unattenuated backscattered photons produce the opposition effect, and the range of near-zero phase angles over which the brightening occurs is a measure of the ratio of the mean spacing between particles of the lunar surface layer to the mean free path of photons within the individual solid particles themselves.

The *bidirectional reflectance* is the ratio of the radiance (or luminance) received by a detector viewing a surface from a specific direction *e* (the *emission angle*) to the radiance (or luminance) from the source, assumed to be illuminating the surface from a direction *i* (*incidence angle*). Hapke's expression for the bidirectional reflectance function (Hapke, 1981, equation 16) is

$$r(\mu_0, \mu, g) = \left(\frac{w}{4\pi} \right) \cdot \left(\frac{\mu_0}{\mu_0 + \mu} \right) \cdot \{ [1 + B(g)]P(g) + H(\mu_0)H(\mu) - 1 \}$$

(where $\mu_0 = \cos i$, the direction cosine for the incident beam; $\mu = \cos e$, the direction cosine for the emerging beam; g = the phase angle; w = the single scattering albedo for a particle; $P(g)$ = the particle phase function normalized so that its surface integral over a sphere equals 4π ; $H(\mu) = [1+2\mu]/[1+2\mu(1-w)^{1/2}]$; and $B(g)$ = the backscatter function for the opposition effect = $B_0\{1 - \tan |g| [3 - \exp(-h/\tan |g|)] [1 - \exp(-h/\tan |g|)]/2h\}$ for $|g| \leq \pi/2$, and $B(g) = 0$ for $|g| > \pi/2$. B_0 is an empirical factor $\approx \exp(-w^2/2)$; h is a parameter depending on particle spacing and has a value approximately equal to 0.4 for lunar soils.

This bidirectional reflectance function is used widely by astronomers and other scientists for remote sensing of planetary surfaces from space-

craft. For such observations, the resolution element on the planetary surface can range from tens of meters to several kilometers across. The terrain may contain craters, mounds, and other topographic features that cause the direction of the local surface normal to vary within a single resolution element. When this happens, local angles of incidence and emission will also vary. When $i > \pi/2$, an area will lie in shadow; when $e > \pi/2$, an area will be on the backside of a slope and invisible to the observer. In addition, one feature may block the view of another. All these conditions associated with macroscopic roughness lead to errors in the predictions of the model. The errors are particularly large when astronomers observe the limb regions of a planet or when spacecraft sensors point to surface regions lying near the horizon.

Hapke (1984) derived an expression for correcting any photometric function for the effects of roughness. The correction works quite well, as he demonstrated. Application of the correction is not difficult, but the explanation is too lengthy to reproduce here. The interested reader will find it discussed in detail in the original paper.

Albedo. The *spherical albedo* or *Bond albedo* is the fraction of sunlight reflected by a planet in all directions. For the Moon, the actual value will depend on which side is illuminated. The values discussed here refer to the Earth-facing hemisphere, or nearside, which contains most of the dark maria.

The Bond albedo of a planet is difficult to measure, and astronomers historically have derived it from measurements of a related quantity, the *geometrical albedo* (p). The geometrical albedo is the ratio of the radiance from a planet at zero phase (e.g., full Moon) to that of a perfectly diffusing planar surface (Lambert reflector) located at the same distance from the sun and normal to the incident radiation (*Kaula*, 1968, p. 260). The geometrical albedo is related to the spherical (Bond) albedo (A) by the simple relationship $A = pq$, where q , the phase integral, is given by

$$q = \int_0^\pi \Phi(g) \sin g \, dg$$

The phase angle g is the angle between the sun and the Earth as seen from the planet, and the phase function Φ describes the variation of brightness of a planet over the range of possible phase angles. The value of the phase integral can be obtained by calculating the area under the phase curve, the plot of $\Phi(g)$. For the Moon the function Φ can be derived from the *Hapke* photometric function. Values quoted in the literature for the phase integral are derived from Earth-based measurements of moonlight.

Finally, the reflectance of a surface element viewed normally (i.e., along the surface normal) at zero phase angle relative to the ideal white diffusing plate is called the *normal albedo* (*Minnaert*, 1961, p. 218). When the angles $i = e = 0$ are substituted into *Hapke's* formula, the result is the normal albedo. The value of the normal albedo for an area of lunar surface will depend on the local chemical and mineralogical composition, particle size, packing density, etc. In general, crater ray systems are the brightest features on the Moon, and highland areas are brighter than maria.

For lunar surface materials, the brightness of any area, observed from the Earth at full Moon (zero phase), yields a value that is virtually that of the normal albedo for that area, irrespective of the orientation of the surface normal to the direction of illumination. However, the formal definition of normal albedo requires the surface element to be illuminated normally.

Maps of the Moon showing the normal albedo of surface features have been produced by *Pohn and Wildey* (1970) and *Wildey* (1978). The earlier map is based on a carefully calibrated full Moon photograph (phase angle = 1.5°) that was digitized by a scanning microdensitometer. The resulting contours of equal film density were converted to radiance using photoelectric observations of a network of lunar surface features, taken at the same time as the photographic exposure. However, as discussed earlier, no photograph of the Moon from Earth can exhibit exact zero phase, and these studies therefore do not rigorously provide the true normal albedo of lunar features.

In the later work, *Wildey* (1978) digitized a series of photographs taken over a range of phase angles between 2.5° and 4.0° . By fitting a parametric function to the data as a function of phase, he was able to extrapolate to develop a lunar "image" of ideal normal albedo as well as a corollary image representing the magnitude of the heiligenschein effect across the nearside of the Moon.

The mapping of lunar surface brightness during a lunation (*Saari and Shorthill*, 1967) included an image taken at a phase angle of -2° , which is, in essence, a map of normal albedo. The data were collected using a photomultiplier to scan the lunar image in the focal plane of the telescope.

Dollfus and Bowell (1971) studied measurements of normal albedo in 9 different reports and derived a best estimate of this quantity for 67 lunar regions; the albedo for these regions ranges from 5.7% to 18.4%.

Single scattering albedo. Modern formulations of reflectance from planetary surfaces are based on the concepts of radiative transfer theory (e.g., *Hapke*,

1981). The fundamental transport equation invokes a hypothetical volume element within the surface that, when illuminated by a pencil of radiation from an arbitrary direction, absorbs a fraction of it and scatters the remainder in various directions relative to the incident direction. The fraction absorbed (*absorption coefficient*), the fraction scattered (*scattering coefficient*), and the distribution function for the scattered component are all parameters in the solution to the transport equation. The *single scattering albedo* is the ratio of the scattering coefficient to the sum of the scattering and absorption coefficients.

In the Mie theory, scattering and absorbing particles are ideal dielectric spheres. In such a situation, the single scattering albedo is related to the physical properties of the material and the size of the particles relative to the wavelength of the radiation. The derivation of the basic radiative transport equation further assumes that the scattering centers in the medium are well separated so that they interact independently with the radiation field. Although the more complicated structure of a real planetary surface violates these assumptions, the Mie theory works well within the limits of various approximations that must be applied to the real problems.

Unfortunately, the considerable unreality of these same approximations blurs the physical meaning of the single scattering albedo values that are derived from applying the theory to actual reflectance measurements. For example, values obtained by fitting *Hapke's* (1981) function to phase curves for lunar regions can be used only for intercomparison with other lunar or planetary data or with laboratory measurements on lunar soils and analogue materials.

Polarization. Sunlight is unpolarized. In other words, the oscillations of the electric and magnetic vectors of the light waves in sunlight are not preferentially aligned in any particular direction. If sunlight is transmitted through a polarizer, its intensity after transmission does not depend on the rotation angle of the polarizer.

If sunlight is reflected from a smooth surface in some direction other than back along the surface normal, the reflected light becomes at least partially plane polarized. (This is a familiar phenomenon associated with Fresnel reflection, and it explains why polaroid sunglasses are effective in reducing glare.)

The polarization of the reflected light is specified by two quantities: the percentage of the intensity attributable to the polarized component and the angle that the direction of the electric vector makes with the normal to the phase plane, i.e., the plane

that contains the incoming and reflected light rays. These quantities are called the *degree of polarization* and the *azimuth of polarization*, respectively.

Although the lunar surface is far from smooth at the dimensions (~0.4–1.0 μm) equivalent to optical wavelengths, moonlight nevertheless is partially polarized. The degree of polarization (P) is given by the relation

$$P = \frac{I_1 - I_2}{I_1 + I_2}$$

where I_1 is the intensity observed normal to the phase plane, and I_2 is the intensity parallel to it (*Dollfus*, 1961). If P is positive the azimuth is assumed to be 180° , while a negative value of P implies an azimuth of 90° . These simple definitions suffice for lunar polarimetry because *Lyot* (1929) discovered that the polarization of moonlight is coincident with the phase plane near full Moon, disappears around phase 23° , and then grows in magnitude but rotated 90° , perpendicular to the phase plane. Similarly, *Gehrels et al.* (1964) failed to find any gradual rotation of the plane of polarization; the polarization vector either lies within or normal to the phase plane. They also observed that the positive maximum in polarization of reflected light from the lunar surface was highest in the UV (0.36 μm), intermediate in the green (0.54 μm), and lowest in the near IR (0.94 μm).

Dollfus and Powell (1971) reviewed and discussed lunar polarization observations, presented new data, and elucidated the details of the polarization mechanism. For example, at a given wavelength, the negative branch of the curve, corresponding to phases of $0 \leq g \leq 23^\circ$, has approximately the same form for all lunar terrains. Similarly, the minimum value of the negative branch, P_{\min} , remains constant for all lunar regions, but it decreases from -10% (-10 parts per thousand) at a wavelength $\lambda = 0.325 \mu\text{m}$ to -12% at $\lambda = 1.050 \mu\text{m}$. The average value for all wavelengths is $P_{\min} = 11.2 \pm 0.3\%$ and $g(P_{\min}) = 9.6 \pm 0.6^\circ$.

On the positive branch of the polarization curve, corresponding to phases $\geq 23^\circ$, the maximum value of polarization (P_m) varies inversely with the albedo of the lunar terrain. The highest value noted for P_m is 350% for a dark mare region in Oceanus Procellarum at $\lambda = 0.325 \mu\text{m}$. However, regions of high albedo, such as highlands or young rayed craters, can display P_m values as low as 30% , a value measured at Aristarchus at $\lambda = 0.6 \mu\text{m}$. The phase angle of maximum polarization, $g(P_m)$, increases with P_m , but the correlation is independent of wavelength. This relation can be expressed by the equation

$$g(P_m) = 97.0 + 0.0517 P_m$$

where $g(P_m)$ is expressed in degrees and P_m in thousandths. *Dollfus and Bowell* (1971) note that uniform behavior of polarization across the entire observable lunar disk provides strong evidence that the properties of the microstructure of the upper lunar surface are remarkably uniform all across the Moon.

A fascinating correlation between the polarization maximum (P_m) and the normal albedo (λ) has also been discovered. The relation is given by

$$\log A = -(0.724 \pm 0.005)\log P_m - (1.81 \pm 0.02)$$

A similar relationship between geometric albedo (q) and the slope of the polarization curve at the inversion point has also been documented in later work (*Zellner et al.*, 1977). This latter correlation has proved to be particularly important in the determination of albedos of asteroids and other small bodies in the solar system. Based on both lunar sample measurements and lunar observations (*Bowell et al.*, 1973), the best-fit relation for the Moon is

$$\log p = -1.04 \log h - 1.88$$

where p is the geometric albedo for a lunar region and h is the inversion slope given in percent per degree. This relation is also consistent with one derived by *Veverka and Noland* (1973) from lunar data published by *Dollfus and Bowell* (1971) and *Dollfus et al.* (1971).

9.3.2. Radar Astronomy

Powerful radar installations built for military purposes during World War II were subsequently utilized in the postwar period to detect echoes reflected from the Moon. The first successful attempts in 1946 produced only marginal returned signals (*DeWitt and Stodola*, 1949), but rapid improvements in the technology soon made possible accurate ranging to the Moon, measurements of the Doppler shifts produced by lunar motions, the detection of Faraday rotation of the polarization vector of the signals in the Earth's ionosphere, the determination of the gross radar scattering law for the lunar surface, and estimates of the Moon's radar cross-section (*Evans*, 1962).

The transmitted radio signal can be pictured as a plane wave traveling from the antenna and striking the Moon. If the Moon behaves like a smooth dielectric sphere, the plane wave will strike it first at the point closest to the antenna—the *subradar point*. The only energy reflected back to the antenna would come from a small zone surrounding the subradar point, corresponding to the area of the first Fresnel zone of the wavefront. The remainder of the

incoming energy would be scattered by the rest of the Moon and would travel in other directions, according to the laws of specular reflection.

Most of the returned energy is observed to come from an area surrounding the subradar point. However, definite radar echoes can be detected from regions out to the lunar limb, implying that the lunar surface is not entirely smooth at radar wavelengths. For these reasons, radar reflection from the Moon is commonly described as “quasispecular,” because the strong central reflection only approximates the expected behavior of an ideally smooth spherical mirror.

Radar backscattering. The brightness (*cross-section*) of the subradar point is a measure of the dielectric constant of the lunar surface, while the shape of the trailing echo (*scattering function*) is a measure of the surface roughness and heterogeneity of the surface on the scale of the wavelength being used. The radar echo from the zone immediately around the subradar point is approximately three orders of magnitude stronger than the echo from the annular region at the lunar limb (*Thompson*, 1979).

Radar systems have the capability to transmit energy with a single mode of polarization and then to detect and analyze the returned energy in both the originally transmitted mode of polarization and the orthogonal mode. Commonly the transmitted signal is circularly polarized to minimize the effects of Faraday rotation during the signal's outward passage through the Earth's ionosphere. The process of reflection from an ideal dielectric sphere reverses the direction of circular polarization. When lunar radar observations are made, the energy returned with the direction of polarization to be expected from an ideal sphere is called *polarized*; the energy received in the other direction of polarization is called *depolarized*. A nonspecular component is also present in the polarized return; this component is qualitatively attributed to flat surfaces that happen to be tilted toward the radar. The depolarized return is attributed to the presence of surface rocks and surface roughness. Radar energy can penetrate a distance of 10 to 50 wavelengths into the extremely dry lunar regolith, allowing subsurface rocks, possibly as deep as several meters, to contribute to the radar reflections returned to Earth.

Although the strengths of the polarized and depolarized returns (echoes) are quite different near the subradar point, the falloff in the strengths of the two types of returns toward the limb regions exhibits somewhat similar behavior (*Hagfors*, 1967). Near the subradar point, the polarized echoes are quite strong, and they decrease sharply and nonuniformly with increasing angle of incidence from the subradar point ($i = 0^\circ$) outward to about $i = 35^\circ$. From about

$i = 35^\circ$ outward, the slope of the angular dependence becomes more gradual, varying as $\cos^{3/2}i$ out to approximately $i = 80^\circ$ (Evans and Hagfors, 1966). Beyond $i = 80^\circ$ to the limb ($0 = 90^\circ$), the dependence is proportional to $\cos i$. In contrast, the strength of the depolarized echo varies uniformly as $\cos i$ from the subradar point outward.

Although the lunar radar backscattering law is similar in form at all wavelengths, the fraction of power in the diffusely scattered component varies considerably, being much greater at higher frequencies (Hagfors, 1970). As a result, the lunar disk appears more uniformly bright when illuminated by the shorter radar wavelengths. Pettengill (discussion following Hagfors, 1970) points out that a plot comparing the lunar scattering laws is misleading when the plots are normalized to unity at the subradar point. Rather, it is more meaningful to scale the areas of the curves to be proportional to the total radar cross-sections at the corresponding wavelengths.

The form of the scattering law that is most widely used for studying the Moon and the inner planets is (Ostro, 1983)

$$\sigma_o(\phi) = 0.5 \rho \beta_{\text{rms}}^2 \times (\cos^4 \phi + \beta_{\text{rms}}^{-2} \sin^2 \phi)^{-3/2}$$

where σ_o is radar cross-section per unit area, ϕ is the angle of incidence, ρ is the Fresnel normal-incidence power reflection, and β_{rms} is the root-mean-square surface slope at wavelength-dependent scales. The theoretical basis for this model can be found in Hagfors (1964, 1970).

Radar cross-section. To understand the radar signal returned from the Moon, we use the basic radar equation that says

$$\begin{aligned} \text{Received Power} = \\ \text{Transmitted Power Density at the Moon} \times \\ \text{Backscatter Cross-Section of the Moon} \times \\ \text{Geometrical Attenuation on Return Path} \times \\ \text{Effective Antenna Aperture} \end{aligned}$$

For a transmitter of power P_t , the power density at the distance of the Moon, R , is given by $P_t G / 4\pi R^2$. The denominator of this expression is just the geometrical attenuation due to the familiar inverse-square law, and the antenna gain G can be related to the effective antenna aperture A by

$$G = 4\pi A / \lambda^2$$

where λ is the wavelength of observation. Combining these terms, we get an expression for received echo power P_r (Ostro, 1983)

$$P_r = P_t \frac{G^2 \lambda^2}{(4\pi)^3 R^4} \sigma$$

where σ is the radar cross-section of the Moon.

The radar *cross-section* σ has the dimensions of an area and is defined as the geometrical cross-section of a metallic sphere whose radar echo has the same strength as the Moon. We can relate this quantity to the physical parameters of the Moon by considering the Moon as an absorbing dielectric sphere of radius a . Following a derivation presented by Bohren and Huffman (1983, p. 120), we can write

$$\sigma / \pi a^2 = g\rho$$

where ρ is the Fresnel reflection coefficient of the dielectric material (Evans and Hagfors, 1964) and g is a gain factor equal to unity for our ideal sphere. Because the Moon is not ideally smooth, some of the returned signal comes from reflections outside the small region surrounding the subradar point. (This is the *diffuse component* of the polarized return.) Because the lunar surface is not perfectly absorbing, some of the returned echo comes from scattering within the surface. (This is the *depolarized component*.) For these reasons, g is larger than unity by some unknown amount.

The product $g\rho$ can be derived directly from observational data. If the gain factor can be independently calculated, then the dielectric constant (ϵ) of the lunar surface can be obtained from the relation

$$\rho = \frac{\sqrt{(\epsilon - 1)}}{\sqrt{(\epsilon + 1)}}$$

Attempts to calculate (Rea et al., 1964, 1965) or estimate (Evans and Hagfors, 1964) the gain factor have resulted in estimates of the dielectric constant, ϵ , given by Hagfors (1970). Further complications can be introduced into these calculations by assuming that the surface consists of layers with differing dielectric properties or that the dielectric properties vary smoothly with depth in some way (Hagfors, 1970), both of which assumptions are more apt to be more realistic representations of the actual lunar surface.

Bistatic radar observations. When spacecraft were placed into orbit about the Moon, it became possible to carry out *bistatic radar* experiments in which the transmitting and receiving antennas are in different places. In the lunar experiments, antennas on Earth could detect both the direct radio or radar transmissions from the spacecraft and the nearly simultaneous reflections of the signals from the lunar surface toward Earth. A small Doppler shift in the reflection wavelength relative to the transmission wavelength allows the two signals to be differentiated. The orbital motion of the radar-

sounding spacecraft causes the point of specular reflection to move across the lunar surface along the ground track. Careful measurement of the intensity and polarization of the returned signals yields information on the reflectivity of the lunar material, possible subsurface layering, and surface slopes (Tyler, 1968b).

The effective surface resolution element in these experiments corresponds to the first Fresnel zone associated with the quasispecular reflection. The size of this zone depends on the altitude of the spacecraft as well as on the surface slope distribution. For measurements made using Explorer 35 in 1967, the surface resolution was approximately 100 km (Tyler, 1968a). For the Apollo 14 and 15 experiments, the resolution elements varied from 10 to 40 km, depending on the nature of terrain overflown (Tyler and Howard, 1973).

During a pass over Oceanus Procellarum, the transmitted signal from Explorer 35 was maintained with its linear polarization lying approximately in the plane of incidence. A Brewster null in the reflected signal was observed at an angle of incidence of $60^\circ \pm 1^\circ$, a result corresponding to a dielectric constant of 3.0 ± 0.2 at a wavelength of 2.2 m (Tyler, 1968a). This measurement was made in mare material located north-northwest of Hansteen Crater, and the result corresponds to the dielectric properties of the surface material averaged over a depth of roughly $\lambda/8$ (25 cm). The reflectivity along groundtracks in Oceanus Procellarum showed quite reproducible enhancements of approximately 30% in echo intensity for mare regions compared to highland areas (Tyler, 1968b). These differences in reflectivity can be explained either by variations in the packing fraction of the regolith or by variations in its depth. The latter explanation appears more physically realistic if one also takes into account the results of Earth-based observations.

The Apollo 14 and 15 missions provided the opportunity to continue bistatic radar investigations at wavelengths of 13 cm and 116 cm (Tyler and Howard, 1973). The signal-to-noise ratio and the surface resolution of these measurements were both an order of magnitude better than previous experiments of the same type. Although the extent of the datasets obtained was limited, the investigators found regions of the lunar surface whose physical properties could not easily be explained by simple models.

For $\lambda = 13$ cm, mare surfaces could be modeled well using a value of the dielectric constant $\epsilon = 3.1$, with few deviations observed. At $\lambda = 116$ cm, much of the mare could also be modeled simply with a similar dielectric constant, but in this case, considerable deviations from the simple characterization

were observed. No successful models for the structure and properties of the anomalous regions could be developed; the authors speculated that their data implied the existence of some frequency dispersive mechanism, such as layering in a high-loss dielectric medium.

In highland regions the longer wavelength (116 cm) data were fitted successfully to a model using a uniform dielectric interface with $\epsilon = 2.8$, a lower value for dielectric constant than that found in the maria. Observations at the shorter wavelength (13 cm) in the Apennine Mountains and in the central highland regions also yielded consistent results, but the data from units in the Palus Somni area and the rim of Mare Crisium could not be fitted with simple models at $\lambda = 13$ cm.

Since the polarization of returned radio signals can be determined, the echoes from the lunar surface also contain information about slopes and surface roughness. The complexity of both the surface and the physical mechanisms that alter the polarization of the signal permit only some general statements with any degree of confidence. In general, slopes in the highlands are higher than slopes in the maria. At $\lambda = 13$ cm, highland rms (root-mean-square) slopes range from 6° to 8° , while mare rms slopes range from 2° to 4° (Tyler and Howard, 1973). Although values derived from the 116-cm observations agree with the 13-cm data in the highlands, the mare values are only half as large as those derived from the 13-cm data. Apparently, small-scale roughness is larger in the maria.

Little work has yet been done on the lunar surface itself to verify the surface structures inferred from radar scattering behavior. A more technical discussion of these issues is found in Tyler (1979).

Apollo Lunar Sounder Experiment (ALSE). The ALSE was a three-channel, synthetic-aperture, orbital radar experiment operated during three orbits of the Apollo 17 mission to infer subsurface electrical conductivity structure, to profile lunar surface topographic variations, and to image the surface along the spacecraft ground track (Phillips et al., 1973a,b). In this experiment, a continuous series of short bursts of radar energy at three frequencies (5, 15, and 150 MHz) was directed from an instrument on the spacecraft toward the lunar surface, and the reflections, received by the same instrument, were measured in terms of intensity, time of arrival, and phase. The very low electrical loss characteristics of the lunar regolith permitted detection of echoes from subsurface features as well as from the surface itself.

Reduction of the ALSE data has been a very complex process, and analysis of the information has been hampered by two fundamental problems (Sharpton et al., 1984). First, the relatively weak

signals returned from subsurface reflectors are obscured by strong surface clutter. Second, time delays associated with signals from subsurface features cannot be unambiguously distinguished from those associated with surface features lying some distance from the ground track. These problems have been overcome to some extent in the data from flat mare regions by correlating reflections from adjacent ground tracks. This correlation allows discrimination between subsurface layers and long linear surface features, which coincidentally parallel the orbital path and produce reflections at a distance from it (Peeples *et al.*, 1978).

Thus far, reflecting subsurface layers have been detected with confidence in both Mare Serenitatis and Mare Crisium. The placement and extent of the reflectors beneath Mare Serenitatis have been used to infer the geological history of the basin (see Fig. 4.31) (Maxwell, 1978; Sharpton and Head, 1982), illustrating the potential of the information in the ALSE dataset.

Range data from the ALSE was used (W. E. Brown *et al.*, 1974) to produce continuous elevation profiles around the Moon. These profiles, which extended along nearly two complete lunar orbits, were constructed from sampling at intervals of about

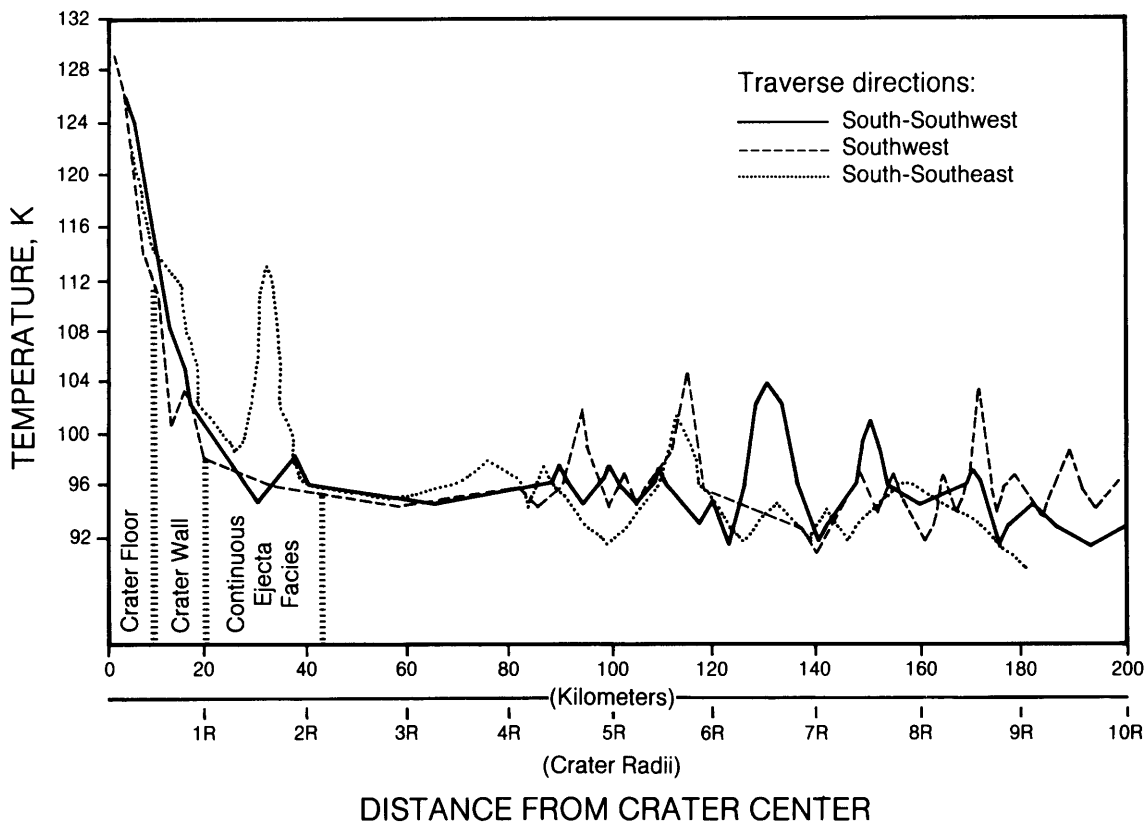


Fig. 9.77. Temperature profiles across Aristarchus Crater, a large central-peak crater emplaced in a mare region. Temperatures were determined from Earth-based thermal infrared measurements. Profiles originate at the center of the crater and traverse the crater in the directions indicated (southwest, south-southwest, and south-southeast). The higher pre-sunrise temperatures of the center indicate that much of the crater interior consists of large blocks of exposed bedrock. The nighttime temperatures fall significantly along the crater floor and are low but somewhat variable across the skirt of continuous ejecta around the crater. The ejecta deposits that occur beyond the limit of near-crater continuous ejecta and as far out as three crater radii (60 km) from the rim have smooth and uniform temperature profiles, unlike the irregular mare surface that is exposed beyond the ejecta. From Schultz and Mendell (1978).

45 m along the orbital ground tracks. *Elachi et al.* (1976) later used these elevation profiles to derive diameter/depth ratios for small craters along the flight path and to study the topography of a few large craters. They also published very accurate (better than ± 25 m in elevation) profiles of Mare Crisium and Mare Serenitatis.

9.3.3. Thermal Infrared Astronomy

The emission of thermal IR ($\lambda = 3\text{--}15\ \mu\text{m}$) radiation from the darkened Moon provides information on heat retention as the lunar surface cools during the two-week-long lunar night. An IR scanning radiometer was operated in the orbiting command module during the Apollo 17 mission. This instrument collected data on lunar surface emissions in the wavelength range from $1.2\ \mu\text{m}$ to about $70\ \mu\text{m}$. The Apollo 17 instrument was capable of resolution on the scale of a 2.2-km-diameter circle on the surface immediately beneath the spacecraft. However, since the collecting mirror on the instrument rotated at right angles to the flight path, the resolvable area degenerated into an ellipse toward the lateral horizons (*Mendell and Low, 1975*). The useful scanned area was within a band of $\pm 6^\circ$ of the command module's orbital latitude. Compared to IR observations made from Earth, which have lunar surface resolutions no better than 20 km and also suffer from atmospheric interference, the Apollo 17 data are an order of magnitude better (*Low and Mendell, 1973*).

The lunar nighttime surface temperature falls from about 100 K at the antisolar meridian to about 90 K at the sunrise terminator. Superimposed on this general nighttime cooling, however, are many "hot spots" that cool more slowly and therefore retain more of their heat during the lunar night. There is a strong correlation between the locations of these

hot spots and the interiors of fresh craters, where large blocks are exposed (*Mendell, 1976*). In a pulverized regolith, composed of small particles and having a large ratio of surface area to particle mass, absorbed heat is lost more rapidly than from large blocks or from outcrops with a small ratio of surface area to mass. *Winter (1970)* showed that rocks smaller than 30 cm tend to have thermal losses just like soil, but rocks larger than 10 m retain heat as if they were solid outcrop.

The most significant result from the Apollo 17 IR radiometer is that its data can be used to provide estimates of minimum large-block sizes and abundances in the centers of young craters. In Aristarchus Crater, for example, the temperature in the crater center just a few hours before sunrise is as high as 120–130 K, whereas the crater walls and the surrounding plains are about 100 K (Fig. 9.77; *Mendell, 1976*; *Schultz and Mendell, 1978*). The thermal retention in Aristarchus is too great to be modeled, even by 3-m blocks, and the thermal behavior is more consistent with a model in which about 11% to 16% of the crater interior is outcrop. Similar extreme temperature differences were recorded in the central peak area of Copernicus Crater. In addition, some smaller fresh craters have heat-retentive rims (e.g., Bessarion A and B Craters; *Mendell and Low, 1975*). Both these central and marginal thermal anomalies disappear in older craters, and this loss of large blocky exposures or outcrops that retain heat can be used as another measure of crater age (see Chapters 4 and 10).

Thermal IR mapping may be a practical method for locating lunar outcrops of large blocks or solid rock. These data would supplement the information on mineralogic composition that would be obtained from shorter wavelength near-IR spectroscopy (Chapter 10).

APPENDIX
SUPPLEMENTARY DATA ON LUNAR PHYSICAL PROPERTIES
(Tables A9.1–A9.16; Figs. A9.1–A9.9)

TABLE A9.1. Particle size distributions of Apollo 17 soils (after *McKay et al.*, 1974), with graphical size parameters (after *Folk and Ward*, 1957); (1) <1-cm data, (2) <1-mm data only.

Sample		Median Grain Size		Graphic Mean		Inclusive Graphic Standard Deviation	Inclusive Graphic Skewness	Graphic Kurtosis
		$M_d \phi$	$M_d \mu\text{m}$	$M_z \phi$	$M_z \mu\text{m}$	$\sigma_1 \phi$	SK_1	K_0
1. 70161,1	(1)	3.91	66.5	3.89	67.5	2.03	-0.06	1.06
	(2)	4.01	62.1	4.08	59.1	1.76	-0.06	0.92
2. 70181,1	(1)	3.93	65.6	3.91	66.5	2.07	-0.08	1.07
	(2)	4.10	58.3	4.12	57.5	1.74	+0.03	0.88
3. 71041,1	(1)	3.58	83.6	3.13	114.2	2.92	-0.27	1.20
	(2)	4.08	59.1	4.15	56.3	1.83	+0.03	0.94
4. 71061,1	(1)	3.13	114.2	2.56	169.6	3.33	-0.25	0.81
	(2)	4.15	56.3	4.11	57.9	1.96	-0.03	0.85
5. 71501,1	(1)	3.75	74.3	3.60	82.5	2.24	-0.16	1.07
	(2)	3.95	64.7	3.94	65.1	1.84	-0.02	0.93
6. 72141,1	(1)	4.35	49.0	4.13	57.1	2.08	-0.18	0.97
	(2)	4.42	46.7	4.31	50.4	1.90	-0.11	0.92
7. 72141,15	(1)	4.40	47.4	4.30	50.8	2.12	-0.12	0.96
	(2)	4.41	47.0	4.45	45.8	1.87	+0.01	0.86
8. 72321,7	(1)	4.40	47.4	4.24	52.9	1.98	-0.16	1.01
	(2)	4.51	43.9	4.40	47.4	1.81	-0.11	0.94
9. 72441,7	(1)	4.18	55.2	3.94	65.1	2.25	-0.22	0.95
	(2)	4.38	48.0	4.23	53.3	1.86	-0.11	0.85
10. 72461,5	(1)	3.95	64.7	3.65	79.7	2.26	-0.26	0.91
	(2)	4.22	53.7	4.03	61.2	1.84	-0.18	0.83
11. 72501,1	(1)	4.07	59.5	3.90	67.0	2.26	-0.15	0.88
	(2)	4.27	51.8	4.14	56.7	1.99	-0.09	0.82
12. 72501,29	(1)	4.11	57.9	3.95	64.7	2.13	-0.17	0.94
	(2)	4.30	50.8	4.18	55.2	1.80	-0.10	0.81
13. 72701,29	(1)	4.17	55.6	4.02	61.6	2.12	-0.16	0.94
	(2)	4.30	50.8	4.20	54.4	1.87	-0.09	0.84
14. 73121,10	(1)	4.18	55.2	3.96	64.2	1.99	-0.19	0.85
	(2)	4.30	50.8	4.11	57.9	1.81	-0.15	0.81
15. 73141,4	(1)	3.81	71.3	3.49	89.0	2.44	-0.23	0.88
	(2)	4.20	54.4	3.99	62.9	1.93	-0.16	0.80
16. 73141,12	(1)	4.00	62.5	3.74	74.8	2.62	-0.19	0.92
	(2)	4.32	50.1	4.26	52.2	2.09	-0.06	0.81
17. 73221,1	(1)	3.82	70.8	3.39	95.4	2.66	-0.26	0.82
	(2)	4.29	49.0	3.96	64.2	2.20	-0.25	0.88
18. 73241,9	(1)	3.62	81.3	2.98	126.7	3.34	-0.28	0.84
	(2)	4.49	44.5	4.29	51.1	2.18	-0.12	0.88
19. 73261,1	(1)	4.00	62.5	3.53	86.6	2.70	-0.27	0.82
	(2)	4.52	43.6	4.17	55.6	2.16	-0.24	0.88
20. 73281,1	(1)	4.00	62.5	3.48	89.6	2.93	-0.31	0.97
	(2)	4.56	42.4	4.36	48.7	1.97	-0.14	0.79
21. 74001,2	(2)	4.53	43.3	4.47	45.1	1.63	-0.07	0.89
22. 74001,10	(2)	4.51	43.9	4.67	39.3	1.69	+0.10	0.91

TABLE A9.1. (continued).

Sample		Median Grain Size		Graphic Mean		Inclusive Graphic Standard Deviation	Inclusive Graphic Skewness	Graphic Kurtosis
		$M_d \phi$	$M_d \mu\text{m}$	$M_z \phi$	$M_z \mu\text{m}$	$\sigma_1 \phi$	SK_1	K_0
23. 74121,12	(1)	4.35	49.0	4.22	53.7	1.95	-0.14	0.92
	(2)	4.45	45.8	4.36	48.7	1.76	-0.09	0.84
24. 74220,6	(2)	4.60	41.2	4.57	42.1	1.58	-0.01	0.93
25. 74220,82	(2)	4.73	37.7	4.65	39.8	1.52	-0.08	0.87
26. 74240,6	(1)	3.38	96.1	2.91	133.0	2.95	-0.23	0.83
	(2)	4.08	59.1	3.93	65.6	2.16	-0.13	0.89
27. 74241,61	(1)	3.50	88.4	3.04	121.6	3.05	-0.21	0.93
	(2)	4.13	57.1	4.15	56.3	2.06	-0.01	0.92
28. 74260,5	(1)	3.53	86.6	2.98	127.0	3.45	-0.30	1.05
	(2)	4.29	51.1	4.17	55.5	2.15	-0.09	0.93
29. 75061,2	(1)	3.12	115.0	2.97	127.6	2.57	-0.17	1.30
	(2)	3.48	89.6	3.63	80.8	1.74	+0.15	0.95
30. 75081,1	(1)	3.58	83.6	3.53	86.6	2.38	-0.09	1.08
	(2)	3.85	69.3	3.91	66.5	1.97	+0.04	0.92
31. 75081,36	(1)	3.66	79.1	3.61	81.9	2.31	-0.12	1.08
	(2)	3.93	65.6	4.00	62.5	1.84	+0.04	0.88
32. 76241,24	(1)	3.80	71.8	3.32	100.1	2.93	-0.28	0.96
	(2)	4.38	48.0	4.25	52.6	2.05	-0.13	0.90
33. 76261,26	(1)	3.75	74.3	3.53	86.6	2.67	-0.19	0.99
	(2)	4.17	55.6	4.12	57.5	2.02	-0.06	0.83
34. 76281,6	(1)	3.82	70.8	3.54	86.0	2.80	-0.19	0.92
	(2)	4.32	50.1	4.24	52.9	2.14	-0.09	0.86
35. 76321,10C	(1)	4.02	61.2	3.85	69.3	2.36	-0.19	1.02
	(2)	4.29	51.1	4.24	52.9	1.86	-0.05	0.85
36. 76501,1	(1)	4.20	54.4	3.90	67.0	2.41	-0.24	1.04
	(2)	4.42	46.7	4.29	51.1	1.90	-0.09	0.88
37. 77531,1	(1)	4.24	52.9	3.99	62.9	2.36	-0.23	1.10
	(2)	4.46	45.4	4.36	48.7	1.90	-0.12	0.94
38. 78221,8B	(1)	4.50	44.2	4.31	50.4	1.94	-0.20	0.97
	(2)	4.62	40.7	4.47	45.1	1.74	-0.13	0.91
39. 78421,1	(1)	4.58	41.8	4.45	45.8	2.04	-0.15	1.03
	(2)	4.69	38.7	4.62	40.7	1.79	-0.06	0.92
40. 78501,1	(1)	4.92	33.0	4.57	42.1	2.26	-0.34	1.16
	(2)	5.15	28.2	4.89	33.7	1.74	-0.23	0.91
41. 79221,1	(1)	4.00	62.5	3.47	90.2	2.70	-0.34	1.01
	(2)	4.42	46.7	4.23	53.2	1.93	-0.19	0.94
42. 79261,1	(1)	3.46	90.9	3.00	125.0	2.88	-0.27	0.86
	(2)	4.11	57.9	3.84	69.8	2.18	-0.23	0.97

TABLE A9.2. Particle shapes: Elongation.

<i>(a) After Mahmood et al. (1974b)</i>										
Sample		Weight of Sample	Weighted Average Elongation							
(1)=14163,148		0.97 g	1.38							
(2)=14259,3		1.26 g	1.31							
(3)=15601,82		0.96 g	1.39							
Fraction		Percent of Sample by Weight			Number of Particles Measured			Elongation (length/width)		
μm	Sieve Nos.	(1)	(2)	(3)	(1)	(2)	(3)	(1)	(2)	(3)
2360-850	8-20	2.3	0.7	3.1	10	6	10	1.38	1.38	1.42
850-425	20-40	6.1	5.8	6.7	18	11	30	1.35	1.27	1.33
425-150	40-100	17.7	22.7	23.2	31	37	115	1.34	1.28	1.38
150-74	100-200	14.2	11.0	20.2	102	181	146	1.31	1.36	1.42
74-45	200-325	12.2	29.9	14.5	-	158	267	-	1.32	1.39
45-	325-	49.5	29.9	32.3	-	14	-	-	1.31	-
					Σ 161	407	568			

(b) After Heywood (1971)

Sample 12057,72: 30 particles with projected area diameter, d_a , of 700 μm

Shape Coefficient	Range
Elongation, n	1.32-1.38
Flatness, m	1.17-1.37
Area ratio, α_a	0.70-0.74
Volume coefficient, $\alpha_{v,a}$	0.32-0.35
Rugosity coefficient, r	1.04-1.10
Specific circularity of profile, ϕ^*	0.93
Specific circularity including effect of rugosity, ϕ_r^*	0.84-0.90

where

n	=	L/B
m	=	B/T
α_a	=	$\pi d_a^2/4LB$
$\alpha_{v,a}$	=	volume of particle/ d_a^3
$\alpha_{v,a}$	=	$\frac{\pi^{3/2}}{8} \cdot \frac{p_r}{\alpha_a^{1/2}} \cdot \frac{1}{mn^{1/2}}$
r	=	perimeter of particle profile (including irregularities) divided by perimeter of smooth curve circumscribing particle profile
ϕ^*	=	$d_a(n+1)/2d_p n^{1/2}$
ϕ_r^*	=	ϕ^*/r
L	=	Length of particle
B	=	width
T	=	thickness ($L > B > T$)
d_a	=	projected area diameter
d_p	=	projected perimeter diameter
p_r	=	prismoidal ratio=mean thickness/ T

TABLE A9.3. Particle shapes: Aspect ratio (after Görz *et al.*, 1971, 1972).

Sample	Size Fraction (μm)	Aspect Ratio Mode (approx. 20% of particles)	Shape Complexity Factor	
			Range	Mode (approx. 80% of particles)
12001,1 (77)	3.2-6.1	0.3-0.4	not reported	
14163,158	1.2-30	0.6-0.7	0.05-1.25	0.75-1.0
15031,44	1.2-30	0.4-0.5	0.3 -1.75	0.75-1.0
15041,50	1.2-30	0.6-0.7	0.3 -1.25	0.75-1.0
15231,49	1.2-30	0.5-0.6	0.3 -1.25	0.75-1.0
15501,25	1.2-30	0.5-0.6 and 0.8-0.9 (bimodal)	0.55-1.25	0.75-1.0
15531,40	1.2-30	0.3-0.4 and 0.7-0.8 (bimodal)	0.6 -1.25	0.75-1.0

Aspect ratio = ratio of minor to major axes of fitted ellipse.

Shape complexity factor = ratio of particle perimeter to ellipse perimeter

> 1 highly angular and complex, with possible reentrant perimeter

= 1 smooth and not reentrant

< 1 regular particle, but not elliptical

TABLE A9.4. Particle shapes: Roundness (after Mahmood *et al.*, 1974b).

Sample	Weighted Average Roundness				Sample weights and size fractions given in Table A9.2.							
	Silhouette		Direct Light									
	Number	Class	Number	Class	Silhouette*			Direct Light†				
Fraction (μm)	Number of Particles Measured			Roundness			Number of Particles Measured			Roundness		
	(1)	(2)	(3)	(1)	(2)	(3)	(1)	(2)	(3)	(1)	(2)	(3)
(1)=14163,148	0.19	Subangular	0.20	Angular								
(2)=14259,3	0.26	Subangular	0.25	Angular								
(3)=15601,82	0.19	Subangular	0.22	Angular								
2360-850	10	6	10	0.16	0.21	0.14	5	7	7	0.20	0.18	0.20
850-425	18	11	30	0.17	0.21	0.14	36	26	14	0.18	0.17	0.17
425-150	31	37	115	0.19	0.25	0.12	124	98	75	0.19	0.21	0.20
159- 74	102	181	146	0.22	0.26	0.23	44	9	84	0.20	0.22	0.27
74- 45	-	158	267	-	0.29	0.23	12	-	-	0.20	-	-
45-	-	14	-	-	0.27	-	28	20	52	0.26	0.17	0.24

* Based on Wadell (1935) and Müller (1967).

† Based on Powers (1953).

TABLE A9.5. Particle shapes: Specific surface area of submillimeter samples (after *Cadenhead et al.*, 1977).

Sample No.	Specific Surface Area (m ² /g)	References
10084	0.59	<i>Gammage and Holmes</i> (1975)
12033	~0.02	<i>Fuller et al.</i> (1971)
12070	0.57	<i>Gammage and Holmes</i> (1975)
14003	0.51	<i>Holmes et al.</i> (1973)
14163,111	0.21	<i>Cadenhead et al.</i> (1972)
14259	0.61	<i>Grossman et al.</i> (1972)
15101,68	0.65	<i>Cadenhead and Jones</i> (1972)
15301	0.68	<i>Cadenhead et al.</i> (1977)
15401	0.48	<i>Cadenhead et al.</i> (1977)
15401	0.40	<i>Grossman et al.</i> (1972)
61221	0.78	<i>Cadenhead et al.</i> (1977)
61241	0.72	<i>Cadenhead et al.</i> (1977)
63321	0.43	<i>Gammage and Holmes</i> (1977)
63341	0.42	<i>Holmes et al.</i> (1973)
74220	0.42	<i>Holmes et al.</i> (1974)
74220	0.46	<i>Cadenhead</i> (1973)
75081	0.50	<i>Cadenhead et al.</i> (1977)

TABLE A9.6. Apollo core tube sample density data.

Core Tube Serial No.*	Sample No.	Returned Sample Weight (g)	Returned Sample Length (cm)	Returned Bulk Density [†] (g/cm ³)	Core Tube Depth (cm)	References
<i>Apollo 11</i>						
2007	10005	52.0	10.0	1.71	>25	<i>Carrier et al. (1971); Costes et al. (1969)</i>
2008	10004	65.1	13.5	1.59	<32	
<i>Apollo 12</i>						
2011	12027	-	17.4	-	~37	<i>Carrier et al. (1971); Scott et al. (1970)</i>
2010 } Double	12025	56.1	9.3	1.98	} 69	
2012 } Double	12028	189.6	31.8	1.96		
2013	12026	102.9	19.4	1.74	37	
<i>Apollo 14</i>						
2045 } Double	14211	39.5	7.5	1.73	13 [§] ; 64 [¶]	<i>Carrier et al. (1972a); Mitchell et al. (1971)</i>
2044 } Double	14210	169.7	31.9	1.75		
2022	14220	80.7	16.5	1.60	15 [§] ; <36 [¶]	
2043**	14230	76.0	~12.5	-	23/45	
<i>Apollo 15</i>						
2003 } Double	15008	510.1	28±1	1.36±0.05	} 70.1	<i>Carrier et al. (1972a); Mitchell et al. (1972a)</i>
2010 } Double	15007	768.7	33.9	1.69		
2007	15009	622.0	36.2	1.30 ^{††}	34.6	
2009 } Double	15011	660.7	29.2±0.5	1.69±0.03	} 67.6	
2014 } Double	15010	740.4	32.9	1.91 ^{††}		
<i>Apollo 16</i>						
2043 } Double	64002	584.1	31.7	1.40 ^{††}	} 65±6	<i>Mitchell et al. (1972b)</i>
2038 } Double	64001	752.3	33.9	1.66		
2029 } Double	68002	583.5	27.4	1.59	} 68.6±0.5	
2036 } Double	68001	840.7	34.9	1.80		
2034 [†]	69001	558.4	-	-	27.5±2	
2045 } Double	60010	635.3	32.3	1.47	} 71±2	
2054 } Double	60009	759.8	33.1	1.72		
2027 } Double	60014	570.3	28.8	1.48 ^{††}	} 70.5±1	
2032 } Double	60013	757.2	34.7	1.63		
<i>Apollo 17</i>						
2031 } Double	73002	429±4	21.8	1.60±0.10 ^{††}	} 70.6±5	<i>Mitchell et al. (1973a)</i>
2046 [†]	73001	809±4	34.9	1.73±0.01		
2035 } Double	74002	910±4	33.3	2.04±0.01	} 71±2	
2044 } Double	74001	1071.4	34.9	2.29		
2048	76001	711.6	34.5	1.57 ^{††}	37.1±0.5	
2037 } Double	79002	409.4	19.4	1.67 ^{††}	} 71±2	
2050 } Double	79001	743.3	31.9	1.74		
2052	70012	434.8	18.4	1.77	28±3 [¶]	

* These equipment numbers identified core tubes. Sample numbers were assigned after the mission in the Lunar Receiving Laboratory. See *Allton (1989)* for equipment descriptions and weights.

[†] CSVC (Core Sample Vacuum Container).

[†] Diameter of samples as follows: Apollo 11, 12, and 14: 1.97 cm; Apollo 15, 16, and 17: 4.13 cm.

[§] Depth before final driving (maximum depth that was photographed).

[¶] Crew estimate: No photograph taken.

** This core tube was driven twice: first on Cone Crater where some or all of the sample fell out; second at North Triplet Crater during the second attempt at a triple core, where some of the sample fell out.

^{††} Corrected for void.

TABLE A9.7. Apollo drill core sample density data.

Sample No.	Returned Sample Weight (g)	Returned Sample Length (cm)	Returned Bulk Density* (g/cm ³)	Drill Stem Depth (cm)	References†
<i>Apollo 15</i>					
15006	210.6	39.9	1.62	} 236±1	<i>Carrier (1974); Mitchell et al. (1972a)</i>
15005	239.1	39.9	1.84		
15004	227.9	39.9	1.75		
15003	223.0	39.9	1.79		
15002	210.1	39.9	1.62		
15001	232.8	37.0	1.93		
<i>Apollo 16</i>					
60007	105.7	22.2±0.5	1.46±0.03	} 224±3	<i>Carrier (1974); Mitchell et al. (1972b)</i>
60006	165.6	35.5±0.5	1.43±0.02		
60005	76.1	disturbed	-		
60004	202.7	39.9	1.56		
60003	215.5	39.9	1.66		
60002	211.9	} 42.5	} 1.75		
60001	30.1				
<i>Apollo 17</i>					
70009	143.3	25±2	1.76±0.14	} 305±1	<i>Carrier (1974); Mitchell et al. (1973a)</i>
70008	260.9	38	2.11		
70007	179.4	34±2	1.62±0.10		
70006	234.2	39.9	1.80		
70005	240.6	39.9	1.85		
70004	238.8	39.9	1.84		
70003	237.8	39.9	1.83		
70002	207.7	} 42.0	} 1.74		
70001	29.8				

* Diameter of samples equals 2.04 cm.

† Also see *Allton and Waltz (1980)* for additional details.

TABLE A9.8. Relative density based on vehicle track data (depth = 0–15 cm).

(a) Average material properties based on Lunokhod 1 (Luna 17); Modular Equipment Transporter (Apollo 14); and Lunar Roving Vehicle (Apollo 15–17). After Costes (1973); Mitchell *et al.* (1973a, 1974).

Location	Soil Consistency	*Penetration Resistance	Relative Density, D_R (%)	
		Gradient, G (N/cm ³)	†	‡
Intercrater Areas	Firm	0.76–1.35	48–63	62–71
Crater Rims	Soft	0.15 (minimum)	30	38

(b) Average material properties based on Modular Equipment Transporter (Apollo 14). After Mitchell *et al.* (1971).

Location	Local Topography	Wheel Sinkage, z (cm)	*Penetration Resistance Gradient, G (N/cm ³)	‡Relative Density D_R (%)
Immediate vicinity of LM	Level, firm	1.3–2.0	1.7–1.0	72–65
	Soft spots	3.8–5.1	0.63–0.40	58–52
ALSEP site	Level, firm	1.3–2.5	1.7–0.87	72–63
Between LM and Station A; immediate vicinity of TV camera	Level, firm	1.3–1.5	1.7–1.3	72–68
A	Level, firm	0.5–1.3	4.7–1.7	86–72
	Crater rim	8.0	0.16	39
B	Level, firm	1.3–1.5	1.7–1.3	72–68
B1	Severe maneuver	5.1	0.40	52
B2	Level, firm	1.3–2.5	1.7–0.87	72–63
B2	Level, soft	2.5–5.1	0.87–0.40	63–52
B3	Level, firm	1.3–3.8	1.7–0.63	72–58
C	Level, firm	1.3–2.0	1.7–1.0	72–65
	Small hummock	2.5–7.6	0.87–0.16	63–39
C	Level, firm	1.3–2.5	1.7–0.87	72–63
	Small hummock	3.8	0.63	58
G	Level, firm	1.3–2.5	1.7–0.87	72–63
Average	Level, firm terrain	1.96	1.03	65
Average	Crater rims, soft spots	5.13	0.40	52

* Inferred average gradient of standard cone penetrometer with depth in lunar surface.

† Based on conversion of G to terrestrial gravity and correlations developed by Corps of Engineers for a variety of soils.

‡ Based on correlations with basaltic lunar soil simulant (Houston and Namiq, 1971).

TABLE A9.9. Compression data for lunar soils (one-dimensional oedometer).

Density, ρ (g/cm ³)	Void Ratio, e	Vertical Applied Stress, σ_v (kPa)	Compression Index, C_c
(a) After <i>Carrier et al.</i> (1972b, 1973c)			
Apollo 12, Sample No. 12001,119			
1.672	0.854*	~0.08	
1.733	0.789	4.41	0.038
1.762	0.759	13.98	0.060
<hr/>			
1.775	0.746	28.59	
1.797	0.725	48.02	0.093
<hr/>			
1.798	0.724	48.02	
1.815	0.708	67.51	0.108
<hr/>			
1.841	0.684	~0.09	
1.860	0.667	2.27	0.012
1.889	0.641	6.96	0.053
1.893	0.638	11.85	0.013
1.923	0.612	31.21	0.062
<hr/>			
1.91	0.62	1.93	0.03
1.94	0.60	11.56	0.05
1.96	0.58	30.95	0.09
1.99	0.56	50.40	0.07
2.00	0.55	69.92	
(b) After <i>Jaffe</i> (1973)			
Apollo 12, Sample No. 12029,8			
0.95	2.26*	0.049	} 0.21 (ave)
1.29	1.40	0.12	
1.38	1.25	0.51	
1.53	1.03	1.29	
1.58	0.96	3.1	
1.62	0.91	8.2	
1.60	0.94	28.0	
1.44	1.15	0.135	} 0.11 (ave)
1.44	1.15	0.27	
1.59	0.95	0.53	
1.53	1.03	1.3	
1.54	1.01	3.1	
1.59	0.95	5.6	
1.58	0.96	8.1	
1.66	0.87	13.0	
1.63	0.90	18.5	
1.64	0.89	28.0	
1.58	0.96	0.135	} 0.04 (ave)
1.62	0.91	0.53	
1.64	0.89	3.1	
1.62	0.91	5.6	
1.68	0.85	28.0	

TABLE A9.9. (continued).

Density, ρ (g/cm ³)	Void Ratio, e	Vertical Applied Stress, σ_v (kPa)	Compression Index, C_c
(c) After Leonovich et al. (1974a, 1975)			
Luna 16			
1.03	1.770 [†]	~0.05	
1.03	1.763	0.1	0.02
1.03	1.757	0.2	0.02
1.04	1.738	0.5	0.05
1.05	1.706	1.0	0.11
1.08	1.647	2.0	0.20
1.14	1.491	5.0	0.39
1.24	1.293	10.0	0.66
1.39	1.053	20.0	0.80
1.55	0.840	50.0	0.54
1.58	0.810	100.0	0.10
(d) After Leonovich et al. (1974a, 1975)			
Luna 20			
0.99	1.890 [†]	~0.05	
0.99	1.880	0.1	0.03
0.99	1.870	0.2	0.03
1.00	1.842	0.5	0.07
1.02	1.796	1.0	0.15
1.05	1.710	2.0	0.29
1.08	1.631	3.0	0.45
1.11	1.559	4.0	0.58
1.14	1.494	5.0	0.67
1.20	1.380	7.0	0.78
1.27	1.243	10.0	0.88
1.44	0.984	20.0	0.86
1.57	0.821	50.0	0.41
1.57	0.810	100.0	0.04

* Specific gravity of 3.1 assumed.

† Specific gravity of 2.85 assumed.

TABLE A9.10. Recompression data for lunar soil (one-dimensional oedometer).

Density, ρ (g/cm ³)	Void Ratio, e^*	Vertical Applied Stress, σ_v (kPa)	Recompression Index, C_r
(a) After <i>Carrier et al.</i> (1972b, 1973c)			
Apollo 12, Sample No. 12001,119			
1.762	0.759	14.0	0.002
1.758	0.763	~0.08	0.001
1.759	0.762	4.2	0.003
1.760	0.761	9.1	
1.797	0.725	48.0	0.000
1.797	0.725	28.4	0.006
1.794	0.728	8.9	0.002
1.795	0.727	28.4	0.013
1.798	0.724	48.0	
(b) After <i>Jaffé</i> (1973)			
Apollo 12, Sample No. 12029,8			
1.70	0.82	0.052	} 0.000 (ave)
1.70	0.82	0.53	
1.71	0.81	1.3	
1.71	0.81	3.1	
1.70	0.82	5.6	
1.68	0.85	8.1	
1.68	0.85	18.5	
1.68	0.85	28.0	
1.87	0.66	0.042	} 0.003 (ave)
1.88	0.65	0.142	
1.87	0.66	0.53	
1.80	0.72	1.3	
1.87	0.66	3.1	
1.86	0.67	5.6	
1.88	0.65	13.0	
1.86	0.67	28.0	

*Specific gravity of 3.1 assumed.

TABLE A9.11. Laboratory hand-penetrometer measurements on lunar soil samples from Apollo 11 (sample no. 10084) (after *Costes et al.*, 1969, 1970a,b; *Costes and Mitchell*, 1970).

Test	Density (g/cm ³)	Force (N)	Area (cm ²)	Pressure (kPa)	Penetration (cm)
1	1.36	<1.8*	0.316	<57	0.64
2	1.36	<1.8*	0.316	<57	1.96
3	1.36	<1.8*	0.316	<57	1.96
4	1.36	<1.8*	0.316	<57	1.96
5	1.36	3.1	2.68	11.4	2.01
6	1.77	1.8	0.316	57	0.81
7	1.77	5.1	0.316	171	1.70
8	1.77	<1.8*	0.316	<57	0.64
9	1.77	9.8	0.316	308	2.54
10	1.77	5.8	0.316	183	2.11
11	1.77	38.7	2.68	143	1.70
12a	1.80	28.9	2.68	108	0.66 [†]
12b	1.80	79.8	2.68	297	1.96 [†]

* Penetrometer did not meet with sufficient resistance to compress the spring. Tabulated force is weight of penetrometer.

[†] Penetrometer was removed after achieving 108 kPa at 0.66 cm of penetration; it was applied again at the same place and pushed into the soil until the applied unit load reached the value 297 kPa at a penetration of 1.96 cm from the original surface of the sample.

TABLE A9.12. Penetrometer data on returned lunar soil from Apollo 12 (Surveyor 3 scoop sample) (sample no. 12029) (after *Jaffe*, 1971a).

Bulk Density (g/cm ³)	Bearing Capacity at Penetration = 1 Indentor Diameter (N/cm ²)	Remarks	Cracking and Bulging
1.15	0.038		No
1.18	0.027		No
1.22	0.038	6-mm cup diameter	—
1.26	0.021		No
1.42	0.048		No (minor bulging)
1.45	0.35		No
1.46	1.9		No
1.48	0.82		No
1.54	1.4		No
1.60	5.6	Extrapolation of stress-penetration curve; 6-mm cup	—
1.61	8.2		Yes
1.62	4.4		No
1.70	6.2		Yes
1.70	10		Yes
1.76	12.5	Extrapolation	Yes
1.79	>6.2	Extrapolation	Yes
1.80	16		Yes
1.82	11	Extrapolation	Yes
1.83	100	At yield	Yes
1.84	33		Yes
1.84	36		Yes
1.86	>6.2	Extrapolation	Yes
1.90	32		Yes
1.93	>6.2	Extrapolation	Yes

TABLE A9.13. Vacuum direct shear test data (Apollo 12, sample no. 12001,119) (after *Carrier et al.*, 1972b, 1973c).

Test No.	Void Ratio,* e	Vertical Stress, σ_v (kPa)	Peak Shear		Friction Angle,† ϕ
			Stress, τ (kPa)	τ/σ_v	
1	0.612	31.21	21.22	0.680	34°
1B	0.55	69.92	50.15	0.717	35°
2	0.708	67.51	36.30	0.538	28°

* At end of consolidation, but prior to shear; specific gravity of 3.1 assumed.

† For cohesion, $c = 0$ to 0.7 kPa.TABLE A9.14. Miniature direct shear test data on returned lunar soil from Apollo 12 (Surveyor 3 scoop sample) (after *Jaffe*, 1973).

Test Series	Initial Bulk Density* (g/cm ³)	Initial Void Ratio†	Cohesion, c (kPa)	Friction Angle, ϕ (deg)
1	0.99	2.12	0.3	13°
2	1.43	1.17	0.1	17°
3	1.60	0.94	0.5	19°
4	1.70	0.82	3.1	14°
5	1.87	0.66	2.8	56°

Test Series	Test Number	Vertical Stress, σ_v (kPa)	Peak Shear Stress, τ (kPa)
1	1	0.048	0.0068
	2	0.119	0.027
	3	0.525	0.17
	4	1.28	0.335
	5	3.25	0.96
	6	8.2	2.25
	7	28.0	6.9
2	1	0.032	0.0283
	2	0.135	0.059
	3	0.273	0.123
	4	0.52	0.325
	5	1.24	0.68
	6	3.13	0.96
	7	5.6	2.23
	8	7.9	2.5
	9	13.0	3.9
	10	17.8	4.8
	11	27.8	8.9
3	1	0.0325	0.029
	2	0.53	0.277
	3	3.2	1.65
	4	5.7	2.2
	5	28.5	9.4

TABLE A9.14. (continued).

Test Series	Test Number	Vertical Stress, σ_v (kPa)	Peak Shear Stress, τ (kPa)
4	1	0.54	0.84
	2	1.27	1.29
	3	3.15	3.15
	4	5.6	4.65
	5	8.05	5.85
	6	13.0	6.25
	7	17.0	7.3
	8	31.0	9.4
5	1	0.0415	0.535
	2	0.138	1.20
	3	0.52	1.85
	4	1.27	3.15
	5	3.10	8.20
	6	5.60	10.7
	7	10.3	19.2
	8	28.0	40.5

* Placement density, prior to consolidation.

† Specific gravity of 3.1 assumed.

TABLE A9.15. Miniature triaxial shear test data on returned lunar soil from Apollo 12 (Surveyor 3 scoop sample) (sample no. 12029,8) (after Scott, 1987, personal communication, 1988).

Void Ratio,* e	Confining Stress, σ_3 (kPa)	Peak Shear Stress, τ (kPa)	Axial Strain at Peak Shear Stress (%)	Friction Angle†, ϕ
0.69	26	157	5.3	59°
0.87	52-55	192	8.9	51°-52°

* At end of consolidation, but prior to shear; specific gravity of 2.9 measured.

† For cohesion, $c = 0$ to 1 kPa.

TABLE A9.16. Summary of dielectric properties of lunar samples.

Sample	ρ g/cm ³	MHz	*	k'	LossTan	%TiO ₂	%FeO	References (electrical; chemical)
10017	3.10	1.0	N	8.80	0.07500	11.74	19.82	<i>Katsube and Collett (1971); LSPET (1969)</i>
10020	3.18	1.0	AN	10.00	0.13000	10.72	19.35	<i>Chung et al. (1970); LSPET (1969)</i>
10022	3.10	450.0	A	4.17	0.13900	12.20	18.90	<i>Gold et al. (1971); Rose et al. (1970)</i>
10046	2.21	1.0	AN	9.00	0.05000	10.35	19.22	<i>Chung et al. (1970); LSPET (1969)</i>
10048	0.00	1.0	AN	3.85	0.12000	n.d.	n.d.	Olhoeft unpublished
10057	2.88	1.0	AN	11.00	0.10000	11.44	19.35	<i>Chung et al. (1970); Engel and Engel (1970a,b)</i>
10059	2.20	450.0	A	5.86	0.11000	7.63	16.16	<i>Gold et al. (1971); Goles et al. (1970a)</i>
10065	2.45	10.0	A	7.30	0.01900	7.35	15.79	<i>Katsube and Collett (1971); Goles et al. (1970a)</i>
10084	1.94	1.0	N	3.80	0.01750	7.56	15.94	<i>Katsube and Collett (1971); LSPET (1972)</i>
10084	1.01	450.0	A	1.80	0.01300	7.56	15.94	<i>Gold et al. (1970); LSPET (1972)</i>
10084	1.25	450.0	A	2.06	0.01700	7.56	15.94	<i>Gold et al. (1970); LSPET (1972)</i>
10084	1.57	450.0	A	2.45	0.02000	7.56	15.94	<i>Gold et al. (1970); LSPET (1972)</i>
12002	3.30	1.0	AN	9.00	0.05000	2.76	19.38	<i>Chung et al. (1971); Grove et al. (1973)</i>
12002	3.10	1.0	N	8.30	0.05100	2.76	19.38	<i>Katsube and Collett (1971); Grove et al. (1973)</i>
12002	3.04	1.0	N	7.80	0.05600	2.76	19.38	<i>Katsube and Collett (1971); Grove et al. (1973)</i>
12002	3.04	1.0	V	8.00	0.06500	2.76	19.38	<i>Olhoeft et al. (1973a); Grove et al. (1973)</i>
12022	3.32	1.0	AN	11.00	0.18000	4.90	21.70	<i>Chung et al. (1971); Brett et al. (1971)</i>
12033	1.19	450.0	A	1.79	0.01000	2.48	14.20	<i>Gold et al. (1971); Cuttitta et al. (1971)</i>
12033	1.40	450.0	A	2.08	0.01200	2.48	14.20	<i>Gold et al. (1971); Cuttitta et al. (1971)</i>
12033	1.72	450.0	A	2.52	0.01300	2.48	14.20	<i>Gold et al. (1971); Cuttitta et al. (1971)</i>
12063	2.90	450.0	A	6.87	0.08000	5.00	21.26	<i>Gold et al. (1971); Willis et al. (1971)</i>
12065	2.90	450.0	A	7.26	0.21000	3.80	22.00	<i>Gold et al. (1971); LSPET (1970)</i>
12070	1.74	1.0	N	3.00	0.02500	2.81	16.40	<i>Katsube and Collett (1973); LSPET (1972)</i>
12070	1.17	450.0	A	1.85	0.00880	2.81	16.40	<i>Gold et al. (1971); LSPET (1972)</i>
12070	1.24	450.0	A	2.02	0.01250	2.81	16.40	<i>Gold et al. (1971); LSPET (1972)</i>
12070	1.32	450.0	A	2.12	0.01210	2.81	16.40	<i>Gold et al. (1971); LSPET (1972)</i>
12070	1.40	450.0	A	2.15	0.01440	2.81	16.40	<i>Gold et al. (1971); LSPET (1972)</i>
12070	1.51	450.0	A	2.32	0.01410	2.81	16.40	<i>Gold et al. (1971); LSPET (1972)</i>
12070	1.80	450.0	A	2.98	0.01580	2.81	16.40	<i>Gold et al. (1971); LSPET (1972)</i>
14003	1.16	450.0	A	2.01	0.00420	1.77	10.45	<i>Gold et al. (1972); Rose et al. (1972)</i>
14003	1.55	450.0	A	2.60	0.00560	1.77	10.45	<i>Gold et al. (1972); Rose et al. (1972)</i>
14163	1.44	450.0	A	2.57	0.00510	1.77	10.41	<i>Gold et al. (1972); Rose et al. (1972)</i>
14163	1.80	450.0	A	3.28	0.00600	1.77	10.41	<i>Gold et al. (1972); Rose et al. (1972)</i>
14163	1.20	1.0	V	2.30	0.00060	1.79	10.35	<i>Strangway et al. (1972); LSPET (1972)</i>
14163	1.71	9375.0	AN	3.59	0.01500	1.79	10.35	<i>Bassett and Shackelford (1972); LSPET (1972)</i>
14163	2.06	9375.0	AN	4.45	0.01500	1.79	10.35	<i>Bassett and Shackelford (1972); LSPET (1972)</i>

TABLE A9.16. (continued).

Sample	ρ g/cm ³	MHz	*	k'	LossTan	%TiO ₂	%FeO	References (electrical; chemical)
14301	2.30	1.0	AN	4.80	0.05000	1.70	9.80	<i>Chung et al. (1972); LSPET (1971a)</i>
14301	2.17	1.0	AN	4.80	0.05000	1.70	9.80	<i>Chung et al. (1972); LSPET (1971a)</i>
14310	2.86	1.0	AN	6.00	0.02000	1.30	7.70	<i>Chung et al. (1972); LSPET (1971a)</i>
14310	2.81	9375.0	AN	6.46	0.00750	1.30	7.70	<i>Bassett and Shackelford (1972); LSPET (1971a)</i>
14310	3.30	1.0	AN	6.40	0.02000	1.30	7.70	<i>Chung et al. (1972); LSPET (1971a)</i>
14310	3.30	1.0	AN	7.00	0.01200	1.30	7.70	<i>Chung et al. (1972); LSPET (1971a)</i>
14310	2.76	450.0	A	6.58	0.00440	1.30	7.70	<i>Gold et al. (1972); LSPET (1971a)</i>
14318	2.30	1.0	AN	5.97	0.00820	1.46	9.50	<i>Chung et al. (1972); Rose et al. (1972)</i>
14321	2.40	1.0	AN	5.28	0.01230	2.40	13.00	<i>Chung et al. (1972); LSPET (1971a)</i>
14321	2.35	1.0	AN	5.90	0.01000	2.40	13.00	<i>Chung et al. (1972); LSPET (1971a)</i>
15001	1.75	450.0	A	2.73	0.00440	2.00	20.00	<i>Gold et al. (1977); Lindstrom et al. (1977b)</i>
15001	1.88	450.0	A	2.82	0.00510	2.00	20.00	<i>Gold et al. (1977); Lindstrom et al. (1977b)</i>
15003	1.33	450.0	A	2.19	0.00470	2.00	20.00	<i>Gold et al. (1977); Lindstrom et al. (1977b)</i>
15003	1.16	450.0	A	1.96	0.00430	2.00	20.00	<i>Gold et al. (1977); Lindstrom et al. (1977b)</i>
15021	1.30	450.0	A	2.13	0.00418	1.80	15.00	<i>Gold et al. (1973); Laul and Schmitt (1973b)</i>
15041	1.45	450.0	A	2.42	0.00486	1.70	14.20	<i>Gold et al. (1973); Laul and Schmitt (1973b)</i>
15065	2.86	1.0	N	6.70	0.01000	1.48	19.18	<i>Chung and Westphal (1973); LSPET (1971)</i>
15081	1.75	450.0	A	3.01	0.00536	1.58	15.28	<i>Gold et al. (1973); Duncan et al. (1975)</i>
15211	1.36	450.0	A	2.34	0.00389	1.34	11.66	<i>Gold et al. (1973); Cuttitta et al. (1973)</i>
15221	1.53	450.0	A	2.57	0.00274	1.27	11.32	<i>Gold et al. (1973); Cuttitta et al. (1973)</i>
15301	1.47	1.0	V	3.20	0.00080	1.17	14.05	<i>Olhoeft et al. (1974); LSPET (1972)</i>
15301	1.60	0.1	V	3.42	0.01220	1.17	14.05	<i>Frisillo et al. (1975); LSPET (1972)</i>
15301	1.62	0.1	V	3.49	0.01240	1.17	14.05	<i>Frisillo et al. (1975); LSPET (1972)</i>
15301	1.64	0.1	V	3.53	0.01250	1.17	14.05	<i>Frisillo et al. (1975); LSPET (1972)</i>
15301	1.68	0.1	V	3.58	0.01220	1.17	14.05	<i>Frisillo et al. (1975); LSPET (1972)</i>
15301	1.80	0.1	V	3.89	0.01250	1.17	14.05	<i>Frisillo et al. (1975); LSPET (1972)</i>
15301	1.83	0.1	V	3.98	0.01220	1.17	14.05	<i>Frisillo et al. (1975); LSPET (1972)</i>
15301	1.58	450.0	A	2.75	0.00438	1.17	14.05	<i>Gold et al. (1973); LSPET (1972)</i>
15401	1.82	450.0	A	3.16	0.00471	0.42	19.66	<i>Gold et al. (1973); Carusi et al. (1972)</i>
15415	2.70	1.0	N	4.20	0.00100	0.02	0.23	<i>Chung and Westphal (1973); LSPET (1972)</i>
15459	2.76	1.0	N	6.62	0.00500	0.91	9.40	<i>Chung and Westphal (1973); Hubbard et al. (1973)</i>
15498	2.40	450.0	A	5.38	0.00810	1.60	17.30	<i>Gold et al. (1973); Laul and Schmitt (1973b)</i>
15555	3.10	1.0	N	6.15	0.02520	2.26	22.47	<i>Chung and Westphal (1973); LSPET (1972)</i>
15597	2.84	450.0	A	6.16	0.00230	1.87	20.17	<i>Gold et al. (1973); Nava (1974)</i>

TABLE A9.16. (continued).

Sample	ρ g/cm ³	MHz	*	k'	LossTan	%TiO ₂	%FeO	References (electrical; chemical)
15601	1.95	450.0	A	3.22	0.00251	1.98	19.79	Gold et al. (1973); LSPET (1971b)
60002	1.21	450.0	A	2.05	0.00390	0.56	6.66	Gold et al. (1977); Nava et al. (1976)
60002	1.04	450.0	A	1.83	0.00330	0.56	6.66	Gold et al. (1977); Nava et al. (1976)
60005	1.12	450.0	A	1.96	0.00290	0.56	6.66	Gold et al. (1977); Nava et al. (1976)
60015	2.76	1.0	N	6.60	0.00020	0.06	0.35	Chung and Westphal (1973); Laul and Schmitt (1973b)
60017	2.32	450.0	A	5.64	0.00250	0.30	2.97	Gold et al. (1973); Rose et al. (1973a)
60025	2.10	450.0	A	4.69	0.00150	0.02	0.67	Gold et al. (1976); Rose et al. (1973a)
60025	2.10	1.0	N	5.00	0.00400	0.02	0.67	Katsube and Collett (1973); Rose et al. (1973a)
60501	1.26	450.0	A	2.14	0.00350	0.61	0.00	Gold et al. (1977); Rose et al. (1975)
60501	1.10	450.0	A	2.03	0.00320	0.61	0.00	Gold et al. (1977); Rose et al. (1975)
61016	2.79	1.0	N	7.82	0.01600	0.69	4.97	Chung and Westphal (1973); Rose et al. (1973a)
61500	1.14	450.0	A	2.00	0.00277	0.56	5.31	Gold et al. (1973); LSPET (1973a)
61500	1.49	450.0	A	2.58	0.00347	0.56	5.31	Gold et al. (1973); LSPET (1973a)
61500	1.91	450.0	A	3.55	0.00503	0.56	5.31	Gold et al. (1973); LSPET (1973a)
62235	2.78	1.0	N	6.52	0.00660	1.21	9.45	Chung and Westphal (1973); LSPET (1973a)
62240	1.38	450.0	A	2.41	0.00364	0.56	5.49	Gold et al. (1973); Rose et al. (1973a)
62240	1.71	450.0	A	3.11	0.00416	0.56	5.49	Gold et al. (1973); Rose et al. (1973a)
62240	1.92	450.0	A	3.30	0.00482	0.56	5.49	Gold et al. (1973); Rose et al. (1973a)
62241	1.34	1.0	V	2.40	0.00100	0.56	5.49	Sill et al. (1973); Rose et al. (1973a)
62295	2.83	1.0	N	6.20	0.01200	0.70	6.40	Katsube and Collett (1973); Rose et al. (1973a)
63501	1.01	450.0	A	1.69	0.00161	0.53	4.72	Gold et al. (1973); Hubbard et al. (1973)
63501	1.42	450.0	A	2.38	0.00253	0.53	4.72	Gold et al. (1973); Hubbard et al. (1973)
63501	1.79	450.0	A	3.22	0.00341	0.53	4.72	Gold et al. (1973); Hubbard et al. (1973)
65015	2.70	1.0	V	7.00	0.00800	1.26	8.59	Sill et al. (1973); Duncan et al. (1973)
65015	2.70	1.0	V	7.70	0.00800	1.26	8.59	Olhoeft et al. (1973a); Duncan et al. (1973)
66041	1.50	1.0	N	2.70	0.00200	0.63	5.80	Katsube and Collett (1973); Rose et al. (1973a)
66041	0.93	450.0	A	1.66	0.00225	0.63	5.80	Gold et al. (1973); Rose et al. (1973a)
66041	1.28	450.0	A	2.25	0.00300	0.63	5.80	Gold et al. (1973); Rose et al. (1973a)
66041	1.53	450.0	A	2.70	0.00388	0.63	5.80	Gold et al. (1973); Rose et al. (1973a)
66055	0.00	1.0	N	3.70	0.01000	1.12	7.45	Katsube and Collett (1973); Fruchter et al. (1974a,b)
66081	1.49	1.0	V	2.80	0.00100	0.67	5.85	Sill et al. (1973); LSPET (1973a)
67601	1.15	450.0	A	1.94	0.00216	0.42	4.09	Gold et al. (1973); LSPET (1973a)
67601	1.43	450.0	A	2.43	0.00258	0.42	4.09	Gold et al. (1973); LSPET (1973a)

TABLE A9.16. (continued).

Sample	ρ g/cm ³	MHz	*	K'	LossTan	%TiO ₂	%FeO	References (electrical; chemical)
67601	1.68	450.0	A	2.94	0.00290	0.42	4.09	Gold et al. (1973); LSPET (1973a)
68121	1.01	450.0	A	1.74	0.00234	0.60	5.20	Gold et al. (1973); Woodcock and Pillinger (1978)
68121	1.41	450.0	A	2.31	0.00312	0.60	5.20	Gold et al. (1973); Woodcock and Pillinger (1978)
68121	1.90	450.0	A	3.24	0.00445	0.60	5.20	Gold et al. (1973); Woodcock and Pillinger (1978)
70051	1.60	500.0	V	3.41	0.00600	5.00	12.00	Bussey (1979); Bussey (1979)
70215	3.27	0.1	V	7.50	0.12300	12.48	19.40	Alvarez (1974c); Rhodes et al. (1974)
72441	1.56	0.1	V	3.04	0.00400	1.53	8.68	Frisillo et al. (1975); Rose et al. (1974a)
72441	1.63	0.1	V	3.11	0.00400	1.53	8.68	Frisillo et al. (1975); Rose et al. (1974a)
72441	1.65	0.1	V	3.13	0.00400	1.53	8.68	Frisillo et al. (1975); Rose et al. (1974a)
72441	1.68	0.1	V	3.15	0.00500	1.53	8.68	Frisillo et al. (1975); Rose et al. (1974a)
72441	1.80	0.1	V	3.27	0.00600	1.53	8.68	Frisillo et al. (1975); Rose et al. (1974a)
72441	1.87	0.1	V	3.35	0.00500	1.53	8.68	Frisillo et al. (1975); Rose et al. (1974a)
73241	1.30	450.0	A	1.95	0.00290	1.73	8.45	Gold et al. (1976); Rose et al. (1974a)
73241	1.75	450.0	A	2.79	0.00410	1.73	8.45	Gold et al. (1976); Rose et al. (1974a)
74220	1.37	1.0	V	2.60	0.01900	8.81	22.04	Olhoeft et al. (1973a,b); LSPET (1973b)
74220	1.44	450.0	A	2.10	0.00660	8.81	22.04	Gold et al. (1976); LSPET (1973b)
74241	1.38	0.1	V	2.20	0.01000	8.61	15.84	Alvarez (1973a); LSPET (1973b)
74241	1.61	0.1	V	2.38	0.01000	8.61	15.84	Alvarez (1973a); LSPET (1973b)
75061	2.16	450.0	A	3.95	0.02360	10.31	18.19	Gold et al. (1976); Rhodes et al. (1974)
75061	1.54	450.0	A	2.47	0.01230	10.31	18.19	Gold et al. (1976); Rhodes et al. (1974)
75081	1.90	1.0	N	3.50	0.01000	9.52	17.41	Katsube (pers. comm.); LSPET (1973b)
75081	2.08	1.0	V	2.40	0.01800	9.52	17.41	Olhoeft et al. (1973a,b); LSPET (1973b)
76315	2.49	450.0	A	5.92	0.00350	0.36	5.29	Gold et al. (1976); Rhodes et al. (1974)
76501	1.08	450.0	A	1.73	0.00410	3.15	10.32	Gold et al. (1976); Rhodes et al. (1974)
79135	2.40	450.0	A	6.23	0.01730	5.15	14.01	Gold et al. (1976); Rhodes et al. (1974)
Luna 16 [†]	1.80	1.0	V	3.31	0.0124			
Luna 20 [†]	1.00	1.0	V	2.07	0.0036			
Luna 20 [†]	1.60	1.0	V	3.20	0.0035			
Luna 20 [†]	1.80	1.0	V	3.46	0.0090			

*A means measured in air, N in nitrogen, and V in vacuum; AN designates those samples that were measured in nitrogen but had previously been exposed to air.

[†] Luna data are not included in the regression analyses. Data are from Golovkin A. R., Dmitriev A. P., Douchowskoy A. E., Novik G. I., Petrotchenkov R. G., Rgevsky V. V., Silin A., and Shvarev V. V. (1974) The result of investigation of the thermal and electric properties of the lunar soil and its earth analogues. In *Lunar Soil from Sea of Fertility*, pp. 559-562. Nauka, Moscow (in Russian); and Golovkin A. R., Douchowskoy A. E., Petrotchenkov R. G., Rgevsky V. V., Silin A. A., and Shvarev V. V. (1979) Electric properties of the Luna 20 soil and its earth analogues. In *Regolith from the Highland Region of the Moon*, pp. 598-603. Nauka, Moscow (in Russian).

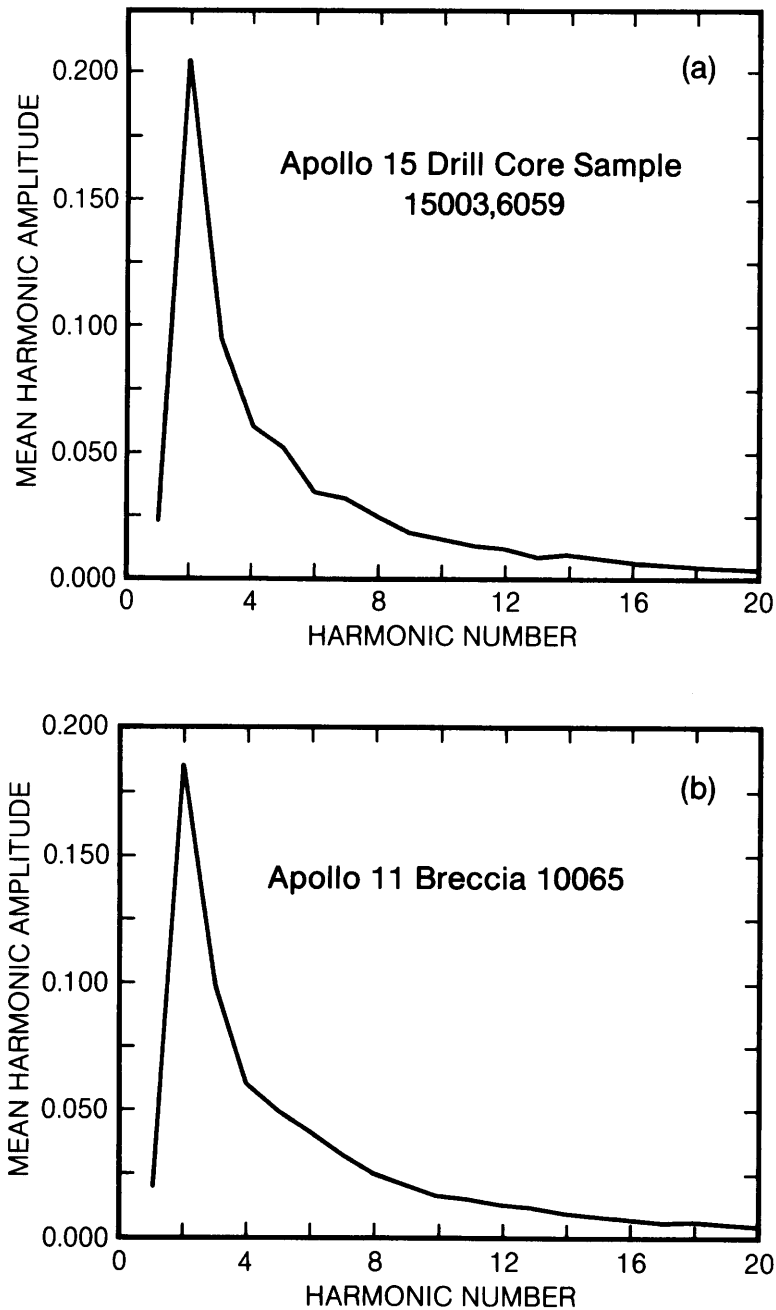


Fig. A9.1. Results of Fourier analyses of measurements of the shapes of individual silicate particles in lunar soil samples: **(a)** impregnated soil sample 15003,6059 from Apollo 15 drill core; **(b)** lunar regolith breccia 10065 from the Apollo 11 site (data from *Kordesh et al.*, 1982; *Kordesh*, 1983a,b). The data represent results of two-dimensional Fourier analyses on individual soil particles, treating the two-dimensional outline of each particle as a polar-coordinate plot of radius and angle. In these plots, mean harmonic amplitude (i.e., the contribution of each harmonic to the particle shape) (vertical axis) is plotted as a function of harmonic number (horizontal axis). The shapes of lunar soil particles can generally be represented by harmonics of number <6, similar to particles in meteoritic breccias, but distinctly different from particles altered by terrestrial media such as wind and water.

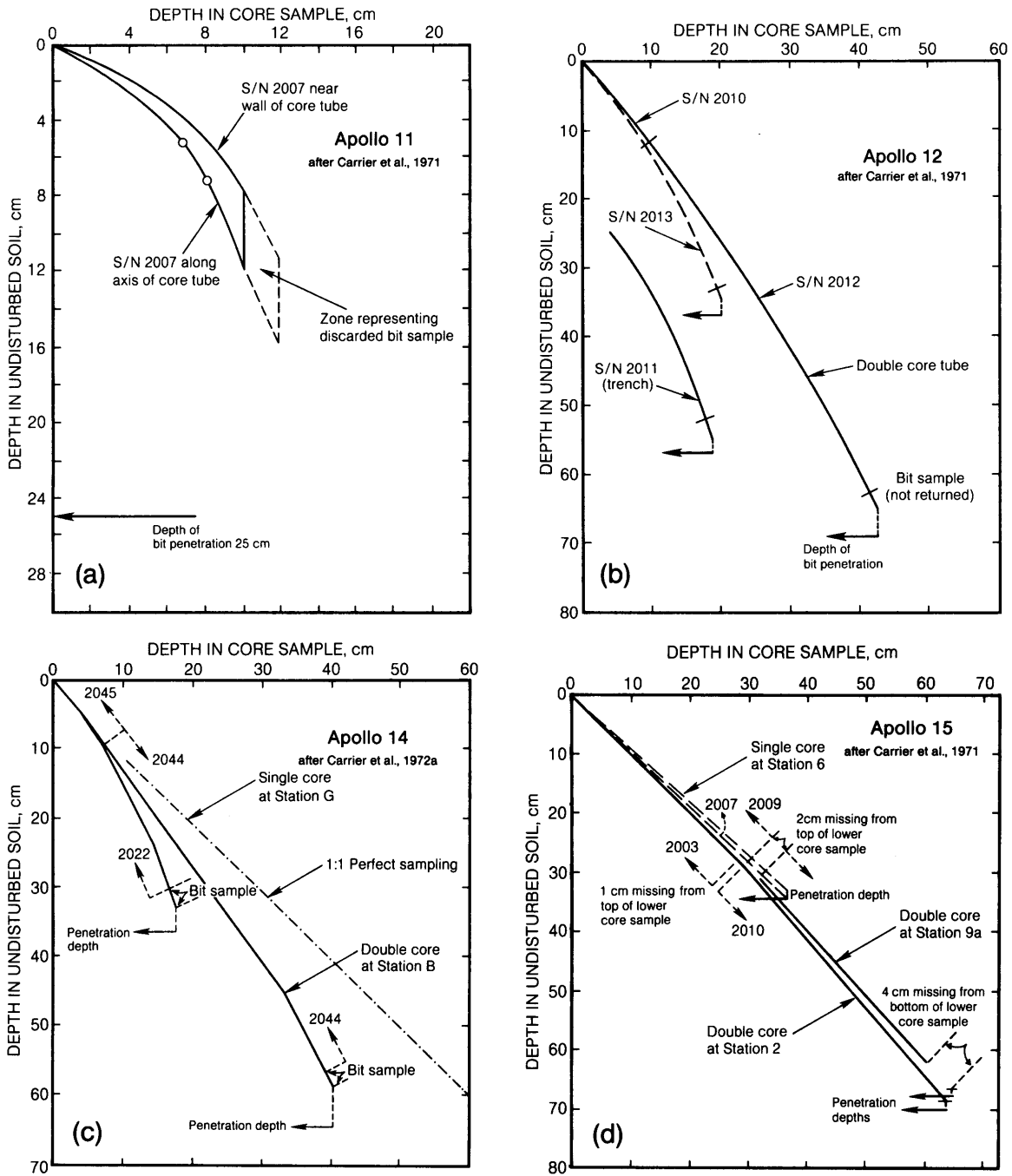


Fig. A92. Depth relations for Apollo core tube samples, showing the divergence between measured sample depth in the core tube (horizontal axis) and the actual depth to which the core was driven in undisturbed soil (vertical axis) (after *Carrier et al., 1971*). If the core tube operated ideally, the data should fall along a line with a 45° slope. The divergence from this ideal line is caused by the fact that, as the tube is driven downward, it gradually becomes plugged with material from shallow depths, until the deeper material can no longer enter. As a result, the material present at a given depth in the core tube was actually collected from a shallower depth than the depth to which the core tube was driven. **(a)** Apollo 11; **(b)** Apollo 12; **(c)** Apollo 14; **(d)** Apollo 15. “S/N” refers to serial numbers of core tubes; all four-digit numbers in **(c)** and **(d)** are also serial numbers.

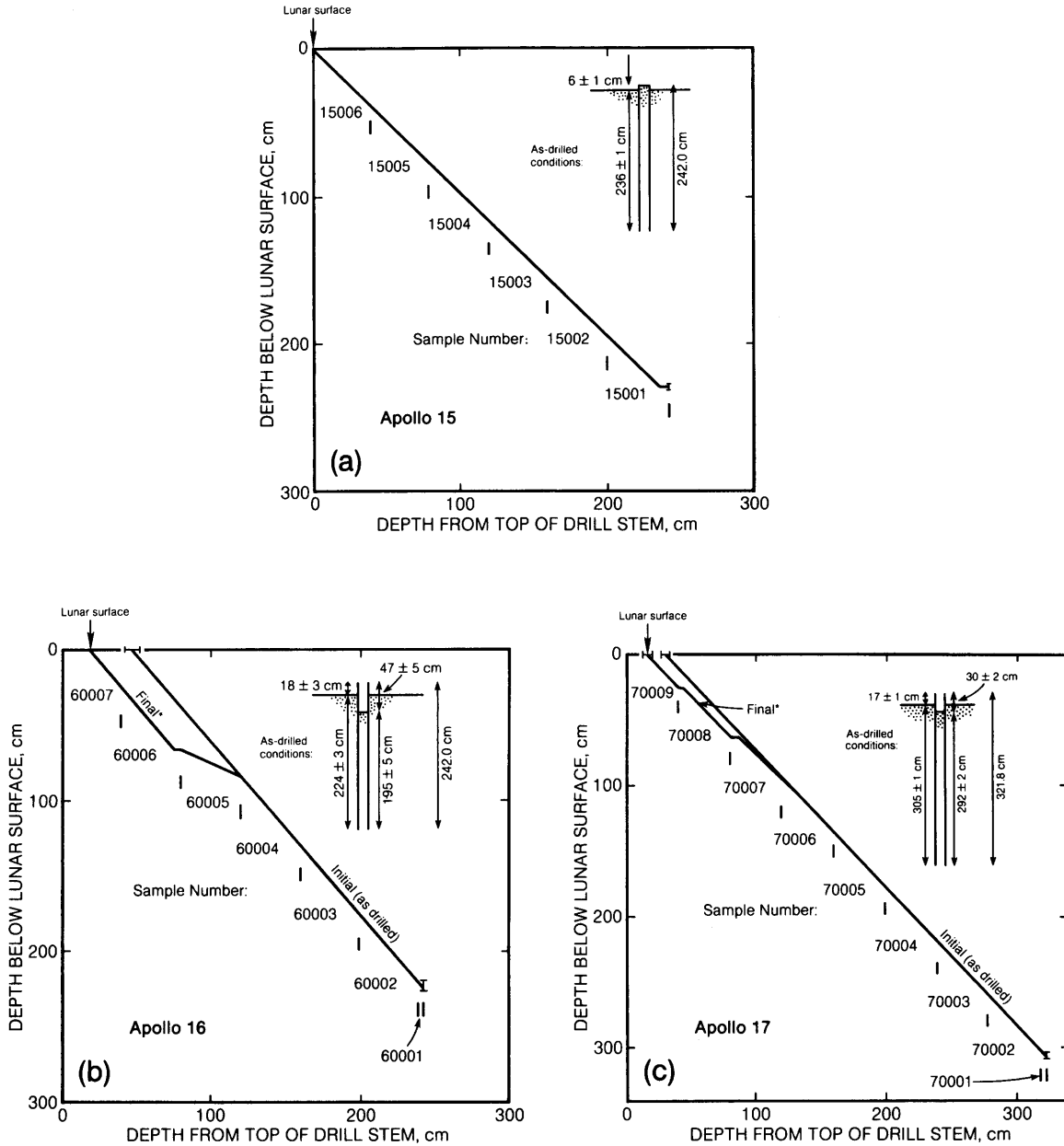


Fig. A9.3. Depth relations for Apollo rotary drill core samples, showing the divergence between measured sample depth in the core tube (horizontal axis) and the actual depth to which the core was driven (vertical axis). Data after *Carrier* (1974) (see also *Allton and Waltz*, 1980 for details). Because these drill cores operated more ideally than the hammered-in core tubes (Fig. A9.2), the data fall closely along the ideal 45° line. **(a)** Apollo 15; **(b)** Apollo 16: asterisk (*) indicates zone where sample moved during return to Earth, leaving a 5-cm void in the bottom of core 60006 and disturbed material along the length of core 60005 (see *Allton and Waltz*, 1980 for an alternate explanation); **(c)** Apollo 17: asterisk (*) indicates zone where sample moved during return to Earth.

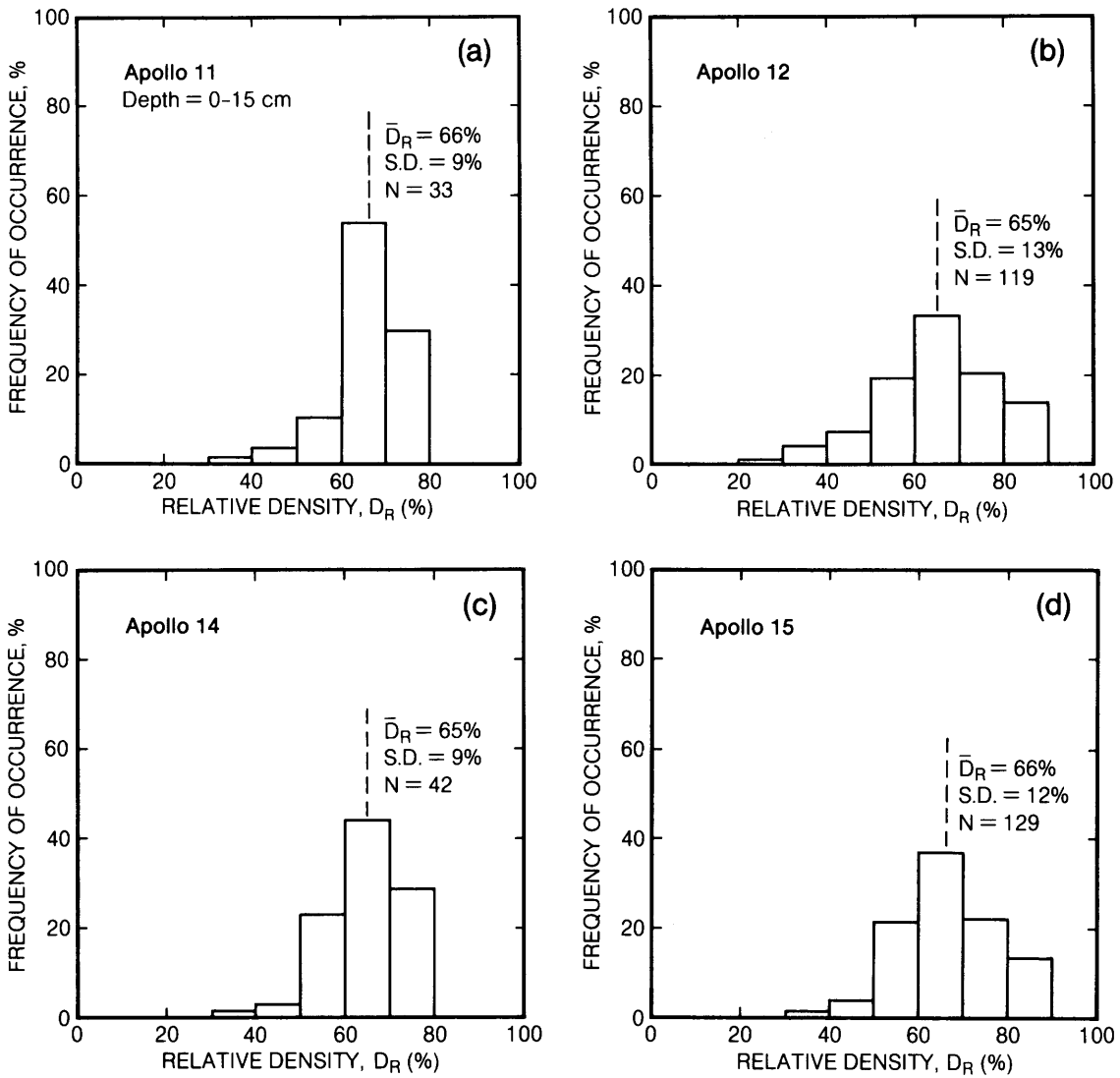


Fig. A9.4. Histograms showing values of relative density of lunar soil determined from measurements of astronaut bootprints in the lunar surface soil (after *Houston et al.*, 1972; *Mitchell et al.*, 1973a,h, 1974). Data include combined measurements from both intercrater areas and crater rims at the **(a)** Apollo 11, **(b)** Apollo 12, **(c)** Apollo 14, **(d)** Apollo 15, **(e)** Apollo 16, and **(f)** Apollo 17 landing sites. At all sites, the lunar soils exhibit high relative densities, mostly in the range 60–80%.

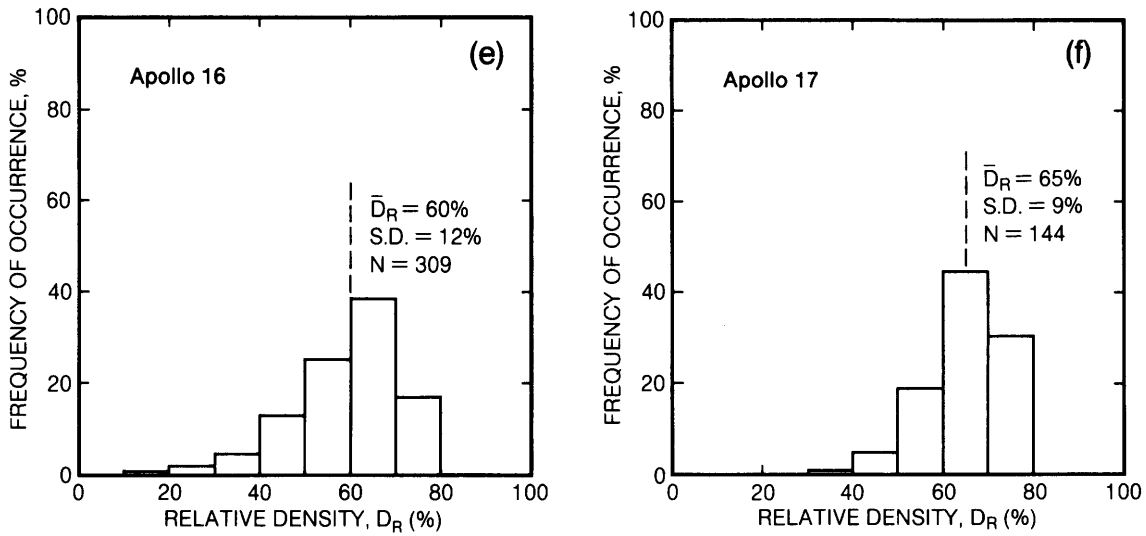


Fig. A9.4. (continued) (e) Apollo 16, and (f) Apollo 17 landing sites. At all sites, the lunar soils exhibit high relative densities, mostly in the range 60–80%.

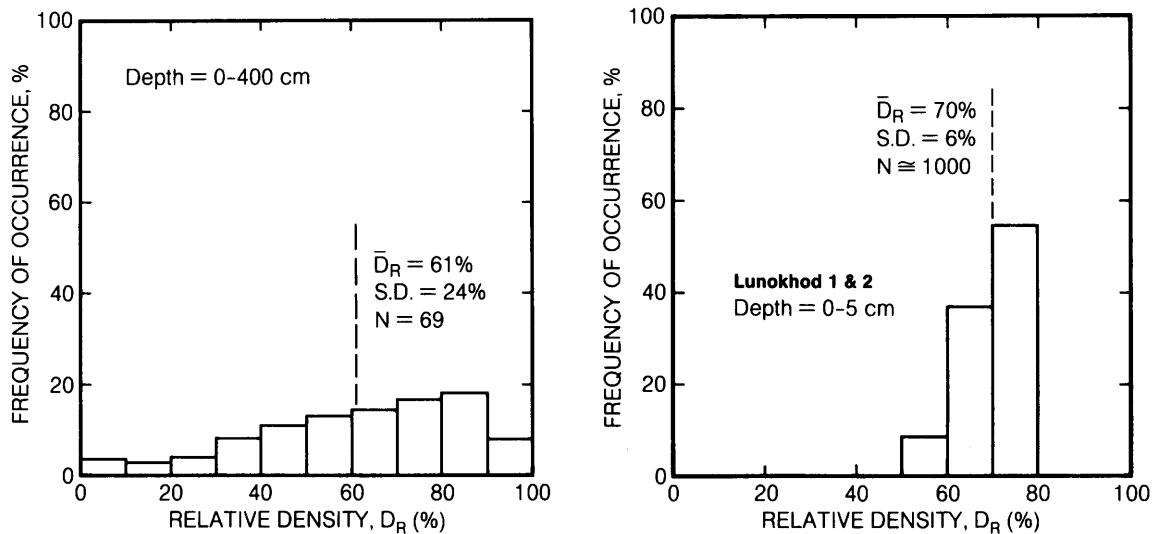


Fig. A9.5. Histogram showing values of relative density of lunar soil determined from measurements of boulder tracks on lunar slopes, chiefly from lunar surface and orbital photographs (after *Houston et al.*, 1972; *Hovland and Mitchell*, 1973; *Mitchell et al.*, 1974). In contrast to the generally high relative densities determined from studies of astronaut bootprints at landing sites (Fig. A9.4), the relative densities of lunar soil on slopes, as inferred from boulder tracks, span a much wider range and do not show a strong concentration at higher relative densities.

Fig. A9.6. Histogram showing measurements of relative density of lunar soil, based on penetration-resistance (cone penetrometer) measurements made by the robotic Lunokhod 1 and 2 roving vehicles during their surface traverses (after *Leonovich et al.*, 1974a). The concentration of measurements at high relative densities (60–80%) is similar to the results obtained at the Apollo landing sites (Fig. A9.4).

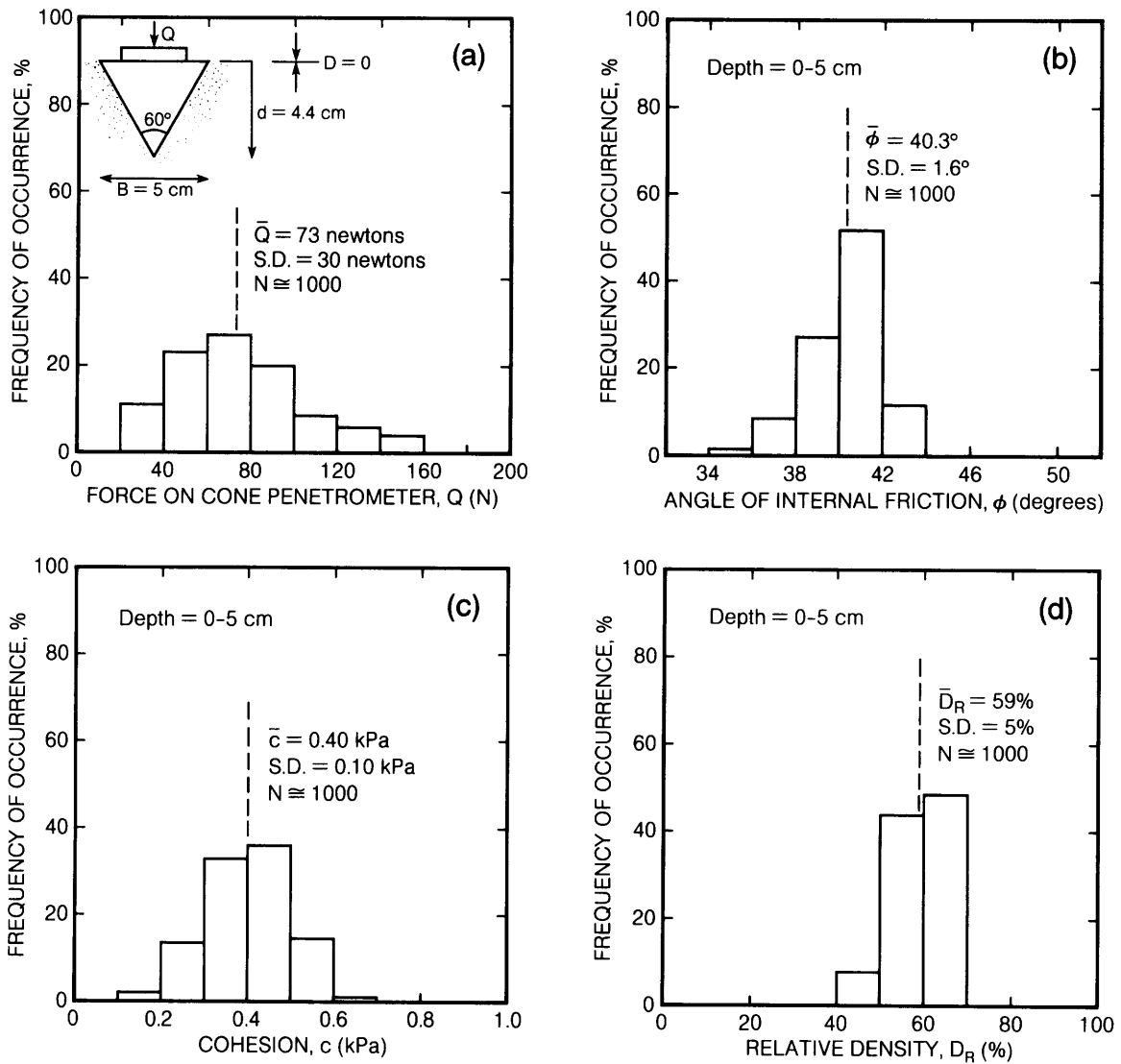


Fig. A9.7. Histograms showing ranges of calculated bearing characteristics of lunar soil, derived from cone penetrometer measurements carried out by the Lunokhod 1 and 2 robotic roving vehicles on their surface traverses (after Leonovich *et al.*, 1974a). **(a)** Force on cone penetrometer required to drive the cone to a tip depth of 4.4 cm; **(b)** friction angle, calculated from bearing capacity theory and data from a basaltic simulant of lunar soil; **(c)** cohesion, calculated from bearing capacity theory and basaltic simulant studies; **(d)** relative density, calculated from data on a basaltic simulant. Note that the range of relative densities calculated in **(d)**, generally 50–70%, is somewhat less than that (60–80%) obtained by other calculations using the same Lunokhod data (Fig. A9.6).

Self-Recording Penetrometer (SRP) data from Apollo 15
(after Mitchell et al., 1972a,d; unpublished data).

Station	SRP Index No.	Penetrometer Tip	Maximum Penetration Depth to Base of Cone/Plate (cm)	Maximum Force to Reach Maximum Depth (N)
8	2	2.03-cm diam. cone	8.2	111
	3	2.03-cm diam. cone	<10.2*	111
	4	2.03-cm diam. cone	5.2	111
	5	2.03-cm diam. cone	<11.2*	111
	6	2.54 × 12.7-cm plate	<9.3*	>111 (~155)†
	7	2.54 × 12.7-cm plate	<6.8*	111

*As shown in the accompanying figures, it is not possible to determine precisely the depth of penetration from the curves for these four tests, because the reference pad assembly apparently rode up the shaft.

†Estimated by astronaut.

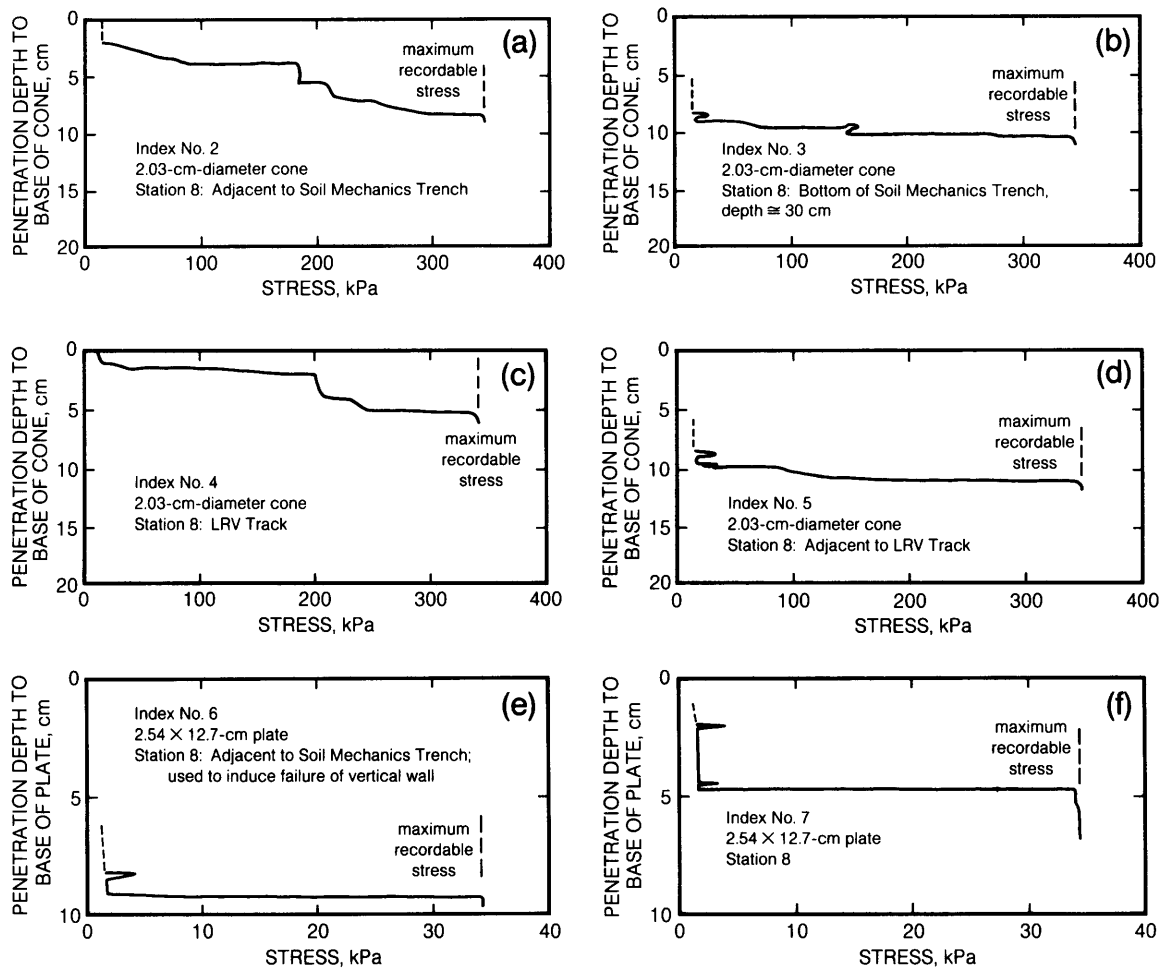


Fig. A9.8. Results of individual penetration measurements made in lunar soil at the Apollo 15 landing site, using the Self-Recording Penetrometer (SRP) (after Mitchell et al., 1972a,d, and unpublished data). Each plot (a-f) represents a single penetration experiment carried out in a different location. Data are plotted as penetration depth to the base of the cone (vertical axis) as a function of the stress applied by the astronaut (horizontal axis). The variety of results from individual penetration experiments (a-f) shows that a significant range of soil behavior exists at different locations, even within the single Apollo 15 landing site.

Self-Recording Penetrometer (SRP) data from Apollo 16
(after Mitchell et al., 1972b, 1973b).

Station	SRP Index No.	Penetrometer Tip	Maximum Penetration Depth to Base of Cone/Plate (cm)	Maximum Force to Reach Maximum Depth (N)
4	5	2.03-cm diam. cone	21.3	215
	6	1.28-cm diam. cone	74	53.5
	7	1.28-cm diam. cone	46	215
10	8	1.28-cm diam. cone	73	199
	10	2.03-cm diam. cone	22	>215
	11	1.28-cm diam. cone	50.5	>215
	12	1.28-cm diam. cone	42	>215
	13	1.28-cm diam. cone	62.5	199
	14	1.28-cm diam. cone	~70	*
	15	2.54 × 12.7-cm plate	9.7	>215
16	2.54 × 12.7-cm plate	6.3	>215	

*No data recorded on SRP cylinder.

As shown in the accompanying figures, an intercept for zero stress on the penetration axis is present in each test. This intercept ranges between 1.9 and 9.0 cm. Careful study of the kinescopes and the test procedures used on the lunar surface indicates that these intercepts most likely resulted from the reference pad assembly riding up on the penetrometer shaft after indexing and positioning. Thus, the penetration curves do not reflect soil conditions above the intercept point, but they are correct below it.

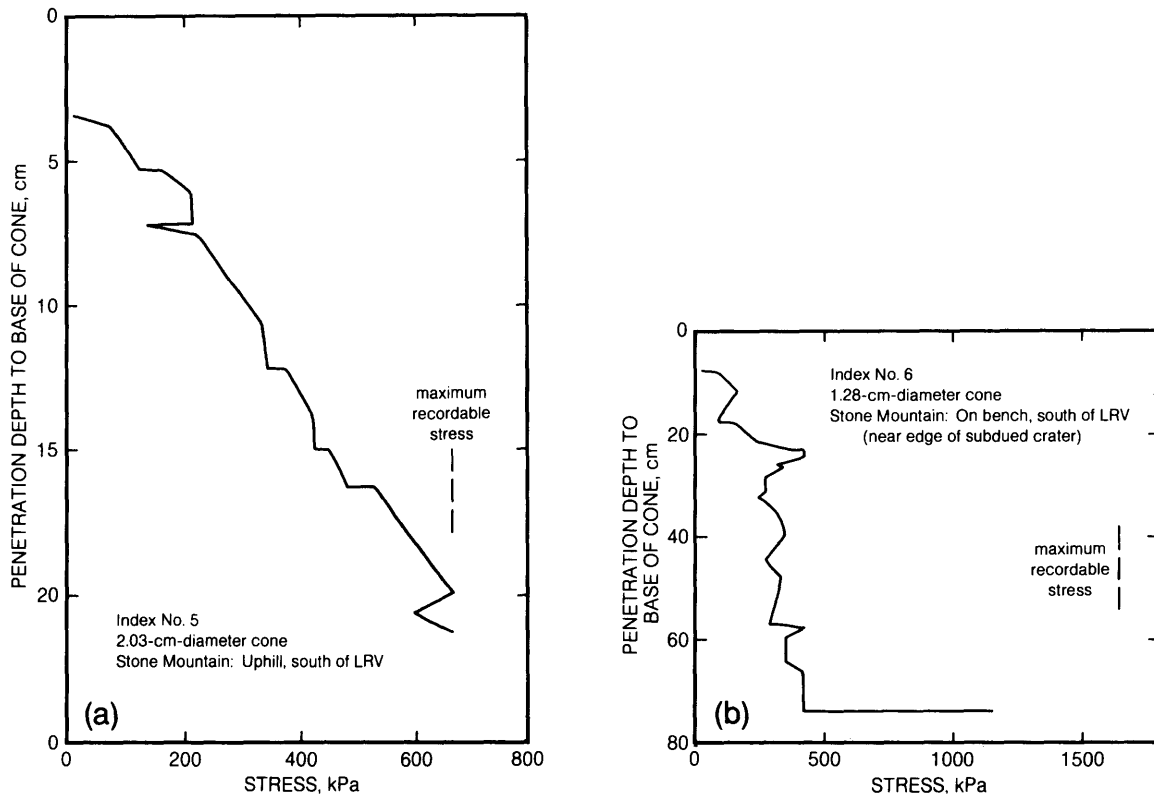


Fig. A9.9. Results of individual penetration measurements made in lunar soil at the Apollo 16 landing site, using the Self-Recording Penetrometer (SRP) (after Mitchell et al., 1972b, 1973b). Each plot (a-j) represents a single penetration experiment carried out in a different location. Data are plotted as penetration depth to the base of the cone (vertical axis) as a function of the stress applied by the astronaut (horizontal axis). The variety of results from individual penetration experiments (a-j) shows that a significant range of soil behavior exists at different locations, even within the single Apollo 16 landing site.

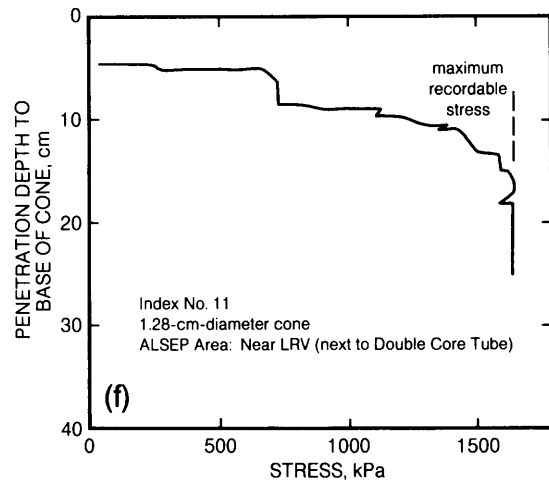
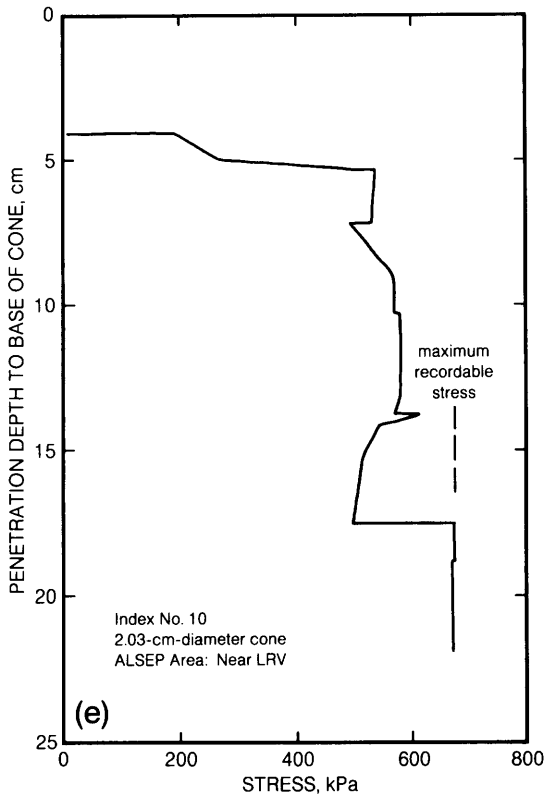
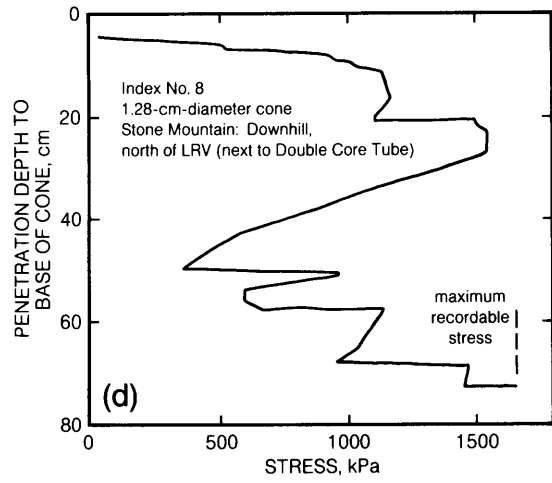
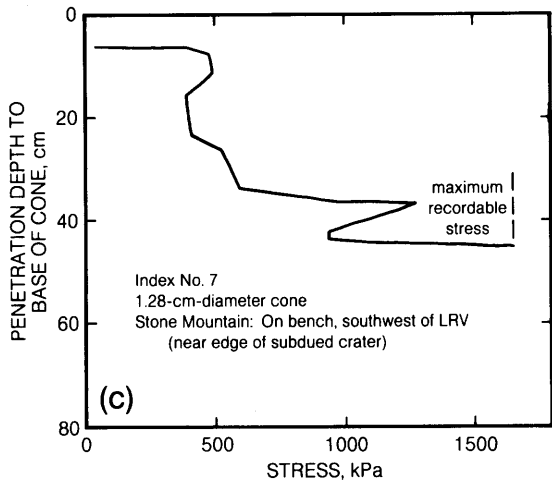


Fig. A9.9. (continued).

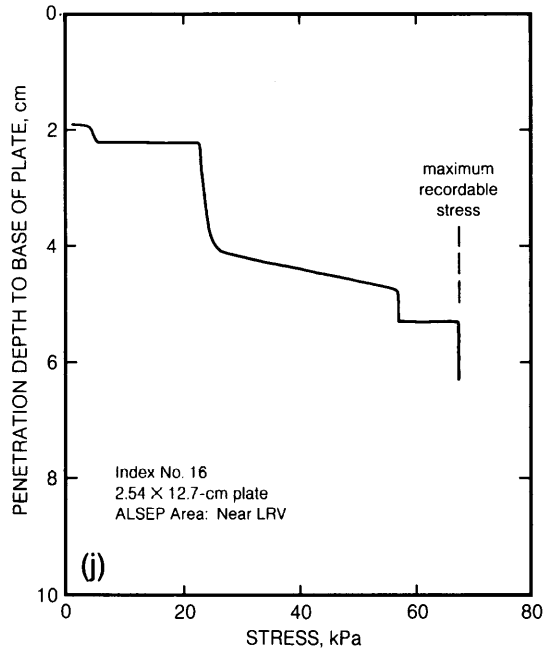
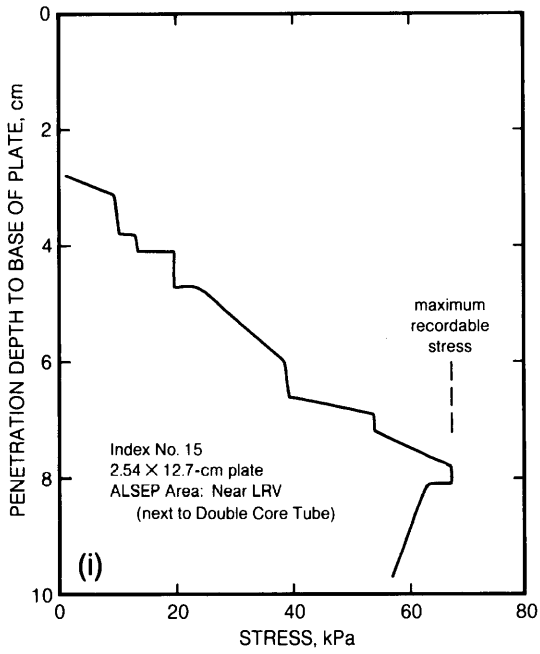
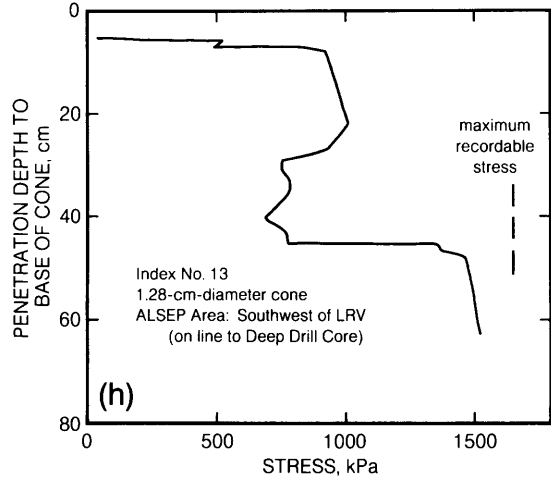
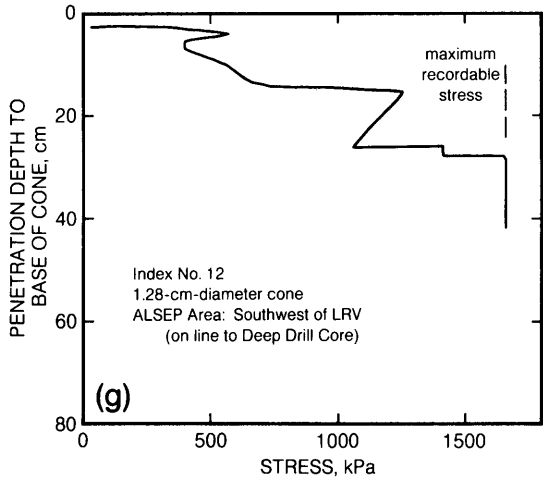


Fig. A9.9. (continued).

GLOBAL AND REGIONAL DATA ABOUT THE MOON

Paul Spudis and Carlé Pieters

Despite the major achievements in studying the Moon during the last quarter-century, our global knowledge is still patchy and incomplete. Although the Moon is so close, access has always been limited. Half of the Moon remained completely unknown until spacecraft could be sent around it. Even with the Apollo program and the Soviet and U.S. robotic lunar explorations, humans have directly explored only 6 sites on the Moon and soft-landed robots at another 10 (not counting the Surveyor 3 site, which was also visited by the Apollo 12 mission; see Table 2.1 and Figs. 2.1 and 2.2). These sites are all on the lunar nearside, and most of them are near the lunar equator. Sample return missions (both human and robotic) have provided information on only nine sites; even with the addition of Antarctic lunar meteorites (whose exact sources are unknown), the lunar sampling grid is still minimal.

To compensate for limited access, lunar scientists have two advantages. One advantage is technical. The instruments used for lunar exploration by both humans and robots, and the techniques used to analyze lunar samples back on Earth, were the most powerful and modern that could be applied. As a result, we have learned things about the Moon in a few years that took decades to learn about the Earth. A second advantage is the nature of the Moon itself. Compared to the Earth, the Moon is a simple world; it lacks the complications produced by plate tectonics, active volcanism, weather, water, and life. The geological history of the Moon, although complex and exciting, is potentially quite decipherable because it is simpler than Earth's. This is why

it has been possible, with only a few landings and sample returns, to establish the outlines of the Moon's origin and development and to identify the new scientific questions to be answered by future missions.

The next step in lunar studies is to acquire complete global information. It is paradoxical that the Apollo program, which provided so much information about a few parts of the Moon, did not also produce full global data about such key lunar characteristics as surface chemistry, surface mineral composition, gravity, magnetic fields, and topography—in short, a scientific database for the whole Moon as a single world.

The need for more global lunar data is clear, and so is the method necessary to collect it—a polar-orbiting spacecraft, equipped with an array of scientific instruments and able to scan the entire Moon over the course of a year. Proposed at various times under various names, the mission is now being actively studied as the Lunar Observer (see section 11.4.6), and is regarded as a key step in the further exploration of the Moon by both robots and human beings.

10.1. GLOBAL AND REGIONAL IMAGERY AND DATA SOURCES

Limited global and regional data for the Moon have so far been obtained primarily from three sources: telescopic observations of the Moon's nearside with Earth-based telescopes; photographs provided in the 1960s by a variety of unmanned

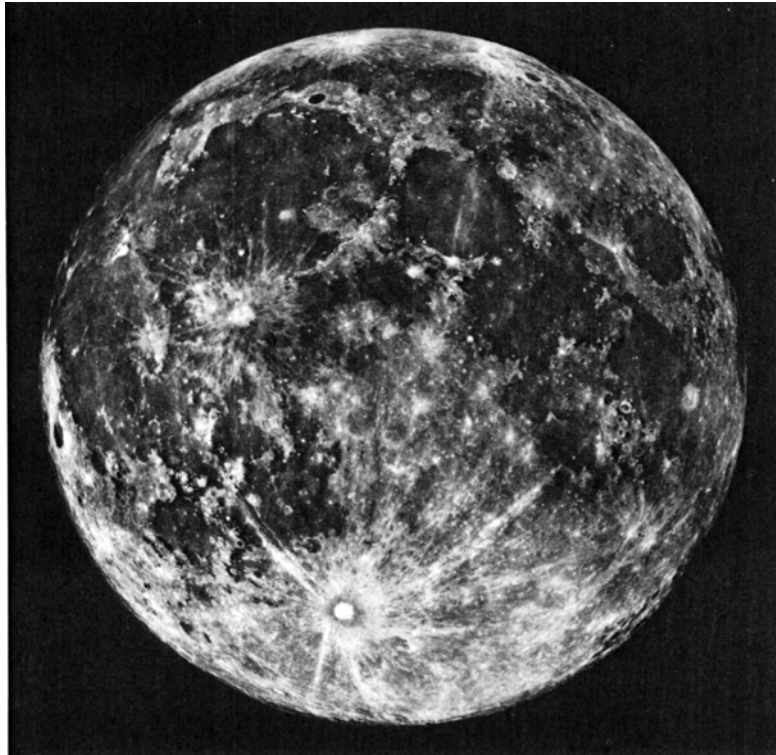


Fig. 10.1. Full-Moon photograph of the lunar nearside, obtained with the 36-in (91-cm) telescope at Lick Observatory, Mt. Hamilton, California. Lunar north is at top. The large, bright-rayed crater at the bottom (south) is Tycho. (Lick Observatory Catalog, Photo #L4. Reproduced by permission.)

missions, including the U.S. Ranger and Lunar Orbiter series, the U.S.S.R. Zond, and others; and measurements using instruments carried in lunar orbit on several Apollo command modules and in subsatellites released during several Apollo missions (1968–1972). Although none of these techniques has provided complete coverage of the entire surface of the Moon, they have provided preliminary information about the lunar magnetic and gravitational fields, the range of different lunar surface materials, and limited information on their distribution. Collections of the photographic images returned by the Lunar Orbiter and Apollo missions are available for examination at the NASA Planetary Data Centers (see front matter of this book).

10.1.1. Earth-based Telescopic Data

Since the first use of telescopes in the 17th century, increasingly larger and more sophisticated instruments have been pointed at the Moon by astronomers wanting to better understand the Earth's nearest neighbor. Current Earth-based observations of the Moon are limited not by telescope design and size, but by atmospheric conditions (weather, atmospheric absorptions, and general atmospheric stability) and by the availability

of appropriate instruments and detectors. Most measurements of moonlight are made through the atmospheric "window" of low absorption between 0.3 μm and 2.5 μm ; almost all the radiation that comes from the Moon in these wavelengths is reflected solar radiation.

Under ideal conditions, the best spatial resolution of lunar features observable from Earth is about 0.5 km near the center of the lunar disk, even for the largest ground-based telescopes. The full Moon photographic image shown in Fig. 10.1 is a good example of the imaging capabilities of Earth-based telescopes. For telescopes in low-Earth orbit above the atmosphere, spatial resolution should easily be about a factor of 10 better than for an equivalent telescope on the ground, and the light reflected from the Moon is not subject to atmospheric absorptions at various wavelengths. However, Earth-based or Earth-orbiting telescopes only allow observation of the nearside of the Moon, the side that always faces the Earth, and even the earliest unmanned missions in the 1960s showed clearly that the nearside is not representative of the whole Moon.

Despite the limited data available from Earth-based observations, the Earth-based vantage point has a number of advantages in convenience that result from the closeness and the ready accessibility

of the Moon. From Earth, individual areas on the Moon can be observed repeatedly under a variety of lighting conditions, allowing small-scale surface features (which cannot be captured in a single photograph) to be identified and studied. Such Earth-based observations were used extensively in the early (pre-Apollo) geological mapping program of the Moon. Furthermore, as technology progresses and new sensing instruments are developed, they can be deployed immediately on existing telescopes to collect new or additional data (see section 10.2.1). Finally, the Moon has been observed by Earth's inhabitants for thousands of years, although at relatively low resolution (about 100 km for a good pair of eyes). Although the Moon appears to have been an inactive planet for much longer than this, one possible large meteoroid impact event on the Moon may have been optically observed and recorded in historic time, about 800 years ago (e.g., *Hartung*, 1976).

10.1.2. Lunar Orbiter Photographic Images

The five Lunar Orbiter spacecraft, placed in lunar orbit in 1966–1967, were designed to carry out three basic activities: (1) photography to obtain both detailed, high-resolution photographs needed for the future Apollo landings and pictures of general scientific interest; (2) geodesy to accurately map the lunar gravitational field; and (3) measurements of the lunar radiation and micrometeoroid environment. The five Lunar Orbiter spacecraft were all successful; they returned 1654 photographs, of which about half were taken near the lunar equator for Apollo site selection purposes. Because the first three Lunar Orbiters obtained all the imagery required for the Apollo site selection, the last two missions, Lunar Orbiters 4 and 5, were placed in polar orbits to systematically map the entire Moon and to photograph regions of high scientific interest.

The Lunar Orbiter cameras recorded two frames simultaneously on film: a wide-angle view (80-mm lens) and a narrow-angle view (160-mm lens). The film was developed onboard the spacecraft in lunar orbit. The resulting images were then optically scanned by a video system and radioed to Earth. This analog (not digital) video signal was then used to expose similar film on Earth. The process was similar to the operation of a conventional FAX or wirephoto machine. The final complete Lunar Orbiter dataset consists of hard-copy, black-and-white photographs assembled from strips (for details, see *Hansen*, 1970).

The data returned by Lunar Orbiter 4 in particular provided nearly complete coverage of the lunar nearside at about 100 m resolution. These photo-

graphs (see Fig. 10.2 and section 10.6 on Apollo landing sites) remain the single most useful collection of photographs of the lunar nearside. A series of high-resolution images provided by Lunar Orbiter 5 and covering small-area scientific targets (e.g., volcanoes within the rings of Mare Orientale) have been used in many subsequent detailed studies (e.g., *Wilhelms*, 1987).

Documents providing compilations and overview of the Lunar Orbiter dataset include an atlas of the entire Moon, based on Lunar Orbiter photographs (*Bowker and Hughes*, 1971), a nearside-only compilation including surface-feature nomenclature (*Gutschewski et al.*, 1971), an excellent user's guide and index to the data collection (*Hansen*, 1970), and useful introductions to both Lunar Orbiter photographs and the general geology of the Moon (*Kosofsky and El-Baz*, 1970; *Schultz*, 1976a).

10.1.3. Apollo Orbital Photography

All the Apollo missions to the Moon, even the ones that did not land, carried out lunar photography, both from lunar approach and in lunar orbit. During the first five lunar missions (Apollo 8 and 10–13), the astronauts took numerous photographs from the command module using a 70-mm Hasselblad handheld camera and a Maurer 16-mm movie camera. In addition, the Apollo 14 mission carried an automated high-resolution mapping camera that unfortunately failed after a few orbits.

In addition to the astronaut-operated cameras in the command module, the last three Apollo missions (Apollo 15–17) carried two automatic cameras in the attached service module. The first, a mapping (metric) camera, was designed to produce moderate-resolution (50 m), cartographic-quality stereo images of the surface along the spacecraft groundtracks (Fig. 10.3). The second was an optical-bar, panoramic camera whose pictures included the surface immediately below the spacecraft at very high resolution (1–2 m) and then included “wings” of progressively lower-resolution imagery out to 54° to each side, perpendicular to the ground track. The photographs produced by these two cameras are of excellent quality, but the coverage is unfortunately limited to the near-equatorial regions overflown by the Apollo 15–17 missions. A series of high-quality topographic maps at 1:250,000 scale (the Lunar Topographic Orthophotomap series) was prepared from the Apollo metric photography by the Defense Mapping Agency (DMA).

Masursky et al. (1978) provide an excellent introduction to the Apollo orbital photography dataset. This superbly illustrated book describes the Apollo photographic systems and gives numerous

Fig. 10.2. Lunar Orbiter 4 photograph showing the typical quality of the high-resolution Lunar Orbiter frames (resolution 100 m), which cover most of the lunar nearside. The area shown is near the southwestern border of Mare Serenitatis. Lunar north is at the top. The photograph shows the boundary between relatively smooth (dark) mare material (upper) and more rugged highlands (lower). The prominent crater is Sulpicius Gallus (12 km diameter). Low-albedo materials in the highlands consist of dark-mantle pyroclastic deposits. The original negatives were developed in the spacecraft and read by a photomultiplier in strips for transmission to Earth; these strips are called "framelets," and the boundaries between framelets cause the horizontal lines seen in this figure. Each framelet shows a strip of lunar surface 11 km wide. The white blemish at the left side is a flaw in the film developed in the spacecraft. (Portion of NASA Photo LOIV-97H.)

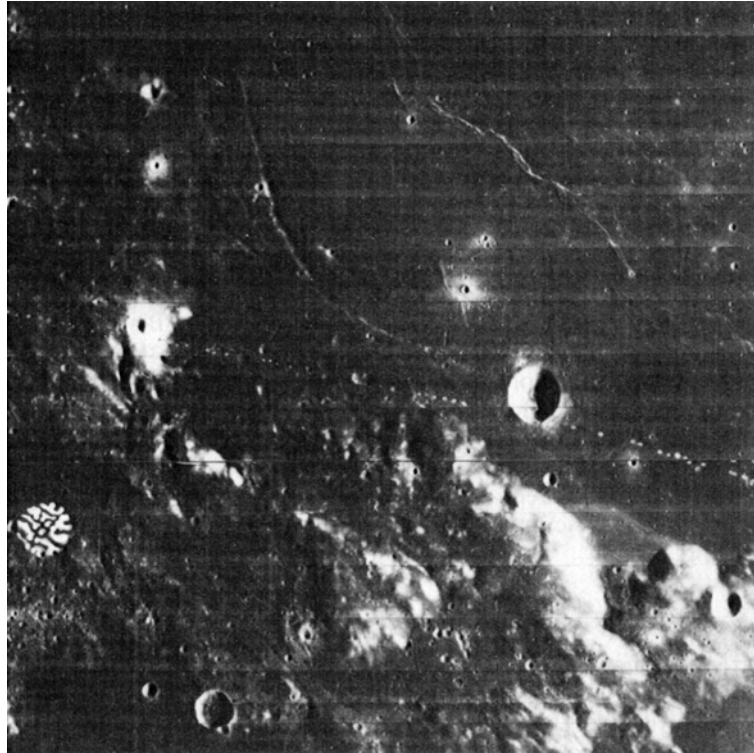


Fig. 10.3. Apollo 17 mapping (metric) camera view of the Sulpicius Gallus region along the southwestern border of Mare Serenitatis. Lunar north is at the top. This figure shows the same boundary region between mare material (upper right) and highlands (lower left) that is shown in Fig. 10.2. This photograph illustrates the general quality of these mapping camera pictures in comparison to Lunar Orbiter imagery (Fig. 10.2). The mapping camera pictures have higher ground resolution (about 50 m) and were taken at lower-angle solar illumination, thus enhancing surface details. Adjacent mapping camera frames have about 30% overlap, permitting stereo viewing. (Apollo 17 Metric Frame 1514.)



examples and geologic interpretations of lunar features using a variety of Apollo photographs. A series of Apollo flight photo indexes and all of the lunar topographic maps prepared from Apollo photographs are obtainable from the National Space Science Data Center (NSSDC) at the NASA/Goddard Space Flight Center in Greenbelt, Maryland; see *Cameron et al.* (1977) for details.

10.1.4. Coverage and Resolution of Lunar Photography

Although virtually the entire lunar surface has been photographed from orbit, the wide variety of missions and photographic systems used in lunar exploration has resulted in an uneven coverage of the Moon in terms of both resolution and image quality (lighting conditions). Virtually all lunar image data is in nondigital (hard copy) form. These image data therefore cannot be digitally processed to enhance contrast and surface detail, nor can they be manipulated to coordinate with other data obtained from the same region. A map showing the variety of resolutions of available lunar surface photographic coverage is given in Fig. 10.4. This map summarizes all available lunar photography from Ranger through Apollo. More detailed discussions of current photographic coverage of the Moon are found in *Heinzen and Peer* (1971) and in the Lunar Geoscience Observer Workshop Report (*LGO Science Workshop Members*, 1986).

10.2. SURFACE MINERALOGIC AND GEOCHEMICAL DATA

Three remote-sensing techniques, involving visible, near-infrared (IR), gamma-ray, and X-ray radiation, have been used successfully to measure the composition of the Moon in selected regions. Spectral measurements of reflected visible and near-IR radiation continue to provide information about the mineralogy of the lunar surface material. All currently available visible and near-IR reflectance data have been acquired using Earth-based telescopes (sections 6.2.1, 6.5, and 7.2). The elemental abundances at the lunar surface have been measured from lunar orbit for Th, U, K, Fe, and Ti using gamma-ray spectrometers, and for Mg, Si, and Al using X-ray spectrometers; both instruments were carried in the Apollo 15 and 16 orbiting spacecraft.

10.2.1. Spectral Reflectance Measurements and Multispectral Imagery (Earth-based)

Even to the naked eye, the surface of the Moon exhibits distinct differences in brightness associated with different geological units; the basaltic maria are dark and the feldspathic highlands are bright (see

discussion of optical astronomy in section 9.3.1). Differences in the relative “redness” or “blueness” between different surface units on the Moon have also been known since the early part of this century (*Wood*, 1912).

The spectral character of radiation reflected from the Moon is controlled largely by the mineralogic composition of the lunar surface. When measured at high spectral resolution (<1%) the reflected solar radiation in the visible and near-IR wavelengths exhibits absorption features that are diagnostic of surface mineralogy (e.g., *Adams*, 1974, 1975; *McCord and Adams*, 1973; see sections 6.2.1, 6.5, and 7.2 for detailed discussions of the spectral characteristics of lunar materials measured in the laboratory). Although mineral composition is the primary factor controlling the spectral character of lunar surface materials, differences in physical properties (e.g., particle size, compaction) and in the results of exposure to the lunar environment (micrometeoroid impact products: glass, agglutinates, etc.) affect both the overall brightness and the relative strengths of individual spectral absorptions.

Reflectance spectra measured on the Moon from Earth-based telescopes currently exist for a few hundred individual areas 5–20 km in diameter for the spectral range 0.3–1.1 μm (e.g., *McCord et al.*, 1972a,b; *Pieters and McCord*, 1976; *Pieters*, 1977). Near-infrared (0.6 to 2.5 μm) spectrometers, capable of producing precise spectra of high spectral resolution, were developed in the mid-1970s, thus making possible telescopic measurements of lunar areas only 3.7 km in diameter (*McCord et al.*, 1981). At these resolutions, compositional variations across relatively small lunar features (e.g., individual craters in the 50- to 100-km-diameter range) can be studied in detail. Detailed remote analysis of the mineral composition of the lunar surface material then became possible with these spectra, and the new compositional information was applied to a variety of important lunar science problems (*Pieters et al.*, 1980, 1983, 1985; *Bell and Hawke*, 1981, 1984; *Hawke and Bell*, 1981; *Pieters*, 1982; *Spudis et al.*, 1984; *Gaddis et al.*, 1985; *Lucey et al.*, 1986; *Smrekar and Pieters*, 1985). Summaries of available spectral reflectance data for the lunar nearside, including both maria and highland crustal regions, can be found in *Pieters* (1978) and *Pieters* (1986), respectively.

Until similar spectroscopic measurements are made from a lunar-orbiting spacecraft, no global spectral data will exist for the Moon, especially for the lunar farside. In the meantime, the information obtained from the slowly increasing number of Earth-based high-resolution spectra obtained for individual small lunar areas are providing a good

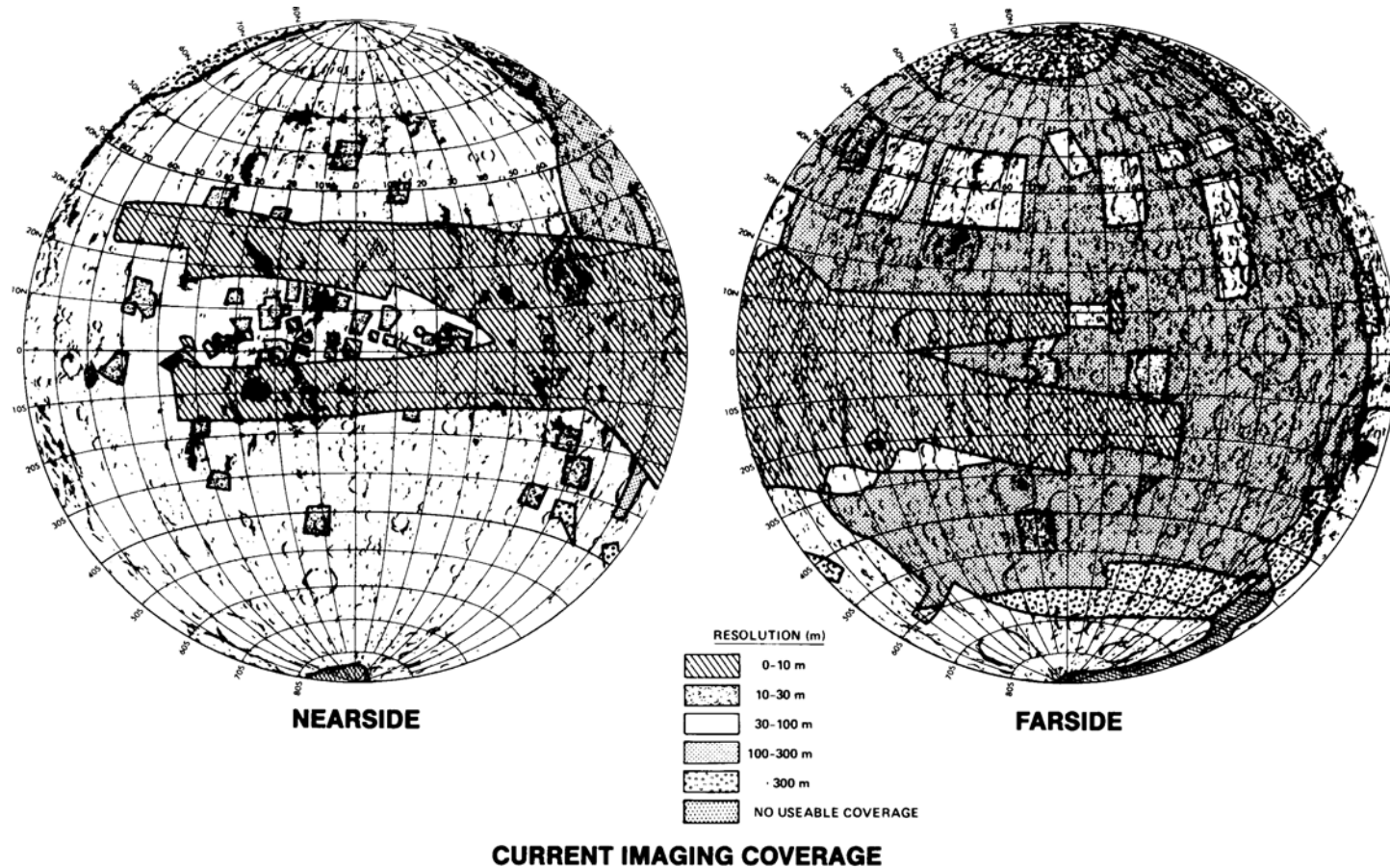


Fig. 10.4. Nearside and farside maps of the Moon showing photographic coverage of the lunar surface from all missions in terms of ground resolution. The best coverage (0–10 m resolution) is in the equatorial “Apollo zone” (east limb, 30°N to 20°S), where the candidate Apollo landing sites were located. However, even in this intensely-covered region, many photographs from longitude 70°E to 100°E were taken under nearly vertical solar illumination, making them less desirable for studying lunar surface features. Data from *Heinzen and Peer* (1971) and the Lunar Cartographic Dossier (*Schirmerman*, 1973).

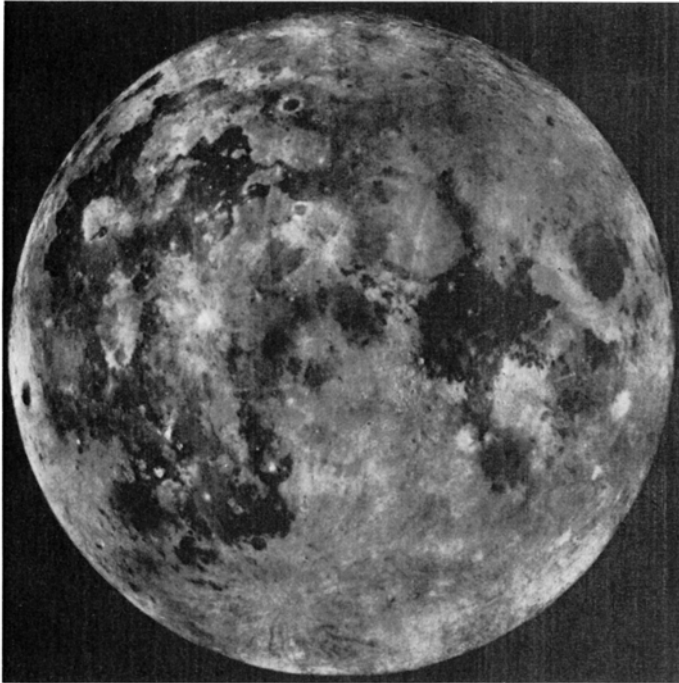


Fig. 10.5. Color-difference photograph of the lunar nearside, obtained in 1973 with the 61-in (155-cm) Catalina (Arizona) reflector (E. Whitaker, personal communication, 1980). Lunar north is at the top. This photograph is a composite image mosaic produced from carefully controlled individual photographs taken at wavelengths of $0.38\ \mu\text{m}$ (negatives) and $0.62\ \mu\text{m}$ (positives). In this figure, relatively blue surface regions appear dark, and relatively red regions appear bright. These color differences are particularly sensitive to the Ti content of lunar mare soils; Ti-rich soils appear bluish and are therefore dark in this image.

characterization of the surprisingly large variety of rock types that are present across the lunar nearside (see discussion in section 10.4.3). It is already clear, for example, that the range of lunar rock types is much greater than represented by the samples returned from the nine Apollo and Luna sites or collected as meteorites in Antarctica.

The spatial extent of spectral variations across the lunar surface is often examined using *multispectral images*, in which surface-image data are gathered for a few selected spectral channels. If the channels chosen are those in which lunar materials exhibit significant spectral contrast, then surface color variations (and hence surface compositional variations) can be mapped using two-dimensional detectors. Although multispectral images do not normally provide the high-spectral-resolution data required to identify individual mineral species, the images are well-suited for efficiently defining the spatial extent of a particular surface unit. Figure 10.5 shows a full-Moon color difference mosaic prepared from composite photographic images taken at $0.38\ \mu\text{m}$ (negative) and $0.62\ \mu\text{m}$ (positive) (E. Whitaker, personal communication, 1980; see Whitaker, 1972 for a discussion of the technique). In this composite image, surface units that have a high $0.38\text{-}\mu\text{m}/0.62\text{-}\mu\text{m}$ reflectance ratio appear dark, and units with a low ratio appear bright. This ratio is

sensitive to the Ti abundance of lunar mare soils (e.g., Charette *et al.*, 1974; Pieters, 1978) and is thus particularly useful for identifying the spatial extent of different basaltic surface units having different Ti contents, e.g., the high-Ti basalts at the Apollo 11 and 17 sites and the low-Ti basalts at the Apollo 12 and 15 sites (see also Plate 10.7 and discussion in section 10.4.1).

High-resolution ($\sim 2\ \text{km}$) digital multispectral images of selected lunar regions were obtained with Earth-based telescopes in the 1970s using vidicon imaging systems (e.g., McCord *et al.*, 1976, 1979; Johnson *et al.*, 1977). Because these images were virtually the only high-precision digital images available during the 1970s and 1980s, they have been extensively used in numerous scientific studies of specific areas on the Moon. The full set of these vidicon images has also provided some of the principal data used to define lunar basalt types on the nearside of the Moon (section 10.4.1). The example shown in Fig. 10.6 is a single set of three visible/near-IR vidicon frames, centered on the Apollo 12 landing site in Oceanus Procellarum (Pieters and McCord, 1976). These images were obtained using filters with bandwidths of $\sim 30\ \text{nm}$ and centered at 0.40 , 0.56 , and $0.95\ \mu\text{m}$. These wavelengths were chosen to be particularly sensitive to (1) the relative brightness of surface features

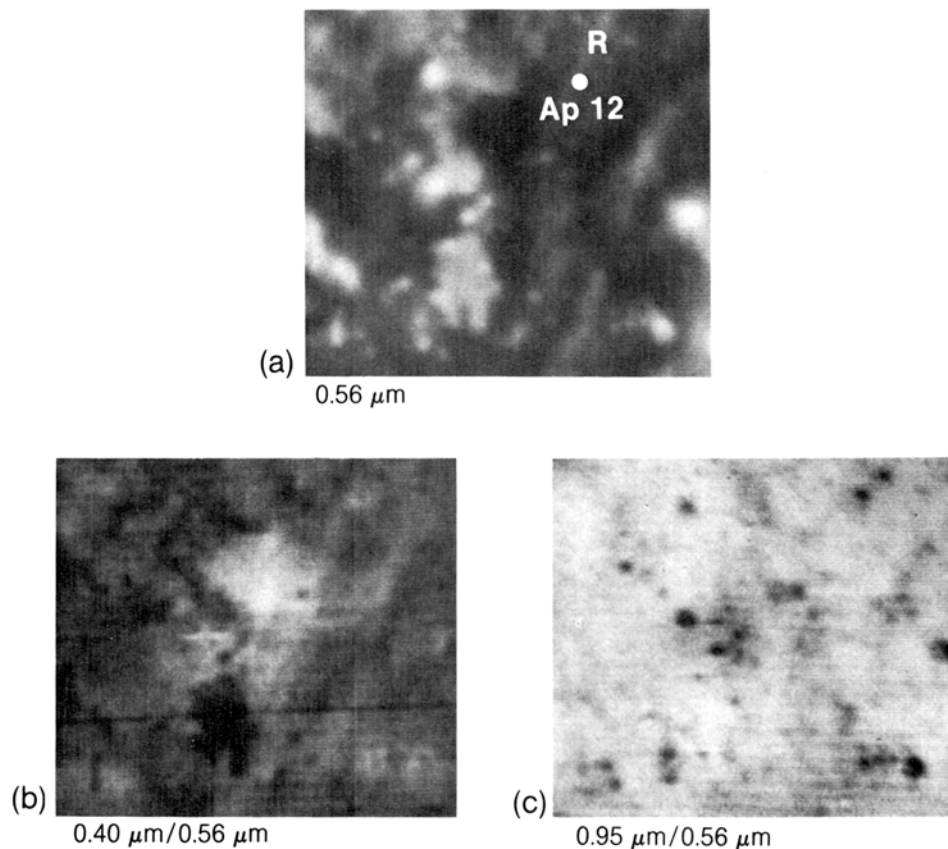


Fig. 10.6. Multispectral images of the Apollo 12 landing site in Oceanus Procellarum, obtained with a vidicon imaging system using Earth-based telescopes. Lunar north is at the top. The 0.56- μm image **(a)** (slightly enhanced) shows prominent albedo variations across the site. Low-albedo surfaces are basaltic mare lavas. Small craters superimposed on the mare and nearby highlands appear bright because they expose fresh material. A crater ray ("R"; thought to be from Copernicus) extends from north to south-southwest across the landing site ("Ap 12"). The two color ratio images **(b,c)** provide different information about surface composition. The 0.40- μm /0.56- μm image **(b)** includes wavelengths that are sensitive to Ti content, and has been enhanced to display the compositional variations of the basaltic surface in this region. A relatively large basalt area (bright area in center), with higher Ti content than most lavas in the Apollo 12 region, occurs to the southwest of the Apollo 12 site. The 0.95- μm /0.56- μm image **(c)** is sensitive to the strength of a mafic mineral absorption band near 1.0 μm . Low values (dark areas in the image) indicate strong absorption and correspondingly high contents of mafic minerals, mostly pyroxene. The freshly-exposed surface material around young craters generally contains a higher component of crystalline material, and these areas therefore exhibit stronger absorptions caused by mafic minerals. Field of view is ~ 150 km.

(0.56 μm), (2) spatial variations in different basaltic surface units (0.40 μm /0.56 μm), and (3) spatial variations of the strength of mafic mineral absorption bands (0.95 μm /0.56 μm).

10.2.2. Apollo Gamma-ray Spectrometer

Both the Apollo 15 and 16 service modules carried a gamma-ray spectrometer with a NaI(Tl) crystal detector. This instrument was capable of measuring

lunar surface gamma-ray radiation and identifying discrete lines in the energy spectrum that were characteristic of individual elements. Two types of lines were observed as signals in the measured spectrum. The first group is caused by natural lunar radioactivity and is produced by the decay of lunar ^{40}K , ^{238}U , and ^{232}Th . The second group of lines results from the bombardment of the Moon by high-energy galactic-cosmic-ray (GCR) particles. This bombardment produces secondary particles (mostly neutrons)

within the lunar surface materials and also excites the nuclei of certain elements. This excitation produces characteristic gamma-ray lines for the elements Fe, Ti, Al, and Si (see discussion in *Arnold et al.*, 1972).

Data from the gamma-ray spectrometers onboard the Apollo 15 and 16 spacecraft have been processed into elemental abundance maps for Th (*Metzger et al.*, 1977; Plate 10.1), Fe (*Davis*, 1980; Plate 10.2), and Ti (*Metzger and Parker*, 1979; *Davis*, 1980; Plate 10.3). The orbital Th data are the most precise (*Metzger et al.*, 1977). The abundance maps for Fe and Ti are derived by a complex iterative process that includes examining the spectra for the expected lines from these elements and then extracting actual concentration levels by comparing the “ground-truth” chemical data derived from laboratory analyses of returned regolith samples from Apollo and Luna landing sites with the gamma-ray spectra measured while flying over those same sites.

The precision of orbital gamma-ray elemental data is dependent on the time spent counting a given area; more counting time results in better statistical precision. Because the time spent in lunar orbit during the Apollo missions was limited, the precision of these orbital data is fairly low (10–25% relative for Fe; 30–50% relative for Ti). The surface or ground resolution of the data is a function of spacecraft altitude, and about 100 km is the nominal resolution of the Apollo gamma-ray data. Detailed discussion of data reduction can be found in *Bielefeld et al.* (1976). Discussions of error analysis and the derivation of Th, Fe, and Ti concentrations are found in *Metzger et al.* (1977), *Metzger and Parker* (1979), and *Davis* (1980), respectively. *Davis and Spudis* (1987) provide error magnitude maps for the Th, Ti, and Fe measurements.

10.2.3. Apollo X-ray Fluorescence Spectrometer

Because the Moon has no absorbing atmosphere, solar radiation at all wavelengths reaches the lunar surface. The Apollo 15 and 16 orbital spacecraft carried X-ray fluorescence spectrometers to measure the fluorescent X-rays produced by the excitation of atoms in the lunar surface by the incident solar X-rays. Measurement of the X-rays given off from the Moon can be used to determine the concentration of elements of atomic number 14 (Si) or less in lunar surface materials. Because no absolute calibration of the incident solar X-ray flux was included on the Apollo spacecraft, the experimental data could only be expressed as ratios of Al/Si and Mg/Si. Surface maps of these ratios were produced along the Apollo 15 and 16 groundtracks

across the hemisphere of the Moon that was sunlit (and therefore exposed to solar X-rays) during these missions (Plates 10.4 and 10.5). The effective ground resolution of the Apollo X-ray data is much greater than that of the gamma-ray data; the nominal surface resolution is about 30 km (*Andre et al.*, 1977).

The Apollo orbital X-ray data provide information on the distribution of the geochemically significant elements Mg and Al, and they have therefore been used in numerous studies relating to the global magmatic history of the Moon (e.g., *Adler et al.*, 1973; *Hubbard*, 1979). Unfortunately, such X-ray data can only be collected from sunlit regions of the Moon; as a result of the relatively short Apollo missions, this information is available for only about 9% of the lunar surface. For details on the Apollo X-ray orbital chemical data, see *Adler et al.* (1972), *Adler and Trombka* (1977), *Clark and Adler* (1978), and *Clark and Hawke* (1981).

10.3. GEOPHYSICAL DATA

Several types of lunar geophysical data have been acquired by lunar-orbiting spacecraft and from Earth-based observations. This section summarizes information on the lunar gravity field, the surface magnetic field, and the radar-backscatter properties of the lunar surface.

10.3.1. Lunar Gravity Field

Current knowledge of the Moon’s gravitational field has come principally from radio-tracking data provided by orbiting lunar spacecraft. These investigations involve measuring the Doppler shift of the spacecraft’s transmitted radio signal as it flies over various lunar features. As the spacecraft’s orbital path is perturbed by lunar mass excesses or deficiencies beneath it, its orbital velocity (and hence the Doppler shift of its signal) changes. These changes can then be used to understand the structure of the lunar gravity field. Because direct spacecraft-to-Earth transmissions have been used with the single-spacecraft missions so far, only gravity data for the lunar nearside are available.

The gravity data obtained from the polar-orbiting Lunar Orbiter 4 and 5 missions (Fig. 10.7) resulted in the discovery of lunar *mascons* (i.e., mass concentrations; *Müller and Sjogren*, 1968, 1969). These mascons are large, positive gravity anomalies associated with some basalt-filled lunar basins. These gravity anomalies still have not been satisfactorily explained. Hypotheses of origin range from the relatively high density of the mare basalts filling the basins (*Phillips et al.*, 1972), to the presence of

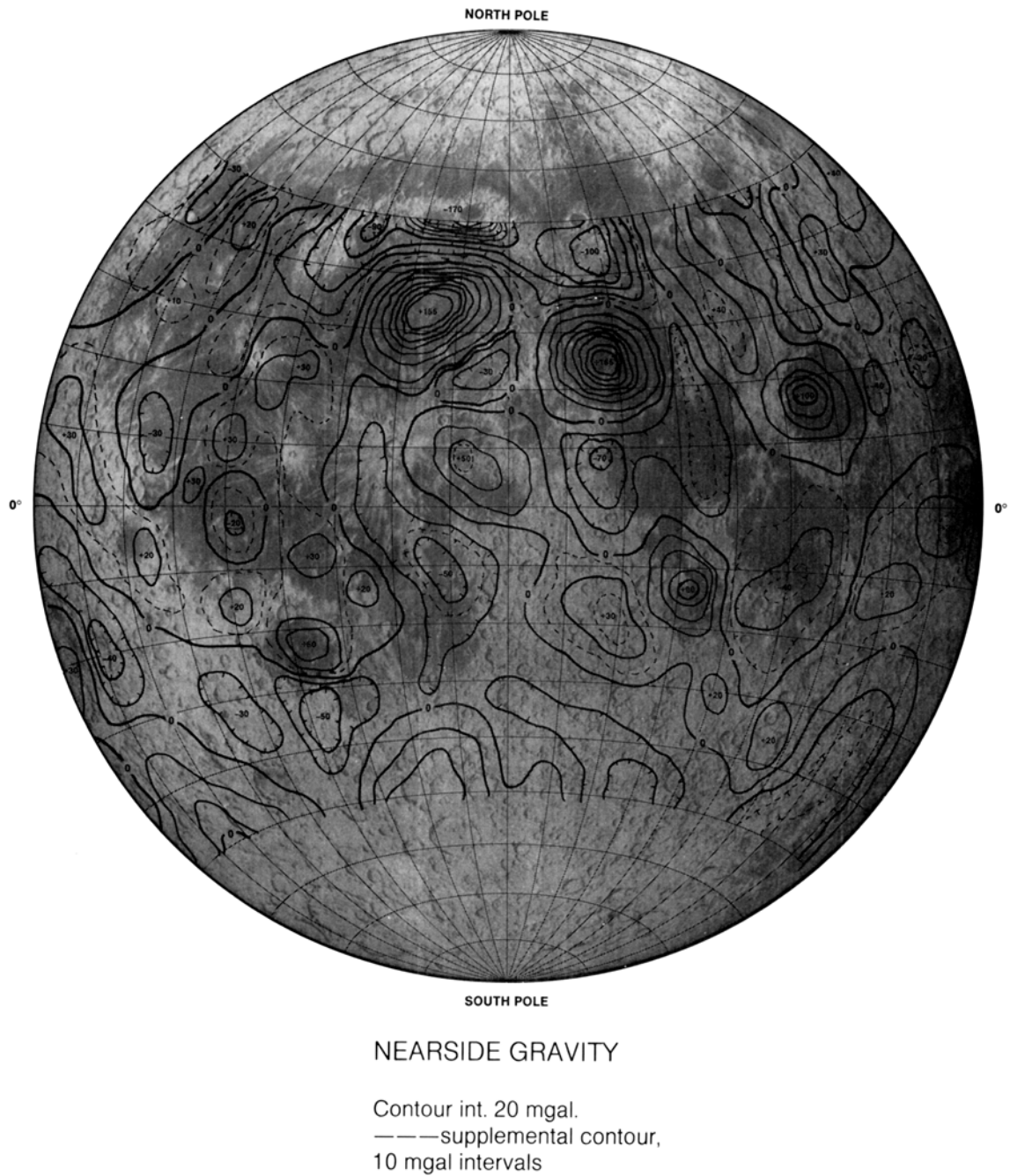


Fig. 10.7. Map of lunar nearside gravity field derived from radio tracking of the Lunar Orbiter 3, 4, and 5 spacecraft (Müller and Sjogren, 1968, 1969). Lunar north is at top. Contour interval is 20 milligals (mgal); supplemental 10-mgal contours (dashed lines) are shown for low-contrast regions. Closed contours around positive values indicate concentrations of excess mass (*mascons*), many of which are associated with the lunar maria. The largest mascon (+165 mgal) is associated with Mare Serenitatis; the second largest (+155 mgal) is associated with Mare Imbrium.

uplifted mantle material (Wise and Yates, 1970), to some combination of the two (Bowin *et al.*, 1975; Phillips and Dvorak, 1981).

10.3.2. Lunar Surface Magnetic Field

It was recognized early in lunar exploration that the Moon possesses at most a very weak internal magnetic field, and it is not yet clear that one exists at all. Surface magnetic measurements were performed by the surface magnetometers deployed at fixed locations at the Apollo 12, 15, and 16 sites. On the Apollo 14 and 16 missions, the astronauts used portable magnetometers to measure the magnetic fields along traverses within the landing area (Dyal *et al.*, 1974). These surface measurements found anomalous local areas with remanent magnetic fields as strong as 300 γ , or 0.24 A/m (a field strength that is still two orders of magnitude less than Earth's; see Table 3.1). Two subsatellites launched into lunar orbit from the Apollo 15 and 16 service modules carried magnetometers (Coleman *et al.*, 1972) to measure surface magnetism directly. These subsatellites also carried electron detectors that could indirectly determine smaller-scale surface magnetic fields by measuring the fluxes of electrons reflected from the lunar surface by magnetic anomalies (Lin *et al.*, 1976; Plate 10.6). The maximum signal detected at the subsatellite was about 0.0080 A/m ($\sim 10 \gamma$), with a sensitivity of 0.0002 A/m (0.2 γ).

The measurements of reflected electrons by the subsatellites (Lin *et al.*, 1976) indicate that about 5% of the lunar maria surfaces have a significant magnetic field (i.e., detected by the subsatellites as a signal >0.0004 A/m, or $>0.4 \gamma$). These measurements also demonstrate that, in general, the lunar maria show relatively weak, bland surface fields, whereas the highlands display a diverse and heterogeneous field strength distribution. For reviews of the interpretations of lunar magnetic data, see Fuller (1974), Dyal *et al.* (1974), and Hood *et al.* (1979).

A major unresolved problem concerning lunar surface magnetism is the existence of localized strong magnetic anomalies detected from orbit (Plate 10.6), including those in the Reiner Gamma region (nearside) and near Van de Graaff Crater (farside). Several of these anomalies occur on the opposite sides of the Moon (antipodal) from young mare impact basins such as Imbrium and Crisium (Hood, 1987). The anomalies are often associated, especially at Reiner Gamma, with a peculiar pattern of light- and dark-colored swirls on the lunar surface.

These anomalies and swirls have generated speculation both during and since the Apollo program, and their origins have not yet been settled.

Extralunar origins such as cometary impact or solar magnetic storms have been proposed, as well as lunar origins such as volcanism or alteration by gases from the lunar interior (El-Baz, 1972). Current hypotheses favor an origin resulting from magnetization of the regions antipodal to some of the major impacts on the Moon (Lin *et al.*, 1988; Hood and Williams, 1989). The origins of the swirls will probably not be resolved until these areas are actually mapped and sampled.

10.3.3. Radar Data for the Lunar Nearside

Radar-reflection data for the nearside of the Moon have been obtained using active Earth-based radio telescopes at both 3.8- and 70-cm wavelengths (Zisk *et al.*, 1974; Thompson, 1987). For any given radar measurement, two different images of the surface are generally produced (see section 9.3.2). In the region away from the *subradar point* (the point on the Moon in direct line from the radar source), the signal returned with the expected polarization sense (called the *polarized* component) produces an image of the lunar surface that appears similar to a surface illuminated by sunlight and includes highlights and shadows. In this case, however, the illumination is incident from the direction of the transmitter. A different signal, returned from the lunar surface with an opposite polarization sense (referred to as the *depolarized* component), is the result of surface scattering properties (i.e., roughness).

Radar-backscatter data for the lunar surface can be used to estimate the roughness of the surface on the scale of the wavelength (e.g., Thompson *et al.*, 1974). The intensity of radar backscatter is controlled chiefly by two sets of properties: the physical structure of the surface (i.e., amounts of blocks and craters) and the magnitude of the electromagnetic discontinuity at the surface, which is a function of the material properties (dielectric constant, loss tangent, and porosity) of the surface material. The major properties of radar-backscatter images are illustrated in the examples in Figs. 10.8–10.10. Fresh craters generally contain blocks and rubble that cause them to appear relatively rough at the scale of the radar wavelength, and they therefore appear bright in the backscatter images. A discussion of radar characteristics of lunar craters can be found in Thompson *et al.* (1974, 1979, 1980). The fine-grained regional pyroclastic (volcanic) deposits, such as the dark-mantle material sampled at the Apollo 17 site (see section 6.1.7), are generally smooth and produce very low radar backscatter. This characteristic is an important diagnostic property that allows major deposits of pyroclastic mantling material to be identified and mapped.

Fig. 10.8. Polarized radar-backscatter image of the nearside of the Moon, obtained during 1981–1984 with the 70-cm radar observatory at Arecibo, Puerto Rico (Thompson, 1987). Lunar north is at top. Since the width of the Arecibo radar antenna beam is only 10 arc-minutes (about one-third the width of the lunar disk as seen from Earth), this image is a calibrated mosaic constructed from 18 separate observations. The size of individual radar cells in the individual frames from which the image was made is 2–5 km. Dark areas correspond to individual maria with relatively smooth surfaces (e.g., Mare Crisium, on the right limb, along the first line of latitude above the equator). Bright splotches correspond to large young craters, which have blocky ejecta blankets and rays (e.g., Tycho, near the bottom center of the disk).

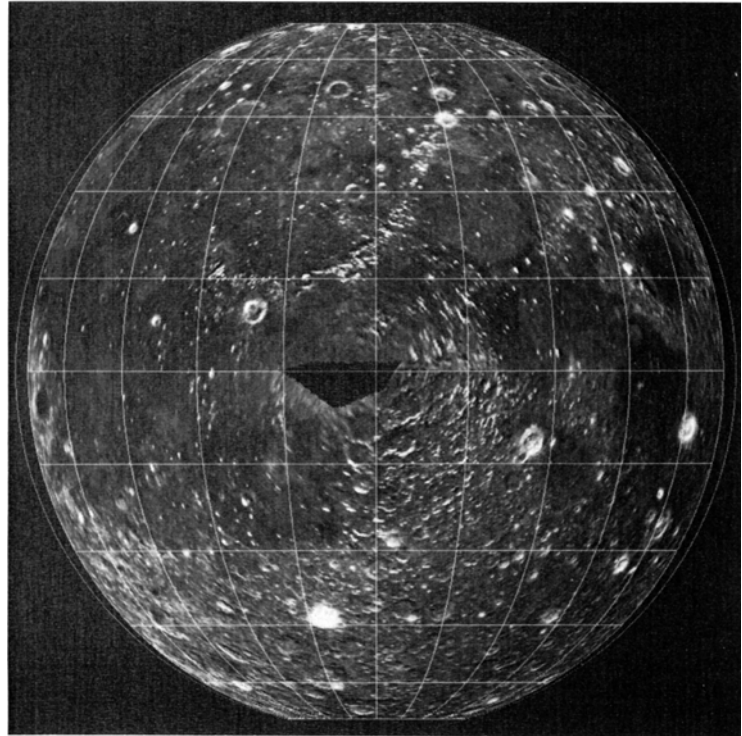
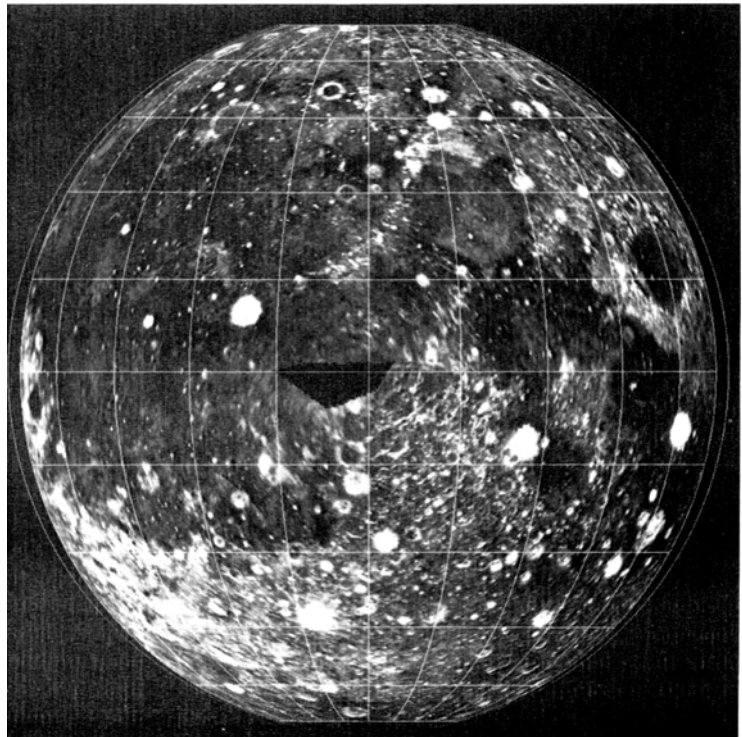


Fig. 10.9. Depolarized 70-cm radar backscatter calibrated image mosaic of the nearside of the Moon, obtained from the Arecibo radar data presented in Fig. 10.8. Lunar north is at top. In addition to high returns (bright areas) from the blocky ejecta surrounding large young craters, significant scattering differences can be observed regionally in the maria. For example, eastern Mare Tranquillitatis and western Oceanus Procellarum (center and left of lunar disk) have weaker return echoes than other maria, while the central portion of Mare Serenitatis and northern Mare Imbrium (upper center) have stronger echoes. In the highland areas on the nearside, areas near Mare Orientale (far left) have stronger echoes than do areas more distant from the Orientale Basin.



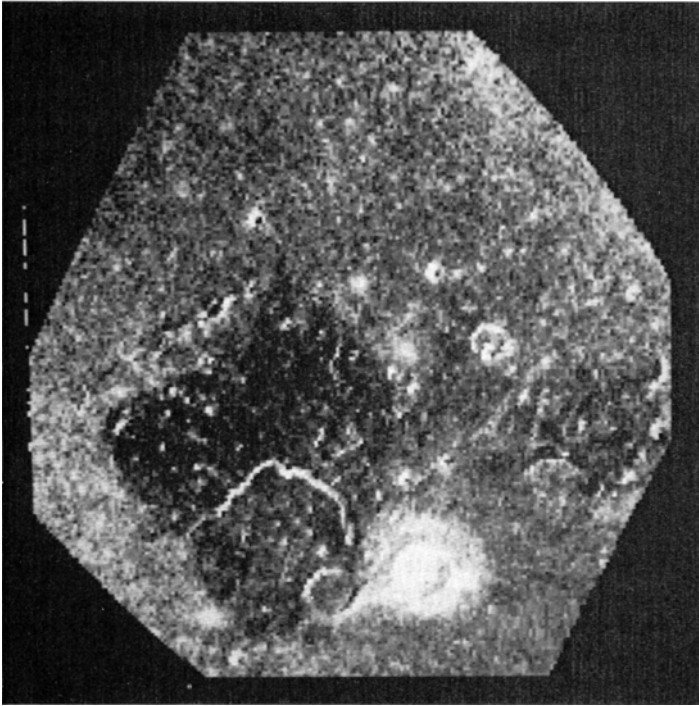


Fig. 10.10. Depolarized 3.8-cm radar backscatter image of the Aristarchus Plateau region of the Moon (ZAC reference area 6.26; Zisk *et al.*, 1974). Lunar north is at top. Radar cell size (equivalent to resolution) is about 3 km. This image provides good examples of the high backscatter from large, fresh lunar craters (bright areas), especially Aristarchus itself (large bright area at bottom), and also shows the exceptionally low backscatter from the pyroclastic deposits that cover much of the plateau (dark areas northwest of Aristarchus). The bright sinuous line west of Aristarchus is a rille (Schröter's Valley).

(Pieters *et al.*, 1973; Gaddis *et al.*, 1985). At longer wavelengths (tens of centimeters), the radar backscatter signal may in part be due to subsurface-volume scattering as well as surface-roughness scattering processes.

10.4. REGIONAL DISTRIBUTION OF LUNAR ROCK TYPES

Although coverage of the lunar surface by remotely-acquired geochemical data is limited, these data are adequate to demonstrate the compositional heterogeneity of the lunar surface. Plates 10.7–10.9 are preliminary maps showing the distribution of different rock types on the lunar surface as derived or inferred from the available remote measurements. From these data, it is clear that the Apollo and Luna collections of samples are not fully representative of the range of lunar materials exposed on the surface.

10.4.1. Mare Basalt Lavas

The compositions of lunar mare basalts from both sampled and unsampled regions of the Moon have been partially determined by using a combination of returned-sample analyses, orbital geochemical data, and Earth-based spectral reflectance measurements.

The Al/Si ratios and the Fe data obtained by orbital X-ray and gamma-ray measurements made on the Apollo 15 and 16 missions (Plates 10.4 and 10.2) clearly indicate that the maria are mafic (low Al/Si and high Fe) and are clearly distinct from the more feldspathic (higher Al/Si and lower Fe) highlands. These data indicate that the fundamental basaltic nature of the maria extends beyond the Apollo and Luna sites and that essentially all the mare regions of the Moon are composed of basaltic lava flows.

The reflectance spectra of mature mare soils, measured by optical telescopes from Earth, provide independent geochemical information at a higher spatial resolution than provided by the orbital X-ray and gamma-ray data. The lateral extent of different mare basalt types on the nearside of the Moon has been mapped at moderately-high spatial resolution (a few kilometers) using data largely acquired with Earth-based telescopes. Multispectral images in the ultraviolet (UV), visible (VIS), and near-IR (0.95 μm) wavelengths, together with albedo images of the lunar nearside and a few hundred spectral reflectance measurements of small (10 km) mare regions, were the principal data used to identify and distinguish different basalt types on the Moon (see review in Pieters, 1978).

Multispectral images in the blue to visible part of the spectrum (0.35 to 0.7 μm) are particularly sensitive to the Ti content of mare soils (e.g., *Charette et al.*, 1974), and a map of lunar basalt types based on inferred Ti content is shown in Plate 10.7. Units are distinguished in terms of estimated Ti content of the soil, based on UV/VIS color ratios and albedo; these estimated Ti concentrations are in qualitative agreement with the lower-resolution orbital data shown in Plate 10.3. Furthermore, the type and abundance of mafic minerals (pyroxenes, olivine, and/or Fe-rich glass) can be independently estimated from variations in absorption features near 1.0 and 2.0 μm (see section 6.2.1), and these quantities can be used to further distinguish lunar basalt types. Blue tones in Plate 10.7 are assigned to relatively Ti-rich soils, red tones indicate relatively Ti-poor soils, and intermediate tones represent soils intermediate in Ti content. Regions of volcanic pyroclastic material (shaded tones), which often mantle highlands near the edges of maria, are identified by their generally low albedo, their exceptionally low radar backscatter, and the frequent presence of a broad glass absorption band (from Fe^{2+}) near 1.0 μm (*Pieters et al.*, 1973; *Adams et al.*, 1975; *Gaddis et al.*, 1985).

From these data it is clear that the maria are heterogeneous, and there appear to be regional differences in chemical composition and in the ages estimated remotely from crater-count data (Plate 10.11). No mare basin is filled with a single type of basalt. Although some series of similar or related basalt flows are extensive, every mare basin or other large region filled with basalt shows a variety of basalt compositions within areas only a few hundred kilometers across.

From the stratigraphic relations deduced from photogeologic studies, it is clear that older basalts often have different compositions than younger ones. The unsampled Ti-rich basalts of Oceanus Procellarum (labelled HDSA and hDSA in Plate 10.7), for example, are superposed on extensive older, low-Ti basalts. These high-Ti basalts in Oceanus Procellarum are among the youngest on the Moon (*Boyce*, 1976), but they are distinct from the Ti-rich basalts of the Moon's eastern hemisphere (e.g., the Apollo 11 basalts, HDWA in Plate 10.7), and they are probably enriched in olivine (*Pieters et al.*, 1980). It is estimated that about two-thirds of the distinct basalt types on the nearside of the Moon have not yet been sampled (*Pieters*, 1978).

10.4.2. Petrologic Map of the Moon from Apollo Gamma-ray Data

It is possible to combine the three Apollo gamma-ray chemical maps (for Th, Fe, and Ti) into a single map showing the distribution of petrologic provinces

on the Moon. *Davis and Spudis* (1985) showed that a plot of orbital chemical data for the Th/Ti ratio against Fe (shown in Plate 10.8a) made it possible to recognize three major lunar rock types across a large fraction of the lunar globe: ferroan anorthosites, mare basalts, and the group of KREEP/Mg-suite norites. These geochemical discriminators are similar to the groupings produced by the systematics of Ti/Sm vs. Mg/(Mg + Fe) ratios used in some studies of pristine highland rocks (*Longhi and Boudreau*, 1979; *Norman and Ryder*, 1980a,b), although the latter ratios were designed to show the effects of ilmenite fractionation in early lunar crustal differentiation.

The fact that the Th/Ti vs. Fe relations (Plate 10.8a) distinguish three major lunar rock types can be used (*Davis and Spudis*, 1987) to reduce all the orbital chemical data to a triangular (ternary) plot of these major rock types. In such a plot, the value of each surface measurement (pixel) of chemical data is included in a ternary space defined by the apices FAN (ferroan anorthosite), MB (mare basalt), and MG (Mg-suite/KREEP) (cf. Plates 10.8b,c). By assigning the three primary colors (red, green, and blue) to the apex components of this ternary plot, the distribution of zones of both "pure" rock types and intermediate compositions can be shown across the Moon (Plates 10.8d,e).

The lunar petrologic map of Plate 10.8 shows that the bulk of the highlands along the Apollo 15 and 16 groundtracks are anorthosite-rich (predominance of blue colors), although other specific petrologic regions are also evident. In fact, the orbital data indicate that the highlands are petrologically heterogeneous and have had a complex evolution, probably involving continuing intrusive activity, deposition of ejecta from large impact basins, and volcanic resurfacing (*Davis and Spudis*, 1985, 1987; *Spudis and Davis*, 1986). The Fe-rich maria are evident as greenish colors, although most mare deposits also show the chemical effects of admixture of highland debris (greenish-cyan colors). For details on this petrological mapping technique, see *Davis and Spudis* (1985, 1987).

10.4.3. Mineralogy of Highland Rock Types Inferred from Near-Infrared Reflectance Spectra

Characteristic near-IR absorption features in the wavelength range 0.90–1.3 μm are diagnostic of various types of pyroxene, olivine, plagioclase, and glass (see sections 6.2.1 and 6.5). These features can be used to identify the presence of these minerals from remotely-acquired reflectance spectra of lunar surface materials. With sufficiently high precision and adequate spectral resolution, mineral abundances can be estimated and thus the rock types

exposed at the surface can be identified (e.g., *Pieters and Mustard*, 1988).

Because of the strongly absorbing nature of soil agglutinates (see section 7.3), absorption features are most readily examined in the reflectance spectra obtained from freshly exposed surfaces, such as those that occur in fresh craters or on steep slopes. Near-IR reflectance spectra have been obtained for freshly-exposed material in almost 100 small lunar regions, each 3–5 km in diameter. Various amounts of low-Ca orthopyroxene, high-Ca clinopyroxene, olivine, and plagioclase have been identified from spectra of these areas (*Pieters*, 1986; see Figs. 6.45 and 6.46) using Earth-based telescopes.

The heterogeneity of the lunar crust can be evaluated by spectral reflectance studies of relatively fresh surfaces exposed by craters. In addition, vertical as well as lateral variability among the crustal rocks can be determined by using the sizes of craters to estimate the original depth of material excavated (*Pieters*, 1986). More than 75% of moderately small highland craters (<15 km in diameter) are dominated by rock types with low-Ca pyroxene as the major mafic mineral, although there are variations in the spectra due to degree of brecciation and pyroxene abundance. Although limited by the number of measurements available, these observations imply that the upper 1–2 km of the lunar highland crust, which is roughly equivalent to the zone often referred to as *megaregolith*, is dominated by a variety of noritic compositions.

Larger craters (>50 km in diameter) probe deeper and, in contrast, excavate a surprising diversity of materials. Evaluation of compositional variations with depth is accomplished by examining different depositional regimes across a crater; for large craters, this type of analysis is within the spatial-resolution capabilities of Earth-based telescopes. The central peaks of large impact craters represent material excavated from the greatest depth (one-sixth to one-tenth the crater diameter), whereas materials forming the rim and the ejecta deposits represent higher stratigraphic units. Crustal stratigraphies reconstructed in this manner are shown in Plate 10.9 (*Pieters*, 1989). In addition to documenting the diversity of lunar crustal materials, these data also provide information on the expected range of materials represented in the returned lunar samples. Noritic (low-Ca pyroxene) and anorthositic (very feldspar rich) compositions dominate the regions surrounding the sampling sites. The occurrence of gabbroic rock types (with high-Ca pyroxene) and the less common troctolites (very olivine-rich), on the other hand, are particularly concentrated in the poorly sampled western hemisphere (*Pieters*, 1986; *Lucey and Hawke*, 1988).

10.5. STRATIGRAPHY AND RELATIVE AGES

The Moon has been mapped geologically at a wide variety of scales. The principles of stratigraphy as applied to lunar history are discussed in section 4.4. *Wilhelms* (1987) has summarized our current knowledge of lunar stratigraphy in the form of an abstract global geologic map (Plate 10.10). On this map, rock-stratigraphic units are subdivided into basin, crater, plains, and mare units. Time-stratigraphic classification (discussed in section 4.4) is indicated for the pre-Nectarian through Copernican systems.

The quantitative study of lunar crater morphology (*morphometry*) and crater density in the lunar maria has permitted subdivision of mare units in terms of relative age (*Boyce*, 1976; *Boyce and Johnson*, 1978; *BVSP*, 1981). A relative age map of the lunar maria is shown in Plate 10.11. This map combines data for the relative ages of mare basalts, obtained from both the so-called “D_i” method (*Soderblom and Lebofsky*, 1972; *Boyce*, 1976) and the cumulative crater density method (*Boyce and Johnson*, 1978). These relative ages are then converted to estimates of absolute ages by comparison to actual age measurements made through isotopic studies of returned basalt samples from the Apollo and Luna landing sites (*Boyce*, 1976).

10.6. GEOLOGY OF THE APOLLO AND LUNA LANDING SITES

Six manned Apollo missions and three robotic Luna missions returned samples from several geologic settings on the Moon. In particular, the later Apollo missions (15–17; the “J” missions) explored increasingly complex geologic terrains. The purpose of this section is to briefly review the regional and local geologic setting of each landing site and to present an interpretive geologic cross-section based on current (and clearly incomplete) understanding.

10.6.1. Apollo 11

The first lunar landing mission, Apollo 11, sampled the relatively old, Ti-rich (“blue”) lunar maria in southwestern Mare Tranquillitatis (landing site: 0.7°N, 24.3°E; Fig. 10.11). The site for the first lunar landing was chosen primarily for safety (relatively flat terrain; few large boulders). This mission provided our first look at the lunar maria, and analysis of the returned samples confirmed the theory that the maria are composed of basaltic lava flows. One “extravehicular activity” (EVA) traverse of two-and-one-half hours was performed by the astronauts on foot (Fig. 10.12).

The Apollo 11 landing site is no closer than about 40 km to the nearest mare/highland boundary, but a significant fraction (a few percent) of the returned regolith samples consists of feldspathic lithic and mineral fragments that were postulated (and subsequently shown) to be derived from highland areas (Wood *et al.*, 1970). The mare basalts range in age from 3.88 to 3.57 b.y. (Sm-Nd ages; BVSP, 1981). These ages are ancient by terrestrial standards, but they are generally younger than the ages inferred for the large multiring basins, whose ejecta deposits were sampled on later missions (e.g., Imbrium; ~3.85 b.y.). At least two chemically distinct groups of basalts of differing ages are present, suggesting the presence of at least two different lava flows in the vicinity of the site. These relations are summarized in the cross-section of Fig. 10.13. More detailed discussions of the geology of the Apollo 11 site are found in Shoemaker *et al.* (1970a) and Beatty and Albee (1978, 1980).

10.6.2. Apollo 12

The Apollo 12 mission was also sent to a relatively flat mare site for safety reasons, but it was the first mission to demonstrate pinpoint landing capability by landing within 200 m of the Surveyor 3 spacecraft in southeastern Oceanus Procellarum (landing site: 3.2°S, 23.4°W; Fig. 10.14). This region of the Moon consists of mare basalts that are lightly cratered relative to those at the Apollo 11 site (hence younger) and of a slightly more “reddish” color (hence different in composition). Some distal ejecta rays from the large Copernicus Crater (400 km to the north) cross the site, leading scientists to hope that this material could be sampled and age-dated to determine the actual time of formation of Copernicus. None of the samples returned, however, could be proven to be from Copernicus. Two EVA traverses on foot were made during this mission (Fig. 10.15).

Samples from the Apollo 12 site indicate the presence of at least three chemically distinct groups of mare basalts ranging in age from 3.29 to 3.08 b.y. (BVSP, 1981). The enigmatic KREEP component was first recognized in the Apollo 12 samples in the form of dark, agglutinitic glasses and a complex polymict breccia (sample 12013). Petrologic and geologic studies of the Apollo 12 site have been used to prepare a tentative cross-section (Fig. 10.16). Detailed discussion of the geology of the Apollo 12 site can be found in Shoemaker *et al.* (1970b), Warner (1970b), Rhodes *et al.* (1977), and Wilhelms (1984).

10.6.3. Apollo 14

The Apollo 14 mission was sent to a hilly region north of Fra Mauro Crater (landing site: 3.7°S, 17.5°W; Fig. 10.17). This landing site was the first in

the lunar highlands, and it was chosen partly because it was believed to contain ejecta from the nearby Imbrium Basin. The Imbrium impact event serves as a major boundary to subdivide lunar geologic history (see section 4.4), and the science objectives for the Apollo 14 mission included both the determination of the absolute age of the Imbrium impact and the examination of the Imbrium Basin ejecta, which was thought to have been derived from deep within the highland crust. Two EVA traverses on foot were performed (Fig. 10.18).

Rocks returned by the Apollo 14 mission included complex polymict fragmental breccias, impact-melt breccias, and clast-poor impact melts with generally basaltic and KREEP-rich compositions; these polymict samples were assembled into their present forms about 3.8 to 3.9 b.y. ago. Their origin still remains contentious. Post-Apollo studies have shown that basin ejecta deposits consist in general of a mixture of primary basin ejecta and admixed local material, although the exact proportions are unknown (cf. Oberbeck, 1975; Schultz and Gault, 1985). As a result, it is still unclear which rocks from the Apollo 14 site represent true Imbrium Basin ejecta; a noncommittal cross-section is presented in Fig. 10.19. The geology of the Fra Mauro (Apollo 14) region is discussed in detail by Chao (1973), Swann *et al.* (1977), Hawke and Head (1977), and Simonds *et al.* (1977).

10.6.4. Apollo 15

Apollo 15 was the first advanced (“J”) mission and the first to be sent to a complex, multiple-objective landing site, the Hadley-Apennine region (landing site: 26.1°N, 3.7°E; Fig. 10.20). This site was chosen to sample and investigate (1) the massifs and highlands that form the rim of the Imbrium Basin and (2) the mare lavas and landforms (e.g., Hadley Rille) of Palus Putredinis. Three extended EVAs were performed (Fig. 10.21), an advance made possible by the first use of the Lunar Roving Vehicle (LRV; see section 9.1.11).

The mare surfaces at the Apollo 15 site provided samples of basaltic lavas of two distinct chemical groups (quartz normative and olivine normative); both groups have virtually the same age (3.3 b.y.). The highland material collected consists of a variety of rock types: anorthosites, Mg-suite plutonic rocks, impact melts, and granulites. Many of these rocks occur as individual clasts in regolith breccias collected from the highland areas at the site. Results from the Apollo 14 and 15 missions together indicate that the Imbrium Basin formed about 3.85 b.y. ago. Two surprising volcanic materials were discovered at the Apollo 15 site: an aluminous, nonmare basalt, rich in KREEP, and an emerald-green glass of

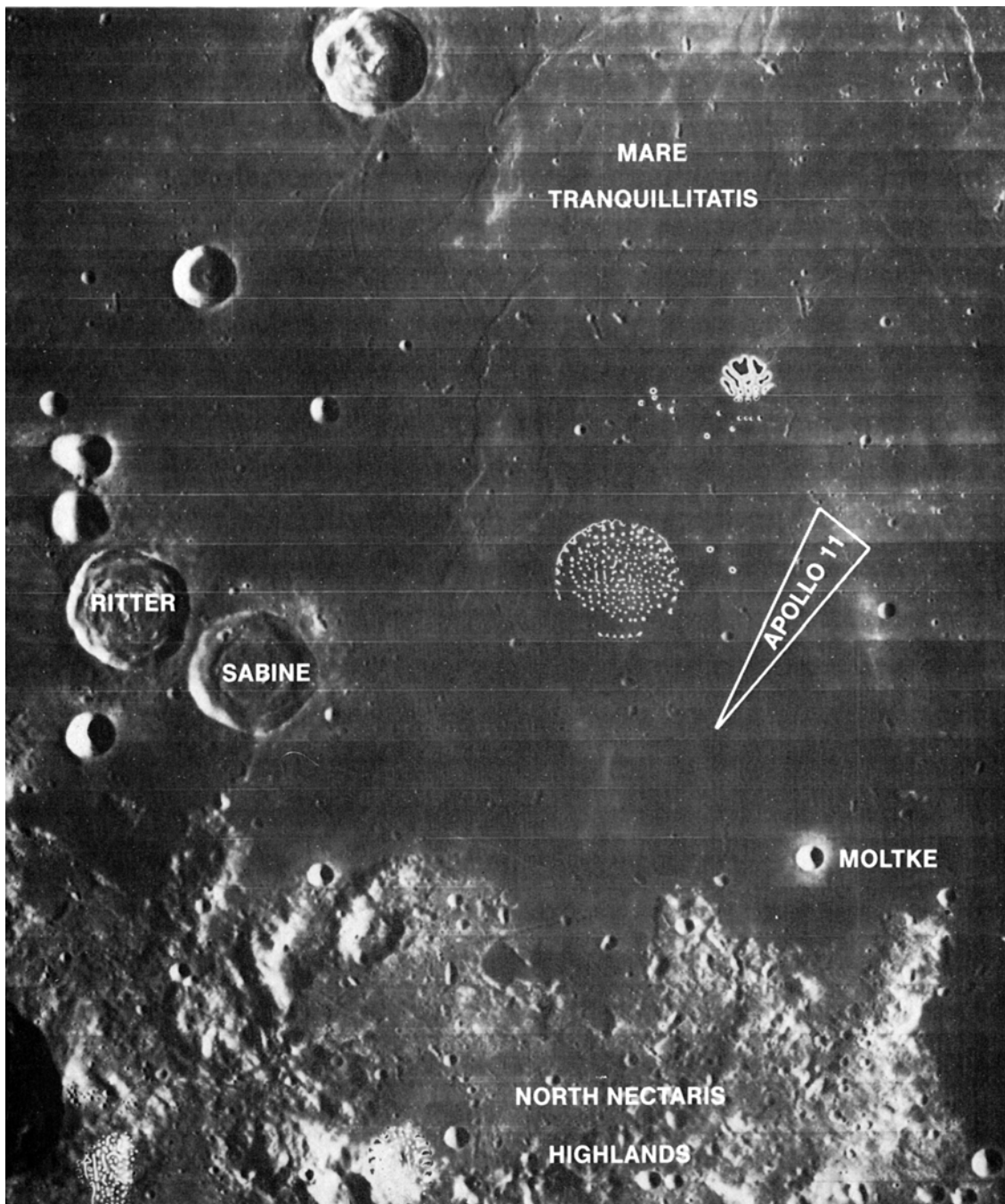


Fig. 10.11. Regional view of southwestern Mare Tranquillitatis, including the Apollo 11 landing site. Lunar north is at top. The actual landing site is on mare basalts of a bluish color and a relatively high crater density (old, high-Ti basalts). The nearest highlands are the circum-Nectaris massifs (bottom), approximately 40 km south of the Apollo 11 site. Horizontal lines are framelet boundaries in this Lunar Orbiter photograph. Each framelet is 12 km wide. The white blemish above the Apollo 11 landing site is a flaw in the film developed in the Lunar Orbiter spacecraft. (NASA Photo LOIV-85H1.)

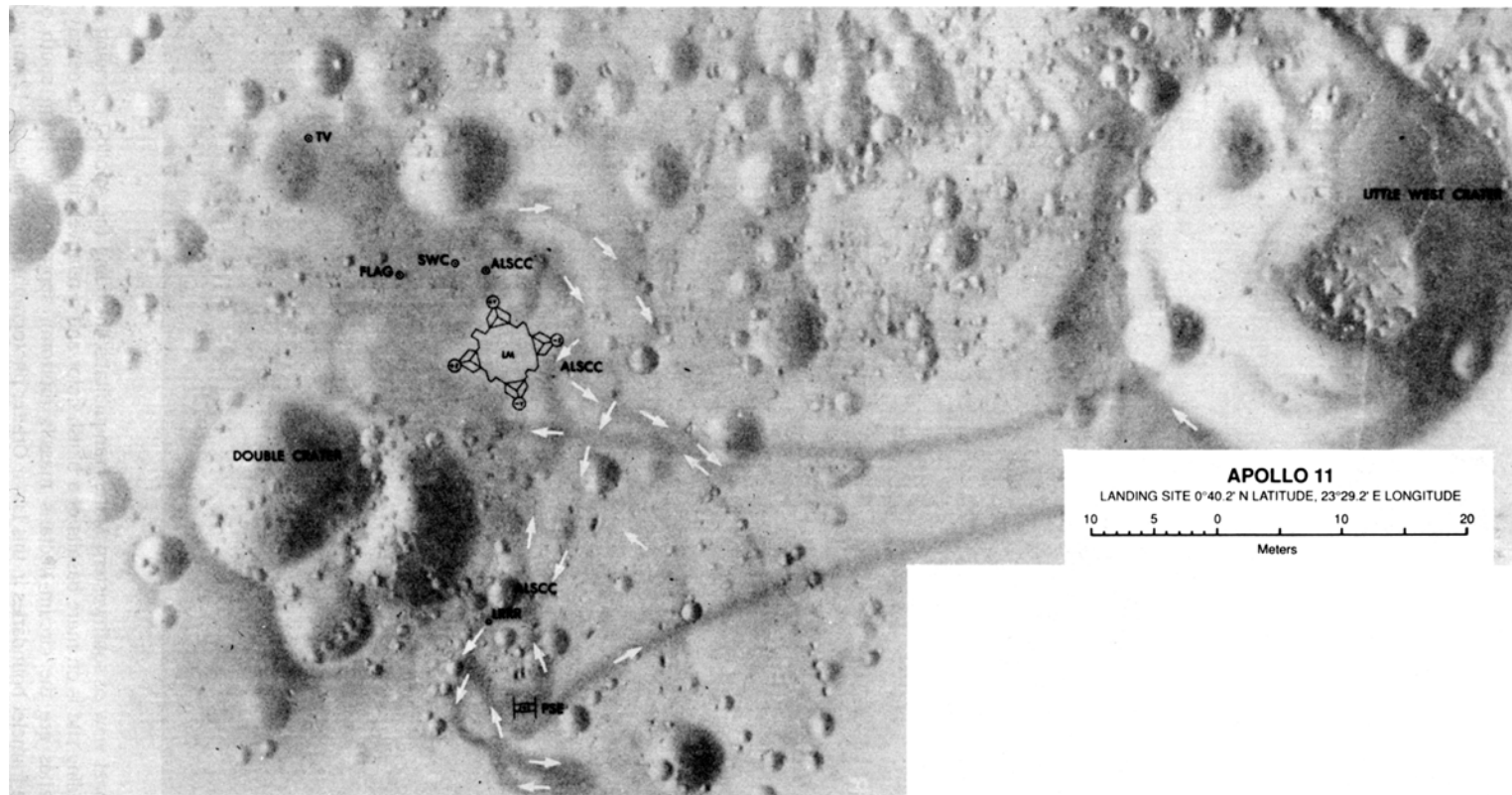


Fig. 10.12. Apollo 11 site traverse map, showing locations of the Lunar Module (LM) and deployed surface experiments. Probable astronaut traverses are shown by the white arrows. (From Defense Mapping Agency; original scale 1:250.) ALSCC = Apollo Lunar Surface Close-up Camera; SWC = Solar-Wind Composition Experiment; PSE = Passive Seismic Experiment; LRRR = Laser Ranging Retroreflector; TV = Television Camera.

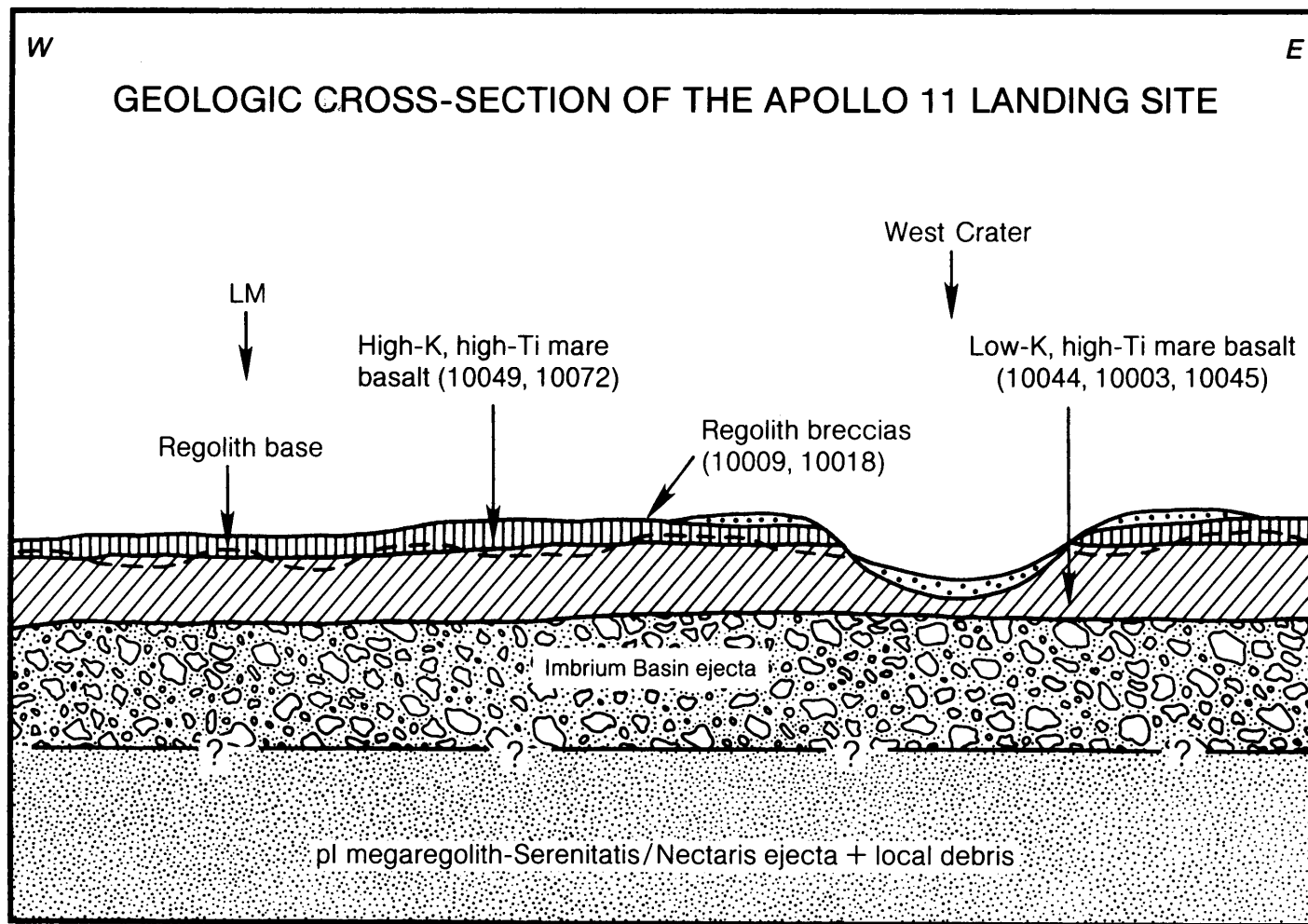


Fig. 10.13. Schematic east-west geologic cross-section through the Apollo 11 landing site, showing at least two basalt lava flow units overlying older ejecta from major impact basins (modified after *Beaty and Albee, 1980*). Presence of the Imbrium ejecta layer is inferred. Numbers refer to specific collected samples representative of the various units inferred to be present. The base of the regolith (dashed line) locally penetrates into the low-K mare basalts. Abbreviation “pl” stands for pre-Imbrian in the deep megaregolith.

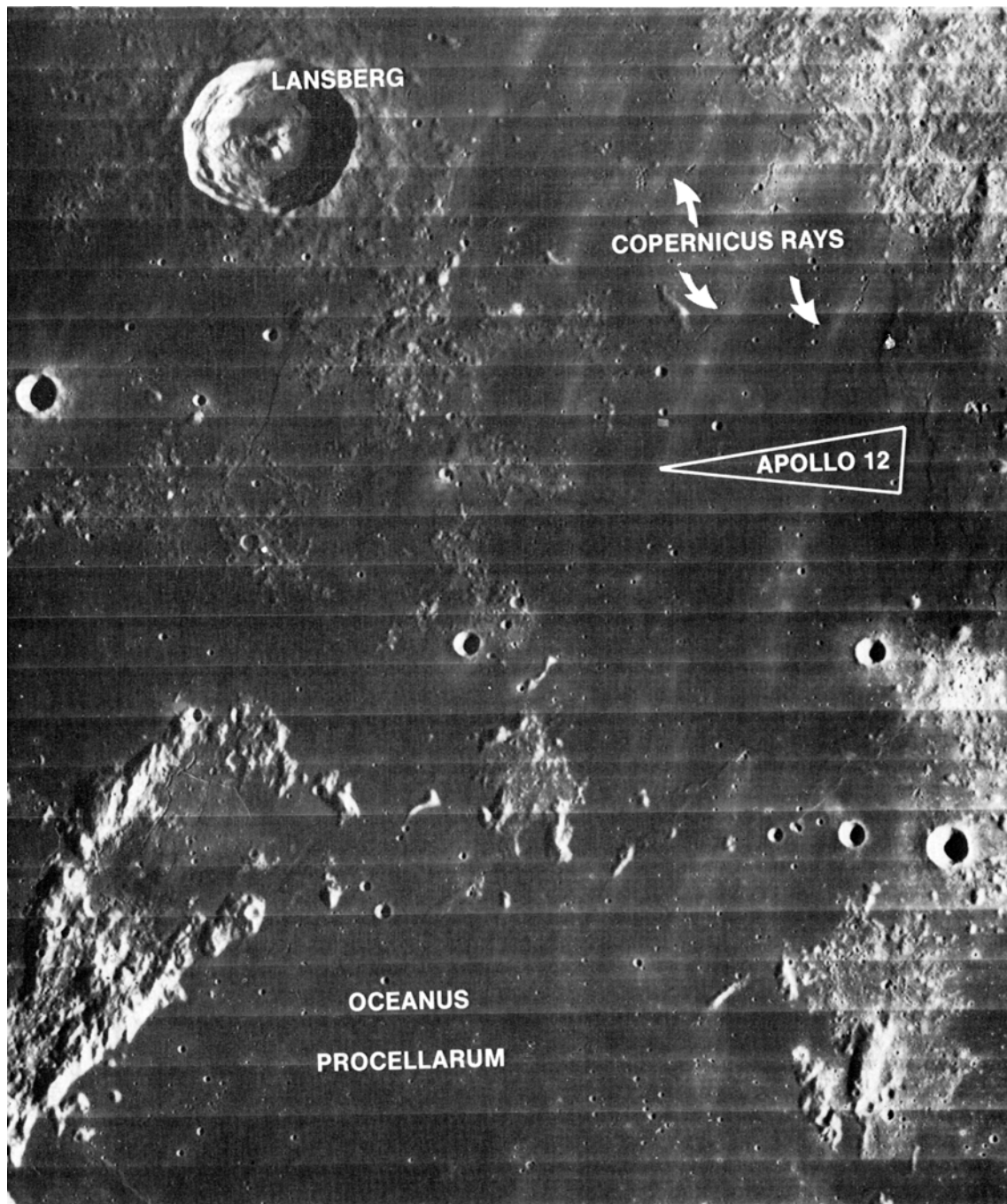


Fig. 10.14. Regional view of southeastern Oceanus Procellarum, showing the Apollo 12 landing site. Lunar north is at top. The actual landing site is on mare basalt with a relatively reddish color and a relatively low crater density (i.e., young, low-Ti basalts). Exposed islands of highland material (light-colored) in the mare suggest that the mare basalt in this region is relatively thin. Rays from Copernicus Crater (light-colored) cross the landing site from northeast to southwest. Horizontal lines are framelet boundaries in this Lunar Orbiter photograph. Each framelet is 12 km wide. (NASA Photo LOIV-125H3.)

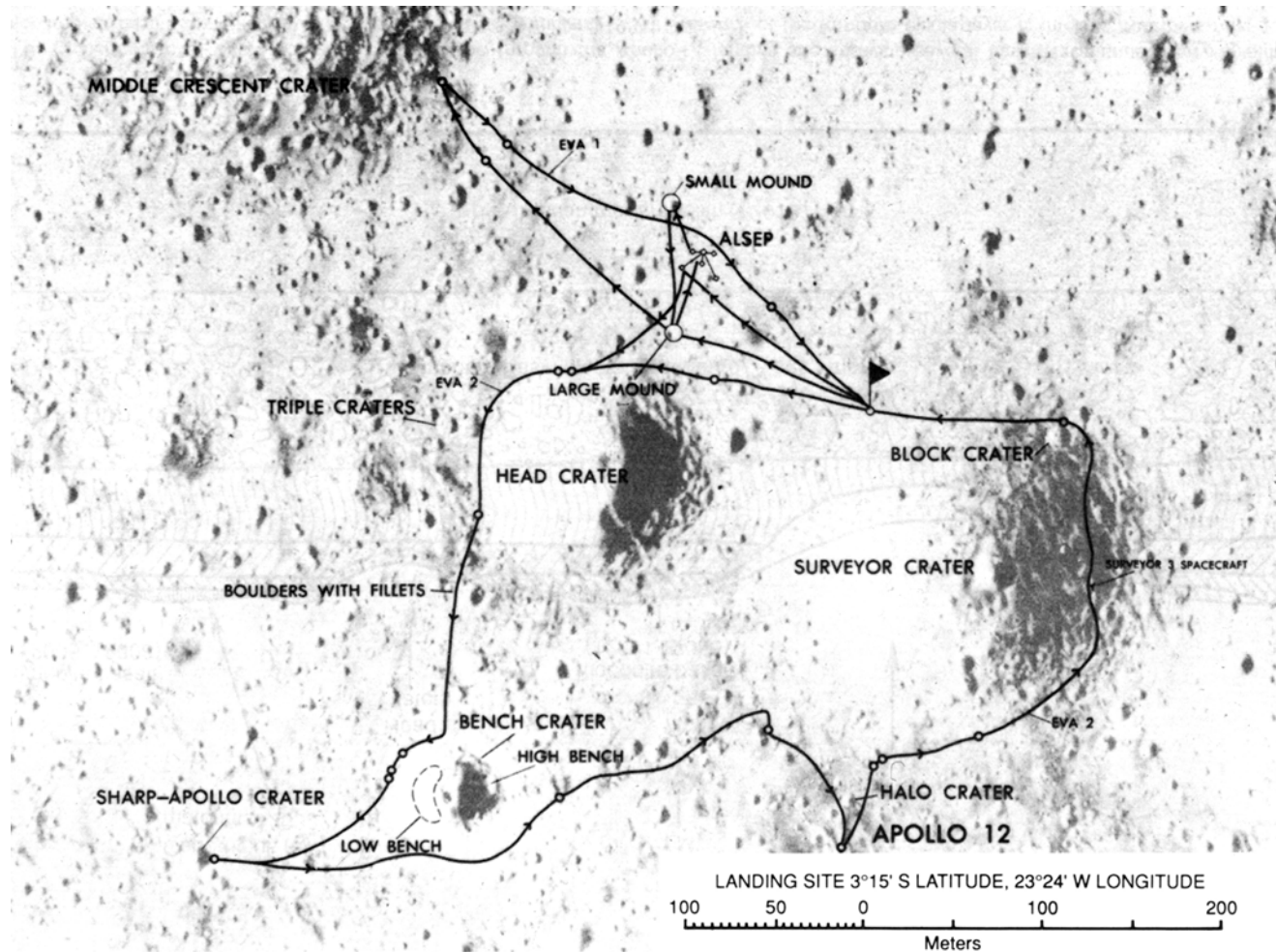


Fig. 10.15. Apollo 12 site traverse map, showing topographic features and scientific sites. The Lunar Module (LM) landing site is shown by the flag on the north rim of Surveyor Crater. The Surveyor 3 spacecraft landed on the east rim of this crater. Solid lines indicate astronaut traverses (extravehicular activity or “EVA”). (From Defense Mapping Agency; original scale 1:2500.) ALSEP = Apollo Lunar Surface Experiments Package.

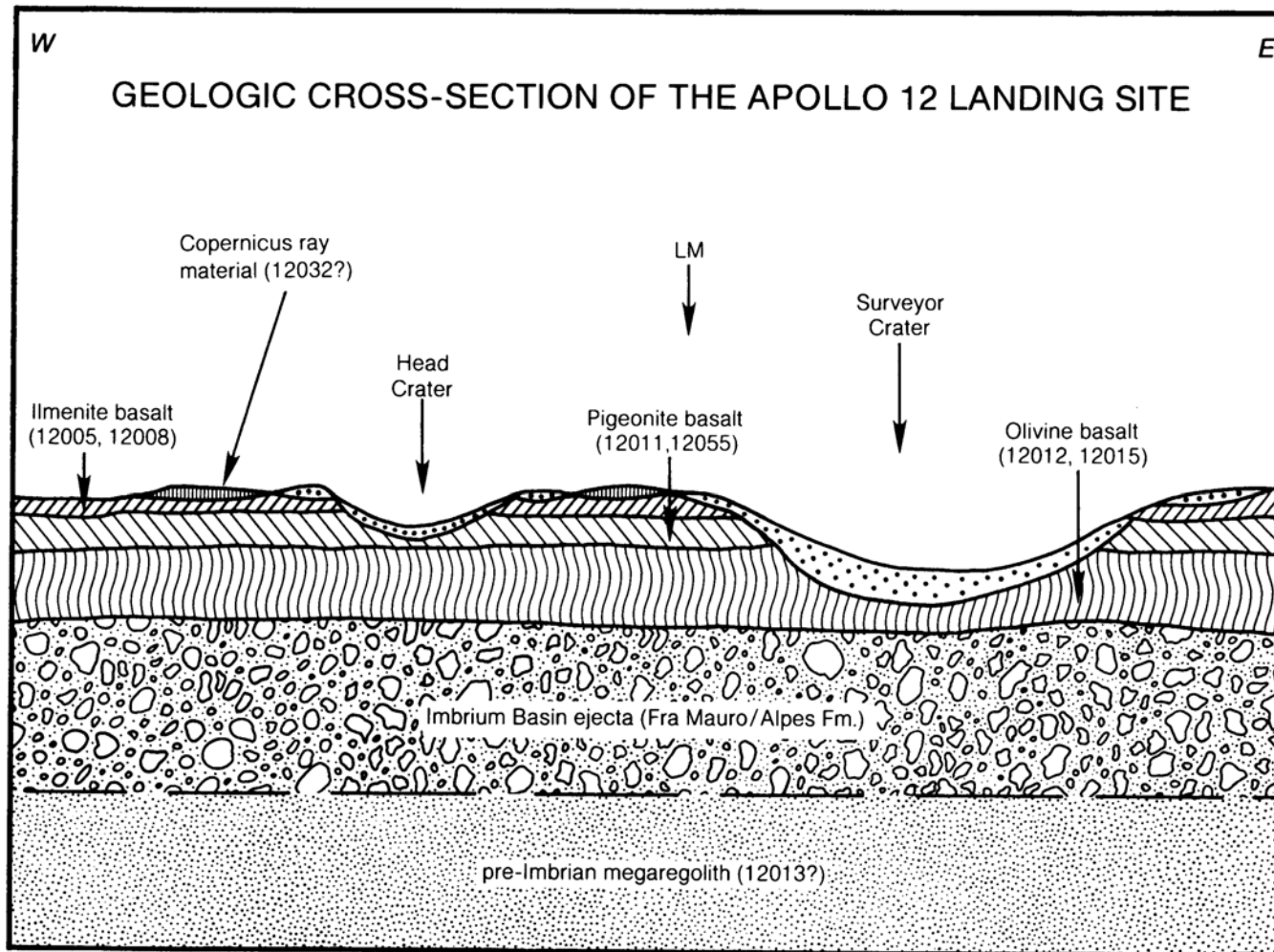


Fig. 10.16. Schematic east-west geological cross-section through the Apollo 12 landing site showing several basalt lava units overlying older ejecta from major impact basins (modified after Rhodes *et al.*, 1977; Wilhelms, 1984). Presence of the Imbrium ejecta layer is inferred. Numbers refer to specific collected samples representative of the various units inferred to be present.



Fig. 10.17. Regional view of the Fra Mauro highlands, showing the Apollo 14 landing site. Lunar north is at top. The actual landing site is on hummocky material (the Fra Mauro Formation) that overlies the pre-Imbrian Fra Mauro Crater; this material is apparently ejecta that was deposited during formation of the Imbrium Basin. Horizontal lines are framelet boundaries in this Lunar Orbiter photograph. Each framelet is 12 km wide. (NASA Photo LOIV-120H3.)

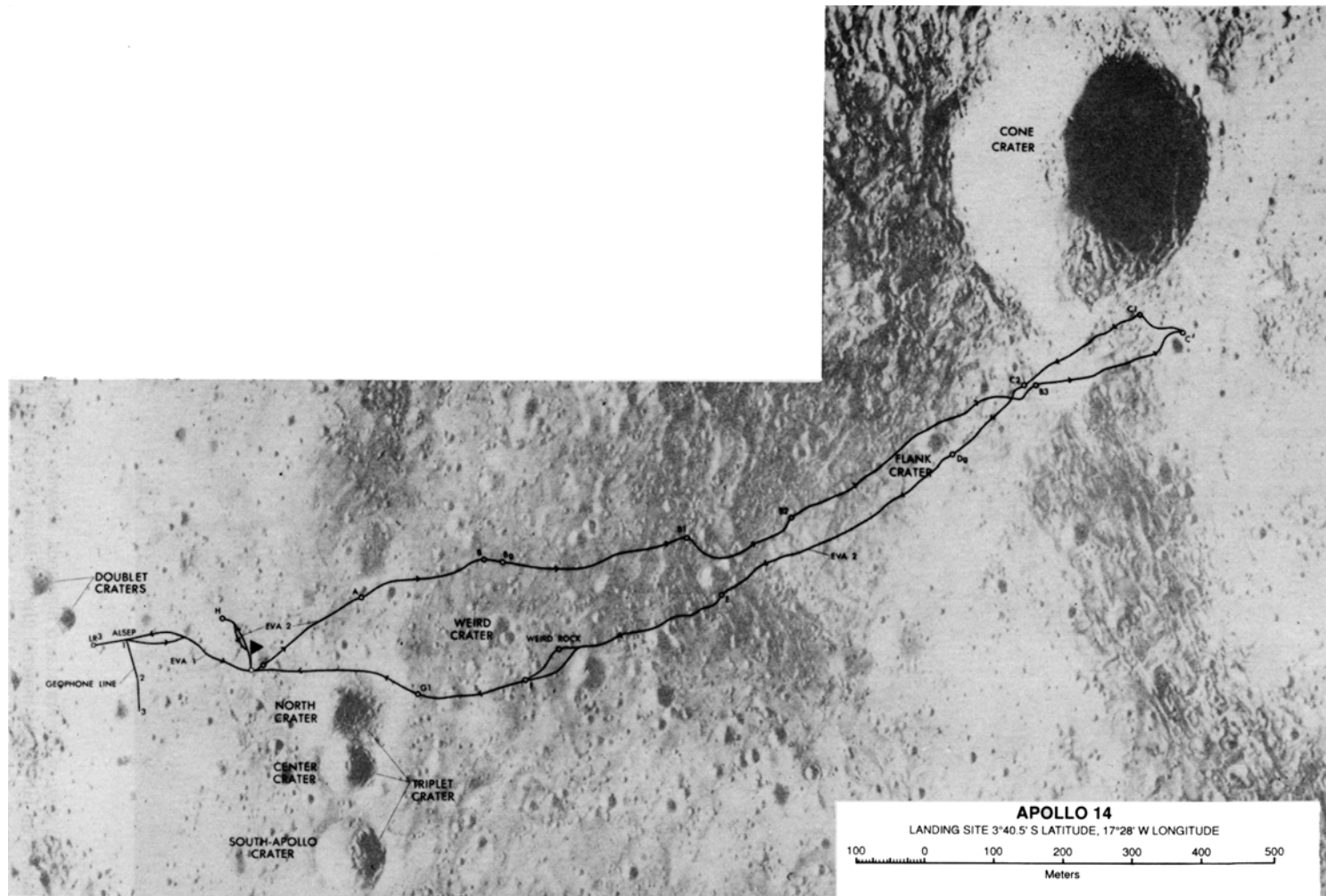


Fig. 10.18. Apollo 14 site traverse map, showing topographic features, scientific sites, and astronaut traverses (solid lines). The Lunar Module (LM) landing site is shown by the flag at the left side. (From Defense Mapping Agency; original scale 1:4000.) Letters are sampling/photo stops; ALSEP = Apollo Lunar Surface Experiments Package; EVA = extravehicular activity.

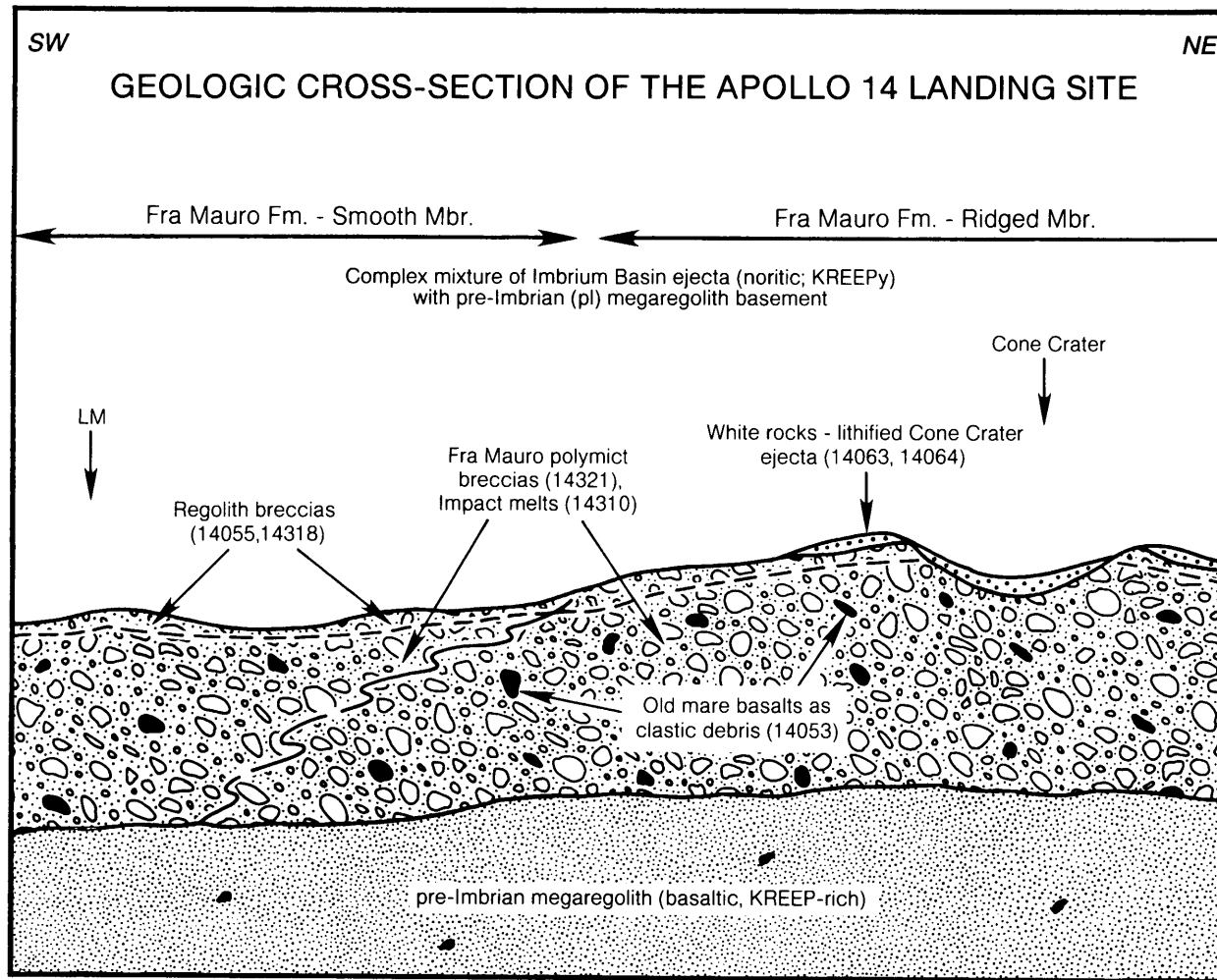


Fig. 10.19. Schematic east-west geologic cross-section through the Apollo 14 landing site, showing contact between “smooth” and “ridged” members (Mbr.) of the Fra Mauro Formation, which is an assemblage of complex impact-produced breccias (after Swann *et al.*, 1977). Numbers refer to specific collected samples that are representative of the units inferred to be present. LM shows where the Lunar Module landed. Dashed line below surface represents the depth of regolith.

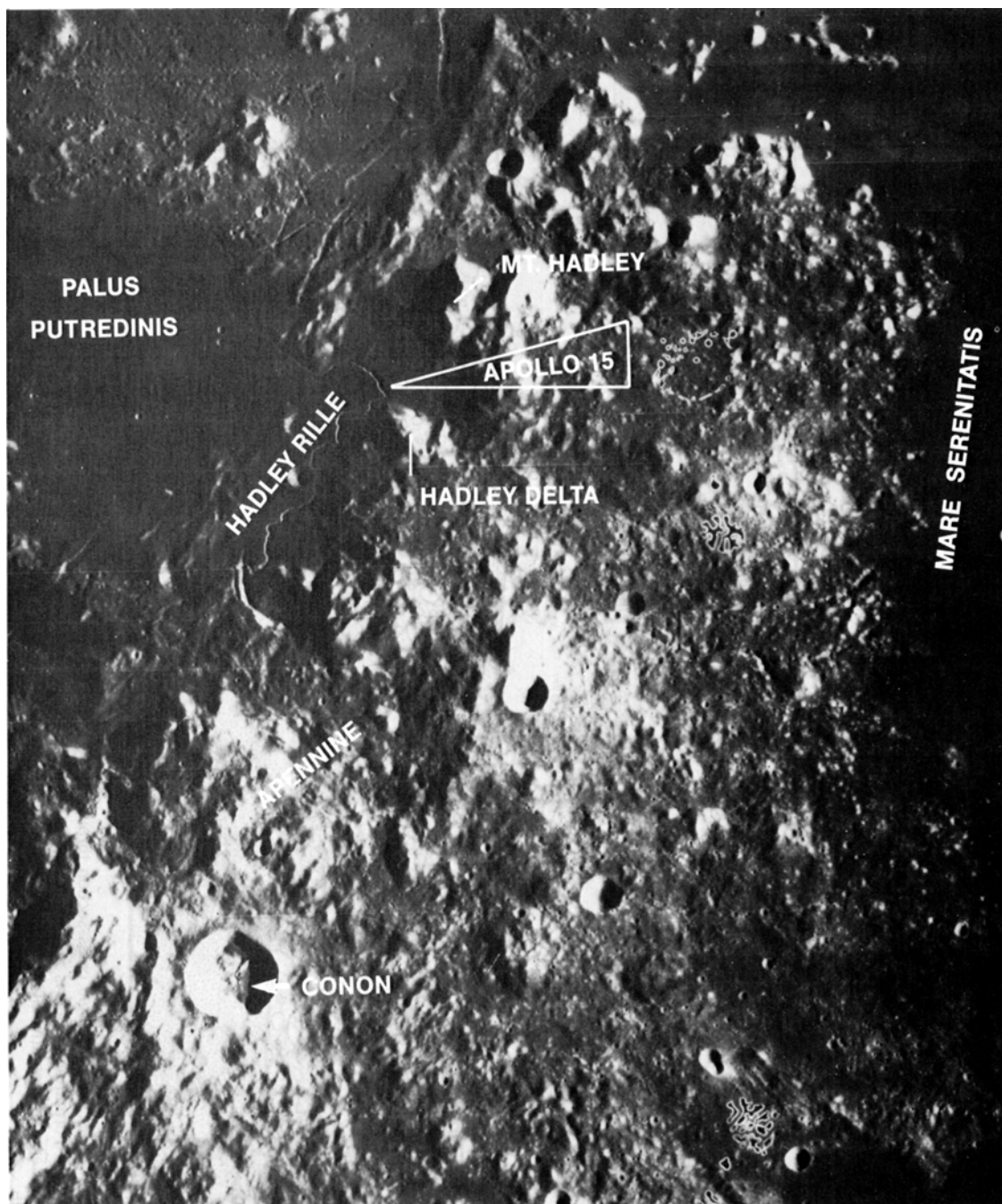


Fig. 10.20. Regional view of the southeastern edge of Mare Imbrium, showing the highland-mare boundary in the Hadley-Apennine area and the Apollo 15 landing site. Lunar north is at top. The actual landing site is located on the reddish (low-Ti) mare basalts of Palus Putredinus, adjacent to the Apennine Scarp, which is part of the main rim of the Imbrium Basin. Hadley Rille is a sinuous rille that runs across the mare material. Horizontal lines are framelet boundaries in this Lunar Orbiter photograph. Each framelet is 12 km wide. Conon Crater is 22 km in diameter. (NASA Photo LOIV-102H3.)



Fig. 10.21. Apollo 15 site traverse map, showing topographic features, scientific sites, and astronaut traverses (solid lines). The Lunar Module landing site is approximately in the center of the picture, on the flat area of mare basalts. Hadley Rille (Rima Hadley) runs along the left side of the picture, and the highland massif (the Apennine Scarp; here called Hadley Delta) is at the bottom. (Defense Mapping Agency Chart 41B4S4(25); original scale 1:25,000.)

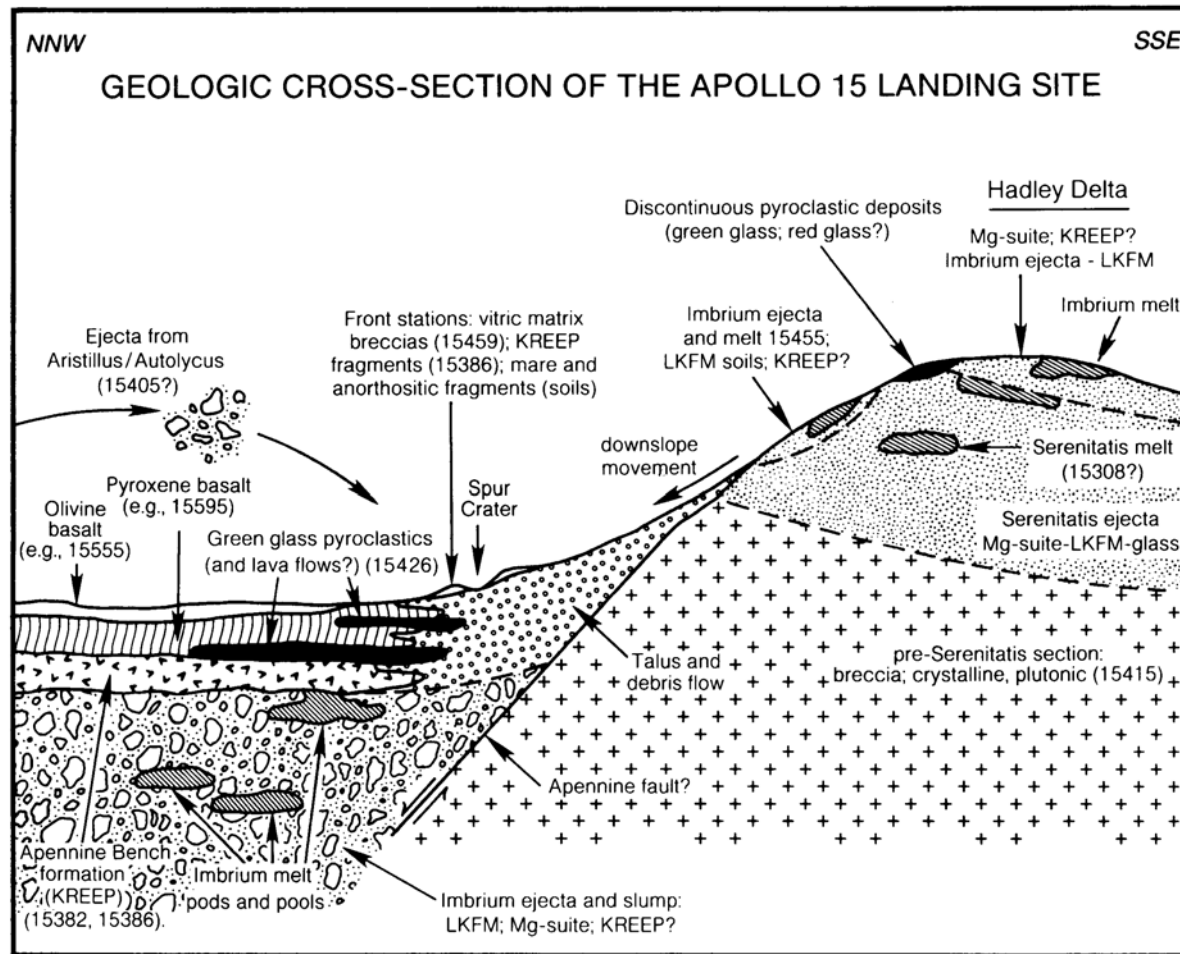


Fig. 10.22. Schematic northwest-southeast geologic cross-section through the Apollo 15 landing site, showing the complex geological transition between mare and highlands (modified from *Spudis and Ryder, 1985; Swann et al., 1972; Swann, 1986*). In the mare (left), post-Imbrian basalt lavas overlie a thick deposit of Imbrium ejecta. In the highland area (Hadley Delta, right), older (pre-Imbrian) ejecta from Mare Serenitatis overlies lunar crustal rocks. Numbers refer to specific collected samples that are representative of the various units inferred to be present.

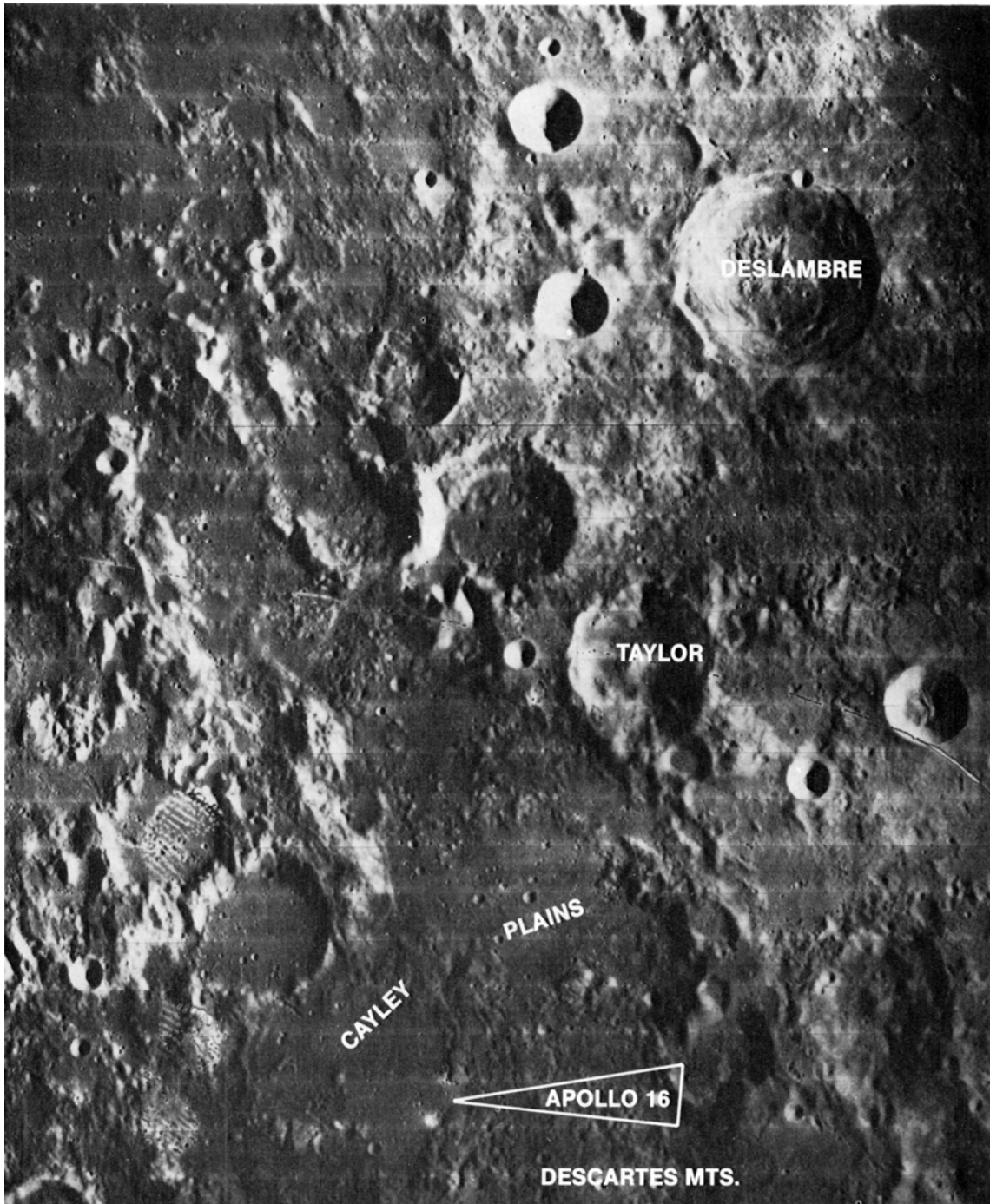


Fig. 10.23. Regional view of the Descartes Highlands, showing the Apollo 16 landing site. Lunar north is at top. Rough, light-colored material near the bottom of frame, making up the Descartes Mountains, is the Descartes Formation, which is interpreted as ejecta from the older Nectaris Basin. The smooth, intermontane plains (darker) are the Cayley Formation, once thought to be a volcanic unit but now interpreted as ejecta from another impact basin (Imbrium?). Horizontal lines are framelet boundaries in this Lunar Orbiter photograph. Each framelet is 12 km wide. Blemishes in the lower left corner are flaws in the film developed in the Lunar Orbiter spacecraft. (NASA Photo LOIV-89H3.)

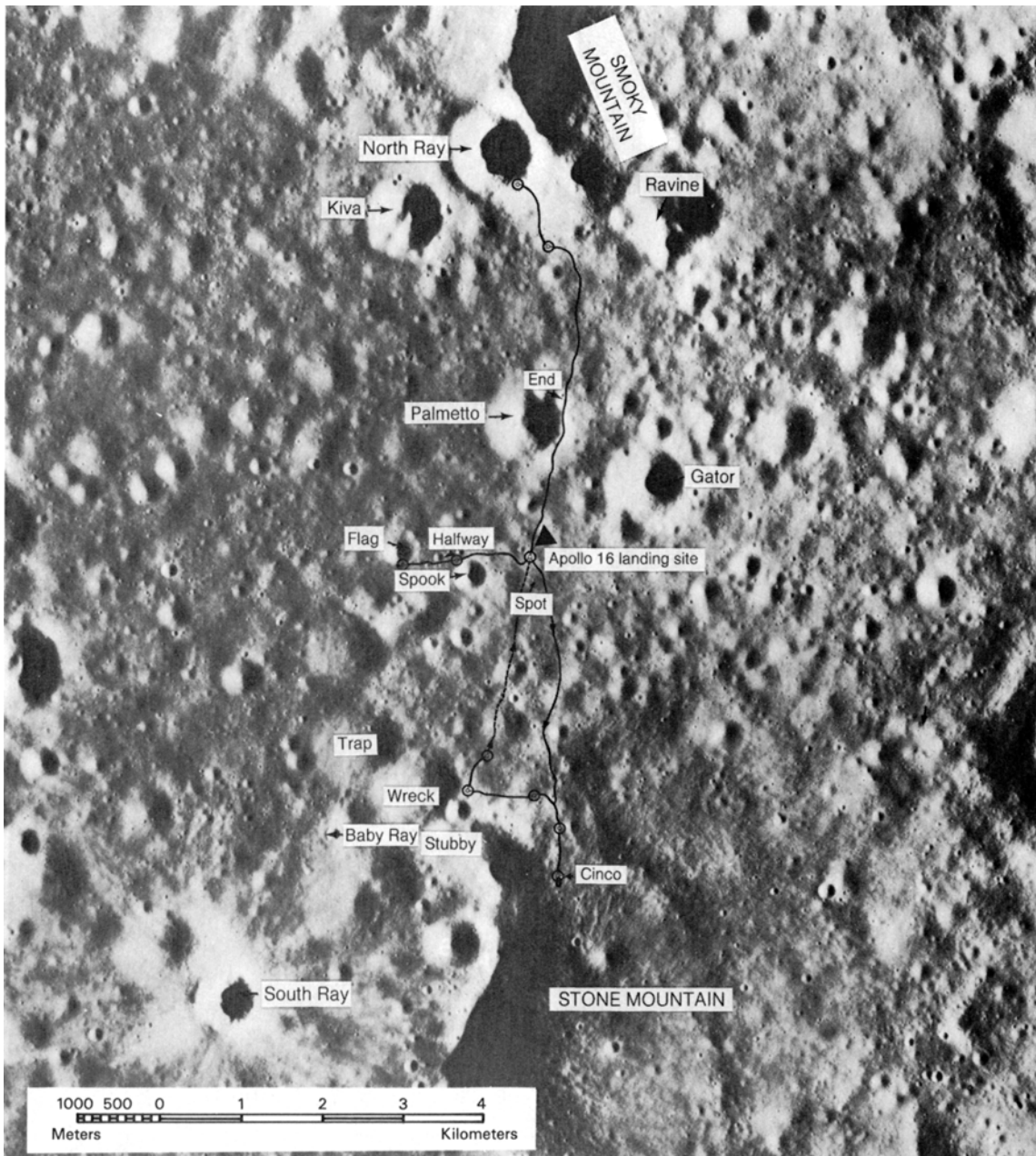


Fig. 10.24. Apollo 16 site traverse map, showing topographic features, scientific sites, and astronaut traverses. Solid lines are used where the traverse is known, dashed lines where the traverse is approximate. The Lunar Module landing site is about in the center of the picture, on the more level plain of the Cayley Formation. This unit was sampled during a short traverse west of the landing site. Longer traverses to north and south sampled the more rugged Descartes Formation at Smoky Mountain/North Ray Crater (north) and at Stone Mountain (south). (Defense Mapping Agency Chart 78D252(25); original scale 1:25,000.)

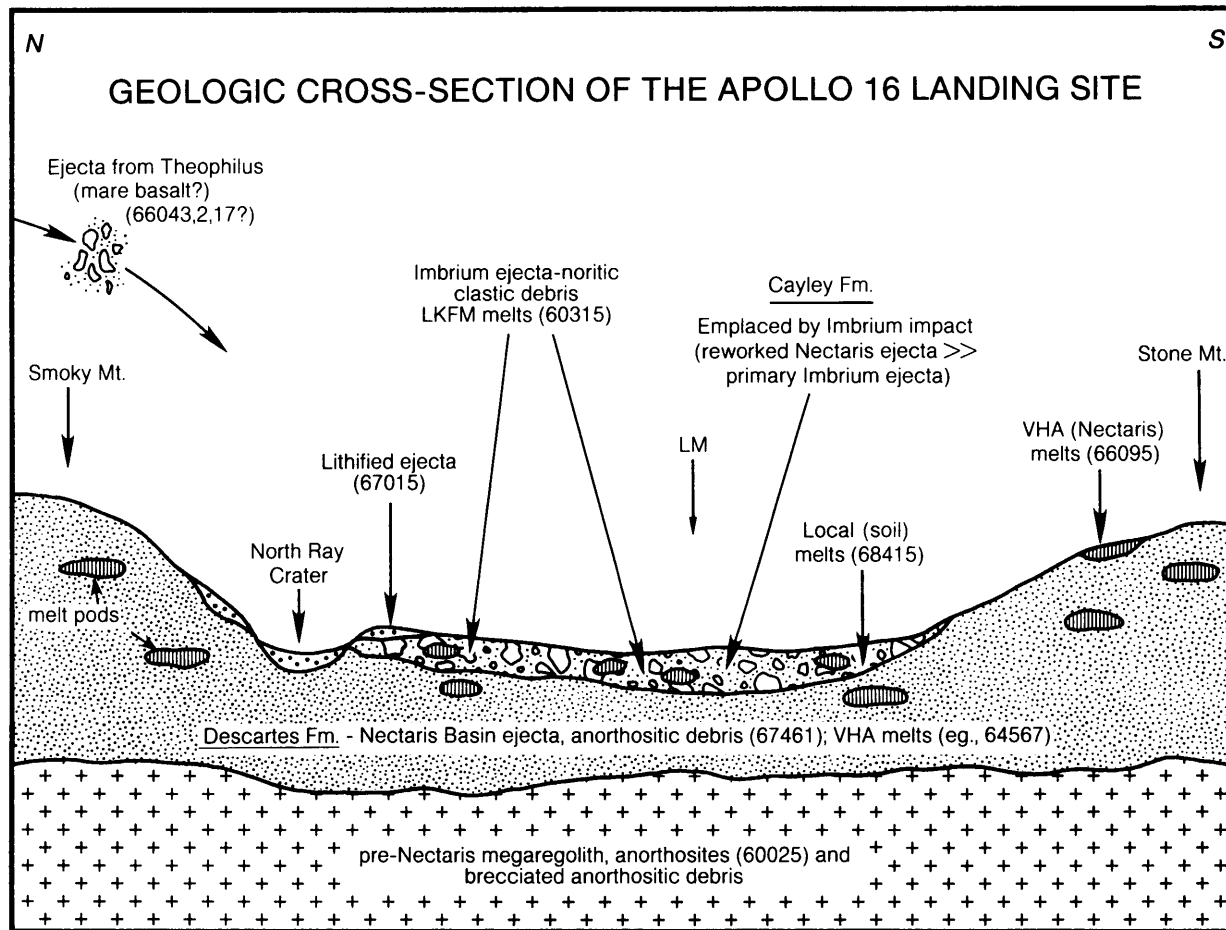


Fig. 10.25. Schematic geologic cross-section through the Apollo 16 landing site, showing the complex interrelations of different units of impact-produced ejecta excavated from large mare basins (modified after *Spudis, 1984; Stöffler et al., 1985*). The Descartes Formation is mostly ejecta from the older Nectaris Basin. The overlying Cayley Formation, emplaced by the younger Imbrian(?) impact event, consists mostly of reworked material from the Descartes Formation with some Imbrian ejecta. Both the Descartes and Cayley Formations are inferred to rest on an older (pre-Nectaris) megaregolith composed of a thick layer of complex debris from many older impact events. Numbers refer to specific collected samples that are representative of the various units inferred to be present. LM shows where the Lunar Module landed.

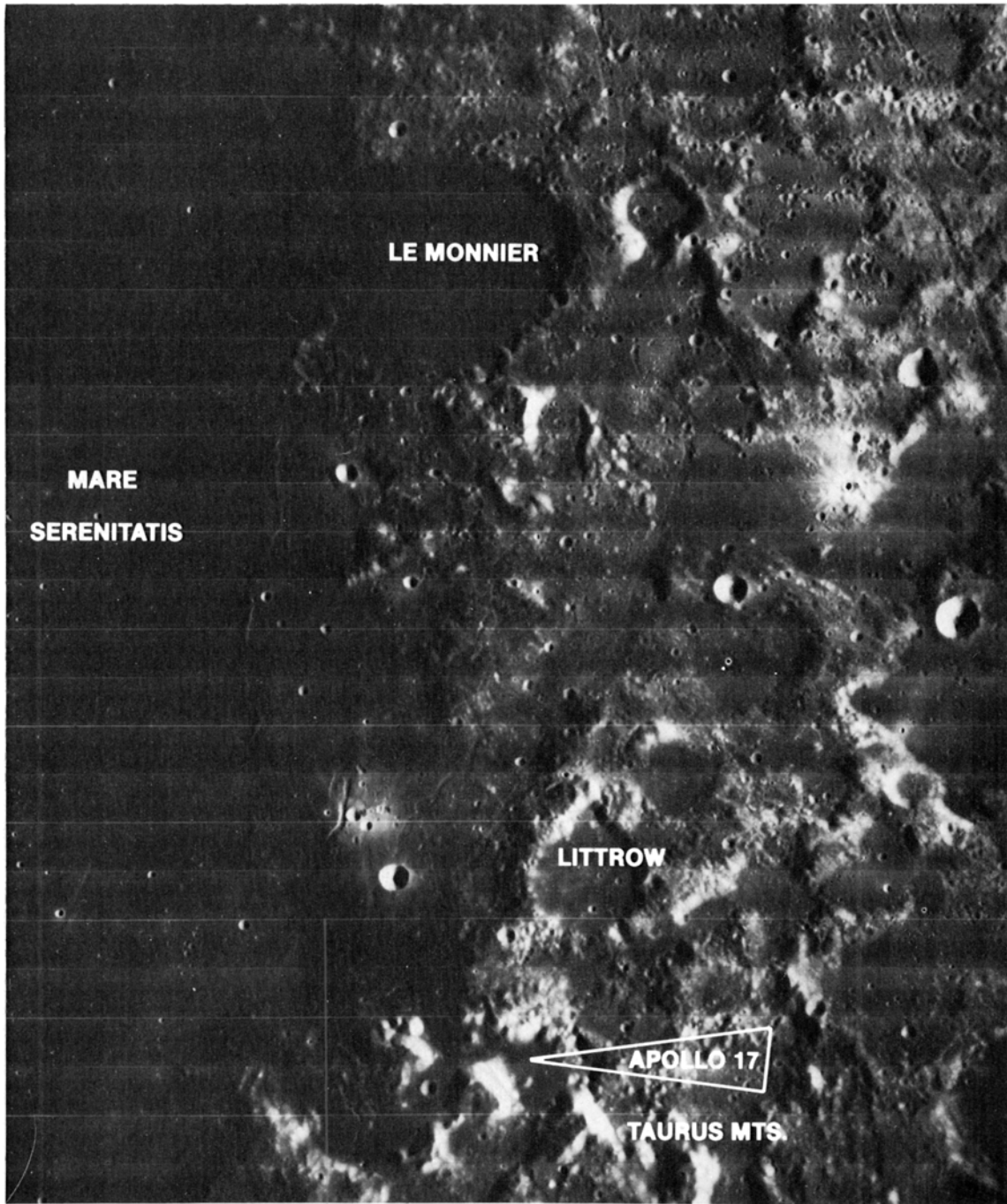


Fig. 10.26. Regional view of the Taurus-Littrow region on the eastern rim of Mare Serenitatis, showing the Apollo 17 landing site. Lunar north is at top. The Taurus Mountains (light-colored highland material at right) form the actual rim of the mare. These massifs are embayed by the later basalt lava flows (darker material at left) of Mare Serenitatis itself. The unusually dark color of the material around the actual landing site (bottom center) is due to the presence of dark-mantle deposits (glass-rich pyroclastic units). Horizontal lines are framelet boundaries in this Lunar Orbiter photograph. Each framelet is 12 km wide. (NASA Photo LOIV-78H3.)

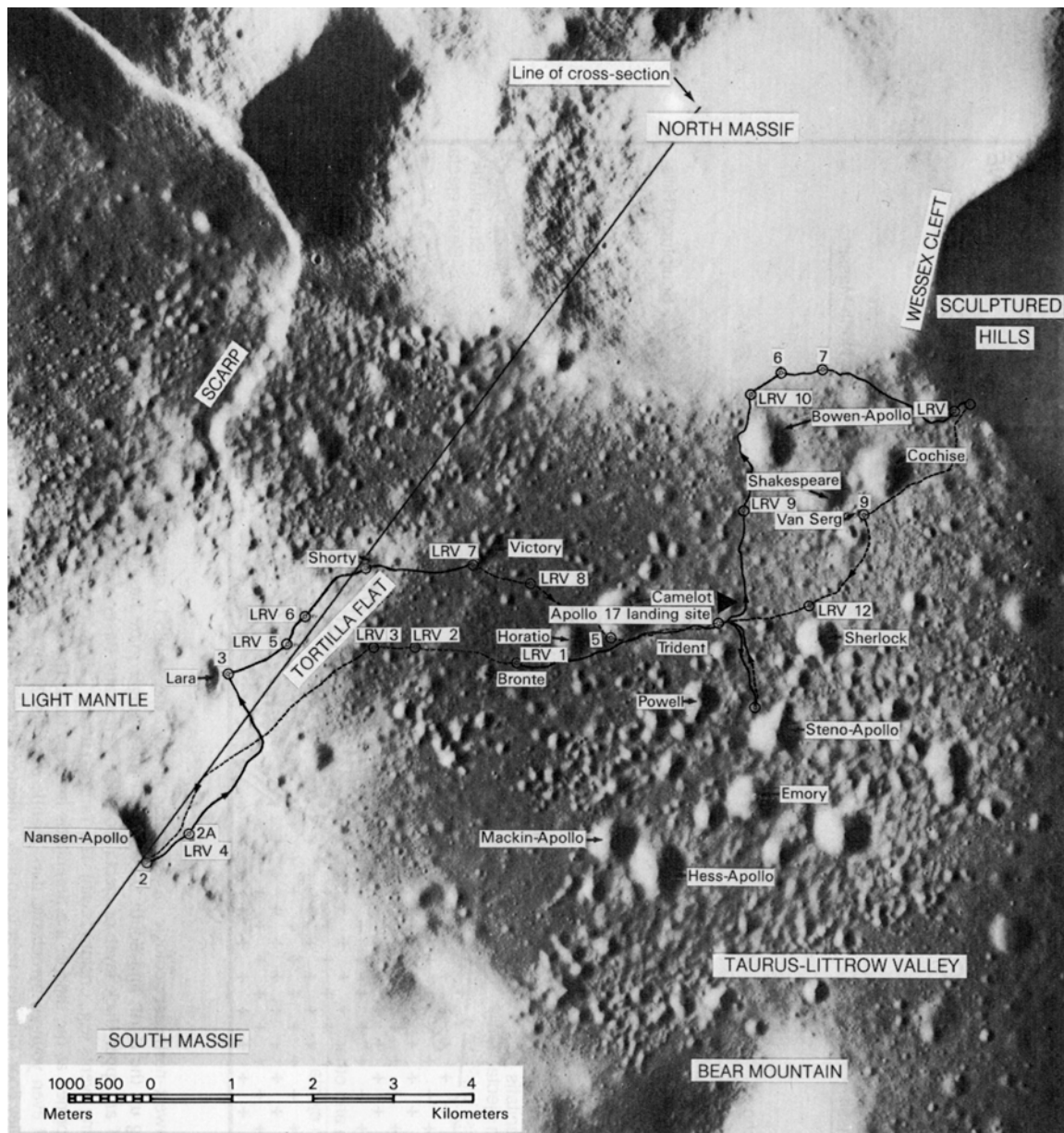


Fig. 10.27. Apollo 17 site traverse map, showing topographic features, informally-named craters, scientific sites, and astronaut traverses. Solid lines are used where the traverse is known, dashed lines where the traverse is approximate. The LM landing site (center flag) is in an east-west-trending valley (Taurus-Littrow Valley) that is floored by basalt lavas and bounded by two high massifs of older highland material (North Massif, South Massif). During traverses with the Lunar Roving Vehicle (marked LRV, with numbered stops), the astronauts studied and sampled both the basalts on the valley floor and the highland material from the massifs. Numbered stations not preceded by "LRV" are formal sampling stations, as opposed to informal samplings made at points of interest during the LRV traverses. (Defense Mapping Agency Chart 43D1S2 (25); original scale 1:25,000.)

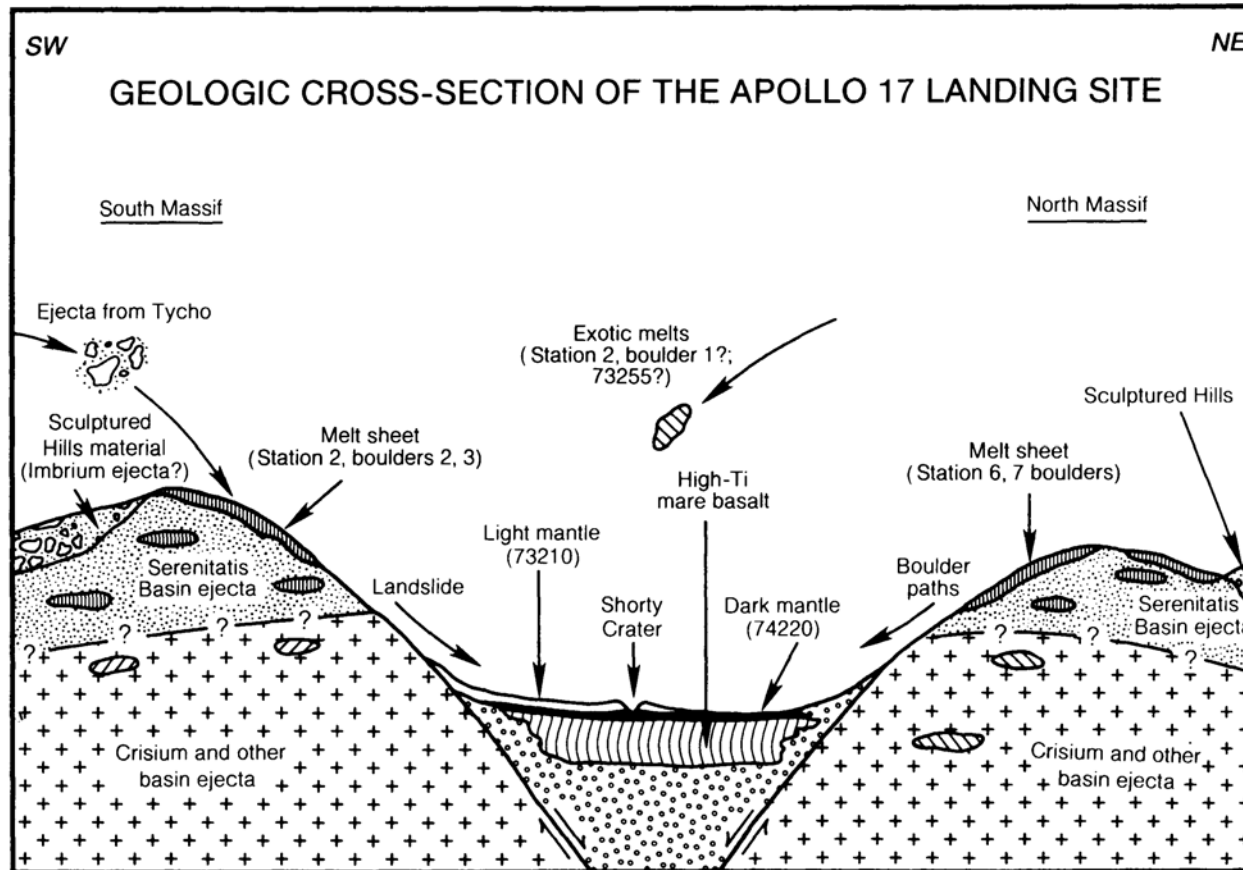


Fig. 10.28. Schematic southwest-northeast geologic cross-section through the Apollo 17 site, showing the complex boundaries between older highland material (ejecta layers making up the North and South Massifs) and the younger mare basalt flows that underlie the valley (modified after Wolfe *et al.*, 1981). The massifs consist of an upper thick layer of ejecta from the Serenitatis Basin, which is inferred to overlie an even thicker layer of complex ejecta from earlier basin-forming events (e.g., Crisium Basin). The Taurus-Littrow Valley developed as a downdropped wedge (graben) between two fractures (faults) that may have been formed at the time of the Serenitatis impact event. The valley was then filled, first with fragmental debris from the massifs, then by basalt lava flows and even younger pyroclastic dark-mantle deposits. More recent geological activity includes landslides and boulder falls from the higher massifs onto the valley floor. Numbers refer to specific collected samples that are representative of the various units inferred to be present.

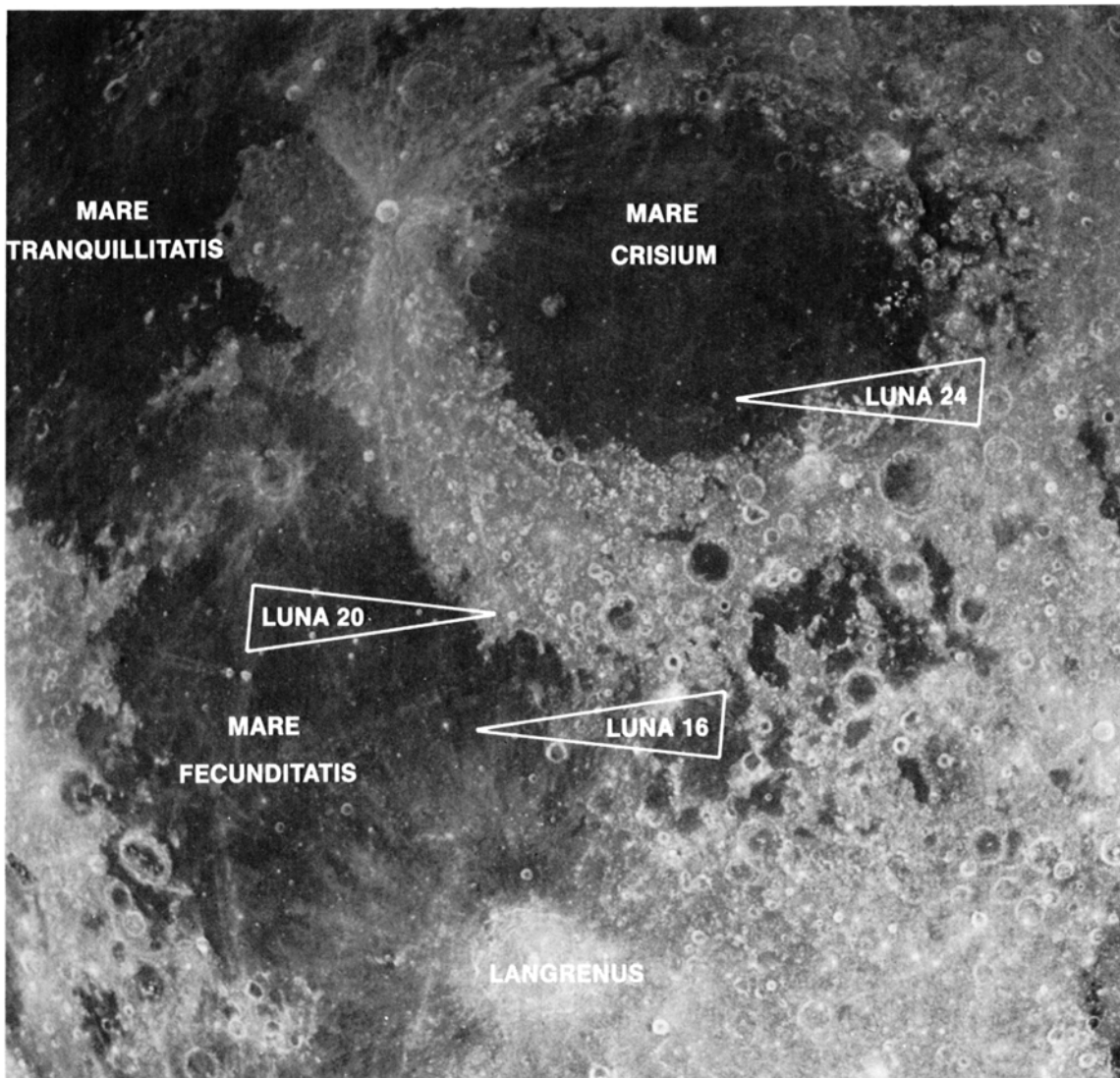


Fig. 10.29. Regional view of the east limb of the Moon, showing landing sites for the U.S.S.R. Luna 16, 20, and 24 robotic sample-return missions. Lunar north is at top; approximate width of view is 1200 km. Luna 16 and 24 sampled mare basalt lavas from Mare Fecunditatis and Mare Crisium, respectively. Luna 20 returned a sample of highland material from the outer edge of the ejecta deposits surrounding Mare Crisium. (Portion of NASA Photo AS11-44-6661.)

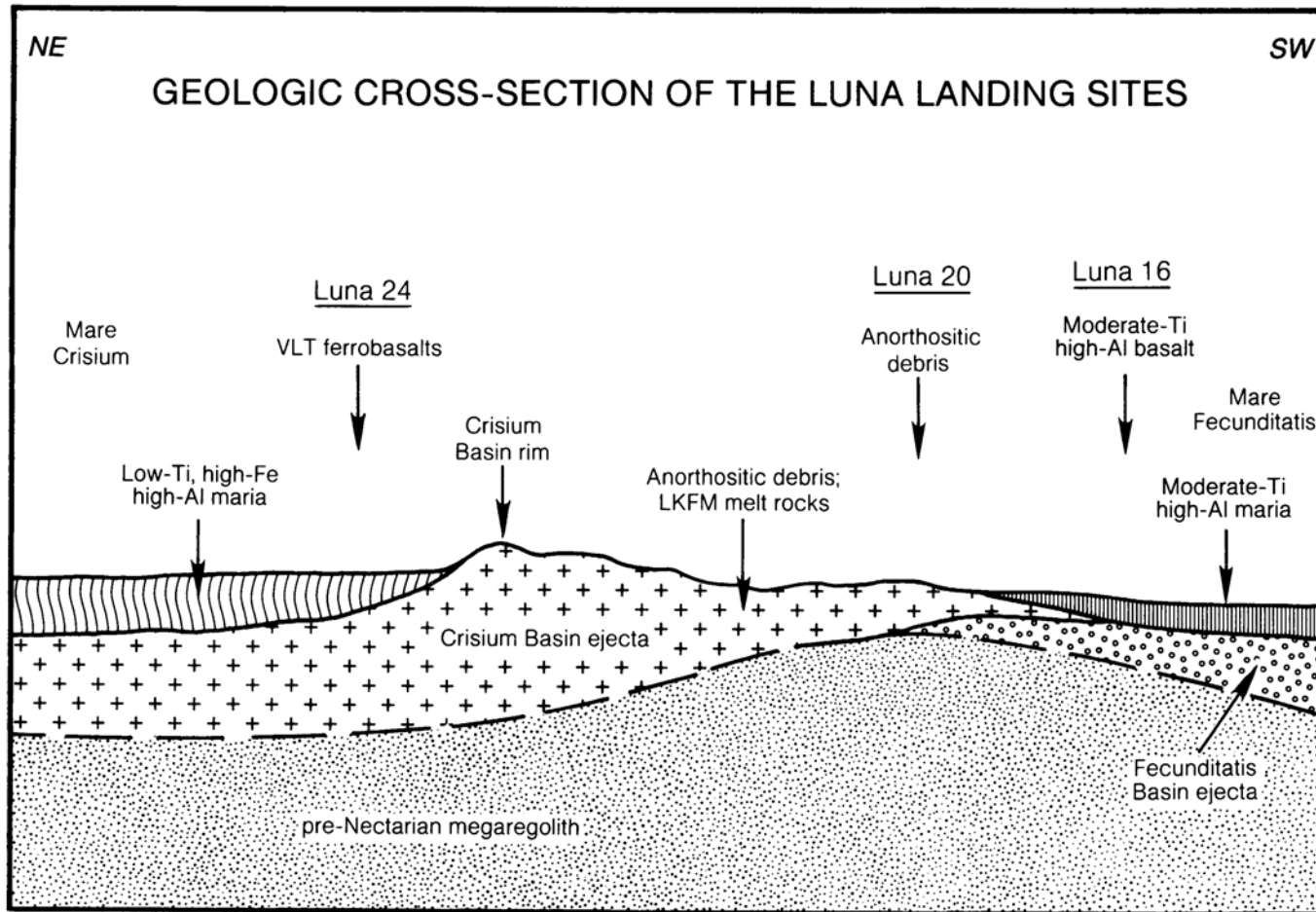


Fig. 10.30. Schematic north-south geologic cross-section through the region of the Luna 16, 20, and 24 landing sites (modified after *Wilhelms*, 1984). The highland regions, whose geology has been inferred from regional relations, consist of layers of complex ejecta deposits from large impact basins, Fecunditatis (older) and Crisium (younger). These units in turn rest on a thick layer of megaregolith consisting of ejecta from even older (pre-Nectarian) impact basins and craters. All ejecta layers were probably deposited before 4.0 b.y. ago and some were subsequently covered by a variety of lava flows. Note that the lavas covering Mare Crisium (left) are significantly different chemically from the flows on Mare Fecunditatis (right).

ultramafic composition and pyroclastic origin. The Apollo 15 site is one of the most geologically complex areas visited by any Apollo mission (Fig. 10.22), and remains the subject of active research. Discussions of the site geology may be found in *Swann et al.* (1972) and *Spudis and Ryder* (1985, 1986).

10.6.5. Apollo 16

The Apollo 16 mission was sent to the central lunar highlands near Descartes Crater (landing site: 9°S, 15.5°E; Fig. 10.23). The main mission objective was to sample two morphologic units representative of highland geology, the relatively smooth Cayley Plains and the hilly and furrowed Descartes material, both of which were suggested prior to the mission to be of volcanic origin. A secondary objective was to examine the lunar highlands at a point distant from any mare. Three long EVAs were performed using the LRV (Fig. 10.24), sampling and examining these two geologic units as well as two recent impact craters 1–2 km in diameter.

In sharp contrast to premission expectations, the returned samples are all impact products, mostly polymict breccias and impact melts (see section 6.4) with some pristine anorthositic rocks (see section 6.3). The extensive Apollo 16 sample suite shows clearly that neither the Cayley nor Descartes unit is volcanic in origin. Current interpretations of these units involve origins as impact-ejecta deposits, somehow related to the formation of the Imbrium and Nectaris Basins, although the exact contribution of each basin to the deposits at the Apollo 16 site is unknown. It is possible to interpret some absolute ages of impact melt rocks from the Apollo 16 site as the time of formation of the Nectaris Basin (3.92 b.y.). One of many possible interpretive cross-sections through the Apollo 16 site is shown in Fig. 10.25. The geology of the Apollo 16 site is discussed in detail by *Ulrich et al.* (1981), *James and Hörz* (1981), *James* (1981), *Spudis* (1984), and *Stöffler et al.* (1985).

10.6.6. Apollo 17

The last Apollo mission was sent to a highland/mare boundary near the southeastern rim of the Serenitatis Basin, the Taurus-Littrow Valley (landing site: 20.2°N, 30.8°E; Fig. 10.26). Planning for this site was probably the best of any Apollo mission, thanks to previous experience and the extensive orbital data obtained from the Apollo 15 mission. Objectives included the examination of two massifs (highlands), where rocks from deep in the lunar crust might be found (as Serenitatis and other basin ejecta), study of the valley subfloor, which was presumed to

consist of mare basalts, and examination of a low-albedo deposit that discontinuously mantles both highlands and mare at the site. Three long traverses were completed with the LRV (Fig. 10.27), and the premission objectives were spectacularly accomplished.

The subfloor of the valley does indeed consist of high-Ti mare basalts, of which several chemical subgroups can be distinguished; they range in age from about 3.8 to 3.7 b.y. The highland massifs bounding the valley consist of complex impact-melt breccias and plutonic igneous rocks of the Mg-suite (see section 6.3.4). The impact-melt breccias show an assembly age of 3.87 b.y. This value may reflect the age of the Serenitatis Basin, but it is uncertain how many cratering or basin-forming events were involved in the origins of these samples. A dark-mantle deposit on the valley floor consists of orange and black pyroclastic fragments, with a high-Ti basaltic composition, about 3.64 b.y. old. A light-mantle unit at the site is an avalanche deposit from the South Massif, apparently initiated by the impact of ejecta from Tycho Crater, about 2000 km away. Cosmic-ray exposure-age measurements of the light mantle material indicate that it was exposed about 100 m.y. ago, and may be interpreted as evidence that both the landslide and the formation of Tycho occurred at that time. The geologic reconstruction of the Apollo 17 site is given in Fig. 10.28; discussions of the geology of the Taurus-Littrow region may be found in *Schmitt* (1973), *Wolfe et al.* (1981), and *Spudis and Ryder* (1981).

10.6.7. The Luna Landing Sites

Between 1970 and 1976, the U.S.S.R. sent three unmanned sample return missions to the Moon, all of which landed (apparently for operational reasons) on the eastern limb of the lunar nearside. Each spacecraft was designed to drill a shallow core into the regolith, remove the core, and return it to Earth. The geology of the specific sites cannot be deciphered directly because of the lack of other data; therefore, this discussion concentrates on the regional geology of the lunar eastern limb.

The Luna 16 mission landed in northern Mare Fecunditatis (landing site: 0.7°S, 56.3°E) in September 1970, Luna 20 landed in the highlands south of the Crisium Basin (landing site: 3.5°N, 56.5°E) in February 1972, and Luna 24 landed in southern Mare Crisium (landing site: 12.7°N, 62.2°E) in August 1976 (Fig. 10.29).

The Luna missions provided us with samples from two different mare deposits and one highland region; the latter site is probably dominated by ejecta from the Crisium Basin. The Luna 16 mission returned

material from a mare basalt regolith; fragments consist of a moderately-high-Ti, high-Al variety of basalt. One "large" basalt fragment (<0.1 g) was successfully age-dated, giving a formation age of 3.41 b.y. Luna 20 returned a small sample from a highland (anorthositic) regolith; most lithic fragments consist of granulites, anorthosites, impact melts, and polymict breccia fragments. The most successful mission in the Luna series, Luna 24, returned a 1.6-m-long core of mare regolith from Mare Crisium. Basalt fragments in the sample are very low in Ti

and high in Fe and Al; measured ages on these basalts range from 3.6 to 3.4 b.y. A regional cross-section showing the general geology of the Luna sites is shown in Fig. 10.30. More detailed discussions of the local and regional geology of these sites are found in the following references: Luna 16, *McCauley and Scott* (1972); Luna 20, *Heiken and McEwen* (1972); Luna 24, *Head et al.* (1978); see also *Wilhelms* (1984) for a discussion of the regional stratigraphy of all three sites.

AFTERWORD

David Vaniman, Bevan French, and Grant Heiken

“Arriving at the lunar module [for the last time], I experience a sense of impending loss. Soon I will leave the Moon, probably forever. And, in a peculiar way, I have come to feel a strange affection for this peaceful, changeless companion of the Earth.” (*Scott, 1973*)

11.1. RETURN TO THE MOON

As the 1990s begin, the Moon is more visible as an object for discussion and planning than at any time since the Apollo program ended nearly 20 years ago. Much of this new interest is scientific. The intervening years have seen a steady stream of new discoveries that have expanded our knowledge about the Moon and have established new ties between the origin of the Moon and the origin of the Earth. But most of the current interest reflects a changed attitude toward the Moon itself. The Moon has become a nearby, familiar, convenient, and accessible world. It has been reached safely by humans, briefly explored, and partly understood. It is natural—almost unavoidable—to think about the Moon when considering the U.S.’s role in the future exploration of space.

Ideas for returning to the Moon with robotic spacecraft and human beings are being heard more often and from higher levels in the government. The goal of using a polar-orbiting spacecraft to make a global scientific survey of the Moon has been studied for nearly two decades (*Lunar Science Institute, 1972*) and has been recommended by several NASA advisory committees (e.g., *Solar System Exploration*

Committee, 1983). In 1986, a presidential commission (*National Commission on Space, 1986*) proposed an ambitious long-term space program that included robotic exploration of the Moon, establishment of a human outpost on the Moon, the use of lunar resources, and human expeditions to Mars. On July 20, 1989, President George Bush marked the 20th anniversary of the Apollo 11 landing by establishing what is now known as the Space Exploration Initiative (SEI), a long-term program of human exploration, first of the Moon and then of Mars.

Since the President’s speech, NASA, the National Space Council, the National Academy of Sciences, and many organizations in the private sector have been actively studying and planning how such exploration could be done. The Moon has suddenly become many things: an exciting focus for planetary science, a target for human occupation, and a resource base for further explorations into the solar system.

11.2. CURRENT UNDERSTANDING OF THE MOON: A BASE FOR PLANNING

11.2.1. The Post-Apollo Moon

The Apollo program’s greatest triumph was to provide enough information about the Moon to plan future exploration and development. Before Apollo,

“ . . . everything we knew about the Moon was based on low-resolution remote sensing, numerical models, and speculation, all carried out by a small number of largely-ignored

scientists. We couldn't even see half of the Moon, we couldn't tell what it was made of, and we had no idea whether it was young or old. To explain any observed lunar phenomenon, there were a variety of theories, all of them untestable, and most of them wrong." (*Briggs*, 1986, pp. iii-iv)

Because of the Apollo program, it is now clear that humans can return to the Moon, that they can live and work on it, and that they can do important scientific work while they are there. Much of the Moon is still an exciting mystery, but its nature is now known to a degree never before possible. The Moon has become an individual world with its own set of unique characteristics.

Dryness. Much to the surprise of almost everyone, the Moon seems to be a completely waterless planet. Its returned rocks contain no water, unlike almost all rocks on the Earth. Water, possibly brought in by cometary impacts, may be preserved at the lunar poles (see section 3.8), but water has apparently never played a major role in the Moon's history.

Lifelessness. The Moon turned out to be just as dead as almost everybody thought it would be. No life, living or fossil, has been found on the Moon. The Moon is even poor in the key chemical elements that are essential for life: hydrogen, carbon, nitrogen, and others. (There is more carbon brought to the Moon by the solar wind than there is in the lunar rocks themselves; see section 8.8.)

Diversity. The Moon is not a homogeneous, uniform world; its surface is made up of a wide range of rocks. The light and dark regions (highlands and maria) seen from Earth are the end result of planet-wide chemical and geological separations during a long period of ancient lunar history. The highlands are made up of ancient, light-colored, Al-rich crustal rocks. The maria are covered by younger, dark-colored, basaltic lavas. All over the Moon there are also complex breccias, fragmental rocks produced by meteoroid impact.

History. The Moon is not just a large meteoroid, primordial and unchanged since the solar system formed. Instead, it is an evolved planet with an exciting and unique history whose outlines have been established by dating the returned samples. The oldest lunar rocks stem from events dating almost to the formation of the solar system, 4.6 b.y. ago. Once formed, the Moon has been modified by a variety of geological forces: widespread primordial melting, intense meteoroid bombardment, internal heating, and the eruption of huge floods of basaltic lava. For about the last 3 b.y., the Moon appears to

have been quiet, although some basaltic volcanism may have occurred in this period. The seismometers placed on the Moon's surface by the Apollo astronauts suggest that it is relatively inactive now.

Surface weathering. Even with no water or air, the Moon is "weathered" by the small cosmic particles that continually bombard its surface. This bombardment has gradually built up the regolith, a powdery layer that covers and conceals the Moon's bedrock. This layer has also trapped and preserved cosmic particles from the sun (the solar wind) and the stars (galactic cosmic rays).

The scientific exploration of the Moon has not ended with the Apollo and Luna programs. Sample analyses, data analyses, and pure serendipity have all expanded the picture of the Moon since the last Luna mission in 1976:

- Small fragments of new lunar rocks and minerals continue to be found in soils and breccia samples, increasing the diversity of known lunar rocks and indicating that the bedrock at the Apollo and Luna sites is not representative of the entire Moon.
- Additional lunar samples have unexpectedly appeared as meteorites collected from the Antarctic ice cap (see section 2.2).
- The solar-wind N trapped in lunar soil breccias shows a significant increase in the isotopic ratio $^{15}\text{N}/^{14}\text{N}$ over geologic time, a change still unexplained by lunar scientists and solar astrophysicists alike (section 7.7).
- As more lunar samples have been analyzed, the uniform primordial "magma ocean" has been splitting into a more complex pattern of smaller "magma seas," leaving behind many unanswered questions about the formation of the lunar crust and the Moon's internal structure (section 2.4.3, especially Fig. 2.5).
- Twenty years of continuing laser ranging to the retroreflectors left by the Apollo astronauts have improved our knowledge of the Moon's motions and orbital dynamics; the Earth-Moon distance, about 400,000 km, can now be measured routinely with a precision of 2–3 cm.
- Finally, a new theory for the origin of the Moon has appeared: the "Giant Impact" of an early planetesimal with the primordial Earth, which spun off heated and vaporized material to make the Moon. This idea is supported (for the

moment at least) by both theoretical studies and the extensive chemical data obtained from returned samples (section 2.4.1).

Scientifically, the Moon has become many different worlds. It is an archive of early planetary history, which preserves for our inspection the records of ancient processes that shaped all the terrestrial planets, including the Earth. The Moon is also a space probe and time machine, for its soil has trapped and preserved the historical records of the sun and the stars. And it is a partner of the Earth, for it now seems clear that the origins of the two worlds—and our own beginnings—are somehow tied together.

The Moon is also a world we can use. Only three days away from Earth by spacecraft and already partially explored, it is a natural target for future human exploration. Geologically, the Moon is still largely unknown, waiting for humans to fill in huge blank areas on its map (see Plates 10.1 to 10.6). The unsolved geological problems of its origin and history can be attacked with the new scientific and exploration capabilities that humans can provide, just as humans have long explored the geology of the Earth. The Moon is also an excellent base for equipment; it is a stable, airless platform on which to erect instruments for many sciences: astronomy, physics, chemistry, life sciences, and a host of others.

Finally, the Moon is a good place to build and launch other things. Its low gravity provides stability for construction, but it is still easy to launch large payloads back to Earth or out to Mars. Oxygen makes up fully half the weight of the Moon's rocks, and much of the remainder consists of potentially useful metals: Fe, Ti, and Al in particular. The Moon could supply many of the materials needed for large operations in space: bulk shielding to protect against radiation, metals and melted glasses for construction, and oxygen for propellants and life support.

11.2.2. Environmental Impacts

Many unfavored and uninhabited regions of the Earth, once ignored as “worthless,” are now valued and preserved as aesthetic monuments because of their austere beauty. Astronaut Edwin (“Buzz”) Aldrin Jr. was stunned by the “magnificent desolation” of the Moon (*Armstrong et al.*, 1970, p. 325). The awe that lunar terrains have produced in their few human visitors is clearly seen in the words and lives of the astronauts who have been exposed to the Moon (*Collins*, 1974).

The lunar surface environment (see Chapters 3 and 4) has been described as dead, harsh, extreme, and hostile. Human survival and scientific operations there are difficult and challenging. Yet many present

lunar environmental features are precisely what make the Moon a desirable place to be. The lack of an atmosphere is good for astronomy, and the large-scale availability of heat and cold makes exciting chemistry and physics experiments possible. The present lunar environment is not to be wasted, and its preservation must be an important part of planning for the future use of the Moon.

The lunar surface environment will be changed greatly when humans return for long visits to do scientific research or to mine lunar resources. The lunar environment is clearly vulnerable to change, and changes have already been produced. The astronaut footprints and the equipment left at the Apollo landing sites will last for several million years (until, of course, they are disturbed by future visitors).

Human effects on the near-vacuum lunar atmosphere are more impressive and potentially more worrisome. Each Apollo mission released on the Moon a mass of gas roughly equal to the existing lunar atmosphere (*Vondrak*, 1974). Measurements of the atmosphere during the Apollo 12 mission found that routine depressurizations of the Lunar Module, many meters away from the detectors, abruptly raised the local gas concentrations by an order of magnitude above the landing-induced local atmosphere of 10^{-6} N/m² (10^{-8} torr). The gas cloud surrounding an astronaut as he moved across the lunar surface was sufficient to saturate the detector (10^{-4} N/m² or 10^{-6} torr) any time the astronaut approached within a few meters (*NASA Manned Spacecraft Center*, 1970). After the Apollo 14 mission was over, continuous monitoring of the Apollo 14 landing site indicates that it will be years before the daytime atmospheric pressure at the site will drop back to the normal 10^{-10} N/m² (10^{-12} torr) (*Johnson et al.*, 1972; see Fig. 3.12). With a low mission rate, the lunar atmosphere can recover from these perturbations, but the effects of continuing missions, large-scale occupation, and lunar mining activities need to be considered in more detail (section 3.9.3).

Planning to minimize the effect of future human explorations on the lunar environment is essential. Some of the possible effects are mitigated by another factor—the growing realization that merely living on the Moon will require a rigidly controlled and largely closed ecological life support system (*MacElroy et al.*, 1985). With all wastes (especially fluids) contained in a closed system for cost and logistics reasons, the dry and airless lunar environment will remain largely unchanged. In addition, human lunar habitations will have to be located underground or beneath thick layers of regolith to provide shielding from lethal cosmic radiation and solar flares. Perhaps much lunar industry will also be carried out underground.

11.3. GOALS FOR FUTURE LUNAR EXPLORATION

The space program has always had two seemingly contradictory themes: pure adventure and pragmatic benefits. To some, these two themes cannot coexist. There is a perception that the adventure ended abruptly with the Apollo landings and that lunar exploration will now be pragmatic and a little boring, an idea equivalent to believing that all adventure in the New World ended with Columbus' fourth voyage. Adventure—perhaps sometimes unwanted—will continue to be a natural part of future lunar exploration. What has changed since the Apollo program is that these explorations and adventures can now be confidently planned. The interest in returning to the Moon has generated a large number of publications (see Appendix A11.1), in which four general goals for future lunar exploration are discussed in detail: science, transportation, resources, and benefits to future astronauts.

11.3.1. Science

Science goals for the Moon fall into two types: *planetary science*, which studies the Moon itself, and *platform science*, in which the Moon is used as a base for instruments for other kinds of scientific observations.

The Moon is an interesting planet in its own right and deserves intensive study with the other terrestrial planets. Initial theories that the Moon might be an unchanged primordial object (similar to a huge meteoroid) were quickly ended by the Apollo missions. The Moon turned out to be something far more interesting: a partly-evolved planet with its own geological history. The Moon preserves an important record of early events that occurred on all the terrestrial planets between about 4.6 and 3 b.y. ago, a record that has been largely destroyed on Earth by our planet's thick atmosphere, abundant water, and crustal movements. Furthermore, the Moon preserves records of the sun's behavior during this same period. Ancient lunar soils, developed and then buried under lava flows or layers of impact ejecta, may provide a record of ancient solar and galactic activity. The study of the Moon's geology is still in its infancy. The rocks returned from the Moon so far are only a tantalizing sample of a planetary geologic record that is different from the Earth's but just as rich.

Astronomy and astrophysics are among the most prominent of the platform sciences that would benefit from a base on the Moon. The lack of atmosphere, the stability of the ground surface on the nearly aseismic Moon, and the radio-quiet zones

present on the lunar farside would make possible many deep-space observations not possible from the Earth's surface or even from Earth orbit. These studies range from radio interferometry (*Burke*, 1985; *Burns*, 1985) to gamma-ray astronomy (*Haymes*, 1985). As one example of experimental physics, the possibility of neutrino detection on the Moon has been proposed (*Cherry and Lande*, 1985). Astronomers and physicists are now thinking more seriously about using the Moon (*Burns and Mendell*, 1988), and the identification of other possible experiments only awaits the application of their imaginations.

11.3.2. Transportation

Small robotic missions to the Moon and into deep space can be launched successfully from the deep gravity well of the Earth's surface. Larger missions, especially human missions headed beyond the Moon, are better launched from places where less fuel is required to overcome Earth's gravity, i.e., from orbit or from the low-gravity surface of the Moon.

The large spacecraft required for a major human mission to Mars, for example, could be assembled in space from materials brought up from the Earth in a series of small launches or supplied from the Moon. Potential lunar resources, especially oxygen and metals, could be used on platforms at the gravitationally stable Lagrange points in the Earth-Moon neighborhood (*Keaton*, 1985), in facilities in lunar orbit, or on the Moon itself (*Duke et al.*, 1985). The Moon is both accessible and fairly well known, and its role as a supporting element in a general space transportation system is likely to increase in importance as flights and commerce in space increase.

11.3.3. Resources

The future use of lunar resources must be considered in terms of two different markets. The first market is in space, and the economic driver is gravity. It is gravitationally easier to transport a given mass (e.g., of oxygen) from the low-gravity lunar surface down to Earth orbit or out to Mars than it is to lift the same mass from the high-gravity surface of the Earth. As the required consumption of oxygen in space increases, a lunar source becomes more attractive, despite the complexity and expense of developing the required facilities on the Moon.

The second market for lunar resources is on Earth, and the economic driver must be terrestrial scarcity. At present, no such market exists, aside from the scientific market for returned lunar samples. Any future resource would have to be both rare and badly needed to overcome the high cost of bringing it back routinely from the Moon.

These two kinds of potential lunar resources are discussed briefly in the following subsections. Detailed discussions of specific resources are given in Appendix A11.2.

Lunar resources for use in space. The most readily available resource on the Moon is bulk lunar regolith for use in radiation shielding. This material can be used either in place or transported from the Moon for use in spacecraft being assembled in low-Earth orbit, in lunar orbit, or at a Lagrange point.

Among possible processed resources, rocket propellants are being given the most serious consideration. Such propellants currently account for the great majority of the total mass that must be lifted from Earth to orbit for current deep-space missions (e.g., 77% for the recently launched Galileo mission to Jupiter), and almost ten times as much propellant must be burned in the launch vehicle just to bring that mass to low-Earth orbit. If near-Earth space traffic becomes considerable, then the cost benefits for lunar propellant production (particularly oxygen) could be considerable (Simon, 1985). Possible methods have been proposed for producing O, H, silane (SiH₄), and even more exotic potential fuels. Other possible resources include metals, glasses, fibers, and concrete. If the recommendations of a recent presidential advisory commission (*National Commission on Space*, 1986) are realized in the next few decades, then propellant production will be the first priority for lunar industry. Thus the ties between future space transportation and the future of lunar mining are very close.

Lunar resources for use on Earth. At present the only market for returned lunar materials is for scientific research. The samples are currently so exotic that they are also potentially valuable to museums and private collectors, if they ever become available to private enterprise. However, this value is artificially inflated by their present rarity; the price of lunar samples would deflate rapidly if large amounts were returned as a consequence of lunar development.

One unique possible lunar resource has recently been identified, the isotope ³He, which originates in the sun and is collected in the lunar regolith by exposure to the solar wind (see sections 8.8.1, 8.8.2, and 8.8.4). Wittenberg *et al.* (1987) have suggested that fusion energy might be more readily and safely obtained on Earth if fusion reactors could use ³He instead of the currently-used tritium (³H). Helium-3 is too rare on Earth, where it is overshadowed by the more common ⁴He produced by radioactive decay. On the Moon, ³He might be extracted economically from the regolith, and Wittenberg *et al.* (1987) calculate that the energy gained by returning it to Earth would be about 250 times the energy used

in obtaining it from the Moon. This idea may not come to pass in the form proposed, but it provides an excellent example of the new ideas for using the Moon that may result from further serious consideration.

11.3.4. Benefits to Future Astronauts: *Terra Firma Nova*

For astronauts in space near the Moon, or even in low-Earth orbit, the Moon can provide an attractive haven from the demands of space itself. At a fundamental level, the Moon provides a massive, solid presence that no spacecraft or space station can duplicate. Everyone, astronauts included, knows the basic desire to step out onto a natural surface and walk around. Beyond psychology, there are real concerns about the physiological effects of long-term weightlessness on human beings. Even short periods of weightlessness in both U.S. and U.S.S.R. orbiting space stations have revealed cardiovascular problems, skeletal and muscular atrophy, and loss of bone calcium, as well as potential psychological problems (Nicogossian *et al.*, 1989; Lorr *et al.*, 1989; Garshnek, 1989; Spangenburg and Moser, 1987). The longer periods spent in weightlessness by U.S.S.R. cosmonauts have verified these problems and have spurred the search for countermeasures.

If humans become numerous in space, the Moon can provide a convenient and accessible remedy for their needs. The low gravity of the Moon may not provide a complete cure for the physiological problems of weightlessness, but low gravity is likely to be better than none. Furthermore, humans in a lunar base can be shielded from the harsh radiation environment of space (especially from short-term solar flares) more easily and for longer periods of time than in a spacecraft or space station. If the future occupation of space is to be prolonged and open to many individuals, the Moon provides an attractive haven for rest, recreation, recovering from weightlessness, avoiding solar flares, and even for taking long walks or otherwise exercising in a gravitational field.

11.4. UNANSWERED QUESTIONS ABOUT THE MOON

Although our current knowledge about the Moon's nature, materials, and surface environment are adequate for detailed planning of future human activities, much important information is still missing from our current knowledge. These gaps are discussed below. The relevant research questions are listed, with emphasis on the scientific details, in Appendix A11.3.

11.4.1. The Lunar Environment

Information on the radiation and thermal environments of the lunar surface (Chapter 3) is critical because both humans and their equipment will require protection from such harsh conditions. Knowledge of radiation exposure conditions at the lunar surface is very good, but detailed biomedical studies of long-term radiation exposure hazards are still needed. For example, we need to know such basic facts as the amount of surface radiation exposure time that can be endured by astronauts on long lunar excursions.

The data on heat flow from the lunar surface are scanty and somewhat uncertain (section 3.6), leaving questions about whether the lunar heat flow is really as high as the Apollo measurements indicate. The available heat-flow data indicate that living quarters, which must be buried to provide protection from radiation, will also need extensive heat-rejection equipment.

Finally, the most unknown lunar regions are the polar areas. There is no information about whether any permanently shadowed (and therefore permanently supercooled) areas exist there, or whether frozen water and other volatiles are present.

11.4.2. Lunar Surface Processes and Evolution

Many problems about early planetary history (sections 2.4 and 8.2) are little better understood for the Moon than for the Earth. Some outstanding questions, like “How old is the oldest volcanism?” or “Are there remnants of the original magma ocean?” stand a better chance of being answered for the Moon than for the Earth. The fact that (in contrast to the Earth) dynamic geological activity ceased on the Moon a long time ago generates other questions like “How young is the youngest lunar volcanism?”

The background to most of these questions is given in the earlier chapters of this book and in Appendix A11.3. Some of these questions deal with speculations that have only been touched on in the earlier chapters, either because of a lack of data or a lack of space. As one example, there is the question (item 13 in Appendix A11.3) of “What causes the lunar transient events?” These “transient events” include enigmatic brightenings or obscurations observed by Earth astronomers, mostly from the Aristarchus Plateau but also associated with a large number of widely scattered impact craters (Tycho, Gassendi, Grimaldi, Humboldt, and many others; see *Middlehurst*, 1977). These events are mentioned briefly in section 9.2.3, where electrostatic charging of lunar surface dust is suggested as one possible cause of the optical effects. It is also

possible that these events are related to gas emissions from the lunar interior, perhaps enhanced in areas of high KREEP content (where gases may form over long timespans by radioactive decay of nongaseous elements), at sites where relatively large but young impact craters have fractured the outer lunar crust, and at sites associated with the extensive fracturing and rille formation along mare-basin rims (see Fig. 4.29c). There is some support for this hypothesis from the Apollo 15 and 16 orbital alpha-particle measurements, which detected areas of enhanced ^{222}Rn (from ^{238}U decay) as well as ^{210}Po (from decay of the Rn daughter ^{210}Pb , accumulated on the lunar surface after several years of Rn diffusion from the lunar interior; see *Gorenstein et al.*, 1974). These areas of enhanced radioactive daughter gases correlate roughly with the sites where optical transient events are concentrated. This explanation of lunar transient events is far different from that of electrostatic charging. A detailed investigation of the transient events may not only resolve the question of their origin, but may also provide one answer to the search for useful concentrations of volatile elements on the Moon.

The Moon will also serve as a field laboratory for studying processes that cannot be studied on Earth. The well-preserved impact craters of the Moon will provide data about the rare and violent changes that accompany impact events, thus leading to a better understanding of how such events affect the surfaces of all the planets and moons in the solar system. Dating the impact melts in the younger craters will help to “calibrate” the impact sizes and frequencies over the last few hundred million years, a calibration that might help to explain the major extinction events in Earth history (*Hörz*, 1985b). There has been much speculation about the cratering process, and the “ground truth” provided by studying the lunar craters is needed to obtain definite answers.

Beyond these problems remain the still-unanswered questions of the origin of the Moon and its relationship to the origin of the Earth itself.

11.4.3. Lunar Minerals, Rocks, and Soils

The extensive datasets provided on lunar minerals (Chapter 5), rocks (Chapter 6), and soils (Chapter 7) still represent a small set of intensely-studied samples rather than the results of a systematic and global sampling of the Moon. It is clear that a large fraction of existing lunar rock types were never sampled by the Apollo or Luna missions. For example, *BVSP* (1981) indicates that about two-thirds of the mare basalts on the lunar surface are unlike any yet sampled; the fraction of unknown pristine highland rocks may well be even higher.

Similarly, there are almost certainly some minerals that occur on the Moon that have not yet been collected (*Vaniman and Bish*, 1990). There are still questions about the existence of (1) economic mineral deposits, (2) primitive lavas that rose directly to the surface from the lunar mantle without losing crystals or becoming contaminated during their ascent, (3) actual fragments of the lunar mantle brought to the surface in volcanic lavas, and (4) large bodies of lunar granitic rock.

Exploration, either by humans or by sophisticated robots, is also needed to determine (1) how thick and widespread are the sheets of impact melt associated with large lunar craters; (2) whether ancient regolith has been preserved under old lava flows; (3) what the highland megaregolith is like, how thick it is, and what underlies it; and (4) how much of the Moon's original and present chemical constituents have been introduced by impacting meteoroids.

11.4.4. Lunar Chemistry

The systematics of lunar chemistry and its variations (Chapter 8) provide a similar variety of unanswered questions, many of which are related to the probable existence of unknown and unsampled lunar rock types. Many current inferences about chemical components (in particular, the ever-present KREEP), depend on ideal assumptions that may be changed or destroyed as more data become available. Even with the current data, it is hard to establish which chemical trends reflect internal lunar processes and which are due solely to the results of impact mixing, melting, and vaporization. Finally, a determination of the true bulk composition of the Moon is still lacking.

11.4.5. Lunar Physical Properties

The gaps in our knowledge of the physical properties of lunar materials (Chapter 9) are due to the same limitations as our knowledge of the lunar surface itself (Chapter 3). Both sets of data rely heavily on the limited studies actually made on the Moon. The lunar conditions of high vacuum and extreme dryness are difficult—often impossible—to duplicate in a terrestrial laboratory on the scale necessary for measurement of many key physical properties.

Nevertheless, the known physical properties indicate several areas where more research is needed to provide the basis for a viable lunar outpost. The foundation material for all structures will almost certainly be lunar regolith; true bedrock may be unavailable at reasonable depths (<5–10 m), except where young lava flows or impact melt sheets are present, on steep slopes within the walls of rilles (see Fig. 3.5), or in crater walls and central peaks (see

Fig. 4.12b and Plate 10.9). It is therefore essential to learn (1) what design limitations are imposed by the fundamental strength of the regolith and its stability in excavations; (2) what deeper excavations (>10 m) into the highland megaregolith might encounter; (3) whether the fine (dust) component of the regolith, which was a constant problem during the Apollo missions, will overcome and destroy our best vacuum- and dust-sealed bearings and other mechanical components; and (4) whether lunar dust will create respiratory problems for humans during long stays on the Moon.

11.4.6. Global Lunar Data and Future Mapping

The Moon is still poorly covered by remote observations, as the existing global maps clearly indicate (Chapter 10). In fact, current maps of the Moon are not nearly as complete as maps of Mars. The orbital information collected by the last Apollo missions is confined to a limited near-equatorial zone (Plates 10.1–10.6), and telescopic multispectral imaging from Earth is limited to the lunar nearside (Plate 10.9).

This incomplete coverage can be filled out by the proposed Lunar Observer mission, probably in time to provide essential data for planning the human return to the Moon. The Lunar Observer spacecraft could carry a wide range of remote-sensing instruments: gamma-ray and X-ray spectrometers, a microwave radiometer, visible- and near-infrared scanning spectrometers, a thermal-infrared spectrometer, camera systems, magnetometers, a variety of spectrometers to measure the lunar atmosphere, and a subsatellite for accurate radio tracking. From a polar orbit, this assemblage could produce complete global maps of the Moon's surface chemistry, surface mineral composition, surface thermal properties, landforms and geological features, magnetic and gravitational fields, and the lunar atmosphere.

These orbital measurements will have a major advantage—they can be calibrated by observing Apollo and Luna sites and using the actual data obtained from samples collected at those points. The increase in knowledge about the Moon as a result of the Lunar Observer mission will be comparable to the increase in knowledge produced by the Apollo program itself. With the new database, planning for the human return to the Moon—in particular the selection of landing sites—can move confidently and rapidly ahead.

11.5. THE NEXT STEPS

The Moon and its future role in space exploration are now being actively debated, and the results of this debate are not yet clear. But if the Moon is to

be explored in any way—for science, for human habitations, for resources, by robotic spacecraft, or with human beings—some specific steps are needed now.

The Lunar Observer mission (section 11.4.6) is generally regarded by both scientists and planners alike as the obvious next step in exploring and understanding the Moon. The data it can provide will raise lunar science to a new level of activity and understanding, for the mission will provide a scientific inventory of the entire Moon and will also place the tremendous amount of Apollo data into a global lunar perspective. Much of this data (e.g., chemical and geological maps, surface imagery, and an accurate lunar gravitational field) will also be important to those who are now planning how humans should return to the Moon, where they should land and establish a base, and what they should do there.

Until the Lunar Observer flies, there is much that can (and should) be done on the ground. The scientific potential of ground-based lunar studies remains high, particularly for such activities as new lunar sample studies, telescopic multispectral scanning of the lunar nearside, ground-based radar probing of the Moon, and the application of modern methods to reanalyze the data from old lunar missions. If lunar resources are to be used, then practical demonstrations of resource production must be made before processing systems are sent to the Moon. These activities, along with other ground-based space-science research, have been delayed or cut back during the last few years as a result of the generally constrained NASA research budgets (*NASA Advisory Council*, 1986). The immediate rebuilding of a healthy and active scientific effort to study the Moon from the ground is an important, relatively inexpensive, and independently valuable step in any rational plan to return to the Moon.

The immediate steps in the return to the Moon are clear, and they are worth taking even if the remainder of the path is still uncertain. It is hard to imagine that humans will choose never to return to the Moon. The Moon is too close, too easy to get

to, too scientifically exciting, and too potentially valuable as a science outpost and a resource base to be ignored indefinitely. Human beings have never yet put their footprints on a new land and then turned back, never to return.

11.6. A PERMANENT PRESENCE

The establishment of a permanent lunar base is not a new idea. Even before the exploration of the Moon by spacecraft, concepts of lunar habitation were being carefully evaluated. Figure 11.1 shows a lunar base concept developed two decades before Apollo 11 reached the lunar surface (see *Clarke*, 1951). The base shown in this figure incorporates many of the features important in current concepts of lunar base construction: It has pressurized buildings, both solar and nuclear power sources, hydroponic farms, and even an electromagnetic launcher under construction for the delivery of lunar resources to assembly areas in space. This base is also designed around the key research element of astronomy, a scientific goal for the use of the lunar base that has only recently been revived.

It is interesting to compare Fig. 11.1 with a current model of the lunar base (Fig. 11.2). This model is much more modest, because it reflects the initial “seed” components of a permanently manned base, but it has much in common with the previous figure that predates it by some 40 years. The single greatest difference between these two figures is one not seen—the accumulated knowledge of lunar surface properties, the space environment, and space travel technology that was still the stuff of science fiction when Fig. 11.1 was made.

The lunar base shown in Fig. 11.2 is possible using slight modifications of current technology. The realization of such a base requires commitment more than research, and awaits only the time when a permanent presence in space is seen to be an advantage. The style of the base that is ultimately built may look much like that shown in Fig. 11.2, but the substance of this base will be a tremendous increase in knowledge and in technological capabilities that cannot presently be visualized.

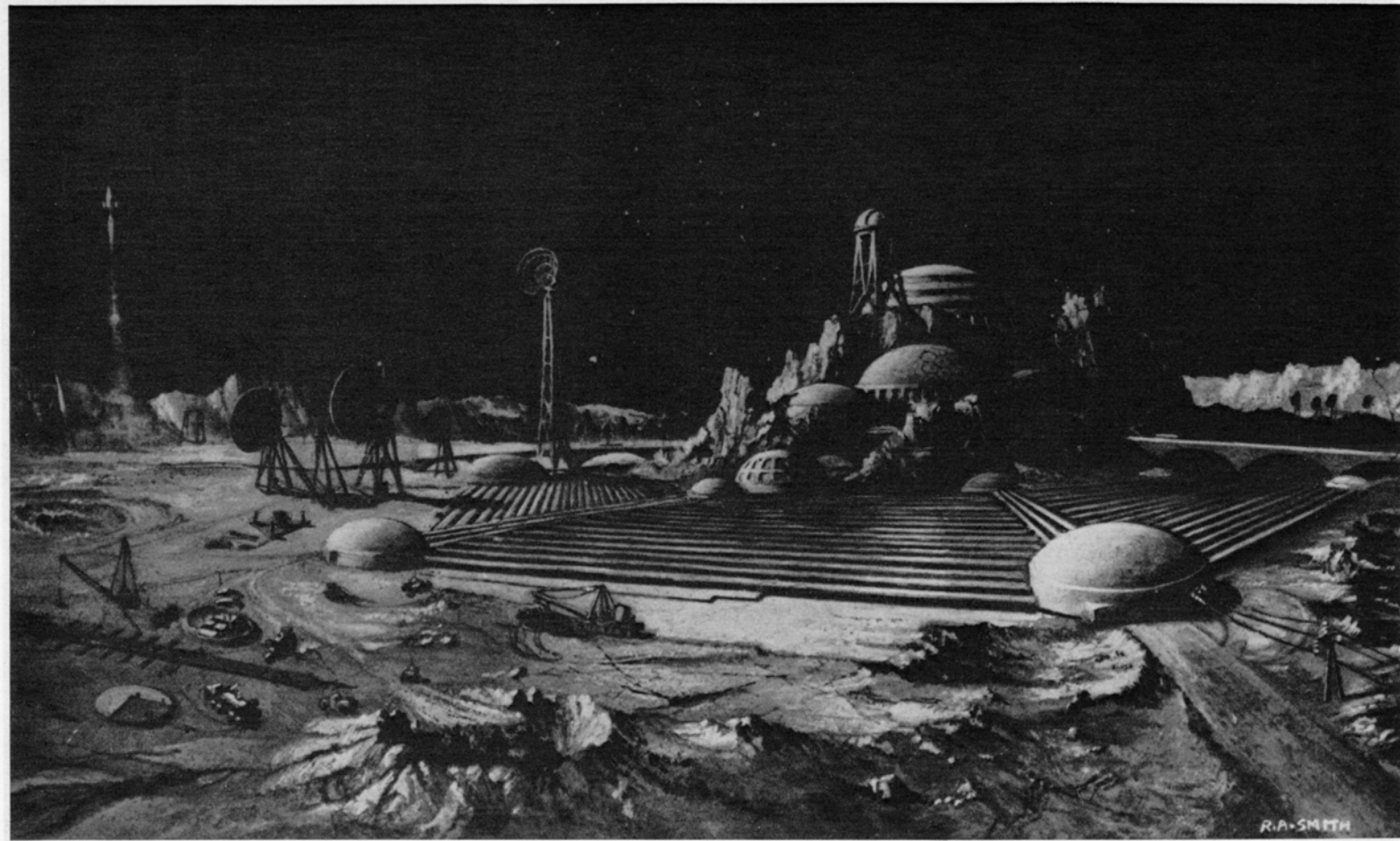
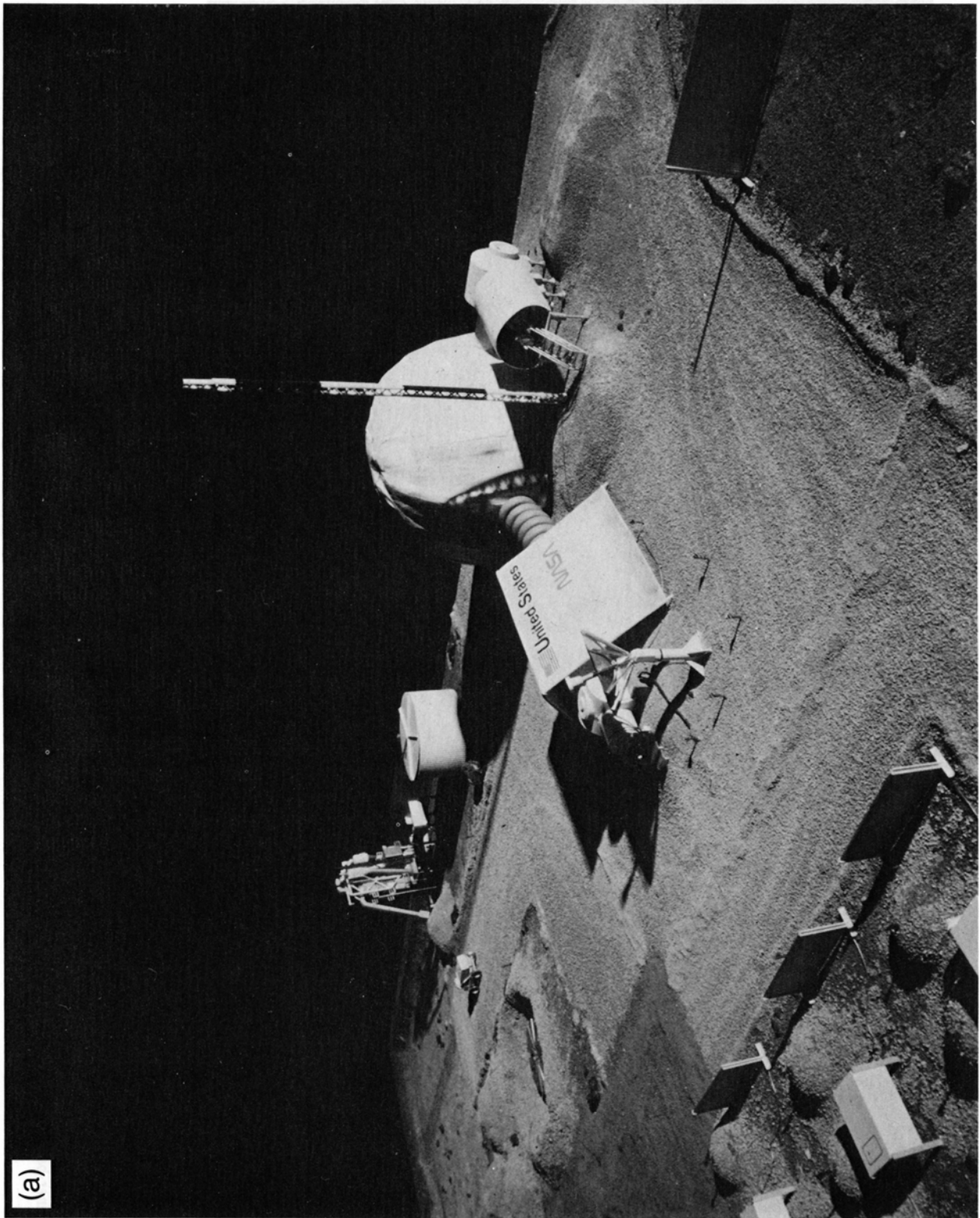


Fig. 11.1. Drawing of a lunar base (ca. 1950) by R. A. Smith (used with permission of the British Interplanetary Society). The base shown is described by *Clarke* (1951). This lunar base concept incorporates solar power (brightly illuminated area in the far distance) and nuclear power systems. The main buildings are set into the central peak of a crater, and surmounted by an astronomical observatory. The space-port is well removed from the living and working areas, a layout that would help to reduce exhaust-driven dust contamination. An electromagnetic launching system for shipment of processed resources is under construction in the left foreground: *Clarke* (1951) suggests the extraction of oxygen from lunar rocks and the production of rocket propellant as key lunar industries. There are some features of this base that would not be considered reasonable given our current knowledge (e.g., the transparent greenhouses arranged in rows around the base's main buildings would probably subject plants and astronauts to unacceptable radiation levels), but the basic features are common to many modern lunar-base concepts.



(b)

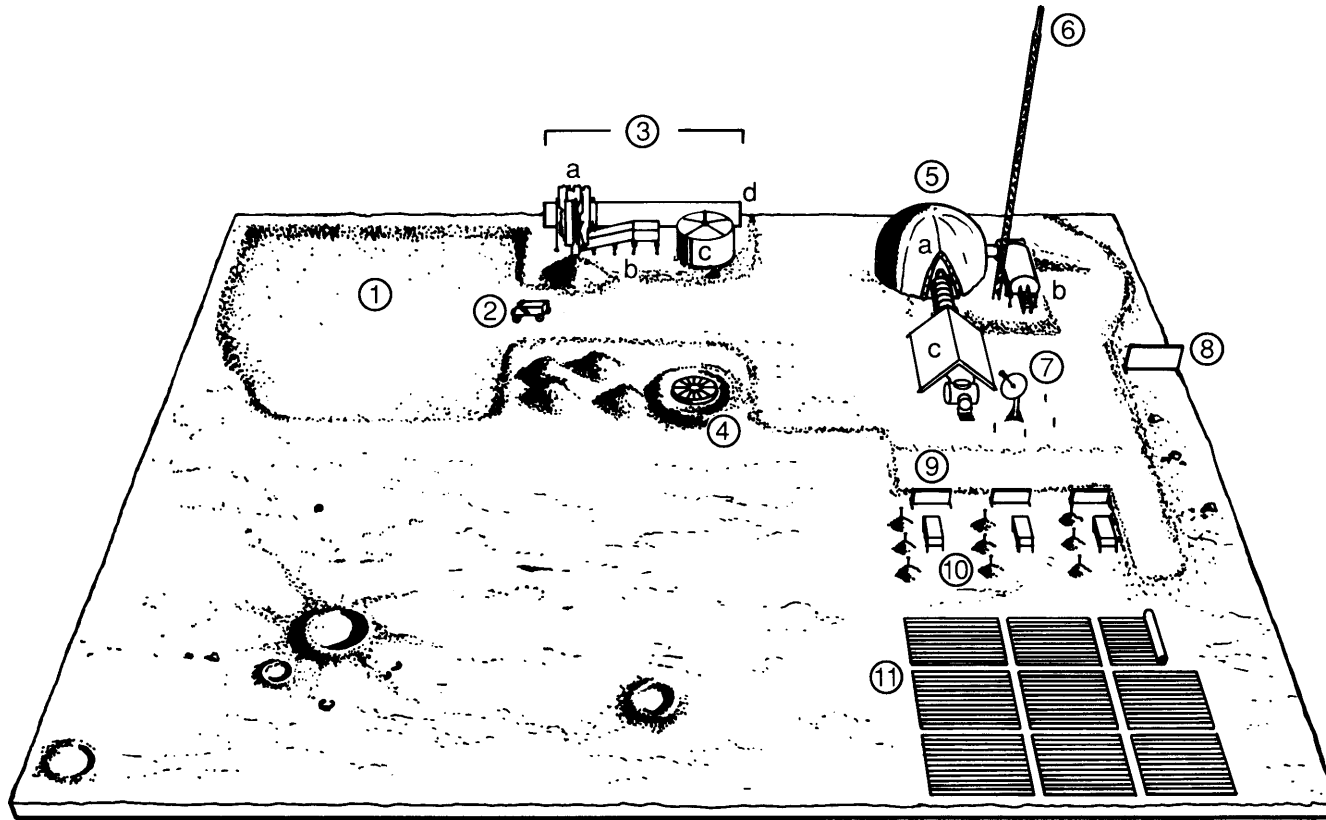


Fig. 11.2. A current NASA model of an initial lunar base (model by Mike Stovall of Eagle Aerospace, Inc.). **(a)** Photograph showing an oblique view of the major structures at the base. **(b)** Diagram showing the main components of the base: (1) A mining pit, excavated by front-end load/haulers (2) to supply a liquified- O_2 propellant production plant (3a). The plant includes tailings storage (3b), 24 t of liquid O_2 storage (3c), and a large radiator for thermal control (3d). The plant is scaled to produce 100 t of liquid O_2 per year by ilmenite reduction. Power for the O_2 plant comes from an SP-100 nuclear reactor (4), buried for radiation protection, that produces 300 kWe. The habitat (5a) is a 16-m dome that houses 12 people and the base operations in five levels, shielded by regolith-filled bags and covered by cloth. The habitat has an airlock (5b) with dust removal systems; remains of the initial base construction shack with a second airlock are shielded by a thermal-protection blanket (5c). The large radio tower (6) provides communications with a pressurized four-man rover (not shown) that may explore areas up to 100 km away; the dish antenna (7) provides high-gain video and data downlinks to Earth. Additional radiators (8 and 9) provide thermal control for the habitat and for fuel cells, respectively. The fuel cells (10) collect energy from Ga-As photovoltaic arrays (11) during the lunar day; each of the three fuel cells provides 25 kWe over the lunar night. Small dirt mounds next to the fuel cells provide thermal shielding for the hydrogen, oxygen, and water that cycle through them.

APPENDIX A 11.1: STUDIES IN LUNAR UTILIZATION

Numerous studies on lunar utilization have been carried out in the last two decades. In considering them, it is first necessary to recognize that the use of the Moon can be considered in several ways. First, there are some things that can be done on the Moon that cannot be done at all on Earth. Getting to the lunar farside to avoid Earth's radio noise and developing processes to take advantage of the extreme lunar daytime vacuum of 10^{-10} N/m² (10^{-12} torr) are two examples. Second, there are lower fuel and energy costs for exporting materials off the Moon (rather than the Earth) for use in space. Schemes for mining the lunar surface for a wide range of materials, from thermal and radiation shielding mass to oxygen-based propellants, make use of this advantage. With the exception of ³He there has been little consideration of lunar exports to Earth (see section 11.3.3), but the development of solar-power satellites using lunar materials is one form of energy export to Earth. Finally, the Moon can be considered useful in its own right as a place worthy of permanent occupation for international scientific and political cooperation. Parallels to the international use of Antarctica have already been made in this regard (Smith, 1985).

This appendix is a brief, annotated historical listing of reports and other publications that represent a wide range of studies on various aspects of lunar utilization. These works are diverse in content, although most view the Moon as "useful" in the second sense defined above, where lunar materials are to be obtained for use elsewhere in space. This listing is not intended to be exhaustive, and many additional individual papers and NASA-sponsored studies are not included. However, the documents cited here provide an excellent entry to the current literature.

1972: Dalton C. and Hohman E., eds., *Conceptual Design of a Lunar Colony*. NASA/ASEE Systems Design Institute. Publication of results from NASA grant NGT-005-114. 506 pp.

Results of an 11-week intensive study by the University of Houston, Rice University, and the NASA Manned Spacecraft Center (now the Johnson Space Center). Sections cover (1) the transition from a base to a colony, with design and function details; (2) a design analysis that includes subsystems and environmental engineering; (3) analysis of physiological, psychological, and safety requirements for the occupants; (4) site selection criteria; (5) oxygen

production schemes; (6) details of a life support system; (7) mining and excavation; (8) a brief discussion of manufacturing; (9) shelter; (10) electric and thermal power generation; and (11) conclusions and recommendations for further study. Written when the Apollo program was at its peak, this is an interesting historical document and one that discusses many details common to later studies of lunar bases and the utilization of the Moon.

from 1974 on: *Acta Astronautica*. Journal of the International Academy of Astronautics. Pergamon, New York.

A journal of 13 issues per year with broad international participation. Papers published are generally aimed at the scientific exploration of space, space utilization, and space development concepts. These papers cover a wide range of topics, some of which are related to lunar utilization. The broad international participation in the production of this journal provides a more global view of space development than obtained from most other publications.

1976: Criswell D. R., ed., *Lunar Utilization*. The Lunar Science Institute, Houston. 188 pp.

A collection of abstracts from a conference held in 1976. Sections include (1) economics; (2) material resources; (3) lunar and space utilization (ideas on processing lunar materials); (4) future exploration of the Moon, asteroids, and comets for utilization purposes; and (5) transportation (getting materials off the Moon).

1977: *Space Manufacturing Facilities—Space Colonies*.

1977: *Space Manufacturing Facilities 2*.

1979: *Space Manufacturing 3*.

1981: *Space Manufacturing 4*.

1985: *Space Manufacturing 5: Engineering with Lunar and Asteroidal Materials*.

1987: *Space Manufacturing 6*.

1989: *Space Manufacturing 7: Space Resources to Improve Life on Earth*.

American Institute of Aeronautics and Astronautics, New York.

These seven books are a collection of papers from nine conferences held at Princeton University. Topics covered include manufacturing in orbit, solar power satellites, space transportation, mass drivers, medical and social topics, international relations, and economics. The papers on lunar materials are mostly concerned with chemical processing or with the electromagnetic ejection of lunar materials from the Moon for use as feedstocks in near-Earth space. Lunar base topics and acquisition of space power for use on Earth receive more emphasis in the later volumes. Future conferences in this series are planned, and more volumes will be added to the series.

1977: O'Neil G. K., ed., *Space-Based Manufacturing from Nonterrestrial Materials*. Progress in Astronautics and Aeronautics, Vol. 57, American Institute of Aeronautics and Astronautics, New York. 177 pp.

Chapters are on (1) transportation (emphasis on mass drivers), (2) materials on the Moon and how to get them off, and (3) systems analysis for space manufacturing in orbit.

1979: Billingham J., Gilbreath W., and O'Leary B., eds., *Space Resources and Space Settlements*. NASA SP-428. 288 pp.

Sections describe (1) regenerative life-support systems, (2) habitats, (3) electromagnetic mass drivers, (4) asteroids as resources, and (5) processing of nonterrestrial materials. The last section includes discussions of a lunar supply base, fiberglass from lunar materials, lunar building materials made with inorganic polymers, assessment of possible lunar ores, chemical extraction of metals and oxygen from lunar materials, and mining and beneficiation of lunar ores.

1980: Williams R. J. and Jadwick J. J., *Handbook of Lunar Materials*. NASA RP-1057, NASA Scientific and Technical Information Office. 120 pp.

This handbook contains sections on (1) general information about the Moon and lunar exploration; (2) physical properties of lunar minerals, with data from their terrestrial analogs where data on lunar samples are lacking; (3) lunar regolith and rock properties; and (4) a summary of the physical properties of SiO₂, Si, Al, Ti, Fe, Ca, Mg, O, and lunar volatiles.

1980-1985: *Space Solar Power Review*. Pergamon, New York.
from 1986 on: *Space Power*. Carfax, Abingdon, England.

A quarterly journal initially dedicated to studies of a particular space technology (solar power satellites) for acquiring energy for use on Earth. After 1985, the scope of the journal was broadened to include all aspects of space resource utilization, space manufacturing, and space colonization. Throughout the journal's publication history, papers on the use of lunar materials for solar-power-satellite manufacture and other purposes have been periodically included.

1982: O'Leary, B., ed., *Space Industrialization*. CRC Press, Boca Raton, Florida. Volume I (167 pp.), Volume II (226 pp.).

Volume I includes an overview, a discussion of near-term products and services, a section on solar power satellites, and a review of possible asteroid resources. Lunar materials are specifically discussed in sections on space manufacturing from nonterrestrial materials (including scaling of processes and research recommendations) and materials processing in space (chemical plant design and chemical processing of lunar materials).

Volume II begins with a section on lunar utilization (including a summary of lunar material properties and possible uses of the Moon as a platform in space, a source of bulk materials, and a source of chemical products). This is followed by sections on large space structures, space transportation, systems analysis and economics, human factors, and the interaction between space industrialization and social science.

1985: Mendell W. W., ed., *Lunar Bases and Space Activities of the 21st Century*. Lunar and Planetary Institute, Houston. 865 pp.

This book is a good introduction to the concepts of establishing a lunar base and using lunar resources. The collected papers are directly relevant to the construction and occupation of a lunar base, with sections on (1) lunar base concepts, (2) transportation to/from the Moon, (3) lunar science from a lunar base, (4) space science from a lunar base, (5) construction on the Moon, (6) materials process-

ing on the Moon, (7) oxygen and hydrogen production on the Moon, (8) life support and health maintenance, (9) social and political implications, and (10) relation to future Mars missions.

(Note: a second volume in this series is based on more recent work and should be released soon by Univelt, San Diego.)

1987: Andrus G. M., ed., *Symposium '86: The First Lunar Development Symposium*. The Lunar Development Council, Pitman, New Jersey. 513 pp.

A collection of 49 papers presented at a 1986 conference that combined interests in lunar development with industrial interests in magnetic-levitation transportation. About 14% of the papers deal exclusively with magnetic levitation, but the remainder either explore the connection between this technology and lunar development or deal specifically with lunar resources, products, architecture, energy systems, and life support.

1988: Johnson S. W. and Wetzel J. P., eds., *Engineering, Construction, and Operations in Space (Proceedings of Space '88)*. American Society of Civil Engineers, New York. 1349 pp.

1990: Johnson S. W. and Wetzel J. P., eds., *Engineering, Construction, and Operations in Space II (Proceedings of Space '90)*. American Society of Civil Engineers, New York. 1598 pp. (two volumes).

These books consist of papers from two conferences with strong representation by civil engineers. Sections directly relevant to lunar utilization include (1) lunar surface properties, (2) processing lunar soils, (3) lunar cement and concrete, (4) lunar construction and surface operations, (5) lunar habitats and mining, (6) lunar base design, and (7) lunar oxygen production. Many other papers deal with orbital operations, robotics, life support, astronomy (especially astronomical observatories based on the Moon), power supplies, and other issues that are common to lunar and other space operations.

The organizers intend to continue holding this conference every two years, with publication of a volume of papers for each conference.

APPENDIX A11.2: LUNAR RESOURCES

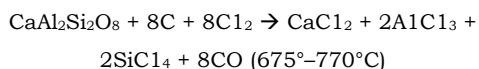
Volumes have been written on the full spectrum of potential lunar resources; Appendix A11.1 is a guide to this literature. In the text below, several major lunar resources are summarized in alphabetical order. Selection of resources for inclusion was based on either (1) abundance on the Moon or (2) a special value attached to the resource. The concepts of lunar resources are constantly changing, and new ideas (such as ^3He , section A11.2.2 below) will probably have to be added to this summary on an almost yearly basis to keep it up-to-date. However, certain resources (e.g., see *oxygen*, section A11.2.5) have already been studied extensively for more than a decade, and they are likely to remain attractive for advanced space exploitation.

A11.2.1. Aluminum

Uses. Aluminum has many potential uses as a light-weight structural metal, as a reflective or coating metal, and perhaps even as a rocket fuel, but Al metal production will probably not be practical until lunar development reaches a scale large enough to support the complex processing required.

Availability. The only practical source of Al on the Moon is the feldspar mineral plagioclase. This mineral is abundant in highland areas, both as single mineral fragments and in anorthositic rocks.

Processing. Concentration of plagioclase from highland regolith is not a well-tested process, but combined sizing and magnetic/electrostatic separation concepts have been considered (see below under *regolith*, section A11.2.6). Concentrations of plagioclase as rich as 90% should be attainable (McKay and Williams, 1979). Plagioclase has been used in terrestrial laboratory and pilot-plant operations for Al production by soda-lime sintering, but this process requires large amounts of Na and Ca carbonate. Several alternative processes are possible; of these, Bhogeswara Rao *et al.* (1979) recommend carbochlorination followed by electrolysis of the chlorides. The initial reaction is



Following this step, the AlCl_3 gas is condensed and mixed with alkali and alkaline earth chlorides for Al extraction by electrolysis. The electrolytic process has been proved by Alcoa (Bhogeswara Rao *et al.*, 1979). To carry out this process on the Moon, carbon, chlorine, and the alkali and alkaline earth chlorides must originally be supplied from Earth, but they can be recycled.

A11.2.2. Helium-3

Uses. A very specific use has been proposed for ^3He in the development of nuclear fusion energy (Wittenberg *et al.*, 1987). The advantages of ^3He fusion over the more studied ^3H fusion method are summarized in section 8.8.4.

Availability. Helium on the Moon is a product of solar wind implantation onto regolith particles. This is a very small amount of He (average of only 10 to 20 $\mu\text{g/g}$ He, concentrated in the most mature regoliths), with ^3He constituting only about 4 to 8 ng/g (about one part in 2500 of total implanted He). Nevertheless, this small amount of ^3He is so much more than found on Earth that it is a potential resource. Helium-3 is presently the only known potential resource from the Moon and cannot be obtained practically on Earth.

Processing. Helium can be extracted from the lunar regolith by heating. Other gases obtained this way are predominantly SO_2 , CO , CO_2 , H_2S , $\text{H}_2\text{O-H}_2$, and N_2 (Gibson, 1973). The gases in the regolith, although rare, could generate pressures up to 10 atm when heated in a sealed collection chamber (see section 8.8.4). All of these co-generated gases also have potential uses (see below under *hydrogen*, section A11.2.3), and fractionation systems to collect all gases would insure the maximum profit from the thermal-extraction process.

The small quantities of He trapped in regolith particles would require thermal processing of large amounts of lunar regolith to obtain useful amounts of the small fraction that is ^3He . Assuming that the average regolith contains 3-4 ng/g collectable ^3He and that only the upper 10 cm of regolith is processed, an area of about 2000 km^2 of unsieved regolith would have to be mined and processed to obtain 1 t of ^3He . This is by far the largest-scale lunar resource processing scheme yet envisioned.

A11.2.3. Hydrogen

Uses. The uses proposed for lunar H_2 fall into three major categories: (1) liquid H_2 and other H-based propellants to fuel rockets (Rosenberg 1985); (2) a reductant for winning oxygen from ilmenite (Gibson and Knudsen, 1985); (3) water production for a wide range of uses.

Availability. Hydrogen is a major constituent of the solar wind, and it is implanted in small amounts in the lunar surface regolith. Although rare, H and other rare regolith gases can be extracted simply by heating. The major constraint on the availability of H_2 is the need to handle large amounts of regolith in order to collect small amounts of gas.

Processing. In addition to conventional furnace heating, other methods of H₂ extraction have been proposed, ranging from microwave heating (*Tucker et al.*, 1985) to microbial extraction (*White and Hirsch*, 1985). In order to extract useful amounts of H, processing must be on a large scale. *Carter* (1985) estimates an average H₂ recovery of about one unit mass for slightly more than 2×10^4 unit masses of <20 μm regolith processed. This would correspond to about 9×10^4 unit masses of unsieved regolith. Assuming processing of only the upper 10 cm of the regolith (as with ³He, see section A11.2.2 above), an area of about 0.7 km² of unsieved regolith would have to be sieved and heated to obtain 1 t of H₂. Although this area is large, it is less than 10⁻³ of the area required to extract a comparable mass of ³He. It is evident that large amounts of H₂ would be co-generated if an ambitious scheme of ³He mining were adopted. The production of ~1 t ³He by heating bulk regolith would release ~5 × 10³ t of H₂.

A11.2.4. Iron

Uses. Iron metal has potential structural uses. Its weight, however, makes it less attractive than aluminum for use off the Moon. Glass, which in vacuum can have great tensile and compressive strength, may also be a competing material for structural uses both on and off the Moon (*Blacic*, 1985). However, Fe could be extracted and used as a byproduct before aluminum and glass plants are in operation, if large-scale O₂ production from ilmenite becomes the first priority in lunar resource uses.

Availability. Iron is common in many lunar minerals and even occurs as small metal beads and fragments in the regolith. Magnetic separation of iron metal from the regolith, however, is complicated by the common occurrence of Fe metal as small inclusions within agglutinates, which are a kind of "slag" produced by micrometeoroid impacts. As with O₂, the energetically most favorable source of Fe is the mineral ilmenite, which is abundant in high-Ti basalts and in the regolith formed over such basalts.

Processing. Extraction of Fe metal beads from the regolith is discussed in section 5.4.3. These beads are extremely fine-grained and are largely enclosed within agglutinates; thus they are unlikely to be a convenient large-scale source of Fe on the Moon. Iron, however, is an almost unavoidable byproduct if O₂ is extracted from lunar ilmenite (FeTiO₃) for life support and propellant uses (see below under *oxygen*, section A11.2.5). For each molecule of O₂ produced, approximately two atoms of Fe are liberated (depending on the ilmenite Fe-Mg composition and the actual processes used). One might also

expect Ti as a byproduct, but substantial additional processing would be necessary to reduce the Ti as well as the Fe to metal.

A11.2.5. Oxygen

Uses. The major use proposed for lunar O₂ is as an oxidizer in rocket propellants. Liquid O₂-liquid H₂ rockets are generally considered most likely, although other liquid propellant mixtures involving oxygen (for example, SiH₄-O₂, CH₃N₂H₃-O₂, S- O₂; *Rosenberg*, 1985; *Vaniman et al.*, 1990) have been considered. Oxygen is also essential for life support functions, and such consumption could become a major factor if the human presence on the Moon becomes substantial.

Availability. Oxygen is almost nonexistent as a free gas on the Moon; lunar rocks are generally reduced (e.g., all Fe is metallic or ferrous, never ferric) and will not readily release O₂. Oxygen production must be based on extraction from silicate or oxide minerals. If oxygen production is based on reduction of ilmenite, a favorable source, then mineral concentrations from high-Ti mare rocks or soils will probably be necessary (see section A11.2.6).

Processing. The importance of O₂ in life support and in space-based propulsion systems has led to several proposed methods for extracting it from lunar rocks. Ilmenite is often specified as the target mineral for oxygen production, because the energy required to reduce the FeO in ilmenite to Fe + 1/2O₂ is relatively low (ΔH for the reaction is about +9.7 kcal/g-mol at 900°C; *Williams and Erstfeld*, 1979). Purity of the ilmenite-enriched feedstock needs to be controlled; in particular, S may be a potential process-poisoning contaminant (*Williams*, 1985). Two basic ilmenite reduction processes are:

1. Using H₂ as a reductant: $\text{FeTiO}_3 + \text{H}_2 \rightarrow \text{Fe} + \text{TiO}_2 + \text{H}_2\text{O}$; followed by splitting of H₂O to produce O₂. The H₂ is recycled (*Gibson and Knudsen*, 1985).
2. Using C as a reductant (carbothermal reduction), a process involving several sequential steps: (a) $\text{FeTiO}_3 + (1 + x)\text{C} \rightarrow \text{FeC}_x + \text{CO} + \text{TiO}_2$; (b) $\text{FeC}_x + x/2\text{O}_2 \rightarrow \text{Fe} + x\text{CO}$; (c) $y\text{CO} + (2y + 1)\text{H}_2 \rightarrow y\text{H}_2\text{O} + \text{C}_y\text{H}_{2y+2}$; (d) $\text{C}_y\text{H}_{2y+2} \rightarrow \text{C}_y + (y + 1)\text{H}_2$; (e) splitting of H₂O to produce O₂. The H₂ and C are recycled (*Cutler and Krag* 1985).

Oxygen may also be separated from the gases used in other processing schemes, for example, reduction of the CO used in metal production by H₂ to produce H₂O, which may then be split to produce O₂ (e.g., some schemes for Fe and Ni extraction; see *Bhogeswara Rao et al.*, 1979). Finally, O₂ might be obtained

by other methods less dependent on a concentrated mineral feedstock. Among these relatively feedstock-insensitive methods are electrolysis of bulk regolith (the "magma electrolysis" method described by *Colson and Haskin*, 1990), or by a variety of other chemical and electrochemical schemes (for a summary see *Waldron*, 1990).

A11.2.6. Regolith

Uses. Regolith uses fall into three broad categories: (1) use of unprocessed bulk regolith for purposes such as shielding from cosmic rays and solar flares, (2) processing of bulk regolith to make glasses or ceramics, and (3) use of minerals separated from regolith as a beneficiated feedstock for other processing schemes.

Availability. Regolith is ubiquitous on the Moon; it is the most readily available of lunar materials. It has a broad range in chemical and mineralogic composition. It also varies in the degree to which its mineralogic constituents are agglomerated into impact-fused soil particles and therefore difficult to separate (see discussion of agglutinates, section 7.1.3). If mineral separates are needed (see preceding sections on *oxygen*, A11.2.5, and *aluminum*, A11.2.1), site selection can be used to optimize the extractability of certain minerals such as ilmenite or feldspar. A special type of regolith, formed on lunar pyroclastic deposits, contains much glass and is enriched in certain volatile elements (see Tables A6.5 and A6.6, as well as section 8.7.5).

Processing. Unprocessed bulk regolith intended for shielding may be scooped, shoveled, or bagged and then put into position. Containerization or

casting into blocks may be necessary, particularly if the regolith shielding is to be transported and used elsewhere, either on the Moon or in space.

Processing of bulk regolith by grain-size separation can enhance certain constituents. Collection of the finest fraction can enrich plagioclase and the KREEP-like mesostasis (section 7.5.3), although the enrichment factors are poor (Fig. 7.30) and the energy and equipment devoted to fine sieving (probably to <20 μm separation) may not be cost-effective. Collection of the coarse fraction, however, can result in significant enrichments of certain minerals. In highland soils such as those at the Apollo 16 site, plagioclase can be expected to make up most of the regolith fragments coarser than 1 cm, perhaps as much as 90% if anorthositic soils can be targeted. In high-Ti mare soils the >1-cm fragments would be dominated by basalts with 10-18% ilmenite. More thorough size-separation systems that remove both the fine (<20 μm) and coarse (>200 μm) splits before magnetic/electrostatic processing may be able to produce concentrates of ~90% plagioclase from some highland soils, or a still-undetermined percentage of ilmenite from high-Ti mare soils (*McKay and Williams*, 1979; *Williams et al.*, 1979; *Agosto*, 1985).

Plagioclase is of interest as a feedstock for Al or ceramic/glass manufacture; ilmenite is of interest as a source of O₂ and Fe. Practical concentration of other phases is more difficult. Deposits of volcanic glass might be considered as a feedstock for surface-deposited volatile elements, but it is uncertain whether their thin volatile-element coatings are sufficient to be considered as a resource (section 8.7.9).

APPENDIX A11.3: SUMMARY OF UNANSWERED QUESTIONS ABOUT THE MOON(modified from *Lunar Geoscience Working Group*, 1986)

Problem	Present Status	Unanswered Questions Requiring Further Research/Exploration
1. Surface history and cratering rate	— Gradual decline in impact rate from 4.6 b.y. ago, with possible spikes	<ul style="list-style-type: none"> — Was there a terminal “cataclysm” ~3.9 b.y. ago? — What is the crater saturation diameter in the highlands? — Has cratering flux varied during the last 3 b.y.? — What were the characteristics of transition from primordial accretion (4.6 b.y. ago) to later heavy bombardment(s)?
2. Cratering mechanisms	<ul style="list-style-type: none"> — Comparison with terrestrial craters, explosions, and experiments to determine processes — Interplanetary comparisons 	<ul style="list-style-type: none"> — What are the variations in cratering flow field with impactor velocity, composition, and target conditions? — Is the proportional-growth model valid for basin-forming events? — How do crater central peaks and rings form? — How are large impact basins formed?
3. Crater and basin ejecta	<ul style="list-style-type: none"> — Basin secondaries abundant — Variable amounts of local rock and original target rock in ejecta — Large melt fraction 	<ul style="list-style-type: none"> — What fraction of primary vs. local ejecta is present in continuous crater/basin deposits? — Is there a consistent pattern of radial and concentric zoning of target stratigraphy in crater ejecta? — What are the shock-level distributions within, outside, and beneath craters? — Are impact melts chemically homogeneous? At what scale does homogenization cease? — What is the provenance of clasts in impact melts? — How are meteoroid siderophile elements added to impact melts? — What are the origins of LKFM and VHA impact melts?

Problem	Present Status	Unanswered Questions Requiring Further Research/Exploration
4. Lunar regolith and the sun's history	<ul style="list-style-type: none"> — Depositional models for regolith maturity indices developed — Evidence for variable solar activity 	<ul style="list-style-type: none"> — What is the nature of the regolith-bedrock interface? — What is the ratio of exotic to local material in the regolith and how did it get there? — What changes have occurred in lateral mixing of ejecta with time and crater size? — What is the nature of regolith stratification? — What are the relative and absolute ages of crater rays? — What has been the flux of micrometeoroids with time? — Determine the history of solar and galactic particles with time: Search for datable soils sandwiched between lava flows
5. Megaregolith	<ul style="list-style-type: none"> — Variable thickness, perhaps as much as 10 km 	<ul style="list-style-type: none"> — What is the exact thickness of the megaregolith? How does it vary across the Moon? — What are the geophysical signatures of the megaregolith? — Is the megaregolith chemically homogeneous?
6. Volcanism	<ul style="list-style-type: none"> — Both thin (<1 km) and thick (>4 km) basin fills are possible 	<ul style="list-style-type: none"> — What is the relationship between mare fill and mass concentrations (mascons)? — How many cooling units (and eruption sequences) are present in a single basin? — What are the thicknesses of individual lava flows? — Has there been ponding of lavas and subsequent differentiation?
— Duration of mare volcanism	— 4.2 to ~1.0 b.y.	<ul style="list-style-type: none"> — How widespread are ancient highland basalts? How old are they? What are their compositions? <ul style="list-style-type: none"> — Where are ancient basalts exposed? — What are the ages of the youngest mare basalts?
— Highland volcanism	— Some possible	<ul style="list-style-type: none"> — Is there molten rock inside the Moon today? <ul style="list-style-type: none"> — What is the origin and which are of impact origin? — When did highland volcanism cease? — Not enough is known about highland volcanism to formulate key questions

Problem	Present Status	Unanswered Questions Requiring Further Research/Exploration
7. Tectonism	— Modeled and compared with images, photos, and geophysical anomalies	<ul style="list-style-type: none"> — What is the global lunar stress history? — What are the origins of lunar wrinkle ridges? — What is the history of lithospheric growth and how did it vary spatially? — Is tectonism around basins associated with the impact event, with the subsequent loading by mare basalts, or both? — What are the ages of young highland scarps? — How do floor-fractured craters form?
8. The lunar crust and “magma ocean”	— Global magma ocean, followed by serial volcanism	<ul style="list-style-type: none"> — How did the lunar crust form? — Did mare basalt source regions form at the same time as ferroan anorthosites? — What is the age range for ferroan anorthosites? — What is the time scale of early lunar differentiation? — Did early heavy impact bombardment interact with early differentiation? — Was there a single moonwide magma ocean, a series of magma seas, or other early magma forms?
— Primary highland rock types	— Represented by pristine clasts	<ul style="list-style-type: none"> — How many magmas contributed to development of the lunar crust? — How and when were these rock types mixed into polymict breccias? — How many of these rock types have been sampled so far? — How and when were intrusions emplaced into the highland crust? — Which rock types were formed in the original magma ocean?
— KREEP (Rocks with high potassium, rare earth elements, and phosphorus)	— Probably global	<ul style="list-style-type: none"> — What is the origin of KREEP? — How does the concentration of KREEP vary spatially within the lunar crust? — Was KREEP absent from the lunar surface 4 b.y. ago? — Are varieties of KREEP associated with granites and rhyolites? — Is KREEP added to the surface by impact or volcanic processes?

Problem	Present Status	Unanswered Questions Requiring Further Research/Exploration
— Crustal structure and composition		— What are the global variations in crustal thickness? — Which isostatic compensation mechanism predominates? — Is the crust layered? — What is the cause of the varied crust thickness and offset between the Moon's center of mass and center of figure? — Have basin-forming impacts excavated complete crustal sections, which can be reconstructed through the study of ejecta?
Compositional	Anorthositic "layer" above noritic "layer"?	
Seismic data:	20–25 km of crust in highlands	
Gravity data:	Unsure about models	
9. The lunar mantle		— What is the composition of the lunar mantle and how does it vary laterally?
— Seismic profile	— Density probably increases with depth	— What is the origin of mantle cumulate rocks?
— Source regions for basaltic lavas	— Heterogeneous	— What is the origin of sublimates from volatile phases present in pyroclastic deposits? What is the composition of these phases?
— Volatiles	— Characterized in pyroclastic ejecta	— What is the structure and location of the volcanic plumbing that served as conduits for mare lavas? What were the eruption mechanisms for lunar pyroclastic deposits? How did they ascend from their source regions?
10. The lunar core	<500 km radius	— Does the Moon have a metal-rich core? If so, is it iron, nickel-iron, or iron sulfide? — What is the nature of the core-mantle boundary? — What are the implications of a lunar core for models of lunar origin?
11. Global properties		— What is the precise moment of inertia?
— Moment of inertia	— 0.3905 ± 0.0023	— What is the global average lunar heat flow? How and why does it vary laterally?
— Heat flow	— About 2 times that of Earth?	— Is there any molten material left in the Moon? — What are the bulk lunar U and Th abundances?

Problem	Present Status	Unanswered Questions Requiring Further Research/Exploration
— Paleomagnetism	<ul style="list-style-type: none"> — Rocks: “fossil magnetism” not understood — Orbital: Bright swirls on the surface are highly magnetic 	<ul style="list-style-type: none"> — What is the origin of lunar paleomagnetism? — Was there once a core magnetic dynamo; if so, when did it start and stop? — What is the origin of Reiner-Gamma-type swirls? — Is the generation of transient magnetic fields an important lunar process? How are they generated? — Is there evidence for polar wandering?
12. Lunar atmosphere	<ul style="list-style-type: none"> — Tenuous; derived from solar-wind gases and radioactive decay of ⁴⁰K to ⁴⁰Ar 	<ul style="list-style-type: none"> — What are the daytime and nighttime concentrations and compositions? — What are the dynamics of the ionosphere? — What is the electron density at the surface? — How will human activities affect the lunar atmosphere?
13. Lunar transient events	<ul style="list-style-type: none"> — Controversial Earth-based observations of clouds or flashes on the Moon — Impact events 	<ul style="list-style-type: none"> — A permanent monitoring system is needed on the lunar surface — Are there gas releases from the lunar interior? — What is the relation between transient events and surface radon emission?
14. Bulk composition of the Moon	<ul style="list-style-type: none"> — Estimates based on a very restricted sample suite 	<ul style="list-style-type: none"> — What is the lunar bulk composition? — What are the implications of the bulk composition for determining the original source of lunar material and its relation to the Earth?
15. Origin of the Moon	<ul style="list-style-type: none"> — Currently favored theory: giant impact on Earth, followed by accretion in orbit around the Earth 	<ul style="list-style-type: none"> — What is the origin of the Moon? — If the collision-ejection hypothesis is valid, are there geochemical signatures in lunar rocks for both projectile and target? — What has been the evolution of the Moon’s orbit through time?

REFERENCES

- Adams J. B. (1974) Visible and near-infrared diffuse reflectance spectra of pyroxenes as applied to remote sensing of solid objects in the solar system. *J. Geophys. Res.*, 79, 4829–4836.
- Adams J. B. (1975) Interpretation of visible and near-infrared diffuse reflectance spectra of pyroxenes and other rock forming minerals. In *Infrared and Raman Spectroscopy of Lunar and Terrestrial Materials* (C. Karr, ed.), pp. 91–116. Academic, New York.
- Adams J. B. and McCord T. B. (1973) Vitrification darkening in the lunar highlands and identification of Descartes material at the Apollo 16 site. *Proc. Lunar Sci. Conf. 4th*, pp. 163–177.
- Adams J. B., Pieters C., and McCord T. B. (1974) Orange glass: Evidence for regional deposits of pyroclastic origin on the Moon. *Proc. Lunar Sci. Conf. 5th*, pp. 171–186.
- Adams J. B., Charette M. P., and Rhodes J. M. (1975) Chemical fractionation of the lunar regolith by impact melting. *Science*, 190, 380–381.
- Adams J. B., Hörz F., and Gibbons R. V. (1979) Effects of shock-loading on the reflectance spectra of plagioclase, pyroxene and glass (abstract). In *Lunar and Planetary Science X*, pp. 1–3. Lunar and Planetary Institute, Houston.
- Adams J. H. Jr. and Shapiro M. M. (1985) Irradiation of the Moon by galactic cosmic rays and other particles. In *Lunar Bases and Space Activities of the 21st Century* (W. W. Mendell, ed.), pp. 315–327. Lunar and Planetary Institute, Houston.
- Adler I. and Trombka J. I. (1977) Orbital chemistry–lunar surface analysis from the X-ray and gamma-ray remote sensing experiments. *Phys. Chem. Earth*, 10, 17–43.
- Adler I., Trombka J., Gerard J., Schmadbeck R., Lowman P., Blodgett H., Yin L., Eller E., Lamoth R., Gorenstein P., Bjorkholm P., Harris B., and Gursky H. (1972) X-ray fluorescence experiment. In *Apollo 15 Preliminary Science Report*, pp. 17–1 to 17–17. NASA SP-289.
- Adler I., Trombka J. I., Schmadbeck R., Lowman P., Blodgett H., Yin L., Eller E., Podwysocki M., Weidner J. R., Bickel A. L., Lum R. K. L., Gerard J., Gorenstein P., Bjorkholm P., and Harris B. (1973) Results of the Apollo 15 and 16 X-ray experiment. *Proc. Lunar Sci. Conf. 4th*, pp. 2783–2791.
- Aggarwal H. R. and Oberbeck V. R. (1979) Monte Carlo simulation of lunar megaregolith and implications. *Proc. Lunar Planet. Sci. Conf. 10th*, pp. 2689–2705.
- Agosto W. N. (1985) Electrostatic concentration of lunar soil minerals. In *Lunar Bases and Space Activities of the 21st Century* (W. W. Mendell, ed.), pp. 453–464. Lunar and Planetary Institute, Houston.
- Agrell S. O., Peckett A., Boyd F. R., Haggerty S. E., Bunch T. E., Cameron E. N., Dence M. R., Douglas J. A. V., Plant A. G., Traill R. J., James O. B., Keil K., and Prinz M. (1970a) Titanian chromite, aluminum chromite, and chromian ulvöspinel from Apollo 11 rocks. *Proc. Apollo 11 Lunar Sci. Conf.*, pp. 81–86.
- Agrell S. O., Scoon J. H., Muir I. D., Long J. V. P., McConnell J. D. C., and Peckett A. (1970b) Observations on the chemistry, mineralogy and petrology of some Apollo 11 lunar samples. *Proc. Apollo 11 Lunar Sci. Conf.*, pp. 93–128.
- Ahrens T. J. and Cole D. M. (1974) Shock compression and adiabatic release of lunar fines from Apollo 17. *Proc. Lunar Sci. Conf. 5th*, pp. 2333–2345.
- Ahrens T. J. and O'Keefe J. D. (1977) Equations of state and impact-induced shock-wave interaction on the Moon. In *Impact and Explosion Cratering* (D. J. Roddy, R. O. Pepin, and R. B. Merrill, eds.), pp. 639–656. Pergamon, New York.
- Albee A. L. and Chodos A. A. (1970) Microprobe investigations on Apollo 11 samples. *Proc. Apollo 11 Lunar Sci. Conf.*, pp. 135–157.
- Albee A. L., Chodos A. A., Gancarz A. J., Haines E. L., Papanastassiou D. A., Ray L., Tera F., Wasserburg G. J., and Wen T. (1972) Mineralogy, petrology, and chemistry of a Luna 16 basaltic fragment, sample B-1. *Earth Planet. Sci. Lett.*, 13, 353–367.
- Aldrin E. E. Jr., Armstrong N. A., and Collins M. (1969) Crew observations. In *Apollo 11 Preliminary Science Report*, pp. 35–39. NASA SP-214.
- Alexander E. C. Jr. and Kahl S. B. (1974) ⁴⁰Ar–³⁹Ar studies of lunar breccias. *Proc. Lunar Sci. Conf. 5th*, pp. 1353–1373.
- Alexander E. C. Jr., Coscio M. R. Jr., Dragon J. C., and Saito K. (1980) K/Ar dating of lunar soils IV: Orange glass from 74220 and agglutinates from 14259 and 14163. *Proc. Lunar Planet. Sci. Conf. 11th*, pp. 1663–1677.
- Alexandrov A. K., Borisov B. M., Garin I. S., Grafov V. I., Ivanov A. G., Kotlov Yu. P., Komarov V. I., Kuleshov A. F., Mishkin V. K., Nikolayev G. B., Polenov L. N., Semenov P. S., and Yakovlev F. P. (1972) Investigations of mobility of Lunokhod 1. In *COSPAR Space Research XII*, pp. 73–82. Akademie-Verlag, Berlin.
- Ali M. Z. and Ehmman W. D. (1977) Chemical characterization of lunar core 60010. *Proc. Lunar Sci. Conf. 8th*, pp. 2967–2981.
- Allen C. C. (1975) Central peaks in lunar craters. *The Moon*, 12, 463–474.
- Allen R. O. Jr., Jovanovic S., and Reed G. W. Jr. (1974) A study of ²⁰⁴Pb partition in lunar samples using terrestrial and meteoritic analogues. *Proc. Lunar Sci. Conf. 5th*, pp. 1617–1623.
- Allen R. O., Jovanovic S., and Reed G. W. Jr. (1975) Agglutinates: Role in element and isotope chemistry and inferences regarding volatile-rich rock 66095 and glass 74220. *Proc. Lunar Sci. Conf. 6th*, pp. 2271–2279.
- Allton J. H. (1989) *Catalog of Apollo Lunar Surface Geological Sampling Tools and Containers*. NASA JSC Publ. No. 23454. 92 pp.
- Allton J. H. and Waltz S. R. (1980) Depth scales for Apollo 15, 16, and 17 drill cores. *Proc. Lunar Planet. Sci. Conf. 11th*, pp. 1463–1477.
- Alvarez L. W., Alvarez W., Asaro F., and Michel H. V. (1980) Extraterrestrial cause for the Cretaceous-Tertiary mass extinction. *Science*, 208, 1095–1108.

- Alvarez R. (1973a) Lunar fines 74241,2, low frequency dielectric variations with density and temperature. *Eos Trans. AGU*, 54, 1129.
- Alvarez R. (1973b) Lunar powder simulator under lunarlike conditions, dielectric properties. *J. Geophys. Res.*, 78, 6833-6844.
- Alvarez R. (1974a) Dielectric comparison of lunar and terrestrial fines at lunar conditions. *J. Geophys. Res.*, 79, 5453-5457.
- Alvarez R. (1974b) Electrical properties of sample 70215 in the lunar temperature range of 100° to 373°K (abstract). In *Lunar Science V*, pp. 15-17. The Lunar Science Institute, Houston.
- Alvarez R. (1974c) Electrical properties of sample 70215; low frequency corrections. *Proc. Lunar Sci. Conf. 5th*, pp. 2663-2671.
- Alvarez R. (1974d) Lunar magnetization and surface charge variations (abstract). In *Lunar Interactions* (D. R. Criswell and J. W. Freeman, eds.), pp. 61-63. The Lunar Science Institute, Houston.
- Alvarez R. (1975) Lunar and terrestrial sample photoconductivity. *Proc. Lunar Sci. Conf. 6th*, pp. 3187-3197.
- Alvarez R. (1977a) On charge transport in the terminator's vicinity (abstract). In *Lunar Science VIII*, pp. 28-30. The Lunar Science Institute, Houston.
- Alvarez R. (1977b) Photoconductive effects on lunar and terrestrial fines. *Proc. Lunar Sci. Conf. 8th*, pp. 1277-1290.
- Anders E. (1968) Chemical processes in the early solar system, as inferred from meteorites. *Acc. Chem. Res.*, 1, 289-298.
- Anders E. (1978) Procrustean science: Indigenous siderophiles in the lunar highlands, according to Delano and Ringwood. *Proc. Lunar Planet. Sci. Conf. 9th*, pp. 161-184.
- Anders E. and Ebihara M. (1982) Solar-system abundances of the elements. *Geochim. Cosmochim. Acta*, 46, 2363-2380.
- Anders E., Ganapathy R., Keays R. R., Laul J. C., and Morgan J. W. (1971) Volatile and siderophile elements in lunar rocks: Comparison with terrestrial and meteoritic basalts. *Proc. Lunar Sci. Conf. 2nd*, pp. 1021-1036.
- Anders E., Ganapathy R., Krähenbühl U., and Morgan J. W. (1973) Meteoritic material on the Moon. *The Moon*, 8, 3-24.
- Anderson A. T. Jr. (1973) The texture and mineralogy of lunar peridotite 15445,10. *J. Geol.*, 81, 219-226.
- Anderson A. T. Jr. and Smith J. V. (1971) Nature, occurrence, and exotic origin of "gray mottled" (Luny Rock) basalts in Apollo 12 soils and breccias. *Proc. Lunar Sci. Conf. 2nd*, pp. 431-438.
- Anderson A. T. Jr., Bunch T. E., Cameron E. N., Haggerty S. E., Boyd F. R., Finger L. W., James O. B., Keil K., Prinz M., Ramdohr P., and El Goresy A. (1970) Armalcolite: A new mineral from the Apollo 11 samples. *Proc. Apollo 11 Lunar Sci. Conf.*, pp. 55-63.
- Andre C. G., Bielefeld M. J., Eliason E., Soderblom L. A., Adler I., and Philpotts J. A. (1977) Lunar surface chemistry: A new imaging technique. *Science*, 197, 986-989.
- Annell C. S. and Helz A. W. (1970) Emission spectrographic determination of trace elements in lunar samples from Apollo 11. *Proc. Apollo 11 Lunar Sci. Conf.*, pp. 991-994.
- Apollo 15 Preliminary Examination Team (1972) Preliminary examination of lunar samples. In *Apollo 15 Preliminary Science Report*, pp. 6-1 to 6-25. NASA SP-289.
- Apollo Soil Survey (1971) Apollo 14: Nature and origin of rock types in soil from Fra Mauro Formation. *Earth Planet. Sci. Lett.*, 12, 49-54.
- Appleman D. E., Nissen H.-U., Stewart D. B., Clark J. R., Dowty E., and Huebner J. S. (1971) Studies of lunar plagioclases, tridymite, and cristobalite. *Proc. Lunar Sci. Conf. 2nd*, pp. 117-133.
- Arkani-Hamed J. (1973) On the thermal history of the Moon. *Proc. Lunar Sci. Conf. 4th*, pp. 2673-2684.
- Arkani-Hamed J. (1974) Lunar mascons as consequences of giant impacts. *The Moon*, 10, 307-322.
- Armstrong N., Collins M., and Aldrin E. E. (1970) *First on the Moon*. Little, Brown and Co., Boston. 511 pp.
- Armstrong T. W. and Alsmiller R. G. Jr. (1971) Calculation of cosmogenic radionuclides in the Moon and comparison with Apollo measurements. *Proc. Lunar Sci. Conf. 2nd*, pp. 1729-1745.
- Arndt J. and von Engelhardt W. (1987) Formation of Apollo 17 orange and black glass beads. *Proc. Lunar Planet. Sci. Conf. 17th*, in *J. Geophys. Res.*, 92, E372-E376.
- Arndt J., Flad K., and Feth M. (1979) Radiative cooling experiments on lunar glass analogues. *Proc. Lunar Planet. Sci. Conf. 10th*, pp. 355-373.
- Arndt J., Hummel W., and Gonzalez-Chabeza I. (1982) Diaplectic labradorite glass from the Manicouagan impact crater. *Phys. Chem. Minerals*, 8, 230-239.
- Arndt J., von Engelhardt W., Gonzales-Cabeza I., and Meier B. (1984) Formation of Apollo 15 green glass beads. *Proc. Lunar Planet. Sci. Conf. 15th*, in *J. Geophys. Res.*, 89, C225-C232.
- Arnold J. R. (1975) Monte Carlo simulation of turnover processes in the lunar regolith. *Proc. Lunar Sci. Conf. 6th*, pp. 2375-2396.
- Arnold J. R. (1979) Ice in the lunar polar regions. *J. Geophys. Res.* 84, 5659-5668.
- Arnold J. R. (1987) Ice at the lunar poles revisited (abstract). In *Lunar and Planetary Science XVIII*, pp. 29-30. Lunar and Planetary Institute, Houston.
- Arnold J. R., Peterson L. E., Metzger A. E., and Trombka J. I. (1972) Gamma-ray spectrometer experiment. In *Apollo 15 Preliminary Science Report*, pp. 16-1 to 16-6. NASA SP-289.
- Arrhenius G. (1974) Electret formation on the lunar surface—adhesion and clustering of dielectric particles in the space environment (abstract). In *Lunar Interactions* (D. R. Criswell and J. R. Freeman, eds.), p. 85. The Lunar Science Institute, Houston.

- Arvidson R., Crozaz G., Drozd R. J., Hohenberg C. M., and Morgan C. J. (1975a) Cosmic ray exposure ages of features and events at the Apollo landing sites. *The Moon*, 13, 67–79.
- Arvidson R., Drozd R. J., Hohenberg C. M., Morgan C. J., and Poupeau G. (1975b) Horizontal transport of the regolith, modification of features, and erosion rates on the lunar surface. *The Moon*, 13, 67–79.
- Arvidson R., Drozd R., Guinness E., Hohenberg C., Morgan C., Morrison R., and Oberbeck V. (1976) Cosmic ray exposure ages of Apollo 17 samples and the age of Tycho. *Proc. Lunar Sci. Conf. 7th*, pp. 2817–2832.
- Ashwal L. D. (1975) Petrologic evidence for a plutonic igneous origin of anorthositic clasts in 67955 and 77017. *Proc. Lunar Sci. Conf. 6th*, pp. 221–230.
- Ashwal L. D. (1990) *Anorthosites*. Springer-Verlag, New York, in press.
- Ashworth D. G. (1977) Lunar and planetary impact erosion. In *Cosmic Dust* (J. A. M. McDonnell, ed.), pp. 427–526. Wiley, New York.
- ASTM D 2487 (1987) Classification of soils for engineering purposes. *Standard Test Method, Vol. 04.08: Soil and Rock; Building Stones*, pp. 395–408. American Society for Testing and Materials, Philadelphia.
- Axon H. J. and Goldstein J. I. (1973) Metallic particles of high cobalt content in Apollo 15 soil samples. *Earth Planet. Sci. Lett.*, 18, 173–180.
- Baedecker P. A., Schaudy R., Elzie J. L., Kimberlin J., and Wasson J. T. (1971) Trace element studies of rocks and soils from Oceanus Procellarum and Mare Tranquillitatis. *Proc. Lunar Sci. Conf. 2nd*, pp. 1037–1061.
- Baedecker P. A., Chou C.-L., and Wasson J. T. (1972) The extralunar component in lunar soils and breccias. *Proc. Lunar Sci. Conf. 3rd*, pp. 1343–1359.
- Baedecker P. A., Chou C.-L., Grudewicz E. B., and Wasson J. T. (1973) Volatile and siderophilic trace elements in Apollo 15 samples: Geochemical implications and characterization of the long-lived and short-lived extralunar components. *Proc. Lunar Sci. Conf. 4th*, pp. 1177–1195.
- Baedecker P. A., Chou C.-L., Sundberg L. L., and Wasson J. T. (1974) Volatile and siderophilic trace elements in the soils and rocks of Taurus-Littrow. *Proc. Lunar Sci. Conf. 5th*, pp. 1625–1643.
- Bakos L., Chayka M., Cher L., Cheke A., Dogadkin N. N., Elek A., Kulchar K., Nagy D. L., Szabo E., Forzats B., and Zemplen E. (1977) Investigation of the composition of the Luna 16 sample. In *The Soviet American Conference on Cosmochemistry of the Moon and Planets* (J. H. Pomeroy and N. J. Hubbard, eds.), pp. 277–280. NASA SP-370.
- Baldrige W. S., Beaty D. W., Hill S. M. R., and Albee A. (1979) The petrology of the Apollo 12 pigeonite basalt suite. *Proc. Lunar Planet. Sci. Conf. 10th*, pp. 141–179.
- Baldwin R. B. (1963) *The Measure of the Moon*. Univ. of Chicago, Chicago. 488 pp.
- Baldwin R. B. (1974) On the origin of the mare basins. *Proc. Lunar Sci. Conf. 5th*, pp. 1–10.
- Baldwin R. B. (1981) On the origin of the planetesimals that produced the multi-ring basins. In *Multi-Ring Basins, Proc. Lunar Planet. Sci. 12A* (P. H. Schultz and R. B. Merrill, eds.), pp. 19–28. Pergamon, New York.
- Bame S. J., Feldman W. C., Gosling J. T., Young D. T., and Zwickl R. D. (1983) What magnetospheric workers should know about solar wind composition. In *Energetic Ion Composition in the Earth's Magnetosphere* (R. G. Johnson, ed.), pp. 73–98. Terra, Tokyo.
- Bansal B. M., Church S. E., Gast P. W., Hubbard N. J., Rhodes J. M., and Wiesmann H. (1972) Chemical composition of soil from Apollo-16 and Luna-20 sites. *Earth Planet. Sci. Lett.*, 17, 29–35.
- Bansal B. M., Gast P. W., Hubbard N. J., Nyquist L. E., Rhodes J. M., Shih C. Y., and Weismann H. (1973) Lunar rock types (abstract). In *Lunar Science IV*, pp. 48–50. The Lunar Science Institute, Houston.
- Barraclough B. L. and Marti K. (1985) In search of the Moon's indigenous volatiles: Noble gases and nitrogen in vesicular lunar glasses (abstract). In *Lunar and Planetary Science XVI*, pp. 31–32. Lunar and Planetary Institute, Houston.
- Barsukov V. L. (1977) Preliminary data for the regolith core brought to earth by the automatic lunar station Luna 24. *Proc. Lunar Sci. Conf. 8th*, pp. 3303–3318.
- Barsukov V. L., Tarasov L. S., Dmitriev L. V., Kolesov G. M., Shevaleevsky I. D., and Garanin A. V. (1977) The geochemical and petrochemical features of regolith and rocks from Mare Crisium (preliminary data). *Proc. Lunar Sci. Conf. 8th*, pp. 3319–3332.
- Barsukov V. L., Dmitriev L. V., Tarasov L. S., Kolesov G. M., Shevaleevsky I. D., Ramendik G. A., and Garanin A. V. (1980) Geochemical and petrological peculiarities of regolith and lithic clasts from Mare Crisium. In *Lunar Soil from Mare Crisium* (V. L. Barsukov, ed.), pp. 158–165. Nauka, Moscow.
- Basford J. R., Dragon J. C., Pepin R. O., Coscio M. R., and Murthy V. R. (1973) Krypton and xenon in lunar fines. *Proc. Lunar Sci. Conf. 4th*, pp. 1915–1955.
- Basilevski A. T. (1976) On the evolution of small lunar craters. *Proc. Lunar Sci. Conf. 7th*, pp. 1005–1020.
- Basilevski A. T., Ivanov B. A., Florensky K. P., Yakolev O. I., Fel'dman V. I., Granovsky L. V., and Snadovskiy M. A. (1983) *Impact Craters on the Moon and Planets*. Nauka, Moscow. 200 pp. (Translated from Russian in NASA TM-77667.)
- Bassett H. L. and Shackelford R. G. (1972) Dielectric properties of Apollo 14 lunar samples at micrometer and millimeter wavelengths. *Proc. Lunar Sci. Conf. 3rd*, pp. 3157–3160.
- Basu A. (1976) Petrology of Holocene fluvial sand derived from plutonic source rocks: Implications to paleoclimatic interpretation. *J. Sed. Petrol.*, 46, 694–709.
- Basu A. (1977) Steady state, exposure age and growth of agglutinates in lunar soils. *Proc. Lunar Sci. Conf. 8th*, pp. 3617–3632.

- Basu A. and Bhattacharya R. N. (1986) A probabilistic approach to ballistite differentiation of surficial soils on moon-like planets (abstract). In *Lunar and Planetary Science XVII*, pp. 32–33. Lunar and Planetary Institute, Houston.
- Basu A. and Bower J. F. (1977) Provenance of Apollo 15 deep drill core sediments. *Proc. Lunar Sci. Conf. 8th*, pp. 2841–2867.
- Basu A. and McKay D. S. (1979) Petrography and provenance of Apollo 15 soils. *Proc. Lunar Planet. Sci. Conf. 10th*, pp. 1413–1424.
- Basu A. and McKay D. S. (1984) Petrologic comparisons of Cayley and Descartes on the basis of Apollo 16 soils from Stations 4 and 11. *Proc. Lunar Planet. Sci. Conf. 14th*, in *J. Geophys. Res.*, 89, B535–B541.
- Basu A. and McKay D. S. (1985) Chemical variability and origin of agglutinitic glass. *Proc. Lunar Planet. Sci. Conf. 16th*, in *J. Geophys. Res.*, 90, D87–D94.
- Basu A., DesMarais D. J., Hayes J. M., and Meinschein W. G. (1975) Integrated investigation of the mixed origin of lunar sample 72161,11. *The Moon*, 14, 129–138.
- Basu A., McKay D. S., and Fruland R. M. (1978) Origin and modal petrography of Luna 24 soils. In *Mare Crisium: The View From Luna 24* (R. B. Merrill and J. J. Papike, eds.), pp. 321–337. Pergamon, New York.
- Basu A., McKay D. S., Griffiths S., and Nace G. (1981) Regolith maturation on the Earth and the Moon with an example from Apollo 15. *Proc. Lunar Planet. Sci. 12B*, pp. 433–449.
- Bates R. L. and Jackson J. A., eds. (1980) *The Glossary of Geology*, 2nd edition. American Geological Institute, Washington. 751 pp.
- Bauer J. F. (1979) Experimental shock metamorphism of mono- and polycrystalline olivine: A comparative study. *Proc. Lunar Planet. Sci. Conf. 10th*, pp. 2573–2596.
- Bean A. L., Conrad C. C. Jr., and Gordon R. F. (1970) Crew observations. In *Apollo 12 Preliminary Science Report*, p. 29–38. NASA SP-235.
- Beaty D. W. and Albee A. L. (1978) Comparative petrology and possible genetic relations among the Apollo 11 basalts. *Proc. Lunar Planet. Sci. Conf. 9th*, pp. 359–463.
- Beaty D. W. and Albee A. L. (1980) The geology and petrology of the Apollo 11 landing site. *Proc. Lunar Planet. Sci. Conf. 11th*, pp. 23–35.
- Beaty D. W., Hill S. M. R., Albee A., Ma M.-S., and Schmitt R. A. (1979) The petrology and chemistry of basaltic fragments from the Apollo 11 soil, Part 1. *Proc. Lunar Planet. Sci. Conf. 10th*, pp. 41–75.
- Becker R. H. (1980) Light elements in lunar soils revisited: Carbon, nitrogen, hydrogen, and helium. *Proc. Lunar Planet. Sci. Conf. 11th*, pp. 1743–1761.
- Becker R. H. and Clayton R. N. (1975) Nitrogen abundances and isotopic compositions in lunar samples. *Proc. Lunar Sci. Conf. 6th*, pp. 2131–2149.
- Becker R. H. and Clayton R. N. (1977) Nitrogen isotopes in lunar soils as a measure of cosmic-ray exposure and regolith history. *Proc. Lunar Sci. Conf. 8th*, pp. 3685–3704.
- Becker R. H. and Epstein S. (1981) Carbon isotope ratios in some low- $\delta^{15}\text{N}$ lunar breccias. *Proc. Lunar Planet. Sci. 12B*, pp. 289–293.
- Becker R. H. and Pepin R. O. (1989) Long-term changes in solar wind elemental and isotopic ratios: A comparison of two lunar ilmenites of different antiquities. *Geochim. Cosmochim. Acta*, 53, 1135–1146.
- Becker R. H., Clayton R. N., and Mayeda T. K. (1976) Characterization of lunar nitrogen compounds. *Proc. Lunar Sci. Conf. 7th*, pp. 441–458.
- Beckmann P. (1965) Radar backscatter from the surface of the Moon. *J. Geophys. Res.*, 70, 2345–2350.
- Beckmann P. (1968) Depolarization of electromagnetic waves backscattered from the lunar surface. *J. Geophys. Res.*, 73, 649–655.
- Beckmann P. and Klemperer W. K. (1965) Interpretation of the angular dependence of backscattering from the Moon and Venus. *J. Res. Natl Bur. Stand.*, 69D, 1669–1677.
- Behrmann C., Crozaz G., Drozd R., Hohenberg C., Ralston C., Walker R., and Yuhas D. (1973) Cosmic-ray exposure history of North Ray and South Ray material. *Proc. Lunar Sci. Conf. 4th*, pp. 1957–1974.
- Bekker M. G. (1969) *Introduction to Terrain—Vehicle Systems*. Univ. of Michigan, Ann Arbor.
- Bell J. F. and Hawke B. R. (1981) The Reiner Gamma formation: Composition and origin as derived from remote sensing observations. *Proc. Lunar Planet. Sci. 12B*, pp. 679–694.
- Bell J. F. and Hawke B. R. (1984) Lunar dark-haloed impact craters: Origin and implications for early mare volcanism. *J. Geophys. Res.*, 89, 6899–6910.
- Bell P. M., Mao H. K., and Rossman G. R. (1975) Absorption spectroscopy of ionic and molecular units in crystals and glasses. In *Infrared and Raman Spectroscopy of Lunar and Terrestrial Minerals* (C. Karr, ed.), pp. 1–38. Academic, New York.
- Bell P. M., Mao H. K., and Weeks R. A. (1976) Optical spectra and electron paramagnetic resonance of lunar and synthetic glasses: A study of the effects of controlled atmosphere, composition, and temperature. *Proc. Lunar Sci. Conf. 7th*, pp. 2543–2559.
- Bence A. E. and Papike J. J. (1972) Pyroxenes as recorders of lunar basalt petrogenesis: Chemical trends due to crystal-liquid interaction. *Proc. Lunar Sci. Conf. 3rd*, pp. 431–469.
- Bence A. E., Papike J. J., and Prewitt C. T. (1970) Apollo 12 clinopyroxenes: Chemical trends. *Earth Planet. Sci. Lett.*, 8, 393–399.
- Berg O. E., Richardson F. F., and Burton H. (1973) Lunar ejecta and meteorites experiments. In *Apollo 17 Preliminary Science Report*, pp. 16–1 to 16–9. NASA SP-330.
- Berg O. E., Richardson F. F., Rhee J. W., and Auer S. (1974) Preliminary results of a cosmic dust experiment on the Moon. *Geophys. Res. Lett.*, 7, 289–230.

- Bernatowicz T., Drozd R. J., Hohenberg C. M., Lugmair G., Morgan C. J., and Podosek F. A. (1977) The regolith history of 14307. *Proc. Lunar Sci. Conf. 8th*, pp. 2763–2783.
- Bernatowicz T. J., Hohenberg C. M., Hudson B., Kennedy B. M., and Podosek F. A. (1978) Argon ages for lunar breccias 14064 and 15405. *Proc. Lunar Planet. Sci. Conf. 9th*, pp. 905–919.
- Bhandari N. and Padia J. T. (1974a) On the variation of the cosmic ray composition in the past. *Proc. Lunar Sci. Conf. 5th*, pp. 2577–2589.
- Bhandari N. and Padia J. T. (1974b) Secular variations in the abundances of heavy nuclei in cosmic rays. *Science*, 185, 1043–1045.
- Bhandari N., Goswami J. N., Gupta S. K., Lal D., Tamhane A. S., and Venkatavaradan V. S. (1972) Collision controlled radiation history of the lunar regolith. *Proc. Lunar Sci. Conf. 3rd*, pp. 2811–2829.
- Bhogeswara Rao D., Choudray U. V., Erstfeld T. E., Williams R. J., and Chang Y. A. (1979) Extraction processes for the production of aluminum, titanium, iron, magnesium, and oxygen from nonterrestrial sources. In *Space Resources and Space Settlements* (J. Billingham et al., eds.), pp. 257–274. NASA SP-428.
- Bianco A. and Taylor L. (1977) Applications of dynamic crystallization studies: Lunar olivine-normative basalts. *Proc. Lunar Sci. Conf. 8th*, pp. 1593–1610.
- Bibring J. P., Burlingame A. L., Langevin Y., Maurette M., and Wszolek P. C. (1974a) Simulation in lunar carbon chemistry: II. Lunar winds contribution. *Proc. Lunar Sci. Conf. 5th*, pp. 1763–1784.
- Bibring J. P., Burlingame A. L., Chaumont J., Langevin Y., Maurette M., and Wszolek P. C. (1974b) Simulation of lunar carbon chemistry: I. Solar wind contribution. *Proc. Lunar Sci. Conf. 5th*, pp. 1747–1762.
- Bickel C. E., Warner J. L., and Phinney W. C. (1976) Petrology of 79215: brecciation of a lunar cumulate. *Proc. Lunar Sci. Conf. 7th*, pp. 1793–1819.
- Bielefeld M. J., Reedy R. C., Metzger A. E., Trombka J. I., and Arnold J. R. (1976) Surface chemistry of selected lunar regions. *Proc. Lunar Sci. Conf. 7th*, pp. 2661–2676.
- Bills B. G. and Ferrari A. J. (1976) Lunar crustal thickness. *Proc. Lunar Sci. Conf. 7th*, frontispiece.
- Binder A. B. (1978) On fission and the devolatilization of a Moon of fission origin. *Earth Planet. Sci. Lett.*, 41, 381–385.
- Binder A. B. (1982) The Moon: Its figure and orbital evolution. *J. Geophys. Res. Lett.*, 9, 33–36.
- Binder A. B. (1986) The initial thermal state of the Moon. In *Origin of the Moon* (W. K. Hartmann, R. J. Phillips, and G. J. Taylor, eds.), pp. 425–433. Lunar and Planetary Institute, Houston.
- Binder A. B. and Gunga H.-C. (1985) Young thrust-fault scarps in the highlands: Evidence for an initially totally molten Moon. *Icarus*, 63, 421–441.
- Binder A. B. and Lange M. A. (1980) On the thermal history, thermal state, and related tectonism of a Moon of fission origin. *J. Geophys. Res.*, 85, 3194–3208.
- Bird M. L. (1971) Distribution of trace elements in olivines and pyroxenes—an experimental study. Ph.D. thesis, Univ. of Missouri, Rolla. 249 pp.
- Bishop A. W. (1955) The use of the slip circle in the stability analysis of earth slopes. *Geotechnique*, 5, 7–17.
- Blacic J. D. (1985) Mechanical properties of lunar materials under anhydrous, hard vacuum conditions: Applications of lunar glass structural components. In *Lunar Bases and Space Activities of the 21st Century* (W. W. Mendell, ed.), pp. 487–495. Lunar and Planetary Institute, Houston.
- Blanchard D. P. and Budahn J. R. (1978) Chemistry of orange/black soils from core 74001/2. *Proc. Lunar Planet. Sci. Conf. 9th*, pp. 1969–1980.
- Blanchard D. P., Haskin L. A., Jacobs J. W., Brannon J. C., and Korotev R. (1975a) Major and trace element chemistry of Boulder 1 at Station 2, Apollo 17. *The Moon* 14, 359–371.
- Blanchard D. P., Korotev R. L., Brannon J. C., Jacobs J. W., Haskin L. A., Reid A. M., Donaldson C. H., and Brown R. W. (1975b) A geochemical and petrographic study of 1–2-mm fines from Apollo 17. *Proc. Lunar Sci. Conf. 6th*, pp. 2321–2341.
- Blanchard D. P., Jacobs J. W., Brannon J. C., and Haskin L. A. (1976) Major and trace element composition of matrix and aphanitic clasts from consortium breccia 73215. *Proc. Lunar Sci. Conf. 7th*, pp. 2179–2187.
- Blanchard D. P., Jacobs J. W., and Brannon J. C. (1977) Chemistry of ANT-suite and felsite clasts from consortium breccia 73215 and of gabbroic anorthosite 79215. *Proc. Lunar Sci. Conf. 8th*, pp. 2507–2524.
- Blanchard D. P., Brannon J. C., Aaboe E., and Budahn J. R. (1978) Major and trace element chemistry of Luna 24 samples from Mare Crisium. In *Mare Crisium: The View from Luna 24* (R. B. Merrill and J. J. Papike, eds.), pp. 613–630. Pergamon, New York.
- Blanford G. E. (1980) Cosmic ray production curves below reworking zones. *Proc. Lunar Planet. Sci. Conf. 11th*, pp. 1357–1368.
- Blanford G. E. (1982) Solar-wind irradiation effects on ilmenite (abstract). In *Lunar and Planetary Science XIII*, pp. 47–48. Lunar and Planetary Institute, Houston.
- Blanford G. E., Fruland R. M., and Morrison D. A. (1975) Long-term differential energy spectrum for solar-flare iron-group particles. *Proc. Lunar Sci. Conf. 6th*, pp. 3557–3576.
- Blanford G. E., Blanford J., and Hawkins J. A. (1979) Irradiation stratigraphy and depositional history of the Apollo 16 double drive tube 60009/10. *Proc. Lunar Planet. Sci. Conf. 10th*, pp. 1333–1349.
- Blau P. J. and Goldstein J. I. (1975) Investigation and simulation of metallic spherules from lunar soils. *Geochim. Cosmochim. Acta*, 39, 309–324.
- Bobrov V. A., Bolotov V. V., Gulbert E. N., Parkhomenko V. S., and Shipitsin Yu. G. (1980) Instrumental neutron activation studies of elemental composition of lunar regolith. In *Lunar Soil from Mare Crisium* (V. L. Barsukov, ed.), pp. 345–351. Nauka, Moscow.

- Bogard D. D. and Hirsch W. C. (1975) Noble gas studies on grain size separates of Apollo 15 and 16 deep drill cores. *Proc. Lunar Sci. Conf. 6th*, pp. 2057-2084.
- Bogard D. D. and Hirsch W. C. (1977) Noble gas evidence for the depositional and irradiational history of 60010-60009 core soils. *Proc. Lunar Sci. Conf. 8th*, pp. 2983-2999.
- Bogard D. D. and Nyquist L. E. (1973) $^{40}\text{Ar}/^{36}\text{Ar}$ variations in Apollo 15 and 16 regolith. *Proc. Lunar Sci. Conf. 4th*, pp. 1975-1985.
- Bogard D. D., Hirsch W. C., and Nyquist L. E. (1974) Noble gases in Apollo 17 fines: Mass fractionation effects in trapped Xe and Kr. *Proc. Lunar Sci. Conf. 5th*, pp. 1975-2003.
- Bogard D. D., McKay D. S., Morris R. V., Wentworth S. J., and Johnson P. (1985) Regolith breccias from Apollo 15 and 16: Petrology, rare gases, and FMR maturity (abstract). In *Lunar and Planetary Science XVI*, pp. 73-74. Lunar and Planetary Institute, Houston.
- Bohren C. F. and Huffman D. R. (1983) *Absorption and Scattering of Light by Small Particles*. Wiley, New York. 530 pp.
- Borchardt R., Knoll H.-D., Bischoff A., Ostertag R., and Stöffler D. (1985) *Microprobe Analyses of Apollo 14 and 16 Lunar Minerals and Rocks*. Institute of Mineralogy, University of Münster. 141 pp.
- Borchardt R., Stöffler D., Spettel B., Palme H., Wänke H., Wacker K., and Jessberger E. K. (1986) Composition, structure, and age of the Apollo 16 subregolith basement as deduced from the chemistry of post-Imbrium melt bombs. *Proc. Lunar Planet. Sci. Conf. 17th*, in *J. Geophys. Res.*, 91, E43-E54.
- Borg J., Chaumont J., Jouret C., Langevin Y., and Maurette M. (1980) Solar wind radiation damage in lunar dust grains and the characteristics of the ancient solar wind. In *The Ancient Sun: Fossil Record in the Earth, Moon and Meteorites* (R. O. Pepin, J. A. Eddy, and R. B. Merrill, eds.), pp. 431-461. Pergamon, New York.
- Bouchet M., Kaplan G., Voudon A., and Bertolotti M.-J. (1971) Spark mass spectrometric analysis of major and minor elements in six lunar samples. *Proc. Lunar Sci. Conf. 2nd*, pp. 1247-1252.
- Bowell E., Dollfus A., Zellner B., and Geake J. E. (1973) Polarimetric properties of the lunar surface and its interpretation Part 6: Albedo determinations from polarimetric characteristics. *Proc. Lunar Sci. Conf. 4th*, pp. 3167-3174.
- Bowin C., Simon B., and Wollenhaupt W. R. (1975) Mascons: A two-body solution. *J. Geophys. Res.*, 80, 4947-4955.
- Bowker D. E. and Hughes J. K. (1971) *Lunar Orbiter Photographic Atlas of the Moon*. NASA SP-206. 675 pp.
- Boyce J. M. (1976) Ages of flow units in the lunar nearside maria based on Lunar Orbiter IV photographs. *Proc. Lunar Sci. Conf. 7th*, pp. 2717-2728.
- Boyce J. M. and Johnson D. A. (1978) Ages of flow units in the far eastern maria and implications for basin-filling history. *Proc. Lunar Planet. Sci. Conf. 9th*, pp. 3275-3283.
- Boyd F. R. and Smith D. (1971) Compositional zoning in pyroxenes from lunar rock 12021, Oceanus Procellarum. *J. Petrol.*, 12, 439-464.
- Boynton W. V. and Hill D. H. (1983) Composition of bulk samples and a pristine clast from Allan Hills A81005. *Geophys. Res. Lett.*, 10, 837-840.
- Boynton W. V. and Wasson J. T. (1977) Distribution of 28 elements in size fractions of lunar mare and highlands soils. *Geochim. Cosmochim. Acta*, 41, 1073-1082.
- Boynton W. V., Baedeker P. A., Chou C.-L., Robinson K. L., and Wasson J. T. (1975) Mixing and transport of lunar surface materials: Evidence obtained by the determination of lithophile, siderophile, and volatile elements. *Proc. Lunar Sci. Conf. 6th*, pp. 2241-2259.
- Boynton W. V., Chou C.-L., Robinson K. L., Warren P. H., and Wasson J. T. (1976a) Lithophiles, siderophiles, and volatiles in Apollo 16 soils and rocks. *Proc. Lunar Sci. Conf. 7th*, pp. 727-742.
- Boynton W. V., Chou C.-L., Bild R. W., Baedeker P. A., and Wasson J. T. (1976b) Element distribution in size fractions of Apollo-16 soils: evidence for element mobility during regolith processes. *Earth Planet. Sci. Lett.*, 29, 21-33.
- Braddy D., Hutcheon I. D., and Price P. B. (1975) Crystal chemistry of Pu and U and concordant fission track ages of lunar zircons and whitlockites. *Proc. Lunar Sci. Conf. 6th*, pp. 3587-3600.
- Bratt S. R., Solomon S. C., and Head J. W. (1986) The evolution of impact basins: Cooling, subsidence, and thermal stress. *J. Geophys. Res.*, 90, 12415-12433.
- Brett R. (1975a) Thicknesses of some lunar mare basalt flows and ejecta blankets based on chemical kinetic data. *Geochim. Cosmochim. Acta*, 39, 1135-1143.
- Brett R. (1975b) Reduction of mare basalts by sulfur loss (abstract). In *Lunar Science VI*, pp. 89-91. The Lunar Science Institute, Houston.
- Brett R. (1976) Reduction of mare basalts by sulfur loss. *Geochim. Cosmochim. Acta*, 40, 997-1004.
- Brett R., Butler P. Jr., Meyer C. Jr., Reid A. M., Takeda H., and Williams R. (1971) Apollo 12 igneous rocks 12004, 12008, 12009, 12022, a mineralogical and petrological study. *Proc. Lunar Sci. Conf. 2nd*, pp. 301-317.
- Brett R., Gooley R. C., Dowty E., Prinz M., and Keil K. (1973) Oxide minerals in lithic fragments from Luna 20 fines. *Geochim. Cosmochim. Acta*, 37, 761-773.
- Briggs G. A. (1986) What good is a new Moon? Foreword to *Lunar Geoscience Working Group, Status and Future of Lunar Geoscience*. NASA SP-484. 54 pp.
- Brown G. M., Emeleus C. H., Holland J. G., and Phillips R. (1970) Mineralogical, chemical and petrological features of Apollo 11 rocks and their relationship to igneous processes. *Proc. Apollo 11 Lunar Sci. Conf.*, pp. 195-219.
- Brown G. M., Emeleus C. H., Holland J. G., Peckett A., and Phillips R. (1971) Picrite basalts, ferrobasalts, feldspathic norites, and rhyolites in a strongly fractionated lunar crust. *Proc. Lunar Sci. Conf. 2nd*, pp. 583-600.
- Brown G. M., Emeleus C. H., Holland J. G., Peckett A., and Phillips R. (1972) Mineral-chemical variations in Apollo

- 14 and Apollo 15 basalts and granitic fractions. *Proc. Lunar. Sci. Conf. 3rd*, pp. 141–157.
- Brown G. M., Peckett A., Phillips R., and Emeleus C. H. (1973) Mineral-chemical variations in the Apollo 16 magnesianfeldspathic rocks. *Proc. Lunar Sci. Conf. 4th*, pp. 505–518.
- Brown G. M., Peckett A., Emeleus C. H., and Phillips R. (1974) Mineral-chemical properties of Apollo-17 mare basalts and terra fragments (abstract). In *Lunar Science V*, pp. 89–91. The Lunar Science Institute, Houston.
- Brown W. E. Jr. (1967) Lunar surface Surveyor radar response. *J. Geophys. Res.*, 72, 791–799.
- Brown W. E. Jr. (1972) Lunar subsurface exploration using coherent radar. In *Lunar Geophysics* (Z. Kopal and D. W. Strangway, eds.), pp. 243–257. Reidel, Dordrecht. (Reprinted in *The Moon*, 4, 113–127.)
- Brown W. E. Jr., Dibos R. A., Gibson G. B., Muhleman D. O., Peake W. H., and Peohls V. J. (1967) Lunar surface electrical properties. In *Surveyor III, a Preliminary Report*, p. 139. NASA SP-146.
- Brown W. E. Jr., Adams G. F., Eggleton R. E., Jackson P., Jordan R., Kobrick M., Peeples W. J., Phillips R. J., Porcello L. J., Schaber G., Sill W. R., Thompson T. W., Ward S. H., and Zelenka J. S. (1974) Elevation profiles of the Moon. *Proc. Lunar Sci. Conf. 5th*, pp. 3037–3048.
- Brunfelt A. O., Heier K. S., and Steinnes E. (1971) Determination of 40 elements in Apollo 12 materials by neutron activation analysis. *Proc. Lunar Sci. Conf. 2nd*, pp. 1281–1290.
- Brunfelt A. O., Heier K. S., Nilssen B., Steinnes E., and Sundvoll B. (1972a) Elemental composition of Apollo 15 samples (abstract). In *The Apollo 15 Lunar Samples* (J. W. Chamberlain and C. Watkins, eds.), pp. 195–197. The Lunar Science Institute, Houston.
- Brunfelt A. O., Heier K. S., Nilssen B., Sundvoll B., and Steinnes E. (1972b) Distribution of elements between different phases of Apollo 14 rocks and soils. *Proc. Lunar Sci. Conf. 3rd*, pp. 1133–1147.
- Brunfelt A. O., Heier K. S., Nilssen B., Steinnes E., and Sundvoll B. (1973a) Elemental composition of Apollo 15 and 16 rocks, fines and minerals (abstract). In *Lunar Science IV*, pp. 100–102. The Lunar Science Institute, Houston.
- Brunfelt A. O., Heier K. S., Nilssen B., Sundvoll B., and Steinnes E. (1973b) Geochemistry of Apollo 15 and 16 materials. *Proc. Lunar Sci. Conf. 4th*, pp. 1209–1218.
- Brunfelt A. O., Heier K. S., Nilssen B., Steinnes E., and Sundvoll B. (1974a) Elemental composition of Apollo 17 fines (abstract). In *Lunar Science V*, pp. 92–94. The Lunar Science Institute, Houston.
- Brunfelt A. O., Heier K. S., Nilssen B., Steinnes E., and Sundvoll B. (1974b) Elemental composition of Apollo 17 fines and rocks. *Proc. Lunar Sci. Conf. 5th*, pp. 981–990.
- Bryan W. B. (1973) Wrinkle ridges as deformed surface crust on ponded mare lava. *Proc. Lunar Sci. Conf. 4th*, pp. 93–106.
- Burke B. F. (1985) Astronomical interferometry on the Moon. In *Lunar Bases and Space Activities of the 21st Century* (W.W. Mendell, ed.), pp. 281–291. Lunar and Planetary Institute, Houston.
- Burke J. D. (1985) Merits of a lunar polar base location. In *Lunar Bases and Space Activities of the 21st Century* (W. W. Mendell, ed.), pp. 77–84. Lunar and Planetary Institute, Houston.
- Burlingame A. L. (1975) The simulated depth history of dust grains in the lunar regolith. *Proc. Lunar Sci. Conf. 6th*, pp. 2397–2415.
- Burnham C. W. (1971) The crystal structure of pyroxferroite from Mare Tranquillitatis. *Proc. Lunar Sci. Conf. 2nd*, pp. 47–57.
- Burns A. A. (1969) Diffuse component of lunar radar echoes. *J. Geophys. Res.*, 74, 6553–6566.
- Burns J. O. (1985) A Moon-Earth radio interferometer. In *Lunar Bases and Space Activities of the 21st Century* (W. W. Mendell, ed.), pp. 293–300. Lunar and Planetary Institute, Houston.
- Burns J. O. and Mendell W. W., eds. (1988) *Future Astronomical Observatories on the Moon* (proceedings of a workshop held in Houston, Texas, January 10, 1986). NASA CP-2489. 134 pp.
- Burns R. G. (1970a) *Mineralogical Applications of Crystal Field Theory*. Cambridge Univ., London. 224 pp.
- Burns R. G. (1970b) Crystal-field spectra and evidence of cation ordering in olivine minerals. *Am. Mineral.*, 55, 1608–1632.
- Burns R. G. and Vaughan D. J. (1975) Polarized electronic spectra. In *Infrared and Raman Spectroscopy of Lunar and Terrestrial Minerals* (C. Karr, ed.), pp. 39–72. Academic, New York.
- Busche F. D., Prinz M., Keil K., and Bunch T. E. (1972) Spinels and the petrogenesis of some Apollo 12 igneous rocks. *Am. Mineral.*, 57, 1729–1747.
- Bussey H. E. (1979) Microwave dielectric measurements of lunar soil with a coaxial line resonator method. *Proc. Lunar Planet. Sci. Conf. 10th*, pp. 2175–2182.
- Butin R., Kotra R. K., Gibson E. K. Jr., Nace G. A., and McKay D. S. (1984) Hydrogen abundances in lunar soils (abstract). In *Lunar and Planetary Science XV*, pp. 112–113. Lunar and Planetary Institute, Houston.
- Butler J. C. and King E. A. (1974) Analysis of grain size-frequency distributions of lunar fines. *Proc. Lunar Sci. Conf. 5th*, pp. 829–841.
- Butler J. C., Greene G. M., and King E. A. (1973) Grain size, frequency distribution and modal analysis of Apollo 16 fines. *Proc. Lunar Sci. Conf. 4th*, pp. 267–278.
- Butler P. Jr. (1972) Compositional characteristics of olivines from Apollo 12 samples. *Geochim. Cosmochim. Acta*, 36, 773–785.
- Butler P. Jr. (1978) Recognition of lunar glass droplets produced directly from endogenous liquids: The evidence from S-Zn coatings. *Proc. Lunar Planet. Sci. Conf. 9th*, pp. 1459–1471.
- Butler P. Jr. and Meyer C. (1976) Sulfur prevails in coatings on glass droplets: Apollo 15 green and brown glasses and Apollo 17 orange and black (devitrified) glasses. *Proc. Lunar Sci. Conf. 7th*, pp. 1561–1581.

- BVSP (Basaltic Volcanism Study Project) (1981) *Basaltic Volcanism on the Terrestrial Planets*. Pergamon, New York. 1286 pp.
- Cadenhead D. A. (1973) Lunar volcanic glass and cinder formation. *Eos Trans. AGU*, 54, 582.
- Cadenhead D. A. and Jones B. R. (1972) The adsorption of atomic hydrogen on 15101,168 (abstract). In *The Apollo 15 Lunar Samples* (J. W. Chamberlain and C. Watkins, eds.), pp. 272-274. The Lunar Science Institute, Houston.
- Cadenhead D. A. and Stetter J. R. (1975) Specific gravities of lunar materials using helium pycnometry. *Proc. Lunar Sci. Conf. 6th*, pp. 3199-3206.
- Cadenhead D. A., Wagner N. J., Jones B. R., and Stetter J. R. (1972) Some surface characteristics and gas interactions of Apollo 14 fines and fragments. *Proc. Lunar Sci. Conf. 3rd*, pp. 2243-2257.
- Cadenhead D. A., Jones B. R., Buerger W. G., and Stetter J. R. (1973) Solar wind and terrestrial atmosphere effects on lunar sample surface composition. *Proc. Lunar Sci. Conf. 4th*, pp. 2391-2401.
- Cadenhead D. A., Stetter J. R., and Buerger W. G. (1974) Pore structure in lunar samples. *J. Colloid Interface Sci.*, 47, 322-336.
- Cadenhead D. A., Brown M. G., Rice D. K., and Stetter J. R. (1977) Some surface area and porosity characterizations of lunar soils. *Proc. Lunar Sci. Conf. 8th*, pp. 1291-1303.
- Cameron A. G. W. and Ward W. R. (1976) The origin of the Moon (abstract). In *Lunar Science VII*, pp. 120-122. The Lunar Science Institute, Houston.
- Cameron E. N. (1971) Opaque minerals in certain lunar rocks from Apollo 12. *Proc. Lunar Sci. Conf. 2nd*, pp. 193-206.
- Cameron K. L. and Cameron M. (1973) Mineralogy of ultramafic nodules from Knippa Quarry, near Uvalde, Texas (abstract). *Geol. Soc. Am. Abstr. with Progr.*, 5, 566.
- Cameron W. S. (1964) An interpretation of Schröter's Valley and other lunar sinuous rilles. *J. Geophys. Res.*, 69, 2523-2430.
- Cameron W. S. (1974) Manifestations and possible sources of lunar transient phenomena (LTP) (abstract). In *Lunar Interactions* (D. R. Criswell and J. R. Freeman, eds.), p. 41. The Lunar Science Institute, Houston.
- Cameron W. S. (1978) *Lunar Transient Phenomena Catalog*. NSSDC/WDC-A-R&S 78-03, NASA Goddard Spaceflight Center, Greenbelt, Maryland.
- Cameron W. S., Mantel E. J., and Miller E. R. (1977) *Catalog of Lunar Mission Data*. NSSDC-77-02, National Space Science Data Center, Washington, DC. 204 pp.
- Campbell C. S. and Brennen C. E. (1985) Chute flows of granular materials; some computer simulations. *J. Appl. Mech.*, 52, 172-178.
- Campbell H. W., Hess P. C., and Rutherford M. J. (1978) Ilmenite crystallization in non-mare basalts (abstract). In *Lunar and Planetary Science IX*, pp. 149-151. Lunar and Planetary Institute, Houston.
- Campbell M. J. and Ulrichs J. (1969) Electrical properties of rocks and their significance for lunar radar observations. *J. Geophys. Res.*, 74, 5867-5881.
- Carlson I. C. and Walton W. J. A. Jr. (1978) *Apollo 14 Rock Samples*. Curatorial Facility Publication 14240, NASA Johnson Space Center, Houston. 413 pp.
- Carlson R. W. and Lugmair G. W. (1979) Sm-Nd constraints on early lunar differentiation and the evolution of KREEP. *Earth Planet. Sci. Lett.*, 45, 123-132.
- Carlson R. W. and Lugmair G. W. (1988) The age of ferroan anorthosite 60025: Oldest crust on a young Moon? *Earth Planet. Sci. Lett.*, 90, 119-130.
- Carr M. H. (1966) Geologic map of the Mare Serenitatis region of the moon. *U.S. Geol. Surv. Misc. Geol. Inv. Map I-489*.
- Carr M. H. (1974) The role of lava erosion in the formation of lunar rilles and Martian channels. *Icarus*, 22, 1-23.
- Carrier W. D. III (1970) Lunar soil mechanics on the Apollo missions (abstract). *Texas Civil Engineering* 40, 7.
- Carrier W. D. III (1973) Lunar soil grain size distribution. *The Moon*, 6, 250-263.
- Carrier W. D. III (1974) Apollo drill core relationships. *The Moon*, 10, 183-194.
- Carrier W. D. III (1984) Geotechnical implications for a lunar base (abstract). In *Papers Presented to the 1984 Symposium on Lunar Bases and Space Activities of the 21st Century*, pp. 75-76. NASA, Washington, DC.
- Carrier W. D. III and Heiken G. (1972) *Apollo 14 Lunar Surface Close-up Photography*. NASA TM X-58072. 51 pp.
- Carrier W. D. III, Johnson S. W., Werner R. A., and Schmidt R. (1971) Disturbance in samples recovered with the Apollo core tubes. *Proc. Lunar Sci. Conf. 2nd*, pp. 1959-1972.
- Carrier W. D. III, Johnson S. W., Carrasco L. H., and Schmidt R. (1972a) Core sample depth relationships: Apollo 14 and 15. *Proc. Lunar Sci. Conf. 3rd*, pp. 3213-3221.
- Carrier W. D. III, Bromwell L. G., and Martin R. T. (1972b) Strength and compressibility of returned lunar soil. *Proc. Lunar Sci. Conf. 3rd*, pp. 3223-3234.
- Carrier W. D. III, Mitchell J. K., and Mahmood A. (1973a) The nature of lunar soil. *J. Soil Mech. Found. Div. Am. Soc. Civ. Eng.*, 99, 813-832.
- Carrier W. D. III, Mitchell J. K., and Mahmood A. (1973b) The relative density of lunar soil. *Proc. Lunar Sci. Conf. 4th*, pp. 2403-2411.
- Carrier W. D. III, Bromwell L. G., and Martin R. T. (1973c) Behavior of returned lunar soil in vacuum. *J. Soil. Mech. Found. Div., Am. Soc. Civ. Eng.*, 99, 979-996.
- Carroll W. F. and Blair P. M. (1971) Discoloration and lunar dust contamination of Surveyor III surfaces. *Proc. Lunar Sci. Conf. 2nd*, pp. 2735-2742.
- Carron M. K., Ansell C. S., Christian R. P., Cuttitta F., Dwornik E. J., Ligon D. T., and Rose H. J. (1972) Elemental analyses of lunar soil samples from Apollo 15 mission (abstract). In *The Apollo 15 Lunar Samples* (J. W. Chamberlain and C. Watkins, eds.), pp. 198-201. The Lunar Science Institute, Houston.

- Carter J. L. (1985) Lunar regolith fines: A source of hydrogen. In *Lunar Bases and Space Activities of the 21st Century* (W.W. Mendell, ed.), pp. 571–581. Lunar and Planetary Institute, Houston.
- Carter J. L. and Padovani E. (1973) Genetic implications of some unusual particles in Apollo 16 less than 1 mm fines 68841,11 and 69941,13. *Proc. Lunar Sci. Conf. 4th*, pp. 323–332.
- Carter J. L., Clanton U. S., Fuhrman R., Laughon R. B., McKay D. S., and Usselman T. M. (1975) Morphology and composition of chalcopyrite, chromite, Cu, Ni-Fe, pentlandite, and troilite in vugs of 76015 and 76215. *Proc. Lunar Sci. Conf. 6th*, pp. 719–728.
- Carusi A., Cavaretta G., Cinotti F., Civitti G., Coradini A., Funicello R., Fulchignoni M., and Taddeucci A. (1972) Lunar glasses as an index of the impacted sites lithology: The source area of the Apollo 15 “green glasses.” *Geol. Romana*, 11, 137–151.
- Cashore J. and Woronow A. (1985) A new Monte Carlo model of lunar megaregolith development. *Proc. Lunar Planet. Sci. Conf. 15th*, in *J. Geophys. Res.*, 90, C811–C815.
- Champhess P. E., Dunham A. C., Gibb F. G. F., Giles H. N., MacKenzie W. S., Stumpfl E. F., and Zussman J. (1971) Mineralogy and petrology of some Apollo 12 samples. *Proc. Lunar Sci. Conf. 2nd*, pp. 359–376.
- Chang S., Lennon K., and Gibson E. K. Jr. (1974a) Abundances of C, N, H, He, and S in Apollo 17 soils from stations 3 and 4: Implications for solar wind exposure ages and regolith evolution. *Proc. Lunar Sci. Conf. 5th*, pp. 1785–1800.
- Chang S., Lennon K., and Gibson E. K. Jr. (1974b) Abundances of C, N, H, He, and S in Apollo 17 soils from Stations 3 and 4: Implications for solar wind exposure ages and regolith evolution (abstract). In *Lunar Science V*, pp. 106–108. The Lunar Science Institute, Houston.
- Chao E. C. T. (1973) Geologic implications of the Apollo 14 Fra Mauro breccias and comparison with ejecta from the Ries crater, Germany. *J. Res. U.S. Geol. Surv.*, 1, 1–18.
- Chao E. C. T., Minkin J. A., Frondel C., Klein C. Jr., Drake J. C., Fuchs L., Tani B., Smith J. V., Anderson A. T., Moore P. B., Zechman G. R. Jr., Traill R. J., Plant A. G., Douglas J. A. V., and Dence M. R. (1970) Pyroxferroite, a new calcium-bearing iron silicate from Tranquillity Base. *Proc. Apollo 11 Lunar Sci. Conf.*, pp. 65–79.
- Chao E. C. T., Boreman J. A., and Desborough G. A. (1971) Unshocked and shocked Apollo 11 and 12 microbreccias: Characteristics and some geologic implications. *Proc. Lunar Sci. Conf. 2nd*, pp. 797–816.
- Chao E. C. T., Minkin J. A., and Best J. B. (1972a) Apollo 14 breccias: General characteristics and classification. *Proc. Lunar Sci. Conf. 3rd*, pp. 645–659.
- Chao E. C. T., Best J. B., and Minkin J. A. (1972b) Apollo 14 glasses of impact origin and their parent rock types. *Proc. Lunar Sci. Conf. 3rd*, pp. 907–925.
- Charette M. P. and Adams J. B. (1977) Spectral reflectance of lunar highland rocks (abstract). In *Lunar Science VIII*, pp. 172–174. The Lunar Science Institute, Houston.
- Charette M. P., McCord T. B., Pieters C. M., and Adams J. B. (1974) Application of remote spectral reflectance measurements to lunar geology classification and determination of titanium content of lunar soils. *J. Geophys. Res.*, 79, 1605–1613.
- Chen H.-K., Delano J. W., and Lindsley D. H. (1982) Chemistry and phase relations of VLT volcanic glasses from Apollo 14 and Apollo 17. *Proc. Lunar Planet. Sci. Conf. 13th*, in *J. Geophys. Res.*, 87, A171–A181.
- Cherkasov I. I., Vakhnin V. M., Kemurjian A. L., Mikhailov L. N., Mikheyev V. V., Misatov A. A., Smorodinov M. A., and Shvarev V. V. (1968) Determination of the physical and mechanical properties of the lunar surface layer by means of Luna 13 automatic station. In *Moon and Planets II* (A. Dollfus, ed.), pp. 70–76. North-Holland, Amsterdam.
- Chernyak Y. B. (1978) On recent lunar atmosphere. *Nature*, 273, 497–501.
- Cherry M. and Lande K. (1985) A lunar neutrino detector. In *Lunar Bases and Space Activities of the 21st Century* (W. W. Mendell, ed.), pp. 335–343. Lunar and Planetary Institute, Houston.
- Choate R., Batterson S. A., Christensen E. M., Hutton R. E., Jaffe L. D., Jones R. H., Ko H. Y., Scott R. F., Spencer R. L., Sperling F. B., and Sutton G. H. (1968) Lunar surface mechanical properties. In *Surveyor Project. Part 1: Project Description and Performance*, pp. 137–194. JPL Tech. Rpt. 32–1265, Jet Propulsion Laboratory, Pasadena.
- Chou C.-L., Baedeker P. A., and Wasson J. T. (1973) Atmophile elements in lunar soils. *Proc. Lunar Sci. Conf. 4th*, pp. 1523–1533.
- Chou C.-L., Baedeker P. A., Bild R. W., and Wasson J. T. (1974) Volatile-element systematics and green glass in Apollo 15 lunar soils. *Proc. Lunar Sci. Conf. 5th*, pp. 1645–1657.
- Chou C.-L., Boynton W. V., Sundberg L. L., and Wasson J. T. (1975) Volatiles on the surface of Apollo 15 green glass and trace-element distributions among Apollo 15 soils. *Proc. Lunar Sci. Conf. 6th*, pp. 1701–1727.
- Christensen E. M., Batterson S. A., Benson H. E., Chandler C. E., Jones R. H., Scott R. F., Shipely E. N., Sperling F. B., and Sutton G. H. (1967) Lunar surface mechanical properties—Surveyor 1. *J. Geophys. Res.*, 72, 801–813.
- Christensen E. M., Batterson S. A., Benson H. E., Choate R., Jaffe L. D., Jones R. H., Ko H. Y., Spencer R. L., Sperling F. B., and Sutton G. H. (1968a) Lunar surface mechanical properties at the landing site of Surveyor III. *J. Geophys. Res.*, 73, 4081–4094.
- Christensen E. M., Batterson S. A., Benson H. E., Choate R., Hutton R. E., Jaffe L. D., Jones R. H., Ko H. Y., Schmidt F. N., Scott R. F., Spencer R. L., Sperling F. B., and Sutton G. H. (1968b) Lunar surface mechanical properties. In *Surveyor VI, A Preliminary Report*, pp. 41–95. NASA SP-166.
- Christian R. P., Berman S., Dwornik E. J., Rose H. J., and Schnepfe M. M. (1976) Composition of some Apollo 14, 15, and 16 lunar breccias and two Apollo 15 fines (abstract). In *Lunar Science VII*, pp. 138–140. The Lunar Science Institute, Houston.

- Chung D. H. (1972) Laboratory studies on seismic and electrical properties of the Moon. *The Moon*, 4, 356–372.
- Chung D. H. and Westphal W. B. (1973) Dielectric spectra of Apollo 15 and 16 lunar solid samples. *Proc. Lunar Sci. Conf. 4th*, pp. 3077–3091.
- Chung D. H., Westphal W. B., and Simmons G. (1970) Dielectric properties of Apollo 11 lunar samples and their comparison with earth materials. *J. Geophys. Res.*, 75, 6524–6531.
- Chung D. H., Westphal W. B., and Simmons G. (1971) Dielectric behavior of lunar samples: electromagnetic probing of the lunar interior. *Proc. Lunar Sci. Conf. 2nd*, pp. 2381–2390.
- Chung D. H., Westphal W. B., and Olhoeft G. R. (1972) Dielectric properties of Apollo 14 lunar samples. *Proc. Lunar Sci. Conf. 3rd*, pp. 3161–3172.
- Chupp E. L. (1988) High-energy particle production in solar flares (SEP, gamma-ray and neutron emissions). *Physica Scripta*, T18, 5–19.
- Cimbalnikova A., Palivcova M., Frana J., and Mastalka A. (1977) Chemical composition of crystalline rock fragments from Luna 16 and Luna 20 fines. In *The Soviet-American Conference on Cosmochemistry of the Moon and Planets* (J. H. Pomeroy and N. J. Hubbard, eds.), pp. 263–275. NASA SP-370, NASA, Washington, DC.
- Cintala M. J., Wood C. A., and Head J. W. (1977) The effects of target characteristics on fresh crater morphology: Preliminary results for the Moon and Mercury. *Proc. Lunar Sci. Conf. 8th*, pp. 3409–3425.
- Cintala M. J., Garvin J. B., and Wetzel S. J. (1982) The distribution of blocks around a fresh mare crater (abstract). In *Lunar and Planetary Science XIII*, pp. 100–101. Lunar and Planetary Institute, Houston.
- Cirlin E. H. and Housley R. M. (1977) A flameless atomic absorption study of the volatile trace metal lead in lunar samples. *Proc. Lunar Sci. Conf. 8th*, pp. 3931–3940.
- Cirlin E. H. and Housley R. M. (1978) Studies of volatiles in Apollo 17 samples and their implication to vapor transport processes. *Proc. Lunar Planet. Sci. Conf. 9th*, pp. 2049–2063.
- Cirlin E. H. and Housley R. M. (1979) Scanning Auger microprobe and atomic absorption studies of lunar volcanic volatiles. *Proc. Lunar Planet. Sci. Conf. 10th*, pp. 341–354.
- Cirlin E. H. and Housley R. M. (1981) Distribution and evolution of Zn, Cd, and Pb in Apollo 16 regolith samples and the average U-Pb ages of the parent rocks. *Proc. Lunar Planet. Sci. 12B*, pp. 529–540.
- Cirlin E. H., Housley R. M., and Grant R. W. (1978) Studies of volatiles in Apollo 17 samples and their implications to vapor transport processes. *Proc. Lunar Planet. Sci. Conf. 9th*, pp. 2049–2063.
- Clanton U. S., McKay D. S., Laughon R. B., and Ladle G. H. (1973) Iron crystals in lunar breccias. *Proc. Lunar Sci. Conf. 4th*, pp. 925–931.
- Clanton U. S., McKay D. S., Waits G., and Fuhrman R. (1978) Sublimate morphology on 74001 and 74002 orange and black glassy droplets. *Proc. Lunar Planet. Sci. Conf. 9th*, pp. 1945–1957.
- Clark P. E. and Adler I. (1978) Utilization of independent solar flux measurements to eliminate non-geochemical variation in X-ray fluorescence data. *Proc. Lunar Planet. Sci. Conf. 9th*, pp. 3029–3036.
- Clark P. E. and Hawke B. R. (1981) Compositional variation in the Hadley Apennine region. *Proc. Lunar Planet. Sci. 12B*, pp. 727–749.
- Clarke A. C. (1951) *The Exploration of Space*. Harper and Bros., New York. 199 pp.
- Clayton D. D. (1968) *Principles of Stellar Evolution and Nucleosynthesis*. McGraw-Hill, New York. 612 pp.
- Clayton R. N. and Thiemens M. H. (1980) Lunar nitrogen: Evidence for secular change in the solar wind. *The Ancient Sun: Fossil Record in the Earth, Moon and Meteorites* (R. O. Pepin, J. A. Eddy, and R. B. Merrill, eds.), pp. 463–473. Pergamon, New York.
- Clayton R. N., Hurd J. M., and Mayeda T. K. (1972) Oxygen isotopic compositions and oxygen concentrations of Apollo 14 and Apollo 15 rocks and soils. *Proc. Lunar Sci. Conf. 3rd*, pp. 1455–1463.
- Clayton R. N., Mayeda T. K., and Hurd J. M. (1974) Loss of oxygen, silicon, sulfur, and potassium from the lunar regolith. *Proc. Lunar Sci. Conf. 5th*, pp. 1801–1809.
- Coleman P. J., Schubert G., Russell C. T., and Sharp L. R. (1972) Satellite measurements of the Moon's magnetic field: A preliminary report. *The Moon*, 4, 419–429.
- Collins M. (1974) *Carrying the Fire*. Ballantine, New York. 488 pp.
- Colson R. O. and Haskin L. A. (1990) Lunar oxygen and metal for use in near-Earth space: Magma electrolysis. In *Engineering Construction, and Operations in Space II: Proceedings of Space 90* (S. W. Johnson and J. P. Wetzel, eds.), pp. 187–196. American Society of Civil Engineers, New York.
- Comer R. P., Solomon S. C., and Head J. W. (1979) Elastic lithosphere thickness on the Moon from mare tectonic features: A formal inversion. *Proc. Lunar Planet. Sci. Conf. 10th*, pp. 2441–2463.
- Compston W., Chappell B. W., Amiens P. A., and Vernon M. J. (1970) The chemistry and age of Apollo 11 material. *Proc. Apollo 11 Lunar Sci. Conf*, pp. 1007–1027.
- Compston W., Berry H., Vernon M. J., Chappell B. W., and Kaye M. J. (1971) Rubidium-strontium chronology and chemistry of lunar material from the Ocean of Storms. *Proc. Lunar Sci. Conf. 2nd*, pp. 1471–1485.
- Compston W., Vernon M. J., Berry H., Rudowski R., Gray C. M., Ware N., Chappell B. W., and Kaye M. (1972a) Age and petrogenesis of Apollo 14 basalts (abstract). In *Lunar Science III*, pp. 151–156. The Lunar Science Institute, Houston.
- Compston W., Vernon M. J., Berry H., Rudowski R., Gray C. M., and Ware N. (1972b) Apollo 14 mineral ages and the thermal history of the Fra Mauro Formation. *Proc. Lunar Sci. Conf. 3rd*, pp. 1487–1503.
- Compston W., Vernon M. J., Chappell B. W., and Freeman R. (1973) Rb-Sr model ages and chemical composition

- of nine Apollo 16 soils (abstract). In *Lunar Science IV*, pp. 158–158b. The Lunar Science Institute, Houston.
- Compston W., Foster J. J., and Gray C. M. (1975) Rb-Sr ages of clasts within Boulder 1, Station 2, Apollo 17. *The Moon*, 14, 445–462.
- Compston W., Foster J. J., and Gray C. M. (1977) Rb-Sr systematics in clasts and aphanites from consortium breccia 73215. *Proc. Lunar Sci. Conf. 8th*, pp. 2525–2549.
- Compston W., Williams I. S., and Meyer C. Jr. (1984a) Age and chemistry of zircon from late-stage lunar differentiates (abstract). In *Lunar and Planetary Science XI*, pp. 182–183. Lunar and Planetary Institute, Houston.
- Compston W., Williams I. S., and Meyer C. (1984b) U-Pb geochronology of zircons from lunar breccia 73217 using a sensitive high mass-resolution ion microprobe. *Proc. Lunar Planet. Sci. Conf. 14th*, in *J. Geophys. Res.*, 89, B525–B534.
- Cooper H. S. F. Jr. (1969) *Apollo on the Moon*. Dial, New York. 144 pp.
- Cooper H. S. F. Jr. (1970) *Moon Rocks*. Dial, New York. 197 pp.
- Cooper M. R., Kovach R. L., and Watkins J. S. (1974) Lunar near-surface structure. *Rev. Geophys. Space Phys.*, 12, 291–308.
- Costes N. C. (1973) Regional variations in physical and chemical properties of lunar surface regolith (abstract). In *Lunar Science IV*, pp. 159–161. The Lunar Science Institute, Houston.
- Costes N. C. and Mitchell J. K. (1970) Apollo 11 soil mechanics investigation. *Proc. Apollo 11 Lunar Sci. Conf.*, pp. 2025–2044.
- Costes N. C., Carrier W. D. III, Mitchell J. K., and Scott R. F. (1969) Apollo 11 soil mechanics investigation. In *Apollo 11 Preliminary Science Report*, pp. 85–122. NASA SP-214.
- Costes N. C., Carrier W. D. III, Mitchell J. K., and Scott R. F. (1970a) Apollo 11: Soil mechanics results. *J. Soil Mech. Found. Div., Am. Soc. Civ. Eng.*, 96, 2045–2080.
- Costes N. C., Carrier W. D. III, Mitchell J. K., and Scott R. F. (1970b) Apollo 11 soil mechanics investigation. *Science*, 167, 739–741.
- Costes N. C., Cohron G. T., and Moss D. C. (1971) Cone penetration resistance test—An approach to evaluating the in-place strength and packing characteristics of lunar soils. *Proc. Lunar Sci. Conf. 2nd*, pp. 1973–1987.
- Costes N. C., Farmer J. E., and George E. B. (1972) *Mobility Performance of the Lunar Roving Vehicle: Terrestrial Studies Apollo 15 Results*. NASA TR-R-401. 87 pp.
- Cour-Palais B. G. (1974) The current micrometeoroid flux at the Moon for masses $\leq 10^{-7}$ g from the Apollo window and Surveyor 3 TV camera results. *Proc. Lunar Sci. Conf. 5th*, pp. 2451–2462.
- Crawford M. L. (1973) Crystallization of plagioclase in mare basalts. *Proc. Lunar Sci. Conf. 4th*, pp. 705–717.
- Crawford M. L. and Hollister L. S. (1974) KREEP basalt: A possible partial melt from the lunar interior. *Proc. Lunar Sci. Conf. 5th*, pp. 399–419.
- Cremers C. J. (1972) Thermal conductivity of Apollo 14 fines. *Proc. Lunar Sci. Conf. 3rd*, pp. 2611–2617.
- Cremers C. J. and Birkebak R. C. (1971) Thermal conductivity of fines from Apollo 12. *Proc. Lunar Sci. Conf. 2nd*, pp. 2311–2315.
- Cremers C. J. and Hsia H. S. (1973) Thermal conductivity of Apollo 15 fines at low density (abstract). In *Lunar Science IV*, pp. 164–166. The Lunar Science Institute, Houston.
- Cremers C. J., Birkebak R. C., and Dawson J. P. (1970) Thermal conductivity of fines from Apollo 11. *Proc. Apollo 11 Lunar Sci. Conf.*, pp. 2045–2050.
- Cripe J. D. and Moore C. B. (1974) Total sulfur contents of Apollo 15 and Apollo 16 lunar samples (abstract). In *Lunar Science V*, pp. 523–525. The Lunar Science Institute, Houston.
- Cripe J. D. and Moore C. B. (1975) Total sulfur contents of Apollo 15, 16 and 17 samples (abstract). In *Lunar Science VI*, pp. 167–168. The Lunar Science Institute, Houston.
- Cripe J. D. and Moore C. B. (1976) Extralunar sulfur in Apollo 16 and 17 lunar fines. *Proc. Lunar Sci. Conf. 7th*, pp. 469–479.
- Criswell D. R. (1972) Lunar dust motion. *Proc. Lunar Sci. Conf. 3rd*, pp. 2671–2680.
- Criswell D. R. (1973) Horizon-low and the motion of lunar dust. In *Photon and Particle Interactions with Surfaces in Space* (R. J. L. Gard, ed.), pp. 545–556. Reidel, Dordrecht.
- Criswell D. R. (1974) Sunset intensification of lunar surface electric fields (abstract). In *Lunar Interactions* (D. R. Criswell and J. R. Freeman, eds.), pp. 100–102. The Lunar Science Institute, Houston.
- Criswell D. R. and De B. R. (1977) Intense localized photoelectric charging in the lunar sunset terminator region II. Supercharging at the progression of sunset. *J. Geophys. Res.*, 82, 1005–1007.
- Croft S. K. (1978) Lunar crater volume: Interpretation by models of impact cratering and upper crustal structure. *Proc. Lunar Planet. Sci. Conf. 9th*, pp. 3711–3733.
- Croft S. K. (1980) Cratering flow field: Implications for the excavation and transient expansion stages of crater formation. *Proc. Lunar Planet. Sci. Conf. 11th*, pp. 2347–2378.
- Croft S. K. (1981) The excavation stage of basin formation: a qualitative model. In *Multi-Ring Basins, Proc. Lunar Planet. Sci. 12A* (P. H. Schultz and R. B. Merrill, eds.), pp. 207–225. Pergamon, New York.
- Crouch D. S. (1971) *Apollo 15 Lunar Surface Drill. Mission Performance and Post-Flight Analysis*. ALSD Proj. Doc. No. MCR-71-318, 30 Oct. 1971, prepared for NASA MSC under Contract No. NAS9-9462 by Martin Marietta Denver Division.
- Crozaz G. (1980) Solar flare and galactic cosmic ray tracks in lunar samples and meteorites: What they tell us about the ancient sun. In *The Ancient Sun: Fossil Record in the Earth, Moon and Meteorites* (R. O. Pepin, J. A. Eddy, and R. B. Merrill, eds.), pp. 331–346. Pergamon, New York.
- Crozaz G. and Plachy A. L. (1976) Origin of the Apollo 17 deep drill coarse-grained layer. *Proc. Lunar Sci. Conf. 7th*, pp. 123–131.

- Crozaz G. and Ross L. M. (1979) Deposition and irradiation of the Apollo 17 deep drill core. *Proc. Lunar Planet. Sci. Conf. 10th*, pp. 1229-1241.
- Crozaz G., Haack U., Hair M., Maurette M., Walker R., and Woolum D. (1970) Nuclear track studies of ancient solar radiations and dynamic lunar surface processes. *Proc. Apollo 11 Lunar Sci. Conf.*, pp. 2051-2080.
- Crozaz G., Walker R. M., and Woolum D. S. (1971) Nuclear track studies of dynamic surface processes on the Moon and the constancy of solar activity. *Proc. Lunar Sci. Conf. 2nd*, pp. 2543-2558.
- Crozaz G., Drozd R., Hohenberg C., Morgan C., Ralston C., Walker R., and Yuhas D. (1974) Lunar surface dynamics: Some general conclusions and new results from Apollo 16 and 17. *Proc. Lunar Sci. Conf. 5th*, pp. 2475-2499.
- Curran D. R., Shockey D. A., Seaman L., and Austin M. (1977) Mechanisms and models of cratering in Earth media. In *Impact Explosion and Cratering* (D. J. Roddy, R. O. Pepin, and R. B. Merrill, eds.), pp. 1057-1087. Pergamon, New York.
- Curtis D. B. and Wasserburg G. J. (1977) Stratigraphic processes in the lunar regolith—additional insight from neutron fluence measurements on bulk soils and lithic fragments from the deep drill cores. *Proc. Lunar Sci. Conf. 8th*, pp. 3575-3593.
- Cutler A. H. and Krag P. (1985) A carbothermal scheme for lunar oxygen production. In *Lunar Bases and Space Activities of the 21st Century* (W. W. Mendell, ed.), pp. 559-569. Lunar and Planetary Institute, Houston.
- Cuttitta F., Rose H. J., Annell C. S., Canon M. K., Christian R. P., Dwornik E. J., Greenland L. P., Helz A. W., and Ligon D. T. (1971) Elemental composition of some Apollo 12 lunar rocks and soils. *Proc. Lunar Sci. Conf. 2nd*, pp. 1217-1229.
- Cuttitta F., Rose H. J. Jr., Annell C. S., Canon M. K., Christia R. P., Ligon D. T. Jr., Dwornik E. J., Wright T. L., and Greenland L. P. (1973) Chemistry of twenty-one igneous rocks and soils returned by the Apollo 15 mission. *Proc. Lunar Sci. Conf. 4th*, pp. 1081-1096.
- Dalton C. and Hoffman E. (1972) *Conceptual Design of a Lunar Colony*. NASA Grant Rpt. NGT 44-005-1 14, Washington, DC. 505 pp.
- Dalton J., Hollister L. S., Kulick C. G., and Hargraves R. B. (1974) The nature of the chromite to ulvöspinel transition in mare basalt 15555 (abstract). In *Lunar Science V*, pp. 160-162. The Lunar Science Institute, Houston.
- Daniels F. B. (1961) A theory of radar return from the Moon and planets. *J. Geophys. Res.*, 66, 1781-1788.
- Darwin G. (1879) On the procession of a viscous spheroid and on the remote history of the Earth. *Philos. Trans. R. Soc. London*, 170, 447-538.
- Davies R. D. and Gardner F. F. (1966) Linear polarization of the Moon at 6, 11, and 21 cm wavelengths. *Aust. J. Phys.*, 19, 823-836.
- Davis J. R. and Rohlfs D. C. (1964) Lunar radio-reflection properties at decimeter wavelengths. *J. Geophys. Res.*, 69, 3257-3262.
- Davis P. A. (1980) Iron and titanium distribution on the Moon from orbital gamma ray spectrometry with implications for crustal evolutionary models. *J. Geophys. Res.*, 85, 3209-3224.
- Davis P. A. and Spudis P. D. (1985) Petrologic province map of the lunar highlands derived from orbital geochemical data. *Proc. Lunar Planet. Sci. Conf. 16th*, in *J. Geophys. Res.*, 90, D61-D74.
- Davis P. A. and Spudis P. D. (1987) Global petrologic variations on the Moon: A ternary-diagram approach. *Proc. Lunar Planet. Sci. Conf. 17th*, in *J. Geophys. Res.*, 92, E387-E395.
- De B. R. and Criswell D. R. (1977) Intense localized photoelectric charging in the lunar sunset terminator region I. Development of potentials and fields. *J. Geophys. Res.*, 82, 999-1004.
- Debrunner H., Flückiger E., Lockwood J. A., and McGuire R.E. (1984) Comparison of the solar cosmic ray events on May 7, 1978, and November 22, 1977. *J. Geophys. Res.*, 89, 769-774.
- Deer W. A., Howie R. A., and Zussman J. (1978) *Rock-Forming Minerals. Vol. 2A: Single-Chain Silicates*. Wiley, New York. 668 pp.
- DeHon R. A. (1974) Thickness of mare material in the Tranquillitatis and Nectaris basins. *Proc. Lunar Sci. Conf. 5th*, pp. 53-59.
- DeHon R. A. (1979) Thickness of the western mare basalts. *Proc. Lunar Planet. Sci. Conf. 10th*, pp. 2935-2955.
- DeHon R. A. and Waskom J. D. (1976) Geologic structure of the eastern mare basins. *Proc. Lunar Sci. Conf. 7th*, pp. 2729-2746.
- Delano J. (1975) Petrology of the Apollo 16 mare component: Mare Nectaris. *Proc. Lunar Sci. Conf. 6th*, pp. 15-47.
- Delano J. W. (1979) Apollo 15 green glass: Chemistry and possible origin. *Proc. Lunar Planet. Sci. Conf. 10th*, pp. 275-300.
- Delano J. (1980) Chemistry and liquidus phase relations of Apollo 15 red glass: Implications for the deep lunar interior. *Proc. Lunar Planet. Sci. Conf. 11th*, pp. 251-288.
- Delano J. (1986) Pristine lunar glasses: Criteria, data, and implications. *Proc. Lunar Planet. Sci. Conf. 16th*, in *J. Geophys. Res.*, 91, D201-D213.
- Delano J. W. and Ringwood A. E. (1978) Siderophile elements in the lunar highlands: Nature of the indigenous component and implications for the origin of the Moon. *Proc. Lunar Planet. Sci. Conf. 9th*, pp. 111-159.
- Delano J. W., Bence A. E., Papike J. J., and Cameron K. L. (1973) Petrology of the 2-4 mm soil fraction from the Descartes region of the Moon and stratigraphic implications. *Proc. Lunar Sci. Conf. 4th*, pp. 537-552.
- Delano J. W., Hughes S. S., and Schmitt R. A. (1986) Collaborative study of the Apollo 15 pristine yellow/brown glasses: An interim report (abstract). In *Lunar and Planetary Science XVII*, pp. 172-173. Lunar and Planetary Institute, Houston.
- Dence M. R. (1973) Dimensional analysis of impact structures (abstract). *Meteoritics*, 8, 343-344.

- Dence M. R., Douglas J. A. V., Plant A. G., and Traill R. J. (1970) Petrology, mineralogy and deformation of Apollo 11 samples. *Proc. Apollo 11 Lunar Sci. Conf.*, pp. 315–340.
- Dence M. R., Douglas J. A. V., Plant A. G., and Traill R. J. (1971) Mineralogy and petrology of some Apollo 12 samples. *Proc. Lunar Sci. Conf. 2nd*, pp. 285–299.
- Dence M. R., Grieve R. A. F., and Robertson P. B. (1977) Terrestrial impact structures: Principal characteristics and energy considerations. In *Impact and Explosion Cratering* (D. J. Roddy, R. O. Pepin, and R. B. Merrill, eds.), pp. 247–275. Pergamon, New York.
- DesMarais D. J. (1978) Carbon, nitrogen, and sulfur in Apollo 15, 16, and 17 rocks. *Proc. Lunar Planet. Sci. Conf. 9th*, pp. 2451–2467.
- DesMarais D. J., Hayes J. M., and Meinschein W. G. (1973) The distribution in lunar soil of carbon released by pyrolysis. *Proc. Lunar Sci. Conf. 4th*, pp. 1543–1558.
- DesMarais D. J., Hayes J. M., and Meinschein W. G. (1974) The distribution in lunar soil of hydrogen released by pyrolysis. *Proc. Lunar Sci. Conf. 5th*, pp. 1811–1822.
- DesMarais D. J., Basu A., Hayes J. M., and Meinschein W. G. (1975) Evolution of carbon isotopes, agglutinates, and the lunar regolith. *Proc. Lunar Sci. Conf. 6th*, pp. 2353–2373.
- Deutsch A. and Stöffler D. (1987) Rb-Sr analyses of Apollo 16 melt rocks and a new age estimate for the Imbrium basin: Lunar basin chronology and the early heavy bombardment of the Moon. *Geochim. Cosmochim. Acta*, 51, 1951–1964.
- Devine J. M., McKay D. S., and Papike J. J. (1982) Lunar regolith: Petrology of the <10 mm fraction. *Proc. Lunar Planet. Sci. Conf. 13th*, in *J. Geophys. Res.*, 87, A260–A268.
- DeWitt J. M. Jr. and Stodola E. K. (1949) Detection of radio signals reflected from the Moon. *Proc. Inst. Radio Eng.*, 37, pp. 229–242.
- Dickinson J. E. and Hess P. C. (1983) Role of whitlockite and apatite in lunar feldspar (abstract). In *Lunar and Planetary Science XIV*, pp. 158–159. Lunar and Planetary Institute, Houston.
- Dickinson T., Taylor G. J., Keil K., Schmitt R. A., Hughes S. S., and Smith M. R. (1985) Apollo 14 aluminous mare basalts and their possible relationship to KREEP. *Proc. Lunar Planet. Sci. Conf. 15th*, in *J. Geophys. Res.*, 90, C365–C374.
- Dietz R. S. (1964) Sudbury structure as an astrobleme. *J. Geol.*, 72, 412–434.
- Ding T. P., Thode H. G., and Rees C. E. (1983) Sulphur content and sulphur isotope composition of orange and black glasses in Apollo 17 drive tube 74002/1. *Geochim. Cosmochim. Acta*, 47, 491–496.
- Dixon J. R. and Papike J. J. (1975) Petrology of anorthosites from the Descartes region of the Moon: Apollo 16. *Proc. Lunar Sci. Conf. 6th*, pp. 263–291.
- Dodd R. T. Jr. (1981) *Meteorites: A Petrologic-Chemical Synthesis*. Cambridge Univ., Cambridge. 368 pp.
- Doe B. R. and Tatsumoto M. (1972) Volatilized lead from Apollo 12 and 14 soils. *Proc. Lunar Sci. Conf. 3rd*, pp. 1981–1988.
- Dolginov Sh. Sh., Yeroshenko Ye. G., Sharova V. A., Vnuchkova T. A., Vanyan L. L., Okulesky B. A., and Bazilevsky A. T. (1976) Study of magnetic field, rock magnetization and lunar electrical conductivity in the Bay Le Monnier. *The Moon*, 15, 3–14.
- Dollfus A. (1961) Polarization studies of the planets. In *The Solar System, Vol. III Planets and Satellites* (G. Kuiper and B. Middlehurst, eds.), pp. 343–399. Univ. of Chicago, Chicago.
- Dollfus A. and Bowell E. (1971) Polarimetric properties of the lunar surface and its interpretation. Part I. Telescopic observations. *Astron. Astrophys.*, 10, 29–53.
- Dollfus A., Geake J. E., and Titulaer C. (1971) Polarimetric properties of the lunar surface and its interpretation. Part 3: Apollo 11 and Apollo 12 lunar samples. *Proc. Lunar Sci. Conf. 2nd*, pp. 2285–2300.
- Donaldson C. H., Usselman T. M., Williams R. J., and Lofgren G. E. (1975) Experimental modeling of the cooling history of Apollo 12 olivine basalts. *Proc. Lunar Sci. Conf. 6th*, pp. 843–869.
- Dorman J., Evans S., Nakamura Y., and Latham G. (1978) On the time-varying properties of the lunar seismic meteoroid population. *Proc. Lunar Planet. Sci. Conf. 9th*, pp. 3615–3626.
- Douchowskoy E. A., Motovilov I. A., Silin A. A., Smorodinov M. I., and Shvarev V. V. (1974) The investigation of the frictional properties of lunar soil and its analogues. In *Lunar Soil from Sea of Fertility*, pp. 582–586. Nauka, Moscow (in Russian).
- Douchowskoy E. A., Markatchev V. V., Silin A. A., Cherkasov I. I., and Shvarev V. V. (1979) The investigation of mechanical properties of Luna 20 soil with the TOR-1 installation. In *Regolith from the Highland Region of the Moon*, pp. 633–634. Nauka, Moscow (in Russian).
- Downs G. S., Goldstein R. M., Green R. R., and Morris G. A. (1971) Mars radar observations, a preliminary report. *Science*, 174, 1324–1327.
- Dowty E., Prinz M., and Keil K. (1973) Composition, mineralogy, and petrology of 28 mare basalts from Apollo 15 rake samples. *Proc. Lunar Sci. Conf. 4th*, pp. 423–444.
- Dowty E., Keil K., and Prinz M. (1974a) Lunar pyroxene-phryic basalts: Crystallization under supercooled conditions. *J. Petrol.*, 15, 419–453.
- Dowty E., Prinz M., and Keil K. (1974b) Ferroan anorthosite: a widespread and distinctive lunar rock type. *Earth Planet. Sci. Lett.*, 24, 15–25.
- Dowty E., Prinz M., and Keil K. (1974c) “Very high alumina basalt”: A mixture and not a magma type. *Science*, 183, 1214–1215.
- Dowty E., Keil K., Prinz M., Gros J., and Takahashi H. (1976) Meteorite-free Apollo 15 crystalline KREEP. *Proc. Lunar Sci. Conf. 7th*, pp. 1833–1844.
- Drake M. J., McCallum I. S., McKay G. A., and Weill D. F. (1970) Mineralogy and petrology of Apollo 12 sample no. 12013. A progress report. *Earth Planet. Sci. Lett.*, 9, 103–123.

- Dran J. C., Durrieu L., Jouret C., and Maurette M. (1970) Habit and texture studies of lunar and meteoritic materials with a 1 MeV electron microscope. *Earth Planet. Sci. Lett.*, 9, 391–400.
- Drozd R. J., Hohenberg C. M., Morgan C. J., and Ralston C. E. (1974) Cosmic-ray exposure history at the Apollo 16 and at other lunar sites: Lunar surface dynamics. *Geochim. Cosmochim. Acta*, 38, 1625–1642.
- Drozd R. J., Hohenberg C. M., Morgan C. J., Podosek F. A., and Wroge M. L. (1977) Cosmic-ray exposure history of Taurus-Littrow. *Proc. Lunar Sci. Conf. 8th*, pp. 3027–3043.
- Duba A., Heard H. C., and Schock R. N. (1976) Electrical conductivity of orthopyroxene to 1400°C and the resulting selenotherm. *Proc. Lunar Sci. Conf. 7th*, pp. 3173–3181.
- Duba A., Dennison M., Irving A. J., Thornber C. R., and Huebner J. S. (1979) Electrical conductivity of aluminous orthopyroxene (abstract). In *Lunar and Planetary Science X*, pp. 318–319. Lunar and Planetary Institute, Houston.
- Duke J. M. (1976) The distribution of the period four transition elements among olivine, calcic pyroxene, and mafic silicate liquid: Experimental results. *J. Petrol.*, 17, 499–521.
- Duke M. B. and Nagle J. S. (1974) *Lunar Core Catalog*. NASA JSC Publication JSC-09252. NASA Johnson Space Center, Houston.
- Duke M. B., Woo C. C., Bird M. L., Sellers G. A., and Finkelman R. B. (1970a) Lunar soil: Size distribution and mineralogical constituents. *Science*, 167, 648–650.
- Duke M. B., Woo C. C., Sellers G. A., Bird M. L., and Finkelman R. B. (1970b) Genesis of lunar soil at Tranquility Base. *Proc. Apollo 11 Lunar Sci. Conf.*, pp. 347–361.
- Duke M. B., Mendell W. W., and Roberts B. B. (1985) Strategies for a permanent lunar base. In *Lunar Bases and Space Activities of the 21st Century* (W. W. Mendell, ed.), pp. 57–68. Lunar and Planetary Institute, Houston.
- Duncan A. R., Erlank A. J., Willis J. P., and Ahrens L. H. (1973) Composition and interrelationships of some Apollo 16 samples. *Proc. Lunar Sci. Conf. 4th*, pp. 1097–1113.
- Duncan A. R., Erlank A. J., Willis J. P., Sher M. K., and Ahrens L. H. (1974) Trace element evidence for a two-stage origin of some titaniferous mare basalts. *Proc. Lunar Sci. Conf. 5th*, pp. 1147–1157.
- Duncan A. R., Sher M. K., Abraham Y. C., Erlank A. J., Willis J. P., and Ahrens L. H. (1975) Interpretation of the compositional variability of Apollo 15 soils. *Proc. Lunar Sci. Conf. 6th*, pp. 2309–2320.
- Duraud J. P., Langevin Y., Maurette M., Comstock G. M., and Burlingame A. L. (1975) The simulated depth history of dust grains in the lunar regolith. *Proc. Lunar Sci. Conf. 6th*, pp. 2397–2415.
- Durgunoglu H. T. and Mitchell J. K. (1975) Static penetration resistance of soils: I—Analysis. *Proc. Specialty Conf. on In Situ Measurement of Soil Properties*, pp. 151–171. American Society of Civil Engineers, Raleigh.
- Dyal P. and Daily W. D. (1979) Electrical conductivity anomalies associated with circular lunar maria. *Proc. Lunar Planet. Sci. Conf. 10th*, pp. 2291–2297.
- Dyal P. and Parkin G. W. (1971) The Apollo 12 magnetometer experiment, internal lunar properties from transient and steady magnetic field measurements. *Proc. Lunar Sci. Conf. 2nd*, pp. 2391–2413.
- Dyal P., Parkin C. W., and Daily W. D. (1974) Magnetism and the interior of the Moon. *Rev. Geophys. Space Phys.*, 12, 568–591.
- Dyal P., Parkin C. W., and Daily W. D. (1976) Structure of the lunar interior from magnetic field measurements. *Proc. Lunar Sci. Conf. 7th*, pp. 3077–3095.
- Dymek R. F., Albee A. L., and Chodos A. A. (1975a) Comparative petrology of lunar cumulate rocks of possible primary origin: Dunite 72415, troctolite 76535, norite 78235, and anorthosite 62237. *Proc. Lunar Sci. Conf. 6th*, pp. 301–341.
- Dymek R. F., Albee A. L., and Chodos A. A. (1975b) Comparative mineralogy and petrology of Apollo 17 mare basalts: Samples 70215, 71055, 74255, and 75055. *Proc. Lunar Sci. Conf. 6th*, pp. 49–77.
- Dymek R. F., Albee A. L., and Chodos A. A. (1976) Petrology and origin of Boulders #2 and #3, Apollo 17 Station 2. *Proc. Lunar Sci. Conf. 7th*, pp. 2335–2378.
- Eberhardt P., Geiss J., Graf H., Grögler N., Krähenbühl U., Schwaller H., Schwarzmüller J., and Stettler A. (1970) Trapped solar wind noble gases, exposure age and K/Ar-age in Apollo 11 lunar fine material. *Proc. Apollo 11 Lunar Sci. Conf.*, pp. 1037–1070.
- Eberhardt P., Geiss J., Graf H., Grögler N., Mendia M. D., Mörgelli M., Schwaller H., Stettler A., Krähenbühl U., and von Gunten H. R. (1972) Trapped solar wind noble gases in Apollo 12 lunar fines 12001 and Apollo 11 breccia 10046. *Proc. Lunar Sci. Conf. 3rd*, pp. 1821–1856.
- Eberhardt P., Geiss J., Grögler N., Mauer P., and Stettler A. (1973) ³⁹Ar–⁴⁰Ar ages of lunar material (abstract). *Meteoritics*, 8, 360–361.
- Eggleton R. E. and Schaber G. E. (1972) Cayley formation interpreted as basin ejecta. In *Apollo 16 Preliminary Science Report*, pp. 29–7 to 29–17. NASA SP-315.
- Ehmann W. D. and Chyi L. L. (1974) Abundances of the group IVB elements, Ti, Zr, and Hf and implications of their ratios in lunar materials. *Proc. Lunar Sci. Conf. 5th*, pp. 1015–1024.
- Ehrlich R. and Weinberg B. (1970) An exact method for characterization of grain shape. *J. Sed. Petrol.*, 40, 205–212.
- Eisentraut K. J., Black M. S., Hileman F. D., Sievers R. E., and Ross W. D. (1972) Beryllium and chromium abundances in Fra Mauro and Hadley-Apennine lunar samples. *Proc. Lunar Sci. Conf. 3rd*, pp. 1327–1333.
- Elachi C., Koblrick M., Roth L., Tiernan M., and Brown W. E. Jr. (1976) Local lunar topography from the Apollo 17 ALSE radar imagery and altimetry. *The Moon*, 15, 119–131.
- Elachi C., Roth L. E., and Schaber G. G. (1984) Spaceborne radar subsurface imaging in hyperarid regions. *IEEE Trans. Geosci. and Rem. Sens.*, GE-22, pp. 383–388.

- El-Baz F. (1972) The Alhazen to Abul Wafa swirl belt: An extensive field of light-colored, sinuous marking. In *Apollo 16 Preliminary Science Report*, pp. 29–93 to 29–97. NASA SP-315.
- El Goresy A. and Ramdohr P. (1975) Subsolidus reduction of lunar opaque oxides: Textures, assemblages, geochemistry, and evidence for a late-stage endogenic gaseous mixture. *Proc. Lunar Sci. Conf. 6th*, pp. 729–745.
- El Goresy A. and Ramdohr P. (1977) Apollo 17 TiO₂-rich basalts: Reverse spinel zoning as evidence for subsolidus equilibration of the spinel-ilmenite assemblage. *Proc. Lunar Sci. Conf. 8th*, pp. 1611–1624.
- El Goresy A., Ramdohr P., and Taylor L. A. (1971a) The geochemistry of the opaque minerals in Apollo 14 crystalline rocks. *Earth Planet. Sci. Lett.*, 13, 121–129.
- El Goresy A., Ramdohr P., and Taylor L. A. (1971b) The opaque minerals in the lunar rocks from Oceanus Procellarum. *Proc. Lunar Sci. Conf. 2nd*, pp. 219–235.
- El Goresy A., Taylor L. A., and Ramdohr P. (1972) Fra Mauro crystalline rocks: Mineralogy, geochemistry, and subsolidus reduction of opaque minerals. *Proc. Lunar Sci. Conf. 3rd*, pp. 333–349.
- El Goresy A., Ramdohr P. and Medenbach O. (1973a) Lunar samples from Descartes site: Opaque mineralogy and geochemistry. *Proc. Lunar Sci. Conf. 4th*, pp. 733–750.
- El Goresy A., Ramdohr P., Pavicevic M., Medenbach O., Müller O., and Gentner W. (1973b) Zinc, lead, chlorine, and FeOOH-bearing assemblages in the Apollo 16 sample 66095: Origin by impact of a comet or a carbonaceous chondrite. *Earth Planet. Sci. Lett.*, 18, 411–419.
- El Goresy A., Prinz M., and Ramdohr P. (1976) Zoning in spinels as an indicator of the crystallization histories of mare basalts. *Proc. Lunar Sci. Conf. 7th*, pp. 1261–1279.
- Engel A. E. J. and Engel C. G. (1970a) Lunar rock compositions and some interpretations. *Science*, 167, 527–528.
- Engel A. E. J. and Engel C. G. (1970b) Lunar rock compositions and some interpretations. *Proc. Apollo 11 Lunar Sci. Conf.*, pp. 1081–1084.
- Engelhardt W., Hurrle H., and Luft E. (1976) Microimpact-induced changes of textural parameters and modal composition of the lunar regolith. *Proc. Lunar Sci. Conf. 7th*, pp. 373–392.
- England A. W. (1975) Thermal microwave emission from a scattering layer. *J. Geophys. Res.*, 80, 4484–4496.
- Epstein S. and Taylor H. P. Jr. (1970) The concentration and isotopic composition of hydrogen, carbon, and silicon in Apollo 11 lunar rocks and minerals. *Proc. Apollo 11 Sci. Conf.*, pp. 1085–1096.
- Epstein S. and Taylor H. P. Jr. (1971) O¹⁸/O¹⁶, Si³⁰/Si²⁸, D/H, and C¹³/C¹² ratios in lunar samples. *Proc. Lunar Sci. Conf. 2nd*, pp. 1421–1441.
- Epstein S. and Taylor H. P. Jr. (1972) O¹⁸/O¹⁶, Si³⁰/Si²⁸, C¹³/C¹², and D/H studies of Apollo 14 and 15 samples. *Proc. Lunar Sci. Conf. 3rd*, pp. 1429–1454.
- Epstein S. and Taylor H. P. Jr. (1973) The isotopic composition and concentration of water, hydrogen, and carbon in some Apollo 15 and 16 soils and in the Apollo 17 orange soil. *Proc. Lunar Sci. Conf. 4th*, pp. 1559–1575.
- Epstein S. and Taylor H. P. Jr. (1974) D/H and ¹⁸O/¹⁶O ratios of H₂O in the “rusty” breccia 66095 and the origin of “lunar water.” *Proc. Lunar Sci. Conf. 5th*, pp. 1839–1854.
- Epstein S. and Taylor H. P. Jr. (1975) Investigation of the carbon, hydrogen, oxygen, and silicon isotope and concentration relationships on the grain surfaces of a variety of lunar soils and in some Apollo 15 and 16 core samples. *Proc. Lunar Sci. Conf. 6th*, pp. 1771–1798.
- Erickson J. E. (1969) Analysis of the meteoroid flux measured by Explorer 16 and Lunar Orbiter. *Astron. J.*, 74, 279–283.
- Eugster O. (1986) Noble gases in grain size fractions of lunar anorthosite 60018: Trapped xenon isotopically similar to terrestrial atmospheric xenon (abstract). In *Lunar and Planetary Science XVII*, pp. 212–213. Lunar and Planetary Institute, Houston.
- Eugster O. and Niedermann S. (1987) Trapped Xe isotopically different from modern solar wind Xe in lunar breccia 60018 and black glass 74001 (abstract). In *Lunar and Planetary Science XVIII*, pp. 275–276. Lunar and Planetary Institute, Houston.
- Eugster O., Eberhardt P., Geiss J., Grögler N., Jungck M., and Mörgeli M. (1975) Solar-wind-trapped and cosmic-ray-produced noble gases in Luna 20 soil. *Proc. Lunar Sci. Conf. 6th*, pp. 1989–2007.
- Eugster O., Grögler N., Eberhardt P., and Geiss J. (1980) Double drive tube 74001/2: Composition of noble gases trapped 3.7 AE ago. *Proc. Lunar Planet. Sci. Conf. 11th*, pp. 1565–1592.
- Evans J. V. (1957) The scattering of radio waves by the Moon. *Proc. Phys. Soc. London*, B70, 1112.
- Evans J. V. (1962) Radio echo studies of the Moon. In *Physics and Astronomy of the Moon* (Z. Kopal, ed.), pp. 429–480. Academic, New York.
- Evans J. V. (1969) Radar studies of planetary surfaces. *Annu. Rev. Astron. Astrophys.*, 7, 201–248.
- Evans J. V. and Hagfors T. (1964) On the interpretation of radar reflections from the Moon. *Icarus*, 3, 151–160.
- Evans J. V. and Hagfors T. (1966) Study of radio echoes from the Moon at 23 centimeters wavelength. *J. Geophys. Res.*, 71, 4871–4889.
- Evans J. V. and Pettengill G. H. (1963) The scattering behavior of the Moon at wavelengths of 3, 6, 68 and 785 centimeters. *J. Geophys. Res.*, 68, 423–447.
- Evans J. V., Evans S., and Thompson J. H. (1959) The rapid fading of Moon echoes at 100 Mc/s. In *Paris Symposium on Radio Astronomy* (R. N. Bracewell, ed.), pp. 8–12. Stanford Univ., Stanford, California.
- Evensen N. M., Hamilton P. J., and O’Nions R. K. (1978) Rare-earth abundances in chondritic meteorites. *Geochim. Cosmochim. Acta*, 42, 1199–1212.
- Fagin S. W., Worrall D. M., and Muehlberger W. R. (1978) Lunar ridge orientations: Implications for lunar tectonic models. *Proc. Lunar Planet. Sci. Conf. 9th*, pp. 3473–3479.
- Fechtig H., Hartung J. B., Nagel K., Neukum G., and Storzer D. (1974) Lunar microcrater studies, derived meteoroid

- fluxes, and comparison with satellite-borne experiments. *Proc. Lunar Sci. Conf. 5th*, pp. 2463-2474.
- Fedorets V. A. (1952) Photographic photometry of the lunar surface. *Publ. Astron. Obs. of the Kharkov State University*, 2, 49-109 (in Russian).
- Feldman W. C., Ashbridge J. R., Bame S. J., and Gosling J. T. (1977) Plasma and magnetic fields from the Sun. In *The Solar Output and its Variation* (O. R. White, ed.), pp. 351-382. Colorado Assoc. Univ., Boulder.
- Fenner M. A., Freeman J. W. Jr., and Hills H. K. (1973) The electric potential of the lunar surface. *Proc. Lunar Sci. Conf. 4th*, pp. 2877-2887.
- Ferrari A. J., Nelson D. L., Sjogren W. L., and Phillips R. J. (1978) The isostatic state of the lunar Apennines and regional surroundings. *J. Geophys. Res.*, 83, 2863-2871.
- Filleux C., Spear R. H., Tombrello T. A., and Burnett D. S. (1978) Direct measurement of surface carbon concentrations for lunar soil breccias. *Proc. Lunar Planet. Sci. Conf. 9th*, pp. 1599-1617.
- Finkelman R. B., Baedeker P. A., Christian R. P., Berman S., Schneppe M. M., and Rose H. J. Jr. (1975) Trace-element chemistry and reducing capacity of size fractions from the Apollo 16 regolith. *Proc. Lunar Sci. Conf. 6th*, pp. 1385-1398.
- Fireman E. L. (1980) Solar activity during the past 10⁴ years from radionuclides in lunar samples. In *The Ancient Sun: Fossil Record in the Earth, Moon and Meteorites* (R. O. Pepin, J. A. Eddy, and R. B. Merrill, eds.), pp. 267-278. Pergamon, New York.
- Firsoff V. A. (1961) *Moon Atlas*. Hutchinson, London. 128 pp.
- Fisher A. D. (1977) A model for microwave intensity propagation in an inhomogeneous medium. *IEEE Trans. Antennas Propag.*, AP-25, 876-882.
- Fisher A. D. and Staelin D. H. (1977) Possible effect of subsurface inhomogeneities on the lunar microwave spectrum. *Icarus*, 32, 98-105.
- Fleischer R. L. and Hart H. R. Jr. (1974) Uniformity of the uranium content of lunar green and orange glasses. *Proc. Lunar Sci. Conf. 5th*, pp. 2251-2255.
- Fleischer R. L., Hart H. R. Jr., and Giard W. R. (1974) Surface history of lunar soil and soil columns. *Geochim. Cosmochim. Acta*, 38, 365-380.
- Fleischer R. L., Price P. B., and Walker R. M. (1975) *Nuclear Tracks in Solids: Principles and Applications*. Univ. of California, Berkeley. 605 pp.
- Floran R. B., Grieve R. A. F., Phinney W. C., Warner J. L., and Simonds C. H. (1978) Manicouagan impact melt, Quebec, 1, stratigraphy, petrology and chemistry. *J. Geophys. Res.*, 83, 2737-2760.
- Florensky C. P., Basilevsky A. T., Ivanov A. V., Pronin A. A., and Rode O. D. (1977) Luna 24: Geologic setting of landing site and characteristics of sample core (preliminary data). *Proc. Lunar Sci. Conf. 8th*, pp. 3257-3279.
- Florensky C. P., Basilevsky A. T., Bobina N. N., Burba G. A., Grebennik N. N., Kuzmin R. O., Polosukhin B. P., Popovich V. D., Pronin A. A., and Ronca L. B. (1978) The floor of crater Le Monier: A study of Lunokhod 2 data. *Proc. Lunar Planet. Sci. Conf. 9th*, pp. 1449-1458.
- Florensky P. V. (1975) The Zhamanschin meteorite crater (the Northern Near-Aral) and its tektites and impactites. *Academy of Sciences of the USSR, Geological Serial*, 10, 74-86.
- Folk R. L. (1968) *Petrology of Sedimentary Rocks*. Hemphill's, Austin. 170 pp.
- Folk R. L. and Ward W. C. (1957) Brazos River bar: A study in the significance of grain size parameters. *J. Sed. Petrol.*, 27, 3-26.
- Fouche K. F. and Smales A. A. (1967) The distribution of trace elements in chondritic meteorites. 2. Antimony, arsenic, gold, palladium and rhenium. *Chem. Geol.* 2, 105-134.
- Freeman J. W. and Ibrahim M. E. (1974) The lunar electric potential and its plasma sheath effects (abstract). In *Lunar Interactions* (D. R. Criswell and J. R. Freeman, eds.), pp. 86-88. The Lunar Science Institute, Houston.
- Freeman J. W. Jr., Hills H. K., and Vondrak R. R. (1972) Water vapor, whence comest thou? *Proc. Lunar Sci. Conf. 3rd*, pp. 2217-2230.
- French B. M. and Short N. M., eds. (1968) *Shock Metamorphism of Natural Materials*. Mono, Baltimore. 644 pp.
- Frick U., Baur H., Funk H., Phinney D., Schafer C., Schultz L., and Signer P. (1973) Diffusion properties of light noble gases in lunar fines. *Proc. Lunar Sci. Conf. 4th*, pp. 1987-2002.
- Fricke S. J., Ingalls R. P., Mason J. C., Stone M. L., and Swift D. W. (1960) Computation and measurement of the fading rate of Moon-reflected UHF signals. *J. Res. Natl. Bur. Stand.*, 64D, 455-465.
- Friedman I., O'Neil J. R., Gleason J. D., and Hardcastle K. (1971) The carbon and hydrogen content and isotopic composition of some Apollo 12 materials. *Proc. Lunar Sci. Conf. 2nd*, pp. 1407-1415.
- Friel J. J. and Goldstein J. I. (1976) An experimental study of phosphate reduction and phosphorus-bearing lunar metal particles. *Proc. Lunar Sci. Conf. 7th*, pp. 791-806.
- Friel J. J. and Goldstein J. I. (1977) The relationship between lunar metal particles and phosphate minerals. *Proc. Lunar Sci. Conf. 8th*, pp. 3955-3965.
- Friel J. J., Harkey R. I., and Ulmer G. C. (1977) Armalcolite stability as a function of pressure and oxygen fugacity. *Geochim. Cosmochim. Acta*, 41, 403-410.
- Frisillo A. L., Olhoeft G. R., and Strangway D. W. (1975) Effects of pressure, temperature and density on the electrical properties of lunar samples 72441,12, 15301,38 and a terrestrial basalt. *Earth Planet. Sci. Lett.*, 24, 345-356.
- Frondel C., Klein C. J., and Ito J. (1971) Mineralogical and chemical data on Apollo 12 lunar fines. *Proc. Lunar Sci. Conf. 2nd*, pp. 719-726.
- Frondel J. W. (1975) *Lunar Mineralogy*. Wiley, New York. 323 pp.
- Fruchter J. S., Robyn M. A., and Goles G. G. (1974a) Compositional affinities of clasts and matrix from breccia 66055 (abstract). In *Lunar Science V*, pp. 251-253. The Lunar Science Institute, Houston.

- Fruchter J. S., Kridelbaugh S. J., Robyn M. A., and Goles G. G. (1974b) Breccia 66055 and related clastic materials from the Descartes region, Apollo 16. *Proc. Lunar Sci. Conf. 5th*, pp. 1035–1046.
- Fruiland R. M. (1983) *Regolith Breccia Workbook*. NASA Planetary Materials Branch Publ. No. 66, NASA Johnson Space Center, Houston. 260 pp.
- Fruiland R. M., Morris R. V., McKay D. S., and Clanton U. S. (1977) Apollo 17 roapy glasses. *Proc. Lunar Sci. Conf. 8th*, pp. 3095–3111.
- Fryxell R. and Heiken G. (1974) Preservation of lunar core samples: Preparation and interpretation of three-dimensional stratigraphic sections. *Proc. Lunar Sci. Conf. 5th*, pp. 935–966.
- Fuchs L. H. (1969) The phosphate mineralogy of meteorites. In *Meteorite Research* (P. M. Millman, ed.), pp. 683–695. Reidel, Dordrecht.
- Fuchs L. H. (1970) Fluorapatite and other accessory minerals in Apollo 11 rocks. *Proc. Apollo 11 Lunar Sci. Conf.*, pp. 475–479.
- Fujiwara A., Kamimoto G., and Tsukamoto A. (1977) Destruction of basaltic bodies by high velocity impact. *Icarus*, 31, 277–288.
- Fukuoka T., Laul J. C., Smith M. R., Hughes S. S., and Schmitt R. A. (1986) Chemistry of Yamato-791197 Antarctic meteorite: Evidence for its lunar highland origin. *Proceedings of the Tenth Symposium on Antarctic Meteorites*, pp. 84–95. Natl. Inst. for Polar Res., Tokyo.
- Fuller E. L., Holmes H. F., Gammage R. B., and Becker K. (1971) Interaction of gases with lunar materials: Preliminary results. *Proc. Lunar Sci. Conf. 2nd*, pp. 2009–2019.
- Fuller M. (1974) Lunar magnetism. *Rev. Geophys. Space Phys.*, 12, 23–64.
- Fung A. K. (1982) A review of volume scatter theories for modeling applications. *Radio Sci.*, 17, 1007–1017.
- Fung A. K. and Moore R. K. (1964) Effects of structure size on moon and earth radar returns of various angles. *J. Geophys. Res.*, 69, 1075–1081.
- Funkhouser J. G., Schaffer O. A., Bogard D. D., and Zahringer J. (1970) Gas analysis of the lunar surface. *Proc. Apollo 11 Lunar Sci. Conf.*, pp. 1111–1116.
- Gaddis L. R., Pieters C. M., and Hawke B. R. (1985) Remote sensing of lunar pyroclastic mantling deposits. *Icarus*, 61, 461–489.
- Gammage R. B. and Holmes H. F. (1975) Specific surface area as a maturity index of lunar fines. *Earth Planet. Sci. Lett.*, 27, 424–426.
- Gammage R. B. and Holmes H. F. (1977) Effect of annealing temperature on the reactivity of lunar fines towards adsorbed water. *Earth Planet. Sci. Lett.*, 34, 445–449.
- Ganapathy R. and Anders E. (1974) Bulk compositions of the Moon and Earth, estimated from meteorites. *Proc. Lunar Sci. Conf. 5th*, pp. 1181–1206.
- Ganapathy R., Keays R. R., Laul J. C., and Anders E. (1970) Trace elements in Apollo 11 lunar rocks: Implications for meteorite influx and origin of Moon. *Proc. Apollo 11 Lunar Sci. Conf.*, pp. 1117–1142.
- Ganapathy R., Morgan J. W., Krähenbühl U., and Anders E. (1973) Ancient meteoritic components in lunar highlands rocks: Clues from trace elements in Apollo 15 and 16 samples. *Proc. Lunar Sci. Conf. 4th*, pp. 1239–1261.
- Ganapathy R., Morgan J. W., Higuchi H., and Anders E. (1974) Meteoritic and volatile elements in Apollo 16 rocks and in separated phases from 14306. *Proc. Lunar Sci. Conf. 5th*, pp. 1659–1683.
- Gancarz A. J., Albee A. L., and Chodos A. A. (1971) Petrologic and mineralogic investigations of some crystalline rocks returned by the Apollo 14 mission. *Earth Planet. Sci. Lett.*, 12, 1–18.
- Gancarz A. J., Albee A. L., and Chodos A. A. (1972) Comparative petrology of Apollo 16 sample 68415 and Apollo 14 samples 14276 and 14310. *Earth Planet. Sci. Lett.*, 16, 307–330.
- Gangadharan S., Sankar-Das M., and Yegnasubramanian S. (1974) Elemental analyses of Luna 16 and 20 regolith samples. In *Further Advances in Lunar Research: Luna 16 and 20 Samples* (N. Bhandari and M. N. Rao, eds.), pp. 47–52. Indian Natl. Sci. Acad., New Delhi.
- Garg A. N. and Ehmann W. N. (1976) Zr-Hf fractionation in chemically defined lunar rock types. *Proc. Lunar Sci. Conf. 7th*, pp. 3397–3410.
- Garshnek V. (1989) Crucial factor: Human. Safely extending the human presence in space. *Space Policy*, August, 201–216.
- Gary B., Stacey J., and Drake F. D. (1965) Radiometric mapping of the Moon at 3 millimeters wavelength. *Astrophys. J. Suppl.* 108, 12, 239–262.
- Gary B. L. and Keihm S. J. (1978) Interpretation of ground-based microwave measurements of the Moon using a detailed regolith properties model. *Proc. Lunar Planet. Sci. Conf. 9th*, pp. 2885–2900.
- Gast P. W. (1968) Trace element fractionation and the origin of tholeiitic and alkaline magma types. *Geochim. Cosmochim. Acta*, 32, 1057.
- Gatehouse B. M., Grey I. E., Lovering J. F., and Wark D. A. (1977) Structural studies on tranquillityite and related synthetic phases. *Proc. Lunar Sci. Conf. 8th*, pp. 1831–1838.
- Gault D. E. (1970) Saturation and equilibrium conditions for impact cratering on the lunar surface: Criteria and implications. *Radio Sci.*, 5, 273–291.
- Gault D. E. (1973) Displaced mass, depth, diameter and effects of oblique trajectories for impact craters formed in dense crystalline rocks. *The Moon*, 4, 32–44.
- Gault D. E. and Greeley R. (1978) Exploratory experiments of impact craters formed in viscous-liquid targets: Analogs for martian rampart craters? *Icarus*, 34, 486–495.
- Gault D. E. and Sonett C. P. (1982) Laboratory simulation of pelagic asteroidal impact: Atmospheric injection, benthic topography, and the surface wave radiation field. In *Geological Implications of Impacts of Large Asteroids and Comets on the Earth* (L. T. Silver and P. H. Schultz, eds.), pp. 69–92. Geol. Soc. Am. Spec. Pap. 190.

- Gault D. E. and Wedekind J. A. (1969) The destruction of tektites by micrometeoroid impact. *J. Geophys. Res.*, 74, 6780–6794.
- Gault D. E., Quaide W. L., and Oberbeck V. R. (1968) Impact cratering mechanics and structures. In *Shock Metamorphism of Natural Materials* (B. M. French and N. M. Short, eds.), pp. 87–99. Mono, Baltimore.
- Gault D. E., Hörz F., Hartung J. B., and Brownlee D. E. (1974) Mixing of the lunar regolith. *Proc. Lunar Sci. Conf. 5th*, pp. 2365–2386.
- Gay P., Bown M. G., and Muir I. D. (1972) Mineralogical and petrographic features of two Apollo 14 rocks. *Proc. Lunar Sci. Conf. 3rd*, pp. 351–362.
- Gehrels T., ed. (1979) *Asteroids*. Univ. of Arizona, Tucson. 1181 pp.
- Gehrels T., Coffeen T., and Owings D. (1964) Wavelength dependence of polarization. III. The lunar surface. *Astron. J.*, 69, 826–852.
- Geiss J. (1973) Solar wind composition and implications about the history of the solar system. In *Papers Presented to the 13th Int. Cosmic Ray Conf.*, 5, pp. 3375–3398. Univ. of Denver, Denver, Colorado.
- Gerstenkorn H. (1955) Über Gezeitenreibung beim Zweikörper-problem. *Zeit. Astrophys.*, 36, 245–274.
- Gibb F. G. F., Stumpfl E. F., and Zussman J. (1970) Opaque minerals in an Apollo 12 rock. *Earth Planet. Sci. Lett.*, 9, 217–224.
- Gibbons R. V., Morris R. V., and Hörz F. (1975) Petrographic and ferromagnetic resonance studies of experimentally shocked regolith analogues. *Proc. Lunar Sci. Conf. 6th*, pp. 3143–3171.
- Gibbons R. V., Hörz F., and Schaal R. B. (1976) The chemistry of some individual lunar soil agglutinates. *Proc. Lunar Sci. Conf. 7th*, pp. 405–422.
- Gibson E. K. Jr. (1973) Thermal analysis—Mass spectrometer computer system and its application to the evolved gas analysis of Green River shale and lunar soil samples. *Thermochim. Acta*, 5, 243–255.
- Gibson E. K. Jr. (1977) Volatile elements, carbon, nitrogen, sulfur, sodium, potassium, and rubidium in the lunar regolith. *Phys. Chem. Earth*, 10, 57–62.
- Gibson E. K. Jr. and Andrawes F. F. (1978a) Sulfur abundances in the 74001/74002 drive tube from Shorty Crater, Apollo 17. *Proc. Lunar Planet. Sci. Conf. 9th*, pp. 2011–2017.
- Gibson E. K. Jr. and Andrawes F. F. (1978b) Nature of the gases released from lunar rocks and soils upon crushing. *Proc. Lunar Planet. Sci. Conf. 9th*, pp. 2433–2450.
- Gibson E. K. Jr. and Bustin R. (1987) Hydrogen abundances vs. depth in the lunar regolith: results from an Apollo double drive tube and deep drill core (abstract). In *Lunar and Planetary Science XVIII*, pp. 324–325. Lunar and Planetary Institute, Houston.
- Gibson E. K. Jr. and Moore G. W. (1973a) Carbon and sulfur distributions and abundances in lunar fines. *Proc. Lunar Sci. Conf. 4th*, pp. 1577–1586.
- Gibson E. K. Jr. and Moore C. B. (1973b) Volatile-rich lunar soil: Evidence of possible cometary impact. *Science*, 179, 69–71.
- Gibson E. K. Jr. and Moore G. W. (1973c) Variable carbon contents of lunar soil 74220. *Earth Planet. Sci. Lett.*, 20, 404–408.
- Gibson E. K. Jr. and Moore G. W. (1974) Sulfur abundances and distributions in the valley of Taurus-Littrow. *Proc. Lunar Sci. Conf. 5th*, pp. 1823–1837.
- Gibson E. K. Jr., Chang S., Lennon K., Moore G. W., and Pearce G. W. (1975) Sulfur abundances and distributions in mare basalts and their source magmas. *Proc. Lunar Sci. Conf. 6th*, pp. 1287–1301.
- Gibson E. K. Jr., Usselman T. M., and Morris R. V. (1976) Sulfur in Apollo 17 basalts and their source regions. *Proc. Lunar Sci. Conf. 7th*, pp. 1491–1505.
- Gibson E. K. Jr., Brett R., and Andrawes F. (1977) Sulfur in lunar mare basalts as a function of bulk composition. *Proc. Lunar Sci. Conf. 8th*, pp. 1417–1428.
- Gibson E. K. Jr., Bustin R., Skaugset A., Can R. H., Wentworth S. J., and McKay D. S. (1987) Hydrogen distributions in lunar materials (abstract). In *Lunar and Planetary Science XVIII*, pp. 326–327. Lunar and Planetary Institute, Houston.
- Gibson M. A. and Knudsen C. W. (1985) Lunar oxygen production from ilmenite. In *Lunar Bases and Space Activities of the 21st Century* (W. W. Mendell, ed.), pp. 543–550. Lunar and Planetary Institute, Houston.
- Gifford A. W. and El-Baz F. (1978) Thickness of mare flow units (abstract). In *Lunar and Planetary Science IX*, pp. 382–384. Lunar and Planetary Institute, Houston.
- Gifford A. W. and El-Baz F. (1981) Thicknesses of lunar mare flow fronts. *Moon and Planets*, 24, 391–398.
- Gillum D. E., Ehmann W. D., Wakita H., and Schmitt R. A. (1972) Bulk and rare earth abundances in the Luna-16 soil levels A and D. *Earth Planet. Sci. Lett.*, 13, 444–449.
- Glasstone S. (1965) *Sourcebook on the Space Sciences*. Van Nostrand, Princeton. 937 pp.
- Goel P. S. and Kothari B. K. (1972) Total nitrogen contents of some Apollo 14 lunar samples by neutron activation analysis. *Proc. Lunar Sci. Conf. 3rd*, pp. 2041–2050.
- Goel P. S., Shukla P. N., Kothari B. K., and Garg A. N. (1975) Total nitrogen in lunar soils, breccias, and rocks. *Geochim. Cosmochim. Acta*, 39, 1347–1352.
- Goins N. R. (1978) Lunar seismology: The internal structure of the Moon. Ph.D. thesis, Massachusetts Institute of Technology, Cambridge, Massachusetts. 666 pp.
- Goins N. R., Toksoz M. N., and Dainty A. M. (1978) Seismic structure of the lunar mantle: An overview. *Proc. Lunar Planet. Sci. Conf. 9th*, pp. 3575–3588.
- Goins N. R., Dainty A. M., and Toksoz M. N. (1980) Seismic energy release from the Moon (abstract). In *Lunar and Planetary Science XI*, pp. 336–338. Lunar and Planetary Institute, Houston.
- Goins N. R., Dainty A. M., and Toksöz N. F. (1981) Seismic energy release of the Moon. *J. Geophys. Res.*, 86, 378–388.
- Gold T. (1966) The Moon's surface. In *The Nature of the Lunar Surface: Proceedings of the 1965 IAU-NASA*

- Symposium* (W. N. Hess, D. H. Menzel, and J. A. O'Keefe, eds.), pp. 107–124. Johns Hopkins, Baltimore.
- Gold T. (1974) The evidence for a surface transport mechanism on the Moon (abstract). In *Lunar Interactions* (D. R. Criswell and J. R. Freeman, eds.), pp. 36–37. The Lunar Science Institute, Houston.
- Gold T. and Williams J. G. (1973) Electrostatic transportation of dust on the Moon. In *Photon and Particle Interactions with Surfaces in Space* (R. L. Grard, ed.), pp. 557–560. Reidel, Dordrecht.
- Gold T. and Williams J. G. (1974) Electrostatic transportation of lunar dust (abstract). In *Lunar Interactions* (D. R. Criswell and J. W. Freeman, eds.), pp. 38–40. The Lunar Science Institute, Houston.
- Gold T., Campbell M. J., and O'Leary B. T. (1970) Optical and high frequency electrical properties of lunar samples. *Proc. Apollo 11 Lunar Sci. Conf.*, pp. 2149–2154.
- Gold T., O'Leary B. T., and Campbell M. (1971) Some physical properties of Apollo 12 lunar samples. *Proc. Lunar Sci. Conf. 2nd*, pp. 2173–2181.
- Gold T., Bilson E., and Yerbury M. (1972) Grain size analysis, optical reflectivity measurements and determination of high frequency electrical properties for Apollo 14 lunar samples. *Proc. Lunar Sci. Conf. 3rd*, pp. 3187–3193.
- Gold T., Bilson E., and Yerbury M. (1973) Grain size analysis and high frequency electrical properties of Apollo 15 and 16 samples. *Proc. Lunar Sci. Conf. 4th*, pp. 3093–3100.
- Gold T., Bilson E., and Baron R. L. (1975) Auger analysis of lunar soil; study of processes which change the surface chemistry and albedo. *Proc. Lunar Sci. Conf. 6th*, pp. 3285–3303.
- Gold T., Bilson E., and Baron R. L. (1976) Electrical properties of Apollo 17 rock and soil samples and a summary of the electrical properties of lunar material at 450 MHz frequency. *Proc. Lunar Sci. Conf. 7th*, pp. 2593–2603.
- Gold T., Bilson E., and Baron R. L. (1977) Electrical properties at 450 MHz of Apollo 15 and 16 deep drill core samples and surface soil samples at the same site. *Proc. Lunar Sci. Conf. 8th*, pp. 1271–1275.
- Goldberg R. H., Burnett D. S., and Tombrello T. A. (1975) Fluorine surface films on lunar samples: Evidence for both lunar and terrestrial origins. *Proc. Lunar Sci. Conf. 6th*, pp. 2189–2200.
- Goldberg R. H., Tombrello T. A., and Burnett D. S. (1976) Fluorine as a constituent in lunar magmatic gases. *Proc. Lunar Sci. Conf. 7th*, pp. 1597–1613.
- Goldstein B. E. (1974) Observations of electrons at the lunar surface. *J. Geophys. Res.*, 79, 23–35.
- Goldstein B. E. (1978) Lunar interaction with the solar wind—effects on lunar electrical conductivity estimates. *Proc. Lunar Planet. Sci. Conf. 9th*, pp. 3093–3112.
- Goldstein J. I. and Axon H. J. (1973) Composition, structure, and thermal history of metallic particles from 3 Apollo 16 soils, 65701, 68501, and 63501. *Proc. Lunar Sci. Conf. 4th*, pp. 751–775.
- Goldstein J. I. and Blau P. J. (1973) Chemistry and thermal history of metal particles in Luna 20 soils. *Geochim. Cosmochim. Acta*, 37, pp. 847–855.
- Goldstein J. I. and Yakowitz H. (1971) Metallic inclusions and metal particles in the Apollo 12 lunar soil. *Proc. Lunar Sci. Conf. 2nd*, pp. 177–191.
- Goldstein J. I., Axon H. J., and Yen C. F. (1972) Metallic particles in the Apollo 14 lunar soil. *Proc. Lunar Sci. Conf. 3rd*, pp. 1037–1064.
- Goldstein J. I., Hewins R. H., and Axon H. J. (1974) Metal silicate relationships in Apollo 17 soils. *Proc. Lunar Sci. Conf. 5th*, pp. 653–671.
- Goles G. G., Randle K., Osawa M., Schmitt R. A., Wakita H., Ehmann W. D., and Morgan J. W. (1970a) Elemental abundances by instrumental activation analyses in chips from 27 lunar rocks. *Proc. Apollo 11 Lunar Sci. Conf.*, pp. 1165–1176.
- Goles G. G., Randle K., Osawa M., Lindstrom D. J., Jerome D. Y., Steinborn T. L., Beyer R. L., Martin M. R., and McKay S. M. (1970b) Interpretations and speculations on elemental abundances in lunar samples. *Proc. Apollo 11 Lunar Sci. Conf.*, pp. 1177–1194.
- Goles G. G., Duncan A. R., Lindstrom D. J., Martin M. R., Beyer R. L., Osawa M., Randle K., Meek L. T., Steinborn T. L., and McKay S. M. (1971) Analyses of Apollo 12 specimens—compositional variations, differentiation processes, and lunar soil mixing models. *Proc. Lunar Sci. Conf. 2nd*, pp. 1063–1082.
- Golombek M. P. (1979) Structural analysis of lunar grabens and the shallow crustal structure of the Moon. *J. Geophys. Res.*, 84, 4657–4666.
- Goodman R. J. (1972) The distribution of Ga and Rb in coexisting groundmass and phenocryst phases of some basic volcanic rocks. *Geochim. Cosmochim. Acta*, 36, 303–317.
- Goodrich C. A., Taylor G. J., Keil K., Kallemeyn G. W., and Warren P. H. (1986) Alkali norite, troctolites, and VHK mare basalts from breccia 14304. *Proc. Lunar Planet. Sci. Conf. 16th*, in *J. Geophys. Res.*, 91, D305–D318.
- Gooley R. C., Brett R., and Warner J. L. (1973) Crystallization history of metal particles in Apollo 16 rake samples. *Proc. Lunar Sci. Conf. 4th*, pp. 799–810.
- Gooley R., Brett R., and Warner J. L. (1974) A lunar rock of deep crustal origin: Sample 76535. *Geochim. Cosmochim. Acta*, 38, 1329–1339.
- Gorenstein P., Golub L., and Bjorkholm P. (1974) Radon emanation from the Moon, spatial and temporal variability. *The Moon*, 9, 129–140.
- Gorshkov E. S., Gus'kova E. G., and Pochtarev V. I. (1972) Magnetic properties of lunar specimens returned by ALS Luna 16. In *COSPAR Space Research XII*, pp. 83–85. Akademie-Verlag, Berlin.
- Gorshkov E. S., Gus'kova E. G., and Pochtarev V. I. (1973) Magnetic investigations of lunar soil delivered by ALS Luna 16. In *COSPAR Space Research XIII*, pp. 961–964. Akademie-Verlag, Berlin.

- Görz H., White W. E., Roy R., and Johnson G. G. (1971) Particle size and shape distributions of lunar fines by CESEMI. *Proc. Lunar Sci. Conf. 2nd*, pp. 2021–2025.
- Görz H., White E. W., Johnson G. G., and Pearson M. W. (1972) CESEMI studies of Apollo 14 and 15 fines. *Proc. Lunar Sci. Conf. 3rd*, pp. 3195–3200.
- Goswami J. N. and Lal D. (1977) Particle track correlation studies in lunar soils: Possible long-term periodic fluctuations in ancient meteoritic flux at 1 A.U. *Proc. Lunar Sci. Conf. 8th*, pp. 813–824.
- Goswami J. N. and Lal D. (1979) Depositional history of the Apollo 17 deep drill core based on particle track record. *Proc. Lunar Planet. Sci. Conf. 10th*, pp. 1253–1267.
- Goswami J. N., Lal D., and Macdougall J. D. (1980) Charge composition and energy spectra of ancient solar flare heavy nuclei. In *The Ancient Sun: Fossil Record in the Earth, Moon and Meteorites* (R. O. Pepin, J. A. Eddy, and R. B. Merrill, eds.), pp. 347–364. Pergamon, New York.
- Goswami J. N., McGuire R. E., Reedy R. C., Lal D., and Jha R. (1988) Solar flare protons and alpha particles during the last three solar cycles. *J. Geophys. Res.*, 93, 7195–7205.
- Graham D. G., Muenow D. W., and Gibson E. K. (1979) Some effects of gas absorption on the high temperature volatile release behavior of a terrestrial basalt, tektite and lunar soil. *Proc. Lunar Planet. Sci. Conf. 10th*, pp. 1617–1627.
- Grant R. W., Housley R. M., Szalkowski F. J., and Marcus H. L. (1974) Auger electron microscopy of lunar samples. *Proc. Lunar Sci. Conf. 5th*, pp. 2423–2439.
- Greeley R. (1971) Lava tubes and channels in the lunar Marius Hills. *The Moon*, 3, 289–314.
- Greeley R. and Hyde J. H. (1972) Lava tubes of the Cave basalts, Mount St. Helens, Washington. *Geol. Soc. Am. Bull.*, 83, 2397–2418.
- Greeley R. and Spudis P. D. (1986) Hadley Rille, lava tubes and mare volcanism at the Apollo 15 site. In *Workshop on the Geology and Petrology of the Apollo 15 Landing Site* (P. D. Spudis and G. Ryder, eds.), pp. 58–61. LPI Tech. Rpt. 86–03, Lunar and Planetary Institute, Houston.
- Green D. H. and Ringwood A. E. (1973) Significance of a primitive lunar basaltic composition present in Apollo 15 soils and breccias. *Earth Planet. Sci. Lett.*, 19, 1–8.
- Green D. H., Ware N. G., Hibberson W. O., and Major A. (1971) Experimental petrology of Apollo 12 basalts: Part 1, sample 12009. *Earth Planet. Sci. Lett.*, 13, 85–96.
- Green D. H., Ringwood A. E., Ware N. G., and Hibberson W. O. (1972) Experimental petrology and petrogenesis of Apollo 14 basalts. *Proc. Lunar Sci. Conf. 3rd*, pp. 197–206.
- Green D. H., Ringwood A. E., Hibberson W. O., and Ware N. G. (1975) Experimental petrology of Apollo 17 mare basalts. *Proc. Lunar Sci. Conf. 6th*, pp. 871–893.
- Greene G. M., King D. T. Jr., Banholzer G. S. Jr., and King E. A. (1975) Size and modal analyses of fines and ultrafines from some Apollo 17 samples. *Proc. Lunar Sci. Conf. 6th*, pp. 517–528.
- Greenwood W. R., Jones R. L., Heiken G. H., Bender M. J., and Hill R. O. (1971) *Lunar Surface Closeup Stereoscopic Photography on the Sea of Tranquility (Apollo 11 Landing Site)*. NASA TM-X-58077. 23 pp.
- Grieve R. A. F. (1981) Impact cratering. *Nature*, 291, 16.
- Grieve R. A. F. (1982) The record of impact on Earth: Implications for major Cretaceous/Tertiary impact event. In *Geological Implications of Impacts of Large Asteroids and Comets on the Earth* (L. T. Silver and P. H. Schultz), pp. 25–38. Geol. Soc. Am. Spec. Pap. 190.
- Grieve R. A. F. and Garvin J. B. (1984) A geometric model for excavation and modification at terrestrial simple craters. *J. Geophys. Res.*, 89, 11561–11572.
- Grieve R. A. F. and Robertson P. B. (1979) The terrestrial cratering record: I. Current status of observations. *Icarus*, 38, 212–229.
- Grieve R. A. F., Dence M. R., and Robertson P. B. (1977) Cratering processes: As interpreted from the occurrence of impact melts. In *Impact and Explosion Cratering* (D. J. Roddy, R. O. Pepin, and R. B. Merrill, eds.), pp. 791–814. Pergamon, New York.
- Grieve R. A. F., Robertson P. B., and Dence M. R. (1981) Constraints on the formation of ring impact structures, based on terrestrial data. In *Multi-Ring Basins, Proc. Lunar Planet. Sci. 12A* (P. H. Schultz and R. B. Merrill, eds.), pp. 37–58. Pergamon, New York.
- Gromov V. V., Leonovich A. K., Lozhkin V. A., Rybakov A. V., Pavlov P. S., Dmitryev A. D., and Shvarev V. V. (1972) Results of investigations of the physical and mechanical properties of the lunar sample from Luna 16. *COSPAR Space Research XII*, pp. 43–52. Akademie-Verlag, Berlin.
- Gromov V. V., Leonovich A. K., Shvarev V. V., Loshkin V. A., Penetrigov V. N., Semenov P. S., Ribakov A. V., Naumov P. N., Grushevsky V. P., and Gubarev V. M. (1979) The results of an investigation of the physical and mechanical properties of lunar soil in nitrogen gas. In *Regolith from the Highland Region of the Moon*, pp. 686–690. Nauka, Moscow (in Russian).
- Gros J., Takahashi H., Hertogen J., Morgan J. W., and Anders E. (1976) Composition of the projectiles that bombarded the lunar highlands. *Proc. Lunar Sci. Conf. 7th*, pp. 2403–2425.
- Grossman J. J., Mukherjee N. R., and Ryan J. A. (1972) Microphysical, microchemical and adhesive properties of lunar material, III. Gas interactions with lunar material. *Proc. Lunar Sci. Conf. 3rd*, pp. 2259–2269.
- Grove T. L. (1978) Cooling histories of Luna 24 very low Ti (VLT) ferrobasalts: An experimental study. *Proc. Lunar Planet. Sci. Conf. 9th*, pp. 565–584.
- Grove T. L. (1982) Use of lamellae in lunar clinopyroxenes as cooling rate speedometers: An experimental calibration. *Am. Mineral.*, 67, 251–268.
- Grove T. L. and Beaty D. W. (1980) Classification, experimental petrology and possible volcanic histories of the Apollo 11 high-K basalts. *Proc. Lunar Planet. Sci. Conf. 11th*, pp. 149–177.
- Grove T. L. and Bence A. E. (1977) Experimental study of pyroxene-liquid interaction in quartz-normative basalt 15597. *Proc. Lunar Sci. Conf. 8th*, pp. 1549–1579.

- Grove T. L. and Bence A. E. (1979) Crystallization kinetics in a multiply saturated basalt magma: An experimental study of Luna 24 ferrobasalt. *Proc. Lunar Planet. Sci. Conf. 10th*, pp. 439–478.
- Grove T. L. and Raudsepp M. (1978) Effects of kinetics on the crystallization of quartz normative basalt 15597: An experimental study. *Proc. Lunar Planet. Sci. Conf. 9th*, pp. 585–599.
- Grove T. L. and Vaniman D. T. (1978) Experimental petrology of very low Ti (VLT) basalts. In *Mare Crisium: The View from Luna 24* (J. J. Papike and R. B. Merrill, eds.), pp. 445–472. Pergamon, New York.
- Grove T. L. and Walker D. (1977) Cooling histories of Apollo 15 quartz-normative basalts. *Proc. Lunar Sci. Conf. 8th*, pp. 1501–1520.
- Grove T. L., Walker D., Longhi J., Stolper E., and Hays J. F. (1973) Petrology of rock 12002 and origin of picritic basalts at Oceanus Procellarum. *Proc. Lunar Sci. Conf. 4th*, pp. 995–1011.
- Grün E., Zook H. A., Fechtig H., and Giese R. H. (1985) Collisional balance of the meteoritic complex. *Icarus*, 62, 244–272.
- Guest J. E. and Murray J. B. (1976) Volcanic features of the nearside equatorial lunar maria. *J. Geol. Soc. Lond.*, 132, 251–258.
- Gurtler C. A. and Grew G. W. (1968) Meteoroid hazard near Moon. *Science*, 161, 462–464.
- Gutschewski G. L., Kinsler D. C., and Whitaker E. (1971) *Atlas and Gazetteer of the Near Side of the Moon*. NASA SP-241. 538 pp.
- Habakov A. V. (1949) *Grundlegende Fragen de Entwicklung der Mondoberfläche*. Moscow.
- Hafner S. S., Niebuhr H. H., and Zeira S. (1973) Ferric iron in plagioclase crystals from anorthosite 15415 (abstract). In *Lunar Science IV*, pp. 326–328. The Lunar Science Institute, Houston.
- Hagfors T. (1961) Some properties of radio waves reflected from the Moon and planets. *J. Geophys. Res.*, 66, 777–785.
- Hagfors T. (1964) Backscattering from an undulating surface with applications to radar returns from the Moon. *J. Geophys. Res.*, 69, 3779–3784.
- Hagfors T. (1966) Relationship of geometric optics and autocorrelation approaches to the analysis of lunar and planetary data. *J. Geophys. Res.*, 71, 379–383.
- Hagfors T. (1967) A study of the depolarization of lunar radar echoes. *Radio Sci.*, 2, 445–465.
- Hagfors T. (1968) Relations between rough surfaces and their scattering properties as applied to radar astronomy. In *Radar Astronomy* (J. V. Evans and T. Hagfors, eds.), pp. 187–218. McGraw-Hill, New York.
- Hagfors T. (1970) Remote probing of the Moon by infrared and microwave emissions and by radar. *Radio Sci.*, 5, 189–227.
- Hagfors T. and Campbell D. B. (1973) Mapping of planetary surfaces with radar. *Proc. IEEE*, 61, 1219–1225.
- Hagfors T. and Evans J. V. (1968) Radar studies of the Moon. In *Radar Astronomy* (J. V. Evans and T. Hagfors, eds.), pp. 219–273. McGraw-Hill, New York.
- Hagfors T., Brockelman R. A., Danforth H. H., Hanson L. B., and Hyed G. M. (1965) Tenuous surface layer on the Moon—evidence derived from radar observations. *Science*, 150, 1153–1156.
- Hagfors T., Green J. L., and Guillen A. (1969) Determination of the albedo of the Moon at a wavelength of 6 meters. *Astron. J.*, 74, 1214–1219.
- Haggerty S. E. (1971a) Compositional variations in lunar spinels. *Nature Phys. Sci.*, 233, 156–160.
- Haggerty S. E. (1971b) Subsolidus reduction of lunar spinels. *Nature Phys. Sci.*, 234, 113–117.
- Haggerty S. E. (1972a) Apollo 14 subsolidus reduction and compositional variations of spinels. *Proc. Lunar Sci. Conf. 3rd*, pp. 305–333.
- Haggerty S. E. (1972b) Chemical characteristics of spinels in some Apollo 15 basalts (abstract). In *The Apollo 15 Lunar Samples* (J. W. Chamberlain and C. Watkins, eds.), pp. 92–97. The Lunar Science Institute, Houston.
- Haggerty S. E. (1972c) Luna 16: An opaque mineral study and a systematic examination of compositional variations of spinels from Mare Fecunditatis. *Earth Planet. Sci. Lett.*, 13, 328–352.
- Haggerty S. E. (1972d) Solid solutions, subsolidus reduction and compositional characteristics of spinels in some Apollo 15 basalts. *Meteoritics*, 7, 353–370.
- Haggerty S. E. (1972e) The mineral chemistry of some decomposition and reaction assemblages associated with Cr-Zr, Ca-Zr, and Fe-Mg-Zr titanites (abstract). In *The Apollo 15 Lunar Samples* (J. W. Chamberlain and C. Watkins, eds.), pp. 88–91. The Lunar Science Institute, Houston.
- Haggerty S. E. (1973a) Armalcolite and genetically associated opaque minerals in the lunar samples. *Proc. Lunar Sci. Conf. 4th*, pp. 777–797.
- Haggerty S. E. (1973b) Luna 20: Mineral Chemistry of spinel, pleonaste, chromite, ulvöspinel, ilmenite, and rutile. *Geochim. Cosmochim. Acta*, 37, 857–867.
- Haggerty S. E. (1977) Apollo 14: Oxide, metal, and olivine mineral chemistries in 14072 with a bearing on the temporal relationships of subsolidus reduction. *Proc. Lunar Sci. Conf. 8th*, pp. 1809–1829.
- Haggerty S. E. (1978a) Luna 24: Systematics in spinel mineral chemistry in the context of an intrusive petrogenetic grid. In *Mare Crisium: The View From Luna 24*, (R. B. Merrill and J. J. Papike, eds.), pp. 523–536. Pergamon, New York.
- Haggerty S. E. (1978b) The redox state of planetary basalts. *Geophys. Res. Lett.*, 5, 443–446.
- Haggerty S. E., Boyd F. R., Bell P. M., Finger L. W., and Bryan W. B. (1970) Opaque minerals and olivine in lavas and breccias from Mare Tranquillitatus. *Proc. Apollo 11 Lunar Sci. Conf.*, pp. 513–538.
- Halajian J. D. (1964) *The Case for a Cohesive Lunar Surface Model*. Grumman Research Dept. Report ADR 04–40–64.2, Grumman Aircraft Engineering Corp., Bethpage, New York.
- Halajian J. D. (1966) *Mechanical, Optical, Thermal, and Electrical Properties of the Surveyor I Landing Site*.

- Grumman Research Dept. Report AS424-4, Grumman Aircraft Engineering Corp., Bethpage, New York.
- Hale W. (1980) Orientations of central peaks in lunar craters: Implications for regional structural trends. In *Proceedings of the Conference on the Lunar Highlands Crust* (J. J. Papike and R. B. Merrill, eds.), pp. 197-209. Pergamon, New York.
- Hale W. S. and Grieve R. A. F. (1982) Volumetric analysis of complex lunar craters: Implications for basin ring formation. *Proc. Lunar Planet. Sci. Conf. 13th*, in *J. Geophys. Res.*, 87, A65-A76.
- Hale W. S. and Head J. W. (1979) Central peaks in lunar craters: Morphology and morphometry. *Proc. Lunar Planet. Sci. Conf. 10th*, pp. 2623-2633.
- Hall J. L., Solomon S. C., and Head J. W. (1981) Lunar floor-fractured craters: Evidence for viscous relaxation of crater topography. *J. Geophys. Res.*, 86, 9357-9552.
- Hanan B. B. and Tilton G. R. (1987) 60025: Relict of primitive lunar crust? *Earth Planet. Sci. Lett.*, 84, 15-21.
- Hansen E. C., Smith J. V., and Steele I. M. (1980) Petrology and mineral chemistry of 67667, a unique feldspathic ilherzolite. *Proc. Lunar Planet. Sci. Conf. 11th*, pp. 523-533.
- Hansen T. P. (1970) *Guide to Lunar Orbiter Photographs*. NASA SP-242. 125 pp.
- Hapke B. W. (1963) A theoretical photometric function for the lunar surface. *J. Geophys. Res.*, 68, 4571-4586.
- Hapke B. (1981) Bidirectional reflectance spectroscopy: 1. Theory. *J. Geophys. Res.*, 86, 3039-3054.
- Hapke B. (1984) Bidirectional reflectance spectroscopy: 3. Correction for macroscopic roughness. *Icarus*, 59, 41-59.
- Hargraves J. K. (1959) Radio observations of the lunar surface. *Proc. Phys. Soc. London*, 73, 536-537.
- Hargraves R. B. and Hollister L. S. (1972) Mineralogic and petrologic study of lunar anorthosite slide 15415,18. *Science*, 175, 430-432.
- Hartmann W. K. (1966) Early lunar cratering. *Icarus*, 5, 406-418.
- Hartmann W. K. (1972) Paleocratering of the Moon. Review of post-Apollo data. *Astrophys. Space Sci.*, 17, 48-64.
- Hartmann W. K. (1975) Lunar "cataclysm": A misconception. *Icarus*, 24, 181-187.
- Hartmann W. K. (1980) Dropping stones in magma oceans: Effects of early lunar cratering. In *Proceedings of the Conference on the Lunar Highlands Crust* (J. J. Papike and R. B. Merrill, eds.), pp. 155-171. Pergamon, New York.
- Hartmann W. K. and Davis D. R. (1975) Satellite-sized planetesimals and lunar origin. *Icarus*, 24, 504-515.
- Hartmann W. K. and Kuiper G. P. (1962) Concentric structures surrounding lunar basins. *Commun. Lunar Planet. Lab.*, 1, 51-66.
- Hartmann W. K. and Wood C. A. (1971) Origin and evolution of multi-ring basins. *The Moon*, 3, 2-78.
- Hartmann W. K., Phillips R. J., and Taylor G. J., eds. (1986) *Origin of the Moon*. Lunar and Planetary Institute, Houston. 781 pp.
- Hartung J. B. (1976) Age of 20-km diameter lunar crater: 797 years, 62 ± 2 days (abstract). In *Lunar Science VII*, pp. 348-350. The Lunar Science Institute, Houston.
- Hartung J. B. and Storzer D. (1974) Lunar microcraters and their solar flare track record. *Proc. Lunar Sci. Conf. 5th*, pp. 2527-2541.
- Hartung J. B., Hauser E. E., Hörz F., Morrison D. A., Schonfeld E., Zook H. A., Mandeville J. C., McDonnell J. A. M., Schaal R. B., and Zinner E. (1978) Lunar surface processes: Report of the 12054 consortium. *Proc. Lunar Planet. Sci. Conf. 9th*, pp. 2507-2537.
- Haselton J. D. and Nash W. P. (1975) A model for the evolution of opaques in mare lavas. *Proc. Lunar Sci. Conf. 6th*, pp. 747-755.
- Haskin L. A. and Korotev R. L. (1977) Test of a model for trace element partition during closed-system solidification of a silicate liquid. *Geochim. Cosmochim. Acta*, 41, 921-939.
- Haskin L. A., Haskin M. A., Frey F. A., and Wildeman T. R. (1968) Relative and absolute abundances of the rare earths. In *Origin and Distribution of the Elements* (L. H. Ahrens, ed.), pp. 889-912. Pergamon, New York.
- Haskin L. A., Allen R. O., Helmke P. A., Paster T. P., Anderson M. A., Korotev R. L., and Zweifel K. A. (1970) Rare earths and other trace elements in Apollo 11 lunar samples. *Proc. Apollo 11 Lunar Sci. Conf.*, pp. 1213-1231.
- Haskin L. A., Helmke P. A., Allen R. O., Anderson M. R., Korotev R. L., and Zweifel K. A. (1971) Rare-earth elements in Apollo 12 lunar materials. *Proc. Lunar Sci. Conf. 2nd*, pp. 1307-1317.
- Haskin L. A., Helmke P. A., Blanchard D. P., Jacobs J. W., and Telunder K. (1973) Major and trace element abundances in samples from the lunar highlands. *Proc. Lunar Sci. Conf. 4th*, pp. 1275-1296.
- Haskin L. A., Shih C.-Y., Bansal B. M., Rhodes J. M., Wiesman H., and Nyquist L. E. (1974) Chemical evidence for the origin of 76535 as a cumulate. *Proc. Lunar Sci. Conf. 5th*, pp. 1213-1225.
- Haskin L. A., Lindstrom M. M., Salpas P. A., and Lindstrom D. J. (1981) On compositional variations among lunar anorthosites. *Proc. Lunar Planet. Sci. 12B*, pp. 41-66.
- Hawke B. R. and Bell J. F. (1981) Remote sensing studies of lunar dark-halo impact craters: Preliminary results and implications for early volcanism. *Proc. Lunar Planet. Sci. 12B*, pp. 665-678.
- Hawke B. R. and Head J. W. (1977) Pre-Imbrian history of the Fra Mauro region and Apollo 14 sample provenance. *Proc. Lunar Sci. Conf. 8th*, pp. 2741-2761.
- Hawke B. K., MacLaskey D., McCord T. B., Adams J. B., Head J. W., Pieters C. M., and Zisk S. H. (1979) Multispectral imaging of the Apollo 15 Apennine region: The identification and distribution of regional pyroclastic deposits. *Proc. Lunar Planet. Sci. Conf. 10th*, pp. 2995-3015.
- Haymes R. C. (1985) Lunar based gamma ray astronomy. In *Lunar Bases and Space Activities of the 21st Century* (W. W. Mendell, ed.), pp. 307-314. Lunar and Planetary Institute, Houston.

- Hazen R. M., Mao H. K., and Bell P. M. (1977) Effects of compositional variation on absorption spectra of lunar olivines. *Proc. Lunar Sci. Conf. 8th*, pp. 1081–1090.
- Hazen R. M., Bell P. M., and Mao H. K. (1978) Effects of compositional variation on absorption spectra of lunar pyroxenes. *Proc. Lunar Planet. Sci. Conf. 9th*, pp. 2919–2934.
- Head J. W. (1974a) Orientale multi-ringed basin interior and implications for the petrogenesis of lunar highland samples. *The Moon*, 11, 327–356.
- Head J. W. (1974b) Stratigraphy of the Descartes Region (Apollo 16): Implications for the origin of samples. *The Moon*, 11, 77–100.
- Head J. W. (1976a) Lunar volcanism in space and time. *Rev. Geophys. Space Phys.*, 14, 265–300.
- Head J. W. (1976b) Evidence for the sedimentary origin of Imbrium sculpture and lunar basin radial texture. *The Moon*, 15, 445–462.
- Head J. W. (1977) Origin of outer rings in lunar multi-ring basins: Evidence from morphology and ring spacing. In *Impact and Explosion Cratering* (D. J. Roddy, R. O. Pepin, and R. B. Merrill, eds.), pp. 567–573. Pergamon, New York.
- Head J. W. (1979) Serenitatis multi-ringed basin: Regional geology and basin ring interpretation. *Moon and Planets*, 21, 439–462.
- Head J. W. (1982) Lava flooding of ancient planetary crusts: Geometry, thickness, and volumes of flooded lunar impact basins. *Moon and Planets*, 26, 61–88.
- Head J. W. and Gifford A. (1980) Lunar mare domes: Classification and mode of origin. *Moon and Planets*, 22, 235–258.
- Head J. W. and McCord T. B. (1978) Imbrian-age highland volcanism on the Moon: The Gruithuisen and Mairan domes. *Science*, 199, 1433–1436.
- Head J. W. and Wilson L. (1979) Alphonsus type dark-halo craters: Morphology, morphometry and eruption conditions. *Proc. Lunar Planet. Sci. Conf. 10th*, pp. 2861–2897.
- Head J. W., Settle M., and Stein R. S. (1975) Volume of material ejected from major basins and implications for the depth of excavation of lunar samples. *Proc. Lunar Sci. Conf. 6th*, pp. 2805–2829.
- Head J. W., Adams J. B., McCord T. B., Pieters C., and Zisk S. (1978) Regional stratigraphy and geologic history of Mare Crisium. In *Mare Crisium: The View from Luna 24* (R. B. Merrill and J. J. Papike, eds.), pp. 43–74. Pergamon, New York.
- Heiken G. (1975) Petrology of lunar soils. *Rev. Geophys. Space Phys.*, 13, 567–587.
- Heiken G. H. and Carrier W. D. III (1971) *Lunar Surface Closeup Stereoscopic Photography on the Ocean of Storms (Apollo 12 Landing Site)*. NASA TM X-58078. 40 pp.
- Heiken G. and McEwen M. C. (1972) The geologic setting of the Luna 20 site. *Earth Planet. Sci. Lett.*, 17, 3–6.
- Heiken G. and McKay D. S. (1974) Petrography of Apollo 17 soils. *Proc. Lunar Sci. Conf. 5th*, pp. 843–860.
- Heiken G. and McKay D. S. (1977) A model for eruption behavior of a volcanic vent in eastern Mare Serenitatis. *Proc. Lunar Sci. Conf. 8th*, pp. 3243–3255.
- Heiken G. H. and McKay D. S. (1978) Petrology of a sequence of pyroclastic rocks from the valley of Taurus-Littrow (Apollo 17 landing site). *Proc. Lunar Planet. Sci. Conf. 9th*, pp. 1933–1943.
- Heiken G. H., McKay D. S., and Fruland R. M. (1973) Apollo 16 soils: Grain size analysis and petrography. *Proc. Lunar Sci. Conf. 4th*, pp. 251–265.
- Heiken G. H., McKay D. S., and Brown R. W. (1974) Lunar deposits of possible pyroclastic origin. *Geochim. Cosmochim. Acta*, 38, 1703–1718.
- Heiken G. H., Morris R. V., McKay D. S., and Fruland R. M. (1976) Petrographic and ferromagnetic resonance studies of the Apollo 15 deep drill core. *Proc. Lunar Sci. Conf. 7th*, pp. 93–111.
- Heinzen C. R. and Peer W. F. (1971) *Lunar Surface Resolution: Coverage of Lunar Orbiter Photography*. JPL Publication 760–63, Jet Propulsion Laboratory, Pasadena. 5 pp.
- Helmke P. A. and Haskin L. A. (1972a) Rare earths and other trace elements in Apollo 15 samples (abstract). In *The Apollo 15 Lunar Samples* (J. W. Chamberlain and C. Watkins, eds.), pp. 217–220. The Lunar Science Institute, Houston.
- Helmke P. A. and Haskin L. A. (1972b) Rare earths and other trace elements in Luna 16 soil. *Earth Planet. Sci. Lett.*, 13, 441–443.
- Helmke P. A., Haskin L. A., Korotev R. L., and Ziege K. E. (1972) Rare earths and other trace elements in Apollo 14 samples. *Proc. Lunar Sci. Conf. 3rd*, pp. 1275–1292.
- Helmke P. A., Blanchard D. P., Jacobs J. W., and Haskin L. A. (1973) Rare earths, other trace elements and iron in Luna 20 samples. *Geochim. Cosmochim. Acta*, 37, 869–874.
- Hertogen J., Janssens M.-J., Takahashi H., Palme H., and Anders E. (1977) Lunar basins and craters: Evidence for systematic compositional changes of bombarding population. *Proc. Lunar Sci. Conf. 8th*, pp. 17–45.
- Heusser E. (1985) ³⁹Ar-⁴⁰Ar Datierungen von Apollo 14 Hochland Gesteinen. Diploma thesis, Max-Planck-Institut, Heidelberg. 45 pp.
- Hewins R. H. and Goldstein J. I. (1974) Metal-olivine associations and Ni-Co contents in two Apollo 12 mare basalts. *Earth Planet. Sci. Lett.*, 24, 59–70.
- Hewins R. H. and Goldstein J. I. (1975) The provenance of metal in anorthositic rocks. *Proc. Lunar Sci. Conf. 6th*, pp. 343–362.
- Heywood H. (1971) Particle size and shape distribution for lunar fines sample 12057,72. *Proc. Lunar Sci. Conf. 2nd*, pp. 1989–2001.
- Higuchi H. and Morgan J. W. (1975) Ancient meteoritic component in Apollo 17 boulders. *Proc. Lunar Sci. Conf. 6th*, pp. 1625–1651.
- Hintenberger H., Weber H. W., Voshage H., Wänke H., Begemann F., and Wlotzka F. (1970) Concentrations and isotopic abundances of the rare gases, hydrogen and nitrogen in Apollo 11 lunar matter. *Proc. Apollo 11 Lunar Sci. Conf.*, pp. 1269–1282.

- Hintenberger H., Weber H. W., and Schultz L. (1974) Solar, spallogenic, and radiogenic rare gases in Apollo 17 soils and breccias. *Proc. Lunar Sci. Conf. 5th*, pp. 2005–2022.
- Hintenberger H., Schultz L., and Weber H. W. (1975) A comparison of noble gases in lunar fines and soil breccias: Implications for the origin of soil breccias. *Proc. Lunar Sci. Conf. 6th*, pp. 2262–2270.
- Hlava P. F., Prinz M., and Keil K. (1972) Niobian rutile in an Apollo 14 KREEP fragment. *Meteoritics*, 7, 479–485.
- Hobbs B. A., ed. (1980) Collective review papers presented at the 4th IAGA Workshop on Electromagnetic Induction in the Earth and Moon. *Geophys. Surv.*, 4, 3–185.
- Hodges C. A. and Wilhelms D. E. (1978) Formation of lunar basin rings. *Icarus*, 34, 294–323.
- Hodges C. A., Muehlberger W. R., and Ulrich G. E. (1973) Geologic setting of Apollo 16. *Proc. Lunar Sci. Conf. 4th*, pp. 1–25.
- Hodges F. N. and Kushiro I. (1974) Apollo 17 petrology and experimental determination of differentiation sequences in model Moon compositions. *Proc. Lunar Sci. Conf. 5th*, pp. 505–520.
- Hodges R. R. Jr. (1973) Helium and hydrogen in the lunar atmosphere. *J. Geophys. Res.*, 78, 8055–8064.
- Hodges R. R. Jr. (1975) Formation of the lunar atmosphere. *The Moon*, 14, 139–157.
- Hodges R. R. Jr. (1980) Lunar cold traps and their influence on argon-40. *Proc. Lunar Planet. Sci. Conf. 11th*, pp. 2463–2477.
- Hodges R. R. Jr., Hoffman J. H., and Johnson F. S. (1974) The lunar atmosphere. *Icarus*, 21, 415–426.
- Hoffman J. H. and Hodges R. R. Jr. (1975) Molecular gas species in the lunar atmosphere. *The Moon*, 14, 159–167.
- Hoffman J. H., Hodges R. R. Jr., Johnson F. S., and Evans D. E. (1973) Lunar atmospheric composition experiment. In *Apollo 17 Preliminary Science Report*, pp. 17–1 to 17–9. NASA SP-330.
- Hohenberg C. M., Marti K., Podosek F. A., Reedy R. C., and Shirck J. R. (1978) Comparisons between observed and predicted cosmogenic noble gases in lunar samples. *Proc. Lunar Planet. Sci. Conf. 9th*, pp. 2311–2344.
- Holcomb R. (1971) Terraced depressions in lunar maria. *J. Geophys. Res.*, 76, 5703–5711.
- Hollister L. S. (1973) Sample 67955: A description and a problem. *Proc. Lunar Sci. Conf. 4th*, pp. 633–641.
- Hollister L. S. and Crawford M. L. (1977) Melt immiscibility in Apollo 15 KREEP: Origin of Fe-rich mare basalts. *Proc. Lunar Sci. Conf. 8th*, pp. 2419–2432.
- Hollister L. S. and Hargraves R. B. (1970) Compositional zoning and its significance in pyroxenes from two coarse grained Apollo 11 samples. *Proc. Apollo 11 Lunar Sci. Conf.*, pp. 541–550.
- Hollister L. S., Trzcinski W. E. Jr., Hargraves R. B., and Kulick C. G. (1971) Petrogenetic significance of pyroxenes in two Apollo 12 samples. *Proc. Lunar Sci. Conf. 2nd*, pp. 529–557.
- Holmes H. F., Fuller E. L., and Gammage R. B. (1973) Interaction of gases with lunar materials: Apollo 12, 14, and 16 samples. *Proc. Lunar Sci. Conf. 4th*, pp. 2413–2423.
- Holmes H. F., Fuller E. L., and Gammage R. B. (1974) Some surface properties of Apollo 17 soils. *Proc. Lunar Sci. Conf. 5th*, pp. 2275–2285.
- Holsapple K. A. and Schmidt R. M. (1986) Point source solutions and coupling parameters in cratering mechanics. *J. Geophys. Res.*, 92, 6350–6376.
- Hood L. L. (1986) Geophysical constraints on the lunar interior. In *Origin of the Moon* (W. K. Hartmann, R. J. Phillips, and G. J. Taylor, eds.), pp. 361–410. Lunar and Planetary Institute, Houston.
- Hood L. L. (1987) Magnetic field and remanent magnetization effects of basin-forming impacts on the Moon. *Geophys. Res. Lett.*, 14, 844–847.
- Hood L. L. and Williams C. R. (1989) The lunar swirls: Distribution and possible origins. *Proc. Lunar Planet. Sci. Conf. 19th*, pp. 99–113.
- Hood L. L., Coleman P. J., and Wilhelms D. E. (1979) Lunar nearside magnetic anomalies. *Proc. Lunar Planet. Sci. Conf. 10th*, pp. 2235–2257.
- Hood L. L., Herbert F., and Sonett C. P. (1982a) Further efforts to limit lunar internal temperatures from electrical conductivity determinations. *Proc. Lunar Planet. Sci. Conf. 13th*, in *J. Geophys. Res.*, 87, A109–A116.
- Hood L. L., Herbert F., and Sonett C. P. (1982b) The deep lunar electrical conductivity profile, structural and thermal inferences. *J. Geophys. Res.*, 87, 5311–5326.
- Hood L. L., Sonett C. P., and Russell C. T. (1985) The next generation geophysical investigation of the Moon. In *Lunar Bases and Space Activities of the 21st Century* (W. W. Mendell, ed.), pp. 253–263. Lunar and Planetary Institute, Houston.
- Horai K. and Winkler J. L. (1975) Thermal diffusivity of lunar rock sample 12002,85. *Proc. Lunar Sci. Conf. 6th*, pp. 3207–3215.
- Horai K. and Winkler J. L. (1976) Thermal diffusivity of four Apollo 17 rock samples. *Proc. Lunar Sci. Conf. 7th*, pp. 3183–3204.
- Horai K. and Winkler J. L. (1980) Thermal diffusivity of two Apollo 11 samples, 10020,44 and 10065,23: Effect of petrofabrics on the thermal conductivity of porous lunar rocks under vacuum. *Proc. Lunar Planet. Sci. Conf. 11th*, pp. 1777–1788.
- Hörz F. (1968) Statistical measurements of deformation structures and refractive indices in experimentally shock loaded quartz. In *Shock Metamorphism of Natural Materials* (B. M. French and N. M. Short, eds.), pp. 243–254. Mono, Baltimore.
- Hörz F. (1977) Impact cratering and regolith dynamics. *Phys. Chem. Earth*, 10, 3–15.
- Hörz F. (1978) How thick are lunar mare basalts? *Proc. Lunar Planet. Sci. Conf. 9th*, pp. 3311–3331.
- Hörz F. (1985a) Lava tubes: Potential shelters for habitats. In *Lunar Bases and Space Activities of the 21st Century* (W. W. Mendell, ed.), pp. 405–412. Lunar and Planetary Institute, Houston.

- Hörz F. (1985b) Mass extinctions and cosmic collisions: A lunar test. In *Lunar Bases and Space Activities of the 21st Century* (W. W. Mendell, ed.), pp. 349–358. Lunar and Planetary Institute, Houston.
- Hörz F. and Quaide W. L. (1973) Debye-Scherrer investigations of experimentally shocked silicates. *The Moon*, 6, 45–82.
- Hörz F. and Schaal R. B. (1980) Asteroidal agglutinate formation and implications for asteroidal surfaces. *Icarus*, 46, 337–353.
- Hörz F., Gibbons R. V., Gault D. E., Hartung J. B., and Brownlee D. E. (1975) Some correlation of rock exposure ages and regolith dynamics. *Proc. Lunar Sci. Conf. 6th*, pp. 3495–3508.
- Hörz F., Gibbons R. V., Hill R. E., and Gault D. E. (1976) Large scale cratering of the lunar highlands: Some Monte Carlo model considerations. *Proc. Lunar Sci. Conf. 7th*, pp. 2931–2945.
- Hörz F., Gall H., Huttner R., and Oberbeck V. R. (1977) Shallow drilling in the “Bunte Breccia” impact deposits, Ries Crater, Germany. In *Impact and Explosion Cratering* (D. J. Roddy, R. O. Pepin, and R. B. Merrill, eds.), pp. 425–558. Pergamon, New York.
- Hörz F., Ostertag R., and Rainey D. A. (1983) Bunte Breccia of the Ries: Continuous deposits of large impact craters. *Rev. Geophys. Space Phys.*, 21, 1667–1725.
- Hörz F., Cintala M. J., See T. H., Cardenas F., and Thompson T. D. (1984) Grain size evolution and fractionation trends in an experimental regolith. *Proc. Lunar Planet. Sci. Conf. 15th*, in *J. Geophys. Res.*, 89, C183–C196.
- Houck K. J. (1982a) Petrologic variations in Apollo 16 surface soils. *Proc. Lunar Planet. Sci. Conf. 13th*, in *J. Geophys. Res.*, 87, A197–A209.
- Houck K. J. (1982b) Modal petrology of six soils from Apollo 16 double drive tube core 64002. *Proc. Lunar Planet. Sci. Conf. 13th*, in *J. Geophys. Res.*, 87, A210–A220.
- Housen K. R., Wilkening L. L., Chapman C. R., and Greenberg R. (1979) Asteroidal regoliths. *Icarus*, 39, 317–351.
- Housley R. M. and Morin F. J. (1972) Electrical conductivity of olivine and the lunar temperature profile. *The Moon*, 4, 35–38.
- Housley R. M., Grant R. W., and Abdel-Gawad M. (1972) Study of excess Fe metal in the lunar fines by magnetic separation, Mössbauer spectroscopy, and microscopic examination. *Proc. Lunar Sci. Conf. 3rd*, pp. 1065–1076.
- Housley R. M., Cirlin E. H., and Grant R. W. (1973a) Characterization of fines from the Apollo 16 site. *Proc. Lunar Sci. Conf. 4th*, pp. 2729–2735.
- Housley R. M., Grant R. W., and Patton N. E. (1973b) Origin and characteristics of excess Fe metal in lunar glass welded aggregates. *Proc. Lunar Sci. Conf. 4th*, pp. 2737–2749.
- Houston W. N. and Mitchell J. K. (1971) Lunar core tube sampling. *Proc. Lunar Sci. Conf. 2nd*, pp. 1953–1958.
- Houston W. N. and Namiq L. I. (1971) Penetration resistance of lunar soils. *J. Terramechanics*, 8, 59–69.
- Houston W. N., Hovland H. J., Mitchell J. K., and Namiq L. I. (1972) Lunar soil porosity and its variation as estimated from footprints and boulder tracks. *Proc. Lunar Sci. Conf. 3rd*, pp. 3255–3263.
- Houston W. N., Moriwaki Y., and Chang C.-S. (1973) Downslope movement of lunar soil and rock caused by meteoroid impact. *Proc. Lunar Sci. Conf. 4th*, pp. 2425–2435.
- Houston W. N., Mitchell J. K., and Carrier W. D. III (1974) Lunar soil density and porosity. *Proc. Lunar Sci. Conf. 5th*, pp. 2361–2364.
- Hovland H. J. and Mitchell J. K. (1971) *Mechanics of Rolling Sphere-Soil Slope Interaction*. Final Report, Vol. II of IV, NASA Contract 8–21432, Space Sciences Laboratory, Univ. of California, Berkeley.
- Hovland H. J. and Mitchell J. K. (1973) Boulder tracks and nature of lunar soil. *The Moon*, 6, 164–175.
- Howard K. A. and Muehlberger W. R. (1973) Lunar thrust faults in the Taurus-Littrow region. In *Apollo 17 Preliminary Science Report*, pp. 31–23 to 31–25. NASA SP-330.
- Howard K. A., Head J. W., and Swann G. A. (1972) Geology of Hadley Rille. *Proc. Lunar Sci. Conf. 3rd*, pp. 1–14.
- Howard K. A., Can M. H., and Muehlberger W. R. (1973) Basalt stratigraphy of southern Mare Serenitatis. In *Apollo 17 Preliminary Science Report*, pp. 29–1 to 29–12. NASA SP-330.
- Howard K. A., Wilhelms P. E., and Scott D. H. (1974) Lunar basin formation and highland stratigraphy. *Rev. Geophys. Space Phys.*, 12, 309–327.
- Hu H.-N. and Taylor L. A. (1978) Soils from Mare Crisium: Agglutinitic glass chemistry and soil development. In *Mare Crisium: The View from Luna 24* (R. B. Merrill and J. J. Papike, eds.), pp. 291–302. Pergamon, New York.
- Hubbard N. J. (1979) Regional chemical variations in lunar basaltic lavas. *Proc. Lunar Planet. Sci. Conf. 10th*, pp. 1753–1774.
- Hubbard N. J., Gast P. W., Meyer C., Nyquist L. E., Shih C.-Y., and Weismann H. (1971) Chemical composition of lunar anorthosites and their parent liquids. *Earth Planet. Sci. Lett.*, 13, 71–75.
- Hubbard N. J., Gast P. W., Rhodes J. M., Bansal B. M., Wiessman H., and Church S. E. (1972a) Nonmare basalts: Part II. *Proc. Lunar Sci. Conf. 3rd*, pp. 1161–1179.
- Hubbard N. J., Nyquist L. E., Rhodes J. M., Bansal B. M., Wiessman H., and Church S. E. (1972b) Chemical features of the Luna 16 regolith sample. *Earth Planet. Sci. Lett.*, 13, 423–428.
- Hubbard N. J., Rhodes J. M., Gast P. W., Bansal B. M., Shih C.-Y., Wiessman H., and Nyquist L. E. (1973) Lunar rock types: the role of plagioclase in non-mare and highland rock types. *Proc. Lunar Sci. Conf. 4th*, pp. 1297–1312.
- Hubbard N. J., Rhodes J. M., Wiessman H., Shih C.-Y., and Bansal B. (1974) The chemical definition and interpretation of rock types returned from the non-mare regions of the Moon. *Proc. Lunar Sci. Conf. 5th*, pp. 1227–1246.
- Hubbard N. J., Vinogradov A. P., Ramendik G. I., and Chupakhin M. S. (1977) New data for the Luna 20 core and a survey of published chemical data. In *The Soviet*

- American Conference on Cosmochemistry of the Moon and Planets* (J. H. Pomeroy and N. J. Hubbard, eds.), pp. 259–262. NASA SP-370.
- Hubner W., Kirsten T., and Kiko J. (1975) Rare gases in Apollo 17 soils with emphasis on analysis of size and mineral fractions of soil 74241. *Proc. Lunar Sci. Conf. 6th*, pp. 2009–2026.
- Huebner J. S., Lipin B. R., and Wiggins L. B. (1976) Partitioning of chromium between silicate crystals and melts. *Proc. Lunar Sci. Conf. 7th*, pp. 1195–1220.
- Huebner J. S., Dupa A., Wiggins L. B., and Smith H. E. (1978) Electrical conductivity of orthopyroxene, measurements and implications. *Proc. Lunar Planet. Sci. Conf. 9th*, pp. 561–563.
- Huebner J. S., Dupa A., and Wiggins L. B. (1979) Electrical conductivity of pyroxene which contains trivalent cations, laboratory measurements and the lunar temperature profile. *J. Geophys. Res.*, *84*, 4652–4656.
- Hughes D. W. (1978) Lunar atmosphere past and present. *Nature*, *273*, 489–490.
- Hughes S. S. and Schmitt R. A. (1984) Confirmation of Zr-Hf fractionation in lunar petrogenesis—an interim report (abstract). In *Lunar and Planetary Science XV*, pp. 385–386. Lunar and Planetary Institute, Houston.
- Hughes S. S. and Schmitt R. A. (1985) Sr-Hf-Ta fractionation during lunar evolution. *Proc. Lunar Planet. Sci. Conf. 16th*, in *J. Geophys. Res.*, *90*, D31–D45.
- Hughes T. C., Keays R. R., and Lovering J. F. (1973) Siderophile and volatile trace elements in Apollo 14, 15 and 16 rocks and fines: Evidence for extralunar component and Ti-, Au-, and Ag-enriched rocks in the ancient lunar crust (abstract). In *Lunar Science IV*, pp. 400–402. The Lunar Science Institute, Houston.
- Hughes V. A. (1962) Diffraction theory applied to radio wave scattering from the lunar surface. *Proc. Phys. Soc.*, *80*, 1117–1127.
- Hulme G. (1973) Turbulent lava flows and the formation of lunar sinuous rilles. *Mod. Geol.*, *4*, 107–117.
- Hundhausen A. J. (1972) *Coronal Expansion and Solar Wind*. Springer-Verlag, New York. 238 pp.
- Huneke J. C. (1978) ⁴⁰Ar-³⁹Ar microanalysis of single 74220 glass balls and 72435 breccia clasts. *Proc. Lunar Planet. Sci. Conf. 9th*, pp. 2345–2362.
- Huneke J. C., Jessberger E. K., Podosek F. A., and Wasserburg G. J. (1973) ⁴⁰Ar-³⁹Ar measurements in Apollo 16 and 17 samples and the chronology of metamorphic and volcanic activity in the Taurus-Littrow region. *Proc. Lunar Sci. Conf. 4th*, pp. 1725–1756.
- Huner W., Kirsten T., and Kiko J. (1975) Rare gases in Apollo 17 soils with emphasis on analysis of size and mineral fractions of soil 74241. *Proc. Lunar Sci. Conf. 6th*, pp. 2009–2026.
- Hunt G. R. (1977) Spectral signatures of particulate minerals in the visible and near-infrared. *Geophysics*, *42*, 501–513.
- Husain L., Schaeffer O. A., Funkhouser J., and Sutter J. (1972) The ages of lunar material from Fra Mauro, Hadley Rille, and Spur Crater. *Proc. Lunar Sci. Conf. 3rd*, pp. 1557–1567.
- Hutcheon I. D., Macdougall D., and Price P. B. (1974) Improved determination of the long-term average Fe spectrum from 1 to 460 MeV/amu. *Proc. Lunar Sci. Conf. 5th*, pp. 2561–2576.
- Hutton R. E. and Evensen D. A. (1972) *Lunar Surface Models*. Report by TRW Systems Groups, Redondo Beach.
- Hutton V. R. S. (1976) The electrical conductivity of the earth and planets. *Rep. Prog. Phys.*, *39*, 487–572.
- Ip W.-H. (1986) Electrostatic charging and dust transport at Mercury's surface. *Geophys. Res. Lett.*, *13*, 1133–1136.
- Irvine W. M. (1966) The shadowing effect in diffuse reflection. *J. Geophys. Res.*, *71*, 2931–2937.
- Irving A. J. (1977) Chemical variation and fractionation of KREEP basalt magmas. *Proc. Lunar Sci. Conf. 8th*, pp. 2433–2448.
- Irving A. J. (1978) A review of experimental studies of crystal/liquid trace element partitioning. *Geochim. Cosmochim. Acta*, *42*, 743–770.
- Irving A. J., Merrill R. B., Singleton D. E. (1978) Experimental partitioning of rare earth elements and scandium among armalcolite, ilmenite, olivine and marebasalt liquid. *Proc. Lunar Planet. Sci. Conf. 9th*, pp. 601–612.
- Ishimaru A. (1978a) *Multiple Scattering Turbulence: Rough Surfaces and Remote Sensing Vol. 2*. Academic, New York. 572 pp.
- Ishimaru A. (1978b) *Single Scattering and Transport Theory: Wave Propagation and Scattering in Random Media, Vol. 1*. Academic, New York. 250 pp.
- Ivanov A. V., Ilin N. P., Loseva L. E., and Senin V. G. (1973a) Composition of metallic iron and some coexisting phases in samples from highland lunar region returned by automatic station Luna-20. *Geochimiya*, *12*, 1782–1792.
- Ivanov A. V., Tarasov L. S., Rode O. D., and Florensky K. P. (1973b) Comparative characteristics of regolith samples delivered from the lunar mare and highland regions by the automatic stations Luna-16 and Luna-20. *Proc. Lunar Sci. Conf. 4th*, pp. 351–364.
- Jackson E. D., Sutton R. L., and Wilshire H. G. (1975) Structure and petrology of a cumulus norite boulder sampled by Apollo 17 in Taurus-Littrow Valley, the Moon. *Geol. Soc. Am. Bull.*, *86*, 433–442.
- Jaffe L. D. (1964) Depth and strength of lunar dust. *Eos Trans. AGU*, *45*, 628.
- Jaffe L. D. (1965) Strength of the lunar dust. *J. Geophys. Res.*, *70*, 6139–6146.
- Jaffe L. D. (1967) Surface structure and mechanical properties of the lunar maria. *J. Geophys. Res.*, *72*, 1727–1731.
- Jaffe L. D. (1969) Lunar surface material: Spacecraft measurements of density and strength. *Science*, *164*, 1514–1516.
- Jaffe L. D. (1971a) Bearing strength of lunar soil. *The Moon*, *3*, 337–345.
- Jaffe L. D. (1971b) Cracking of lunar mare soil. *Nature*, *234*, 402–403.
- Jaffe L. D. (1973) Shear strength of lunar soil from Oceanus Procellarum. *The Moon*, *8*, 58–72.

- Jaffe L. D. et al. (1968) Principal science results from the Surveyor project. In *Surveyor Project Final Report, Part 2: Science Results*, pp. 15–20. JPL Tech. Rpt. 32–1265, Jet Propulsion Laboratory, Pasadena.
- James O. D. (1973) *crystallization History of Lunar Basalt 14310*. U.S. Geol. Surv. Prof. Pap. 841. 29 pp.
- James O. B. (1976) Petrology of aphanitic lithologies in consortium breccia 73215. *Proc. Lunar Sci. Conf. 7th*, pp. 2145–2178.
- James O. B. (1977) Lunar highlands breccias generated by major impacts. In *The Soviet-American Conference on Cosmochemistry of the Moon and Planets* (J. H. Pomeroy and N. J. Hubbard, eds.), pp. 637–658. NASA SP-370.
- James O. B. (1980) Rocks of the early lunar crust. *Proc. Lunar Planet. Sci. Conf. 11th*, pp. 365–393.
- James O. B. (1981) Petrologic and age relations in Apollo 16 rocks: Implications for subsurface geology and the age of the Nectaris basin. *Proc. Lunar Planet. Sci. 12B*, pp. 209–233.
- James O. B. and Flohr M. K. (1983) Subdivision of the Mg-suite noritic rocks into Mg-gabbro-norites and Mg-norites. *Proc. Lunar Planet. Sci. Conf. 13th*, in *J. Geophys. Res.*, 88, A603–A614.
- James O. B. and Hammarstrom J. G. (1977) Petrology of four clasts from consortium breccia 73215. *Proc. Lunar Sci. Conf. 8th*, pp. 2459–2494.
- James O. B. and Hörz F., eds. (1981) *Workshop on Apollo 16*. LPI Tech. Rpt. 81–01, Lunar and Planetary Institute, Houston. 157 pp.
- James O. B., Lindstrom M. M., and Flohr M. K. (1983) Petrology and geochemistry of alkali gabbro-norites from lunar breccia 67975. *Proc. Lunar Planet. Sci. Conf. 17th*, in *J. Geophys. Res.*, 92, E314–E330.
- James O. B., Flohr M. K., and Lindstrom M. M. (1984) Petrology and chemistry of lunar dimict breccia 61015. *Proc. Lunar Planet. Sci. Conf. 15th*, in *J. Geophys. Res.*, 89, C63–C86.
- James O. B., Lindstrom M. M., and Flohr M. K. (1987) Petrology and geochemistry of alkali gabbro-norites from lunar breccia 67975. *Proc. Lunar Planet. Sci. Conf. 17th*, in *J. Geophys. Res.*, 92, E314–E330.
- Jeffreys H. (1962) *The Earth*. Cambridge Univ., Cambridge. 438 pp.
- Jerde E. A., Warren P. H., Morris R. V., Heiken G. H., and Vaniman D. T. (1987) A potpourri of regolith breccias: "New" samples from the Apollo 14, 16 and 17 landing sites. *Proc. Lunar Planet. Sci. Conf. 17th*, in *J. Geophys. Res.*, 92, E526–E536.
- Jerome D. Y. and Philippot J.-C. (1973) Chemical composition of Luna 20 soil and rock fragments. *Geochim. Cosmochim. Acta*, 37, 909–914.
- Jerome D. Y., Philippot J.-C., and Brichet E. (1972) Determination of 29 elements in Luna 16 soil by non-destructive activation analysis. *Earth Planet. Sci. Lett.*, 13, 436–440.
- Jessberger E. K. (1983) ^{40}Ar - ^{39}Ar dating of North Ray Crater ejecta (abstract). In *Lunar and Planetary Science XIV*, pp. 349–350. Lunar and Planetary Institute, Houston.
- Jessberger E. K., Huneke J. C., Podosek F. A., and Wasserburg G. J. (1974) High-resolution argon analysis of neutron-irradiated Apollo 16 rocks and separated minerals. *Proc. Lunar Sci. Conf. 5th*, pp. 1419–1449.
- Jessberger E. K., Dominik B., Kirsten T., and Staudacher T. (1977) New ^{40}Ar - ^{39}Ar ages of Apollo 16 breccias and 4.42 AE old anorthosites (abstract). In *Lunar Science VIII*, pp. 511–513. The Lunar Science Institute, Houston.
- Johnson F. S., Evans D. E., and Carroll J. M. (1970) Cold cathode gage (lunar atmosphere detector). In *Apollo 12 Preliminary Science Report*, pp. 93–97. NASA SP-235.
- Johnson F. S., Carroll J. M., and Evans D. E. (1972) Lunar atmosphere measurements. *Proc. Lunar Sci. Conf. 3rd*, pp. 2231–2242.
- Johnson N. L. (1979) *Handbook of Soviet Lunar and Planetary Exploration*. American Astronautical Society, Science and Technology Series Vol. 47. 262 pp.
- Johnson T. V., Mosher J. A., and Matson D. L. (1977) Lunar spectral units: A northern hemispheric mosaic. *Proc. Lunar Sci. Conf. 8th*, pp. 1013–1028.
- Jones J. H. and Drake M. J. (1982) An experimental geochemical approach to early planetary differentiation (abstract). In *Lunar and Planetary Science XIII*, pp. 369–370. Lunar and Planetary Institute, Houston.
- Jones J. H. and Drake M. J. (1986) Geochemical constraints on core formation in the Earth. *Nature*, 322, 221–228.
- Jovanovic S. and Reed G. W. Jr. (1973) Volatile trace elements and the characterization of the Cayley Formation and the primitive lunar crust. *Proc. Lunar Sci. Conf. 4th*, pp. 1313–1324.
- Jovanovic S. and Reed G. W. Jr. (1974) Labile and nonlabile element relationships among Apollo 17 samples. *Proc. Lunar Sci. Conf. 5th*, pp. 1685–1701.
- Jovanovic S. and Reed G. W. Jr. (1975) Cl and P₂O₅ systematics: Clues to early lunar magmas. *Proc. Lunar Sci. Conf. 6th*, pp. 1737–1751.
- Jovanovic S. and Reed G. W. Jr. (1976a) Convection cells in the early lunar magma ocean: Trace-element evidence. *Proc. Lunar Sci. Conf. 7th*, pp. 3447–3459.
- Jovanovic S. and Reed G. W. Jr. (1976b) Trace elements and the evolution of lunar rocks (abstract). In *Lunar Science VII*, pp. 437–439. The Lunar Science Institute, Houston.
- Jovanovic S. and Reed G. W. Jr. (1977) Trace element geochemistry and the early lunar differentiation. *Proc. Lunar Sci. Conf. 8th*, pp. 623–632.
- Jovanovic S. and Reed G. W. Jr. (1978) Trace element evidence for a laterally inhomogeneous Moon. *Proc. Lunar Planet. Sci. Conf. 9th*, pp. 59–80.
- Jovanovic S. and Reed G. W. Jr. (1979) Regolith layering processes based on studies of low-temperature volatile elements in Apollo core samples. *Proc. Lunar Planet. Sci. Conf. 10th*, pp. 1425–1435.
- Jovanovic S. and Reed G. W. Jr. (1980a) Cl, P₂O₅, U and Br associated with mineral separates from a low and a high Ti mare basalt. *Proc. Lunar Planet. Sci. Conf. 11th*, pp. 125–134.
- Jovanovic S. and Reed G. W. Jr. (1980b) Candidate samples for the earliest lunar crust. In *Proceedings of the*

- Conference on the Lunar Highlands Crust (J. J. Papike and R. B. Merrill, eds.), pp. 101–111. Pergamon, New York.
- Jovanovic S. and Reed G. W. Jr. (1981) Aspects of the history of 66095 based on trace elements in clasts and whole rock. *Proc. Lunar Planet. Sci. 12B*, pp. 295–304.
- Jovanovic S., Jensen K. J., and Reed G. W. Jr. (1978) Luna 24 origins: Some trace element constraints. In *Mare Crisium: The View from Luna 24* (R. B. Merrill and J. J. Papike, eds.), pp. 695–700. Pergamon, New York.
- Juan V. C., Chen J. C., Huang C. K., Chen P. Y., and Wang Lee C. M. (1972) Petrology and chemistry of some Apollo 14 lunar samples. *Proc. Lunar Sci. Conf. 3rd*, pp. 687–705.
- Kaczaral P. W., Dennison J. E., and Lipschutz M. E. (1986) Yamato-791197: A volatile trace element rock lunar highlands sample from Antarctica. *Proceedings of the Tenth Symposium on Antarctic Meteorites*, pp. 76–83. Natl. Inst. for Polar Res., Tokyo.
- Kallemeyn G. W. and Warren P. H. (1983) Compositional implications regarding the lunar origin of the ALHA81005 meteorite. *Geophys. Res. Lett.*, 10, 833–836.
- Kaplan I. R. and Petrowski C. (1971) Carbon and sulfur isotope studies on Apollo 12 lunar samples. *Proc. Lunar Sci. Conf. 2nd*, pp. 1397–1406.
- Kaplan I. R., Smith J. W., and Ruth E. (1970) Carbon and sulfur concentration and isotopic composition in Apollo 11 samples. *Proc. Apollo 11 Lunar Sci. Conf.*, pp. 1317–1330.
- Kaplan I. R., Kerridge J. F., and Petrowski C. (1976) Light element geochemistry of the Apollo 15 site. *Proc. Lunar Sci. Conf. 7th*, pp. 481–492.
- Katsube T. J. and Collett L. S. (1971) Electrical properties of Apollo 11 and Apollo 12 lunar samples. *Proc. Lunar Sci. Conf. 2nd*, pp. 2367–2379.
- Katsube T. J. and Collett L. S. (1973a) Electrical characteristics of Apollo 16 lunar samples. *Proc. Lunar Sci. Conf. 4th*, pp. 3101–3110.
- Katsube T. J. and Collett L. S. (1973b) Electrical characteristics of rocks and their application to planetary and terrestrial EM-sounding. *Proc. Lunar Sci. Conf. 4th*, pp. 3111–3131.
- Kaula W. M. (1968) *An Introduction to Planetary Physics: The Terrestrial Planets*. Wiley, New York. 490 pp.
- Keaton P. W. (1985) A Moon base/Mars base transportation depot. In *Lunar Bases and Space Activities of the 21st Century* (W. W. Mendell, ed.), pp. 141–154. Lunar and Planetary Institute, Houston.
- Keays R. R., Ganapathy R., Laul J. C., Anders E., Herzog G. F., and Jeffery P. M. (1970) Trace elements and radioactivity in lunar rocks: Implications for meteorite infall, solar-wind flux, and formation conditions of the Moon. *Science*, 167, 490–493.
- Keihm S. J. and Langseth M. G. (1973) Surface brightness temperature at the Apollo 17 heat flow site: Thermal conductivity of the upper 15 cm of regolith. *Proc. Lunar Sci. Conf. 4th*, pp. 2503–2513.
- Keihm S. J. and Langseth M. G. (1975a) Lunar microwave brightness temperature observations reevaluated in the light of Apollo program findings. *Icarus*, 24, 211–230.
- Keihm S. J. and Langseth M. G. (1975b) Microwave emission spectrum of the Moon: Mean global heat flow and average depth of the regolith. *Science*, 187, 64–66.
- Keihm S. J., Peters K., Langseth M. G., and Chute J. L. (1973) Apollo 15 measurement of lunar surface brightness temperatures: Thermal conductivity of the upper 1.5 meters of regolith. *Earth Planet. Sci. Lett.*, 19, 337–351.
- Keil K., Bunch T. E., and Prinz M. (1970) Mineralogy and composition of Apollo 11 lunar samples. *Proc. Apollo 11 Lunar Sci. Conf.*, pp. 561–598.
- Keil K., Prinz M., and Bunch T. E. (1971) Mineralogy, petrology and chemistry of some Apollo 12 samples. *Proc. Lunar Sci. Conf. 2nd*, pp. 319–341.
- Keil K., Kurat G., Prinz M., and Green J. (1972) Lithic fragments, glasses and chondrules from Luna 16 fines. *Earth Planet. Sci. Lett.*, 13, 243–256.
- Kerridge J. F. (1975) Solar nitrogen: Evidence for a secular change in the ratio of nitrogen-15 to nitrogen-14. *Science*, 188, 162–164.
- Kerridge J. F. (1980) Secular variations in composition of the solar wind: Evidence and causes. In *The Ancient Sun: Fossil Record in the Earth, Moon and Meteorites* (R. O. Pepin, J. A. Eddy, and R. B. Merrill, eds.), pp. 475–489. Pergamon, New York.
- Kerridge J. F. (1989) What has caused the secular increase in solar nitrogen-15? *Science*, 245, 480–486.
- Kerridge J. F. and Kaplan I. R. (1978) Sputtering: Its relationship to isotopic fractionation on the lunar surface. *Proc. Lunar Planet. Sci. Conf. 9th*, pp. 1687–1709.
- Kerridge J. F., Kaplan I. R., and Petrowski C. (1975a) Evidence for meteoritic sulfur in the lunar regolith. *Proc. Lunar Sci. Conf. 6th*, pp. 2151–2162.
- Kerridge J. F., Kaplan I. R., Petrowski C., and Chang S. (1975b) Light element geochemistry of the Apollo 16 site. *Geochim. Cosmochim. Acta*, 39, 137–162.
- Kesson S. E. (1975) Mare basalts: Melting experiments and petrogenetic interpretations. *Proc. Lunar Sci. Conf. 6th*, pp. 921–944.
- Kesson S. E. and Lindsley D. H. (1975) The effect of Al³⁺, Cr³⁺, and Ti³⁺ on the stability of armalcolite. *Proc. Lunar Sci. Conf. 6th*, pp. 911–920.
- Kesson S. E. and Lindsley D. H. (1976) Mare basalt petrogenesis—a review of experimental studies. *Rev. Geophys. Space Phys.*, 14, 361–373.
- Kharkar D. P. and Turekian K. K. (1971) Analyses of Apollo 11 and Apollo 12 rocks and soils by neutron activation. *Proc. Lunar Sci. Conf. 2nd*, pp. 1301–1305.
- Kieffer S. W. (1971) Shock metamorphism of the Coconino Sandstone at Meteor Crater, Arizona. *J. Geophys. Res.*, 76, 5449–5473.
- Kieffer S. W. (1975) From regolith to rock by shock. *The Moon*, 13, 301–320.
- Kiko J., Warhaut M., and Kirsten T. (1979) Solar wind noble gas distribution in lunar ilmenites and correlated element fractionation (abstract). In *Lunar and Planetary Science X*, pp. 664–666. Lunar and Planetary Institute, Houston.
- King E. A. Jr. and Butler J. C. (1977) Rosin's law and the lunar regolith. *The Moon*, 17, 177–178.

- King E. A. Jr., Carman M. F., and Butler J. C. (1970) Mineralogy and petrology of coarse particulate material from the lunar surface at Tranquility Base. *Proc. Apollo 11 Lunar Sci. Conf.*, pp. 599–606.
- King J. H. (1974) Solar proton fluences for 1977–1983 space missions. *J. Spacecraft Rockets*, 11, 401–408.
- Kinslow R., ed. (1970) *High-Velocity Impact Phenomena*. Academic, New York. 575 pp.
- Kipp M. E. and Melosh H. J. (1986) Short note: A preliminary numerical study of colliding planets. In *Origin of the Moon* (W. K. Hartmann, R. J. Phillips, and G. J. Taylor, eds.), pp. 643–647. Lunar and Planetary Institute, Houston.
- Kirsten T. and Horn P. (1974) Chronology of the Taurus-Littrow region III: Ages of mare basalts and highland breccias and some remarks about the interpretation of highland rocks. *Proc. Lunar Sci. Conf. 5th*, pp. 1451–1475.
- Kirsten T., Horn P., and Kiko J. (1973) ^{39}Ar - ^{40}Ar dating and rare gas analysis of neutron-irradiated Apollo 16 rocks and soils. *Proc. Lunar Sci. Conf. 4th*, pp. 1757–1784.
- Klein C. Jr. and Drake J. C. (1972) Mineralogy, petrology, and surface features of some fragmental material from the Fra Mauro site. *Proc. Lunar Sci. Conf. 3rd*, pp. 1095–1113.
- Klein C. Jr., Drake J. C., and Frondel C. (1971) Mineralogical, petrological, and chemical features of four Apollo 12 lunar microgabbros. *Proc. Lunar Sci. Conf. 2nd*, pp. 265–284.
- Koch G. S. Jr. and Link R. F. (1970) *Statistical Analysis of Geological Data*. Wiley, New York. 375 pp.
- Koeberl C., Warren P. H., Lindstrom M. M., Spettel B., and Fukuoka T. (1989) Preliminary examination of the Yamato-86032 lunar meteorite: II. Major and trace element chemistry. In *Proceedings of the Thirteenth Symposium on Antarctic Meteorites*, pp. 15–24. Natl. Inst. for Polar Res., Tokyo.
- Kohl J. W., Boström C. O., and Williams D. J. (1973) Particle observations of the August 1972 solar events by Explorers 41 and 43. In *Collected Data Reports on August 1972 Solar-Terrestrial Events* (H. E. Coffey, ed.), pp. 330–333. Report UAG-28, Part II, World Data Center A for Solar-Terrestrial Physics, NOAA, Boulder, Colorado.
- Kolesov G. M. and Surkov Yu. A. (1980) Neutron-activation analysis of regolith samples from Mare Crisium. In *Lunar Soil from Mare Crisium* (V. L. Barsukov, ed.), pp. 238–243. Nauka, Moscow.
- Kordesh K. (1983a) Comparative Fourier grain shape analysis of meteoritic breccias and lunar soils (abstract). In *Lunar and Planetary Science XIV*, pp. 387–388. Lunar and Planetary Institute, Houston.
- Kordesh K. (1983b) Fourier grain analysis of clasts in achondrites utilizing shape frequency distributions (abstract). *Meteoritics*, 18, 327.
- Kordesh K., Blakely R., Basu A., and Pachut J. (1982) Fourier grain shape analysis of clasts in a chondrite (abstract). *Meteoritics*, 17, 236.
- Korotev R. L. (1976) Geochemistry of grain-size fractions of soils from the Taurus-Littrow valley floor. *Proc. Lunar Sci. Conf. 7th*, pp. 695–726.
- Korotev R. L. (1981) Compositional trends in Apollo 16 soils. *Proc. Lunar Planet. Sci. 12B*, pp. 577–605.
- Korotev R. L. (1982) Comparative geochemistry of Apollo 16 surface soils and samples from cores 64002 and 60002 through 60007. *Proc. Lunar Planet. Sci. Conf. 13th, J. Geophys. Res.*, 87, A269–A278.
- Korotev R. L. (1985) Geochemical survey of Apollo 15 regolith breccias (abstract). In *Lunar and Planetary Science XVI*, pp. 459–460. Lunar and Planetary Institute, Houston.
- Korotev R. L. (1987a) The meteoritic component of Apollo 16 noritic impact melt breccias. *Proc. Lunar Planet. Sci. Conf. 17th, Geophys. Res.*, 92, E491–E512.
- Korotev R. L. (1987b) The nature of the meteoritic components of Apollo 16 soil, as inferred from correlations of iron, cobalt, iridium, and gold with nickel. *Proc. Lunar Planet. Sci. Conf. 17th, Geophys. Res.*, 92, E447–E461.
- Korotev R. L. and Haskin L. A. (1987) Does the lunar crust have a Eu anomaly? (abstract). In *Lunar and Planetary Science XVIII*, pp. 507–508. Lunar and Planetary Institute, Houston.
- Korotev R. L., Haskin L. A., and Lindstrom M. M. (1980) A synthesis of lunar highlands compositional data. *Proc. Lunar Planet. Sci. Conf. 11th*, pp. 395–429.
- Korotev R. L., Lindstrom M. M., Lindstrom D. J., and Haskin L. A. (1983) Antarctic meteorite ALHA81005—not just another lunar anorthositic breccia. *Geophys. Res. Lett.*, 10, 829–832.
- Korotev R. L., Morris R. V., and Lauer H. V. (1984) Stratigraphy and geochemistry of the Stone Mountain double drive tube (64001/2). *Proc. Lunar Planet. Sci. Conf. 15th, in J. Geophys. Res.*, 89, C143–C160.
- Kosofsky L. J. and El-Baz F. (1970) *The Moon as Viewed by Lunar Orbiter*. NASA SP-200. 152 pp.
- Kothari B. K. and Goel P. S. (1973) Nitrogen in lunar samples. *Proc. Lunar Sci. Conf. 4th*, pp. 1587–1596.
- Kovach R. L. and Watkins J. S. (1973) The velocity structure of the lunar crust. *The Moon*, 7, 63–75.
- Krähenbühl U. (1980) Distribution of volatile and non-volatile elements in grain-size fractions of Apollo 17 drive tube 74001/2. *Proc. Lunar Planet. Sci. Conf. 11th*, pp. 1551–1564.
- Krähenbühl U., Ganapathy R., Morgan J. W., and Anders E. (1973) Volatile elements in Apollo 16 samples: Implications for highland volcanism and accretion history of the Moon. *Proc. Lunar Sci. Conf. 4th*, pp. 1325–1348.
- Krähenbühl U., Grütter A., von Gunten H. R., Meyer G., Wegmüller F., and Wyttenbach A. (1977) Volatile and non-volatile elements in grain size fractions of Apollo 17 soils 75081, 72461 and 72501. *Proc. Lunar Sci. Conf. 8th*, pp. 3901–3916.
- Krotikov V. D. (1962) Some electrical properties of earth rocks and their comparison with those of the lunar surface layer. *Izv. Vyssh. Uchebn. Zaved. Radiofiz.*, 5, 1057–1061.
- Krotikov V. D. and Troitsky V. S. (1963) Radio emission and the nature of the Moon. *Usp. Fiz. Nauk.*, 81, 589–639.

- Krotikov V. D. and Troitsky V. S. (1964) Detecting heat flow from the interior of the Moon. *Soviet Astron.*, 7, 822–826.
- Kroupenio N. N. (1972) Some characteristics of the Venus surface. *Icarus*, 17, 692–698.
- Kroupenio N. N. (1973) Results of radar experiments performed on automatic stations Luna 16 and Luna 17. In *COSPAR Space Research XIII*, pp. 969–973. Akademie-Verlag, Berlin.
- Kroupenio N. N., Balo A. G., Ruzskii E. G., Ladyghin V. A., Cherkasov V. V., and Fomin V. S. (1975) Results of radar experiments performed aboard the Luna 19 and 20 automatic stations. In *COSPAR Space Research XV*, pp. 615–620. Akademie-Verlag, Berlin.
- Kuiper G. P., ed. (1960) *Photographic Lunar Atlas*. Univ. of Chicago, Chicago. 23 pp.
- Kuiper G. P. (1965) Surface structure of the Moon. In *The Nature of the Lunar Surface* (W. N. Hess, D. Menzel, and J. A. O'Keefe, eds.), Chapter 4. Johns Hopkins, Baltimore.
- Kurat G., Keil K., and Prinz M. (1974) Rock 14318: A polymict lunar breccia with chondritic texture. *Geochim. Cosmochim. Acta*, 38, 1133–1146.
- Kushiro I. and Nakamura Y. (1970) Petrology of some lunar crystalline rocks. *Proc. Apollo 11 Lunar Sci. Conf.*, pp. 607–626.
- Lakatos S., Heymann D., and Yaniv A. (1973) Green spherules from Apollo 15: Inferences about their origin from inert gas measurements. *The Moon*, 7, 131–148.
- Lambe T. W. and Whitman R. V. (1969) *Soil Mechanics*. Wiley, New York. 553 pp.
- Lambeck K. (1975) Effects of tidal dissipation in the oceans on the Moon's orbit and the Earth's rotation. *J. Geophys. Res.*, 80, 2917–2925.
- Lammlin D. R. (1977) Lunar seismicity and tectonics. *Phys. Earth Planet. Inter.*, 14, 224–273.
- Lammlin D. R., Latham G. V., Dorman J., Nakamura Y., and Ewing M. (1974) Lunar seismicity, structure, and tectonics. *Rev. Geophys. Space Phys.*, 12, 1–21.
- Lange M. A. and Ahrens T. J. (1979) Impact melting early in lunar history. *Proc. Lunar Planet. Sci. Conf. 10th*, pp. 2707–2725.
- Langevin Y. (1982) Evolution of an asteroidal regolith: Granulometry, mixing and maturity. In *Workshop on Lunar Breccias and Soils and Their Meteoritic Analogs* (G. J. Taylor and L. L. Wilkening, eds.), pp. 87–93. LPI Tech. Rpt. 82–02, Lunar and Planetary Institute, Houston.
- Langevin Y. and Arnold J. R. (1977) The evolution of the lunar regolith. *Annu. Rev. Earth Planet. Sci.*, 5, 449–489.
- Langseth M. G. and Keihm S. J. (1977) In-situ measurements of lunar heat flow. In *Soviet-American Conference on Geochemistry of the Moon and Planets*, pp. 283–293. NASA SP-370.
- Langseth M. G. Jr., Clark S. P. Jr., Chute J. L. Jr., Keihm S., and Wechsler A.E. (1972) Heat-flow experiment. In *Apollo 15 Preliminary Science Report*, pp. 11–1 to 11–23. NASA SP-289.
- Langseth M. G. Jr., Keihm S. J., and Chute J. L. Jr. (1973) Heat-flow experiment. In *Apollo 17 Preliminary Science Report*, pp. 9–1 to 9–24. NASA SP-330.
- Langseth M. G., Keihm S. J., and Peters K. (1976) Revised lunar heat-flow values. *Proc. Lunar Sci. Conf. 7th*, pp. 3143–3171.
- Lanzerotti L. J. and Brown W. L. (1981) Ice in the polar regions of the moon. *J. Geophys. Res.*, 86, 3949–3950.
- LAPST (Lunar and Planetary Sample Team) (1985) *Horizons and Opportunities in Lunar Sample Science*. LPI Tech. Rpt. 85–04, Lunar and Planetary Institute, Houston. 32 pp.
- Latham G. V., McDonald W. G., and Moore H. J. (1970a) Missile impacts as sources of seismic energy on the Moon. *Science*, 168, 242–245.
- Latham G. V., Ewing M., Dorman J., Press F., Toksoz M. N., Sutton G., Meissner R., Duennebie F., Nakamura Y., Kovach R., and Yates M. (1970b) Seismic data from manmade impacts on the Moon. *Science*, 170, 620–626.
- Latham G. V., Ewing M., Press F., Sutton G., Dorman J., Nakamura Y., Toksoz N., Wiggins R., Derr J., and Duennebie F. (1970c) Apollo 11 passive seismic experiment. *Proc. Apollo 11 Lunar Sci. Conf.*, pp. 2309–2320.
- Latham G., Ewing M., Dorman J., Press F., Toksoz N., Sutton G., Duennebie F., and Nakamura Y. (1972) Moonquakes and lunar tectonism. *The Moon*, 4, 3–12.
- Latham G. V., Dorman H. J., Horvath P., Ibrahim A. K., Koyama J., and Nakamura Y. (1978) Passive seismic experiment: A summary of current status. *Proc. Lunar Planet. Sci. Conf. 9th*, pp. 3609–3613.
- Laul J. C. and Papike J. J. (1980) The lunar regolith: Comparative chemistry of the Apollo sites. *Proc. Lunar Planet. Sci. Conf. 11th*, pp. 1307–1340.
- Laul J. C. and Schmitt R. A. (1973a) Chemical composition of Luna 20 rocks and soil and Apollo 16 soils. *Geochim. Cosmochim. Acta*, 37, 927–942.
- Laul J. C. and Schmitt R. A. (1973b) Chemical composition of Apollo 15, 16 and 17 samples. *Proc. Lunar Sci. Conf. 4th*, pp. 1349–1367.
- Laul J. C. and Schmitt R. A. (1975a) Dunite 72417: A chemical study and interpretation. *Proc. Lunar Sci. Conf. 6th*, pp. 1231–1254.
- Laul J. C. and Schmitt R. A. (1975b) Chemical composition of Apollo 17 samples: Boulder breccias (2), rake breccias (8), and others (abstract). In *Lunar Science VI*, pp. 489–491. The Lunar Science Institute, Houston.
- Laul J. C., Morgan J. W., Ganapathy R., and Anders E. (1971) Meteoritic material in lunar samples: Characterization from trace elements. *Proc. Lunar Sci. Conf. 2nd*, pp. 1139–1158.
- Laul J. C., Wakita H., Showalter D. L., Boynton W. V., and Schmitt R. A. (1972a) Bulk, rare earth, and other trace elements in Apollo 14 and 15 and Luna 16 samples. *Proc. Lunar Sci. Conf. 3rd*, pp. 1181–1201.
- Laul J. C., Ganapathy R., Morgan J. W., and Anders E. (1972b) Meteoritic and non-meteoritic trace elements in Luna 16 samples. *Earth Planet. Sci. Lett.*, 13, 450–454.
- Laul J. C., Hill D. W., and Schmitt R. A. (1974) Chemical studies of Apollo 16 and 17 samples. *Proc. Lunar Sci. Conf. 5th*, pp. 1047–1066.

- Laul J. C., Vaniman D. T., Papike J. J., and Simon S. (1978a) Chemistry and petrology of size fractions of Apollo 17 deep drill core 70009-70006. *Proc. Lunar Planet. Sci. Conf. 9th*, pp. 2065-2097.
- Laul J. C., Vaniman D. T., and Papike J. J. (1978b) Chemistry, mineralogy and petrology of seven >1 mm fragments from Mare Crisium. In *Mare Crisium: The View from Luna 24* (J. J. Papike and R. B. Merrill, eds.), pp. 537-568. Pergamon, New York.
- Laul J. C., Papike J. J., and Simon S. B. (1981) The lunar regolith: Comparative studies of the Apollo and Luna sites. Chemistry of soils from Apollo 17, Luna 16, 20, and 24. *Proc. Lunar Planet. Sci. 12B*, pp. 389-407.
- Laul J. C., Smith M. R., and Schmitt R. A. (1983) ALHA 81005 meteorite: Chemical evidence for a lunar highland origin. *Geophys. Res. Lett.*, 10, 825-828.
- Laul J. C., Smith M. R., Papike J. J., and Simon S. B. (1984) Agglutinates as recorders of regolith evolution: Application to the Apollo 17 drill core. *Proc. Lunar Planet. Sci. Conf. 15th*, in *J. Geophys. Res.*, 89, C161-C170.
- Laul J. C., Rode O. D., Simon S. B., and Papike J. J. (1987) The lunar regolith: Chemistry and petrology of Luna 24 grain size fractions. *Geochim. Cosmochim. Acta*, 51, 661-673.
- Leich D. A., Kahl S. B., Kirschbaum A. R., Niemeyer S., and Phinney D. (1975) Rare gas constraints on the history of Boulder 1, Station 2, Apollo 17. *The Moon*, 14, 407-444.
- Leonovich A. K., Gromov V. V., Rybakov A. V., Petrov V. K., Pavlov P. S., Cherkasov I. I., and Shvarev V. V. (1971) Studies of lunar ground mechanical properties with the self-propelled Lunokhod-1. In *Peredvizhnaya Laboratoriya na Luna-Lunokhod-1 ('Lunokhod 1'—Mobile Lunar Laboratory)*, pp. 120-135. Nauka, Moscow.
- Leonovich A. K., Gromov V. V., Rybakov A. V., Petrov V. N., Pavlov P. S., Cherkasov I. I., and Shvarev V. V. (1972) Investigations of the mechanical properties of the lunar soil along the path of Lunokhod I. In *COSPAR Space Research XII*, pp. 53-64. Akademie-Verlag, Berlin.
- Leonovich A. K., Gromov V. V., Dmitriyev A. D., Penetrigov V. N., Semenov P. S., and Shvarev V. V. (1974a) The main peculiarities of the processes of the deformation and destruction of lunar soil. In *The Soviet American Conference on Cosmochemistry of the Moon and Planets*, pp. 735-743. NASA SP-370 (1977); also available in NASA Technical Translation F-16034 (1974).
- Leonovich A. K., Gromov V. V., Dmitriyev A. D., Loshkin V. A., Pavlov P. S., Rybakov A. V., and Shvarev V. V. (1974b) The results of investigations of the physical and mechanical properties of lunar soil in nitrogen gas within a research box. In *Lunar Soil from Sea of Fertility*, pp. 563-570. Nauka, Moscow (in Russian).
- Leonovich A. K., Gromov V. V., Semyonov P. S., Penetrigov V. N., and Shvartov V. V. (1975) Luna 16 and 20 investigations of the physical and mechanical properties of lunar soil. In *COSPAR Space Research XV*, pp. 607-616. Akademie-Verlag, Berlin.
- Letaw J. R., Silberberg R., and Tsao C. H. (1987) Radiation hazards on space missions. *Nature*, 330, 709-710.
- Levinson A. A. and Taylor S. R. (1971) *Moon Rocks and Minerals*. Pergamon, New York. 222 pp.
- Levy C., Christophe-Michel-Levy M., Picot P., and Caye R. (1972) A new titanium and zirconium oxide from the Apollo 14 samples. *Proc. Lunar Sci. Conf. 3rd*, pp. 1115-1120.
- Lewis J. S., Jones T. D., and Farrand W. H. (1988) Carbonyl extraction of lunar and asteroidal materials. In *Engineering Construction and Operations in Space: Proceedings of Space '88* (S. W. Johnson and J. P. Wetzel, eds.), pp. 111-122. American Society of Civil Engineers, New York.
- LGO Science Workshop Members (1986) *Contributions of a Lunar Geoscience Observer (LGO) Mission to Fundamental Questions in Lunar Science*. Southern Methodist Univ., Dallas, Texas. 86 pp.
- Lightner B. D. and Marti K. (1974) Lunar trapped xenon. *Proc. Lunar Sci. Conf. 5th*, pp. 2023-2031.
- Lin R. P., Anderson K. A., Bush R., McGuire R. E., and McCoy J. E. (1976) Lunar surface remanent magnetic fields detected by the electron reflection method. *Proc. Lunar Sci. Conf. 7th*, pp. 269 1-2703.
- Lin R. P., Anderson K. A., and Hood L. L. (1988) Lunar surface magnetic field concentrations antipodal to young large impact basins. *Icarus*, 74, 529-541.
- Lincoln Laboratory (1970) *Radar Studies of the Moon*. Final report, NASA Contract NAS-9-7830. MIT, Lexington. 50 pp.
- Lindsay J. F. (1973) Evolution of lunar soil grain size and shape parameters. *Proc. Lunar Sci. Conf. 4th*, pp. 215-224.
- Lindsay D. H. (1967) The join hedenbergite-ferrosilite at high pressures and temperatures. *Carnegie Inst. Wash. Yearb.*, 65, 230-232.
- Lindsay D. H. and Burnham C. W. (1970) Pyroxferroite: Stability and X-ray crystallography of synthetic $\text{Ca}_{0.15}\text{Fe}_{0.85}\text{SiO}_3$ pyroxenoid. *Science*, 168, 364-367.
- Lindsay D. H. and Munoz J. L. (1969) Subsolidus relations along the join hederbergite-ferrosilite. *Am. J. Sci.*, 267A, 295-324.
- Lindsay D. H., Papike J. J., and Bence A. E. (1972) Pyroxferroite: Breakdown at low pressure and high temperature (abstract). In *Lunar Science III*, pp. 483-485. The Lunar Science Institute, Houston.
- Lindsay D. H., Kesson S. E., Hartzman M. J., and Cushman M. K. (1974) The stability of armalcolite: Experimental studies in the system Mg-Fe-Ti-O. *Proc. Lunar Sci. Conf. 5th*, pp. 521-534.
- Lindstrom D. J. (1976) Experimental study of the partitioning of the transition metals between clinopyroxene and coexisting silicate liquids. Ph.D. thesis, Univ. of Oregon. 188 pp.
- Lindstrom D. J. and Semkow K. W. (1986) Electrochemical monitoring of crystal growth for silicate melts. In *Lunar and Planetary Science XVII*, pp. 484-485. Lunar and Planetary Institute, Houston.
- Lindstrom D. J., Haskin L. A., Semkow K. W., and Lewis R. H. (1986) Conductivities of silicate melts; applications to lunar smelting (abstract). In *Lunar and Planetary Science XVII*, pp. 482-483. Lunar and Planetary Institute, Houston.

- Lindstrom M. M. (1984) Alkali gabbro-norite, ultra-KREEPY melt rock and the diverse suite of clasts in North Ray Crater feldspathic fragmental breccia 67975. *Proc. Lunar Planet. Sci. Conf. 15th*, in *J. Geophys. Res.*, 90, C50-C62.
- Lindstrom M. M. and Lindstrom D. J. (1986) Lunar granulites and their precursor anorthositic norites of the early lunar crust. *Proc. Lunar Planet. Sci. Conf. 16th*, in *J. Geophys. Res.*, 91, D263-D276.
- Lindstrom M. M., Duncan A. R., Fruchter J. S., McKay S. M., Stoesser J. W., Goles G. G., and Lindstrom D. J. (1972) Compositional characteristics of some Apollo 14 clastic materials. *Proc. Lunar Sci. Conf. 3rd*, pp. 1201-1215.
- Lindstrom M. M., Nava D. F., Lindstrom D. J., Winzer S. R., Lum R. K. L., Schuhmann P. J., Schuhmann S., and Philpotts J. A. (1977a) Geochemical studies of the white breccia boulders at North Ray Crater, Descartes region of the lunar highlands. *Proc. Lunar Sci. Conf. 8th*, pp. 2137-2151.
- Lindstrom M. M., Nielsen R. L., and Drake M. J. (1977b) Petrology and geochemistry of lithic fragments separated from the Apollo 15 deep-drill core. *Proc. Lunar Sci. Conf. 8th*, pp. 2869-2888.
- Lindstrom M. M., Knapp S. A., Shervais J. W., and Taylor L. A. (1984) Magnesian anorthosites and associated troctolites and dunite in Apollo 14 breccias. *Proc. Lunar Planet. Sci. Conf. 15th*, in *J. Geophys. Res.*, 90, C41-C49.
- Lindstrom M. M., Lindstrom D. J., Korotev R. L., and Haskin L. A. (1986) Lunar meteorite Yamato-791197: A polymict anorthositic norite breccia. *Proceedings of the Tenth Symposium on Antarctic Meteorites*, pp. 58-75. Natl. Inst. for Polar Res., Tokyo.
- Lingenfelter R. E. and Hudson H. S. (1980) Solar particle fluxes and the ancient Sun. In *The Ancient Sun: Fossil Record in the Earth, Moon and Meteorites* (R. O. Pepin, J. A. Eddy, and R. B. Merrill, eds.), pp. 69-79. Pergamon, New York.
- Lingenfelter R. E., Canfield E. H., and Hess W. N. (1961) The lunar neutron flux. *J. Geophys. Res.*, 66, 2665-2671.
- Lingenfelter R. E., Canfield E. H., and Hampel V. E. (1972) The lunar neutron flux revisited. *Earth Planet. Sci. Lett.*, 16, 355-369.
- Linsky J. L. (1973) The Moon as a proposed radiometric standard for microwave and infrared observations of extended sources: *Astrophys. J. Suppl.* 216, 25, 163-204.
- Lipin B. R. and Muan A. (1974) Equilibria bearing on the behavior of titanate phases during crystallization of iron silicate melts under strongly reducing conditions. *Proc. Lunar Sci. Conf. 5th*, pp. 535-548.
- Lofgren G. E. (1974) An experimental study of plagioclase crystal morphology: Isothermal crystallization. *Am. J. Sci.*, 274, 243-273.
- Lofgren G. E. (1975) Dynamic crystallization experiments on mare basalts (abstract). In *Papers Presented to the Conference on Origins of Mare Basalts and Their Implications for Lunar Evolution*, pp. 99-103. The Lunar Science Institute, Houston.
- Lofgren G. E. (1977) Dynamic crystallization experiments bearing on the origin of textures in impact-generated liquids. *Proc. Lunar Sci. Conf. 8th*, pp. 2079-2095.
- Lofgren G. E. (1980) Experimental studies on the dynamic crystallization of silicate melts. In *Physics of Magmatic Processes* (R. B. Hargraves, ed.), pp. 487-551. Princeton Univ., Princeton, New Jersey.
- Lofgren G. E. (1983) Effect of heterogeneous nucleation on basaltic textures: A dynamic crystallization study. *J. Petrol.*, 24, 229-255.
- Lofgren G. E., Donaldson C. H., Williams R. J., Mullins O. Jr., and Usselman T. M. (1974) Experimentally reproduced textures and mineral chemistry of Apollo 15 quartz normative basalts. *Proc. Lunar Sci. Conf. 5th*, pp. 549-567.
- Lofgren G. E., Donaldson C. H., and Usselman T. M. (1975) Geology, petrology, and crystallization of Apollo 15 quartz-normative basalts. *Proc. Lunar Sci. Conf. 6th*, pp. 79-99.
- Lofgren G. E., Smith D. P., and Brown R. W. (1978) Dynamic crystallization and kinetic melting of the lunar soil. *Proc. Lunar Planet. Sci. Conf. 9th*, pp. 959-976.
- Longhi J. (1978) Pyroxene stability and the composition of the lunar magma ocean. *Proc. Lunar Sci. Conf. 9th*, pp. 285-306.
- Longhi J. and Ashwal L. D. (1985) Two-stage models for lunar and terrestrial anorthosites: Petrogenesis without a magma ocean. *Proc. Lunar Planet. Sci. Conf. 15th*, in *J. Geophys. Res.*, 90, C571-0584.
- Longhi J. and Boudreau A. E. (1979) Complex igneous processes and the formation of primitive lunar crustal rocks. *Proc. Lunar Planet. Sci. Conf. 10th*, pp. 2085-2105.
- Longhi J. and Pan V. (1986) The architecture of the ol-pl-qtz pseudoternary liquidus diagram (abstract). In *Lunar and Planetary Science XVII*, pp. 492-493. Lunar and Planetary Institute, Houston.
- Longhi J., Walker D., and Hays J. F. (1972) Petrography and crystallization history of basalts 14310 and 14072. *Proc. Lunar Sci. Conf. 3rd*, pp. 131-139.
- Longhi J., Walker D., Grove T. L., Stolper E. M., and Hays J. M. (1974) The petrology of the Apollo 17 mare basalts. *Proc. Lunar Sci. Conf. 5th*, pp. 447-469.
- Longhi J., Walker D., and Hays J. F. (1976) Fe, Mg, and silica in lunar plagioclase (abstract). In *Lunar Science VII*, pp. 501-503. The Lunar Science Institute, Houston.
- Longhi J., Walker D., and Hays J. F. (1978) The distribution of Fe and Mg between olivine and lunar basaltic liquids. *Geochim. Cosmochim. Acta*, 42, 1545-1558.
- Lorr D. B., Garshenk V., and Cadoux C., eds. (1989) *Working in Orbit and Beyond: The Challenge of Space Medicine*. Science and Technology Series, Vol. 72 (supplement to *Advances in the Astronautical Sciences*), Univelt, San Diego. 188 pp.
- Lovering J. F. and Hughes T. C. (1971) Rhenium and osmium abundance determinations and meteoritic contamination levels in Apollo 11 and Apollo 12 lunar samples. *Proc. Lunar Sci. Conf. 2nd*, pp. 1331-1335.

- Lovering J. F. and Ware N. G. (1970) Electron-probe microanalyses of minerals and glasses in Apollo 11 lunar samples. *Proc. Apollo 11 Lunar Sci. Conf.*, pp. 633–654.
- Lovering J. F. and Wark D. A. (1971) Uranium-enriched phases in Apollo 11 and Apollo 12 basaltic rocks. *Proc. Lunar Sci. Conf. 2nd*, pp. 151–158.
- Lovering J. F. and Wark D. A. (1975) The lunar crust: Chemically defined rock groups and their K-U fractionation. *Proc. Lunar Sci. Conf. 6th*, pp. 1203–1217.
- Lovering J. F., Wark D. A., Reid A. F., Ware N. G., Keil K., Prinz M., Bunch T. E., El Goresy A., Ramdohr P., Brown G. M., Peckett A., Phillips R., Cameron E. N., Douglas J. A. V., and Plant A. G. (1971) Tranquillityite: A new silicate mineral from Apollo 11 and Apollo 12 basaltic rocks. *Proc. Lunar Sci. Conf. 2nd*, pp. 39–45.
- Low F. J. and Davidson A. W. (1965) Lunar observations at a wavelength of 1 millimeter. *Astrophys. J.*, 142, 1278–1282.
- Low F. J. and Mendell W. W. (1973) Infrared scanning radiometer. In *Apollo 17 Preliminary Science Report*, pp. 24–1 to 24–6. NASA SP-330.
- Lowrance W. W. (1976) *Of Acceptable Risk: Science and the Determination of Safety*. William Kaufmann, Los Altos, California. 180 pp.
- LSPET (Lunar Sample Preliminary Examination Team) (1969) Preliminary examination of lunar samples from Apollo 11. *Science*, 165, 121 1–1227.
- LSPET (Lunar Sample Preliminary Examination Team) (1970) Preliminary examination of lunar samples from Apollo 12. *Science*, 167, 1325–1339.
- LSPET (Lunar Sample Preliminary Examination Team) (1971a) Preliminary examination of lunar samples from Apollo 14. *Science*, 173, 681–693.
- LSPET (Lunar Sample Preliminary Examination Team) (1971b) *Lunar Sample Information Catalog: Apollo 15*. NASA MSC-03209.
- LSPET (Lunar Sample Preliminary Examination Team) (1972) The Apollo 15 lunar samples: A preliminary description. *Science*, 175, 363–375.
- LSPET (Lunar Sample Preliminary Examination Team) (1973a) The Apollo 16 lunar samples: Petrographic and chemical description. *Science*, 179, 23–34.
- LSPET (Lunar Sample Preliminary Examination Team) (1973b) Apollo 17 lunar samples, chemical and petrographic description. *Science*, 182, 659–672.
- Lucchitta B. K. (1976) Mare ridges and related highland scarps—Results of vertical tectonism? *Proc. Lunar Sci. Conf. 7th*, pp. 2761–2782.
- Lucchitta B. K. (1978) Geologic map of the north side of the Moon. *U.S. Geol. Surv. Map 1–1062*.
- Lucchitta B. K. and Watkins J. A. (1978) Age of graben systems on the moon. *Proc. Lunar Planet. Sci. Conf. 9th*, pp. 3459–3472.
- Lucey P. G. and Hawke B. R. (1988) A remote mineralogic perspective on gabbroic units in the lunar highlands. *Proc. Lunar Planet. Sci. Conf. 18th*, pp. 355–363.
- Lucey P. G., Hawke B. R., Pieters C. M., Head J. W., and McCord T. B. (1986) A compositional study of the Aristarchus region of the Moon using near-infrared reflectance spectroscopy. *Proc. Lunar Planet. Sci. Conf. 16th*, in *J. Geophys. Res.*, 91, D344–D354.
- Lugmair G. W. (1987) The age of the lunar crust: 60025—Methuselah's legacy (abstract). In *Lunar and Planetary Science XVIII*, pp. 584–585. Lunar and Planetary Institute, Houston.
- Lugmair G. W., Marti K., Kurtz J. P., and Scheinin N. B. (1976) History and genesis of lunar troctolite 76535 or: How old is old? *Proc Lunar Sci. Conf. 7th*, pp. 2009–2033.
- Lunar Geoscience Working Group (1986) *Status and Future of Lunar Geoscience* NASA SP-484. 54 pp.
- Lunar Science Institute (1972) *Post Apollo Lunar Science*. Report of a study by The Lunar Science Institute, Houston, Texas, July 1972. 104 pp.
- Lunatic Asylum (1970) Mineralogic and isotopic investigations on lunar rock 12013. *Earth Planet. Sci. Lett.*, 9, 137–163.
- Lynn V. L., Sohigian M. D., and Crocker E. A. (1964) Radar observations of the Moon at a wavelength of 8.6 millimeter. *J. Geophys. Res.*, 69, 781–783.
- Lot B. (1929) Recherches sur la polarisation de la lumiere des planetes et de quelques substances terrestres. *Annales de l'Observatoire de Paris, Section de Meudon, VIII*, No. 1. Translated to English in NASA Technical Translation F-187 (1964).
- Ma M.-S. and Schmitt R. A. (1980) Chemistries of lithic fragments from the Apollo 17 drill core sections 70003, 70005, and 70007—III—Anorthosites and chemically unique fragments (abstract). In *Lunar and Planetary Science XI*, pp. 640–642. Lunar and Planetary Institute, Houston.
- Ma M.-S. and Schmitt R. A. (1982) Chemistry of the matrix, the glass coating and an olivine clast from polymict ANT breccia 60035 (abstract). In *Lunar and Planetary Science XIII*, pp. 453–454. Lunar and Planetary Institute, Houston.
- Ma M.-S., Schmitt R. A., Taylor G. J., Warner R. D., Lange D., and Keil K. (1978) Chemistry and petrology of Luna 24 lithic fragments and <250 μ m soils: Constraints on the origin of VLT mare basalts. In *Mare Crisium: The View from Luna 24* (J. J. Papike and R. B. Merrill, eds.), pp. 569–592. Pergamon, New York.
- Ma M.-S., Schmitt R. A., Nielsen R. L., Taylor G. J., Warner R. D., and Keil K. (1979) Petrogenesis of Luna 16 aluminous mare basalts. *Geophys. Res. Lett.*, 6, 909–912.
- Ma M.-S., Schmitt R. A., Taylor G. J., Warner R. D., and Keil K. (1981a) Chemical and petrographic study of spinel troctolite in 67435: Implications for the origin of Mg-rich plutonic rocks (abstract). In *Lunar and Planetary Science XI*, pp. 640–642. Lunar and Planetary Institute, Houston.
- Ma M.-S., Liu Y.-G., and Schmitt R. A. (1981b) A chemical study of individual green glasses and brown glasses from 15426: Implications for their petrogenesis. *Proc. Lunar Planet. Sci. 12B*, pp. 915–933.
- MacDonald G. A. (1972) *Volcanoes*. Prentice-Hall, Englewood Cliffs, New Jersey. 510 pp.

- MacDonald G. J. F. (1964) Tidal friction. *Rev. Geophys.*, 2, 467-541.
- MacDougall J. D. and Kothari B. K. (1976) Formation chronology for C2 meteorites. *Earth Planet. Sci. Lett.*, 33, 36-44.
- MacDougall J. D., Rajan R. S., Hutcheon I. D., and Price P. B. (1973) Irradiation history and accretionary processes in lunar and meteoritic breccias. *Proc. Lunar Sci. Conf. 4th*, pp. 2319-2336.
- MacElroy R. D., Klein H. P., and Avern M. M. (1985) The evolution of CELSS for lunar bases. In *Lunar Bases and Space Activities of the 21st Century* (W. W. Mendell, ed.), pp. 623-633. Lunar and Planetary Institute, Houston.
- Mackin J. H. (1969) Origin of the lunar maria. *Geol. Soc. Am. Bull.*, 80, 735-748.
- Mahmood A., Mitchell J. K., and Carrier W. D. III (1974a) Grain orientation in lunar soil. *Proc. Lunar Sci. Conf. 5th*, pp. 2347-2354.
- Mahmood A., Mitchell J. K., and Carrier W. D. III (1974b) Particle shapes of three lunar soil samples. Unpublished report, available from W. D. Carrier III.
- Malvin D. J. and Drake M. J. (1987) Experimental determination of crystal/melt partitioning of Ga and Ge in the system forsterite-anorthite-diopside. *Geochim. Cosmochim. Acta*, 51, 2117-2128.
- Manka R. H. and Michel F. C. (1971) Lunar atmosphere as a source of lunar surface elements. *Proc. Lunar Sci. Conf. 2nd*, pp. 1717-1728.
- Mantel E. J. and Miller E. R., eds. (1977) *Catalog of Lunar Mission Data*. National Space Science Data Center, World Data Center A for Rockets and Satellites, Goddard Space Flight Center, Greenbelt, MD. 204 pp.
- Mark R. K., Lee-Hu C.-N., and Wetherill G. W. (1974) Rb-Sr age of lunar igneous rocks 62295 and 14310. *Geochim. Cosmochim. Acta*, 38, 1643-1648.
- Marsh S. P. (1980) *LASL Shock Hugoniot Data*. Univ. of California, Berkeley. 658 pp.
- Marti K., Lugmair G. W., and Urey H. C. (1970) Solar wind gases, cosmic-ray spallation products and the irradiation history of Apollo 11 samples. *Proc. Apollo 11 Lunar Sci. Conf.*, pp. 1357-1367.
- Marti K., Aeschlimann U., Eberhardt P., Geiss J., Grögler N., Jost D. T., Laul J. C., Ma M.-S., Schmitt R. A., and Taylor G. J. (1983) Pieces of the ancient lunar crust: Ages and composition of clasts in consortium breccia 67915. *Proc. Lunar Planet. Sci. Conf. 14th*, in *J. Geophys. Res.*, 88, B165-B175.
- Martin R. T., Winkler J. L., Johnson S. W., and Carrier W. D. III (1973) Measurement of conductance of Apollo 12 lunar simulants taken in the molecular flow range for helium, argon, and krypton gases. Unpublished report.
- Marvin U. B. (1971) Lunar niobian rutile. *Earth Planet. Sci. Lett.*, 11, 7-9.
- Marvin U. B. and Lindstrom M. M. (1983) Rock 67015: A feldspathic fragmental breccia with KREEP-rich melt clasts. *Proc. Lunar Planet. Sci. Conf. 13th*, in *J. Geophys. Res.*, 87, A659-A670.
- Marvin U. B. and Walker D. (1978) Implications of a titanium-rich glass clod at Oceanus Procellarum. *Am. Mineral.*, 63, 924-929.
- Marvin U. B. and Walker D. (1985) A transient heating event in the history of a highlands troctolite from Apollo 12 soil 12033. *Proc. Lunar Sci. Conf. 15th*, in *J. Geophys. Res.*, 90, C421-C429.
- Marvin U. B. and Warren P. H. (1980) A pristine eucritlike gabbro from Descartes and its exotic kindred. *Proc. Lunar Planet. Sci. Conf. 11th*, pp. 507-521.
- Marvin U. B., Wood J. A., Taylor G. J., Reid J. B. Jr., Powell B. N., Dickey J. S. Jr., and Bower J. F. (1971) Relative proportion and probable sources of rock fragments in the Apollo 12 soil samples. *Proc. Lunar Sci. Conf. 2nd*, pp. 679-699.
- Marvin U. B., Lindstrom M. M., Bernatowicz T. J., Podosek F. A., and Sugiura N. (1987) The composition and history of breccia 67015 from North Ray Crater. *Proc. Lunar Planet. Sci. Conf. 17th*, in *J. Geophys. Res.*, 90 E4 71-E490.
- Masaytis V. L., Mikhailov M. V., and Selivanovskaya T. V. (1975) *The Popigay Meteorite Crater*. Nauka, Moscow. 124 pp.
- Mason B. (1971) *Handbook of Elemental Abundances in Meteorites*. Gordon and Breach, New York. 566 pp.
- Mason B. (1979) *Cosmochemistry, Part 1: Meteorites*. U.S. Geol. Surv. Prof. Pap. 440B-1.
- Mason B., Simkin T., Norman A. F., Switzer G. S., Nelen J. A., Thompson G., and Melson W. G. (1973) Composition of Apollo 16 fines 60051, 60052, 64811, 67711, 67712, 68821 and 68822 (abstract). In *Lunar Science IV*, pp. 505-507. The Lunar Science Institute, Houston.
- Mason R. J., Guest J. E., and Cooke G. N. (1976) An Imbrium pattern of graben on the moon. *Proc. Geol. Assoc. London*, 87, pp. 161-168.
- Masuda A., Nakamura N., Kurasawa H., and Tanaka T. (1972) Precise determination of rare-earth elements in the Apollo 14 and 15 samples. *Proc. Lunar Sci. Conf. 3rd*, pp. 1307-1315.
- Masuda A., Nakamura N., and Tanaka T. (1973) Fine structures of mutually normalized rare-earth patterns of chondrites. *Geochim. Cosmochim. Acta*, 37, 239-248.
- Masuda A., Tanaka T., Nakamura N., and Kurasawa H. (1974) Possible REE anomalies of Apollo 17 REE patterns. *Proc. Lunar Sci. Conf. 5th*, pp. 1247-1253.
- Masursky H. (1964) A preliminary report on the role of isostatic rebound in the geological development of the lunar crater Ptolemaeus. In *Astrogeological Studies*, pp. 102-134. U.S. Geol. Surv. Open File Annu. Prog. Rpt., Part A. 134 pp.
- Masursky H., Colton G. W., and El-Baz F. (1978) *Apollo Over the Moon: A View from Orbit* NASA SP-362. 255 pp.
- Matsui T., Waza T., Kani K., and Suzuki S. (1982) Laboratory simulation of planetesimal collision. *J. Geophys. Res.*, 87, 10968-10982.
- Maxwell D. E. (1977) Simple Z model of cratering, ejection and the overturned flap. In *Impact and Explosion Cratering* (D. J. Roddy, R. O. Pepin, and R. B. Merrill, eds.), pp. 1003-1008. Pergamon, New York.

- Maxwell J. A., Peck L. C., and Wiik H. B. (1970) Chemical composition of Apollo 11 lunar samples 10017, 10020, 10072, and 10084. *Proc. Apollo 11 Lunar Sci. Conf.*, pp. 1369–1374.
- Maxwell T. A. (1978) Origin of multi-ring basin ridge systems: An upper limit to elastic deformation based on a finite-element model. *Proc. Lunar Planet. Sci. Conf. 9th*, pp. 3541–3559.
- Maxwell T. A., El-Baz F., and Ward S. H. (1975) Distribution, morphology, and origin of ridges and arches in Mare Serenitatis. *Geol. Soc. Am. Bull.*, 86, 1273–1278.
- May T. W. (1976) Holographic analysis and interpretation of the 5 megahertz radar imagery of the Apollo Lunar Sounder experiment in Maria Serenitatis and Crisium. M.Sc. thesis, Univ. of Utah. 91 pp.
- McCallister R. H. and Taylor L. A. (1973) Kinetics of ulvöspinel reduction—synthetic study and applications to lunar rocks. *Earth Planet. Sci. Lett.*, 17, 357–364.
- McCallum I. S. and Mathez E. A. (1975) Petrology of noritic cumulates and a partial melting model for the genesis of Fra Mauro basalts. *Proc. Lunar Sci. Conf. 6th*, pp. 395–414.
- McCallum I. S., Mathez E. A., Okamura F. P., and Ghose S. (1974) Petrology and crystal chemistry of poikilitic anorthositic gabbro 77017. *Proc. Lunar Sci. Conf. 5th*, pp. 287–302.
- McCauley J. F. (1967) Geologic map of the Hevelius region of the Moon. *U.S. Geol. Surv. Misc. Inv. Map I-491*.
- McCauley J. F. and Scott D. H. (1972) The geologic setting of the Luna 16 landing site. *Earth Planet. Sci. Lett.*, 13, 225–232.
- McCord T. B. and Adams J. B. (1973) Progress in remote optical analysis of lunar surface composition. *The Moon*, 7, 453–474.
- McCord T. B., Charette M. P., Johnson T. V., Lebofsky L. A., Pieters C., and Adams J. B. (1972a) Lunar spectral types. *J. Geophys. Res.*, 77, 1349–1359.
- McCord T. B., Charette M. P., Johnson T. V., Lebofsky L. A., and Pieters C. (1972b) Spectrophotometry (0.3 to 1.1 μm) of visited and proposed Apollo lunar landing sites. *The Moon*, 5, 52–89.
- McCord T. B., Pieters C. M., and Feierberg M. A. (1976) Multi-spectral mapping of the lunar surface using groundbased telescopes. *Icarus*, 29, 1–34.
- McCord T. B., Grabow M., Feierberg M. A., MacLaskey D., and Pieters C. M. (1979) Lunar multispectral maps: Part H of the lunar nearside. *Icarus*, 37, 1–28.
- McCord T. B., Clark R. N., Hawke B. R., McFadden L. A., Owensby P. D., Pieters C. M., and Adams J. B. (1981) Moon: Near-infrared spectral reflectance, a first good look. *J. Geophys. Res.*, 86, 10883–10892.
- McCoy J. E. (1976a) Additional photometric studies of light scattering above the lunar terminator from Apollo orbital corona photography (abstract). In *Lunar Science VII*, pp. 515–517. The Lunar Science Institute, Houston.
- McCoy J. E. (1976b) Astronaut observations (abstract). In *Abstracts for Special Symposium on Recent Activity in the Moon, Supplement to Lunar Science VII*, pp. 11–13. The Lunar Science Institute, Houston.
- McCoy J. E. and Criswell D. R. (1974a) Additional astronaut observations of possible light scattering by lunar dust atmosphere. In *Lunar Interactions* (D. R. Criswell and J. R. Freeman, eds.), pp. 105–106. The Lunar Science Institute, Houston.
- McCoy J. E. and Criswell D. R. (1974b) Evidence for a high altitude distribution of lunar dust. *Proc. Lunar Sci. Conf. 5th*, pp. 2991–3005.
- McDonnell J. A. M. (1977) The role of accretionary particles on lunar exposure and aging processes—lunar dust slows lunar clocks. *COSPAR Plenary Meeting 20th*, p. 6. Tel Aviv, Israel.
- McDonnell J. A. M., ed. (1978) *Cosmic Dust* Wiley, New York. 693 pp.
- McDonnell J. A. M. (1979) Lunar surface grain motion: Electrostatic charging, supercharging (electret effects) and mechanical bonding. In *COSPAR Space Research XIX*, pp. 455–458. Pergamon, New York.
- McDonnell J. A. M. and Flavill R. P. (1977) Lunar surface microscale transportation phenomena: I. In *COSPAR Space Research XVII*, pp. 611–616. Pergamon, New York.
- McGetchin T. R. and Head J. W. (1973) Lunar cinder cones. *Science*, 180, 68–71.
- McGetchin T. R., Settle M., and Head J. W. (1973) Radial thickness variation in crater ejecta: Implications for lunar basin models. *Earth Planet. Sci. Lett.*, 20, 226–236.
- McGetchin T. R., Settle M., and Head J. W. (1973) Radial thickness variation in crater ejecta: Implications for lunar basin models. *Earth Planet. Sci. Lett.*, 20, 226–236.
- McGuire R. E. and von Rosenvinge T. T. (1984) The energy spectra of solar energetic particles. *Adv. Space Res.*, 4, 117–125.
- McGuire R. E., von Rosenvinge T. T., and McDonald F. B. (1986) The composition of solar energetic particles. *Astrophys. J.*, 301, 938–961.
- McKay D. S. and Basu A. (1983) The production curve for agglutinates in planetary regoliths. *Proc. Lunar Planet. Sci. Conf. 14th*, in *J. Geophys. Res.*, 88, B193–B199.
- McKay D. S. and Williams R. J. (1979) A geologic assessment of potential lunar ores. In *Space Resources and Space Settlements* (J. Billingham et al., eds.), pp. 243–256. NASA SP-428.
- McKay D. S., Greenwood W. R., and Morrison D. A. (1970) Origin of small lunar particles and breccia from the Apollo 11 site. *Proc. Apollo 11 Lunar Sci. Conf.*, pp. 673–694.
- McKay D. S., Heiken G. H., Taylor R. M., Clanton U. S., Morrison D. A., and Ladle G. H. (1972) Apollo 14 soils: Size distribution and particle types. *Proc. Lunar Sci. Conf. 3rd*, pp. 983–995.
- McKay D. S., Clanton U. S., and Ladle G. (1973) Scanning electron microscope study of Apollo 15 green glass. *Proc. Lunar Sci. Conf. 4th*, pp. 225–238.
- McKay D. S., Fruland R. M., and Heiken G. H. (1974) Grain size and evolution of lunar soils. *Proc. Lunar Sci. Conf. 5th*, pp. 887–906.

- McKay D. S., Dungan M. A., Morris R. V., and Fruland R. M. (1977) Grain size, petrographic, and FMR studies of the double core 60009/10: A study of soil evolution. *Proc. Lunar Sci. Conf. 8th*, pp. 2929–2952.
- McKay D. S., Heiken G. H., and Waits G. (1978a) Core 74001/2: Grain size and petrology as a key to the rate of *in-situ* reworking and lateral transport on the lunar surfaces. *Proc. Lunar Planet. Sci. Conf. 9th*, pp. 1913–1932.
- McKay D. S., Basu A., and Waits G. (1978b) Grain size and the evolution of Luna 24 soils. In *Mare Crisium: The View from Luna 24* (R. B. Merrill and J. J. Papike, eds.), pp. 125–136. Pergamon, New York.
- McKay D. S., Basu A., and Nace G. (1980) Lunar core 15010/11: Grain size, petrology, and implications for regolith dynamics. *Proc. Lunar Planet. Sci. Conf. 11th*, pp. 1531–1550.
- McKay D. S., Bogard D. D., Morris R. V., Korotev R. L., Johnson D., and Wentworth S. J. (1986) Apollo 16 regolith breccias: Characterization and evidence for early formation in the mega-regolith. *Proc. Lunar Planet. Sci. Conf. 16th*, in *J. Geophys. Res.*, 91, D277–D303.
- McKay G. A. and Weill D. F. (1976) Petrogenesis of KREEP. *Proc. Lunar Sci. Conf. 7th*, pp. 2427–2447.
- McKay G. A. and Weill D. F. (1977) KREEP petrogenesis revisited. *Proc. Lunar Sci. Conf. 8th*, pp. 2339–2335.
- McKay G. A., Wiesmann H., Bansal B. M., and Shih C.-Y. (1979) Petrology, chemistry, and chronology of Apollo 14 KREEP basalts. *Proc. Lunar Planet. Sci. Conf. 10th*, pp. 181–205.
- McKinley J. P., Taylor G. J., Keil K., Ma M.-S., and Schmitt R. A. (1984) Apollo 16: Impact melt sheets, contrasting nature of the Cayley Plains and Descartes Mountains, and geologic history. *Proc. Lunar Planet. Sci. Conf. 14th*, in *J. Geophys. Res.*, 89, pp. B513–B524.
- McSween H. Y. Jr. (1985) SNC meteorites: Clues to martian petrologic evolution? *Rev. Geophys.*, 23, 391–416.
- Mehta S. and Goldstein J. I. (1979) Analytical electron microscopy study of submicroscopic metal particles in glassy constituents of lunar breccias 15015 and 60095. *Proc. Lunar Planet. Sci. Conf. 10th*, pp. 1507–1521.
- Mehta S., Goldstein J. I., and Friel J. J. (1979) Investigations of submicron sized metal particles in glass coatings of lunar breccia 15286. *Proc. Lunar Planet. Sci. Conf. 10th*, pp. 1523–1530.
- Melosh H. J. (1975) Large impact craters and the Moon's orientation. *Earth Planet. Sci. Lett.*, 26, 353–360.
- Melosh H. J. (1977) Crater modification by gravity: A mechanical analysis of slumping. In *Impact and Explosion Cratering* (D. J. Roddy, R. O. Pepin, and R. B. Merrill, eds.), pp. 1245–1260. Pergamon, New York.
- Melosh H. J. (1978) The tectonics of mascon loading. *Proc. Lunar Planet. Sci. Conf. 9th*, pp. 3513–3525.
- Melosh H. J. (1982) A schematic model of crater modification by gravity. *J. Geophys. Res.*, 87, 371–380.
- Mendell W. W. (1976) Degradation of large, period II craters. *Proc. Lunar Sci. Conf. 7th*, pp. 2705–2716.
- Mendell W. W., ed. (1985) *Lunar Bases and Space Activities of the 21st Century*. Lunar and Planetary Institute, Houston. 865 pp.
- Mendell W. W. and Low F. J. (1975) Infrared orbital mapping of lunar features. *Proc. Lunar Sci. Conf. 6th*, pp. 2711–2719.
- Mendell W. W. and McKay D. S. (1975) A lunar soil evolution model. *The Moon*, 13, 285–292.
- Merlivat L., Lelu M., Nief G., and Roth E. (1974) Deuterium, hydrogen, and water content of lunar material. *Proc. Lunar Sci. Conf. 5th*, pp. 1885–1895.
- Metzger A. E. and Parker R. E. (1979) The distribution of titanium on the lunar surface. *Earth Planet. Sci. Lett.*, 45, 155–171.
- Metzger A. E., Trombka J. I., Peterson L. E., Reedy D. C., and Arnold J. R. (1973) Lunar surface radioactivity: Preliminary results of the Apollo 15 and Apollo 16 gamma-ray spectrometer experiments. *Science*, 179, 800–803.
- Metzger A. E., Haines E. L., Parker R. E., and Radocinski R. G. (1977) Thorium concentrations in the lunar surface. I: Regional values and crustal content. *Proc. Lunar Sci. Conf. 8th*, pp. 949–999.
- Meyer C. (1978) Ion microprobe analyses of aluminous lunar glasses: A test of the "rock type" hypothesis. *Proc. Lunar Planet. Sci. Conf. 9th*, pp. 1551–1570.
- Meyer C. Jr. and Schonfeld E. (1977) Ion microprobe study of glass particles from lunar sample 15101 (abstract). In *Lunar Science VIII*, pp. 661–663. The Lunar Science Institute, Houston.
- Meyer C. Jr., McKay D. S., Anderson D. H., and Butler P. Jr. (1975) The source of sublimates on the Apollo 15 green and Apollo 17 orange glass samples. *Proc. Lunar Sci. Conf. 6th*, pp. 1673–1699.
- Meyer H. O. A. and Boctor N. Z. (1974) Opaque mineralogy: Apollo 17 rock 75035. *Proc. Lunar Sci. Conf. 5th*, pp. 707–716.
- Meyer H. O. A. and McCallister R. H. (1977) The Apollo 16 deep drill core. *Proc. Lunar Sci. Conf. 8th*, pp. 2889–2907.
- Michel R., Herpers U., Kulus H., and Herr W. (1972) Isotopic anomalies in lunar rhenium. *Proc. Lunar Sci. Conf. 3rd*, pp. 1917–1925.
- Middlehurst B. M. (1977) A survey of lunar transient phenomena. *Phys. Earth Planet. Inter.*, 14, 185–193.
- Miller M. D., Pacer R. A., Ma M.-S., Hawke B. R., Lookhart G. L., and Ehmann W. D. (1974) Compositional studies of the lunar regolith at the Apollo 17 site. *Proc. Lunar Sci. Conf. 5th*, pp. 1079–1086.
- Minkin J. A., Thompson C. L., and Chao E. C. T. (1977) Apollo 16 white boulders consortium samples 67455 and 67475: Petrologic investigation. *Proc. Lunar Sci. Conf. 8th*, pp. 1967–1986.
- Minnaert M. (1961) Photometry of the Moon. In *The Solar System, Vol. III: Planets and Satellites* (G. Kuiper and B. Middlehurst, eds.), pp. 213–248. Univ. of Chicago, Chicago. 601 pp.
- Misra K. C. and Taylor L. A. (1975a) Characteristics of metal particles in Apollo 16 rocks. *Proc. Lunar Sci. Conf. 6th*, pp. 615–639.

- Misra K. C. and Taylor L. A. (1975b) Correlation between native metal compositions and the petrology of Apollo 16 rocks (abstract). In *Lunar Science VI*, pp. 566–568. The Lunar Science Institute, Houston.
- Mitchell J. K. (1976) *Fundamentals of Soil Behavior*. Wiley, New York. 422 pp.
- Mitchell J. K. and Durgunoglu H. T. (1973) *In-situ* strength by static cone penetration test. *Proc. Intl. Conf. on Soil Mech. and Found. Eng., Vol. 1*, pp. 279–286.
- Mitchell J. K. and Houston W. N. (1974) Static penetration testing on the Moon. *European Symposium in Penetration Testing 1st*, pp. 277–284. Intl. Soc. for Soil Mech. and Found. Eng.
- Mitchell J. K., Bromwell L. G., Carrier W. D. III, Costes N. C., and Scott R. F. (1971) Soil mechanics experiment. In *Apollo 14 Preliminary Science Report*, pp. 87–108. NASA SP-272.
- Mitchell J. K., Bromwell L. G., Carrier W. D. III, Costes N. C., Houston W. N., and Scott R. F. (1972a) Soil-mechanics experiments. In *Apollo 15 Preliminary Science Report*, pp. 7–1 to 7–28. NASA SP-289.
- Mitchell J. K., Carrier W. D. III, Houston W. N., Scott R. F., Bromwell L. G., Durgunoglu H. T., Hovland H. J., Treadwell D. D., and Costes N. C. (1972b) Soil mechanics. In *Apollo 16 Preliminary Science Report*, pp. 8–1 to 8–29. NASA SP-315.
- Mitchell J. K., Bromwell L. G., Carrier W. D. III, Costes N. C., and Scott R. F. (1972c) Soil mechanical properties at the Apollo 14 site. *J. Geophys. Res.*, 77, 5641–5664.
- Mitchell J. K., Houston W. N., Scott R. F., Costes N. C., Carrier W. D. III, and Bromwell L. G. (1972d) Mechanical properties of lunar soil: Density, porosity, cohesion, and angle of friction. *Proc. Lunar Sci. Conf. 3rd*, pp. 3235–3253.
- Mitchell J. K., Carrier W. D. III, Costes N. C., Houston W. N., Scott R. F., and Hovland H. J. (1973a) Soil mechanics. In *Apollo 17 Preliminary Science Report*, pp. 8–1 to 8–22. NASA SP-330.
- Mitchell J. K., Carrier W. D. III, Costes N. C., Houston W. N., and Scott R. F. (1973b) Surface soil variability and stratigraphy at the Apollo 16 site. *Proc. Lunar Sci. Conf. 4th*, pp. 2437–2445.
- Mitchell J. K., Houston W. N., Carrier W. D. III, and Costes N. C. (1974) *Apollo Soil Mechanics Experiment S-200*. Final report, NASA Contract NAS 9-11266, Space Sciences Laboratory Series 15, Issue 7, Univ. of California, Berkeley.
- Moore C. B. and Lewis C. F. (1976) Total nitrogen contents of Apollo 15, 16, and 17 lunar rocks and breccias (abstract). In *Lunar Science VII*, pp. 571–573. The Lunar Science Institute, Houston.
- Moore C. B., Lewis C. F., Larimer J. W., Delles F. M., Gooley R., and Nichiporuk W. (1971) Total carbon and nitrogen abundances in Apollo 12 lunar samples. *Proc. Lunar Sci. Conf. 2nd*, pp. 1343–1350.
- Moore C. B., Lewis C. F., Cripe J., Delles F. M., Kelly W. R., and Gibson E. K. Jr. (1972) Total carbon, nitrogen, and sulfur in Apollo 14 lunar samples. *Proc. Lunar Sci. Conf. 3rd*, pp. 2051–2058.
- Moore C. B., Lewis C. F., and Gibson E. K. Jr. (1973) Total carbon contents of Apollo 15 and 16 lunar samples. *Proc. Lunar Sci. Conf. 4th*, pp. 1613–1623.
- Moore C. B., Lewis C. F., and Cripe J. D. (1974) Total carbon and sulfur contents of Apollo 17 lunar samples. *Proc. Lunar Sci. Conf. 5th*, pp. 1897–1906.
- Moore H. J. (1970) *Estimates of the Mechanical Properties of Lunar Surface Using Tracks and Secondary Craters Produced by Blocks and Boulders*. U.S. Geol. Surv. Interagency Report, Astrogeology, 22.
- Moore H. J. (1972) Large blocks around lunar craters. In *Analysis of Apollo 10 Photography and Visual Observations*, p. 26. NASA SP-232 (1971).
- Moore H. J., Hodges C. A., and Scott D. H. (1974) Multiringed basins—illustrated by Orientale and associated features. *Proc. Lunar Sci. Conf. 5th*, pp. 71–100.
- Moore R. K. (1983) Radar fundamentals and scatterometers. In *Manual of Remote Sensing Vol. 1*, 2nd edition (R. N. Colwell, ed.), pp. 369–428. American Society of Photogrammetry, Falls Church, Virginia.
- Morgan J. W. and Petrie R. K. (1979) Breccias 73215 and 73255: Siderophile and volatile trace elements. *Proc. Lunar Planet. Sci. Conf. 10th*, pp. 789–801.
- Morgan J. W. and Wandless G. A. (1979) 74001 drive tube: Siderophile elements match IIB iron meteorite pattern. *Proc. Lunar Planet. Sci. Conf. 10th*, pp. 327–340.
- Morgan J. W. and Wandless G. A. (1984) Surface-correlated trace elements in 15426 lunar glass (abstract). In *Lunar and Planetary Science XV*, pp. 562–563. Lunar and Planetary Institute, Houston.
- Morgan J. W., Krähenbühl U., Ganapathy R., and Anders E. (1972a) Trace elements in Apollo 15 samples: Implications for meteorite influx and volatile depletion on the Moon. *Proc. Lunar Sci. Conf. 3rd*, pp. 1361–1376.
- Morgan J. W., Laul J. C., Krähenbühl U., Ganapathy R., and Anders E. (1972b) Major impacts on the Moon: Characterization from trace elements in Apollo 12 and 14 samples. *Proc. Lunar Sci. Conf. 3rd*, pp. 1377–1395.
- Morgan J. W., Krähenbühl U., Ganapathy R., Anders E., and Marvin U. (1973) Trace element abundances and petrology of separates from Apollo 15 soils. *Proc. Lunar Sci. Conf. 4th*, pp. 1379–1398.
- Morgan J. W., Ganapathy R., Higuchi H., Krähenbühl U., and Anders E. (1974) Lunar basins: Tentative characterization of projectiles from meteoritic elements in Apollo 17 boulders. *Proc. Lunar Sci. Conf. 5th*, pp. 1703–1736.
- Morgan J. W., Higuchi H., and Anders E. (1975) Meteoritic material in a boulder from the Apollo 17 site: Implications for its origin. *The Moon*, 14, 373–383.
- Morgan J. W., Higuchi H., Takahashi H., and Hertogen J. (1978) A “chondritic” eucrite parent body: Inference from trace elements. *Geochim. Cosmochim. Acta*, 42, 27–38.
- Morris R. V. (1976) Surface exposure indices of lunar rocks: A comparative FMR study. *Proc. Lunar Sci. Conf. 7th*, pp. 315–335.
- Morris R. V. (1977) Origin and evolution of the grain-size dependence of the concentration of fine-grained metal

- in lunar soils: The maturation of lunar soils to a steady-state stage. *Proc. Lunar Sci. Conf. 8th*, pp. 3719–3747.
- Morris R. V. (1978a) In situ reworking (gardening) of the lunar surface: Evidence from the Apollo cores. *Proc. Lunar Planet. Sci. Conf. 9th*, pp. 1801–1811.
- Morris R. V. (1978b) The surface exposure (maturity) of lunar soils; some concepts and I_s/FeO compilation. *Proc. Lunar Planet. Sci. Conf. 9th*, pp. 2287–2297.
- Morris R. V. (1980) Origins and size distribution of metallic iron particles in the lunar regolith. *Proc. Lunar Planet. Sci. Conf. 11th*, pp. 1697–1712.
- Morris R. V. (1985) Determination of optical penetration depths from reflectance and transmittance measurements on albite powders (abstract). In *Lunar and Planetary Science XVI*, pp. 581–582. Lunar and Planetary Institute, Houston.
- Morris R. V. and Gose W. A. (1976) Ferromagnetic resonance and magnetic studies of cores 60009/10 and 60003: Compositional and surface-exposure stratigraphy. *Proc. Lunar Sci. Conf. 7th*, pp. 1–11.
- Morris R. V., Lauer H. V. Jr., and Gose W. A. (1979) Characterization and depositional and evolutionary history of the Apollo 17 deep drill core. *Proc. Lunar Planet. Sci. Conf. 10th*, pp. 1141–1157.
- Morris R. V., Score R., Dardano C., and Heiken G. (1983) *Handbook of Lunar Soils*. JSC Publ. No. 19069, Planetary Materials Branch Publ. 67. NASA Johnson Space Center, Houston. 914 pp.
- Morris R. V., See T. H., and Hörz F. (1986) Composition of the Cayley Formation at Apollo 16 as inferred from impact melt splashes. *Proc. Lunar Planet. Sci. Conf. 17th*, in *J. Geophys. Res.*, 91, E21–E42.
- Morrison D. A. and Clanton U. S. (1979) Properties of microcraters and cosmic dust of less than 1000 Å dimensions. *Proc. Lunar Planet. Sci. Conf. 10th*, pp. 1649–1663.
- Morrison G. H., Gerard J. T., Kashuba A. T., Gangadharam E. V., Rothenberg A. M., Potter N. M., and Miller G. B. (1970) Elemental abundances in lunar soil and rock. *Proc. Apollo 11 Lunar Sci. Conf.*, pp. 1383–1392.
- Morrison G. H., Gerard J. T., Potter N. M., Gangadharam E. V., Rothenberg A. M., and Burdo R. A. (1971) Elemental abundances of lunar soil and rocks from Apollo 12. *Proc. Lunar Sci. Conf. 2nd*, pp. 1169–1185.
- Morrison G. H., Nadkarni R. A., Jaworski J., Botto R. I., and Roth J. R. (1973) Elemental abundances of Apollo 16 samples. *Proc. Lunar Sci. Conf. 4th*, pp. 1399–1405.
- Morrison R. H. and Oberbeck V. R. (1975) Geomorphology of crater and basin deposits — emplacement of the Fra Mauro Formation. *Proc. Lunar Sci. Conf. 6th*, pp. 2503–2530.
- Morrison R. H. and Oberbeck V. R. (1978) A composition and thickness model for lunar impact crater and basin deposits. *Proc. Lunar Planet. Sci. Conf. 9th*, pp. 3763–3785.
- Muehlberger W. R. (1974) Structural history of southeastern Mare Serenitatis and adjacent highlands. *Proc. Lunar Sci. Conf. 5th*, pp. 101–110.
- Muehlberger W. R., Batson R. M., Boudette E. L., Duke C. M., Eggleton R. E., Elston D. P., England A. W., Freeman V. L., Hait M. H., Hall T. A., Head J. W., Hodges C. A., Holt H. E., Jackson E. D., Jordan J. A., Larson K. B., Milton D. J., Reed V. S., Rennilson J. J., Schaber G. G., Schafer J. P., Silver L. T., Stuart-Alexander D., Sutton R. L., Swann G. A., Tyner R. L., Ulrich G. E., Wilshire H. G., Wolfe E. W., and Young J. W. (1972) Preliminary geologic investigation of the Apollo 16 landing site. In *Apollo 16 Preliminary Science Report*, pp. 6–1 to 6–81. NASA SP-315.
- Muehlberger W. R., Batson R. M., Cernan E. A., Freeman V. L., Hait M. H., Holt H. E., Howard K. A., Jackson E. D., Larson K. B., Reed V. S., Rennilson J. J., Schmitt H. H., Scott D. H., Sutton R. L., Stuart-Alexander D., Swann G. A., Trask N. J., Ulrich G. E., Wilshire H. G., and Wolfe E. W. (1973) Preliminary geologic investigation of the Apollo 17 landing site. In *Apollo 17 Preliminary Science Report*, pp. 6–1 to 6–91. NASA SP-330.
- Muhleman D. O. (1964) Radar scattering from Venus and the Moon. *Astron. J.*, 69, 34–41.
- Muhleman D. O. (1972) Microwave emission from the Moon. In *Thermal Characteristics of the Moon*, Vol. 28 (J. Lucas, ed.), pp. 51–81. MIT, Cambridge.
- Muhleman D. O., Brown W. E. Jr., and Davids L. (1968a) Radar reflectivity analysis, lunar surface electromagnetic properties, part I. In *Surveyor 7 Preliminary Report*, pp. 181–186. NASA SP-173.
- Muhleman D. O., Brown W. E. Jr., and Davids L. (1968b) Lunar surface electromagnetic properties: Radar reflectivity analysis. In *Surveyor 7 Mission Report, Part 2: Science Results*, pp. 209–220. JPL Tech. Rpt. 32–1264, Jet Propulsion Laboratory, Pasadena.
- Muhleman D. O., Brown W. E. Jr., Davids L., Negus de Wys J., and Peake W. H. (1969) Lunar surface electromagnetic properties. In *Surveyor Program Results*, pp. 203–269. NASA SP-184.
- Mukherjee N. R. (1975) Solar-wind interactions: Nature and composition of the lunar atmosphere. *The Moon*, 14, 169–186.
- Müller G. (1967) *Methods in Sedimentary Petrology*, pp. 100–101. Hafner, New York.
- Müller O. (1972) Chemically bound nitrogen abundances in lunar samples, and active gases released by heating at lower temperatures (250–500°C). *Proc. Lunar Sci. Conf. 3rd*, pp. 2059–2068.
- Müller O. (1973) Chemically bound nitrogen contents of Apollo 16 and Apollo 15 lunar fines. *Proc. Lunar Sci. Conf. 4th*, pp. 1625–1634.
- Müller O. (1974) Solar wind nitrogen and indigenous nitrogen in Apollo 17 lunar samples. *Proc. Lunar Sci. Conf. 5th*, pp. 1907–1918.
- Müller P. M. and Sjogren W. L. (1968) Mascons: Lunar mass concentrations. *Science*, 161, 680–684.
- Müller P. M. and Sjogren W. L. (1969) Lunar gravimetry and mascons. *Appl. Mech. Rev.*, 22, 955–959.
- Murali A. V., Ma M.-S., and Schmitt R. A. (1977) Chemistry of 30 Apollo 17 rake basalts; 71597 a product of partial

- olivine accumulation (abstract). In *Lunar Science VIII*, pp. 703–705. The Lunar Science Institute, Houston.
- Murali A. V., Pawaskar P. B., and Reedy G. R. (1979) Chemical studies of two Luna-24 regolith samples. In *Advances in Lunar Research: Luna 24 Samples* (S. K. Trehan and H. Y. Mohan Ram, eds.), pp. 49–58. Indian Natl. Sci. Acad., New Dehli.
- Murali A. V., Zolensky M. E., and Blanchard D. P. (1987) Tektite-like bodies at Lona Crater, India: Implications for the origin of tektites. *Proc. Lunar Planet. Sci. Conf. 17th*, in *J. Geophys. Res.*, 92, E729–E735.
- Murase T. and McBirney A. R. (1970) Viscosity of lunar lavas. *Science*, 167, 1491–1493.
- Murray B. C., Belton M. J. S., Danielson G. E., Davies M. E., Hapke B., O'Leary B. T., Strom R. G., Suomvi V. E., and Trask N. J. (1974) Preliminary description and interpretation from Mariner 10 pictures. *Science*, 185, 169–179.
- Murray J. B. (1980) Oscillating peak model of basin and crater formation. *Moon and Planets*, 22, 269–291.
- Murthy V. R., Evensen N. M., Jahn B.-M., and Coscio M. R. Jr. (1972) Apollo 14 and 15 samples: Rb-Sr ages, trace elements, and lunar evolution. *Proc. Lunar Sci. Conf. 3rd*, pp. 1503–1514.
- Mustard J. F. and Pieters C. M. (1987) Quantitative abundance estimates from bidirectional reflectance measurements. *Proc. Lunar Planet. Sci. Conf. 17th*, in *J. Geophys. Res.*, 92, E617–E626.
- Mutch T. A. (1970) *Geology of the Moon—A Stratigraphic View*. Princeton Univ., Princeton, New Jersey. 324 pp.
- Nagasawa H., Schreiber H. D., and Blanchard D. P. (1976) Partition coefficients of REE and Sc in perovskite, melilite, and spinel and their implications for Allende inclusions (abstract). In *Lunar Science VII*, pp. 588–590. The Lunar Science Institute, Houston.
- Nakamura N. (1974) Determination of REE, Ba, Fe, Mg, Na and K in carbonaceous and ordinary chondrites. *Geochim. Cosmochim. Acta*, 38, 757–775.
- Nakamura N., Unruh D. M., and Tatsumoto M. (1986) REE, Rb-Sr, and Pb isotopic characteristics of the Yamato-791197 meteorite: Evidence for a lunar highland origin. *Proceedings of the Tenth Symposium on Antarctic Meteorites*, pp. 106–115. Natl. Inst. for Polar Res., Japan.
- Nakamura Y. (1978) A₁ moonquakes: Source distribution and mechanism. *Proc. Lunar Planet. Sci. Conf. 9th*, pp. 3589–3607.
- Nakamura Y. (1980) Shallow moonquakes: How they compare with earthquakes. *Proc. Lunar Planet. Sci. Conf. 11th*, pp. 1847–1853.
- Nakamura Y., Latham G. V., and Dorman H. J. (1982) Apollo lunar seismic experiment—final summary. *Proc. Lunar Planet. Sci. Conf. 13th*, in *J. Geophys. Res.*, 87, A117–A123.
- Naney M. T., Crowl D. M., and Papike J. J. (1976) The Apollo 16 drill core: Statistical analysis of glass chemistry and the characterization of a high alumina-silica poor (HASP) glass. *Proc. Lunar Sci. Conf. 7th*, pp. 155–184.
- NASA (1969) *Analysis of Apollo 8 Photography and Observations*. NASA SP-201. 337 pp.
- NASA Advisory Council (1986) *The Crisis in Space and Earth Science: A Time for New Commitment*. Report by the Space and Earth Science Advisory Committee of the NASA Advisory Council, Washington, DC, November 1986. 84 pp.
- NASA Manned Spacecraft Center (1970) *Apollo 12 Preliminary Science Report*. NASA SP-235. 227 pp.
- Nash W. P. and Hansel W. D. (1973) Partial pressures of oxygen, phosphorus and fluorine in some lunar lavas. *Earth Planet. Sci. Lett.*, 20, 13–27.
- National Commission on Space (1986) *Pioneering the Space Frontier*. Bantam, New York. 211 pp.
- Nava D. F. (1974) Chemistry of some rock types and soils from the Apollo 15, 16 and 17 lunar sites (abstract). In *Lunar Science V*, pp. 547–549. The Lunar Science Institute, Houston.
- Nava D. F. and Philpotts J. A. (1973) A lunar differentiation model in light of new chemical data on Luna 20 and Apollo 16 soils. *Geochim. Cosmochim. Acta*, 37, 963–973.
- Nava D. F., Lindstrom M. M., Schuhmann P. J., Lindstrom D. J., and Philpotts J. A. (1976) The remarkable chemical uniformity of Apollo 16 layered deep drill core section 60002. *Proc. Lunar Sci. Conf. 7th*, pp. 133–139.
- Nava D. F., Winzer S. R., Lindstrom D. J., Meyerhoft M., Lum R. K. L., Schuhmann P. J., Lindstrom M. M., and Philpotts J. A. (1977) Rind glass and breccia: A study of lunar sample 15255 (abstract). In *Lunar Science VIII*, pp. 720–722. The Lunar Science Institute, Houston.
- Nehru C. E., Prinz M., Dowty E., and Keil K. (1974) Spinel-group minerals and ilmenite in Apollo 15 rock samples. *Am. Mineral.*, 59, 1220–1234.
- Nehru C. E., Warner R. D., and Keil K. (1976) *Electron Microprobe Analyses of Opaque Mineral Phases from Apollo 11 Basalts*. Univ. of New Mexico Spec. Publ. 17, Albuquerque.
- Neukum G. (1977) Different ages for lunar light plains. *The Moon*, 17, 383–393.
- Neukum G. and Wise D. U. (1976) Mars: A standard crater curve and possible new time scale. *Science*, 194, 1381–1387.
- Neukum G., Konig B., Fechtig H., and Storzer D. (1975) Cratering in the Earth-Moon system: Consequences for age determinations by crater counting. *Proc. Lunar Sci. Conf. 6th*, pp. 2597–2620.
- Newsom H. E. (1986) Constraints on the origin of the Moon from the abundance of molybdenum and other siderophile elements. In *Origin of the Moon* (W. K. Hartmann, R. J. Phillips, and G. J. Taylor, eds.), pp. 203–229. Lunar and Planetary Institute, Houston.
- Newton R. C., Anderson A. T., and Smith J. V. (1971) Accumulation of olivine in rock 12040 and other basaltic fragments in the light of analysis and synthesis. *Proc. Lunar Sci. Conf. 2nd*, pp. 575–582.
- Nicogossian A. E., Huntton C. L., and Pool S. L., eds. (1989) *Space Physiology and Medicine*, 2nd edition. Lea and Febiger, Philadelphia. 401 pp.
- Nord G. L. Jr. and James O. B. (1978) Consortium breccia 73255: Thermal and deformational history of bulk

- breccia and clasts, as determined by electron petrography. *Proc. Lunar Planet. Sci. Conf. 9th*, pp. 821–839.
- Nord G. L. Jr. and Wandless M.-V. (1983) Petrology and comparative thermal and mechanical histories of clasts in breccia 62236. *Proc. Lunar Planet. Sci. Conf. 13th*, in *J. Geophys. Res.*, 88, A645–A657.
- Nord G. L. Jr., Christie J. M., Heuer A. H., and Lally J. S. (1975) North Ray Crater breccias: an electron petrographic study. *Proc. Lunar Sci. Conf. 6th*, pp. 779–797.
- Nordmeyer E. F. (1967) *Lunar Surface Mechanical Properties Derived from Track Left by Nine-Meter Boulder*. MSC Internal Note No. 67–TH-1, NASA Manned Spacecraft Center, Houston.
- Norman M. D. (1981) Petrology of suevitic lunar breccia 67016. *Proc. Lunar Planet. Sci. 12B*, pp. 235–252.
- Norman M. D. and Ryder G. (1980a) Geochemical evidence for the role of ilmenite and clinopyroxene in the early lunar differentiation (abstract). In *Lunar and Planetary Science XI*, pp. 821–823. Lunar and Planetary Institute, Houston.
- Norman M. D. and Ryder G. (1980b) Geochemical constraints on the igneous evolution of the lunar crust. *Proc. Lunar Planet. Sci. Conf. 11th*, pp. 531–559.
- Norris S. J., Swart P. K., Wright I. P., Grady M. M., and Pillinger C. T. (1983) A search for correlatable, isotopically light carbon and nitrogen in lunar soils and breccias. *Proc. Lunar Planet. Sci. Conf. 14th*, in *J. Geophys. Res.*, 88, B200–B210.
- Nunes P. D. and Tatsumoto M. (1973) Excess lead in “rusty rock” 66095 and implications for an early lunar differentiation. *Science*, 182, 916–920.
- Nunes P. D., Tatsumoto M., Knight R. J., Unruh D. M., and Doe B. R. (1973) U-Th-Pb systematics of some Apollo 16 lunar samples. *Proc. Lunar Sci. Conf. 4th*, pp. 1797–1822.
- Nunes P. D., Knight R. J., Unruh D. M., and Tatsumoto M. (1974a) The primitive nature of the lunar crust and the problem of initial Pb isotopic compositions of a lunar rock: A Rb-Sr and U-Th-Pb study of Apollo 16 samples (abstract). In *Lunar Science V*, pp. 559–561. The Lunar Science Institute, Houston.
- Nunes P. D., Tatsumoto M., and Unruh D. M. (1974b) U-Th-Pb systematics of some Apollo 17 samples (abstract). In *Lunar Science V*, pp. 562–564. The Lunar Science Institute, Houston.
- Nunes P. D., Tatsumoto M., and Unruh D. (1974c) U-Th-Pb systematics of some Apollo 17 lunar samples and implications for a lunar basin excavation chronology. *Proc. Lunar Sci. Conf. 5th*, pp. 1487–1514.
- Nunes P. D., Tatsumoto M., and Unruh D. M. (1975) U-Th-Pb systematics of anorthositic gabbros 78155 and 77017—implications for early lunar evolution. *Proc. Lunar Sci. Conf. 6th*, pp. 1431–1444.
- Nyquist L. E. (1977) Lunar Rb-Sr chronology. *Phys. Chem. Earth*, 10, 103–142.
- Nyquist L. E. (1982) Radiometric ages and isotopic systematics of pristine plutonic lunar rocks (abstract). In *Workshop on Magmatic Processes of Early Planetary Crusts* (D. Walker and I. S. McCallum, eds.), pp. 114–120. LPI Tech Rpt. 82–01, Lunar and Planetary Institute, Houston.
- Nyquist L. E., Wiesmann H., Shih C.-Y., and Bansal B. M. (1977) REE and Rb-Sr analysis of 15405 quartz-monzodiorite (super-KREEP) (abstract). In *Lunar Science VIII*, pp. 738–740. The Lunar Science Institute, Houston.
- Nyquist L. E., Wiesmann H., Bansal B., Wooden J., and McKay G. (1978) Chemical and Sr-isotopic characteristics of the Luna 24 samples. In *Mare Crisium: The View from Luna 24* (R. B. Merrill and J. J. Papike, eds.), pp. 631–656. Pergamon, New York.
- Nyquist L. E., Shih C.-Y., Wooden J. L., Bansal B. M., and Wiesmann H. (1979) The Sr and Nd isotopic record of Apollo 12 basalts: Implications for lunar geochemical evolution. *Proc. Lunar Planet. Sci. Conf. 10th*, pp. 77–114.
- Oberbeck V. R. (1975) The role of ballistic erosion and sedimentation in lunar stratigraphy. *Rev. Geophys. Space Phys.*, 13, 377–362.
- Oberbeck V. R. (1977) Application of high explosive cratering to planetary problems. In *Impact and Explosion Cratering* (D. J. Roddy, R. O. Pepin, and R. B. Merrill, eds.), pp. 45–66. Pergamon, New York.
- Oberbeck V. R. and Quaide W. L. (1968) Genetic implications of lunar regolith thickness variations. *Icarus*, 9, 446–465.
- Oberbeck V. R., Quaide W. L., and Greeley R. (1969) On the origin of lunar sinuous rilles. *Mod. Geol.*, 1, 75–80.
- Oberbeck V. R., Greeley R., Morgan R. B., and Lovas M. J. (1971) *Lunar Rilles—A Catalog and Method of Classification*. NASA TM X-62,088. 83 pp.
- Oberbeck V. R., Morrison R. H., Hörz F., Quaide W. L., and Gault D. E. (1974) Smooth plains and continuous deposits of craters and basins. *Proc. Lunar Sci. Conf. 5th*, pp. 111–136.
- Oberst J. and Nakamura Y. (1986) Distinct meteoroid families identified on the lunar seismograms. *Proc. Lunar Planet. Sci. Conf. 17th*, in *J. Geophys. Res.*, 91, E769–E773.
- O'Hara M. J. and Humphries D. J. (1975) Armalcolite crystallization, phenocryst assemblages, eruption conditions and origin of eleven high titanium basalts from Taurus Littrow (abstract). In *Lunar Science VI*, pp. 619–621. The Lunar Science Institute, Houston.
- O'Hara M. J., Biggar G. M., Hill P. G., Jeffries B., and Humphries D. J. (1974) Plagioclase saturation in lunar high-Ti basalt. *Earth Planet. Sci. Lett.*, 21, 253–268.
- O'Keefe J. D. and Ahrens T. J. (1975) Shock effects from a large impact on the moon. *Proc. Lunar Sci. Conf. 6th*, pp. 2831–2844.
- Olhoef G. R. (1979) Impulse radar studies of near surface geological structure (abstract). In *Lunar and Planetary Science X*, pp. 943–945. Lunar and Planetary Institute, Houston.
- Olhoef G. R. (1984) Applications and limitations of ground penetrating radar. In *Expanded Abstracts, 54th Ann. Int. Meeting and Expo. of the Soc. of Explor. Geophys.*, pp. 147–148. Atlanta, Georgia.

- Olhoeft G. R. and Strangway D. W. (1975) Dielectric properties of the first 100 meters of the Moon. *Earth Planet. Sci. Lett.*, 24, 394–404.
- Olhoeft G. R., Strangway D. W., and Frisillo A. L. (1973a) Lunar sample electrical properties. *Proc. Lunar Sci. Conf. 4th*, pp. 3133–3149.
- Olhoeft G. R., Strangway D. W., Pearce G. W., Frisillo A. L., and Gose W. A. (1973b) Electrical and magnetic properties of Apollo 17 soils. *Eos Trans. AGU*, 54, pp. 601.
- Olhoeft G. R., Frisillo A. L., Strangway D. W., and Sharpe H. (1974a) Temperature dependence of electrical conductivity and lunar temperatures. *The Moon*, 9, 79–87.
- Olhoeft G. R., Frisillo A. L., and Strangway D. W. (1974b) Electrical properties of lunar soil sample 15301,38. *J. Geophys. Res.*, 79, 1599–1604.
- Olhoeft G. R., Strangway D. W., and Pearce G. W. (1975) Effects of water on electrical properties of lunar fines. *Proc. Lunar Sci. Conf. 6th*, 3333–3342.
- Olhoeft G. R., Schaefer B., and Johnson G. R. (1979) Experimental measurements of surface and volume scattering processes at microwave wavelengths (abstract). In *Lunar and Planetary Science X*, pp. 946–948. Lunar and Planetary Institute, Houston.
- Onorato P. I. K., Uhlmann D. R., and Simonds C. H. (1976) Heat flow in impact melts: Apollo 17 Station 6 Boulder and some application to other breccias and xenolith laden melts. *Proc. Lunar Sci. Conf. 7th*, pp. 2449–2467.
- Onorato P. I. K., Uhlmann D. R., Taylor L. A., Coish R. A., and Gamble R. P. (1978) Olivine cooling speedometers. *Proc. Lunar Planet. Sci. Conf. 9th*, pp. 613–628.
- Orphal D. L. (1977) Calculations of explosive cratering—II: Cratering mechanics and phenomenology. In *Impact and Explosion Cratering* (D. J. Roddy, R. O. Pepin, and R. B. Merrill, eds.), pp. 907–918. Pergamon, New York.
- Orphal D. L., Borden W. F., Larson S. A., and Schultz P. H. (1980) Impact melt generation and transport. *Proc. Lunar Planet. Sci. Conf. 11th*, pp. 2309–2323.
- Ostertag R. (1983) Shock experiments on feldspar crystals. *Proc. Lunar Planet. Sci. Conf. 14th*, in *J. Geophys. Res.*, 88, B364–B376.
- Ostertag R., Stöffler D., Bischoff A., Palme H., Schulz L., Spettel B., Weber H., Weckwerth G., and Wänke H. (1986) Lunar meteorite Yamato-791197: Petrography, shock history and chemical composition. *Proceedings of the Tenth Symposium on Antarctic Meteorites*, pp. 17–44. Natl. Inst. for Polar Res., Tokyo.
- Ostertag R., Stöffler D., Borchardt R., Palme H., Spettel B., and Wänke H. (1987) Precursor lithologies and metamorphic history of granulitic breccias from North Ray Crater, Station 11, Apollo 16. *Geochim. Cosmochim. Acta*, 51, 131–142.
- Ostro S. J. (1983) Planetary radar astronomy. *Rev. Geophys. Space Phys.*, 21, 186–196.
- Ozima M. and Podosek F. A. (1983) *Noble Gas Geochemistry*. Cambridge Univ., New York. 400 pp.
- Palme H. (1980) The meteoritic contamination of terrestrial and lunar impact melts and the problem of indigenous siderophiles in the lunar highlands. *Proc. Lunar Planet. Sci. Conf. 11th*, pp. 481–506.
- Palme H., Baddenhausen H., Blum K., Cendales M., Dreibus G., Hofmeister H., Kruse H., Palme C., Spettel B., Vilcsek E., Wänke H., and Kurat G. (1978) New data on lunar samples and achondrites and a comparison of the least fractionated samples from the Earth, the Moon and the Eucrite Parent Body. *Proc. Lunar Planet. Sci. Conf. 9th*, pp. 25–57.
- Palme H., Spettel B., Weckwerth G., and Wänke H. (1983) Antarctic meteorite ALHA 81005, a piece from the ancient lunar crust. *Geophys. Res. Lett.*, 10, 817–820.
- Palme H., Spettel B., Wänke H., Bischoff A., and Stöffler D. (1984) Early differentiation of the Moon: Evidence from trace elements in plagioclase. *Proc. Lunar Planet. Sci. Conf. 15th*, in *J. Geophys. Res.*, 89, C3–C15.
- Papanastassiou D. A. and Wasserburg G. J. (1971) Rb-Sr ages of igneous rocks from the Apollo 14 mission and the age of the Fra Mauro Formation. *Earth Planet. Sci. Lett.*, 12, 36–48.
- Papanastassiou D. A. and Wasserburg G. J. (1972) The Rb-Sr age of a crystalline rock from Apollo 16. *Earth Planet. Sci. Lett.*, 16, 289–298.
- Papanastassiou D. A. and Wasserburg G. J. (1976) Rb-Sr age of troctolite 76535. *Proc. Lunar Sci. Conf. 7th*, pp. 2035–2054.
- Papike J. J. and Bence A. E. (1978) Lunar mare versus terrestrial midocean ridge basalts: Planetary constraints on basaltic volcanism. *Geophys. Res. Lett.*, 5, 803–806.
- Papike J. J. and Cameron M. (1976) Crystal chemistry of silicate minerals of geophysical interest. *Rev. Geophys. Space Phys.*, 14, 37–80.
- Papike J. J. and Vaniman D. T. (1978) Luna 24 ferrobasalts and the mare basalt suite: Comparative chemistry, mineralogy, and petrology. In *Mare Crisium: The View from Luna 24* (J. J. Papike and R. B. Merrill, eds.), pp. 371–401. Pergamon, New York.
- Papike J. J., Bence A. E., Brown G. E., Prewitt C. T., and Wu C. H. (1971) Apollo 12 clinopyroxenes: Exsolution and epitaxy. *Earth Planet. Sci. Lett.*, 10, 307–315.
- Papike J. J., Bence A. E., and Lindsley D. H. (1974) Mare basalts from the Taurus-Littrow region of the Moon. *Proc. Lunar Sci. Conf. 5th*, pp. 471–504.
- Papike J. J., Hodges F. N., Bence A. E., Cameron M., and Rhodes J. M. (1976) Mare basalts: Crystal chemistry, mineralogy, and petrology. *Rev. Geophys. Space Phys.*, 14, 475–540.
- Papike J. J., Simon S. B., White C., and Lau J. C. (1981) The relationship of the lunar regolith <10 mm fraction and agglutinates. Part I: A model for agglutinate formation and some indirect supportive evidence. *Proc. Lunar Planet. Sci. 12B*, pp. 409–420.
- Papike J. J., Simon S. B., and Lau J. C. (1982) The lunar regolith: Chemistry, mineralogy, and petrology. *Rev. Geophys. Space Phys.*, 20, 761–826.
- Parker M. N. and Tyler G. L. (1973) Bistatic-radar estimation of surface-slope probability distributions with applications to the Moon. *Radio Sci.*, 8, 177–184.

- Pearce G. W. and Chou C. L. (1976) Relationships between siderophile elements and metallic iron contents of Apollo 16 and 17 lunar soils (abstract). In *Lunar Science VII*, pp. 673–675. The Lunar Science Institute, Houston.
- Pearce G. W., Gose W. A., and Lindsay J. (1975) Reduction of iron and regolith soil maturity (abstract). In *Lunar Science VI*, pp. 634–636. The Lunar Science Institute, Houston.
- Peckett A., Phillips R., and Brown G. M. (1972) New zirconium-rich minerals from Apollo 14 and 15 lunar rocks. *Nature*, 236, 215–217.
- Peeples W. J., Sill W. R., May T. W., Ward S. H., Phillips R. J., Jordan R. L., Abbott E. A., and Killpack T. J. (1978) Orbital radar evidence for lunar subsurface layering in Maria Serenitatis and Crisium. *J. Geophys. Res.*, 83, 3459–3468.
- Pepin R. O. (1980) Rare gases in the past and present solar wind. In *The Ancient Sun: Fossil Record in the Earth, Moon and Meteorites* (R. O. Pepin, J. A. Eddy, and R. B. Merrill, eds.), pp. 411–421. Pergamon, New York.
- Pepin R. O., Nyquist L. E., Phinney D., and Black D. C. (1970) Rare gases in Apollo 11 lunar material. *Proc. Apollo 11 Lunar Sci. Conf.*, pp. 1435–1454.
- Pepin R. O., Basford J. R., Dragon J. C., Coscio M. R., and Murthy V. R. (1974) Rare gases and trace elements in Apollo 15 drill core fines: Depositional chronologies and K-Ar ages, and production rates of spallation-produced ^3He , ^{21}Ne , ^{38}Ar versus depth. *Proc. Lunar Sci. Conf. 5th*, pp. 2149–2184.
- Pepin R. O., Dragon J. C., Johnson N. L., Bates A., Coscio M. R., and Murthy V. R. (1975) Rare gases and Ca, Sr, and Ba in Apollo 17 drill-core fines. *Proc. Lunar Sci. Conf. 6th*, pp. 2027–2055.
- Pepin R. O., Eddy J. A., and Merrill R. B., eds. (1980) *The Ancient Sun: Fossil Record in the Earth, Moon and Meteorites*. Pergamon, New York. 581 pp.
- Perry C. H., Agrawal D. K., Anastassakis E., Lowndes R. P. and Tornberg N. E. (1972) Far infrared and Raman spectroscopic investigations of lunar materials from Apollo 11, 12, 14 and 15. *Proc. Lunar Sci. Conf. 3rd*, pp. 3077–3095.
- Peterson D. W. and Swanson D. A. (1974) Observed formation of lava tubes. *Speleology*, 2, 209.
- Petrov G. I. (1972) Investigation of the Moon with the Lunokhod 1 space vehicle. In *COSPAR Space Research XII*, pp. 1–12. Akademie-Verlag, Berlin.
- Petrowski C., Kerridge J. F., and Kaplan I. R. (1974) Light-element geochemistry of the Apollo 17 site. *Proc. Lunar Sci. Conf. 5th*, pp. 1939–1948.
- Pettengill G. H. (1978) Physical properties of the planets and satellites from radar observations. *Annu. Rev. Astron. Astrophys.*, 17, 265–292.
- Pettengill G. H. and Thompson T. W. (1968) A radar study of the lunar crater Tycho at 3.8 cm and 70 cm wavelengths. *Icarus*, 8, 457–471.
- Pettengill G. H., Zisk S. H., and Thompson T. W. (1974) The mapping of lunar radar scattering characteristics. *The Moon*, 10, 3–16.
- Pettijohn F. J., Potter P. E., and Siever R. (1973) *Sand and Sandstone*. Springer-Verlag, New York. 618 pp.
- Phillips R. J. and Dvorak J. (1981) The origin of lunar mascons: Analysis of the Bouguer gravity associated with Grimaldi. In *Multi-Ring Basins, Proc. Lunar Sci. Conf. 12A* (P. H. Schultz and R. B. Merrill, eds.), pp. 91–104. Pergamon, New York.
- Phillips R. J. and Lambeck K. (1980) Gravity fields of the terrestrial planets: Long wavelength anomalies and tectonics. *Rev. Geophys. Space Phys.*, 18, 27–76.
- Phillips R. J., Conel J. E., Abbott E. A., Sjogren W. L., and Morton J. B. (1972) Mascons: Progress toward a unique solution for mass distribution. *J. Geophys. Res.*, 77, 7106–7114.
- Phillips R. J., Adams G. F., Brown W. E. Jr., Eggleton R. E., Jackson P., Jordan R., Linlor W. I., Peeples W. J., Porcello L. J., Ryu J., Schaber G., Sill W. R., Thompson T. W., Ward S. H., and Zelenka J. S. (1973a) Apollo Lunar Sounder Experiment. In *Apollo 17 Preliminary Science Report*, pp. 22–1 to 22–6. NASA SP-330.
- Phillips R. J., Adams G. F., Brown W. E. Jr., Eggleton R. E., Jackson, P., Jordan R., Peeples W. J., Porcello L. J., Ryu J., Schaber G., Sill W. R., Thompson T. W., Ward S. H., and Zelenka J. S. (1973b) The Apollo 17 lunar sounder. *Proc. Lunar Sci. Conf. 4th*, pp. 2821–2831.
- Philpotts J. A. and Schnetzler C. C. (1970) Apollo 11 samples: K, Rb, Sr, Ba, and rare-earth concentrations in some rocks and separated phases. *Proc. Apollo 11 Lunar Sci. Conf.*, pp. 1471–1486.
- Philpotts J. A., Schnetzler C. C., Bottino M. L., Schuhmann S., and Thomas H. H. (1972) Luna 16: Some Li, K, Rb, Sr, Ba, rare-earth, Zr, and Hf concentrations. *Earth Planet. Sci. Lett.*, 13, 429–435.
- Philpotts J. A., Schuhmann S., Kouns C. W., Lum R. K. L., and Winzer S. (1974) Origin of Apollo 17 rocks and soils. *Proc. Lunar Sci. Conf. 5th*, pp. 1255–1267.
- Phinney D., Kahl S. B., and Reynolds J. H. (1975) ^{40}Ar - ^{39}Ar dating of Apollo 16 and Apollo 17 rocks. *Proc. Lunar Sci. Conf. 6th*, pp. 1593–1608.
- Phinney W. C. and Simonds C. H. (1977) Dynamical implications of the petrology and distribution of impact melt rocks. In *Impact and Explosion Cratering* (D. J. Roddy, R. O. Pepin, and R. B. Merrill, eds.), pp. 771–790. Pergamon, New York.
- Phinney W. C., Warner J. L., and Simonds C. H. (1977) Lunar highland rock types: Their implications for impact-induced fractionation. In *The Soviet-American Conference on Cosmochemistry of the Moon and Planets*, pp. 91–126. NASA SP-370.
- Pieters C. M. (1977) Characterization of lunar mare basalt types—II: Spectral classification of fresh mare craters. *Proc. Lunar Sci. Conf. 8th*, pp. 1037–1048.
- Pieters C. M. (1978) Mare basalt types on the front side of the Moon. *Proc. Lunar Planet. Sci. Conf. 9th*, pp. 2825–2849.
- Pieters C. M. (1982) Copernicus crater central peak: Lunar mountain of unique composition. *Science*, 215, 59–61.

- Pieters C. M. (1983) Strength of mineral absorption features in the transmitted component of near-infrared reflected light: First results from RELAB. *J. Geophys. Res.*, 88, 9534–9544.
- Pieters C. M. (1986) Composition of lunar highland crust from near-infrared spectroscopy. *Rev. Geophys.*, 24, 557–578.
- Pieters C. M. (1989) Compositional diversity and stratigraphy of the lunar highland crust (abstract). In *Lunar and Planetary Science XX*, pp. 848–849. Lunar and Planetary Institute, Houston.
- Pieters C. M. and McCord T. B. (1976) Characterization of lunar mare basalt types: I. A remote sensing study using reflection spectroscopy of surface soils. *Proc. Lunar Sci. Conf. 7th*, pp. 2677–2690.
- Pieters C. M. and Mustard J. F. (1988) Exploration of crustal/mantle material for the Earth and Moon using reflectance spectroscopy. *Remote Sens. Environ.*, 24, 151–178.
- Pieters C., McCord T. B., Zisk S., and Adams J. B. (1973) Lunar black spots and nature of the Apollo 17 landing site. *J. Geophys. Res.*, 78, 5867–5875.
- Pieters C., Head J., McCord T. B., Adams J. B., and Zisk S. H. (1975) Geochemical and geological units of Mare Humorum: Definition using remote sensing and lunar sample information. *Proc. Lunar Sci. Conf. 6th*, pp. 2689–2710.
- Pieters C. M., Head J. W., Adams J. B., McCord T. B., Zisk S. H., and Whitford-Stark J. L. (1980) Late high-titanium basalts of the western maria: Geology of the Flamsteed region of Oceanus Procellarum. *J. Geophys. Res.*, 85, 3913–3938.
- Pieters C. M., Hawke B. R., Gaffey M. J., and McFadden L. A. (1983) Possible lunar source areas of meteorite ALHA81005: Geochemical remote sensing information. *Geophys. Res. Lett.*, 10, 813–816.
- Pieters C. M., Adams J. B., Mougini-Mark P., Zisk S. H., Smith M. O., Head J. W., and McCord T. B. (1985) The nature of crater rays: The Copernicus example. *J. Geophys. Res.*, 90, 12393–12413.
- Pike R. J. (1968) *Preliminary Models of Slope Distributions on the Moon*. U.S. Geological Survey, unpublished manuscript.
- Pike R. J. (1974a) Ejecta from large craters on the Moon: Comments on the geometric model of McGetchin et al. *Earth Planet. Sci. Lett.*, 23, 265–274.
- Pike R. J. (1974b) Depth/diameter relations of fresh lunar craters: Revision from spacecraft data. *Geophys. Res. Lett.*, 1, 291–294.
- Pike R. J. (1976) Crater dimensions from Apollo data and supplemental sources. *The Moon*, 15, 463–477.
- Pike R. J. (1977) Apparent depth/apparent diameter relation for lunar craters. *Proc. Lunar Sci. Conf. 8th*, pp. 3427–3436.
- Pike R. J. (1980) Formation of complex impact structures: Evidence from Mars and other planets. *Icarus*, 43, 1–19.
- Pike R. J. and Spudis P. (1987) Basin-ring spacing on the Moon, Mercury, and Mars. *Earth, Moon and Planets*, 39, 129–194.
- Pillinger C. T., Davis P. R., Eglinton G., Gowar A. P., Jull A. J. T., Maxwell J. R., Housley R. M., and Cirlin E. H. (1974) The association between carbide and finely divided metallic iron in lunar fines. *Proc. Lunar Sci. Conf. 5th*, pp. 1949–1961.
- Piwinskii A. J. and Duba A. G. (1975) Feldspar electrical conductivity and the lunar interior. *Proc. Lunar Sci. Conf. 6th*, pp. 2899–2907.
- Podosek F. A. and Huneke J. C. (1973) Argon in Apollo 15 green glass spherules (15426): ^{40}Ar - ^{39}Ar age and trapped argon. *Earth Planet. Sci. Lett.*, 19, 413–421.
- Pohl J., Stöffler D., Gall H., and Ernstson K. (1977) The Ries impact crater. In *Impact and Explosion Cratering* (D. J. Roddy, R. O. Pepin, and R. B. Merrill, eds.), pp. 343–404. Pergamon, New York.
- Pohn H. A. and Wildey R. L. (1970) *A Photoelectric-Photographic Study of the Normal Albedo of the Moon*. U.S. Geol. Surv. Prof. Pap. 599E.
- Pohn H. A., Radin H. W., and Wildey R. L. (1969) The Moon's photometric function near zero phase angle from Apollo 8 photography. *Astrophys. J.*, 157, L193–L195.
- Pollack J. B. and Whitehill L. (1972) A multiple-scattering model of the diffuse component of lunar radar echoes. *J. Geophys. Res.*, 77, 4289–4303.
- Pomerantz M. A. and Duggal S. P. (1974) The sun and cosmic rays. *Rev. Geophys. Space Phys.*, 12, 343–361.
- Porcello L. J., Jordan R. L., Zelenka J. S., Adams G. F., Phillips R. J., Brown W. E. Jr., Ward S. H., and Jackson P. L. (1974) The Apollo Lunar Sounder Radar System. *Proc. IEEE*, 62, 769–783.
- Powell B. N. and Weiblen P. W. (1972) Petrology and origin of lithic fragments in the Apollo 14 regolith. *Proc. Lunar Sci. Conf. 3rd*, pp. 837–852.
- Powell B. N., Aitken F. K., and Weiblen P. W. (1973) Classification, distribution, and origin of lithic fragments from the Hadley-Apennine region. *Proc. Lunar Sci. Conf. 4th*, pp. 445–460.
- Powers M. C. (1953) A new roundness scale for sedimentary particles. *J. Sed. Petrol.*, 23, 117–119.
- Prinz M. and Keil K. (1977) Mineralogy, petrology and chemistry of ANT-suite rocks from the lunar highlands. *Phys. Chem. Earth*, 10, 215–237.
- Prinz M., Dowty E., Keil K., and Bunch T. E. (1973) Spinel troctolite and anorthosite in Apollo 16 samples. *Science*, 179, 74–76.
- Quaide W. and Bunch T. (1970) Impact metamorphism of lunar surface materials. *Proc. Apollo 11 Lunar Sci. Conf.*, pp. 711–729.
- Quaide W. L. and Oberbeck V. R. (1975) Development of the mare regolith: Some model considerations. *The Moon*, 13, 27–55.
- Quaide W., Oberbeck V., Bunch T., and Polkowski G. (1971) Investigations of the natural history of the regolith at the Apollo 12 site. *Proc. Lunar Sci. Conf. 2nd*, pp. 701–718.
- Quick J. E., James O. B., and Albee A. L. (1981a) Petrology and petrogenesis of lunar breccia 12013. *Proc. Lunar Planet. Sci. 12B*, pp. 117–172.

- Quick J. E., James O. B., and Albee A. L. (1981b) A reexamination of the Rb-Sr isotopic systematics of lunar breccia 12013. *Proc. Lunar Planet. Sci. 12B*, pp. 173-184.
- Ramdohr P. (1972) Lunar pentlandite and sulfidization reactions in microbreccia 14315, 9. *Earth Planet. Sci. Lett.*, 15, 113-115.
- Ramdohr P. and El Goresy A. (1970) Opaque minerals of the lunar rocks and dust from Mare Tranquillitatis. *Science*, 167, 615-618.
- Rammensee W. and Wänke H. (1977) On the partition coefficient of tungsten between metal and silicate and its bearing on the origin of the Moon. *Proc. Lunar Sci. Conf. 8th*, pp. 399-409.
- Rao D. B., Chondary U. V., Erstfeld T. E., Williams R. J., and Chang Y. A. (1979) Extraction processes for the production of aluminum, titanium, iron, magnesium, and oxygen from nonterrestrial sources. In *Space Resources and Space Settlements* (J. Billingham et al., eds), pp. 257-274. NASA SP-428.
- Ravine M. A. and Grieve R. A. F. (1986) An analysis of morphologic variation in simple lunar craters. *Proc. Lunar Planet. Sci. Conf. 17th*, in *J. Geophys. Res.*, 91, E75-E83.
- Rea D. G., Hetherington N., and Mifflin R. (1964) The analysis of radar echoes from the Moon. *J. Geophys. Res.*, 69, 5217-5223.
- Rea D. G., Hetherington N., and Mifflin R. (1965) A note on "The analysis of radar echoes from the Moon." *J. Geophys. Res.*, 70, 1565.
- Reasoner D. L. (1975) Lunar nightside electron fluxes. *Proc. Lunar Sci. Conf. 6th*, pp. 3023-3032.
- Reed G. W. Jr. and Jovanovic S. (1970) Halogens, mercury, lithium, and osmium in Apollo 11 lunar samples. *Proc. Apollo 11 Lunar Sci. Conf.*, pp. 1487-1492.
- Reed G. W. Jr. and Jovanovic S. (1971) The halogens and other trace elements in Apollo 12 samples and the implications of halides, platinum metals, and mercury on surfaces. *Proc. Lunar Sci. Conf. 2nd*, pp. 1261-1276.
- Reed G. W. Jr. and Jovanovic S. (1972) Trace element comparisons between mare and Apennine-Front non-mare samples (abstract). In *The Apollo 15 Lunar Samples* (J. W. Chamberlain and C. Watkins, eds.), pp. 247-249. The Lunar Science Institute, Houston.
- Reed G. W. Jr. and Jovanovic S. (1973a) The halogens in Luna 16 and Luna 20 soils. *Geochim. Cosmochim. Acta*, 37, 1007-1009.
- Reed G. W. Jr. and Jovanovic S. (1973b) Fluorine in lunar samples: Implications concerning fluorapatite. *Geochim. Cosmochim. Acta*, 37, 1457-1471.
- Reed G. W. Jr. and Jovanovic S. (1979) Near-surface daytime thermal conductivity in the lunar regolith. *Proc. Lunar Planet. Sci. Conf. 10th*, pp. 1637-1647.
- Reed G. W. Jr., Goleb J. A., and Jovanovic S. (1971a) Surface-related Hg in lunar samples. *Science*, 172, 258-261.
- Reed G. W. Jr., Jovanovic S., and Fuchs L. H. (1971b) Fluorine and other trace elements in lunar plagioclase concentrates. *Earth Planet. Sci. Lett.*, 11, 354-358.
- Reed G. W. Jr., Jovanovic S., and Fuchs L. (1972) Trace element relations between Apollo 14 and 15 and other lunar samples, and the implications of a Moon-wide Cl-KREEP coherence and Pt-metal noncoherence. *Proc. Lunar Sci. Conf. 3rd*, pp. 1989-2001.
- Reed G. W. Jr., Allen R. O. Jr., and Jovanovic S. (1977) Volatile metal deposits on lunar soils—relation to volcanism. *Proc. Lunar Sci. Conf. 8th*, pp. 3917-3930.
- Reed S. J. B. and Taylor S. R. (1974) Meteoritic metal in Apollo 16 samples. *Meteoritics*, 9, 23-34.
- Reedy R. C. (1977) Solar proton fluxes since 1956. *Proc. Lunar Sci. Conf. 8th*, pp. 825-839.
- Reedy R. C. (1978) Planetary gamma-ray spectroscopy. *Proc. Lunar Planet. Sci. Conf. 9th*, pp. 2961-2984.
- Reedy R. C. (1980) Lunar radionuclide records of average solar-cosmic-ray fluxes over the last ten million years. In *The Ancient Sun: Fossil Record in the Earth, Moon and Meteorites* (R. O. Pepin, J. A. Eddy, and R. B. Merrill, eds), pp. 365-386. Pergamon, New York.
- Reedy R. C. (1987) Nuclide production by primary cosmic-ray protons. *Proc. Lunar Planet. Sci. Conf. 17th*, in *J. Geophys. Res.*, 92, E703-E709.
- Reedy R. C. and Arnold J. R. (1972) Interaction of solar and galactic cosmic-ray particles with the Moon. *J. Geophys. Res.*, 77, 537-555.
- Reedy R. C., Arnold J. R., and Lal D. (1983) Cosmic-ray record in solar system matter. *Annu. Rev. Nucl. Part Sci.*, 33, 505-537.
- Rees C. E. and Thode H. G. (1972) Sulfur concentrations and isotope ratios in lunar samples. *Proc. Lunar Sci. Conf. 3rd*, pp. 1479-1485.
- Rees C. E. and Thode H. G. (1974) Sulfur concentrations and isotope ratios in Apollo 16 and 17 samples. *Proc. Lunar Sci. Conf. 5th*, pp. 1963-1973.
- Reid A. M., Meyer C., Harmon R. S., and Brett R. (1970) Metal grains in Apollo 12 igneous rocks. *Earth Planet. Sci. Lett.*, 9, 1-5.
- Reid A. M., Warner J. L., Ridley W. I., and Brown R. W. (1973) Luna 20 soil: Abundance and composition of phases in the 45-125 micron fraction. *Geochim. Cosmochim. Acta*, 37, 1011-1030.
- Reid A. M., Duncan A. R., and Richardson S. H. (1977) In search of LKFM. *Proc. Lunar Sci. Conf. 8th*, pp. 2321-2338.
- Reid J. B. (1971) Apollo 12 spinels as petrogenetic indicators. *Earth Planet. Sci. Lett.*, 10, 351-356.
- Reimold W. U. and Stöffler D. (1978) Experimental shock metamorphism of dunite. *Proc. Lunar Planet. Sci. Conf. 9th*, pp. 2805-2824.
- Reimold W. U., Nyquist L. E., Bansal B. M., Wooden J. L., Shih C.-Y., Weismann H., and Mackinnon I. D. R. (1985) Isotope analysis of crystalline impact melt rocks from Apollo 16 Stations 11 and 13, North Ray Crater. *Proc. Lunar Planet. Sci. Conf. 15th*, in *J. Geophys. Res.*, 89, C431-C448.
- Rennilson J. J. and Criswell D. R. (1974) Surveyor observations of lunar horizon-glow. *The Moon*, 10, 121-142.

- Rhee J. W., Berg O. E., and Wolf H. (1977) Electrostatic dust transport and Apollo 17 LEAM experiment. In *COSPAR Space Research XVII*, pp. 627–629. Pergamon, New York.
- Rhodes J. M. (1977) Some compositional aspects of lunar regolith evolution. *Philos. Trans. R. Soc. London, A285*, 293–301.
- Rhodes J. M. and Blanchard D. P. (1980) Chemistry of Apollo 11 low-K mare basalts. *Proc. Lunar Planet. Sci. Conf. 11th*, pp. 49–66.
- Rhodes J. M. and Blanchard D. P. (1981) Apollo 11 breccias and soils: Aluminous mare basalts or multi-component mixtures? *Proc. Lunar Planet. Sci. 12B*, pp. 607–620.
- Rhodes J. M. and Hubbard N. J. (1973) Chemistry, classification, and petrogenesis of Apollo 15 mare basalts. *Proc. Lunar Sci. Conf. 4th*, pp. 1127–1148.
- Rhodes J. M., Rodgers K. V., Shih C., Bansal B. M., Nyquist L. E., Wiesmann H., and Hubbard N. J. (1974) The relationships between geology and soil chemistry at the Apollo 17 landing site. *Proc. Lunar Sci. Conf. 5th*, pp. 1097–1117.
- Rhodes J. M., Adams J. B., Blanchard D. P., Charette M. P., Rodgers K. V., Jacobs J. W., Brannon J. C., and Haskin L. A. (1975) Chemistry of agglutinate fractions in lunar soils. *Proc. Lunar Sci. Conf. 6th*, pp. 2291–2307.
- Rhodes J. M., Hubbard N. J., Wiesmann H., Rodgers K. V., Brannon J. C., and Bansal B. M. (1976) Chemistry, classification, and petrogenesis of Apollo 17 mare basalts. *Proc. Lunar Sci. Conf. 7th*, pp. 1467–1489.
- Rhodes J. M., Blanchard D. P., Dungan M. A., Brannon J. C., and Rogers K. V. (1977) Chemistry of Apollo 12 mare basalts: Magma types and fractionation processes. *Proc. Lunar Sci. Conf. 8th*, pp. 1305–1338.
- Richart F. E., Hall J. R., and Woods R. D. (1970) *Vibrations of Soils and Foundations*. Prentice-Hall, Englewood Cliffs, New Jersey.
- Richter D., Simmons G., and Siegfried R. (1976) Microcracks, micropores and their petrologic interpretation for 72415 and 15418. *Proc. Lunar Sci. Conf. 7th*, pp. 1901–1923.
- Ridley W. I., Brett R., Williams R. J., Takeda H., and Brown R. W. (1972) Petrology of Fra Mauro basalt 14310. *Proc. Lunar Sci. Conf. 3rd*, pp. 159–170.
- Ridley W. I., Hubbard N. J., Rhodes J. M., Weismann H., and Bansal B. (1973) The petrology of lunar breccia 15445 and petrogenetic implications. *J. Geol.*, 81, 621–631.
- Ringwood A. E. (1970) Petrogenesis of Apollo 11 basalts and implications for lunar origin. *J. Geophys. Res.*, 75, 6453–6479.
- Ringwood A. E. (1978) Origin of the Moon (abstract). In *Lunar and Planetary Science IX*, pp. 961–963. Lunar and Planetary Institute, Houston.
- Ringwood A. E., Seifert S., and Wänke H. (1987) A komatiite component in Apollo 16 highland breccias: Implications for the nickel-cobalt systematics and bulk composition of the Moon. *Earth Planet. Sci. Lett.*, 81, 105–117.
- Roberts W. A. (1968) Shock crater characteristics. In *Shock Metamorphism of Natural Materials* (B. M. French and N. M. Short, eds.), pp. 101–114. Mono, Baltimore.
- Robertson P. B. and Grieve R. A. F. (1977) Shock attenuation at terrestrial impact structures. In *Impact and Explosion Cratering* (D. J. Roddy, R. O. Pepin, and R. B. Merrill, eds.), pp. 687–702. Pergamon, New York.
- Robertson P. B., Dence M. R., and Vos M. A. (1986) Deformation in rock-forming minerals from Canadian craters. In *Shock Metamorphism of Natural Materials* (B. M. French and N. M. Short, eds.), pp. 433–452. Mono, Baltimore.
- Roddy D. J., Ullrich G. W., Sauer F. M., and Jones G. H. S. (1977) Cratering motions and structural deformation in the rim of the Prairie Flat multiring explosion crater. *Proc. Lunar Sci. Conf. 8th*, pp. 3389–3407.
- Roedder E. and Weiblen P. W. (1972a) Petrographic features and petrologic significance of melt inclusions in Apollo 14 and 15 rocks. *Proc. Lunar Sci. Conf. 3rd*, pp. 251–279.
- Roedder E. and Weiblen P. W. (1972b) Occurrence of chromian, hercynitic spinel (“pleonaste”) in Apollo 14 samples and its petrologic implications. *Earth Planet. Sci. Lett.*, 15, 376–402.
- Rose H. J. Jr., Cuttitta F., Dwornik E. J., Canon M. K., Christian R. P., Lindsay J. R., Ligon D. T. Jr., and Larson R. R. (1970) Semimicro X-ray fluorescence analysis of lunar samples. *Proc. Apollo 11 Lunar Sci. Conf.*, pp. 1493–1497.
- Rose H. J. Jr., Cuttitta F., Ansell C. S., Canon M. K., Christian R. P., Dwornik E. J., Greenland L., and Dignon D. T. Jr. (1972) Compositional data for twenty-one Fra Mauro lunar materials. *Proc. Lunar Sci. Conf. 3rd*, pp. 1215–1229.
- Rose H. J. Jr., Cuttitta F., Berman S., Carron M. K., Christian R. P., Dwornik E. J., Greenland L. P., and Ligon D. T. Jr. (1973a) Compositional data for twenty-two Apollo 16 samples. *Proc. Lunar Sci. Conf. 4th*, pp. 1149–1158.
- Rose H. J. Jr., Canon M. K., Christian R. P., Cuttitta F., Dwornik E. J., and Dignon D. T. Jr. (1973b) Elemental analysis of some Apollo 16 samples (abstract). In *Lunar Science IV*, pp. 631–633. The Lunar Science Institute, Houston.
- Rose H. J. Jr., Cuttitta F., Berman S., Brown F. W., Canon M. K., Christian R. P., Dwornik E. J., and Greenland L. P. (1974a) Chemical composition of rocks and soils at Taurus-Littrow. *Proc. Lunar Sci. Conf. 5th*, pp. 1119–1133.
- Rose H. J. Jr., Brown F. W., Canon M. K., Christian R. P., Cuttitta F., Dwornik E. J., and Ligon D. T. Jr. (1974b) Composition of some Apollo 17 samples (abstract). In *Lunar Science V*, pp. 645–646. The Lunar Science Institute, Houston.
- Rose H. J. Jr., Baedeker P. A., Berman S., Christian R. P., Dwornik E. J., Finkelman R. B., and Schnepfe M. M. (1975) Chemical composition of rocks and soils returned by the Apollo 15, 16 and 17 missions. *Proc. Lunar Sci. Conf. 6th*, pp. 1363–1373.
- Rosenberg S. D. (1985) A lunar-based propulsion system. In *Lunar Bases and Space Activities of the 21st Century* (W. W. Mendell, ed.), pp. 169–176. Lunar and Planetary Institute, Houston.
- Ross M., Bence A. E., Dwornik E. J., Clark J. R., and Papike J. J. (1970) Mineralogy of lunar clinopyroxenes, augite and pigeonite. *Proc. Apollo 11 Lunar Sci. Conf.*, pp. 839–848.

- Ross M., Huebner J. S., and Dowty E. (1973) Delineation of the one atmosphere augite-pigeonite miscibility gap for pyroxenes from lunar basalt 12021. *Am. Mineral.*, 58, 619–635.
- Rossiter J. R. (1977) Interpretation of radio interferometry depth sounding, with emphasis on random scattering from glaciers and the lunar surface. Ph.D. thesis, Univ. of Toronto. 220 pp.
- Russ G. P. III and Emerson M. T. III (1980) ^{53}Mn and ^{26}Al evidence for solar cosmic ray constancy—an improved model for interpretation. In *The Ancient Sun: Fossil Record in the Earth, Moon and Meteorites* (R. O. Pepin, J. A. Eddy, and R. B. Merrill, eds.), pp. 387–399. Pergamon, New York.
- Rust D. M. (1982) Solar flares, proton showers, and the space shuttle. *Science*, 216, 939–946.
- Rutherford M. J., Dixon S., and Hess P. (1980) Ilmenite saturation at high pressure in KREEP basalts: Origin of KREEP and Hi-TiO₂ in mare basalts (abstract). In *Lunar and Planetary Science XI*, pp. 966–967. Lunar and Planetary Institute, Houston.
- Ryder G. (1976) Lunar sample 15405: Remnant of a KREEP basalt-granite differentiated pluton. *Earth Planet. Sci. Lett.*, 29, 255–268.
- Ryder G. (1979) The chemical components of highlands breccias. *Proc. Lunar Planet. Sci. Conf. 10th*, pp. 561–581.
- Ryder G. (1981) Distribution of rocks at the Apollo 16 landing site. In *Workshop on Apollo 16* (O. B. James and F. Hörz, eds.), pp. 112–119. LPI Tech. Rpt. 81–01, Lunar and Planetary Institute, Houston.
- Ryder G. (1982) Lunar anorthosite 60025, the petrogenesis of lunar anorthosites, and the composition of the Moon. *Geochim. Cosmochim. Acta*, 46, 1591–1601.
- Ryder G. (1984) Olivine in lunar dunite 72415, a rather shallow-origin cumulate (abstract). In *Lunar and Planetary Science XV*, pp. 709–710. Lunar and Planetary Institute, Houston.
- Ryder G. (1985) *Catalog of Apollo 15 Rocks*. JSC Publ. No. 20787, Curatorial Branch Publ. 72. NASA Johnson Space Center, Houston. 1296 pp.
- Ryder G. (1987) Petrographic evidence for nonlinear cooling rates and a volcanic origin for Apollo 15 KREEP basalts. *Proc. Lunar Planet. Sci. Conf. 17th*, in *J. Geophys. Res.*, 92, E331–E339.
- Ryder G. and Blair E. (1982) KREEP glass and the exotic provenance of polymict breccia 66055. *Proc. Lunar Planet. Sci. Conf. 13th, J. Geophys. Res.*, 87, A147–A158.
- Ryder G. and Bower J. F. (1976) Poikilitic KREEP impact melts in the Apollo 14 white rocks. *Proc. Lunar Sci. Conf. 7th*, pp. 1925–1948.
- Ryder G. and Bower J. F. (1977) Petrology of Apollo 15 black-and-white rocks 15445 and 15455—fragments of the Imbrium impact melt sheet? *Proc. Lunar Sci. Conf. 8th*, pp. 1895–1923.
- Ryder G. and Norman M. D. (1978) *Catalog of Pristine Non-Mare Materials Part 2. Anorthosites*. JSC Publ. No. 14603, NASA Johnson Space Center, Houston. 86 pp.
- Ryder G. and Norman M. D. (1979) *Catalog of Pristine Non-Mare Materials Part 1. Non-Anorthosites (Revised)*. JSC Publ. No. 14565, NASA Johnson Space Center, Houston. 147 pp.
- Ryder G. and Norman M. D. (1980) *Catalog of Apollo 16 Rocks*. JSC Publ. No. 16904, Curatorial Branch Publ. 52, NASA Johnson Space Center, Houston. 1144 pp.
- Ryder G. and Spudis P. D. (1980) Volcanic rocks in the lunar highlands. In *Proceedings of the Conference on the Highlands Crust* (J. J. Papike and R. B. Merrill, eds.), pp. 353–375. Pergamon, New York.
- Ryder G. and Taylor G. J. (1976) Did mare-type volcanism commence early in lunar history? *Proc. Lunar Sci. Conf. 7th*, pp. 1741–1755.
- Ryder G. and Wood J. A. (1977) Serenitatis and Imbrium impact melts: Implications for large-scale layering in the lunar crust. *Proc. Lunar Sci. Conf. 8th*, pp. 655–668.
- Ryder G., Stoesser D. B., Marvin U. B., Bower J. F., and Wood J. A. (1975) Boulder 1, Station 2, Apollo 17: Petrology and petrogenesis. *The Moon*, 14, 327–357.
- Ryder G., Stoesser D. B., and Wood J. A. (1977) Apollo 17 KREEPy basalt: A rock type intermediate between mare and KREEP basalts. *Earth Planet. Sci. Lett.*, 35, 1–13.
- Ryder G., Norman M. D., and Score R. A. (1980) The distinction of pristine and meteorite-contaminated highlands rocks using metal compositions. *Proc. Lunar Planet. Sci. Conf. 11th*, pp. 471–479.
- Saari J. M. and Shorthill R. W. (1967) *Isothermal and Isophotoc Atlas of the Moon*. NASA CR-855, prepared by Boeing Scientific Research Laboratories under contract NASW-982. 186 pp.
- Salomonovich A. E. and Losovskii B. Ya. (1963) Radio brightness distribution on the lunar disk at 0.8 cm. *Soviet Astron. A. J.*, 6, 833–839.
- Salpas P. A., Taylor L. A., and Lindstrom M. M. (1987) Apollo 17 KREEPy basalts: Evidence for nonuniformity of KREEP. *Proc. Lunar Planet. Sci. Conf. 17th*, in *J. Geophys. Res.*, 92, E340–E348.
- Sato M. (1978) Oxygen fugacity of basaltic magmas and the role of gas forming elements. *Geophys. Res. Lett.*, 5, 447–449.
- Sato M. (1979) The driving mechanism of lunar pyroclastic eruptions inferred from the oxygen fugacity behavior of Apollo 17 orange glass. *Proc. Lunar Planet. Sci. Conf. 10th*, pp. 311–325.
- Sato M., Hickling N. L., and McLane J. E. (1973) Oxygen fugacity values of Apollo 12, 14, and 15 lunar samples and reduced state of lunar magmas. *Proc. Lunar Sci. Conf. 4th*, pp. 1061–1079.
- Schaal R. B. and Hörz F. (1977) Shock metamorphism of lunar and terrestrial basalts. *Proc. Lunar Sci. Conf. 8th*, pp. 1697–1729.
- Schaal R. and Hörz F. (1980) Experimental shock metamorphism of lunar soil. *Proc. Lunar Planet. Sci. Conf. 11th*, pp. 1679–1695.
- Schaal R. B., Hörz F., Thompson T. D., and Bauer J. F. (1979) Shock metamorphism of granulated, lunar basalt. *Proc. Lunar Planet. Sci. Conf. 10th*, pp. 2547–2571.

- Schaber G. G. (1973a) Lava flows in Mare Imbrium: Geologic evaluation from Apollo orbital photography. *Proc. Lunar Sci. Conf. 4th*, pp. 73–92.
- Schaber G. G. (1973b) Eratosthenian volcanism in Mare Imbrium: Source of youngest lava flows. In *Apollo 17 Preliminary Science Report*, pp. 30–17. NASA SP-330.
- Schaber G. G., Thompson T. W. and Zisk S. H. (1975) Lava flows in Mare Imbrium, an evaluation of anomalously low Earth-based radar reflectometry. *The Moon*, 13, 395–423.
- Schaber G. G., Boyce J. M., and Moore H. J. (1976) The scarcity of mappable flow lobes on the lunar maria: Unique morphology of the Imbrium flows. *Proc. Lunar Sci. Conf. 7th*, pp. 2783–2800.
- Schaber G. G., McCauley J. F., Breed C. S., and Olhoeft G. R. (1986) Shuttle imaging radar—physical controls on signal penetration and subsurface scattering in the Eastern Sahara. *IEEE Trans. Geosci. Remote Sens.*, GE-24, 603–623.
- Schaeffer O. A. and Husain L. (1973) Isotopic ages of Apollo 17 lunar material. *Eos Trans. AGU*, 54, 614.
- Schaeffer O. A., Husain L., and Schaeffer G. A. (1976) Ages of highland rocks: The chronology of lunar basin formation revisited. *Proc. Lunar Sci. Conf. 7th*, pp. 2067–2092.
- Schimerman L. A. (1973) *Lunar Cartographic Dossier*. Defense Mapping Agency, St. Louis and NASA, Washington, DC.
- Schloerb F. P., Muhleman D. O., and Berge G. L. (1976) Lunar heat flow and regolith structure inferred from interferometric observations at a wavelength of 49.3 cm. *Icarus*, 29, 329–341.
- Schmidt O. Y. (1959) *A Theory of the Origin of the Earth*. Lawrence and Wishart, London. 139 pp.
- Schmitt H. H. (1973) Apollo 17 report on the valley of Taurus-Littrow. *Science*, 182, 681–690.
- Schmitt H. H. and Cernan E. A. (1973) A geological investigation of the Taurus-Littrow Valley. In *Apollo 17 Preliminary Science Report*, pp. 5–1 to 5–21. NASA SP-330.
- Schnetzler C. C. and Philpotts J. A. (1970) Partition coefficients of rare-earth elements between igneous matrix material and rock-forming mineral phenocrysts—II. *Geochim. Cosmochim. Acta*, 34, 331.
- Schnetzler C. C. and Philpotts J. A. (1971) Alkali, alkaline earth, and rare earth element concentrations in some Apollo 12 soils, rocks, and separated phases. *Proc. Lunar Sci. Conf. 2nd*, pp. 1101–1122.
- Schock R. N., Duba A., and Stocker R. L. (1980) Defect production and electrical conductivity in olivine (abstract). In *Lunar and Planetary Science XI*, pp. 987–989. Lunar and Planetary Institute, Houston.
- Schonfeld E. and Bielefeld M. J. (1978) Correlation of dark mantle deposits with high Mg/Al ratios. *Proc. Lunar Planet. Sci. Conf. 9th*, pp. 3037–3048.
- Schonfeld E. and Meyer C. Jr. (1972) The abundances of components of the lunar soils by a least-squares mixing model and the formation age of KREEP. *Proc. Lunar Sci. Conf. 3rd*, pp. 1397–1420.
- Schubert G., Lingenfelter R. E., and Peale S. J. (1970) The morphology, distribution, and origin of lunar sinuous rilles. *Rev. Geophys. Space Phys.*, 8, 199–224.
- Schubert G., Schwartz K., Sonett C. P., Colburn D. S., and Smith B. F. (1973) Lunar electromagnetic scattering II. Magnetic fields and transfer functions for parallel propagation. *Proc. Lunar Sci. Conf. 4th*, pp. 2909–2923.
- Schultz L., Weber H. W., Spettel B., Hintenberger H., and Wänke H. (1977) Noble gas and element distribution in agglutinate and bulk grain size fractions of soil 15601. *Proc. Lunar Sci. Conf. 8th*, pp. 2799–2815.
- Schultz P. H. (1976a) *Moon Morphology*. Univ. of Texas, Austin. 626 pp.
- Schultz P. H. (1976b) Floor-fractured lunar craters. *The Moon*, 15, 241–273.
- Schultz P. H. and Gault D. E. (1975a) Seismic effects from major basin formations on the Moon and Mercury. *The Moon*, 12, 159–177.
- Schultz P. H. and Gault D. E. (1975b) Seismically induced modification of lunar surface features. *Proc. Lunar Sci. Conf. 6th*, pp. 2845–2862.
- Schultz P. H. and Gault D. E. (1985) Clustered impacts: Experiments and implications. *J. Geophys. Res.*, 90, 3701–3732.
- Schultz P. H. and Mendell W. (1978) Orbital infrared observations of lunar craters and possible implications for impact ejecta emplacement. *Proc. Lunar Sci. Conf. 9th*, pp. 2857–2883.
- Schultz P. H. and Merrill R. B., eds. (1981) *Multi-Ring Basins*, *Proc. Lunar Planet. Sci. 12A*. Pergamon, New York. 295 pp.
- Schultz P. H. and Spudis P. D. (1979) Evidence for ancient mare volcanism. *Proc. Lunar Planet. Sci. Conf. 10th*, pp. 2899–2918.
- Schultz P. H. and Spudis P. D. (1983) Beginning and end of lunar mare volcanism. *Nature*, 302, 233–236.
- Schultz P. H., Greeley R., and Gault D. E. (1976) Degradation of small surface features. *Proc. Lunar Sci. Conf. 7th*, pp. 985–1003.
- Schurmann K. and Hafner S. S. (1972) On the amount of ferric iron in plagioclases from lunar igneous rocks. *Proc. Lunar Sci. Conf. 3rd*, pp. 615–621.
- Schwerer F. C., Nagata T., and Fisher R. M. (1971) Electrical conductivity of lunar surface rocks and chondritic meteorites. *The Moon*, 2, 408–422.
- Schwerer F. C., Huffman G. P., Fisher R. M., and Nagata T. (1972) Electrical conductivity and Mossbauer study of Apollo lunar samples. *Proc. Lunar Sci. Conf. 3rd*, pp. 3173–3185.
- Schwerer F. C., Huffman G. P., Fisher R. M., and Nagata T. (1973) Electrical conductivity of lunar surface rocks at elevated temperatures. *Proc. Lunar Sci. Conf. 4th*, pp. 3151–3166.
- Schwerer F. C., Huffman G. P., Fisher R. M., and Nagata T. (1974) Electrical conductivity of lunar surface rocks; laboratory measurements and implications for lunar

- interior temperatures. *Proc. Lunar Sci. Conf. 5th*, pp. 2673–2687.
- Sclar C. B. and Bauer J. F. (1973) Shock effects in experimentally shocked terrestrial ilmenite, lunar ilmenite of rock fragments in the 1–10 mm fines (10085,19), and lunar rock 60015. *Proc. Lunar Sci. Conf. 4th*, pp. 841–859.
- Sclar C. B. and Bauer J. F. (1975) Shock-induced subsolidus reduction-decomposition of orthopyroxene and shock-induced melting in norite 78235. *Proc. Lunar Sci. Conf. 6th*, pp. 799–820.
- Scoon J. H. (1971) Chemical analyses of lunar samples 12040 and 12064. *Proc. Lunar Sci. Conf. 2nd*, pp. 1259–1260.
- Scoon J. H. (1972) Chemical analyses of lunar samples 14003, 14311, and 14321. *Proc. Lunar Sci. Conf. 3rd*, pp. 1335–1336.
- Scoon J. H. (1974) Chemical analysis of lunar samples from the Apollo 16 and 17 collections (abstract). In *Lunar Science V*, pp. 690–692. The Lunar Science Institute, Houston.
- Scott D. H., McCauley J. F., and West M. N. (1977) Geologic map of the west side of the Moon. *U.S. Geol. Surv. Map I-1034*, scale 1:5,000,000.
- Scott D. R. (1973) What is it like to walk on the Moon? *Nat. Geo.*, 144, 326–329.
- Scott R. F. (1968) The density of lunar surface soil. *J. Geophys. Res.*, 73, 5469–5471.
- Scott R. F. (1987) Failure. *Geotechnique*, 37, 423–466.
- Scott R. F. and Ko H. Y. (1968) Transient rocket-engine gas flow in soil. *AIAA J.*, 6, 258–264.
- Scott R. F. and Roberson F. I. (1967) Soil mechanics surface sampler: Lunar tests, results, and analyses. In *Surveyor 3 Mission Report. Part 2: Scientific Data and Results*, pp. 69–110. JPL Tech. Rpt. 32–1177, Jet Propulsion Laboratory, Pasadena.
- Scott R. F. and Roberson F. I. (1968a) Surveyor III—Soil mechanics surface sampler: Lunar surface tests, results, and analysis. *J. Geophys. Res.*, 73, 4045–4080.
- Scott R. F. and Roberson F. I. (1968b) Soil mechanics surface sampler. In *Surveyor Project Final Report, Part 2: Science Results*, pp. 195–206. JPL Tech. Rpt. 32–1265, Jet Propulsion Laboratory, Pasadena.
- Scott R. F. and Roberson F. I. (1969) Soil mechanics surface sampler. In *Surveyor Program Results*, pp. 171–179. NASA SP-184.
- Scott R. F. and Zuckerman K. A. (1971) Examination of returned Surveyor III surface sampler. *Proc. Lunar Sci. Conf. 2nd*, pp. 2743–2751.
- Scott R. F., Carrier W. D. III, Costes N. C., and Mitchell J. K. (1970) Mechanical properties of the lunar regolith, Part C of Preliminary geological investigation of the Apollo 12 landing site. In *Apollo 12 Preliminary Science Report*, pp. 161–182. NASA SP-235.
- Scott R. F., Carrier W. D. III, Costes N. C., and Mitchell J. K. (1971) Apollo 12 soil mechanics investigation. *Geotechnique*, 21, 1–14.
- Scrutton C. T. (1978) Periodic growth features in fossil organisms and length of day and month. In *Tidal Friction and the Earth's Rotation* (P. Brosche and J. Sundermann, eds.), pp. 154–196. Springer-Verlag, Heidelberg.
- See T. H., Hörz F., and Morris R. V. (1986) Apollo 16 impact-melt splashes: Petrography and major-element composition. *Proc. Lunar Planet. Sci. Conf. 17th*, in *J. Geophys. Res.*, 91, E3–E20.
- Sen P. N., Scala C., and Cohen M. H. (1981) A self-similar model for sedimentary rocks with application to the dielectric constant of fused glass beads. *Geophysics*, 46, 781–795.
- Shapiro I. I., Zisk S. H., Rogers A. E. E., Slade M. A., and Thompson T. W. (1972) Lunar topography—global determination by radar. *Science*, 178, 939–948.
- Sharpton V. L. (1985) Analysis of topography and implications for the tectonic evolution of the Moon and Venus. Ph.D. thesis, Brown Univ., Providence, Rhode Island. 175 pp.
- Sharpton V. L. and Head J. W. III (1982) Stratigraphy and structural evolution of southern Mare Serenitatis: A reinterpretation based on Apollo Lunar Sounder Experiment data. *J. Geophys. Res.*, 87, 10983–10998.
- Sharpton V. L., Head J. W., and Shorthill R. W. (1984) Analysis and interpretation of the Apollo Lunar Sounder data: A status report (abstract). In *Lunar and Planetary Science XV*, pp. 762–763. Lunar and Planetary Institute, Houston.
- Shaw H. R. and Swanson D. A. (1970) Eruption and flow rates of flood basalts. *Proceedings of the Second Columbia River Basalt Symposium* (E. H. Gilmour and D. Stradling, eds.), pp. 271–299. Eastern Washington State College, Cheney.
- Shervais J. W. and Taylor L. A. (1983) Micrographic granite: More from Apollo 14 (abstract). In *Lunar and Planetary Science XIV*, pp. 696–697. Lunar and Planetary Institute, Houston.
- Shervais J. W. and Taylor L. A. (1986) Petrologic constraints on the origin of the Moon. In *Origin of the Moon* (W. K. Hartmann, R. J. Phillips, and G. J. Taylor, eds), pp. 173–201. Lunar and Planetary Institute, Houston.
- Shervais J. W., Taylor L. A., and Laul J. C. (1983) Ancient crustal components in the Fra Mauro breccias. *Proc. Lunar Planet. Sci. Conf. 14th*, in *J. Geophys. Res.*, 88, B177–B192.
- Shervais J. W., Taylor L. A., and Laul J. C. (1984a) Very high potassium (VHK) basalt: A new type of aluminous mare basalt from Apollo 14 (abstract). In *Lunar and Planetary Science XV*, pp. 768–769. Lunar and Planetary Institute, Houston.
- Shervais J. W., Taylor L. A., Laul J. C., and Smith M. R. (1984b) Pristine highland clasts in consortium breccia 14305: Petrology and geochemistry. *Proc. Lunar Planet. Sci. Conf. 15th*, in *J. Geophys. Res.*, 89, C25–C40.
- Shervais J. W., Taylor L. A., and Lindstrom M. M. (1985a) Apollo 14 mare basalts: Petrology and geochemistry of clasts from consortium breccia 14321. *Proc. Lunar Planet. Sci. Conf. 15th*, in *J. Geophys. Res.*, 89, C375–C395.

- Shervais J. W., Taylor L. A., Laul J. C., Shih C.-Y., and Nyquist L. E. (1985b) Very high potassium (VHK) basalt: Complications in mare basalt petrogenesis. *Proc. Lunar Planet. Sci. Conf. 16th*, in *J. Geophys. Res.*, 90, D3-D18.
- Shih C.-Y., Haskin L. A., Wiesmann H., Bansal B. M., and Brannon J. C. (1975) On the origin of high-Ti mare basalts. *Proc. Lunar Sci. Conf. 6th*, pp. 1255-1285.
- Shih C.-Y., Nyquist L. E., Bogard D. D., Wooden J. L., Bansal B. M., and Wiesmann H. (1985) Chronology and petrogenesis of a 1.8 g lunar granite clast: 14321,1062. *Geochim. Cosmochim. Acta*, 49, 411-426.
- Shih C.-Y., Nyquist L. E., Bogard D. D., Bansal B. M., Wiesmann H., Johnson P., Shervais J. W., and Taylor L. A. (1986) Geochronology and petrogenesis of Apollo 14 very high potassium basalts. *Proc. Lunar Planet. Sci. Conf. 16th*, in *J. Geophys. Res.*, 91, D214-D228.
- Shirley D. N. (1983) A partially molten magma ocean model. *Proc. Lunar Planet. Sci. Conf. 13th*, in *J. Geophys. Res.*, 88, A519-A527.
- Shoemaker E. M. (1962) Interpretation of lunar craters. In *Physics and Astronomy of the Moon* (Z. Kopal, ed.), pp. 283-359. Academic, New York.
- Shoemaker E. M. (1965) *Preliminary Analysis of the Fine Structure of Mare Cognitum*. JPL Tech. Rpt. 32-700, Jet Propulsion Laboratory, Pasadena. 35 pp.
- Shoemaker E. M. (1970) Origin of fragmental debris on the lunar surface and the history of bombardment of the Moon. *Instituto de Investigaciones Geologicas de la Diputacion Provincial XXV*, pp. 27-56. Universidad de Barcelona. (Published in 1971.)
- Shoemaker E. M. (1972) Cratering history and early evolution of the Moon (abstract). In *Lunar Science III*, pp. 696-698. The Lunar Science Institute, Houston.
- Shoemaker E. M. (1977) Why study impact craters? In *Impact and Explosion Cratering* (D. J. Roddy, R. O. Pepin, and R. B. Merrill, eds.), pp. 1-10. Pergamon, New York.
- Shoemaker E. M. (1983) Asteroid and comet bombardment of the Earth. *Annu. Rev. Earth Planet. Sci.*, 11, 15-41.
- Shoemaker E. M. and Hackman R. J. (1962) Stratigraphic basis for a lunar time scale. In *The Moon* (Z. Kopal, ed.), pp. 289-300. Academic, New York.
- Shoemaker E. M., Hackman R. J., and Eggleton R. E. (1962) Interplanetary correlation of geologic time. *Adv. Astron. Sci.*, 8, 70-89.
- Shoemaker E. M., Morris E. C., Batson R. M., Holt H. E., Larson K. B., Montgomery D. R., Rennilson J. J., and Whitaker E. A. (1968) Television observations from Surveyor. In *Surveyor Project Final Report, Part II*, pp. 21-136. JPL Tech. Rpt. 32-1265, Jet Propulsion Laboratory, Pasadena.
- Shoemaker E. M., Bailey N. G., Batson R. M., Dahlem D. H., Foss T. H., Grolier M. J., Goddard E. M., Hait M. H., Holt H. E., Larson K. B., Rennilson J. J., Schaber G. G., Schleicher D. L., Schmitt H. H., Sutton R. L., Swann G. A., Waters A. C., and West M. N. (1970a) Geologic setting of the lunar samples returned by the Apollo 11 Mission. In *Apollo 11 Preliminary Science Report*, pp. 41-84. NASA SP-214.
- Shoemaker E. M., Batson R. M., Bean A. L., Conrad C. Jr., Dahlem D., Goddard E. N., Hait M. T., Larson K. B., Schaber G. G., Schleicher D. L., Sutton R. L., Swann G. A., and Waters A. C. (1970b) Preliminary geologic investigation of the Apollo 12 landing site. Part A. Geology of the Apollo 12 landing site. In *Apollo 12 Preliminary Science Report*, pp. 113-182. NASA SP-235.
- Short N. M. and Foreman M. L. (1972) Thickness of impact crater ejecta on the lunar surface. *Mod. Geol.*, 3, 69-91.
- Sievers R. E., Eisentraut K. J., Griest D. J., Richardson M. F., Wolf W. R., Ross W. D., Frew N. M., and Isenhour T. L. (1971) Variations in beryllium and chromium contents in lunar fines compared with crystalline rocks. *Proc. Lunar Sci. Conf. 2nd*, pp. 1451-1459.
- Silberberg R., Tsao C. H., Adams J. H. Jr., and Letaw J. R. (1985) Radiation transport of cosmic ray nuclei in lunar material and radiation doses. In *Lunar Bases and Space Activities of the 21st Century* (W. W. Mendell, ed.), pp. 663-669. Lunar and Planetary Institute, Houston.
- Sill W. R., Hansen W., Ward S. H., Katsube T. J., and Collett L. S. (1973) The dielectric properties of Apollo 14 and 16 rock and soil samples. Talk presented at the Conference on Geophysical and Geochemical Exploration of the Moon and Planets, January 10-12, The Lunar Science Institute, Houston.
- Silver L. T. (1970) Uranium-thorium-lead isotopes in some Tranquillity Base samples and their implication for lunar history. *Proc. Apollo 11 Lunar Sci. Conf.*, pp. 1533-1574.
- Silver L. T. (1972) Uranium-thorium-lead isotopes and the nature of the mare surface debris at Hadley-Apennine (abstract). In *The Apollo 15 Lunar Samples* (J. W. Chamberlain and C. Watkins, eds.), pp. 388-390. The Lunar Science Institute, Houston.
- Silver L. T. (1974a) Implications of volatile leads in orange, grey and green lunar soils for an Earth-like Moon (abstract). *Eos Trans. AGU*, 55, 681.
- Silver L. T. (1974b) Patterns of U-Th-Pb distributions and isotope relations in Apollo 17 soils (abstract). In *Lunar Science V*, pp. 706-708. The Lunar Science Institute, Houston.
- Silver L. T. and Schultz P. H., eds. (1982) *Geological Implications of Impacts of Large Asteroids and Comets on Earth*. Geol. Soc. Am. Spec. Pap. 190. 528 pp.
- Simkin T., Noonan A., Switzer G. S., Mason B., Nelen J. A., Melson W. G., and Thompson G. (1973) Composition of Apollo 16 fines 60051, 60052, 64811, 64812, 68821, and 68822. *Proc. Lunar Sci. Conf. 4th*, pp. 279-289.
- Simmons G., Strangway D. W., Bannister L., Baker R., Cubley D., La Torraca G., and Watts R. (1972) The surface electrical properties experiment. In *Lunar Geophysics* (Z. Kopal and D. W. Strangway, eds.), pp. 258-271. Reidel, Dordrecht.
- Simmons G., Strangway D., Annan P., Baker R., Bannister L., Brown R., Cooper W., Cubley D., deBettencourt J., England A. W., Groener J., Kong J., La Torraca G., Meyer J., Nanda V., Redman D., Rossiter J., Tsang L., Urner J., and

- Watts R. (1973) Surface electrical properties experiment. In *Apollo 17 Preliminary Science Report*, pp. 15-1 to 15-14. NASA SP-380.
- Simnett G. M. (1974) Relativistic electron events in interplanetary space. *Space Sci. Rev.*, 16, 257-323.
- Simnett G. M. (1976) Solar cosmic radiation during August 1972. *Space Sci. Rev.*, 19, 579-610.
- Simon M. C. (1985) A parametric analysis of lunar oxygen production. In *Lunar Bases and Space Activities of the 21st Century* (W. W. Mendell, ed.), pp. 531-541. Lunar and Planetary Institute, Houston.
- Simon S. B. and Papike J. J. (1985) Petrology of the Apollo 12 highland component. *Proc. Lunar Planet. Sci. Conf. 16th*, in *J. Geophys. Res.*, 90, D47-D60.
- Simon S. B., Papike J. J., and Laul J. C. (1981) The lunar regolith: Comparative studies of the Apollo and Luna sites. Petrology of soils from Apollo 17, Luna 16, 20, and 24. *Proc. Lunar Planet. Sci. 12B*, pp. 371-388.
- Simon S. B., Papike J. J., and Laul J. C. (1982) The Apollo 14 regolith: Petrology of cores 14210/14211 and 14220 and soils 14141, 14148, and 14149. *Proc. Lunar Planet. Sci. Conf. 13th*, in *J. Geophys. Res.*, 87, A232-A246.
- Simon S. B., Papike J. J., and Shearer C. K. (1984) Petrology of Apollo 11 regolith breccias. *Proc. Lunar Planet. Sci. Conf. 15th*, in *J. Geophys. Res.*, 89, C 109-C 132.
- Simon S. B., Papike J. J., Gosselin D. C., and Laul J. C. (1985) Petrology and chemistry of Apollo 12 regolith breccias. *Proc. Lunar Planet. Sci. Conf. 16th*, in *J. Geophys. Res.*, 90, D75-D86.
- Simon S. B., Papike J. J., Gosselin D. C., and Laul J. C. (1986a) Petrology, chemistry and origin of Apollo 15 regolith breccias. *Geochim. Cosmochim. Acta*, 50, 2675-2691.
- Simon S. B., Papike J. J., Hörz F., and See T. H. (1986b) An experimental investigation of agglutinate melting mechanisms: Shocked mixtures of Apollo 11 and 16 soils. *Proc. Lunar Planet. Sci. Conf. 17th*, in *J. Geophys. Res.*, 91, E64-E74.
- Simon S. B., Papike J. J., Laul J. C., Hughes S. S., and Schmitt R. A. (1988) Apollo 16 regolith breccias and soils: Recorders of exotic component addition to the Descartes region of the moon. *Earth Planet. Sci. Lett.*, 89, 147-162.
- Simonds C. H. (1975) Thermal regimes in impact melts and the petrology of the Apollo 17 Station 6 boulder. *Proc. Lunar Sci. Conf. 6th*, pp. 641-672.
- Simonds C. H. (1981) Physics of the magma ocean: A critical review (abstract). In *Workshop on Apollo 16* (O. B. James and F. Hörz, eds.), pp. 123-128. LPI Tech. Rpt. 81-01, Lunar and Planetary Institute, Houston.
- Simonds C. H., Warner J. L., and Phinney W. C. (1973) Petrology of Apollo 16 poikilitic rocks. *Proc. Lunar Sci. Conf. 4th*, pp. 613-632.
- Simonds C. H., Warner J. L., and Phinney W. C. (1975) The petrology of the Apennine Front revisited (abstract). In *Lunar Science VI*, pp. 744-746. The Lunar Science Institute, Houston.
- Simonds C. H., Warner J. L., Phinney W. C., and McGee P. E. (1976) Thermal model for impact breccia lithification: Manicouagan and the Moon. *Proc. Lunar Sci. Conf. 7th*, pp. 2509-2528.
- Simonds C. H., Phinney W. C., Warner J. L., McGee P. E., Geeslin J., Brown R. W., and Rhodes J. M. (1977) Apollo 14 revisited, or breccias aren't so bad after all. *Proc. Lunar Sci. Conf. 8th*, pp. 1869-1893.
- Simoneit B. R., Christiansen P. C., and Burlingame A. L. (1973) Volatile element chemistry of selected lunar, meteoritic, and terrestrial samples. *Proc. Lunar Sci. Conf. 4th*, pp. 1635-1650.
- Simpson J. A. (1983) Elemental and isotopic composition of the galactic cosmic rays. *Annu. Rev. Nucl. Part. Sci.*, 33, 323-381.
- Simpson P. R. and Bowie S. H. V. (1971) Opaque phases in Apollo 12 samples. *Proc. Lunar Sci. Conf. 2nd*, pp. 207-218.
- Simpson R. A. and Tyler G. A. (1982) Radar scattering laws for the lunar surface. *IEEE Trans. Antennas and Propag.*, 30, 438-449.
- Sippel R. F. (1971) Luminescence petrography of the Apollo 12 rocks and comparative features in terrestrial rocks and meteorites. *Proc. Lunar Sci. Conf. 2nd*, pp. 247-263.
- Skinner B. J. (1970) High crystallization temperatures indicated for igneous rocks from Tranquillity Base. *Proc. Apollo 11 Lunar Sci. Conf.*, pp. 891-895.
- Smith E. I. (1973) Identification, distribution, and significance of lunar volcanic domes. *The Moon*, 6, 3-31.
- Smith E. I. and Sanchez A. G. (1973) Fresh lunar craters: Morphology as a function of diameter, a possible criterion for crater origin. *Mod. Geol.*, 4, 51-59.
- Smith J. V. (1974) Lunar mineralogy: A heavenly detective story, Presidential Address, Part 1. *Am. Mineral*, 59, 231-243.
- Smith J. V. and Steele I. M. (1974) Intergrowths in lunar and terrestrial anorthosites with implications for lunar differentiation. *Am. Mineral*, 59, 673-680.
- Smith J. V. and Steele I. M. (1976) Lunar mineralogy: A heavenly detective story. Part II. *Am. Mineral*, 61, 1059-1116.
- Smith J. V., Anderson A. T., Newton R. C., Olsen E. J., Wyllie P. J., Crewe A. V., Isaacson M. S., and Johnson D. (1970) Petrologic history of the Moon inferred from petrography, mineralogy, and petrogenesis of Apollo 11 rocks. *Proc. Apollo 11 Lunar Sci. Conf.*, pp. 897-925.
- Smith J. W. (1974) Carbon, nitrogen, and sulfur in lunar fines 15012 and 15013: Abundances, distributions and isotopic compositions. *Geochim. Cosmochim. Acta*, 38, 853-872.
- Smith J. W., Kaplan I. R., and Petrowski C. (1973) Carbon, nitrogen, sulfur, helium, hydrogen, and metallic iron in Apollo 15 drill stem fines. *Proc. Lunar Sci. Conf. 4th*, pp. 1651-1656.
- Smith P. M. (1985) Lunar stations: Prospects for international cooperation. In *Lunar Bases and Space Activities of the 21st Century* (W. W. Mendell, ed.), pp. 717-723. Lunar and Planetary Institute, Houston.

- Smith W. B., Ingalls R. P., Shapiro I. I., and Ash M. E. (1970) Surface height variations on Venus and Mercury. *Radio Sci.*, 5, 411–423.
- Smrekar S. and Pieters C. M. (1985) Near-infrared spectroscopy of probable impact melt from three large lunar highland craters. *Icarus*, 63, 442–452.
- Smyth J. R. (1974) The crystal chemistry of armalcolites from Apollo 17. *Earth Planet. Sci. Lett.*, 24, 262–270.
- Smyth J. R. (1975) Intracrystalline cation order in a lunar crustal troctolite. *Proc. Lunar Sci. Conf. 6th*, pp. 821–832.
- Soderblom L. A. (1970) A model for small-impact erosion applied to the lunar surface. *J. Geol. Res.*, 75, 2655–2661.
- Soderblom L. A. and Lebofsky L. A. (1972) Technique for rapid determination of relative ages of lunar areas from orbital photography. *J. Geophys. Res.*, 77, 279–296.
- Solar System Exploration Committee (1983) *Planetary Exploration Through Year 2000, A Core Program*. U.S. Government Printing Office, Washington, DC. 167 pp.
- Solar System Exploration Committee (1986) *Planetary Exploration Through Year 2000, An Augmented Program*. U.S. Government Printing Office, Washington, DC. 239 pp.
- Solomon S. C. (1986) On the early thermal state of the Moon. In *Origin of the Moon* (W. K. Hartmann, R. J. Phillips, and G. J. Taylor, eds.), pp. 435–452. Lunar and Planetary Institute, Houston.
- Solomon S. C. and Chaiken J. (1976) Thermal expansion and thermal stress in the Moon and terrestrial planets: Clues to early thermal history. *Proc. Lunar Sci. Conf. 7th*, pp. 3229–3243.
- Solomon S. C. and Head J. W. (1979) Vertical movement in the mare basins: Relation to the mare emplacement, basin tectonics, and lunar thermal history. *J. Geophys. Res.*, 84, 1667–1682.
- Solomon S. C. and Head J. W. (1980) Lunar mascon basins: Lava flooding, tectonics, and evolution of the lithosphere. *Rev. Geophys. Space Phys.*, 18, 107–141.
- Solomon S. C., Corner R. P., and Head J. W. (1982) The evolution of impact basins: Viscous relaxation of topographic relief. *J. Geophys. Res.*, 87, 3975–3992.
- Sonett C. P. (1982) Electromagnetic induction in the Moon. *Rev. Geophys. Space Phys.*, 20, 411–456.
- Sonett C. P. and Duba A. (1975) Lunar temperature and global heat flux from laboratory electrical conductivity and lunar magnetometer data. *Nature*, 258, 118–121.
- Sonett C. P., Giampapa M., and Matthews M. S., eds. (1990) *The Sun in Time*. Univ. of Arizona, Tucson, in press.
- Spangenburg R. and Moser D. (1987) A question of gravity. *Space World, February*, 8–11.
- Spudis P. D. (1984) Apollo 16 site geology and impact melts: Implications for the geologic history of the lunar highlands. *Proc. Lunar Planet. Sci. Conf. 15th*, in *J. Geophys. Res.*, 89, C95–C107.
- Spudis P. D. and Davis P. A. (1986) A chemical and petrologic model of the lunar crust and implications for lunar crustal origin. *Proc. Lunar Planet. Sci. Conf. 17th*, in *J. Geophys. Res.*, 91, E84–E90.
- Spudis P. D. and Ryder G. (1981) Apollo 17 impact melts and their relation to the Serenitatis basin. In *Multi-Ring Basins, Proc. Lunar Planet. Sci. 12A* (P. H. Schultz and R. B. Merrill, eds.), pp. 133–148. Pergamon, New York.
- Spudis P. D. and Ryder G. (1985) Geology and petrology of the Apollo 15 landing site: Past present, and future understanding. *Eos Trans. AGU*, 66, 721–726.
- Spudis P. D. and Ryder G., eds. (1986) *Workshop on the Geology and Petrology of the Apollo 15 Landing Site*. LPI Tech. Rpt. 86–03, Lunar and Planetary Institute, Houston. 126 pp.
- Spudis P. D., Hawke B. R., and Lucey P. (1984) Compositions of Orientale Basin deposits and implications for the lunar basin-forming process. *Proc. Lunar Planet. Sci. Conf. 15th*, in *J. Geophys. Res.*, 89, C197–C210.
- Stahle V. (1972) Impact glasses from the suevite of the Nordlinger Ries. *Earth Planet. Sci. Lett.*, 17, 275–293.
- Stanin F. T. and Taylor L. A. (1979a) Armalcolite/ilmenite: Mineral chemistry, paragenesis, and origin of textures. *Proc. Lunar Planet. Sci. Conf. 10th*, pp. 383–405.
- Stanin F. T. and Taylor L. A. (1979b) Ilmenite/armalcolite: Effects of rock composition, oxygen fugacity and cooling rate (abstract). In *Lunar and Planetary Science X*, pp. 1160–1162. Lunar and Planetary Institute, Houston.
- Stanin F. T. and Taylor L. A. (1980) Armalcolite: An oxygen fugacity indicator. *Proc. Lunar Planet. Sci. Conf. 11th*, pp. 117–124.
- Staudacher T., Jessberger E. K., Dominik B., Kirsten T., and Schaeffer O. (1982) $^{40}\text{Ar}/^{39}\text{Ar}$ ages of rocks and glasses from the Nordlinger Ries Crater and the temperature history of impact breccias. *J. Geophys. Res.*, 87, 1–11.
- Steele I. M. (1974) Ilmenite and armalcolite in Apollo 17 breccias. *Am. Mineral.*, 59, 681–689.
- Steele I. M. and Smith J. V. (1972) Ultrabasic lunar samples. *Nature Phys. Sci.*, 240, 5–6.
- Steele I. M. and Smith J. V. (1975) Minor elements in lunar olivine as a petrologic indicator. *Proc. Lunar Sci. Conf. 6th*, 451–467.
- Steele I. M. and Smith J. V. (1976) Mineralogy and petrology of complex breccia 14063,14. *Proc. Lunar Sci. Conf. 7th*, pp. 1949–1964.
- Steele I. M., Smith J. V., and Grossman L. (1972) Mineralogy and petrology of Apollo 15 rake samples: I. Basalts. In *The Apollo 15 Lunar Samples* (J. W. Chamberlain and C. Watkins, eds.), pp. 158–160. The Lunar Science Institute, Houston.
- Stephenson A., Collinson D. W., and Runcorn S. K. (1978) Rock magnetic and paleomagnetic studies on Luna 24 samples. In *Mare Crisium: The View from Luna 24* (R. B. Merrill and J. Papike, eds.), pp. 701–709. Pergamon, New York.
- Stettler A., Eberhardt P., Geiss J., Grögler N., and Maurer P. (1973) $\text{Ar}^{39}\text{-Ar}^{40}$ ages and $\text{Ar}^{37}\text{-Ar}^{38}$ exposure ages of lunar rocks. *Proc. Lunar Sci. Conf. 4th*, pp. 1865–1888.
- Stewart D. B. (1975) Apollonian metamorphic rocks—the products of prolonged subsolidus equilibration (abstract). In *Lunar Science VI*, pp. 774–776. The Lunar Science Institute, Houston.
- Stoener R. W., Davis R. Jr., Norton E., and Bauer M. (1974) Radioactive rare gases, tritium, hydrogen, and helium in

- the sample return container, and in the Apollo 16 and 17 drill stems. *Proc. Lunar Sci. Conf. 5th*, pp. 2211–2229.
- Stoeser D. B., Wolfe R. W., Wood J. A., and Bower J. F. (1974) Petrology. In *Interdisciplinary Studies of Samples from Boulder 1, Station 2, Apollo 17* (J. A. Wood, ed.), pp. 35–109. Smithsonian Astrophysical Observatory, Cambridge, Massachusetts.
- Stöffler D. (1971) Progressive metamorphism and classification of shocked and brecciated crystalline rocks at impact craters. *J. Geophys. Res.*, 76, 5541–5551.
- Stöffler D. (1972) Deformation and transformation of rock-forming minerals by natural and experimental shock processes. I. Behavior of minerals under shock compression. *Fortschr. Mineral.*, 49, 5477–5488.
- Stöffler D. (1974) Deformation and transformation of rock forming minerals by natural and experimental shock processes. II. Physical properties of shocked minerals. *Fortschr. Mineral.*, 51, 256–289.
- Stöffler D. (1981) Cratering mechanics: Data from terrestrial and experimental craters and implications for the Apollo 16 site (abstract). In *Workshop on Apollo 16* (O. B. James, ed.), pp. 132–141. LPI Tech. Rpt. 81–01, Lunar and Planetary Institute, Houston.
- Stöffler D. (1982) Physical properties of rocks. Density of minerals and rocks under shock compression. In *Numerical Data and Functional Relationships in Science and Technology, Group V. Geophysics and Space Research* (G. Angenheister, ed.), pp. 120–183. Springer-Verlag, Berlin.
- Stöffler D. (1984) Glasses formed by hypervelocity impact. *J. Noncryst. Solids*, 67, 465–505.
- Stöffler D., Dence M. R., Graup G., and Abadian M. (1974) Interpretation of ejecta formations at the Apollo 14 and 16 sites by a comparative analysis of experimental, terrestrial, and lunar craters. *Proc. Lunar Sci. Conf. 5th*, pp. 137–150.
- Stöffler D., Gault D. E., Wedekind J., and Polkowski G. (1975) Experimental hypervelocity impact into sand: Distribution and shock metamorphism of ejecta. *J. Geophys. Res.*, 80, 4062–4077.
- Stöffler D., Knöll H.-D., and Maerz U. (1979) Terrestrial and lunar impact breccias and the classification of lunar highland rocks. *Proc. Lunar Planet. Sci. Conf. 10th*, pp. 639–675.
- Stöffler D., Knöll H.-D., Marvin U. B., Simonds C. H., and Warren P. H. (1980) Recommended classification and nomenclature of lunar highland rocks—a committee report. In *Proceedings of the Conference on the Lunar Highlands Crust* (J. J. Papike and R. B. Merrill, eds.), pp. 51–70. Pergamon, New York.
- Stöffler D., Ostertag R., Reimold U., Borchardt R., Malley J., and Rehfeldt A. (1981) Distribution and provenance of lunar highland rock types at North Ray Crater, Apollo 16. *Proc. Lunar Planet. Sci. 12B*, pp. 185–207.
- Stöffler D., Bischoff A., Borchardt R., Burgehele A., Deutsch A., Jessberger E. K., Ostertag R., Palme H., Spettel B., Reimold W. U., Wacker K., and Wänke H. (1985) Composition and evolution of the lunar crust in the Descartes Highlands, Apollo 16. *Proc. Lunar Planet. Sci. Conf. 15th*, in *J. Geophys. Res.*, 89, C449–0506.
- Stolper E. M. (1974) Apollo 15 green glass. A.B. thesis, Harvard University. 178 pp.
- Stolper E. M. (1977) Experimental petrology of eucritic meteorites. *Geochim. Cosmochim. Acta*, 41, 587–611.
- Stone C. D., Taylor L. A., McKay D. S., and Morris R. V. (1982) Ferromagnetic resonance intensity: A rapid method for determining lunar glass bead origin. *Proc. Lunar Planet. Sci. Conf. 13th*, in *J. Geophys. Res.*, 87, A182–A196.
- Strangway D. W. (1969) Moon, electrical properties of the uppermost layers. *Science*, 165, 1012–1013.
- Strangway D. W. and Olhoeft G. R. (1977) Electrical properties of planetary surfaces. *Philos. Trans. R. Soc. London*, A285, 441–450.
- Strangway D. W., Chapman W. B., Olhoeft G. R., and Carnes J. (1972) Electrical properties of lunar soil—dependence upon frequency, temperature and moisture. *Earth Planet. Sci. Lett.*, 16, 275–281.
- Strangway D. W., Annan A. P., Redman J. D., Rossiter J. R., Rylaarsdam J. A., and Watts R. D. (1974) *Surface Electrical Properties Experiment, Parts 1, 2, and 3*. NASA Reports CR-141471, 141472, and 141473. 1355 pp. (total).
- Strangway D. W., Pearce G. W., and Olhoeft G. R. (1975) Magnetic and dielectric properties of lunar samples. In *Proceedings of the Soviet-American Conference on Cosmochemistry of the Moon and Planets*, pp. 712–728. Nauka, Moscow. Reprinted as NASA SP-370 (1977).
- Strasheim A., Hackson P. F. S., Coetzee J. H. J., Strelow F. W. E., Wybenga F. T., Gricius A. J., Kokot M. L., and Scott R. H. (1972) Analysis of lunar samples 14163, 14259, and 14321 with isotopic data for $^7\text{Li}/^6\text{Li}$. *Proc. Lunar Sci. Conf. 3rd*, pp. 1337–1342.
- Strom R. G. (1964) Analysis of lunar lineaments. I. Tectonic maps of the moon. *Commun. Lunar Planet. Lab.*, 2, 205–216.
- Strom R. G. (1977) Origin and relative age of lunar and mercurian intercrater plains. *Phys. Earth Planet. Inter.*, 15, 156–172.
- Stuart-Alexander D. E. (1978) Geologic map of the central farside of the Moon. *U.S. Geol. Survey Map I-1047*.
- Sung C. M., Abu-Eid R. M., and Burns R. G. (1974) $\text{Ti}^{3+}/\text{Ti}^{4+}$ ratios in lunar pyroxenes: Implications to depth of origin of mare basalt magma. *Proc. Lunar Sci. Conf. 5th*, pp. 717–726.
- Surkov Yu. A. and Kolesov G. M. (1979) Contents of rock-forming minor and trace elements as gauges of Luna 20 regolith characteristics. In *Regolith from the Highland Region of the Moon* (V. L. Barsukov and Yu. A. Surkov, eds.), pp. 345–354. Nauka, Moscow.
- Svitek T. and Murray B. C. (1988) Lunar polar ice—A reappraisal (abstract). In *Lunar and Planetary Science XIX*, p. 1160. Lunar and Planetary Institute, Houston.
- Swann G. A. (1986) Some observations on the geology of the Apollo 15 landing site (abstract). In *Workshop on the Geology and Petrology of the Apollo 15 Landing Site* (G. Ryder and P. D. Spudis, eds.), pp. 108–112. LPI Tech. Rpt. 86–03, Lunar and Planetary Institute, Houston.

- Swann G. A., Bailey N. G., Batson R. M., Freeman V. L., Hait M. H., Head J. W., Holt H. E., Howard K. A., Irwin J. B., Larson K. B., Muehlberger W. R., Reed V. S., Rennilson J. J., Schaber G. G., Scott D. R., Silver L. T., Sutton R. L., Ulrich G. E., Wilshire H. G., and Wolfe E. W. (1972) Preliminary geologic investigations of the Apollo 15 landing site. In *Apollo 15 Preliminary Science Report*, pp. 5-1 to 5-112. NASA SP-289.
- Swann G. A., Bailey N. G., Batson R. M., Eggleton R. E., Hait M. H., Holt H. E., Larson K. B., Reed V. S., Schaber G. G., Sutton R. L., Trask N. A., Ulrich G. E., and Wilshire H. G. (1977) *Geology of the Apollo 14 Landing Site in the Fra Mauro Highlands*. U.S. Geol. Surv. Prof. Pap. 800. 103 pp.
- Takeda H., Miyamoto M., Ishii T., and Lofgren G. E. (1975) Relative cooling rates of mare basalts at the Apollo 12 and 15 sites as estimated from pyroxene exsolution data. *Proc. Lunar Sci. Conf. 6th*, pp. 987-996.
- Takeda H., Mori H., Miyamoto M., and Ishii T. (1983) Mesostasis-rich lunar and eucritic basalts with reference to REE-rich minerals (abstract). In *Lunar and Planetary Science XIV*, pp. 842-843. Lunar and Planetary Institute, Houston.
- Tarasov L. S., Nazarov M. A., Shevaleevsky I. D., Kudryashova A. F., Gaverdovskaya A. S., and Korina M. I. (1977) Mineralogy and petrography of lunar rocks from Mare Crisium (preliminary data). *Proc. Lunar Sci. Conf. 8th*, pp. 3333-3356.
- Tatsumoto M. (1970) Age of the Moon: An isotopic study of U-Th-Pb systematics of Apollo 11 lunar samples—II. *Proc. Apollo 11 Lunar Sci. Conf.*, pp. 1595-1612.
- Tatsumoto M. (1973) U-Th-Pb measurements of Luna 20 soil. *Geochim. Cosmochim. Acta*, 37, 1079-1086.
- Tatsumoto M. and Unruh D. M. (1976) KREEP basalt age: Grain by grain U-Th-Pb systematics study of the quartz monzodiorite clast 15405, 88. *Proc. Lunar Sci. Conf. 7th*, pp. 2107-2129.
- Tatsumoto M., Knight R. J., and Doe B. R. (1971) U-Th-Pb systematics of Apollo 12 lunar samples. *Proc. Lunar Sci. Conf. 2nd*, pp. 1521-1546.
- Tatsumoto M., Hedge C. E., Doe B. R., and Unruh D. M. (1972a) U-Th-Pb and Rb-Sr measurements on some Apollo 14 lunar samples. *Proc. Lunar Sci. Conf. 3rd*, pp. 1531-1555.
- Tatsumoto M., Hedge C. E., Knight R. J., Unruh D. M., and Doe B. R. (1972b) U-Th-Pb, Rb-Sr, and K measurements on some Apollo 15 and Apollo 16 samples (abstract). In *The Apollo 15 Lunar Samples* (J. W. Chamberlain and C. Watkins, eds.), pp. 391-395. The Lunar Science Institute, Houston.
- Tatsumoto M., Nunes P. D., Knight R. J., Hedge C. E., and Unruh D. M. (1973) U-Th-Pb, Rb-Sr, and K measurements of two Apollo 17 samples (abstract). *Eos Trans. AGU*, 54, 614-615.
- Tatsumoto M., Premo W. R., and Unruh D. M. (1987) Origin of lead from green glass of Apollo 15426: A search for primitive lunar lead. *Proc. Lunar Planet. Sci. Conf. 17th*, in *J. Geophys. Res.*, 92, E361-E371.
- Taylor D. W. (1937) Stability of earth slopes. *Journal of the Boston Society of Civil Engineers*. Reprinted in *Contributions to Soil Mechanics 1925-1940*, pp. 337-386. Boston Society of Civil Engineers (1940).
- Taylor D. W. (1948) *Fundamentals of Soil Mechanics*. Wiley, New York.
- Taylor G. J. and Spudis P. D. (1990) *Geoscience and a Lunar Base: A Comprehensive Plan for Lunar Exploration*. NASA CP-3070. 73 pp.
- Taylor G. J., Warner R. D., and Keil K. (1978) VLT mare basalts: Impact mixing, parent magma types, and petrogenesis. In *Mare Crisium: The View from Luna 24* (J. J. Papike and R. B. Merrill, eds.), pp. 357-370. Pergamon, New York.
- Taylor G. J., Warner R. D., and Keil K. (1979) Stratigraphy and depositional history of the Apollo 17 drill core. *Proc. Lunar Planet. Sci. Conf. 10th*, pp. 1159-1184.
- Taylor G. J., Warner R. D., Keil K., Ma M.-S., and Schmitt R. A. (1980) Silicate liquid immiscibility, evolved lunar rocks and the formation of KREEP. In *Proceedings of the Conference on the Lunar Highlands Crust* (J. J. Papike and R. B. Merrill, eds.), pp. 339-352. Pergamon, New York.
- Taylor H. P. and Epstein S. (1973) O^{18}/O^{16} and Si^{30}/Si^{28} studies of some Apollo 15, 16, and 17 samples. *Proc. Lunar Sci. Conf. 4th*, pp. 1657-1679.
- Taylor L. A. (1988) Generation of native Fe in lunar soil. In *Engineering, Construction, and Operations in Space: Proceedings of Space '88* (S. W. Johnson and J. P. Wetzel, eds.), pp. 67-77. American Society of Civil Engineers, New York.
- Taylor L. A. and Cirlin E.-H. (1986) A review of ESR studies on lunar samples. In *ESR Dating and Dosimetry*, pp. 19-29. Ionics, Tokyo.
- Taylor L. A. and Hunter R. H. (1981) The significance of Cl/P₂O₅ ratios from lunar samples. *Proc. Lunar Planet. Sci. 12B*, pp. 323-331.
- Taylor L. A. and Lu F. (1990) The formation of ore mineral deposits on the Moon: A feasibility study. In *The Second Conference on Lunar Bases and Space Activities of the 21st Century* (W. W. Mendell, ed.). Univelt, San Diego, in press.
- Taylor L. A. and McCallister R. H. (1972) Experimental investigation of significance of zirconium partitioning in lunar ilmenite and ulvöspinel. *Earth Planet. Sci. Lett.*, 17, 105-111.
- Taylor L. A. and Williams K. L. (1973) Cu-Fe-S phases in lunar rocks. *Am. Mineral.*, 58, 952-954.
- Taylor L. A., Kullerud G., and Bryan W. B. (1971) Opaque mineralogy and textural features of Apollo 12 samples and a comparison with Apollo 11 rocks. *Proc. Lunar Sci. Conf. 2nd*, pp. 855-871.
- Taylor L. A., Williams R. J., McCallister R. H. (1972) Stability relations of ilmenite and ulvöspinel in the Fe-Ti-O system and application of these data to lunar mineral assemblages. *Earth Planet. Sci. Lett.*, 16, 282-288.
- Taylor L. A., Mao H. K., and Bell P. M. (1973a) "Rust" in the Apollo 16 rocks. *Proc. Lunar Sci. Conf. 4th*, pp. 829-839.

- Taylor L. A., McCallister R. H., and Sardi O. (1973b) Cooling histories of lunar rocks based on opaque mineral geothermometers. *Proc. Lunar Sci. Conf. 4th*, pp. 819–828.
- Taylor L. A., Williams K. L., and Sardi O. (1973c) Selected Apollo 17 soils: Mineralogy and geochemistry of opaque and non-opaque phases. *Earth Planet. Sci. Lett.*, 21, 6–12.
- Taylor L. A., Mao H. K., and Bell P. M. (1974) Identification of the hydrated iron oxide mineral akaganeite in Apollo 16 lunar rocks. *Geology*, 2, 429–432.
- Taylor L. A., Uhlmann D. R., Hopper R. W., and Misra K. C. (1975) Absolute cooling rates of lunar rocks: Theory and application. *Proc. Lunar Sci. Conf. 6th*, pp. 181–191.
- Taylor L. A., Onorato P. I. K., Uhlmann D. R., and Coish R. A. (1978) Subophitic basalts from Mare Crisium: Cooling rates. In *Mare Crisium: The View From Luna 24* (R. B. Merrill and J. J. Papike, eds.), pp. 473–482. Pergamon, New York.
- Taylor L. A., Shervais J. W., Hunter R. H., Shih D.-Y., Bansal B. M., and Nyquist L. E. (1983) Pre-4.2 AE mare basalt volcanism in the lunar highlands. *Earth Planet. Sci. Lett.*, 66, 33–47.
- Taylor S. R. (1975) *Lunar Science: A Post Apollo View*. Pergamon, New York. 372 pp.
- Taylor S. R. (1982) *Planetary Science: A Lunar Perspective*. Lunar and Planetary Institute, Houston. 481 pp.
- Taylor S. R., Rudowski R., Muir P., Graham A., and Kaye M. (1971) Trace element chemistry of lunar samples from the Ocean of Storms. *Proc. Lunar Sci. Conf. 2nd*, pp. 1083–1099.
- Taylor S. R., Kaye M., Muir P., Nance W., Rudowski R., and Ware N. (1972) Composition of the lunar uplands: Chemistry of Apollo 14 samples from Fra Mauro. *Proc. Lunar Sci. Conf. 3rd*, pp. 1231–1249.
- Taylor S. R., Gorton M. P., Muir P., Nance W., Rudowski R., and Ware N. (1973a) Lunar highlands compositions: Apennine Front. *Proc. Lunar Sci. Conf. 4th*, pp. 1445–1459.
- Taylor S. R., Gorton M. P., Muir P., Nance W. B., Rudowski R., and Ware N. (1973b) Composition of the Descartes region, lunar highlands. *Geochim. Cosmochim. Acta*, 37, 2665–2683.
- Tera F. and Wasserburg G. J. (1972a) U-Th-Pb analyses of soil from the Sea of Fertility. *Earth Planet. Sci. Lett.*, 13, 457–466.
- Tera F. and Wasserburg G. J. (1972b) U-Th-Pb systematics in lunar highland samples from the Luna 20 and Apollo 16 missions. *Earth Planet. Sci. Lett.*, 17, 36–51.
- Tera F. and Wasserburg G. J. (1976) Lunar ball games and other sports (abstract). In *Lunar Science VII*, pp. 858–860. The Lunar Science Institute, Houston.
- Tera F., Eugster O., Burnett D. S., and Wasserburg G. J. (1970) Comparative study of Li, Na, K, Rb, Cs, Ca, Sr, and Ba abundances in achondrites and in Apollo 11 lunar samples. *Proc. Apollo 11 Lunar Sci. Conf.*, pp. 1637–1657.
- Tera F., Ray L. A., and Wasserburg G. J. (1972) Distribution of Pb-U-Th in lunar anorthosite 15415 and inferences about its age (abstract). In *The Apollo 15 Lunar Samples* (J. W. Chamberlain and C. Watkins, eds.), pp. 396–401. The Lunar Science Institute, Houston.
- Tera F., Papanastassiou D. A., and Wasserburg G. J. (1974) Isotopic evidence for a terminal lunar cataclysm. *Earth Planet. Sci. Lett.*, 22, 1–21.
- Thiemens M. H. and Clayton R. N. (1980) Solar and cosmogenic nitrogen in the Apollo 17 deep drill core. *Proc. Lunar Planet. Sci. Conf. 11th*, pp. 1435–1451.
- Thode H. G. and Rees C. E. (1976) Sulphur isotopes in grain size fractions of lunar soils. *Proc. Lunar Sci. Conf. 7th*, pp. 459–468.
- Thompson A. C. and Stevenson D. J. (1983) Two-phase gravitational instabilities in thin disks with application to the origin of the Moon (abstract). In *Lunar and Planetary Science XIV*, pp. 787–788. Lunar and Planetary Institute, Houston.
- Thompson T. W. (1987) High-resolution lunar radar map at 70-cm wavelength. *Earth, Moon and Planets*, 37, 59–70.
- Thompson T. W. (1974) Atlas of lunar radar maps at 70-cm wavelength. *The Moon*, 10, 51–85.
- Thompson T. W. (1979) A review of Earth-based radar mapping of the Moon. *Moon and Planets*, 20, 179–198.
- Thompson T. W. (1986) High resolution radar map of the Moon (abstract). In *Lunar and Planetary Science XVII*, pp. 895–896. Lunar and Planetary Institute, Houston.
- Thompson T. W. and Saunders R. S. (1986) Lunar and Venusian radar bright rings (abstract). In *Lunar and Planetary Science XVII*, pp. 897–898. Lunar and Planetary Institute, Houston.
- Thompson T. W. and Zisk S. H. (1972) Radar mapping of lunar surface roughness. In *Thermal Characteristics of the Moon* (J. W. Lucas, ed.), pp. 83–117. AIAA, New York.
- Thompson T. W., Pollack J. B., Campbell M. J., and O'Leary B. T. (1970) Radar maps of the Moon at 70-cm wavelength and their interpretation. *Radio Sci.*, 5, 253–262.
- Thompson T. W., Howard K. A., Shorthill R. W., Tyler G. L., Sisk S. H., Whitaker E. A., Schaber G. G., and Moore H. J. (1973) Remote sensing of Mare Serenitatis. In *Apollo 17 Preliminary Science Report*, pp. 33–1 to 33–10. NASA SP-330.
- Thompson T. W., Masursky H., Shorthill R. W., Tyler G. L., and Zisk S. H. (1974) A comparison of infrared, radar, and geologic mapping of lunar craters. *The Moon*, 10, 87–117.
- Thompson T. W., Roberts W. J., Hartmann W. K., Shorthill R. W., and Zisk S. H. (1979) Implications about the lunar megaregolith. *Moon and Planets*, 21, 319–342.
- Thompson T. W., Cutts J. A., Shorthill R. W., and Zisk S. H. (1980) Infrared and radar signatures of lunar craters: Implications about crater evolution. In *Proceedings of the Conference on the Lunar Highlands Crust* (J. J. Papike and R. B. Merrill, eds.), pp. 483–499. Pergamon, New York.
- Tikhonova T. V. and Troitsky V. S. (1969) Effect of heat from within the Moon on its radio emission for the case of lunar properties which vary with depth. *Soviet Astron.*, 13, 120–128.
- Titly S. R. (1966) Seismic energy as an agent of morphologic modification on the Moon. In *Astrogeologic Studies Ann. Prog. Rep. July 1965 July 1966, Pt A*, pp. 87–103. U.S. Geol. Surv. Open File Report.

- Toksoz M. N., Dainty A. M., Solomon S. C., and Anderson K. R. (1973) Velocity structure and evolution of the Moon. *Proc. Lunar Sci. Conf. 4th*, pp. 2529–2547.
- Trask N. J. (1971) Geologic comparison of mare materials in the equatorial belt, including Apollo 11 and 12 landing sites. In *Geological Survey Research 1971*, pp. D138–D144. U.S. Geol. Surv. Prof. Pap. 750–D.
- Trask N. J. (1972) *The Contribution of Ranger Photographs to Understanding the Geology of the Moon*. U.S. Geol. Surv. Prof. Pap. 599–I. 16 pp.
- Tsay F.-D., Chan S. I., and Manatt S. L. (1971) Ferromagnetic resonance of lunar samples. *Geochim. Cosmochim. Acta*, 5, 865–875.
- Tsay F.-D., Manatt S. L., Live D. H., and Chan S. J. (1973) Metallic Fe phases in Apollo 16 fines: Their origin and characteristics as revealed by electron spin resonance studies. *Proc. Lunar Sci. Conf. 4th*, pp. 2751–2761.
- Tucker D. S., Vaniman D. T., Anderson J. L., Clinard F. W. Jr., Feber R. C. Jr., Frost H. M., Meek T. T., and Wallace T. C. (1985) Hydrogen recovery from extraterrestrial materials using microwave energy. In *Lunar Bases and Space Activities of the 21st Century* (W. W. Mendell, ed.), pp. 583–590. Lunar and Planetary Institute, Houston.
- Tucker M. E. (1981) *Sedimentary Petrology*. Blackwell, Oxford. 252 pp.
- Turekian K. K. and Kharkar D. P. (1970) Neutron activation analysis of milligram quantities of Apollo 11 lunar rocks and soil. *Proc. Apollo 11 Lunar Sci. Conf.*, pp. 1659–1664.
- Turner G. and Cadogan P. H. (1975) The history of lunar bombardment inferred from ^{40}Ar - ^{39}Ar dating of highland rocks. *Proc. Lunar Sci. Conf. 6th*, pp. 1509–1538.
- Turner G., Cadogan P. H., and Yonge C. J. (1973) Argon selenochronology. *Proc. Lunar Sci. Conf. 4th*, pp. 1889–1914.
- Tyler G. L. (1968a) Brewster angle of the lunar crust. *Nature*, 219, 1243–1244.
- Tyler G. L. (1968b) Oblique-scattering radar reflectivity of the lunar surface: Preliminary results from Explorer 35. *J. Geophys. Res.*, 73, 7609–7620.
- Tyler G. L. (1979) Comparison of quasi-specular radar scatter from the Moon with surface parameters obtained from images. *Icarus*, 37, 29–45.
- Tyler G. L. and Howard H. T. (1973) Dual-frequency bistatic-radar investigations of the Moon with Apollos 14 and 15. *J. Geophys. Res.*, 78, 4852–4874.
- Tyler G. L., Simpson R. A., and Moore H. J. (1971) Lunar slope distributions, comparison of bistatic-radar and photographic results. *J. Geophys. Res.*, 76, 2790–2795.
- Uhlmann D. R., Klein L., Kritchevsky G., and Hopper R. W. (1974) The formation of lunar glasses. *Proc. Lunar Sci. Conf. 5th*, pp. 2317–2331.
- Uhlmann D. R., Onorato P. I. K., Yinnon H., and Taylor L. A. (1979) Partitioning as a cooling rate indicator (abstract). In *Lunar and Planetary Science X*, pp. 1253–1255. Lunar and Planetary Institute, Houston.
- Ulaby F. T., Moore R. K., and Fung A. K., eds. (1982) *Microwave Remote Sensing Vol. 2: Surface Scattering and Emission Theory*. Addison-Wesley, Reading. 1064 pp.
- Ulich B. L., Cogdell J. R., Davis J. H., and Calvert T. A. (1974) Observations and analysis of lunar radio emission at 3.09 mm wavelength. *The Moon*, 10, 163–174.
- Ullrich G. W., Roddy D. J., and Simmons G. (1977) Numerical simulations of a 20-ton TNT detonation at the earth's surface and implications concerning the mechanics of central uplift formation. In *Impact and Explosion Cratering* (D. J. Roddy, R. O. Pepin, and R. B. Merrill, eds.), pp. 959–982. Pergamon, New York.
- Ulrich G. E., Hodges C. A., and Muehlberger W. R., eds. (1981) *Geology of the Apollo 16 Area, Central Lunar Highlands*. U.S. Geol. Surv. Prof. Pap. 1048. 539 pp.
- Unruh D. M. and Tatsumoto M. (1978) Implications from Luna 24 sample 24170 to U-Pb evolution of the lunar mantle. In *Mare Crisium: The View from Luna 24* (R. B. Merrill and J. J. Papike, eds.), pp. 679–694. Pergamon, New York.
- Unruh D. M., Nakamura N., and Tatsumoto M. (1977) History of the Pasamonte achondrite: Relative susceptibility of the Sm-Nd, Rb-Sr, and U-Pb systems to metamorphic events. *Earth Planet. Sci. Lett.*, 37, 1–12.
- Urey H. C. (1965) Meteorites and the Moon. *Science*, 147, 1262–1265.
- Urey H. C. (1966) The capture hypothesis of the origin of the Moon. In *The Earth-Moon System* (B. G. Marsden and A. G. W. Cameron, eds.), pp. 210–212. Plenum, New York.
- Usselman T. M. and Lofgren G. E. (1976) The phase relations, textures, and mineral chemistries of high titanium mare basalts as a function of oxygen fugacity and cooling rate. *Proc. Lunar Sci. Conf. 7th*, pp. 1345–1363.
- Usselman T. M. and Pearce G. W. (1974) Grain growth of iron: Implications for the thermal conditions in a lunar ejecta blanket (abstract). In *Lunar Science V*, pp. 809–811. The Lunar Science Institute, Houston.
- Usselman T. M., Lofgren G. E., Donaldson C. H., and Williams R. J. (1975) Experimentally reproduced textures and mineral chemistries of high-titanium mare basalts. *Proc. Lunar Sci. Conf. 6th*, pp. 997–1020.
- van Diggelen J. (1959) Photometric properties of lunar crater floors. *Recherches Astronomiques de l'Observatoire d'Utrecht*, 14, no. 2. Translated to English as NASA Technical Translation F-209 (1964).
- Van Hollebeke M. A. I., Ma Sung L. S., and McDonald F. B. (1975) The variation of solar proton energy spectra and size distribution with heliolongitude. *Solar Phys.*, 41, 189–223.
- Vaniman D. T. (1990) Glass variants and multiple HASP trends in Apollo 14 regolith breccias. *Proc. Lunar Planet. Sci. Conf. 20th*, pp. 209–217.
- Vaniman D. T. and Bish D. L. (1990) Yoshiokaite, a new Ca,Al-silicate mineral from the Moon. *Am. Mineral.*, 75, 676–686.
- Vaniman D. T. and Papike J. J. (1977a) The Apollo 17 drill core: Characterization of the mineral and lithic component (sections 70007, 70008, 70009). *Proc. Lunar Sci. Conf. 8th*, pp. 3123–3159.

- Vaniman D. T. and Papike J. J. (1977b) The Apollo 17 drill core: Modal petrology and glass chemistry (sections 70007, 70008, 70009). *Proc. Lunar Sci. Conf. 8th*, 3161–3193.
- Vaniman D. T. and Papike J. J. (1977c) Very low Ti (VLT) basalts: A new mare rock type from the Apollo 17 drill core. *Proc. Lunar Sci. Conf. 8th*, pp. 1443–1471.
- Vaniman D. T. and Papike J. J. (1980) Lunar highland melt rocks: Chemistry petrology and silicate mineralogy. In *Proceedings of the Conference on the Lunar Highlands Crust* (J. J. Papike and R. B. Merrill, eds.), pp. 271–337. Pergamon, New York.
- Vaniman D. T., Lellis S. F., Papike J. J., and Cameron K. L. (1976) The Apollo 16 drill core: Modal petrology and characterization of the mineral and lithic component. *Proc. Lunar Sci. Conf. 7th*, pp. 199–239.
- Vaniman D. T., Labotka T. C., Papike J. J., Simon S. B., and Laul J. C. (1979) The Apollo 17 drill core: Petrologic systematics and the identification of a possible Tycho component. *Proc. Lunar Planet. Sci. Conf. 10th*, pp. 1185–1227.
- Vaniman D. T., Meek T. T., and Blake R. D. (1986) Fusing of lunar materials with microwave energy; Pt. II. Melting of a simulated glassy Apollo 11 soil (abstract). In *Lunar and Planetary Science XVII*, pp. 911–912. Lunar and Planetary Institute, Houston.
- Vaniman D., Pettit D., and Heiken G. (1990) Uses of lunar sulfur. In *The Second Conference on Lunar Bases and Space Activities of the 21st Century* (W. W. Mendell, ed.). Univelt, San Diego, in press.
- Vanyan L. L., Vnuchlkova T. A., Egorov I. V., Basilevsky A. T., Eroshenko E. G., Fainberg E. B., Dyal P., and Daily W. D. (1979) Electrical conductivity anomaly beneath Mare Serenitatis detected by Lunokhod 2 and Apollo 16 magnetometers. *Moon and Planets*, 21, 185–192.
- Vedder J. F. and Mandeville J.-C. (1974) Microcraters formed in glasses by projectiles of various densities. *J. Geophys. Res.*, 79, 3247–3256.
- Vedenin A. I., Douchowskoy E. A., Markatchev V. V., Silin A. A., Cherkasov I. I., and Shvarev V. V. (1974) The investigation of mechanical properties of lunar soil and its analogs in different atmospheres and vacuum in the TOR-1 installation. In *Lunar Soil from Sea of Fertility*, pp. 571–581. Nauka, Moscow (in Russian).
- Verkouteren R. M., Dennison J. E., and Lipschutz M. E. (1983) Siderophile, lithophile and mobile trace elements in the lunar meteorite Allan Hills 81005. *Geophys. Res. Lett.*, 10, 821–824.
- Veverka J. and Noland M. (1973) Asteroid reflectivities from polarization curves: Calibration of the “slope-albedo” relationship. *Icarus*, 19, 230–239.
- Vinogradov A. P. (1971) Preliminary data on lunar ground brought to Earth by automatic probe “Luna-16.” *Proc. Lunar Sci. Conf. 2nd*, pp. 1–16.
- Vinogradov A. P. (1972) Preliminary data on lunar regolith returned by automatic probe “Luna-20.” *Geokhimiya*, 7, 763–774.
- Vinogradov A. P. (1973) Preliminary data on lunar soil collected by the Luna 20 unmanned spacecraft. *Geochim. Cosmochim. Acta*, 37, 721–729.
- Vondrak R. R. (1974) Creation of an artificial lunar atmosphere. *Nature*, 248, 657–659.
- von Engelhardt W. V., Luft E., Arndt J., Shock H., and Weiskichner W. (1987) Origin of moldavites. *Geochim. Cosmochim. Acta*, 51, 1425–1443.
- von Gunten H. R., Wegmuller F., and Krähenbühl U. (1982) Low temperature volatilization on the Moon. *Proc. Lunar Planet. Sci. Conf. 13th*, in *J. Geophys. Res.*, 87, A279–A282.
- Wadell H. (1935) Volume, shape and roundness of quartz particles. *J. Geol.*, 43, 250–280.
- Wakita H., Schmitt R. A., and Rey P. (1970) Elemental abundances of major, minor and trace elements in Apollo 11 lunar rocks, soil and core samples. *Proc. Apollo 11 Lunar Sci. Conf.*, pp. 1685–1717.
- Wakita H., Rey P., and Schmitt R. A. (1971) Abundances of the 14 rare-earth elements and 12 other trace elements in Apollo 12 samples—five igneous and one breccia rocks and four soils. *Proc. Lunar Sci. Conf. 2nd*, pp. 1319–1330.
- Waldron R. D. (1990) Alternatives for *in situ* resource processing. In *Engineering Construction, and Operations in Space II: Proceedings of Space '90* (S. W. Johnson and J. P. Wetzel, eds.), pp. 216–225. American Society of Civil Engineers, New York.
- Walker D. (1983) Lunar and terrestrial crust formation. *Proc. Lunar Planet. Sci. Conf. 14th*, in *J. Geophys. Res.*, 88, B17–B25.
- Walker D., Longhi J., and Hays J. F. (1972) Experimental petrology and origin of Fra Mauro rocks and soil. *Proc. Lunar Sci. Conf. 3rd*, pp. 797–817.
- Walker D., Longhi J., Grove T. L., Stolper E., and Hays J. F. (1973a) Experimental petrology and origin of rocks from the Descartes highlands. *Proc. Lunar Sci. Conf. 4th*, pp. 1013–1032.
- Walker D., Grove T. L., Longhi J., Stolper E. M., and Hays J. F. (1973b) Origin of lunar feldspathic rocks. *Earth Planet. Sci. Lett.*, 20, 325–336.
- Walker D., Longhi J., Stolper E. M., Grove T. L., and Hays J. F. (1975) Origin of titaniferous lunar basalts. *Geochim. Cosmochim. Acta*, 39, 1219–1235.
- Walker D., Kirkpatrick R. J., Longhi J., and Hays J. F. (1976) Crystallization history of lunar picritic basalt sample 12002: Phase equilibria and cooling rate studies. *Geol. Soc. Am. Bull.*, 87, 646–656.
- Walker D., Longhi J., Lasaga A. C., Stolper E. M., Grove T. L., and Hays J. F. (1977) Slowly cooled microgabbros 15555 and 15065. *Proc. Lunar Sci. Conf. 8th*, pp. 1521–1547.
- Walker D., Powell M. A., Lofgren G. E., and Hays J. F. (1978) Dynamic crystallization of a eucrite basalt. *Proc. Lunar Planet. Sci. Conf. 9th*, pp. 1369–1391.
- Walker R. J. and Papike J. J. (1981) The relationship of the lunar regolith <10 mm fraction and agglutinates. Part II: Chemical composition of agglutinate glass as a test of the “fusion of the finest fraction” (F³) model. *Proc. Lunar Planet. Sci. 12B*, pp. 421–431.

- Walker R. M. (1975) Interaction of energetic nuclear particles in space with the lunar surface. *Annu. Rev. Earth Planet. Sci.*, 3, 99–128.
- Walker R. M. (1980) Nature of the fossil evidence: Moon and meteorites. In *The Ancient Sun: Fossil Record in the Earth, Moon and Meteorites* (R. O. Pepin, J. A. Eddy, and R. B. Merrill, eds.), pp. 11–28. Pergamon, New York.
- Walker R. and Yuhas D. (1973) Cosmic ray track production rates in lunar materials. *Proc. Lunar Sci. Conf. 4th*, pp. 2379–2389.
- Walton J. R., Lakatos S., and Heymann D. (1973) Distribution of inert gases in fines from the Cayley-Descartes region. *Proc. Lunar Sci. Conf. 4th*, pp. 2079–2095.
- Wänke H., Rieder R., Baddenhausen H., Spettel B., Teschke Quijano-Rico M., and Basacescu A. (1970a) Major and trace elements in lunar materials. *Proc. Apollo 11 Lunar Sci. Conf.*, pp. 1719–1727.
- Wänke H., Wlotzka F., Jagoutz E., and Begemann F. (1970b) Composition and structure of metallic iron particles in lunar fines. *Proc. Apollo 11 Lunar Sci. Conf.*, pp. 931–936.
- Wänke H., Wlotzka F., Baddenhausen H., Balacescu A., Spettel B., Teschke F., Jagoutz E., Kruse H., Quijano-Rico M., and Rieder R. (1971) Apollo 12 samples: Chemical composition and its relation to sample locations and exposure ages, the two component origin of the various soil samples and studies on lunar metallic particles. *Proc. Lunar Sci. Conf. 2nd*, pp. 1187–1208.
- Wänke H., Baddenhausen H., Balacescu A., Teschke F., Spettel B., Dreibus G., Palme H., Quijano-Rico M., Kruse H., Wlotzka F., and Begemann F. (1972) Multielement analyses of lunar samples and some implications of the results. *Proc. Lunar Sci. Conf. 3rd*, pp. 1251–1268.
- Wänke H., Baddenhausen H., Dreibus G., Jagowitz E., Kruse H., Palme H., Spettel B., and Teschke F. (1973) Multielement analyses of Apollo 15, 16, and 17 samples and the bulk composition of the Moon. *Proc. Lunar Sci. Conf. 4th*, pp. 1461–1481.
- Wänke H., Palme H., Baddenhausen H., Dreibus G., Jagoutz E., Kruse H., Spettel B., Teschke F., and Thacker R. (1974) Chemistry of Apollo 16 and 17 samples: Bulk composition, late stage accumulation and early differentiation of the Moon. *Proc. Lunar Sci. Conf. 5th*, pp. 1307–1335.
- Wänke H., Palme H., Baddenhausen H., Dreibus G., Jagoutz E., Kruse H., Palme C., Spettel B., Teshke F., and Thacker R. (1975) New data on the chemistry of lunar samples: Primary matter in the lunar highlands and the bulk composition of the Moon. *Proc. Lunar Sci. Conf. 6th*, pp. 1313–1340.
- Wänke H., Palme H., Kruse H., Baddenhausen H., Cendales M., Dreibus G., Hofmeister H., Jagoutz E., Palme C., Spettel B., and Thacker R. (1976) Chemistry of lunar highland rocks: A refined evaluation of the composition of the primary matter. *Proc. Lunar Sci. Conf. 7th*, pp. 3479–3499.
- Wänke H., Baddenhausen H., Blum K., Cendales M., Dreibus Hofmeister H., Kruse H., Jagoutz E., Palme C., Spettel B., Thacker R., and Vilček E. (1977) On the chemistry of lunar samples and achondrites. Primary matter in the lunar highlands: A re-evaluation. *Proc. Lunar Sci. Conf. 8th*, pp. 2191–2213.
- Wänke H., Dreibus G., and Palme H. (1978) Primary matter in the lunar highlands: The case of siderophile elements. *Proc. Lunar Planet. Sci. Conf. 9th*, pp. 83–110.
- Warhaut M., Kiko J., and Kirsten T. (1979) Microdistribution patterns of implanted rare gases in a large number of individual lunar soil particles. *Proc. Lunar Planet. Sci. Conf. 10th*, pp. 1531–1546.
- Warner J. L. (1970) *Apollo 12 Lunar Sample Information*. NASA TR-R-353. 391 pp.
- Warner J. L. (1971) Lunar crystalline rocks: Petrology and geology. *Proc. Lunar Sci. Conf. 2nd*, pp. 469–480.
- Warner J. L. (1972) Metamorphism of Apollo 14 breccias. *Proc. Lunar Sci. Conf. 3rd*, pp. 623–643.
- Warner J. L., Simonds C. H., and Phinney W. C. (1973) Apollo 16 rocks: Classification and petrogenetic model. *Proc. Lunar Sci. Conf. 4th*, pp. 481–504.
- Warner J. L., Simonds C. H., and Phinney W. C. (1976a) Genetic distinction between anorthosites and Mg-rich plutonic rocks: New data from 76255 (abstract). In *Lunar Science VII*, pp. 915–917. The Lunar Science Institute, Houston.
- Warner J. L., Simonds C. H., and Phinney W. C. (1976b) Apollo 17, Station 6 boulder sample 76255: Absolute petrology of breccia matrix and igneous clasts. *Proc. Lunar Sci. Conf. 7th*, pp. 2233–2250.
- Warner J. L., Phinney W. C., Bickel C. E., and Simonds C. H. (1977) Feldspathic granulitic impactites and pre-final bombardment lunar evolution. *Proc. Lunar Sci. Conf. 8th*, pp. 2051–2066.
- Warner R. D., Planner H. N., Keil K., Murali A. V., Ma M.-S., Schmitt R. A., Ehmman W. D., James W. D. Jr., Clayton R. N., and Mayeda T. K. (1976a) Consortium investigation of breccia 67435. *Proc. Lunar Sci. Conf. 7th*, pp. 2379–2402.
- Warner R. D., Barkley J. L., Manaker W. L., Warren R. G., and Keil K. (1976b) *Electron Microprobe Analyses of Spinel, Fe Oxides, and Metal from Apollo 17 Rake Sample Mare Basalts*. Inst. of Meteoritics Spec. Publ. 16, Univ. of New Mexico, Albuquerque. 114 pp.
- Warner R. D., Keil K., Nehru C. E., and Taylor G. J. (1976c) *Catalogue of Apollo 16 Rake Samples from the LM area and Station 5*. Inst. of Meteoritics Spec. Publ. 13, Univ. of New Mexico, Albuquerque. 87 pp.
- Warner R. D., Keil K., Nehru C. E., and Taylor G. J. (1978a) *Catalogue of Apollo 17 Rake Samples from Stations 1A, 2, 7 and 8*. Inst. of Meteoritics Spec. Publ. 18, Univ. of New Mexico, Albuquerque. 88 pp.
- Warner R. D., Nehru C. E., and Keil K. (1978b) Opaque oxide mineral crystallization in lunar high-titanium mare basalts. *Am. Mineral.*, 63, 1209–1224.
- Warner R. D., Taylor G. J., Conrad G. H., Northrop H. R., Barker S., and Keil K. (1979a) Apollo 17 high-Ti mare basalts: New bulk compositional data, magma types, and petrogenesis. *Proc. Lunar Planet. Sci. Conf. 10th*, pp. 225–247.

- Warner R. D., Taylor G. J., Wentworth S. J., Huss G. R., Mansker W. L., Planner H. N., Sayeed U. A., and Keil K. (1979b) *Electron Microprobe Analyses of Glasses from Apollo 17 Rake Sample Breccias and Apollo 17 Drill Core*. Inst. of Meteoritics Spec. Publ. 20, Univ. of New Mexico, Albuquerque. 20 pp.
- Warren P. H. (1985) The magma ocean concept and lunar evolution. *Annu. Rev. Earth Planet. Sci.*, 13, 201–240.
- Warren P. H. (1986) Anorthosite assimilation and the origin of the Mg/Fe-related bimodality of pristine Moon rocks: Support for the magmasphere hypothesis. *Proc. Lunar Planet. Sci. Conf. 16th*, in *J. Geophys. Res.*, 91, D331–D343.
- Warren P. H. and Jerde E. (1987) Composition and origin of Nuevo Laredo Trend eucrites. *Geochim. Cosmochim. Acta*, 51, 713–725.
- Warren P. H. and Kallemeyn G. W. (1984) Pristine rocks (8th foray): “Plagiophile” element ratios, crustal genesis, and the bulk composition of the moon. *Proc. Lunar Planet. Sci. Conf. 15th*, in *J. Geophys. Res.*, 89, C16–C24.
- Warren P. H. and Kallemeyn G. (1986) Geochemistry of lunar meteorite Yamato-791197: Comparison with ALHA81005 and other lunar samples. *Proceedings of the Tenth Symposium on Antarctic Meteorites*, pp. 3–16. Natl. Inst. for Polar Res., Tokyo.
- Warren P. H. and Kallemeyn G. W. (1987) Major elements and trace siderophile elements in four lunar meteorites. *Proceedings of the Eleventh Symposium on Antarctic Meteorites*, pp. 1–20. Natl. Inst. for Polar Res., Tokyo.
- Warren P. H. and Taylor G. J. (1981) Geochemical constraints on lateral transport during basin formation (abstract). In *Workshop on Apollo 16* (O. B. James and F. Hörz, eds.), pp. 147–149. LPI Tech. Rpt. 81–01, Lunar and Planetary Institute, Houston.
- Warren P. H. and Wasson J. T. (1977) Pristine nonmare rocks and the nature of the lunar crust. *Proc. Lunar Sci. Conf. 8th*, pp. 2215–2235.
- Warren P. H. and Wasson J. T. (1978) Compositional-petrographic investigation of pristine nonmare rocks. *Proc. Lunar Planet. Sci. Conf. 9th*, pp. 185–217.
- Warren P. H. and Wasson J. T. (1979a) The origin of KREEP. *Rev. Geophys. Space Phys.*, 17, 73–88.
- Warren P. H. and Wasson J. T. (1979b) The compositional-petrographic search for pristine nonmare rocks: Third foray. *Proc. Lunar Planet. Sci. Conf. 10th*, pp. 583–610.
- Warren P. H. and Wasson J. T. (1980) Further foraging for pristine nonmare rocks: Correlations between geochemistry and longitude. *Proc. Lunar Planet. Sci. Conf. 11th*, pp. 431–470.
- Warren P. H., Afiatalab F., and Wasson J. T. (1978) Investigation of unusual KREEPy samples: Pristine rock 15386, Cone Crater soil fragments 14143, and 12023, a typical Apollo-12 soil. *Proc. Lunar Planet. Sci. Conf. 9th*, pp. 653–660.
- Warren P. H., Taylor G. J., Keil K., Marshall C., and Wasson J. T. (1981) Foraging westward for pristine nonmare rocks: Complications for petrogenetic models. *Proc. Lunar Planet. Sci. 12B*, pp. 21–40.
- Warren P. H., Taylor G. J., Keil K., Kallemeyn G. W., Rosener P. S., and Wasson J. T. (1983a) Sixth foray for pristine nonmare rocks and an assessment of the diversity of lunar anorthosites. *Proc. Lunar Planet. Sci. Conf. 13th*, in *J. Geophys. Res.*, 88, A615–A630.
- Warren P. H., Taylor G. J., Keil K., Shirley D. N., and Wasson J. T. (1983b) Petrology and chemistry of two “large” granite clasts from the Moon. *Earth Planet. Sci. Lett.*, 64, 175–185.
- Warren P. H., Taylor G. J., Keil K., Kallemeyn G. W., Shirley D. N., and Wasson J. T. (1983c) Seventh foray: Whitlockite-rich lithologies, a diopside-bearing troctolitic anorthosite, ferroan anorthosites, and KREEP. *Proc. Lunar Planet. Sci. Conf. 14th*, in *J. Geophys. Res.*, 88, B151–B164.
- Warren P. H., Taylor G. J., and Keil K. (1983d) Regolith breccia Allan Hills A81005: Evidence of lunar origin, and petrography of pristine and nonpristine clasts. *Geophys. Res. Lett.*, 10, 779–782.
- Warren P. H., Shirley D. N., and Kallemeyn G. W. (1986) A potpourri of pristine Moon rocks, including a VHK mare basalt and a unique, augite-rich Apollo 17 anorthosite. *Proc. Lunar Planet. Sci. Conf. 16th*, in *J. Geophys. Res.*, 91, D319–D330.
- Warren P. H., Jerde E., and Kallemeyn G. W. (1987) Pristine moon rocks: A “large” felsite and a metal-rich ferroan anorthosite. *Proc. Lunar Planet. Sci. Conf. 17th*, in *J. Geophys. Res.*, 92, E303–E313.
- Warren P. H., Jerde E. A., and Kallemeyn G. W. (1989) Lunar meteorites: Siderophile element contents, and implications for the composition and origin of the Moon. *Earth Planet. Sci. Lett.*, 91, 245–260.
- Wasserburg G. J. and Papanastassiou D. A. (1971) Age of Apollo 15 mare basalt: Lunar crust and mantle evolution. *Earth Planet. Sci. Lett.*, 13, 97–104.
- Wasserburg G. J., Papanastassiou D. A., Tera F., and Huneke J. C. (1977) Outline of a lunar chronology. *Philos. Trans. R. Soc. London*, A285, 7–22.
- Wasson J. T. (1985) *Meteorites: Their Record of Early Solar-System History*. Freeman, New York. 267 pp.
- Wasson J. T. and Baedeker P. A. (1970) Ga, Ge, In, Ir and Au in lunar, terrestrial and meteoritic basalts. *Proc. Apollo 11 Lunar Sci. Conf.*, pp. 1741–1750.
- Wasson J. T., Chou C.-L., Bild R. W., and Baedeker P. A. (1973) Extralunar materials in Cone-Crater soil 14141. *Geochim. Cosmochim. Acta*, 37, 2349–2353.
- Wasson J. T., Chou C.-L., Robinson K. L., and Baedeker P. A. (1975a) Siderophiles and volatiles in Apollo-16 rocks and soils. *Geochim. Cosmochim. Acta*, 39, 1475–1485.
- Wasson J. T., Boynton W. V., Chou C.-L., and Baedeker P. A. (1975b) Compositional evidence regarding the influx of interplanetary materials onto the lunar surface. *The Moon*, 13, 121–141.
- Wasson J. T., Boynton W. V., Kallemeyn G. W., Sundberg L. L., and Wai C. M. (1976) Volatile compounds released during lunar lava fountaining. *Proc. Lunar Sci. Conf. 7th*, pp. 1583–1595.
- Wasson J. T., Warren P. H., Kallemeyn G. W., McEwing C. E., Mittlefehldt D. W., and Boynton W. V. (1977) SCCR, a

- major component of highlands rocks. *Proc. Lunar Sci. Conf. 8th*, pp. 2237–2252.
- Watkins J. S. and Kovach R. L. (1973) Seismic investigation of the lunar regolith. *Proc. Lunar Sci. Conf. 4th*, pp. 2561–2574.
- Watson E. B. and Green T. H. (1981) Apatite/liquid partition coefficients for the rare earth elements and strontium. *Earth Planet. Sci. Lett.*, 56, 405–421.
- Wechsler A. E. and Glaser P. E. (1965) Pressure effects on postulated lunar materials. *Icarus*, 4, 335–352.
- Wechsler B. A. and Prewitt C. T. (1977) Structural chemistry of armalcolite and ilmenite at high temperatures (abstract). In *Lunar Science VIII*, pp. 1000–1001. The Lunar Science Institute, Houston.
- Wechsler B. A., Prewitt C. T., and Papike J. J. (1976) Chemistry and structure of lunar and synthetic armalcolite. *Earth Planet. Sci. Lett.*, 29, 91–103.
- Weigand P. W. (1972) Petrology of pyroxene vitrophyre 15597. In *The Apollo 15 Lunar Samples* (J. W. Chamberlain and C. Watkins, eds.), pp. 187–188. The Lunar Science Institute, Houston.
- Weigand P. W. and Hollister L. S. (1973) Basaltic vitrophyre 15597: An undifferentiated melt sample. *Earth Planet. Sci. Lett.*, 19, 61–74.
- Weill D. F. and McKay G. A. (1975) The partitioning of Mg, Fe, Sr, Ce, Sm, Eu and Yb in lunar igneous systems and a possible origin of KREEP by equilibrium partial melting. *Proc. Lunar Sci. Conf. 6th*, pp. 1143–1158.
- Weill D. F., Grieve R. A., McCallum I. S., and Bottinga Y. (1971) Mineralogy-petrology of lunar samples: Micro-probe studies of samples 12021 and 12022; Viscosity of melts of selected lunar compositions. *Proc. Lunar Sci. Conf. 2nd*, pp. 413–430.
- Weismann P. R. (1982) Terrestrial impact rates for long and short-period comets. In *Geological Implications of Impacts of Large Asteroids and Comets on the Earth* (L. T. Silver and P. H. Schultz, eds.), pp. 15–24. Geol. Soc. Am. Spec. Pap. 190.
- Wenk H. R. and Wilde W. R. (1973) Chemical anomalies of lunar plagioclase, described by substitution vectors and their relation to optical and structural properties. *Contrib. Mineral. Petrol.*, 41, 89–104.
- Wentworth S., Taylor G. J., Warner R. D., Keil K., Ma M.-S., and Schmitt R. A. (1979) The unique nature of Apollo 17 VLT mare basalts. *Proc. Lunar Planet. Sci. Conf. 10th*, pp. 207–232.
- Wetherill G. W. (1977) Evolution of the Earth's planetesimal swarm subsequent to the formation of the Earth and Moon. *Proc. Lunar Sci. Conf. 8th*, pp. 1–16.
- Wetherill G. W. (1981) Nature and origin of basin-forming projectiles. In *Multi-Ring Basins*, *Proc. Lunar Planet. Sci. 12A* (P. H. Schultz and R. B. Merrill, eds.), pp. 1–18. Pergamon, New York.
- Whipple E. C. (1981) Potentials of surfaces in space. *Rep. Progr. Phys.*, 44, 1197–1250.
- Whipple F. L. (1963) On meteoroids and penetration. *Geophys. Res.*, 68, 4929–4939.
- Whitaker E. A. (1972) Lunar color boundaries and their relationship to topographic features: A preliminary survey. *The Moon*, 4, 348–355.
- White D. C. and Hirsch P. (1985) Microbial extraction of hydrogen from lunar dust. In *Lunar Bases and Space Activities of the 21st Century* (W. W. Mendell, ed.), pp. 591–602. Lunar and Planetary Institute, Houston.
- Wieler R., Etique P., Signer P., and Poupeau G. (1980) Record of the solar corpuscular radiation in minerals from lunar soils: A comparative study in noble gases and tracks. *Proc. Lunar Planet. Sci. Conf. 11th*, pp. 1369–1393.
- Wiesmann H. and Hubbard N. J. (1975) *A Compilation of the Lunar Sample Data Generated by the Gast Nyquist and Hubbard Lunar Sample PI Ships*. NASA Johnson Space Center, Houston. 50 pp.
- Willey R. L. (1978) The Moon in heiligenschein. *Science*, 200, 1265–1267.
- Willey R. L. and Pohn H. A. (1964) Detailed photoelectric photometry of the Moon. *Astron. J.*, 69, 619–634.
- Willey R. L. and Pohn H. A. (1969) The normal albedo of the Apollo 11 landing site and intrinsic dispersion on the lunar heiligenschein. *Astrophys. J.*, 158, L129–L130.
- Wilhelms D. E. (1970) *Summary of Lunar Stratigraphy—Telescopic Observations*. U.S. Geol. Surv. Prof. Pap. 599–F. 47 pp.
- Wilhelms D. E. (1972) *Geologic Mapping of the Second Planet*. U.S. Geol. Surv. Open File Rept., Astrogeologic Studies 55. 36 pp.
- Wilhelms D. E. (1984) The Moon. In *The Geology of the Terrestrial Planets* (M. Carr et al., eds.), pp. 107–205. NASA SP-469.
- Wilhelms D. E. (1987) *The Geologic History of the Moon*. U.S. Geol. Surv. Prof. Pap. 1348. 302 pp.
- Wilhelms D. E. and Davis D. E. (1971) Two former faces of the Moon. *Icarus*, 15, 368–372.
- Wilhelms D. E. and El Baz F. (1977) Geologic map of the east side of the Moon. *U.S. Geol. Surv. Map I-948*, scale 1:5,000,000.
- Wilhelms D. E. and McCauley J. F. (1971) Geologic map of the nearside of the Moon. *U.S. Geol. Surv. Map I-703*.
- Wilhelms D. E., Oberbeck U. R., and Aggarwal H. R. (1978) Size-frequency distributions of primary and secondary lunar impact craters. *Proc. Lunar Planet. Sci. Conf. 9th*, pp. 3735–3762.
- Wilhelms D. E., Howard K. A., and Wilshire H. G. (1979) Geologic map of the south side of the Moon. *U.S. Geol. Surv. Map I-1162*.
- Wilkening L., ed. (1982) *Comets*. Univ. of Arizona, Tucson. 76 pp.
- Williams G. J. (1974) Electrostatic migration, surface exposure and layering. In *Lunar Interactions* (D. R. Criswell and J. R. Freeman, eds.), pp. 55–56. The Lunar Science Institute, Houston.
- Williams K. L. and Taylor L. A. (1974) Optical properties and chemical compositions of Apollo 17 armalcolites. *Geology*, 2, 5–8.
- Williams R. J. (1985) Oxygen extraction from lunar materials: An experimental test of an ilmenite reduction

- process. In *Lunar Bases and Space Activities of the 21st Century* (W. W. Mendell, ed.), pp. 551–558. Lunar and Planetary Institute, Houston.
- Williams R. J. and Erstfeld T. E. (1979) *High Temperature Electrolyte Recovery of Oxygen from Gaseous Effluents from the Carbo-Chlorination of Lunar Anorthite and the Hydrogenation of Ilmenite*. NASA TM-58214. 51 pp.
- Williams R. J. and Jadwick J. J. (1980) *Handbook of Lunar Materials*. NASA RP-1057. 120 pp.
- Williams R. J., McKay D. S., Giles D., and Bunch T. E. (1979) Mining and beneficiation of lunar ores. In *Space Resources and Space Settlements*, pp. 275–288. NASA SP-428.
- Willis J. P., Ahrens L. H., Danchin R. V., Erlank A. J., Gurney J. J., Hofmeyr P. K., McCarthy T. S., and Orren M. J. (1971) Some interelement relationships between lunar rocks and fines and stony meteorites. *Proc. Lunar Sci. Conf. 2nd*, pp. 1123–1138.
- Willis J. P., Erlank A. J., Gurney J. J., Theil R. H., and Ahrens L. H. (1972) Major, minor, and trace element data for some Apollo 11, 12, 14, and 15 samples. *Proc. Lunar Sci. Conf. 3rd*, pp. 1269–1273.
- Wilshire H. G. and Howard K. A. (1968) Structural pattern in central uplifts of cryptoexplosion structures as typified by Sierra Madera. *Science*, 162, 258–261.
- Wilshire H. G. and Jackson E. D. (1972) *Petrology and Stratigraphy of the Fra Mauro Formation at the Apollo 14 Site*. U.S. Geol. Surv. Prof. Pap. 785. 26 pp.
- Winter D. F. (1970) The infrared Moon: Data, interpretations, and implications. *Radio Sci.*, 5, 229–240.
- Winzer S. R., Nava D. F., Schumann S., Kouns C. W., Lum R. K. L., and Philpotts J. (1974) Major, minor and trace element abundances in samples from the Apollo 17 Station 7 boulder: Implications for the origin of early lunar crustal rocks. *Earth Planet. Sci. Lett.*, 23, 439–444.
- Wise D. U. and Yates M. T. (1970) Mascons as structural relief on a lunar “moho.” *J. Geophys. Res.*, 75, 261–268.
- Wiskerchen M. J. and Sonett C. P. (1977) A lunar metal core? *Proc. Lunar Sci. Conf. 8th*, pp. 515–535.
- Wittenberg L. J., Santarius J. F., and Kulcinski G. L. (1987) Lunar source of ^3He for commercial fusion power. *Fusion Technol.*, 10, 167–178.
- Wlotzka F., Jagouz E., Spettel B., Baddenhausen H., Balacescu A., and Wänke H. (1972) On lunar metallic particles and their contribution to the trace element content of Apollo 14 and 15 soils. *Proc. Lunar Sci. Conf. 3rd*, pp. 1077–1084.
- Wlotzka F., Spettel B., and Wänke H. (1973) On the composition of metal from Apollo 16 fines and the meteoritic component. *Proc. Lunar Sci. Conf. 4th*, pp. 1483–1491.
- Wolf R. and Anders E. (1980) Moon and Earth: Compositional differences inferred from siderophiles, volatiles, and alkalis in basalts. *Geochim. Cosmochim. Acta*, 44, 2111–2124.
- Wolf R., Woodrow A., and Anders E. (1979) Siderophile and volatile elements in the Earth and Moon: Similar or not (abstract). In *Lunar and Planetary Science X*, pp. 1361–1363. Lunar and Planetary Institute, Houston.
- Wolfe E. W., Bailey N. G., Lucchitta B. K., Muehlberger W. R., Scott D. H., Sutton R. L., and Wilshire H. G. (1981) *The Geologic Investigation of the Taurus-Littrow Valley: Apollo 11 Landing Site*. U.S. Geol. Surv. Prof. Pap. 1080. 280 pp.
- Wolfe S. H. (1971) Potassium-argon ages of the Manicouagan-Mushalagan structure, Quebec, Canada. *J. Geophys. Res.*, 76, 5424–5436.
- Wood C. A. and Andersson L. (1978) *The Lunar and Planetary Laboratory Catalog of Lunar Craters, Pt. 1: Nearside*. Unpublished manuscript.
- Wood J. A., Dickey J. S., Marvin U. B., and Powell B. N. (1970) Lunar anorthosites and a geophysical model of the Moon. *Proc. Apollo 11 Lunar Sci. Conf.*, pp. 965–988.
- Wood R. W. (1912) Selective absorption of light on the Moon's surface and lunar petrography. *Astrophys. J.*, 36, 74.
- Woodcock M. R. and Pillinger C. T. (1978) Major element chemistry of agglutinate size fractions. *Proc. Lunar Planet. Sci. Conf. 9th*, pp. 2195–2214.
- Woolum D. S., Burnett D. S., and Bauman C. A. (1973) Lunar neutron probe experiment. In *Apollo 17 Preliminary Science Report*, pp. 18–1 to 18–12. NASA SP-330.
- Wright D. A. (1971) Electrical conductivity of lunar rock. *Nature*, 231, 169–170.
- Wright D. L., Olhoeft G. R., and Watts R. D. (1984) Ground-penetrating radar studies on Cape Cod. In *Surface and Borehole Geophysical Methods in Ground Water Investigations* (D. M. Nielsen, ed.), pp. 666–680. National Water Well Association, Worthington, Ohio.
- Wright R. A., Cocks F. H., Vaniman D. T., Blake R. D., and Meek T. T. (1986) Fusing of lunar materials with microwave energy; Pt. I. Studies of doping media (abstract). In *Lunar and Planetary Science XVII*, pp. 958–959. Lunar and Planetary Institute, Houston.
- Wszolek P. C., Simoneit B. R., and Burlingame A. L. (1973) Studies of magnetic fines and volatile-rich soils: Possible meteoritic and volcanic contributions to lunar carbon and light element chemistry. *Proc. Lunar Sci. Conf. 4th*, pp. 1693–1706.
- Yaniv A. and Heymann D. (1972) Atmospheric Ar⁴⁰ in lunar fines. *Proc. Lunar Sci. Conf. 3rd*, pp. 1967–1980.
- York D., Kenyon W. J., and Doyle R. J. (1972) Ar-Ar ages of Apollo 14 and 15 samples (abstract). In *Lunar Science III*, pp. 822–824. The Lunar Science Institute, Houston.
- Young J. W., Mattingly T. K., and Duke C. M. (1972) Crew observations. In *Apollo 16 Preliminary Science Report*, pp. 5–1 to 5–6. NASA SP-315.
- Young R. A. (1976) The morphological evolution of mare-highland contacts: A potential measure of relative mare surface age. *Proc. Lunar Sci. Conf. 7th*, pp. 2801–2816.
- Yuhas D. and Walker R. (1973) Long term behavior of VH cosmic rays as observed in lunar rocks. *Papers Presented to the 15th Intl. Cosmic Ray Conf.*, 2, 1116–1121.
- Zellner B., Leake M., Leberte T., Duseaux M., and Dollfus A. (1977) The asteroid albedo scale. I. Laboratory polarimetry of meteorites. *Proc. Lunar Sci. Conf. 8th*, pp. 1091–1110.

- Zinner E. (1980) On the constancy of solar particle fluxes from track, thermoluminescence and solar wind measurements in lunar rocks. In *The Ancient Sun: Fossil Record in the Earth, Moon and Meteorites* (R. O. Pepin, J. A. Eddy, and R. B. Merrill, eds.), pp. 201–226. Pergamon, New York.
- Zisk S. H. (1970) *Radar Atlas of the Moon*. Lincoln Laboratory, Lexington. 4 pp., 180 p1.
- Zisk S. H. (1972a) A new, Earth-based radar technique for the measurement of lunar topography. *The Moon*, 4, 296–306.
- Zisk S. H. (1972b) Lunar topography—first radar interferometer measurements of the Alphonsus-Ptolemaeus-Arzachel region. *Science*, 178, 977–980.
- Zisk S. H. (1978) Mare Crisium area topography: A comparison of Earth-based radar and Apollo mapping camera results. In *Mare Crisium: The View from Luna 24* (R. B. Merrill and J. J. Papike, eds.), pp. 75–80. Pergamon, New York.
- Zisk S. H., Pettengill G. H., and Catuna G. W. (1974) High-resolution radar maps of the lunar surface at 3.8-cm wavelength. *The Moon*, 10, 17–50.
- Zisk S. H., Hodges C. A., Moore H. J., Shorthill R. W., Thompson T. W., Whitaker E. A., and Wilhelms D. E. (1977) The Aristarchus-Harbinger region of the Moon: Surface geology and history from recent remote-sensing observations. *The Moon*, 17, 59–99.
- Zito R. R. (1989) A new mechanism for lunar transient phenomena. *Icarus*, 82, 419–422.
- Zonnenshtral G. A. and Pel'dman Iu. I. (1970) Specific effective scattering area of the lunar surface determined from measurements by the Luna-9 and Luna-13 automatic stations. *Cosmic. Res.*, 8, 541–546.
- Zook H. A. (1975) The state of meteoritic material on the Moon. *Proc. Lunar Sci. Conf. 6th*, pp. 1653–1672.
- Zook H. A. (1980) On lunar evidence for a possible large increase in solar flare activity 2×10^4 years ago. In *The Ancient Sun: Fossil Record in the Earth, Moon and Meteorites* (R. O. Pepin, J. A. Eddy, and R. B. Merrill, eds.), pp. 245–266. Pergamon, New York.
- Zook H. A. and Berg O. E. (1975) A source for hyperbolic cosmic dust particles. *Planet. Space Sci.*, 23, 183–203.

SAMPLE INDEX*

10002	346,478	12018	142, 146, 170, 172, 175	14082	244
10003	190, 196, 204, 261, 262, 613	12020	159	14083	244,396,397
10004	327, 482, 572	12021	159, 163, 175, 179, 180	14141	478
10005	327, 482, 487, 572	12022	166, 172, 175, 177, 199, 204, 581	14148	312,346
10009	613	12023	346	14149	313,346
10017	159, 169, 172, 196, 581	12024	320	14156	312, 346
10018	613	12025	322, 327, 572	14163	291, 292, 300, 344, 347, 349, 404, 414, 478, 479, 482, 497, 545, 546, 569, 570, 571, 581
10020	166, 169, 175, 206, 482, 581	12026	322, 327, 572	14168	159
10021	177	12027	322, 327, 572	14191	177
10022	159, 163, 166, 581 10024 159, 163	12028	322, 327, 423, 430, 436, 572	14210	327,572
10044	166, 196, 613	12029	482, 497, 502, 575, 577, 578, 580	14211	327,572
10045	159, 163, 166, 169, 613	12030	320, 346	14220	327,572
10046	581	12032	169, 346, 616	14230	327, 572
10047	170	12033	132, 165, 168, 230, 276, 291, 292, 300, 303, 320, 346, 347, 349, 571, 581	14257	172
10048	532, 581			14258	172
10049	190, 204, 261, 262, 613	12034	169, 353	14259	193, 308, 479, 482, 497, 569, 570, 571
10050	163	12035	166, 175, 199	14276	161, 164, 180, 253, 254, 282
10057	172, 193, 581	12036	178	14298	312
10058	159, 169, 172, 175, 178, 180	12037	316, 320, 346	14301	582
10059	177, 581	12038	178, 193	14303	132, 217, 219, 220, 221, 269, 270
10062	196	12039	169,170	14304	190, 215, 230, 396, 397
10065	480, 482, 581, 585	12040	159	14305	159, 163, 166, 169, 181, 190, 191, 193, 225, 230, 231, 261, 263
10068	177	12041	346	14310	87, 150, 161, 164, 167,172, 175, 178, 181, 194, 213, 214, 234, 242, 243, 253, 254, 282, 283, 545, 546, 550, 551, 582, 619
10071	177,204	12042	320, 346	14313	385
10072	172, 206, 613	12044	320, 346	14318	216, 234, 257, 582, 619
10084	177, 180, 291, 292, 296, 297, 304, 308, 320, 344, 347, 349, 404, 413, 482, 497, 571, 578, 581	12051	180,261,262	14321	132, 134, 169, 178, 181, 190, 191, 194, 225, 229, 230, 232, 261, 263, 276, 313, 394, 395, 396, 397, 399, 482, 582, 619
10085	74, 169, 172, 180, 181	12052	159, 166, 175, 193	14422	312
		12053	194		
		12055	616		
		12056	199		
		12057	479, 480, 482, 569		
		12063	159, 163, 166, 172, 175, 179, 193, 210, 581	15001	323, 327, 329, 337, 338, 573, 582, 587
12001	291, 292, 300, 320, 344, 346, 347, 349, 404, 414, 478, 497, 502, 504, 505, 570, 575, 577, 579	12064	191,261,262	15002	323, 327, 329, 337, 338, 573, 587
12002	172, 175, 191, 193, 203, 204, 207, 208, 261, 262, 482, 502, 532, 549, 550, 581	12065	159, 169, 172, 175, 581	15003	323, 327, 329, 337, 338, 480, 573, 582, 585, 587
12003	320,344	12070	169, 178, 193, 308, 316, 320, 346, 571, 581	15004	323, 327, 329, 337, 338, 573, 587
12004	179, 180, 199	12073	222, 230, 231, 276	15005	323, 327, 329, 337, 338, 573, 587
12005	199, 616	14003	346, 478, 571, 581		
12008	616	14047	230,231,276		
12009	166, 175, 194, 199, 204, 208	14053	147, 151, 159, 163, 172, 175, 195, 261, 263, 619		
12011	616	14055	619		
12012	616	14063	234, 242, 244, 277, 619		
12013	132, 134, 135, 169, 181, 232, 368, 381, 610, 616	14064	244, 278, 619		
12015	616	14066	243, 250, 280, 281		
		14068	243, 252, 280, 281		
		14072	147, 151, 175, 207		
		14073	150, 175		

* Lunar meteorites are listed in the subject index.

15006	323, 327, 329, 337, 338, 432, 573, 587	15403	346	60002	314, 318, 327, 573, 583, 587
15007	216, 327, 409, 572	15405	134, 217, 218, 219, 220, 221, 232, 269, 270, 368, 391, 393, 409, 425, 622	60003	327, 573, 587
15008	327, 572			60004	327, 573, 587
15009	327, 572	15410	346	60005	327, 573, 583, 587
15010	323, 327, 498, 572	15415	162, 165, 221, 222, 224, 228, 272, 273, 370, 393, 409, 582, 622	60006	327, 573, 587
15011	323, 327, 498, 572			60007	327, 573, 587
15012	346			60009	318, 323, 324, 327, 329, 331, 332, 337, 339, 341, 343, 572
15013	346	15418	243, 283, 284, 532		
15015	482	15423	239	60010	318, 323, 324, 327, 329, 331, 332, 337, 339, 341, 343, 572
15016	159, 163, 201, 204	15426	190, 203, 204, 261, 263, 428, 622		
15017	242, 278, 279, 280			60013	327, 572
15020	346	15431	320	60014	327, 572
15021	313, 82	15434	161, 164, 218	60015	162, 165, 213, 224, 248, 272, 273, 317, 583
15030	346	15445	178, 280, 281	60016	153, 257
15031	497, 570	15455	225, 229, 234, 243, 252, 274, 275, 345, 622	60017	153, 583
15040	346			60018	248
15041	320, 535, 570, 582	15459	582	60019	234, 248
15058	159, 194, 197, 532	15470	346	60025	162, 165, 221, 224, 225, 242, 248, 583, 625
15065	207, 582	15471	320	60035	248, 394, 395
15070	346	15476	197	60050	346
15071	180, 320	15486	197	60066	248
15076	198	15495	193	60095	74, 234, 237, 242, 248, 278, 280
15080	346, 443	15498	582		
15081	582	15499	159, 204, 210	60115	234
15085	175, 198	15500	346	60135	221, 248
15090	346	15501	320, 570	60215	242, 248, 394, 395
15091	308, 320	15530	346	60315	153, 161, 167, 243, 250, 252, 280, 281, 625
15100	346, 413, 414	15531	320, 570	60335	153, 161, 164, 167, 177, 180, 243, 250, 280, 281, 345
15101	320, 482, 571	15536	408	60500	346
15102	177	15545	191, 203, 261, 262	60501	583
15205	247, 317, 353	15555	159, 166, 172, 175, 532, 582, 622	60527	248
15210	346	15595	194, 197, 622	60601	320
15211	320, 582	15596	197	60629	248
15220	478	15597	159, 175, 191, 197, 261, 262, 345, 582	60635	253, 254
15221	288, 291, 292, 320, 344, 346, 347, 349, 582			60639	248, 413, 462, 465
15230	346	15600	346, 348, 350	60657	248
15231	320, 570	15601	288, 293, 301, 302, 320, 345, 348, 350, 414, 479, 482, 497, 498, 499, 569, 570, 583	60665	248
15250	346			61015	234, 237, 240, 242, 248, 256
15251	313, 320	15684	74	61016	153, 162, 165, 180, 248, 583
15255	278, 279			61121	320
15261	180			61140	346
15270	346, 478			61141	20
15271	291, 292, 300, 320, 344, 347, 349	21000	291, 292, 348, 350	61156	220, 269, 270
15290	346	21013	191, 261, 263	61161	346
15299	234, 394, 395, 396, 397	22001	177, 291, 292, 348, 350	61180	346, 478
15300	346	22002	178	61195	248
15301	320, 531, 532, 545, 547, 548, 571, 582	22003	178	61220	346, 413, 478
15306	353	24077	318, 320, 326	61221	445, 446, 571
15308	622	24109	190, 261, 263, 320, 326	61224	226, 229, 274, 275
15363	224, 272, 273, 405, 408	24149	320, 326	61240	346
15382	216, 217, 218, 220, 269, 270, 622	24174	159, 163, 166, 190, 261, 263, 320, 326	61241	320, 571
15386	161, 164, 187, 191, 216, 217, 218, 220, 229, 269, 270, 622	24182	320, 326		
15400	346, 478	24210	320, 326		
15401	210, 211, 320, 571, 582	24999	291, 292, 348, 350		
		60001	327, 573, 587		

61500	346, 583	65035	248	67639	244
61501	320	65055	253	67645	244
61538	248	65056	248	67647	244
61576	248	65075	248	67649	244
62231	308, 320	65095	153, 248	67655	244
62235	161, 164, 167, 243, 250, 280, 281, 583	65315	74, 165, 224, 231, 248, 272, 393	67656	244
62236	221, 222, 224, 225, 272, 273	65325	248	67657	244
62237	168, 221, 222, 223, 224, 272, 273, 409	65366	248	67667	227, 229
62240	346, 583	65500	346, 413	67669	244
62241	583	65700	346	67695	248
62246	248	65701	320	67700	346
62255	234, 242, 248	65795	254	67706	244
62280	346, 478	65901	320	67707	244
62295	153, 164, 167, 180, 234, 240, 243, 253, 254, 281, 282, 283, 583	66031	320	67710	346
63320	346	66035	223, 224	67715	252
63321	571	66040	346	67747	253, 254
63335	153	66041	583	67749	216, 217
63340	346	66043	625	67768	244
63341	571	66055	583	67915	229, 274, 275, 394, 395, 396, 397
63355	153	66080	346, 413	67955	153, 234, 243, 255, 283, 284
63500	346, 398, 413	66081	583	67960	320
63501	534, 583	66095	150, 151, 153, 161, 164, 167, 179, 180, 238, 250, 279, 280, 281, 345, 429, 430, 431, 447, 625	67975	215, 230, 244, 248, 276
63549	161, 164	66156	177	68001	328, 572
63565	248	67015	153, 234, 241, 242, 277, 278, 625	68002	328, 572
63566	242, 248, 278, 279	67016	237, 238, 241, 242, 255, 277, 278	68035	248
63567	248	67025	248	68115	153, 180
63575	248	67095	248	68121	584
63576	248	67115	248, 277, 278	68415	74, 153, 164, 167, 180, 234, 237, 239, 242, 243, 253, 254, 282, 283, 532, 625
63588	244	67215	243, 283, 284	68416	153, 161, 167, 253
63595	244	67415	215, 243, 283, 284	68500	346, 478
64001	327, 329, 332, 333, 334, 572	67435	226, 228, 229, 243, 248, 274, 275, 394, 395, 396, 397	68515	248
64002	327, 329, 332, 333, 334, 572	67455	231, 234, 241, 242, 244, 257, 272, 273, 277, 278	68516	248
64420	346	67457	244	68519	248
64435	248	67460	346	68536	248
64453	317	67461	291, 292, 320, 344, 347, 350, 625	68815	234, 237, 238, 242, 246, 278, 532
64455	81, 82, 161, 164, 167, 242, 243, 248, 253, 278, 279, 280, 282, 283, 316, 317	67475	280, 281	68820	346
64475	234	67480	346	68841	179
64500	346, 478	67495	242, 244	69001	328, 572
64501	291, 292, 295, 300, 320, 344, 347, 349	67511	320	69920	346
64535	248	67517	244	69921	320
64567	251, 252, 625	67526	244	69935	153, 180
64568	251	67527	244	69940	346
64569	251	67528	244	69955	153
64800	346	67545	244	70001	328, 329, 332, 335, 336, 340, 341, 573, 587
64801	320	67549	244	70002	294, 325, 328, 329, 332, 336, 340, 341, 573, 587
64811	320	67559	161, 164, 167, 253, 254	70003	294, 328, 329, 332, 335, 340, 341, 573, 587
64815	251	67569	248	70004	294, 328, 329, 332, 335, 336, 340, 341, 573, 587
64816	251	67600	346	70005	294, 328, 329, 332, 335, 336, 340, 341, 573, 587
65015	153, 164, 167, 239, 242, 252, 281, 531, 583	67601	583, 584		
65016	248	67618	248		
		67635	168		

70006	294, 328, 329, 332, 335, 336, 340, 341, 573, 587	72441	290, 330, 567, 584	76241	318, 568
70007	166, 190, 200, 204, 261, 263, 294, 328, 329, 332, 335, 336, 340, 341, 396, 397, 573, 587	72460	346	76246	346
70008	159, 163, 166, 294, 328, 329, 332, 335, 336, 340, 341, 573, 587	72461	314, 398, 567	76255	165
70009	159, 200, 294, 325, 328, 329, 332, 335, 336, 340, 341, 344, 573, 587	72500	346, 478	76260	346
70011	346	72501	291, 292, 314, 347, 350, 567	76261	568
70012	328, 572	72701	320, 567	76280	346
70017	159, 177, 190, 204, 482	73001	328, 572	76281	568
70035	159, 177, 196	73002	328, 572	76315	252, 281, 584
70051	584	73120	346	76320	346
70135	372, 373, 390	73121	567	76321	443, 568
70160	346	73122	320	76500	346
70161	567	73131	320	76501	91, 292, 348, 350, 568, 584
70180	346, 478	73140	346	76535	162, 165, 168, 226, 228, 229, 274, 275, 409
70181	567	73141	567	77017	234, 237, 240, 243, 255, 283, 284
70215	166, 177, 204, 208, 261, 262, 482, 551, 552, 584	73151	320	77035	227, 482
70251	320	73155	87	77135	161, 164, 167, 237, 242, 250, 280, 281
70271	320	73210	628	77215	229, 274, 275
70311	320	73211	320	77511	320
71035	196	73215	232, 237, 239, 243, 250, 280, 281, 317	77530	346
71040	346	73217	134	77531	568
71041	567	73220	346	78121	320
71055	166, 317	73221	567	78155	234, 243, 283, 284
71060	346	73235	252	78220	346, 478
71061	289, 318, 330, 567	73240	478	78221	291, 292, 320, 348, 350, 477, 568
71131	320	73241	567, 584	78231	320
71151	320	73255	229, 628	78235	162, 165, 228
71500	346, 478	73261	306, 567	78236	229
71501	306, 307, 320, 567	73280	346	78238	162, 165
71535	395, 396	73281	567	78241	568
71569	206	74001	210, 211, 303, 325, 328, 343, 567, 572	78420	346
72131	320	74002	303, 325, 328, 343, 572	78421	306
72140	478	74111	320	78440	346
72141	306, 318, 567	74120	346	78441	320
72160	346	74121	568	78460	346
72161	320	74220	190, 194, 204, 206, 210, 211, 261, 262, 320, 398, 428, 434, 436, 478, 568, 571, 584, 628	78480	346
72221	320	74240	568	78481	320
72235	209	74241	177, 568, 584	78500	478
72241	320	74242	177	78501	568
72255	229	74260	568	78526	190, 191, 204, 261, 263
72261	320	74275	159, 204, 208	78598	395, 396, 397
72275	216, 217, 218, 220, 221, 242, 244, 269, 270, 277, 278, 409	75035	172, 193	79001	328, 572
72320	346	75055	190, 204	79002	328, 572
72321	567	75060	346	79121	320
72395	243, 280, 281, 482	75061	568, 584	79135	584
72415	162, 168, 225, 227, 229, 274, 275	75080	346	79155	74
72417	229, 395, 405, 406, 408, 409, 412	75081	177, 308, 318, 413, 568, 571, 584	79175	234
72431	320	75083	163	79215	234, 240, 243, 283, 284
72440	346	76001	328, 572	79220	346
		76015	234, 243, 280, 281, 317	79221	568
		76031	320	79240	346
		76055	252	79241	320
		76121	320	79261	568
		76131	320	79511	320
		76215	317		
		76221	320		

SUBJECT INDEX

- Accretion of the Moon
(chemistry) 419
- Aeronautical Chart and
Information Center
(ACIC) 60
- Age dating 134
 highland rocks 218, 219, 225, 228, 245, 250,
 253, 255, 256
 mare basalts 208, 209
 methods 134, 223
- Agglutinates 288, 296–299, 301, 339, 414
 and siderophile elements 414
 chemistry 299
 description 296
 F³ model 299
 genesis 298
 mineralogy 297
 native Fe in 154
 petrography 298
 physical properties 296
 solar-wind elements in 301
- Akaganeite 150
- Albedo 59, 558, 560, 561
 absorption coefficient 561
 Bond albedo 560
 geometrical albedo 560
 normal albedo 560
 scattering coefficient 561
 single scattering albedo 560
 spherical albedo 560
- Albite 127, 363, 368
- Aldrin, Edwin E., Jr. 27–30
- Alkali anorthosite 228, 381, 398, 399
 high strontium, gallium
 content 399
- Alkali gabbro 370
- Alkali gabbroonorite 230, 368
- Alkali norite 230
- Allan Hills 81005 9, 223, 224, 234
- Alpha particles 56
- Alphonsus Crater 102
- Altai Mountains 117
- Aluminum 363–372, 603
 as a resource 647
 mapping from orbit 603, Plate 10.4
- Ancient regolith 352
- Anorthite 127, 363
- Anorthosite 9, 19, 363, 405, 408, 409,
 453, 458
- Antimatter 47, 52
- Antimony 413
- Apatite 154, 181, 384, 391, 398, 434
 chemical composition 181
- Apennine Bench Formation 114, 622
- Apennine Front 37, 348, 353, 621
- Apennine Mountains 33, 564
- Apennine Scarp 620
- Aphelion 34
- Apogee 57
- Apollo 5, 8, 596–598, 602, 603, 605
- Apollo 11 30, 609, 611–613
 geology 613
 landing site 611, 612
- Apollo 12 610, 614–616
 geology 616
 landing site 614, 615
- Apollo 14 31, 610, 617–619
 geology 619
 landing site 617, 618
- Apollo 15 33, 36, 37, 337, 348, 620–
 622
 geology 622
 heat flow 36, 37
 landing site 620, 621
- Apollo 16 32, 341, 351, 623–625, 631
 geology 625
 landing site 623, 624
- Apollo 17 35, 37, 341, 348, 626–628,
 631
 geology 628
 heat flow 37
 landing site 626, 627
- Apollo command module
 experiments 596
- Apollo Lunar Module (LM) 22, 476
- Apollo Lunar Sample Return
 Containers (ALSRC) 22
- Apollo Lunar Sounder
 Experiment (ALSE) 564
- Apollo Self-Recording
 Penetrometer (SRP) 508, 512, 591
- Apollo Simple Penetrometer
 (ASP) 506
- Apollo sample summary 9
- Apollo samples 8, 21, 22
 bulk sample 22
 contingency sample 21
 cores 22
 documented sample 22
 rake sample 22
 selected sample 22
- Apollo subsatellite
 experiments 596
- Archimedes Crater 114
- Arecibo Observatory 606
- Argon 42, 437–443
- Aristarchus Crater 70, 565
- Aristarchus Plateau 101, 607
- Aristillus Crater 622
 ejecta at Apollo 15 622
- Armalcolite 137, 147, 148, 176
 chemical composition 148, 176
 crystal structure 147, 148
- Armstrong, Neil A. 475

- Astronauts 8, 27, 475
- Astronomy from the Moon 636
- Asuka 31 (unbrecciated cumulate) 9
- Atmosphere 28, 40–45, 439, 440, 445, 635
- ambient “pressure” 635
 - contamination 41
 - gas abundances 45
 - lunar paleoatmosphere 44
 - permanent 45
 - pollution 635
 - scale height 45
- Augite 126
- Autolycus Crater 622
- ejecta at Apollo 15 622
- Avalanches 34, 522
- Baby Ray Crater 624
- Baddeleyite 137, 149, 178
- chemical composition 178
- Basalt 9, 94, 183, 186–202, 205, 206
- aluminous low-Ti basalt 186, 188
 - chemical compositions 186, 187, 261–268
 - classification 186
 - comparison with other planetary basalts 192
 - cooling history 194
 - cooling rates 200, 201
 - crystallization experiments 198
 - experimental petrology 205
 - fractionation trends 187
 - gas phase 201
 - genesis 94, 206
 - high-Ti basalt 186, 187, 195
 - ilmenite basalt 188
 - low-Ti basalt 186, 188, 198
 - melting 206
 - mineralogy 193
 - modal mineral abundances 188
 - olivine basalt 188
 - oxygen partial pressures (fugacities) 193
 - phase relations 206
 - physical properties 186
 - pigeonite basalt 188
 - textures 195
 - trace elements 135, 187
 - very-high-K (VHK) basalt 135, 186, 190
 - very-low-Ti (VLT) basalt 186, 192, 198
 - vesicles 201
 - viscosity 95, 99, 139, 193, 194
- Basaltic volcanism 94, 95, 100, 103, 105, 184, 186, 208, 209
- ages 208
 - area on lunar surface 95
 - distribution of lava 209
 - duration 95
 - “fire fountains” 95
 - fissure vents 103, 105
 - gas phases 105
 - genesis 105
 - landforms 100
 - lava flows 95, 184
 - magma generation 95
 - partial melting 186
 - petrologic models 103
 - pyroclastic deposits 184
 - reflectance spectra 209
- Basins 61, 64, 68, 69, 105, 118
- ages 118
 - basin-forming process 69
 - central peak 64
 - excavation depth 68
 - location 118
 - multiring 64
 - peak-ring 64
 - ring basins 68
 - ring structure 105
 - size 118
- Bean, Alan L. 28–30
- Bear Mountain 627
- Bedrock 33
- Bench Crater 615
- Beryllium 52
- Bessarion Craters 566
- Bidirectional reflectance (optical) 559
- Biogenic elements (hydrogen, carbon, and nitrogen) 443–447
- and soil maturity 445
 - combination with oxygen 447
 - correlations 445, 446
 - from meteoroids 445–447
 - in agglutinates 447
 - surface correlation 447
- Biological Preparation Laboratory 25
- Bistatic radar observations 563
- Block Crater 615
- Bond albedo 560
- Bootprints (astronauts) 498, 635
- Bornite (chemical composition) 179
- Boron 52, 374
- Boulder tracks 499, 589
- Boulders 31–33
- Bowen-Apollo Crater 627
- Breccias 9, 81, 85, 183, 185, 186, 212, 213, 232–235, 241, 242, 252, 257, 285
- chemical composition 213
 - classification 233–235
 - clast-poor 185
 - clast-poor impact melt 252
 - clasts 233
 - components 233
 - crystalline melt 185
 - dimict 186, 235
 - facies 242

- | | | | |
|--------------------------------|-------------------------------|-----------------------------|---------------------------------|
| fragmental | 185 | origin | 254 |
| genesis of | 242 | petrography | 252 |
| glassy melt | 185 | Clasts | 78, 185 |
| granulitic (metamorphic) | 186 | Closed-ecology life support | 635 |
| matrix | 233 | Cobalt | 411 |
| monomict | 81, 185, 213 | Cochise Crater | 627 |
| petrography | 241 | Coesite | 132 |
| polymict | 81, 185, 232, 233, 234, 235 | Cold Cathode Gage | |
| regolith breccias | 186, 257 | experiments | 41 |
| Bridge Crater | 621 | Colors | 30 |
| Briggs, G. A. | 633, 634 | Compressibility | 500 |
| Brightness | 59 | Compressional ridges | 110 |
| Brightness longitude | 29, 59 | Compton Crater | 63 |
| Bronte Crater | 627 | Cone Crater | 32, 237, 381, 572, 618, 619 |
| Brooks Air Force Base | | Cone penetrometer | 589 |
| (BAFB) | 9, 23 | Conon Crater | 620 |
| Bulk density | 484, 490, 492, 572, 573 | Contamination of samples | 8, 24, 406, 443 |
| Bulk density (soil) | 483 | protection from | 24 |
| density vs. depth | 492 | Continuous deposits | 73 |
| in core tubes | 572 | Coordination (mineralogy) | 121 |
| in drill cores | 573 | Copernican Period | 116 |
| | | Copernicus Crater | 34, 63, 114, 566, 602, 610, 614 |
| Cachari meteorite | 408 | Cordillera Mountains | 70 |
| Camelot Crater | 627 | Core samples | 8, 9, 321–342, 487 |
| Canyon Diablo meteorite | 433 | Core tube sampler | 485 |
| Carbochlorination | 647 | Core tube samples (reported | |
| Carbothermal reduction | 648 | vs. actual depth) | 586 |
| Cartography | 60 | Core tubes (bit design) | 486 |
| Cataclysm (cratering) | 83 | Cosmic rays | 49–53, 315 |
| Catena | 60 | Crater degradation | 65 |
| Cayley Formation | 247, 623–625, 631 | Crater frequency | 79 |
| Cayley Plains | 245, 249 | Crater morphometry | 65 |
| Celsius | 127 | Cratering | 85, 86 |
| Center Crater | 618 | flux models | 85, 86 |
| Central peaks of craters | 259 | Craters | 32, 62–85, 108, 115 |
| spectral properties | 259 | ages | 85 |
| Chalcophile | 358 | apparent | 68 |
| Chalcopyrite | 151, 179 | breccia lens | 81 |
| chemical composition | 179 | central peaks | 61, 68 |
| Chemical statistics (cautions, | | complex | 61, 68 |
| data limitations) | 361 | cross-sections | 81 |
| Chemistry | 357–474 | degradation | 65, 115 |
| chemistry of soil size | 344, 347, 349, 385, 391, 398, | densities | 83, 84 |
| fractions | 413, 440 | ejecta | 66 |
| contamination | 443 | excavation cavity | 66 |
| guide to individual element | | history | 92 |
| discussions | 360 | isostatic adjustment | 108 |
| reliability of data | 361, 390, 400, 403, 432, 443 | mechanics | 65 |
| replicate analyses | 403 | melt zone | 78 |
| sample size limitations | 403 | microcraters | 82 |
| statistical summaries | 449–474 | morphometry | 65, 66 |
| Chondrites | 359, 379, 404 | pit craters | 87 |
| iridium content | 404 | population | 88 |
| REE concentrations | 379 | processes | 61, 65, 68 |
| Chromite | 397, 399 | production rates | 84 |
| as an ore | 399 | relative age dating | 83 |
| Cinco Crater | 624 | secondary | 7, 71, 73 |
| Cinder cones | 101 | shapes | 65 |
| Clast-poor impact melt | 252–254 | simple | 61, 67 |
| ages | 253 | size-frequency distribution | 82 |
| chemistry | 252 | | |

slope angles	32	mechanics	485
spall zone	87	Dune Crater	621
spectral properties	258	Dunite	185, 365, 368–370, 378, 395, 396, 398, 405, 406, 408, 409, 411, 412
transient cavity	66	REE pattern	378
true	68	Duricrust	492, 493
Crisium Basin	605, 628, 630, 631	Dust	34, 478
ejecta at Apollo 17	628	adhesion	34
ejecta at Luna landing	630	Earth-based telescopic data	
sites	630	(see Observation of the	
Cristobalite	132, 217	Moon from Earth)	596
Crust	15, 17, 92, 93, 212, 609	Earthlight Crater	621
cross-section	93	Earth-Moon distance	634
fracturing	92	Earthshine	29
mineralogy	609	Ecliptic	58
origin	15	Ejecta	66, 70, 71, 73, 85, 92, 94
velocity structure	92	composition	94
Crystal growth from magma	200	continuous	73
Crystal nucleation	200	curtain	71
Crystalline melt breccias		deposits	71
(impact melt breccias)	249–252	diameter of blocks	73
ages	250	lateral mass transport	92
modal analysis	250	lunar meteorites	92
texture	250	primary	71
Cubanite	151, 179	processes	71
chemical composition	179	radial distance from crater	73
Cumulate texture	223	rays	73
Curation history	25	sampling lunar crust	94
		secondary	71
Dark-haloed craters	101, 102	stratigraphic units	85
Defense Mapping Agency	597	thickness	73
Density (bulk Moon)	28, 362	trajectories	73
Density (of soil) (see relative		Elastic scattering	53
density)	496	Elbow Crater	351, 621
Depth perception	29	Electrical and	
Descartes Crater	631	electromagnetic	
Descartes Formation	245, 254, 623–625, 631	properties	530–558
Descartes Highlands	32, 253, 623	DC conductivity	531, 532
Deslambre Crater	623	dielectric permittivity	536
Deuterium	436, 447	dielectric properties	581
Diaplectic feldspar glass	74	electrical conductivities	531
Diaplectic glasses	76	electrostatic charging	532
Dielectric permittivity	536, 549	loss tangent	531, 545, 550
as a function of frequency	549	photoconductivity	532
increase with stress		temperature dependence	545
(density)	549	Electrical conductivity	531
Dielectric properties	581	Electromagnetic sounding	552, 554, 556
Differentiation (of the Moon)	15	Hagfors RMS slope	554
Differentiation (planetary,		radar cross-section	554
chemical)	362	scattering from the Moon	556
Dimict breccia	256–257	volume scattering	554
Diopside	363	Electron spin resonance	129
Dolerite	9	Electrostatic charging and	
Dorsa	60	dust migration	532
Double Crater	612	Elephant Moraine 87521	9
Doublet Craters	618	Elevation measurements	
Drill core	9	(radar)	565
Drill core samples	587	Emory Crater	627
sample depth vs. actual		Emsland iron meteorite	408
depth	587		
Drill cores (mechanics)	485		
Drive tubes	8, 9		

- End Crater 624
- Energy consumption (astronauts) 28
- Engineering problems 475
- Enstatite 125, 363, 368
- Environment 34, 44, 635
 fragility 635
 human impact 34, 44
- Equation of state 74
- Equivalent surface area ratio (ESAR) 481
- Eratosthenes Crater 114
- Eratosthenian Period 116
- Erosion 87
- Escape velocity 28
- Eucritic meteorites 408
- Europium anomalies 18, 188
- Explorer 46, 564
 meteoroid data 46
- Exposure age parameters 338, 339
- Exposure ages 56, 316, 307, 343
- Exsolution 126, 129
- Extinction (impact hypothesis) 638
- Falling (astronauts) 28
- Farringtonite 228
- Fault scarps 34
- Fault systems 108
- Fayalite 130, 363
- Fecunditatis Basin 630
 ejecta at Luna landing sites 630
- Feldspar (see Plagioclase feldspar, Potassium feldspar) 137
- Felsite 132, 135, 230, 368
- Ferroan anorthosite 13, 16, 18, 185, 220, 221, 378, 396, 608
 “genesis rock” 221
 REE pattern 378
 texture 221
- Ferrophile 391, 395, 398
 tendencies of cobalt and nickel to be ferrophile 398
- Ferrosilite 125, 363, 368
- Fission tracks 134
- Flag Crater 624
- Flank Crater 618
- Forsterite 130, 363
- Fractional crystallization 208
- Fractionation of magma 21, 187
- Fragmental breccias 235, 237, 244, 245
 ages 245
 chemistry 237
 clast types 244
 origins 245
 petrography 237
- Fra Mauro basalt 214
- Fra Mauro Crater 610, 617
- Fra Mauro Formation 31, 617, 619
- Fused soil component 288
- Future exploration 636
- Future research (outstanding questions) 636, 637
- Gabbro 185, 365
- Galactic-cosmic-ray history 356
- Galactic cosmic rays (GCR) 47, 51–55, 310
 cascade effects 54
 depth of penetration 55
 energy 52
 flux 52, 53
 interstellar 53
 isotropy 52
 modulation 52, 53
 penetration 53, 54
 protons 51, 53
 secondary radiation 54
 spallation 52
- Gamma rays 47, 53, 56
 remote mapping 56
- Gamma-ray spectrometry 602, 608
- Gardening (regolith) 87–89, 337, 342, 343
- Gas adsorption (rocks, soil) 41
- Gas condensation (lunar surface) 42
- Gas losses (thermal, ionization) 42, 44, 45
- Gassendi Crater 638
- Gator Crater 624
- Geikielite 140
- Geography 60
- Geology of landing sites 609–632
- Geometrical albedo 560
- Geophysical data 603
- Geotechnical properties 475
- Germanium 409
- Glass particles 100–102, 202–205, 303
 surface coatings 268, 303, 427–430
- Glassy melt breccias 246, 247
 ages 247
 origin 247
 texture 247
- Global data (limitations) 595
- Global stress field 108
- Gnomon 22
- Gold 406
- Grabens 108, 109
- Granite 132, 230, 232, 365, 368, 381, 391, 395, 396, 412
 ages 232
 cobalt-aluminum content 412
- Granulites 92, 254, 255
- Granulitic breccia 254, 255
 ages 255
 chemical composition 254
 chemistry 255
 origin 255
 petrography 255
 texture 254
- Gravity 27, 28, 139

Gravity anomalies	603	Imbrium Basin	32, 103, 114, 117, 245, 605, 610, 616, 617, 619, 620, 622, 625, 631
Gravity field	603	ejecta at Apollo 11	616
Green glass	101, 102, 202–205, 610, 622	ejecta at Apollo 14	619
Grimaldi Crater	638	ejecta at Apollo 15	622
Ground level enhancement (GLE)	48, 52	ejecta at Apollo 16	625, 631
Ground-penetrating radar	530	maria	103
H-phase (seismology)	40	Impact	61
Hadley Delta	33, 37, 621, 622	Impact basins (map of)	12
Hadley Rille	33, 37, 100, 348, 353, 610, 620, 621	Impact destruction of surface rocks	88
Hagfors RMS slope	554	Impact-glass beads	302
Halfway Crater	624	Impact glasses	246, 302
Halo Crater	615	chemistry	246
Halogens	434	distinction from volcanic glasses	246
Hansteen Crater	564	petrography	246
Head Crater	615, 616	texture	246
Heat flow	28, 36–38	Impact melt	73–80, 83
Heat flow probes	36, 37	Impact melt breccia	
Heat retention (regolith)	566	(crystalline melt breccia)	249, 250
Hedenbergite	363	Impact melt rocks	233, 285
Heiligenschein	559	age	83
Helium	42, 505	chemical composition	79
Helium-3	448, 637	distinction between impact melts and igneous rocks	78
Hess-Apollo Crater	627	sheets	78
Highland compositions (Mg-Fe ratios)	366	Impact processes	61, 62, 85–87, 108, 311
Highland monomict rocks	213, 361	abrasion	86, 87
Highland pristine rocks	184, 212–232	collisional fragmentation	86, 87
Highlands	10, 11	energy	62
Historic meteoroid impacts	597	erosion	86, 87
History (lunar)	61, 115–120	impact velocities	62
Horatio Crater	627	production of new particles	311
Hugoniot Elastic Limit	76	regolith formation	311
Humboldt Crater	113, 638	shock induration	311
Hydrogen	42, 436–448	vapor fractionation	311
as a resource	647, 648	Impact structures	61–64
Hydrogen reduction	648	morphologic elements	64
Hydrothermal fluids	406	Inclination (Moon)	28
Ice	40	Incompatible trace elements	17, 372–390
Igneous highland rocks	185, 228, 230	abundances	372
alkali anorthosite	228	and KREEP	372
alkali gabbronorite	230	concentration in rare minerals	383
alkali norite	230	correlations in general	379
felsites	230	correlations in highland materials	381
ferroan anorthosite	185	correlations in mare basalt	386, 387
granite	228	partitioning	372
KREEP rocks	185	Index Crater	621
Mg-rich rocks	185	Inner Rook Mountains	105
Ilmenite	137, 140, 141, 171, 363, 441, 445	Instrumental neutron activation analysis (INAA)	403
as a source of oxygen	141	Integrated mass depth	493
chemical composition	140, 171	Internal forces	111
crystal structure	140	contraction	111
helium retention	445	thermal stress	111
high helium and neon content in soil	441		
Imbrian Period	117		

- International Astronomical Union 60
- Ionization (of atmosphere) 44
- Ionization (of regolith) 53
- Ionization chambers 47
- Ionizing radiation 315
- Iridium 404
- Iron 363–372, 413, 603
- as a resource 648
 - as a siderophile element 413
 - chemical composition 151, 180
 - iron metal 138, 151–154, 180, 371
 - mapping from orbit 603, Plate 10.2
 - valence 128, 129
- I_s/FeO 315, 319–343
- Isotopes 415, 428, 430, 433, 436, 437, 439, 447
- helium 436
 - hydrogen 436
 - lead 428, 430, 638
 - nitrogen 447
 - noble gases 437
 - oxygen 311–313
 - polonium 638
 - plutonium 439
 - radon 638
 - silicon 311–313
 - strontium-rubidium 415
 - sulfur 433
 - thorium 430
 - uranium 430, 439
- Isotopic compositions (lunar soils) 311–313
- Janssen Formation 117
- Johnson Space Center (JSC) 9, 23
- Johnston compositional prism 143
- Juvinas meteorite 408
- Kamacite 151, 399
- Kiva Crater 624
- KREEP 16, 18, 19, 218, 220, 306, 378–380, 409, 608, 610
- abundance 220
 - age 218
 - and germanium 409
 - chemical definition 218, 380
 - KREEP rocks 15, 185, 216–220
 - REE concentrations 379
 - REE pattern 378
 - urKREEP 19
- Lacus (definition) 60
- Lagrange points 636
- Lakangaon meteorite 408
- Lalande Crater 63
- Landslides 39
- Langrenus Crater 629
- Lansberg Crater 614
- Lara Crater 627
- Last Crater 621
- Lava flows 33, 95, 98, 99, 186
- area 95
 - flux 99
 - lava tubes 101, 186
 - length 95
 - thickness 95, 99
 - viscosity 95, 99
- Lava terraces 101
- Lava tubes 101, 186
- Law of Superposition 111
- Lawrencite 150, 430, 447
- Leaching (of halogens) 434
- Le Monnier Crater 626
- Leuconorite 365
- Libration 58, 59
- diurnal 59
 - latitudinal 58, 59
 - longitudinal 58
- Life (absence of) 26, 634
- Lithium 52
- Lithophile 358
- Little West Crater 612
- Littrow Crater 626
- Lunar Crater 79
- Loss tangent 536–552, 581–584
- Low-K Fra Mauro (LKFM) 19, 250, 622, 625
- Luna 3 11
- Luna 16 630
- Luna 16 basalt 398
- high strontium concentrations 398
- Luna 20 630
- Luna 24 630
- Luna landing sites 629–631
- geology 630
- Luna missions 5, 7, 10, 23, 25, 483
- Luna samples 23, 25
- Lunar Atmospheric Composition Experiment (LACE) 41
- Lunar bases 640–643
- Lunar “dust storms” 536
- Lunar ejecta and meteorites experiment (LEAM) 536
- Lunar exploration 5–7
- history 7
- Lunar farside 11
- Lunar geologic mapping 114
- Lunar grid system 111
- Lunar highlands 10, 11, 92
- Lunar history 83–85, 111–120, 609–632
- Lunar interior (electrical, thermal properties) 533
- Lunar landing sites (map) 6
- Lunar magmatic evolution 19
- Lunar meteorites 6, 9, 23, 92, 394
- iron/manganese test of origin 394
- Lunar minerals 121–181, 298, 320
- apatite 122, 154

- armalcolite 122, 137, 147–150
 baddeleyite 137
 chalcopyrite 151
 chemical composition 155–181
 chromite 122
 cohenite 122
 comparison with minerals
 of the Earth 135–137, 139
 cubanite 151
 definition (mineral) 121
 endmember (definition) 121
 hercynite 122
 ilmenite 122, 137, 140
 kamacite 151
 mackinawite 151
 metallic iron 151–154, 298, 320
 meteoritic contamination 151
 native iron 122, 151
 niningerite 122
 olivine 130–132
 oxides 137–150, 178
 pentlandite 151
 phosphate minerals 154, 155
 plagioclase feldspar 122, 126–129, 163, 165, 385
 potassium feldspar 133, 135
 proportions in soils 123
 pyroxene 122, 123–126
 pyroxferroite 133, 134
 rutile 137
 schreibersite 122
 silica minerals 132
 sphalerite 151
 spinels 122, 137, 143–147
 sulfide minerals 150
 taenite 151
 tranquillityite 133
 troilite 122, 150
 ulvöspinel 122
 whitlockite 122, 154
 yoshiokaite 123
 zircon 134
 zirconolite 137
 Lunar module (LM)
 exhaust gases 41, 42
 footpads (regolith
 compression) 518
 Lunar month 58
 Lunar motorcycle 524, 525
 Lunar Observer 19, 595, 639
 Lunar Orbiter 5, 46, 60, 596, 597, 603, 604
 Lunar Orbiter 4
 meteoroid data 46
 photographic data 597
 Lunar Receiving Laboratory
 (LRL) 8, 25, 443
 Lunar regolith
 evolution 285–356
 grain size 307
 maturity 305, 307, 315, 323
 physical properties 475–594
 pre-Apollo models 476
 spectral properties 307
 stratigraphy 323
 surface exposure 315
 surface exposure age 307
 thickness 305
 Lunar rock erosion 86
 Lunar rocks 183–284
 chemical composition 261–284
 classification 184
 igneous 184
 pristine 184
 Lunar Roving Vehicle (LRV) 5, 32, 522–530, 610, 627
 Lunar Sample Building 23
 Lunar sample curation 10, 23, 24
 Lunar Sample Data Base
 (LSDB) 25
 Lunar sample identification 8
 Lunar sample numbering 10
 Lunar Sample Preliminary
 Examination Team
 (ISPET) 8, 22
 Lunar sample records 24
 Lunar samples 6–10
 Lunar soil 88–92, 287–307, 475–482
 agglutinates 288, 296, 299, 301, 339, 414
 chemical composition 306, 314, 331–352, 449–474
 components 294, 302
 definition 287
 density 483–500, 572–574, 588, 589
 description 287
 erosion of particles 304
 fused soil component 288
 glass beads 302
 grain shapes 304, 478–481, 569, 570, 585
 grain size 304, 477, 478, 567, 568
 grain surfaces and
 coatings 304
 maturity 294, 307–321
 modal analyses 123, 289–296
 particles 304
 petrography 288, 295
 volatile elements 314, 414–436
 Lunar stratigraphy 111–120
 Lunar Topographic
 Orthophotomap series 597
 Lunar transient events 532, 638
 polonium 638
 radon 638
 Lunar utilization (annotated
 bibliography) 644–646
 Lunar vehicles 32, 483, 499, 510–512,
 522–530
 Apollo Lunar Roving
 Vehicle (LRV) 5, 32, 522–530, 610, 627
 design 526
 future design 529
 lunar motorcycle 524, 525
 Lunokhod 483, 510–512, 523, 589
 Modularized Equipment
 Transporter (MET) 523
 performance 524, 526

- tracks 499
 trafficability parameters 526
 Lunokhod 483, 510–512, 523, 589

 MacAlpine Hills 88104 9
 MacAlpine Hills 88105 9
 Mackin-Apollo Crater 627
 Mackinawite 151
 Magma 138, 139
 crystal settling 138
 viscosity 95, 99, 139, 193
 Magma ocean 15, 16, 184, 224
 Magnesium 363–372, 602, 603
 mapping from orbit 602, 603, Plate 10.5
 Magnesium-rich rocks 14, 19, 185, 225–228
 Magnetic anomalies 604, 605
 Magnetic field 28, 604, 605, Plate 10.6
 Magnetotail (Earth's) 47
 Major elements 363–372
 abundances and correlations 366
 abundances ranked by volume 363
 abundances ranked by weight 363
 ores 371
 Mandel'shtam Scarp 113
 Manicouagan Crater 79
 Manned Spacecraft Center (MSC) 25
 Mantle compositions 386
 Maps 60, 604, 607–609, Plate 10.7, Plate 10.8, Plate 10.10, Plate 10.11
 geologic 609, Plate 10.10
 gravity field 604
 magnetic field Plate 10.6
 mare basalts 607, Plate 10.7
 petrologic (Th/Ti vs. Fe) 608, Plate 10.8
 Mare (see Maria)
 Mare basalt 17, 18, 94–107, 140, 186–212, 608, Plate 10.7
 age range by remote sensing 609, Plate 10.11
 chemical data 261–268, 359, 449–472
 mineralogy 140, 188, 193–195
 sampled and unsampled types 608
 source areas 17, 18, 205–208, 386
 Mare basin (definition) 95
 Mare Crisium 11, 557, 564, 565, 606, 629, 630, 632
 Mare domes 101
 Mare Fecunditatis 398, 629, 631
 Mare Humboldtianum 60
 Mare Imbrium 98, 380, 604, 606, 620
 Mare Orientale 105, 597
 Mare Serenitatis 100, 107, 565, 598, 604, 606, 620, 626
 Mare Smythii 60
 Mare Tranquillitatis 606, 611, 629

 Maria 10, 11, 95–107
 age of lava (known) 208, 209
 age of lava (suspected) 99
 area 105
 composition 95, 359, 261–268, 449–472
 definition 95
 history 102, 103
 hypotheses for origin 95
 lava filling 95, 102
 “mascons” 107
 origin of term 60
 structure 103
 thickness 97, 103, 105
 volcanic eruptions 103
 volume of lava 105
 Marius Hills 100, 101
 Mascons 107, 111, 603, 604
 Mass (Moon) 28
 Mass wasting 33
 Maturation (of lunar regolith) 294, 307–321
 Maturity indices 317–321, 331, 332, 336–344
 agglutinates 288, 296–299, 319
 grain size 318, 319, 321, 344
 I_s/FeO 298, 315, 319–343
 particle track index 315–317, 319, 337–342
 solar wind 315, 319, 337–342
 Maunder Minimum 53, 56
 Megaregolith 92, 212, 286
 Mercury (Hg) 432
 as a surface-exposure index 432
 mobility due to daily heating 432
 Mesostasis 366, 372, 373
 sodium enrichment 366
 Metamict 134
 Meteorite (definition) 46, 358
 Meteorites (chemistry) 358
 Meteorite Working Group 23
 Meteoroids 83, 85
 bombardment 45–47, 62–94, 310–315
 definition 46, 358
 hazards 46, 47
 impact frequency 39, 41, 79–85
 intermixture in lunar samples 151, 404–413, 419, 421
 micrometeoroids 45, 61
 showers 39
 size/mass distribution 46, 61, 81–83
 variation in composition with time 420
 velocities 46, 62
 Metric mapping camera 597
 Middle Crescent Crater 615
 Mineralogy (see also Lunar Minerals) 121–181
 remote sensing 608
 Miscellaneous minor elements 390–399
 correlations 391, 394
 in major minerals 394

- | | | | |
|---|------------------------------|------------------------------------|---|
| partitioning | 394 | North Ray Crater | 237, 245, 247, 249, 361, 624, 625 |
| Mösting A Crater | 60 | North Triplet Crater | 572 |
| Mösting C Crater | 211 | Nuclear particle effects | 310 |
| Moderate-titanium high-aluminum maria | 630 | Nuclear reactions | 53, 315 |
| Modularized Equipment Storage Assembly (MESA) | 22 | Observation of the Moon from Earth | 34, 36, 60, 558–566, 595–597, 599–605 |
| Modularized Equipment Transporter (MET) | 523 | Obstacles to travel | 32–34 |
| Moltke Crater | 63, 611 | boulders | 32 |
| Molybdenum | 401, 411 | rilles | 33 |
| Moment of inertia (Moon) | 28 | Oceanus (definition) | 60 |
| Monazite | 372 | Oceanus Procellarum | 31, 564, 602, 606, 608, 610, 614 |
| Monomict breccias | 81, 185, 213, 358, 400 | Oedometer test | 501, 502 |
| Mons (definition) | 60 | definition | 501 |
| Monte Carlo technique | 86, 342 | Olivine | 130–132, 137, 166–168, 363 |
| Montes d’Alembert | 60 | chemical composition | 130, 166–168 |
| Montes Harbinger | 60 | crystal structure | 130 |
| Montes Leibnitz | 60 | Opposition effect (optical) | 559 |
| Moonquakes | 39, 108, 109 | Optical astronomy | 558–561 |
| Morozov Scarp | 113 | albedo | 560 |
| Morphometry (craters) | 65, 609 | phase angle (optical) | 29, 59, 558 |
| Mounds | 31 | phase plane (optical) | 29, 558 |
| Mount Hadley | 33, 620 | photometric function | 558–559 |
| Mount La Hire | 98 | polarization | 561 |
| Mountains of perpetual light | 40 | single scattering albedo | 560 |
| Mountains (slope angles) | 32, 33 | Orange soils | 102, 184, 202–205, 427–430 |
| Multispectral images | 601, 602 | Orbital gamma-ray data | 602 |
| resolution | 601 | Orbital gravity data | 603 |
| vidicon imaging | 601 | Orbital magnetic data | 605 |
| Multispectral maps | Plate 10.7 | Orbital photography | 597, 599, 600 |
| Muons | 47, 54 | coverage | 600 |
| | | panoramic camera | 597 |
| Naming lunar features | 60 | resolution | 600 |
| Nansen-Apollo Crater | 627 | stereo photos from orbit | 598 |
| NASA planetary data centers | xix, 596 | Orbital plane (Moon) | 58 |
| National Space Science Data Center | xix, 599 | Orbital X-ray fluorescence data | 603 |
| Native iron | 138, 151–154, 180, 371 | Ores | 138, 371, 385, 388, 398, 414, 435, 448, 647–649 |
| chemical composition | 151, 180 | Oriente Basin | 69, 70, 103, 105, 117, 606 |
| distribution in lunar rocks | 152 | maria within | 103 |
| genesis | 154 | Origin of the Moon | 13, 14, 361–363 |
| Navigation | 29 | collision hypothesis | 14 |
| Nectarian Period | 117 | Osmium | 408 |
| Nectaris Basin | 245, 257, 623, 625, 631 | Outcrop (in craters) | 566, Plate 10.9 |
| ejecta at Apollo 16 | 625, 631 | Outcrop (in rilles) | 32, 33 |
| Nectaris Highlands | 611 | Outer Rook Mountains | 105 |
| Neon (in lunar atmosphere) | 42, 43 | Oxide minerals | 137–150, 178 |
| Nested crater hypothesis | 68 | chemical composition | 138, 178 |
| Neutron capture | 53 | crystal structure | 138 |
| Neutrons in galactic cosmic rays (GCR) | 55 | petrogenesis | 138 |
| Nickel | 411 | Oxygen (as a resource) | 637, 648, 649 |
| Noble gases | 437–443 | Palladium | 409 |
| isotopic ratios | 437 | Palmetto Crater | 624 |
| Norite | 185, 363, 368, 380, 453, 608 | Palus (definition) | 60 |
| Normal albedo | 560 | Palus Putredinis | 610, 621 |
| Normal faulting | 111 | Palus Somni | 564 |
| North Crater | 618 | Particle shapes (soil) | 478–481, 569–571, 585 |
| North Massif (Apollo 17) | 348, 627, 628 | aspect ratio | 479, 570 |

- elongation 479, 569
- Fourier analyses 479, 585
- roundness 479, 570
- specific surface area 479, 571
- volume coefficient 479
- Particle size distributions (soil) 477, 478, 567, 568
- Particle tracks (radiation) 315, 316, 441
- Partition coefficient 373
- Partitioning (chemical) 373, 394, 400, 411
 - incompatible trace elements 373
 - miscellaneous minor elements 394
 - nickel 411
 - siderophile elements 400
- Pentlandite 151
- Perigee 57
- Perihelion 34
- Phase angle 29, 59
- Phase plane 29
- Phases of the Moon 57
- Phi (ϕ) scale (grain size) 304–306, 477, 478
 - definition 477, 478
- Phosphate minerals 154, 155, 181
 - chemical compositions 181
- Photoconductivity 532, 534
- Photography (color-difference) 601
- Photometric function 558–560
- Pigeonite 126, 198, 225
- Pions 53, 54, 55
- Piton B Crater 211
- Plagioclase feldspar 126, 127, 385
 - and calcium separation 385
 - chemical composition 127, 163–165
 - crystal structure 126
- Plagiophile (terminology) 398
- Planetary Materials Laboratory (PML) 21, 23
- Planetary separation processes 361
- Planetary vs. platform science 636
- Plasma (solar wind) 48, 436, 437
- Platinum 408
- Pleonaste 147
- Polar cap absorption (PCA) 47
- Polar environment 39
- Polarization 561, 562
 - azimuth 561
 - degree 561
- Polymict breccias 81, 185, 232–257, 358, 400
 - chemical data 277–284, 449–474
 - nomenclature 233–235
- Porosity of lunar soil 481–483, 492, 496
 - intergranular 481
 - intragranular 481, 496
 - subgranular 481
- Potassium feldspar 127, 135, 385
 - and barium separation 385
 - celsian 135
 - chemical composition 135
 - crystal structure 135
- Powell Crater 627
- Pre-Nectarian Period 117
- Primary magmas 208
- Pristine igneous highland rocks 212–232
 - ages 229
 - alkali anorthosite 214
 - anorthosite/norite/troctolite (ANT) 214
 - classification 214–216
 - ferroan anorthosite 214
 - “Fra Mauro basalt” 214
 - granite 214
 - “highland basalt” 214
 - KREEP 214
 - Mg-rich rocks 214
 - modal data 217, 224, 229, 230
 - pyroxene compositions in 225
- Pristine (relation to monomict) 185
- Pristine (sample handling) 8, 9, 24
- Pristine (sample origins) 152, 184, 213, 358, 400
 - definition 213
- Promontorium (definition) 60
- Propellant production 637, 640, 647–649
- Protons (ionizing radiation) 48–56
- Pseudotachylite 256
- Pyrochlore 228
- Pyroclastic deposits 95, 101, 102, 202–205, 210, 325, 366, 398, 427–430, 434, 608
 - chemical composition 264–268, 427–430
 - comparison with soils 366
 - cooling rates 203
 - distribution 210
 - gas phase 202, 205, 427–430
 - green glass 102, 202–205, 427–430
 - “lava fountaining” 105
 - orange glass 102, 184, 202–205, 427–430
 - recognition 202
 - reflectance spectra 210
 - remote sensing 608
 - strontium, gallium concentrations 398
 - textures 203
- Pyroxene 123–126, 135, 157–162, 363
 - chemical composition 125, 157–162
 - crystal structure 123
- Pyroxferroite 130, 134
 - composition 134, 169
 - crystal structure 134
- Q (seismic) 39, 516, 517
- Quarantine (lunar samples) 25
- Quartz 132, 217, 230
- Quartz monzodiorite 221, 368, 370, 381, 425

- Radar 530, 552–558, 562–566, 605–607
- Radar astronomy 562–564, 605–607
- Apollo Lunar Sounder Experiment (ALSE) 564
- bistatic radar observation 563
- diffuse component 563
- penetration 562
- polarization 562
- scattering function 562
- subradar point 562
- Radar backscattering 562
- Radar cross-section 554, 563
- Radar data (Earth-based) 605–607
- crater features 605
- pyroclastic deposits 605
- Radar data (orbital) 564–566
- Radar images 606, 607
- Radar maps 557–558
- Radar scattering 557
- Radiation (ionizing) 47–56, 310, 315–317
- cascade 53
- crystal defects 54, 315–317
- damage by 315–317
- doses 55
- effects 56, 315–317
- elastic scattering 53
- energy 47, 48, 310, 315–317
- exposure ages 56, 87, 88
- hazards 51, 52, 56
- neutron capture 53
- particle tracks 316
- particles 48
- penetration 48, 56, 310
- radionuclide production 310
- secondary radiation 53–55
- shielding 52
- spallation 53
- Radiation damage 54, 315–317
- Radiation energy 47, 315–317
- Radiation from the Moon 558–566
- Radio communications 531
- Radiochemical neutron activation analysis (RNAA) 403
- Radius (Moon) 28
- Ranger 5, 596
- Rare earth elements (REE) 18, 190, 191, 204, 220, 231, 242, 243, 372–390
- Rarefaction waves 65
- Ravine Crater 624
- Recompression index 504
- Reflection and emission of radiation 558–566
- Regolith 87–92, 285–356, 475
- antiquity vs. maturity 355
- as a resource 649
- as construction material 286
- chemical composition 329, 334, 344
- chemical variation between sites 351
- chemical variation within sites 345
- comparison of soil composition with rock composition 345
- definition 285
- depth variation 321
- differential comminution 344
- dynamics 342
- evolution 88–90
- gardening 87–89, 337, 342, 343
- gas absorption 443
- gas adsorption 41, 443
- gas release on crushing 447
- grain size 318, 343
- KREEP 345
- mass wasting 89
- maturity 294, 317, 318, 332, 338
- mercury (Hg) as exposure index 432
- meteoroid content 405
- mixing 332
- models 87
- models for formation 342
- Monte Carlo models 88
- path I, path II 321
- petrography 329, 334
- processes 321, 337, 342.
- processes of regolith formation 285
- pyrolysis 447
- radiation history 354
- seismic properties 288, 516, 517
- solar-wind retention 441–443
- sorting 321
- stratigraphy 321, 325, 337
- surface exposure ages 338
- thickness 89, 90, 91, 92, 286
- variation with depth 325–336
- Regolith breccias 257, 354–361
- Reiner Gamma 605
- Relative density (soil) 476, 494–500, 574, 588, 589
- Remote sensing 552–566, 599–607
- Resources 138, 141, 154, 186, 414, 636, 644–649
- aluminum 647
- annotated bibliography 644–646
- carbonyl processing of FeNi 414
- for use in space 636
- for use on Earth 636
- from mare basalt 186
- helium-3 647
- hydrogen 647
- ilmenite 648
- iron 648
- iron metal 154
- oxygen 138, 141, 648
- plagioclase 647
- regolith 649
- Revolution of the Moon 57

- Rhenium 408
- Rhodium 409
- Rhysling Crater 621
- Ridges 32
- Ries Crater 79, 92
- Rilles 33, 99, 101, 113
 - hypotheses of origin 101
 - sinuous 99
 - slope angles 33
- Rima (definition) 60
- Rima Hadley 621
- Ring basins 68
- Ritter Crater 611
- Rock types (summary) 156, 184–186, 359–361
- Rook Mountains 70
- Ropy glasses 302
- Rotation of the Moon 58
- Roughness of lunar surface
 - and trafficability 30–34, 526–530
- Rugosity 479, 569
- Ruthenium 409
- Rutile 137, 149, 178
 - chemical composition 178
- Sabine Crater 611
- Saint George Crater 621
- Sampling history (Apollo) 21
- Schlieren 74, 78, 202
- Schreibersite 150, 391
- Schrödinger Crater 63
- Schröter's Valley 607
- Schwantke molecule 128
- Scott, David R. 28, 633
- Sculptured Hills 348, 627, 628
- Secondary craters 33
- Secondary particles 53
- Seismic activity 38, 41
- Seismic attenuation (Q) 39, 516, 517
- Seismic energy 28, 108
 - of impacts 108
- Seismic experiments 38, 41
- Seismic properties (regolith) 288, 516, 517
- Seismic velocities (regolith) 288
- Seismograms 40
- Selenodesy 60
- Self-Recording Penetrometer (SRP) 508, 512, 591
- Serenitatis Basin 103, 107, 622, 628, 631
 - ejecta at Apollo 15 622
 - ejecta at Apollo 17 628
 - maria 103
- Serial magmatism 17, 18
- Shadows 30, 36
- Shakespeare Crater 627
- Shape complexity factor 570
- Sharp-Apollo Crater 615
- Shear strength 506–516
- Sherlock Crater 627
- Shock melting 73–79
- Shock metamorphism 73–79
 - effects on minerals and rocks 74
 - energy 73
 - fracturing 76
 - pressures 73, 74, 77
 - regolith 77
 - rocks 77
 - schlieren 74
 - shatter cones 76
 - shock lamellae 74
 - temperatures 73
- Shock pressure attenuation 74
- Shock vaporization 73, 302, 424
- Shock waves 65
- Shocked minerals 302
- Shorty Crater 102, 427, 428, 627, 628
- Sidereal month 57
- Sidereal rotation 28
- Siderophile elements 358, 399–414
 - analytical difficulties 400
 - correlations 406
 - data limitations 403
 - partitioning 399
- Silica minerals 132, 215, 229, 230
 - chemical composition 132, 169
 - coesite 132
 - crystal structures 132
 - quartz 132, 217, 230
 - stishovite 132
 - tridymite 132
- Silicon 603
 - mapping from orbit 603, Plate 10.4, Plate 10.5
- Sinuuous rilles 99
- Sinus (definition) 60
- Sirsalis Rille 112
- Skaergaard intrusion 225
- Slope stability 39, 521, 522
 - constructed slopes 521
 - dumped soil 521
 - excavations 521
 - factor of safety 522
 - natural slopes 522
- Smithsonian Institution 23
- Smoky Mountain 32, 351, 624, 625
- S/N (serial number of core tubes) 572
- Soft soil (trafficability) 499, 529
- Soil (definition; also see Regolith) 287–307, 475
- Soil bearing capacity 517–521, 590–594
 - allowable bearing capacity (dynamic) 520
 - allowable bearing capacity (static) 519
 - penetrometer measurements 590–594, 578–580
 - settlement depths 520
 - ultimate bearing capacity (dynamic) 518

- | | | | |
|--|-------------------------------------|---------------------------------|---------------------------------|
| ultimate bearing capacity (static) | 517 | Spectral properties | 209–211, 257–260, 307, 608, 609 |
| Soil compressibility | 500–506, 575–577 | highland rocks | 257–260 |
| coefficient of lateral stress | 506 | mare basalts | 209–211 |
| compression index | 501 | regolith | 307 |
| gas release | 505 | Sphalerite | 151, 179, 434 |
| maximum past pressure | 504 | chemical composition | 179 |
| oedometer data | 575, 576 | Spherical albedo | 560 |
| recompression index | 504, 577 | Spinel | 137, 143–147, 173–175 |
| Soil diffusivity | 517 | chemical composition | 143, 173 |
| Soil permeability | 517 | chromian ulvospinel | 145 |
| Soil porosity | 481–483, 492, 496 | chromite | 143 |
| Soil shear strength | 506–517, 578–580, 589–594 | compositions in highland rocks | 147 |
| Apollo Self-Recording Penetrometer (SRP) | 508, 512–516, 591 | crystal structure | 143 |
| cohesion | 506 | hercynite | 145 |
| cone penetrometer data | 510–516, 578 | pleonaste | 145 |
| direct shear tests | 579 | spinel (<i>sensu strictu</i>) | 145 |
| field measurement | 506 | stability relations | 147 |
| friction angle | 506 | subsolidus reduction | 147 |
| laboratory measurements | 514 | titanian chromite | 145 |
| Soils and regolith breccias | 352–354, 361 | ulvöspinel | 143 |
| chemical data | 449–474 | Spook Crater | 624 |
| Solar cosmic rays (SCR) | 47–52, 54, 310, 315–317 | Spot Crater | 624 |
| anisotropy | 49 | Spur Crater | 351, 621, 622 |
| composition | 49 | Sputtering | 54 |
| penetration | 54 | Static electricity hazards | 536 |
| protons | 50, 51 | Steno-Apollo Crater | 627 |
| secondary radiation | 54 | Stishovite | 132 |
| travel times | 49 | Stone Mountain | 32, 351, 514, 624, 625 |
| Solar cycle | 49, 50, 52, 56 | Stubby Crater | 624 |
| Solar flares (see Solar cosmic rays) | | Sulfide minerals | 150, 151, 179 |
| Solar history | 354–356 | chalcopyrite | 151 |
| Solar maximum | 49 | chemical composition | 179 |
| Solar nebula | 361 | cubanite | 151 |
| Solar protons | 51 | mackinawite | 151 |
| Solar radiation (history of measurement) | 47, 52 | pentlandite | 151 |
| Solar wind | 47, 48, 54, 310, 315, 436, 440, 552 | sphalerite | 151 |
| composition | 48 | troilite | 150 |
| cumulative abundance | 54 | Sulfur | 422, 432–434 |
| penetration | 54 | abundance in mare basalt | 422 |
| saturation of regolith | 440 | as metamorphic fluid | 434 |
| Solar-flare history | 356 | correlation with titanium | |
| Solar-wind history | 355 | in mare basalt | 432 |
| Solar-wind-implanted elements | 436–448 | in pyroclastic deposits | 434 |
| and soil maturity | 315, 319, 337–342 | isotopic fractionation | 433 |
| as resources | 448, 647 | Sulpicius Gallus | 598 |
| Solid solutions | 121 | Sunspots | 49, 50 |
| South-Apollo Crater | 618 | Surface area (Moon) | 28 |
| South Massif (Apollo 17 site) | 34, 348, 627, 628 | Surface temperatures | 28, 34, 36, 566 |
| South Ray Crater | 32, 249, 256, 257, 624 | Surveyor | 5, 483 |
| Space Exploration Initiative | 633 | Surveyor 3 | 5, 34, 610 |
| Spacesuits | 27, 28 | Surveyor Crater | 31, 615, 616 |
| Spallation | 53 | Synodic month | 57 |
| Specific circularity | 569 | Taenite | 151, 399 |
| Specific gravity | 481, 482 | Taurus Mountains | 100, 626 |
| Specific surface area (SSA) | 480 | Taurus-Littrow Valley | 33, 37, 41, 627, 631 |
| | | Taylor Crater | 623 |
| | | Tectonic activity | 107–110 |
| | | compression | 110 |

- extension 109
 Tektites 79
 Telescopic data (See
 Observation of the Moon
 from Earth) 596, 597
 resolution 596
 wavelengths 596
 Temperature (lunar surface) 28, 34, 36, 566
 Temperature profiles (across
 craters) 565
 Terminal cataclysm 120, 212
 Terrain 30–34
 ejecta ridges 31
 highland 32
 mare 31
 mare-highland boundaries 32
 Tetraenaite 151, 399
 Textures of mare basalts 195–201
 intergranular 195
 intersertal 195
 ophitic 195
 pilotaxitic 201
 porphyritic 195
 radiate 198
 trachytic 201
 vitrophyric 195
 Theophilus Crater 625
 ejecta at Apollo 16 625
 Thermal conductivity
 (regolith) 37, 38
 Thermal infrared astronomy 566
 Thermal insulation (regolith) 38
 Thermal solifluction 493
 Thermoluminescence 54
 Thorium 603
 mapping from orbit 603, Plate 10.1
 Thrust faults 111, 113
 Tidal forces 108
 Tides 27, 109
 Titanium 603
 mapping from orbit 603, Plate 10.3
 valence states 126, 148
 Tortilla Flat 627
 Track density 54, 316, 339
 Track maturity 339
 Track maturity index 315–317, 319, 337–342
 Trafficability 522–530
 parameters 526
 Tranquillityite 133, 170
 chemical composition 133, 170
 crystal structure 133
 Trap Crater 624
 Trident Crater 627
 Tridymite 132
 Triple Craters 615
 Triplet Craters 618
 Troctolite 185, 365, 368, 369, 370, 409,
 453
 Troilite 150, 179, 398, 432–434
 chemical composition 150, 179
 Tsunami hypothesis (basin
 formation) 68
 Tungsten 413
 Tycho Crater 39, 596, 606, 628, 631, 638
 age 631
 impact effects at Apollo 17 628
 Unanswered questions 650–654
 Unconformities
 (stratigraphic) 88
 Uranium-thorium correlation 431
 Vallis (definition) 60
 Vallis Schröter 60
 Van de Graaf Crater 605
 Van Serg Crater 627
 Vapor-mobilized elements 205, 414–436
 correlation with each other 426
 correlation with maturity 421
 correlations with rubidium
 and cesium 423
 depletion in monomict
 rocks 415
 indigenous concentrations 422
 in pyroclastic deposits 205, 427
 in vesicles 428
 leaching 428
 minimal solar-wind
 contribution 422
 surface correlation on
 pyroclastic fragments 268, 303, 428
 thermal mobilization 430
 vapor-phase transport 424
 whole-Moon composition 424
 Very-high-alumina (VHA)
 melt 247, 250, 625
 Very-high-K (VHK) basalt 135, 186, 190
 Very-low-Ti (VLT) basalt 186, 192, 198
 Vesicles 105, 428
 Victory Crater 627
 Viscosity (of magmas) 95, 99, 193
 Visibility (astronauts) 29
 Void ratios (of soil)
 minimum and maximum 496
 Volatility 406, 410, 413, 415, 422, 431
 antimony 413
 germanium 410
 gold 406
 lead 431
 rubidium, cesium, sodium,
 potassium 422
 sodium 415
 vapor-mobilized elements 415
 Volcanism 94, 95, 100, 103, 105, 184,
 186, 208, 209
 Volcanic glasses 186, 303
 Walking (astronauts) 28
 Waste heat 38
 Water 39, 40, 56, 150, 406, 634

Weightlessness		Yamato 791197	9, 394, 395, 397
(physiological problems)	637	Yamato 793274	9
Weird Crater	618	Yamato 82192	9
Weird Rock	618	Yamato 82193	9
Wessex Cleft	627	Young, John W.	30
West Crater	613		
Whitlockite	154, 181, 372, 384, 391, 398,	Zhamanshin impact	
chemical composition	434	structure	79
Wollastonite	181	Zircon	134, 372, 384
Wreck Crater	125	chemical composition	134, 169
Wrinkle ridges	624	structure	134
Wüstite	108	Zirconolite	137, 150
	138	Zond	5, 596

L · U · N · A · R

s o u r c e b o o k

a user's guide to the moon

The *Lunar Sourcebook*, a concisely presented collection of data gathered during the American and Soviet missions, is an accessible and complete one-volume reference encyclopedia of current scientific and technical information about the Moon. This book provides a thorough introduction to lunar studies and a summary of current information about the nature of the lunar environment. It explores the formation and evolution of the Moon's surface, the chemical and mineralogical nature of lunar rocks and soils, and the current state of scientific knowledge about the nature, origin, and history of the Moon.

The book is written and edited by scientists active in every field of lunar research, all of whom are veterans of the Apollo program. The contributors are from universities, national laboratories, industry, and NASA.

Engineers, mission planners, planetary scientists, educators, and students interested in scientific study and exploration of the Moon will find this book to be a unique and essential reference. Cover design by Christy Owens.

Cambridge University Press

CAMBRIDGE
UNIVERSITY PRESS

ISBN 0-521-33444-6



9 780521 334440